Basic Performance, Optimization, and Safety and Risk Evaluation of Next-Generation Refrigerants and Refrigerating and Air Conditioning Technologies

Final report

Research Committee for Next-Generation Refrigerants,

Japan Society of Refrigerating and Air Conditioning Engineers

January 31, 2023

Table of Contents

1. Introduction

Japan Society of Refrigerating and Air Conditioning Engineers
Chair, Research Project Committee for Next-Generation Refrigerants
Norihiro Inoue (Tokyo University of Marine Science and Technology)

The 1987 Montreal Protocol mandated a gradual reduction in the production of substances that deplete the ozone layer. These substances include fluorocarbons (CFCs and HCFCs) and certain hydrofluorocarbons (HFCs), which have been developed as substitutes for CFCs that have been used and emitted in increasing amounts since this protocol was implemented. Similarly, the Kyoto Protocol (COP3), which was formulated to prevent global warming, designated HFC refrigerants as greenhouse gases. In the 2015 Paris Agreement (COP21), Japan set a target to reduce CO_2 emissions by 26% from 2013 levels by 2030 and by 80% by 2050. Since then, greenhouse gas emission regulations have become even more stringent. In October 2020, Japan declared that it would aim to achieve carbon neutrality by 2050. To achieve this goal, Japan aims to reduce greenhouse gas emissions by 46% compared with 2013 emissions by 2030. Notably, the current climate conditions call for countries to take on the challenge of further reductions in emissions.

Similarly, the Kigali Amendment to the Montreal Protocol was proposed in 2016. Developed countries agreed to gradually reduce the production and consumption of HFCs and CFCs by 85% by 2036 based on 2011–2013 production volumes. Under current domestic and international climate conditions, an urgent need arises to switch from HFCs and CFCs to low global warming potential (GWP) working fluids and natural fluids as next-generation working fluids for power, industry/household refrigeration, and air-conditioning equipment. Therefore, an ever-increasing need for the evaluation of the basic physical properties of newly developed and proposed low-GWP refrigerants and for the early development and optimization methods of energy-saving refrigeration and air-conditioning equipment using these refrigerants arises. Additionally, safety issues with low-GWP next-generation refrigerants (including hydrocarbon-based types), which are candidates for new alternatives (i.e., flammability and chemical instability) arise. Therefore, the basic characteristics of next-generation refrigerants should be elucidated, and a standard evaluation method for safety and risk associated with their use should be established. In this context, the Japan Society of Refrigerating and Air Conditioning Engineers was commissioned through the New Energy and Industrial Technology Development Organization (NEDO) research project titled "Development of optimization and evaluation methods for next-generation refrigeration and air-conditioning technology for energy-saving and low-greenhouse effects" (September 2018–March 2023) and has conducted research on new refrigerants and related equipment for five years since September 2018.

During this time, working groups (WGs) were established within the Research Project Committee for Next-Generation Refrigerants to examine each of the following themes: NEDO-commissioned project R&D item (1) "Acquisition and evaluation of data on basic characteristics of next-generation refrigerants" as WG I, R&D item (2) "Development of safety and risk assessment methods of next-generation refrigerants" as WG II, R&D item (3) "Survey of trends on regulations, standards, equipment development, and performance evaluation related to next-generation refrigerants in Japan and overseas" as WG III, and "Evaluation methods for performance of air-conditioning equipment" as WG IV, established in 2021. Summaries are provided four to five times a year by each WG, focusing on business operators, progress reports regarding R&D and survey items, and information exchange. The Research Project Committee, which consists of representatives of various business operators and expert members, meets four times a year (April, July, October, and January) to efficiently link the results of R&D efforts to international standards and international standardization by exchanging and summarizing information on the progress and results of each R&D item in this commissioned project, evaluating the basic characteristics of next-generation refrigerants, conducting early R&D and optimization of associated energy-saving refrigeration and air-conditioning equipment, and establishing relevant safety/risk assessments and performance evaluation methods.

This report summarizes valuable results obtained over the past five years for each WG. In Part 1, we report the results of WGI, including the physical properties and heat transfer performance of next-generation refrigerants, cycle performance, various performance analyses, development of evaluation methods, simulator development, and machine learning approaches. In Part 2, we report the results of WGII, which includes refrigerant leakage models, ignition possibility evaluation, ignitability evaluation, low-GWP mixed refrigerant combustion characteristics evaluation, and risk assessment of room air conditioners and built-in showcases using A3 refrigerant, summarized as safety and risk assessment methods for next-generation refrigerants. In Part 3, we report the results of WGIII, which include surveys of trends in domestic and international regulations and standards obtained through the project commissioned by the Japan Society of Refrigerating and Air Conditioning Engineers, and an overseas survey (Europe, United States, and China) regarding current and next-generation refrigerant trends. In Part 4, we report the results of WGIV, which include the evaluation methods for the performance of air-conditioning equipment conducted by the Japan Air Conditioning and Refrigeration Testing Laboratory, University of Tokyo, and Waseda University. In the limited period of five years, these WGs have produced many valuable results to the extent possible under current conditions, and some of the results have already been reflected in international standards and specifications.

However, although a wide variety of next-generation refrigerants are being developed, no prospect for a refrigerant that is highly safe and efficient and optimal for use in equipment intended to limit global warming is realizable. Although the NEDO project will soon come to an end, R&D will continue in the future. Moreover, many ongoing results will be published that will lead to updated international standards and specifications. Additionally, this R&D is essential for maintaining leadership in international academic research and the refrigeration and air-conditioning industry, and simultaneously for Japan to lead the way in safety, high efficiency, and reliability in the refrigeration and air-conditioning industry and for its continued development along with related industries. We believe that the government, private sector, and industry will continue to work together to ensure sustainable development of industries related to next-generation refrigerants, as international environmental regulations are expected to become even more stringent in the future.

2. Research Project Committee Objectives, Structure, and Results of Activities

Japan Society of Refrigerating and Air Conditioning Engineers
Vice Chair, Research project committee for Next-Generation Refrigerants
Shigehiro Uemura (Japan Society of Refrigerating and Air Conditioning Engineers)

2.1 Introduction

Since FY2018, the Japan Society of Refrigerating and Air Conditioning Engineers (JSRAE) has been conducting the NEDO research project, "Development of technology and assessment techniques for next-generation refrigerants with a low global warming potential (GWP)." To conduct this project, a research project committee and working groups (WGs) were established in FY2018 to exchange information and establish plans.

Herein, we present the final report that summarizes the results of our activities over five years until FY2022.

2.2 Background

The 2016 Kigali Amendment to the Montreal Protocol added an obligation to gradually reduce the production and consumption of hydrofluorocarbons (HFCs). Therefore, an ever-increasing need for the evaluation of refrigerants with low GWP and the establishment of performance evaluation methods for related energy-saving refrigeration and air-conditioning equipment arise. Furthermore, safety issues (i.e., flammability and chemical instability) associated with next-generation refrigerant candidates (low-GWP refrigerants) arise. Therefore, establishing standard safety and risk assessment methods when using these next-generation refrigerants is essential.

2.3 Research objectives

In the NEDO-commissioned project "Development of technology and assessment techniques for next-generation refrigerants with a low GWP value," R&D item (1) "Acquisition and evaluation of data on basic characteristics of next-generation refrigerants" and R&D item (2) "Development of safety and risk assessment methods for next-generation refrigerants" have been promoted. The research project conducted by JSRAE compiles information such as identifying and resolving issues that accompany the progress of each R&D item in the commissioned project and disseminates the information both domestically and overseas to efficiently link these R&D results to international standardization. Therefore, we surveyed methods and results related to the evaluation of the basic properties of next-generation refrigerants, performance evaluation of energy-saving refrigeration, and air-conditioning equipment with next-generation refrigerants for early development and optimization. We also surveyed safety and risk assessments related to applications in refrigeration and air-conditioning equipment.

2.4 Research structure

A research project committee consisting of NEDO project R&D implementers and experts from industry, government, and academia was established within JSRAE. Furthermore, four WGs were established within the committee to explore different issues. Fig. 2-1 shows an organizational chart.

1) Research project committee

The research project committee has the following functions:

-Exchanging information on the implementation status of each WG and confirming and organizing the overall progress.

-Deliberating the organization of the provided information and the content for external communication.

-Content compiled by each WG will be published as a Progress Report each fiscal year and as a Final Report in the final fiscal year.

-The committee will meet approximately four times a year.

Table 2-1 shows the composition of the research project committee.

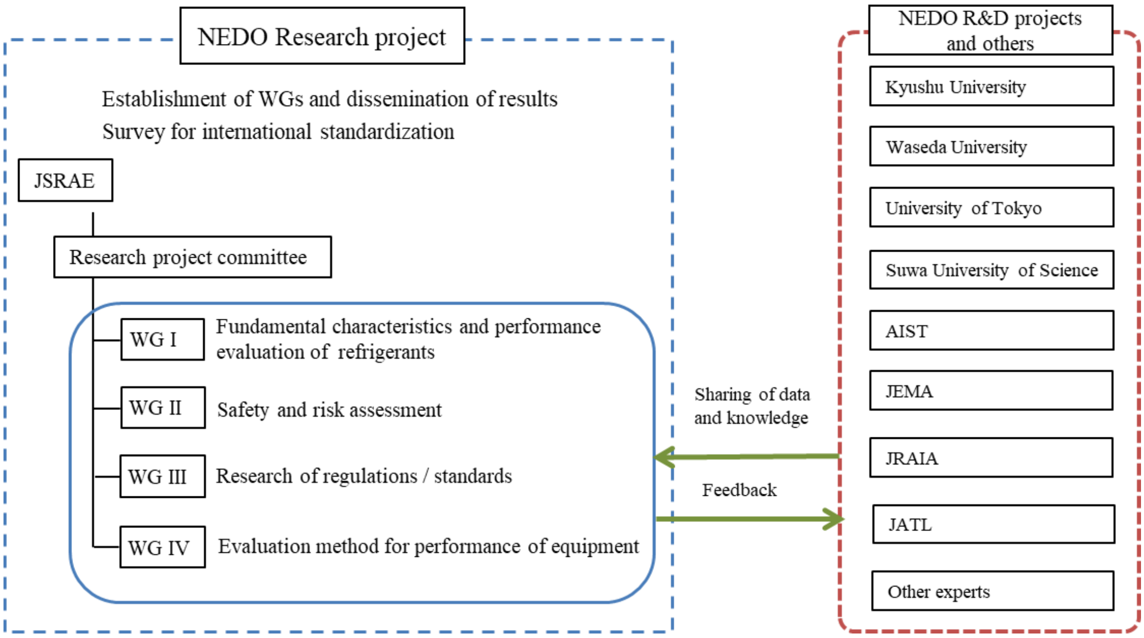

Figure 2-1 Structure of research project

Table 2-1 Members of the research project committee (As of January 2023)

	Name	Affiliation
Chair	Norihiro Inoue	Professor, Tokyo University of Marine Science and Technology
Vice Chair	Shigehiro Uemura	JSRAE
Committee members		
Experts	Noboru Kagawa	Professor, National Defense Academy
	Kazuya Koshino	Director, High-Pressure Gas Safety Institute of Japan
	Tetsuro Kishimoto	Managing Director, Environment and Energy Network 21 (WG III Chief)
	Osami Kataoka	Chief, ISO Domestic Subcommittee, JSRAE
	Akio Miyara	Chief, ASHRAE Japan Domestic Subcommittee, JSRAE
	Shinichiro Sato	Director, General Affairs and Administration/Accounting, JSRAE
NEDO-commissioned operators	Yukihiro Higashi	Professor, Kyushu University
	Kenji Takizawa	Chief Researcher, AIST
	Kiyoshi Saito	Professor, Waseda University (WG I, WG IV Chief)
	Eiji Hihara	Professor, National Institution for Academic Degrees and Quality Enhancement of Higher Education (WG II Chief)
	Tomohiko Imamura	Associate Professor, Suwa University of Science
	Hiroumi Shiina	Chief Researcher, AIST
Industry (JRAIA)	Tetsuji Okada	Managing Director, JRAIA
	Takeshi Sakai	Technical Department Manager, JRAIA
Observers	Ayumi Kodama, Momoe Ikeda	Fluoride Gases Management Office, Ministry of Economy, Trade and Industry
	Satoshi Fujigaki, Tomokazu Mori, Makoto Gocho, Tatsuhiko Takahashi Takuma Ooishi	NEDO Environment Department
Secretariat	Kyoji Kouno	Secretary-General, JSRAE
	Akira Nishiguchi	JSRAE

NEDO : New Energy and Industrial Technology Development Organization
JSRAE : Japan Society of Refrigerating and Air Conditioning Engineers
AIST : National Institute of Advanced Industrial Science and Technology
JRAIA : Japan Society of Refrigerating and Air Conditioning Engineers
JEMA : Japan Electrical Manufacturers' Association
JATL : Japan Air Conditioning ana Refrigeration Testing Laboratory

2) WGs

WGs have the following functions:

- Exchanging information between NEDO-commissioned project R&D implementers, industry groups, and other experts.
- Exchanging opinions on progress on time and coordinating the information to be provided to the research project committee based on discussions.

The four WGs include WG I -WG III, which have been active since the establishment of the research project committee, and WG IV, established in 2021.

WG I Fundamental characteristics and performance evaluation of next-generation refrigerants.
WG II Safety and risk assessment of next-generation refrigerants
WG III Research on regulations/standards for next-generation refrigerants.
WG IV Evaluation methods for air-conditioning equipment performance

Table 2-2 presents the lists of the members of each WG.

Table 2-2 Members of each working group (As of January 2023)

WG	Content	Chief	Members
WG I	Next-generation refrigerant - Basic characteristics data-sharing - Performance analysis method investigation *Should be based on international standardization.	Kiyoshi Saito Professor, Waseda University	Yukihiro Higashi (Kyushu University), Akio Miyara (Saga University), Ryo Akasaka (Kyushu Sangyo University), Seiichi Yamaguchi, Jongsoo Jeong (Waseda University), Koji Enoki (University of Electro-Communications) * NEDO and JRAIA participated as observers.
WG II	Next-generation refrigerant - Safety / risk assessment (starting with items mainly related to HCs)	Eiji Hihara Professor, National Institution for Academic Degrees and Quality Enhancement of Higher Education	Kenji Takizawa (National Institute of Advanced Industrial Science and Technology), Tomohiko Imamura (Suwa University of Science), Hiroumi Shiina (National Institute of Advanced Industrial Science and Technology), Makoto Ito (University of Tokyo) * NEDO and JRAIA participated as observers.
WG III	Next-generation refrigerants - Regulation / standards survey - International standardization proposal survey	Tetsuro Kishimoto Managing Director, Environment and Energy Network 21	Osami Kataoka (Daikin Industries), Masato Miyata (National Institute for Land and Infrastructure Management), Kenji Tojo (Waseda University), Kazuya Matsumoto (High Pressure Gas Safety Institute of Japan) * NEDO participated as observer
WG IV	Equipment performance - Test method verification - Performance evaluation Investigation	Kiyoshi Saito Professor, Waseda University	Eiji Hihara (National Institution for Academic Degrees and Quality Enhancement of Higher Education), Jongsoo Jeong (Waseda University), Yu Chen, Makoto Ito (University of Tokyo), Osami Kataoka, Katsunori Murata (Daikin Industries), Satoshi Sakashita (Panasonic), Hidetomo Nakagawa (Mitsubishi Electric), Ryoichi Takafuji (Hitachi Johnson Controls Air Conditioning), Tatsuya Tani, Ryota Hirata (Japan Air Conditioning and Refrigeration Testing Laboratory), Koji Muruzono (Japan Refrigeration and Air Conditioning Industry Association)

2.5 Survey content

The following information will be collected and summarized concerning the basic characteristics, optimization, performance evaluation, and safety/risk assessment of refrigerants related to the practical development of energy-saving refrigeration and air-conditioning equipment that uses next-generation refrigerants.

1) Survey on trends in aspects, such as regulations and standards, related to next-generation refrigerants (Research project committee WG III-related item)

- Collecting and organizing information on regulatory trends and existing safety standards (e.g., international standards and industry standards) related to next-generation refrigerants in Japan and overseas, as well as information related to new developments, revisions, and other trends.
- Collecting and organizing information on trends in research and standardization of basic characteristics of next-generation refrigerants in Japan and overseas and trends in optimization and performance evaluation in equipment development, as well as collecting and organizing information relating to trends in the standardization of new basic characteristics, performance evaluations, and equipment development.

2) Extraction of issues related to basic characteristics, optimization, safety, and risks when using next-generation refrigerants and related equipment, and surveying possible methods for responding to these issues (research project committee WG I, II, IV-related items)

- Extraction of issues related to the basic characteristics of next-generation refrigerants and early development and optimization of energy-saving refrigeration and air-conditioning equipment, progress roadblocks, and survey methods for responding to these issues.
- Extracting issues related to system optimization and performance evaluation of energy-saving refrigeration and air-conditioning equipment using next-generation refrigerants, progress roadblocks, and survey methods for responding to these issues.
- Collecting and organizing information on the optimal and safe usage of next-generation refrigerants and equipment that uses new refrigerants.
- Extracting issues related to the development of safety and risk assessment methods for next-generation refrigerants, progress roadblocks, and survey methods to respond to these issues.

3) Surveying the international standardization of safety and risk assessment methods for next-generation refrigerants and related equipment (Research project committee WG III-related item)

- Collecting and organizing information on the content that should be proposed for international standards based on survey results in 1) and 2) and R&D results relating to safety and risk assessment methods of next-generation refrigerants in the NEDO-commissioned project “Development of technology and assessment techniques for next-generation refrigerants with a low GWP value.”

2.6 Results of research project committee activities

1) Dates held and main agenda

Table 2-3 Results of research project committee meetings (1)

Total number	Date held	Main agenda
1st	2019/2/4 (Mon.) 13:30-15:30 JSRAE conference room	- "NEDO project background and policy trends" (lecture by Fluoride Gases Management Office Director Minagawa) - Position and role of research project committee/WG - Overview of NEDO research project
2nd	2019/4/22 (Mon.) 13:30-15:30 JSRAE conference room	- Explanation of contents by each WG in FY2018 progress report - FY2019 plan for the research project - Holding workshops at Annual JSRAE Conference
3rd	2019/7/24 (Wed.) 13:30-15:30 JSRAE conference room	- "Latest trends in Fluoro-carbon countermeasures" (lecture by Fluoride Gases Management Office Director Tone) - Progress report for each WG and opinion exchange - “Trends in revision of international standards” (report by committee member Kataoka) - External communication plan (Annual JSRAE Conference, ICR2019, IEA Heat Pump Conference)
4th	2019/11/11 (Mon.) 13:30-15:30 JSRAE conference room	- Progress report for each WG and opinion exchange - As part of the WG III report, trends in the revision of international standards, the introduction of AHRTI new refrigerant database construction P/J (committee member Kataoka) - Results of the Annual JSRAE Conference - FY2019 progress report
5th	2020/2/26 (Wed.) 13:30-16:00 JSRAE conference room	- “Prospects for use of fluorocarbons” (Kiyota, Fluoride Gases Management Office) - Progress status of each WG, how to proceed in future, issues, opinion exchange - External communication proposals (ASHRAE Winter Conference)
6th	2020/5/15 (Fri.) E-mail discussion	- Discussion on the content of the FY2019 progress report
7th	2020/7/15 (Wed.) 13:30-15:40 Online meeting	- Progress report for each WG and plans, opinion exchange - Discussion of progress report content and publication schedule - Changes in situation and responses regarding external communication due to COVID-19 - Interim evaluation implementation planning and schedule for the current fiscal year
8th	2020/10/22 (Thu.) 13:30-15:15 Online meeting	- Progress report for each WG and plans (road map, etc.) - How to proceed with the research project (review of survey methods, etc.) - Review and adjustment of external publications - Creation of FY2020 progress report
9th	2021/1/20 (Wed.) 15:00-16:45 Online meeting	- Progress status of each WG and plans for next fiscal year onwards, opinion exchange - As part of the WG III report, the introduction of “Trends in performance standards” (committee member Kataoka) - Requests regarding changes in the status of external communications and - FY2020 progress report (confirmation of English translation, etc.)

Table 2-3 Results of research project committee meetings (2)

Total number	Date held	Main agenda
10th	2021/4/20 (Tue.) 13:30-15:20 Online meeting	- Discussion of FY2020 progress report - FY2021 plans for each WG - External communication and Annual JSRAE Conference WS
11th	2021/7/15 (Thu.) 13:30-15:20 Online meeting	- Publication status of FY2020 progress report - Progress status of each WG - Regarding establishment of WG IV - Planning for hosting international conference
12th	2021/10/21 (Thu.) 13:30-15:20 Online meeting	- Progress status of each WG - Creation of FY2021 progress report - External communication (associated international conference hosting status, planning) - Ozone Layer Protection / Global Warming Prevention Award report
13th	2022/1/20 (Thu.) 13:30-15:15 Online meeting	- Progress status of each WG and planning for next fiscal year - External communication - Creation of FY2022 final report
14th	2022/4/26 (Tue.) 13:30-15:30 Online meeting	- Discussion on FY2021 progress report - Progress status of each WG and plan for next fiscal year - External communication and Annual Conference workshop - Research project committee plan for this fiscal year
15th	2022/7/15 (Fri.) 13:30-15:30 Online meeting	- Progress status of each WG - Reflecting on results of each WG in standard revisions - Annual Conference workshop
16th	2022/10/20 (Thu.) 13:30-15:30 Online meeting	- Progress report for each WG, opinion exchange - Discussion on summary table for reflecting results of each WG in standard revisions - Confirmation of plans for this fiscal year, such as preparation of final report
17th	2023/1/20 (Fri.) 13:30-15:30 Online meeting	- Progress status of each WG - Reflecting on results of each WG in standard revisions - Annual Conference workshop

2) Results of external communication

The major external communications that have taken place to date are as follows:

1. Progress report

The results for each fiscal year from FY2018 to FY2021 were published as a progress report on the JSRAE website.

https://www.jsrae.or.jp/committee/jisedai_R/jisedai_R.html (2018-2021 whole Japanese)

https://www.jsrae.or.jp/jsrae/committee/jisedai_R/2020_ProgressR_Part2-e.pdf (2020 WG II English)

2. Annual JSRAE Conference

At each Annual JSRAE Conference from 2019 to 2022, the research project committee organized a workshop termed "Next-generation low-GWP refrigerant safety, physical properties, heat transfer, and cycle performance evaluation" and reported the results.

3. Presentations at major international conferences

- Japan Refrigeration and Air Conditioning Industry Association "Environment and New Refrigerant International Symposium" (2018, 2021)
- IEA Heat Pump Conference 2020 (2021)

- HFO2021 Conference (2021)   - Purdue Conference (2022)

4. Other

Many presentations and contributions have been made in associated domestic and international conferences, seminars, and specialized journals.

2.7 Working group (WG) activity results

The five-year implementation results for each WG were as follows:

1) WG I (Fundamental characteristics and performance evaluation of next-generation refrigerants
Chief: Professor Saito, Waseda University)

A total of 18 meetings were held to report the progress of each R&D item and exchange opinions with the Japan Refrigeration and Air Conditioning Industry Association. Data on refrigerant physical properties, which are basic characteristics, and heat transfer, which is an applied characteristic, are summarized. Additionally, performance evaluation and analysis methods were adjusted and directed from a practical point of view to determine a more efficient way forward.

Finally, several public presentations on R&D results, which were well received, were made.

Table 2-4 Results of WG I meetings (1)

Total number	Date held	Main agenda
1st	2019/5/28 (Tue.) 17:30-18:40 JSRAE conference room	- Consultation on ways forward based on the “Refrigeration and air-conditioning equipment evaluation technology construction proposal” by Chief Saito - Share information with JRAIA members
2nd	2019/8/9 (Fri.) 15:15-17:10 Kikai Shinko Kaikan	- Progress report on new refrigerant physical properties, equations of state, and heat transfer characteristics - Report on status of mathematical model development, system performance evaluation equipment, and simulator development
3rd	2019/10/10 (Thu.) 15:45-17:45 Kikai Shinko Kaikan	- Overview of system performance evaluation equipment and test content - Methods for linking future target substances and system evaluations regarding basic properties of refrigerants (physical properties, heat transfer)
4th	2019/12/26 (Thu.) 15:50-18:00 Kikai Shinko Kaikan	- Issues on physical property evaluation (mixtures of 3-component, REFPROP-related matters, etc.) - Status of heat transfer property evaluation - FY2019 progress report
5th	2020/4/8 (Wed.) 15:00-16:40 Online meeting	- Progress status of performance analysis technology and performance evaluation technology at Waseda University - Progress status of physical property measurements at Kyushu University - Refrigerants to be evaluated in the future
6th	2020/6/24 (Wed.) 15:00-16:30 Online meeting	- Heat transfer database construction - Progress on dynamic system performance evaluation equipment - Draft international standardization road map for system performance evaluation
7th	2020/9/4 (Fri.) 15:00-17:00 Online meeting	- Measurements of physical properties of refrigerants including CF3I - Development status of actual operation evaluation equipment - Support for BAM round robin test
8th	2020/11/6 (Fri.) 15:15-16:30 Online meeting	- Test plan using actual operation evaluation equipment - Refrigerant types and test equipment in above-mentioned plan - FY2020 progress report creation schedule

Table 2-4 Results of WG I meetings (2)

Total number	Date held	Main agenda
9th	2021/1/19 (Tue.) 15:00-16:45 Online meeting	- Results of this fiscal year of evaluation of basic properties such as thermo-physical properties and heat transfer properties - Development status of equipment performance evaluation method and next fiscal year plan - Summary of progress report and external communication plan
10th	2021/4/16 (Fri.) 15:00−16:40 Online meeting	- Confirmation of FY2020 progress report - Discussion on path forward for Kyushu University G and Waseda G - Participation in JRAIA International Symposium and Annual JSRAE Conference
11th	2021/6/25 (Fri.) 15:00−17:00 Online meeting	- Introduction of HFO thermodynamic table (JAREF) - Explanation of research status of mixed refrigerant boiling heat transfer, Q&A - Development status of performance simulator
12th	2021/9/17 (Fri.) 15:00−17:00 Online meeting	- Status of external communication related to refrigerant thermo-physical properties - Progress of experiments using refrigerant charging amount evaluation equipment - Test results obtained by performance evaluation equipment
13th	2021/12/3 (Fri.) 15:00−17:10 Online meeting	- Status of research on physical properties and equations of state of R13I1 - Progress status of Waseda University G implementation themes (mixed refrigerant boiling heat transfer experiment, R290 drop-in test, etc.)
14th	2022/2/8 (Tue.) 16:30−18:40 Online meeting	- Physical properties and equations of state of R13I1 mixed system - Progress status of Waseda University G implementation themes (simulator development, refrigerant charging amount evaluation, etc.)
15th	2022/4/6 (Wed.) 15:00−17:10 Online meeting	- Status of next-generation refrigerant heat transfer performance and heat transfer database - Void fraction measurement by capacitance method - Verification of dynamic performance evaluation test method (confirmation of emulator method)
16th	2022/6/30 (Thu.) 15:00−16:30 Online meeting	- Research on physical properties of R32+R1123+CF3I and R1123+R290 - Evaporator refrigerant flow path optimization by simulation - Boiling heat transfer and pressure loss prediction by AI
17th	2022/9/15 (Thu.) 15:00−17:00 Online meeting	- Summary of five years of physical property measurement results (four types of single refrigerants, 20 types of mixtures) - Overview of research by Waseda University to date - Summary of methods for final report and deadline
18th	2022/12/22 (Thu.) 15:00−17:00 Online meeting	- Confirmation of the contents of the final report and future plans - Progress status of Waseda Univ. (Drop-in test, AI-based heat transfer property evaluation))

2) WG II (Safety and risk assessment of next-generation refrigerants: Chief: Professor Hihara, National Institution for Academic Degrees and Quality Enhancement of Higher Education).

Because of the progress reports on each R&D item and the exchange of opinions with the Japan Refrigeration and Air Conditioning Industry Association, the types and methods of data accumulation for future standard revision proposals were confirmed, and ways forward were clarified.

Additionally, many external presentations on R&D results have been made, and they have been well received.

Table 2-5 Results of WG II meetings (1)

Total number	Date held	Main agenda
1st	2018/12/26 (Wed.) 16:00-17:00 Kikai Shinko Kaikan	- Establishment of WG, implementation content, process - How to share information with JRAIA members - Summary of activity results
2nd	2019/2/25 (Mon.) 13:30-17:00 Kikai Shinko Kaikan	- R&D status reports and opinion exchange (University of Tokyo, Suwa University of Science, AIST, JRAIA) - Creation of progress report
3rd	2019/4/19 (Fri.) 13:30-17:00 Japan Electro-Heat Center conference room	- R&D status reports and opinion exchange (University of Tokyo, Suwa University of Science, AIST, JRAIA) - Correspondence with candidates for external presentations - Progress report results
4th	2019/7/11 (Fri.) 13:30-17:00 JSRAE conference room	- R&D status reports and opinion exchange (University of Tokyo, Suwa University of Science, AIST, JRAIA) - Correspondence with Annual JSRAE Conference, ICR workshop
5th	2019/10/4 (Fri.) 13:30-17:00 JSRAE conference room	- R&D status reports and opinion exchange (University of Tokyo, Suwa University of Science, AIST) - Schedule for FY2019 progress report
6th	2019/12/19 (Thu.) 13:30-17:00 JSRAE conference room	- R&D status reports and opinion exchange (University of Tokyo, Suwa University of Science, AIST) - FY2019 progress report content, schedule confirmation
7th	2020/5/28 (Thu.) 13:30-17:30 Online meeting	- R&D status reports and opinion exchange (University of Tokyo, Suwa University of Science, AIST) - Changes in external presentation policy and plan due to COVID-19 - Summary of FY2019 progress report
8th	2020/9/24 (Thu.) 9:00-11:50 Online meeting	- R&D status reports and opinion exchange (University of Tokyo, Suwa University of Science, AIST) - Moving forward
9th	2020/11/26 (Thu.) 9:30-11:30 Online meeting	- R&D status reports and opinion exchange (University of Tokyo, Suwa University of Science, AIST) - Creation of FY2020 progress report
10th	2021/1/14 (Thu.) 10:00-12:10 Online meeting	- Report on status of each R&D item and future planning, opinion exchange (University of Tokyo, Suwa University of Science, AIST) - Confirmation of progress report creation guidelines (implementation of English translation)

Table 2-5 Results of WG II meetings (2)

Total number	Date held	Main agenda
11th	2021/4/15 (Thu.) 10:00−12:10 Online meeting	- Purpose and schedule for summary version of FY2020 progress report and publication of English version - Explanation of this fiscal years' plan for four implementation themes, Q&A
12th	2021/7/8 (Thu.) 13:30−15:40 Online meeting	- Process and schedule for creating English translation (all volumes) of FY2020 progress report - Explanation of progress status of four implementation themes, Q&A
13th	2021/9/22 (Wed.) 13:30−15:20 Online meeting	- Explanation of progress status of four implementation themes, Q&A (in particular, risk evaluation, ignition source analysis, combustibility mechanism of mixed systems, etc.) - Presentation themes for JRAIA symposium
14th	2021/12/2 (Thu.) 13:30−15:50 Online meeting	- Analysis and evaluation of degree of danger when igniting refrigerant - Laser breakdown ignition possibility experiment results - Combustibility evaluation involving mixed-system concentration distributions
15th	2022/2/17 (Thu.) 13:30−16:00 Online meeting	- Risk assessment by leakage simulation - Physical hazard evaluation during rapid leakage on full-scale model - Next fiscal year's final report (Japanese / English) creation schedule
16th	2022/4/14 (Thu.) 13:30−16:00 Online meeting	- Evaluation of degree of danger when flammable refrigerant is ignited outdoors - Physical risk assessment method during refrigerant combustion - Combustibility evaluation of mixed refrigerants (R1123+32)
17th	2022/7/6 (Wed.) 13:30−15:30 Online meeting	- R&D status report and opinion exchange (Suwa University of Science, AIST) - Confirmation of final report content and schedule creation
18th	2022/9/21 (Wed.) 13:30−16:00 Online meeting	- R&D status report and opinion exchange (University of Tokyo, Suwa University of Science, AIST) - Combustibility of refrigerants mixed with lubricating oil
19th	2022/11/25 (Fri.) 13:30−16:00 Online meeting	- R&D status report and opinion exchange (Suwa Tokyo University of Science, AIST Safety Science Division) - Confirmation of the schedule for the completion of the final report

3) WG III (Research of regulations/standards for next-generation refrigerants: Chief: Director Kishimoto, Environment, and Energy Network 21)

Discussions were held on relevant regulations, the scope of surveys on standards, domestic and international regulations, trends in standard revisions, and the direction of target next-generation refrigerants. Additionally, proposals were made and support was provided for survey projects implemented by the JSRAE (e.g., international surveys and HFC alternative refrigerant trend surveys), and contributions were made to the directions of the surveys.

Table 2-6 Results of WG III meetings (1)

Total number	Date held	Main agenda
1st	2019/2/8 (Fri.) 10:30-12:00 JSRAE conference room	- Establishment of WG, implementation content, process - Scope of regulations and standards to be surveyed - Refrigerants to be surveyed
2nd	2019/3/25 (Mon.) 10:30-12:00 JSRAE conference room	- List of related regulations and standards - FY2018 progress report draft review - Ways forward, such as cooperation with other WGs and various industries
3rd	2019/5/28 (Tue.) 15:00-16:30 Japan Electro-Heat Center conference room	- Opinion exchange based on “Background and future of corresponding with international standards” (report by committee member Kataoka) - Research on conditions required for next-generation refrigerants - Domestic correspondence system with ISO and IEC
4th	2019/7/25(Thu.) 10:30-12:00 JSRAE conference room	- Future implementation content and plan for survey project (prioritization of regulations and standards, methods of information collection, etc.) - Latest standard revision trends
5th	2019/10/16 (Wed.) 10:30-12:15 JSRAE conference room	- International survey plan - Methods for surveys involving trends associated with low-GWP refrigerants - Energy conservation regulations for buildings
6th	2019/12/13 (Fri.) 10:30-12:00 JSRAE conference room	- Destinations and schedule for international surveys (Europe and United States) - Evaluation methods for systems using next-generation refrigerants - Draft table of contents for FY2019 progress report
	2020/4 E-mail discussion	- Content of FY2019 progress report
7th	2020/7/9 (Thu.) 10:40-12:10 Online meeting	- Opinion exchange based on “Latest trends in international standards” (report by committee member Kataoka) : particularly items related to refrigerant safety - Progress of survey project and future plans
8th	2020/10/16 (Fri.) 10:30-11:50 Online meeting	- Opinion exchange based on “Latest trends in international standards” (report by committee member Kataoka) : addition of items related to performance evaluation - This fiscal year’s survey content and ways forward (e.g., additional patent surveys)
9th	2021/1/8 (Fri.) 10:30-12:00 Online meeting	- Opinion exchange based on “Latest trends in international standards :equipment performance test, evaluation methods” (report by committee member Kataoka) - Content of FY2020 progress report
10th	2021/4 E-mail discussion	- Content of FY2020 progress report
11th	2021/7/6 (Tue.) 15:00−16:40 Online meeting	- Process for this year’s survey project - Latest trends in related international standards (committee member Kataoka) - Establishment of new WG(WG IV)

Table 2-6 Results of WG III meetings (2)

Total number	Date held	Main agenda
12th	2021/10/5 (Tue.) 15:00−16:20 Online meeting	- Explanation of this fiscal year's survey implementation, Q&A - Recent trends in construction-related regulations and standards (committee member Miyata) - Introduction of GWP review in IPCC Sixth Assessment Report
13th	2022/1/6 (Thu.) 13:30−15:00 Online meeting	- Survey on refrigerant trends in China (interim report) - Proposal for this fiscal year's progress report - Introduction of WG I, II, and IV activities
14th	2022/3/28 (Mon.) 16:00−17:40 Online meeting	- Explanation of latest standard trend information, Q&A (committee member Kataoka) (safety standards, performance standards) - Content of this fiscal year's progress report
15th	2022/5/25 (Wed.) 10:30−12:00 Online meeting	- Proposal of items to be implemented in this fiscal year's survey project, opinion exchange - Content of WG III results reported in Annual JSRAE Conference - Status and prospects for reflecting research results of each WG in international standards, etc.
16th	2022/7/27 (Wed.) 10:30−12:00 Online meeting	- Final report draft composition - Review of ISO period performance evaluation standards and support for fixed load tests (explanation and opinion exchange from committee member Kataoka)
17th	2022/10/7 (Fri.) 10:30−12:00 Online meeting	- Final report content - Results and plans for reflecting research results of each WG in international standards, etc. - Trends in PFAS regulations (committee member Kataoka)
18th	2023/1/12 (Thu.) 10:30−12:00 Online meeting	- Confirmation of the contents of the final report - Latest information on standard revisions - Impressions of each committee member at the final round

4) WG IV (Evaluation Methods for Performance of Air-Conditioning Equipment Chief: Professor Saito, Waseda University)

WG IV was established in FY2021.

Based on the status report of ongoing R&D content, opinions related to data collection, evaluation methods, and test methods for equipment performance evaluation were exchanged, and research was performed on identified issues and ways forward.

Table 2-7 Results of WG IV meetings

Total number	Date held	Main agenda
1st	2021/9/14 (Tue.) 15:00−17:30 Online meeting	- Background, purpose, and structure of WG IV - Introduction of efforts by NEDO operators and related organizations - Process moving forward
2nd	2021/11/25 (Thu.) 13:30−15:45 Online meeting	- Progress status of NEDO operators (University of Tokyo, Waseda University), Q&A - Issues and support for fixed load tests (committee member Kataoka) - Implementation status of fixed load test (JATL)
3rd	2022/3/2 (Wed.) 13:30−15:30 Online meeting	- Results of non-fixed compressor frequency performance test (University of Tokyo) - Results of emulator usage performance test (Waseda University): - Explanation of efforts by JEMA, JRAIA
4th	2022/5/12 (Thu.) 13:30−15:40 Online meeting	- Confirmation of 2021 progress report - Progress status of NEDO operators (University of Tokyo, Waseda University), Q&A - Related organization activity report (JEMA, JATL)
5th	2022/7/5 (Tue.) 15:00−16:50 Online meeting	- Results of load tests by air enthalpy method (University of Tokyo) - Results of R290 and R454C drop-in tests on R22 machine (Waseda University) - IoT data aggregation report (JRAIA)
6th	2022/9/27 (Tue.) 13:30−15:30 Online meeting	- Evaluation of dynamic load test results (University of Tokyo) - Research of performance differences due to test conditions and test methods (Waseda University) - Final report composition and schedule confirmation
7th	2022/12/23 (Fri.) 13:30−15:30 Online meeting	- Status of dynamic load test, exchange of opinions (University of Tokyo) - Round-robin test results, exchange of opinions (Waseda University) - Confirm the contents of the final report

2.8 Regarding this final report

The final report, which summarizes the results over a five-year period, describes an overview of the NEDO research project, a promotion system adopted by the research project committee and WGs, and an overview of the activities, which consists of the following four separate volumes that provide a detailed introduction to each WG's activities.

Part 1: WG I Fundamental characteristics and performance evaluation of next-generation refrigerants
Part 2: WG II Safety and risk assessment of next-generation refrigerants.
Part 3: WG III Research on regulations/standards for next-generation refrigerants
Part 4: WG IV Evaluation methods for performance of air-conditioning equipment

The content of the publication is a summary of the results obtained through the NEDO project via the research project committee and is premised on publication. Therefore, the content is limited and not necessarily a progress report for the NEDO project as a whole. Additionally, the report includes reports on related achievements by industry groups that were not part of the NEDO project.

Basic Performance, Optimization, and Safety and Risk Evaluation of Next-Generation Refrigerants and Refrigerating and Air Conditioning Technologies

Part 1: Fundamental Characteristics and Performance Evaluation of Next-Generation Refrigerants

WG I Final Report

Research Committee for Next-Generation Refrigerants,

Japan Society of Refrigerating and Air-Conditioning Engineers

January 31, 2023

Table of contents

1. INTRODUCTION

With the global demand for carbon neutrality, there are major scientific and technological challenges to overcome. To overcome such challenges, Japan pledged to achieve carbon neutrality by 2050 and is currently progressing toward this objective.

Under these conditions, refrigeration and air conditioning technology has been widely applied to refrigeration, air conditioning, water heating, and industrial technology as a cold/heat control technology to realize energy conservation. The applications of this technology are increasing, as it represents a prospective driving force of the economy.

In recent years, refrigeration and air conditioning technology has been recognized as a technology that can prevent heat stroke by controlling temperature under extreme conditions and preventing viruses, among other infectious diseases, from spreading to humans by humidity control. The realization of low temperature and excellent temperature control allows for the provision of safe and secure food as the core technology of the cold chain, which can additionally be used for the production of drinking water from air. Thus, refrigeration and air conditioning technology has evolved into a technology that protects the environment and human life.

Notably, refrigerants cause ozone layer depletion and global warming problems. The refrigerant problem can be attributed to ozone depletion; however, in recent years, several refrigerants were found to demonstrate a more significant greenhouse effect greater than that of carbon dioxide. Following the Kigali Amendment to the Montreal Protocol, a major reduction in the use of refrigerants was targeted. Therefore, it is essential to install equipment that uses low global warming potential (GWP) refrigerants.

To accelerate the introduction of low-GWP equipment to the market, academic and public research institutes should establish basic technologies, including the risk assessment of refrigerants, basic thermodynamic properties of refrigerants necessary for equipment design, and the evaluation of technologies and optimization tools for the entire system. It is essential to establish a system that can support the marketing of equipment employing next-generation low-GWP refrigerants within a fully Japanese framework.

In this WG I, the Kyushu University group and the Waseda University group can be considered as implementers, who in addition to industrial firms such as METI and NEDO, discussed the establishment of fundamental technologies that can support equipment design and evaluation.

The Kyushu University group established a database and equation of state for the evaluation of various refrigerant properties, developed a heat transfer database, and formulated heat transfer correlations to establish a foundation for equipment design. The Waseda University group developed a device, system, and life-cycle climate performance (LCCP) simulators that can evaluate the theoretical performance of the equipment. In addition, they developed a system testing facility to obtain actual driving data; from which a fundamental performance evaluation base was established.

This report summarizes the results of this five-year project and establishes a system for evaluating equipment that uses next-generation low-GWP refrigerants, to facilitate the selection of appropriate refrigerants and accelerate the development of equipment that uses next-generation low-GWP refrigerants. Accordingly, this report makes a significant contribution to the proliferation of low-GWP of refrigerants.

Waseda university Kiyoshi Saito

The composition of WG I members is shown in Table 1.

Table 1-1 WG I members list

	Name	Affiliation
Chair	Kiyoshi SAITO	Waseda University
Committee member	Yukihiro HIGASHI	Kyushu University
	Akio MIYARA	Saga University
	Ryo AKASAKA	Kyushu Sangyo University
	Seiichi YAMAGUCHI	Waseda University
	Jongsoo JEONG	Waseda University
	Koji ENOKI	The University of Electro-Communications
Observer	Yoichi MIYAOKA	Waseda University
	Niccolo GIANNETTI	Waseda University
	Moojoong KIM	Waseda University
	Norihiro INOUE	Tokyo University of Marine Science and Technology
	Eiji HIHARA	National Institute for Academic Degrees Quality Enhancement of Higher Education
	Koji YAMASHITA	The Japan Refrigeration and Air Conditioning Industry Association (Mitsubishi Electric Corporation)
	Shigeharu TAIRA	The Japan Refrigeration and Air Conditioning Industry Association (Daikin Industries, Ltd.)
	Takumi SAKMOTO	The Japan Refrigeration and Air Conditioning Industry Association (Sharp Corporation)
	Tomoyuki HAIKAWA	The Japan Refrigeration and Air Conditioning Industry Association (Daikin Industries, Ltd.)
	Masami TANIGUCHI	The Japan Refrigeration and Air Conditioning Industry Association (Denso Corporation)
	Kohei MARUKO	The Japan Refrigeration and Air Conditioning Industry Association (Toshiba Carrier Corporation)
	Seishi IITAKA	The Japan Refrigeration and Air Conditioning Industry Association (Panasonic Corporation)
	Ryoichi TAKAFUJI	The Japan Refrigeration and Air Conditioning Industry Association (Johnson Controls - Hitachi Air Conditioning)
	Keisuke MITOMA	The Japan Refrigeration and Air Conditioning Industry Association (Mitsubishi Heavy Industries Thermal Systems, Ltd.)
	Komei NAKAJIMA	The Japan Refrigeration and Air Conditioning Industry Association (Mitsubishi Electric Corporation)
	Hayato NUNO	The Japan Refrigeration and Air Conditioning Industry Association (Daikin Industries, Ltd.)
	Kazutaka HORI	The Japan Refrigeration and Air Conditioning Industry Association (Daikin Industries, Ltd.)
	Takashi INOUE	The Japan Refrigeration and Air Conditioning Industry Association (Johnson Controls - Hitachi Air Conditioning)
	Taiki IIZUKA	The Japan Refrigeration and Air Conditioning Industry Association (Johnson Controls - Hitachi Air Conditioning)
	Yoshihiro HARA	The Japan Refrigeration and Air Conditioning Industry Association (Mitsubishi Heavy Industries Thermal Systems, Ltd.)

Table 1-1 WG I members list (continued)

	Name	Affiliation
Observer	Akira HIWATA	The Japan Refrigeration and Air Conditioning Industry Association (Panasonic Corporation)
	Hiroichi YAMAGUCHI	The Japan Refrigeration and Air Conditioning Industry Association (Toshiba Carrier Corporation)
	Kenji MATSUDA	The Japan Refrigeration and Air Conditioning Industry Association (Mitsubishi Heavy Industries Thermal Systems, Ltd.)
	Takeshi SAKAI	The Japan Refrigeration and Air Conditioning Industry Association
	Koji MUROZONO	The Japan Refrigeration and Air Conditioning Industry Association
	Kazuhiro HASEGAWA	The Japan Refrigeration and Air Conditioning Industry Association
	Satoshi FUJIGAKI	New Energy and Industrial Technology Development Organization
	Tomokazu MORI	New Energy and Industrial Technology Development Organization
	Tatsuhiko TAKAHASHI	New Energy and Industrial Technology Development Organization
	Makoto GOCHO	New Energy and Industrial Technology Development Organization
	Takuma OISHI	New Energy and Industrial Technology Development Organization
Secretriat	Kyoji KONO	Japan Society of Refrigerating and Air Conditioning Engineers
	Shigehiro UEMURA	Japan Society of Refrigerating and Air Conditioning Engineers
	Akira NISHIGUCHI	Japan Society of Refrigerating and Air Conditioning Engineers

The authors of this report are listed in Table 1-2.

Table 1-2 Author list

	Author
1. Introduction	Kiyoshi SAITO (Waseda University)
2. Measurement 0f thermophysical properties and performance evaluation for next-generation refrigerants	Yukihiro HIGASHI (Kyushu University), Naoya SAKODA, Takahiko MIYAZAKI, Kyaw THU, Hiroyuki MIYAMOTO (Toyama Prefectural University), Katsuyuki TANAKA (Nihon University), Chieko KONDOU (Nagasaki University), Yuya KANO (National Institute of Advanced Industrial Science and Technology), Ryo AKASAKA (Kyushu Sangyo University), Sho FUKUDA, Akio MIYARA (Saga University), Keishi KARIYA
3. Experiment, modeling, and formulation of components	Akio MIYARA (Saga University), Keishi KARIYA, Chieko KONDOU (Nagasaki University), Yufei LIU, Sho FUKUDA (Kyushu Sangyo University), Norihiro INOUE (Tokyo University of Marine Science and Technology), Daisuke JIGE, Kiyoshi SAITO (Waseda University), Seiichi YAMAGUCHI, Niccolo GIANNETTI, Jongsoo JEONG, Moojoong KIM, Kenji TOJO, Koji ENOKI (The University of Electro-Communications), Yohei INOUE, Yuichi SEI
4. System analysis	Kiyoshi SAITO (Waseda University), Niccolo GIANNETTI, Jongsoo JEONG, Yoichi MIYAOKA, Yuichi SEI (The University of Electro-Communications)
5. Conclusin	Yukihiro HIGASHI (Kyushu University)

Disclaimer

Although every effort has been made to ensure the accuracy of the information contained in this report, the authors and JSRAE assume no responsibility for any actions taken by users based on the information contained in this report. Likewise, the authors and JSRAE assume no responsibility for any damages or disadvantage incurred by users resulting from the use of this report.

2. MEASUREMENTS OF THERMOPHYSICAL PROPERTIES AND PERFORMANCE EVALUATION FOR NEXT-GENERATION REFRIGERANTS

2.1 Thermophysical Property Measurements of Next-Generation Refrigerants

2.1.1 Thermodynamic property measurements including the critical region

2.1.1.1 Experimental apparatus

In the NEXT-RP (Research Center of next-generation refrigerant properties, I^2CNER, Kyushu University), the thermodynamic property measurements, that is, *PvT* properties, saturation pressures, saturated densities, and critical parameters, were conducted. The experimental setup for measuring the *PvT* properties, saturation pressures, and critical pressures is shown in Fig. 2.1.1-1. Whereas, that employed for measuring the saturation densities, critical temperature, and critical density is shown in Fig. 2.1.1-2[1,2].

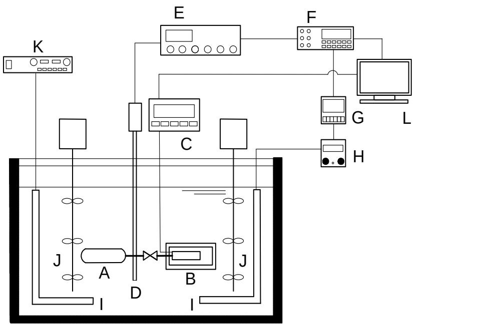

Fig. 2.1.1-1 Experimental apparatus for *PvT* property measurements. A: pressure vessel, B: pressure transducer, C: pressure indicator, D: 25 Ω standard platinum resistance thermometer, E: thermometer bridge, F: digital multimeter, G: PID controller, H: voltage transformer, I: heater, J: stirrer, K: AC power supply, L: computer.

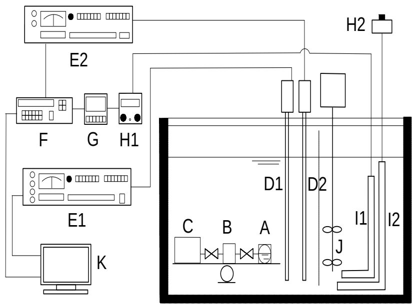

Fig.2.1.1-2 Experimental apparatus for vapor-liquid coexistence curve measurements. A: optical cell, B: expansion vessel, C: supplying vessel, D1, D2: 25 Ω standard platinum resistance thermometer, E1, E2: thermometer bridge, F digital multimeter, G: PID controller, H1, H2: voltage transformer, I1, I2: heater, J: stirrer, K: computer.

In the *PvT* property measurement apparatus shown in Fig. 2.1.1-1, a stainless steel pressure vessel with a pre-measured inner volume was filled with a sample whose mass was adjusted as per the desired density. The pressure vessel was directly connected to a high-precision pressure sensor and immersed in a liquid thermostatic bath in a silicon oil medium with a temperature fluctuation within ±1 mK. Temperature measurements were performed using a 25 Ω standard platinum resistance thermometer and an AC temperature measuring bridge and calculation were performed employing an ITS90. The sample density was calculated based on the filling mass of the sample and the inner volume of the pressure vessel with thermal correction for temperature. Further, pressure measurements are performed using a pressure transducer corrected for vacuum, and the temperature dependence of the pressure transducer was pre-calibrated. The measurement uncertainties were estimated to be within ±10 mK for temperature, ±1 kPa for pressure, and ±0.15% for density, although they varied slightly depending on the refrigerant type and temperature range. In addition, the refrigerant mixture composition was calculated as the ratio of the filling masses, and the uncertainty was estimated to be within ±0.05% using an electronic balance with a resolution of up to mg.

Figure 2.1.1-2 shows the apparatus employed for determining the saturation density and critical parameters by directly observing the meniscus disappearance with the naked eye. The apparatus comprised three cylindrical pressure vessels: an optical cell with Pyrex viewing windows to observe the meniscus behavior, a supplying vessel that was also used for initial sample filling, and an expansion vessel used for changing the density in the optical cell. Through the use of three vessels, up to eight data can be obtained in a single filling. This method is extremely effective for refrigerant blend measurements for which sample preparation is challenging, or for the measurement of novel fluids such as next-generation refrigerants, which has limited sample supply. The temperature of this apparatus is also measured using a 25 Ω standard platinum resistance thermometer, and the density is calculated based on the filling mass of the sample and the inner volume of the three pressure vessels while considering thermal compensation for the temperature. As this apparatus was not equipped with a pressure measurement system, critical pressure measurements were performed using the *PvT* property measurement apparatus shown in Fig. 2.1.1-1. The accuracy of the measurement differs for each refrigerant measurement; however, in general, the accuracies of temperature and density measurements are within ±10 mK and ±0.15 to 0.2%, respectively. In particular, the uncertainty of density is affected by the number of expansions; thus. each measurement exhibits a different uncertainty.

2.1.1.2 Targeted single refrigerants and refrigerant blends

In this research targeting next-generation refrigerants, their performance as refrigeration equipment and their ozone depletion potential (ODP) and global warming potential (GWP) as a measure against global environmental problems must be focused upon. In the course of the research, it has also become clear that other chemical properties, such as flammability, disproportionation reactions, and polymerization of refrigerant blends, are also important factors to be considered in the selection of next-generation refrigerants. Furthermore, the availability of refrigerants was also found to be a major selection factor, and the refrigerants targeted during the five years of the project are summarized in Table 2.1.1-1.

The references presented in Table 2.1.1-1, indicate the information already published in conference presentations along with published Journal papers. In addition to these, certain information has also been published in the 2018 (first year) and 2021 (previous year) editions of this progress report. This report focuses on the information that has not yet been published; thus, please refer to previous publications and progress reports. Moreover, that raw data for unpublished information will not be published in this report as well, as the publication of in advance is not possible.

Table 2.1.1-1 List of measured refrigerants/blends.

Year	Refrigerants/Blends	GWP	Ref.
2018	HFO1336mzz(E)	16	3, 4
	HCFO1224yd(Z)	1	5, 6
	R455A	151	7
2019	HFC32/HFO1123/HFO1234yf [21.2/59.5/19.3 mass%]	150	to be presented
	HFC32/HFO1123/HFO1234yf [21.2/40.3/38.5 mass%]	150	to be presented
	HFC32/HFO1123[additional experiment]	--	8
	HFO1123[additional experiment]	1	9
2020	R465A	148	7
	CF_3I	5	10, 11, 12
	HFC32/CF_3I [50/50 mass%]	355	13, 14
	HFC32/CF_3I [50/50 mol%]	152	13, 14
	HFO1123/CF_3I [50/50 mass%]	2.5	15
	HFO1123/CF_3I [50/50 mol%]	3.5	15
	HC290/HFO1234yf [50/50 mass%]	1	16
2021	HFC32/HFO1123/CF_3I [22/73/5 mass%]	155	to be presented
	HFC32/HFO1123/CF_3I [22/68/10 mass%]	156	to be presented
	HFC32/HFO1123/CF_3I [30/65/5 mass%]	212	to be presented
	HFC32/HFC125/CF_3I [49/11.5/39.5 mass%]	744	7, 11
	HFC125/CF_3I [50/50 mass%]	1728	14
2022	HFO1123/HC290 [80/20 mass%]	1	to be presented
	HFO1123/HC290/HFO1234yf [48/12/40 mass%]	1	to be presented
	HFO1123/HC290/HFO1234yf [32/8/60 mass%]	1	to be presented
	HFC32/HFO1336mzz(E) [40/60 mass%]	270	ongoing

	HFO1234yf/HFO1336mzz(E) [40/60 mass%]	1	ongoing
	HFO1234ze(E)/HFO1336mzz(E) [40/60 mass%]	1	ongoing

2.1.1.3 Thermodynamic properties of ternary refrigerant blends containing CF_3I

To evaluate the thermodynamic properties of ternary refrigerant blends containing CF_3I as a component refrigerant, the thermodynamic properties of binary refrigerant blends must be evaluated in advance. The ternary refrigerant blends considered in this project are the HFC32/HFO1123/CF_3I and HFC32/HFC125/CF_3I blends that have been approved by ASHRAE 34 as R466A; thus, they may be considered as targets. The binary refrigerant blends were HFC32/HFO1123, HFC32/CF_3I, HFO1123/CF_3I, HFC125/CF_3I, and HFC32/HFC125 blends. Among these, the HFC32/HFC125 blend provides reliable information because information on its thermodynamic properties had already been gathered when the R410A refrigerant blend began to be widely used. The thermodynamic properties of the HFC32/HFO1123 blend have already been evaluated in the previous project of the current NEDO project, and the HFC32/CF_3I and HFO1123/CF_3I blends were also introduced in the progress report prepared in FY2021 and summarized in Table 2.1.1-1. This report presents the results of the HFC125/CF_3I binary and ternary refrigerant blends, which were necessary for the evaluation of R466A.

(1) HFC125/CF_3I binary refrigerant blend

For the HFC125/CF_3I [50/50 mass%] binary refrigerant blend, the *PvT* properties were measured in the temperature range of 305 to 400 K, pressure range of 1214 to 6868 kPa, and density range of 105 to 1402 kg m^{-3}. A total of 96 data points were obtained along eight isochores for both 1- and 2-phase regions. The measured *PVT* properties of this blend are shown in the *PT* diagrams presented in Fig. 2.1.1-3, wherein the solid line indicates the isochores calculated from REFPROP 10.0. Comparisons of the measured and calculated values revealed a large difference, particularly in the liquid phase region. This difference may be attributed to the equation of state of CF_3I, and the lack of thermophysical properties of a single component for CF_3I.

For the saturation density of HFC125/CF_3I [50/50 mass%], seven saturated vapor densities, five saturated liquid densities, and one datum in the very vicinity of the critical density were measured through meniscus disappearance observations. Moreover, four saturated densities were also determined from the inflection point of the isochores. The measured results are shown in Fig. 2.1.1-4. Further, vapor-liquid coexistence curves for both components calculated from REFPROP 10.0 were also drawn. The orange curve in Fig. 2.1.1-4 is the calculated vapor-liquid coexistence curve from REFPROP 10.0. Similar to that observed in Fig. 2.1.1-3, there is a large difference between the experimental and measured values.

The critical point of the HFC125/CF_3I [50/50 mass%] blend was determined based on the meniscus disappearance position and the intensity of the critical opalescence based on the results of this experiment. The results were T_c=353.79 K, P_c=3815 kPa, and ρ_c=705 kg m^{-3}. Further, the composition dependence of the critical locus determined by the correlation method[17)], which has been conventionally used to correlate the critical locus of CFC refrigerants, is also depicted in the $T\rho$ diagram in Fig. 2.1.1-4.

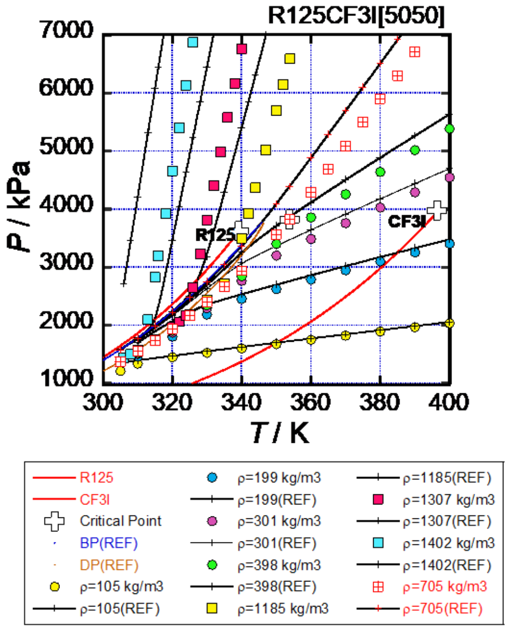

Fig. 2.1.1-3 *PVT* property measurements of HFC125/ CF_3I [50/50 mass%]. Solid line is the isochores drawn by REFPROP 10.0

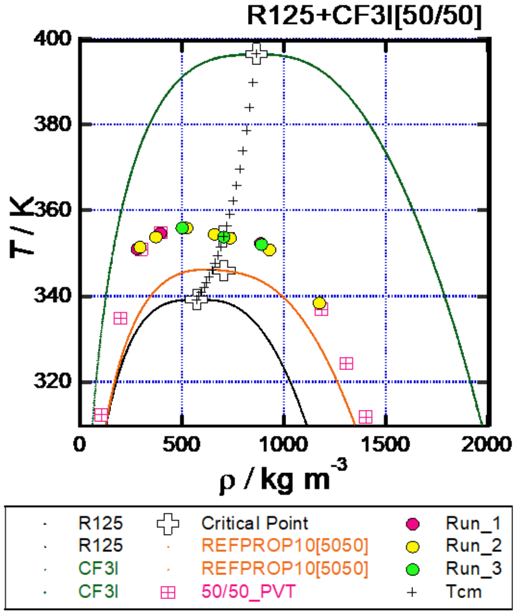

Fig. 2.1.1-4 Vapor-liquid coexistence curve of HFC125/ CF_3I [50/50 mass%]. Orange line is the vapor-liquid coexistence curve drawn by REFPROP 10.0.

(2) HFC32/HFC125/CF_3I ternary refrigerant blend

In the ternary HFC32/HFC125/CF_3I blend, the composition ratio of 49/11.5/39.5 mass%, for which the ASHRAE refrigerant designation was obtained as R466A, was measured. The *PvT* properties were measured at temperatures of 300 K to 400 K, pressures of 1690 to 6715 kPa, and densities of 101 to 1105 kg m^{-3}, and a total of 79 data points from both 1- and 2-phase regions were obtained along seven isochores. The measured *PvT* property data are shown in the *PT* diagram presented in Fig. 2.1.1-5, wherein the solid line indicates the isochores calculated from REFPROP 10.0. However, in REFPROP 10.0, all the mixing parameters for this system have not been determined, and thus, the reliability of the calculations cannot be guaranteed.

In the measurement of the saturation density of HFC32/HFC125/CF_3I [49/11.5/39.5 mass%], five saturated vapor densities and seven saturated liquid densities were measured based on meniscus disappearance observations. In addition, six saturation densities were determined from the inflection point of the isochores obtained in this project. The results are shown in Fig. 2.1.1-6, together with the vapor-liquid coexistence curves of the two components and the vapor-liquid coexistence curve calculated from REFPROP 10.0. It is evident that the REFPROP 10.0 results differed significantly from the experimental results shown in the plots. This may be attributed to the mixing parameters of HFC125/CF_3I not being optimized as of yet.

The critical point of the HFC32/HFC125/CF3I [49/11.5/39.5 mass%] blend was determined to be T_c=351.34 K, P_c=5295 kPa, and ρ_c=578 kg m^{-3} from the meniscus disappearance position and the intensity of the critical opalescence. The measured critical parameters of this ternary refrigerant blend have also not been reported until now. Whereas, the critical parameters presented in REFPROP 10.0 are T_c = 346.28 K, P_c = 5283 kPa, and ρ_c = 569 kg m^{-3}. The differences between the two were approximately 5 K, 12 kPa, and 9 kg m^{-3}, for the critical temperature, pressure, and density, respectively.

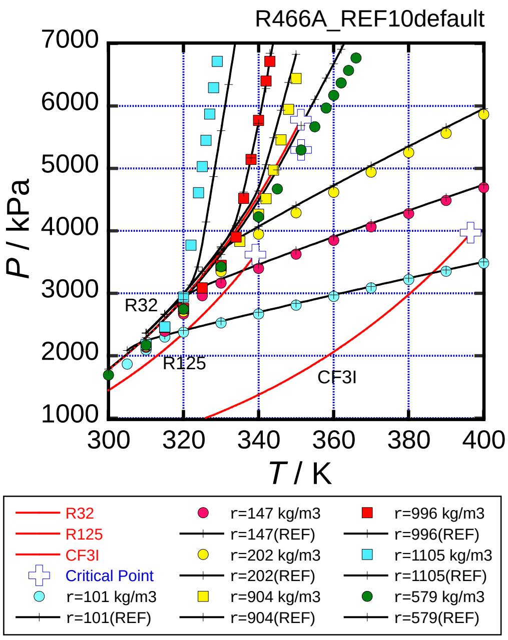

Fig. 2.1.1-5 *PVT* property measurements of HFC32/HFC125/CF3I [49/11.5/39.5 mass%=R466A]. Solid line is the isochores drawn by REFPROP 10.0.

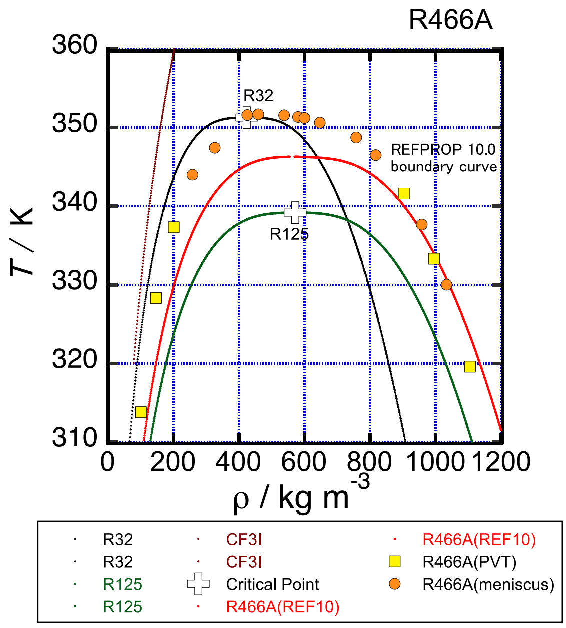

Fig. 2.1.1-6 Vapor-liquid coexistence curve of HFC32/HFC125/CF3I [49/11.5/39.5 mass%= R466A]. Orange curve is the coexistence curve drawn by REFPROP 10.0.

(3) HFC32/HFO1123/CF3I ternary refrigerant blend

The *PvT* properties of ternary HFC32/HFO1123/CF3I blend including the low GWP refrigerant HFO1123 developed by AGC company in a previous NEDO project were measured for three composition ratios of (1) 22/68/10 mass%, (2) 22/73/5 mass%, and (3) 30/65/5 mass%. Measurements were performed in the temperature range of room temperature to 400 K and pressure range up to 7 MPa, with two vapor-phase and two liquid-phase isochores. The compositions were selected based on advice from the project leader. The initial plan was to measure the critical parameters and saturation density as well as the *PvT* properties of this ternary refrigerant blend; however, this was interrupted during the measurement of the HFO1123/CF3I refrigerant mixture because of a change in the sample inside the sample vessel, which may interfere with the measurement equipment. Thus, the measurement had to be suspended. This phenomenon has been confirmed through several subcontractors. Consequently, the isochores near the critical density could not be measured in Figs. 2.1.1-7 to 2.1.1-9.

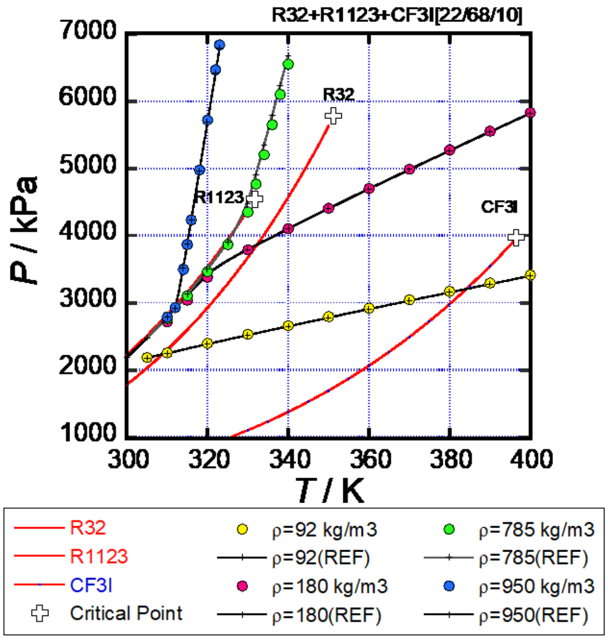

Fig. 2.1.1-7 *PvT* property measurements of HFC32/HFO1123/CF_3I [22/68/10 mass%].
Solid line is the isochores drawn by REFPROP 10.0.

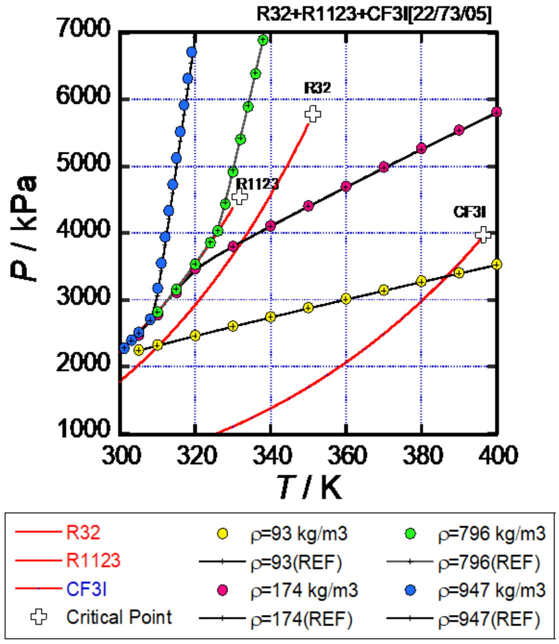

Fig. 2.1.1-8 *PvT* property measurements of HFC32/HFO1123/CF_3I [22/73/5 mass%].
Solid line is the isochores drawn by REFPROP 10.0.

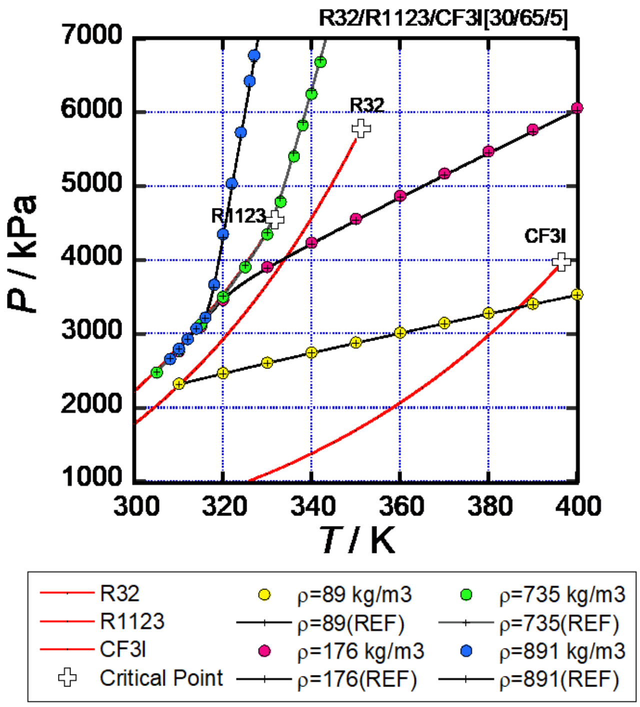

Fig. 2.1.1-9 *PvT* property measurements of HFC32/HFO1123/CF_3I [30/65/5 mass%].
Solid line represents the isochores drawn by REFPROP

Comparisons of the measured plots in the figure and the calculated results of REFPROP 10.0, shown as solid lines, with other refrigerant blends that have already been measured and compared, revealed consistency for this blend. In terms of density deviation, the maximum deviation was within 1%, and a majority of the average deviations were within 0.5%. Considering the reproducibility of the aforementioned CF_3I refrigerant blend in the liquid phase, it was initially thought that calculation accuracy could not be expected to be very high; however, the weight of CF_3I was low in all three compositions, and it was assumed that the majority of the calculation accuracy was dependent on the binary HFC32/HFO1123 blend. We speculate that most of this is dependent on the calculation accuracy of the binary HFC32/HFO1123 blend. For the binary HFC32/HFO1123 blend, the thermodynamic properties of both the single-component refrigerant and their blends have already been measured by this research team[18, 19], and reliable equations of state and mixing parameters have already been published, which may have led to the results shown in this study.

2.1.1.4 Thermodynamic properties of the binary HFO1123/HC290 refrigerant blend

As mentioned in Section 2.1.1.3(c), HFO1123 was newly developed as a domestically produced refrigerant in the NEDO project. HFO1123 exhibits a relatively low critical temperature ($T_c = 331.73$ K) compared to other low-GWP refrigerants. Moreover, its thermodynamic properties are similar to those of HFC32, which renders it a refrigerant suitable for use in air conditioners. However, it may result in disproportionation reactions, which hinders its development. In this project, a group led by the University of Tokyo has been conducting research from a risk assessment perspective, and it has emerged that mixing HFO1123 with HC290 may potentially suppress the disproportionation reaction. Therefore, to further advance the performance evaluation of HFO1123/HC290, a priority was assigned to the evaluation of the HFO1123/HC290 blend in this study.

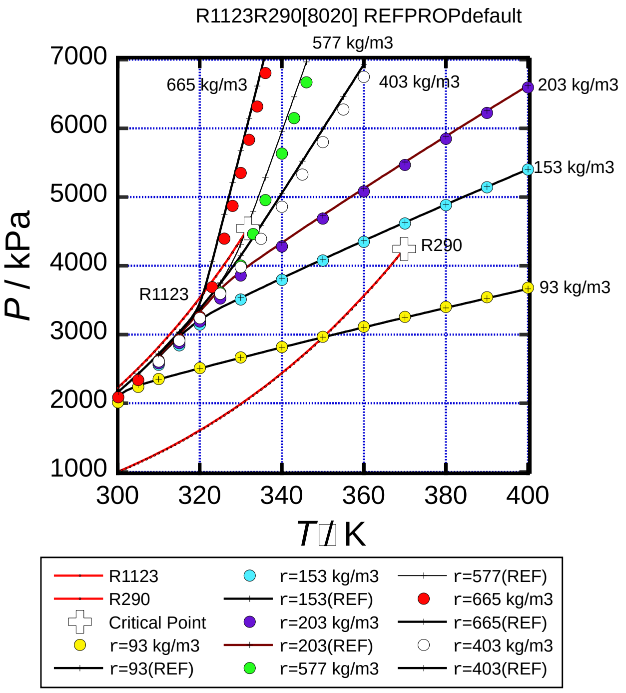

Fig. 2.1.1-10 *PvT* property measurements of HFO1123/ HC290 [80/20 mass%]. Solid line is the isochores drawn by REFPROP 10.0

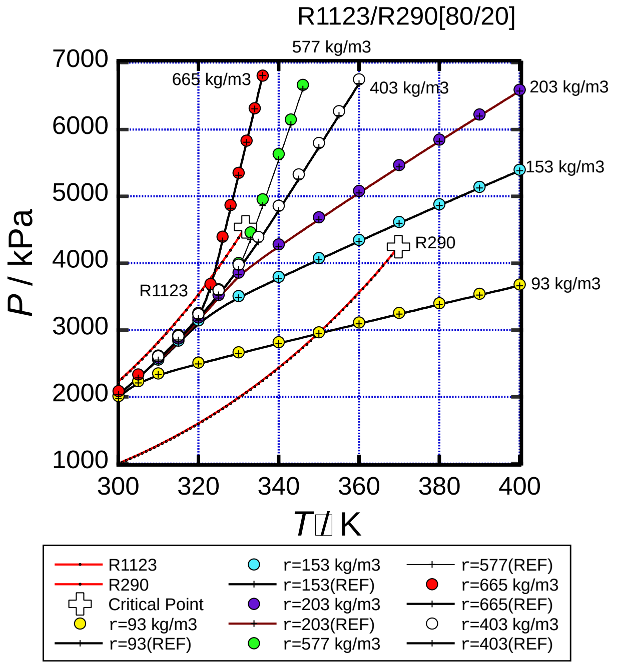

Fig. 2.1.1-11 *PvT* property measurements of HFO1123/ HC290 [80/20 mass%]. Solid line is the isochores drawn by REFPROP 10.0 modified by this project

For the binary HFO1123/HC290[80/20 mass%] blend, *PvT* properties were measured in the temperature range of 300 to 400 K, pressure range of 2013 to 6806 kPa, and density range of 93 to 665 kg m^{-3}, and a total of 67 data points were obtained along six isochores, including both one- and two-phase regions. The experimental results of the *PvT* properties for this blend are shown in the two *PT* plots presented in Figs. 2.1.1-10 and Fig. 2.1.1-11. The plots of these two figures show the same data; however, there is a difference in the isochores drawn in them. Figure 2.1.1-10 shows the calculation results using the default version of REFPROP 10.0, which is widely available, whereas Fig. 2.1.1-11 shows the results using the binary mixing parameters of HFO1123/HC290 blend determined in this project. Specifically, Fig. 2.1.1-11 shows the calculation results using the binary mixing parameters of the HFO1234yf/HC290 blend, which were determined using the measured refrigerant properties data of this project. Although determining and calculating the binary mixing parameters specifically for HFO1123/HC290 using the results of this project would be ideal, it was not possible at the time this report was prepared (end of October 2022). However, compared to the REFPROP 10.0 default version, which used estimated mixing parameters, the improved version of the calculation exhibited better data reproducibility, particularly on the liquid side. When using mixing parameters with inferred results, certain uncertainties are unavoidable, such as the agreement or lack of agreement depending on the type of refrigerant mixture. In conclusion, optimization verification based on measured data is essential.

When measuring the saturation density of HFO1123/HC290[80/20 mass%], four saturated vapor densities, five saturated liquid densities, and one datum in the very vicinity of the critical density were measured through meniscus disappearance observations. Moreover, the saturation densities at five points were determined from the inflection point of the isochores. The results are shown in Fig. 2.1.1-12, along with the vapor-liquid coexistence curves for both components calculated from REFPROP 10.0. The blue curve in the figure is the calculated vapor-liquid coexistence curve for the REFPROP 10.0 default, and the orange curve represents the calculated result by fitting the mixing parameters of HFO1234yf/HC290 blend to the HFO1123/HC290 blend. The latter exhibited a behavior closer to that of the experimental data, indicating that it has been improved.

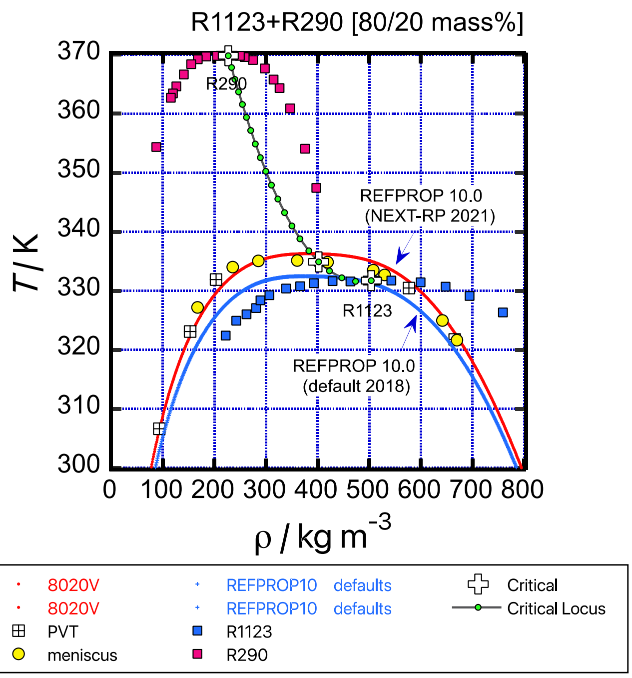

Fig. 2.1.1-12 Vapor-liquid coexistence curve of HFO1123/HC290 blends. Blue coexistence curve is the REFPROP 10.0(default) calculation. Orange coexistence curve is the REFPROP 10.0 calculation modified by this project. In this figure, critical locus is also

The critical point of the HFO1123/HC290 [80/20 mass%] refrigerant blend was determined to be T_c=334.914 K, P_c=4392 kPa, ρ_c=402 kg m^{-3} based on the meniscus disappearance position and the intensity of the critical opalescence. There have been no experimental reports on the critical parameters of this binary refrigerant blend till date.

The critical parameters presented in REFPROP 10.0 are T_c = 332.44 K, P_c = 4353 kPa, and ρ_c = 395 kg m^{-3}. The differences between the two were approximately 2.5 K, 39 kPa, and 7 kg m^{-3} for the critical temperature, pressure, and density, respectively. Figure 2.1.1-12 shows the predicted critical locus of this blend.

2.1.1.5 Thermodynamic properties of the binary HFO1123/HC290 refrigerant blend

In the development of next-generation refrigerants, a low global warming potential (GWP) is the most important requirement. However, in addition to these conditions, safety must be ensured. In addition, measures to reduce flammability must be adopted. However, the binary blend refrigerant HFO1123/HC290, which was newly evaluated in Section 2.1.1.4, mixes HFO1123, an A2 refrigerant, with HC290, an A3 refrigerant; thus, the flammability issue is yet to be completely resolved. As a countermeasure, the third refrigerant with low flammability can be blended with the HFO1123/HC290 system as a third refrigerant from the refrigerant perspective. We began evaluating a ternary blend of HFO1123/HC290/HFO1234yf with the addition of HFO1234yf, an A2L refrigerant. Although HFO1234yf is actually a specific inert gas and not a completely nonflammable refrigerant, it was selected for its availability.

For the compositions measured, two types were selected for HFO1123/HC290/HFO1234yf: (1) 48/12/40 mass% and (2) 32/8/60 mass%. However, a sample of HFO1123 ran out during the course of the measurements, and additional supplies could not be procured in time; thus, this report is not complete with respect to the determination of the saturation density and critical point.

For the ternary HFO1123/HC290/HFO1234yf [48/12/40 mass%], *PvT* properties were measured in the temperature range of 305 to 400 K, pressure range of 1650 to 6888 kPa, and density range of 88 to 804 kg m^{-3}. The measured *PvT* properties of this blend are shown in the *PT* diagram presented in Fig. 2.1.1-13, wherein, the solid lines show the isochores calculated from REFPROP 10.0. Further, the mixing parameters for HFO1123/HC290 have not yet been determined, as explained in the previous section, and the mixing parameters for HFO1234yf/HC290 were used in this calculation. As evident from Fig. 2.1.1-13, the reproducibility between the experimental and calculated values was satisfactory. Further improvement in accuracy can be achieved if the mixing parameters can be determined in the future when vapor-liquid equilibrium data become available.

For the ternary HFO1123/HC290/HFO1234yf [32/8/60 mass%] blend, *PvT* properties were measured in the temperature range of 305 to 400 K, pressure range of 1387 to 6888 kPa, and density range of 101 to 804 kg m^{-3}. The results of the *PvT* measurements for this blend are shown in the *PT* diagram presented in Fig. 2.1.1-14. Comparisons of Fig. 2.1.1-14 with Fig. 2.1.1-13 revealed a slight discrepancy between the measured and calculated values; particularly in the isochores on the liquid phase. As mentioned above, the optimization of the mixing parameters for this blend was not complete at this time, and we surmise that this may be because of the differences in composition.

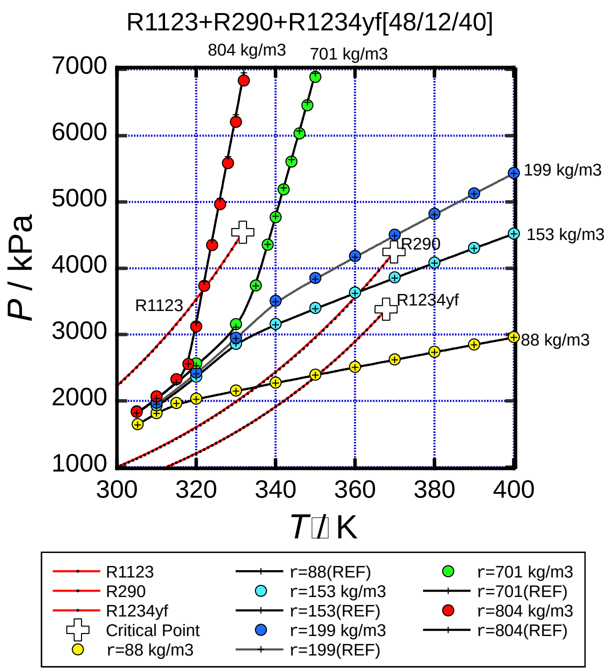

Fig. 2.1.1-13 *PVT* property measurements of HFO1123/HC290/HFO1234yf [48/12/40 mass%]. Solid line is the isochores drawn by REFPROP 10.0.

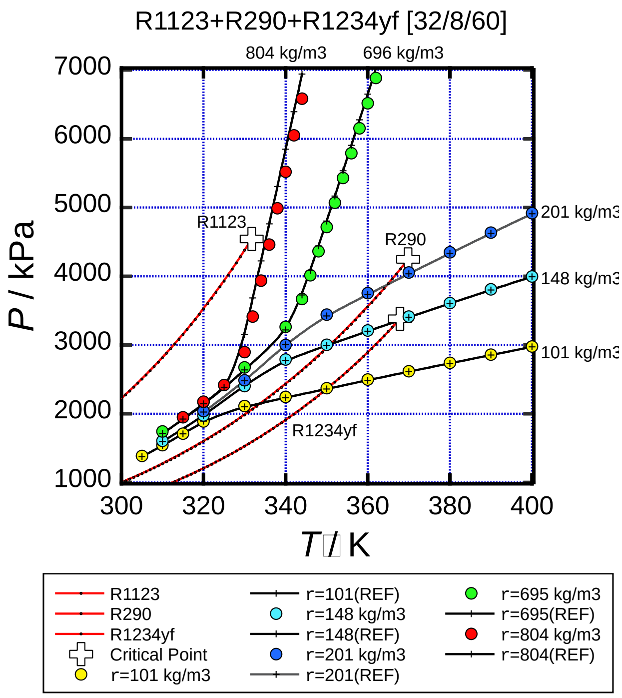

Fig. 2.1.1-14 *PVT* property measurements of HFO1123/HC290/HFO1234yf [32/8/60 mass%]. Solid line is the isochores drawn by REFPROP 10.0.

References

1) R. Akasaka, S. Fukuda, K. Miyane, and Y. Higashi: J. Chem. Eng. Data, 67, 346(2022).
2) R. Akasaka, Y. Kayukawa, and Y. Higashi: Int. J. Thermophys., 43:159, (2022).
3) N. Sakoda and Y. Higashi: Proc. of the 2019 JSRAE Annual Conference, Tokyo, D144(2019).
4) N. Sakoda, Y. Higashi, and R. Akasaka: J. Chem. Eng. Data, 66, 734(2021).
5) N. Sakoda and Y. Higashi: Proc. of the 39th Japan Symposium on Thermophysical Properties, Nagoya, B311(2018).
6) N. Sakoda and Y. Higashi: J. Chem. Eng. Data, 64, 3983(2019).
7) Y. Higashi, K. Miyane: Proc. of the 2022 JSRAE Annual Conference, Okayama, A114(2022).
8) H. Miyamoto, T. Saito, N. Sakoda, U. Perera, T. Ishii, K. Thu and Y. Higashi: Int. J. Refrig., 1198, 340(2020).
9) N. Sakoda, Md. A. Isram, Y. Takata, S. Koyama, and R. Akasaka: J. Chem. Eng. Data, 63(2). 417 (2018).
10) U. A. Perera, K. Thu, N. Sakoda, K. Miyane, and Y. Higashi: J. Chem. Eng. Data, 67. 2182(2022).
11) U. A. Perera, K. Thu, T. Miyazaki, N. Sakoda and Y. Higashi : presented at 21st Symposium on Thermophysical Properties, Boulder, USA (2021, June).
12) N. Sakoda and Y. Higashi: presented at 21st Symposium on Thermophysical Properties, Boulder, USA (2021, June).
13) N. Sakoda and Y. Higashi: presented at 6th IIR Conference on Thermophysical Properties and Transfer Processes of Refrigerants (TPTPR2021), Vicenza, Italy, (2021, Sept.)
14) R. Akasaka, Y. Kayukawa, and Y. Higashi: Int. J. Thermophysics, 43:159 (2022).
15) K. Kitabatake, H. Ishimaru, N. Sakoda, and Y. Higashi: Presented at 13th Asian thermophysical Properties Conference, OS17-2-03, Sendai, Japan(2022, Sept.)
16) R. Akasaka, S. Fukuda, K. Miyane, and Y. Higashi: J. Chem. Eng. Data, 67, 346(2022).
17) Y. Higashi, Y. Kabata, M. Uematsu, and K. Watanabe: J. Chem. Eng. Data, 33(1), 23(1988).
18) Y. Higashi and R. Akasaka: Proc. 16th Int. Refrigeration and Air Conditioning Conference, Purdue, USA(2016).
19) R. Akasaka: Proc. 11th Asian Thermophys. Prop. Conf., Yokohama, Japan (2016).

2.1.2 Vapor-liquid equilibrium measurements

The results of Toyama Prefectural University (Section 2.1.2.1) and Kyushu University (Section 2.1.2.2) are reported below for vapor-liquid equilibrium property measurements. References are attached together after Section 2.1.2.2.

2.1.2.1 Vapor-liquid equilibrium measurements at Toyama Prefectural University

Toyama Prefectural University has been measuring the vapor-liquid equilibrium properties (boiling point and dew point pressure, saturated liquid density) and associated $P\rho Tx$ properties. The recirculation-type vapor-liquid equilibrium property measuring apparatus can be employed for measuring vapor-liquid equilibrium properties, and is characterized based on the fact that equilibrium disruption owing to pressure fluctuations during sample collection is small, and the reliability of this measurement is high. Figure 2.1.2-1 shows a schematic of the equipment[1)]. The apparatus includes (a) sample recirculation section, (b) expansion section, (c) GC section, and (d) injection machine for sample filling and an evacuation section. The sample circulation section (a) comprised a 380 cm^3 optical cell A and two circulation loops. Each loop artificially reproduced the vapor-liquid interface (meniscus), and circulated 1. vapor → liquid and 2. liquid → vapor. Circulation was performed using a piston-type liquid transfer pump D. It was devised to prevent droplets and air bubbles that can cause data failure. Following confirmation that the circulation reached an equilibrium state on the output screen of BenchVue (manufactured by Keysight Technologies), a small amount of each circulation sample was scooped. The entire system was installed in a liquid constant temperature bath, and the temperature of the heat medium (water) was measured and controlled via a platinum resistance thermometer and a thermometer bridge F201 (manufactured by Chino Co., Ltd.). The pressure inside the optical cell was measured using a quartz oscillation pressure gauge 31K-101 (Paroscientific Inc., USA). Whereas, in the expansion part (b), the small amount of sample sandwiched in (a) was completely gasified at 100 °C, and then entirely mixed with He (purity 99.999 vol%) for uniformity. It comprised two loops as in (a). Thereafter, the sample was instantaneously pinched via a 6-way valve from each loop and sent to the capillary column PoraPLOT Q

(Agilent Technologies, Inc.) in the gas chromatograph GC-3200 (GL Sciences, TCD type) (c). The column had a length of 25 m, an inner diameter of 0.53 mm, and a film thickness of 20 µm. The area fraction (area%) of the substance can be obtained from the *V-t* diagram output by the GC, with the arrival time at the outlet indicating the type of substance whereas the intensity of the detected value indicates the quantity. The composition (mol%) was obtained from this numerical value and the calibration curve prepared separately. Further, the sample was prepared by filling each component individually into the optical cell of (a) using a piston-cylinder gas injection machine in the sample filling section (d). The cylinder had a capacity and compression ratio of 300 cm^3 and 4, respectively, and was equipped with a safety device capable of determining the pressure required to stop compression.

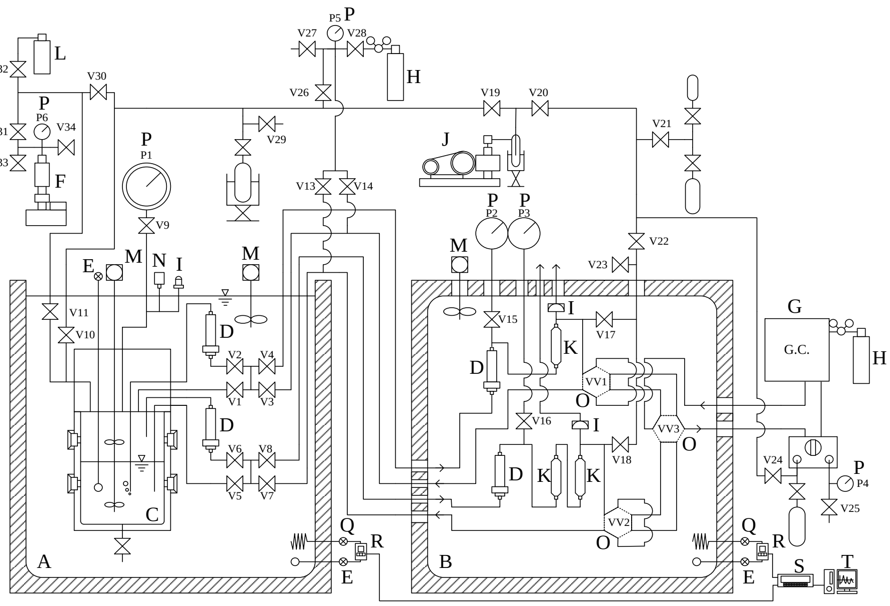

(A) Liquid thermostat bath
(B) Air thermostat bath
(C) Optical cell
(D) Circulation pump
(E)Platinum resistance thermometer
(I) Safety valve
(J) Vacuum pump
(K) Expansion vessel
(L) Sample container
(M) Stirrer
(N) Pressure gauge
(Q) Heater
(R) PID controller
(S) Digital multimeter

Fig. 2.1.2-1 Recirculation-type vapor-liquid equilibrium apparatus.

For calibrating the values obtained by the gas chromatograph, the following calibration equation, Eq. (2.1.2-1), was regressed based on the present data, that obtained by Nagasaki university, and that obtained by Kyushu university. Based on this equation, the composition (mol fraction) of the sample was calculated from the measured value (area%) via a gas chromatograph.

$$M_{\mathrm{comp\ 1}} = A_{\mathrm{comp\ 1}} + a \times A_{\mathrm{comp\ 1}}\,(1 - A_{\mathrm{comp\ 1}}) \tag{2.1.2-1}$$

As an example, Fig. 2.1.2-2 shows the distribution of the calibration data for the R32/R1123 and R32/R1234yf binary mixtures and the calculated values from the calibration equations. This ensures the reliability of the composition measurement values.

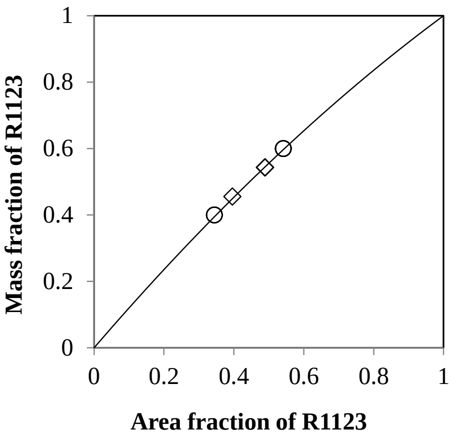

(a) R32/R1123 mixtures

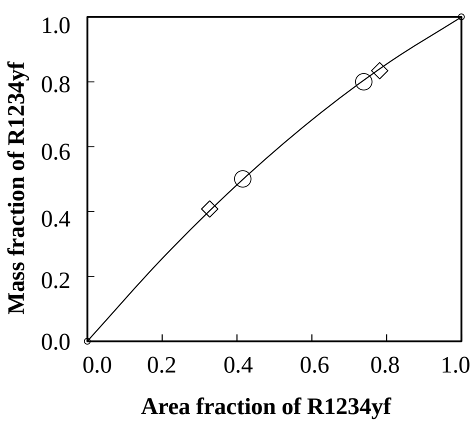

(b) R32/R1234yf mixtures

Fig. 2.1.2-2 Distributions of the calibration data. ◇ : Toyama prefectural University, ○ : Kyusyu University.

The expanded uncertainty (with the coverage factor, k=2,) of this measurement apparatus was 0.03 K for temperature, 0.60% for pressure, and 0.51 mol% for composition measurements. The uncertainty budget table is shown in Table 2.1.2-1.

Table 2.1.2-1 Expanded uncertainties (k = 2) and uncertainty sources for the measurements in this study

	For the temperature measurements	
$u_{T,1}$	temperature fluctuation	0.01 K
$u_{T,2}$	uncertainty of the sensor	0.01 K
U_T	Expanded Uncertainty	0.03 K
	For the pressure measurements	
$u_{P,1}$	uncertainty of the sensor	0.28%
$u_{P,2}$	uncertainty of the dynamic strain measuring instrument	0.11%
U_P	Expanded Uncertainty	0.60%
	For the composition measurements	
$u_{x,1}$	repeatability of the GC data	0.214 mol%
$u_{x,2}$	uncertainty regarding the present calibration factor	0.136 mol%
$U_{x,\mathrm{isopentane}}$	Expanded Uncertainty	0.51 mol%

Next, the bellows variable volumometer type vapor-liquid equilibrium property measurement apparatus is described. The principle of this device is the variable volume method, and it facilitates precise measurements of the vapor-liquid equilibrium and the accompanying $P\rho Tx$ properties in the temperature range of 280 to 600 K and pressure range of up to 30 MPa. Figure 2.1.2-3 shows the schematic of this apparatus. In this measurement, the mass and composition of the sample were prepared and measured in advance in a separate container. After connecting this container to bellows container A, the temperature difference ($\triangle T$ = approximately 200 °C) was applied to this container to fill the sample. The mass and composition of the sample were determined from the mass before and after filling the container and the composition of the remaining sample after filling. Subsequently, the volume of the sample was controlled and measured considering a resolution of 0.2 μℓ after controlling the state of the sample at an arbitrary temperature and pressure. Further, the density was calculated from the sample mass and measurement volume. Consequently, the $P\rho Tx$ properties can be clarified with high accuracy. As the measured values can be obtained on the isothermal line, we carefully clarified the vapor-liquid equilibrium properties (boiling point pressure and saturated liquid density) from the inflection point of the isotherm in the saturated state. The distributions of the obtained measured values on the $P\rho$ diagrams are shown later. The expanded uncertainties (k = 2) of this apparatus were 3 mK for temperature measurement, 1.43 kPa ($P \leq 7$ MPa) and 0.06% (7 MPa < $P \leq 30$ MPa) for pressure measurement, and 0.11% for density measurements.

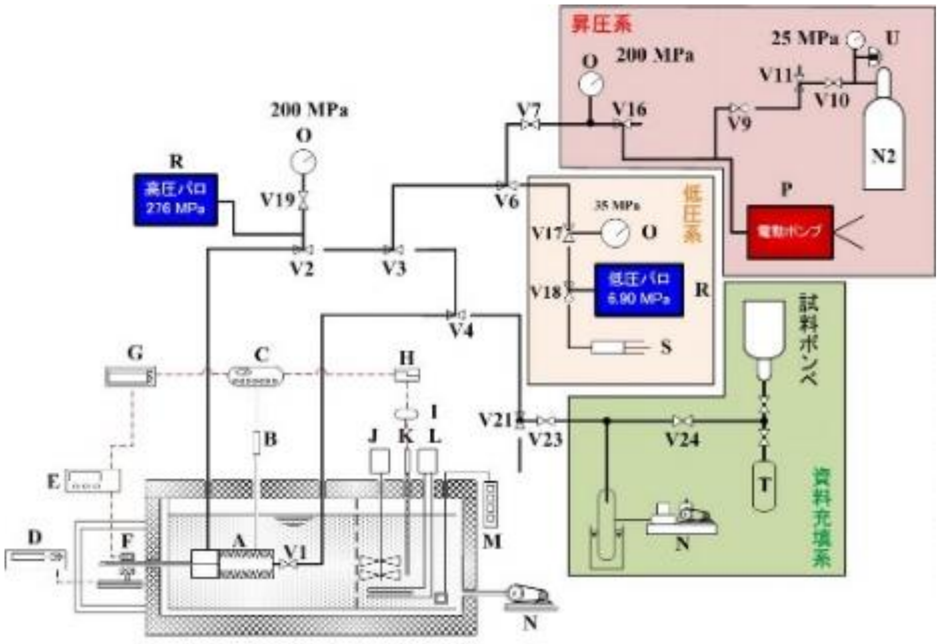

(A) Pressure vessel and Bellows
(B) Platinum resistance thermometer
(C) Thermometer bridge
(D) Magnescale
(F) Difference transformer
(G) Data logger
(H) PID controller
(I) Thyristor regulator
(K) Sub heater
(L) Main heater
(M) Cooler
(N) Vacuum pump
(P) Electric pump
(R) Pressure gauge
(U) Safety valve

Fig. 2.1.2-3 Bellows variable volumometer type vapor-liquid equilibrium property measurement apparatus.

The present measurement results are summarized in Table 2.1.2-2. In particular, for HFC32/HFO1234yf/HFO1123 mixtures, a total of 621 measured values were obtained for 3 types of binary and ternary mixtures, which were published by the authors as original papers[10-13]. The details are reported below.

Table 2.1.2-2 Present measurement data for the binary and ternary mixtures

Mixtures	Temperatures(K)	Pressures(MPa)	Data points	
HFC32/HFO1123[10]	300-330	2.1-4.4	22	
HFC32/HFO1234yf[11]	300-330	1.0-2.9	56	
HFO1234yf/HFO1123[12]	300-330	1.0-3.3	116	
HFC32/HFO1234yf /HFO1123(1) [13]	303-328	1.9-3.2	32 (P_{bub}, P_{dew}) 7 (ρ')	Same as AMOLEA 150Y4,5
HFC32/HFO1234yf /HFO1123(2) [13]	278-328	0.9-6.4	53 (P_{bub}, P_{dew}) 14 (ρ') 321 ($P\rho Tx$)	Other compositions
HFO1123/CF_3I	303-333	1.8-3.9	30 (P_{bub}, P_{dew})	
HFO1123/HC290	303-333		measuring	

First, we report the measurement results of binary mixtures, HFC32/HFO1123, HFC32/HFO1234yf, and HFO1123/HFO1234yf. In this study, reliable boiling point and dew point pressure measurements were performed for these binary systems in temperature, pressure, and composition ranges of 300 to 330 K, pressures of 1.0 to 4.4 MPa, and mole fractions of 0.1 to 0.9. Figures 2.1.2-4 to 6 show the distribution of these measured values on the Px diagram. For reference, Figs. 2.1.2-7 to 9 show the relative pressure deviations of the boiling point and dew point based on the latest REFPROP ver. 10.0 (Kuntz-Wagner mixing rule). Because the latest REFPROP ver. 10.0 has not been regressed to each measured value obtained by the authors for the first time, remarkable deviations were observed for certain binary mixtures. To confirm the validity of this deviation, we attempted to correlate it with the measured values using the modified Peng-Robinson equation of state. The modified Peng-Robinson equation of state correlated in this study is shown in Eqs. 2.1.2-2 to 7 as follows;

$$P = \frac{RT}{V_\mathrm{m} - b} - \frac{a}{V_\mathrm{m}(V_\mathrm{m}+b)+b(V_\mathrm{m}-b)} \tag{2.1.2-2}$$

where

$$a_\mathrm{i} = 0.45724\alpha_\mathrm{i}\frac{R^2T_\mathrm{ci}^2}{p_\mathrm{ci}} \quad b_\mathrm{i} = 0.07780\frac{RT_\mathrm{ci}}{p_\mathrm{ci}} \tag{2.1.2-3}$$

$$\alpha_\mathrm{i}(T) = \left[1 + c_1\left(1-\sqrt{\frac{T}{T_\mathrm{C}}}\right) + c_2\left(1-\sqrt{\frac{T}{T_\mathrm{C}}}\right)^2 + c_3\left(1-\sqrt{\frac{T}{T_\mathrm{C}}}\right)^3\right]^2 \tag{2.1.2-4}$$

Here, the mixing rules are:

$$a = \sum_\mathrm{i}\sum_\mathrm{j} x_\mathrm{i}x_\mathrm{j}a_\mathrm{ij} \tag{2.1.2-5}$$

$$a_\mathrm{ij} = \left(1-k_\mathrm{ij}\right)\sqrt{a_\mathrm{i}a_\mathrm{j}} \tag{2.1.2-6}$$

$$b = \sum_\mathrm{i} x_\mathrm{i}b_\mathrm{i} \tag{2.1.2-7}$$

Table 2.1.2-3 Parameters of the modified Peng-Robinson equation of state

	C_1	C_2	C_3	k_{ij}
R32	0.85	-0.92	3.0	
R1234yf	0.83	-0.77	2.7	
R1123	0.78	-1.00	5.3	
R32/R1234yf				0.042
R32/R1123				0.039
R1123/R1234yf				-0.006

Each parameter is shown in Table 2.1.2-3. The calculation results from this equation of state are plotted as a solid line (boiling point) and a broken line (dew point) in the Figs. The mixing rule adopted in this equation of state was a simple Lorentz-Berthelot mixing rule, with only one parameter for each binary mixture. Therefore, the deviation diagrams show that the measured values indicate thermodynamically reasonable compositional behavior. Akasaka and Lemmon developed a new Helmholtz free-energy type equation of state (abbreviated as Akasaka and Lemmon equation of state below) using these measured values as input values. This model will be implemented in the next version of REFPROP. As an example, the deviation from the Akasaka and Lemmon equation of state is shown in Fig. 2.1.2-10. Owing to the good correlation, the improvement in the reliability was confirmed.

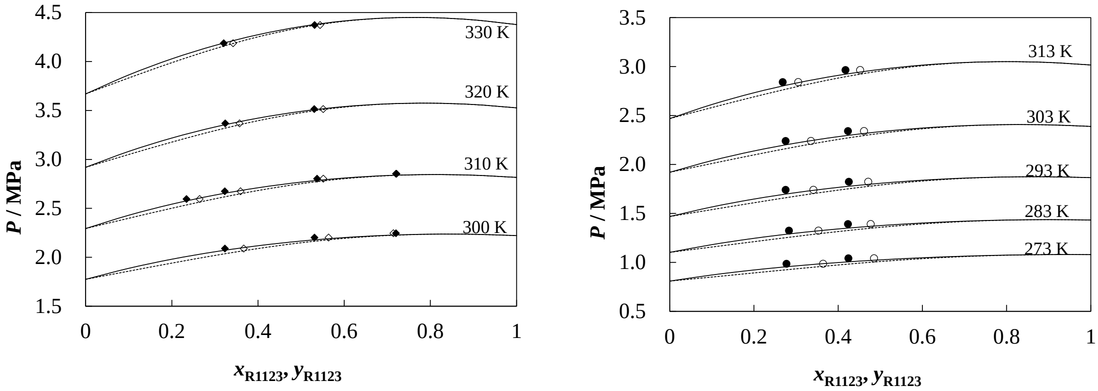

Fig. 2.1.2-4 Distribution of the present VLE data for HFC32/HFO1123 binary mixtures. (◆◇) Toyama prefectural university, (●○) Kyushu university, (— --) bubble and dew point pressure values from the Akasaka model[4] calculated using the REFPROP 10.0[5] software package. The left figure shows measured data at temperature values that were close to the integer values in absolute temperature, whereas the right figure shows data at temperature values that were close to the integer values in degrees Celsius.

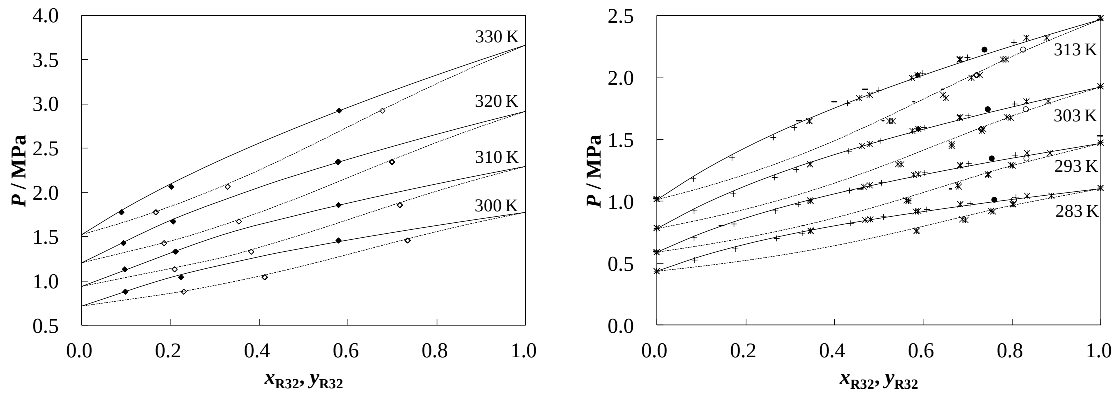

Fig. 2.1.2-5 Distribution of the present VLE data for HFC32/HFO1234yf binary mixtures. (◆◇) Toyama prefectural university, (●○) Kyushu university, (∗, -, +) Literature data, (— --) bubble and dew point pressure values from the Akasaka model[6] calculated using the REFPROP 10.0[5] software package.

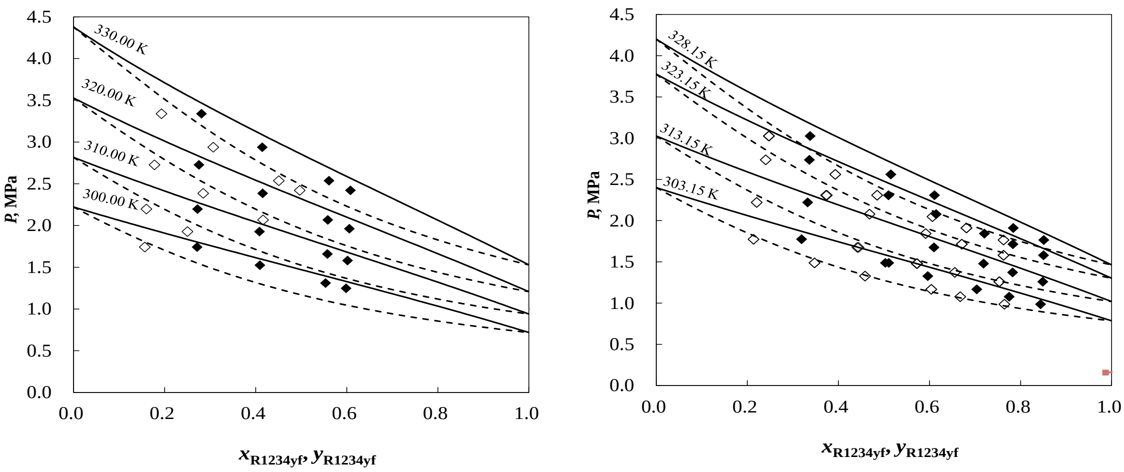

Fig. 2.1.2-6 Distribution of the present VLE data for HFO1123/HFO1234yf binary mixtures. (◆◇) Toyama prefectural university, (— --) bubble and dew point pressure values calculated using the REFPROP 10.0[5] software package.

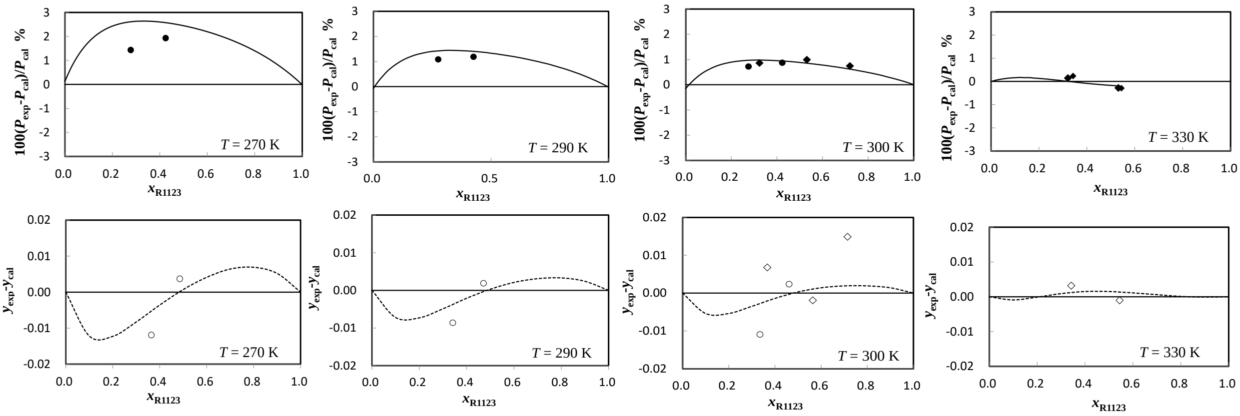

Fig. 2.1.2-7 Deviation plots of the present VLE data for HFC32/HFO1123 binary mixtures using the Akasaka model[4]. (◆◇) Toyama prefectural university, (●○) Kyushu university, (— --) bubble point pressure and vapor phase mole fraction values from the present Peng-Robinson equation of state modified by Mathias and Copeman[7]. The baseline represents values from the Akasaka model[4] calculated using the REFPROP 10.0[5].

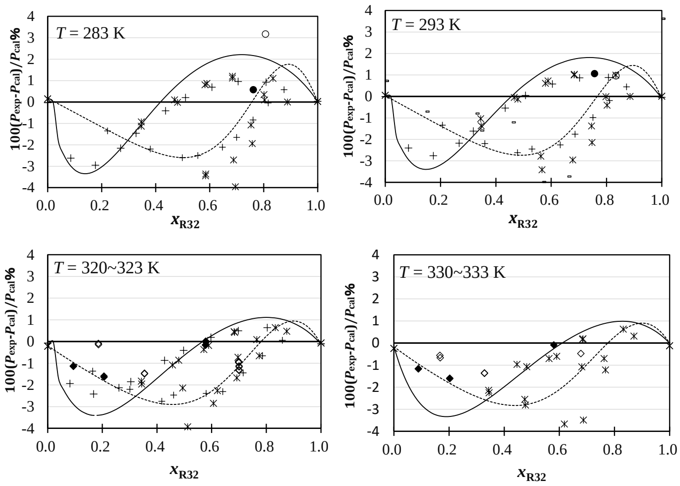

Fig. 2.1.2-8 Deviation plots of the present VLE data for HFC32/HFO1234yf binary mixtures using the Akasaka model (with the vapor-liquid equilibrium properties calculated using the REFPROP ver. 10.0 software program). (◆◇) Toyama prefectural university, (●○) Kyushu university, (＊, -, +) Literature data, (— --) bubble point and dew point pressure values from the present Peng-Robinson equation of state modified by Mathias and Copeman[7]. The baseline represents values from the Akasaka model[6] calculated using the REFPROP 10.0[5].

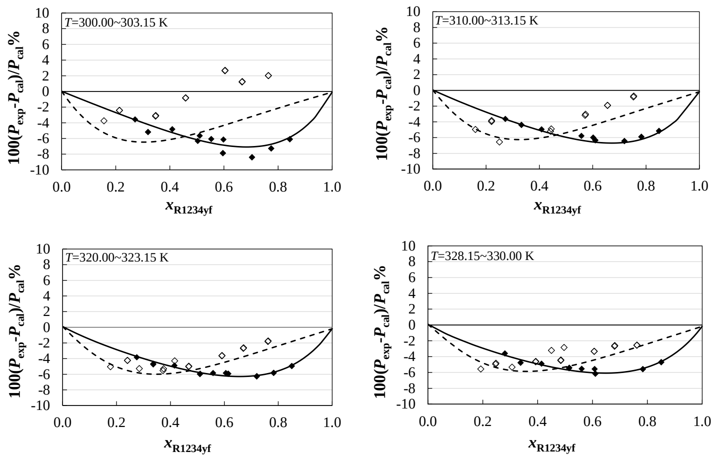

Fig. 2.1.2-9 Deviation plots of the present VLE data for HFO1123/HFO1234yf binary mixtures using the REFPROP ver. 10.0[5]. (◆◇) Toyama prefectural university, (— --) bubble point and dew point pressure values from the present Peng-Robinson equation of state modified by Mathias and Copeman[7]. The baseline represents values calculated using the REFPROP 10.0[5].

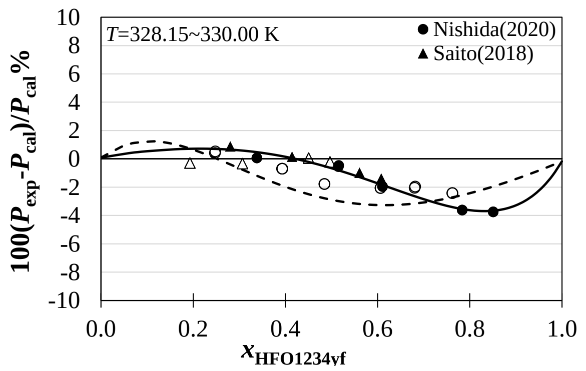

Fig. 2.1.2-10 Deviation plots of the present VLE data for HFO1123/HFO1234yf binary mixtures from Akasaka and Lemmon model[8]. (●○, ▲△) Toyama prefectural university.

Next, we report the measurement results of the ternary mixture HFC32/HFO1234yf/HFO1123. First, Fig. 2.1.2-11 shows the results of measurement using a bellows variable volumometer type vapor-liquid equilibrium property measurement apparatus.

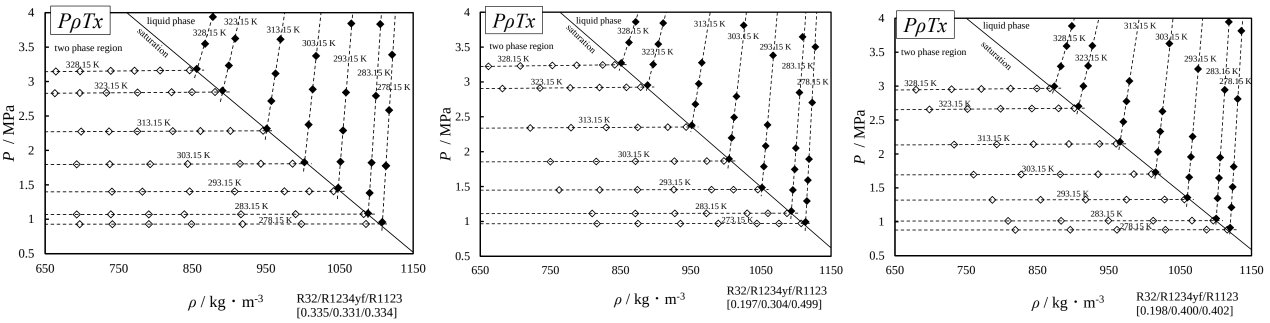

Fig. 2.1.2-11 Distribution of the present VLE and $P\rho Tx$ property data for HFC32/HFO1234yf/HFO1123 ternary mixtures. (◆◇) Toyama prefectural university, ----, linear expression regressed based on the measured values of each isotherm; —, values of the saturated liquid densities calculated from the Akasaka and Lemmon model[8].

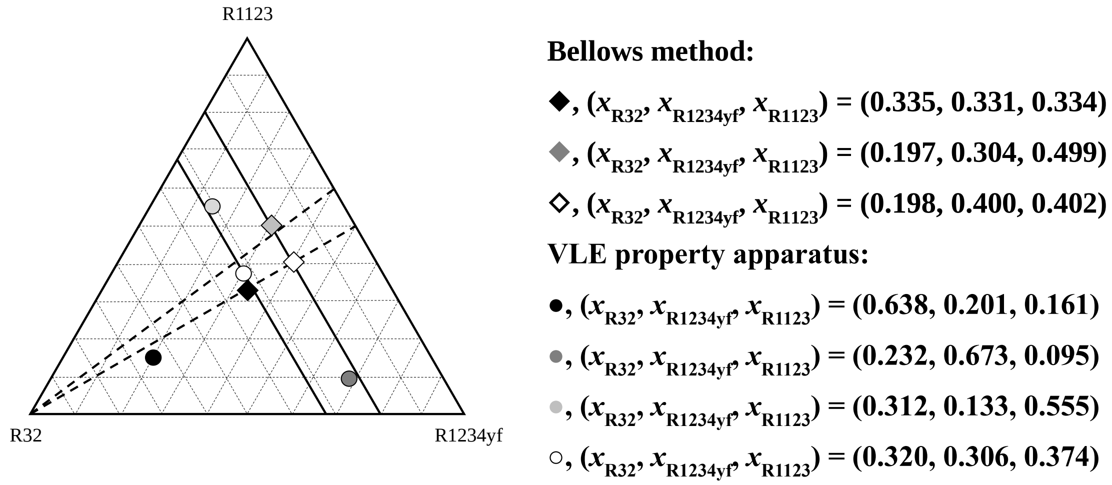

Fig. 2.1.2-12 Composition distribution map of the present measurements. ◆●, compositions of the present data; —, the case where the composition of R32 is fixed; ----, the case where the composition of the R1234yf/R1123 binary system is fixed.

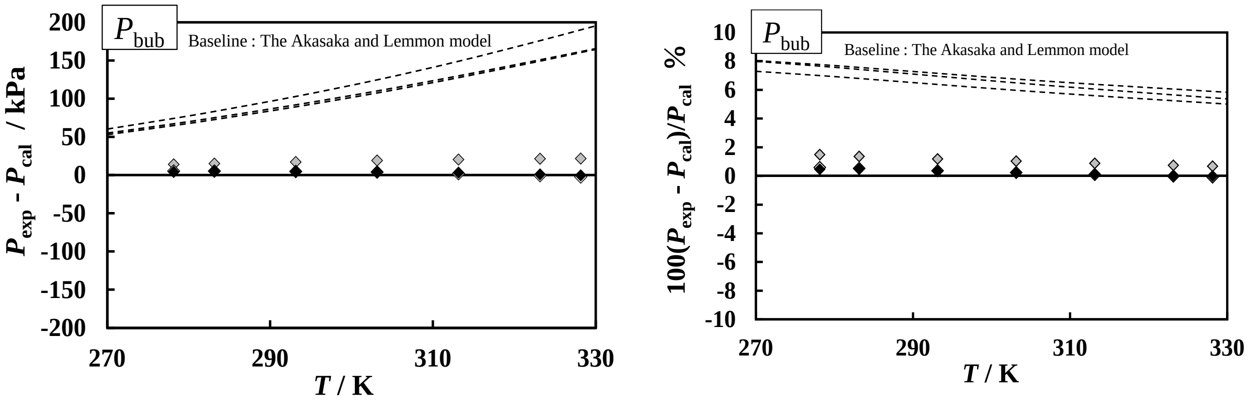

Fig. 2.1.2-13 Absolute (left) and relative (right) pressure deviation plots of the present bubble-point pressures using the bellows method from the Akasaka and Lemmon model[8] (with the vapor–liquid equilibrium properties calculated using the REFPROP ver. 10.0[5] for R32/R1123/R1234yf ternary mixtures). ◆, (x_{R32}, $x_{R1234yf}$, x_{R1123}) = (0.335, 0.331, 0.334); ◆, (x_{R32}, $x_{R1234yf}$, x_{R1123}) = (0.197, 0.304, 0.499); ◇, (x_{R32}, $x_{R1234yf}$, x_{R1123}) = (0.198, 0.400, 0.402); ----, values from the REFPRO P ver. 10.0[5].

The dashed lines connecting the measured values of $P\rho Tx$ properties in the figure indicate each isotherm, and the boiling point pressure and saturated liquid density can be clarified from the inflection point at the boiling point. In addition, measurements using a recirculation-type vapor-liquid equilibrium property measurement apparatus were also performed. Figure 2.1.2-12 shows the composition distribution of the measurement results for the ternary mixtures in this study. In addition, the latest Akasaka and Lemmon's estimated vapor-liquid equilibrium properties for a ternary system including binary parameters (abbreviated as Akasaka and Lemmon model in the figure, unofficially decided as default model in the next version of the REFPROP) are also plotted in Fig. 2.1.2-13. Moreover, the figure includes the calculation results from REFPROP ver. 10.0 (released in 2018); however, the new Akasaka and Lemmon model (baseline) exhibited a maximum relative deviation of approximately 6%. Consequently, it can be concluded that the improvement in the reproducibility of the equation of state for the binary mixtures contributed to the improvement in the reproducibility of the thermodynamic properties of the ternary mixture model.

From 2021, measurements of the HFO1123/CF_3I and HFO1123/HC290 binary mixtures have been performed. First, the measurement results of the HFO1123/CF_3I binary mixtures are shown in Fig. 2.1.2-15.

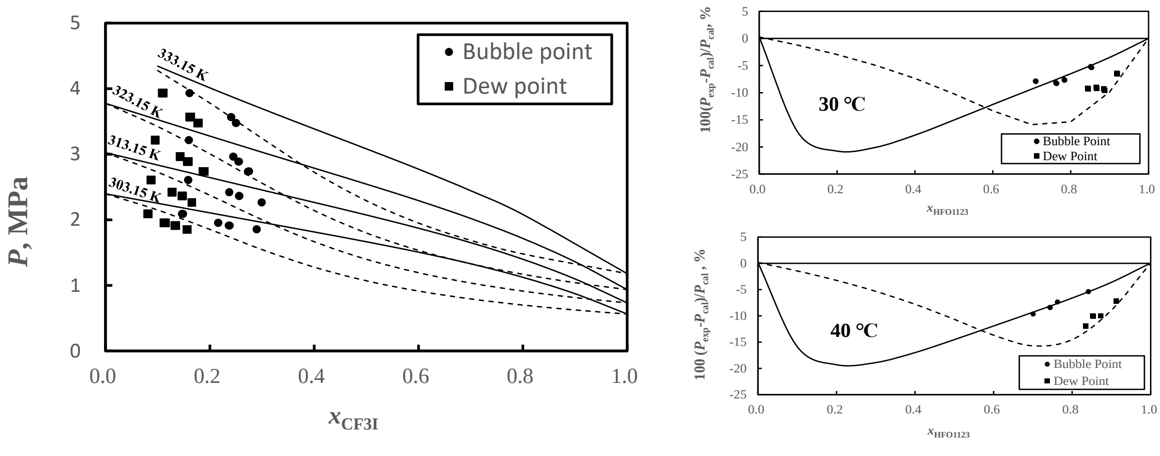

Fig. 2.1.2-15 Deviation plots of the present VLE property data versus estimated values by the REFPROP ver. 10.0[5] (including the equation of state for CF_3I by Akasaka[9]). ●,■; This work (bubble and dew point pressures), —, ----; modified Peng-Robinson equation of state (Right figures).

For the HFO1123/CF_3I binary mixtures, a total of 30 measured values were obtained at temperatures ranging from 30 and 60 °C. The curve and baseline in the left and right figures are the values estimated by REFPROP 10.0[5] using the Akasaka[9] formula [preliminary version] for CF_3I; however, the correlation for binary mixtures preset in REFPROP are uncorrected, and thus a significant difference was confirmed between the measured and estimated values. In addition, in the relative pressure deviation diagram on the right, a good correlation result with the calculated results obtained using the modified Peng-Robinson equation of state correlated in this study was also confirmed. Although only the measured values for the low CF_3I composition were obtained, only one mixing rule parameter existed in the modified Peng-Robinson equation of state. Moreover, the calculation results for the high CF_3I composition cannot be corrected. It was inferred that when performing measurements, the actual measurement value agreed with this Peng-Robinson equation of state with a large negative relative pressure deviation from the Helmholtz free-energy type model. There were plans to further add measurements with an increased CF_3I composition; however, following the completion of the latest measurement, the window of the optical cell of the recirculation-type vapor-liquid equilibrium property measurement apparatus became cloudy, which resulted in difficulties for further measurements. Therefore, the measurement of the CF_3I high composition side and the CF_3I pure substance was discontinued. Consequently, the entire sample system of the recirculation type vapor-liquid equilibrium and bellows variable volumometer type vapor-liquid equilibrium property measurement apparatus was disassembled and cleaned.

Subsequently, following the conduction of calibration experiments for both devices again, from 2022, measurement of the HFO1123/HC290 binary mixtures will be undertaken. Till date, we have obtained experimental vapor-liquid equilibrium properties for two types of compositions. We aim to continue this measurement, and to perform systematically comparisons with the existing Helmholtz free-energy type equation of state.

2.1.2.2 Vapor-liquid equilibrium measurements at Kyushu University

Vapor-liquid equilibrium (VLE) of refrigerant mixtures at low temperature range of 263 to 323 K were measured based on the circulation method. A schematic of the experiment apparatus is shown in Fig. 2.1.2-16[10]. An equilibrium cell (A) with inner volume of 265 cm^3 was filled with a sample of refrigerant mixtures in the vapor-liquid equilibrium condition. Following the maintenance of the cell temperature constant, the equilibrium pressure was measured, and a small amount of vapor and liquid phase samples were extracted. The concentrations of the samples were measured using a gas chromatograph (Q), and the VLE properties of temperature T, pressure P, liquid phase mole fraction x and vapor phase mole fraction y were determined. Further, the equilibrium cell was equipped with sight glasses to confirm the vapor-liquid equilibrium condition and enable the observance of the vapor-liquid meniscus. A quartz-type pressure transducer (B), circulation pump (V), and hexagon valve (U) were directly connected to the equilibrium cell, and immersed in a thermostatic bath using silicone oil as a heat transfer medium during the measurements. The sample pressure was measured precisely with an uncertainty of 2 kPa. Further, the circulation pump circulated the vapor-phase sample to the liquid phase, and stirred the entire sample. The vapor-phase sample was extracted from a valve above the equilibrium cell to a sample cylinder. Subsequently, the liquid-phase sample was extracted from the hexagon valve to a tube, which was expanded to a sample cylinder in the vapor condition. The silicone oil of the thermostatic bath was stirred using stirrers (M). The temperature of the oil was roughly adjusted to a target temperature with a main heater (M) and circulation bath (L), and the output power of a sub-electric heater was precisely controlled employing a PID controller (J) to maintain a constant oil temperature. The temperature of the bath was measured according to ITS-90 using a standard platinum resistance thermometer (E) and thermometer bridge (D). Consequently, the uncertainty of the temperature measurement was estimated to be 10 mK. The components of refrigerant mixtures were detected by the thermal conductivity detector (TCD) of the gas chromatograph. An evacuated sampling tube of the gas chromatograph was filled with the extracted sample at the atmospheric pressure, and it was transferred to the TCD by the carrier gas, helium. The peak areas were obtained depending on the amount of the components. A Propak Q column (mesh: 50/80, length: 3 m) was adopted to separate the components.

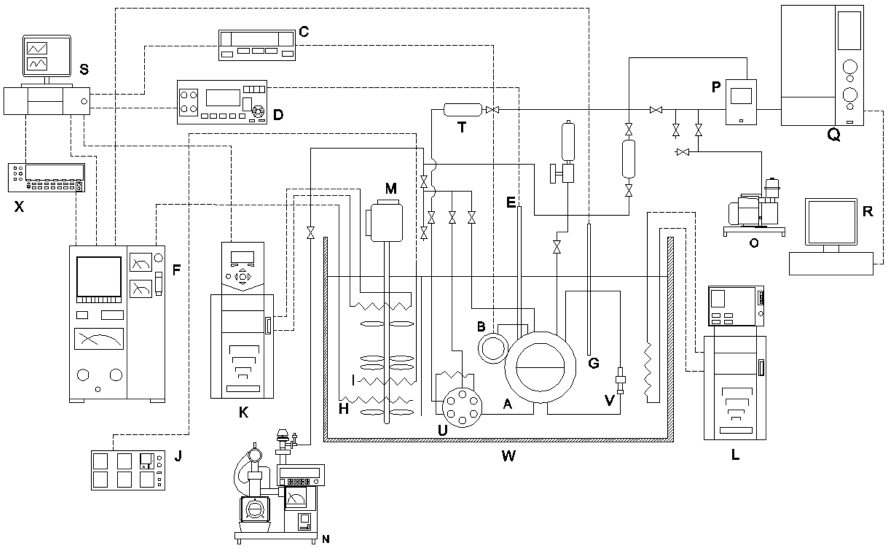

A: Equilibrium cell; B: Pressure transducer; C: Digital pressure indicator; D: Thermometer bridge; E: Standard platinum resistance thermometer; F: Temperature controller; G: Platinum resistance thermometer; H: Main-electric heater; I: Sub-electric heater; J: Temperature controller; K, L: Circulation bath; M: Stirrer; N, O: molecular pump; P: Auto gas sampler; Q: Gas chromatograph; R, S: Computers; T: Sample cylinder; U:Hexagon valve; V: Magnetic circulation pump; W: Thermostatic bath; X: AC/DC converter

Fig. 2.1.2-16 Schematic of the vapor-liquid equilibrium measurement apparatus at low temperatures

VLE measurement results of binary refrigerant mixtures including CF_3I or HFO1123 are shown in Figs. 2.1.2-17 to 21, and the VLE calculations from a cubic equation of state (EOS) and the Peng-Robinson EOS were illustrated as well[14, 15]. The interaction parameter, k_{12}, of the PR EOS was determined based on the experimental data. The EOS encountered difficulty in representing the experimental densities adequately; however, it can represent the VLE properties of temperature, pressure, and composition. From Figs. 2.1.2-17 to 21, it was confirmed that the EOS with the fitted interaction parameter represented the experimental data.

Figure 2.1.2-22 shows the VLE measurement results of ternary mixtures of HFC32/HFC125/CF_3I and HFC32/HFO1123/CF_3I at 283 K [16]. The VLE calculation of PR EOS has been illustrated in this figure using only binary interaction parameters. For the ternary mixtures, a relatively larger difference between the experimental data and EOS calculations were observed than in case of the binary mixtures. The obtained experimental data can aid in determining the mixing parameters of highly-accurate Helmholtz-type EOSs, to improve representation of the composition dependence.

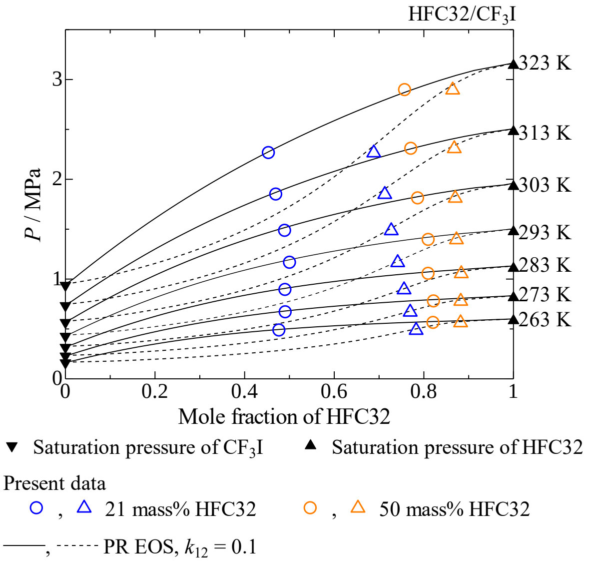

Fig. 2.1.2-17 VLE measurement results of HFC32/CF$_3$I

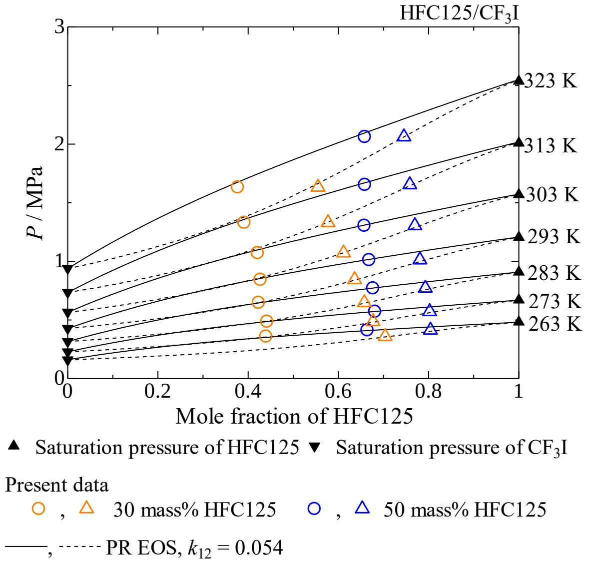

Fig. 2.1.2-18 VLE measurement results of HFC125/CF$_3$I

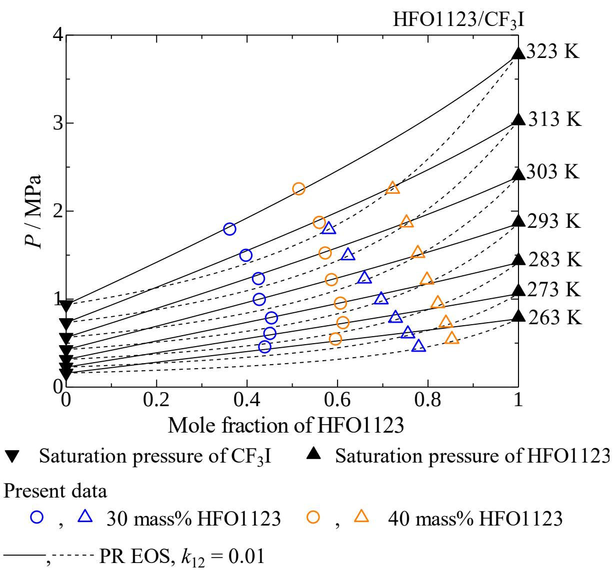

Fig. 2.1.2-19 VLE measurement results of HFO1123/CF$_3$I

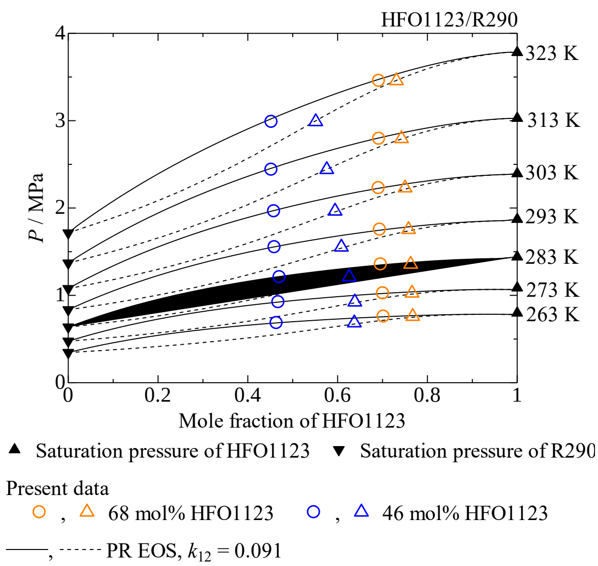

Fig. 2.1.2-20 VLE measurement results of HFO1123/R290

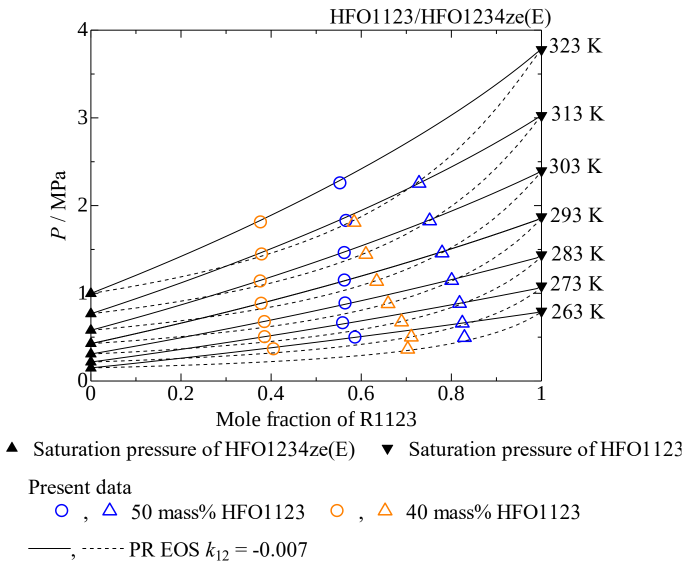

Fig. 2.1.2-21 VLE measurement results of HFO1123/HFO1234ze(E)

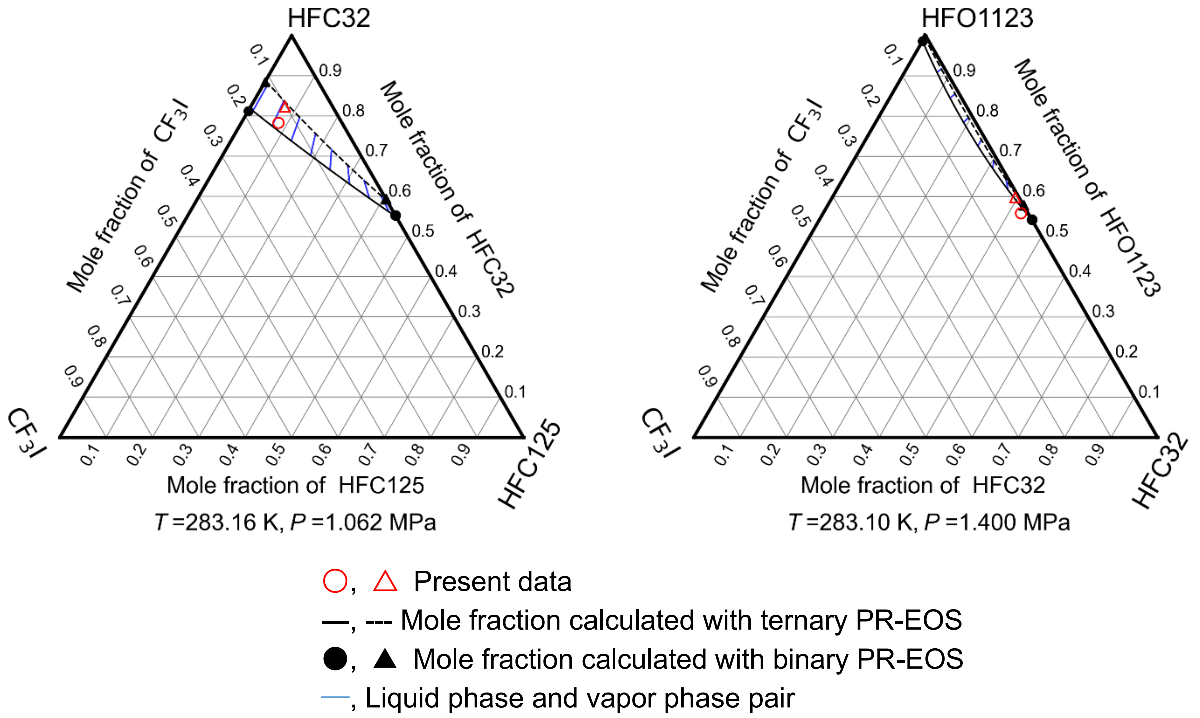

Fig. 2.1.2-22 VLE measurement results of HFC32/HFC125/CF_3I and HFC32/HFO1123/CF_3I

References

1) Y. Nagata, K. Mizutani, H. Miyamoto: J. Chem. Thermodyn. 43(3), pp. 244-247 (2011).
2) H. Miyamoto, Y. Shoji, R. Akasaka, E. W. Lemmon: Int. J. Thermophys., 38(10), pp. 157-166 (2017).
3) T. Matsumoto, H. Miyamoto: J. Chem. Thermodyn., 101, pp. 150-156, (2016).
4) R. Akasaka: The 11th Asian Thermophysical Properties Conference (ATPC 2016), Yokohama, Japan (2016).
5) E. W. Lemmon, I. H. Bell, M. L. Huber, M. O. McLinden: REFPROP ver. 10.0, NIST Standard Reference Database, 23, (2018).

6) R. Akasaka: Fluid Phase Equilib., 358, pp. 98-104 (2013).
7) P. M. Mathias, T. W. Copeman: Fluid Phase Equilib., 13, pp. 91-108 (1983).
8) R. Akasaka, E. W. Lemmon: to be presented at The Sixth IIR Conference on Thermophysical Properties and Transfer Processes of Refrigerants (TPTPR2021), September 1-3, Vicenza, Italy, (2021).
9) R. Akasaka: "Helmholtz free-energy type equation of state for CF_3I", private communication (2021).
10) H. Miyamoto, T. Saito, N. Sakoda, U. Perera, T. Ishii, K. Thu, Y. Higashi: Int. J. Refrig., 119, pp. 340-348 (2020).
11) T. Yamada, H. Miyamoto, N. Sakoda, Y. Higashi: Int. J. Thermophys., 41, 167 (2020).
12) H. Miyamoto, M. Nishida, T. Saito: J. Chem. Thermodyn., 158, 106456 (2021).
13) H. Miyamoto, Y. Nakamura, K. Minai, T. Yamada: Fluid Phase Equilib., 558, 113440 (2022).
14) N. Sakoda, Y. Higashi, The Sixth IIR Conference on Thermophysical Properties and Transfer Processes of Refrigerants (TPTPR2021), September 1-3, Vicenza, Italy, (2021).
15) K. Kitabatake, H. Ishimaru, Y. Higashi, N. Sakoda, The 13th Asian Thermophysical Properties Conference (ATPC2022), Sept. 26-30, Sendai, Japan (2022).
16) H. Ishimaru, K. Kitabatake, Y. Higashi, N. Sakoda, 2022 JSRAE Annual Conference, Sept. 7-9, Okayama, Japan (2022).

2.1.3 Measurements of *PvTx* properties in high temperatures and isobaric specific heat

2.1.3.1 *PvTx* property measurements in high temperatures

(1) Experimental apparatus

PvTx properties including the high-temperature range and isobaric specific heat capacity of next-generation refrigerants were measured at College of Science and Engineering, Nihon University. Experimental apparatus for *PvTx* property measurements based on the isochoric method with constant volume and expansion vessels, are shown in Fig. 2.1.3-1.

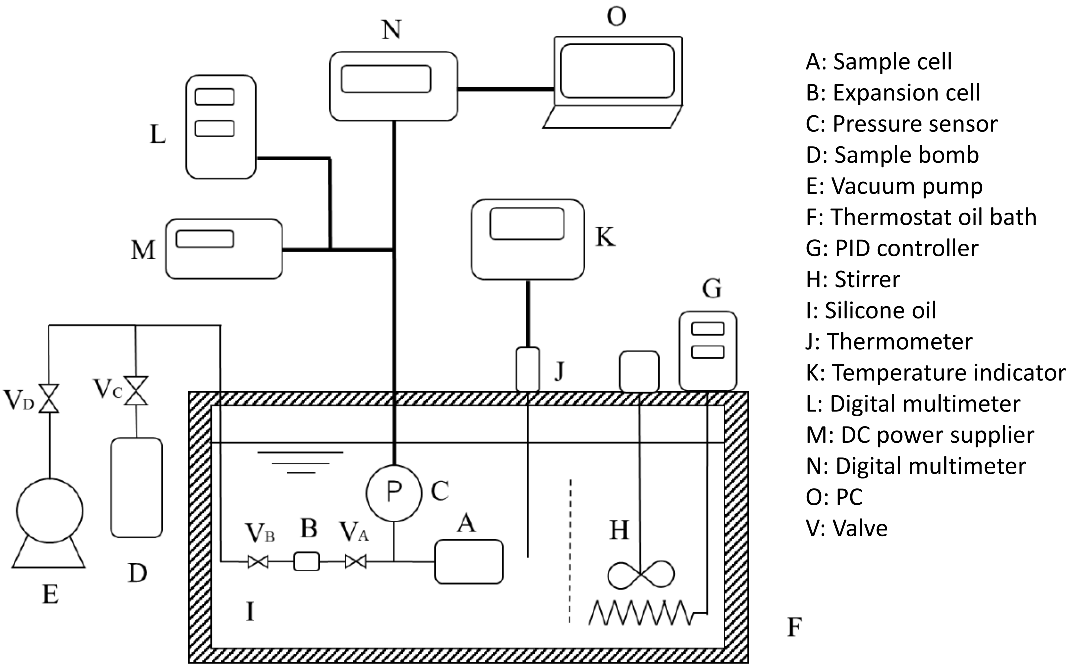

Fig. 2.1.3-1 Experimental apparatus for PVTx property measurements based on the isochoric method with a constant volume vessel and an expansion vessel.

The apparatus for the *PvT* property measurement shown in Fig. 2.1.3-1 had a pressure sensor installed in a constant volume vessel, and the pressure was measured at an arbitrary temperature using a thermostatic oil bath under an isochoric line with an arbitrary filling mass. In particular, the pressure sensor employed a sensor capable of measuring even in a high temperature range, and used nitrogen gas whose pressure was adjusted prior to measurement to calibrate the pressure dependence of the sensor. In the isochoric method, the density is changed through changes in the filling amount of the sample, and data is obtained along isochoric lines. Although the composition must be adjusted, the expansion vessel was provided to reduce the operation, accelerate the measurement, and measure the same composition. In particular, as the temperature is frequently high during expansion, a bellows valve was used. The volume of the pressure vessel equipped with the pressure sensor is approximately 8 cc. Further, the expansion vessel exhibits a volume of approximately 3 cc, and each expansion sets the mass (that is, density) of the sample in the pressure vessel to a value that was approximately, 1/4 lower than before expansion while the composition remained constant. The measurement temperature range was in is from 323 to 453 K and the pressure was up to 10 MPa. The measurement was also performed using an isochoric apparatus comprising a single container without an expansion vessel, similar to this apparatus. Because the apparatus does not have an expander; the sample must be adjusted and filled each time the density was changed. It can be measured by setting arbitrary composition and density.

(2) Experimental results for *PvTx* properties including high temperature

As shown in Table 2.1.3-1, *PvTx* properties including high temperature were measured using HCFO1224yd(Z), CF_3I [R13I1], HFO1123 for pure substances, and HFO1336mzz(E)/HFO1336mzz(Z) for binary mixtures, Whereas, the HFO1234yf/HFC32, HFO1234yf/CO_2, HFC32/CO_2, HFC32/CF_3I, HFO1123/CF_3I, HFO1123/HC290, HFO1123/HFO1234yf, HFO1234yf/HFC32/CO_2 were ternary mixtures.

Table 2.1.3-1 Results of isobaric specific heat capacity measurements of at 25 °C, 50 kPa and 101 kPa.

Refrigerant	Composition	Reference
	Pure substance	
HCFO1224yd(Z)		2
CF_3I		3
HFO1123		to be published
	Binary mixture	
HFO1336mzz(E)/HFO1336mzz(Z)	43.80/56.20 mass%	to be published
HFO1234yf+HFC32	37.41/62.59 mass% 23.29/76.71 mass%	1, to be published
HFO1234yf+CO_2	97.38/2.62 mass%	1, to be published
HFC32+CO_2	97.25/2.75 mass%	1, to be published
HFC32+CF_3I	87.5/12.5 mass% 95.5/4.5 mass%	to be published
HFO1123+CF_3I	10/90 mass%	to be published
HFO1123+HC290	50/50 mass%	ongoing
HFO1123+HFO1234yf	50/50 mass%	ongoing
	Ternary mixture	
HFC32+HFO1234yf+CO_2	30.31/67.12/2.57 mass% 39.59/56.18/4.22 mass% 54.28/42.88/2.85 mass% 26.66/70.02/3.32 mass%	1, to be published

(a) Results for pure substances

HCFO1224yd(Z) was measured at 169 data points along 17 isochoric lines in the range of 323 to 453 K and at 10 MPa[2)]. In addition, 14 isotherms were obtained using the obtained data. Fig. 2.1.3-2 shows the measurement results along the isochoric lines, and Fig. 2.1.3-3 shows the results organized into isotherm lines.

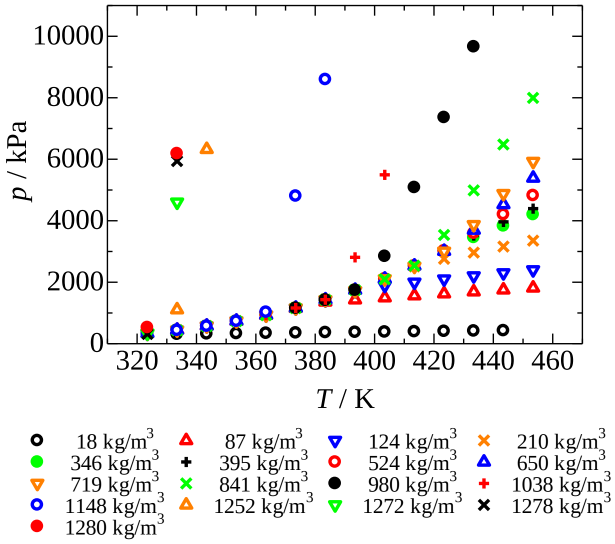

Fig. 2.1.3-2 *PvTx* property measurements of HCFO1224yd(Z). [*P*-*T* diagram]

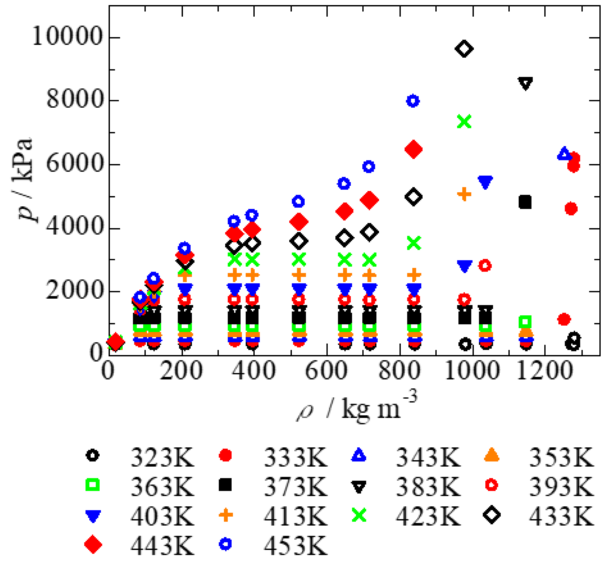

Fig. 2.1.3-3 *PvTx* property measurements of HCFO1224yd(Z). [*P*-ρ diagram]

CF_3I [R13I1] was measured at 116 data points along 19 isochoric lines in the range of 323 to 453 K at 10 Mpa[3]. Further, 14 isotherms were obtained using the obtained data. Figure 2.1.3-4 shows the results of measurement along the isochoric lines, and Fig. 2.1.3-5 shows the results organized into isotherm lines.

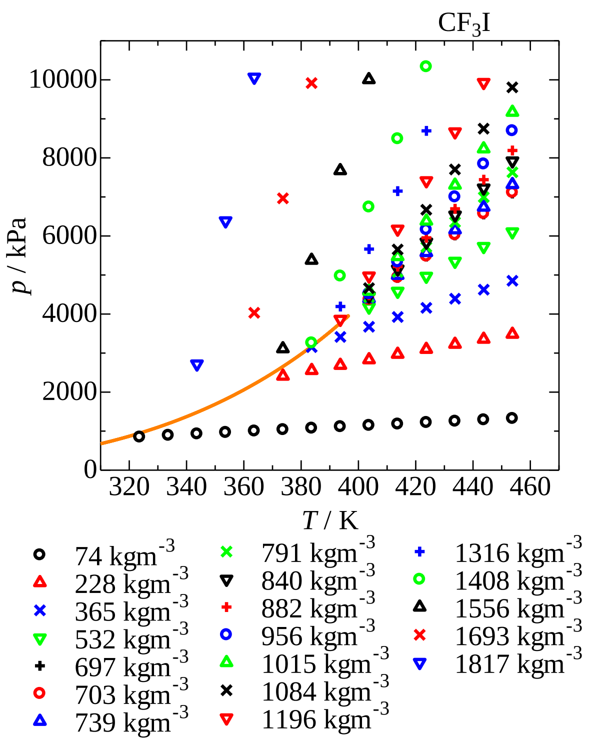

Fig. 2.1.3-4 *PvTx* property measurements of CF_3I. [*P*-*T* diagram]

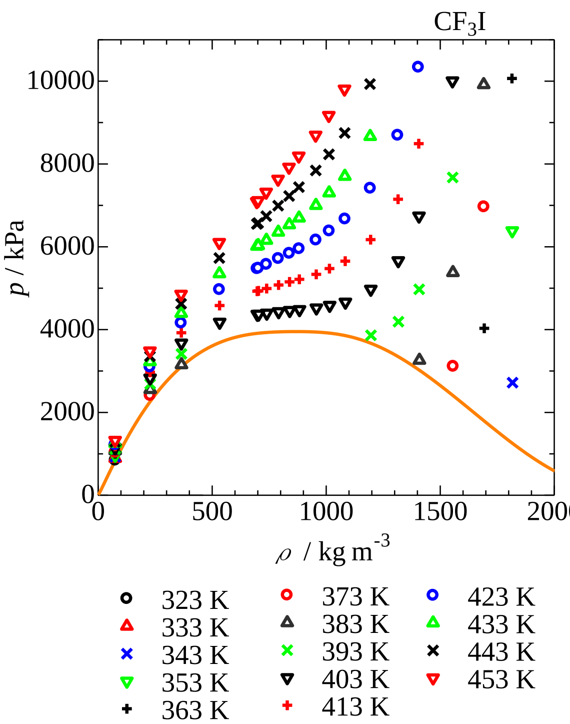

Fig. 2.1.3-5 *PvTx* property measurements of CF_3I. [*P*-ρ diagram]

HFO1123 was measured at 74 points along 6 isochoric lines in the range of 323 to 453 K and 10 MPa. In addition, 14 isotherms were obtained using the obtained data. Figure 2.1.3-6 shows the measurement results along the isochoric line, and Fig. 2.1.3-7 shows the result of those organized into the isotherm line.

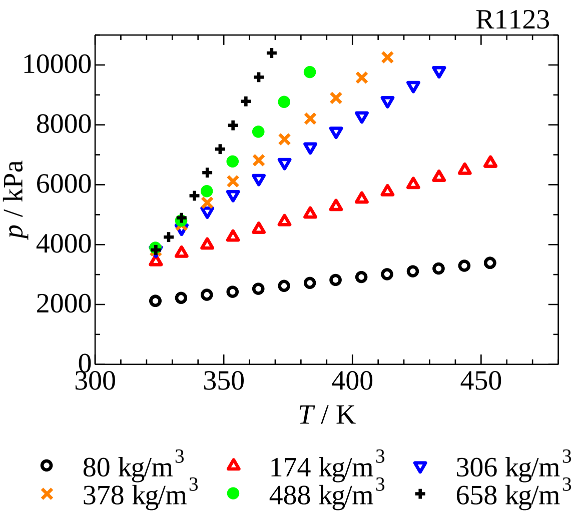

Fig. 2.1.3-6 *PvTx* property measurements of HFO1123. [*P*-*T* diagram]

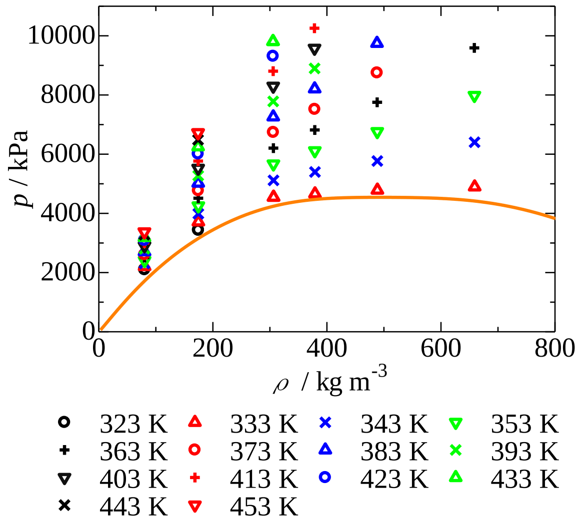

Fig. 2.1.3-7 *PVTx* property measurements of HFO1123. [*P*-*ρ* diagram]

(b) Results for binary refrigerant mixtures

For HFO1336mzz(E)/HFO1336mzz(Z) refrigerant mixture, 42 measurement results were obtained along three isochores for one composition. Figure 2.1.3-8 shows the *PT* (pressure-temperature) diagram of HFO1336mzz(E)/HFO1336mzz(Z) [43.80/56.20 mass%].

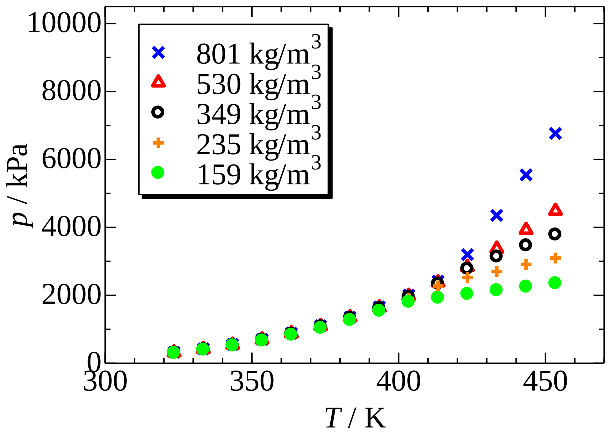

Fig. 2.1.3-8 *PvTx* property measurements of HFO1336mzz(E)/HFO1336mzz(Z) [43.80/56.20 mass%].

Regarding HFO1234yf/HFC32, HFO1234yf/CO_2, and HFC32/CO_2 for each binary mixture of HFO1234yf, HFC32, and CO_2, a total of 233 measurements were obtained along 21 isochores. The *PT* (pressure-temperature) diagrams are shown in Fig. 2.1.3-9 for HFC32/CO_2 [97.25/2.75 mass%], in Fig. 2.1.3-10 for HFO1234yf/CO_2 [97.38/2.62 mass%], in Fig. 2.1.3-11 for HFC32/ HFO1234yf [62.59/37.41 mass%], in Fig. 2.1.3-12 for HFC32/ HFO1234yf [23.29/76.71 mass%].

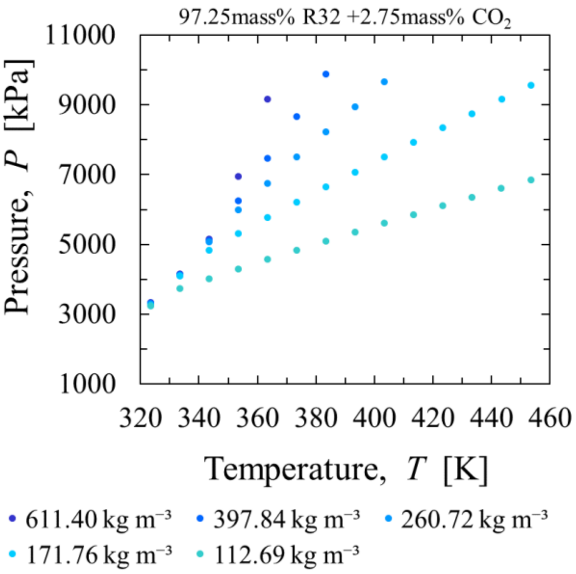

Fig. 2.1.3-9 *PvTx* property measurements of HFC32/CO_2 [97.25/2.75 mass%].

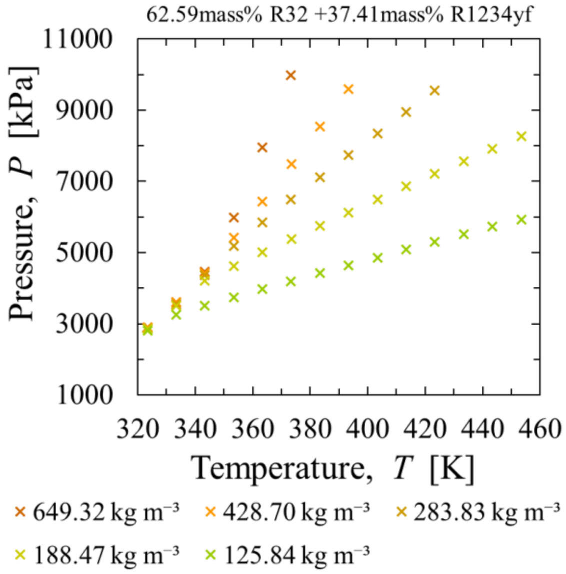

Fig. 2.1.3-11 *PvTx* property measurements of HFC32/ HFO1234yf [62.59/37.41 mass%].

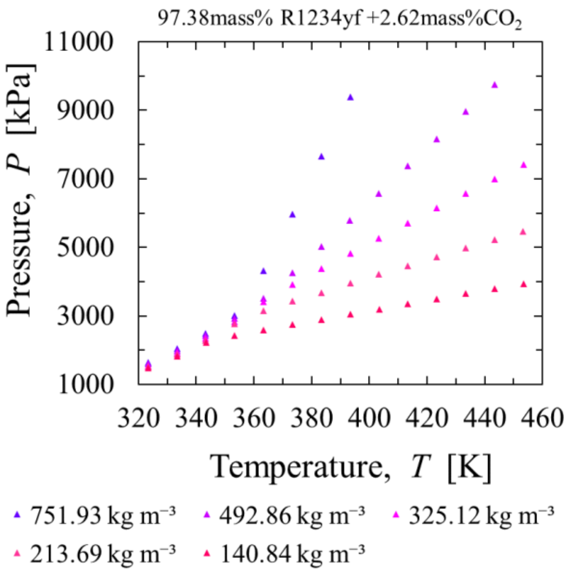

Fig. 2.1.3-10 *PvTx* property measurements of HFO1234yf/CO_2 [97.38/2.62 mass%].

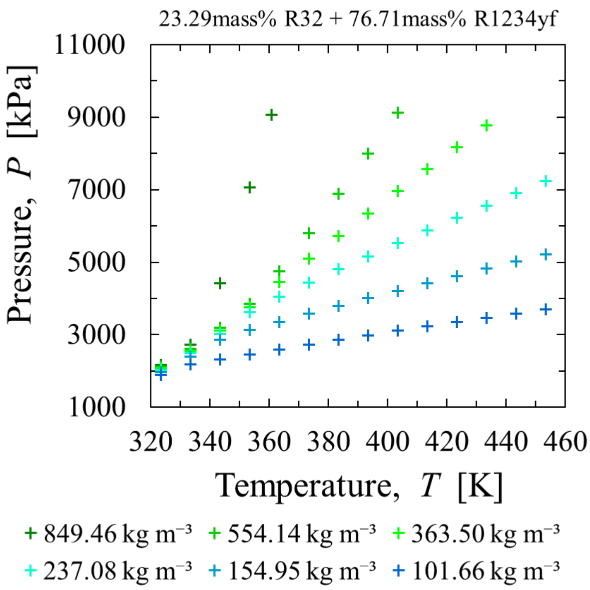

Fig. 2.1.3-12 *PvTx* property measurements of HFC32/ HFO1234yf [23.29/76.71 mass%].

For the HFC32/CF_3I binary refrigerants, 105 measurement results were obtained along 11 isochores for two compositions[4)]. Figure 2.1.3-13 shows the *PT* (pressure-temperature) diagram of HFC32/CF_3I [87.5/12.5 mass%] and Fig. 2.1.3-14 shows the *PT* (pressure-temperature) diagram of HFC32/CF_3I [95.5/4.5 mass%].

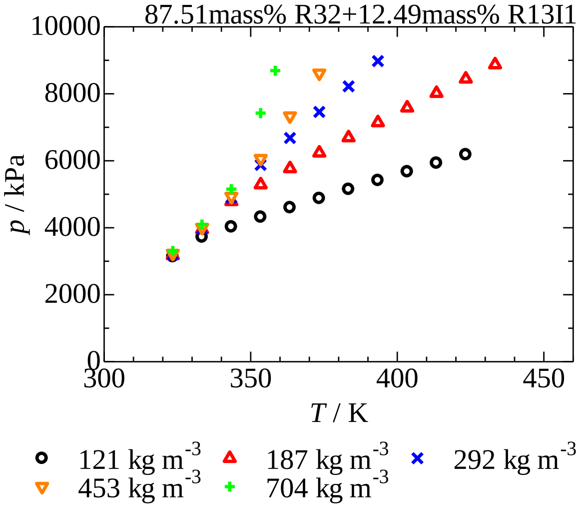

Fig. 2.1.3-13 *PvTx* property measurements of HFC32/CF_3I [87.5/12.5 mass%].

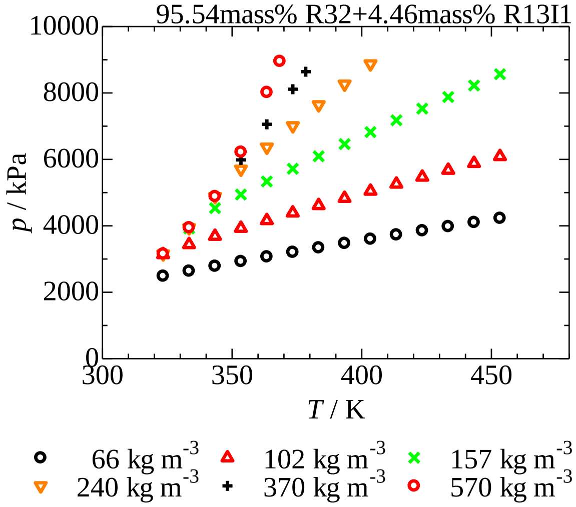

Fig. 2.1.3-14 *PvTx* property measurements of HFC32/CF_3I [95.5/4.5 mass%].

Regarding the HFO1123/CF_3I binary refrigerants, 80 measurement results were obtained along 5 isochores for one composition. Figure 2.1.3-15 shows the *PT* (pressure-temperature) diagram of HFO1123/CF_3I [10/90 mass%].
In case of the HFO1123/HFO1234yf binary refrigerants, 33 measurement results were obtained along four isochores for one composition. Figure 2.1.3-16 shows the *PT* (pressure-temperature) diagram of HFO1123/HFO1234yf [50/50 mass%].

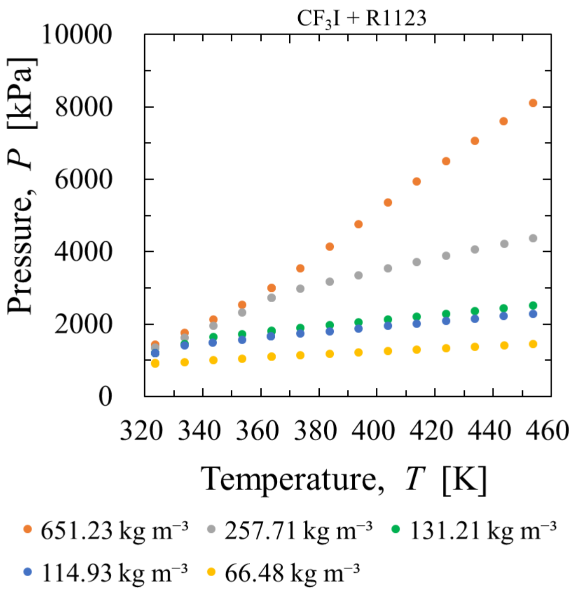

Fig. 2.1.3-15 *PvTx* property measurements of HFO1123/CF_3I [10/90 mass%].

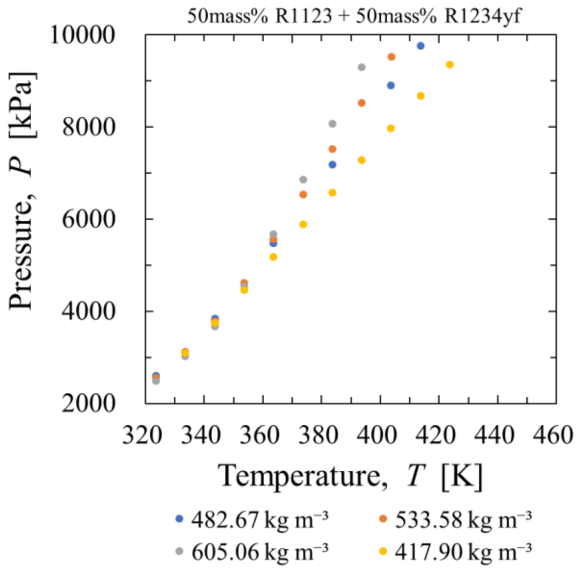

Fig. 2.1.3-16 *PvTx* property measurements of HFO1123/HFO1234yf [50/50 mass%].

Regarding the HFO1123/HC290 binary mixtures, 110 measurement results were obtained along 9 isochores in one composition. Figure 2.1.3-17 shows the *PT* (pressure-temperature) diagram of HFO1123/HC290 [50/50 mass%].

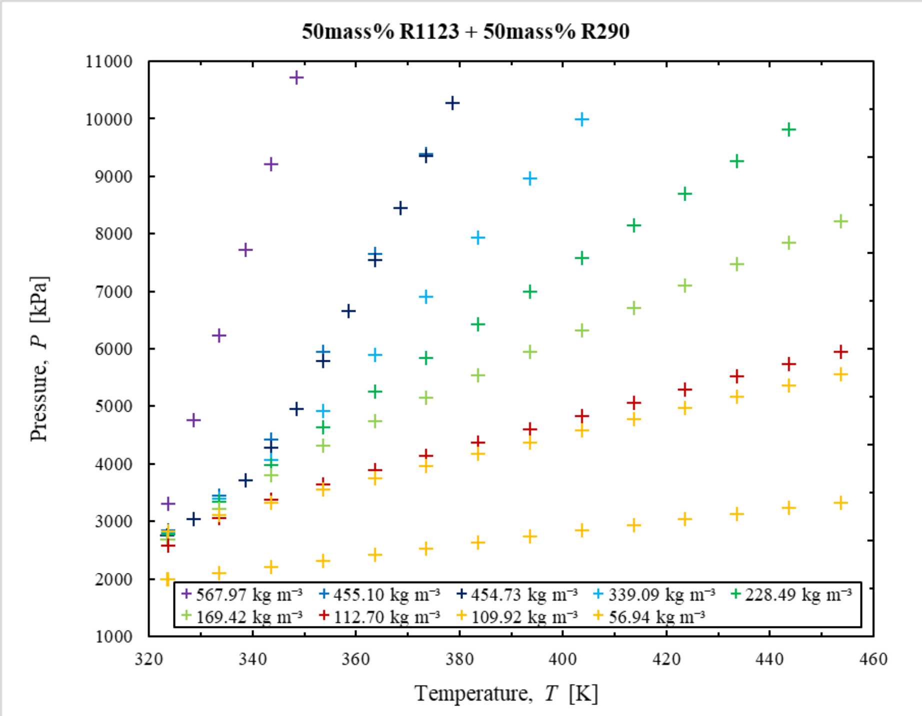

Fig. 2.1.3-17 *PVTx* property measurements of 50 mass% HFO1123/50 mass% HC290.

(c) Results for ternary refrigerant mixtures

In case of the HFO1234yf/HFC32/CO_2 ternary refrigerants, 183 measurement results were obtained along 10 isotherms for 4 compositions[1)]. *PT* (pressure and temperature) diagram are shown in the Fig. 2.1.3-18 for HFC32/HFO1234yf/CO_2 [30.31/67.12/2.57 mass%], Fig. 2.1.3-19 shows that for HFC32/HFO1234yf/CO_2 [39.59/56.18/4.22 mass%], Fig. 2.1.3-20 shows that for HFC32/HFO1234yf/CO_2 [54.28/42.88/2.85 mass%], and Fig. 2.1.3-21 shows that for HFC32/HFO1234yf/CO_2 [26.66/70.02/3.32 mass%].

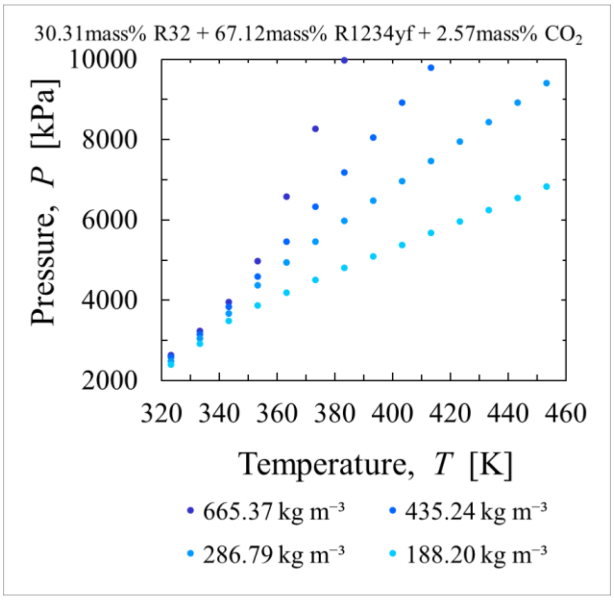

Fig. 2.1.3-18 *PvTx* property measurements of HFC32/HFO1234yf/CO_2 [30.31/67.12/2.57 mass%]

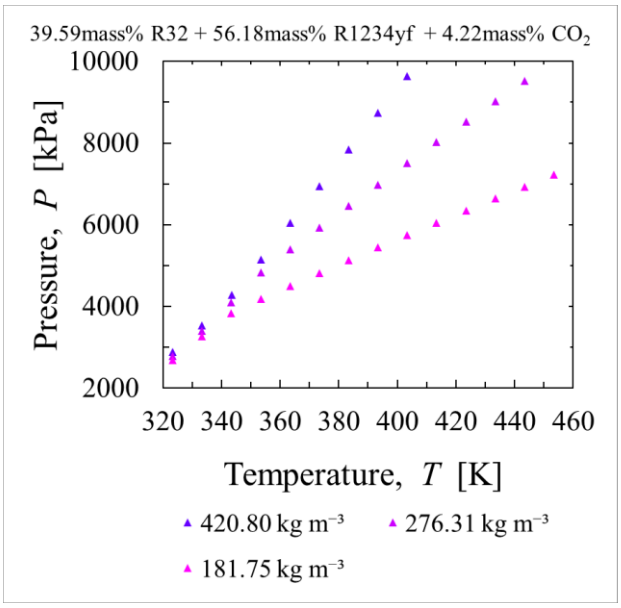

Fig. 2.1.3-19 *PvTx* property measurements of HFC32/HFO1234yf/CO_2[39.59/56.18/4.22 mass%]

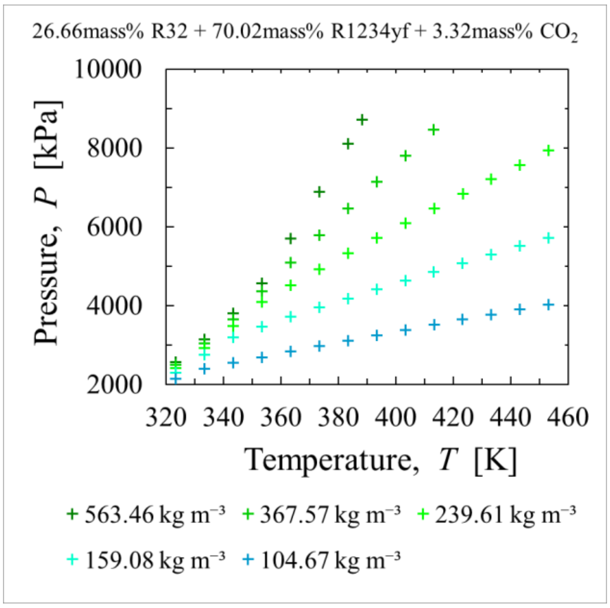

Fig. 2.1.3-20 *PvTx* property measurements of HFC32/HFO1234yf/CO_2 [54.28/42.88/2.85 mass%]

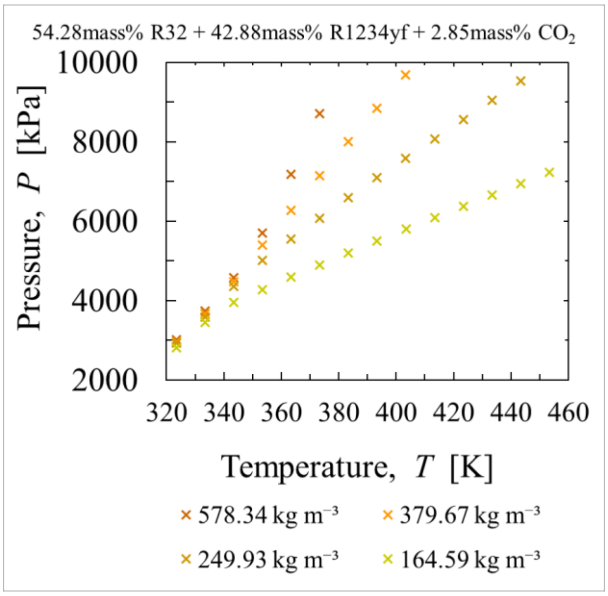

Fig. 2.1.3-21 *PvTx* property measurements of HFC32/HFO1234yf/CO_2 [26.66/70.02/3.32 mass%]

2.1.3.2 Isobaric-specific heat capacity

(1) Experimental apparatus

Figure 2.1.3-22 shows the apparatus for measuring the isobaric-specific heat capacity[5)]. A thermal flowmeter, which operates as a calorimeter, was connected in series with a Coriolis flowmeter with the flow being identical to that of the mass flow rate. A temperature sensor was installed at the front of the flow path of the thermal flow meter, whereas a pressure sensor was installed at the rear. Further, flow rate control valves were installed at the front and behind the flow path of the flow meter for flow rate and pressure adjustments. A 500 cc cylinder was filled with several grams of the sample and placed under a constant temperature bath together with a flow meter. The thermostat air bath was used, and a fan Was installed in the bath for air circulation. After passing through the flowmeter, the sample was recovered in a recovery cylinder cooled with liquid nitrogen. Subsequently, the outputs of the thermal and Coriolis flowmeters were input to a personal computer via a digital multimeter.

The flow method was used as the principle of measuring the isobaric-specific heat capacity. In the flow method, the sample was circulated at a constant flow rate and heated using a heater, as shown in Eq. 2.1.3-1. The constant pressure specific heat is inversely proportional to the amount of temperature change with respect to the amount of heat $\dot{Q}$.

$$\dot{Q} = \dot{m} c_p \frac{dT}{dt} \qquad (2.1.3\text{-}1)$$

Using a Coriolis flowmeter, the mass flow rate indicates an output voltage V_c that is proportional to the mass flow rate. If the apparatus constant of the Coriolis flowmeter is K_c, it can be expressed as Eq. 2.1.3-2.

$$\dot{m} = K_c V_c \qquad (2.1.3\text{-}2)$$

A thermal flowmeter outputs a voltage V_T that is inversely proportional to the isobaric-specific heat capacity. If the device constant of the thermal flowmeter is K_T, Eq. 2.1.3-1 can be expressed as Eq. 2.1.3-3.

$$\dot{m} = \frac{\dot{Q}}{c_p \frac{dT}{dt}} = \frac{K_T V_T}{c_p} \qquad (2.1.3\text{-}3)$$

When the Coriolis flowmeter and the thermal flowmeter are connected in series and the same mass flow rate flows, from Eq. 2.1.3-2 and Eq. 2.1.3-3,

$$K_c V_c = \frac{K_T V_T}{c_p} \tag{2.1.3-4}$$

Further, arranging Eq. 2.1.3-4 in terms of isobaric-specific heat capacity,

$$c_p = \frac{K_T V_T}{K_c V_c} = K\frac{V_T}{V_c} \tag{2.1.3-5}$$

where K is the integrated apparatus constant of the flowmeter. Using a substance whose isobaric specific heat capacity is well known in advance, the output voltage V_c of the Coriolis flowmeter and the output voltage V_T of the thermal flowmeter was measured, and the apparatus constant K was decided. Similarly, by measuring the output voltage V_c of the Coriolis flowmeter and the output voltage V_T of the thermal flowmeter, the isobaric specific heat capacity can be obtained from Eq. 2.1.3-5.

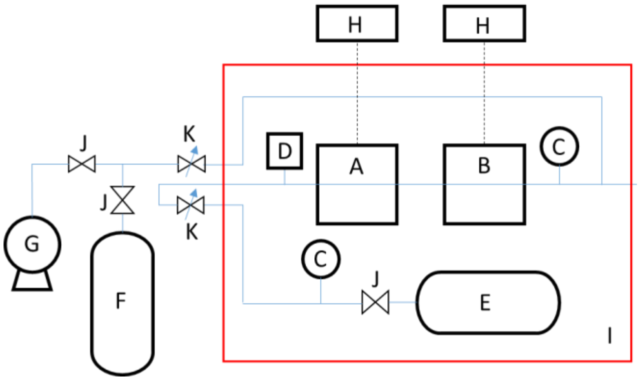

Fig. 2.1.3-22 Experimental apparatus for isobaric-specific heat capacity measurements based on a flow calorimeter. A: Calorimeter(thermal flow meter), B: Coriolis flow meter, C: Pressure sensor, D: Temperature sensor, E: Sample bomb, F: Recovery bomb, G: Vacuum pump, H: Digital multimeter, I: Thermostat, J: Valve, K: Flow control valve

(2) Experimental results of isobaric specific heat capacity

The isobaric-specific heat capacity was measured at 50 and 101 kPa at 25°C. The samples used to determine the device constants were CO_2, HCFC22, HFC134a, HFC125, and Ar. The measurement results are presented in Table 2.1.3-2. Figure 2.1.3-23 shows the measurement results[5)] with variation in the composition ratio of the binary refrigerant HFC32/HFO1234yf. At this time, when the composition ratio was mol and the unit of specific heat was summarized on a mol basis, the obtainment of an ideal mixture on a mol basis was confirmed.

Table 2.1.3-2 Results of isobaric specific heat capacity measurements of at 25 °C, 50 kPa and 101 kPa.

25℃	50 kPa	101 kPa	Composition ratio
Refrigerants	c_p[kJ/ kg K]		
CO_2	0.842	0.851	
HCFC22	0.656	0.662	
HFC134a	0.847	0.851	
HFC125	0.790		
Ar		0.522	
HFC32	0.821	0.844	
HFO1234yf	0.899	0.912	
CF_3I	0.403	0.399	
HFO1123	0.858	0.845	
HCFO1224yd(Z)	0.784	0.817	
HFO1243zf	0.941	0.987	
HCFO1233zd(E)	0.820		
HFO1336mzz(E)	0.871		
R407C	0.823		
HFC32/CF_3I		0.489	49.38/50.62 mol%
HFC32/HFC125/CF_3I		0.66	49.0/11.5/39.5 mol%
HFO1123/HC290			50.0/50.0 mass%
HFO1123/HFO1234yf			50.0/50.0 mass%

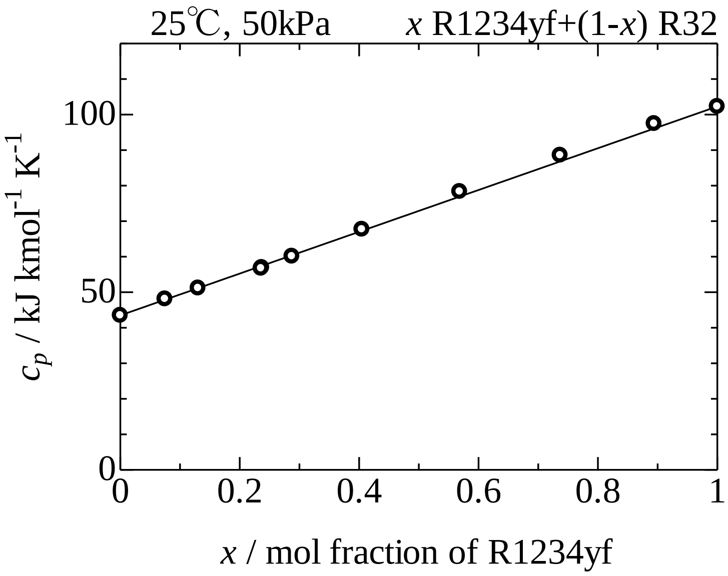

Fig. 2.1.3-23 Composition dependence of isobaric-specific heat capacity for HFC32/HFO1234yf mixture

References

1) E. Tanaka, K. Tanaka, Proc. of the 2021 JSRAE Annual Conference D231, pp.1-2, Tokyo (online) (2021).

2) K. Tanaka, Proc. of 12th Asian Thermophysical Properties Conference, p.31, Xi'an (2019).

3) K. Tanaka, Netubussei, 35(4), 140 (2021).

4) K. Tanaka, Proc. of the 2021 JSRAE Annual Conference D232, pp.1-2, Tokyo (online) (2021).

5) K. Tanaka, Proc. of the 2021 JSRAE Annual ConferenceD233 p.1-2, Tokyo(online) (2021).

2.1.4 Surface tension measurements

Nagasaki University provided the surface tension measurement data using the differential capillary rise method for new refrigerants. This method was based on the phenomenon that the balance between the surface tension and volumetric force of the liquid column determined the height of a liquid column in a glass capillary. As shown in the left of Fig. 2.1.4-1, the differential height Δh_m measured at the bottom of the meniscuses was precisely measured, and the lifted volume of the hemispherical meniscus was corrected. Figure 2.1.4-1 right-hand side shows the measurement setup designed for the capillary rise method. Three capillary glass tubes with different inner radii were vertically set in a pressure vessel (A), and sample refrigerant was filled approximately halfway from the bottom of the capillary tubes. Thereafter, the pressure vessel was placed in a thermostatic bath (B) filled with propylene glycol. The bath temperature was controlled within ±10 mK using a PID controller (K), three stirrers (E), an electric heater (F), and a chiller (G). Further, the temperature near the pressure vessel was measured using a platinum resistance thermometer (M) and a bridge ASL F-500(C) calibrated to ITS-90. In addition, the differential capillary height of the liquid columns was measured through a glass window of the thermostatic bath using a digital traveling microscope (D), a CCD camera (I), and an external monitor (J). The glass capillaries and pressure vessel were cleansed with an alkaline solution and distilled water using an ultrasonic bath. The estimated measurement uncertainty of 95% coverage Was 0.22 mNm-1. Here, the measurement reproducibility was considered satisfactory because the measured surface tensions of R134a, R32, and R245fa were consistent with the literature data to within ±0.15 mNm-1. Further, the composition of the mixture was calculated employing the weight method performed at the time of sample mixing and was confirmed to be in general having ±1% agreement using a gas chromatograph with the recovered sample after the measurement.

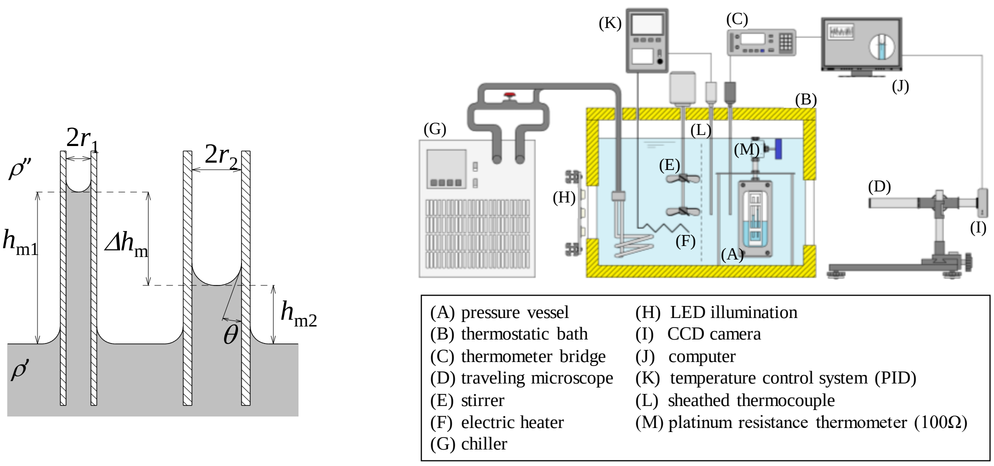

Fig. 2.1.4-1 Measurement method. Principle of a differential capillary rise height (left) and measurement setup (right).

The surface tension of thirteen refrigerants was measured in this project, as summarized in Fig. 2.1.4-2. However, this included certain refrigerants re-measured for the measurement of mixtures owing to insufficient data at low temperatures. For most of the substance, the surface tension data were provided at temperatures up to 225 K. The solid lines indicate the surface tension calculated through van der Waals-type empirical correlations. The empirical correlation is summarized in Table 2.1.4-1. The critical temperatures in the listed empirical correlations were mainly provided by Kyushu university. In Table 2.1.4-1, parachor of these substances are listed. The parachor method obtains the surface tension from the molar density difference between saturated vapor and liquid, $\tilde{\rho}'$ and $\tilde{\rho}''$, in mol cm^{-3}, as follows.

$$\sigma = \left\{ \left[P_i \right] \left(\tilde{\rho}' - \tilde{\rho}'' \right) \right\}^4 \tag{2.1.4-1}$$

The values of parachor are almost independent of the temperature except near the critical point. Further, constant values were obtained except for that at R1336mzz(E), which was expressed as a function of temperature because the temperature dependence in case of R1336mzz(E) was not negligible.

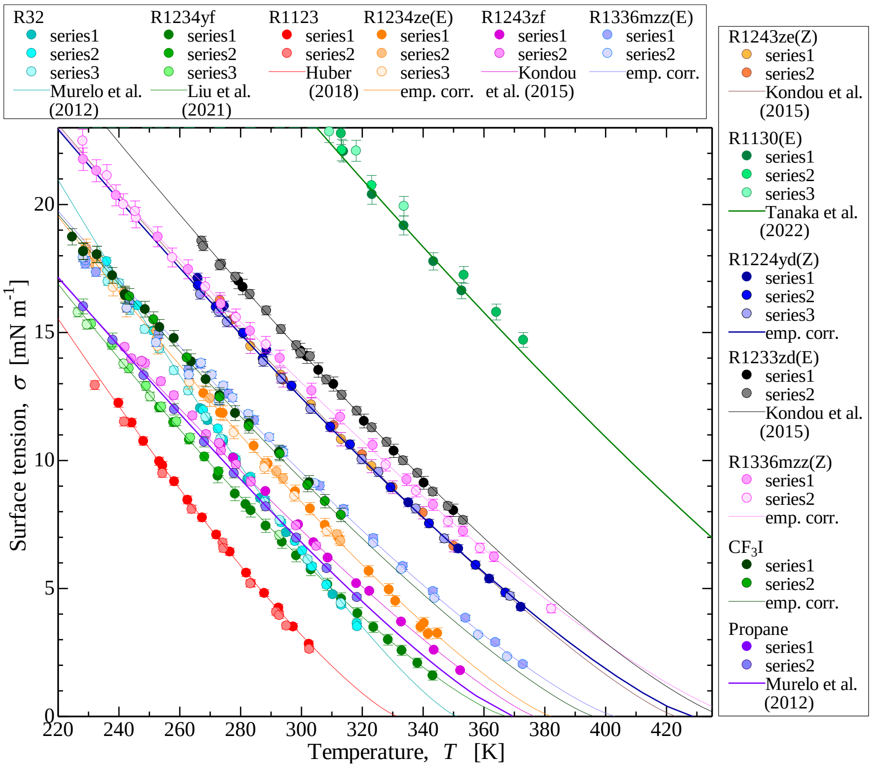

Fig. 2.1.4-2 Surface tension measured for low GWP refrigerants and mixture components.

Table 2.1.4-1 Empirical correlation and Parachor for single components.

Compound	Empirical correlation for σ [mN m^{-1}]	Parachor	References for correlation for crit. temp.
HFO1123	$\sigma = 61.2\left(1-\dfrac{T}{331.73}\right)^{1.26}$	123.3	JAREF[1] Higashi[7]
HFO1234yf	$\sigma = 55.24\left(1-\dfrac{T}{367.85}\right)^{1.30}$	172.0	JAREF[1] JAREF[1]
HFO1234ze(E)	$\sigma = 61.98\left(1-\dfrac{T}{382.51}\right)^{1.281}$	171.9	Mulero[6] Higashi[9]
HFO1243zf	$\sigma = 53.30\left(1-\dfrac{T}{378.93}\right)^{1.247}$	167.7	JAREF[1] Higashi[11]
HFO1234ze(Z)	$\sigma = 56.57\left(1-\dfrac{T}{423.27}\right)^{1.22}$	177.6	JAREF[1] Higashi[10]
HCFO1233zd(E)	$\sigma = 61.95\left(1-\dfrac{T}{438.75}\right)^{1.277}$	202.4	JAREF[1] Hulse[14]
HCFO1224yd(Z)	$\sigma = 57.02\left(1-\dfrac{T}{428.69}\right)^{1.265}$	207.0	JAREF[1] Higashi[8]
HFO1336mzz(E)	$\sigma = 53.71\left(1-\dfrac{T}{403.53}\right)^{1.27}$	237.45-0.0483T	Iwasaki[2] Sakoda[5]
HFO1336mzz(Z)	$\sigma = 55.48\left(1-\dfrac{T}{444.5}\right)^{1.29}$	230.04	Unpublished Tanaka[12]
HCO1130(E)	$\sigma = 70.21\left(1-\dfrac{T}{516.5}\right)^{1.25}$	173.4	Tanaka[3] Tanaka[3]

CF_3I	$\sigma = 53.53\left(1-\dfrac{T}{396.495}\right)^{1.24}$	170.24	Numadate[4] Perera[13]
HC290	$\sigma = 53.34\left(1-\dfrac{T}{369.89}\right)^{1.235} - 17.48\left(1-\dfrac{T}{369.89}\right)^{4.404}$	151.62	Mulero[15] Lemmon [16]

Subsequently, the surface tension of the refrigerant mixture was measured. In Figs. 2.1.4-3~5 below, the symbols show the measurement results based on composition, and the solid lines show the calculation results of REFPROP10.0. The parachor method is implemented in REFPROP10.0[17] to calculate the surface tension for mixtures, as shown below.

$$\sigma = \left\{\sum_{i=1}^{N}[P_i](\tilde{\rho}' x_i - \tilde{\rho}'' y_i)\right\}^4 \qquad (2.1.4\text{-}2)$$

Where x_i and y_i are the mole fractions of i species in the liquid and vapor phases, respectively. The composition and saturation density calculations were performed by REFPROP10.0. The results presented below were obtained from the equations of state developed for each refrigerant and the optimized mixing parameters in this project.

First, the surface tension was measured for a ternary mixture of HFO1123/HFC32/HFO1234yf refrigerants, as shown in Fig. 2.1.4-3 (c), and their constituent binary mixtures, as shown in Figs. 2.1.4-3(a)~3(b). The measured results for HFC32/HFO1234yf were consistent with the calculations, and the equation of state, mixing parameters, and Parachor were all obtained with high accuracy. In case of HFO1123/HFO1234yf, the measured data were slightly higher than REFPORP10.0 above 260 K. Further, for HFO1123/HFC32/HFO1234y with relatively low HFO1234yf compositions of 18 and 8 mass%, the measured results were slightly lower than the calculated results below 250 K; whereas, above 270 K, the measured results were slightly higher. However, there was consistency throughout the entire measurement range.

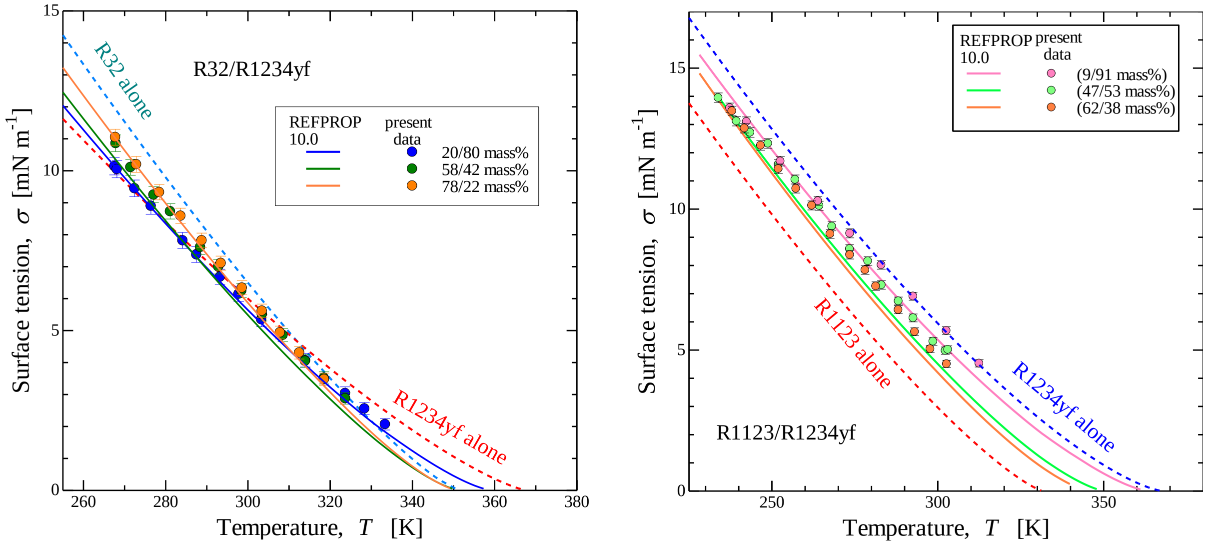

(a)HFC32/HFO1234yf (b) HFO1123/HFO1234yf

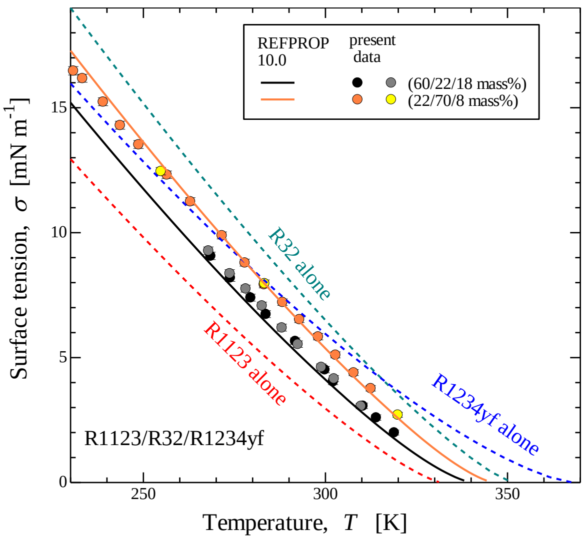

(c) HFO1123/HFC32/HFO1234yf

Fig. 2.1.4-3 Surface tension measured for HFO1123/HFC32/HFO1234yf and its constituent binary mixtures[18)]

Figure 2.1.4-4 shows the HFO1123/HFC32/CF_3I ternary mixture. The constituent binary mixture HFO1123/CF_3I was checked because few measurements, such as density, were available, and mixing parameters were not optimized for this mixture. The results are shown in Fig. 2.1.4-4(a). The solid line indicates the calculated surface tension using the mixing parameters automatically generated by REFPROP10.0. Further, the measured data deviated from the calculated results, particularly toward the critical point, where the difference wa more evident. Kyushu University (NEXT-RP) also noted a significant difference between the measurement and calculation for the saturation density near the critical point; thus, the critical temperature is also expected to yield a substantial calculation error. The surface tension measurement data suggested approximately 5 K higher critical temperature than the calculation for this binary mixture. Figures 2.1.4-4(b)~4(d) show the results for compositions of 65/30/5, 68/22/10, and 73/22/5 mass%, respectively. The measured and calculated results were consistent because of the low mass fraction of CF_3I. In addition, the values calculated using the parachor method and REFPROP10.0 were consistent, thereby confirming that the parachor method was well implemented in REFPROP10.0 for this combination.

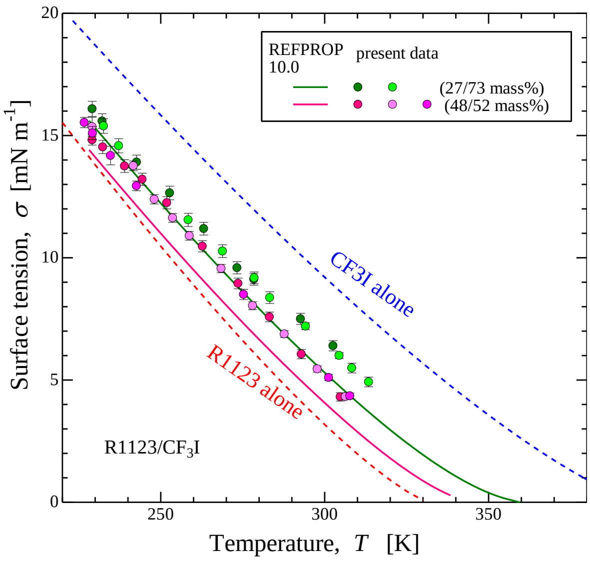

(a) HFO1123/CF_3I

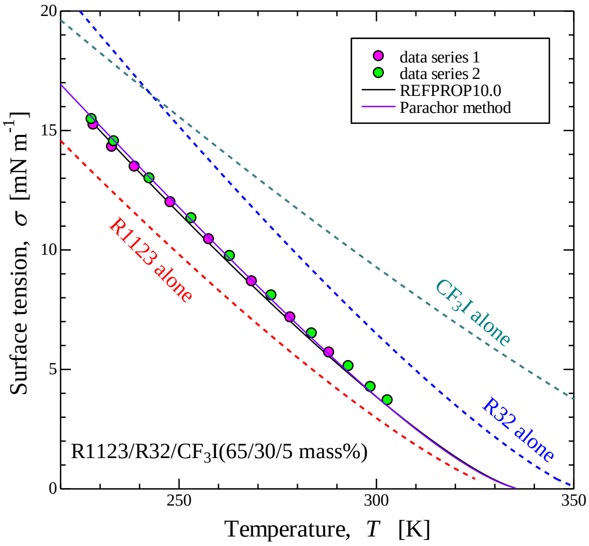

(b) 65/30/5 mass%

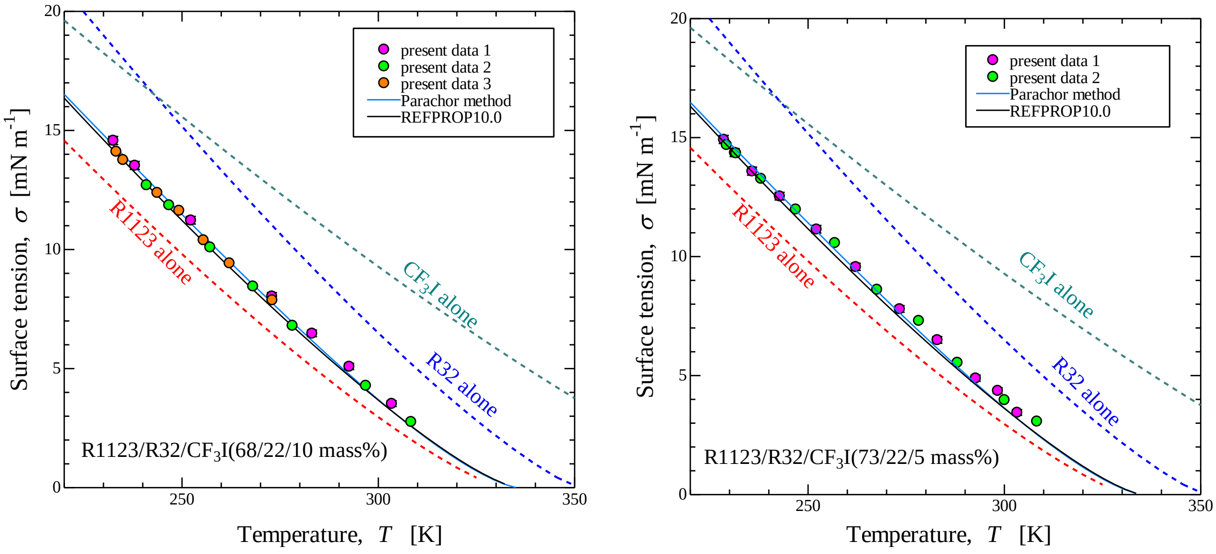

(c) 68/22/10 mass% (d) 73/22/5 mass%

Fig. 2.1.4-4 Surface tension measured for HFO1123/HFC32/CF_3I[19)]

Figure 2.1.4-5 shows the surface tension measurements of the HFO1123/HC290 binary mixture. Two measurements were performed at a composition of 78/22 mass%. The results were close to those of the surface tension of HFO1123 alone, and the REFPROP 10.0 estimates exhibited qualitative consistency. However, the mixing parameters for this binary system were not yet optimized; thus, better consistency is expected after optimization.

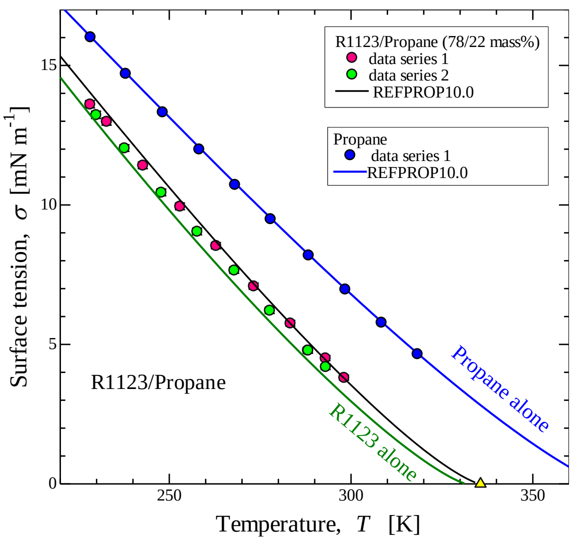

Fig. 2.1.4-5 Surface tension measured for HFO1123/HC290

In addition, the surface tension of R455A (HFO1234yf/HFC32/R744: 75.5/21.5/3.0 mass%) and R488A (HFC32/HFC125/HFO1234yf/HFC134a/HFO1234ze(E): 26/26/20/21/7 mass%) were also measured, which are already registered with ASHRAE. The results are shown in Fig. 2.1.4-6. These premixed refrigerants were compared to the previous version, REFPROP 9.1, and to REFPROP 10.0, which included the mixing parameters developed in this project. The measured results for R455A were consistent with REFPROP 10.0, although REFPROP 9.1 yielded slightly higher results. However, because R488A is a quintet mixture, certain combinations, such as HFC125/HFO1234ze(E), have not been investigated. Thus, the mixing parameter was not yet optimized for all combinations. However, REFPROP10.0 with optimized parameters yielded values considerably closer to the measured values. As confirmed above, the optimization of mixing parameters significantly affected the calculation of surface tension.

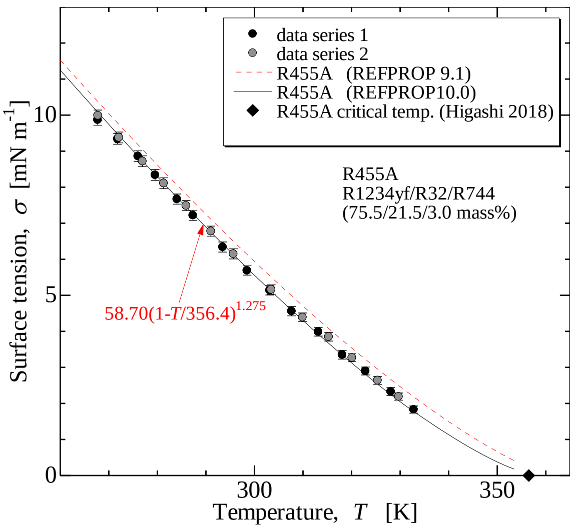

(a) R455[20)]

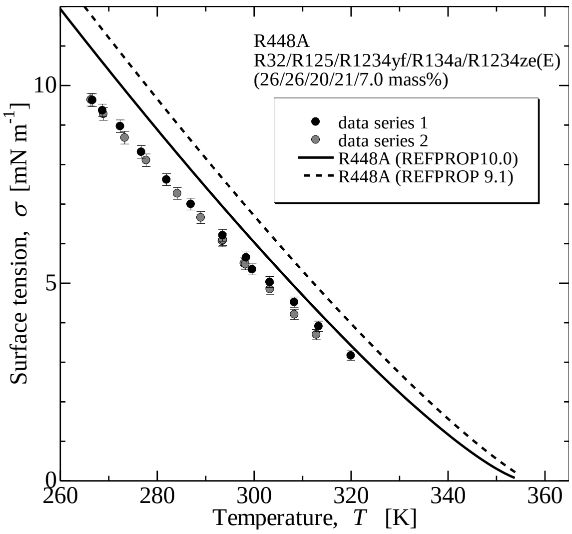

(b) R448A[21)]

Fig. 2.1.4-6 Surface tension measured for premixed refrigerants R455A and R448A

References

1) Y. Kayukawa, C. Kondou, N. Sakoda, K. Kariya, S. Fukuda: "JSRAE Thermodynamic Tables, Vol. 5. HFOs and HCFOs,Ver.1.0" Japan Society of Refrigerating and Air Conditioning Engineers, Tokyo (2021).
2) S. Iwasaki, C. Kondou, Y. Higashi: Trans. JSRAE. 37, 73 (2020). (in Japanese).
3) K. Tanaka, C. Kondou, S. Fukuda, R. Akasaka: Int. J. Thermophys., 43, 69 (2022).
4) T. Numadate, Y. Jojima, Y. Otsubo, Y. Liu, C. Kondou: JSRAE Annual Conference, D212, Tokyo (held on the web) (2021).
5) N. Sakoda, Y. Higashi, R. Akasaka, R.: J. Chem. Eng. Data., 66, 734 (2020).
6) A. Mulero, I. Cachadiña: J. Phys. Chem. Ref. Data 43, 023104 (2014).
7) Y. Higashi, R. Akasaka: Proc.16th Int. Refrigeration and Air Conditioning Conference at Purdue, Paper ID: 1688, West Lafayette, Indiana (2016).
8) Y. Higashi, R. Akasaka: Proc. the 11th Asian Thermophysical Properties Conference, Yokohama, Japan (2016).
9) Y. Higashi, K. Tanaka, T. Ichikawa: J. Chemical & Engineering Data, 55(4), 1594 (2010).
10) Y. Higashi, S. Hayasaka, C. Shirai, R. Akasaka: Int. J. Refrig., 52, 100 (2015).
11) Y. Higashi, N. Sakoda: J. Chem. Eng. Data, 63(10), 3818 (2018).
12) K. Tanaka, R. Akasaka, E. Sakaue, J. Ishikawa, K. K. Kontomaris: J. Chem. Eng. Data, 62(3), 1135 (2017).
13) U.A. Perera, K. Thu, N. Sakoda, M. Kozue, Y. Higashi: J. Chem. Eng. Data. 67(9) 2182 (2022).
14) R.J. Hulse, R.S. Basu, R.R. Singh, R.H.P. Thomas: J. Chem. Eng. Data, 57(12), 3581 (2012).
15) A. Mulero, I. Cachadiña, M.I. Parra: J. Phys. Chem. Ref. Data, 41(4), 043105 (2012).
16) E.W. Lemmon, M.O. McLinden, W. Wagner: J. Chem. Eng. Data, 54, 3141(2009).
17) E.W. Lemmon, I.H. Bell, M.L. Huber, M.O. McLinden: Reference Fluid Properties, version 10.0, Applied Chemicals and Materials Division National Institute of Standards and Technology, Boulder.
18) Y. Otsubo, T. Numadate, Y. Jojima, T. Kawahara, C. Kondou, Y. Liu: Proc. the 91st JIME Annual Conf. no. 106, Kobe (2021).
19) Y. Otsubo, T. Kawahara, R. Nonaka, C. Kondou: 2022 JSRAE Annual Conf., Okayama, C312 (2022).
20) C. Kondou, Y. Higashi: Proc. the 88th JIME Annual Conf., no. 207, Okayama, (2018).
21) T. Numadate, S. Iwasaki, Y. Jojima, C. Kondou, Y. Higashi: Proc. the 89th JIME Annual Conf., OS2-8, pp. 173-174. Hakodate, (2019).

2.1.5 Speed of sound measurements

In AIST, we performed speed of sound measurements for a refrigerant in the vapor phase using an acoustic-microwave cylindrical resonator[1)–3)]. Figures 2.1.5-1 Fig. 2.1.5-2 show a photograph of the cylindrical resonator and a schematic of the speed of sound and dielectric permittivity measurement apparatus, respectively. The cylindrical resonator was composed of oxygen-free copper with very high thermal and electrical conductivity. The cylindrical cavity length and diameter were approximately 50 and 24 mm, respectively. The cylindrical resonator was mounted in a pressure vessel composed of SUS316 to minimize the cavity shape deformation owing to the sample gas pressure. A sample gas was admitted into the pressure vessel and went into the cylindrical cavity through the hole placed at the side wall of the resonator. During the acoustic and microwave resonance measurements, the sample admission hole was plugged with a customized bellows valve to create an ideal cylindrical cavity shape.

The acoustic resonance was measured using two condenser microphones (B&K, 4192, one as a transmitter, and the other a receiver), attached to both end plates of the cylindrical resonator. The receiver microphone preamplifier (GRAS, 26AC) and transmitter microphone adapter (GRAS, RA0086) were connected to the respective microphones through hand-made hermetic feedthroughs with triaxial cables. Further, the acoustic resonance frequency curve was measured using an audio-frequency response analyzer (NF, FRA51062). The output signal from FRA51062 was amplified via a driving amplifier (GRAS, 14AA) to excite the transmitter microphone, and the detected signal with the receiver microphone at a locked frequency of the transmitter oscillation was measured using an FRA51062 through a microphone power module (GRAS, 12AR). Consequently, by sweeping the frequency of the output signal, an acoustic resonance frequency curve was obtained.

Meanwhile, the microwave resonance was measured with two antennas attached on both end plates of the cylindrical resonator. The antennas were made from copper semirigid coaxial cables and attached to the resonator such that their front edges were flushed with the interior surface of the cylindrical cavity. Thereafter, the microwave resonance frequency curve was measured using a vector network analyzer (R&S, ZVB20) to obtain the microwave transmission characteristics (S-parameter) in the cylindrical resonator.

The pressure vessel installing the cylindrical resonator was immersed in a liquid thermostat to control its temperature within 5 mK. The temperature was measured using a standard platinum resistance thermometer (Netsushin, NSR-LT40), which was calibrated in accordance with ITS-90, and a precision thermometer bridge (ASL, F700B). Silicon oil (Barrel Silicon MA20) was used as a heating medium in the thermostat. The sample gas pressure was directly measured with a quartz-oscillation type pressure transducer (Paroscientific, 2400A), which was placed at a head space in the thermostat to minimize the temperature gradient of the sample gas.

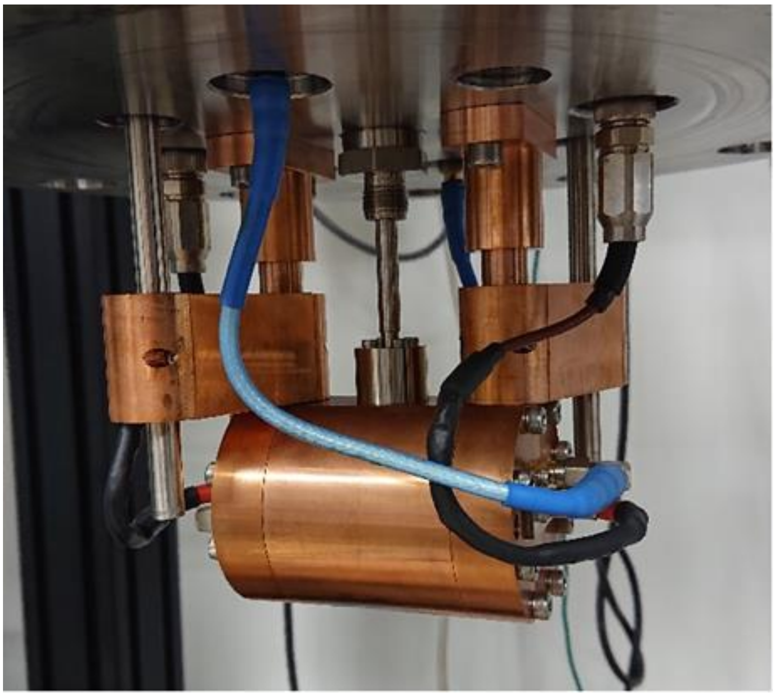

Fig. 2.1.5-1 Photograph of the acoustic-microwave cylindrical resonator.

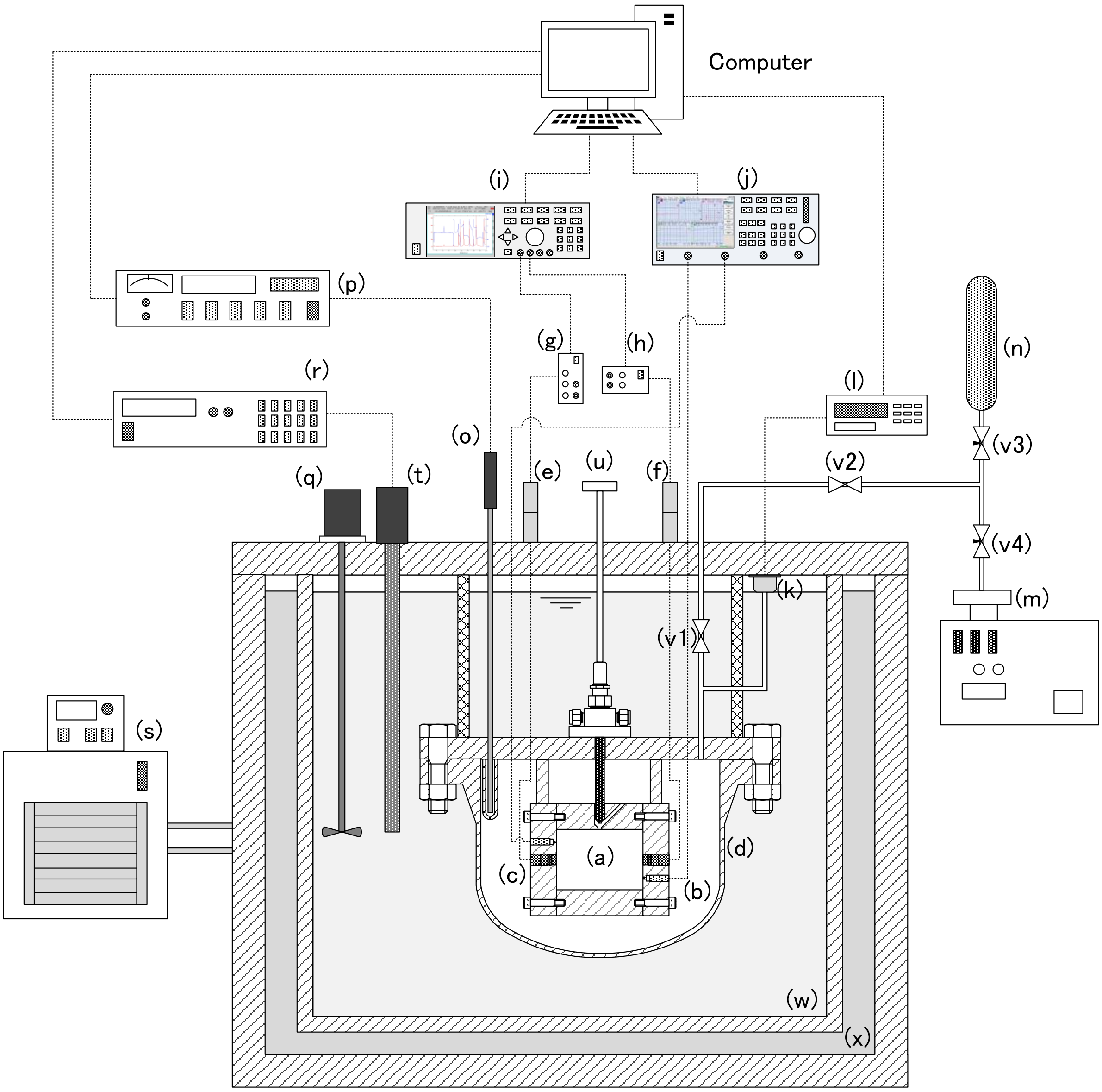

Fig. 2.1.5-2 Schematic of the speed of sound and dielectric permittivity measurement apparatus.
(a) cylindrical cavity resonator; (b) antennas; (c) microphones; (d) pressure vessel; (e) transducer microphone adapter; (f) receiver microphone preamplifier; (g) transducer microphone power supply; (h) receiver microphone power supply; (i) acoustic resonance frequency analyzer; (j) vector network analyzer; (k) quartz oscillation type pressure sensor; (l) pressure display; (m) vacuum pump; (n) sample gas cylinder; (o) standard platinum resistance thermometer; (p) AC resistance bridge; (q) centrifugal type stirrer; (r) DC programmable power supply; (s) external refrigerated circulator; (t) sheath heater; (u) sample admission valve; (v1–4) valves; (w) main thermostatic bath; (x) outer thermostatic layer.

In this study, the speed of sound was obtained through acoustic resonance frequency measurements in the five pure longitudinal modes in the range of (2, 0) to (6, 0). Based on the measurement of the acoustic resonance frequency in the longitudinal mode $f_{l,0}$, the speed of sound w, of the sample gas was using the following relation.

$$w = \frac{2L\left(f_{l,0} + \Delta f_{AC}\right)}{l} \tag{2.1.5-1}$$

where L and l represent the cylindrical cavity length and acoustic resonance mode index, respectively, and Δf_{AC} is the acoustic resonance frequency correction owing to nonideal resonance effects. Further, the microwave resonance frequency in the cylindrical cavity f_{pqs}, is associated with the dielectric permittivity of the sample gas ε_r, and the speed of light in vacuum c, as follows.

$$f_{pqs} = \frac{c}{2\pi\sqrt{\varepsilon_r}}\sqrt{\left(\frac{\phi_{pq}}{r}\right)^2 + \left(\frac{\pi s}{L}\right)^2} - \Delta f_{EM} \tag{2.1.5-2}$$

where s and ϕ_{pq} は are the microwave resonance mode index and the eigenvalue of the microwave resonance, respectively, and Δf_{EM} is microwave resonance frequency correction because of nonideal resonance effects. Therefore, the microwave resonance measurement in the evacuated cavity ($\varepsilon_r = 1$) resulted in the cylindrical cavity dimensions at a measurement temperature. In addition, the relative dielectric permittivity of the sample gas was determined considering the ratio of the microwave resonance frequencies between the evacuated and sample gas-filled cavity. The measurement uncertainties ($k = 2$) of the present apparatus were estimated to be 14 mK, 0.28 kPa, 0.04%, and 0.02% for temperature, pressure, speed of sound, and dielectric permittivity, respectively.

Moreover, a new speed of sound measurement apparatus in the liquid phase was developed under this project as illustrated in Fig. 2.1.5-3. Using an ultra-sonic pulse transmission type of sensor (Anton Parr, L-Sonic 6100), the speed of sound in a liquid sample was determined by measuring the traveling time, t, of the ultra-sonic pulse propagating between a transmitter and a receiver in the liquid.

$$w = \frac{L_0(1 + \alpha T)(1 + \beta p)}{t - \mathrm{D}_0(1 + \mathrm{D}_1 T + \mathrm{D}_2 T^2)} \tag{2.1.5-3}$$

where L_0 is the traveling distance between the transmitter and the receiver at a calibration temperature, α is the temperature correction factor of the traveling distance, and D_0～D_2 are the time-delay correction factors of the traveling time that were calibrated by the manufacturer based on the speed of sound of in pure water. In addition, β represents the pressure correction factor for the traveling distance and was set as 0.0007 in this study by referring to a previous report[4)] using the same type of the sensor. Moreover, the measurement uncertainty ($k = 2$) of the speed of sound in the liquid phase was estimated to be approximately 0.1 %.

The speed of sound sensor for the liquid sample was immersed in a liquid thermostat with glycol brine (Barrel Brine E) to control the temperature within 5 mK. The temperature was measured using a platinum resistance thermometer (Chino, R900), calibrated in advance based on the ITS-90, and a digital temperature indicator (ASL, F200). Further, the sample pressure was directly measured with a quartz-oscillation type pressure transducer (Paroscientific, 31K101). The measurement uncertainties ($k = 2$) of temperature and pressure were estimated to be approximately 20 mK and 1 kPa, respectively.

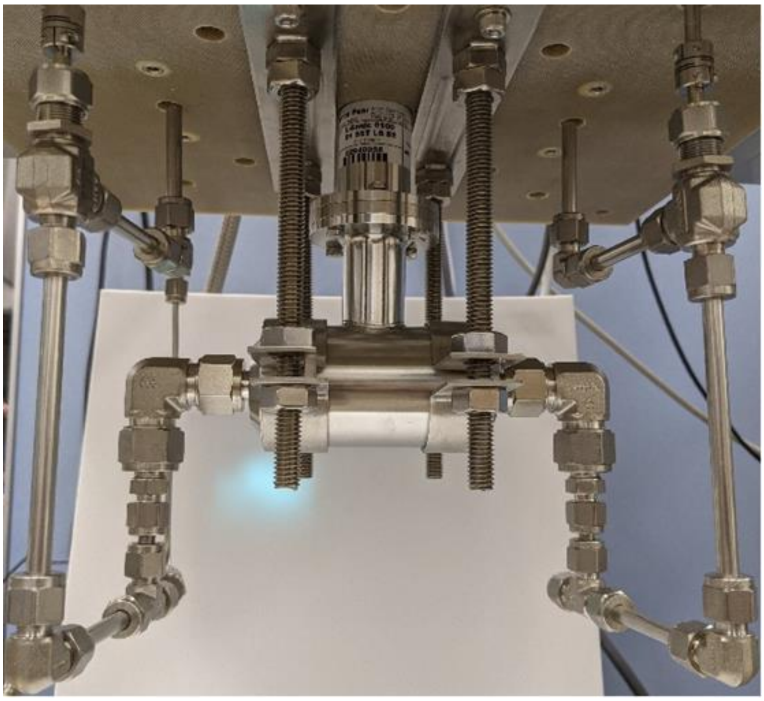

Fig. 2.1.5-3 Photograph of the speed of sound measurement apparatus in the liquid phase.

Table 2.1.5-1 summarizes the sample of the refrigerants, measurement temperature range, measurement pressure range, and speed of sound data obtained in this project. For each refrigerant sample, pressure and temperature dependences of the measured speed of sound data are illustrated in Fig. 2.1.5-4 and Fig. 2.1.5-5, respectively.

Table 2.1.5-1 List of the measured refrigerants.

Refrigerants	Temperature range / K	Pressure range / kPa	Number of speed of sound data	Reference
HFO1336mzz(E)	303 – 403	40 – 900	36 (vapor)	5), 6), 7)
HFO1336mzz(Z)	303 – 403	40 – 1000	36 (vapor)	6), 8)
	383 – 343	40 – 6500	95 (liquid)	9)
R454C	283 – 313	130 – 490	18 (vapor)	10)
R455A	283 – 313	150 – 780	17 (vapor)	10)
CF_3I	280 – 343	300 – 6800	35 (liquid)	9)

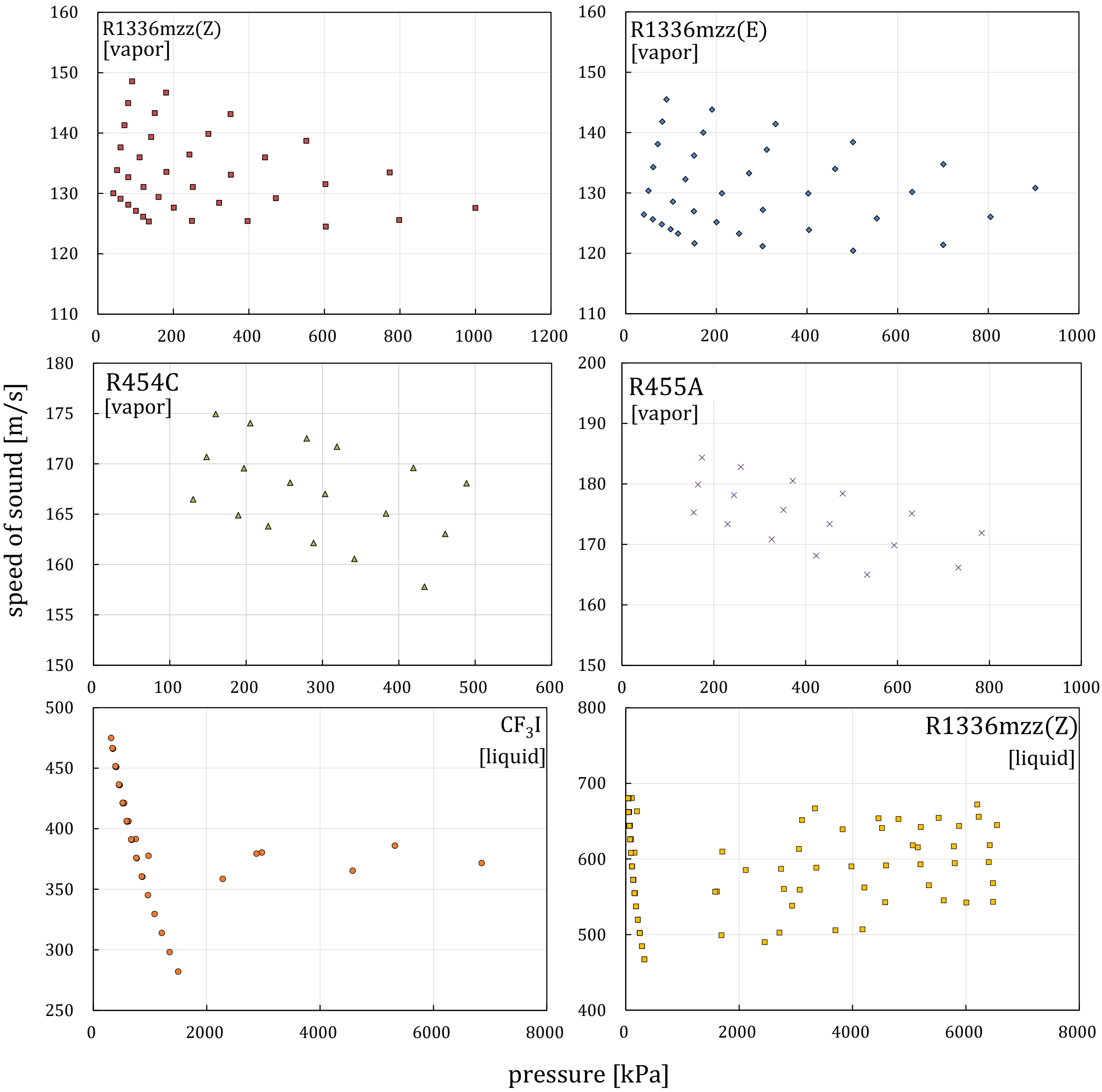

Fig. 2.1.5-4 Pressure dependence of the measured speed of sound data.

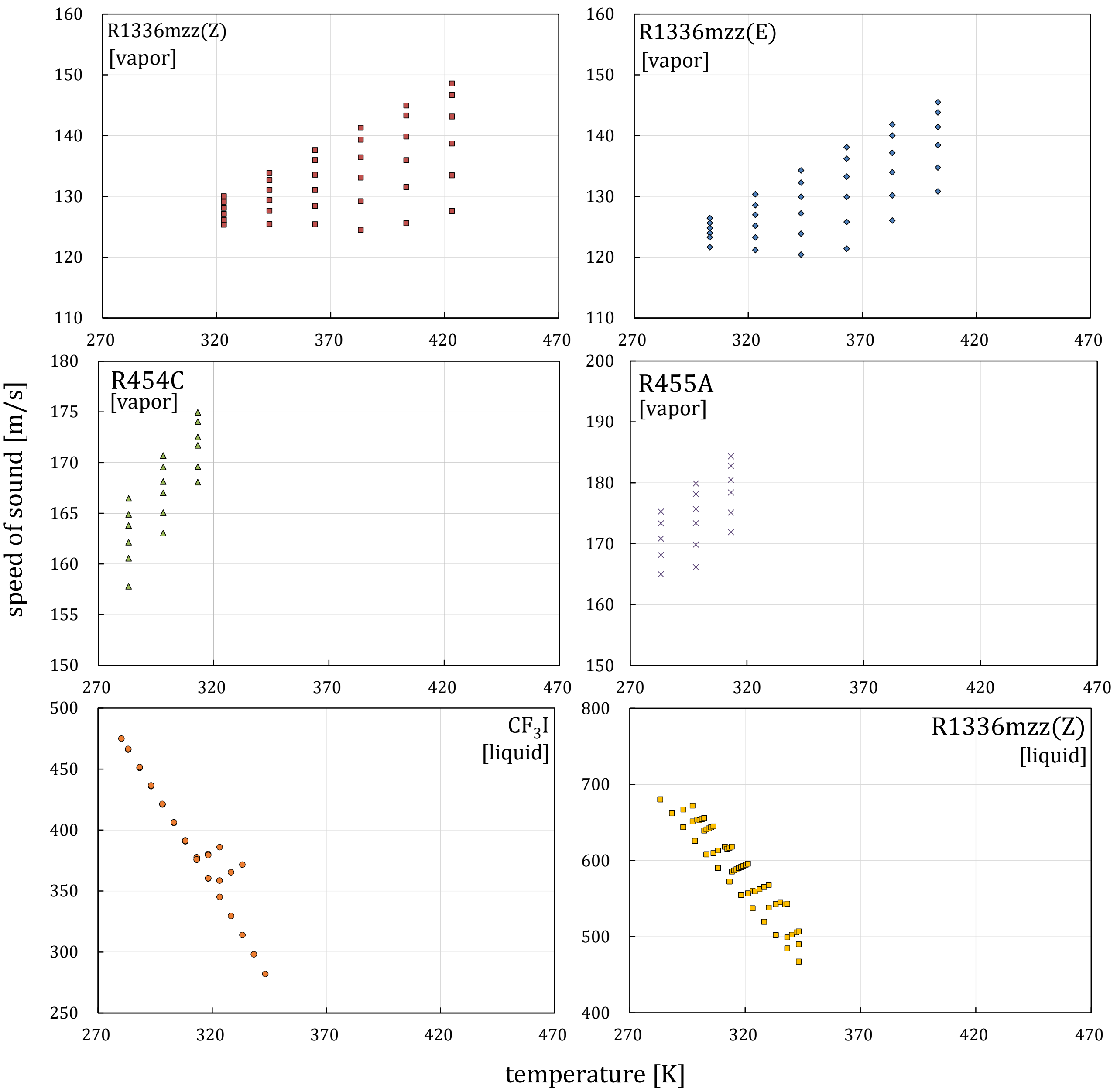

Fig. 2.1.5-5 Temperature dependence of the measured speed of sound data.

Furthermore, based on the vapor speed of sound data for HFO1336mzz(Z) and HFO1336mzz(E), the isobaric heat capacity in the ideal gas state, $c_p{}^{o}$, were determined by extrapolating the squared speed of sound on each isotherm to zero pressure as follows.

$$\lim_{p \to 0} w^2 = \frac{RTc_p^o}{M\left(c_p^o - R\right)} \tag{2.1.5-4}$$

where R is the gas constant and M is the molar mass. Figure 2.1.5-6 shows the temperature dependences of the determined ideal gas heat capacities for HFO1336mzz(Z) and HFO1336mzz(E). Using the determined ideal gas heat capacities, the following Plank-Einstein type of temperature correlations were formulated.

$$\frac{c_p^o}{R} = 4 + \sum_{i=1}^{n} \frac{\mathrm{d}_i(\mathrm{c}_i/T)^2 \exp\,(\mathrm{c}_i/T)}{[\exp(\mathrm{c}_i/T) - 1]^2} \tag{2.1.5-5}$$

where c_i and d_i are the fitted parameters reproducing the determined ideal gas heat capacities, whose numerical values are described in the literature[2)] for HFO1336mzz(Z) and the that[3)] for HFO1336mzz(E).

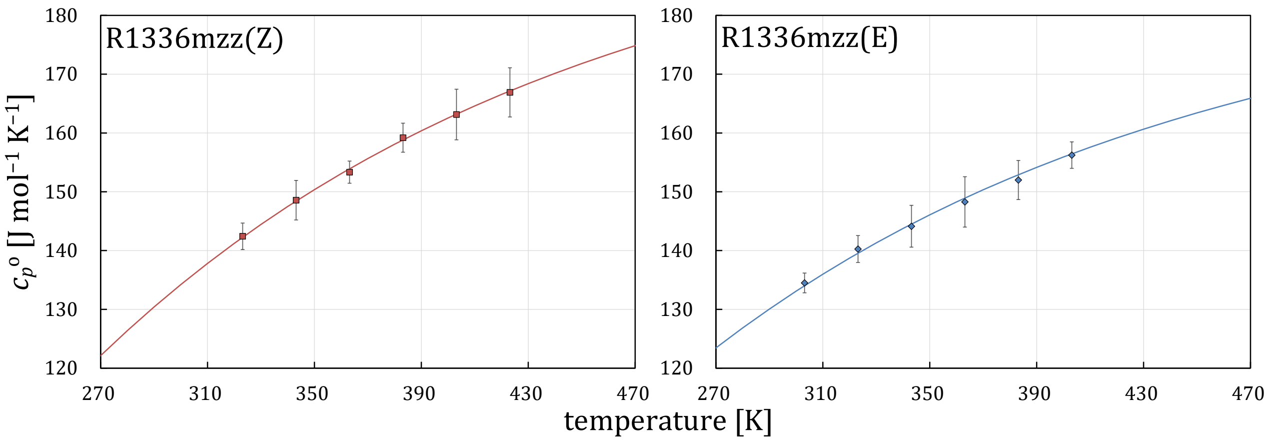

Fig. 2.1.5-6 Temperature dependence of the determined ideal gas heat capacities of HFO1336mzz(Z) and HFO1336mzz(E) in the ideal gas states.

References

1) Y. Kano, Y. Kayukawa, Y. Fujita, Dipole moment and heat capacity in the ideal gas state derived from relative permittivity and speed of sound measurements for HFO-1123 and HCFO-1224yd(Z), *Int. J. Refrig*. 118, 354 – 364, 2020.
2) Y. Kano, Thermophysical properties of 1,1,1,3,3,3-Hexafluoro-2-methoxypropane (HFE-356mmz) in the vapor phase measured by using an acoustic-microwave resonance technique, *Energies* 13, 5525, 2020.
3) Y. Kano, Multi-property evaluation for a gas sample based on the acoustic and electromagnetic resonances measurement in a cylindrical cavity, *J. Chem. Thermodyn*. 159, 106448, 2021.
4) T. Nishiyama, T. Kurakari, L. Gao, Y. Higashi, R. Akasaka: Proc. of the 2nd IIR Conference on HFOs and Low GWP blends, Japan, 2021. DOI : 10.18462/iir.HFO.2021.1028
5) Y. Kano, Y. Kayukawa, Y. Fujita, Speed of sound and dielectric constant measurements for HFO-1336mzz(E) in the gas phase, 2nd Pacific Rim Thermal Engineering Conference, 2019.
6) Y. Kano, Y. Kayukawa, N. Kuramoto, Speed of sound and dielectric permittivity measurements for R1336mzz(Z) and R1336mzz(E) in the vapor phases, 13th Asian Thermophysical Properties Conference, 2022.
7) Y. Kano: submitted to *J. Chem. Eng. Data*, 2022.
8) Y. Kano: submitted to *J. Therm. Anal. Calorim.* 2022.
9) Y. Kano: to be presented at 22nd European Conference on Thermophysical Properties (ECTP2023).
10) Y. Kano: to be presented at 2023 JSRAE Annual Conference.

2.1.6 Thermal conductivity and viscosity

At Saga university, the thermal conductivity and viscosity of HFO refrigerants were measured and the calculation model was estimated to reproduce the measurement results. The experimental apparatus is shown in Fig. 2.1.6-1. This apparatus facilitates simultaneous measurement of thermal conductivity and viscosity at different temperature and pressure conditions.

The thermal conductivity was measured using the thin-wire method; Fig. 2.1.6-2 shows the thermal conductivity measurement circuit. The thermal conductivity was determined by measuring the non-equilibrium potential difference of the Wheatstone bridge circuit caused by the change in electrical resistance of the long and short platinum wires in the bridge upon electrical heating of the refrigerant via the two wires measuring 15 μm in diameter. The refrigerant's thermal conductivity λ can be obtained by Eq. (2.1.6-1). In the equation q, E, T and t represent the heat load per unit length of the wire, non-equilibrium potential difference, refrigerant temperature, and time, respectively. To reduce the influence of current oscillations immediately following the start of electric conduction, current was applied to the dummy circuit on the left side of the figure in advance and was switched via a relay switch to the bridge circuit. The relationship between E and ln(t) was a straight line, and the thermal conductivity was obtained from the slope of the diagram plotting values. Figure 2.1.6-3 shows an example of the measurement. The plots in the figure show the measured values and the solid line is a straight line that reproduces the measured values. The synthetic standard uncertainty of the thermal conductivity obtained with this system was up to ±2.52 %.

$$\frac{dE}{d\ln t} = \frac{1}{\lambda}\frac{q}{4\pi}\frac{dE}{dT} \qquad (2.1.6\text{-}1)$$

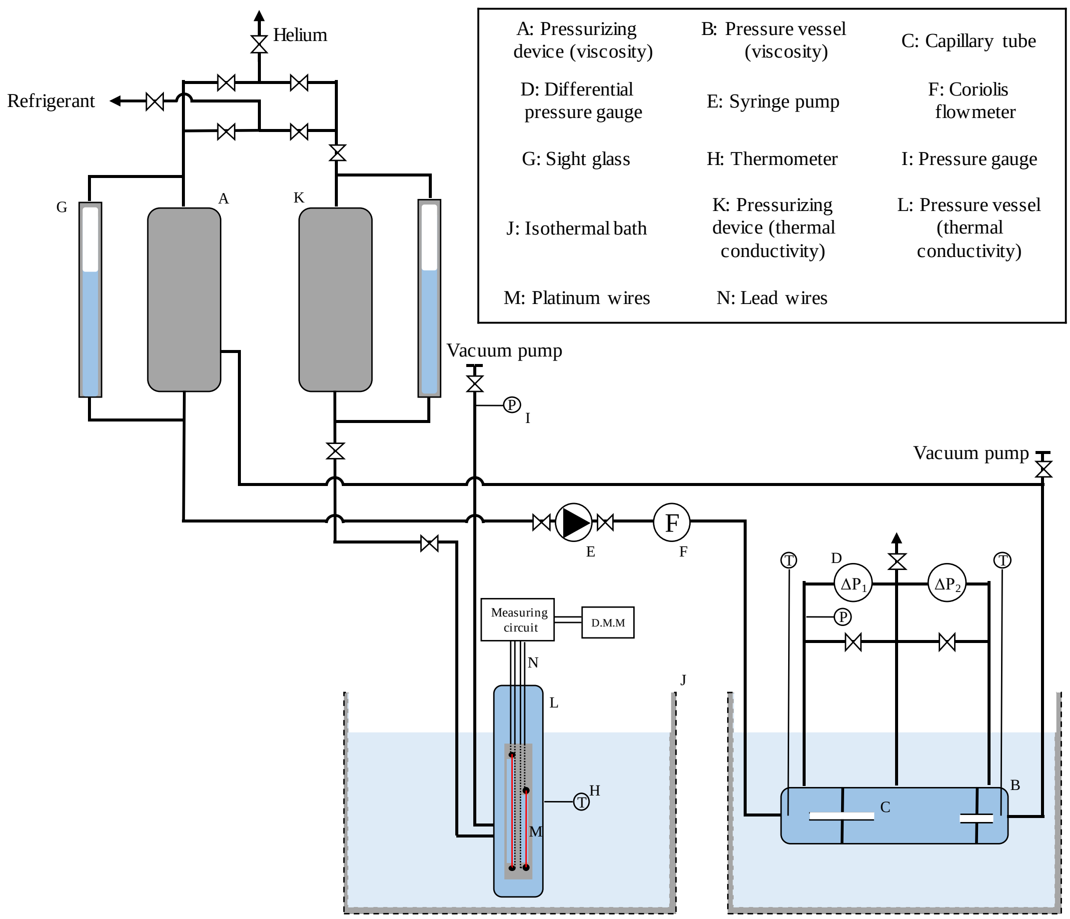

Fig. 2.1.6-1 Experimental apparatus for thermal conductivity and viscosity measurement

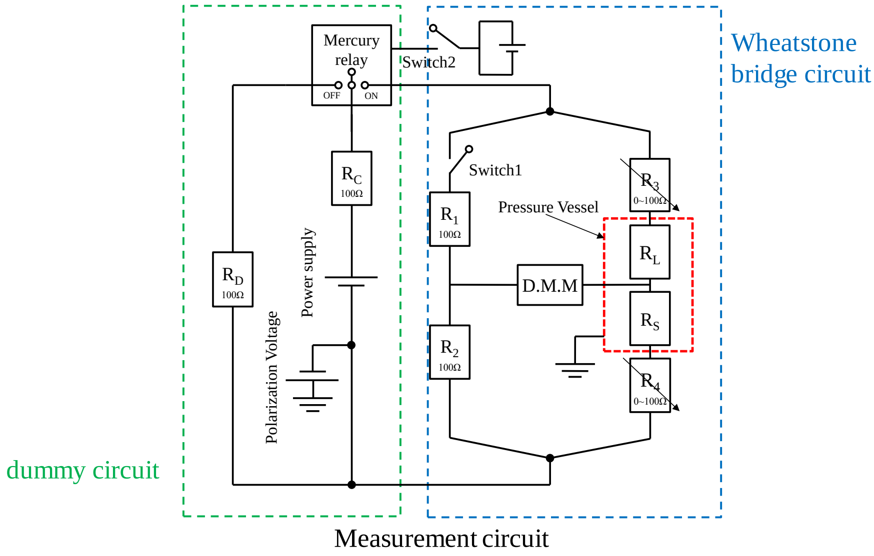

Fig. 2.1.6-2 Measurement circuit for thermal conductivity

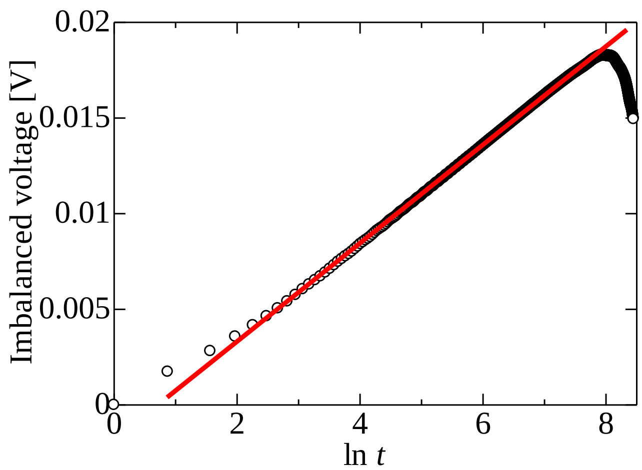

Fig. 2.1.6-3 Typical experimental result of thermal conductivity

To perform viscosity measurements, the tandem capillary tube method was used to eliminate the pressure drop at the inlet/outlet end. In the tandem capillary tube method, the viscosity can be obtained from the differential pressure of the long and short capillary tubes with an inner diameter of 0.1 mm and flow rate by laminar flow. Thus, the previously required device constants can be discarded and the viscosity can be obtained directly from the following equation (2.1.6-2). The synthetic standard uncertainty of the viscosity obtained with this apparatus reached up to ± 3.10 %.

$$\eta = \frac{\pi(a_L^4 \Delta P_L - a_S^4 \Delta P_S)}{8q(L_L - L_S)} \tag{2.1.6-2}$$

Table 2.1.6-1 lists the refrigerants measured in this project. The measured data included refrigerants that have not yet been published, as well as data obtained to confirm deviations in REFPROP calculations, such as HFC32 and HFO1234yf. The calculated values of HFO1234yf reproduced the measured values with a deviation of less than ±3% on the liquid side, and that less than ±5% on the vapour side in the high pressure range and approximately +10% in the low pressure range. Under practical conditions, the REFPROP calculated values were consistent with the measured values.

Table 2.1.6-1 List of measured refrigerants/blends

Refrigerants/Blends	**Properties**	**Measurement range Pressure, Temperature**	**Prediction method**	**Reference**
HFC32	Thermal conductivity	1 to 4 MPa 40 to 140 ℃	REFPROP Ver. 10.0	To be published
	Viscosity	1 to 4 MPa 40 to 140 ℃	REFPROP Ver. 10.0	To be published
HFO1234yf	Thermal conductivity	1 to 4 MPa 40 to 140 ℃	REFPROP Ver. 10.0	To be published
	Viscosity	1 to 4 MPa 40 to 140 ℃	REFPROP Ver. 10.0	To be published
HFO1336mzz(E)	Thermal conductivity	0.25 to 4 MPa 40 to 180 ℃	ECS model (NIST)	1, 2, 3
	Viscosity	0.25 to 4 MPa 40 to 180 ℃	ECS model (NIST)	2, 4, 5, 6, 7
CF_3I	Thermal conductivity	0.5 to 4 MPa 40 to 120 ℃	ECS model by modified EOS	To be published
	Viscosity	0.5 to 4 MPa 40 to 120 ℃	ECS model by modified EOS	8
HFC32/HFO1234yf [68.9/31.1 mass%]	Thermal conductivity	1 to 4 MPa -40 to 20 ℃	REFPROP Ver. 10.0	Ongoing
	Viscosity	1 to 4 MPa -40 to 20 ℃	REFPROP Ver. 10.0	Ongoing

In this report, the measurement results of thermal conductivity and viscosity values are not published. The measured data of the new refrigerant candidates will be published in the future. Further, the thermal conductivity and viscosity data of the published refrigerants can be found in the references. This report summarized the results of the comparison of the measured data with REFPROP ver. 10 and the prediction modified or newly developed in this project. The comparison results are shown in Figs. 2.1.6-4 to 6. The range of the various refrigerants to be measured and the type of prediction calculation model are presented in Table 2.1.6-1. The calculation model of HFO1336mzz(E) was obtained with the aid of Dr. Huber (NIST), and the transport properties of CF_3I were calculated employing the extended corresponding state model (ECS model) using equation of state developed in this project.

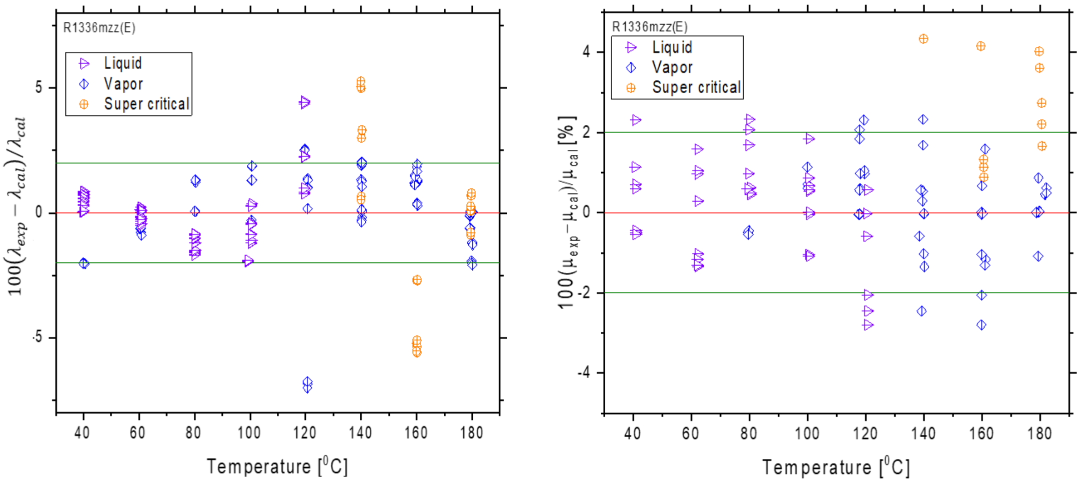

(a) Thermal conductivity (b) Viscosity

2.1.6-4 Deviation between experimental and correlated [9] transport properties of HFO1336mzz(E)

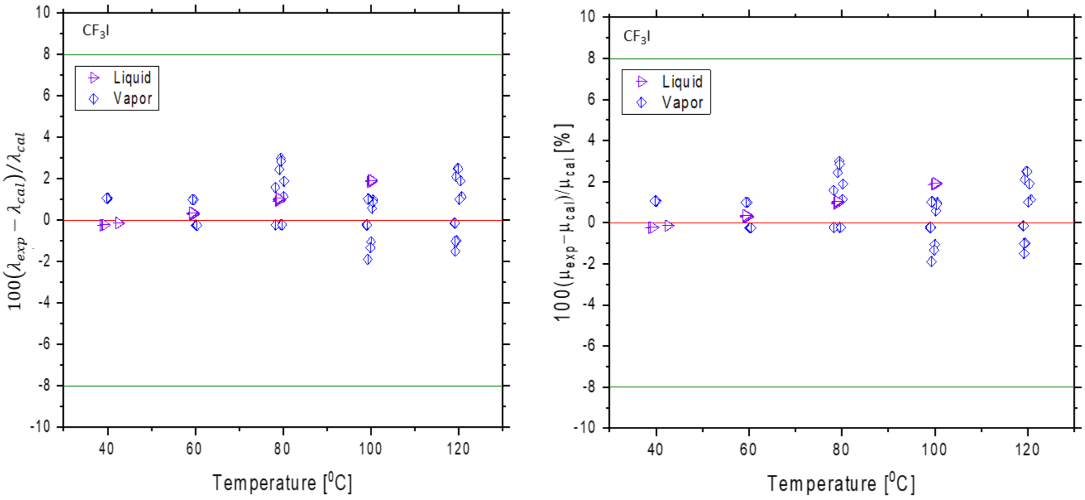

(a) Thermal conductivity (b) Viscosity

2.1.6-5 Deviation between experimental and correlated [10] transport properties of CF_3I

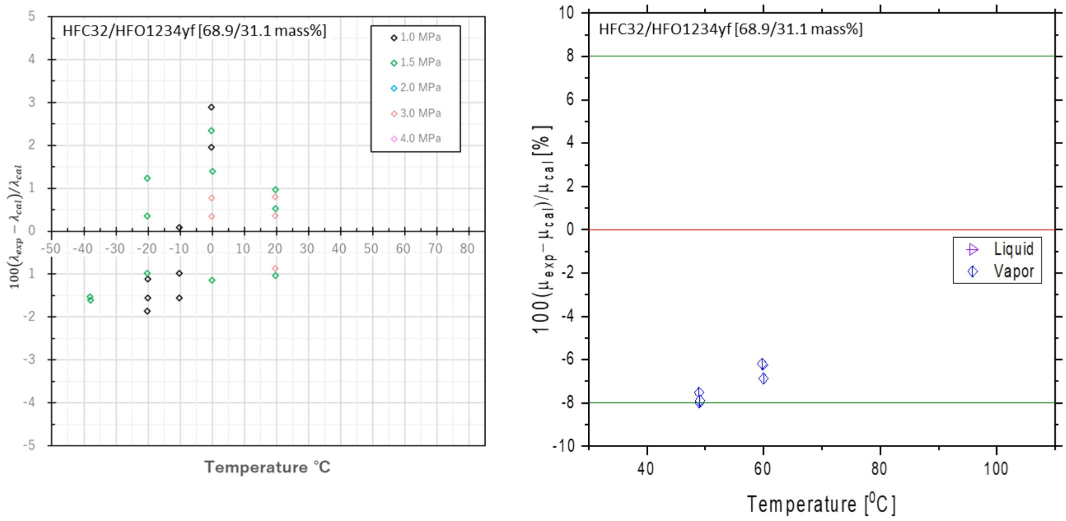

(a) Thermal conductivity (b) Viscosity

2.1.6-6 Deviation between experimental and correlated transport properties of HFC32+HFO1234yf [68.9/31.1 mass%]

For R1336mzz(E) in Fig. 2.1.6-4, most of the data for thermal conductivity and viscosity can be reproduced within ±2%, implying that the calculated values were consistent with the measured values. Certain data deviations in the supercritical pressure region were as large as 5%; however, this was because of the abrupt changes in physical properties near the pseudo-critical temperature; therefore, deviations of approximately 5% are acceptable. The deviation between the calculation and measured CF_3I values in Fig. 2.1.6-5 was small indicating consistency. For HFC32+HFO1234yf [68.9/31.1 mass%] in Fig. 2.1.6-5, the calculated results of thermal conductivity were consistent; however, the deviation in the viscosity Was -8%. Currently, there is still a lack of data, therefore modifications of the model should be considered along with the enrichment of the data.

References

1） D. Mondal, K. Kariya, A. R. Tuhin, K. Miyoshi, A. Miyara, Int. J. Refrig., 129, 109-117 (2021)

2） A. R. Tuhin, D. Mondal, N. Amakusa, K. Kariya, A. Miyara, 2021 JSRAE Annual Conference, D211, Tokyo (Online) (2021) (in Japanese)

3） K. Miyoshi, D. Mondal, A. R. Tuhin, K. Kariya, A. Miyara, 2020 JSRAE Annual Conference, D113 Mie (Online) (2020) (in Japanese)

4） D. Mondal, K. Kariya, A. R. Tuhin, N. Amakusa, A. Miyara, Int. J. Refrig., 133, 267-275 (2022)

5） N. Amakusa, D. Mondal, A. R. Tuhin, K. Kariya, A. Miyara, HFO2021 2nd IIR Conference on HFOs and Low GWP blends, 1015, Online (2021)

6） A. R. Tuhin, D. Mondal, N. Amakusa, K. Kariya, A. Miyara, 21st symposium on thermophysiacl properties, Boulder (Web conference) (2021)

7） M. Morshed, A. R. Tuhin, K. Kariya, A. Miyara, The 13th Asian thermophysical properties conference (ATPC2022), 5103-1 (2022)

8） A. R. Tuhin, D. Mondal, K. Kariya, A. Miyara, 2022 JSRAE Annual Conference, A112 Okayama (2022) (in Japanese)

2.2 Development of equations of state for next-generation refrigerants

2.2.1 Helmholtz energy equations of state

For the performance analysis of refrigeration cycles and design of heat exchangers, compressors, and piping, thermodynamic properties, including saturation properties, PVT behavior, enthalpy, heat capacities, and sound speed, are frequently calculated from various independent variables, where an equation of state is required which can calculate these properties with a similar uncertainty to their experimental uncertainties. Helmholtz energy equations of state are thermodynamic property models that ensure this requirement, and they are often used for equations of state for refrigerants.

2.2.2 Equations of state for pure refrigerants

Typically, Helmholtz energy equations of state use several terms compared to cubic equations of state, such as the Peng-Robinson equation. Thus, to optimize the functional form, further experimental data is needed as along with a highly developed statistical analysis. This type of equation of state is composed of the ideal-gas and residual parts expressing ideal-gas properties and representing the differences between ideal gases and real fluids, respectively, which originate from the intermolecular forces. The ideal-gas part is analytically calculated from the ideal-gas isobaric heat capacity obtained from estimation techniques or extrapolation of experimental vapor-phase sound speed data. Whereas, the residual part is generally determined by fitting an empirical functional form to the experimental data. These studies[1-3] closely present the fitting procedure. Table 2.2.2-1 summarizes equations of state developed in this project, as well as their valid ranges and expected uncertainties. The outlines of each equation are presented below.

Table 2.2.2-1 Pure-refrigerant equations of state developed in this project

Refrigerant	Valid range			Expected relative uncertainty (k = 2)			Reference
	T_{min} (K)	T_{max} (K)	p_{max} (MPa)	Vapor pressure	Density	Sound speed	
HCFO1224yd(Z) (Interim)	263	473	10	0.05	L: 0.1	V: 0.03	4
HCFO1224yd(Z) (Final)	158	473	35	0.03	L: 0.03 V: 0.3	V: 0.03 L: 0.03	5
HFO1123	196	480	20	0.05	L: 0.05 V: 0.2	V: 0.02	6
HFO1336mzz(E)	200	410	5.7	0.1	L: 0.15 V: 0.5	V: 0.05	7, 8
HFO1234yf	122	410	100	0.1	L: 0.1 V: 0.2	V: 0.02 L: 0.05	2
HCFO1233zd(E)	166	450	100	0.07	L: 0.05 V: 0.15	V: 0.05 L: 0.08	3
CF_3I (Interim)	300	400	6	0.2	L: 0.2 V: 0.5		unpublished

HCFO1224yd(Z)（Interim model）

An interim equation was developed for HCFO1224yd(Z)[4], which was based on experimental data measured in this project. The ideal-gas part was formulated from ideal-gas isobaric heat capacities obtained through quantum analysis and those from the extrapolation of experimental vapor-phase sound speed data. Further, the residual part was fitted with experimental data, including the critical parameters, vapor pressures, saturated liquid densities, PVT behavior, and vapor-phase sound speeds. These properties are represented by the equation of state almost within their experimental uncertainties. The equation is available on REFPROP10.0. Liquid density data[9] and liquid-phase sound speed data[10], which were published after the interim equation was established and were located at the extrapolated region. Moreover, the exhibited larger deviations than their uncertainties.

HCFO1224yd(Z) （Final model）
The interim model was updated by refitting to the data with deviations higher than their experimental uncertainties. The final equation represents the liquid density data of Fedele et al. [9] within the experimental uncertainties and well expresses the liquid sound speed data of Lago. [10] The evaluation of this equation by NIST has been completed, and will be available in the next version of REFPROP. Figure 2.2.2-1 shows the deviations in the experimental densities from values calculated using the equation of state. [5]

HFO1123
The interim equation for HFO1123 developed in the last project[11] was updated via the addition of new experimental densities in the lower-temperature regions to the fitting. The final equation[6] improved the density deviations and extrapolated behavior by revising functional forms. Its evaluation using NIST has been completed, and will be available in the next version of REFPROP.

HFO1336mzz(E)
An interim equation of state for HFO1336mzz(E) [7] was developed by fitting to experimental data measured in this project, including the critical parameters, saturation properties, PVT behavior, vapor-phase sound speeds, and ideal-gas isobaric heat capacities. These properties are represented by the interim equation almost within their experimental uncertainties. In addition, the parameters of the extended corresponding states (ECS) model for transport properties were fitted to experimental viscosities and thermal conductivities measured in this project. These properties are also well represented by the ECS model. The equation of state and ECS model were successfully used in the heat transfer analysis at NIST[12]. Further, the heat transfer coefficients calculated using these models were consistent with experimental values. A paper discussing the formulations of the equation of state and ECS model[8] will be published shortly, and the equation will be available in the next version of REFPROP.

HFO1234yf
It has recently been found that the equation of state in REFPROP10.0[13] is less reliable in the calculations of liquid-phase sound speeds, and thus it was updated in this project. Various knowledge and techniques obtained during the fitting of the updated equation were applied to the development of the equations for HCFO1224yd(Z), HFO1123, and HFO1336mzz(E). The final equation[2] was selected by ISO TC96/SC8/WG7 as an international standard formulation (ISO 17584, refrigerant property) [14] for HFO1234yf.

HCFO1233zd(E)
It was found that an inconsistent dataset could be used in the fitting of the equation of state for HCFO1233zd(E) in REFPROP10.0[15]; therefore, it was updated in this project. In addition, new knowledge was acquired in this fitting, and it was employed in the development of other equations of state in this project, coupled with those obtained in the fitting for HFO1234yf. The final equation[3] was recommended by ISO TC96/SC8/WG7 to an international standard formulation for HCFO1233zd(E) of ISO 17584[14]. Figure 2.2.2-2 shows the deviations in experimental densities from values calculated with the final equation of state. [3]

CF_3I (Interim model)
The equation of state for CF_3I in REFPROP10.0[16] exhibited considerably large deviations from experimental densities measured in this project, and thus the project attempted to update it. An interim equation of state fitted to the density data exhibits better consistency with experimental surface tensions or results from molecular simulations compared to the Lemmon and Span equation.[16] However, in this project, the measurements of liquid density at high pressures and vapor-phase sound speed were postponed owing to the difficulty in experimental handling of this fluid, and thus, the equation of state has not yet been completed.

Controlling behavior in the critical and extrapolated regions
The fitting of the residual part controls the values, slopes, and curvatures of various derived properties such that the equation of state behaves well over wide ranges of temperature and pressure. Studies[2,3] have discussed this procedure in detail. This is essential particularly for equations with an empirical functional form to control the trend of derived properties. Consequently, the equations developed in this project exhibited reasonable extrapolation

behavior even in regions away from the experimental data. Figure 2.2.2-3 shows the changes in isochoric and isobaric heat capacities calculated from the equation of state[2].

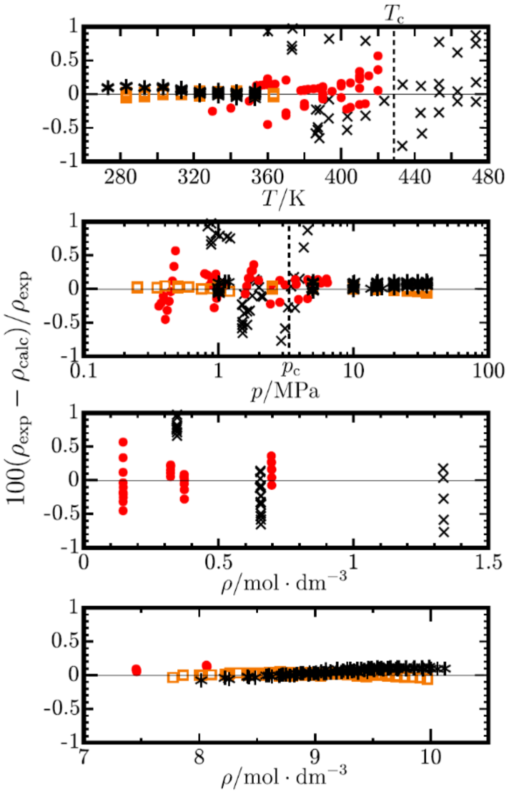

Fig. 2.2.2-1 Relative deviations in the experimental density from calculated value with the equation of state for HCFO1224yd(Z)[5]: (✕) Fukushima et al.;[17] (●) Sakoda and Higashi; [18] (*) Romeo et al.; [19] (□) Fedele et al. [9]

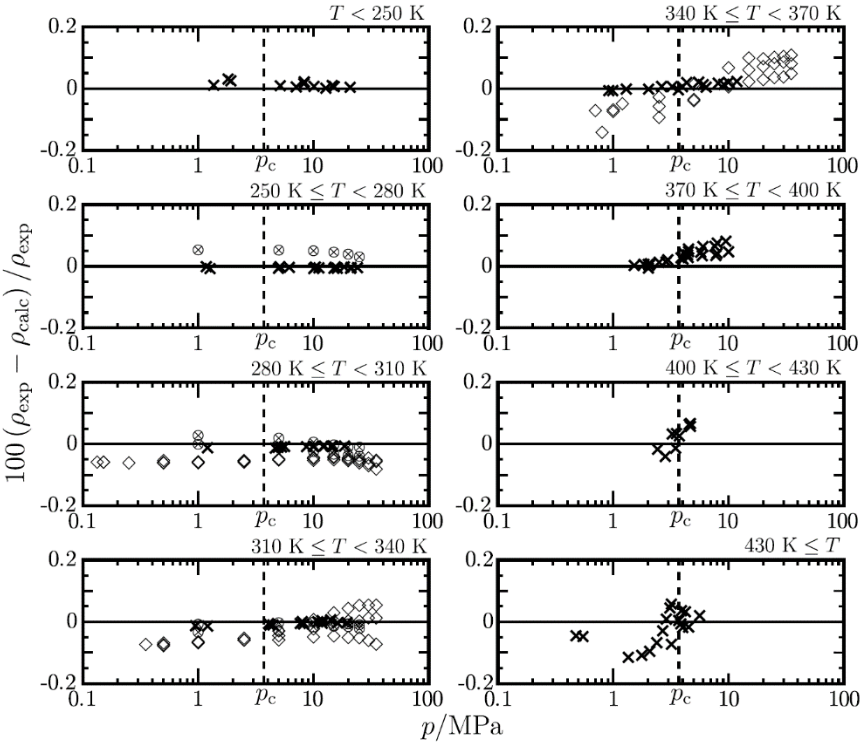

Fig. 2.2.2-2 Relative deviations in the experimental density from calculated value with the equation of state for HCFO1233zd(E)[3]: (✕) Mondéjar al.;[15] (⊗) Romeo et al.; [20] (◇) Fedele et al. [21]

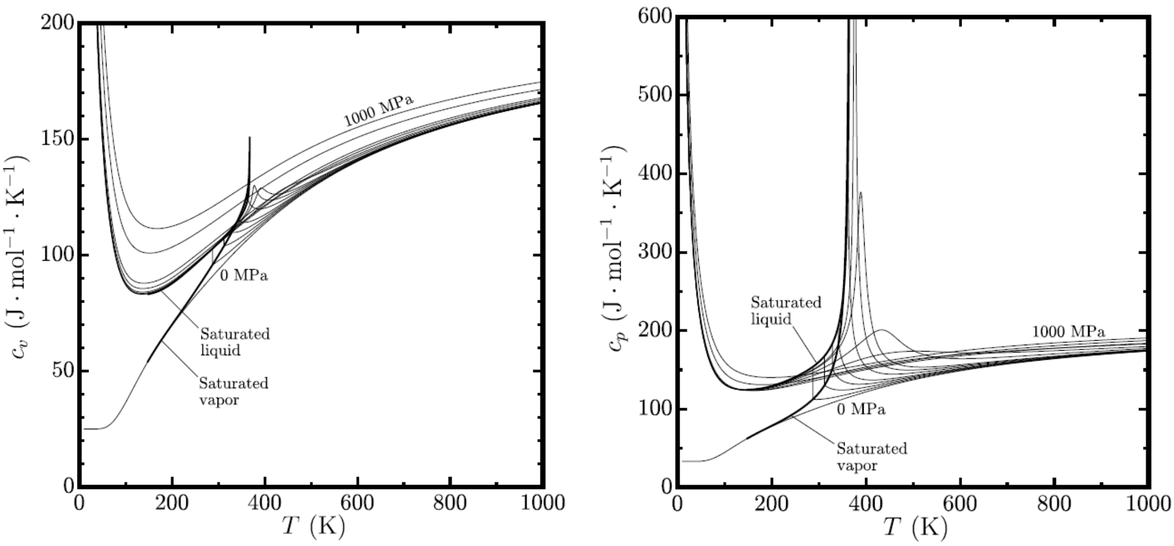

Fig. 2.2.2-3 Isochoric heat capacity (left panel) and isobaric heat capacity (right panel) calculated from the equation of state for HFO1234yf [2]. Isobars are shown at pressures of 0 (ideal gas), 0.5, 1, 1.5, 2, 3, 4, 5, 10, 20, 50, 100, 500, and 1000 MPa.

2.2.3 Mixture model for refrigerant mixtures

Equations of state for refrigerant mixtures were formulated with the multi-fluid model based on a mixing rule of pure-fluid Helmholtz energy equations. In contrast to cubic equations, wherein the same functional form is used both for pure fluids and mixtures, the multi-fluid model can directly employ accurate Helmholtz energy equations for pure fluids. In this project, the formulation was created following the fashion of the Kunz-Wagner (KW) model. [22,23] This model is used for property calculations of mixtures in REFPROP10.0. The model includes five adjustable parameters, which are normally determined through the fitting of experimental data for the vapor-liquid equilibrium (VLE) and PVT behavior of the mixture of interest. Studies[22,23] have reported the details of the KW model. An example of the application of the KW model to refrigerant mixtures is provided in Ref. [24] Table 2.2.3-1 summarizes the mixture models developed in this project, as well as their expected uncertainties for the VLE and density. The outlines of each mixture model are given below.

Table 2.2.3-1 Mixture models developed in this project

Refrigerant mixture	Pure-fluid EOS	Expected relative uncertainty (k = 2)		Reference
		VLE†	Density	
HFC32/HFO1123	HFC32: Tillner-Roth and Yokozeki[25] HFO1123: Akasaka et al.[6]	0.2	L: 0.2 V: 1.0	27
HFO1123/HFO1234yf	HFO1123: Akasaka et al.[6] HFO1234yf: Richter et al.[13]	1.0	L: 0.2 V: 1.0	27
HFO1234yf/HC290	HFO1234yf: Richter et al. [3] HC290: Lemmon et al.[26]	0.2	L: 0.2 V: 0.4	28

†Uncertainties in the VLE indicate relative deviations between experimental and calculated bubble-point pressures.

HFC32/HFO1123 mixture

A mixture model[27] was fitted to the experimental data for the VLE and PVT behavior obtained in this project. The equation of state for HFC32 by Tillner-Roth and Yokozeki[25] and that for HFO1123 by Akasaka et al. [6] were used for the fitting of the mixture model. The final mixture model was observed to well represent the experimental data[28], and the critical temperature calculated from the model was generally consistent with an experimental value. Figure 2.2.3-1 shows the bubble- and dew-point curve calculated from the mixture model, as well as the experimental isothermal VLE data. [28]

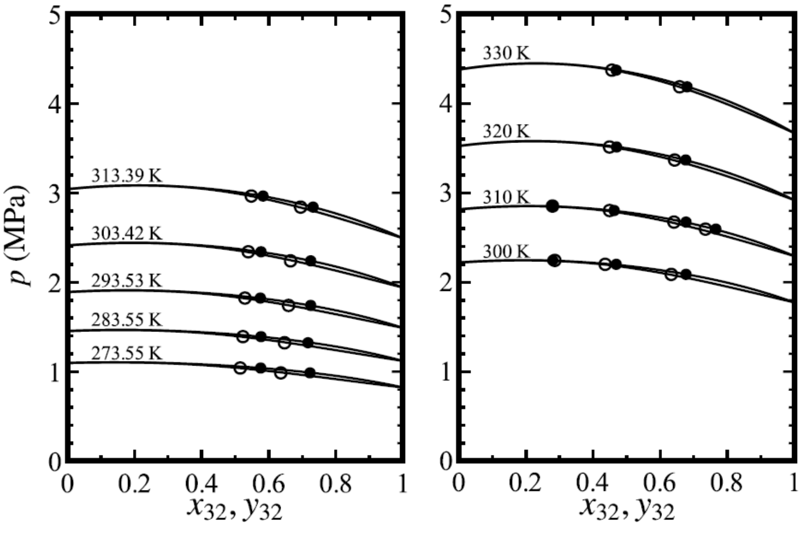

Fig. 2.2.3-1 Bubble- and dew-point curves calculated from the mixture model for HFO32/HFO1123 mixtures[27] and experimental data for the isothermal vapor-liquid equilibrium.[28]

HFO1123/HFO1234yf mixture

A mixture model[27)] was formulated with the experimental data for the VLE and PVT behavior measured in this project. The equation of state for HFO1123 by Akasaka et al.[6)] and that for HFO1234yf by Richter et al. [13)] was used for the mixture model. The experimental data[28,29)] were observed to be represented almost within their uncertainties. Moreover, the model yielded similar uncertainties, even when applying the equation of state for HFO1234yf by Lemmon and Akasaka[2)]. Figure 2.2.3-2 shows the bubble- and dew-point curves calculated from the final mixture model and the experimental isothermal VLE data. [28,29)]

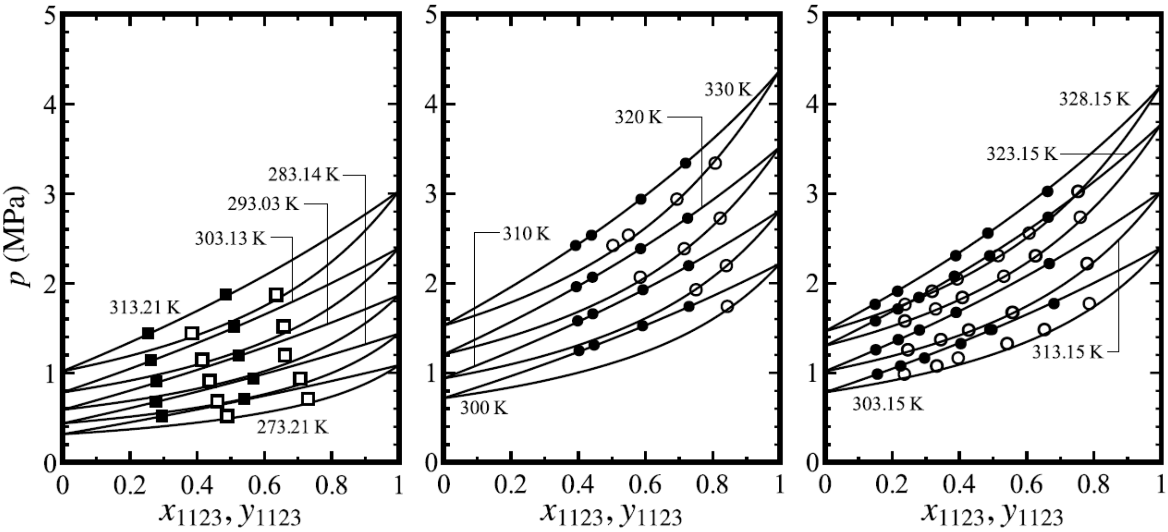

Fig. 2.2.3-2 Bubble- and dew-point curves calculated from the mixture model for HFO1123/HFO1234yf mixtures[27)] and experimental data for the isothermal vapor-liquid equilibrium.[28,29)]

HFO1234yf/HC290 mixture

A mixture model[31)] was developed from the PVT data measured in this project and experimental VLE data from the literature.[30)] These data were adequately represented by the mixture model. Furthemore, the model exhibited better numerical stability than the available model[32)] in the property calculations near the critical point.

2.2.4 REFPROP 10.0N

REPROP10.0N is a version obtained based on the pure-fluid equations of state and mixture models in this project. It was added to the original REFPROP10.0. 10.0N to include additional FLD files and mixing parameters presented in Table 2.2.4-1. This version was shared among the members of this project. Figure 2.2.4-1 shows a *p*-*h* diagram of HFO1336mzz(E) depicted using REFPROP10.0N.

Table 2.2.4-1 FLD files and mixing parameters included in REFPROP10.0N

FLD file	R1224YDZ.FLD, R1123.FLD, R1234YF.FLD, R1233ZDE.FLD, R1336MZZE.FLD, CF3I.FLD
Additional mixing parameters in HMX.BNC	HFC32/HFO1123, HFO1123/HFO1234yf, HFO1234yf/HC290

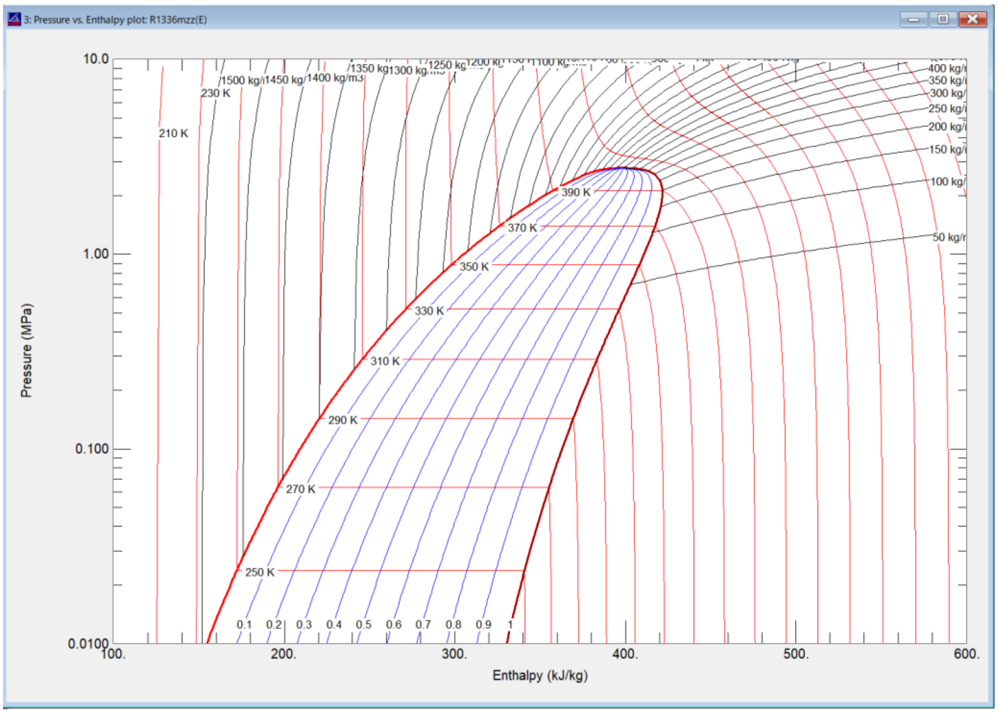

Fig. 2.2.4-1 Pressure-enthalpy diagram of HFO1336mzz(E) plotted on REFPROP 10.0N.

References

1) E.W. Lemmon, R.T. Jacobsen: J. Phys. Chem. Ref. Data 34, 69 (2005).
2) E. W. Lemmon, R. Akasaka: Int. J. Thermophys., 43, 119 (2022).
3) R. Akasaka, E. W. Lemmon: J. Phys. Chem. Ref. Data, 51, 023101 (2022).
4) R. Akasaka, M. Fukushima, and E. W. Lemmon: 21st European Conference on Thermophysical Properties, Graz, Austria, September 3-8. (2017).
5) R. Akasaka, E. W. Lemmon: 21th Symposium on Thermophysical Properties (online), June 20-25, (2021).
6) R. Akasaka, Y. Higashi, N. Sakoda, S. Fukuda, and E. W. Lemmon: Int. J. Refrig., 119, 457 (2020).
7) R. Akasaka, L. D. Simoni, and E. W. Lemmon: 19th International Refrigeration and Air Conditioning Conference at Purdue (online), West Lafayette, IN, USA, July 11-14, (2022).
8) R. Akasaka, M. L. Huber, L. D. Simoni, and E. W. Lemmon, to be published in Int. J. Thermophys., (2022).
9) L. Fedele, S. Bobbo, M. Scattolini, C. Zilio, and R. Akasaka: Int. J. Refrig., 118, 139 (2020).
10) S. Lago, private communication, (2020).
11) R. Akasaka, M. Fukushima, and E. W. Lemmon: 16th International Refrigeration and Air Conditioning Conference at Purdue, West Lafayette, IN, USA, July 11-14, (2016).
12) M.A. Kedzierski, L. Lin: Tech. Rep. NIST Technical Note 2125, National Institute of Standards and Technology, Gaithersburg, MD, USA (2020).
13) M. Richter, M.O. McLinden, and E.W. Lemmon: J. Chem. Eng. Data 56, 3254 (2011).
14) International Organization for Standardization: ISO/DIS 17584 Refrigerant Properties (2022).
15) M. E. Mondéjar, M. O. McLinden, and E. W. Lemmon: J. Chem. Eng. Data 60, 2477 (2015).
16) E. W. Lemmon, R. Span: J. Chem. Eng. Data, 60, 3745 (2015).
17) M. Fukushima, H. Hayamizu, and M. Hashimoto; 16th International Refrigeration and Air Conditioning Conference at Purdue, West Lafayette, IN, USA, July 11-14, (2016).
18) N. Sakoda, Y. Higashi; J. Chem. Eng. Data 64, 3983 (2019).
19) R. Romeo, S. Lago, and P. A. Giuliano Albo: Proceedings of the 12th Asian Thermophysical Properties Conference, Xi'an, China, (2019).
20) R. Romeo, P. A. Giuliano Albo, S. Lago, and J. S. Brown, Int. J. Refrig. 79, 176 (2017).
21) L. Fedele, M. Pierantozzi, G. Di Nicola, J. S. Brown, and S. Bobbo, J. Chem. Eng. Data 63, 225 (2018).
22) O. Kunz, W. Klimeck, W. Wagner, M. Jaeschke: GERG Technical Monograph, Vol. 15 (2004).
23) O. Kunz, W. Wagner: J. Chem. Eng. Data 57, 3032 (2012).

24) R. Akasaka: Fluid Phase Equilib. 358, 98, (2013).
25) R. Tillner-Roth, A. Yokozeki: J. Phys. Chem. Ref. Data, 26, 1273 (1997).
26) E. W. Lemmon, M. O. McLinden, and W Wagner: J. Chem. Eng. Data, 54, 3141 (2009).
27) R. Akasaka, E. W. Lemmon: The 6th IIR Conference on Thermophysical Properties and Transfer Processes of Refrigerants (online), September 1-3, (2021).
28) H. Miyamoto, T. Saito, N. Sakoda, U. Perera, T. Ishii, K. Thu, and Y. Higashi: Int. J. Refrig., 119, 340 (2020).
29) N. Sakoda, J. Shiheng, M. Nakazaki, Y. Takata, and Y. Higashi: The 25th IIR International Congress of Refrigeration, Montreal, Canada, (2019).
30) Q. Zhong, X. Dong, Y. Zhao, H. Li, H. Zhang, H. Guo, and M. Gong: Int. J. Refrig. 81, 26 (2017).
31) R. Akasaka, S. Fukuda, K. Miyane, and Y. Higashi: J. Chem. Eng. Data, 67, 346 (2022).
32) Q. Zhong, X. Dong, Y. Zhao, H. Zhang, J. Wanga, H. Guo, J. Shen, and M. Gong: J. Chem. Thermodyn., 129, 36 (2019).

2.3 Performance Evaluation of Next-Generation Refrigerants Considering Cycle Characteristics

2.3.1 Thermodynamic analysis of fundamental characteristics for heat pump cycle

Kyushu Sangyo University performed thermodynamic analysis to calculate the cycle of the refrigerant mixture and consequently examine the optimal composition of the refrigerant mixture.

First, to examine the differences in calculation results with respect to the conditions, the calculations were performed for the ternary mixture of HFO1234yf/HFC32/CO_2 refrigerants with varying condensation temperatures. Table 2.3.1-1 presents the calculation conditions. Because of the temperature glide in the refrigerant mixture, calculations were performed such that the average temperatures of the dew and boiling points were the condensation and evaporation temperatures, respectively. The adiabatic compression efficiency of the compressor was set to 0.85.

Figure 2.3.1-1 shows the calculation results. The solid and dashed lines were the COP and GWP contours, and the COP result was the ratio to the COP of R410A. Except for the case of high CO_2 ratios, the overall COP contours did not exhibit significant changes. Therefore, unless the temperature conditions are close to or exceed the critical temperature, the condensation temperature does not affect the COP because of differences in refrigerant composition. Moreover, the evaporation temperature was also changed in a similar manner; however, the difference in refrigerant composition had minimal effect on the COP.

Table 2.3.1-1 Calculation conditions of HFO1234yf/HFC32/CO_2

Refrigerants	Condensation temperature、°C	Evaporation temperature、°C	Superheat、K	supercooling、K
HFOR1234yf HFC32 CO_2	20 30 40	0	3	0

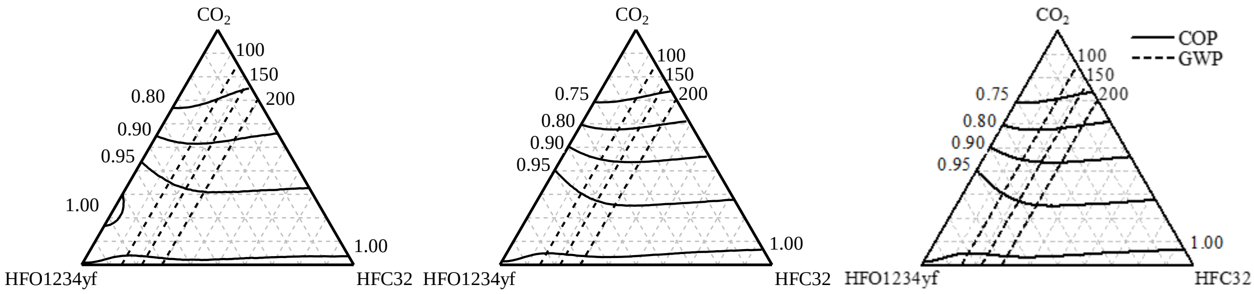

(a) Cond. Temp. 20 °C (a) Cond. Temp. 30 °C (c) Cond. Temp. 40 °C

Fig. 2.3.1-1 Calculation results of HFO1234yf/HFC32/CO2 by condensation temperature.

Next, cycle calculations were performed for the CF_3I/HFC32/HFC125 mixture at condensation and evaporation temperatures of 25°C and -3°C, respectively, and superheat and supercooling of 3 and 0 K, respectively. Figure 2.3.1-2 shows the calculation results, where (a), (b), (c) and (d) show the COP ratio to R410A, the volume capacity ratio to R410A, GWP, and temperature glide in the evaporator, respectively. The COP ratio was the highest when the ratio of CF_3I was approximately 0.8, and the lowest when the ratio of CF_3I/HFC32 was approximately 70/30 mass% and pure HFC125. However, the overall COP ratio was similar to that of R410A. The volume capacity ratio increased with increase in the ratio of HFC32. Further, the GWP increased with increase in the ratio of HFC125, and the composition range of GWP below 500 was only from pure CF_3I to approximately 40/60 mass% CF_3I/HFC32 ratio. In addition, the temperature glide was higher than 10 K in the region of high CF_3I ratio and reduced with increase in the ratios of HFC32 and HFC125. Consequently, the optimal composition region for the CF_3I/HFC32/HFC125 mixture refrigerant was determined based on these results.

Figure 2.3.1-3 shows a triangular diagram of CF_3I/HFC32/HFC125 with COP ratio contours of 0.98 and 0.95, and volume capacity ratio, GWP, and temperature contours of 1.00, 500, and 5K, respectively. Moreover, the selection conditions for the optimum composition were a COP ratio of approximately 1, volume capacity of at least 1, GWP less than 500, and temperature glide less than 5K. The composition that satisfied all these conditions is indicated by the red region in the figure.

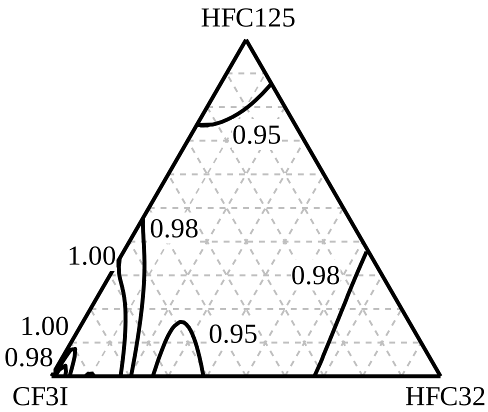

(a) COP

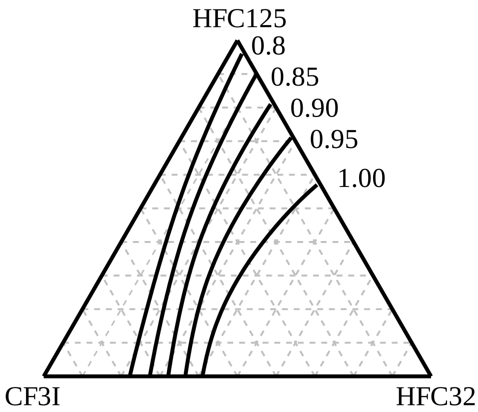

(b) volumetric capacity

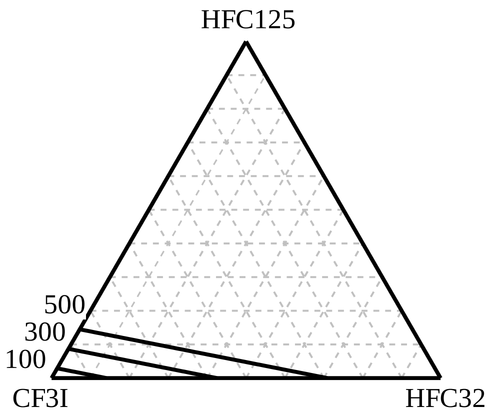

(c) GWP

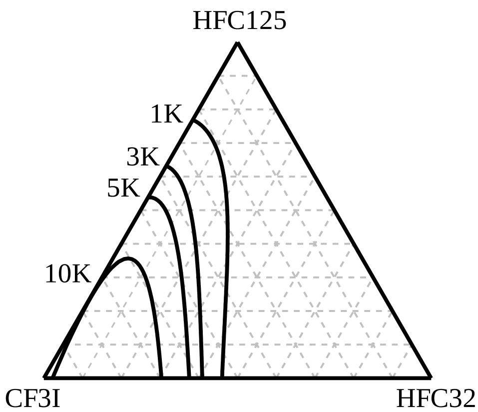

(d) Temperature glid of eva.

Fig. 2.3.1-2 Calculation results of CF_3I/HFC32/HFC125

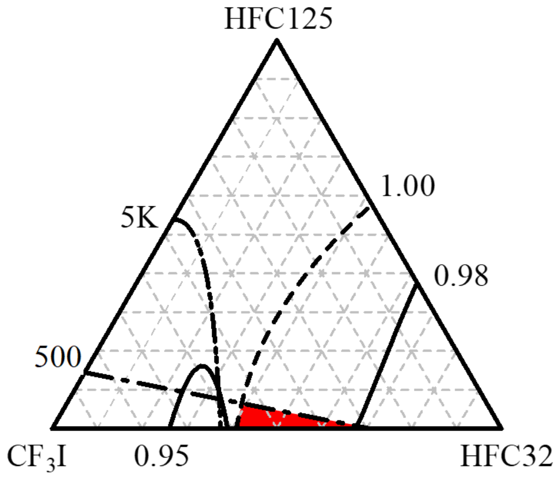

Fig. 2.3.1-3 optimum mix composition of CF_3I/HFC32/HFC125

Thereafter, cycle calculations were performed for the CF_3I/HFC32/HFO1123 mixture under similar conditions. Figure 2.3.1-4 shows the calculation results. The COP ratio was slightly lower in the region where the ratio of HFO1123 was high; the overall trend was similar to that of R410A in other ratios. The volume capacity ratio increased with increase in the ratio of HFC32 and HFO1123. Further, the GWP increased with increase in the ratio of HFC32, with the composition range of GWP less than 500 having a ratio of HFC32 less than 0.7 mass%. The temperature glide was higher than 15 K in the region with high CF_3I ratio, and less than 1 K when CF_3I ratio was 0.3 or lesser. Consequently, the optimal composition region of the CF_3I/HFC32/HFO1123 mixed refrigerant was determined based on these results.

Figure 2.3.1-5 shows a triangular diagram of CF_3I/HFC32/HFO1123 with COP ratio contours of 0.98 and 0.95, volume capacity ratio contour of 1.00, GWP contours of 300 and 500, and temperature glide contour of 1K. The selection conditions for the optimum composition were a COP ratio of approximately 1, volume capacity of at least 1, GWP less than 500, and temperature glide less than 1K. The composition that satisfied all these conditions is indicated as the red region in the figure. Therefore, the optimal composition of CF_3I/HFC32/HFO1123 mixed refrigerant had a wide selection range, and an optimal composition range was observed for cases even below GWP of 300.

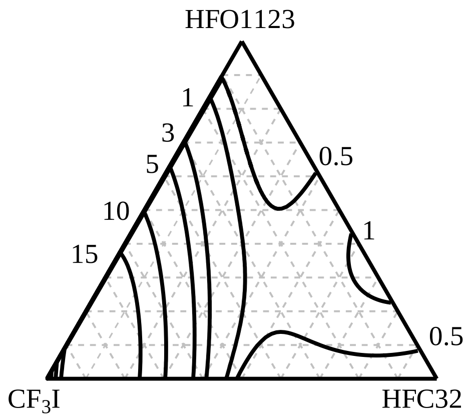

(a) COP

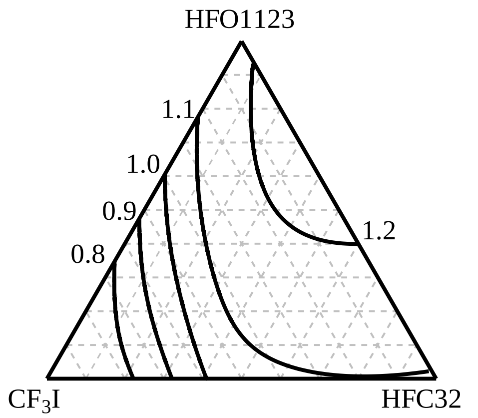

(b) volumetric capacity

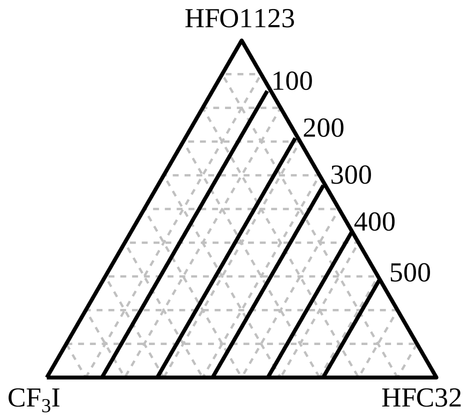

(c) GWP

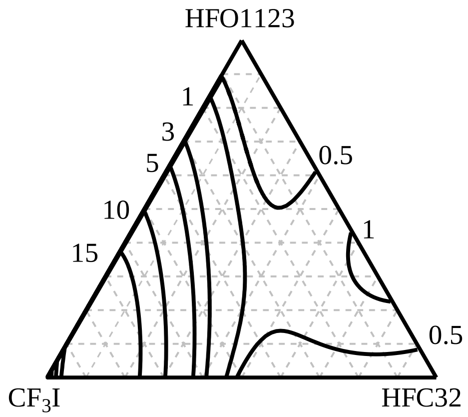

(d) Temperature glid of eva.

Fig. 2.3.1-4 Calculation results of CF_3I/HFC32/HFO1123

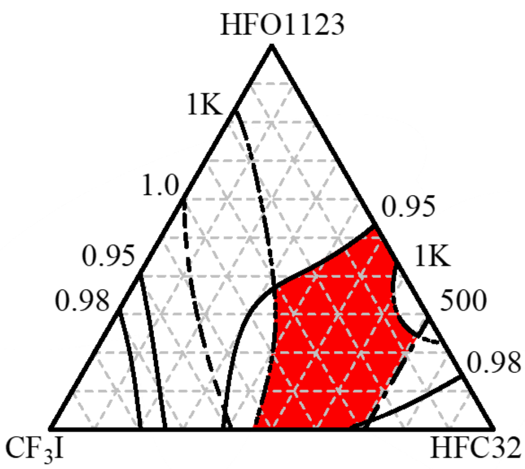

Fig. 2.3.1-5 Optimum mix composition of CF_3I/HFC32/HFC125

The optimum composition has been studied through thermodynamic analysis. However, these results may differ from those obtained when the heat pump is actually operated. For example, thermodynamic analysis shows that low-pressure refrigerants tend to have higher COP. However, in the actual cycle, the pressure loss of low-pressure refrigerants tended to be higher, and COP tended to be lower than that of high-pressure refrigerants. Therefore, the comparison of COP and determination of the optimal composition without considering pressure loss is difficult. In addition, in case of temperature glide, no limit for the dew and boiling points was observed in the theoretical calculations. In contrast, in the actual equipment, a limit to the temperature exists because of the temperature on the heat source fluid side where the heat exchange occurs. Therefore, calculations were performed considering the heat exchanger performance and pressure drop.

Figure 2.3.2-6 shows the temperature distribution of the refrigerant and source fluid in the heat exchanger. The red, blue, and light blue lines represent the refrigerant in the condenser, the refrigerant in the evaporator, and the heat source fluid, respectively. The temperature changes inside the heat exchanger were subdivided to facilitate their liner approximation, and calculations were performed such that KA (heat passage coefficient x heat transfer area), which indicates heat exchanger performance, was constant in the following equation. In actual equipment, KA is determined by various factors such as the type of heat exchanger and heat transfer coefficient of the refrigerant; however, keeping KA constant implies the use of an optimized heat exchanger for each refrigerant.

$$\delta Q = \delta(KA_c(0))\, \Delta T_{mc}(0) \tag{2.3.2-1}$$

$$\Delta T_{mc}(0) = \frac{[T_c(0) - t_{wc}(0)] - [T_c(1) - t_{wc}(1)]}{\ln\left(\frac{[T_c(0) - t_{wc}(0)]}{[T_c(1) - t_{wc}(1)]}\right)} \tag{2.3.2-2}$$

$$KA = \sum_{i=0}^{m} \delta(KA_c(i)) \tag{2.3.2-3}$$

Next, the pressure loss is explained. Similar to heat exchanger performance, pressure loss was also determined by various factors such as the type of heat exchanger and the type of refrigerant. However, it is impossible to determine the shape of the heat exchanger in advance when considering the optimal composition. Figure 2.3.2-7 shows the experimental results of pressure loss in a heat exchanger measured in the past. The horizontal axis represents the volume capacity. The experimental refrigerants used in the results are listed, and refrigerants of various working pressures were used. The solid line in the figure is the correlation equation developed from these results.

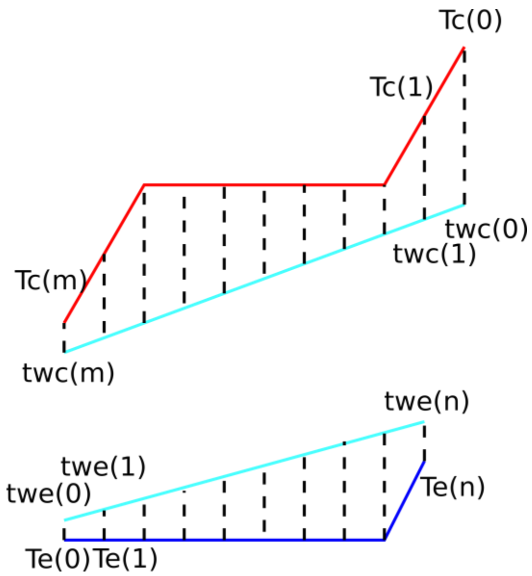

Fig. 2.3.1-6 Temperature distribution in heat exchanger

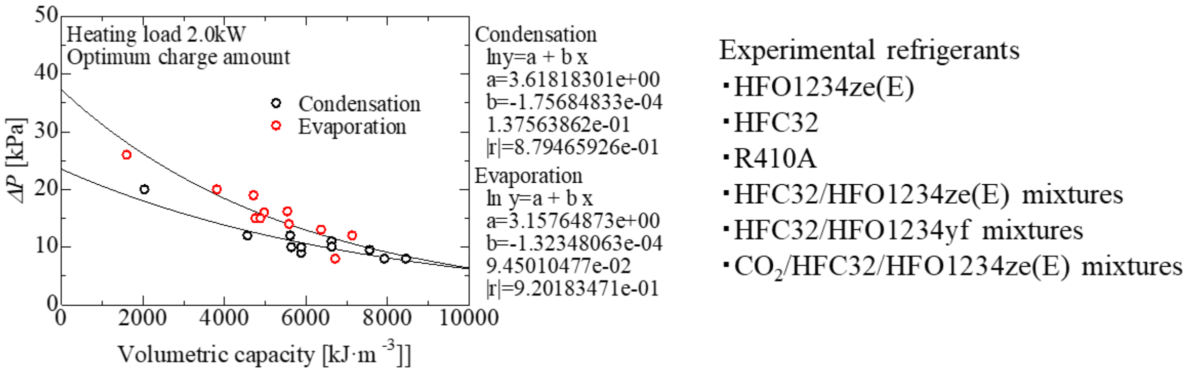

Fig. 2.3.1-7 Pressure loss in heat exchanger

The COP of the HFC32/HFO1234yf mixture was calculated using this calculation method, and Table 2.3.1-1 shows the calculated conditions, where T_w, SH, and η_{adi} are the inlet/outlet temperature of the source water flowing through the heat exchanger, superheat, and adiabatic compression efficiency, respectively. Figure 2.3.2-8 shows the COP ratio (R410A ratio) for the ratio of HFC32 in the mixture. Red and blue are the calculation results considering the heat exchanger performance and pressure drop, respectively, and the theoretical thermodynamic analysis. In the calculation results considering heat exchanger performance and pressure loss, the COP ratio increased with increase in the ratio of HFC32. This is because the increase in the HFC32 ratio increased the volume capacity and decreased the pressure drop. This is the same trend as the results of the cycle experiments. However, the thermodynamic analysis results showed that the COP ratio was lowest in case of HFC32/HFO1234yf (0.6/0,4 mass%). Thus, by considering the heat exchanger performance and pressure drop, the COP ratios that are similar to the results of the cycle experiments can be calculated, thereby rendering the study of optimal composition easier.

Table 2.3.1-2 Calculation condition

	in	out
Tw_cond [°C]	30	45
Tw_eva [°C]	15	7
SH [K]	3	
η_adi	0.85	
KA	0.25	

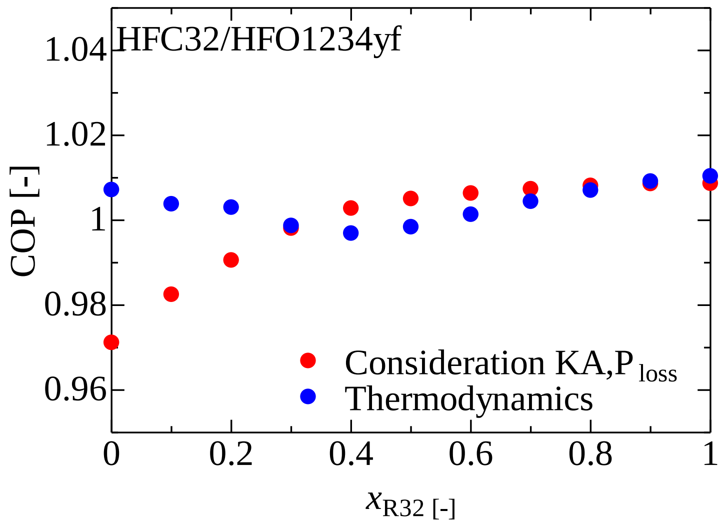

Fig. 2.3.1-8 Calculation results of HFC32/HFO1234yf

2.3.2 Experimental evaluation of fundamental characteristics for heat pump cycle

2.3.2.1 Experimental apparatus

Figure 2.3.2-1 shows a schematic of the experimental apparatus for heat pump cycle experiment. The specifications of heat exchangers and a compressor are presented in Tables 2.3.2-1 and 2.3.2-2. The system was designed as a water-cooled system to facilitate accurate evaluation of the heat exchange performance.

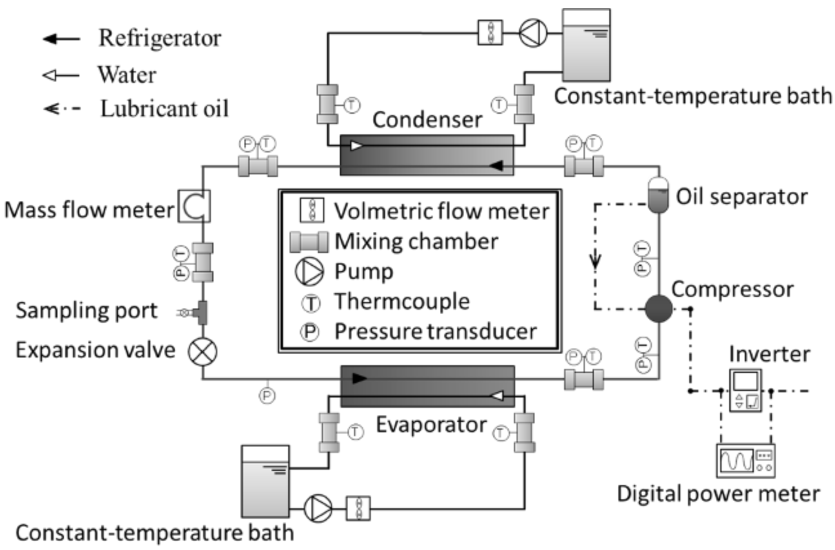

Fig. 2.3.2-1 Experimental apparatus

Table 2.3.2-1 Heat exchangers (Double tube type)

		Outer diameter [mm]	Inner diameter [mm]	Length [mm]	Tube
Condenser and Evaporator	Outer tube	15.88	13.88	7200	Smooth
	Inner tube	9.53	7.53	7200	Grooved

Table 2.3.2-2 Compressor

Type	Scroll compressor
RPM range	1500 – 1600 rpm
Upper limit of discharge temperature	120 °C
Lubricant oil	POE VG68
Cylinder volume	11 cm^3

2.3.2.2 Refrigerant and experimental conditions

Table 2.3.2-3 lists the refrigerants used in the study. The experimental conditions are summarized in Table 2.3.2-4.

Table 2.3.2-3 List of refrigerants used in the study

Refrigerant	**Experimental conditions**	**Publications**
R410A	Heating (High), Heating (Low), Cooling (Air), Cooling (Water)	Applied Thermal Engineering 181 (2021) 115952[1)]
HFC32	Heating (High), Heating (Low), Cooling (Air)	Purdue Conferences 2018, 2339[2)]: Heating (High), Heating (Low), Cooling (Air)
R32/R1234yf (42/58 mass%)		Applied Thermal Engineering 181 (2021) 115952[1)]
R32/R1234yf (22/78 mass%) (R454C equivalent)	Heating (High), Heating (Low), Cooling (Air), Cooling (Water)	Applied Thermal Engineering 181 (2021) 115952[1)]: Heating (High), Heating (Low) Heat Transfer Engineering, DOI: 10.1080/01457632.2020.1776997[3)]: Cooling (Air)
R32/R1234yf/R744 (22/72/6 mass%)		International Journal Refrigeration 121 (2021) 289-301[4)]: Heating (High), Heating (Low), Cooling (Air)
R32/R1123 (58/42 mass%)	Heating (High), Heating (Low), Cooling (Air)	Purdue Conferences 2018, 2339[2)]: Heating (High), Heating (Low), Cooling (Air)
R32/R1123 (46/54 mass%)		
R32/R1123 (42/58 mass%)		
R32/R1234yf/R1123 (21/19/60 mass%)	Heating (High), Heating (Low), Cooling (Air), Cooling (Water)	to be presented
R32/R1234yf/R1123(21/39/40 mass%)		
R404A	Cooling (Water), Refrigeration	
R32/R1234yf/CO2(22/72/6 mass%)	Cooling (Water)	
R32/R1234yf/CO2(22/75/3 mass%) (R455A equivalent)	Cooling (Water), Refrigeration	

Table 2.3.2-4

Conditions	Condenser side heat transfer media [ºC]	Evaporator side heat transfer media [ºC]
Heating (High load)	20 → 45	15 → 9
Heating (Low load)	20 → 30	15 → 9
Cooling (Air source)	30 → 45	20 → 10
Cooling (Water source)	30 → 35	12 → 7
Refrigeration	30 → 35	Cond. 1: 10 → 0 Cond. 2: 7 → -3 Cond. 3: 4 → -6

2.3.2.3 Results

A binary mixture, HFO1234yf/HFC32 (78/22 mass%, and ternary mixture, HFO1234yf/HFC32/CO_2 (72/22/6 mass%) were tested and the results are shown in Fig. 2.3.2-2. It was shown that the binary mixture of HFC32/HFO1234yf achieved a COP equivalent to that of R410A at a certain load range. COP of the binary mixture decreased with increase in HFO1234yf; however, the ternary mixture, HFC32/HFO1234yf/CO2 = 22/72/6 had an COP lower or equivalent to HFC32/HFO1234yf = 22/78.

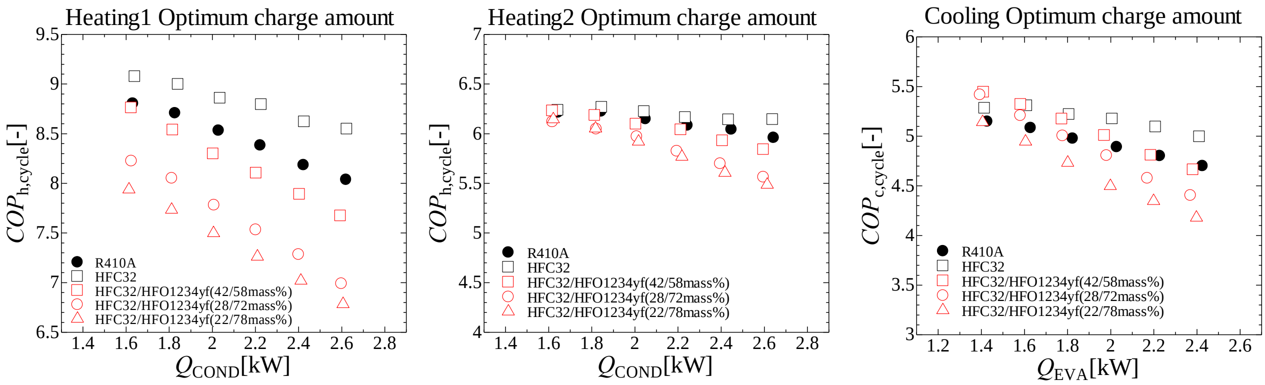

Fig. 2.3.2-2 Compare COP of zeotropic mixture refrigerants of HFC32/HFO1234yf with that of existing refrigerant.
(Heating 1 = Low load: Evaporator 15°C→ 9°C, Condenser 20°C→30°C,
Heating 2 = High load: Evaporator 15°C→ 9°C, Condenser 20°C→45°C,
Cooling = Air source: Evaporator 20°C→ 10°C, Condenser 30°C→45°C).

Drop-in experiments were conducted using a ternary mixture of HFC32/HFO1234yf/HFO1123 with the mass composition of 21.2/38.5/40.3 for high-load heating, low-load heating, and cooling modes. The results were compared with the target refrigerant, that is, R410A and the previously evaluated binary mixture (HFC32/HFO1234yf with 22/78 mass%) and the ternary mixture (HFC32/HFO1234yf/CO_2 with 22/72/6 mass %) in Fig. 2.3.2-3. The present ternary mixture exhibited comparable COP_{sys} values to those of R410A, that is, higher than HFC32/HFO1234yf and HFC32/HFO1234yf/CO_2 blends for the low heating mode. Thus, the system performance was sensitive to the condenser temperature and the coolant temperature difference across the compressor. The larger temperature difference across the condenser resulted in lower performance.

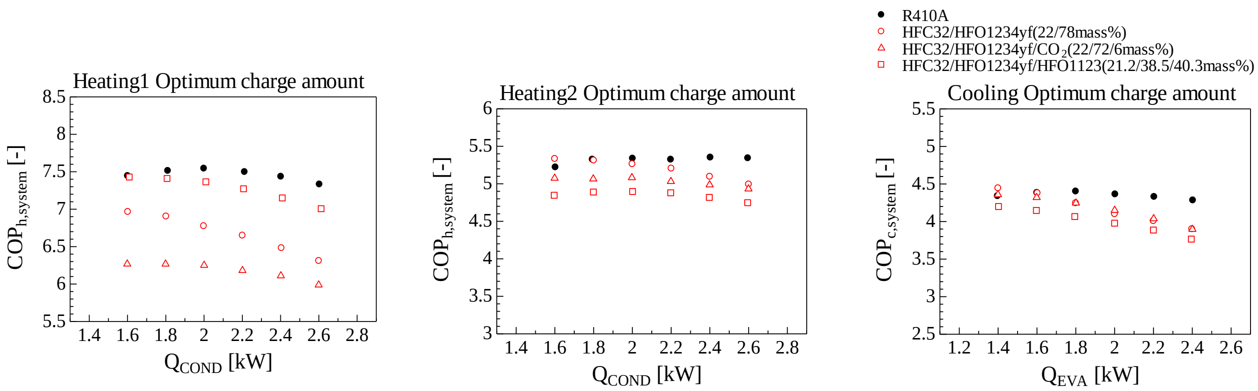

(a) Low heating mode (b) High heating mode (c) Cooling mode

Fig. 2.3.2-3 The system COP of HFO1123 mixture

Figure 2.3.2-4 shows the results of HFC32/HFO1234yf/HFO1123 = 21/19/60 mass%. The results showed that HFO1123 ternary mixture resulted in lower COP than HFC32/HFO1234yf = 22/78 mass% in low load regions, but unlike to the HFC32/HFO1234yf = 22/78 mass%, the degradation of performance was small.

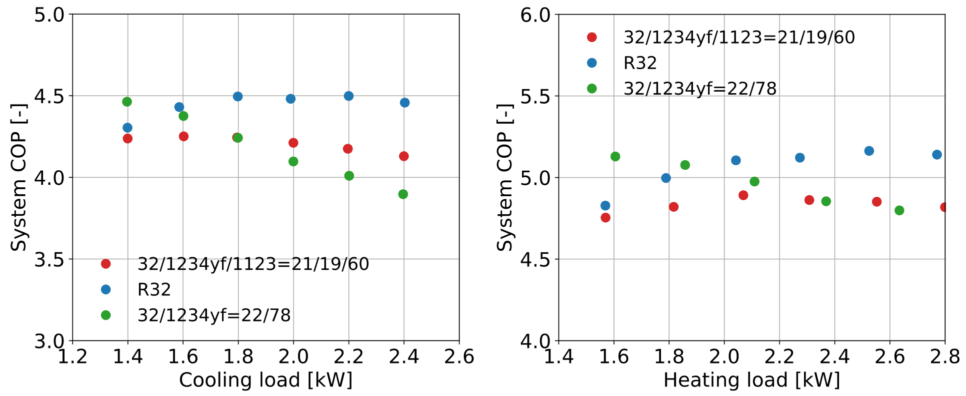

(a) Cooling (Air source) (b) Heating (High load)

Fig.2.3.2-4 Comparison of the system COP of a HFO1123 mixture

R404A and R445A were tested and the results are shown in Figs. 2.3.2-5 and 2.3.2-6. It was found that the R455A resulted in a larger pressure ratio and higher discharge temperature, and the optimum refrigerant charge for R455A was smaller than that of R404A in the current set up.

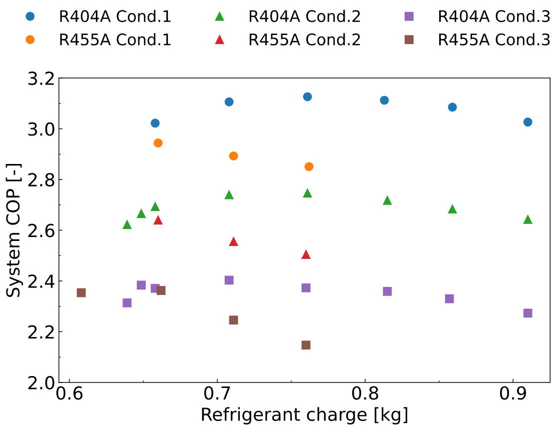

Fig.2.3.2-5 Comparison of R404A and R455A at 1.0 kW

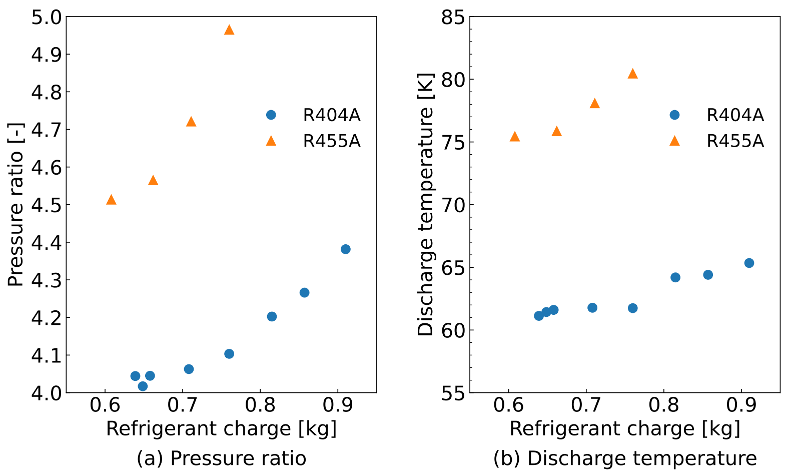

Fig. 2.3.2-6 Pressure ratio and discharge temperature at 1.0 kW in condition 3

Reference

1) K. Thu, K. Takezato, N. Takata, T. Miyazaki, Y. Higashi: Applied Thermal Engineering 181, 115952 (2021).
2) S. Koyama, T. Miyazaki, J. Hirayama, N. Takata, Y. Higashi: Purdue Conferences 2018, 2339 (2018).
3) T. Takezato, S. Senba, T. Miyazaki, N. Takata, Y. Higashi, K. Thu: Heat Transfer Engineering, 42, 13 (2021).
4) K. Thu, K. Takezato, N. Takata, T. Miyazaki, Y. Higashi, International Journal Refrigeration 121, 289, (2021) .

3. EXPERIMENT, MODELING, AND FORMULATION OF COMPONENTS

3.1 Heat Exchanger

3.1.1 Experiments on heat transfer characteristics and performance of heat exchangers

3.1.1.1 Phase change heat transfer in circular tubes

(1) Experimental method

Fig. 3.1.1.1-1 shows the experimental setup comprising a vapor-compression forced-circulation loop with a bypass loop connecting the outlet of the oil separator to the inlet of the compressor. The heat sink water is delivered from the thermostatic bath to the precooler, condensation test section, and supercooler. Simultaneously, the heat source water is circulated throughout the evaporation test section and superheater. The refrigerant vapor quality can be adjusted to the desired test section inlet conditions in the precooler and preheater, while the refrigerant mass flow rate and pressure can be controlled by the compressor speed, expansion valve open width, and bypass. For refrigerant mixtures, a small amount of circulating liquid refrigerant is instantaneously collected from the sampling port into a vessel and a gas chromatograph is used to measure the composition.

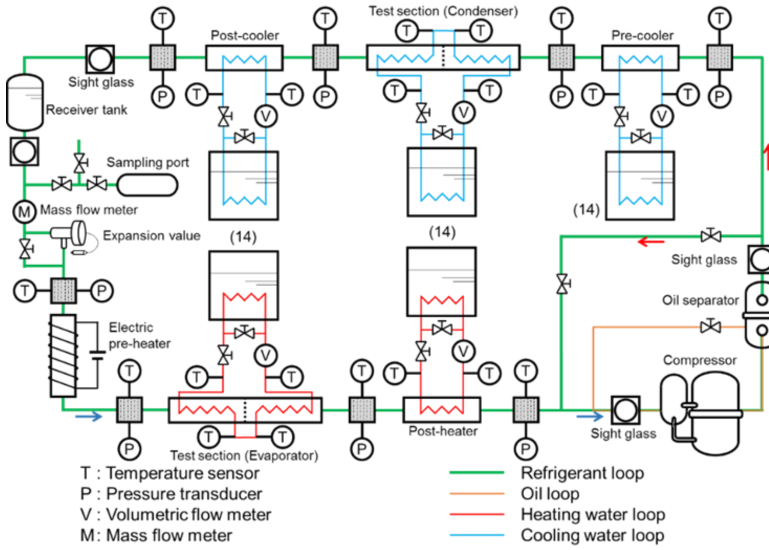

Fig. 3.1.1.1-1 Measurement setup.

Figs. 3.1.1.1-2(a) and (b) show the condenser and evaporator test sections, respectively. The test sections consist of two double-tube counter-flow heat exchangers (subsections). A refrigerant flows in the inner tube, while water flows in the annular channel. The refrigerant pressure and average mixing temperature were measured in the mixing chambers using absolute pressure gauges and K-type thermocouples, respectively. Differential pressure transducers were used to measure the differential pressure over the subsections. The measured pressure-drop section length in each subsection was 604 mm, and the effective heat-transfer length was 414 mm. T-type thermocouples were embedded at four points on the outer wall of the test tubes set horizontally at the center of each subsection to measure the wall temperature. The saturation temperature (the average of dew and boiling points for mixed refrigerants) was set at 40 °C and 10 °C for the condensation and evaporation experiments, respectively. The physical properties of mixed refrigerants were determined using REFPROP Ver. 10.0[1].

Table 3.1.1.1-1 lists the specifications of the smooth (ST) and inner helical microfin (MT) tubes used in the experiment, where d_{eq} is the equivalent inner diameter defined as the inner diameter of the representative ST with a cross-sectional free flow area equal to the actual area of the MT and η_A is the surface enlargement defined as the ratio of the actual heat transfer area of the MT to that of the equivalent inner diameter.

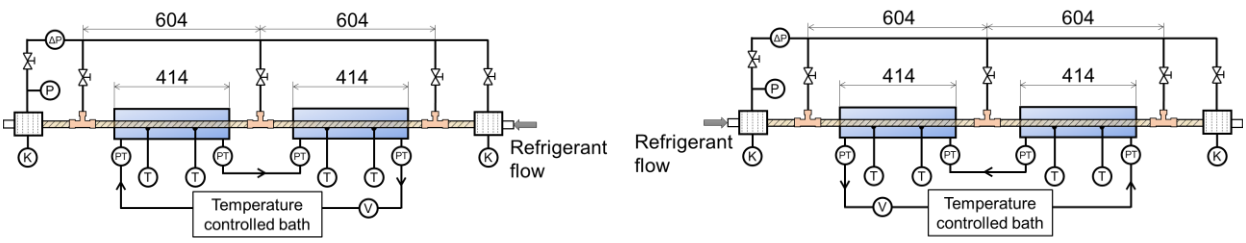

(a) Condenser (b) Evaporator

Fig. 3.1.1.1-2 Test sections

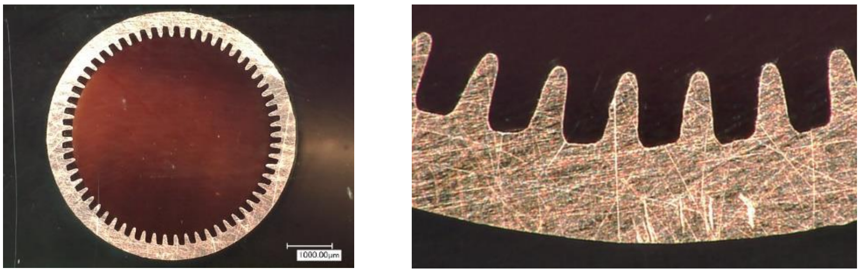

Fig. 3.1.1.1-3 Cross-sectional view of the MT used in the experiment

Table 3.1.1.1-1 Dimensions of the ST and MT used in the experiment

	ST	MT60
Outer diameter d_o [mm]	6.02	6.03
Equivalent inner diameter d_{eq} [mm]	5.22	5.21
Fin height h_{fin} [mm]	-	0.269
Helical angle β [°]	-	18
Apex angle γ [°]	-	15
Number of fins N_{fin}	-	60
Surface enlargement η_A	1	2.62

(2) Heat transfer coefficient and pressure drop for condensation flow

・Pure refrigerants of HFC32, HFO1234ze(E), and HFO1234yf

Fig. 3.1.1.1-4 shows the measured condensation heat transfer coefficients of HFC32, HFO1234ze(E), and HFO1234yf flowing in a ST and the results in correlation to that predicted by Haraguchi et al.[2)] The heat transfer coefficient was highest for HFC32, lowest for HFO1234yf, while HFO1234ze(E) had a heat transfer coefficient almost equal to that of HFO1234yf. Fig. 3.1.1.1-5 shows the measured pressure gradient of HFC32, HFO1234ze(E), and HFO1234yf flowing in the ST and the results in correlation to that predicted by Miyara et al.[3)] The pressure drop decreased in the order of HFO1234ze(E), HFO1234yf, and HFC32.

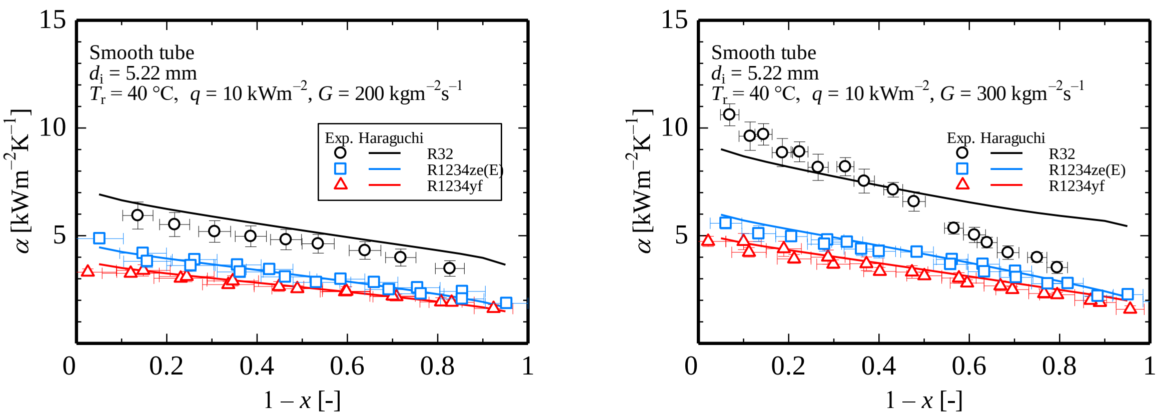

(a) G = 200 kg m^{-2}s^{-1} (b) G = 300 kg m^{-2}s^{-1}

Fig. 3.1.1.1-4 Measured condensation heat transfer coefficients of HFC32, HFO1234ze(E), and HFO1234yf

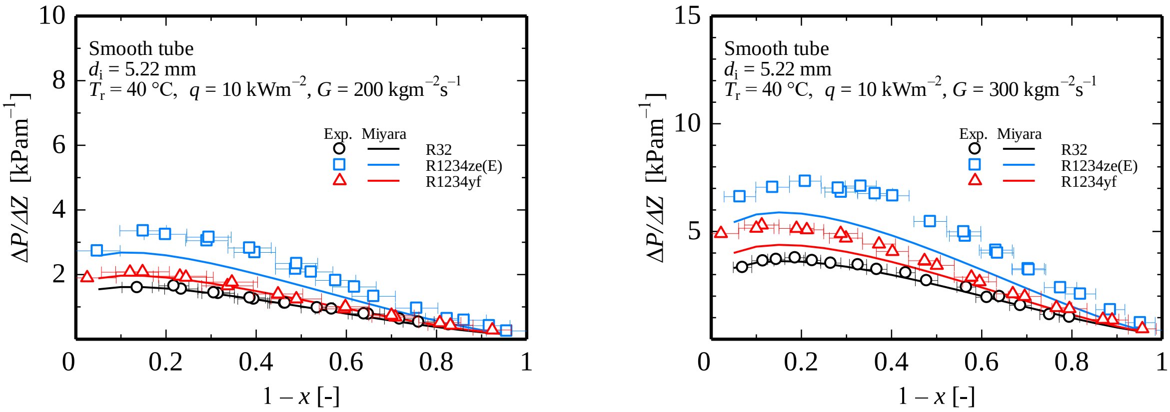

(a) G = 200 kg m^{-2}s^{-1} (b) G = 300 kg m^{-2}s^{-1}

Fig. 3.1.1.1-5 Measured condensation pressure gradients of HFC32, HFO1234ze(E), and HFO1234yf

・Binary mixture of HFO1123/HFC32

Fig. 3.1.1.1-6(a) shows the experimentally quantified condensation heat transfer coefficient of the HFO1123/HFC32 mixture at an average saturation temperature of 40 °C, heat flux of 10 kW m^{-2}, and mass–velocity range of 200–400 kg m^{-2}s^{-1}, while Fig. 3.1.1.1-6(b) shows a comparison between the pressure gradients of the HFO1123/HFC32 mixture and HFC32. The pressure drop of the HFO1123/HFC32 mixture was approximately 25% lower than that of HFC32. The results in Fig. 3.1.1.1-6(c) show a comparison between the condensation heat transfer coefficients of the HFO1123/HFC32 mixture and HFC32 and that of the HFO1123/HFC32 mixture flowing in the ST and MT. The temperature glide of the HFO1123/HFC32 mixture was small, approximately 1.0 K, resulting in a slight degradation of heat transfer. The heat transfer coefficient of MT increased significantly with a decrease in liquid quality. Heat transfer enhancement in the HFO1123/HFC32 mixture and HFC32 was similar at a mass–velocity of 200 kg m^{-2}s^{-1}. Conversely, the heat transfer enhancement increased with an increase in mass–velocity for the HFO1123/HFC32 mixture when compared to that for single compounds.

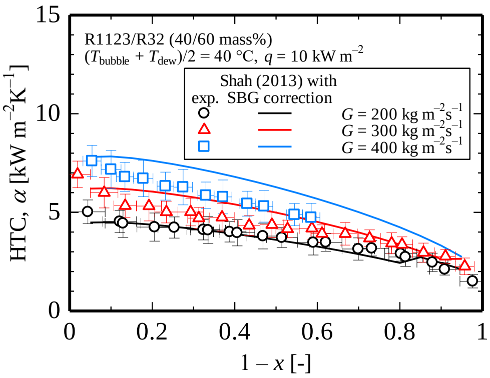

(a) Heat transfer coefficient

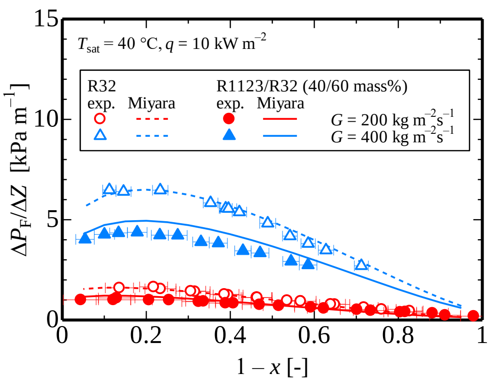

(b) Pressure gradient

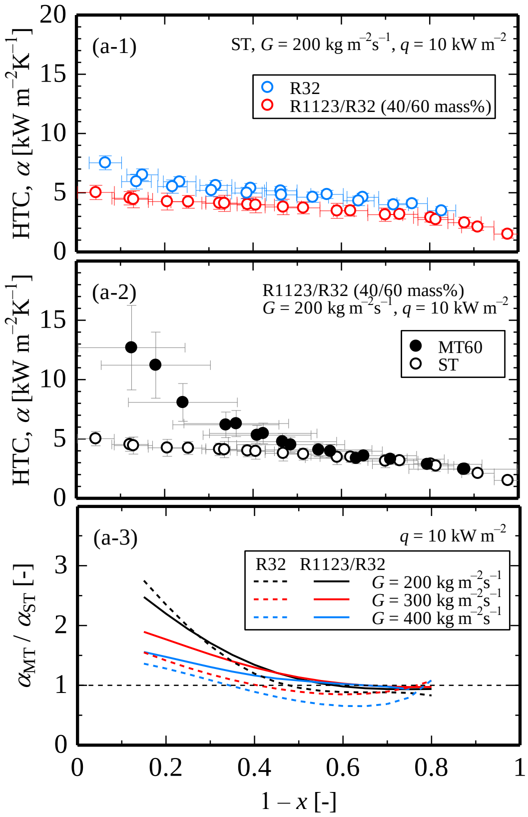

(c) Comparison between heat transfer coefficients of ST and MT

Fig. 3.1.1.1-6 Condensation flow of the HFO1123/ HFC32 mixture

・Premixed ternary mixture R455A (HFC32/HFO1234yf/CO_2; 21.5/75.5/3.0 mass%)

Figs. 3.1.1.1-7(a) and (b) show the condensation heat transfer coefficient and pressure gradient measured for R455A (HFC32/HFO1234yf/CO_2; 21.5/75.5/3.0 mass%) at an average saturation temperature of 40 °C, heat flux of 10 kW m^{-2}, and mass–velocities of 200, 300, and 400 kg m^{-2}s^{-1}. A comparison of the heat transfer coefficients of the pure, binary mixture, and ternary mixture refrigerants is shown in Fig. 3.1.1.1-7(c). The heat transfer coefficient was highest for HFC32, followed by HFO1123/HFC32 (40/60 mass%), and lowest for R455A. The results indicate a substantial causal effect between temperature gradient and heat transfer degradation.

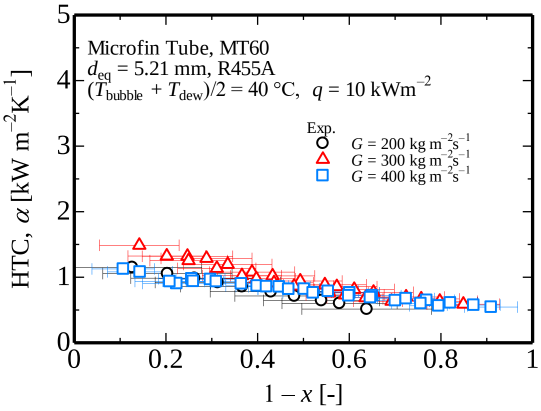

(a) Heat transfer coefficient

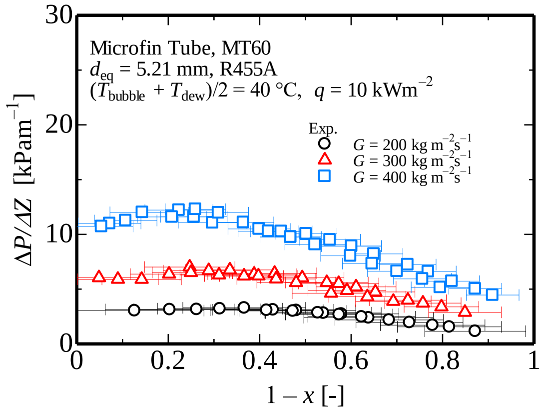

(b) Pressure gradient

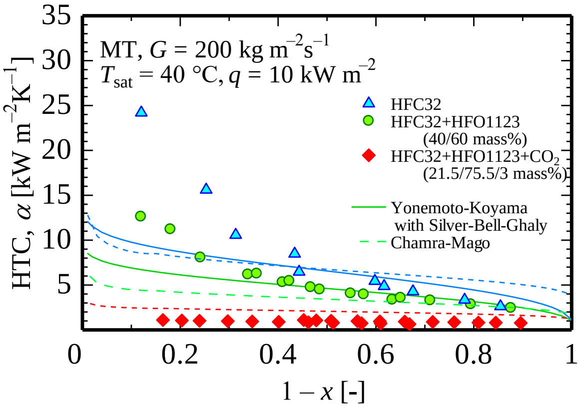

(c) Effect of the volatility difference[7,8)]

Fig. 3.1.1.1-7 Condensation flow of R455A

・Binary mixture of HFO1234ze(E)/HFC32

Fig. 3.1.1.1-8 shows the condensation pressure gradient and heat transfer coefficient measured for the HFO1234ze(E)/HFC32 mixture flowing in a ST, where the solid and dashed lines are the predicted results for HFC32 and HFO1234ze(E), respectively. The pressure drop increased with the composition of HFO1234ze(E). Fig. 3.1.1.1-9 shows the composition dependence of the condensation heat transfer coefficients in ST and MT48 reported by Mishima[9)], where the horizontal axis shows the HFC32 composition and the vertical axis shows the heat transfer coefficient, ratio of heat transfer degradation to ideal heat transfer coefficient of the mixtures, and temperature gradient in each graph. For example, at a HFC32 composition of approximately 0.23, where the temperature gradient was maximized, the heat transfer coefficient decreased the most.

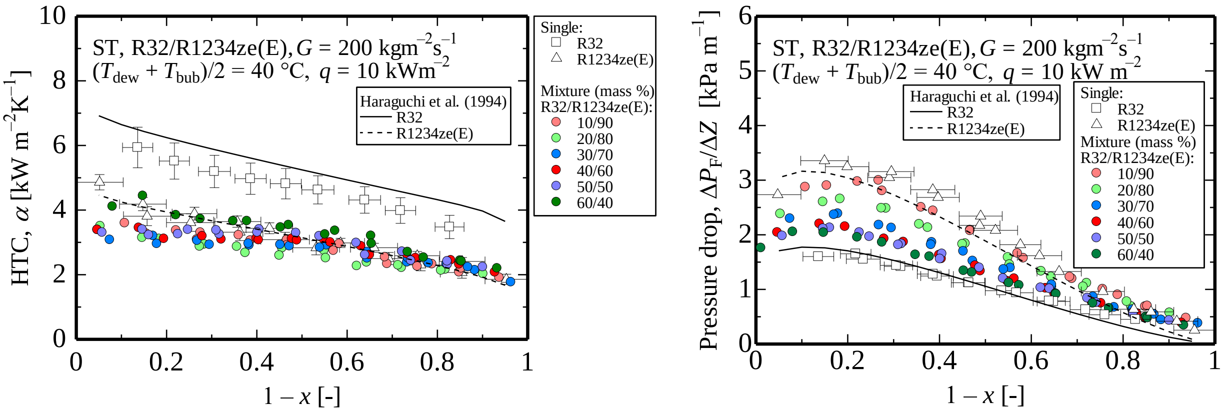

(a) Heat transfer coefficient (b) Pressure gradient

Fig. 3.1.1.1-8 Condensation flow of the HFO1234ze(E)/HFC32 mixture

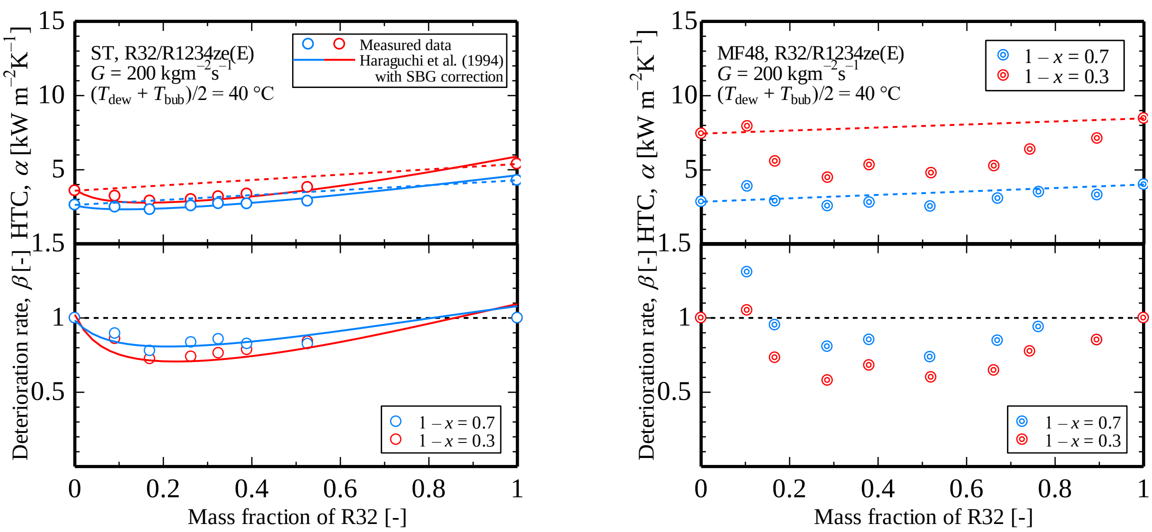

(a) ST (b) MT48

Fig. 3.1.1.1-9 Condesation flow of the HFO1234ze(E)/HFC32 mixture

・Binary mixture of HFO1234yf/HFC32

Fig. 3.1.1.1-10 shows the measured pressure gradient and heat transfer coefficient of the HFO1234yf/HFC32 mixture flowing in a ST. The pressure drop and condensation heat transfer coefficient of the HFO1234yf/HFC32 mixture showed similar trends to those of the HFO1234ze(E)/HFC32 mixture condensation flow. The heat transfer coefficients significantly decreased for compositions with large temperature gradients, while the pressure drop decreased as the composition of HFC32 increased.

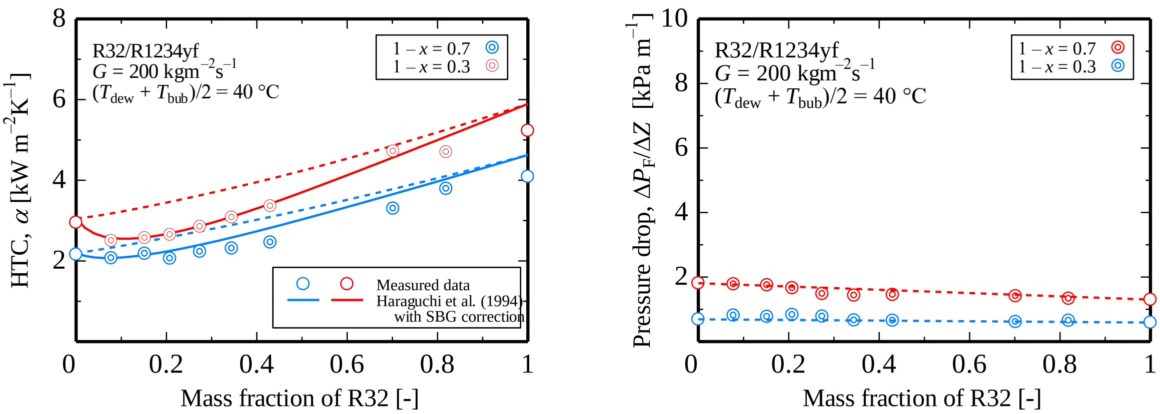

(a) Heat transfer coefficient (b) Pressure gradient

Fig. 3.1.1.1-10 Condensation flow of the HFO1234yf/HFC32 mixture

(3) Heat transfser coefficient and pressure drop for evaporation flow

・Pure refrigerants of HFC32, HFO1234ze(E) and HFO1234yf

Figs. 3.1.1.1-11 and -12 show the measured evaporative heat transfer coefficients and pressure gradients, respectively, of HFC32, HFO1234ze(E), and HFO1234yf. The heat transfer coefficient was highest for HFC32, followed by those of HFO1234ze(E) and HFO1234yf. HFC32 exhibited the highest heat transfer coefficient at vapor qualities below 0.8; however, the difference in heat transfer coefficients among the three refrigerants was the lowest at vapor qualities above 0.8. HFO1234ze(E) exhibited the most significant pressure drop, followed by HFO1234yf and HFC32.

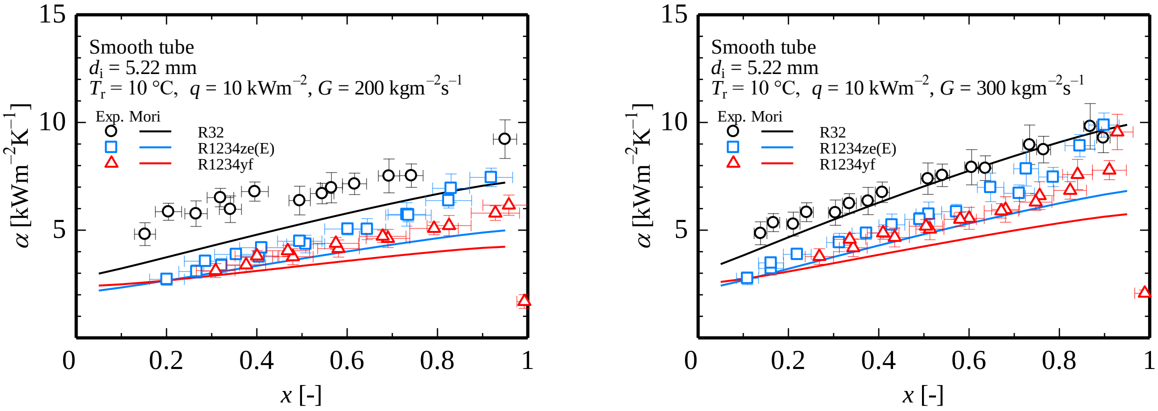

(a) G = 200 kg m^{-2}s^{-1} (b) G = 300 kg m^{-2}s^{-1}

Fig. 3.1.1.1-11 Measured evaporative heat transfer coefficients of HFC32, HFO1234ze(E), and HFO1234yf [10)]

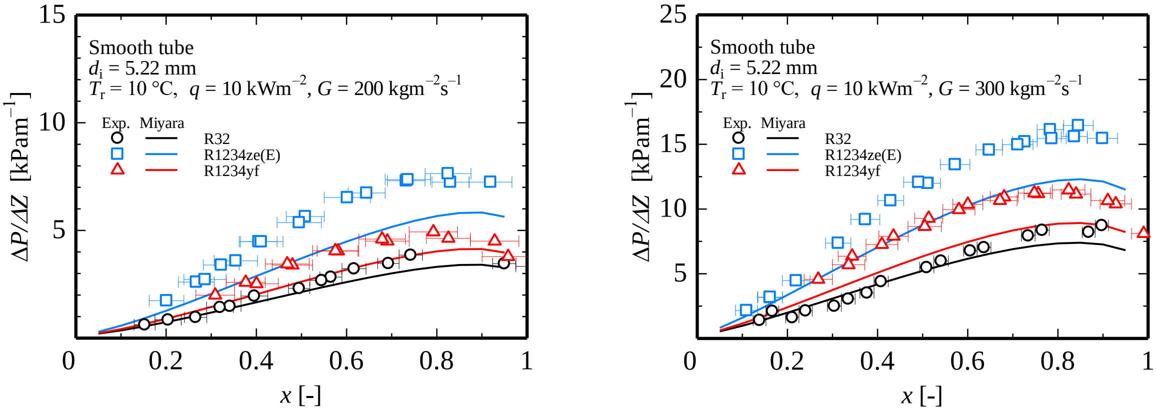

(a) G = 200 kg m^{-2}s^{-1} (b) G = 300 kg m^{-2}s^{-1}

Fig. 3.1.1.1-12 Measured evaporative pressure gradients of HFC32, HFO1234ze(E), and HFO1234yf

・Binary mixture of HFO1123/HFC32

Figs. 3.1.1.1-13(a) and (b) show the measured evaporative heat transfer coefficient and pressure gradient, respectively, of the HFO1123/HFC32 mixture measured at an average saturation temperature of 10 °C, heat flux of 10 kW m^{-2}, and mass–velocity of 200 kg m^{-2}s^{-1}. Furthermore, the results correlated to that predicted by Takamatsu et al. [11)] for other refrigerant mixtures are shown. First, the onset and post-dry-out heat transfer coefficients were calculated using the equations defined by Yoshida et al.[12)] and Mori et al.[13)], respectively. Second, the heat transfer coefficient between the two calculated values was calculated by linear interpolation. Fig. 3.1.1.1-13(c) shows a comparison of the evaporative heat transfer coefficients of the HFO1123/HFC32 mixture and HFC32 in the ST and MT. The heat transfer coefficient of the HFO1123/HFC32 mixture was slightly lesser than that of HFC32. At lower vapor qualities, MT showed a lower heat transfer coefficient than that of ST; however, at vapor qualities above 0.6, MT showed a higher heat transfer coefficient. The heat transfer enhancement ratios based on the ST of the HFO1123/HFC32 mixture and HFC32 were similar.

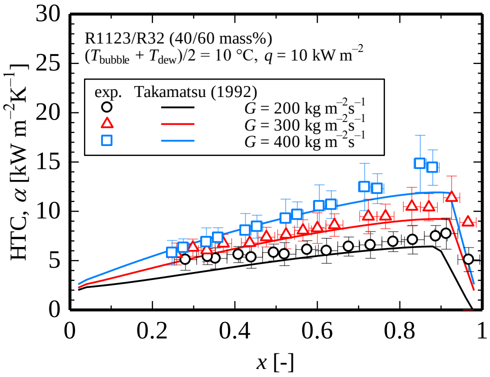

(a) Heat transfer coefficient

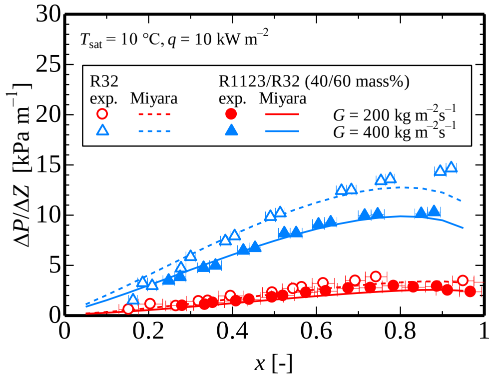

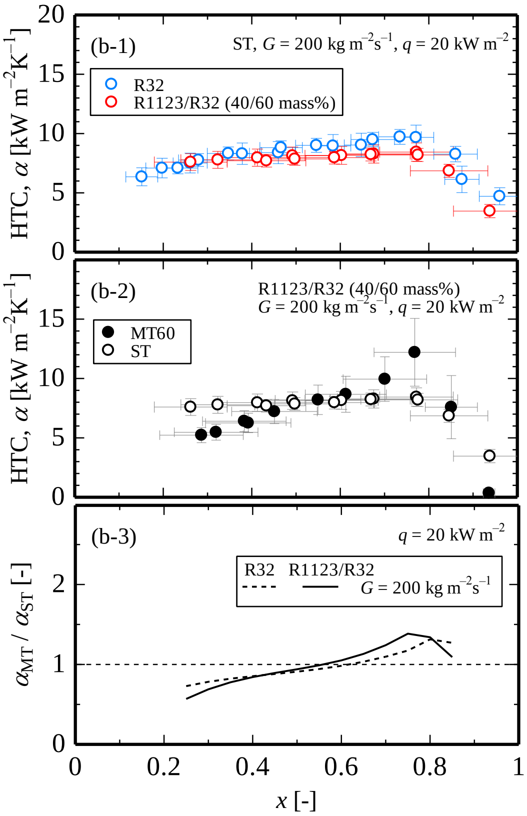

(b) Pressure gradient (c) Comparison between heat transfer coefficients of ST and MT

Fig. 3.1.1.1-13 Evaporation flow of the HFO1123/HFC32 mixture

・Pure refrigerant of HCFO1224yd(Z)

Fig. 3.1.1.2.3-14 shows the measured evaporative heat transfer coefficient and pressure gradient of HCFO1224yd(Z) compared to those of HFC32 and the HFO1123/HFC32 mixture (40/60 mass%). The heat transfer coefficient of HCFO1224yd(Z) at a saturation temperature of 10 °C and mass–velocity of 100 kg m^{-2}s^{-1} was lower than that of HFC32 at a mass–velocity of 200 kg m^{-2}s^{-1}, while the pressure drop of HCFO1224yd(Z) was approximately 1.5 times higher than that of HFC32.

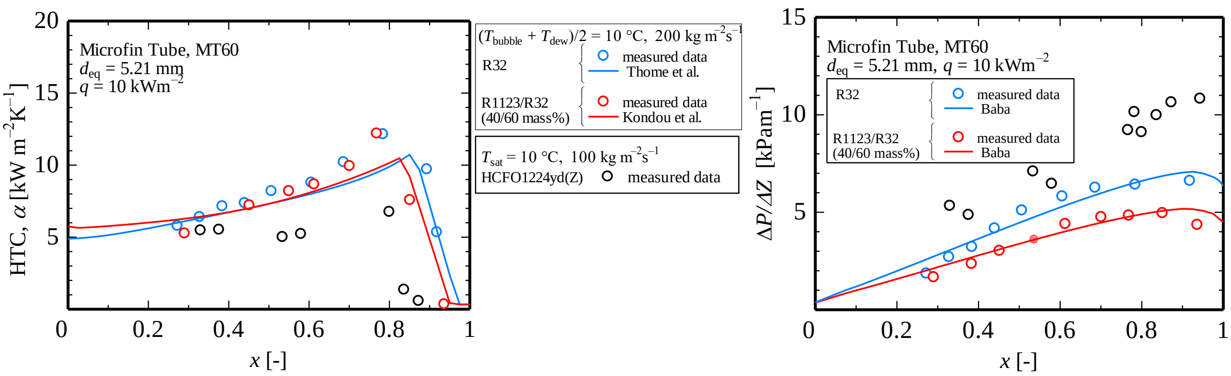

(a) Heat transfer coefficient[14,15] (b) Pressure gradient[16]

Fig. 3.1.1.1-14 Evaporation flow of HCFO1224yd(Z)

・Binary mixture of HFO1234ze(E)/HFC32

Fig. 3.1.1.1-15 shows the measured evaporative pressure gradient and heat transfer coefficient of the HFO1234ze(E)/HFC32 mixture flowing in a ST. The solid and dashed lines show the predicted values for

HFO1234ze(E) and HFC32, respectively. The amount of pressure drop of the HFO1234ze(E)/HFC32 mixture was between that of the pressure drops of HFO1234ze(E) and HFC32. The pressure drop increased in the mixture as the HFO1234ze(E) composition increases. Fig. 3.1.1.1-16 shows the composition dependence of the evaporative heat transfer coefficient in ST and MT48. The heat transfer coefficient in the MT exhibited a more significant evaporative heat transfer degradation than in the condensation process.

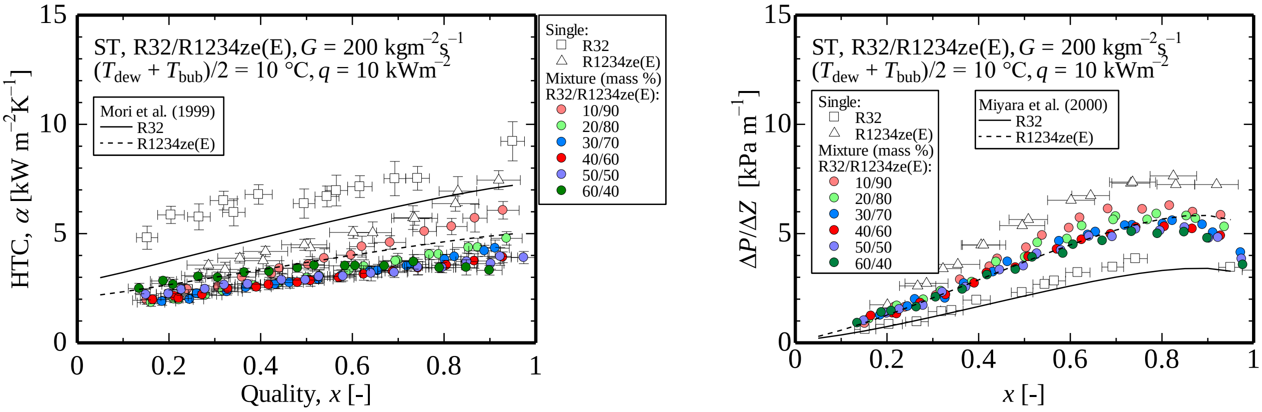

(a) Heat transfer coefficient (b) Pressure gradient

Fig. 3.1.1.1-15 Evaporation flow of the HFO1234ze(E)/HFC32 mixture

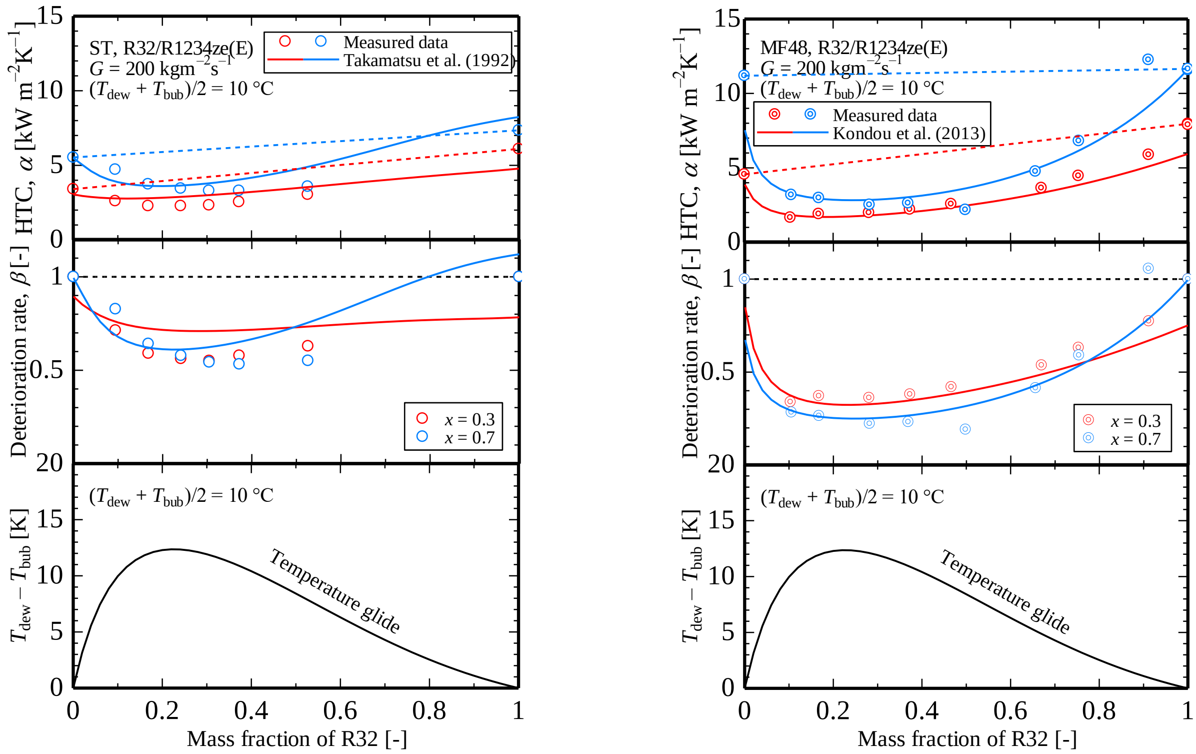

(a) ST (b) MT48

Fig. 3.1.1.1-16 Evaporation flow of the HFO1234ze(E)/HFC32 mixture

・Binary mixture of HFO1234yf/HFC32

Fig. 3.1.1.1-17 shows the measured evaporative pressure gradient and heat transfer coefficient of the HFO1234yf/HFC32 mixture flowing in a ST. Similar to that of the HFO1234ze(E)/HFC32 mixture, the heat transfer coefficient of the HFO1234ze(E)/HFC32 mixture decreased significantly at compositions with large temperature gradients, and the pressure drop increased with increase in the composition of HFO1234ze(E).

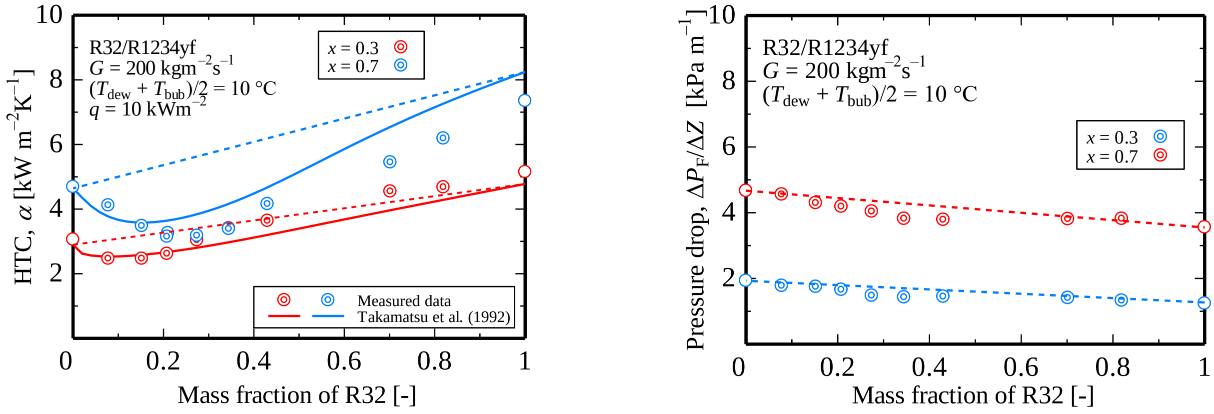

(a) Heat transfer coefficient (b) Pressure gradient

Fig. 3.1.1.1-17 Evaporation flow of the HFO1234yf/HFC32 mixture

References

1) E. W. Lemmon, I. H. Bell, M. L. Huber, and M. O. McLinden, NIST Standard Reference Database 23 (2018).
2) H. Haraguchi, S. Koyama, and T. Fujii, Trans. JSME (B), 60(574), 2117(1994). (in Japanese)
3) A. Miyara, K. Kuwahara, and S. Koyama, JSME Kyushu Branch 57th, 117(2005). (in Japanese)
4) M. M. Shah, ASHRAE Transactions, Denver, 119(2), 3(2013).
5) L. Silver, Trans. Inst. Chem. Engrs., 25, 30(1947).
6) K. J. Bell and M. A. Ghaly, AIChE Symp. Ser., 69, 72(1973).
7) R. Yonemoto and S. Koyama, Trans. JSRAE., 24(2), 139(2007). (in Japanese)
8) L. M. Chamra and P. J. Mago, Int. J. Heat Mass Transf., 49(11–12), 1915(2006).
9) F. Mishima, Doctoral dissertation, IGSES Kyushu University (2014). (in Japanese)
10) H. Mori, S. Yoshida, Y. Kakamoto, and K. Ohishi, Trans. JSRAE., 16(2), 177(1999). (in Japanese)
11) H. Takamatsu, S. Momoki, and T. Fujii, Trans. JSME(B), 58(551), 2198(1992). (in Japanese)
12) S. Yoshida, H. Mori, Y. Kakamoto, and K. Ohishi, Trans. JSRAE., 17(4), 511(2000). (in Japanese)
13) H. Mori, S. Yoshida, Y. Kakamoto, K. Ohishi, and K. Fukuda, Trans. JSRAE., 17(4), 521(2000). (in Japanese)
14) J.R. Thome, Convective Flow and Pool Boiling Conference (1997).
15) C. Kondou, D. Baba, F. Mishima, and S. Koyama, Int. J. Refrig., 36, 2366(2013).
16) D. Baba, Doctoral dissertation, IGSES Kyushu University (2013). (in Japanese)

3.1.1.2 Phase change heat transfer in a multiport tube

Measurements of condensation and evaporation heat transfer coefficients and pressure drops of next-generation refrigerants flowing in an aluminum multiport tube were performed. Fig. 3.1.1.2-1 shows a schematic of the experimental apparatus used for the experiment. The experimental apparatus consisted of a forced-circulation loop with a pump. The test refrigerant flowed through the pump, Coriolis flow meter, water preheater, and electric preheater to the test section. The refrigerant condenses or evaporates in the test section and then returns to the pump through a cooler, receiver, and supercooler. The flow rate of the refrigerant was mainly regulated by the pump speed and bypass loop, while the refrigerant pressure was mainly regulated by the heat exchange rate of the condenser.

During the evaluation, the heat transfer coefficient and pressure drop were measured by varying the mass–velocity, vapor quality, and heat flux. For refrigerant mixtures, circulating composition was determined by sampling the refrigerants using gas chromatography.

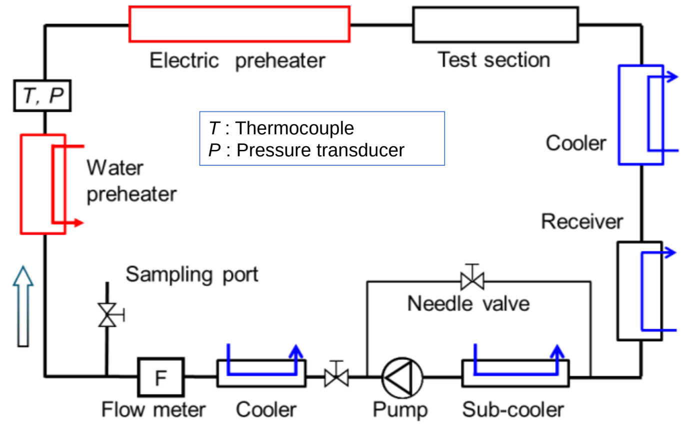

Fig. 3.1.1.2-1 Experimental setup

Fig. 3.1.1.2-2 shows a schematic of the test section. The multiport tube under test was cooled or heated from the top and bottom using a copper jacket through which cool or hot water flowed. Heat flux was controlled by the water temperature in the copper jacket using heat flux sensors, which were inserted between the test tube and copper jacket. The outer wall temperature was measured using K-type thermocouples (accuracy ±0.05 K) attached to the outer wall surface of the test tube, while the pressure and differential pressure of the refrigerant in the test section were measured using absolute pressure *P* (accuracy ±3 kPa) and differential pressure Δ*P* (accuracy of ±40 Pa) transducers, respectively. The multiport tube under test was 16 mm wide and 1.5 mm thick, while the cross-section of the channel consisted of square mini-channels with a hydraulic diameter of 0.82 mm.

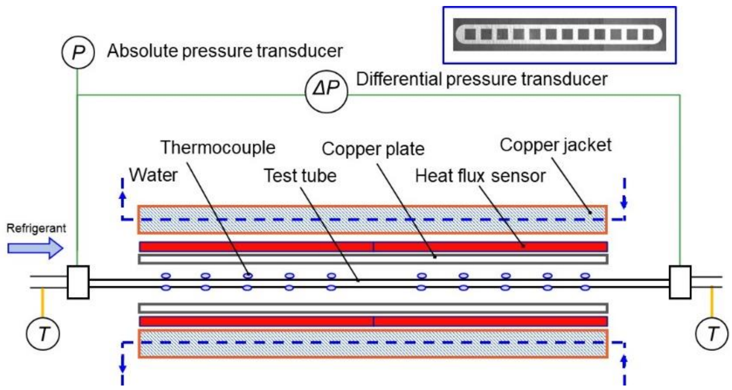

Fig. 3.1.1.2-2 Test section

Fig. 3.1.1.2-3 shows the evaluation results of the pure refrigerants, HFC32 and HFO1234yf; binary refrigerant mixtures, R410A and HFC32/HFO1234yf (48/52mass%, 27/73mass%), HFO1123/HFC32 (39/61mass%),

$HFC32/CF_3I$ (90/10 mass%); and ternary refrigerant mixtures, HFO1123/HFC32/HFO1234yf (59/21/20 mass %) and CO_2/HFC32/HFO1234yf (2/20/78 mass%). For pure refrigerants, the evaluation was conducted at a refrigerant pressure at which the refrigerant saturation temperature was 40 °C. For non-azeotropic mixtures, the evaluation was conducted at a refrigerant pressure at which the average temperature between the dew and boiling points was 40 °C. The condensation heat transfer coefficient can be calculated as

$$\alpha = \frac{q}{T_r - T_w}, \quad (3.1.1.2\text{-}1)$$

where q is the heat flux measured based on the actual heat transfer area inside the tube, T_r is the refrigerant temperature, and T_w is the inner-wall temperature of the tube, which can be obtained from the measured outer-wall temperature of the tube. The physical properties of the refrigerants were measured using REFPROP Ver. 10.0 [1].

The condensation heat transfer coefficient was highest for the pure refrigerant HFC32, whereas that for HFO1234yf, $HFC32/CF_3I$, and HFO1123/HFC32 were similar or slightly better than that for R410A. However, the refrigerant mixtures containing HFO1234yf with a large temperature glide showed a lower heat transfer coefficient than that for R410A and HFO1234yf. The related results of condensation heat transfer in multiport tubes have been reported in previous studies [2–8].

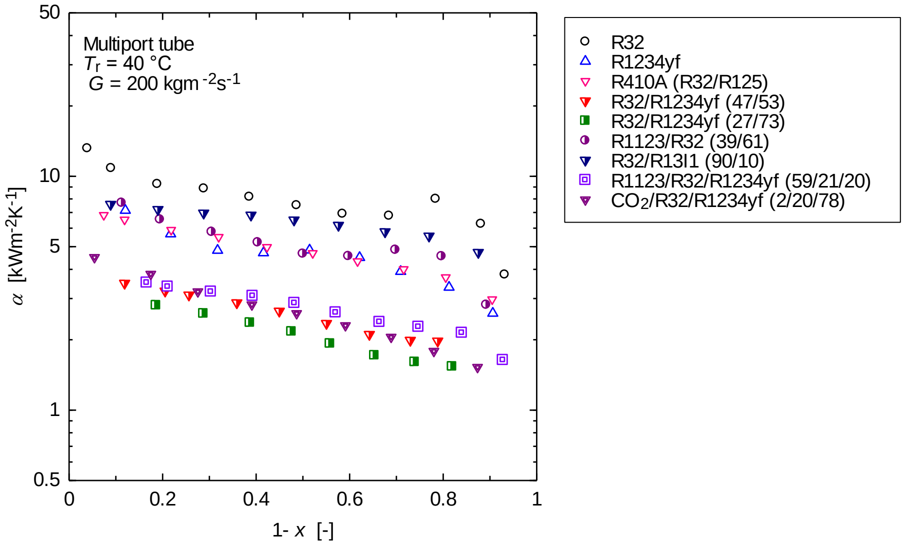

Fig. 3.1.1.2-3 Condensation heat transfer coefficients of pure and mixed refrigerants inside the horizontally placed multiport tube

Fig. 3.1.1.2-4 shows the evaluation results of the pure refrigerants, HFC32 and HFO1234yf; binary refrigerant mixtures, R410A, HFC32/HFO1234yf (50/40 mass%, 18/82 mass%), HFO1123/HFC32 (39/61 mass%), $HFC32/CF_3I$ (90/10 mass%); and ternary refrigerant mixtures, HFO1123/HFC32/HFO1234yf (59/21/20 mass %), and CO_2/HFC32/HFO1234yf (4/16/80 mass%). For pure refrigerants, the evaluation was conducted at a refrigerant pressure at which the refrigerant saturation temperature was 15 °C. For non-azeotropic mixtures, the evaluation was conducted at a refrigerant pressure at which the average temperature between the dew and boiling points was 15 °C. The evaporative heat transfer coefficient can be calculated as

$$\alpha = \frac{q}{T_w - T_r} \quad (3.1.2.2\text{-}2)$$

where q is the heat flux measured based on the actual heat transfer area inside the tube, T_r is the refrigerant temperature of the tube, and T_w is the inner-wall temperature of the tube.

The evaporative heat transfer coefficient was highest for the pure refrigerant HFC32, whereas that for the $HFC32/CF_3I$ and HFO1123/HFC32 mixtures were similar or better than that for R410A and better than that for

HFO1234yf. Conversely, refrigerant mixtures containing HFO1234yf with a larger temperature glide showed lower heat transfer coefficients than R410A and HFO1234yf. The related results of evaporative heat transfer in multiport tubes have been reported in previous studies [9–12)].

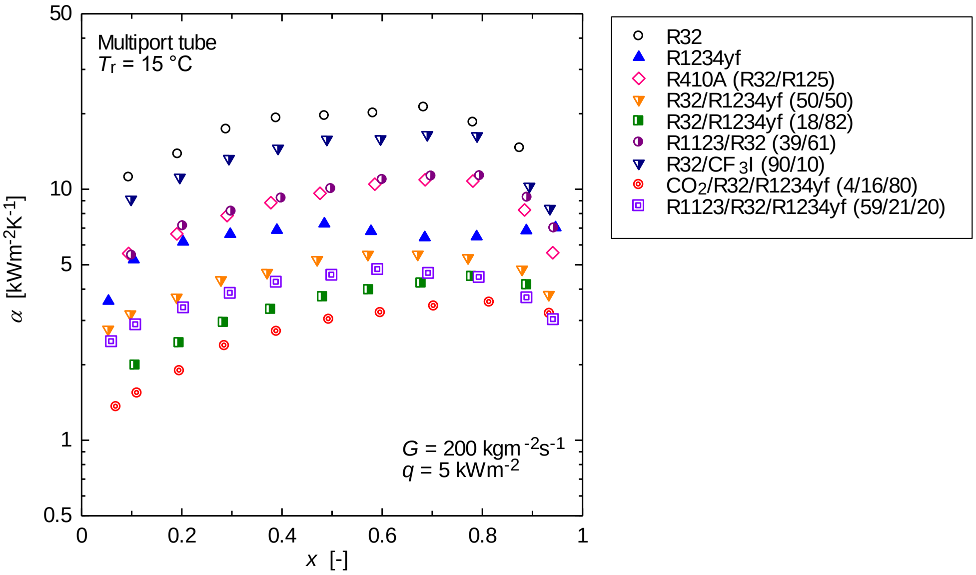

Fig. 3.1.1.2-4 Evaporative heat transfer coefficients of pure and mixed refrigerants inside the horizontally placed multiport tube

Fig. 3.1.1.2-5 shows the frictional pressure drop in the condensation flow of pure refrigerants, R32 and R1234yf; binary mixtures, R410A and R32/R1234yf (48/52 mass%, 27/73 mass%), R1123/R32 (39/61 mass%), R32/R13I1 (90/10 mass%); and ternary mixtures, R1123/R32/R1234yf (59/21/20) and CO2/R32/R1234yf (2/20/78). For pure refrigerants, the evaluation was conducted at a refrigerant pressure at which the refrigerant saturation temperature reached 40 °C, whereas the non-azeotropic mixtures were evaluated at a refrigerant pressure at which the average temperature of the dew and boiling point reaches 40 °C. The frictional pressure drop of the pure refrigerant R1234yf was the highest in the high to medium vapor quality range when compared under the same mass–velocity conditions; R32, R32/R1234yf, and CO2/R32/R1234yf had similar pressure drops. The pressure drops of the R410A, R1123/R32, and R1123/R32/R1234yf mixtures were lower than those of other refrigerants.

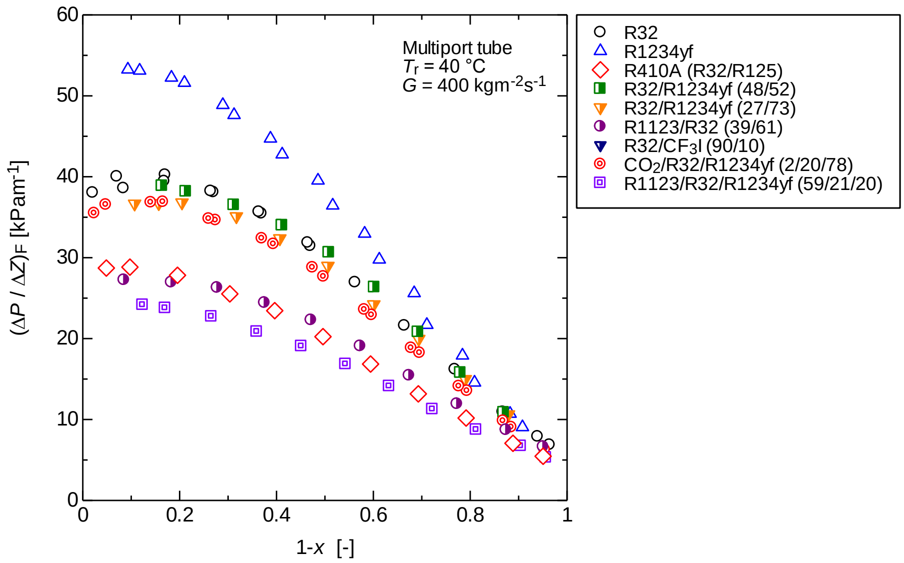

Fig. 3.1.2.2-5 Pressure gradients of pure and mixed refrigerants inside the horizontally placed multiport tube

References

2-1) E. W. Lemmon, I. H. Bell, M. L. Huber, and M. O. McLinden, NIST Standard Reference Database 23 (2018).

2-2) D. Jige, N. Mikajiri, S. Kikuchi, and N. Inoue, J. Int. Acad. Refrig., 120, 200–208(2020). https://doi.org/10.1016/j.ijrefrig.2020.08.029.

2-3) D. Jige, N. Mikajiri, S. Kikuchi, and N. Inoue, A313, JSRAE Annual Conf., Tokyo, (2020).

2-4) N. Mikajiri, S. Kikuchi, D. Jige, and N. Inoue, B122, JSRAE Annual Conf., Tokyo, (2020)

2-5) M. Nobunaga, N. Mikajiri, D. Jige, N. Inoue, 54th Japanese Joint Conference on Air-conditioning and Refrigeration, (2021).

2-6) M. Nobunaga, N. Mikajiri, D. Jige, and N. Inoue, International Symposium on New Refrigerants and Environmental Technology (2021).

2-7) D. Jige, M. Nobunaga, T. Nogami, and N. Inoue, Submitted to the Int. J. Heat Mass Transf.

2-8) D. Jige, N. Mikajiri, M. Nobunaga, and N. Inoue, Int. J. Heat Mass Transf., 195, 23146(2022). ISSN 0017-9310, https://doi.org/10.1016/j.ijheatmasstransfer.

2-9) D. Jige, S. Kikuchi, H. Eda, and N. Inoue, Int. J. Heat Mass Transf., 144, 118668(2019). https://doi.org/10.1016/j.ijheatmasstransfer.2019.118668.

2-10) D. Jige, S. Kikuchi, N. Mikajiri, and N. Inoue, Int. J. Refrig., 119, 390–400(2020). ISSN 0140-7007, https://doi.org/10.1016/j.ijrefrig.2020.04.036.

.2-11) N. Mikajiri, M. Nobunaga, D. Jige, and N. Inoue, B133, JSRAE Annual Conf., Tokyo, (2021).

2-12) M. Nobunaga, D. Jige, and N. Inoue, A142, JSRAE Annual Conf., Okayama (2022).

3.1.1.3 Phase change heat transfer in a plate heat exchanger channel

At Saga University, the characteristics of local condensation and boiling heat transfer coefficients in a plate heat exchanger for various HFO refrigerants were investigated. Transparent plate heat exchanger channels were fabricated to observe the flow characteristics and measure the void fraction by using the shutoff method.

Figs. 3.1.1.3-1 and -2 show schematics of the plate heat exchanger under test for measurement and visualization of heat transfer coefficient, respectively. For both the experiments, herringbone pattern was grooved on the test channels, having a channel length and width of 186 mm and 84 mm, respectively. For the visualization test, a test plate with a channel length of 372 mm was also prepared.

A 10 mm thick stainless-steel plate was brazed to both the outer surfaces of the test plate, with horizontal grooves of diameter 1.6 mm on both sides, into which T-type sheath thermocouples were inserted to measure the temperatures of the heat transfer surfaces on both the refrigerant and water sides. The heat transfer surface temperatures were measured in the flow direction at 23.2, 45.6, 68.0, 90.4, and 112.8 mm from the inlet, taking the upper side of the refrigerant flow path as a reference. The water-side heat-transfer surface temperature was measured using the same type of thermocouple placed at the same position as on the refrigerant side. The temperature was measured by moving the thermocouples in the width direction after they reached a steady state. The measurement points are indicated by red circles in Fig. 3.1.1.3-1. A little further outside the plate, a 6 mm thick stainless-steel plate with a 5 mm deep rectangular channel was superimposed, through which the heat source water flowed from the stainless-steel pipe attached to the header.

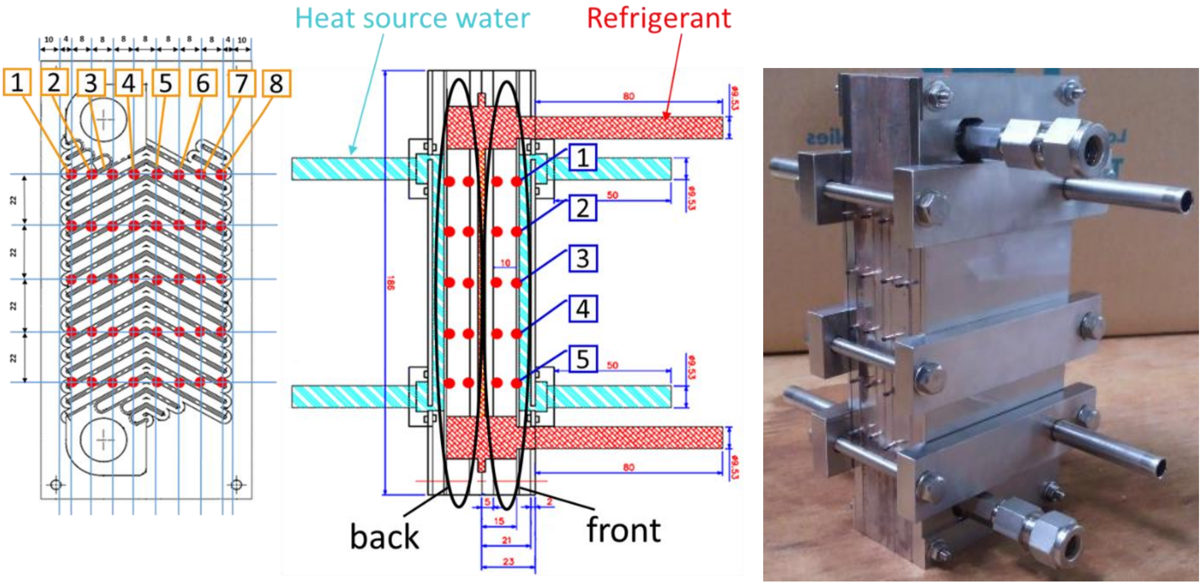

Fig. 3.1.1.3-1 Test channel of plate heat exchanger (Heat transfer experiment)

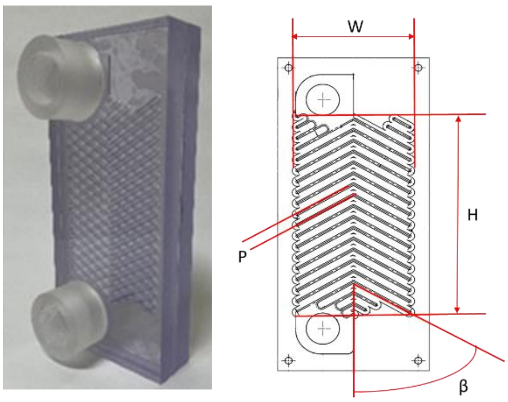

Corrugation type	Chevron
Fluid flow plate length H (mm)	186（short）372(long)
Plate width W (mm)	64
Area of the plate (m^2)	0.0075
Chevron angle β (deg)	60
Corrugation pitch P (mm)	5.6
Corrugation depth (mm)	1.5
Hydraulic equivalent diameter (mm)	2.6
Inlet and outlet pipe	same side

Fig. 3.1.1.3-2 Test channel of plate heat exchanger and its specifications (Visualization experiment)

The paths of refrigerant and heat-source water flow are shown by red and light blue marking in the Fig. 3.1.1.3-1. The refrigerant inlets and outlets were located at the same position in the vertical direction, where the test plate with the inlet was the front and the test plate without the inlet was the back. The refrigerants measured and the experimental conditions for the evaporation and condensation heat transfer coefficient measurements are listed in Tables 3.1.1.3-1 and -2, respectively. Some of the refrigerants measured included unpublished results and data that have to be re-estimated. The final unpublished data will be published as soon as they are finalized. Table 3.1.1.3-3 lists the conditions necessary for the visualization experiment.

Table 3.1.1.3-1 List of measured refrigerants/blends for evaporation experiment (upward flow)

Refrigerants/Blends	Mass–velocity G kg/(m^{2}s)	Saturation temperature ℃	Quality x -	Reference
HFC32	10 to 50	10 to 30	0.0 to 1.0	1, 2
HFO1234yf	10 to 50	10 to 20	0.0 to 1.0	3, 4
CF_3I	20, 50	15 to 35	0.0 to 1.0	To be published
HFC32/HFO1234yf [68.9/31.1 mass%]	10	11.5	0.0 to 1.0	To be published
HFC32/HFO1234yf [21.5/78.5 mass%]	10,50	20	0.0 to 1.0	5

Table 3.1.1.3-2 List of measured refrigerants/blends for condensation experiment (downward flow)

Refrigerants/Blends	Mass–velocity G kg/(m^{2}s)	Saturation temperature ℃	Quality x -	Reference
HFC32	10 to 50	20 and 35	1.0 to 0.0	1,2
HFO1234yf	20, 50	20 and 30	1.0 to 0.0	3,4
CF_3I	20, 50	10	1.0 to 0.0	To be published
HFC32/HFO1234yf [68.9/31.1 mass%]	10	40	1.0 to 0.0	6
HFC32/HFO1234yf [21.5/78.5 mass%]	10, 50	30	1.0 to 0.0	5

Table 3.1.1.3-3 Experimental conditions necessary for visualization experiment

Working fluid	Flow direction	Mass–velocity G kg/(m^{2}s)	Quality x -	Reference
FC-72	10 to 50	20 and 35	1.0 to 0.0	7

For example, the results of local evaporation and condensation heat transfer coefficients of HFO1234yf at mass–velocity G = 20 kg/(m^{2}s) are shown in Figs. 3.1.1.3-3 and -4, respectively, where the vertical axis represents the local heat transfer coefficient and the horizontal axis shows the position on the plate width direction. The evaporation heat transfer coefficient was relatively high from the left end where the refrigerant inlets and outlets were located, whereas the heat transfer coefficients at both ends, where the refrigerant flow seemed to be low, were lower. The local heat transfer coefficient in the high-quality region (x = 0.90) decreased with distance from the inlet/outlet owing to the dry-out coefficient. The condensation heat transfer coefficients at both ends of the flow path, where the liquid film appeared to be thicker, were relatively lesser than those at the center of the flow path.

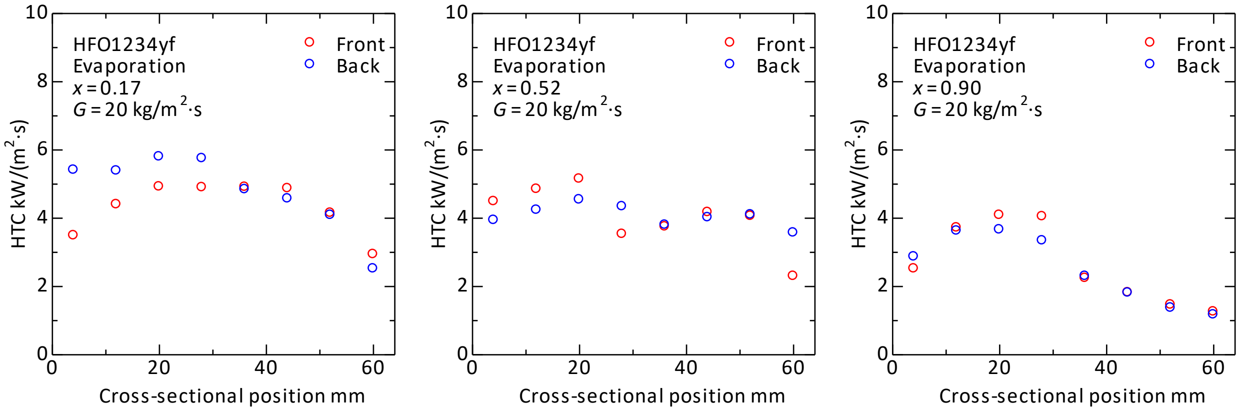

Fig. 3.1.1.3-3 Local evaporative heat transfer coefficient

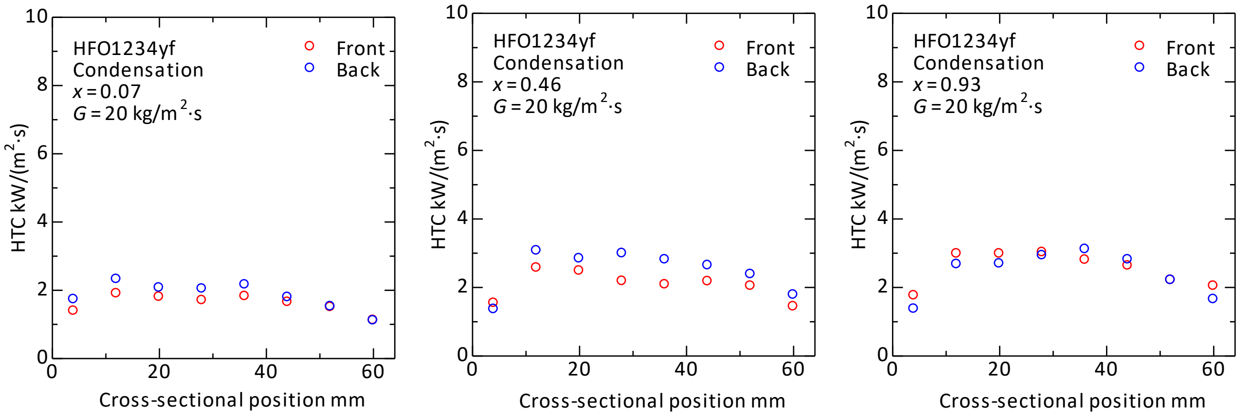

Fig. 3.1.1.3-4 Local condensation heat transfer coefficient

Furthermore, the evaporative/condensation heat transfer coefficients of various HFO refrigerants were compared. Fig. 3.1.1.3-5 shows the cross-sectional average evaporative heat transfer coefficient plotted for each refrigerant. The results for HFO1234ze(E)[8], previously measured by our research group, are also shown for comparison. It was observed that the heat transfer coefficient for HFC32 was the highest for all mass–velocities. In mixed refrigerants, the heat transfer coefficients decreased with a decrease in the mass concentration of HFC32, and the heat transfer coefficient for the HFC32/HFO1234yf mixture (21.5/78.5 mass%) was lower than that for the pure refrigerant HFO1234yf.

Fig. 3.1.1.3-6 shows the cross-sectional average values of the condensation heat-transfer coefficient. Similar to the evaporative heat transfer results, HFC32 had the highest heat transfer coefficient. The heat transfer coefficients for the mixed refrigerants were significantly lower than that for the pure refrigerants. Although the effect of concentration gradient inside the liquid film may have caused the decrease in value, a different trend from that of the evaporative heat transfer results was observed. Hence, we are currently examining for are any errors in the data reduction.

Finally, the results of visualization observations and void fraction measurements of the plate channel are reported, and Fig. 3.1.1.3-7(a) shows the flow observation results obtained for the upstream flow. At low flow rates, a slug flow was observed, which transitioned to an annular flow with an increase in flow and quality, as shown in Figs. 3.1.1.3-8(a) and (b), respectively. Fig. 3.1.1.3-7(b) shows the results of the void fraction measured using the shut-off method. In general, the void fraction increased with an increase in the flow and quality.

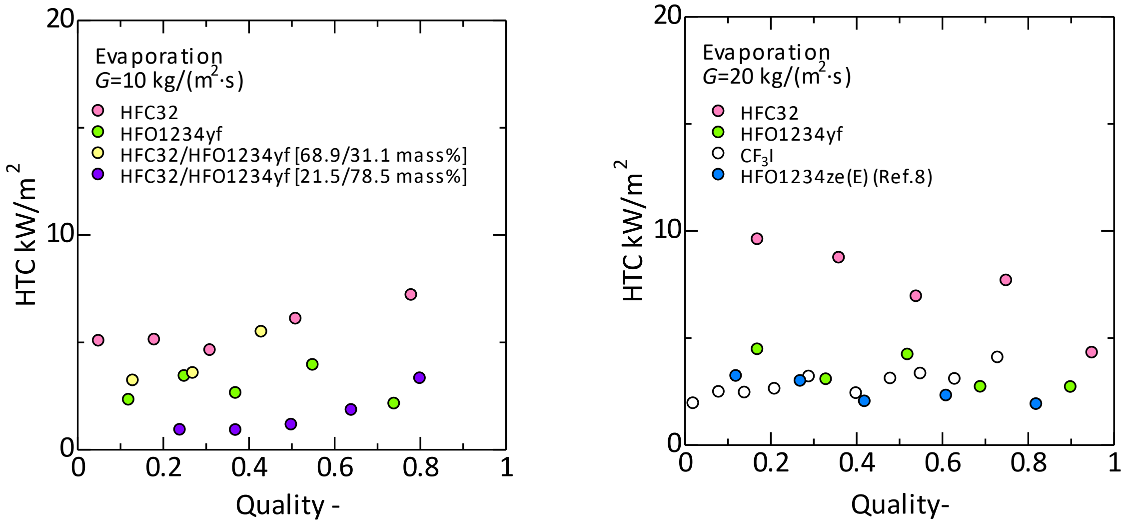

Fig. 3.1.1.3-5 Cross–sectional average of evaporative heat transfer coefficient

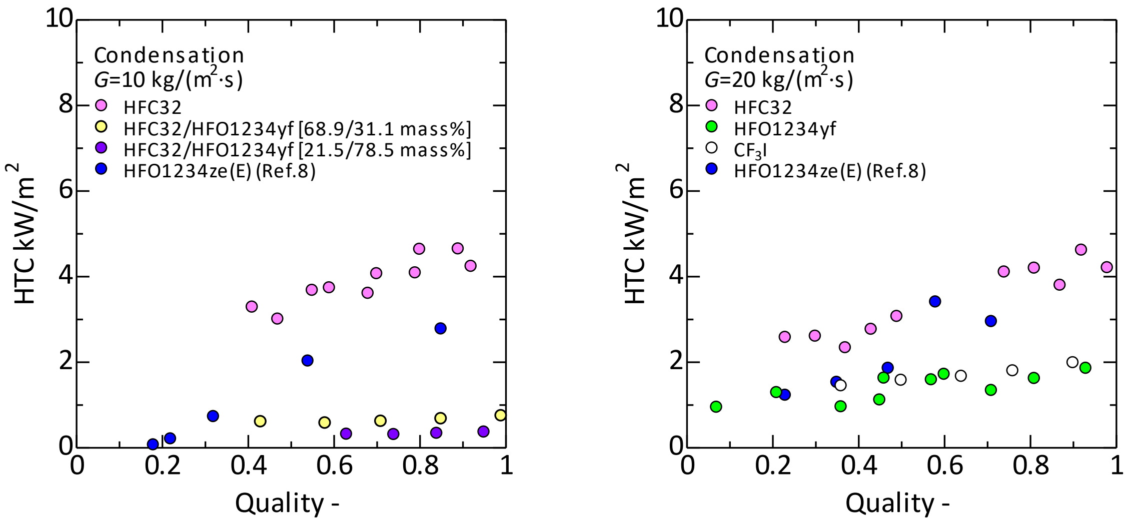

Fig. 3.1.1.3-6 Cross–sectional average of condensation heat transfer coefficient

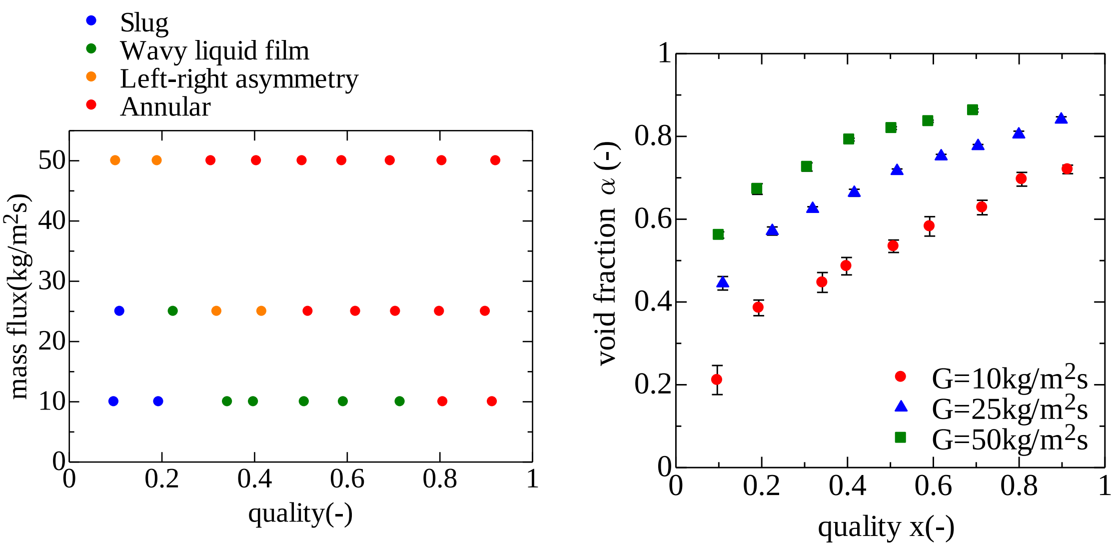

(a) Flow pattern (b) Void fraction.

Fig. 3.1.1.3-7 Flow pattern and void fraction of the plate heat exchanger channel

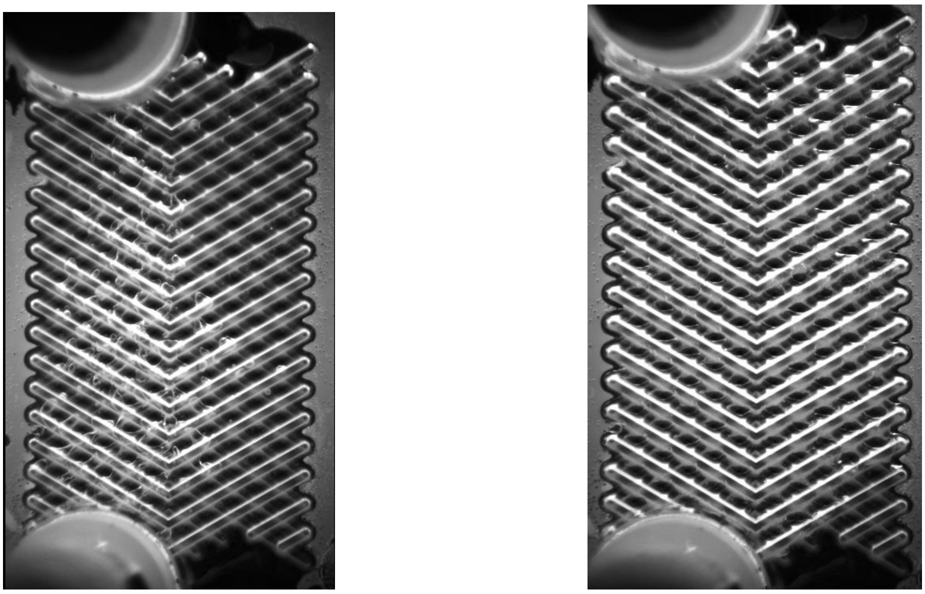

(a) Slug flow (x = 0.1, G = 10 kg/m^{2}s) (b) Annular flow (x = 0.9, G = 10 kg/m^{2}s)

Fig. 3.1.1.3-8 Observation of flow patterns

References

K. Kariya, K. Sonoda, and A. Miyara, Purdue Conferences, USA, 2565(2018).

K. Kariya and A. Miyara, 25th IIR International Congress of Refrigeration, Canada, 1363(2019).

S. Diaw, T. Tun, K. Yoshida, K. Kariya and A. Miyara, 2020 JSRAE Annual Conference, Online, B321(2020) (in Japanese).

S. Diaw, T. Tun, K. Yoshida, K. Kariya, and A. Miyara, Purdue Conferences, Online, 2509(2021).

T. Tun, K. Yoshida, S. Diaw, K. Kariya, and A. Miyara, HFO2021 2nd IIR Conference on HFOs and Low GWP Blends, Online, 1067(2021).

M. M. Rahman, T. Tun, K. Kariya, and A. Miyara, 2022 JSRAE Annual Conference, Okayama, D145(2022) (in Japanese).

S. Hyodo, K. Kariya, and A. Miyara, HFO2021 2nd IIR Conference on HFOs and Low GWP blends, Online, 1046(2021).

K. Kariya, M. S. Mahmud, and A. Miyara, Purdue Conferences, USA, 2600(2016).

3.1.1.4 Condensation on a horizontal tube and verification of thermophysical property estimation

Kyushu Sangyo University measured the condensation heat transfer outside a circular tube in a horizontally placed ST. The validity of the thermophysical properties was verified by comparing the measured values with theoretical values. Conversely, the validity of the thermophysical property estimates calculated from the equation of state created by the measured thermophysical properties was verified.

Fig. 3.1.1.4-1 shows a schematic of the experimental apparatus, which consisted mainly of a condenser, evaporator, refrigerant circulation loop, and heat source water loop. The liquid refrigerant condensed in the condenser flows down by gravity to fill the evaporator, while the vapor refrigerant evaporated in the evaporator returns to the condenser. The refrigerant pressure in the evaporator was measured using an absolute pressure transducer (P) installed near the test tube, and the wall temperature of the test tube was measured using the electrical resistance method.

Fig. 3.1.1.4-2 shows an overview of the ST used for the measurement. Cooling water flows inside the ST, while the refrigerant cooled by the cooling water condenses and flows to the bottom of the ST. The heat transfer coefficient can be calculated as

$$\alpha = \frac{Q_{\mathrm{H_2O}}}{A(T_{\mathrm{sat}} - T_{\mathrm{wall}})} \quad , \tag{3.1.1.4-1}$$

where Q_{H2O}, A, T_{sat}, and T_{wall} are the heat exchange rate of the cooling water, effective heat transfer area, refrigerant saturation temperature calculated from the pressure gauge, and test tube wall temperature, respectively. The heat exchange rate of the cooled water can be calculated as

$$Q_{\mathrm{H_2O}} = V_{H_2O}\rho_{\mathrm{H_2O}}\Delta h_{\mathrm{H_2O}} - Q_{\mathrm{loss}}, \tag{3.1.1.4-2}$$

where ρ_{H2O}, $\dot{V}_{H2O}$, and Δh_{H2O} are the density, volumetric flow rate, and specific enthalpy difference, respectively, at the inlet and outlet of the test tube. Q_{loss} is the heat loss, which is given by the temperature difference between the source water and ambient air and is pre-tested. The outer wall temperature T_{wall} of the heat transfer tube was measured using the electrical resistance method.

The experimental results obtained were compared with the values calculated from the theoretical equation based on Nusselt's liquid film theory, such that

$$\alpha = \frac{\lambda_l}{D_o} Nu = 0.728 \left(\frac{\mathrm{GaPr_l}}{\mathrm{Ja}}\right)^{0.25} \left(\frac{\lambda_l}{D_o}\right)$$

$$= 0.728 \left[\frac{g}{D_{\mathrm{o}}(T_{\mathrm{sat}} - T_{\mathrm{wall}})}\right]^{0.25} \left\{\lambda_{\mathrm{l}}^{0.75} \cdot [\rho_{\mathrm{l}}(\rho_{\mathrm{l}} - \rho_{\mathrm{v}})]^{0.25} \cdot h_{\mathrm{fg}}^{0.25} \cdot \mu_{\mathrm{l}}^{-0.25}\right\} \tag{3.1.14-3}$$

where λ, ρ, h_{fg}, and μ are the heat transfer coefficient, density, latent heat of evaporation, and viscosity of the refrigerant, respectively. The subscripts l and v represent the saturated liquid and vapor, respectively. The values calculated from the equation of state were assigned to the thermophysical properties, g and D_{o}, the acceleration due to gravity and the outer diameter of the ST, respectively.

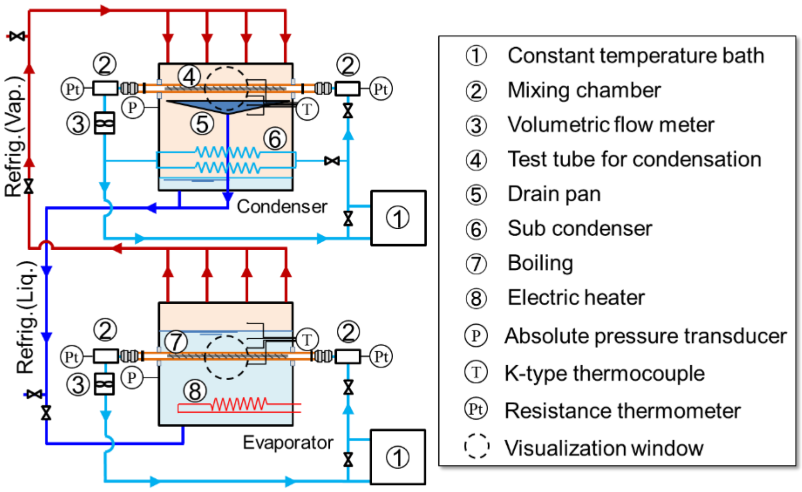

Fig. 3.1.1.4-1 Schematic of the experimental apparatus

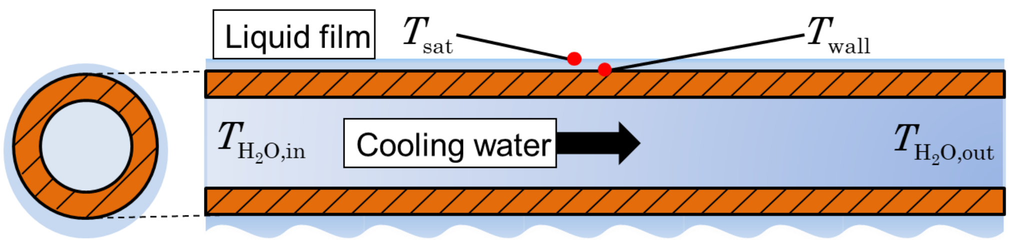

Fig. 3.1.1.4-2 Schematic of the ST under test

First, to confirm the integrity of the experimental apparatus, the condensation heat transfer outside the tube was measured in a ST using R134a. Fig. 3.1.1.4-3 shows the experimental results of heat transfer coefficient against wall supercooling, where the circle, triangle, and square plots represent the results for saturation temperatures of 20, 30, and 40 °C, respectively, bars represent errors, and lines represent the calculated values using the theoretical equation based on Nusselt's liquid film theory. The experimental results were in good agreement with the experimental uncertainty, thus confirming the integrity of the experimental setup.

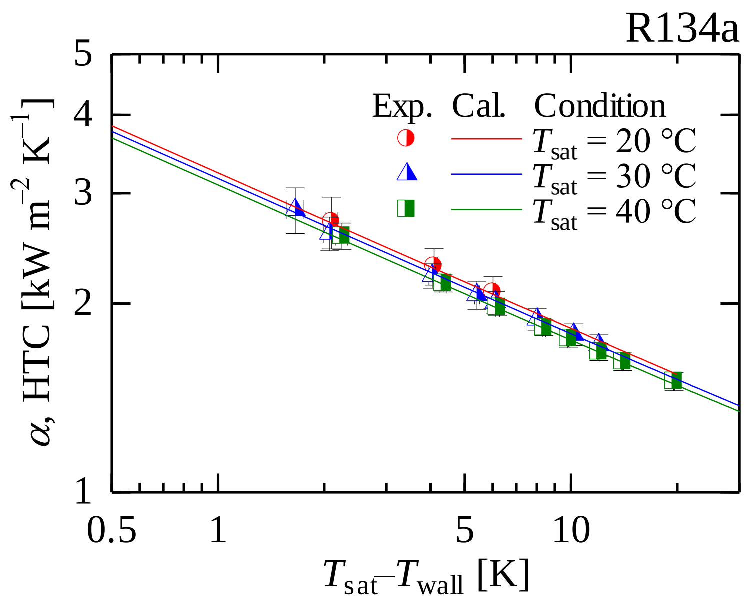

Fig. 3.1.1.4-3 Experimental results of R134a

Second, the outside condensation heat transfer was measured in the same ST for the new refrigerant candidates R1336mzz(E) and CF3I. Figs. 3.1.1.4-4 and -5 show the experimental results of heat transfer coefficient against wall supercooling for R1336mmz(E) and CF3I, respectively. For R1336mzz(E), the heat transfer coefficient for wall supercooling at approximately 2 K showed a large difference from the calculated value due to the uncertainty of the measurement equipment, as indicated by the large error bars. Moreover, R1336mzz(E) has a high normal boiling point. However, the experimental and calculated results of other wall supercooling methods were in good agreement because the Nusselt's liquid film theory assumed no turbulence in the liquid film flowing through the heat transfer tube; however, as the wall supercooling increases in reality, the amount of condensate increases and turbulence occurs in the liquid film. Similar phenomenon was also observed in R134a.

For CF3I, the experimental results were similar to that of the R1336mmz(E), where large error bars in the experimental results around a wall supercooling temperature of 2 K were observed. The experimental results were higher than the calculated values for all wall supercoolings. Thus, a disturbance to the liquid film occurred similar to that in the R1336mzz(E) results.

Fig. 3.1.1.4-6 compares the experimental and calculated results for R1336mzz(E) and CF3I. The vertical and horizontal axes represent the calculated and experimental results, respectively, while the dashed line indicates a 10% difference between the experimental and calculated results. The experimental results for R1336mzz(E) and CF3I were within 10% of the calculated values, and the estimated physical properties used to calculate the calculated values were considered to be sufficiently accurate for practical purposes, such as cycle analysis and heat transfer coefficient calculations.

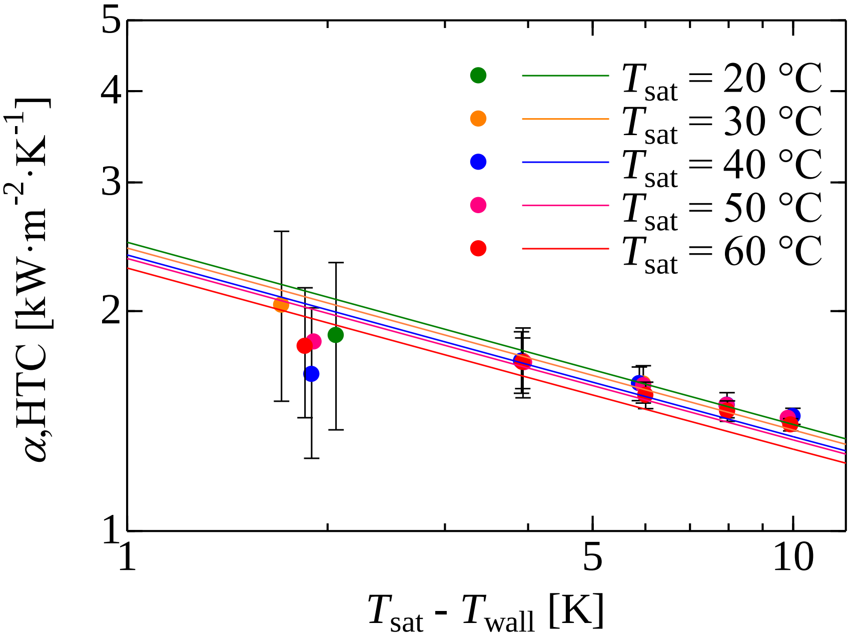

Fig. 3.1.1.4-4 Experimental results for R1336mmz(E)

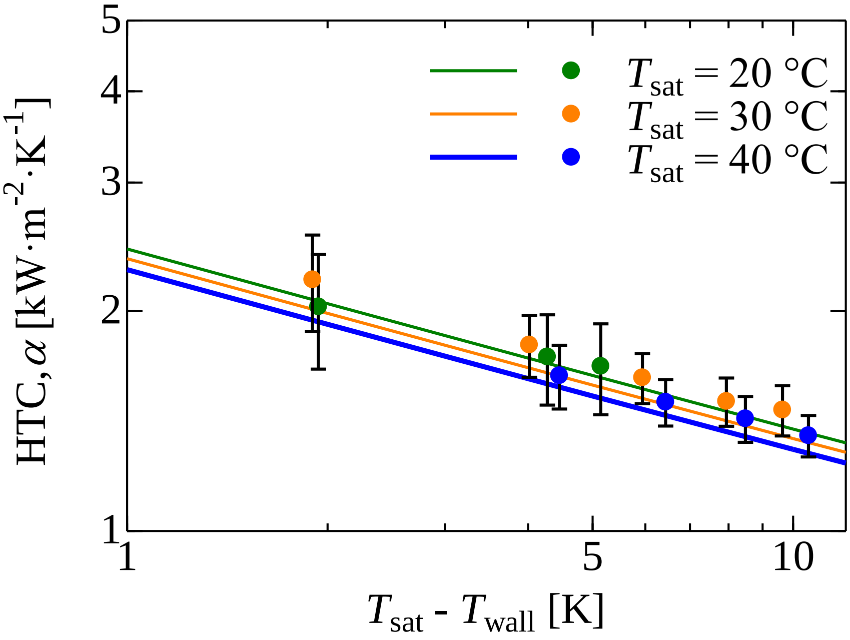

Fig. 3.1.1.4-5 Experimental results for CF_3I

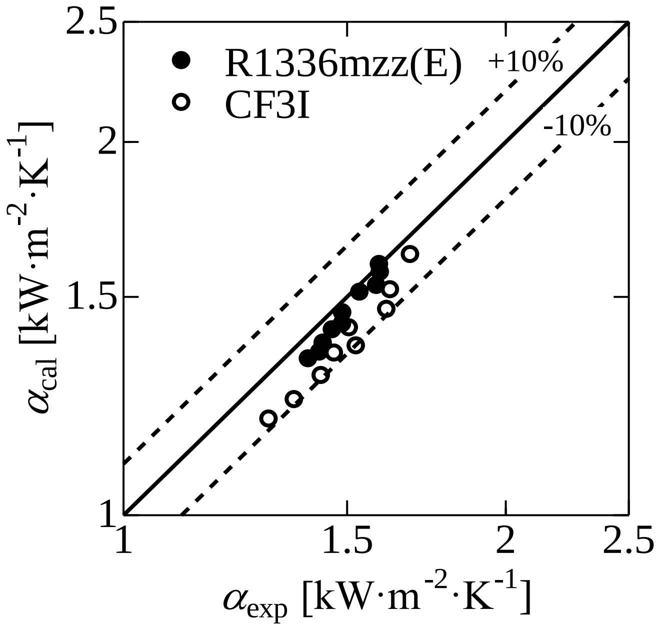

Fig. 3.1.1.4-6 Comparison of experimental and calculation results

3.1.2 Building Heat Transfer Database

3.1.2.1 Outline of the heat transfer database

Since heat transfer and pressure drop characteristics of refrigerants are affected by the type of heat exchanger and shape of the heat transfer surface, creating tables and developing software to calculate heat transfer and pressure drop coefficients, such as thermophysical properties, pose a challenge. Many correlations have been proposed for predicting heat transfer coefficient and pressure drop. However, no correlations applicable to all heat exchangers and heat transfer surface shapes exist. There are no general correlations to predict all situations of heat transfer. However, numerous experimental data have been reported for condensation and evaporation in round tubes, multiport tubes, and plate heat exchangers. Several heat transfer data points have been reported for different types of MT, channel shapes of multiport tubes, and surface shapes of plate heat exchangers. Since data are usually reported as plotted symbols in figures of research papers, secondary usage, such as comparison and correlation development, becomes complex. Thus, developing a heat transfer database with experimental data obtained in this study and data reported in other journals will be useful for the evaluation of heat transfer coefficients of new refrigerants and design of heat exchangers.

Fig. 3.1.2.1-1 shows an outline of the heat transfer database network configured for this study. The collected data are accumulated in a web system, which users can easily search, browse, and compare on the internet.

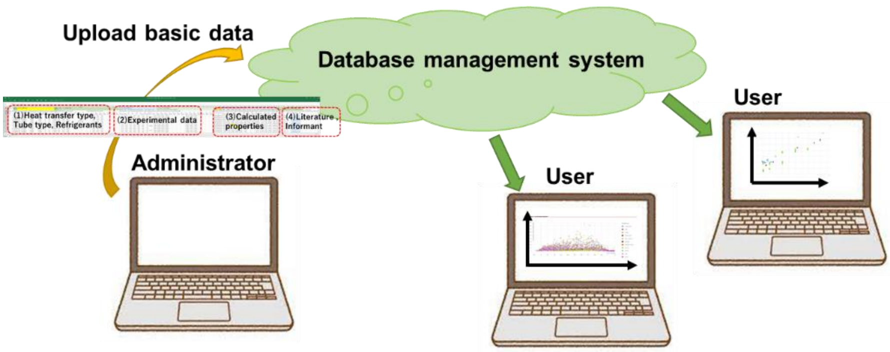

Fig. 3.1.2.1-1 Network configuration of heat transfer database

3.1.2.2 Data collection from existing literature

The collection procedure and basic data format of the heat transfer data are shown in Fig. 3.1.2.2-1. The collected data were given as input to a formatted Excel sheet. From the left of the sheet, data groups were set as (1) type of heat transfer process, tube type, refrigerant name, and mass fraction; (2) experimental data, such as heat transfer coefficient, temperature, pressure, mass–velocity, quality, and pressure gradient; (3) thermophysical properties calculated using REFPROP with experimental data; and (4) information on data, such as DOI, paper title, journal name, and volume. Thus, the data collected from this study and cooperating members were set in the aforementioned format.

For the data reported in journal papers, information for group (1) was taken from the main document or figures. The data for group (2) were obtained from figures used in the journal papers using a digitizer. Other data that were not provided in figures were obtained from documents explaining the data. Similarly, the information required by groups (3) and (4) were given as input. New experimental data and the data reported in journal papers were input into an Excel file for each paper or condition, which were then uploaded individually to the database web system.

Data on heat transfer and pressure gradient were set with the data on mass–velocity, quality, heat flux, pressure, refrigerant temperature, and wall temperature. For mixed refrigerants, the calculated mass fractions of liquid and vapor were also given as input. The calculated thermophysical properties along the same line can be used to analyze the data.

The uploaded data in the Excel file were stored in a structured database system MySQL, using which data search, browsing, and condition settings could be efficiently conducted.

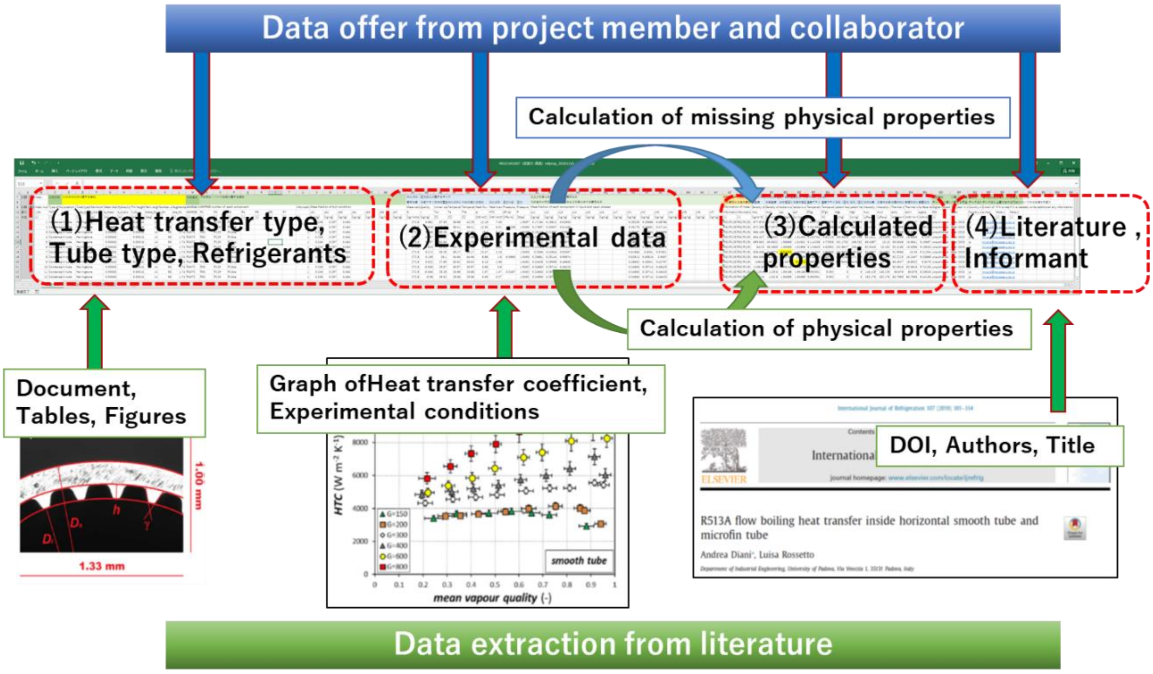

Fig. 3.1.2.2-1 Data collection scheme and data structure in Excel file

3.1.2.3 Data conversion of JSRAE_DD_HT

From 2000 to 2010, the Japan Society of Refrigerating and Air Conditioning Engineers (JSRAE) built a heat transfer database (JSRAE_DD_ HT) by collecting data from Kyushu University, Tokyo University of Marine Science and Technology, Okayama Prefectural University, and Saga University. In JSRAE_DD_HT, documents on experimental apparatus, data reduction, and uncertainty analysis were stored along with experimental data, where unpublished and detailed data on properties, such as wall temperature distribution, were included. Using JSRAE_DD_HT, heat transfer characteristics could be analyzed in detail. However, different data formats were used by each researcher, making it difficult to handle the data in a uniform manner, and data reported in journal papers by other researchers could not be included in JSRAE_DD_HT. Since enormous valuable data were included in JSRAE_DD_HT, the data had to be transferred to the new database.

Fig. 3.1.2.3-1 shows an example of the experimental data uploaded in the JSRAE_DD_HT. The data were given as input to an Excel sheet, where the upper part of the sheet displayed experimental conditions, such as the type of tested tube, tube size, refrigerant name and composition, and mass–velocity. The lower part of the sheet listed measured data, such as distributions of quality, temperature, heat transfer coefficient, and pressure. The yellow marked line shows missing values of quality, refrigerant temperature, and others details corresponding to a heat transfer coefficient. In the experiment, measurements were carried out at the inlet and outlet of a subsection, and the heat transfer coefficient was calculated as the average value of the subsection. However, some values corresponding to the heat transfer coefficient were not given as input. To transfer data from JSRAE_DD_HT to the new database, vacant data were given an average value lying between those measured at the inlet and outlet of the subsection.

In JSRAE_DD_HT, the experimental data of HCFC22, HCFC123, HFC125, HFC134a, R407C, and R410A were included. However, data on some refrigerants could not be obtained because the refrigerants were phased out. For specific conditions, series of experimental data from the inlet to the outlet of the condenser or evaporator tube were included in files. A total of 434 data files were transferred to the new database.

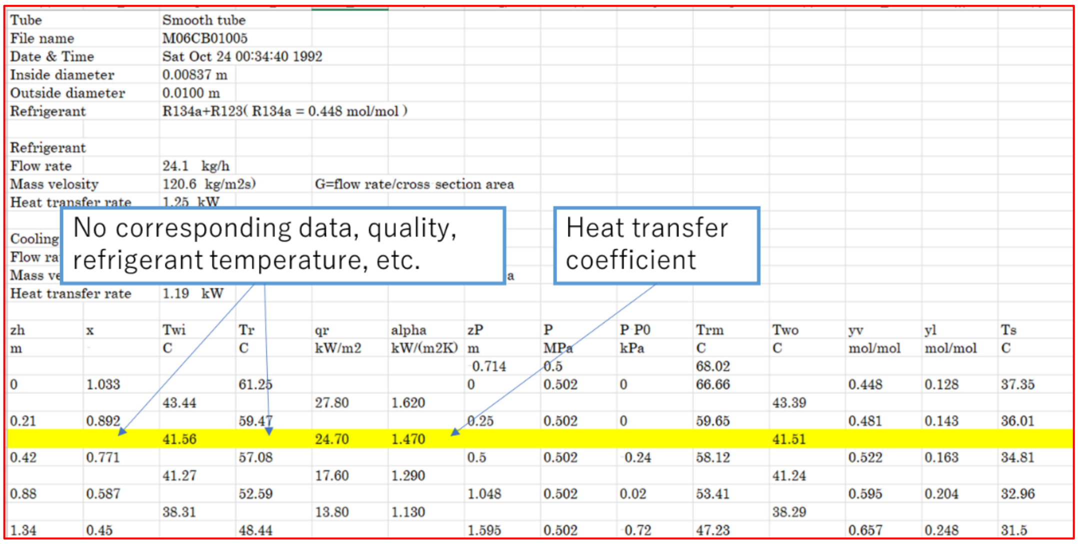

Fig. 3.1.2.3-1 Data format of the JSRAE_DD_HT built in 2000

3.1.2.4 Utilization of the heat transfer database

The data on heat transfer were stored in the web system as MySQL, built for this project, and the database could be accessed using a web browser. Fig. 3.1.2.4-1(a) shows the top page of the database system. The heat transfer and pressure drop data collected during the condensation and boiling of refrigerants in round tubes, multiport tubes, and plate heat exchangers were stored. By clicking on the heat exchanger type, the screen jumps to the next page, as shown in Fig. 3.1.2.4-1(b), where users can select boiling, condensation, or adiabatic two-phase flow. Adiabatic two-phase flow experiments were conducted to measure the frictional pressure loss. As aforementioned, the data measured in this study, obtained from existing literature, and transferred from JSRAE_DD_HT were all included in the new database. Unpublished data from this study will be added after finalizing and reporting them in literature.

There are numerous types of pure and mixed refrigerants, some of which do not have ASHRAE numbers. In most cases, the ASHRAE number is used to differentiate refrigerants, pure or mixed. However, refrigerants with no ASHRAE numbers are also available in the new database system.

Examples of browsing data are shown in Figs. 3.1.2.4-2(a)‐(d), where the browsing results of boiling heat transfer are introduced. After selecting the heat exchanger type, boiling is selected in the “Select Heat Transfer Type” option and the refrigerant is selected in the “Select Substance” option. For this example, several refrigerants were selected. After refrigerant selection, on clicking the “Search” button, the next page shows the data plot, where the users can select the parameters of the x- and y-axes. Fig. 3.1.2.4-2(a) shows the distribution of the mass–velocities and pressures. The existing experimental conditions can be identified from this graph. In the right column, a legend of the refrigerants is indicated. The data symbols in the graph can be highlighted by placing the mouse pointer on the refrigerant symbol in the legend. In addition, by placing the mouse pointer on a data symbol, detailed information on the data appears.

Fig. 3.1.2.4-2(b) shows the distribution of the heat transfer coefficients with respect to quality. Since data of different refrigerants and experimental conditions were plotted together in graph, identifying the characteristics of each refrigerant and the effects of each condition was difficult. The desired data to be observed can be plotted by narrowing the filter conditions. In addition, the graph-browsing conditions created under the desired conditions can be saved and reused. Fig. 3.1.2.4-2(c) shows the relationship between the heat transfer coefficient and heat flux by narrowing the conditions to spiral MT with qualities between 0.4 and 0.5. As a whole, the heat transfer coefficients are known to increase with the increase in heat flux. Conversely, the variations in heat transfer coefficient with mass–velocity are shown in Fig. 3.1.2.4-2(d), for two groups of refrigerants. The heat transfer coefficients of one group increased with an increase in the mass–velocity. Contrarily, the heat transfer coefficients of the other group decreased with an increase in mass–velocity.

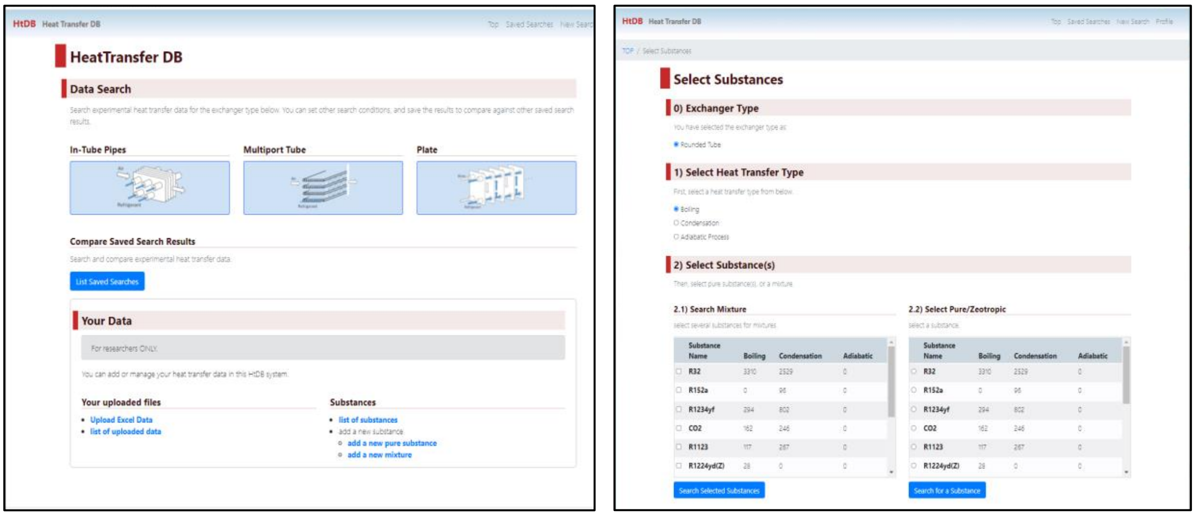

(a) Top page (b) Selection of heat transfer type and refrigerants

Fig. 3.1.2.4-1 Webpage of the heat transfer database

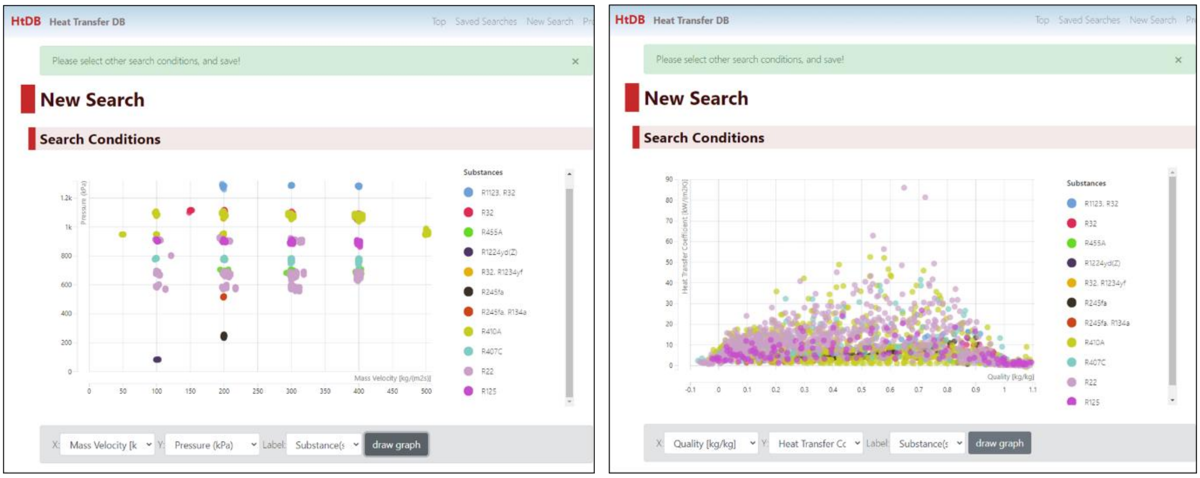

(a) Mass–velocity and pressure conditions (b) Heat transfer coefficient against vapor quality

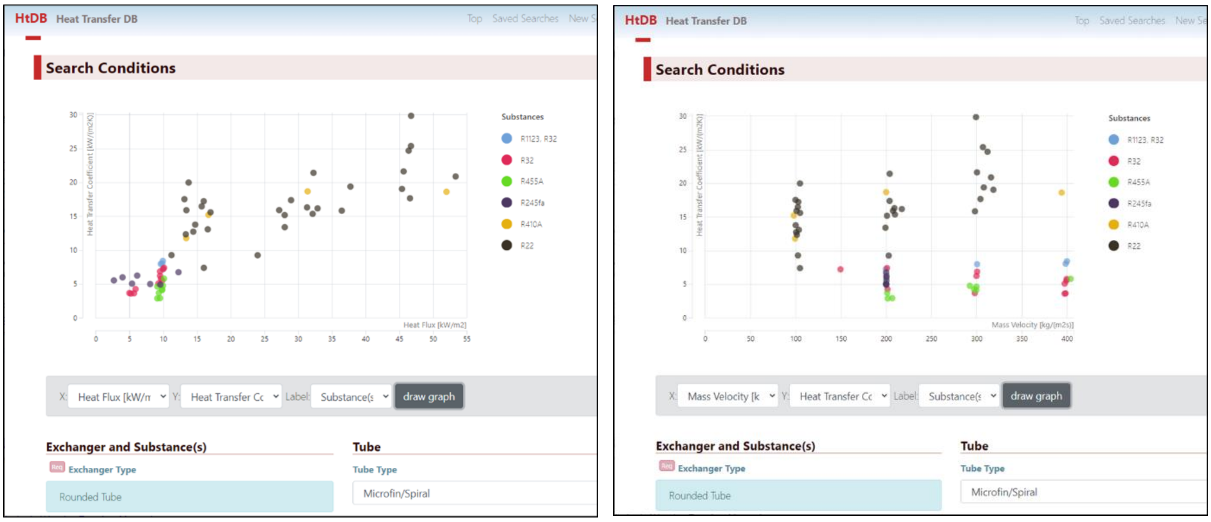

(c) Heat transfer coefficient against heat flux (d) Heat transfer coefficient against mass–velocity

Fig. 3.1.2.4-2 Examples of data displayed on the webpage

3.1.3 Correlations for Heat Transfer and Pressure Drop of Each Heat Exchanger

3.1.3.1. Prediction models for condensation and evaporation in circular tubes

The heat transfer and pressure drop models for condensation and evaporative flows in horizontally placed ST and MT were verified for new low global warming potential (GWP) refrigerants. The predicted results were compared with the measured data obtained in this study.

(1) Condensation process

・Condensation flow of single compounds in ST

Figs. 3.1.3.1-1(a) and (b) show the heat transfer coefficients of HFO1234yf and HFO1234ze(E) at a saturation temperature of 40 °C. The measured heat transfer coefficients were compared with those of the models discussed by Cavallini[1)], Dobson-Chato[2)], Shah[3)], and Haraguchi et al.[4)]. As shown in Fig. 3.1.3.1-1, the values calculated by Dobson-Chato[2)], Shah[3)], and Haraguchi et al.[4)] agreed with the experimental results, whereas those by Cavallini et al.[1)] yielded values smaller than the experimental results over the entire range of vapor quality. Table 3.1.3.1-1 summarizes the correlations of Haraguchi et al.[4)]

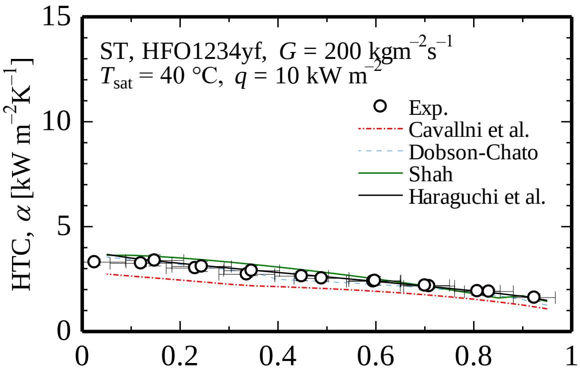

(a) HFO1234yf, $G = 200$ kg m^{-2}s^{-1}

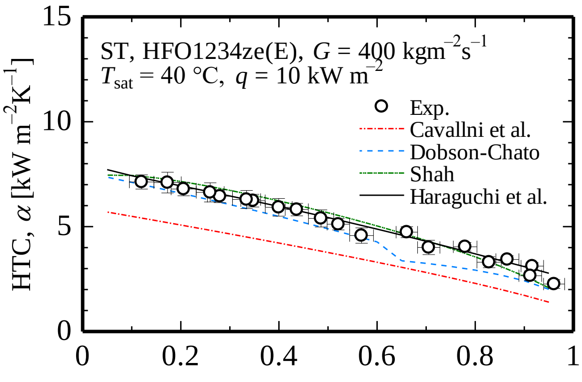

(b) HFO1234ze(E), $G = 400$ kg m^{-2}s^{-1}

Fig. 3.1.3.1-1 Comparison between the calculated and experimental condensation heat transfer coefficients for single components

Table 3.1.3.1-1 Haraguchi et al.[4)] correlation

$$Nu = \frac{\alpha d_i}{\lambda_L} = \sqrt{Nu_F^2 + Nu_B^2}$$

Natural convection term Nu_B: $Nu_B = 0.725 H(\xi)\left(\frac{Ga_L Pr_L}{H_L}\right)^{1/4}$

$H(\xi)$: Function of void fraction, $H(\xi) = \xi + \left\{10\left[(1-\xi)^{0.1} - 1\right] + 1.7\times10^{-4} Re\right\}\sqrt{\xi}\left(1-\sqrt{\xi}\right)$

Ga_L: Galilei number, $Ga_L = \frac{g \rho_L^2 d_i^3}{\mu_L^2}$, H_L: ratio of sensible latent heat, $H_L = \frac{c_{pL}(T_{sat} - T_{wi})}{\Delta h_{LV}}$

Forced convection term Nu_F: $Nu_F = 0.0152\left(1 + 0.6 Pr_L^{0.8}\right)\left(\Phi_V / X_{tt}\right) Re_L^{0.77}$

Φ_V: Friction multiplier, $\Phi_V = 1 + 0.5\left[\frac{G}{\sqrt{g d_i \rho_V (\rho_L - \rho_V)}}\right]^{0.75} X_{tt}^{0.35}$,

X_{tt}: Lockhart-Martinelli parameters, $X_{tt} = \left(\frac{1-x}{x}\right)^{0.9}\left(\frac{\rho_V}{\rho_L}\right)^{0.5}\left(\frac{\mu_L}{\mu_V}\right)^{0.1}$

・Condensation flow of binary refrigerant mixtures in ST

Figs. 3.1.3.1-2(a) and (b) show the measured condensation heat transfer coefficients in a ST at a mass–velocity of 200 kg m^{-2}s^{-1} for the HFO1234ze(E)/HFC32 and HFO1234yf/HFC32 mixtures, respectively. The horizontal axis shows the composition, and the red and blue plots represent the results for liquid qualities of 0.3 and 0.7, respectively. The dashed line represents the predicted results proposed by Haraguchi et al.[4)] for single compounds. The predictions were overestimated for both the mixtures relative to the measured data. As the temperature glide increased, heat transfer degradation became more evident, and the predictions deviated significantly from the measurement data. Therefore, a correction method was introduced by Silver-Bell-Ghaly[5,6)] using Eq. (3.1.3.1-1).

The equation of Haraguchi et al.[4)] was substituted for the heat transfer coefficient calculation of single compounds in the first term.

$$\frac{1}{\alpha_{\mathrm{mix}}} = \frac{1}{\alpha_{\mathrm{cal}}} + x\,c_{p\mathrm{V}}\left(\frac{\Delta T}{\Delta h}\right)\frac{1}{\alpha_{\mathrm{V}}}\,, \tag{3.1.3.1-1}$$

where α_{cal} is the heat transfer coefficient of single compounds calculated using the physical properties of the mixtures and α_{V} is the heat transfer coefficient for a vapor phase calculated from the Dittus-Boelter equation. ΔT is the temperature glide and Δh is the specific enthalpy change during the isobaric condensation process of the refrigerant mixtures. The predicted results calculate using the Silver-Bell-Ghaly[5,6)] correction model, shown by solid lines, agreed satisfactorily with the experimental data for the HFO1234ze(E)/HFC32 and HFO1234yf/HFC32 mixtures.

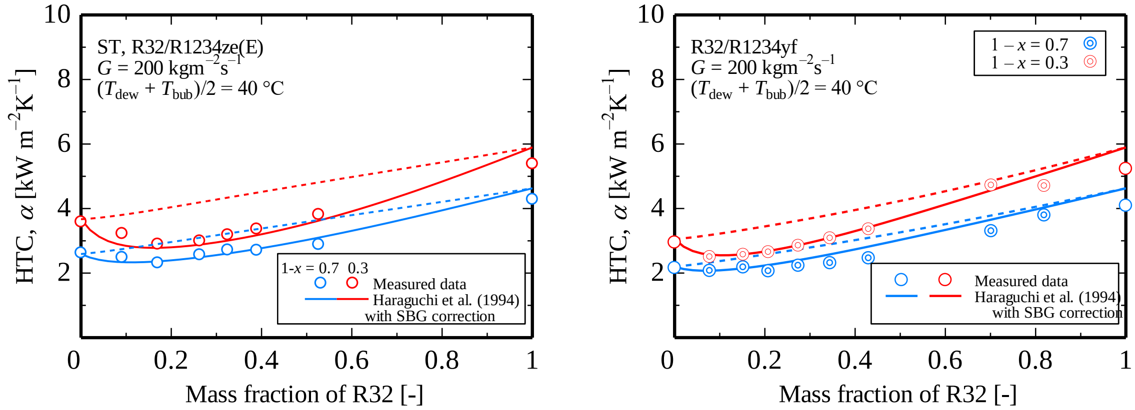

(a) HFO1234ze(E)/HFC32 (b) HFO1234yf/HFC32

Fig. 3.1.3.1-2 Comparison between the calculated and experimental condensation heat transfer coefficients for binary mixtures in ST

・Condensation flow of a single compound in MT

Fig. 3.1.3.1-3(a) shows the measured condensation heat transfer coefficients of HFC32 at mass–velocities of 150, 200, 300, and 400 kg $m^{-2}s^{-1}$ and that of the prediction model of Yonemoto-Koyama[7)]. Although the Yonemoto-Koyama[7)] model predicted lower value of heat transfer coefficients than the measured data at liquid qualities below 0.4, the measurement uncertainty in the region was substantial. Thus, the correlation agreed satisfactorily with the measured data. Particularly, for liquid qualities above 0.5, the predicted results agreed well with the measured data. Table 3.1.3.1-2 summarizes the correlations of Yonemoto-Koyama[7)].

・Condensation flow of binary refrigerant mixtures in MT

The Silver-Bell-Ghaly[5,6)] correction model was applied to predict the heat transfer coefficients of refrigerant mixtures in MT, similar to that in ST. The heat transfer coefficient term for a single refrigerant was substituted in the equation by the predicted values of Yonemoto-Koyama et al.[7)] Fig. 3.1.3.1-3(b) compares the predicted and measured results for the HFO1123/HFC32 mixture at mass–velocities of 200, 300, and 400 kg $m^{-2}s^{-1}$. The heat transfer coefficients considering the zeotropicity in the refrigerant mixture calculated using the Yonemoto-Koyama[7)] and Silver-Bell-Ghaly[5-6)] models are shown as solid lines. The values predicted by these correlations agreed well with the measured data for the entire range of liquid quality.

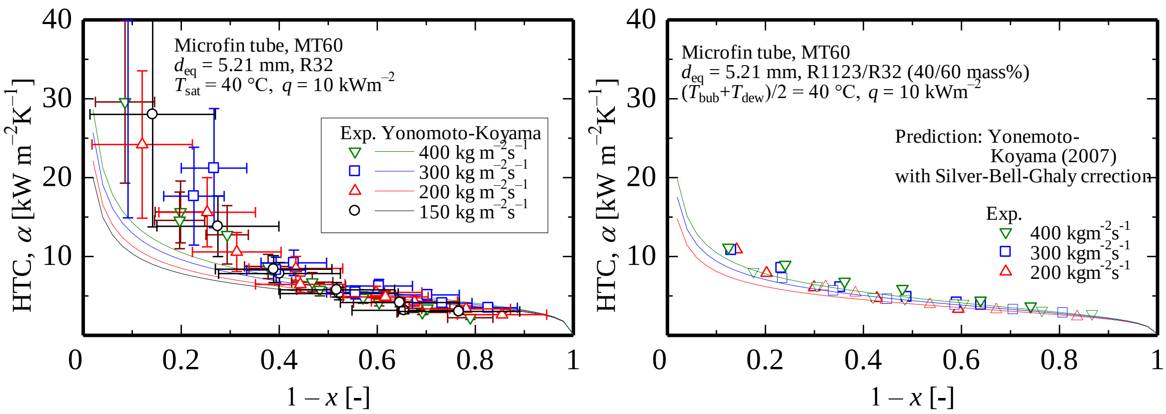

(a) HFC32 (b) HFO1123/HFC32

Fig. 3.1.3.1-3 Comparison between the calculated and experimental condensation heat transfer coefficients for binary mixtures in MT

Table 3.1.3.1-2 Yonomoto-Koyama[7] correlation

$Nu = \dfrac{\alpha\, d_{\mathrm{eq}}}{\lambda_{\mathrm{L}}} = \left(Nu_{\mathrm{F}}^2 + Nu_{\mathrm{B}}^2\right)^{1/2}$
Natural convection term Nu_{B}: $Nu_{\mathrm{B}} = \dfrac{1.98}{\eta^{0.5}} H(\xi) \dfrac{1}{Bo^{0.1}} \left(\dfrac{Ga_{\mathrm{L}} Pr_{\mathrm{L}}}{Ph_{\mathrm{L}}}\right)^{1/4}$
ξ: Void fraction, $\xi = 0.81\xi_{\mathrm{Smith}} + 0.19 x^{100(\rho_{\mathrm{V}}/\rho_{\mathrm{L}})^{0.8}} \xi_{\mathrm{Homo}}$,
$H(\xi)$: Function of void fraction, $H(\xi) = \xi + \left[10(1-\xi)^{0.1} - 8.9\right]\sqrt{\xi}\left(1-\sqrt{\xi}\right)$,
ξ_{Smith}: Smith correlation, $\xi_{\mathrm{Smith}} = \left\{1 + \dfrac{\rho_{\mathrm{V}}}{\rho_{\mathrm{L}}}\left(\dfrac{1-x}{x}\right)\left(0.4 + 0.6\sqrt{\dfrac{\dfrac{\rho_{\mathrm{L}}}{\rho_{\mathrm{V}}} + 0.4\dfrac{1-x}{x}}{1 + 0.4\dfrac{1-x}{x}}}\right)\right\}^{-1}$
ξ_{Homo}: Void fraction of homogeneous flow, $\xi_{\mathrm{Homo}} = \left[1 + \left(\dfrac{1-x}{x}\right)\dfrac{\rho_{\mathrm{V}}}{\rho_{\mathrm{L}}}\right]^{-1}$
Bo: Bond number, $Bo = \dfrac{(p-t) d_{\mathrm{eq}} g (\rho_{\mathrm{L}} - \rho_{\mathrm{V}})}{\sigma}$, Ga_{L}: Galilei number, $Ga_{\mathrm{L}} = \dfrac{G \rho_{\mathrm{L}}^2 d_{\mathrm{eq}}^3}{\mu_{\mathrm{L}}^2}$
Ph_{L}: Ratio of sensible latent heat, $Ph_{\mathrm{L}} = \dfrac{c_{p\mathrm{L}}(T_{\mathrm{sat}} - T_{\mathrm{wi}})}{\Delta h_{\mathrm{LV}}}$
Forced convection term Nu_{F}: $Nu_{\mathrm{F}} = 2.12\sqrt{f_{\mathrm{V}}}\Phi_{\mathrm{V}}\left(\dfrac{\rho_{\mathrm{L}}}{\rho_{\mathrm{V}}}\right)^{0.5}\left(\dfrac{x}{1-x}\right) Pr_{\mathrm{L}}^{0.5} Re_{\mathrm{L}}^{0.5}$
f_{V}: Vapor friction coefficient, $f_{\mathrm{V}} = 0.046 Re_{\mathrm{V}}^{-0.2} \dfrac{d_{\mathrm{eq}}}{d_{\mathrm{h}}} (\sec\theta)^{0.75}$
Φ_{V}: Friction multiplier, $\Phi_{\mathrm{V}} = 1 + 1.2 Fr^{0.05} X_{\mathrm{tt}}^{0.5}$
Re_{L} and Re_{V}: Liquid and vapor Reynolds numbers: $Re_{\mathrm{L}} = \dfrac{G(1-x) d_{\mathrm{eq}}}{\mu_{\mathrm{L}}}$, $Re_{\mathrm{V}} = \dfrac{G x d_{\mathrm{eq}}}{\mu_{\mathrm{V}}}$
Fr: Froude number, $Fr = \dfrac{G}{\sqrt{g\, d_{\mathrm{eq}} \rho_{\mathrm{V}} (\rho_{\mathrm{L}} - \rho_{\mathrm{V}})}}$

(2) Evaporation process

Several prediction models for measurement of evaporative heat transfer coefficients in horizontally placed tubes have been derived from the method proposed by Chen[8], which was based on the idea of heat transfer being represented by nucleate boiling and forced convection heat transfers. Nucleate and forced convection boiling are mutually dependent and the heat transfer coefficient can be expressed as the sum of their contributions, such that

$$\alpha = \alpha_{\mathrm{cv}} + \alpha_{\mathrm{nb}} = F\alpha_{\mathrm{LO}} + S\alpha_{\mathrm{pb}} , \qquad (3.1.3.1\text{-}2)$$

where α_{cv} and α_{nb} are the forced convective and nucleate boiling contributions, respectively, α_{L} is the convective heat transfer coefficient, as only liquid flows through the tube, and α_{pb} is the heat transfer coefficient obtained from the pool-boiling heat transfer correlation. F is the two-phase flow multiplier obtained from the Lockhart-Martinelli parameter and S is the nucleate boiling suppression factor.

・Evaporation flow of single compounds in ST

The measured evaporative heat transfer coefficients of HFO1234yf and HFO1234ze(E) in a ST were compared with those predicted by the correlations of Mori et al.[9], Saitoh et al.[10], Takamatsu et al.[11], and Yu et al.[12]. Figs. 3.1.3.1-4(a) and (b) show the heat transfer coefficients at a saturation temperature of 10 °C for HFO1234yf and HFO1234ze(E), respectively. Mori et al.[9], Saitoh et al.[10], and Yu et al.[12] reported slightly lesser values than the measured data. Simultaneously, the calculated results by Takamatsu et al.[11] was in close agreement with the measured data over the entire range of vapor quality. Tables 3.1.3.1-3 summarize the correlations of Takamatsu et al.[11]

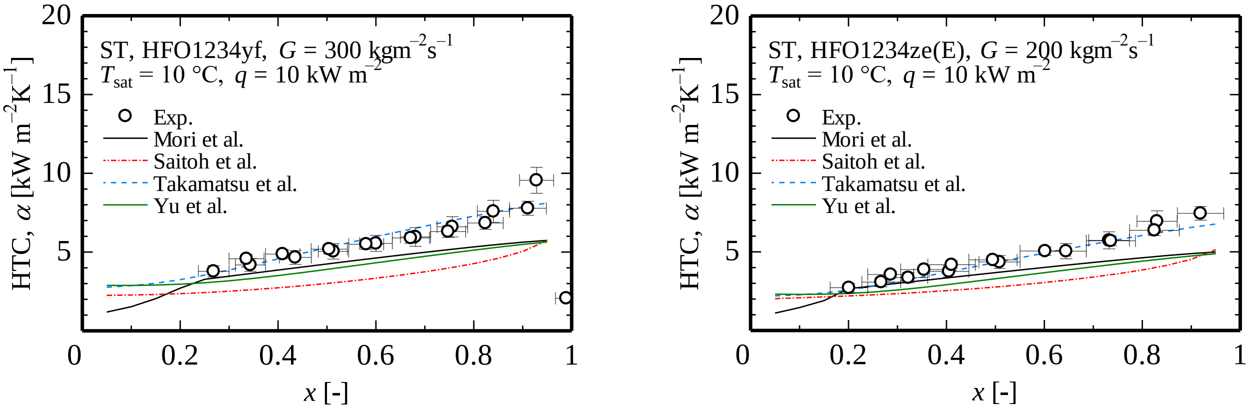

(a) HFO1234yf, $G = 300$ kg m^{-2}s^{-1} (b) HFO1234ze(E), $G = 200$ kg m^{-2}s^{-1}

Fig. 3.1.3.1-4 Comparison between the calculated and experimental evaporative heat transfer coefficients for single components

Table 3.1.3.1-3 Takamatsu et al.[11)] correlation

$$\alpha = \alpha_{cv} + \alpha_{nb} = F\alpha_L + S\alpha_b$$

Nucleate boiling heat transfer, α_{nb}: $\alpha_{nb} = S\,K^{0.745}\alpha_{pb}$

S: Suppression factor, $S = \dfrac{\left(1-e^{-\xi}\right)}{\xi}$, $\xi = 3.3\times10^{-5}\,J\ddot{a}^{1.25} La\left(\dfrac{\alpha_{cv}}{\lambda_L}\right)$

K: Heat flux ratio, $K^{0.745} = \dfrac{1}{1+0.875\eta+0.518\eta^2-0.159\eta^3+0.7907\eta^4}$

Stephan-Abdelsalam correlation: $\alpha_{pb} = 1.35\times 207\dfrac{\lambda_L}{d_b}\left(\dfrac{q\,d_b}{\lambda_L T_{sat}}\right)^{0.745}\left(\dfrac{\rho_V}{\rho_L}\right)^{0.581} Pr_L^{0.533}$

La: Laplace number, $La = \sqrt{\dfrac{2\sigma}{g(\rho_L-\rho_V)}}$, $J\ddot{a}$: Jakob number, $J\ddot{a} = \dfrac{\rho_L c_{pL}}{\rho_V \Delta h_{LV}} T_{sat}$

Forced convection heat transfer,

$\alpha_{cv} = 0.0116F\,Re_{LO}^{0.89} Pr_L^{0.4}\dfrac{\lambda_L}{d_i}$, F: Reynolds number factor, $F = F_\gamma^{0.89/0.8} = \left(1+2X_{tt}^{-0.88}\right)^{0.89/0.8}$

Re_{LO}: Liquid Reynolds number, $Re_{LO} = \dfrac{G(1-x)d_i}{\mu_L}$

・Evaporation flow of binary refrigerant mixtures in ST

Figs. 3.1.3.1-5(a) and (b) show the measured evaporative heat transfer coefficients of the HFO1234ze(E)/HFC32 and HFO1234yf/HFC32 mixtures at a mass–velocity of 200 kg m^{-2}s^{-1}. The horizontal axis shows the HFC32 mass fraction, and red and blue indicate results at vapor qualities of 0.3 and 0.7, respectively. The solid lines indicate the correlation reported by Takamatsu et al.[13)], which modified the nucleate boiling term representing the thermal resistance effect in the vapor phase, caused by the heating of the sensible heat portion owing to the temperature glide. Although the correlation of Takamatsu et al.[13)] overpredicted the heat transfer coefficients of the HFO1234ze(E)/HFC32 and HFO1234yf/HFC32 mixtures by approximately 20% at higher mass fractions, the prediction accuracy was overall sufficient. Table 3.1.3.1-4 summarizes the correlations of Takamatsu et al.[13)]

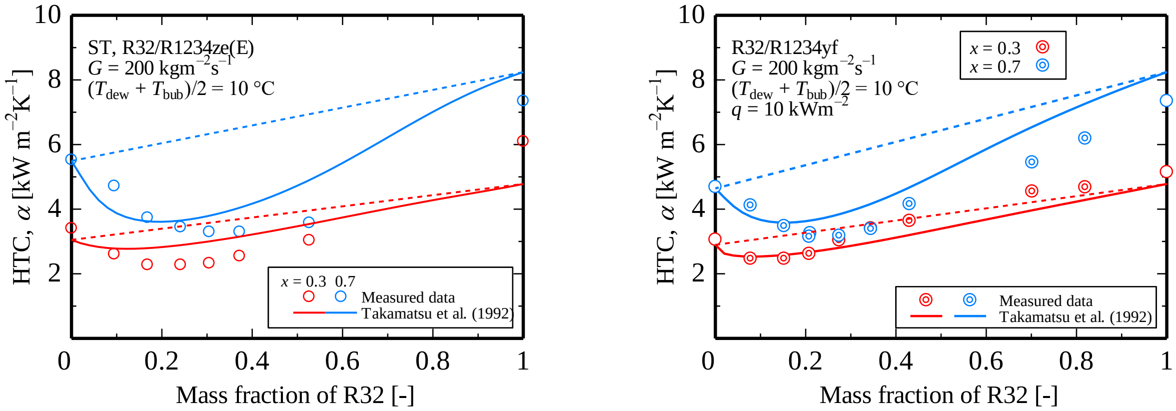

(a) HFO1234ze(E)/HFC32 (b) HFO1234yf/HFC32

Fig. 3.1.3.1-5 Comparison between the calculated and experimental evaporative heat transfer coefficients for binary mixtures

Table 3.1.3.1-4 Takamatsu et al.[13] correlation.

$$\alpha = \alpha_{\mathrm{cvm}} + \alpha_{\mathrm{nbm}} = S_{\mathrm{cvm}}\,\alpha_{\mathrm{cv}} + K^{0.745} S_{\mathrm{m}}\,\alpha_{\mathrm{pbm}}$$

Nucleate boiling heat transfer, α_{pbm}: $$\alpha_{\mathrm{pbm}} = \frac{\alpha_{\mathrm{pb1}}\alpha_{\mathrm{pb2}}}{\alpha_{\mathrm{pb2}} y_{\mathrm{L1}} + \alpha_{\mathrm{pb1}}\left(1 - y_{\mathrm{L1}}\right)}\left(\frac{1}{1 + 4.8\left|y_{\mathrm{V}} - y_{\mathrm{L}}\right|}\right)$$

S_{m}: Suppression factor, $$S_{\mathrm{m}} = S_{\mathrm{cvm}}\frac{1}{\xi}\left(1 - e^{-\xi}\right) + \left(1 - S_{\mathrm{cvm}}\right), \quad \xi = 3.3\times10^{-5} J\ddot{a}^{1.25} La\left(\frac{\alpha_{\mathrm{cv}}}{\lambda_{\mathrm{L}}}\right),$$

La: Laplace number, $$La = \sqrt{\frac{2\sigma}{g\left(\rho_{\mathrm{L}} - \rho_{\mathrm{V}}\right)}},$$ $J\ddot{a}$: Jakob number, $$J\ddot{a} = \frac{\rho_{\mathrm{L}} c_{p\mathrm{L}}}{\rho_{\mathrm{V}} \Delta h_{\mathrm{LV}}} T_{\mathrm{sat}}$$

S_{cvm}: Suppression factor for mixtures, $$S_{\mathrm{cvm}} = \frac{1}{1 + 0.30x^{1.39}\left(1 - x\right)^{-0.39}\left(\left|y_{\mathrm{V}} - y_{\mathrm{L}}\right| + \left|y_{\mathrm{V}} - y_{\mathrm{L}}\right|^{2}\right)}$$

Stephan-Abdelsalam correlation: $$\alpha_{\mathrm{pb}} = C_1 \alpha_{\mathrm{SA}} = 1.35\times 207\frac{\lambda_{\mathrm{L}}}{d_{\mathrm{b}}}\left(\frac{q\,d_{\mathrm{b}}}{\lambda_{\mathrm{L}}\,T_{\mathrm{sat}}}\right)^{0.745}\left(\frac{\rho_{\mathrm{V}}}{\rho_{\mathrm{L}}}\right)^{0.581} Pr_{\mathrm{L}}^{0.533}$$

K: Heat flux ratio, $$K^{0.745} = \frac{1}{1 + 0.875\eta + 0.518\eta^{2} - 0.159\eta^{3} + 0.7907\eta^{4}}, \quad \eta = \frac{\alpha_{\mathrm{cvm}}}{S_{\mathrm{m}}\,\alpha_{\mathrm{pbm}}}$$

Forced convection heat transfer $$\alpha_{\mathrm{cv}} = 0.0116 F Re_{\mathrm{LO}}^{0.89} Pr_{\mathrm{L}}^{0.4}\frac{\lambda_{\mathrm{L}}}{d_{\mathrm{i}}}$$

Re_{LO}: Liquid Reynolds number, $$Re_{\mathrm{LO}} = \frac{G\left(1 - x\right)d_{\mathrm{i}}}{\mu_{\mathrm{L}}},$$

F: Reynolds number factor: $$F = F_{\gamma}^{0.89/0.8} = \left(1 + 2X_{\mathrm{tt}}^{-0.88}\right)^{0.89/0.8}$$

・Evaporation flow of single compounds in MT

Fig. 3.1.3.1-6(a) shows the measured evaporative heat transfer coefficient of HFC32 in MT at mass–velocities of 200, 300, and 400 kg m^{-2}s^{-1}. The selected correlation for comparison was that of Thome[14]. Onset-dryout quality and post-dryout heat transfer coefficients were calculated using the correlations of Yoshida et al.[15] and Mori et al.[16], respectively. The heat transfer coefficients for the dryout interval were linearly interpolated between the values calculated by Thome[14] at the onset of dryout and those calculated by Mori et al.[16] at the dryout termination. Fig. 3.1.3.1-6(a) shows that the correlation of Thome[14] satisfactorily agreed with the measured data. However, it was predicted to be lower than the measured data at a mass–velocity of 400 kg m^{-2}s^{-1}. Table 3.1.3.1-5 summarizes the correlation of Thome[14]. The correlations of Yoshida et al.[15] for the onset-dryout quality and Mori et al.[16] for the post-dryout heat transfer coefficient successfully represented the measured results quantitatively. Table 3.1.4.1-6 summarizes the correlations of Yoshida et al.[15] and Mori et al.[16].

Table 3.1.3.1-5 Thome[14] correlation

$\alpha = E_{\mathrm{mf}}\left[\alpha_{\mathrm{nb}}^3 + \left(E_{\mathrm{RB}}\alpha_{\mathrm{CV}}\right)^3\right]^{1/3}$
Forced convection heat transfer: $\alpha_{\mathrm{cv}} = 0.0133 Re_{\mathrm{L,film}}^{0.69} Pr_{\mathrm{L}}^{0.4}\left(\lambda_{\mathrm{L}}/\delta\right)$
$Re_{\mathrm{L,film}}$: Liquid film Reynolds number, $Re_{\mathrm{L,film}} = \dfrac{4G(1-x)}{\delta\left[(1-\xi)\mu_{\mathrm{L}}\right]}$,
ξ: Void fraction, $\xi = \dfrac{x}{\rho_{\mathrm{V}}}\left\{1+0.12(1-x)\left(\dfrac{x}{\rho_{\mathrm{V}}}+\dfrac{1-x}{\rho_{\mathrm{L}}}\right)+\dfrac{1.18(1-x)\left[g\sigma\left(\rho_{\mathrm{L}}-\rho_{\mathrm{V}}\right)\right]^{0.25}}{G\rho_{\mathrm{L}}^{0.5}}\right\}^{-1}$
E_{mf}: Enhancement factor for microfin tubes, $E_{\mathrm{mf}} = 1.89\left(\dfrac{G}{G_{\mathrm{ref}}}\right)^2 - 3.7\dfrac{G}{G_{\mathrm{ref}}} + 3.02$, $G_{\mathrm{ref}} = 500\ \mathrm{kgm^{-2}s^{-1}}$
Nucleate boiling heat transfer:
Cooper pool boiling correlation: $\alpha_{\mathrm{nb}} = 55P_{\mathrm{R}}^{0.12}\left(-\log_{10} p_{\mathrm{R}}\right)^{-0.55} M^{-0.5} q^{0.67}$
E_{RB}: Convection enhancement factor, $E_{\mathrm{RB}} = \left(1+\left[2.64 Re_{\mathrm{L}}^{0.036}\left(\dfrac{h_{\mathrm{fin}}}{d_{\max}}\right)^{0.212}\left(\dfrac{p_{\mathrm{fin}}}{d_{\max}}\right)^{-0.21}\left(\dfrac{\beta_{\mathrm{fin}}}{90°}\right)^{0.29} Pr_{\mathrm{L}}^{-0.024}\right]^7\right)^{1/7}$
Re_{L}: Liquid Reynolds number, $Re_{\mathrm{L}} = \dfrac{G(1-x)d_{\max}}{\mu_{\mathrm{L}}}$, p_{fin}: groove pitch, $p_{\mathrm{fin}} = \dfrac{\pi d_{\max}}{N_{\mathrm{fin}}\tan\beta_{\mathrm{fin}}}$

Table 3.1.3.1-6 Yoshida et al.[15] and Mori et al.[16] correlations

x_{di}: Dryout inception quality $x_{\mathrm{di}} = \min\left(x_{\mathrm{di1}}, x_{\mathrm{di2}}\right)$ $x_{\mathrm{di}} = 0.92$, $x_{\mathrm{di2}} = \min\left(x_{\mathrm{di2a}}, x_{\mathrm{di2b}}\right)$, $x_{\mathrm{di2a}} = 0.44 Fr_{\mathrm{V}}^{0.04} Bo^{-0.07}$, $x_{\mathrm{di2b}} = 0.63 Fr_{\mathrm{V}}^{0.02} Bo^{-0.33}$ x_{de}: Dryout completion quality $x_{\mathrm{de}} = \min\left(x_{\mathrm{de1}}, x_{\mathrm{de2}}\right)$ $x_{\mathrm{de1}} = 1$, $x_{\mathrm{de2}} = \min\left(x_{\mathrm{de2a}}, x_{\mathrm{de2b}}\right)$, $x_{\mathrm{de2a}} = 0.76 Fr_{\mathrm{V}}^{0.023} Bo^{-0.022}$, $x_{\mathrm{de2b}} = 0.405 Fr_{\mathrm{V}}^{0.01} Bo^{-0.11}$ Fr_{V}: Vapor Froude number $Fr_{\mathrm{V}} = \dfrac{G^2}{g d_{\mathrm{eq}}\rho_{\mathrm{V}}\left(\rho_{\mathrm{L}}-\rho_{\mathrm{V}}\right)}$, Bo: Bond number, $Bo = \dfrac{q}{G\Delta h_{\mathrm{LV}}}$
Post-dryout heat transfer coefficient $\alpha = \dfrac{\lambda_{\mathrm{V}}}{d_{\mathrm{eq}}} \times \dfrac{(f/2)\left(Re_{\mathrm{V}}-1000\right)Pr_{\mathrm{V}}}{1+12.7\sqrt{f_{\mathrm{V}}/2}\left(Pr_{\mathrm{V}}^{2/3}-1\right)}$ f_{V}: Vapor friction coefficient, $f_{\mathrm{V}} = 0.308 Re_{\mathrm{V}}^{-0.33}$, Re_{V}: Vapor Reynolds number, $Re_{\mathrm{V}} = \dfrac{G x d_{\mathrm{eq}}}{\mu_{\mathrm{V}}}$

・Evaporation flow of binary refrigerant mixtures in MT

Fig. 3.1.3.1-6(b) shows a comparison of the predicted and experimental results for the HFO1123/HFC32 mixture at mass–velocities of 200, 300, and 400 kg $\mathrm{m^{-2}s^{-1}}$, where the heat transfer coefficients calculated by Kondou et al.[17] are indicated by solid lines. The correlation of Kondou et al.[17] was in reasonable agreement with the measured data over the entire range of vapor quality. Table 3.1.3.1-7 summarizes the correlation of Kondou et al.[17]

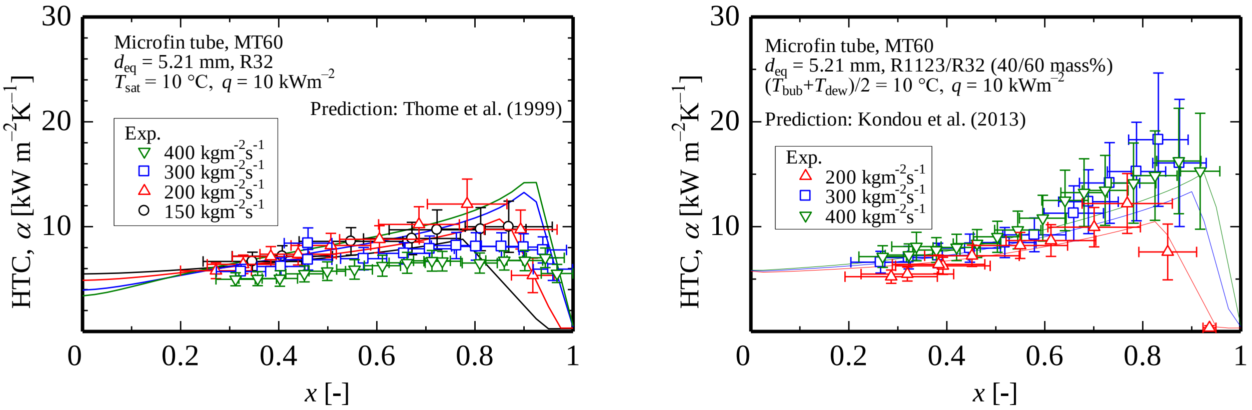

(a) HFC32 (b) HFO1123/HFC32

Fig. 3.1.3.1-6 Comparison between the calculated and experimental evaporative heat transfer coefficients for single and binary mixtures in MT (Solid lines show the prediction results of selected correlation)

Table 3.1.3.1-7 Kondou et al.[17] correlation

$$\alpha = \left[\frac{1}{\alpha_V}\left(x c_{pV}\left.\frac{\mathrm{d}T_{sat}}{\mathrm{d}h}\right|_p\right) + \frac{1 + C_{ir}\left(\tilde{Y}_1 - \tilde{X}_1\right)}{\alpha_{CV} + \alpha_{nb,mix}}\right]^{-1}, \quad \alpha_V = \left(\frac{\lambda_V}{d_{eq}}\right)0.023\left(\frac{G_r d_{eq}}{\mu_V}\right)Pr_L^{1/3}, \quad \left.\frac{\mathrm{d}T_{sat}}{\mathrm{d}h}\right|_p \cong \frac{T_{dew} - T_{bub}}{\Delta h_{LV}}$$

Forced convection heat transfer

Carnavos correlation: $\alpha_{cv} = F\alpha_{L\_Carnavos}$

$$F = 1 + C_{cv}/X_{tt}, \quad C_{cv} = 10\left(Re_L \times 10^{-4}\right)^{-0.6}\left[1 - 0.93\exp\left(-4Re_L \times 10^{-4}\right)\right]\left(\rho_V/\rho_L\right)^{0.35}$$

$$\alpha_{L\_Carnavos} = \frac{\lambda_L}{\left(d_{eq}/\eta_A\right)}0.023\left[\frac{G_r(1-x)\left(d_{eq}/\eta_A\right)}{\mu_L}\right]^{0.8} Pr^{0.4} F_{Carnavos}, \quad F_{Carnavos} = \left(\frac{d_{eq}}{d_{max}}\right)^{0.2}\left(\frac{d_{max}}{d_{eq}\eta_A}\right)^{0.5}\left(\frac{1}{\cos\beta}\right)^3$$

Nucleate boiling heat transfer:

$$\alpha_{nb,m} = \left(\frac{\tilde{X}_1}{\alpha_{nb,1}} + \frac{\tilde{X}_2}{\alpha_{nb,2}}\right)^{-1} N_{Sn}^{7/5} \qquad N_{Sn} = \left[1 - \left(\tilde{Y}_1 - \tilde{X}_1\right)\left(\frac{\alpha_L}{D_{12,L}}\right)^{1/2}\left(\frac{C_{pL}}{\Delta h_{LV,L}}\right)\left(\frac{dT_{bub}}{d\tilde{X}_1}\right)\right]^{-1}$$

$\alpha_{nb,1}$ and $\alpha_{nb,2}$ are calculated by means of Momoki et al.[19] for each component.

(3) Pressure drop of condensation and evaporation flow in MT

The measured pressure drops in the condensation and evaporative flows of HFC32 and the HFO1123/HFC32 mixture in MT were compared with predicted results based on the correlation of Baba[20] for single compounds. Fig. 3.1.3.1-7 shows the experimental pressure drop measured at mass–velocities of 200 and 400 kg m^{-2}s^{-1}, heat flux of 10 kg m^{-2}s^{-1}, and predicted pressure drop by Baba[20]. The correlation of Baba[20] was in good agreement with the measured data of both refrigerants under test and represented the effect of physical properties on the pressure drop. The agreement was also consistent with previous findings, where the pressure drop of the refrigerant mixtures was not affected by mass transfer resistance or temperature glide but was only affected by physical properties, such as vapor density and liquid viscosity, as in the case of single compounds. Table 3.1.3.1-8 summarizes the correlations of Baba[20].

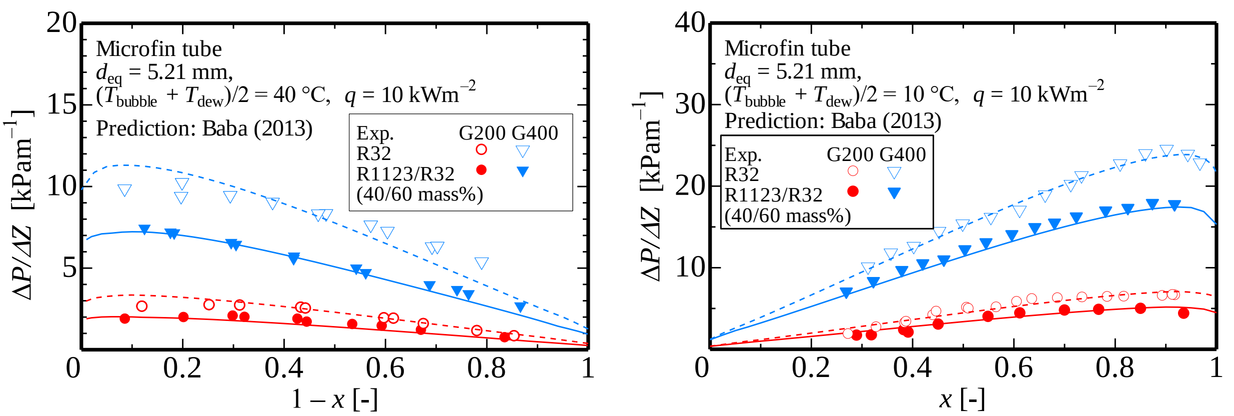

(a) Condensation (b) Evaporation

Fig. 3.1.3.1-7 Comparison between the calculated and experimental pressure drops values

Table 3.1.3.1-8 Baba[20] correlation.

$$\left(\frac{\Delta P_{\mathrm{F}}}{\Delta Z}\right)_{\mathrm{TP}} = \Phi_{\mathrm{VO}}^2 \left(\frac{2 f_{\mathrm{VO}} G^2}{d_{\mathrm{eq}} \rho_{\mathrm{V}}}\right)$$

Condensation flow: $\Phi_{\mathrm{VO}}^2 = x^{1.8} + (1-x)^{1.8} \left(\frac{\rho_{\mathrm{V}} f_{\mathrm{LO}}}{\rho_{\mathrm{L}} f_{\mathrm{VO}}}\right) + 0.63 x^{0.9} (1-x)^{0.52} \left(\frac{\rho_{\mathrm{V}}}{\rho_{\mathrm{L}}}\right)^{0.5} \left(\frac{\mu_{\mathrm{L}}}{\mu_{\mathrm{V}}}\right)^{1.05}$

Evaporation flow: $\Phi_{\mathrm{VO}}^2 = x^{1.8} + (1-x)^{1.8} \left(\frac{\rho_{\mathrm{V}} f_{\mathrm{LO}}}{\rho_{\mathrm{L}} f_{\mathrm{VO}}}\right) + 1.22 x^{0.97} (1-x)^{0.61} \left(\frac{\rho_{\mathrm{V}}}{\rho_{\mathrm{L}}}\right)^{0.5} \left(\frac{\mu_{\mathrm{L}}}{\mu_{\mathrm{V}}}\right)^{0.71}$

$$f_{\mathrm{LO}} = 0.046 \left(\frac{Re_{\mathrm{LO}} d_{\mathrm{eq}}}{d_{\max}}\right)^{-0.2} \left(\frac{\eta_{\mathrm{A}} d_{\mathrm{eq}}}{d_{\max}}\right)^{0.8} (\cos\beta)^{-1.3} \left[1 + \left(\frac{10.8 p_{\mathrm{fin}}}{d_{\max}}\right)^{3.3}\right] \left(\frac{d_{\mathrm{eq}}}{d_{\max}}\right)^5$$

$$f_{\mathrm{VO}} = 0.046 \left(\frac{Re_{\mathrm{VO}} d_{\mathrm{eq}}}{d_{\max}}\right)^{-0.2} \left(\frac{\eta_{\mathrm{A}} d_{\mathrm{eq}}}{d_{\max}}\right)^{0.8} (\cos\beta)^{-1.3} \left[1 + \left(\frac{10.8 p_{\mathrm{fin}}}{d_{\max}}\right)^{3.3}\right] \left(\frac{d_{\mathrm{eq}}}{d_{\max}}\right)^5$$

Re_{LO} and Re_{VO}: Liquid and vapor Reynolds number, $Re_{\mathrm{LO}} = \frac{G d_{\mathrm{eq}}}{\mu_{\mathrm{L}}}$, $Re_{\mathrm{VO}} = \frac{G d_{\mathrm{eq}}}{\mu_{\mathrm{V}}}$

p_{fin}: Groove pitch, $p_{\mathrm{fin}} = \frac{\pi d_{\max} \cos\beta}{N_{\mathrm{fin}}}$

References

1) Cavallini, D. Col, L. Doretti, M. Matkovic, L. Rossetto, C. Zilio, and G. Censi, Heat Transf. Eng., 27(8), 31(2006).
2) M. K. Dobson and J. C Chato, J. Heat Mass Transf., 120(1), 193(1998).
3) M. M. Shah, ASHRAE Transactions, Denver, 119(2), 3(2013).
4) H. Haraguchi, S. Koyama, and T. Fujii, Trans. JSME(B), 60 (574), 2117(1994). (in Japanese)
5) L. Silver, Trans. Inst. Chem. Engrs., 25, 30(1947).
6) K. J. Bell and M. A. Ghaly, AIChE Symp. Ser., 69, 72(1973).
7) R. Yonemoto and S. Koyama, Trans. JSRAE., 24(2), 139(2007). (in Japanese)
8) J. C. Chen, Ind. Eng. Chem., 5(3), 322(1966).
9) H. Mori, S. Yoshida, Y. Kakamoto, and K. Ohishi: Trans. JSRAE., 16(2), 177(1999). (in Japanese)
10) S. Saitoh, H. Daiguji, and E. Hihara, Int. J. Heat Mass Transf., 50, 5215(2007).
11) H. Takamatsu, S. Momoki, and T. Fujii, Trans. JSME(B), 58(550), 1875(1992). (in Japanese)
12) J. Yu, S. Momoki, and S. Koyama, Int. J. Heat Mass Transf., 42(10), 1909(1999).
13) H. Takamatsu, S. Momoki, and T. Fujii, Trans. JSME(B), 58(551), 2198(1992). (in Japanese)
14) J.R. Thome, Convective Flow and Pool Boiling Conference, (1997).
15) S. Yoshida, H. Mori, Y. Kakamoto, and K. Ohishi, Trans. JSRAE., 17(4), 511(2000). (in Japanese)
16) H. Mori, S. Yoshida, Y. Kakamoto, K. Ohishi, and K. Fukuda, Trans. JSRAE., 17(4), 521(2000). (in Japanese)
17) Kondou, D. Baba, F. Mishima, and S. Koyama, Int. J Refrig., 36, 2366(2013).
18) J.R. Thome: AIChE. Symp. Ser., 77(208), 238(1981).
19) S. Momoki, J. Yu, S. Koyama, T. Fujii and H. Honda: Trans. JSRAE., 12(2), 177(1995). (in Japanese)
20) Baba, Doctoral dissertation, IGSES Kyushu University (2013). (in Japanese)

3.1.3.2 Phase change heat transfer in multiport tube

Table 3.1.3.2-1 shows the recommended correlation of condensation heat transfer for pure and mixed refrigerants inside multiport tube[1]. Fig. 3.1.3.2-1 shows the comparison of the correlation[1] with the measured condensation heat transfer coefficients.

Table 3.1.3.2-1 Recommended correlation of condensation heat transfer inside multiport tube [1]

$$\alpha_{\mathrm{pure}} = \frac{\lambda_{\mathrm{L}} Nu}{D_{\mathrm{h}}} \quad \text{for pure refrigerants}$$

$$\alpha_{\mathrm{mix}} = \left(\frac{1}{\alpha_{\mathrm{pure}}} + \frac{3xc_{p\mathrm{V}}(\Delta T_{\mathrm{glide}} / \Delta h_{\mathrm{LV}})}{\alpha_{\mathrm{V}}} \right)^{-1} \quad \text{for mixtures}$$

$$\alpha_{\mathrm{V}} = 0.023 \left(\frac{GxD_{\mathrm{h}}}{\mu_{\mathrm{V}}} \right)^{0.8} \left(\frac{\mu_{\mathrm{V}} c_{p\mathrm{V}}}{\lambda_{\mathrm{V}}} \right)^{0.4} \left(\frac{\lambda_{\mathrm{V}}}{D_{\mathrm{h}}} \right)$$

$$Nu = \left(Nu_{\mathrm{F}}^3 + Nu_{\mathrm{S}}^3 \right)^{1/3}$$

$$Nu_{\mathrm{F}} = 0.023 \left[\frac{G(1-x)D_{\mathrm{h}}}{\mu_{\mathrm{L}}} \right]^{0.8} \left(\frac{\mu_{\mathrm{L}} c_{p\mathrm{L}}}{\lambda_{\mathrm{L}}} \right)^{0.3} \left[1 + 0.22 \left(\frac{x}{1-x} \right) \left(\frac{\rho_{\mathrm{L}}}{\rho_{\mathrm{V}}} \right)^{-0.1} \left(\frac{\mu_{\mathrm{L}}}{\mu_{\mathrm{V}}} \right)^{1.18} \right]$$

$$Nu_{\mathrm{S}} = 0.56 \beta Co^{-0.3} \left[\frac{\rho_{\mathrm{L}} \Delta h_{\mathrm{LV}} \sigma D_{\mathrm{h}}}{\mu_{\mathrm{L}} \lambda_{\mathrm{L}} (T_{\mathrm{r}} - T_{\mathrm{w}})} \right]^{1/4}$$

$$\beta = \frac{x}{x + (1-x)(\rho_{\mathrm{V}} / \rho_{\mathrm{L}})}, \quad Co = \frac{\sqrt{\sigma / \{ g(\rho_{\mathrm{L}} - \rho_{\mathrm{V}}) \}}}{D_{\mathrm{h}}}$$

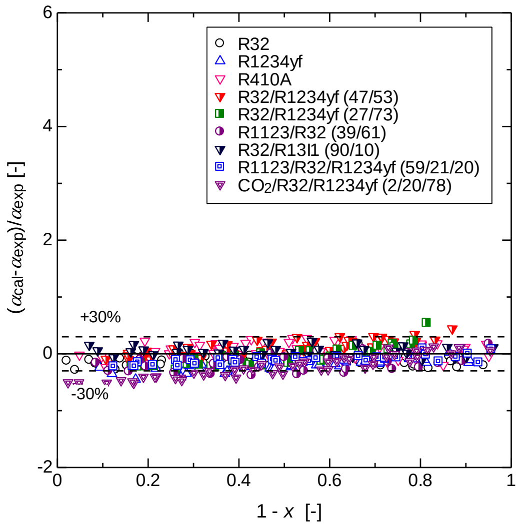

Fig. 3.1.3.2-1 Comparison of the correlation with the measured condensation heat transfer coefficients

Table 3.1.3.2-2 shows the recommended correlation of evaporative heat transfer coefficient for pure and mixed refrigerants inside multiport tube [2,3]. The correlation was proposed considering nucleate boiling, forced convection, and thin-liquid heat transfer inside multiport rectangular minichannels and their heat transfer deterioration. Fig. 3.1.3.2-2 shows the comparison of the measured data with the correlation[2,3] of evaporative heat transfer coefficients. The deviation of the correlation of evaporative heat transfer coefficients from the experimental results was larger than those for the condensation heat transfer coefficients. Thus, improvement in predictability is required for onset and end dryout at low mass–velocities.

Table 3.1.3.2-2 Recommended correlation of evaporative heat transfer inside multiport tube [2,3]

$$\alpha_{\mathrm{tp,mix}} = \left[(\alpha_{\mathrm{cb,mix}})^5 + (\alpha_{\mathrm{nb,mix}})^5\right]^{1/5} \quad \text{for mixtures}$$

$$\alpha_{\mathrm{tp,pure}} = \left[(\alpha_{\mathrm{cb,id}})^5 + (\alpha_{\mathrm{nb,id}})^5\right]^{1/5} \quad \text{for pure refrigerants}$$

$$\alpha_{\mathrm{cb,mix}} = \max\left(\alpha_{\mathrm{fc,mix}},\, \alpha_{\mathrm{lf,mix}}\right), \quad \alpha_{\mathrm{cb,id}} = \max\left(\alpha_{\mathrm{fc,id}},\, \alpha_{\mathrm{lf,id}}\right)$$

$$\alpha_{\mathrm{nb,mix}} = \alpha_{\mathrm{nb,id}}\left\{1 + \frac{\Delta T_{\mathrm{glide}}}{q/a_{\mathrm{nb,id}}}\left[1 - \exp\left(\frac{-q}{0.0003\rho_{\mathrm{L}}\Delta h_{\mathrm{LV}}}\right)\right]\right\}^{-1}$$

$$\alpha_{\mathrm{nb,id}} = 10\frac{\lambda_{\mathrm{L}}}{D_{\mathrm{b}}}\left(\frac{q\,D_{\mathrm{b}}}{\lambda_{\mathrm{L}}T_r}\right)^{C}\left(\frac{P_{\mathrm{r}}}{P_{\mathrm{crit}}}\right)^{0.1}\left(1 - \frac{T_{\mathrm{r}}}{T_{\mathrm{crit}}}\right)^{-1.4}\left(\frac{\mu_{\mathrm{L}}c_{p\mathrm{L}}}{\lambda_{\mathrm{L}}}\right)^{-0.25},$$

$$C = 0.855\left(\frac{\rho_{\mathrm{V}}}{\rho_{\mathrm{L}}}\right)^{0.309}\left(\frac{P_{\mathrm{r}}}{P_{\mathrm{crit}}}\right)^{-0.437}, \quad D_{\mathrm{b}} = 0.511\sqrt{\frac{2\sigma}{g(\rho_{\mathrm{L}} - \rho_{\mathrm{V}})}}$$

$$\alpha_{\mathrm{fc,mix}} = \alpha_{\mathrm{fc,id}} = \left[1 + 2\left(\frac{1}{X_{\mathrm{tt}}}\right)^{0.88}\right] \times 0.023\frac{\lambda_{\mathrm{L}}}{D_{\mathrm{h}}}\left[\frac{G(1-x)D_{\mathrm{h}}}{\mu_{\mathrm{L}}}\right]^{0.8}\left(\frac{\mu_{\mathrm{L}}c_{p\mathrm{L}}}{\lambda_{\mathrm{L}}}\right)^{0.4}$$

$$a_{\mathrm{lf,mix}} = \frac{\alpha_{\mathrm{lf,id}}}{1 + (\alpha_{\mathrm{lf,id}}/q)(T_{\mathrm{w}} - T_{\mathrm{r}})}$$

For annular and churn flow regimes:

$$\alpha_{\mathrm{lf,id}} = \beta\frac{\lambda_{\mathrm{L}}}{\delta_{\mathrm{e}}}, \quad \delta_{\mathrm{e}} = 0.014Ca^{0.1}D_{\mathrm{h}}, \quad \beta = x/\left[x + (1-x)(\rho_{\mathrm{V}}/\rho_{\mathrm{L}})\right]$$

For plug and slug-annular flow regimes:

$$\alpha_{\mathrm{lf,id}} = F_{\mathrm{dp}}\left(\beta\frac{\lambda_{\mathrm{L}}}{\delta_{\mathrm{e}}}\right), \quad \delta_{\mathrm{e}} = 0.005Ca^{0.05}\left(\rho_{\mathrm{L}}/\rho_{\mathrm{V}}\right)^{0.2}D_{\mathrm{h}}$$

$$F_{\mathrm{dp}} = \min\left[7.8Co^{-1.0}\left(\frac{q}{G\Delta h_{\mathrm{LV}}} \times 10^4\right)^{-0.3}\left(\frac{\rho_{\mathrm{V}}}{\rho_{\mathrm{L}}}\right)^{0.2}\left(\frac{GD_{\mathrm{h}}}{\mu_{\mathrm{L}}}\right)^{-0.16},\ 1\right]$$

Flow pattern transition boundaries:

- Annular flow regime: $We_{\mathrm{V}} / Co \geq 75$
- Plug flow regime: $\dfrac{We_{\mathrm{L}}}{Co} > 2.3\times10^{-4}\left(\dfrac{We_{\mathrm{V}}}{Co}\right)^{3.7}$
- Slug-annular flow regime: $\dfrac{We_{\mathrm{L}}}{Co} \leq 2.3\times10^{-4}\left(\dfrac{We_{\mathrm{V}}}{Co}\right)^{3.7}$ and $We_{\mathrm{Lo}} < 4$
- Churn flow regime: $\dfrac{We_{\mathrm{L}}}{Co} \leq 2.3\times10^{-4}\left(\dfrac{We_{\mathrm{V}}}{Co}\right)^{3.7}$ and $We_{\mathrm{Lo}} \geq 4$

For dryout region (post dryout region)[3)]:

$$\alpha = \alpha_{x\mathrm{di}} - \frac{x - x_{\mathrm{di}}}{x_{\mathrm{de}} - x_{\mathrm{di}}}\left(\alpha_{x\mathrm{di}} - \alpha_{x\mathrm{de}}\right)$$

where $\alpha_{x\mathrm{di}}$ is the heat transfer coefficient calculated at $x = x_{\mathrm{di}}$

$$x_{\mathrm{di}} = \min\left(x_{\mathrm{di1}}, x_{\mathrm{di3a}}, x_{\mathrm{di3b}}\right)$$

$$x_{\mathrm{di1}} = 0.94 - 1.75\times10^{-6}(Re_{\mathrm{Vo}}Bo)^{1.75}\left(\rho_{\mathrm{V}}/\rho_{\mathrm{L}}\right)^{-0.86}$$

$$x_{\mathrm{di3a}} = 0.253 Fr_{\mathrm{Vo}}^{-0.32} Bo^{-0.12} We_{\mathrm{Vo}}^{0.48}\left(\rho_{\mathrm{V}}/\rho_{\mathrm{L}}\right)^{0.16}$$

$$x_{\mathrm{di3b}} = Fr_{\mathrm{Vo}}^{-1.00} Bo^{-0.21} We_{\mathrm{Vo}}{}^{0.70}$$

$$\alpha_{x\mathrm{de}} = 0.023\frac{\lambda_{\mathrm{V}}}{D_{\mathrm{h}}}\left[\frac{GD_{\mathrm{h}}}{\mu_{\mathrm{V}}}\right]^{0.8}\left[\frac{\mu_{\mathrm{V}} c_{p\mathrm{V}}}{\lambda_{\mathrm{V}}}\right]^{0.4}$$

$$X_{\mathrm{tt}} = \left(\frac{1-x}{x}\right)^{0.9}\left(\frac{\rho_{\mathrm{V}}}{\rho_{\mathrm{L}}}\right)^{0.5}\left(\frac{\mu_{\mathrm{L}}}{\mu_{\mathrm{V}}}\right)^{0.1}, \quad Ca = \left\{x/\rho_{\mathrm{V}} + (1-x)/\rho_{\mathrm{L}}\right\}\mu_{\mathrm{L}} G/\sigma, \quad Co = \sqrt{\sigma / \{g(\rho_{\mathrm{L}} - \rho_{\mathrm{V}})\}}\Big/D_{\mathrm{h}}$$

$$We_{\mathrm{L}} = G^2(1-x)^2 D_{\mathrm{h}} / (\rho_{\mathrm{L}}\sigma), \quad We_{\mathrm{Lo}} = G^2 D_{\mathrm{h}} / (\rho_{\mathrm{L}}\sigma), \quad We_{\mathrm{V}} = G^2 x^2 D_{\mathrm{h}} / (\rho_{\mathrm{V}}\sigma)$$

$$We_{\mathrm{Vo}} = G^2 D_{\mathrm{h}} / (\rho_{\mathrm{V}}\sigma), \quad Re_{\mathrm{Vo}} = GD_{\mathrm{h}}/\mu_{\mathrm{V}}, \quad Bo = q/(G\Delta h_{\mathrm{LV}}), \quad Fr_{\mathrm{Vo}} = G^2\big/\left[gD_{\mathrm{h}}\rho_{\mathrm{V}}\left(\rho_{\mathrm{L}} - \rho_{\mathrm{V}}\right)\right]$$

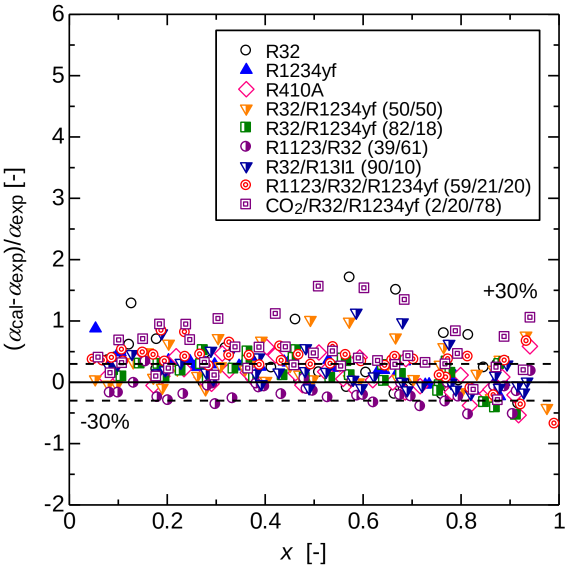

Fig. 3.1.3.2-2 Comparison of measured data with the correlations of evaporative heat transfer coefficients

Table 3.1.3.2-3 lists the recommended correlations of the pressure drop inside the multiport tube[4,5]. For frictional pressure drops, the predicted correlations proposed for pure refrigerants could be applied to refrigerant mixtures. Fig. 3.1.3.2-3 shows a comparison between the correlations for the frictional pressure drops[4,5] and the measured data of pure and mixed refrigerants in condensation flow.

Table 3.1.3.2-3 Recommended correlations of pressure drop inside multiport tube [4,5]

$$\left(\frac{\Delta P}{\Delta Z}\right)_{\mathrm{F}} = \Phi_{\mathrm{Vo}}^2 \left(\frac{\Delta P}{\Delta Z}\right)_{\mathrm{Vo}} = \left[x^{1.8} + (1-x)^{1.8}\frac{\rho_{\mathrm{V}}}{\rho_{\mathrm{L}}}\frac{f_{\mathrm{Lo}}}{f_{\mathrm{Vo}}} + 0.65x^{0.68}(1-x)^{0.43}\left(\frac{\mu_{\mathrm{L}}}{\mu_{\mathrm{V}}}\right)^{1.25}\left(\frac{\rho_{\mathrm{V}}}{\rho_{\mathrm{L}}}\right)^{0.75}\right]\left(\frac{2 f_{\mathrm{Vo}} G^2}{D\rho_{\mathrm{V}}}\right)$$

$$f_{\mathrm{Vo}} = \begin{cases} C_1 / (GD/\mu_{\mathrm{V}}), & \text{for } (GD/\mu_{\mathrm{V}}) \leq 1500 \\ 0.046/(GD/\mu_{\mathrm{V}})^{0.2}, & \text{for } (GD/\mu_{\mathrm{V}}) > 1500 \end{cases}$$

$$f_{\mathrm{Lo}} = \begin{cases} C_1 / (GD/\mu_{\mathrm{L}}), & \text{for } (GD/\mu_{\mathrm{L}}) \leq 1500 \\ 0.046/(GD/\mu_{\mathrm{L}})^{0.2}, & \text{for } (GD/\mu_{\mathrm{L}}) > 1500 \end{cases}$$

$C_1 = 16$ for circular minichannels

$C_1 = 24\left(1 - 1.355a^* + 1.947a^{*2} - 1.701a^{*3} + 0.956a^{*4} - 0.254a^{*5}\right)$ for rectangular minichannels

a^* : Aspect ratio of shorter side to longer side of the rectangular minichannel

$$\left(\frac{\Delta P}{\Delta Z}\right)_{\mathrm{F}}=\Phi_{\mathrm{f}}^{2}\left(\frac{\Delta P}{\Delta Z}\right)_{\mathrm{f}}$$

$$\left(\frac{\Delta P}{\Delta Z}\right)_{\mathrm{f}}=\frac{2f_{\mathrm{f}}G^2(1-x)^2}{D\rho_{\mathrm{f}}},\ \left(\frac{\Delta P}{\Delta Z}\right)_{\mathrm{g}}=\frac{2f_{\mathrm{g}}G^2x^2}{D\rho_{\mathrm{g}}}$$

$$f_{\mathrm{k}}=C_1/Re_{\mathrm{k}} \qquad \text{for } Re_{\mathrm{k}}<2000$$

$$f_{\mathrm{k}}=0.079/Re_{\mathrm{k}}^{0.25} \qquad \text{for } 2000\le Re_{\mathrm{k}}<20000$$

$$f_{\mathrm{k}}=0.049/Re_{\mathrm{k}}^{0.2} \qquad \text{for } 20000\le Re_{\mathrm{k}}$$

For laminar flow in rectangular channel

$$f_{\mathrm{k}}Re_{\mathrm{k}}=24\left(1-1.3553a^{*}+1.9467a^{*2}-1.7012a^{*3}+0.9564a^{*4}-0.2537a^{*5}\right)$$

$$C=0.39Re_{\mathrm{fo}}^{0.03}Su_{\mathrm{go}}^{0.10}(\rho_{\mathrm{f}}/\rho_{\mathrm{g}})^{0.35} \quad \text{for turbulent/turbulent}$$

$$C=8.7\times10^{-4}Re_{\mathrm{fo}}^{0.17}Su_{\mathrm{go}}^{0.50}(\rho_{\mathrm{f}}/\rho_{\mathrm{g}})^{0.14} \quad \text{for turbulent/laminar}$$

$$C=0.0015Re_{\mathrm{fo}}^{0.59}Su_{\mathrm{go}}^{0.19}(\rho_{\mathrm{f}}/\rho_{\mathrm{g}})^{0.36} \quad \text{for laminar/turbulent}$$

$$C=3.5\times10^{-5}Re_{\mathrm{fo}}^{0.44}Su_{\mathrm{go}}^{0.50}(\rho_{\mathrm{f}}/\rho_{\mathrm{g}})^{0.48} \quad \text{for laminar / laminar}$$

$$Su_{\mathrm{Vo}}=\frac{\rho_{\mathrm{V}}\sigma D_{\mathrm{h}}}{\mu_{\mathrm{V}}^{2}}$$

a^{*} : aspect ratio of shorter side to longer side of the rectangular minichannel

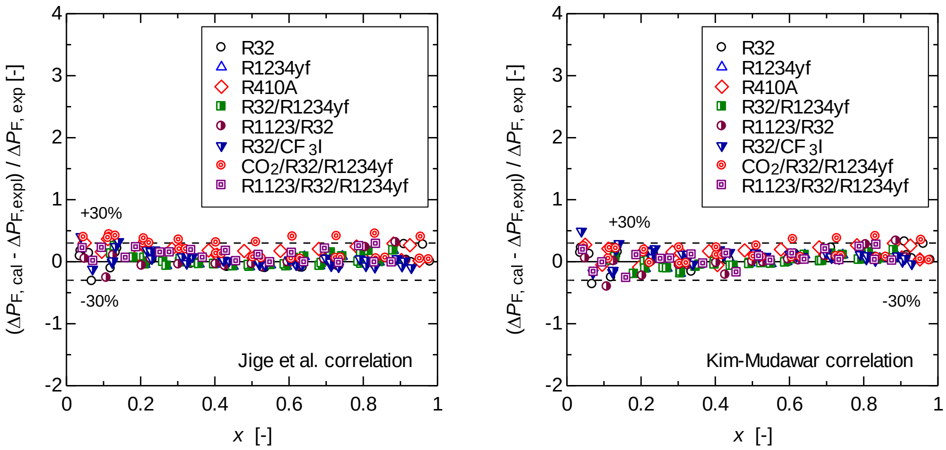

(a) Jige et al.[4] (b) Kim and Mudawar[5]

Fig. 3.1.3.2-3 Comparison of measured data with the correlations of pressure drop

References

1) D. Jige, M. Nobunaga, T. Nogami, and N. Inoue, Submitted to the Int. J. Heat Mass Transf.
2) D. Jige, S. Kikuchi, H. Eda, and N. Inoue, Int. J. Refrig., 95, 154–164(2018).
3) D. Jige, S. Kikuchi, H. Eda, and N. Inoue, Int. J. Heat Mass Transf., 144, 118668(2019)
4) D. Jige, N. Inoue, and S. Koyama, Int. J. Refrig., 67, 202–213(2016).
5) S. M. Kim and I. Mudawar, . Int. J. Heat Mass Transf., 55, 3246–3261(2012).

3.1.3.3 Correlations of condensation and evaporative heat transfer coefficient in a plate heat exchanger

Based on the experimental data for condensation and evaporative heat transfer coefficients in plate heat exchangers reported in Section 3.1.1.3, the correlations of the heat transfer coefficients were estimated. A comparison between the existing condensation heat transfer coefficient correlations[1–4], experimental data of this study, and data of a previous study[5] is shown in Fig. 3.1.3.3-1, where the agreement of the calculated values of HFC32 with the measured values was better than the results for the other refrigerants, but the deviations for the other refrigerants were larger. The correlations discussed in this section, or in general, are mainly focused on forced convection condensation, which is found in regions of high mass–velocity or quality. The mass–velocity conditions in this study were partly different. Further studies will be carried out and a correlation for the conditions of this study will be developed in the future. Table 3.1.3.3-1 shows the correlation suggested by Longo et al.[3], which was applicable up to the natural-convection condensation region.

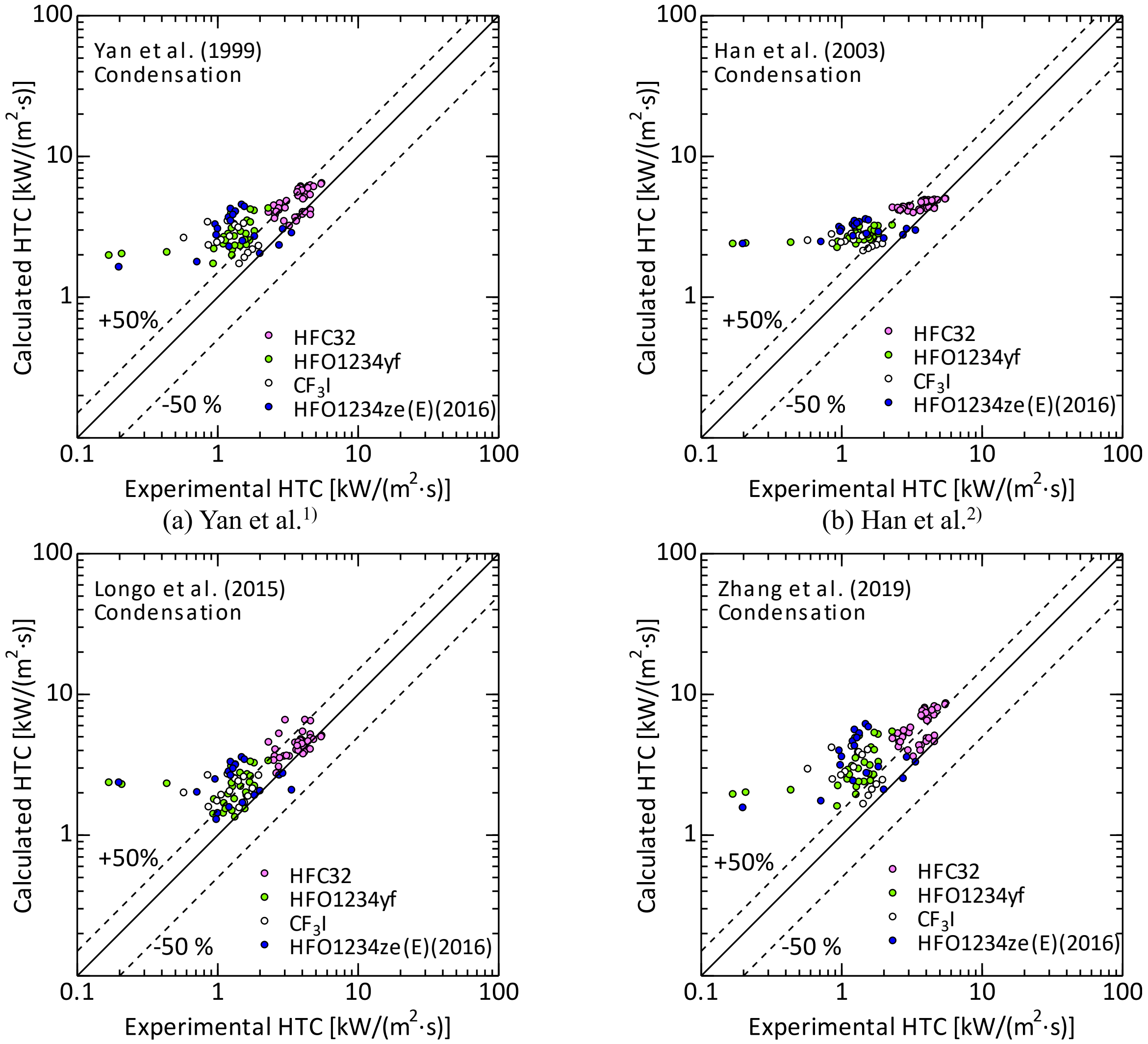

(a) Yan et al.[1] (b) Han et al.[2]

(c) Longo et al.[3] (d) Zhang et al.[4]

Fig. 3.1.3.3-1 Agreement between measured experimental data and calculated values

Table 3.1.3.3-1 Correlation of condensation heat transfer coefficient for HFO refrigerants

Reference	Correlation
Longo et al.[3)]	$h = 0.943\phi\left[\frac{k_L^3\rho_L^2 g\Delta J_{LG}}{\mu_L\Delta TL}\right]^{\frac{1}{4}} \quad (Re_{eq} < 1600)$ $h = 1.875\phi\frac{k_L}{D_h}Re_{eq}^{0.445}Pr_L^{1/3} \quad (Re_{eq} \geq 1600)$ $Re_{eq} = \frac{G\left[(1-x)+x\left(\frac{\rho_L}{\rho_V}\right)^{0.5}\right]D_h}{\mu_l}$

A similar estimation of correlation for evaporative heat transfer coefficient revealed that the correlation suggested by Longo et al.[6)], as shown in Table 3.1.3.3-2, reproduced the presented experimental data well. The value of the surface roughness Ra_0 was set to 3.2 μm, which is the standard value for the tested plate (machined surface). The values correlated by Gorenflo et al.[7)] were used for calculating parameters related to pool boiling, which were not mentioned by Longo et al.[6)]. The correlations of Longo et al.[6)] are provided in Table 3.1.3.3-2. Fig. 3.1.3.3-2 shows that the calculated evaporative heat transfer coefficient reproduced most of the measured values within ±30% or lesser. The data that deviate significantly from the calculated values were due to the occurrence of dryout. Thus, within practical limits, the correlation can be used to predict the heat transfer coefficient inside a plate heat exchanger. Correlations for condensation[8)] and evaporative[9)] heat transfer coefficients of zeotropic mixed refrigerants have been proposed in recent years; however, the application was limited to plate geometries and has not been generalized. The data obtained in this study were also based on a limited number of refrigerant types and measurement conditions; therefore, estimation or development of correlations for zeotropic mixed refrigerants was challenging. In the future, data will be acquired, evaluated, and examined for various HFO refrigerant mixtures and experimental conditions.

Table 3.1.3.3-2 Correlation of evaporative heat transfer coefficient for presented plate heat exchanger[10)]

Reference	Correlation
Longo et al.[6)] Gorenflo et al.[7)]	$h = MAX(h_{cb}, h_{nb})$ $h_{cb} = 0.122\phi\frac{k_L}{D_h}Re_{eq}^{0.8}Pr_L^{1/3}$ $Re_{eq} = \frac{G\left[(1-x)+x\left(\frac{\rho_L}{\rho_V}\right)^{0.5}\right]D_h}{\mu_L}$ $h_{nb} = C_{nb}\phi h_0 C_{Ra}F(p^*)\left(\frac{q}{q_0}\right)^{0.467}$ $C_{nb} = 0.58$ $h_0 = 3.58P_f^{0.6}$ $P_f = \left[\left(\frac{dp}{dT}\right)_{VPC}/\sigma\right]_{p_0^*=0.1}$ $F(p^*) = 1.2p^{*0.27} + [2.5 + 1/(1-p^*)]p^*$ $C_{Ra} = \left(\frac{R_a}{0.4\mu m}\right)^{0.1333}$ $q_0 = 20$ $Ra_0 = 0.4$ (Original, for smooth copper tube) $Ra_0 = 3.2$ (Present report, for cutting SUS304 plate) $p_0^* = 0.1$

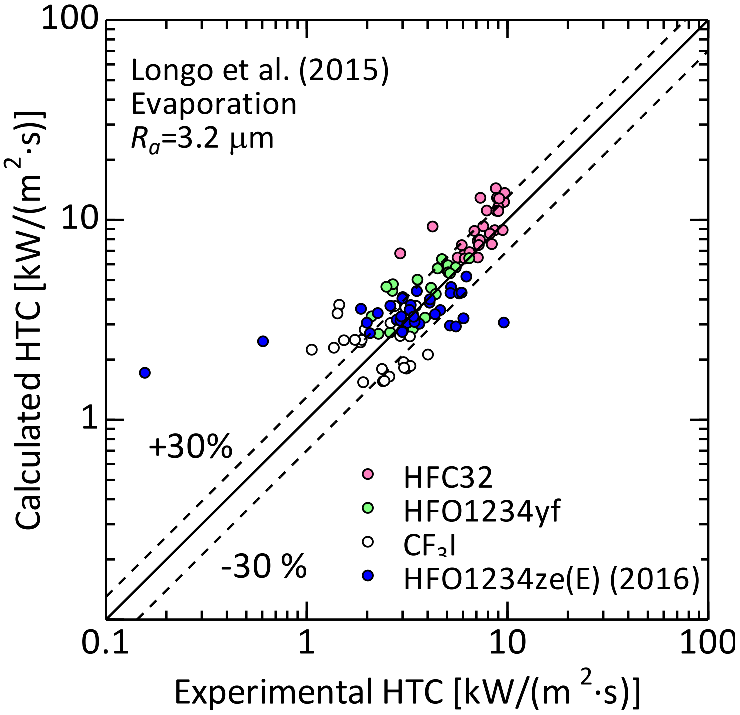

Fig. 3.1.3.3-2 Agreement between the experimental and calculated values of heat transfer coefficients by Longo et al.[6] correlation

Nomenclature used

D_h	Hydraulic diameter	m
g	Gravity acceleration	m/s^2
G	Mass–velocity	$kg/(m^2 \cdot s)$
h	Heat transfer coefficient	W/m^2
J_{LG}	Specific latent heat of condensation	J/kg
k	Thermal conductivity	$W/(m \cdot K)$
L	Flow length of the plate	m
Pr	Prandtl number	-
q	Heat flux	W/m^2
Re	Reynolds number	-
Ra	Mean roughness	μm
x	Vapor quality	-
ΔT	Difference between saturation and wall temperature	K
ϕ	Enlargement factor	-
μ	Viscosity	$Pa \cdot s$
ρ	Density	kg/m^3

Subscripts

l	Saturated liquid
v	Saturated vapor

References

1) Y. Y. Yan, H. C. Lio, T. F. Lin, G. A. Longo, S. Mancin, G. Righetti, and Claudio Zilio, Int. J. Heat Mass Transf., 42, 993–1006(1999).
2) D. H. Han, K. J. Lee, and Y. H. Kim, J. Korean Phys. Soc., 43(1), 66–73(2003).
3) G. A. Longo, G. Righetti, and C. Zilio, Int. J. Heat Mass Transf., 82, 530–536(2015).
4) J. Zhang, M. R. Kærn, T. Ommen, B. Elmegaard, and F. Haglind, Int. J. Heat Mass Transf., 128, 136–149(2019).
5) K. Kariya, M. S. Mahmud, and A. Miyara, Purdue Conference, 2600(2016)
6) G. A. Longo, S. Mancin, G. Righetti, and C. Zilio, Int. J. Heat Mass Transf., 91, 144–149(2015).
7) D. Gorenflo, U. Chandra, S. Kotthoff, and A. Luke, Int. J. Refrig., 27, 492–502(2004).
8) X. Huang, J. Zhang, and F. Haglind, Int. J. Refrig., 137, 166–167(2022).
9) R. Prabakaran, M. Salman, P. G. Kumar, D. Lee, and S. C. Kim, Appl. Therm. Eng., 216, 119070(2022).
10) K. Kariya, M. Rahman, and A. Miyara, JSME heat transfer engineering conference 2022, C214(2022).

3.1.4 Prediction of heat transfer coefficient and pressure loss using AI

For the optimal design of a heat exchanger, the phase-change heat-transfer coefficient in a tube should be determined. Therefore, we first determined the accuracies of the boiling heat-transfer coefficient formulas proposed by various researchers. Data samples for the evaluation were collected from other researchers to ensure objectivity and an unbiased evaluation. The proposed correlation for the prediction of heat-transfer coefficient is not applicable to a wide variety of refrigerants, as the prediction accuracy differs significantly for refrigerants with different properties. This is a critical issue with respect to the completion of this project, as it increases the difficulty associated with realizing an optimal heat exchanger design. We investigated a solution to this problem and reported the results.

A database of natural refrigerants, HFO refrigerants, and Freon was compiled. The considered tube diameters were within a range of 0.5–4 mm, which is within the range of prospective heat exchangers in the field of refrigeration and air conditioning. The database set included horizontal flow data, in addition to upward and downward flow data. The total number of data points was 1,388.

The correlations for the prediction of heat transfer used in the evaluation are shown in Table 3.1.4-1. A Visual Basic for an application (VBA) program was developed to extract the characteristics and reliability of each equation using Refprop10, namely, software for calculating physical properties. The equations above were automatically computed and compared by simply inputting the experimental conditions.

The results of each formula were compared in graph form, and in the case of comparisons with experimental values, the standard deviation (SD) and percentage of prediction accuracy within 20% and 30% of the total experimental values were outputted as percentages.

Table 3.1.4-1 Data Sample

Source	Fluid	Saturation pressure MPa (Temperature ℃)	Inside diameter mm	Flow direction	Mass flux $kg \cdot m^{-2} \cdot s^{-1}$	Heat flux $kW \cdot m^{-2}$	N
Lazarek and Black	R 113	0.17 (64)	3.15	Upward	502	114, 178	3
	R 113	0.17 (64)	3.15	Downward	502	64 - 178	11
Wambsganss et al.	R 113	0.13 - 0.16 (55 - 62)	2.92	Horizontal	50 - 300	8.8 - 90.8	72
Tran et al.	R 12	0.83 (34)	2.46	Horizontal	66.3 - 300	7.5 - 59.4	59
Kew and Cornwell	R 141b	0.10 (32)	2.87, 3.69	Horizontal	188, 212	9.7 - 90	67
Bao et al.	R 11	0.29 - 0.47 (57 - 76)	1.95	Horizontal	167 - 560	52 - 125	81
	R 123	0.35 - 0.51 (67 - 82)	1.95	Horizontal	167 - 452	39 - 125	80
Kuwahara et al.	R 134a	0.88 (35)	0.84	Horizontal	525	15.6	15
Sumith et al.	H_2O	0.10 (100)	1.45	Upward	23.4 - 152.7	36 - 391	65
Saitoh et al.	R 134a	0.41 (10)	0.51, 1.12, 3.1	Horizontal	150, 300	12 - 29	75
Yamashita et al.	CO_2	5.00 (14)	1.02	Horizontal	300 - 1000	30 - 50	62
Miyata et al.	R 410A	1.09 (10)	1.00	Upward	30 - 200	1 - 16	170
	R 410A	1.09 (10)	1.00	Downward	30 - 200	1 - 16	206
Li et al.	R 32	1.28 (15)	2.00	Horizontal	200	6 - 24	44
	R 1234yf	0.51 (15)	2.00	Horizontal	100 - 400	6 - 24	91
Enoki et al.	R 410A	1.09 (10)	1.00	Horizontal	30 - 400	2 - 24	287

In Table 3.1.4-1, the following references were made: Lazarek and Black [3.1.4-1)], Wambsganss et al.[3.1.4-2)], Tran et al.[3.1.4-3)], Kew and Cornwell[3.1.4-4)], Bao et al.[3.1.4-5)], Kuwahara et al.[3.1.4-6)], Sumith et al.[3.1.4-7)], Saitoh et al.[3.1.4-8)], Yamashita et al.[3.1.4-9)], Miyata et al.[3.1.4-10), 3.1.4-11)], Li et al.[3.1.4-12)], and Enoki et al.[3.1.4-13).]

Fig. 3.1.4-1 presents the accuracies of the nine formulas (the references are from [3.1.4-14)] to [3.1.4-22)]), with the exception of that by Enoki et al., and Fig. 3.1.4-2 presents the accuracies obtained by Enoki et al.[3.1.4-23)] with the experimental values on the horizontal axis, and the calculation results of each study on the vertical axis.

The accuracies of the correlations for the prediction of heat transfer were characterized as follows: the calculated values were lower than the 45° diagonal line, which indicates 100% accuracy. In particular, the calculated values were lower than the experimental results because the increase in heat-transfer coefficient caused by the thin liquid film was not considered.

Fig. 3.1.4-2 presents the accuracy obtained by Enoki et al. from the University of Electro-Communications (the representative of the subcontracted research), which was significantly higher than those of the other formulae. This may be because of the addition of the heat conduction evaporation term of the liquid film proposed by Miyata et al. as a linear sum based on recent observations of refrigerants and flow phases specific to horizontal flow.

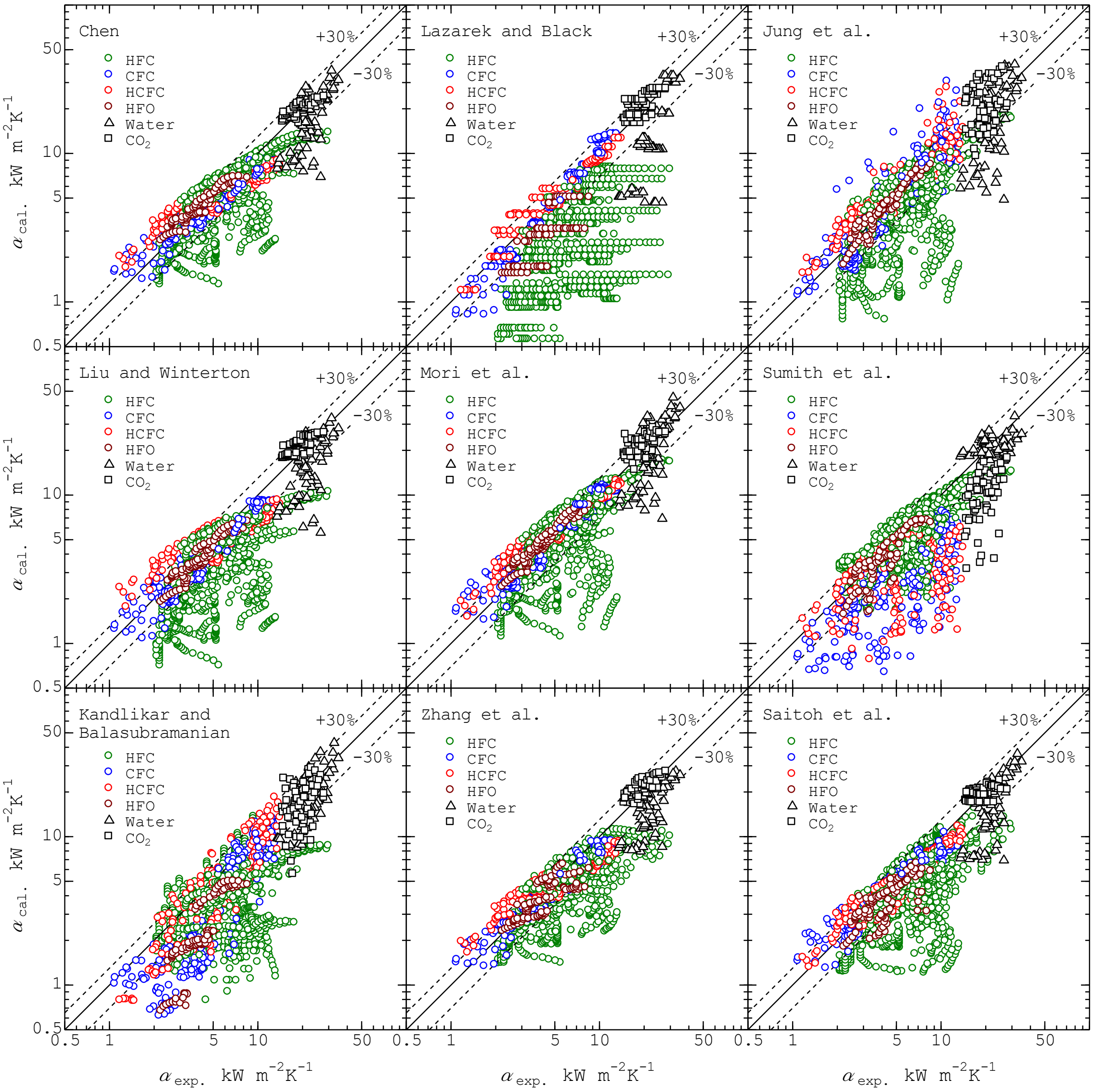

Fig. 3.1.4-1 Accuracy of boiling heat transfer coefficient predictions for data from nine researchers, excluding Enoki et al.

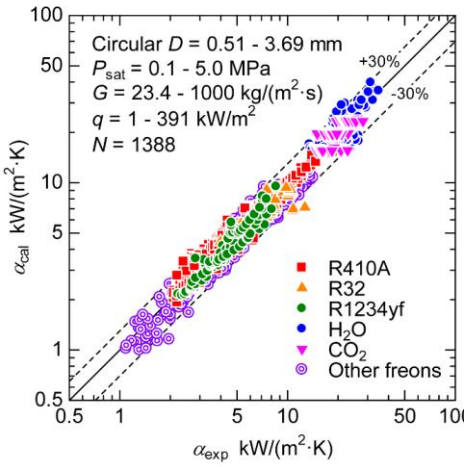

Fig. 3.1.4-2 Accuracy of boiling heat transfer coefficient prediction by Enoki et al.

Notably, these equations apply only to circular flow paths and not to rectangular flow paths, as observed in recent heat transfer tubes. Furthermore, if complex boiling phenomena caused by mixed refrigerants are considered in future research, changes in the local properties of the heat transfer surface will represent a major problem with respect to the development of heat exchangers for microchannel tubes with evaporative heat transfer, as there is no general formula that can be applied to any heat transfer tube shape or refrigerant. In particular, there is currently no formula that can be used in the heat exchangers of RAC equipment.

In this project, the following study was conducted to provide a clear method for the optimal design of heat exchangers, which is of utmost importance. The University of Electro-Communications (i.e., the subcontractor) previously examined whether phase-change heat transfer can be predicted using artificial intelligence (AI). Therefore, it was considered possible. However, because of the black-box nature of the method, we proposed a novel method devised during this time-period (3.1.4.1).

A prediction model for frictional pressure loss was developed. Furthermore, we proposed a method for constructing a machine learning model that achieves a higher accuracy than individual predictions by combining it with phase-change heat transfer data. Thereafter, we visualized the deep-learning model (3.1.4.2).

3.1.4.1 Prediction of boiling heat transfer coefficients for mini channels

In recent years, heat transfer in mini channels with internal diameters of 1–4 mm was studied with respect to several applications such as refrigeration, air conditioning, radiators, heat pipes for electronics, heat radiation in space, and heart-lung machines. In particular, in the refrigeration and air conditioning field, several studies were conducted on heat transfer in mini-channels owing to their capacity to considerably improve heat transfer efficiency. In addition, mini-channels render the heat exchanger compact, and aid in reducing the amount of refrigerants that negatively influence the global environment. This improvement can be attributed to the heat transmission phenomena that occur in mini channels. Heat transfer in mini channels includes forced convection evaporation, in addition to nucleate boiling, which is similar to that in normal channels. The use of thin channels leads to the promotion of liquid film-conductive evaporation with an increase in the effect of surface tension. Subsequently, the thickness of the liquid film (which causes thermal resistance) around the gas plug decreases in the area where slag flow occurs.

Although mini channels provide numerous advantages, as previously described, the prediction of their heat transfer coefficients is extremely difficult because the heat transfer area during liquid film-conductive evaporation varies based on changes in the gas plug, flow condition, and flow direction with respect to the flow amount and quality.

We previously proposed equations for predicting the heat transfer coefficients of mini channels. These equations can predict the heat-transfer coefficients with a higher accuracy than those proposed in existing studies. However, the improvement of the prediction accuracy is critical.

Given ample data for heat transfer obtained under various conditions, AI technologies can be used as an alternative method for the prediction of heat transfer coefficients. Numerous research fields and actual applications such as image recognition and natural language processing use AI technologies for prediction tasks. However, with reference to the available literature, our previous study represents the first report of the application of deep learning, which can be referred to as deep neural networks (DNNs), to multiphase flow and the prediction of heat transfer coefficients, regardless of single-phase flow or vapor–liquid two-phase flow. We are currently solving various thermal engineering and informatics issues, including multiphase flow. This research area is referred to as "thermoinformatics," which is a new field that combines thermal engineering and informatics.

In the previous study, we demonstrated the capacity of deep learning to predict heat transfer coefficients with a relatively high accuracy. However, the prediction accuracy can be further improved. Moreover, although values such as heat transfer coefficients can be predicted, deep learning does not return the uncertainties of the predicted values, and may therefore provide significantly different predicted values. In such cases, the use of mini channels negatively influences the heat-transfer efficiency. Therefore, a method is required to predict heat transfer coefficients, regardless of the inner diameter of the tube, channel geometry, refrigerant, and flow direction. However, the aim of this study was to investigate the basic horizontal flow for circular mini channels.

Herein, we combined deep learning and Gaussian process regression (GPR) to predict the heat-transfer coefficients and corresponding uncertainties based on their variances. The proposed system reiterates the training and prediction phases. Moreover, the proposed system yields a predicted heat-transfer coefficient and its uncertainty in each prediction phase. Finally, based on the uncertainties, the system generates a final predicted heat-transfer coefficient that minimizes the expectation of the prediction error and its uncertainty.

(1) Preliminaries

(a) Deep neural networks (DNN)

Although there are several existing machine-learning algorithms, neural networks such as DNNs have attracted considerable attention in various research areas. For example, DNNs can estimate potential diseases or risk factors based on the status of patients or the river stage, and can be used for image analysis. However, no research was conducted on the use of DNNs for the prediction of heat-transfer coefficients, with the exception of our previous study.

Fig. 3.1.4-3 illustrates the calculation process of each node in a DNN during the prediction of the heat transfer coefficients, and Fig. 3.1.4-4 depicts the overall structure. Let $L^{(l)}$ represent the lth layer of the DNN.

The input layer is $L^{(0)}$ and the output layer is $L^{(\mathcal{L})}$; thus, the DNN has $\mathcal{L}+1$ layers.

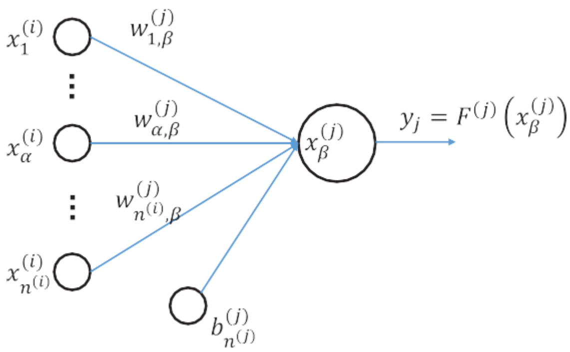

Fig. 3.1.4-3 Calculation process of a node

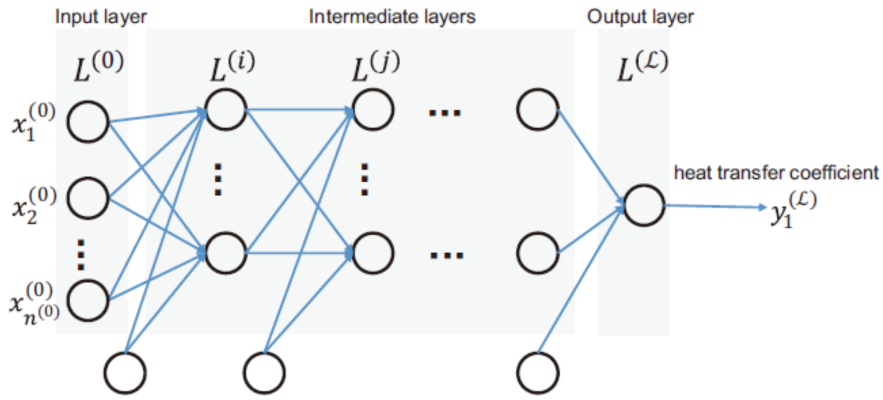

Fig. 3.1.4-4 Overall structure of deep neural networks

Let $N_i^{(l)}$ represent the ith node of Layer $L^{(l)}$, and let $n^{(l)}$ represent the number of nodes in layer $L^{(l)}$. Layer $L^{(l)}$ contains Nodes $N_1^{(l)}, N_2^{(l)}, \dots, N_{n^{(l)}}^{(l)}$. Let $\mathrm{w}_{\mathrm{ij}}^{(\mathrm{l})}$ represent the weight between Nodes $\mathrm{N}_{\mathrm{i}}^{(\mathrm{l-1})}$ and $\mathrm{N}_{\mathrm{j}}^{(\mathrm{j})}$, and $\mathrm{b}_{\mathrm{j}}^{(\mathrm{l})}$ represent the bias connected to Node $\mathrm{N}_{\mathrm{j}}^{(\mathrm{l})}$.

Nodes of Layer $L^{(l)}$ share an activation function $\mathrm{F}^{(\mathrm{l})}$. The input and output values of Node $\mathrm{N}_{\mathrm{i}}^{(\mathrm{l})}$ are $\mathrm{x}_{\mathrm{i}}^{(\mathrm{l})}$ and $\mathrm{y}_{\mathrm{i}}^{(\mathrm{l})}$, respectively. The values are calculated as follows:

$$\mathrm{x}_{\mathrm{i}}^{(\mathrm{l})} = \sum_{j=1}^{n^{l-1}} y_j^{l-1} w_{ji}^{(l)} + b_i^{(l)}, \tag{3.1.4-1}$$

$$\mathrm{y}_{\mathrm{i}}^{(\mathrm{l})} = F^{(l)}(x_i^{(l)}). \tag{3.1.4-2}$$

We use $\mathrm{y}^{(\mathcal{L})}$ (not $\mathrm{y}_1^{(\mathcal{L})}$) as the output of the final DNN layer because the DNN predicting the heat-transfer coefficients contains only one node in its final layer. Let t represent the target value of $\mathrm{y}^{(\mathcal{L})}$ (i.e., the ground truth value of the heat transfer coefficient) and let E represent the loss function. Notably, E receives $\mathrm{y}^{(\mathcal{L})}$ and t as arguments and returns the error value between them.

Based on the inputs of the DNN $(\mathrm{x}_1^{(0)}, x_2^{(0)}, \dots, x_{n^{(0)}}^{(0)})$ and the value of the error $(\mathrm{E}(\mathrm{y}^{(\mathcal{L})}, \mathrm{t}))$, the DNN updates all the weights and biases. There are several existing optimization algorithms, such as the stochastic gradient descent, MomentumSGD, and Adam optimizer.

(b) Gaussian Process Regression

Gaussian process regression is a fully probabilistic model used in various research fields. Moreover, GPR can be used for supervised learning. It receives x as its input and returns y = f(x) as its output. The objective of GPR is to generate accurate f (x) values. Moreover, GPR can return the corresponding uncertainty of the predicted value.

For example, we assumed an underlying true function, as follows:

$$\mathrm{y} = \mathrm{x} + \sin(5 * \mathrm{x}) \tag{3.1.4-3}$$

Sample data were obtained from the function with noise underlying a normal distribution and a standard deviation of 0.2. Figure 3.1.4-5 depicts the true function and sampled data.

Gaussian process regression approaches the true function based on sampled data (i.e., training data). Figure 3.1.4-6 presents an example of the GPR output. In the figure, "mean" represents the predicted value, and "confidence" represents the 95% confidence of the prediction. The confidence width was narrow when the prediction points were close to the training data, and wide when the prediction points were far from the training data.

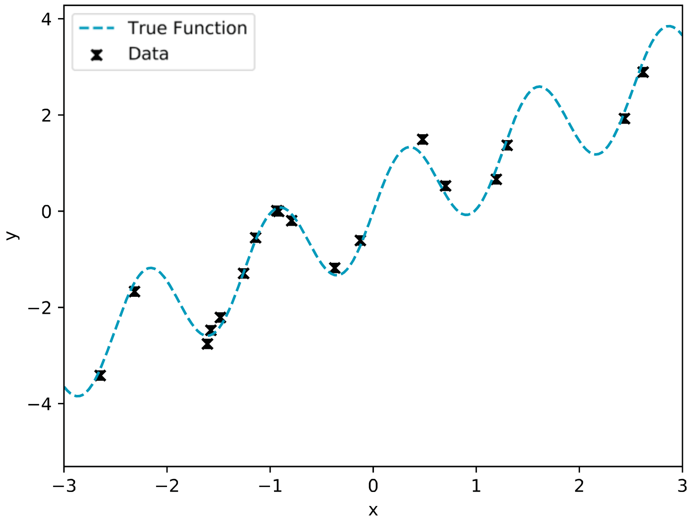

Fig. 3.1.4-5 Example of a true function [y = x + sin(5 ∗ x)] and training data [x + sin(5 ∗ x) + N (0, 0.22)]

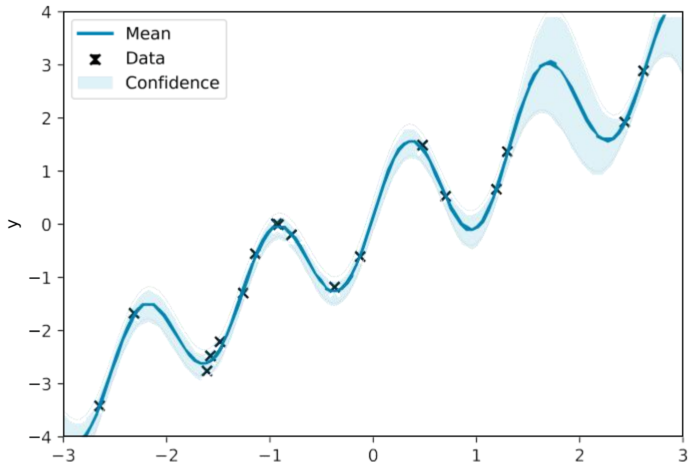

Fig. 3.1.4-6 The GPR output (prediction mean and 95% confidence) and training data.

(2) Databases and methods

(a) Databases

Databases containing horizontal flow data were used. Table 3.1.4-2 presents a summary of the databases, including the five experimental conditions.

(b) Physical Properties

We used the 16 physical properties listed in Table 3.1.4-3, which are considered to influence heat transfer. Table 3.1.4-3 presents the maximum, minimum, and average values of each physical property. The value ranges of these physical properties are wide. Therefore, these databases were considered appropriate for the evaluation of the proposed algorithm. The physical property values were calculated using REFPROP Ver. 10.0, as provided by the National Institute of Standards and Technology.

(c) Method

Figure 3.1.4-7 depicts the overall architecture of the proposed system. The system comprises two phases: the training phase and the prediction phase (see Figs. 3.1.4-8 and 3.1.4-9). In the training phase, the architecture learns a prediction function f(x), where x represents five experimental conditions and 16 physical properties, and f(x) returns the predicted heat-transfer coefficient and its corresponding uncertainty. In the prediction phase, the system outputs the predicted heat-transfer coefficient and its corresponding uncertainty based on the target input x*.

The training phase involves two steps. In the first step, the DNN is trained using the training data. The training data comprises the physical conditions, experimental conditions, and corresponding heat-transfer coefficients. The training data $X = \{x_1, x_2, \ldots, x_n\}$ should be standardized owing to the significant difference between the value ranges of each condition (see Tables 3.1.4-2 and 3.1.4-3), which leads to the low accuracy of the machine learning algorithms. Let x_i represent the ith sample of the training dataset, where x_i comprises 21 conditions (16 physical conditions and five experimental conditions), and x_{ij} represent the value of the jth condition for the ith sample. For each i and j, the following is calculated:

$$x'_{ij} \leftarrow \frac{x_{ij} - Mean(\{x_{1j},\ldots,x_{nj}\})}{Std(\{x_{1j},\ldots,x_{nj}\})}, \tag{3.1.4-4}$$

where Mean(·) and Std(·) represent the mean and standard deviation, respectively.

Table 3.1.4-2 Experimental conditions (quality, saturation pressure, inner diameter, mass flux, and heat flux) of data points obtained from existing studies on mini channels

Source	Fluid	Quality	Saturation Pressure MPa	Inside Diameter mm	Mass Flux $kg \cdot m^{-2} \cdot s^{-1}$	Heat Flux $kW \cdot m^{-2}$	N
3.1.4-1)	R113	0.01–0.71	0.12–0.16	2.92	50–300	8.8–90.8	72
3.1.4-3)	R12	0.20–0.77	0.83	2.46	66.3–300	7.5–59.4	59
3.1.4-4)	R141b	0.00–0.90	0.10	2.87, 3.69	188, 212	9.7–90	67
3.1.4-5)	R11	0.01–0.64	0.29–0.47	1.95	167–560	52–125	81
	R123	0.01–0.68	0.35–0.51	1.95	167–452	39–125	80
3.1.4-6)	R134a	0.01–0.66	0.88	0.84	525	15.6	15
3.1.4-8)	R134a	0.22–0.91	0.41	0.51, 1.12, 3.1	150,300	12–29	75
3.1.4-9)	CO_2	0.01–0.85	5.00	1.02	300–1000	30–50	62
3.1.4-12)	R32	0.28–0.86	1.28	2.00	200	4–24	44
	R1234yf	0.22–0.92	0.51	2.00	100–400	6–24	91
3.1.4-13)	R410A	0.05–0.95	1.09	1.00	30–400	2-24	287
3.1.4-24)	NH_3	0.03–0.78	0.43	1.00	100	20	132
3.1.4-25)	R32	0.13–0.65	1.28	2.00	300	10	14
3.1.4-26)	R1234ze(E)	0.11-0.74	0.31	4.00	200	20	15
3.1.4-27)	R600a	0.06–0.26	0.55	1.10	400	35	5
	R1234ze(E)	0.04–0.29	0.60	1.10	500	25–35	12
						Total	1111

Table 3.1.4-3 Physical properties used for deep learning and their maximum, minimum, and average values

	Saturation temperature, T_{sat} (K)	Critical pressure, P_{crit} (MPa)	Critical temperature, T_{crit} (K)	Vapor density, ρ_V (kg m^{-3})	Liquid density, ρ_L (kg m^{-3})	Ratio of V-L density, ρ_V/ρ_L	Vapor viscosity, μ_V (μPa s)	Liquid viscosity, μ_L (μPa s)
Max	354.74	11.33	487.21	156.67	1492.63	189.38×10^{-3}	16.81	469.23
Min	273.15	3.38	304.13	3.46	529.87	3.97×10^{-3}	7.94	75.6
Ave.	298.22	5.32	392.11	33.55	1122.75	32.05×10^{-3}	11.75	203.81

	Vapor thermal conductivity, λ_V (mW m^{-1} K^{-1})	Liquid thermal conductivity, λ_L (mW m^{-1} K^{-1})	Specific heat at const. p, Cp_L (J kg^{-1} K^{-1})	Specific Heat at Const. Vol., Cv_L (J kg^{-1} K^{-1})	Surface tension, σ (mN m^{-1})	Latent heat, Δhv (kJ kg^{-1})	Thermal diffusivity, α_L (m^2 s^{-1})	Prandtl number, Pr_L
Max	27.32	559.20	4616.54	2800.29	26.30	1262.24	18.97×10^{-8}	6.71
Min	9.83	62.26	918.02	610.63	2.07	133.73	3.34×10^{-8}	1.40
Ave.	14.42	141.41	1839.56	1070.40	11.18	314.49	6.82×10^{-8}	3.11

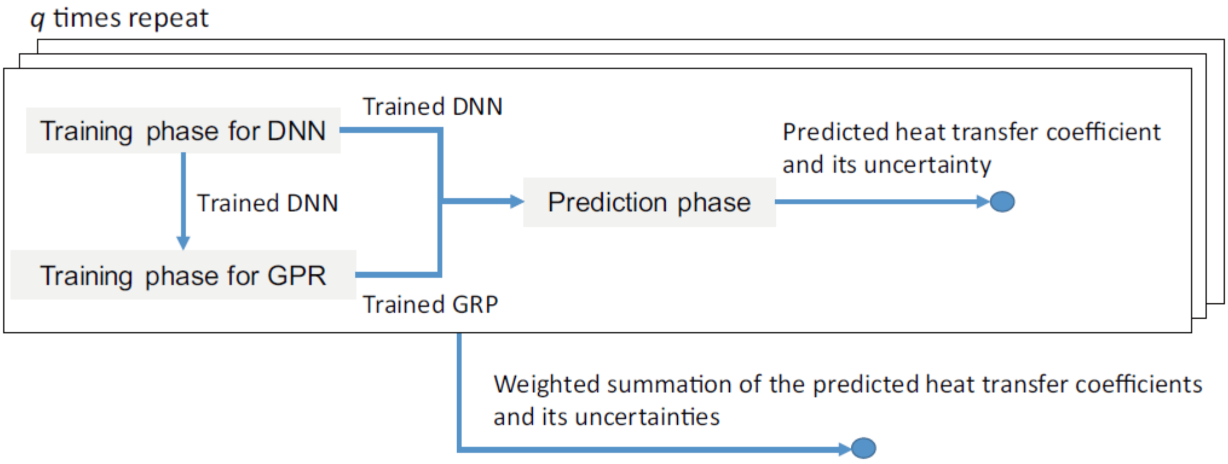

Fig. 3.1.4-7 Overall architecture

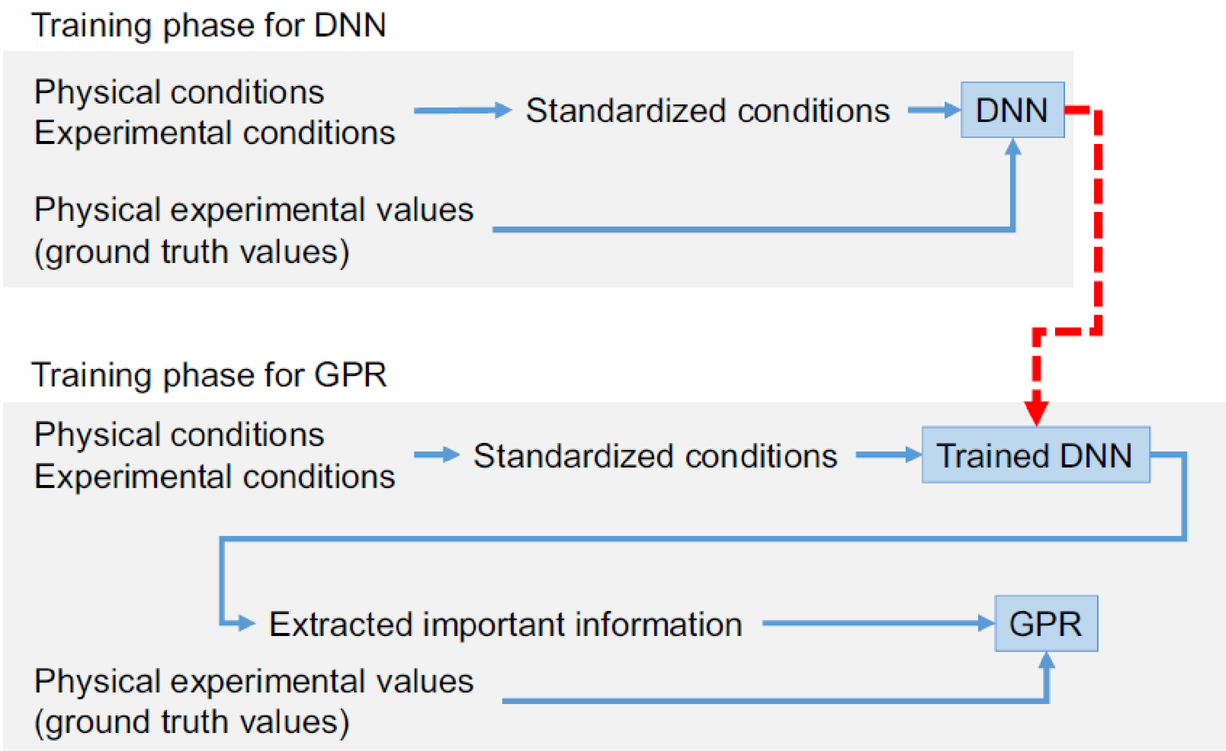

Fig. 3.1.4-8 Training phase

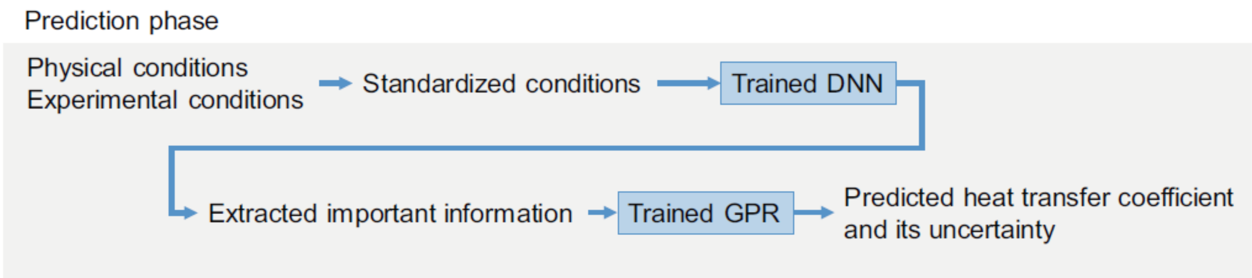

Fig. 3.1.4-9 Prediction phase

Let $\hat{X}$ represent the standardized training data set, that is, $\hat{X} = \{\widehat{x_1}, \widehat{x_2}, \dots, \widehat{x_n}\}$, where $\widehat{x_i} = \{\widehat{x_{i,1}}, \widehat{x_{i,2}}, \dots, \widehat{x_{i,21}}\}$.

In the second step of the training phase, the GPR is trained based on the output of layer $L^{\mathcal{L}-1}$ of the DNN and the corresponding heat-transfer coefficient y. Instead of the final output value of the DNN, the $y^{\mathcal{L}-1}$ value of the DNN is used. The DNN processes the original input into a different parameter space $y^{\mathcal{L}-1}$, such that the correlation with the heat transfer coefficient is simpler. In particular, the hidden layer immediately before the DNN output contains compressed information that can accurately predict the heat-transfer coefficient. Therefore, by transferring this information to the GPR, the prediction accuracy is improved.

In the prediction phase, the samples for which the heat transfer coefficients should be determined, that is, $X^* = \{x_1^*, \dots, x_m^*\}$, are first standardized based on the following:

$$\widehat{x_{ij}^*} \leftarrow \frac{\left(x_{ij}^* - Mean(\{x_{1j}, \dots, x_{nj}\})\right)}{\left(Std(\{x_{1j}, \dots, x_{nj}\})\right)} \tag{3.1.4-5}$$

The values of $Mean(\{x_{1j}, \dots, x_{nj}\})$ and $Std(\{x_{1j}, \dots, x_{nj}\})$ for each j in Equation (3.1.4.2) are the same as those in Equation (3.1.4.1) in the training phase. Subsequently, $y^{\mathcal{L}-1}$ of the DNN is obtained based on the standardized samples. The GPR yields the predicted heat-transfer coefficients and corresponding uncertainties of the target samples based on $y^{\mathcal{L}-1}$. The training and prediction phases are repeated q times, where q is a pre-defined hyperparameter.

Finally, we integrate the results of q. However, the results may exhibit different uncertainties. Therefore, a weighted summation of the results is executed by considering the uncertainties.

Under the assumption that the difference between the true value of the ith sample (represented by t_i) and the predicted value of the ith sample in the jth turn (represented by y_{ij}) is in accordance with a normal distribution, the probability of the predicted value becoming y_{ij} is represented by the following:

$$\mathrm{p}(\mathrm{y_{ij}}) = \frac{1}{\sqrt{2\pi v_{ij}}} \exp\left(-\frac{1}{2v_{ij}}(t_i - y_{ij})^2\right) \tag{3.1.4-6}$$

where v_{ij} represents the variance of the normal distribution of the i^{th} sample at the j^{th} turn.

The probability of obtaining y_{ij} for $j = 1, \dots, q$ is represented by the following:

$$\prod_{\mathrm{j=1}}^{\mathrm{q}} p(y_{ij}) = (\prod_{j=1}^{q} \frac{1}{\sqrt{2\pi v_{ij}}}) \exp\left[-\sum_{j=1}^{q} \frac{1}{2v_{ij}}(t_i - y_{ij})^2\right] \tag{3.1.4-7}$$

The value of t_{i} that maximizes Equation (3.1.4-7) is the most probable value. When the following equation is satisfied, Equation (3.1.4-7) is maximized.

$$\sum_{\mathrm{j=1}}^{\mathrm{q}} \frac{1}{2v_{ij}}(t_i - y_{ij}) = 0 \tag{3.1.4-8}$$

Let $\widehat{y_i}$ represent the most probable value of $\mathrm{t_i}$ that maximizes Equation (3.1.4-7). In this case, the following is obtained:

$$\widehat{y_i} \leftarrow (\sum_{j=1}^{q} \frac{y_{ij}}{v_{ij}}) / \sum_{j=1}^{q} \frac{1}{v_{ij}}. \tag{3.1.4-9}$$

The resulting variance is obtained based on the propagation of the error formula. Consider the function $\mathrm{z} = \mathrm{f}(\mathrm{t_1}, \mathrm{t_2}, \dots, \mathrm{t_q})$, where the variance of $\mathrm{t_j}$ is $\mathrm{v_j}$. The variance $v(z)$ of z is represented by

$$\mathrm{v(z)} = \sum_{\mathrm{j=1}}^{\mathrm{q}} \left(\frac{\partial \mathrm{z}}{\partial \mathrm{t_j}}\right)^2 v_j. \tag{3.1.4-10}$$

Therefore, the following can be obtained:

$$\widehat{v_i} \leftarrow \frac{1}{\sum_{j=1}^{q} \frac{1}{v_{ij}}}. \tag{3.1.4-11}$$

The DNN model comprises four intermediate layers, each containing 20 nodes. The activation function is a rectified linear unit (ReLU), which is represented by $\mathrm{F}^{(\mathrm{l})}(x_i^{(l)}) = \max(0, x_i^{(l)})$, and the learning optimization algorithm is an Adam optimizer. With respect to the parameters of the Adam optimizer, we set the learning rate as 0.001; exponential decay rates for the moment estimates β_1 and β_2 as 0.9 and 0.999, respectively; ϵ as e^{-7}, where e represents the base of the natural logarithm; and the weight decay as 0.0.

The loss function is defined as follows:

$$\frac{1}{\mathrm{B}} \sum_i \left(\frac{\widehat{y_i} - t_i}{t_i}\right)^2, \tag{3.1.4-11}$$

where B represents the DNN batch size, and $\widehat{y_i}$ and $\mathrm{t_i}$ represent the predicted heat-transfer coefficient and true value of the i-th target sample, respectively.

We set the number of epochs as 200, batch size (B) as 10 and repeat time (q) as 10. The GPR kernel function combines the Gaussian kernel and bias kernel.

Algorithm 3.1.4.1 illustrates the procedure of the proposed system.

Algorithm 3.1.4.1 Prediction of heat transfer coefficients of target samples

Input: Training data set $X = \{x_1, \ldots, x_n\}$, corresponding heat transfer coefficient $y = \{y_1, \ldots, y_n\}$, target samples $T = \{t_1, \ldots, t_m\}$
Output: Predicted heat transfer coefficients $\hat{Y} = \{\hat{y_1}, \ldots, \hat{y_m}\}$ and corresponding uncertainty $\hat{V} = \{\hat{v_1}, \ldots, \hat{v_m}\}$
/** Standardization */
for $j = 1, \ldots, 21$ **do**
  for $i = 1, \ldots, n$ **do**
    $x'_{ij} \leftarrow \dfrac{x_{ij} - \text{Mean}(\{x_{1j}, \ldots, x_{nj}\})}{\text{Std}(\{x_{1j}, \ldots, x_{nj}\})}$.
  end for
  for $i = 1, \ldots, m$ **do**
    $t'_{ij} \leftarrow \dfrac{t_{ij} - \text{Mean}(\{x_{1j}, \ldots, x_{nj}\})}{\text{Std}(\{x_{1j}, \ldots, x_{nj}\})}$.
  end for
end for
Create an empty array y_s and v_s.
for $i = 1, \ldots, q$ **do**
  Initialize and train the DNN model M_{D} based on $\acute{X}$ and y.
  Initialize and train the GPR model M_{G} based on M_{D} output of layer $(\mathcal{L}-1, \acute{X})$ and y.
  y_{pred} and $v_{\text{pred}} \leftarrow M_{\text{G}}$ predict $(M_{\text{D}}$ output of layer $(\mathcal{L}-1, \acute{T}))$
  Substitute y_{pred} and v_{pred} in y_s and v_s, respectively.
end for
for $i = 1, \ldots, m$ **do**
  $\hat{y_i} \leftarrow$ Eq. (13) using y_s and v_s.
  $\hat{v_i} \leftarrow$ Eq. (15) using v_s.
end for
return $\hat{Y}$ and $\hat{V}$

(3) Evaluation

We assume that there are N samples of test data. Let α_i^{cal} and α_i^{exp} represent the ith estimated value calculated using the proposed algorithm and the ith experimental value (i.e., the ground truth value in this evaluation) of the boiling heat transfer, respectively. Furthermore, we can consider SD as a utility metric, which is expressed as follows:

$$\text{SD} = \sqrt{\frac{1}{N}\sum_i^N \left(\frac{\alpha_i^{cal} - \alpha_i^{\exp}}{\alpha_i^{\exp}}\right)^2}. \qquad (3.1.4\text{-}12)$$

A 10-cross validation was conducted in this study, that is, we randomly divided the 1111 samples into 10 datasets, where d_i represents the ith dataset ($i = 1, \ldots, 10$). The proposed method learned a prediction model from nine datasets (training dataset containing 999 or 1000 samples) and predicted the heat transfer coefficients for the remaining datasets (test dataset that contains 111 or 112 samples). This process was repeated ten times by varying the training and test datasets. For example, in the first round, the training dataset represented the set of $d_2, \ldots, d_{10}$ and the test dataset represented d_1; in the second round, the training dataset represented the set of $d_1, d_3, \ldots, d_{10}$ and the test dataset represented d_2, etc.

The relationships between the physical experimental values (i.e., the ground truth value) α^{exp} and the predicted values α^{cal} are illustrated in Fig. 3.1.4-10, which depicts the prediction accuracies obtained using the equations proposed by Enoki et al. (2015), Saitoh et al. (2007), and Zhang et al. (2004). The prediction accuracy predicted by the DNN (Enoki et al., 2017) is shown in Fig. 3.1.4-10. The DNN parameters were set as the same values as those used by Enoki et al. (2017). The equations proposed by Enoki et al. and Saitoh et al. demonstrated high generality; however, they could not comprehensively describe the management of NH_3. Therefore, we calculated the prediction values by adapting the Stephan–Abdelsalam equation for refrigerants (Stephan and Abdelsalam, 1980) to estimate the contribution of nucleate boiling, which is similar to that of CO_2.

In Fig. 3.1.4-10, the SD, in addition to R20 and R30, which represent the percentages by which the predicted values were within ± 20 and ± 30 of the ground truth, respectively, are depicted. Table 3.1.4-4 comprehensively presents the SD, R20, and R30 results. In Table 3.1.4-4, the most accurate values are italicized, and the second most accurate values are marked in bold. The SD values of the proposed method are the minimum from 15 of the 16 datasets. As can be seen from the figures, the proposed method outperformed the other prediction methods. Moreover, to confirm that the proposed system (which is based on a combination of DNN and GPR) can outperform the GPR-only system, we conducted the same experiment using GPR. The final SD, R20, and R30 results were 8.49, 96.6, and 99.5, respectively, which were poorer than those of the proposed and DNN-only systems (Enoki et al., 2017).

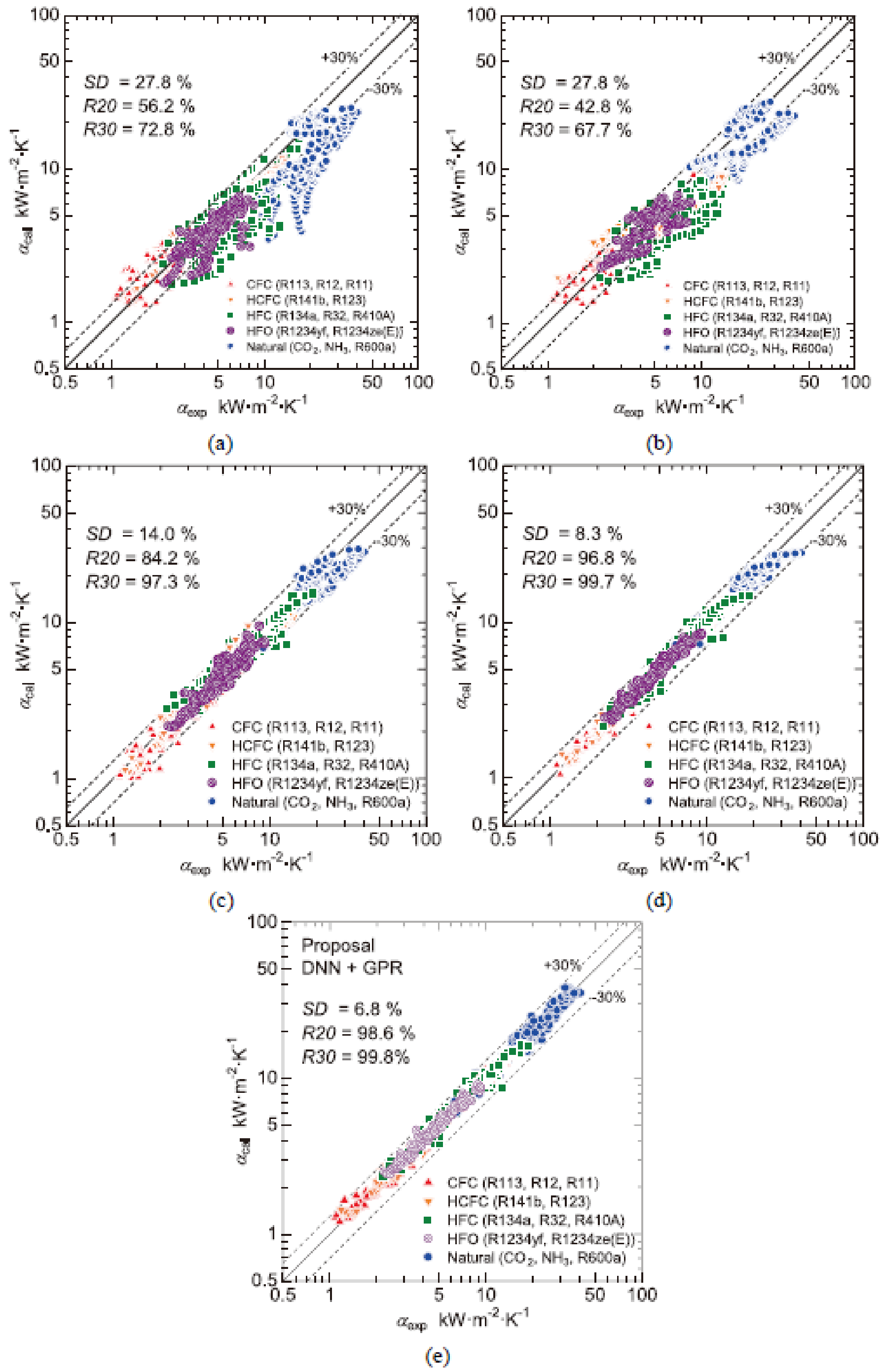

Fig. 3.1.4-10 Comparison of predictions and experimental data: (a) results obtained by Saitoh et al.[3.1.4-22], (b) Zhang et al.[3.1.4-21], (c) Enoki et al.[3.1.4-23], (d) Enoki et al.[3.1.4-28], and (e) the proposed method.

Table 3.1.4-4: The SD, R20, and R30 results

Source	No.	%	Zhang et al. (2004)	Saitoh et al. (2007)	Enoki et al. (2015)	Enoki et al. (2017)	Proposed System
Wambsganss		SD	21.1	27.1	17.7	8.6	8.4
2.92 mm	72	R20	55.6	55.6	68.1	95.8	98.6
R113		R30	83.3	75.0	94.4	100.0	98.6
Tran		SD	17.0	17.1	6.2	6.0	5.9
2.46 mm	59	R20	71.2	66.1	100.0	100.0	100.0
R12		R30	96.6	98.3	100.0	100.0	100.0
Kew		SD	32.7	22.8	15.6	8.0	6.7
2.87–3.69 mm	67	R20	35.8	62.7	82.1	95.5	98.5
R141b		R30	56.7	82.1	98.5	100.0	100.0
Bao		SD	25.1	21.1	15.8	4.7	4.7
1.95 m	81	R20	32.1	48.1	79.0	100.0	100.0
R11		R30	72.8	91.4	100.0	100.0	100.0
Bao		SD	27.6	15.1	16.7	4.0	4.0
1.95 mm	80	R20	25.0	86.3	71.3	100.0	100.0
R123		R30	67.5	96.3	100.0	100.0	100.0
Kuwahara		SD	24.3	27.2	23.4	9.6	9.2
0.84 mm	15	R20	53.3	33.3	26.7	100.0	93.3
R134a		R30	73.3	80.0	93.3	100.0	100.0
Saitoh		SD	18.8	18.8	10.9	5.8	5.1
0.51–3.1 mm	75	R20	73.3	76.0	93.3	100.0	98.7
R134a		R30	85.3	89.3	100.0	100.0	100.0
Yamashita		SD	16.0	13.7	12.3	11.3	9.9
1.02 mm	62	R20	74.2	87.1	90.3	93.5	93.5
CO2		R30	95.2	96.8	96.8	100.0	100.0
Li		SD	22.8	35.5	14.6	12.8	11.3
2 mm	44	R20	59.1	40.9	90.9	96.9	93.2
R32		R30	81.8	52.3	93.2	95.5	97.7
Li		SD	19.3	22.9	11.9	5.6	4.8
2 mm	91	R20	65.9	68.1	91.2	98.9	100.0
R1234yf		R30	84.6	78.0	100.0	100.0	100.0
Enoki		SD	34.9	28.5	9.3	7.8	5.5
1 mm	287	R20	22.3	58.2	97.2	96.9	99.0
R410A		R30	50.5	70.0	99.7	100.0	100.0
Yokoyama		SD	30.9	47.8	18.9	11.8	8.3
2 mm	132	R20	31.8	0.0	65.9	92.4	99.2
NH3		R30	48.5	8.3	87.9	99.2	100.0
Wu		SD	44.6	13.1	17.2	8.5	5.8
2 mm	14	R20	0.0	85.7	78.6	92.9	100.0
R32		R30	0.0	100.0	85.7	100.0	100.0
Longo		SD	18.3	19.0	18.7	8.1	9.7
4 mm	15	R20	80.0	53.3	60.0	100.0	93.3
R1234ze		R30	86.7	100.0	100.0	100.0	100.0
Sempe´rtegui		SD	16.8	15.2	12.9	11.9	8.8
1.1 mm	5	R20	80.0	80.0	80.0	89.4	100.0
R600a		R30	100.0	100.0	100.0	100.0	100.0
Sempe´rtegui		SD	22.4	18.0	17.4	10.1	7.0
1.1 mm	12	R20	50.0	66.7	75.0	100.0	100.0
R1234ze(E)		R30	91.7	100.0	100.0	100.0	100.0
		SD	27.8	27.8	14.0	8.3	6.8
Total	1111	R20	42.8	56.2	84.2	96.8	98.6
		R30	67.7	72.8	97.3	99.7	99.8

Figure 3.1.4-11 depicts the relationship between the mean squared errors (MSEs) and variances outputted using the proposed method. The variances can be considered uncertainties. We categorized 1111 samples based on their variances and calculated the MSE of each category. The MSE increased as the variance increased. Moreover, a confidence range (where a is an arbitrary value ranging from 0–1) could be determined for each sample.

Thereafter, we conducted an additional experiment to better understand the relationship between variances and MSEs. We removed all samples from one dataset and used the remaining datasets as training data. Subsequently, we predicted the heat-transfer coefficients of the removed samples. In particular, the first system learned a prediction model based on all the datasets, except for the dataset from Wambsganss et al.[3.1.4-1)], and subsequently predicted the heat transfer coefficients for the dataset from Wambsganss et al.[3.1.4-1)] Thereafter, the system learned a prediction model based on all the datasets, except for the Tran et al.[3.1.4-3)] dataset, and then predicted the heat transfer coefficients for the Tran et al.[3.1.4-3)] dataset, etc. Given that the physical properties and experimental conditions of these datasets were significantly different, the prediction task was challenging. The results are shown in Fig. 3.1.4-12. The MSEs and variances (uncertainties) demonstrated strong correlations. The model trained without Yamashita et al.[3.1.4-9)] or Yokoyama et al.[3.1.4-24)] datasets yielded large errors and uncertainties in their dataset predictions. The former was the only dataset containing data on CO_2, whereas the latter was the only dataset containing data on NH_3. In particular, when the training data contained only the data that were significantly different from the data to be predicted, the prediction accuracy decreased.

The variance map reveals that more data are required to improve the data-driven heat transfer correlation, which will be experimentally verified in future research.

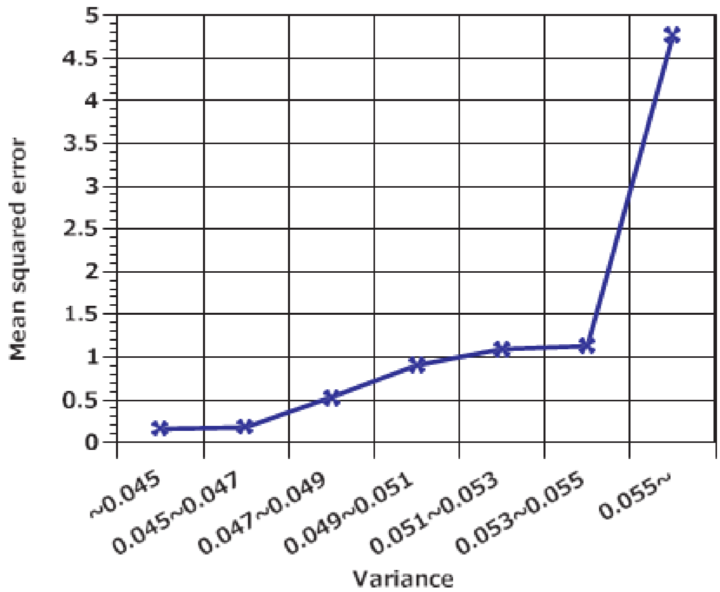

Fig. 3.1.4-11 Variance (uncertainty) with respect to the MSE

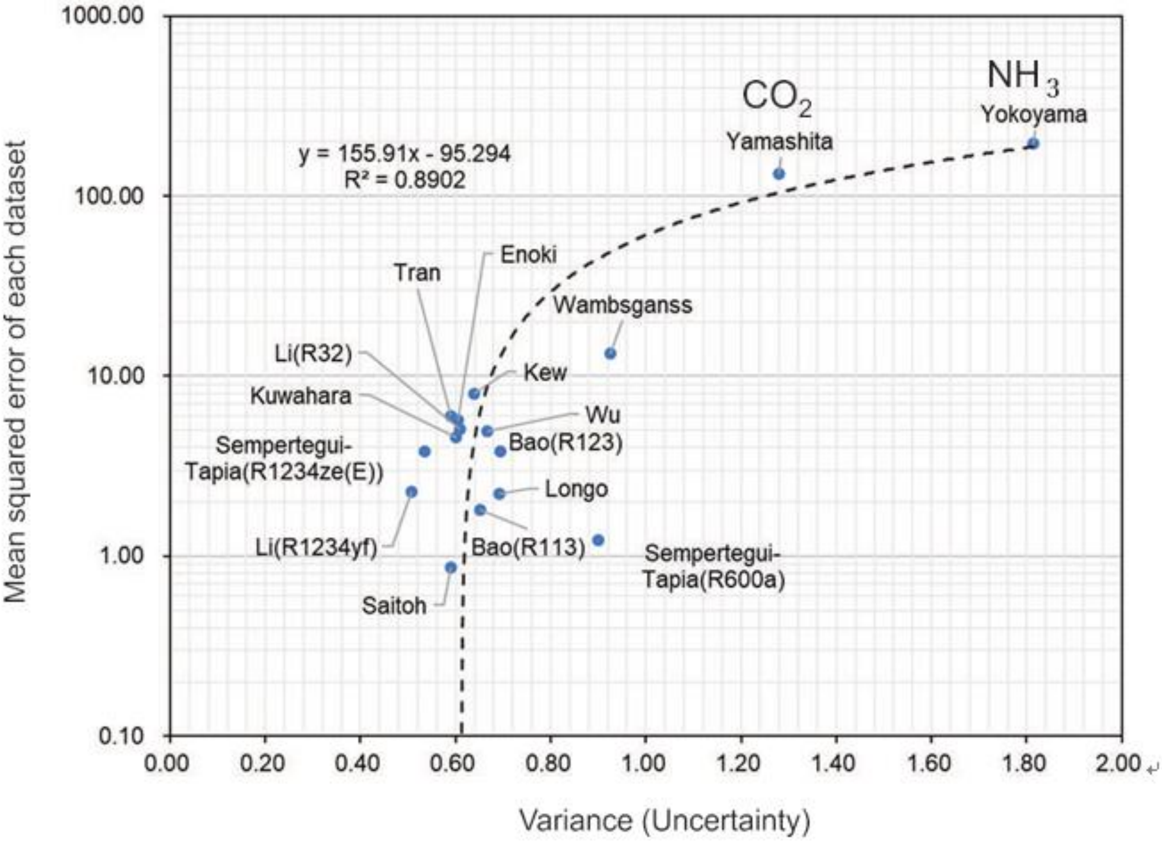

Fig. 3.1.4-12: Variance (uncertainty) with respect to the MSE, where all samples were removed in a training phase for each data set

(4) Discussion

(a) Learning Accuracy With Respect to Heat Transfer Characteristics

Figure 3.1.4-13 depicts the relationship between the heat transfer coefficients and quality with respect to the dataset obtained by the authors, which is a part of the dataset (Enoki et al.[3.1.4-23]). We validated the learning accuracy of the proposed method by comparing it with the physical experimental results and the equation proposed by Enoki et al.[3.1.4-23]. The predictions based on the equation proposed by Enoki et al.[3.1.4-23] and those based on the DNN (Enoki et al.[3.1.4-28]) and the proposed method were highly similar to the physical experimental values.

The heat transfer α in mini channels includes forced convection evaporation α_{fc} and nucleate boiling α_{nb}, which are similar to those in normal channels, in addition to liquid film-conductive evaporation α_{lf}, which is specific to mini channels. This relationship is defined as follows (Enoki et al.[3.1.4-23]):

$$\alpha = \alpha_{fc} + \alpha_{nb} + \alpha_{lf} \tag{3.1.4-13}$$

First, we examined the values predicted by the proposed method at G = 400 $kgm^{-2}s^{-1}$, which indicated that the mass flux (rate of mass flow per unit area) was large. The heat transfer coefficient increased with an increase in the heat flux and quality. However, when the heat flux was high and the quality was low, the heat-transfer coefficient was not influenced by the change in quality. The impact of heat flux on the heat-transfer coefficient decreased as the quality increased. The proposed method [and the equation proposed by Enoki et al. (2015)] reproduced these characteristics.

When the mass flux was small (G = 30 and 100 $kgm^{-2}s^{-1}$), effective heat transmission occurred (Enoki et al.[3.1.4-13), 3.1.4-29]; Miyata et al.[3.1.4-11]). When the quality was low and the heat flux was small (2 kW m^{-2}), the heat transfer coefficient of G = 30 $kgm^{-2}s^{-1}$ was the largest among the other settings of G. Based on this observation, we concluded that liquid film-conductive evaporation influences the heat-transfer coefficient. When G = 100 $kgm^{-2}s^{-1}$ and the heat flux was low, the heat-transfer coefficient decreased, given that the liquid film decreased in thickness when the flow condition changed from a slag flow to a wavy flow. The proposed method reproduced the effect caused by liquid film-conductive evaporation.

In particular, the derivation of an equation for the heat transfer coefficient, which exhibits complex variations with the flow rate, heat flux, and quality, is based on a substantial understanding of physical phenomena. However, considerable time is required to determine the effects and extent of these experimental conditions. Nevertheless, by using a credible database as the training data, the DNN and the proposed method were effective in realizing the above-mentioned complex heat-transfer mechanism.

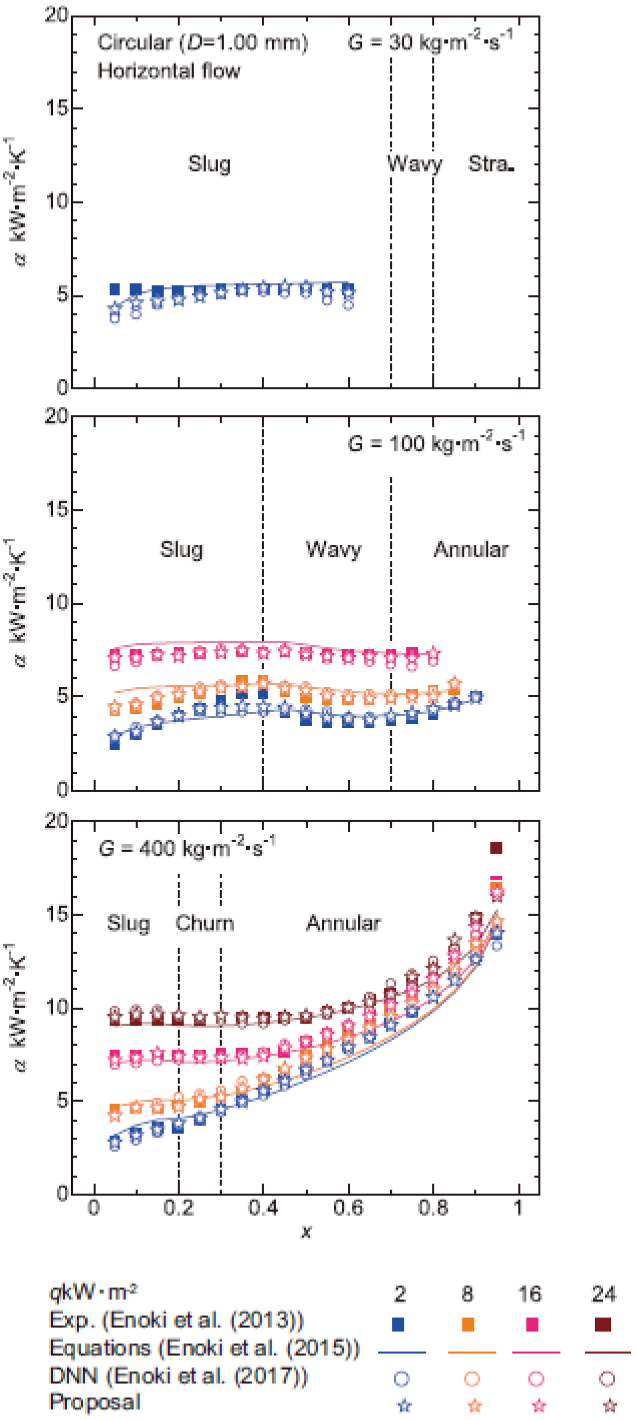

Fig. 3.1.4-13 The relationship between the heat transfer coefficients and quality

(b) Challenges of AI and Future Prospective

This study demonstrated that AI is a promising approach for the prediction of heat-transfer coefficients. However, this method has two major disadvantages. First, it is difficult for humans to understand the computation of the results obtained by the AI model. In contrast, the prediction equations proposed by Enoki et al.[3.1.4-23] can be rationalized. Therefore, prediction equations should be considered to understand the computation of the generated results. Second, the AI model may return impractical values when the input values differ significantly from the training data.

In the first case, several studies can provide an improved understanding of the behaviors of AI models. The findings of these studies will be combined in future research. In the second case, the proposed GPR method can mitigate this drawback. Gaussian process regression provides several advantages over general machine-learning algorithms. First, as previously indicated, GPR can be used to predict heat-transfer coefficients and uncertainties based on their variances. Therefore, a system using the proposed method can determine whether the predicted heat-transfer coefficients are accurate based on their uncertainties. Second, because of the uncertainties in the predicted values for each experimental condition, we can determine the optimal experimental conditions that increase the accuracy of the proposed method. For example, as shown in Fig. 3.1.4-12, the model generated relatively inaccurate predictions under the experimental conditions of the

Yamashita et al.[3.1.4-9] or Yokoyama et al.[3.1.4-24] data sets, as their uncertainties are large. This was confirmed because the dataset is publicly available, and the proposed method predicted the heat-transfer coefficients of the datasets. However, even if the dataset was not available, the accuracy of the predicted values can be determined based on the experimental conditions of the datasets. This is because the proposed model can yield uncertainties without true values of the heat-transfer coefficients.

We are currently developing hybrid prediction methods that can aid researchers in establishing a more general and accurate heat-transfer correlation using AI. Figure 3.1.4-12 depicts the reliability of developing a DNN with certain experimental data removed from the database, and predicting the experimental data removed using GPR. Figure 3.1.4-12 illustrates that a DNN constructed by removing CO_2 and NH_3 loses its reliability. These data are indispensable for the construction of a generalized heat transfer correlation.

To better understand the unreliability of the DNN when CO_2 and NH_3 were removed, we sorted them with respect to their vapor-to-liquid density ratio, which is a critical property in the investigation of phase-change heat transfer, as depicted in Fig. 3.1.4-14. The significantly high vapor-to-liquid density ratios of CO_2 and NH_3 played a critical role when compared with other datasets. By further analyzing this type of data through databasing and importing, improved formulae can be constructed. Furthermore, by conducting such an analysis of other physical properties, objective indices can be obtained using AI. This demonstrates an effective application of thermoinformatics, which is applicable to other fields of thermal engineering.

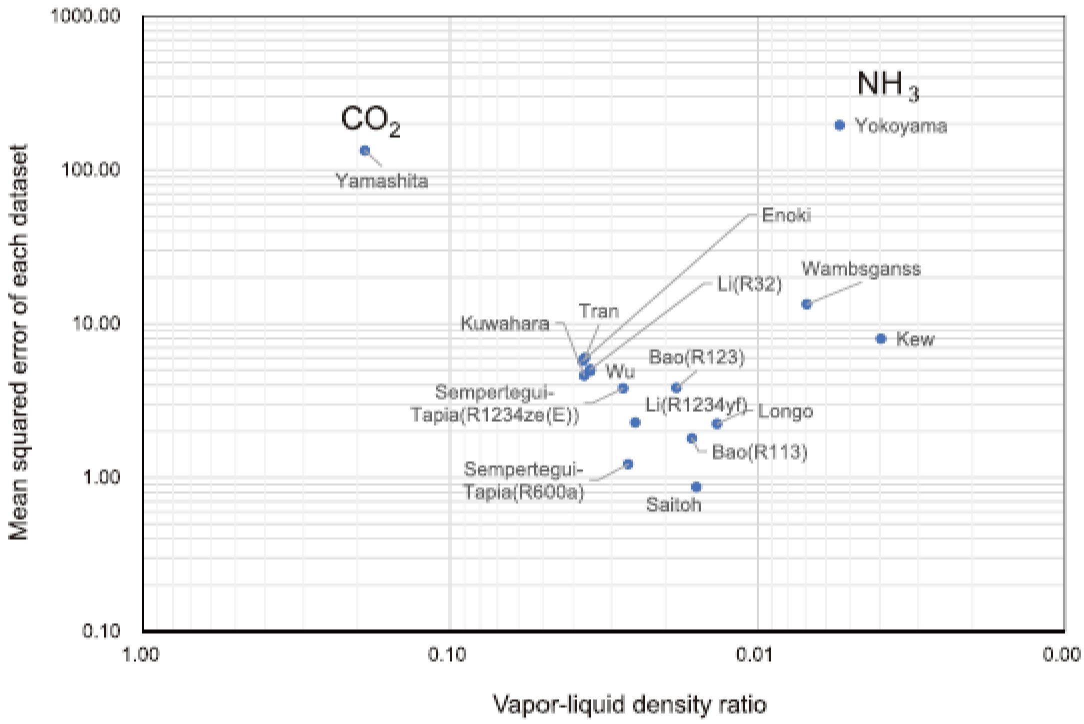

Fig. 3.1.4-14 Vapor-to-liquid density ratio with respect to the MSE, where all samples were removed for each data set in the training phase

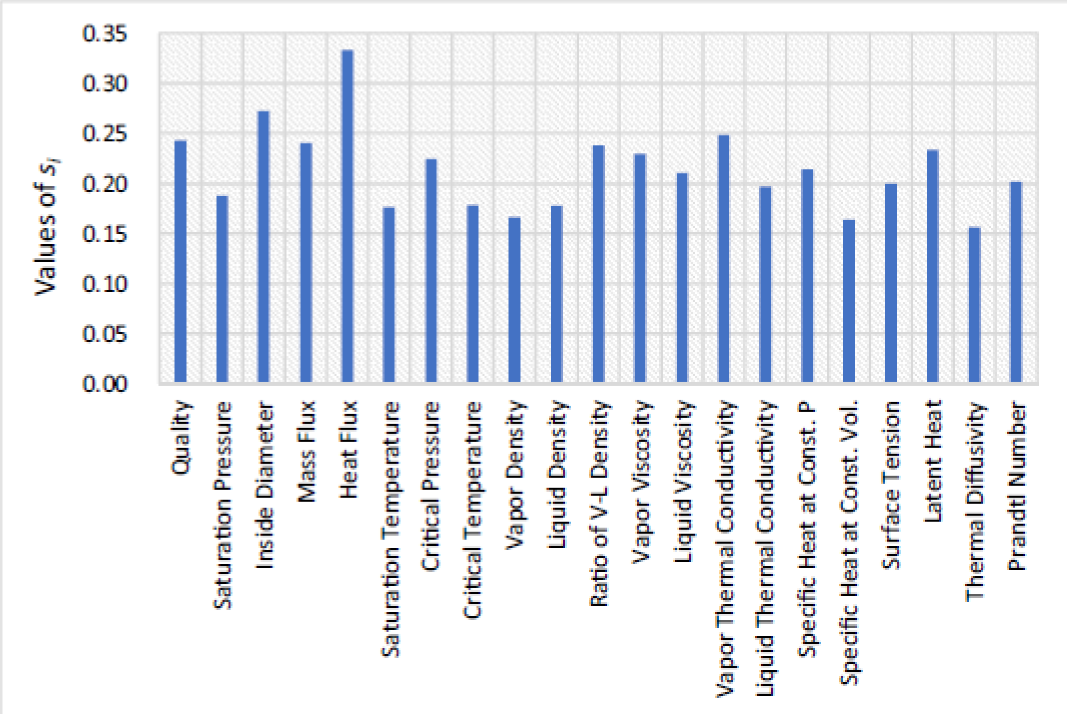

Fig. 3.1.4-15 Average absolute value of the weights connecting the first and second layers

(c) Analysis of DNN Weight Parameters

By analyzing the weight parameters that connect the first and second layers, the features of the data that have a significant influence on the prediction can be determined. For each feature, we calculated the average absolute values of the weights connecting the first and second layers using the following expression:

$$\mathrm{s_i} = \sum_{\mathrm{j=1}}^{\mathrm{n^{(l)}}} \left| w_{i,j}^{(l)} \right| \qquad (3.1.4.14)$$

Figure 3.1.4-15 presents these results. Figure 3.1.4-15 reveals that the quality, inner diameter, heat flux, the ratio of V–L density, and latent heat may be the most critical parameters for prediction. The vapor thermal conductivity was considerably high; however, because it is strongly correlated with the liquid thermal conductivity, further investigation should be conducted considering the physical mechanism. In future research, frameworks will be employed to better understand the computation of the DNN output results, such as LIME[3.1.4-30)] and SHAP[3.1.4-31)].

3.1.4.1.5 Conclusion

To promote thermoinformatics by combining thermal engineering and informatics, we proposed an AI system that can predict the heat-transfer coefficients in mini channels using DNNs and GPR. The proposed system can predict the heat-transfer coefficients of freon refrigerants and natural gases (CO_2, NH_3, and R600a), in addition to low-GWP refrigerants, with high accuracy. Moreover, the proposed system can generate the uncertainties of the predicted values. Thus, AI techniques, including the proposed system, can contribute to the advancement of the multiphase flow research field. In future research, we will develop an AI system that can describe the computations underlying the return of the predicted values by incorporating physical attributes such as the flow path, gravity, thermodynamics, and heat transfer.

3.1.4.2 Prediction of phase-change heat transfer and frictional pressure loss using transfer learning and fine-tuning

We developed AI models to predict phase-change heat transfer and frictional pressure loss. First, we developed a machine-learning database. A total of 6,684 data points were obtained, including 4,863 data points for phase-change heat transfer and 1,821 data points for frictional pressure loss for various pipe diameters and flow directions, which were obtained only for pure refrigerants (12 types, including olefin refrigerants, CFC substitutes, and ammonia).

Using AI technology, a model was developed to predict phase-change heat transfer and friction pressure loss from the data. The model was developed as follows:

Model 1. A deep learning model (DLM) trained on phase-change heat transfer data to predict phase-change heat transfer.

Model 2. A combined deep learning/Gaussian regression model to predict frictional pressure loss, in which the deep learning model trained on phase-change heat transfer data was fine-tuned on frictional pressure loss data and trained in combination with GPR.

Model 3. A combined deep learning/Gaussian regression model for predicting friction pressure loss, in which a deep learning model trained on phase-change heat transfer data was trained on friction pressure loss data by transfer learning combined with GPR.

Model 4. A DLM trained on friction pressure loss data to predict the friction pressure loss.

Model 5. A combined deep learning/Gaussian regression model to predict phase-change heat transfer, where the DLM trained on friction pressure loss data was fine-tuned on phase-change heat transfer data and trained in combination with GPR.

Model 6. A combined deep learning/GPR model to predict phase-change heat transfer, in which a DLM trained on frictional pressure loss data was transfer-trained on phase-change heat transfer data and trained in combination with GPR.

Specific methods for each AI model are described below.

The training phase of Model 1 is shown in Fig. 3.1.4-16, where the experimental setup information such as the saturation pressure, inner diameter, mass flux, and heat flux (in addition to physical properties such as the saturation pressure, critical pressure, and critical temperature) are inputted to train the deep learning (DNN) model for the prediction of the phase-change heat transfer. In particular, the model is a five-layer model with ReLU as the activation function, Adam optimizer as the optimization algorithm, mean absolute value error as the loss function, and a total of 200 epochs.

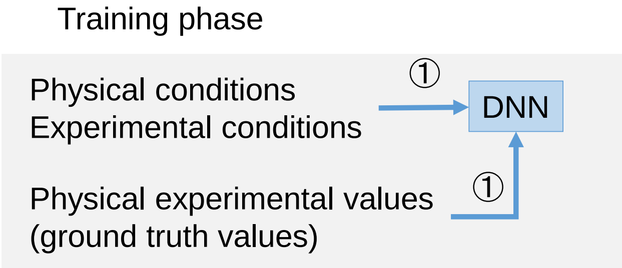

Fig. 3.1.4-16 Training phase of Model 1

Fig. 3.1.4-17 presents the flow of predicting phase change heat transfer from untrained data using the trained Model 1.

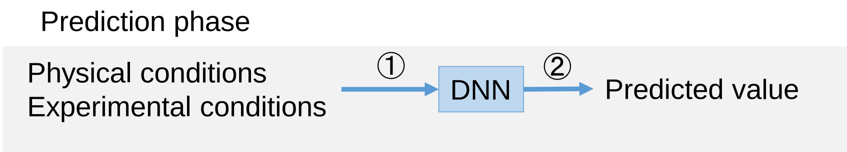

Fig. 3.1.4-17 Prediction phase of Model 1

The predicted heat-transfer coefficient values are outputted by inputting the experimental setup information and physical property information.

The training phase of Model 2 is shown in Fig. 3.1.4-18. In Model 2, the DLM is trained on the phase-change heat transfer data, as in Model 1 (Fig. 3.1.4-18 ①. Database A contains phase-change heat-transfer data). Thereafter, the final layer of the trained DLM is initialized (Fig. 3.1.4-18, ②). This DLM (Fig. 3.1.4-18③) is re-trained using the friction pressure loss data (Fig. 3.1.4-18 ④. Database B contains the friction pressure loss data). Here, the DLM in Fig. 3.1.4-18③ is trained with phase-change heat transfer data for layers other than the final layer. Therefore, it can extract the information necessary to predict phase-change heat transfer data. However, in Model 2, layers other than the final layer are re-learned; therefore, this functionality is not utilized unchanged, and is instead tuned for the friction pressure loss data. This method is referred to as fine tuning.

If sufficient friction pressure loss training data are available, there is a slight advantage in performing this type of fine-tuning. Otherwise, fine-tuning is expected to achieve a high accuracy with a small amount of data by pre-training based on similar data, and then fine-tuning the model learned from the pre-training stage.

In this study, the fine-tuned DLM was used (Fig. 3.1.4-18 ⑥ and ⑦. Database B contains friction pressure loss data) to train an AI technique referred to as GPR (Fig. 3.1.4-18 ⑧). We demonstrated that a combination of DLMs and GPR can achieve a higher forecasting accuracy. Furthermore, by using GPR, the predicted value can be generated, in addition to the reliability of the prediction. Hence, the model can only be used when uncertainty is low.

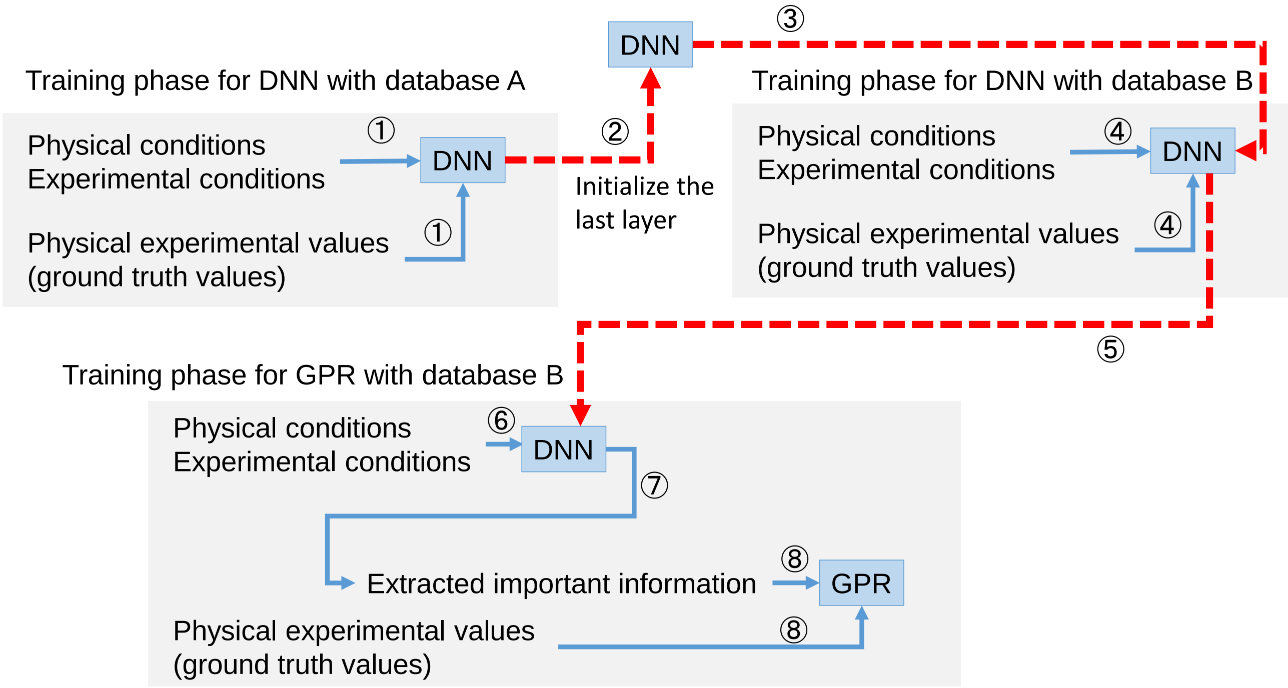

Fig. 3.1.4-18 Training phase of Model 2

The prediction phase of Model 2 is shown in Fig. 3.1.4-19. The predicted friction pressure loss and its uncertainty value are outputted by entering the experimental setup and physical property information. Here, Data B contains information on the experimental conditions and physical properties for which the friction pressure loss should be predicted.

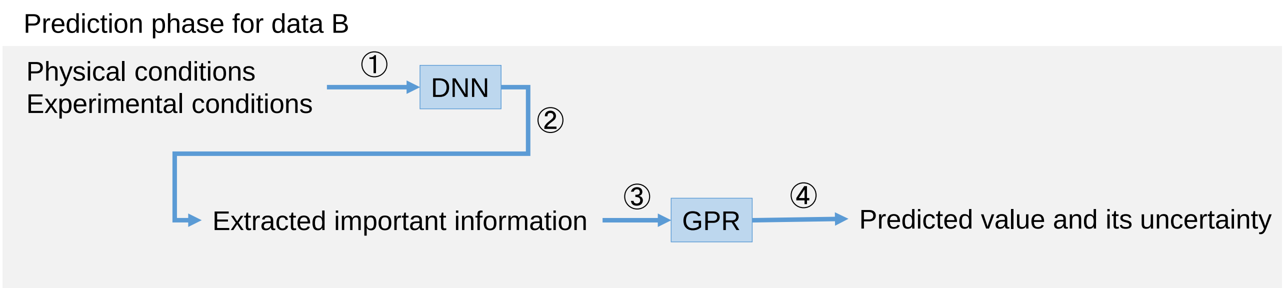

Fig.3.1.4-19 Prediction phase of Model 2

The process of Model 3 is almost identical to that of Model 2 (Fig. 3.1.4-18 and 3.1.4-19). The difference is that in Fig. 3.1.4-18, when the DLM is re-trained in step ④, all layers, except the final layer, are fixed. In particular, the DLM obtained in Step ① is used for all layers except for the final layer. This is different from fine-tuning and is referred to as transfer learning. If the properties of the dataset used for initial training and the dataset used for retraining are almost the same, the accuracy of transfer learning increases.

Models 4–6 are the datasets used in Models 1–3, but with different datasets. In particular, Database A contains friction pressure loss data, Database B contains phase-change heat transfer data and information on the experimental conditions and physical properties for which the phase-change heat transfer data are to be predicted.

To evaluate the accuracy of the predictions made by the proposed model, a 10-cross-validation is performed to separate the training data from the test data. For the models generated by fine-tuning and transfer learning, the evaluation method can be described using Model 2 as an example, as follows. First, the DLM is trained using all the phase-change heat transfer data. Thereafter, fine-tuning is performed using 9/10 of the friction pressure loss data. The obtained model is used to train the GPR model. The model is predicted and evaluated using the remaining 1/10th of the friction pressure loss data. This procedure is then repeated ten times.

The evaluation indices are the MSE, SD, R20, and R30. Let n be the number of test data points. For a given experimental condition and property data i, let $v_e(i)$ be the value obtained experimentally and $v_p(i)$ be the value predicted by the AI model. The MSE value is then calculated as follows:

$$MSE = \frac{1}{n}\left(v_e(i) - v_p(i)\right)^2. \tag{3.1.4-15}$$

Moreover, the SD is calculated as follows:

$$SD = \sqrt{\frac{1}{n}\sum_i^n \left(\frac{v_e(i)-v_p(i)}{v_e(i)}\right)^2}. \tag{3.1.4-16}$$

Consider Function r that outputs 1 when it receives a value greater than or equal to 0 as an argument, and 0 when it receives a value less than or equal to 0. The R20 value is calculated using the following equation:

$$R20 = \frac{1}{n}\sum_i^n r\left(0.2 - \frac{|v_e(i)-v_p(i)|}{v_e(i)}\right). \tag{3.1.4-17}$$

Similarly, the R30 value is calculated using the following equation:

$$R30 = \frac{1}{n}\sum_i^n r\left(0.3 - \frac{|v_e(i)-v_p(i)|}{v_e(i)}\right). \tag{3.1.4-18}$$

The R20 and R30 values are the percentages of data for which the relative error is within 20% and 30% of the true value, respectively.

Table 3.1.4-5 presents the prediction results for the phase-change heat transfer data, and Table 3.1.4-6 presents the prediction results for the friction pressure loss data.

Table. 3.1.4-5 Heat transfer coefficient results

	Deep neural network (Model 1)	Fine-tuning (Model 5)	Transfer learning (Model 6)
MSE (smaller is better)	4.16	**3.70**	12.1
SD (smaller is better)	0.0562	**0.0505**	0.227
R20 (larger is better)	0.861	**0.897**	0.690
R30 (larger is better)	0.932	**0.942**	0.792

Table.3.1.4-6 Pressure drop results

	Deep neural network (Model4)	Fine-tuning (Model 2)	Transfer learning (Model 3)
MSE (smaller is better)	7.50	**2.10**	78.6
SD (smaller is better)	1.18	**1.07**	370
R20 (larger is better)	0.740	**0.791**	0.337
R30 (larger is better)	0.834	**0.860**	0.433

In both results, the combination of fine-tuning deep learning and GPR (fine-tuning (Model 5) and fine-tuning (Model 2)) demonstrated the highest accuracy for all indicators. This is because neither the phase-change heat transfer data nor the friction pressure loss data were sufficiently large to maximize the accuracy of deep learning. Fine-tuning the models that were pre-trained with different data allowed for learning based on more relevant data. Thus, the fine-tuned model was considered to demonstrate the highest accuracy.

The model pre-trained with frictional pressure loss data and fine-tuned with phase-change heat transfer data (Model 5) exhibited an 11% reduction in the MSE when compared with the DLM (Model 1). Moreover, the model pre-trained with phase-change heat transfer data and fine-tuned with friction pressure loss data (Model 2) significantly reduced the MSE by 72% when compared with the DLM (Model 4). This is because the initial amount of friction pressure loss data was significantly smaller, and the effect of pre-training with phase-change heat transfer data in predicting the friction pressure loss data was significant.

The results reveal that the accuracy was reduced when transfer learning was employed. This may be because the feature information required to predict the phase-change heat transfer data did not completely match the feature information required to predict the friction pressure loss data.

Thereafter, we examined the influence of each feature on the predictions by checking the SHapley Additive exPlanations (SHAP) values. However, because this is not directly applicable to complex models, such as that used in this study, SHAP values were checked for DLMs (simple deep learning models, fine-tuning models, and transfer learning models), and not for GPRs.

The SHAP values of the DLMs for the phase-change heat transfer data are shown in Fig. 3.1.4-20.

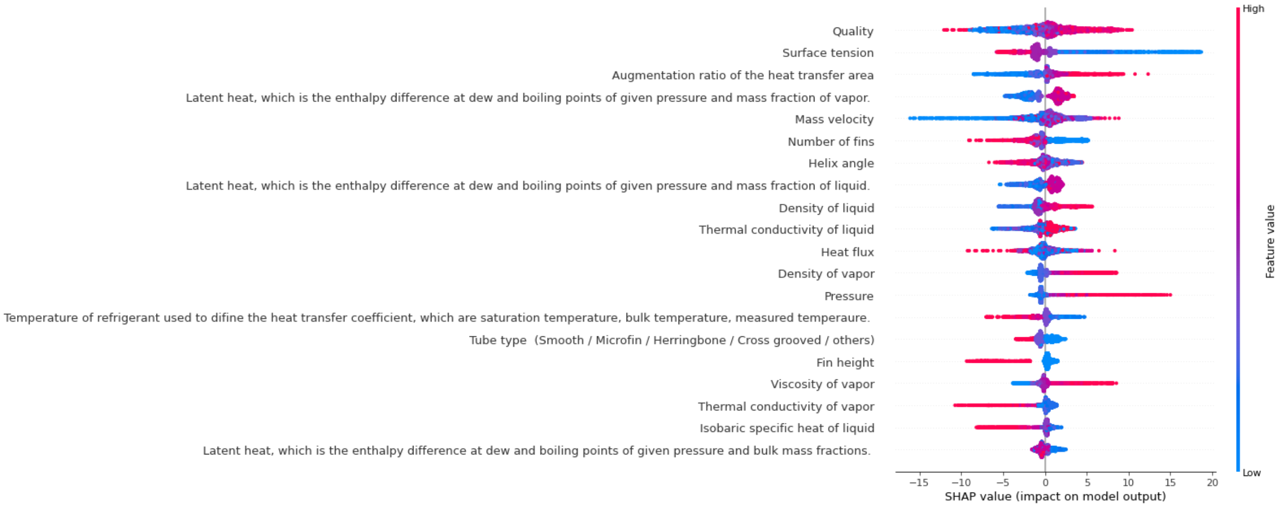

Fig.3.1.4-20 The SHAP values of the DNN for the heat transfer coefficient (Model 1)

The experimental conditions and physical properties are listed on the left side of the figure in order of influence of the predicted results, from top to bottom. For example, for quality, more red dots were plotted on the right side. This indicates that with an increase in the value of quality, the predicted value increased. Moreover, more blue dots were plotted for the surface tension from left to right. This indicates that with an increase in the surface tension value, the predicted value decreased.

Figures 3.1.4-21–3.1.4-25 present the results of the analysis of the SHAP values for the other models.

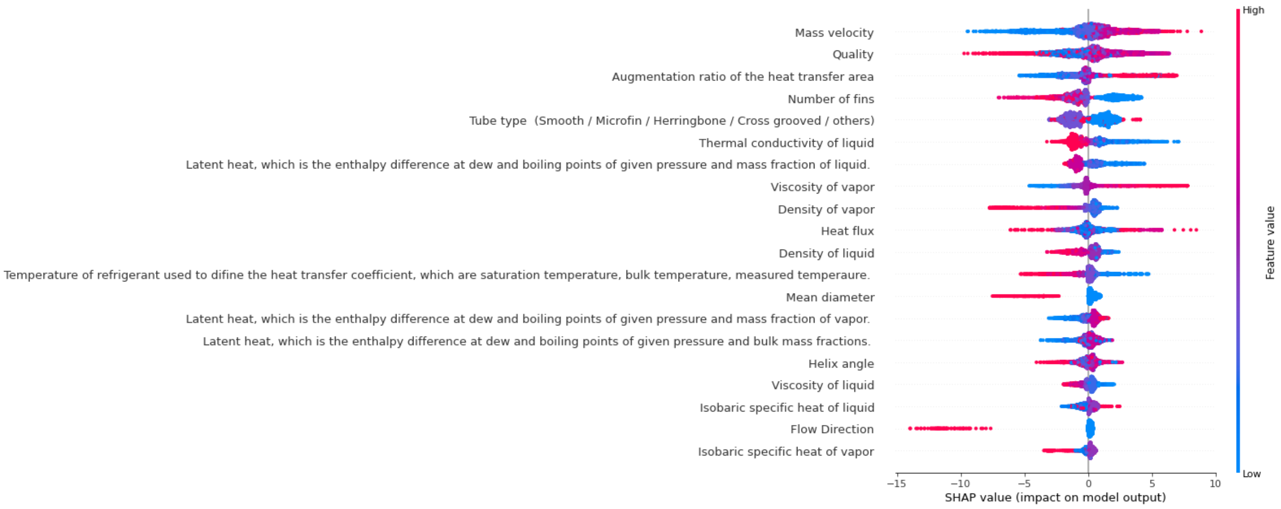

Fig. 3.1.4-21 The SHAP values of the fine-tuning model for the heat transfer coefficient (Model 5)

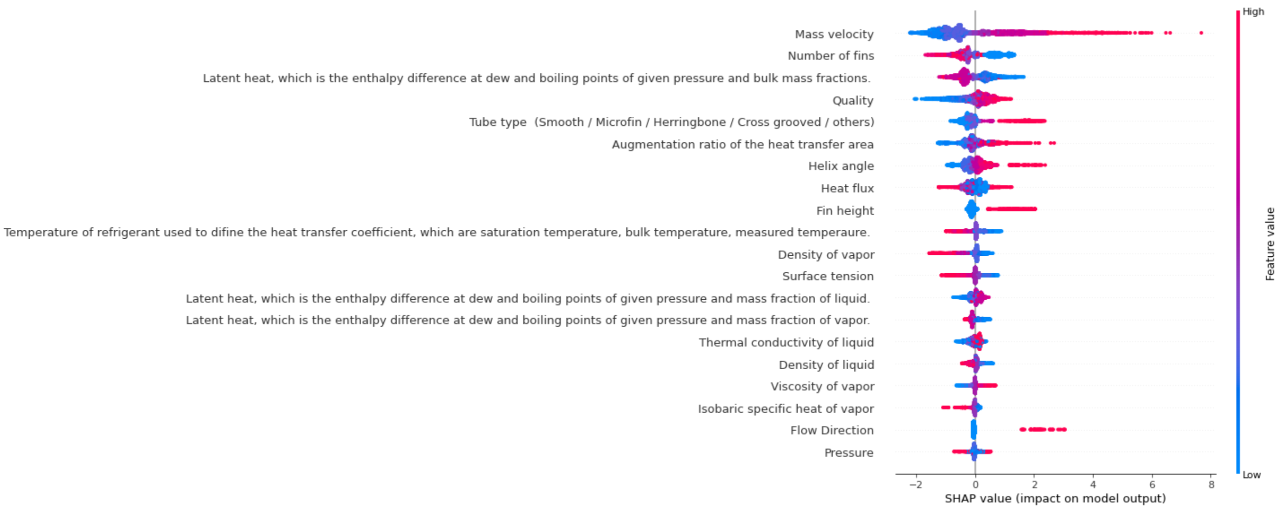

Fig. 3.1.4-22 The SHAP values of the fine-tuning model for the heat transfer coefficient (Model 6)

Fig. 3.1.4-23 The SHAP values of DNN for the pressure drop (Model 4)

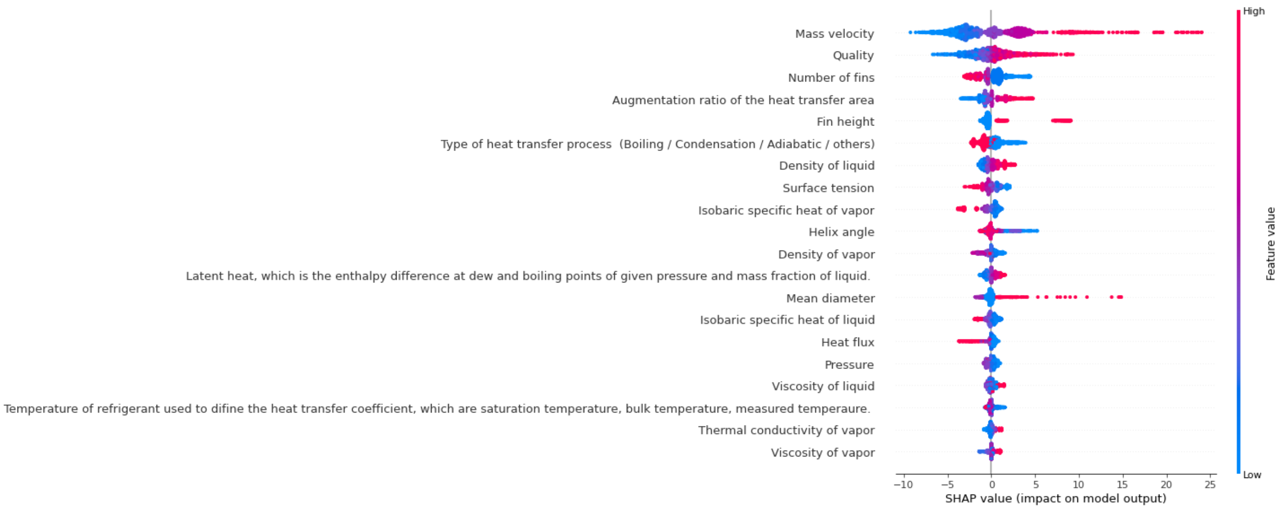

Fig. 3.1.4-24 The SHAP values of the fine-tuning model for the pressure drop (Model 2)

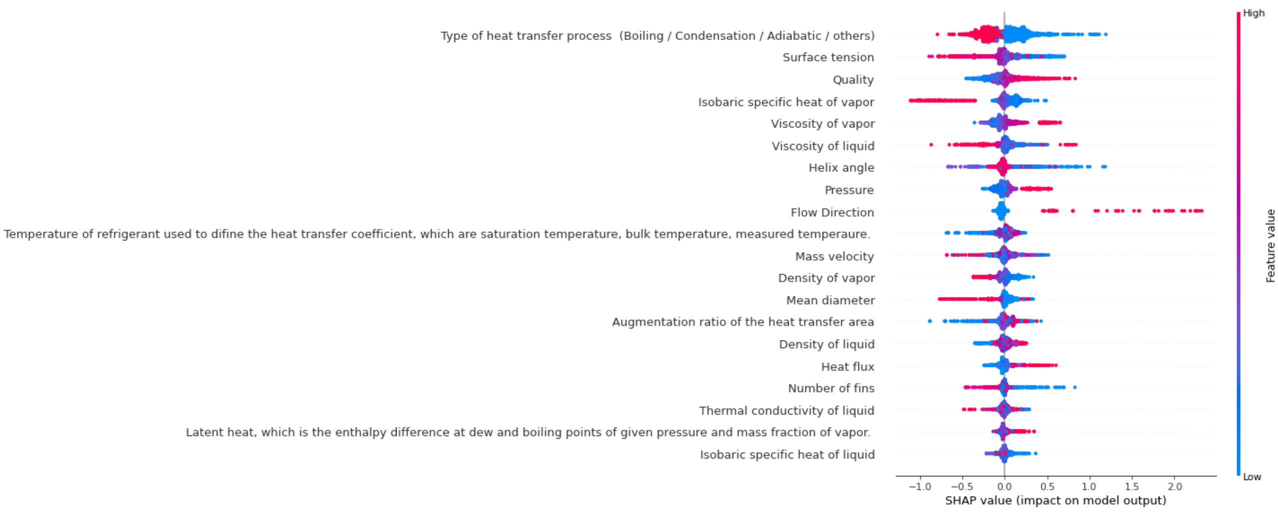

Fig. 3.1.4-25 The SHAP values for the transfer learning mode of the pressure drop (Model 3)

As can be seen from these figures, there were differences between the methods used to construct the DLMs in terms of the influencing features of the models, and their corresponding influences on the models. However, because the fine-tuning models (Models 2 and 5) achieved the highest accuracies, these results should be given more preference. Model 5 for the phase-change heat transfer data reveals that the influence of mass velocity was the most significant, and with an increase in the mass velocity, the value of the phase-change heat transfer increased. The same trend was observed in Model 2 for the pressure loss data. The use of this SHAP value-based visualization technique alleviates the problem associated with deep learning, which renders the trained models a black box.

References

1) Lazarek, G.M., Black, S.H., Evaporative heat transfer, pressure drop and critical heat flux in a small vertical tube with R-113, Int. J. Heat and Mass Transfer, 1982, 25(7), pp. 945-960.
2) Wambsganss, M.W., France, D.M., Jendrzejczyk, J.A., Tran, T.N., Boiling heat transfer in a horizontal small diameter tube, Trans. ASME J. Heat Transfer, 1993, 115, pp. 963-972.
3) Tran, T.N., Wambsganss, M.W., France, D.M., Small circular- and rectangular-channel boiling with two refrigerants, Int. J. Multiphase Flow, 1996, 22(3), pp. 485-498.
4) Kew, P.A., Cornwell, K., Correlations for the prediction of boiling heat transfer in small-diameter channels, Applied Thermal Engineering, 1997, 17, pp. 705-715.
5) Bao, Z.Y., Fletcher, D.F., Haynes, B.S., Flow boiling heat transfer of Freon R11 and HCFC123 in narrow passages, Int. J. Heat and Mass Transfer, 2000, 43, pp. 3347-3358.
6) Kuwahara, K., Koyama, S., Hashimoto, Y., Characteristics of evaporation heat transfer and flow pattern of pure refrigerant HFC134a in horizontal capillary tube, JSME Int. J., 2000, 43(4), pp. 640-646.
7) Sumith, B., Kaminaga, F., Matsumura, K., Saturated flow boiling of water in a vertical small diameter tube, Experimental Thermal and Fluid Science, 2003, 27(7), pp. 789-801.
8) Saitoh, S., Daiguji, H., Hihara, E., Effect of tube diameter on boiling heat transfer of R-134a in horizontal small-diameter tubes, Int. J. Heat and Mass Transfer, 2005, 48, pp. 4973-4984.
9) Yamashita, H., Ueda, Y., Ishihara, I., Matsumoto, R., Forced convection boiling heat transfer of carbon dioxide in microchannel, Proc. JSME, 2005, No. 054-1(12), pp. 7-8. (in Japanese)
10) Miyata, K., Mori, H., Ohishi, K., Hamamoto, Y., Boiling Heat Transfer and Pressure Drop of a Refrigerant Flowing Vertically Upward in a Small Diameter Tube, Trans. of the JSRAE, 2007, 24(4), pp. 359-369. (in Japanese)
11) Miyata, K., Mori, H., Ohishi, K., Hamamoto, Y., Boiling Heat Transfer of a Refrigerant Flowing Vertically Downward in a Mini-channel, Trans. of the JSRAE, 2009, 26(3), pp. 347-357. (in Japanese)
12) Li, M., Dang, C., Hihara, E., Flow boiling heat transfer of HFO1234yf and R32 refregerant mixtures in a smooth horizontal tube: Part1. Experimental investigation, Int. J. Heat and Mass Transfer, 2012, 55, pp. 3437-3446.
13) Enoki, K., Mori, H., Miyata, K., Kariya, K., Hamamoto, Y., Boiling Heat Transfer and Pressure Drop of a Refrigerant Flowing in Small Horizontal Tubes, Proc. of the 3rd Int. Forum on Heat Transfer, Nagasaki, Japan (2012), IFHT2012-193.
14) Chen, J.C., Correlation for boiling heat transfer to saturated fluids in convective flow, 1996, Ind. Engng. Chem. Proc. Des. Dev. 5, pp. 322-329
15) Lazarek, G.M., and Black, S., Evaporative heat transfer, pressure drop and critical heat flux in a small vertical tube with R-113. Int. J. Heat Mass Transfer, 1982, 25, pp. 945-960
16) Jung, D.S., A study of flow boiling heat transfer with refrigerant mixtures, Int. J. Heat Mass Transfer 32, 1989, pp. 1751-1764
17) Liu, Z., and Winterton, R., A general correlation for saturated and subcooled flow boiling in tubes and annuli, based on a nucleate pool boiling equation, Int. J. Heat Mass Transfer, 34, 1991, pp. 2759-2766
18) Mori, H., Yoshida, S., Kakimoto, Y., Ohishi, K., Reform of the Correlation for the Prediction of Heat Transfer Coefficient for Refrigerants Flowing in Horizontal Evaporator Tubes, 1999, Trans. JSRAE, 16, pp. 177-187 (in Japanese)
19) Sumith, B., et al, Saturated flow boiling water in a vertical small diameter tube, 2003, Experimental Thermal Fluid Science, 27, pp. 789-801
20) Kandlikar, S.G., Balasubramaian, K., Balasubramaian, P, An extension of the flow boiling correlation to transition, laminar, and deep laminar flows in minichannels and microchannels, 2004, Heat Transfer Eng., 25, pp. 86-93
21) Zhang, W., et al., Correlation for flow boiling heat transfer in mini-channels. Int. J. Heat Mass Transfer, 47, 2004, pp. 5749-5763
22) Saitoh, S., et al., Correlation for boiling heat transfer of R-134a in horizontal tubes including effect of tube diameter, 2007, Int. J. Heat Mass Transfer, 50, pp. 5215–5225
23) Enoki, K., Miyata, K., and Mori, H., Modification of the Prediction Correlation for Flow Boiling Heat Transfer in Small Diameter Tubes, Trans. JSRAE, 2015, 32(3), pp. 275–283 (in Japanese)

24) Yokoyama, S., Saito, K., and Kato, M., The Characteristics of Evaporation Heat Transfer in Flowing a Circular Mini-Channel, Proc. of 47th Air Conditioning and Refrigeration Union Lecture, JSRACE, 2013, p. 21 (Tokyo, Japan).
25) Wu, X., Zhu, Y., and Huang, X., Influence of 0± Helix Angle Micro Fins on Flow and Heat Transfer of R32 Evaporating in a Horizontal Mini Multichannel Flat Tube, Exp. Thermal Fluid Sci., 2015, 68, pp. 669-680.
26) Longo, G.A., Mancin, S., Righetti, G., and Zilio, C., Saturated Flow Boiling of HFC134a and Its Low GWP Substitute HFO1234ze(E) inside a 4 mm Horizontal Smooth Tube, Int. J. Refrig., 2016, 64, pp. 32–39.
27) Semp´ertegui-Tapia, D.F., Ribatski, G., Flow Boiling Heat Transfer of R134a and Low GWP Refrigerants in a Horizontal Micro-Scale Channel, Int. J. Heat Mass Transf., 2017, 108, pp. 2417-2432.
28) Enoki, K., Sei, Y., Okawa, T., Saito, K., Prediction for Flow Boiling Heat Transfer in Small Diameter Tube Using Deep Learning, J. Multiph. Flow, 2017, 31(4), pp. 412-421.
29) Enoki, K., Miyata, K., Mori, H., Kariya, K., and Hamamoto, Y., Boiling Heat Transfer and Pressure Drop of a Refrigerant Flowing Vertically Upward in Small Rectangular and Triangular Tubes, 2013, Heat Transf. Eng., 34(11-12), pp. 966-975, 2013.
30) Ribeiro, M. T., Singh, S., and Guestrin, C., Why should I trust you?-Explaining the predictions of any classifier. In KDD, 2016.
31) Lundberg, S.M., Lee, S.I., A unified approach to interpreting model predictions, Adv. Neu. Inf. Process. Syst., 2017, 30.

3.1.5 Evaluation of void fraction

Low-GWP refrigerants are currently used to prevent global warming due to conventional refrigerants, among other factors. Consequently, the flammability and toxicity of low-GWP refrigerants has attracted significant research attention. To reduce the flammability and toxicity risks of low-GWP refrigerants, it is necessary to establish a refrigerant charge prediction technique that reduces or optimizes the refrigerant usage. However, the prediction of the amount of refrigerant in an actual cooling system is a complex problem, as reported by various studies on the refrigerant evaluation WG of the Japan Refrigeration and Air Conditioning Industry Association. In this section, research was performed using an experimental apparatus that can visualize and characterize a two-phase refrigerant pipe. The two-phase flow phenomenon was clarified based on the following steps:

1) Development of a capacitance-based void fraction sensor and establishment of a measurement method
2) Void fraction measurement using a refrigerant charging amount evaluation apparatus
3) Accurate void fraction prediction correlation, considering the characteristics of low-GWP refrigerants
4) Prediction of the refrigerant charging amount and evaluation of the void fraction prediction correlation

3.1.5.1 Development of a capacitance-based void fraction sensor and establishment of a measurement method

A capacitance-based sensor is an alternative measurement method that exploits the electrostatic properties of the two-phase flow between two electrodes[1–5]. Given that this technique utilizes a relatively simple configuration, enables real-time measurements, and exhibits the characteristics of a non-contact method, it has attracted significant attention for application to refrigerants. In particular, the characteristics of the real-time measurement of a void fraction allow for the evaluation of recent heat exchangers with a complex refrigerant flow distribution structure, to improve their performance. The electrostatic property used in this technique is the dielectric constant. The capacitance measured using two electrodes is dependent on the type of fluid, void fraction, and flow pattern. The relationship between the capacitance and void fraction (i.e., the C–α relation) is not linear, and the C–α relationship changes according to the flow pattern. Therefore, there is a dependency on the flow pattern. In particular, the two-phase flow pattern depends on the mass flux, temperature, flow rate, and refrigerant type. Thus, using a capacitance-based sensor to determine the void fraction requires the C–α relationship to be quantified according to the two-phase flow pattern (i.e., by using a calibration method).

As detailed in this section, we developed a high-precision void fraction measurement method for refrigerants with macro- and micro-sized tubes using a capacitance-based sensor with asymmetric electrodes designed for cryogenic fuel[2,3].

(1) Capacitance-based void fraction sensor with asymmetric electrodes

Various types of electrodes were proposed by multiple researchers. Most of these electrodes consist of a pair of arc-shaped electrodes attached to the outside of the circular tube (Fig. 3.1.5-1(a)). It was reported that a sensor with arc-shaped electrodes exhibits a measurement error of up to 30% in horizontal flow tests. The distortion of the electric field caused by the influence of the metal shield, which is installed to reduce noise from the outside, was reported as the source of error, as shown in Fig. 3.1.5-1(a).

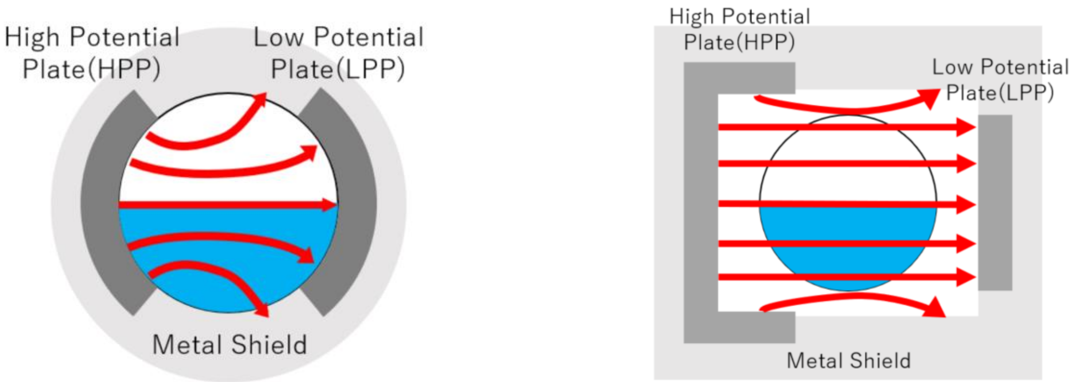

(a) (b)

Fig. 3.1.5-1 Electric field lines according to the shape of the electrode
(a) Symmetrical arc-shaped electrodes and (b) parallel asymmetric electrodes

In this study, to reduce the distortion of the electric field caused by the shield, a sensor with parallel asymmetric electrodes was developed (Fig. 3.1.5-1(b)),[3] wherein the high-potential plate with the larger area was folded to reduce the electric field distortion between the electrode plates. Hence, the measurement error was reduced to 6.5%.

(2) Optimal design of capacitance-based void fraction sensor

Electric field analysis (EFA) was performed using Elmer, which is an open-source finite element method (FEM) software. A capacitance-based void fraction sensor was implemented as an EFA model. The relationship between the capacitance (C) and void fraction (α) was established to account for changes in the electrode parameters and flow patterns, and an error analysis was performed. In addition, the electrode size parameters were optimized to achieve maximum the measurement accuracy by applying a design of experiments. In particular, as shown in Fig. 3.1.5-2, EFA was performed using four elements: the high-potential electrode height (HPH), high-potential electrode side-wall length (HPS), low-potential electrode height (LPH), and plate distance (PD) for the three evaluation levels. The electrode size parameters were determined to minimize the error between the void fraction derived from the calculated capacitance and the input void fraction.

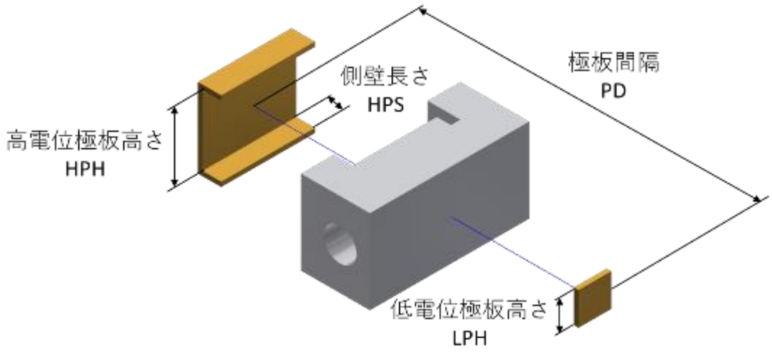

Fig. 3.1.5-2 Design parameters of a capacitance-based void fraction sensor

When fabricating a capacitance-based void fraction sensor, it is necessary to use a material with dielectric characteristics for the pipe; therefore, it is unsuitable to use a metal material such as copper, which is typically used for refrigerant pipes. Generally, in void fraction sensors for silicone oil or liquid hydrogen, acrylic resin is used as a piping material. However, because the working fluid used in this study was a refrigerant, it was necessary to consider its compatibility with the piping material. Based on their physical properties, polymers cause expansion, strength loss, and dissolution due to chemical reactions with the refrigerant, thus leading to system failure and a decrease in the measurement accuracy.

Table 3.1.5-1 presents the material compatibility test results for various refrigerants and polymers used as piping materials. These results reveal the [weight change rate]/[volume change rate] ratio after each plastic material was immersed in each refrigerant at 50 °C for five days. As can be seen from this Table 3.1.5-1, most refrigerants and acrylic resins are incompatible.

Table 3.1.5-1 Effects of refrigerants on polymer materials[6)]

Materials	R410A	R407C	R404A	R507A	R32	R125	R134a	R143a	R22
Polyvinyl chloride	2/2	1/1	0/0	0/0	5/5	0/-2	0/0	-3/-4	12/13
Polyethylene	1/1	1/1	1/1	1/1	1/1	1/1	1/0	1/-4	3/2
Polypropylene	2/2	2/2	3/2	2/2	0/0	1/-1	2/1	3/-1	6/4
Polystyrene	6/4	3/2	1/1	0/0	10/8	1/-1	1/1	1/-2	meltdown
Acrylic resin	34/29	39/33	0/0	0/0	34/35	6/5	34/28	0/-1	meltdown
Polycarbonate	6/4	3/2	0/0	0/0	11/14	0/0	0/0	0/1	meltdown
Phenolic resin	-1/-1	-1/-1	-1/-1	-1/-1	0/0	0/0	-1/-1	0/2	0/0
Epoxy resin	0/-1	0/-1	0/-1	0/-1	0/0	0/0	2/3	0/1	-2/-2
Polyphenylene oxide	6/4	3/2	0/0	0/1	10/8	0/0	0/-1	1/1	12/8
ABS resin	9/13	7/5	0/0	0/0	19/16	0/0	1/1	0/-1	meltdown

In addition, because the refrigeration system operates under a relatively high system pressure, sufficient strength should be considered for the piping material. Therefore, it is necessary to select materials other than the general-purpose plastics listed in Table **3.1.5-1**. In this study, polyether ether ketone (PEEK), which is a type of engineering plastic, was applied to the void fraction sensor. In particular, PEEK was developed by ICI, United Kingdom (UK), in 1978 and registered as a "VictrexPEEK" trademark. It is recognized for its excellent mechanical strength and chemical resistance. In addition, it demonstrates high compatibility with low-GWP refrigerants such as R32 and R454C. The dielectric constant of PEEK is approximately 3.3, which is close to that of an acrylic resin (3.0). These characteristics are sufficient with respect to electromagnetism.

(3) Validation of capacitance-based void fraction sensor prototype

A void fraction sensor prototype (Fig. 3.1.5-3(a)) was fabricated using a macro-tube with an inner diameter of 7.1 mm. In addition, the validation of the simulated stratified flow pattern was performed using Novec7300 (3M), which has a well-known dielectric constant. In this validation, the measured void fraction (α) due to the capacitance (C) was compared with the actual void fraction; and the measurement accuracy of the void fraction sensor and validity of the electric field analysis (EFA) were confirmed. Fig. 3.1.5-3(b) presents the measured and calculated results of designed capacitances for the simulated stratified flow pattern. The measured capacitance was different from the designed capacitance; however, this can be addressed by normalization, as shown in Fig. 3.1.5-3(c).

Moreover, the measurement accuracy can be improved by considering the $C-\alpha$ relationship for different flow patterns. Fig. 3.1.5-3(d) presents the $C-\alpha$ relationship derived from EFA for different R22 flow patterns. As can be seen from the figure, the $C-\alpha$ relationship exhibited a deviation of up to 10% with respect to the simple linear relationship, which indicates that it is essential to consider the appropriate flow pattern for the capacitance-based void fraction sensor.

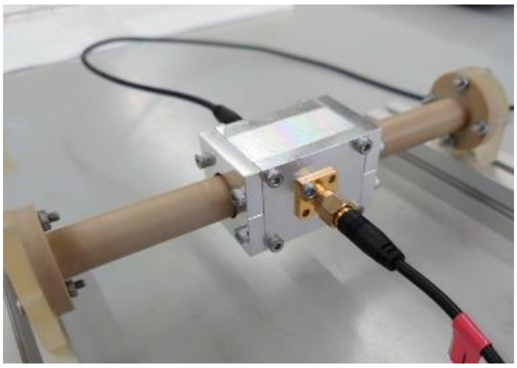

(a)

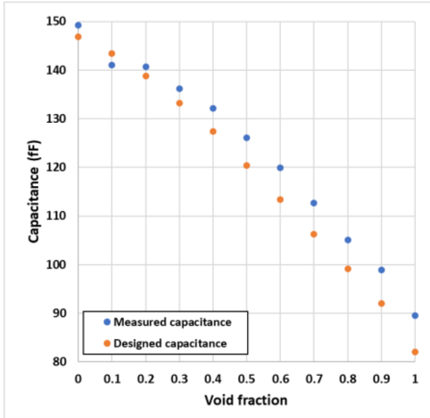

(b)

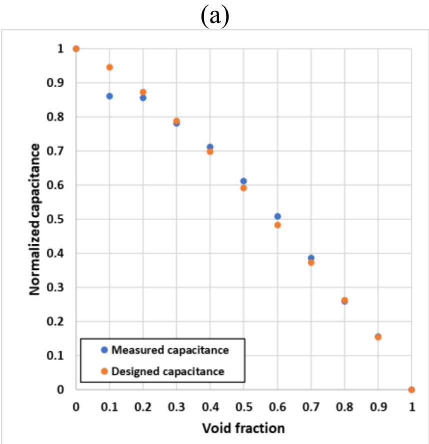

(c)

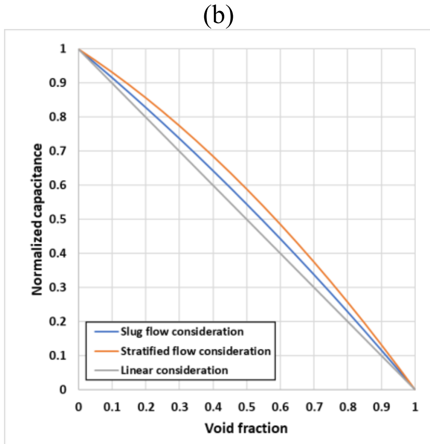

(d)

Fig. 3.1.5-3 Prototype of a capacitance-based sensor and its validation results: (a) prototype of capacitance-based sensor, (b) capacitance with respect to void fraction [Novec 7300], (c) normalized capacitance with respect to void fraction [Novec 7300], and (d) $C-\alpha$ relationship derived from EFA for different R22 flow patterns

To verify the validity of the fabricated void fraction sensor with respect to the refrigerant, the void fraction was measured for the R22 refrigerant. The validation was performed in a macro-tube with an inner diameter of 7.1 mm at a temperature of 20 °C and flow rate of 123.5 kg/m^{2}s. The measured void fraction was compared with various void fraction prediction correlations (Smith, Zivi, Fang, Chisholm, and Steiner), where Smith, Zivi, and Fang used the slip ratio model, Chisholm used the Kah model, and Steiner used the drift-flux model.

Fig. 3.1.5-4(a) presents a comparison of the experimental results for different correlations. The blue points represent the measured void fraction in this experiment, and the red points represent the experimental data from Hashizume measured using the quick closing valve (QCV) method under the same conditions. The two sets of experimental results demonstrated a similar trend and were in good agreement. Moreover, the void fraction measured by the prototype sensor was well-fitted with Steiner drift-flux model of correlation. Fig. 3.1.5-4(b) presents the results for the slug flow pattern, and Fig. 3.1.5-4(c) presents the results for the stratified flow pattern. The difference between Fig. 3.1.5-4(b) and Fig. 3.1.5-4(c) indicates that the measurement result of the void fraction can be significantly different depending on the C–α relationship applied to data reduction.

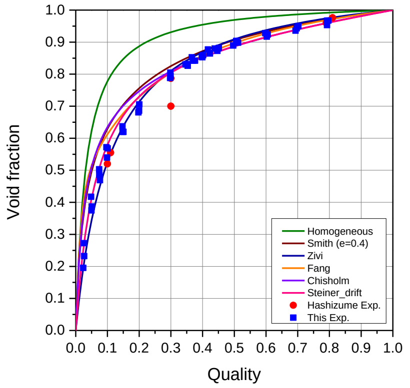

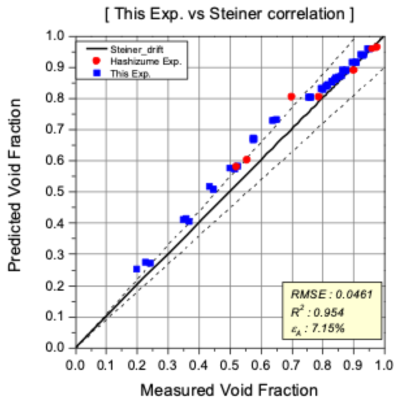

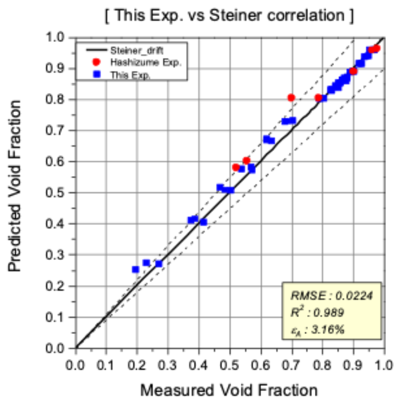

(a) (b) (c)

Fig. 3.1.5-4 Comparison of R22 void fraction measurement results: (a) comparison of measured void fraction with various correlations [R22], (b) comparison of slug flow considered while measuring void fraction with Steiner correlation, and (c) comparison of stratified flow considered while measuring void fraction with Steiner correlation

(4) High precision of capacitance-based void fraction sensor considering the flow pattern transition of the microchannel

As is evident from the above EFA results and the experimental validation for the prototype sensor, the relationship between the void fraction (α) and the measured capacitance (C) ($C-\alpha$ relationship) was not linear and was significantly dependent on the flow pattern. Given that the flow pattern depends on the type of refrigerant, temperature, mass flux, etc., it is necessary to determine the $C-\alpha$ relationship using various flow patterns, to accurately measure the void fraction using the capacitance-based sensor.

The aim of this study was to validate a capacitance method for void fraction measurement using a capacitance-based sensor with low sensitivity to flow patterns. Accordingly, a calibration method was established based on the characteristics of various flow patterns visualized using a high-speed camera. The observed flow pattern was reflected in the electric field analysis (EFA), using finite element method (FEM), results to derive the $C-\alpha$ relation for the capacitance-based sensor. The proposed calibration method was validated with respect to the QCV method, which was simultaneously applied to the horizontal flow of the smoothed circular macro-tube of the R32 refrigerant at a saturation temperature of 25 °C, mass flux range of 100–400 kg/m²s , and vapor quality of x = 0.025–0.900.

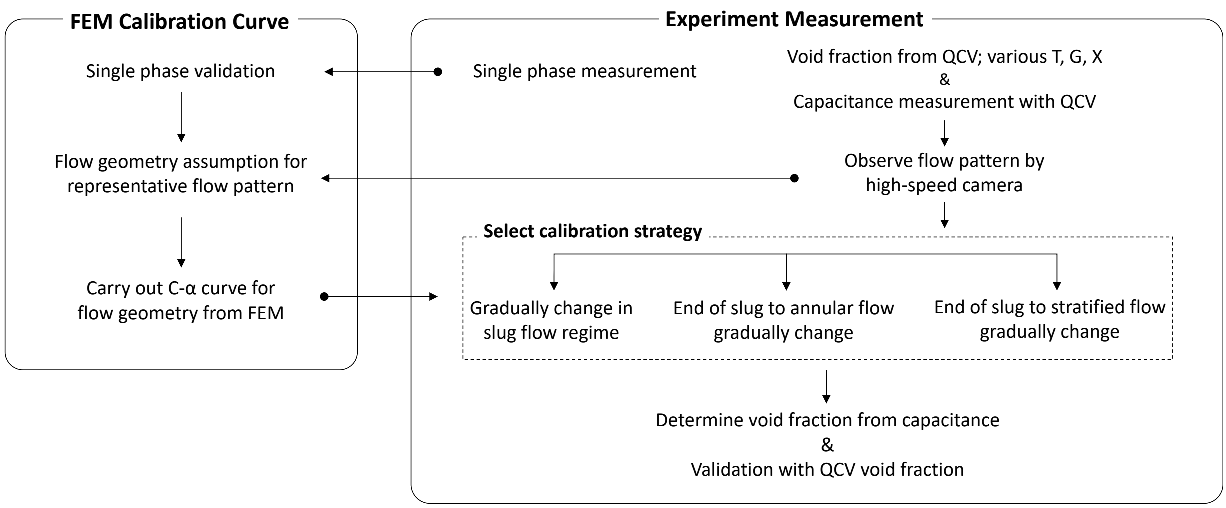

Fig. 3.1.5-5 Measurement and calibration for the capacitance method[7)]

Fig. 3.1.5-6 presents the representative transition of flow patterns visualized using a high-speed camera. A gradual transition in the flow pattern was observed as the inlet quality increased.

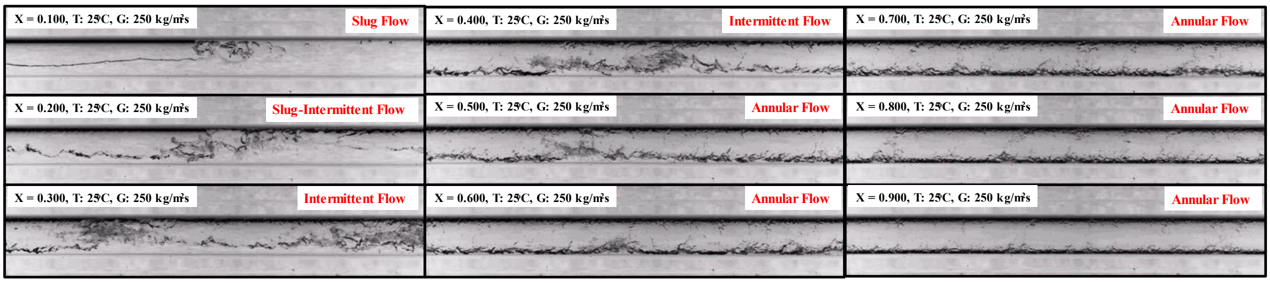

Fig. 3.1.5-6 The flow pattern change and change in vapor inlet quality (R32, T = 25 °C, and G = 250 kg/m²s)

In particular, the gradual transition in the slug flow region required separate consideration given the transient characteristics of slug flow. Fig. 3.1.5-7 presents the raw signal of the capacitance-based sensor, which reflects the flow pattern transition in the slug flow region.

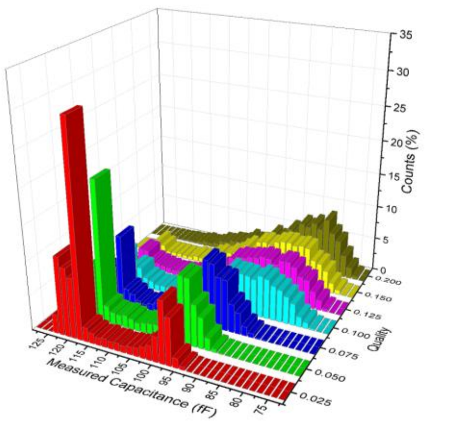

Fig. 3.1.5-7 The characteristics of capacitance distribution of the low-quality region, that is, slug flow (R32, T = 25 °C, and G = 100 kg/m²s)[7)]

Fig. 3.1.5-7 presents the distribution of the measured capacitance. When the distribution graph exhibited one peak, this indicates a stable flow, and when there were two or more peaks, this indicates an unstable flow. As the quality increased, the flow pattern was gradually stabilized.

Given that the capacitance-based sensor with asymmetric electrodes used in this study exhibited a relatively low sensitivity to the flow pattern, a slight variation in the flow pattern exhibited no significant influence on the measurement. Based on this characteristic, bubble, stratified, and annular flow were determined as representative flow patterns for EFA in this study. For these flow patterns, the $C-\alpha$ relationship was derived, as shown in Fig. 3.1.5-8. In addition, the linear $C-\alpha$ relationship considering no flow pattern is presented for comparison.

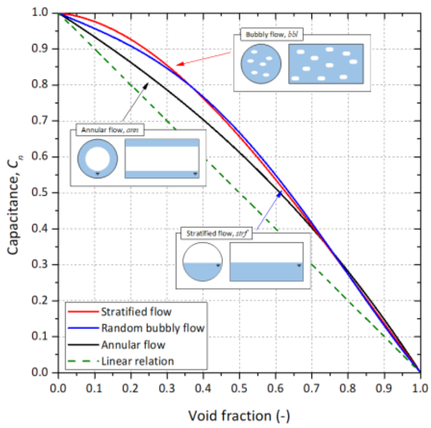

Fig. 3.1.5-8 The $C-\alpha$ relationship curve derived from EFA analysis for each representative flow pattern [7)]

Considering the above flow pattern analysis result and the $C-\alpha$ relationships derived from the EFA, a correction formula can be derived, which corresponds to the void fraction for the transition between slug and stratified flow, as expressed by Equations (3.1.5-1) and (3.1.5-2).

$$\alpha_{slug} = \frac{Count_{fp}}{Count_{tot}}\alpha_{strf} + \frac{Count_{sp}}{Count_{tot}}\alpha_{bbl} \tag{3.1.5-1}$$

where $Count_{fp}$ and $Count_{sp}$ are the number of signals corresponding to the first and second distributions, respectively, and $Count_{tot}$ denotes the total number of signals.

$$\alpha_{intm} = \frac{(x - x_{IS})}{(x_{EA} - x_{IS})}\alpha_{ann} + \frac{(x_{IA} - x)}{(x_{EA} - x_{IS})}\alpha_{strf} \tag{3.1.5-2}$$

Here, x_{IS} is the quality at which the intermittent and slug flow transitions occur in the flow pattern map, and x_{EA} is the quality at the end of annular flow.

In Fig. 3.1.5-9, the three types of void fraction measurement results are shown: the capacitance-based sensor result, which is based on the proposed correction formula, the void fraction measured by the QCV method, and the uncorrected linear $C - \alpha$ relationship.

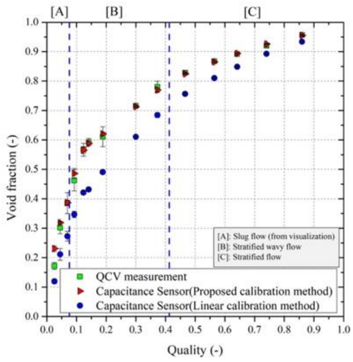

(a)

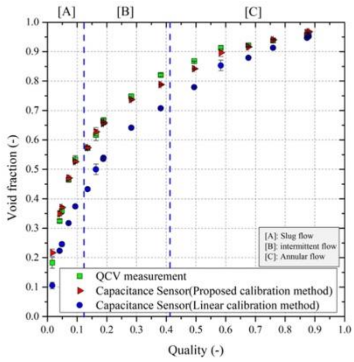

(b)

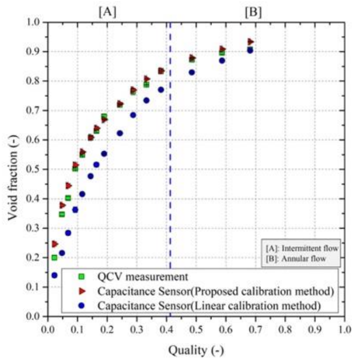

(c)

Fig. 3.1.5-9 Comparison between the void fraction results derived using the QCV method and those obtained using the capacitance method with proposed and linear calibration
(a) R32, T = 25 °C, and G = 100 kg/m²s; (b) R32, T = 25 °C, and G = 250 kg/m²s; and (c) R32, T = 25 °C, and G = 400 kg/m²s[7)]

Each measurement result, whether or not the correction formula was applied, was compared with the void fraction derived from the QCV method, and the measurement errors for each flow pattern are summarized in Table. 3.1.5-2.

Table. 3.1.5-2 Summary of the calibration results of the capacitance-based method for each flow pattern

	E_R		R^2	
	Linear calibration	Proposed calibration	Linear calibration	Proposed calibration
Slug	30.4%	7.8%	0.287	0.966
Intermittent	25.33%	2.24%	-0.198	0.986
Stratified	9.02%	0.63%	0.499	0.997
Annular	4.54%	1.36%	-1.307	0.776
All	19.53%	2.99%	0.711	0.994

In the entire flow pattern, the capacitance-based sensor with the proposed calibration method was well matched with the QCV method result as the value of R^2 = 0.994. It was found that the capacitance-based void fraction sensor, to which the calibration technique was developed in this study, can perform non-contact, real-time, and high-precision measurements.

(5) Capacitance-based void fraction sensor development for a microchannel

A tube with an inner diameter of 1 mm or less is classified as a microchannel. The two-phase flow in microchannels exhibits various characteristics that are useful in multiple applications such as microelectronic cooling, microelectromechanical systems, and microchannel heat exchangers. In particular, a microchannel heat exchanger has a heat flux of 1 kW/cm² or higher and is one of the most advanced heat exchangers. However, owing to the minimal diameter, it is difficult to analyze the flow characteristics of the two-phase flow inside the microchannel. In particular, the void fraction is one of the most difficult parameters to measure among the various microchannel characteristics. The void fraction of microchannels is generally measured using the QCV method. Given that the QCV method requires the recovery the two-phase refrigerant in the tube and weight measurement, multiple errors ranging from 10–30% have been reported. Moreover, when analyzing a single microchannel, which is the basis of characterization, it is difficult to measure the void fraction owing to its small internal volume.

In this study, a novel sensor capable of measuring the void fraction of microchannels based on a capacitance-based void fraction sensor for a macro-sized tube was developed and implemented. Capacitance-based sensors with asymmetric electrodes are difficult to use in small tubes. This is partly because the size of the low-potential electrode is limited by the diameter of the tube, which reduces the resolution of the sensor. Therefore, the capacitance-based sensor developed in this study optimizes the width of each electrode to compensate for the reduced resolution and sets the aspect ratio of the high- and low-potential electrodes to 1:9.48 and 1:8.24, respectively.

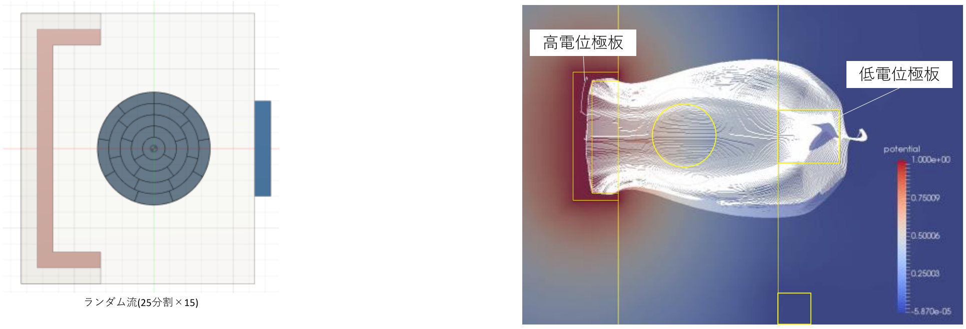

(a) (b)

Fig. 3.1.5-10 Example of finite element method of sensor:
(a) EFA modeling and (b) EFA result

As shown in Fig. 3.1.5-10, the capacitance-based sensor for the microchannel was analyzed based on EFA, as identified in the sensor design for the macro-tube. The C–α relationship was derived for various flow patterns. The flow pattern considered by EFA is a typical flow pattern for microchannels, as shown in Fig. 3.1.5-11. The flow pattern in the microchannel varied from plug flow to annular flow with respect to the vapor quality.

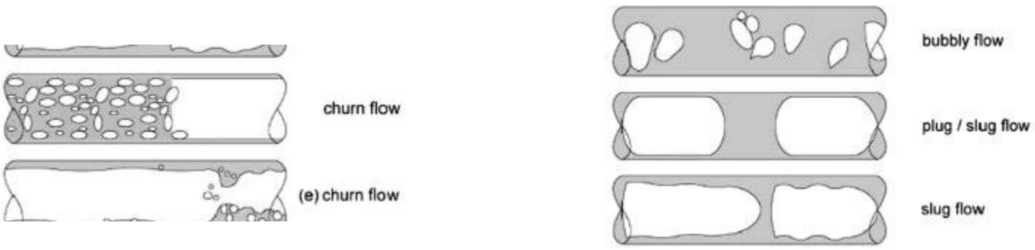

Fig. 3.1.5-11 Various two-phase flow patterns in a microchannel

However, because the capacitance-based void fraction sensor applied in this study has a relatively low sensitivity to the flow pattern owing to the influence of the characteristic asymmetric electrode, the effects on measurements and analysis were not significant. Therefore, in this study, plug, annular, and churn flows were selected as representative flow patterns to derive and evaluate the $C-\alpha$ relationship. Fig. 3.1.5-12 presents the $C-\alpha$ relationship derived for the three flow modes with an error of approximately 1.7%.

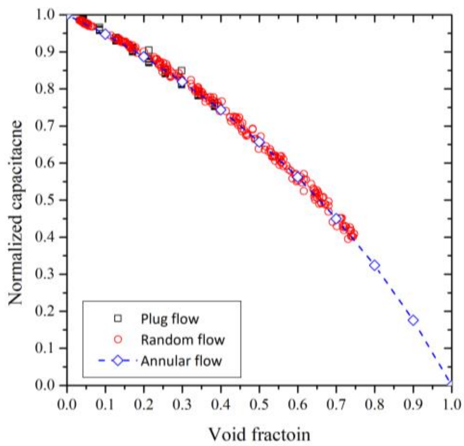

Fig. 3.1.5-12 The $C-\alpha$ relationship for different microchannel flow patterns

The slight differences between the $C-\alpha$ relationships for the different flow patterns were because of the relatively symmetrical two-phase flow in the microchannel when compared with that in the macro-tube. Finally, a comprehensive $C-\alpha$ relationship can be derived by considering all three flow patterns, as expressed by Equations (3.1.5-3) and (3.1.5-4).

$$\alpha_{R1234yf} = -0.2596C_n^3 - 0.7379C_n + 0.9997 \tag{3.1.5-3}$$

$$\alpha_{R32} = -0.3797C_n^3 - 0.0604C_n^2 - 0.5597C_n + 1.0024 \tag{3.1.5-4}$$

where C_n is the normalized value of the capacitance measured by the sensor.

(6) Fabrication of a void fraction sensor

Considering the electrode shape, material selection, and flow pattern described above, a highly accurate void fraction sensor with a macro-tube and microchannel with inner diameters of 7.1 mm and 1 mm, respectively, was fabricated for the R32 and R454C refrigerants. Fig. 3.1.5-13 presents the designed computer-aided design (CAD) model and actual fabricated sensor.

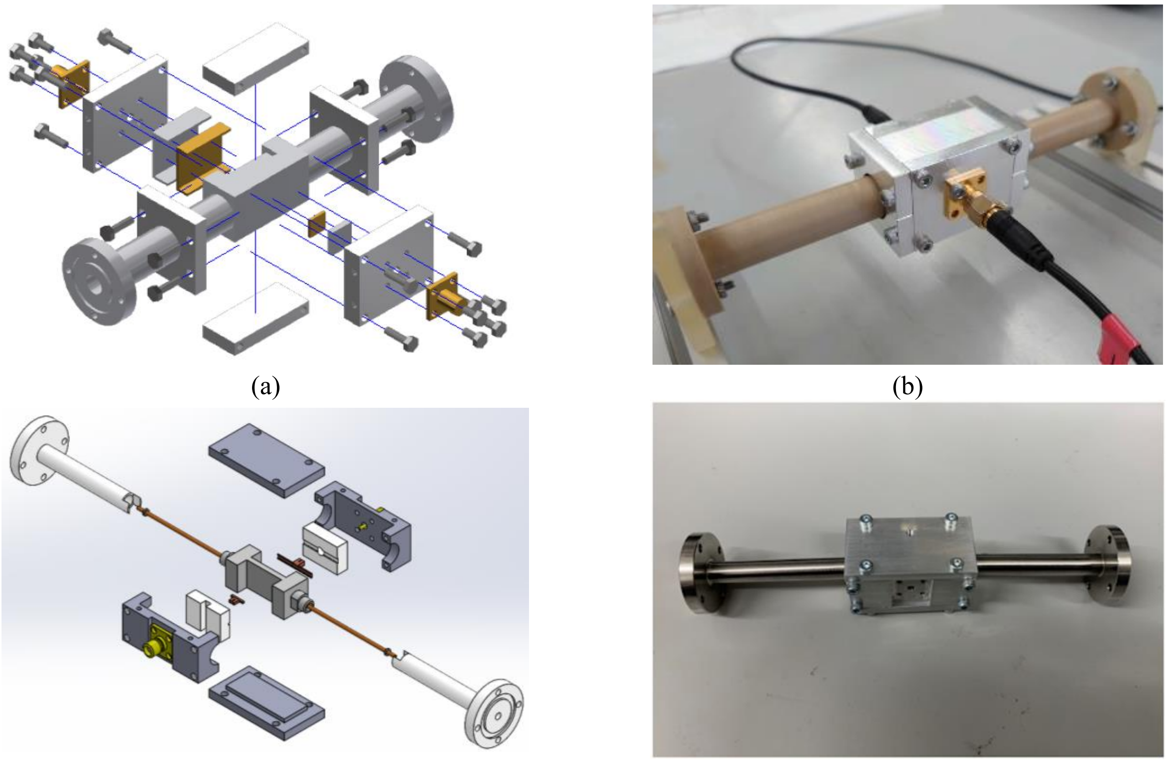

(a) (b) (c) (d)

Fig. 3.1.5-13 Capacitance-based sensor design: (a) CAD model for the macro-tube, (b) actual sensor for macro-tube, (c) CAD model for the microchannel, and (d) actual sensor for microchannel

(7) Summary

The developed capacitance-based void fraction sensor, as detailed in this section, is a measurement method with a simple configuration using a capacitance, which varies depending on the void fraction and flow pattern. This sensor allows for the real-time non-contact measurement of the void fraction. In addition, it has a measurement accuracy (3–5%), which is comparable to that of the existing traditional QCV technique (approximately 1–3%); thereby, it is multi-purpose.

The following items were investigated and verified during the sensor development process:

- Sensor optimization and the C–α relationship analysis using EFA
- Calibration for accurate void fraction measurements using the capacitance-based sensor
- Validation of the capacitance-based sensor for various refrigerants and diameters using the conventional QCV method

3.1.5.2 Void fraction measurement for various refrigerants and diameters using an evaluation apparatus of the refrigerant charge amount

(1) Development of an evaluation apparatus for refrigerant charge amount analysis under a wide range of experimental conditions

Fig. 3.1.5-14 presents a schematic of the experimental apparatus used to measure the void fraction and evaluate the refrigerant charge amount. The designed experimental apparatus can efficiently change the size of test sections from the macro-tube (inner diameter of 7.1 mm) to microchannel (inner diameter of 1 mm) dimensions. The main aspects of this study were as follows.

- The QCV method was applied as a reference measurement method.
- A wide range of compatible heating capacities was used for various refrigerants and mass flow rates.
- The test section was sufficiently large to accommodate various tube diameters.

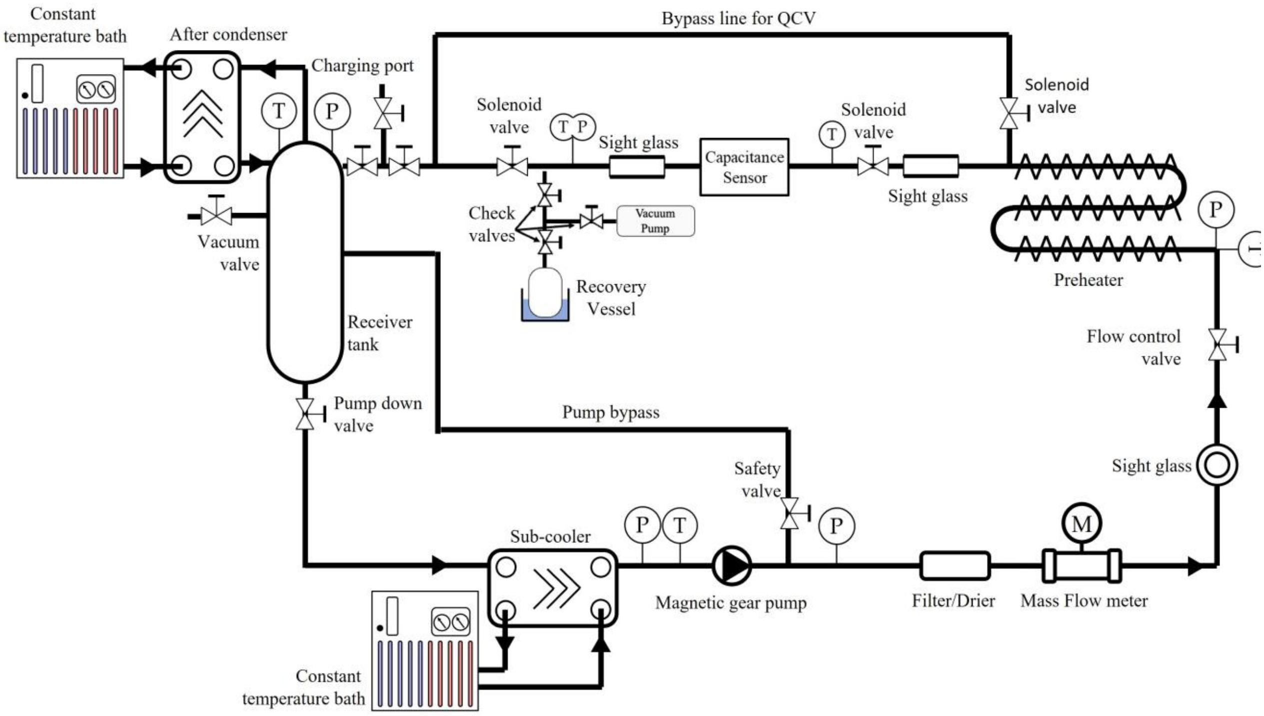

Fig. 3.1.5-14 Schematic of the refrigerant charge amount evaluation apparatus design

The refrigerant loop was made of a copper tube with an inner diameter of 7.1 mm; the flow from the receiver tank to the pre-heater through the subcooler was ensured by a magnetic geared pump (GA series, MICROPUMP) to prevent oil mixing and pulsation caused by the compressor and centrifugal pump. Typically, an air conditioner uses a compressor to circulate the refrigerant. However, the compressor requires lubrication for smooth mechanical operation, and there is a high probability that the lubricant oil mixes with the refrigerant, thereby influencing the refrigerant characteristics. Therefore, it should be excluded from element studies. If a centrifugal pump is used to circulate the refrigerant, it may induce flow pulsation. The aforementioned oil mixing and pulsation problems constitute error factors in the experiment. In this study, the refrigerant in the supercooled state was heated by the pre-heater and converted into a two-phase state with a specific inlet vapor quality. The refrigerant in the two-phase system was returned to the refrigerant tank and passed through the test section. Thereafter, the gas phase of the refrigerant was then condensed in the aftercondenser. The entire experimental apparatus was insulated using AEROFLEX insulation with a thickness of 15 mm, to prevent heat loss to the surrounding environment. The flow rate of the refrigerant was controlled by adjusting the revolutions per minute of the magnetic geared pump, and was measured using a flow meter (OVAL, ALTImass II type U) with an accuracy of ± 0.05%.

The inlet vapor quality was adjusted using an electric pre-heater with a capacity of 5.6 kW. The power consumption of the heater was measured using a power analyzer (YOKOGAWA, WT332E) with an accuracy of ± 0.1%. The saturation temperature and pressure in the test section were controlled using a separate external temperature control system, to regulate the cooling capacity of the condenser. Simultaneously, the pressure was measured using a pressure transducer (YOKOGAWA, EJA430J) with a full-scale accuracy of ± 0.1%, and the temperature was measured using a PT100 RTD sensor (SAKAGUCHI, Class A) with an accuracy of ± 0.15 °C. The uncertainty of the experimental apparatus for the inlet vapor quality was ± 2.12% (x = 0.5, 25 °C, and 250 kg/m²s). A high-speed camera (IDT, NR4-ANM1) was installed in the visualization section mounted downstream of the test section, to observe the flow pattern under all inlet vapor-quality conditions. The high-speed camera system, operated with 1016 × 1016 pixels and a sensor of 1 million pixels, was equipped with a 50 mm f/2.8 macro-lens (Nikon), and 2 s of flow was captured at 5000 fps and 139 μs of exposure time. Fig. 3.1.5-15 presents an actual image of the evaluation apparatus of the refrigerant charge amount.

Fig.3.1.5-15 Overview of refrigerant charge amount evaluation apparatus

(2) Void fraction measurement of R32 and R454C in a macro-sized tube

The R32 refrigerant is an essential component of several low-GWP refrigerants. It is used as a replacement refrigerant for R410A in 600 GWP units, and in mixed refrigerants such as R452B, R454B, R454C, and R466A. Therefore, owing to the significance of this refrigerant, sufficient void fraction measurements for R32 should be conducted. Moreover, R454C is a representative low-GWP refrigerant composed of a mixture of R1234yf and R32 in the ratio 78.5:21.5, which exhibits the characteristics of a zeotropic refrigerant. Additionally, R454C is currently under investigation for application to various systems. In particular, it is a refrigerant that requires investigation to improve the accuracy of the prediction of the refrigerant charging amount, which was the aim of this study. For void fraction measurement, the evaluation apparatus of the refrigerant charge amount developed in 2020 was used. In addition, a capacitance-based sensor with the calibration method and conventional QCV method was applied to measure the void fractions of R32 and R454C. In addition, this evaluation apparatus provided a high measurement accuracy of 1.07% for the uncertainty of the QCV method, and 3.47% for the uncertainty of the capacitance-based sensor based on the pure refrigerant (R32). The measurements were performed at three saturation temperatures (10 °C, 25 °C, and 40 °C), three mass fluxes (100, 250, and 400 kg/m²s), and with an inner diameter of 7.1 mm. However, R454C was measured at three saturation pressures (0.79 MPa, 1.19 MPa, and 1.72 MPa) instead of three saturation temperatures, owing to the characteristics of zeotropic refrigerants.

As shown in Table. 3.1.5-3, the measurement results were compared with the six void fraction prediction correlations presented in the literature, and the capacity of the existing prediction correlations to predict the void fraction of the new refrigerant was investigated.

Table 3.1.5-3 Various correlations for void fraction prediction

	Correlation
Chisholm[8)]	$\alpha = \left[1 + \left(\frac{1-x}{x}\right)\left(\frac{\rho_g}{\rho_l}\right)\sqrt{1 - x\left(1 - \frac{\rho_l}{\rho_g}\right)}\right]^{-1}$
Yashar[9)]	$\alpha = \left(1 + \frac{1}{Ft} + X_{tt}\right)^{-0.321}$
Smith[10)]	$\alpha = \left\{1 + \left(\frac{1-x}{x}\right)\left(\frac{\rho_g}{\rho_l}\right)\left[K + (1-K)\sqrt{\frac{\frac{\rho_l}{\rho_g} + K\frac{(1-x)}{x}}{1 + K\frac{(1-x)}{x}}}\right]\right\}^{-1}$
Steiner[11)]	$\alpha = \frac{U_{sg}}{C_0 U_m + U_{gm}}$, $C_0 = 1 + 0.12(1-x)$, $U_{gm} = \frac{1.18(1-x)}{\rho_l^{0.5}}\left[g\sigma\left(\rho_l - \rho_g\right)\right]^{0.25}$
Zivi[12)]	$\alpha = \left[1 + \left(\frac{1-x}{x}\right)\left(\frac{\rho_g}{\rho_l}\right)^{2/3}\right]^{-1}$
Homogeneous	$\alpha_h = \left[1 + \left(\frac{1-x}{x}\right)\left(\frac{\rho_g}{\rho_l}\right)\right]^{-1}$

Fig. 3.1.5-16 presents the void fraction measurement results for R32 and the existing void fraction prediction correlations. Most of the correlations, except for the homogeneous and Yashar correlations, predicted the void fraction of R32 within an acceptable error range. The measured void fraction was in good agreement with Steiner's correlation.

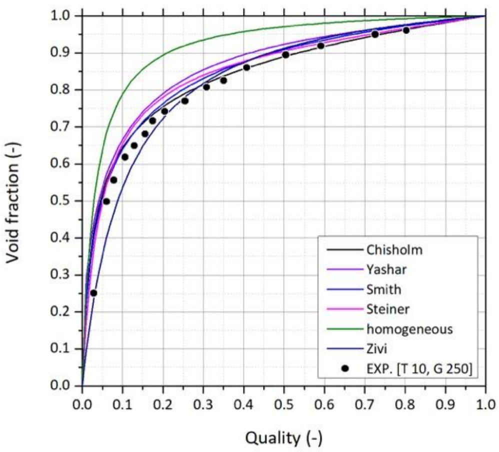

(a) T = 10 °C and G = 250 kg/m²s

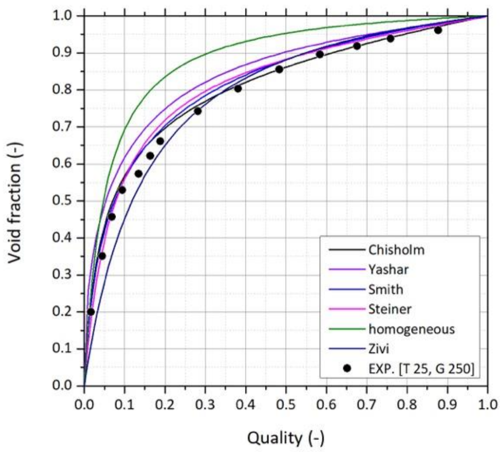

(b) T = 25 °C and G = 250 kg/m²s

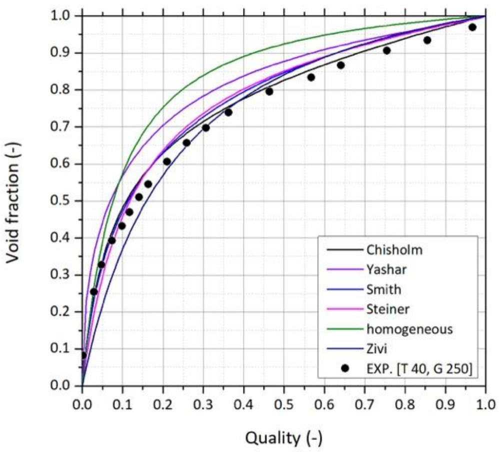

(c) T = 40 °C and G = 250 kg/m²s

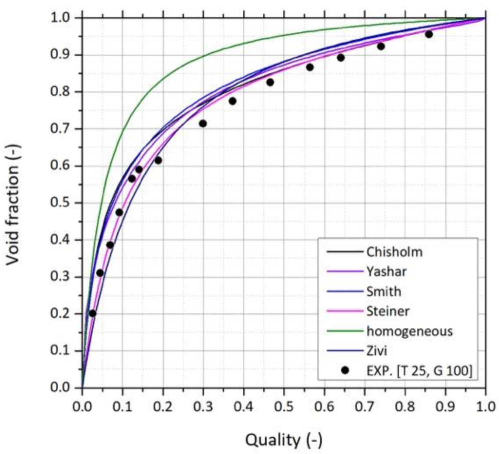

(d) T = 25 °C and G = 100 kg/m²s

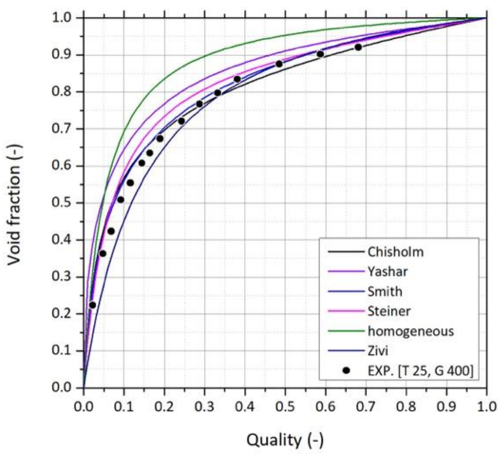

(e) T = 25 °C and G = 400 kg/m²s

Fig. 3.1.5-16 The R32 void fraction measurement and comparison with correlations

Fig. 3.1.5-17 presents the void fraction measurement results for R454C and the existing void fraction prediction correlations. Most of the correlations, except for the homogeneous and Zivi correlations, predicted the void fraction of R454C within an acceptable error range. Nevertheless, the measured void fraction was in good agreement with the correlation by Smith.

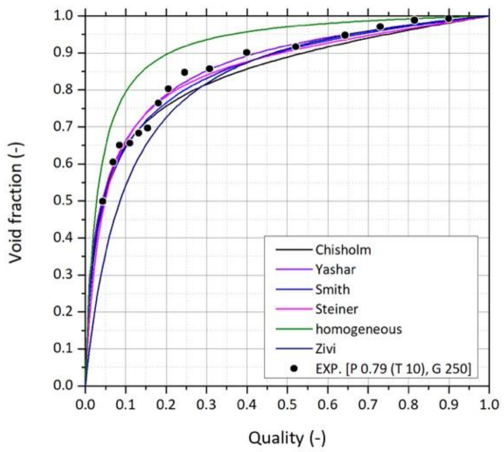

(a) P = 0.79 MPa (T = 10 °C) and G = 250 kg/m²s

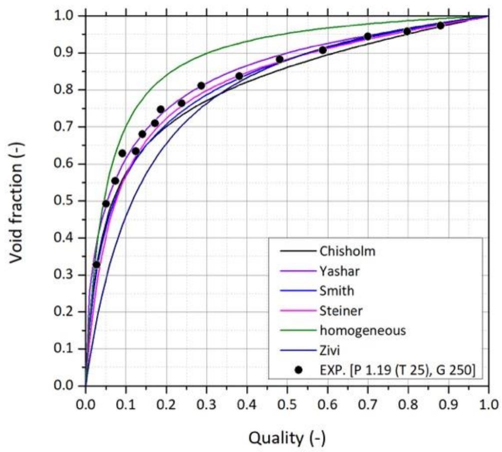

(b) P = 1.19 MPa (T = 25 °C) and G = 250 kg/m²s

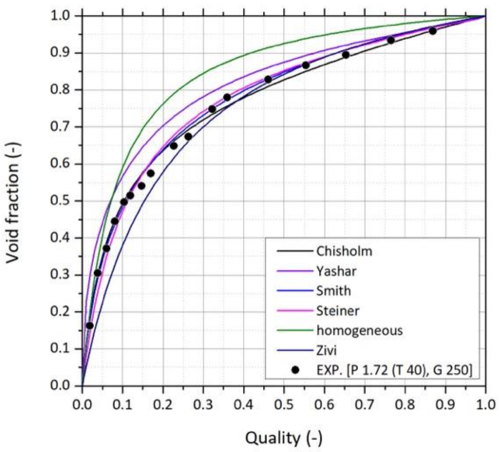

(c) P = 1.72 MPa (T = 40 °C) and G = 250 kg/m²s

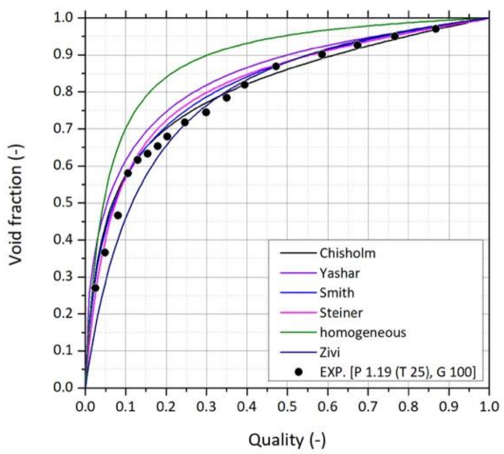

(d) P = 1.19 MPa (T = 25 °C) and G = 100 kg/m²s

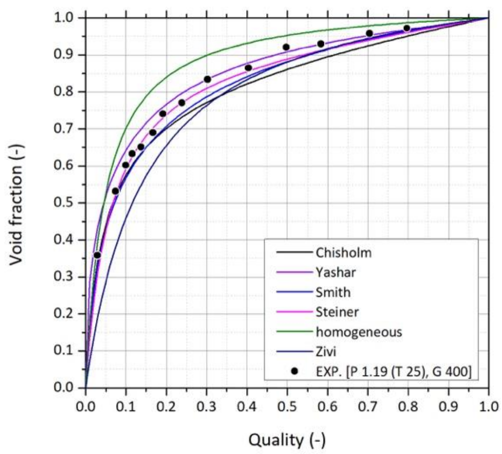

(e) P = 1.19 MPa (T = 25 °C) and G = 400 kg/m²s

Fig. 3.1.5-17 The R454C void fraction measurement and comparison with correlations

Table. 3.1.5-4 quantifies and summarizes the differences between the measurement results of the void fraction of each refrigerant and the six prediction correlations. As described above, in predicting the void fraction of each refrigerant, the optimal correlations differed. In addition, Steiner's correlation was demonstrated to exhibit a relatively low error and can therefore be generally used. However, although Steiner's correlation is general, a deviation occurred depending on the refrigerant. This deviation may be an error factor in the prediction of the refrigerant charging amount. Therefore, it is necessary to develop a new correlation that has a low effect on the refrigerant and a low error.

Table 3.1.5-4 Void fraction prediction errors of various correlations

Refrigerant	Correlation	Error (%) All quality range	Error (%) Low quality range	RMSE	R^2
R32	Chisholm	7.8	12.4	0.042	0.96
	Yashar	15.1	22.7	0.081	0.87
	Smith	7.9	11.5	0.042	0.96
	Steiner	7.0	10.0	0.039	0.96
	Zivi	9.4	14.3	0.049	0.94
	Homogeneous	23.4	33.1	0.135	0.62
R454C	Chisholm	3.8	4.7	0.028	0.98
	Yashar	7.1	9.1	0.045	0.97
	Smith	3.6	4.5	0.028	0.98
	Steiner	4.7	6.2	0.032	0.99
	Zivi	11.7	17.5	0.100	0.95
	Homogeneous	14.7	15.6	0.079	0.97

(3) The void fraction measurement of R1234yf and R32 in a microchannel

R1234yf and R32 refrigerants are important low-GWP pure refrigerants with GWPs of 4 and 675, respectively, and are used in various refrigeration systems. In addition, they are used as components in low-GWP refrigerants; therefore, the acquisition of sufficient information on the void fraction and examination of characteristics are required. However, with reference to the available literature, the measurement result of the void fraction of the refrigerant in a single microchannel has not been reported. In this study, the abovementioned capacitance-based sensor was applied to the microchannel, and the void fractions of R1234yf and R32 flowing in a single microchannel were measured. The void fraction measurement was performed by attaching a test section with an inner diameter of 1 mm to the evaluation apparatus of the refrigerant charge amount presented in Section 3.1.5. A detailed test section is shown in Fig. 3.1.5-18.

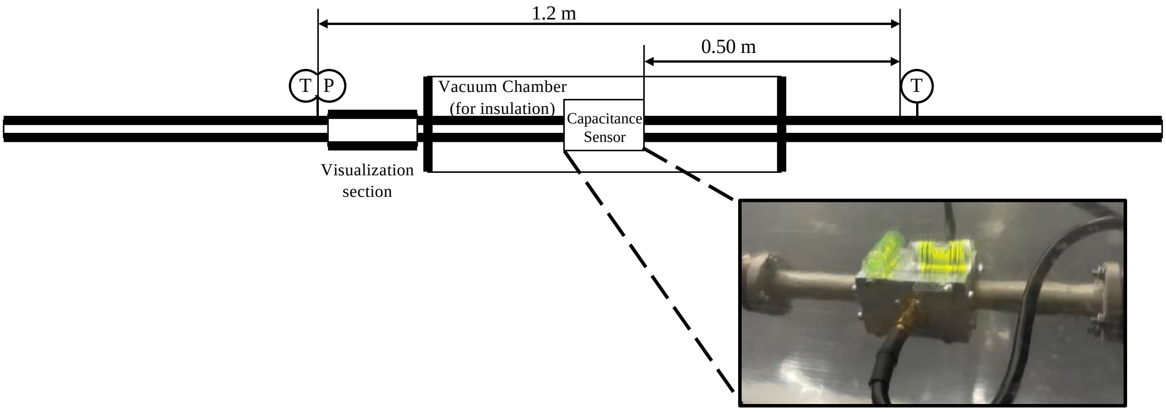

Fig. 3.1.5-18 Test section of microchannel void fraction measurement

As shown in Fig. 3.1.5-18, the QCV method was not applied to the measurement of the void fraction in the microchannel, unlike the measurement in the 7.1 mm macro-tube. The capacitance-based void fraction sensor exhibited sufficient measurement reliability in the studies conducted in 2020 and 2021. Additionally, the QCV method is not suitable for a single microchannel because the absolute amount of refrigerant in the tube directly influences the measurement error. The uncertainty of the void fraction measurement of the microchannel using the capacitance-based sensor was 6.32%, which is larger than the uncertainty for the macro-tube with a diameter of 7.1 mm, and lower than the uncertainty of the QCV method for the microchannel (10–30%). The measurements were performed at two mass flow rates (300 kg/m²s and 600 kg/m²s) and two saturation temperatures (20 °C and 30 °C). A high-speed camera was used for visualization.

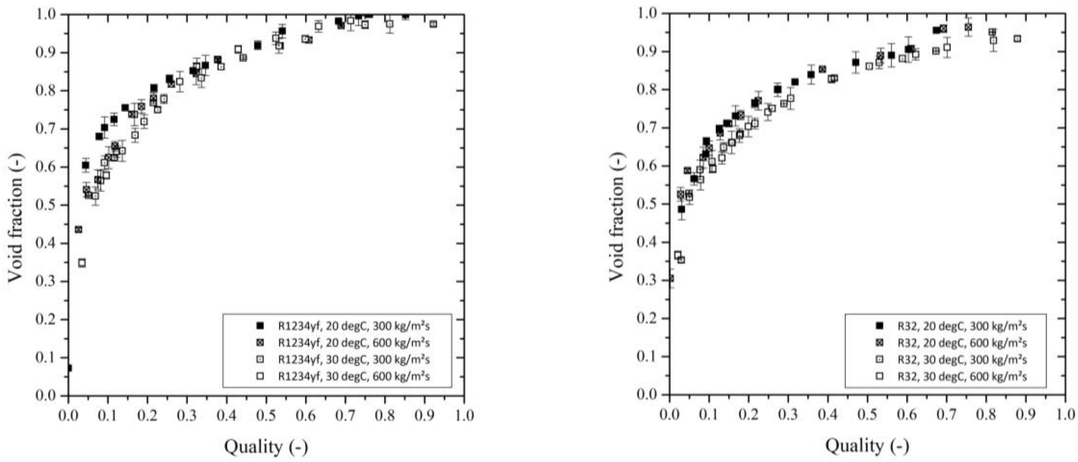

(a) (b)

Fig. 3.1.5-19 Microchannel void fraction results for each refrigerant: (a) R1234yf and (b) R32

Fig. 3.1.5-19 presents the void fraction measurement results for each refrigerant condition. Although there was no significant change between the two temperature conditions, the result at the saturation temperature of 30 °C was slightly lower at the same quality because of the slight temperature difference between the conditions.

In the case of the mass flux, the difference between the two refrigerants with respect to the mass flow rate was relatively small. Fig. 3.1.5-20 presents the flow patterns inside the microchannel captured in this study with respect to the quality of the two mass fluxes.

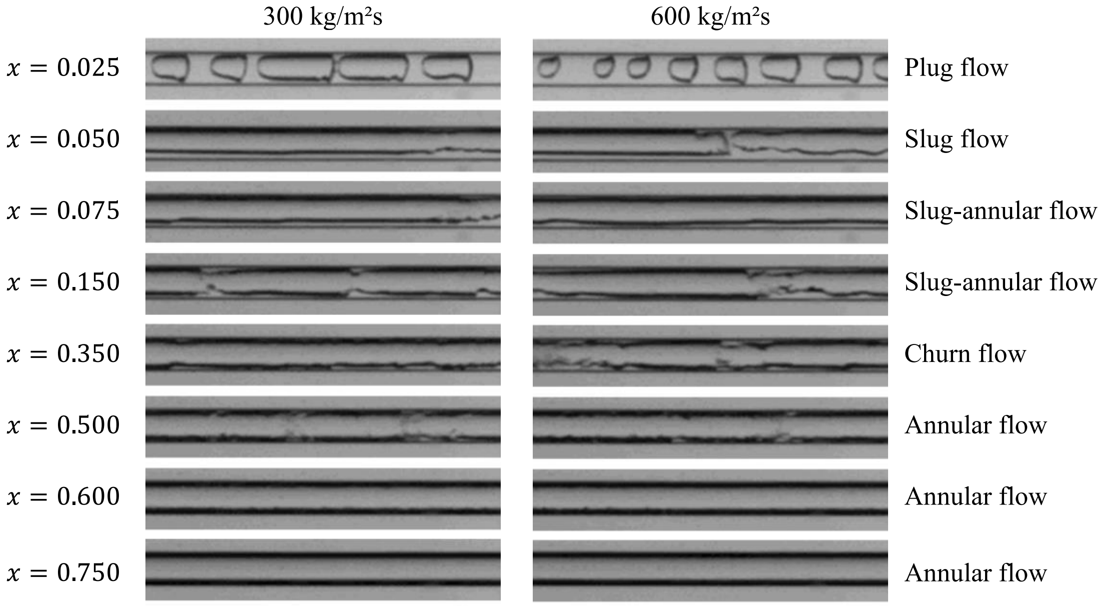

Fig. 3.1.5-20 Visualization results of microchannel with respect to the mass flux [R1234yf]

The change in flow pattern is one of the main reasons for the void fraction differences with respect to the mass flux change. However, the visualization results reveal only a slight difference between the two mass fluxes. In the visualization results, there was additional information on the characteristics of the low-quality two-phase flow in a microchannel. The vapor generated in the low-quality region flowed while pushing the liquid phase under the influence of surface tension and viscosity. In particular, the slip ratio (u_g/u_l) was close to 1 and exhibited a relatively close homogenous characteristic.

In addition, changes in the void fraction according to the refrigerant were discussed. In the relationship between the quality and void fraction, as expressed by Equation 2, the density ratio (ρ_g/ρ_l) exhibited a significant dependence on the refrigerant. As the density ratio increased, the void fraction at the same quality decreased. As shown in Table 3.1.5-5, the density ratio of R32 was more significant than that of R1234yf, which resulted in a relatively low void fraction.

$$\alpha = \left[1 + \left(\frac{1-x}{x}\right)\left(\frac{\rho_g}{\rho_l}\right)\left(\frac{u_g}{u_l}\right)\right]^{-1} \qquad (3.1.5\text{-}5)$$

Table 3.1.5-5 Density and density ratio of each refrigerant

Refrigerant	Temperature	ρ_l (kg/m^3)	ρ_g (kg/m^3)	ρ_g/ρ_l
R1234yf	20 ℃	1109.857	32.796	0.0296
	30 ℃	1073.298	43.729	0.0407
R32	20 ℃	981.384	40.856	0.0416
	30 ℃	939.624	54.776	0.0583

The measured void fraction was compared with six void fraction prediction correlations (Table 3.1.5-3). However, given that Yashar's correlation in Table 3.1.5-3 was significantly different from the measured results, it was replaced with the Armand-Massena's correlation. Table 3.1.5-6 presents the six predicted correlations.

Table 3.1.5-6 Various correlations for the void fraction prediction

	Correlation
Chisholm[8)]	$\alpha = \left[1 + \left(\frac{1-x}{x}\right)\left(\frac{\rho_g}{\rho_l}\right)\sqrt{1 - x\left(1 - \frac{\rho_l}{\rho_g}\right)}\right]^{-1}$
Armand-Massena[13)]	$\alpha = (0.833 + 0.167x)\alpha_h$
Smith[10)]	$\alpha = \left\{1 + \left(\frac{1-x}{x}\right)\left(\frac{\rho_g}{\rho_l}\right)\left[K + (1-K)\sqrt{\frac{\frac{\rho_l}{\rho_g} + K\frac{(1-x)}{x}}{1 + K\frac{(1-x)}{x}}}\right]\right\}^{-1}$
Steiner[11)]	$\alpha = \frac{U_{sg}}{C_0 U_m + U_{gm}}$, $C_0 = 1 + 0.12(1-x)$, $U_{gm} = \frac{1.18(1-x)}{\rho_l^{0.5}}\left[g\sigma(\rho_l - \rho_g)\right]^{0.25}$
Zivi[12)]	$\alpha = \left[1 + \left(\frac{1-x}{x}\right)\left(\frac{\rho_g}{\rho_l}\right)^{2/3}\right]^{-1}$
Homogeneous	$\alpha_h = \left[1 + \left(\frac{1-x}{x}\right)\left(\frac{\rho_g}{\rho_l}\right)\right]^{-1}$

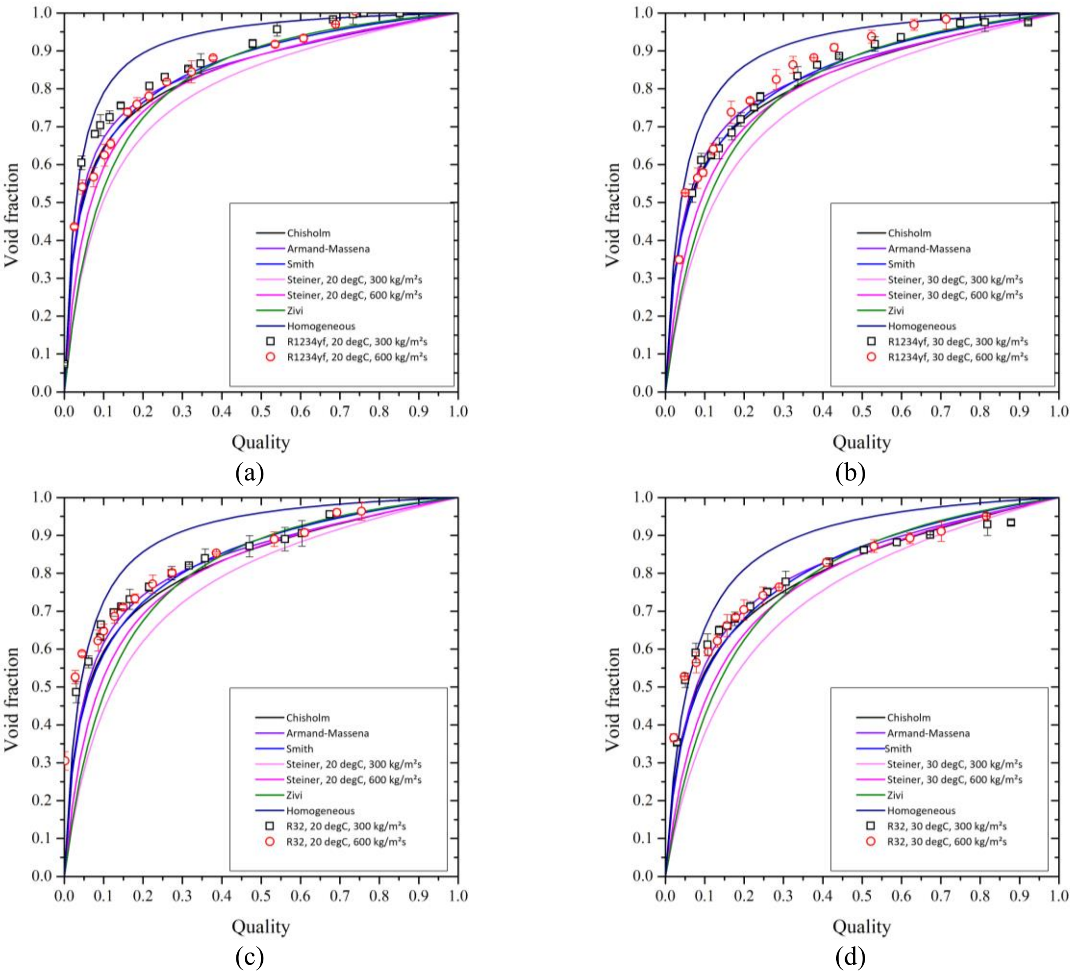

Fig. 3.3-21 Prediction results of considered correlations with experimental data:
(a) R1234yf, T = 20 °C; (b) R1234yf, T = 30 °C; (c) R32, T =n20 °C; and (d) R32, T = 30 °C

Fig. 3.1.5-21 presents the prediction results from the existing six correlations, in addition to the measurement results. In contrast to the measurement results of the void fraction in the macro-tube with a diameter of 7.1 mm, the measured void fraction was generally higher than in the existing six prediction correlations. In particular, it was measured relatively close to the homogeneous model, which indicates that the void fraction of the microchannel was higher than the void fraction of the macro-tube at the same quality. The void fraction was higher because the influences of the surface tension and viscosity on the fluid were relatively significant at small diameters, as demonstrated by Nino[14,15] and Shedd[4] in previous studies. As the effect of the surface tension increased, a characteristic flow pattern was observed, and the slip ratio between the vapor and liquid phases decreased close to 1. As expressed by Equation (3.1.5-5), the vapor phase and liquid phase velocities directly influenced the void fraction. In the microchannel, the slip ratio decreased over the entire area and intensified at a low quality. In plug flow, as shown in Fig. 3.1.5-20, the bubbles generated by boiling pushed the liquid refrigerant while the slip ratio between the vapor and liquid phases approached 1. As the boiling amount gradually increased (and the quality increased), the gas phase volume and velocity ratio increased. However, it was relatively small when compared with that of the macro-tube.

Table 3.1.5-7 Void fraction prediction errors of various correlations for microchannels

Refrigerant	Correlation	Error (%)	RSME	R^2
R1234yf	Chisholm	6.0	0.098	0.96
	Armand-Massena	5.6	0.098	0.96
	Smith	5.4	0.095	0.97
	Steiner	12.7	0.177	0.71
	Zivi	12.0	0.189	0.75
	Homogeneous	12.2	0.178	0.71
R32	Chisholm	8.3	0.137	0.83
	Armand-Massena	6.8	0.136	0.85
	Smith	8.6	0.145	0.81
	Steiner	18.8	0.270	0.09
	Zivi	17.9	0.266	0.21
	Homogeneous	12.1	0.150	0.67

The prediction errors for the six aforedescribed correlations were quantified, as shown in Table 3.1.5-7. Because of the aforementioned characteristics of the microchannels, the correlation results of Armand-Massena based on the homogeneous model were in relatively good agreement with the measurement results. In addition, the slip ratio model was relatively accurate for the void fraction of the microchannel owing to the change in the significant influencing factors of the slip ratio. However, the Steiner drift-flux model, which is generally suitable for most refrigerants and conditions, exhibited a significant difference.

(4) Summary

In this section, the void fractions of the R32, R1234yf, and R454C refrigerants in the macro-tube and microchannel are discussed. R32 and R1234yf are critical as low-GWP refrigerants and components of the R454C low-GWP mixed refrigerant. The void fraction was measured under adiabatic conditions, with the saturation temperature (for pure refrigerant), saturation pressure (for mixed refrigerant), and mass flux as variables.

The differences in the void fraction characteristics between pure and mixed refrigerants were because of the differences in features. However, these result were obtained under adiabatic conditions. For mixed refrigerants, the composition changes during evaporation or condensation. This may induce unsteady changes in physical properties (density, viscosity, surface tension, etc.) that influence the void fraction. However, in the case of adiabatic conditions, because the quality of the inlet/outlet of the test section is maintained, an unsteady composition change does not occur. In further studies, experiments under various heat transfer modes (evaporation and condensation) are required to clarify the effects of unsteady changes in the mixed refrigerant on the void fraction characteristics.

Under the same quality condition, the measured void fraction result of the microchannel was relatively higher than that of the macro-tube, and the trend was particularly significant in the low-quality region. The reason for these trends is that the influence of the surface tension and viscosity is significant in microchannels. This causes a symmetrical flow pattern, in which the velocities of the gas and liquid phases are equalized (the slip ratio approaches 1). These characteristics are more promoted with a decrease in the diameter of the tube; therefore, further research is required.

In addition, the measured void fraction results were compared with various prediction correlations. The accuracy of the prediction correlation differed with respect to the tube diameter. In the macro-tube and microchannel cases, the Steiner and Armand-Massena correlations exhibited relatively high accuracies. Given that the precise prediction correlations are dependent on the difference between the refrigerant and tube diameter, the refrigerant charge amount evaluation using one existing correlation may cause significant errors. Therefore, a correlation that maintains a high accuracy, even with various refrigerants and tube diameters, is required; as described in the followed section.

3.1.5.3 New void fraction correlation for various refrigerants and tube diameters

(1) New drift-flux model

In this study, a relatively highly accurate drift-flux model was selected to derive a new void fraction prediction correlation. Zuber proposed the drift-flux model expressed by Equation (3.1.5-6). It is a model based on two measurable velocities, namely, the vapor phase superficial velocity (U_{sg}) and the liquid phase superficial velocity (U_{sl}), in addition to the vapor phase average velocity (u_g), which is expressed as a two-phase average velocity:

$$u_g = C_0 U_M + U_{gm} \tag{3.1.5-6}$$

where $U_M = U_{sg} + U_{sl}$, U_{gm} is the drift velocity and C_0 is a 'distribution parameter,' which is a parameter that changes according to the distribution of the gas-liquid phase in the cross-section. A physical interpretation represents the relationship between the velocity distribution, assuming homogeneous flow, and the actual velocity distribution. The gas-phase average velocity (u_g) and void fraction (α) are expressed by Equations (3.1.5-7) and (3.1.5-8) using the gas-phase superficial velocity.

$$u_g = \frac{U_{sg}}{\alpha} \tag{3.1.5-7}$$

$$\alpha = \frac{U_{sg}}{C_0 U_M + U_{gm}} \tag{3.1.5-8}$$

According to the report by Bhagwat et al.[16,17], the drift-flux model was concluded as the most versatile. This is because it is sensitive to the flow rate changes and considers changes in the flow pattern. In addition, De Kerpel et al.[5] and Wojtan et al.[18] compared the experimental values with the correlation. They concluded that the Steiner correlation of the drift-flux model exhibited the highest accuracy. However, the Steiner drift-flux model exhibited a deviation in the prediction accuracy depending on the refrigerant and tube diameter, and has been investigated only for pure refrigerants. As described above, C_0 and U_{gm} shown in Equations (3.1.5-6) are the most critical parameters in the drift-flux model. Fig. 3.1.5-22 presents a comparison between the Steiner model (Table 3.1.5-6), which is a widely used drift-flux model, and C_0 and U_{gm} reducted from the experimental values in this study.

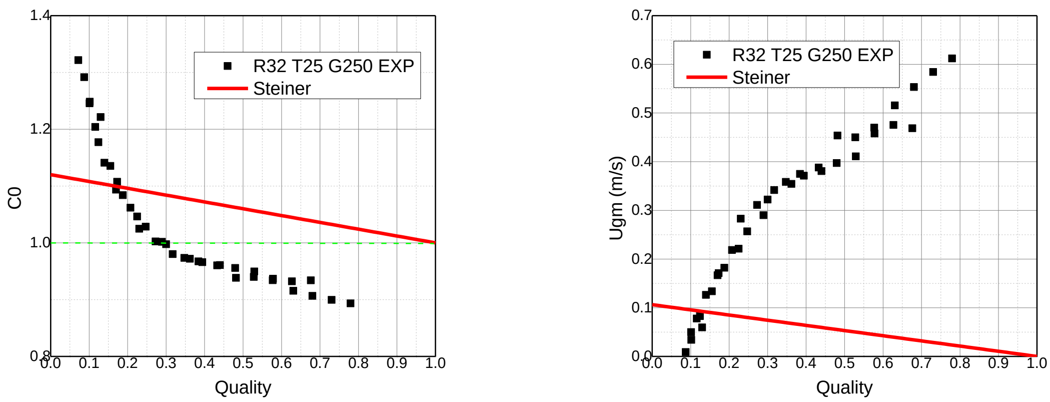

(a) C_0 (b) U_{gm}

Fig. 3.1.5-22 Comparison of Steiner correlation and the experimental results in C_0 and U_{gm}

One of the causes of the difference in C_0 and U_{gm} between Steiner's correlation and the experimental value is the linear relationship that does not consider the flow pattern in Steiner's correlation. The Steiner correlation constructs the equation linearly, such that $C_0 = 1$ for quality $x = 1$. The drift velocity (U_{gm}) is expressed in a form that considers the bubble velocity rising in a vertical flow. The terminal velocity of the rising bubble can be derived from the balance between the buoyancy and drag by considering the size and shape of the bubble, as reported by Harmathy. However, because the buoyancy force on the horizontal flow has a slight effect on the two-phase flow when compared with the vertical flow, additional consideration is required.

Therefore, this paper proposes a correlation that reflects the flow pattern change in horizontal flow. Given that the flow pattern changes according to the quality, the equations are expressed with respect to quality. The equations for the two parameters are expressed by Equations (3.1.5-9) and (3.1.5-10).

$$
\boldsymbol{C_0} = \begin{cases} 0 < x < x_{c1}, & C_{0,p1} + \dfrac{C_{0,p2} - C_{0,p1}}{x_{c1}} x \\ x_{c1} < x < x_{c2}, & \dfrac{x_{c2} - x}{x_{c2} - x_{c1}} C_{0,p2} + \dfrac{x - x_{c1}}{x_{c2} - x_{c1}} C_{0,p3} \\ x_{c2} < x < 1, & \dfrac{1 - x}{1 - x_{c2}} C_{0,p3} + \dfrac{x - x_{c2}}{1 - x_{c2}} C_{0,SP} \end{cases} \tag{3.1.5-9}
$$

$$
\boldsymbol{U_{gm}} = \begin{cases} 0 < x < x_{c1}, & U_{gm,p1} + \dfrac{U_{gm,p2} - U_{gm,p1}}{x_{c1}} x \\ x_{c1} < x < x_{c2}, & \dfrac{x_{c2} - x}{x_{c2} - x_{c1}} U_{gm,p2} + \dfrac{x - x_{c1}}{x_{c2} - x_{c1}} U_{gm,p3} \\ x_{c2} < x < 1, & \dfrac{1 - x}{1 - x_{c2}} U_{gm,p3} + \dfrac{x - x_{c2}}{1 - x_{c2}} U_{gm,SP} \end{cases} \tag{3.1.5-10}
$$

where x_{c1} and x_{c2} are based on Kattan's flow pattern map[19,20] and are calculated as expressed by Equation (3.1.5-11).

$$
x_{c1} = \frac{x_{p1-2} + x_{p2-3}}{2} \tag{3.1.5-11a}
$$

$$
x_{c2} = \frac{x_{p2-3} + 1}{2} \tag{3.1.5-11b}
$$

Let us assume a representative case in which three types of flow patterns change as the quality changes at a given temperature and flow rate. The subscripts such as “p1” and “p2” indicate the flow mode of each sequence according to the transition process of the flow mode; and x_{p1-2} and x_{p2-3} are the transition boundary quality of Flow modes p1 and p2 and the transition boundary quality of Flow modes p2 and p3, respectively. Given that the flow pattern should differ with respect to the refrigerant, temperature, flow rate, and tube diameter, an appropriate transition boundary quality should be selected. Table 3.1.5-8 summarizes the parameters C_0 and U_{gm} for each flow pattern based on the experimental values.

Table 3.1.5-8 Parameters C_0 and U_{gm} of each flow pattern for the proposed correlation

Flow pattern	C_0	$\boldsymbol{U_{gm}}$
Slug	1.2	0
Stratified	1.03	$0.1434\left(\frac{\mu_g}{\mu_L}\right)^{0.67} Re^{-0.13} v_g\big\|_{x=1}$
Plug	1	$0.1434\left(\frac{\mu_g}{\mu_L}\right)^{0.67} v_g\big\|_{x=1}$
Annular	$0.8845\left(\frac{\rho_g}{\rho_L}\right)^{-0.04} Re^{0.04}$	$0.0417\left(\frac{\mu_g}{\mu_L}\right)^{1.48} Re^{-1} We^{0.29} v_g\big\|_{x=1}$
Slug-annular	$0.8845\left(\frac{\rho_g}{\rho_L}\right)^{-0.04}$	$0.0417\left(\frac{\mu_g}{\mu_L}\right)^{1.48} We^{0.29} v_g\big\|_{x=1}$
Single-phase	1	0

In this study, C_0 and U_{gm} of the slug flow and single-phase flow were determined based on Ishii's modified one-dimensional (1D) drift-flux model to obtain valid values. The other flow pattern parameters were derived from the experimental results. From Table 3.1.5-8 and Equations (3.1.5-9) and (3.1.5-10), C_0 and U_{gm} can be derived considering the gradual transition in the flow pattern.

Fig. 3.1.5-23 presents C_0 and U_{gm} from the experimental results, Steiner's correlation, and proposed prediction correlation. The new prediction correlation proposed in this study yielded a value closer to the experimental value than that of the Steiner's correlation for C_0 and U_{gm}, which implies that it accurately reflects the physical characteristics of horizontal two-phase flow.

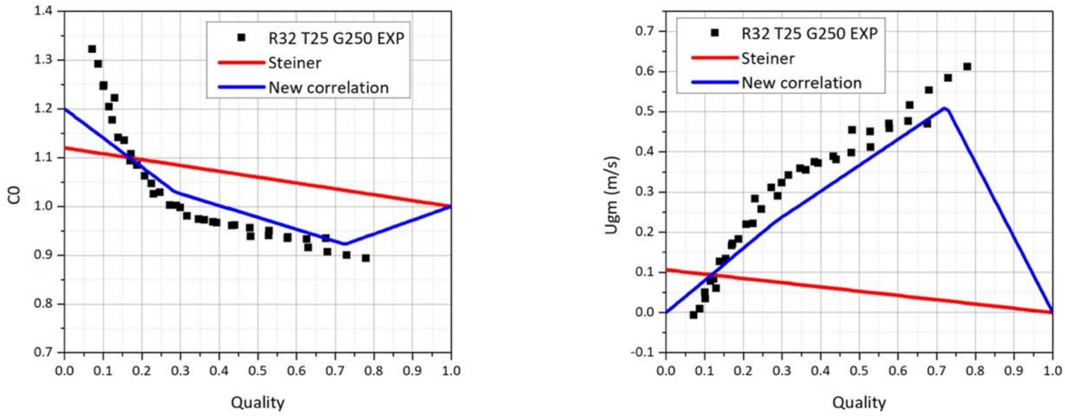

(a) C_0 (b) U_{gm}

Fig. 3.1.5-23 Comparison of C_0 and U_{gm} from the proposed correlation, Steiner correlation, and experimental results for the macro-tube

(2) Comparison with the experimental results of macro-tube void fraction

The proposed prediction correlation and measured void fraction were compared, as shown in Fig. 3.1.5-24.

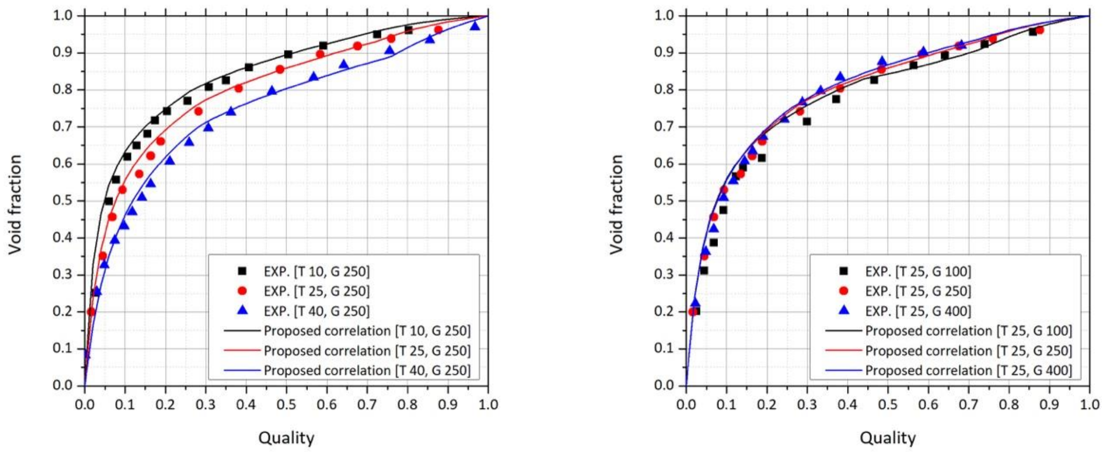

(a) R32 temperature change (b) R32 mass flux change

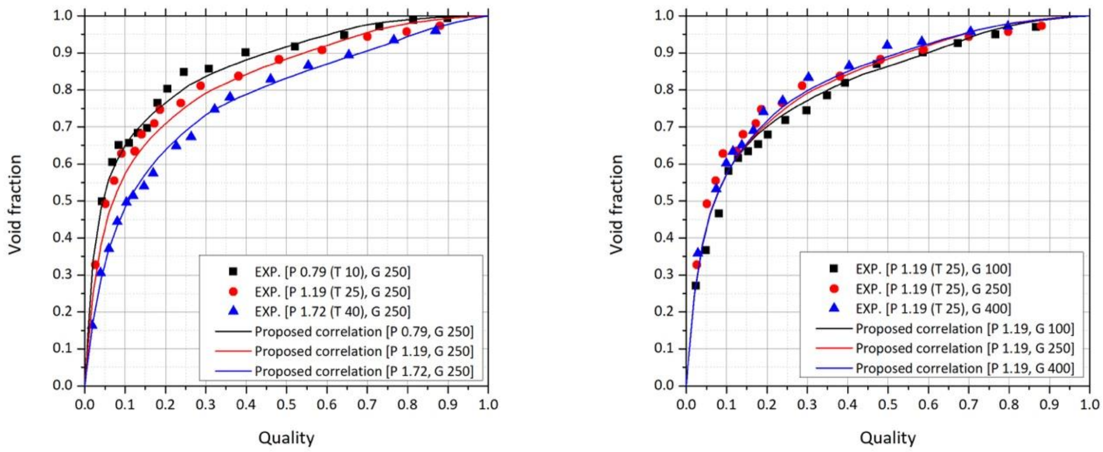

(c) R454C pressure change (d) R454 mass flux change

Fig. 3.1.5-24 Comparison of the proposed correlation with the experimentally measured void fraction

Table 3.1.5-9 presents the quantitative analysis of the error between the measured and predicted void fractions. The predicted error of Steiner's correlation is shown for comparison. The prediction correlation proposed in this study yielded a relatively higher accuracy than Steiner's correlation. Moreover, it yielded a relatively stable and high prediction accuracy for refrigerant changes.

Table 3.1.5-9 Void fraction prediction error of the proposed correlation

Refrigerant	Correlation	Error (%)		RMSE	R^2
		All quality range	Low quality range		
R32	Present research	5.5	7.8	0.034	0.98
	Steiner	7.0	10.0	0.039	0.96
R454C	Present research	4.5	5.1	0.031	0.99
	Steiner	4.7	6.2	0.032	0.99

(3) Comparison with the experimental results of microchannel void fraction

The Steiner drift-flux model uses the coefficient C_0 (distribution parameter) to explain the distribution of the gas and liquid phases of the refrigerants in the tube. It was assumed that there was an asymmetric distribution of the gas and liquid phases. However, the microchannel flow pattern differed from Steiner's drift-flux model, as it exhibited a symmetric flow pattern owing to the significant influence of the surface tension and viscosity. In particular, C_0 converged to 1 for highly symmetric flow patterns (e.g., high-quality annular flow). Therefore, when C_0 of Steiner's drift-flux model was fixed as '1' for all qualities, the prediction results were close to the measured result of the microchannel, as shown in Fig. 3.1.5-25.

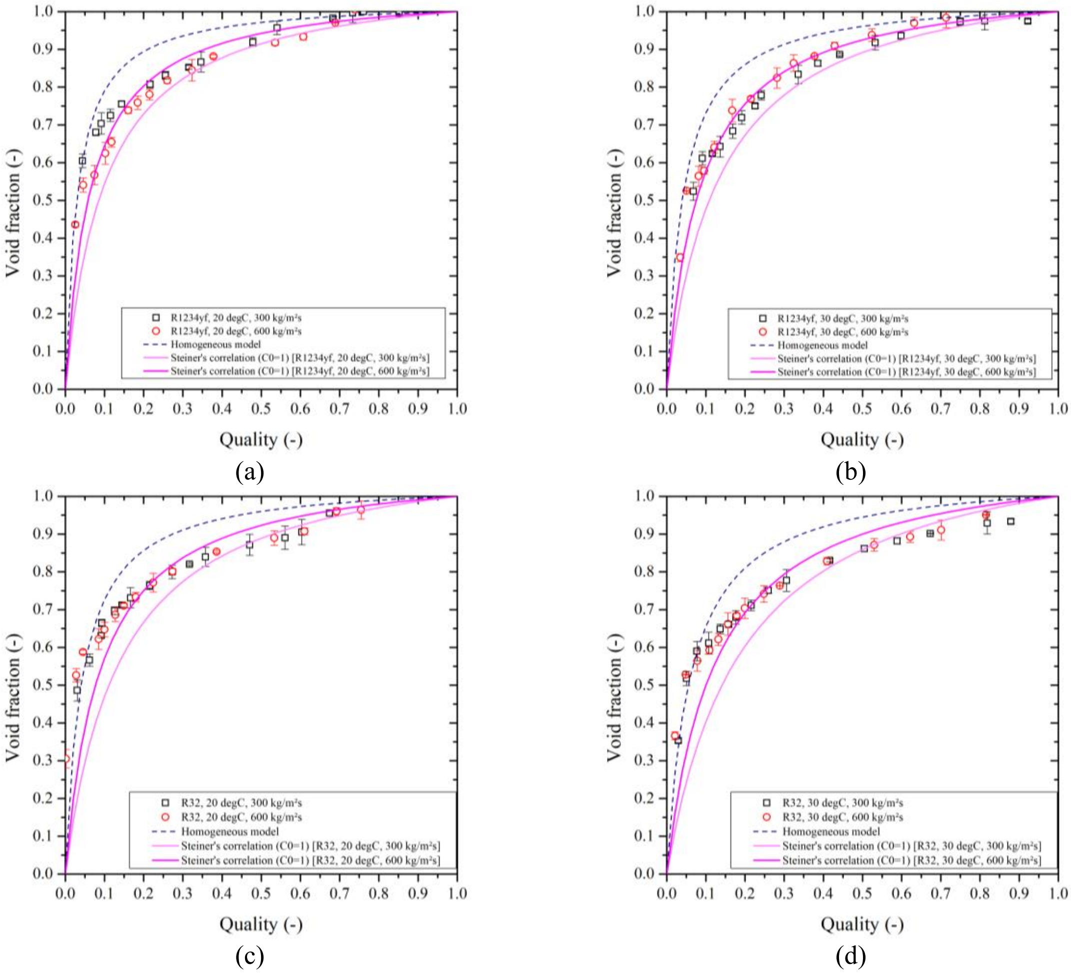

Fig. 3.1.5-25 Prediction results of corrected Steiner correlation with experimental data: (a) R1234yf, T = 20 °C; (b) R1234yf, T = 30 °C; (c) R32, T = 20 °C; and (d) R32, T = 30 °C

Thus, considering the symmetric flow pattern is essential to the distribution parameter C_0. When the parameters that considered flow patterns were applied to the prediction of the microchannel void fraction, as shown in Table 3.1.5-8, the results were as shown in Fig. 3.1.5-26.

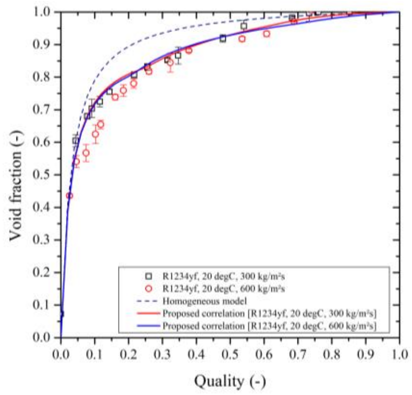

(a)

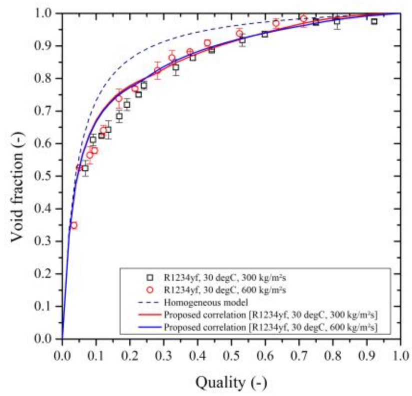

(b)

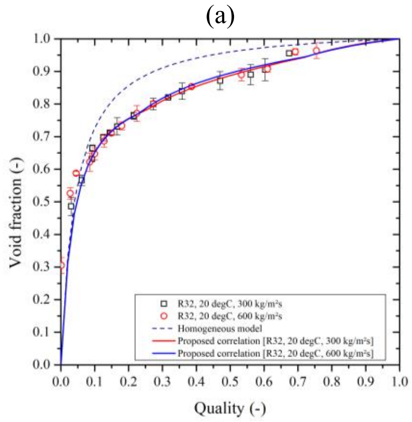

©

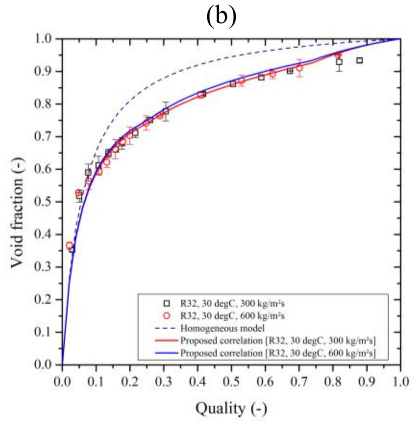

(d)

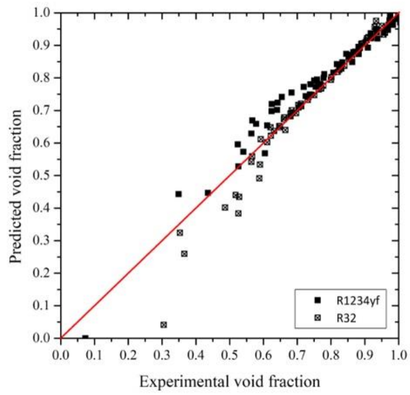

Fig. 3.3-26 Prediction results for microchannel void fraction from the proposed correlation of this study: (a) R1234yf, T = 20 ℃; (b) R1234yf, T = 30 ℃; (c) R32, T = 20 ℃; (d) R32, T = 30 ℃; and (e) experimental vs. prediction values

As shown in Fig. 3.1.5-26, the prediction results were in good agreement with the measurement results, and the quantified error is shown in Table 3.1.5-10.

Table 3.1.5-10 The void fraction prediction errors of various correlations for the microchannel

Refrigerant	Error (%)	RSME	R^2
R1234yf	5.8	0.121	0.94
R32	4.9	0.107	0.91

The new prediction correlation proposed in this study, which predicts the void fraction with a relatively high accuracy with respect to various tube diameters, refrigerants, temperatures, and flow rates, was investigated.

As a further study, a capacitance-based sensor and test section for the micro-fin tube were manufactured, and a void fraction measurement experiment is currently in progress. The void fraction characteristics for the micro-fin tube from this study will be reflected in the prediction correlation and refrigerant charging amount simulation.

(4) Summary

This section describes new prediction correlations, which considered R32, R1234yf, and R454C proposed for macrochannels and microchannels. The proposed correlation is a drift-flux model that considers a gradual flow-pattern transition.

The new void fraction correlation based on the drift-flux model yielded stable prediction results of less than 6% over the entire range of tube diameters, refrigerants, temperatures, and flow rates considered in the experiment. However, comprehensive studies of various refrigerants and tube diameters are required to evaluate the accuracy of the correlations over a broader range.

References

1) G. Portillo, T. A. Shedd, K. H. Lehrer, G., Portillo, and T. A: Proc. Int. Ref. and Air Cond. Conf., p.887 (2008),

2) Y. Sakamoto, H. Kobayashi, Y. Naruo, Y. Takesaki, Y. Nakajima, A. Furuichi, H. Tsujimura, K. Kabayama, and T. Sato: Int J Hydrogen Energy, 44(33), 18483 (2019).

3) Y. Sakomoto, T. Sato, and H. Kobayashi: J. Fluid Sci. Technol., 11(2), JFST0008 (2016).

4) T. A. Shedd:「Void Fraction and Pressure Drop Measurements for Refrigerant R410A Flows in Small Diameter Tubes」, (2012).

5) K. de Kerpel, B. Ameel, C. T’Joen, H. Canière, and M. de Paepe: Int. J. Refrig., 36(2), 390 (2013).

6) AGC Chemicals Company Technical Documents. URL: https://www.agc-chemicals.com/jp/ja /products/detail/index.html?pCode=JP-JA-G007

7) M. Kim, K. Komeda, J. Jeong, M. Oinuma, T. Sato, and K. Saito: Sensors, 22(9), 3511 (2022).

8) D. Chisholm: Int. J. Heat Mass Transf., 16(2), (1973).

9) D. A. Yashar, T. A. Newell, and J. C. Chato: Experimental investigation of void fraction during horizontal flow in smaller diameter refrigeration applications, (1998).

10) S. L. Smith: Proc. Inst. Mech. Eng., 184(1), 647 (1969).

11) D. Steiner: Heat Transfer to Boiling Saturated Liquids, Düsseldorf, (1993).

12) S. M. Zivi: J. Heat Transfer, 86(2), 247 (1964).

13) W. A. Massena: Steam-Water Pressure Drop and Critical Discharge Flow - A Digital Computer Program, Richland, Wash, (1960).

14) V. G. Niño, P. S. Hrnjak, and T. A. Newell: Characterization of Two-Phase Flow in Microchannels, (2002).

15) W. T. Payne, . G Nino, P. S. Hrnjak, and T. A. Newell: Void Fraction and Pressure Drop in Microchannels, (2000).

16) S. M. Bhagwat and A. J. Ghajar: Int. J. Multiph. Flow, 59, 186 (2014).

17) A. J. Ghajar and S. M. Bhagwat: “Frontiers and Progress in Multiphase Flow I,” pp.157–212, Springer International Publishing, (2014).

18) L. Wojtan, T. Ursenbacher, and J. R. Thome: Exp. Therm. Fluid Sci., 29(3), 383 (2005).

19) N. Kattan, J. R. Thome, and D. Favrat: J. Heat Transfer, 120(1), 140 (1998).

20) N. Kattan, J. R. Thome, and D. Favrat: J. Heat Transfer, 120(1), 148 (1998).

3.1.6 Mathematical model

The following is the mathematical model of a heat exchanger.

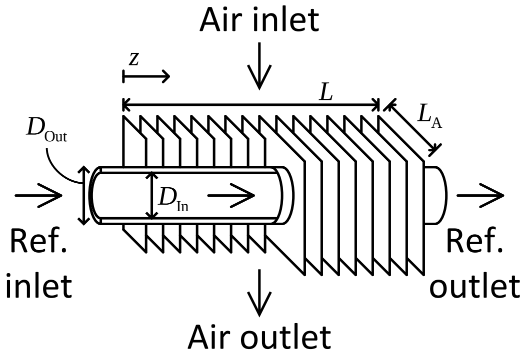

Fig. 3.3.6-1 Fin tube type heat exchanger

Assumption

In the mathematical model of this heat exchanger, the heat transfer coefficient and pressure drop equations characterize the various heat transfer and pressure correlations proposed in this study.

Refrigerant-side continuity equation:

$$\frac{\partial \rho_{\mathrm{R}}}{\partial t}+\frac{\partial\left(\rho_{\mathrm{R}} v_{\mathrm{R}}\right)}{\partial z}=0 . \qquad (3.1.6\text{-}1)$$

Refrigerant-side pressure drop:

$$\frac{\partial P_{\mathrm{R}}}{\partial z}=-f_{\mathrm{R}} \frac{1}{d_{\mathrm{In}}} 2 \rho_{\mathrm{R}} v_{\mathrm{R}}^{2} . \qquad (3.1.6\text{-}2)$$

Refrigerant-side energy equation:

$$\frac{\partial\left(\rho_{\mathrm{R}} u_{\mathrm{R}}\right)}{\partial t}+\frac{\partial\left(\rho_{\mathrm{R}} v_{\mathrm{R}} h_{\mathrm{R}}\right)}{\partial z}=-\frac{L c_{\mathrm{In}}}{S_{\mathrm{In}}} q_{\mathrm{In}} . \qquad (3.1.6\text{-}3)$$

Inner-tube energy equation:

$$\rho_{\mathrm{M}} C_{\mathrm{M}} \frac{\partial T_{\mathrm{M}}}{\partial t}=\frac{L c_{\mathrm{In}}}{S_{\mathrm{M}}} q_{\mathrm{In}}-\frac{A_{\mathrm{Pipe}}+\eta_{\mathrm{FIN}} A_{\mathrm{FIN}}}{S_{\mathrm{M}} L}\left(q_{\mathrm{Out}}+j_{\mathrm{Out}} h v_{\mathrm{Wat}}\right) . \qquad (3.1.6\text{-}4)$$

Air-side continuity equations:

$$\rho_{\mathrm{A,O}} v_{\mathrm{A,O}} L_{\mathrm{A,O}}-\rho_{\mathrm{A,I}} v_{\mathrm{A,I}} L_{\mathrm{A,I}}=\frac{A_{\mathrm{Pipe}}+\eta_{\mathrm{FIN}} A_{\mathrm{FIN}}}{L} j_{\mathrm{Out}} , \qquad (3.1.6\text{-}5)$$

$$\rho_{\mathrm{A,O}} v_{\mathrm{A,O}} L_{\mathrm{A,O}}=G_{\mathrm{A,O}} , \qquad (3.1.6\text{-}6)$$

$$\rho_{\mathrm{A,I}} v_{\mathrm{A,I}} L_{\mathrm{A,I}}=G_{\mathrm{A,I}} . \qquad (3.1.6\text{-}7)$$

Air-side pressure drop:

$$P_{\mathrm{A,O}}-P_{\mathrm{A,I}}=-f_{A} \frac{2 L_{x} \rho_{A} V_{ac}^{2}}{D_{ec}} . \qquad (3.1.6\text{-}8)$$

Air-side vapor continuity equation:

$$\rho_{\mathrm{A,O}} v_{\mathrm{A,O}} X_{\mathrm{A,O}} L_{\mathrm{A,O}} - \rho_{\mathrm{A,I}} v_{\mathrm{A,I}} X_{\mathrm{A,I}} L_{\mathrm{A,I}} = \frac{A_{\mathrm{Pipe}} + \eta_{\mathrm{FIN}} A_{\mathrm{FIN}}}{L} j_{\mathrm{Out}} . \tag{3.1.6-9}$$

Air-side energy equation:

$$\rho_{\mathrm{A,O}} v_{\mathrm{A,O}} h_{\mathrm{A,O}} L_{\mathrm{A,O}} - \rho_{\mathrm{A,I}} v_{\mathrm{A,I}} h_{\mathrm{A,I}} L_{\mathrm{A,I}} = \frac{A_{\mathrm{Pipe}} + \eta_{\mathrm{FIN}} A_{\mathrm{FIN}}}{L} \left(q_{\mathrm{Out}} + j_{\mathrm{Out}} hv_{\mathrm{Wat}} \right). \tag{3.1.6-10}$$

If the air outlet temperature reaches the dew point, j is calculated under the assumption that dehumidification is performed to equalize the air outlet temperature and dew point. If the air outlet temperature is higher than the dew point, no dehumidification is assumed.

$$j_{\mathrm{Out}} = \begin{cases} 0 & T_{\mathrm{DP,A,O}} < T_{\mathrm{A,O}} \\ f\left(P_{\mathrm{A,O}}, h_{\mathrm{A,O}}, T_{\mathrm{DP,A,O}}\right) & T_{\mathrm{DP,A,O}} = T_{\mathrm{A,O}} \end{cases} \tag{3.1.6-11}$$

Heat transfer equation:

$$q_{\mathrm{In}} = \alpha_{\mathrm{In}} \left(T_{\mathrm{R}} - T_{\mathrm{M}} \right) . \tag{3.1.6-12}$$

Void fraction equation:

$$\alpha = \left[1 + s\left(\frac{1-x}{x}\right)\left(\frac{\rho_g}{\rho_l}\right)\right]^{-1}. \tag{3.1.6-13}$$

In the gas–liquid two-phase flow model, the slip ratio stated in Equation 3.1.6-13 is obtained using the Smith equation for the heat exchanger and piping as a slip flow model. For the other elements, a homogeneous flow is assumed with s = 1.

NOMENCLATURE

A	: Area, m^2	α	: Heat transfer coefficient, $W \cdot m^{-2} \cdot K^{-1}$
D	: Diameter, m	ρ	: Density, $kg \cdot m^{-3}$
f	: Fanning friction factor, -	η	: Efficiency, -
G	: Mass flow rate, $kg \cdot s^{-1}$	λ	: Thermal conductivity, $W \cdot m^{-1} \cdot K^{-1}$
h	: Specific enthalpy, $J \cdot kg^{-1}$	Nu	: Nusselt number, -
j	: Mass flux, $kg \cdot m^{-2} \cdot s^{-1}$	V	: Volume, m^3
L	: Length, m	F	: Fin length, m
P	: Pressure, Pa	μ	: Viscosity, Pa・s
q	: Heat flux, $W \cdot m^{-2}$	ν	: Kinematic viscosity, $m^2 \cdot s^{-1}$
S	: Cross sectional area, m^2	Cp	: Specific heat capacity, $J \cdot kg^{-1} \cdot K^{-1}$
t	: Time, s	Ga	: Galileo number, -
u	: Specific internal energy, $J \cdot kg^{-1}$	hv	: Latent heat of vaporization, $J \cdot kg^{-1}$
v	: Velocity, $m \cdot s^{-1}$	H	: Sensible heat factor, -

SUBSCRIPTS

A	: Air	Vap	: Vapor
DP	: Dew point	EVA	: Evaporator
FC	: Fin collar	SAT	: Saturated
FIN	: FIN	Pipe	: Pipe
I	: Inlet	F	: Front

In	: Inside	P	: Pitch
M	: Metal	T	: Thickness
O	: Outlet	W	: Wall
Out	: Outside	C	: Collar
R	: Refrigerant	Cha	: Characteristic
Liq	: Liquid	Wat	: Water

3.2 Compressor

As social awareness of global warming increases, conventional refrigerants are regulated at different stages. To select safe and environment-friendly next-generation refrigerants for highly efficient heat pump systems, a performance evaluation method by simulation technologies should be established to overcome the limitations of experiments involving a wide variety of refrigerants. This study was focused on the complex refrigerant behavior inside a compressor, which considerably influences the system performance. Additionally, the aim of this study was to develop detailed simulation models that can reflect the change in the refrigerant state in the compressor, considering the differences in refrigerant properties. The details of the system performance were further clarified based on the proposed compressor model. The compressor efficiency was calculated and compared with respect to different refrigerants based on a model that considers the effects of the leakage and heat transfer of the refrigerant containing lubricant. Compressor performance tests were conducted to verify the validity of the model. Heat pump cycle simulations were performed using the compressor efficiency values, and the effects of different refrigerant properties on the characteristics and performance of the entire heat pump cycle were accordingly clarified.

3.2.1 Modeling

The compressors studied were scroll- and rotary-type compressors, which are widely used in the refrigeration and air-conditioning fields. Their structures are shown in Fig. 3.2-1, and an equivalent compressor model is depicted in Fig.3.2-2. Both types of compressors consist of a compression mechanism that draws in and pressurizes the refrigerant gas, a motor that drives the compression mechanism, and a sealed casing that houses them. The refrigerant is compressed and discharged through the suction, compression, and discharge chambers. In these processes, the leakage of refrigerant from the high-pressure side to the low-pressure side should be considered, in addition to the heat transfer to and from the wall surface of the working chamber and effects of the lubricating oil.

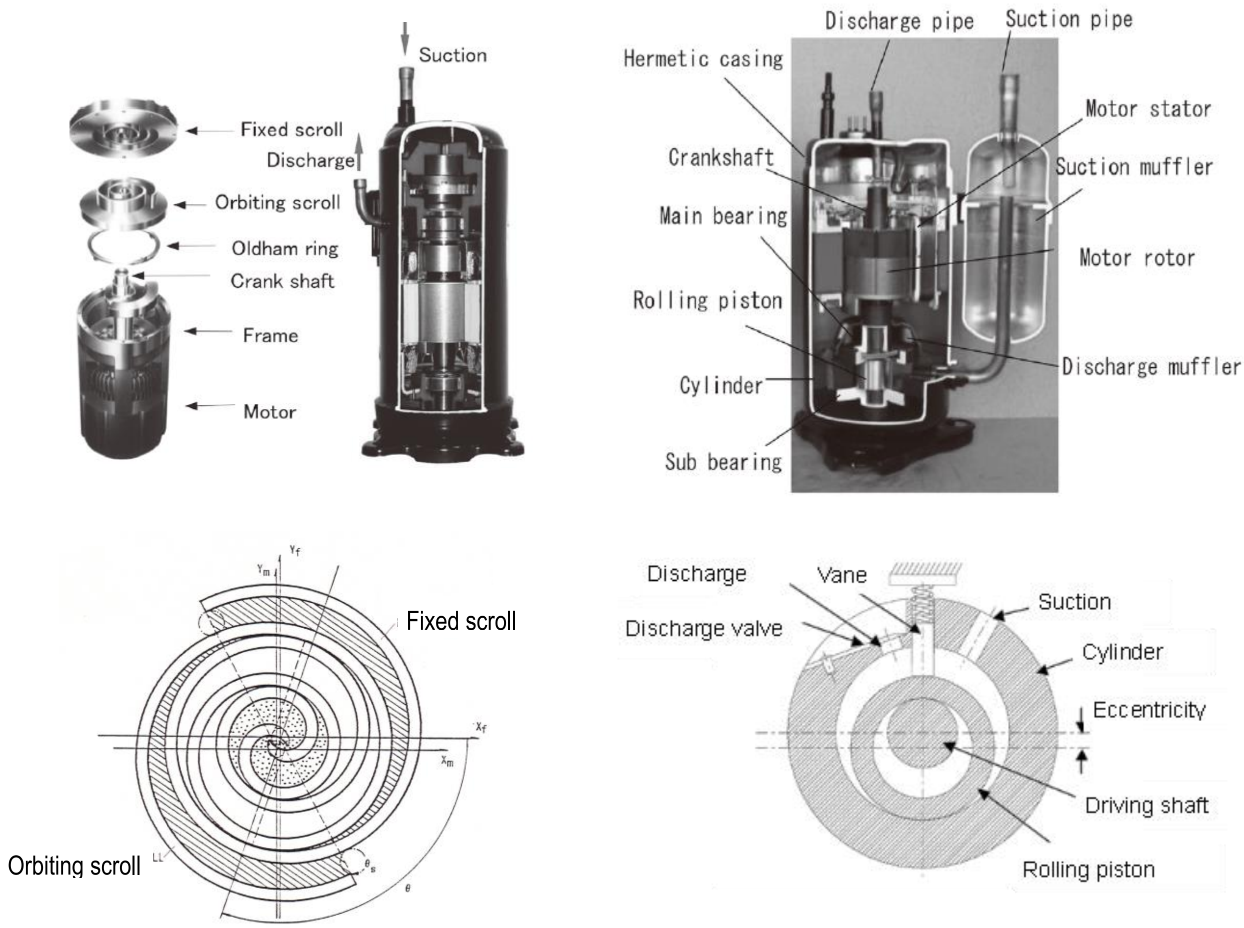

Scroll compressor[4] Rotary compressor[1]

Fig. 3.2-1 Scroll- and rotary-type compressors

In general, when modeling a compressor, as shown in Fig.3.2-2, the thermo-fluid characteristics of the refrigerant in the compression chamber, mechanical characteristics of the bearings and sliding parts in the compression mechanism, and electrical characteristics of the inverter and motor are considered. However, in this study, the mechanical and electrical characteristics that are considered to be less affected by the refrigerant's physical properties. Accordingly, they are expressed using the motor efficiency, inverter efficiency, etc.

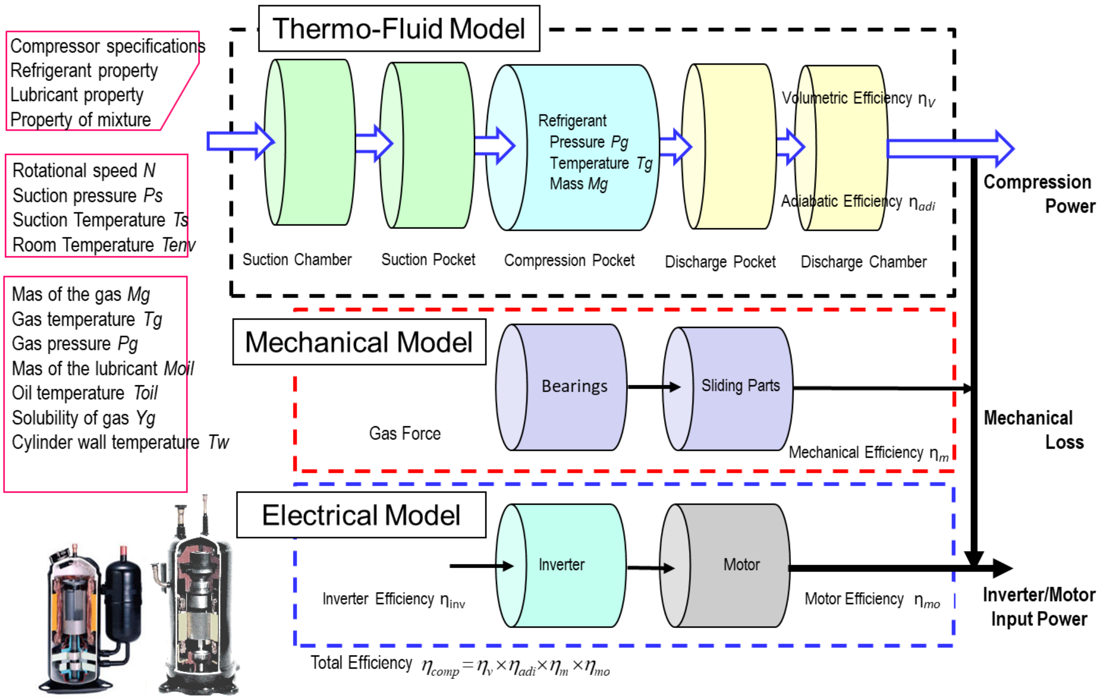

Fig. 3.2-2 Compressor model

3.2.2 Compression Chamber Model

A positive displacement compressor draws refrigerant gas into the compression chamber, reduces its volume using mechanical power, and discharges it at a higher pressure. Owing to heat, mass, and work transfer during gas compression, the state of the refrigerant in the compression chamber continuously changes over time. The amount of work done on the compressed refrigerant, leakages between adjacent chambers with different pressures, and heat transfer between the gas, wall surface, and lubricant are considered, as represented in Fig. 3.2-3. We can assume that the gas and lubricant do not undergo phase changes, and the specific volume of the latter does not change with pressure. Moreover, we can further assume that the lubricant acts as an immiscible mist contained in the gas, and that there is no heat transfer between the lubricant and wall surface (heat transfer to/from the wall surface is assumed to be performed only by refrigerant gas).

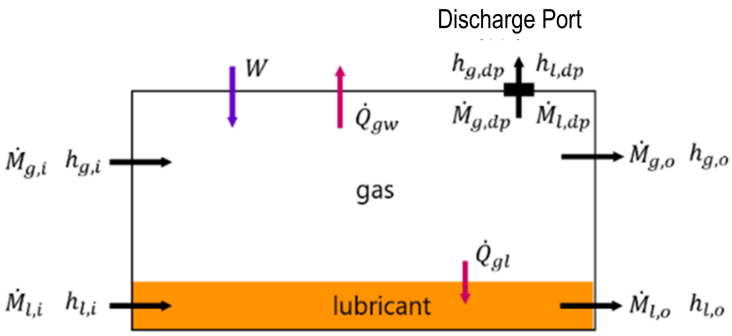

Fig. 3.2-3 Compression chamber model

3.2.2.1 Fundamental equations

The energy and mass conservation of the gas and lubricant in the compression chamber can be expressed by Eqs. (3.2-1)-(3.2-4).

$$\frac{dM_g u_g}{dt} = \dot{M}_{g,i}h_{g,i} - \left(\dot{M}_{g,out} + \dot{M}_{g,dp}\right)h_{g,o} + \dot{W} - \dot{Q}_{gw} - \dot{Q}_{gl} \tag{3.2-1}$$

$$\frac{dM_l u_l}{dt} = \dot{M}_{l,i}h_{l,i} - \left(\dot{M}_{l,o} + \dot{M}_{l,dp}\right)h_{l,o} + \dot{Q}_{gl} \tag{3.2-2}$$

$$\frac{dM_g}{dt} = \dot{M}_{g,i} - \dot{M}_{g,o} - \dot{M}_{g,dp} \tag{3.2-3}$$

$$\frac{dM_l}{dt} = \dot{M}_{l,i} - \dot{M}_{l,o} - \dot{M}_{l,dp} \tag{3.2-4}$$

3.2.2.2 Leakage

The refrigerant gas and lubricating oil flow from the high-pressure section to the low-pressure section of the compressor through the gap between them. Figures 3.2-4 and 3.2-5 present the typical leakage paths for each compressor.

Typical leakage paths in a scroll compressor are as follows:
① Axial clearance between the top of the scroll wrap and the bottom of the mating scroll wrap (axial gap δa)
② Radial clearance between the side of the scroll wrap and the side of the mating scroll wrap (radial gap δr)

Typical leakage paths in a rotary compressor are as follows:
① Radial clearance between the rolling piston and cylinder
② End-face clearance between the vane and cylinder side surface
③ End-face clearance between the rolling piston and cylinder side surface
④ Clearance between the vane and vane groove surface

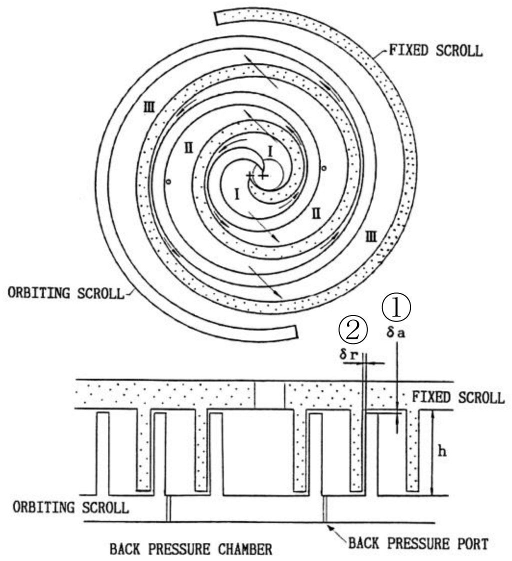

Fig. 3.2-4 Leakage pass (scroll compressor) [4)]

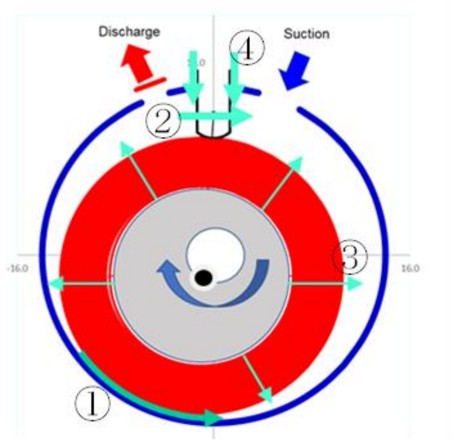

Fig. 3.2-5 Leakage pass (rotary compressor)

The amount of leakage is calculated using the apparent specific heat ratio and gas temperature, assuming the thermal equilibrium and homogeneity of the two-phase flow of gas and lubricant, as realized in the model proposed by Fujiwara et al. (1985). Regarding the mixture of refrigerant and lubricant, the lubricant is included in the mass fraction φ. The mass flow rate of the leaked gas and lubricant flowing through the gap of the high-pressure side (Chamber 1) to the low-pressure side (Chamber 2) (Leakage paths ① and ② shown in Fig. 2) is calculated using Equation (3.2-7), which corresponds to the mass flow rate of a compressible fluid passing through an orifice. The apparent specific heat ratio of the mixture is obtained using Equation (3.2-9).

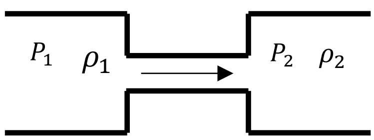

Fig. 3.2-6 Nozzle flow (compressible flow)

$$\dot{M}_g = (1-\varphi)\dot{M} \tag{3.2-5}$$

$$\dot{M}_l = \varphi\dot{M} \tag{3.2-6}$$

$$\dot{M} = \begin{cases} cA\sqrt{\frac{2\kappa}{\kappa-1}P_1\rho_1\left\{\left(\frac{P_2}{P_1}\right)^{\frac{2}{\kappa}} - \left(\frac{P_2}{P_1}\right)^{\frac{\kappa+1}{\kappa}}\right\}} & (P_2 > P_{\mathrm{ch}}) \\ cA\sqrt{P_1\rho_1\kappa\left(\frac{2}{\kappa+1}\right)^{\frac{\kappa+1}{\kappa-1}}} & (P_2 \leqq P_{\mathrm{ch}}) \end{cases} \tag{3.2-7}$$

$$P_{\mathrm{ch}} = P_1\left(\frac{2}{\kappa+1}\right)^{\frac{\kappa}{\kappa-1}} \tag{3.2-8}$$

$$\kappa = \frac{C_p M_g + C_l M_l}{C_v M_g + C_l M_l} \tag{3.2-9}$$

Moreover, a portion of the lubricating oil supplied between the inside of the rolling piston and drive shaft of the rotary compressor leaks into the compression chamber through the end-face clearance between the rolling piston and cylinder side (Leakage path (3)). In addition, the lubricating oil acting on the back of the vane leaks into the compression chamber through the clearance between the vane and vane groove (Leakage path ④). The flow rates of lubricating oil through these gaps are calculated as a viscous fluid flow (laminar flow) using Equation (3.2-10).

$$\dot{M}_l = \frac{b\rho_l}{12L\mu_l}(P_i - P_o)\delta^3 \tag{3.2-10}$$

3.2.2.3 Heat transfer

The heat transfer area between the gas and wall is equivalent to the inner surface area of the compression chamber, which is the sum of the top, bottom, and side surfaces, and can be determined by the geometric parameters. The heat transfer coefficients between the refrigerant and wall surface are calculated using the Nusselt number and equation for the forced convection heat transfer in a circular tube (Kays and Crawford, 1980).

$$\dot{Q}_{gw} = h_{gw}S_{gw}(T_g - T_w) \tag{3.2-11}$$

$$\dot{Q}_{gl} = h_{gl}S_{gl}(T_g - T_l) \qquad (3.2\text{-}12),$$

$$Nu = CRe^m Pr^n (C = 0.022, m = 0.8, n = 0.5) \tag{3.2-13}$$

3.2.2.4 Discharge valve (Relief valve)

The discharge valve, which prevents backflow from the discharge chamber to the compression chamber, opens when the pressure difference between the compression and discharge chambers exceeds a certain value, thus discharging refrigerant gas from the compression to the discharge chamber. The model is shown in Fig. 3.2-7. The displacement and velocity of the valve are determined using Eq. (3.2-14) and Eq. (3.2-15), respectively. We can assume that the opening area is proportional to the displacement.

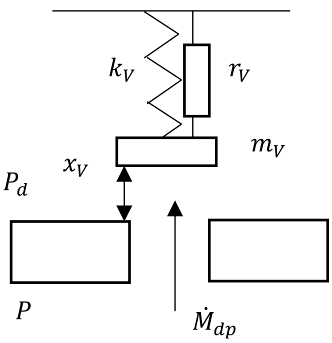

Fig. 3.2-7 Discharge (Relief) Valve

$$\frac{dx_V}{dt} = v_V \tag{3.2-14}$$

$$\frac{dv_V}{dt} = \frac{1}{m_V}(F_{gv} - r_V v_V - k_V x_V) \tag{3.2-15}$$

3.2.3 Refrigerant

In this study, R410A and its alternatives (R32 and R466A) were selected. Table 3.2-2 presents the composition and typical properties of these refrigerants, and the cooling effect and coefficient of performance (COP) in the theoretical cycle under the conditions listed in Table 3.2-1.

Table 3.2-1 Cycle conditions of temperature

Condensing temperature	℃	42
Evaporating temperature	℃	8.5
Superheat	K	5
Subcool	K	3

Table 3.2-2 Properties of refrigerant

Refrigerant	R410A	R32	R466A
Composition (Mass %)	R32/R125 = 50/50	R32 = 100	R32/R125/CF3I = 49/11.5/39.5
GWP (AR4)	2090	675	733
Safety classification	A1	A2L	A1
Specific heat ratio	1.38	1.49	1.43
Density ($kg \cdot m^{-3}$)	38.5	27.8	45.8
Cooling effect ($kJ \cdot kg^{-1}$)	165	250	149
Cooling effect ($kJ \cdot m^{-3}$)	6374	6953	6837
Theoretical COP	6.65	6.81	6.71
COP ratio	1.000	1.02	1.01

3.2.4 Compressor simulation

3.2.4.1 Calculation methods

Based on the model depicted in the previous section, simulations were performed using R410A, R32, and R466A as refrigerants, assuming a compressor for a residential R410A air conditioner, to clarify the effects of refrigerant properties on the compressor characteristics and performance. Based on the inlet and outlet conditions of the compressor, the state of the refrigerant from the suction to discharge stages was calculated for each angle in MATLAB using the Runge–Kutta method. The physical properties of the refrigerant were obtained using REFPROP10. Table 3.2-3 lists the compressor specifications and operating conditions used in the calculations. The scroll and rotary compressors had stroke volumes of 8.0 cc/rev and 7.25 cc/rev, respectively.

Table 3.2-3 Specifications of compressor simulation

Displacement volume	cc	Scroll/rotary 8.0/7 .25
Rotational speed	rps	Scroll/rotary 50/60
Evaporating temperature	℃	8.5
Super heat	K	5
Lubricant circulating ratio	%	2.0

3.2.4.2 Results of compressor simulation

(1) Leakage and heat transfer

Fig. 3.2-8 presents the leakage in a scroll compressor at a condensation temperature of 42 ℃ (Leakage path ①). The vertical axis denotes the ratio of the leakage mass flow rate to the mass of the refrigerant in the compression chamber at suction completion, and the horizontal axis denotes the rotational angle from the start of the suction process. The effects of heat transfer to and from the wall surface of the working chamber are shown in Fig. 3.2-9. The vertical axis denotes the ratio of the heat transfer rate to the heat capacity of the refrigerant in the compression chamber at suction completion, and the horizontal axis denotes the rotational angle from the start of the suction process.

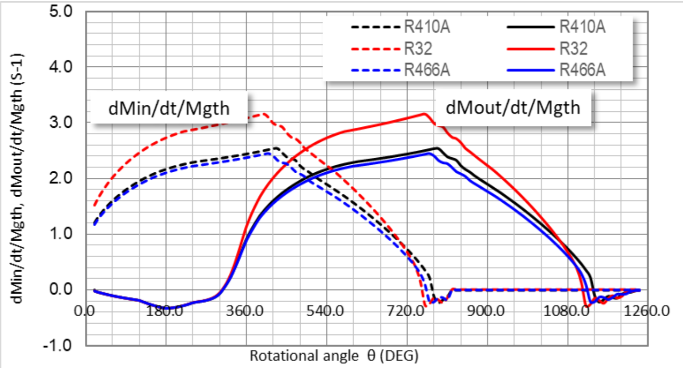

Fig. 3.2-8 Leakage flow rate through Leakage path ① (scroll compressor)

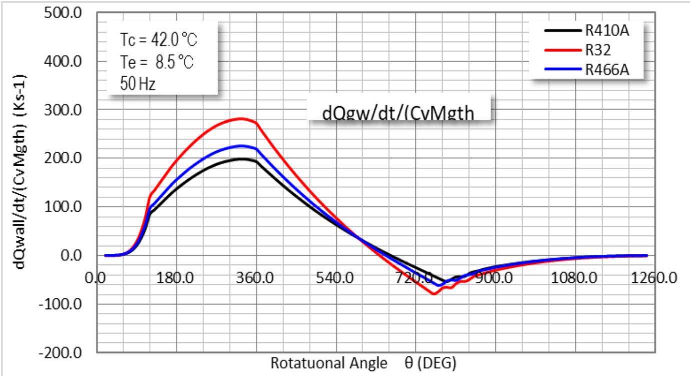

Fig. 3.2-9 Heat transfer between gas and compression chamber wall (scroll compressor)

The effect of leakage in the rotary compressor (Leakage paths (1), (2), (3), and (4)) is shown in Fig. 3.2-10, and effect of the heat transfer is shown in Fig. 3.2-11.

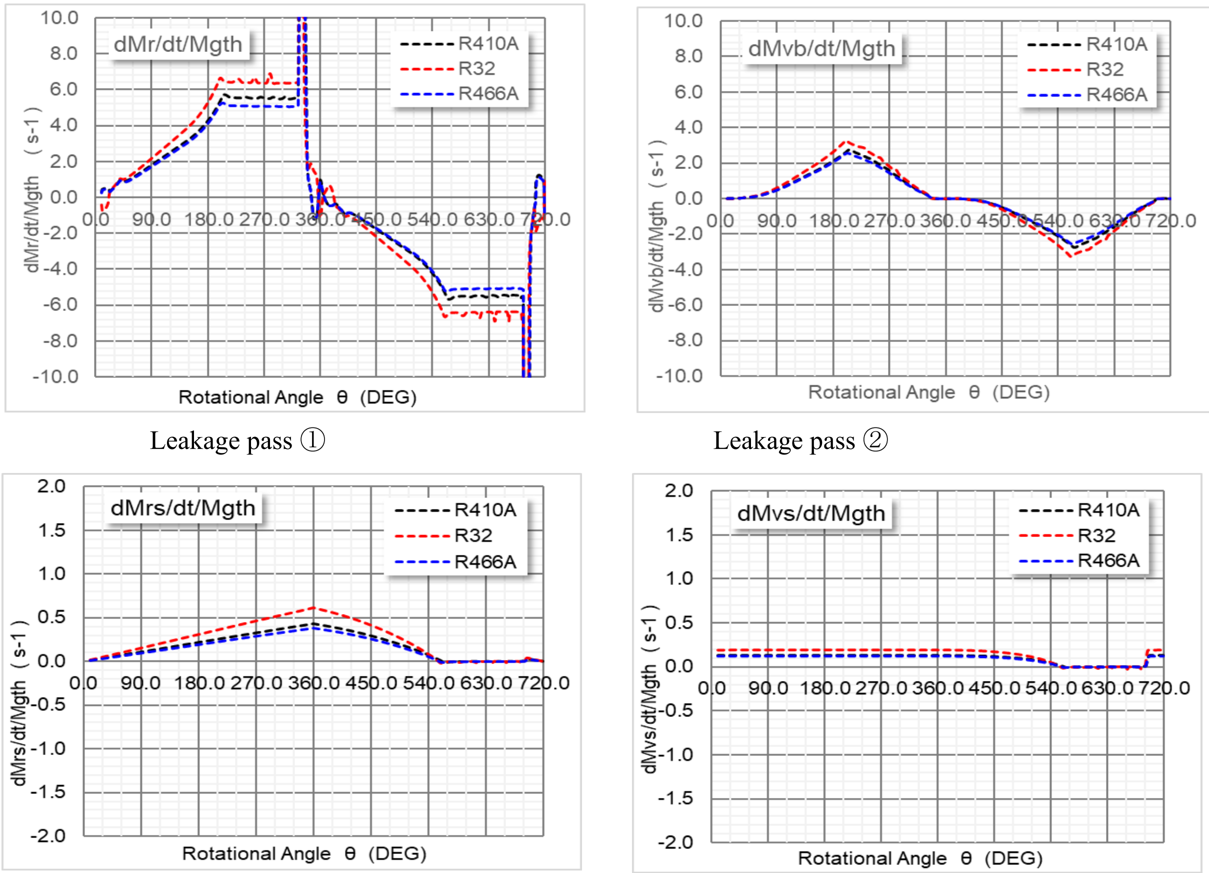

Leakage pass ①

Leakage pass ②

Leakage pass ③

Leakage pass ④

Fig. 3.2-10 Leakage flow rate through four different leakage paths (rotary compressor)

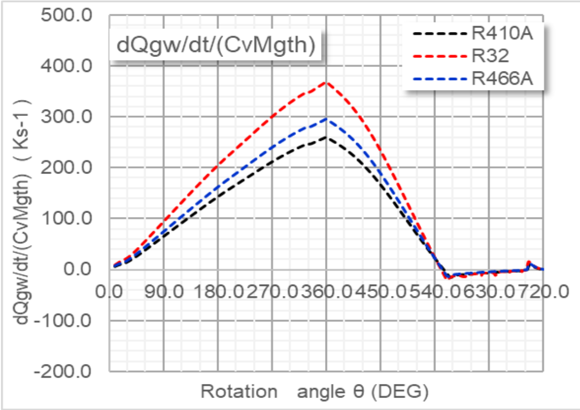

Fig. 3.2-11 Heat transfer between gas and compression chamber wall (rotary compressor)

These results indicate that R32 is more influenced by leakage and heat transfer than R410A and R466A. This can be attributed to the higher specific heat ratio and lower density of R32 than those of the other refrigerants.

(2) Performance of the compressor

The compressor performance values were obtained when the evaporation temperature (0.08 °C) was kept constant and condensation temperature (pressure ratio) was varied. Fig. 3.2-12 presents the volumetric and adiabatic efficiencies of a scroll compressor, and Fig. 3.2-13 presents the volumetric and adiabatic efficiencies of a rotary compressor. Both are expressed as ratios (relative values) with respect to efficiencies obtained with R410A at a pressure ratio of 2.4. Fig. 3.2-14 presents the refrigerant temperature at the end of the suction process and at discharge in the rotary compressor as a ratio (relative value) to the suction temperature. The horizontal axis represents the compression ratio, which is the ratio of the discharge pressure to the suction pressure.

The volumetric efficiency decreased with an increase in the compression ratio, whereas the suction completed temperature and discharge temperature increased. Adiabatic efficiency reached its maximum at pressure ratios of approximately 2.4 and 2.0 for the scroll and rotary compressors, respectively.

When R466A was used, the volumetric efficiency was similar to that of R410A, whereas the adiabatic efficiency was slightly higher. Moreover, R32 exhibited higher temperatures at suction completion and discharge than R410A, thus resulting in a 2%–5% decrease in volumetric efficiency and 1–3% decrease in adiabatic efficiency. This was mainly because of the higher specific heat ratio and lower density of R32 than the other refrigerants.

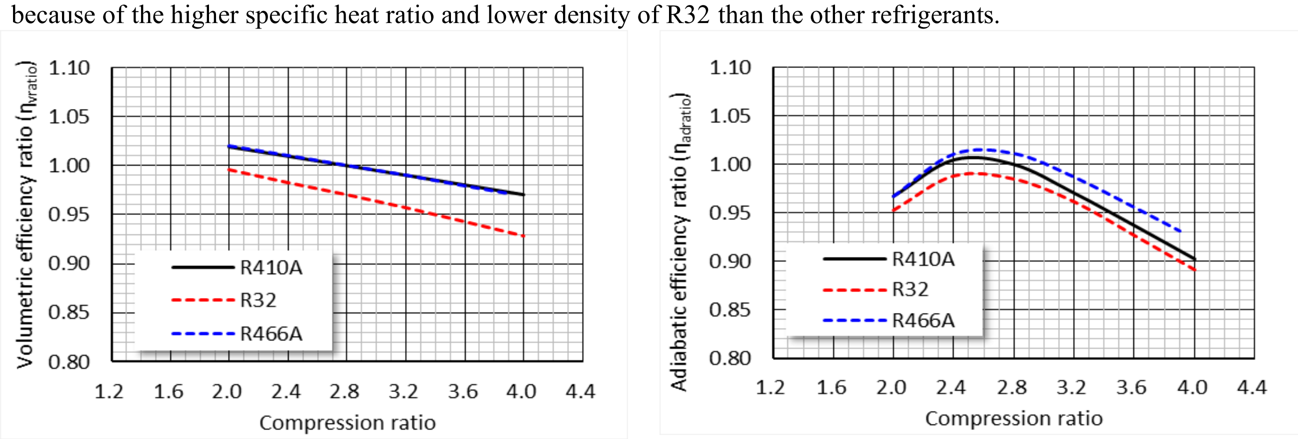

Fig. 3.2-12 Performance of scroll compressor (50 Hz)

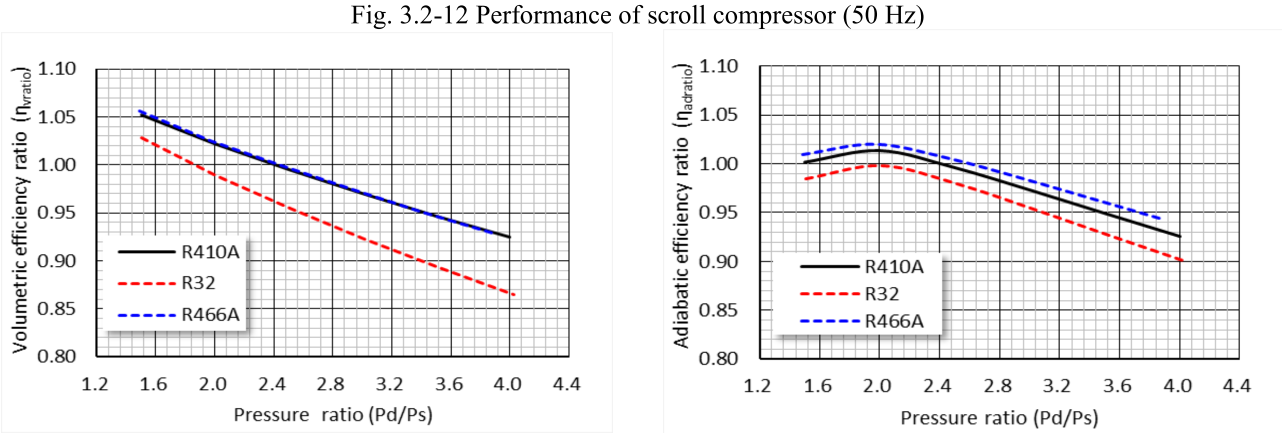

Fig. 3.2-13 Performance of rotary compressor (60 Hz)

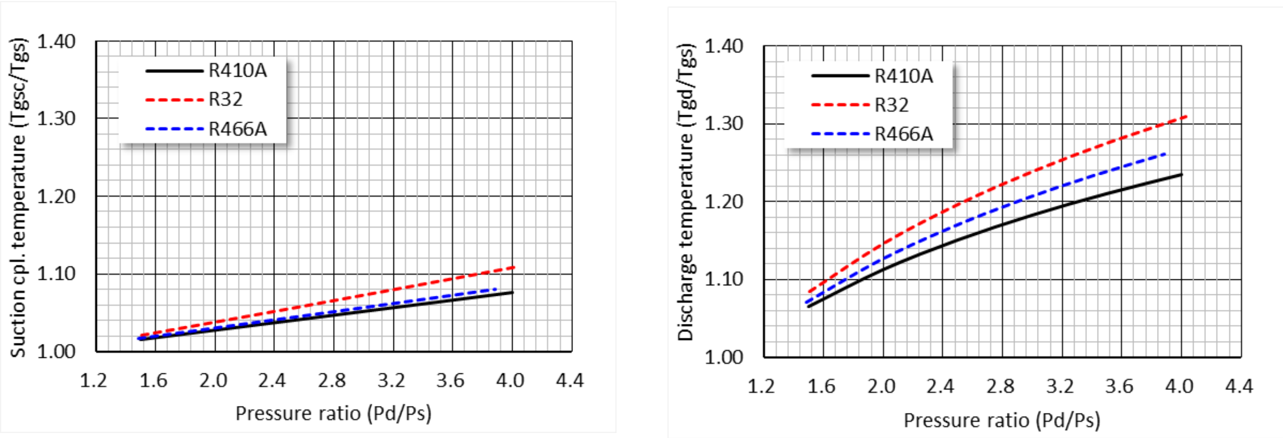

Fig. 3.2-14 Suction completion and discharge temperature of rotary compressor (60 Hz)

3.2.5 Experiment

3.2.5.1 Experimental setup

Using the refrigerant circuit shown in Fig. 3.2-15, a performance test was conducted by driving a scroll or rotary compressor for a residential air conditioner. Tests conducted with R410A and R32 revealed the effects of the refrigerant properties on the compressor performance and verified the simulation model.

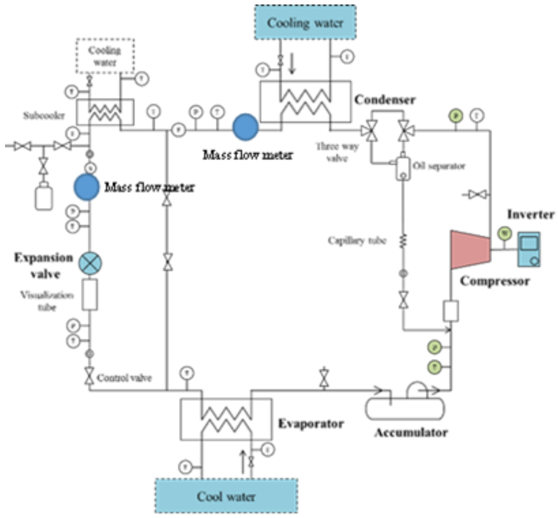

Fig. 3.2-15 Compressor test stand

3.2.5.2 Result of experiment

The compressor characteristics were verified using the pressure ratio as a parameter by maintaining the suction pressure and varying the discharge pressure. The results of the test conducted at 50 Hz using R410A and R32 with a scroll compressor are shown in Fig. 3.2 -16, the results of the test conducted at 50 Hz using R410A with a rotary compressor are shown in Fig. 3.2 -17, and the results of the test conducted at 60 Hz using R410A and R32 are shown in Fig. 3.2 -18. The results of the test conducted at 50 Hz using R410A and R32 with a scroll compressor are shown in Fig. 3.2 -16, and the results of the test conducted at 50 Hz using R410A and that at 60 Hz using R410A and R32 with a rotary compressor are shown in Figs. 3.2-17 and 3.2-18, respectively. These are expressed as ratios (relative values) with respect to each efficiency value obtained from a simulation conducted at a pressure ratio of 2.4 by using R410A and are shown with the simulation results.

The volumetric efficiency decreased uniformly as the pressure ratio increased, with a larger decrease observed for R32 than for R410A. The total compressor efficiency for scroll compressors reached a maximum at a pressure ratio of 2.5, whereas for rotary compressors, it reached a maximum at a pressure ratio of 2.0. Comparing the results of the tests and simulations conducted under similar conditions, we confirmed that the results obtained from the simulations were approximately valid.

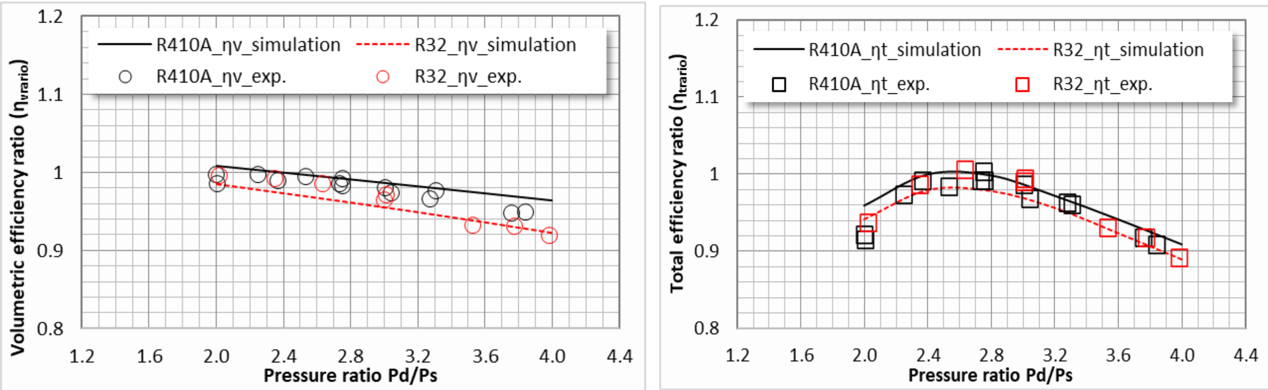

Fig. 3.2-16 Results of the experiment and simulation (scroll compressor, 50 Hz: R410A and R32)

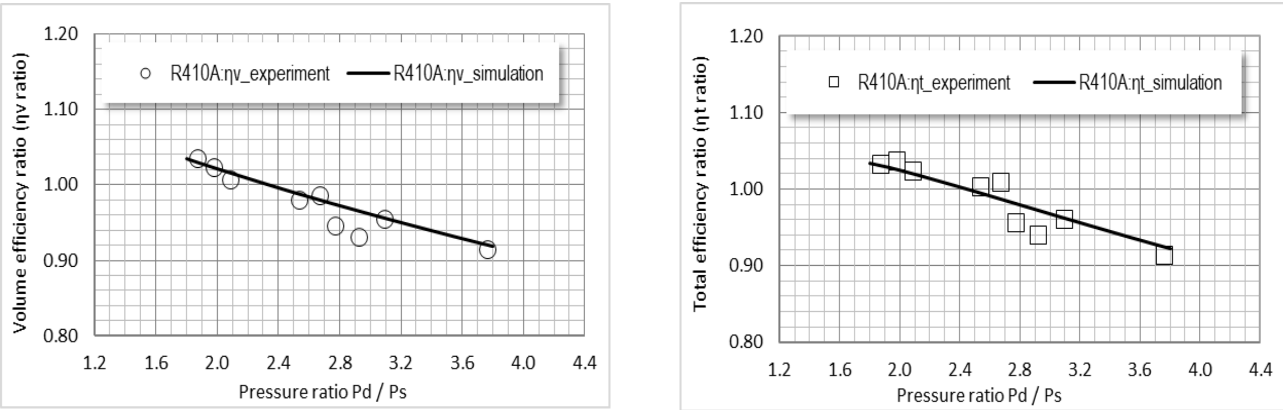

Fig. 3.2-17 Results of the experiment and simulation (rotary compressor, 50 Hz: R410A)

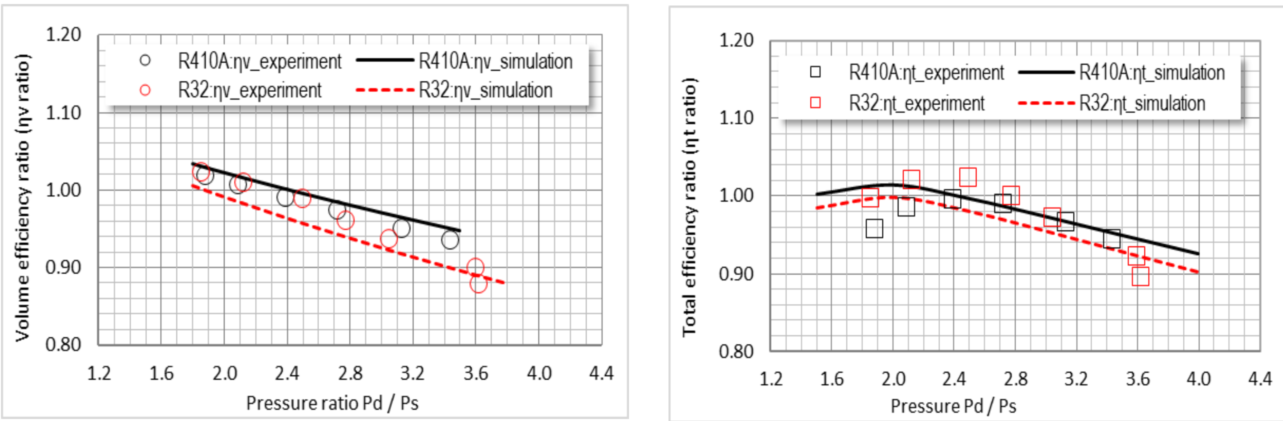

Fig. 3.2-18 Results of experiment and simulation (rotary compressor, 60 Hz: R410A and R32)

3.2.6 Heat pump cycle simulation

3.2.6.1 Calculation method

A cycle simulation (EFM + M)[20] was performed for refrigerants R410A, R32, and R466A, assuming the cooling operation of a residential air conditioner and using the volumetric and adiabatic efficiencies obtained from the compressor simulation to clarify the effects of refrigerant properties on cycle performance. REFPROP10 was used to determine the refrigerant properties. The compressor stroke volume was determined for each refrigerant to achieve a cooling capacity of 2.8 kW under the standard cooling conditions listed in Table 3.2-4, whereas the refrigerant charge amount was determined to maximize the COP, as listed in Table 3.2-5.

Table 3.2-4 Specifications of heat pump cycle simulation

Cooling capacity	kW	2.8
Compressor rotational speed	rps	Scroll/rotary 50/60
Indoor fan power consumption	W	20
Outdoor fan power consumption	W	40
Indoor temperature	℃	27
Outdoor temperature	℃	35

Table 3.2-5 Calculation conditions

Refrigerant	Mass charge	Displacement volume
	kg	Scroll/rotary (cc)
R410A	0.87	8.00/7.25
R32	0.66	7.50/6.80
R466A	0.92	7.95/7.20

3.2.6.2 Simulation results

The following figure depicts the obtained cycle performance when the indoor air temperature was kept constant (27 °C) and outdoor air temperature was changed. Figs. 3.2-19 and 3.2-20 present the simulated cooling capacity and COP with a scroll compressor, whereas Figs. 3.2-21 and 3.2-22 present the results with a rotary compressor. In both cases, the simulation results revealed that the cooling capacity and COP decreased as the outdoor air temperature increased. In the case of R32, the COP was 4–5% higher than that of R410A, whereas that of R466A was similar to that of R410A. Under high outdoor air temperature conditions, R32 had a slightly higher cooling capacity than the others.

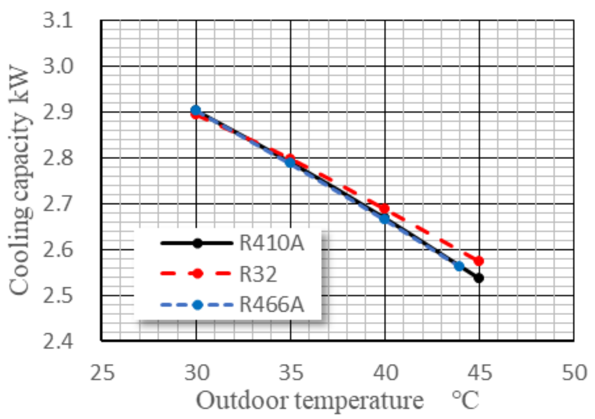

Fig. 3.2-19 Cooling capacity (scroll compressor)

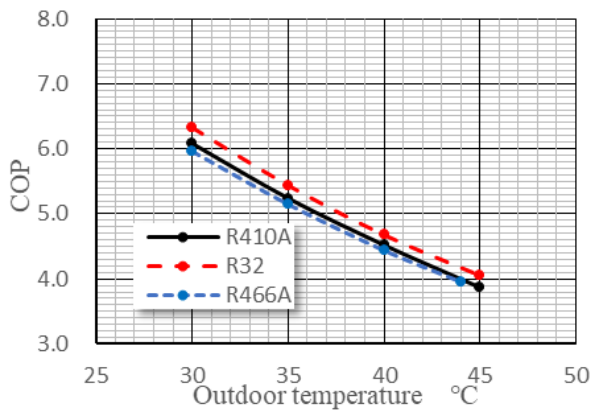

Fig. 3.2-20 Cycle COP (scroll compressor)

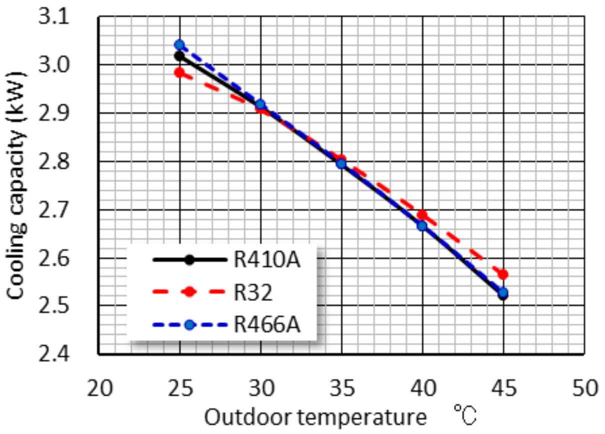

Fig. 3.2-21 Cooling capacity (rotary compressor)

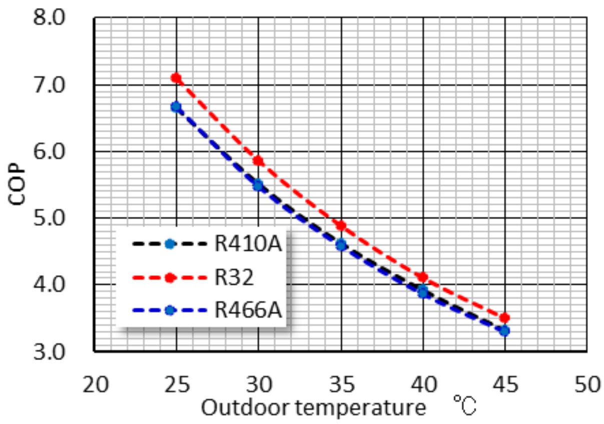

Fig. 3.2-22 Cycle COP (rotary compressor)

3.2.7 Conclusions

In this study, compressor simulations, performance tests, and heat pump cycle simulations were conducted for a residential R410A room air conditioner using three types of refrigerants (R410A, R32, and R466A). Accordingly, the following conclusions were obtained:

(1) The results of the compressor simulation confirmed that the constructed model can appropriately evaluate the effects of the refrigerant properties on the compressor performance. We determined that when R32 was used, the effects of leakage and heat transfer were larger than those of R410A, whereas the volumetric and adiabatic efficiencies were lower.

(2) Performance tests using a scroll and rotary compressor for room air conditioners yielded similar trends with respect to the compressor simulation results, thus confirming the validity of the model.

(3) By applying the results of the compressor simulation to the heat pump cycle simulation, the cycle performance could be more comprehensively evaluated based on the properties of the refrigerant.

NOMENCLATURE

A	: leakage pass area, m^2	*v*	: velocity, $m \cdot s^{-1}$
c	: flow coefficient, -	*W*	: work, kJ
h	: specific enthalpy, $kJ \cdot kg^{-1}$	*x*	: vane displacement, m
h	: heat transfer coefficient, $kW \cdot m^{-2} \cdot K^{-1}$	*Pr*	: Prandtl number, -
M	: mass, kg	*Nu*	: Nusselt number, -
N	: compressor rotational speed, s^{-1}	*Re*	: Reynolds number, -
P	: pressure, Pa	η	: efficiency, -
Q	: heat transfer, kJ	θ	: rotational angle, rad
S	: surface area, m^2	κ	: specific heat ratio, -
T	: temperature, K	ρ	: density, $kg \cdot m^{-3}$
t	: time, s	φ	: mass ratio, -
u	: specific internal energy, $kJ \cdot kg^{-1}$		
V	: volume, m^3		

SUBSCRIPTS

a	: axial	*o*	: outer
ad	: adiabatic	*dp*	: discharge port
ch	: choke	*s*	: suction
d	: discharge	*sc*	: suction completed
l	: lubricant	*th*	: theoretical
mech	: mechanical	*w*	: wall
mot	: motor		

References

1) JSRAE , “Compressor for Air conditioning and Refrigeration “, JSRAE Technical Book series, pp. 1-33, 51-79, 83-98, 187-202 (2018).
2) Fujiwara M., Kasuya K., Matsunaga T., Watanabe M., “Performance Analysis of Screw Compressor”, Trans. Jpn. Soc. Mech. Eng., Vol. 51, No. 466, pp. 1816-1824 (1985) (in Japanese).
3) Kays W. M., Crawford M. E., “Convective Heat and Mass Transfer”, McGraw-Hill, pp. 238-248 (1980).
4) Tojo K., Ikegawa M., Maeda N., Machida S., Shiibayashi M., Uchikawa N., “Computer Modeling of Scroll Compressor with Self-Adjusting Back Pressure Mechanism”, Proc of the 8th Int. Comp. Eng. Conf. at Purdue (1986).
5) Suefuji K., Shiibayashi M., Tojo K., “Performance Analysis of Hermetic Scroll Compressor”, Trans. JAR, Vol. 10, No. 2, pp. 319-326 (1993) (in Japanese).
6) Chen Y., Groll E. A., Halm N. P., Braun J. E., “A Comprehensive Model of Scroll Compressor”, Int. Journal of Refrigeration., Vol. 25, pp. 731-750 (2002).
7) Itoh T., Fujitani M., Sakai Y., “Leakage Characteristics of Scroll Compressor by Two Phase Flow Model in Consideration of Wall Oil Film Thickness”, Trans. Jpn. Soc. Mech. Eng., Vol. 68, No. 671 (2002) (in Japanese)
8) Kawamura R., Iwatake W., Shimizu M., Tatsuwaki K., “Analysis of Thermal Fluid Behavior during Compression Process of Scroll Compressor”, Mitsubishi Denki Gihou, 93(6), pp. 27-30 (2019) (in Japanese).
9) Tojo K., “Evolution and Future Prospects of Scroll Compressor Technology”, Trans. JAR, Vol. 37, No. 2, pp. 123-144 (2020) (in Japanese).
10) Bell I. H., Lemort V., Groll E. A., Braum J. E., King G. B., Horton W. Tr., “Liquid-flooded Compression and Expansion in Scroll Compressor”, Int. Journal of Refrigeration, Vol. 35, pp. 1878-1889 (2012).
11) Shimizu T., Shiga T., Tyuu I., ”Some Investigation on the Pressure Change Characteristics of a Rotary Compressor”, Trans. JAR, Vol. 50, No. 573 (1975) (in Japanese).
12) Tojo K., Kan T, Arai A., “Dynamic Behavior of Sliding Vane in Small Rotary Compressors", Proc of the 3rd Int. Comp. Eng. Conf. at Purdue (1978).
13) Yanagisawa T., “Leakage Loss Analysis of Rotary Compressor (1)”, Trans. Jpn. Soc. Mech. Eng., Vol. 48, No. 426 (1982) (in Japanese).
14) Yanagisawa T., Shimizu T., Nakamura M., “Leakage Loss Analysis of Rotary Compressor (2)”, Trans. Jpn. Soc. Mech. Eng., Vol. 48, No. 431 (1982) (in Japanese).
15) Yanagisawa T., “Piston behavior and Mechanical Loss Analysis of Rotary Compressor”, Trans. Jpn. Soc. Mech. Eng., Vol. 48, No. 429 (1982) (in Japanese).
16) Nakamura M., Hata H., Nakamura Y., Endo T., Izuka K., “Study on Vibration Reduction of a Rolling Piston-Type Compressor by Motor Torque Control”, Trans. Jpn. Soc. Mech. Eng., Vol. 56, No. 522 (1990) (in Japanese).
17) Fukuta M., Yanagisaw T., Shimizu T., Suzuki Y., “Mathmatical Model of Vane Compressors for Computer Simulation of Automotive Air Conditioning Cycle”, Trans. Jpn. Soc. Mech. Eng., Vol. 59, No. 561 (1993) (in Japanese).
18) Matsui M., et al., ” Development of High-Efficiency Technology of Two-Stage Rotary Expander for CO2 Refrigerant”, Proc of the 19th Int. Comp. Eng. Conf. at Purdue, C1237 (2008)
19) Shida S., Shishimoto T., Toda H., “A3 and A4 Series Compact Large-Capacity Rotary Compressors for VRF Air-Conditioning Systems”, TOSHIBA Review, Vol. 75, No. 4 (2020) (in Japanese).
20) K. Ohno, K. Saito, Proceedings of the 46th Japanese Joint Conference on Air-conditioning and Refrigeration, 119 (2012).

3.3 Expansion valve

This section discusses the construction of a correlation equation for predicting the characteristics of the expansion valve, which can be used in the system analysis.

The role of the expansion valve, which is a component of an air conditioner, is to ensure the superheat of the refrigerant flowing into the compressor, and to prevent liquid refrigerant from flowing into the compressor.

Considering the cooling operation as an example, the flow rate of the refrigerant flowing through the expansion valve decreases and the pressure difference between the inlet and outlet of valves increases when the valve opening is reduced because of the general characteristics of valves.

With a decrease in the flow rate, the refrigerant evaporates more readily in the evaporator, and the superheat at the evaporator outlet (≒ compressor inlet) increases. The opposite is true when the valve opening is increased, and the superheat is reduced.

Thus, the superheat control by the expansion valve plays a critical role in the control of air conditioners. During the normal operation of an air conditioner, the refrigerant is subcooled at the inlet of the expansion valve.

Refrigerant that flows into the expansion valve in a subcooled state undergoes isenthalpic expansion at the valve to reduce pressure. In the case of refrigerants used in air conditioners, the refrigerant pressure is reduced in the expansion valve and is in a saturated two-phase state.

This indicates that a phase change occurs during the expansion process. It is common knowledge that the characteristics of the expansion valve (the relationship between the valve opening, flow rate, and pressure difference) are significantly dependent on how the fluid passes through the trough of the valve, and the relationship between the phase change during the expansion process and this trough is critical.

Furthermore, in actual air conditioner operation, the refrigerant is not always subcooled at the inlet of the expansion valve, and there are cases wherein the refrigerant is in a gas–liquid two-phase state. This can occur, for example, owing to relatively rapid transient changes in operating conditions such as startup and shutdown, temperature setpoint changes, and abrupt changes in room load.

The relationship between the pressure difference at the inlet and outlet of the expansion valve and the flow rate, which is generally used in conventional simulations of air conditioners as a whole, is expressed by the following equation:

$$\dot{m} = c_d A \sqrt{\rho_i (P_i - P_o)} \tag{3.3-1}$$

This equation is obtained from Bernoulli's law assuming the incompressibility of the fluid flowing through the expansion valve and has been extensively used under conditions where the refrigerant at the expansion valve inlet is a subcooled liquid under normal operating conditions. Moreover, c_d is the flow coefficient, which is generally considered as a constant value for simple prediction. However, when attempting to predict the performance and characteristics of air conditioners under a wide range of actual operating conditions, it is necessary to vary the flow coefficient with respect to the specific case.

Therefore, we attempted to develop an experimental correlation equation for the flow coefficient that can be used in system simulations of air conditioners and can be applied under various conditions.

3.3.1 Experiment

Fig. 3.3-1 presents images of the expansion valve used in this experiment. The expansion valve was a common type widely used in home air conditioners. The valve opening of the expansion valve could be adjusted by moving the needle shown in the figure up and down using a stepping motor at the top of the valve.

Fig. 3.3-2 presents an image of the experimental apparatus. Fig. 3.3-3 presents a flow diagram of the experimental apparatus. The experimental apparatus consisted of a vapor compression heat pump cycle, and the electronic expansion valve in this cycle was the subject of this study.

In this study, it was necessary to understand the characteristics of the expansion valve under various conditions, as described above, to develop a correlation equation for the expansion valve. Hence, several innovations were made to the experimental apparatus.

First, a needle valve was installed at the bottom of the expansion valve, such that the outlet pressure of the expansion valve could be set arbitrarily without changing the low and high pressures of the experimental apparatus.

A bypass pipe and flow control valve were installed from the inlet of the expansion valve to allow for the flow rate through the valve to be set as desired.

An oil separator was installed to maximally reduce the influence of the compressor lubricating oil on the expansion valve.

The evaporator and condenser exchanged heat via chilled and cooled water, respectively.

A chilled water tank, cooling water tank, chiller for temperature control, and boiler for temperature control were installed outside the apparatus; thus, and chilled water and cooling water of any temperature and flow rate could be supplied to the experimental apparatus.

The main measurement points related to the characterization of the expansion valve were as follows. The inlet and outlet pressures of the expansion valve were measured using a capacitance pressure gauge. The inlet temperature of the expansion valve was measured using a platinum resistance temperature detector. The flow rate at the inlet of the expansion valve was measured using a Coriolis flowmeter.

If the inlet state was supercooled liquid, the density was calculated from the pressure and temperature using a physical property function (REFPROP10).

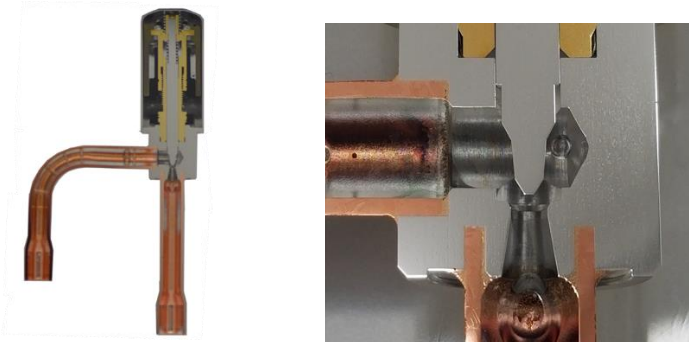

(a) Cut-model of expansion valve (b) Magnified image of throat and needle
Fig. 3.3-1 Images of expansion valve used in the experiment

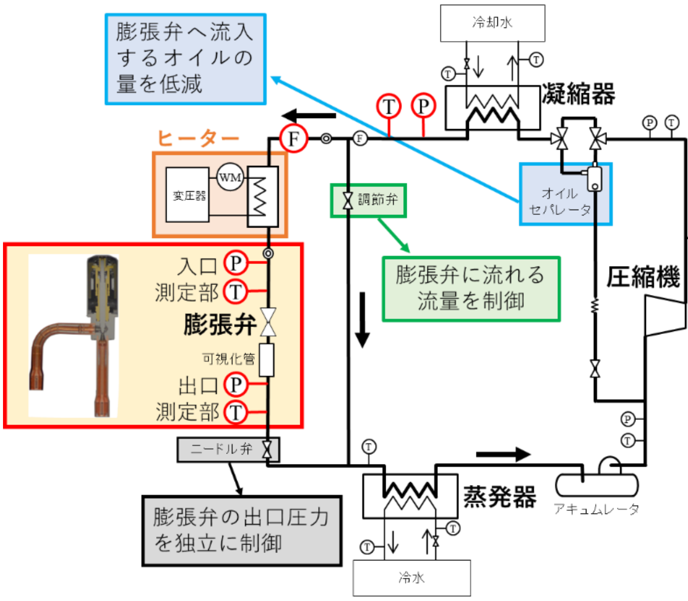

Fig. 3.3-2 Experimental apparatus Fig. 3.3-3 Flow diagram of experimental apparatus

3.3.2 Experimental conditions

Table 3.3-1 presents the experimental conditions for which R32 refrigerant was adopted. The experimental parameters were the valve opening, inlet pressure, and inlet degree of subcooling and pressure difference between inlet and outlet. Fig. 3.3-4 presents plots of the experimental conditions. Fig. 3.3-4 (a) is a PQ diagram, and each plot indicates the resistance value of the expansion valve. Fig. 3.3-4 (b) presents the inlet condition of the pressure and degree of subcooling. The experiment was conducted under a wide range of inlet pressures.

The number of data obtained in the experiment was 2827.

Table 3.3-1 Experimental conditions

Refrigerant	R32
Valve opening, %	7.0–20.0
Inlet pressure, MPa	1.4–2.9
Inlet subcooling, K	0–12.1
Pressure difference, MPa	0.4–2.0

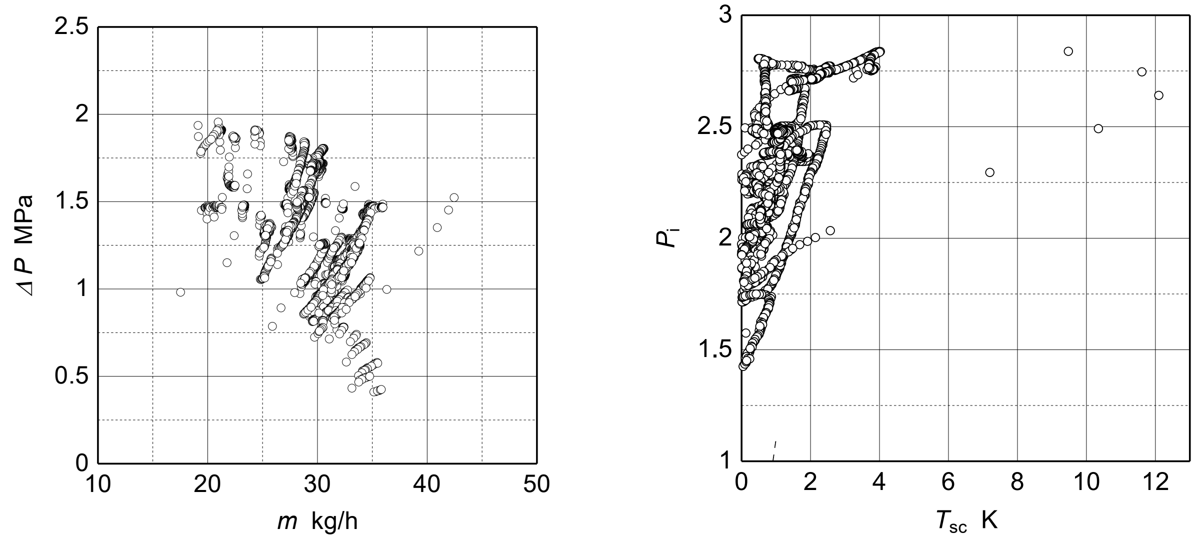

(a) Pressure difference and mass flow rate

(b) Inlet pressure and degree of subcooling

Fig. 3.3-4 Experimental conditions

3.3.3 Results

3.3.3.1 Data reduction

The flow coefficients defined in the following equation were evaluated in this study as an index of the expansion valve performance.

$$c_d = \frac{\dot{m}}{A\sqrt{\rho_i(P_i - P_o)}} \tag{3.3-2}$$

The correlation between the flow coefficients and the other physical quantities (i.e., valve opening, inlet state, pressure difference and flow rate) were analyzed, Finally, the experimental correlation equation of the flow coefficients was constructed.

3.3.3.2 Experimental Correlation

Fig. 3.3-5 presents the correlation diagram between the flow coefficient, inlet pressure, mass flow rate, inlet degree of subcooling, and pressure difference. These results indicate that there are three patterns of correlations: linear correlation, non-linear correlation, and no correlation. With respect to the flow coefficient, a negative linear correlation was observed with the inlet pressure and pressure difference; whereas, a positive linear correlation was observed with the mass flow rate. Furthermore, there was an upward convex curvilinear correlation between the valve opening and the flow coefficient. No clear correlation was observed between the degree of subcooling and flow coefficient.

3.3.3.3 Experimental correlation equation for and its accuracy

The experimental correlation of the flow coefficients was analyzed, and the experimental correlation was developed as expressed by Eq. (3.3-2). Given that the valve opening z was the only component that exhibited a curvilinear correlation with the flow coefficient, a quadratic curve approximation was applied. A comprehensive analysis of the experimental data revealed that there was a lower limit of z_0 at which the flow rate was zero, and an opening z_{fo} at which no change in flow rate occurred, even if the valve opening was raised.

The effects of the differential pressure, inlet pressure, inlet subcooling, and mass flow rate were first-order approximations. The effects of the differential pressure, inlet pressure, inlet supercooling, and mass flow rate were approximated by linear functions. The pressure and temperature were non-dimensionalized to the critical pressure and critical temperature, respectively. However, within the scope of the experiments conducted in this study, the effect of the inlet pressure difference on the flow coefficient was sufficiently small when compared with the other parameters that the coefficient is set to zero.

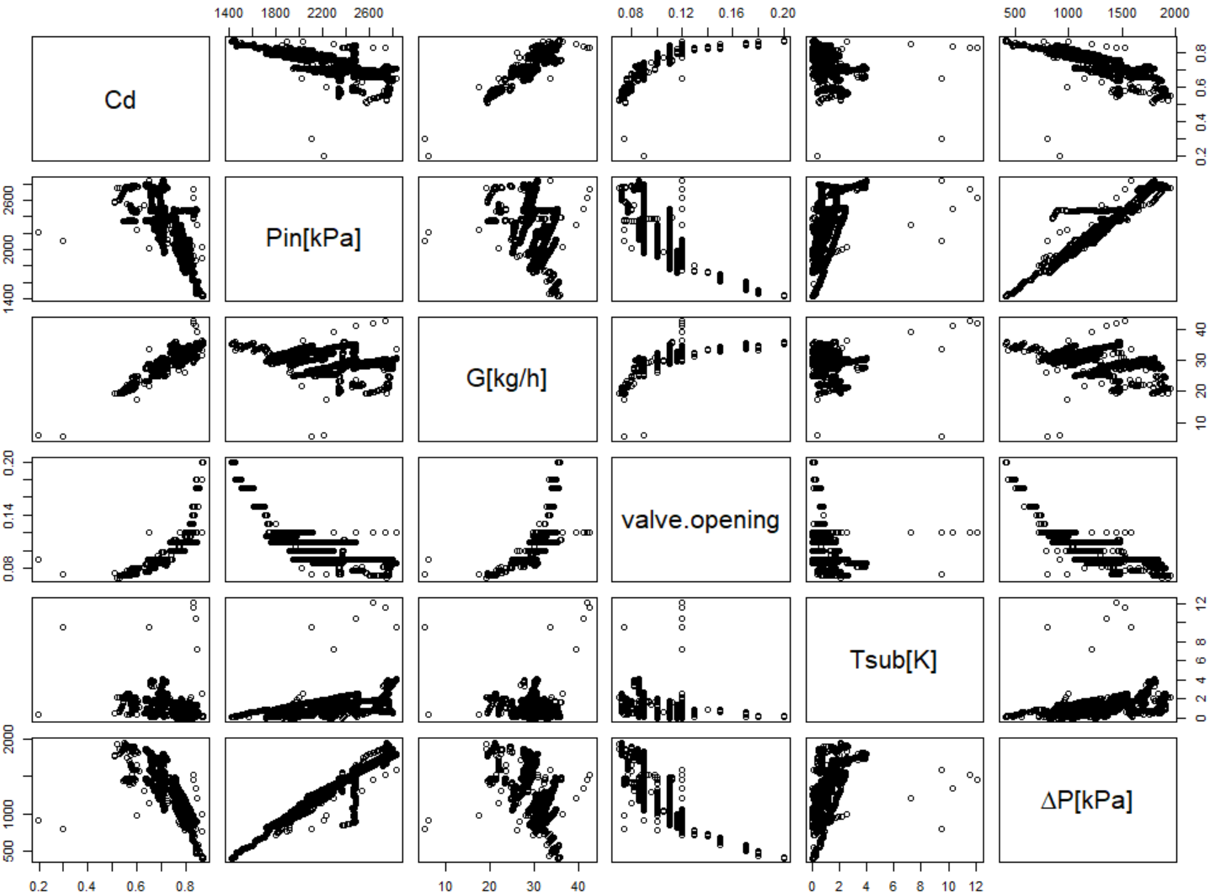

Fig. 3.3-5 Correlation diagram of experimental data

$$c_d = a_z\left(\frac{z-z_0}{z_{fo}-z_0}\right)^2 + a_{\Delta P}\left(\frac{\Delta P}{P_c}\right) + a_{P_i}\left(\frac{P_i}{P_c}\right) + a_{T_{sc}}\left(\frac{T_{sc}}{T_c}\right) + a_{\dot{m}}\left(\frac{\dot{m}}{\dot{m}_{max}}\right) + a_0 \qquad (3.3\text{-}2)$$

Table 3.3-1 Values of constants in Eq (3.3-2)

a_z	-0.05537
$a_{\Delta P}$	-0.8425
a_{P_i}	0
$a_{T_{sc}}$	1.571
$a_{\dot{m}}$	0.3250
a_0	0.6606
z_0	0.13
z_{fo}	0.2
$\dot{m}_{max}$	0.3250

To verify the accuracy of the correlation equation, the flow coefficients calculated from the correlation equation and the experimental flow coefficients were compared using all the data.

Fig. 3.3-6 presents a comparison of the predicted and experimental values based on the correlation equation. The line where the relative error was 10% is shown. It can be seen that the relative error between the predictions and the experimental values was within 10 % for almost all the data. The average relative error was 1.83%.

Fig. 3.3-7 presents the relationship between the flow coefficient and the relative error. The results reveal that the relative error was largest when the flow coefficient was approximately 0.45, and smallest when the flow coefficient was approximately 0.7.

3.3.3.4 Comparison between experimental values and experimental correlation equation

This section presents a comparison of the experimental flow coefficients obtained by entering the experimental values of each parameter into the experimental correlation equation for flow coefficients presented in the previous section, namely, Eq. (3.3-2). This verified that the correlation equation can be used to predict the characteristics of the expansion valve.

Fig. 3.3-7 presents the comparison results. The black plots present the experimental values and the red plots present the predicted values using the correlation equation. First, it can be concluded that the experimental results accurately reproduced the influence of each parameter on the flow coefficient within the range considered in this experiment. In particular, the effect of the opening angle was well represented by a curve that was consistent with the experimental values, thus suggesting that this correlation equation can be used for system control studies.

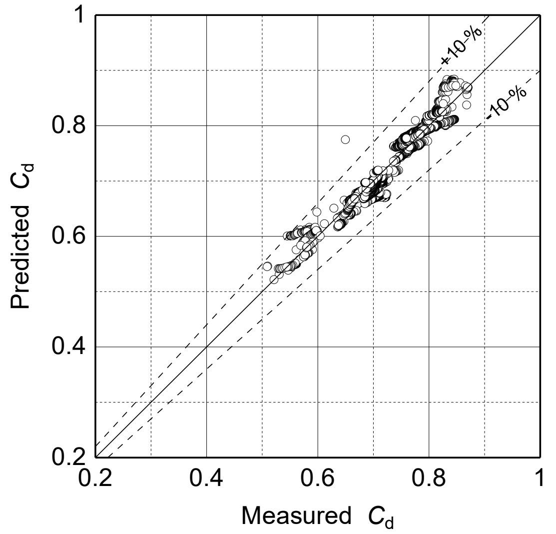

Fig. 3.3-6 Accuracy of experimental correlation equation

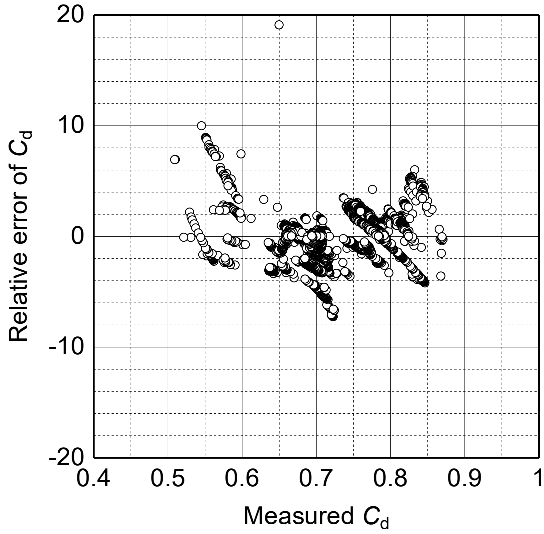

Fig. 3.3-7 Relative errors

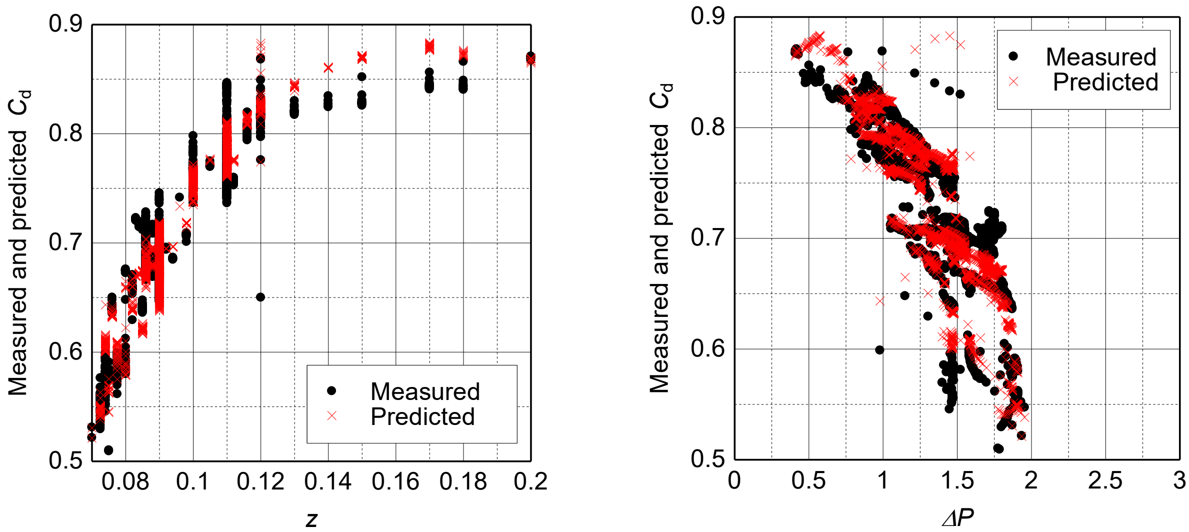

(a) Effect of valve opening

(b) Effect of pressure difference

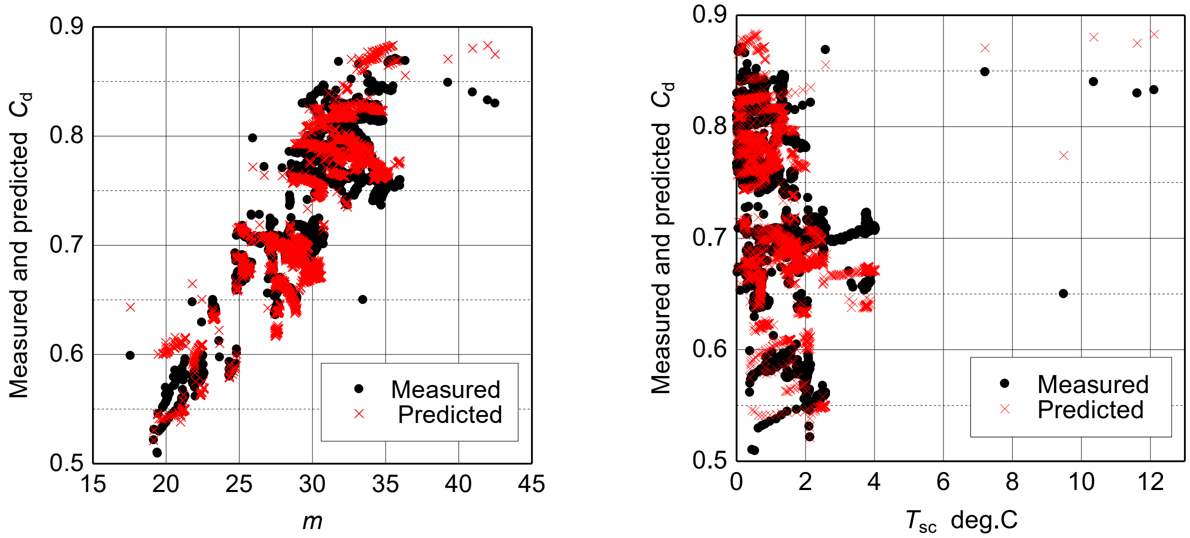

(c) Effect of mass flow rate

(d) Effect of subcooling degree

Fig. 3.3-7 Comparison between the predicted flow coefficients using Eq. (3.3-2) and the measured flow coefficients

3.3.4 Summary

We attempted to develop a correlation equation for the flow coefficient by clarifying and analyzing the correlation between the parameters that influence the characteristics of the expansion valve and the flow coefficient, which is a critical indicator of the characteristics of the expansion valve of a residential air conditioner when R32 is used as a refrigerant.

As a result, the study can be summarized as follows.

(1) Experiments were conducted for various expansion valve openings, inlet pressures, inlet supercooling, differential pressures, and mass flow rates, and nearly 3,000 data points were obtained.
(2) As a result, a quadratic correlation was observed between the valve opening and flow coefficient, and a linear correlation with other parameters.
(3) Based on these results, a correlation equation was developed, and its accuracy was verified.

Based on the above, the experimental correlation of flow coefficient can be used to predict the performance and analyze the behavior of the system, including the expansion valve.

NOMENCLATURE

A	: area, m^3	$\dot{m}$	: mass flow rate, kg/s
c_d	: flow coefficient, -	T	: temperature, K
$\dot{m}$	: mass flow rate, kg/s	Tsc	: degree of subcooling, K
P	: pressure, Pa	ρ	: density, kg·m^{-3}
ΔP	: pressure difference, Pa		

SUBSCRIPMTS

c	: critical point	max	: maximum
fo	: fully opened	o	: outlet
i	: inlet		

4. SYSTEM ANALYSIS

4.1 Acquisition of system data

4.1.1 Development of emulator-based hybrid dynamic air conditioning performance test facility

4.1.1.1 Overview

The improved performance of devices such as heat exchangers and compressors, in addition to the progression of various technological innovations such as inverters[1)2)3)4)5)], has resulted in a significant improvement in the annual performance of air conditioning systems. In particular, the annual performance factor (APF)[6)], which expresses the annual energy consumption efficiency, as specified by the Japanese Industrial Standards (JIS), exceeded 7.0, and it was conjectured that the limit has almost been reached[7)8)9)]. However, several issues associated with the APF-based evaluation method were identified. Specifically, an air conditioner is operated in the dynamic state by changing its compressor rotation speed, expansion valve opening, etc., as required under the current operating conditions in accordance with commands from its control system. However, international standards such as the JIS estimate the APF using several discrete points of operating data in the steady state. These points exclude changes due to indoor air temperature control, which is the core function of the control system, by maintaining the compressor rotation speed. This assumption can be made because the performance of an air conditioner is significantly influenced by the parameters of the test equipment and control system. Hence, the prescribed APF test method prioritizes the capacity to rapidly and efficiently assess the performance of air conditioning equipment in a reproducible manner, regardless of the test equipment performance parameters.

Such a simplified quantification of annual performance using only the steady state results in a large discrepancy with respect to the actual driving performance. This was identified as a limitation to the promotion of effective energy savings and CO_2 emissions reduction. The problem extends beyond the limits of the evaluation method; in that the actual operating performance is not accurately evaluated, which discourages manufacturers from developing new equipment, and represents a bottleneck with respect to the improvement of equipment performance. In particular, this is among the greatest challenges preventing the realization of carbon neutrality in the refrigeration and air conditioning industry.

To overcome these issues, the dynamic performance of air conditioning equipment should be clearly understood, such that the same dynamic performance can be consistently obtained across different test facilities. To achieve this objective, the test conditions should be applied on the building side to consistently reflect characteristics such as the building load and building heat capacity, both of which considerably influence the dynamic performance of air conditioning equipment, regardless of the test equipment employed. In practice, such conditions are impractical to simulate, even when using the same hardware. Although a dynamic performance evaluation method was previously proposed[10)], the resulting dynamic performance varies depending on the specific test equipment employed, even when the type of equipment is the same.

Therefore, in this study, we revised the conventional steady-state performance test method to compensate for the building-side test conditions by calculating them virtually using emulator software, thereby realizing a novel, reproducible, and dynamic performance test method. To achieve this, we first developed an epoch-generating performance test device equipped with an emulator and evaluated its stability. The realization of a reliable dynamic test method can facilitate the effective use of conventional test equipment to unify air conditioner product standard performances and actual operating performances, which is relevant to users after the installation of their equipment.

Although we previously studied duct-type test equipment[11)], in this study, a test facility was developed to evaluate the dynamic performance of air conditioning systems with a high accuracy based on calorimeter measurements in a test chamber. The concept and configuration of the proposed test facility, evaluation of its methodological soundness, and the evaluation of the dynamic operation performance of air conditioning equipment are accordingly reported herein.

4.1.1.2 Concept of air conditioning load and test facility performance

To study the dynamic performance of air conditioners, we organized the basic concept of energy flow in a building and defined the necessary parameters based on the building energy exchange shown in Fig. 4.1.1-1. Assuming the summer season, heat enters the building via outside air and sun on the walls and windows and outside air brought in by ventilation. Furthermore, human occupants generate heat and steam. These heat sources are collectively referred to as "the building load."

In addition, the conditions inside the building, as indicated by the red dashed line in the figure, are influenced by the state of the air supplied by the air conditioner, the building load, and the quantity of indoor air and heat capacity of the building, which includes the fixtures, walls, and room temperature changes. The building-specific conditions that determine the changes in building load and temperature are referred to as the "building-side air conditions."

On the air conditioner side, the room air is considered as intake air and cooled. This cooled air is directed into the building as supply air. The cooling provided by the air conditioner at this stage is referred to as the "air conditioning load." The conditions that determine the operational status of the air conditioner, which are enclosed by the blue dashed line, are referred to as the "equipment-side air conditions."

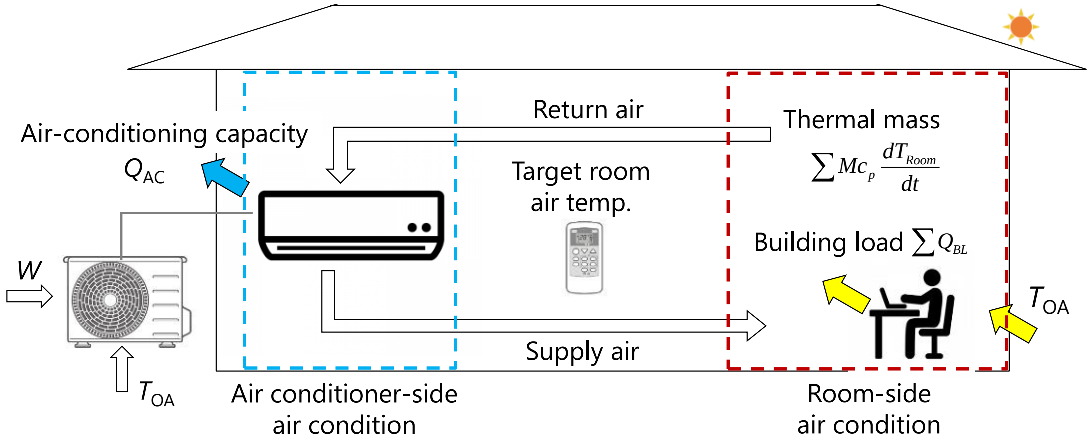

Fig. 4.1.1-1 Heat flow inside a building during the summer

Fig. 4.1.1-2 depicts a series of load–time curves relating the changes in a building, air conditioning load, and room temperature.

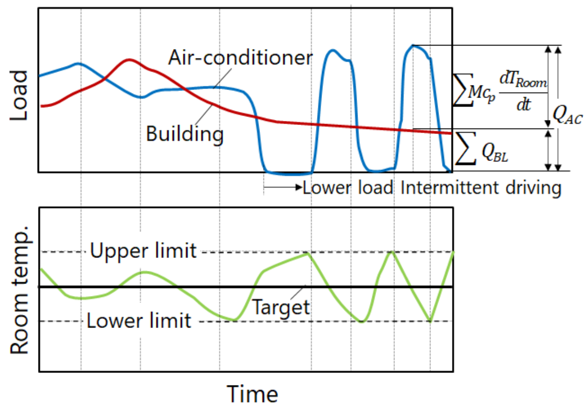

Fig. 4.1.1-2 Load and temperature changes inside a building

The "building load" and "air conditioning load" are different in the dynamic state than in the static state. This difference is influenced by the heat capacity inside the building, which results in changes in the indoor air temperature.

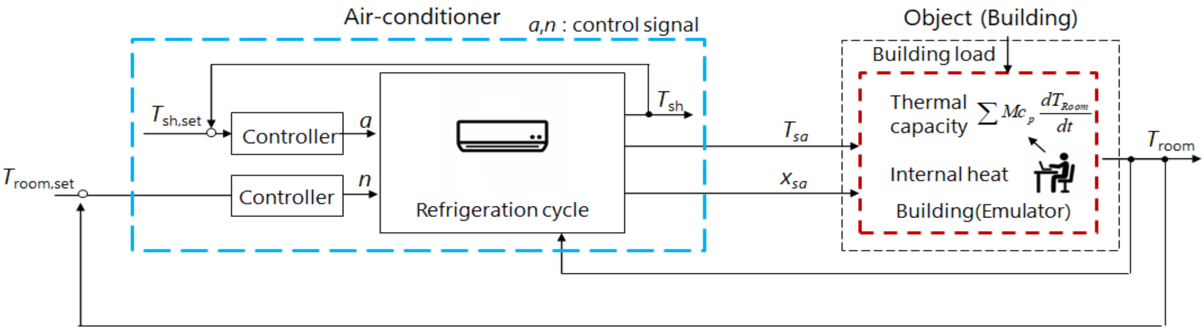

Fig. 4.1.1-3 Air-conditioner control method

Additionally, the dynamic performance evaluation represents an investigation of the air conditioning system control performance. As shown in Fig. 4.1.1-3, indoor air temperature control, which is the primary objective of the air conditioner, is performed for the interior of the building and the entire building. The building characteristics exert a significant influence on the control performance accordingly. Therefore, the same air conditioner performance can only be obtained when using the same equipment, whereas the "building-side air conditions" are set as the same, to an extent. Although this explanation was provided in terms of heat exchange, given that the "building-side air conditions" and the "equipment-side air conditions" exert a mutual influence on the humidity (i.e., the material equilibrium of water); it is necessary to consider this exchange.

4.1.1.3 Current representative performance test facilities

Typical air conditioner performance tests employ calorimeters, which were developed for measurements in the steady state at fixed compressor speeds. Such tests are generally conducted in “air enthalpy” or “balance” test facilities. The characteristics, measurement principles, and issues that arise when attempting to determine dynamic performance using each of these test facilities are described in this section.

(1) Air enthalpy test facility

The air enthalpy test facility is shown in Fig. 4.1.1-4, and comprises an indoor room in which an indoor unit was installed, and an outdoor room in which the outdoor unit was installed. Condition generators were installed in both rooms to control the temperature and humidity to the pre-determined levels. The primary feature of this test facility is its capacity to directly measure the air conditioning load by determining the temperature, humidity, and air volume to describe the air conditions. Because of the difficulty associated with the measurement of the air volume, the test results obtained using the air enthalpy facility are slightly less accurate than those obtained in the balanced test facility, although the former approach was recently improved to achieve near parity with the latter.

Notably, when analyzing the dynamic performance of an air conditioning system using the air enthalpy test facility, the performance will differ according to the specific parameters of the facility unless a method is introduced to provide the same “building-side air conditions”, regardless of the specific facility employed.

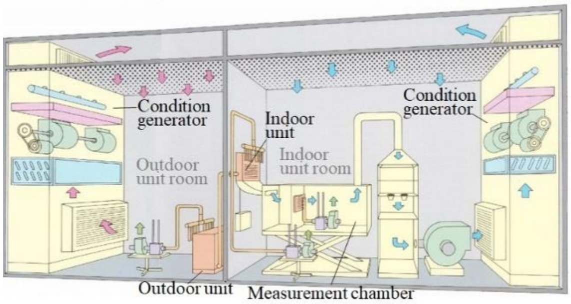

Fig. 4.1.1-4 Air enthalpy test facility[12)]

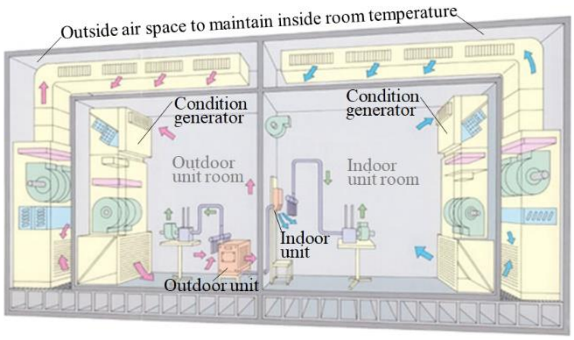

Fig. 4.1.1-5 Balance test facility[12)]

(2) Balance test facility

Fig. 4.1.1-5 presents the balance test facility, which was developed to similarly comprise an indoor unit room and an outdoor unit room, each of which was equipped with a condition generator to provide a constant room temperature and humidity. A notable feature of this facility is that it enables the measurement of the building load using a condition generator installed in the indoor unit room. If the load is steady, this value is equal to the air conditioning load, thereby allowing for the air conditioning load to be measured indirectly. Owing to this balance between the air conditioning and building loads, this facility is referred to as “balanced.” In addition, a space was provided outside both rooms to prevent heat from leaking through the room walls, thus helping to maintain a temperature consistent with the air inside. However, unless measures are implemented to ensure that the “building-side air conditions,” which cause changes in the temperature and humidity of the indoor air, are the same (even in different test facilities), the performance of the evaluated air conditioner will differ depending on the test equipment employed. This issue is similar to that for the air enthalpy test facility.

4.1.1.4 Proposed dynamic performance test facility

A new emulator-based dynamic performance test facility was developed to address the problems associated with the abovementioned conventional air enthalpy and balance test facilities.

(1) Basic concept of evaluation equipment

Fig. 4.1.1-6 illustrates the basic concept underlying the dynamic performance test facility. Fig. 4.1.1-7 depicts the control system when the air conditioning equipment was dynamically driven by the test equipment. As previously mentioned, the “building-side air conditions,” as presented in the red frame, exert a considerable influence on the dynamic performance of an air conditioner; thus, different dynamic driving performances yield different results.

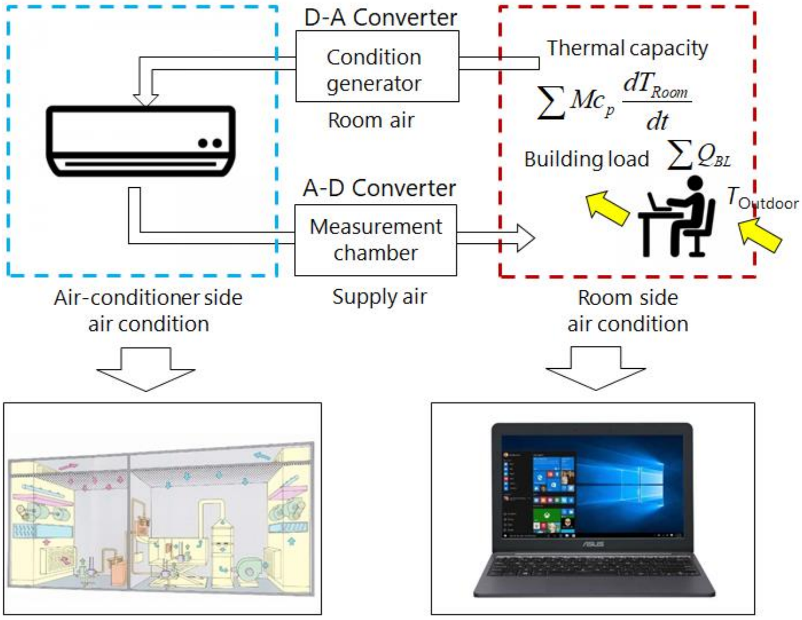

Fig. 4.1.1-6 Dynamic performance test method for air conditioners

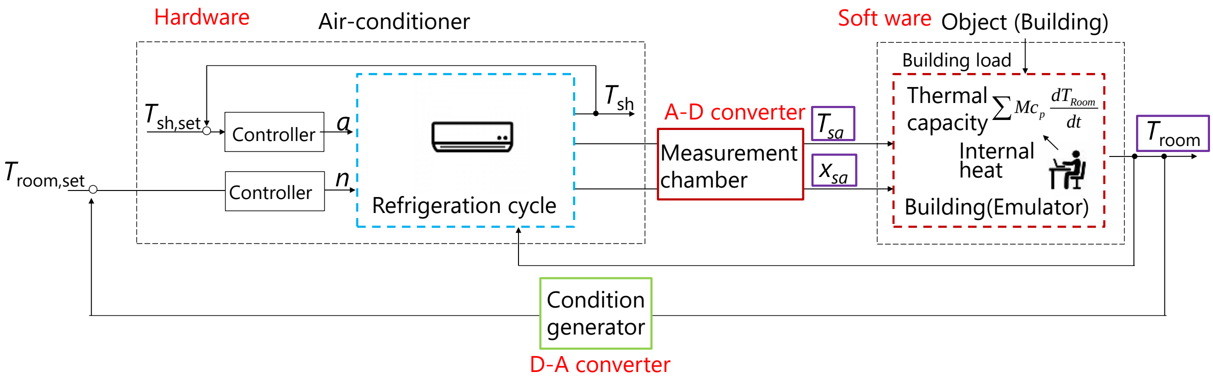

Fig. 4.1.1-7 Air-conditioner control system considering dynamic conditions

Numerous factors influence the performance of an air conditioning system in dynamic operation, such as the walls of the test facility, heat capacity of the installed measurement equipment, and size of the test equipment. The uniformity of the hardware conditions across facilities cannot be ensured. Therefore, we devised a new test method to compensate for the differences due to the test facility and equipment by virtually deriving the "building-side air conditions" using computer emulation. As it remains necessary to directly measure the load and power consumption of the air conditioning system, it is physically installed in the test facility, and actual measurements can be conducted while emulation software virtually calculates the built-in "building-side air conditions." The "equipment-side air conditions" are then demonstrated in the actual indoor air by the condition generator based on the indoor air conditions calculated by the emulator. The blown air generated by the air conditioner is measured in the measurement chamber and transmitted to the emulator as a digital signal.

In this test system, the condition generator and measurement chamber should not be considered as devices that generate loads and measure performance. Instead, they should be considered as devices that play the roles of digital-to-analog or analog-to-digital converters mediating between the emulator and performance evaluation device.

The most beneficial feature of the proposed dynamic performance test method is that the test facility can be used in its existing form when it is based on air enthalpy. Balance test-based facilities can be used by introducing a measurement chamber. In addition, by changing the mathematical model employed as the emulator, both the static and dynamic characteristics can be evaluated under various conditions.

In particular, the proposed method allows for the use of conventional test equipment, and can be readily employed to evaluate product development standards by unifying emulator architecture for example. In addition, by developing an emulator that reflects the conditions in an actual building, air conditioner performance can be measured under actual operating conditions. This allows for the analysis of the actual operating performance of air conditioners in different countries by accounting for their specific building and weather conditions. Thus, the same testing equipment can be used for general evaluations ranging from product development standards to the dynamic performance required by users under actual operation, thus realizing a unified test facility.

(2) Configuration of the dynamic performance test facility

The evaluation system employed in the proposed dynamic test facility is configured as shown in Fig. 4.1.1-8. The hardware comprises a test facility and an emulator installed on a computer to calculate the building-side air conditions, which are then physically generated by the condition generator. The air blown by the air conditioner is subsequently measured in the measurement chamber and transmitted to the emulator as a digital signal.

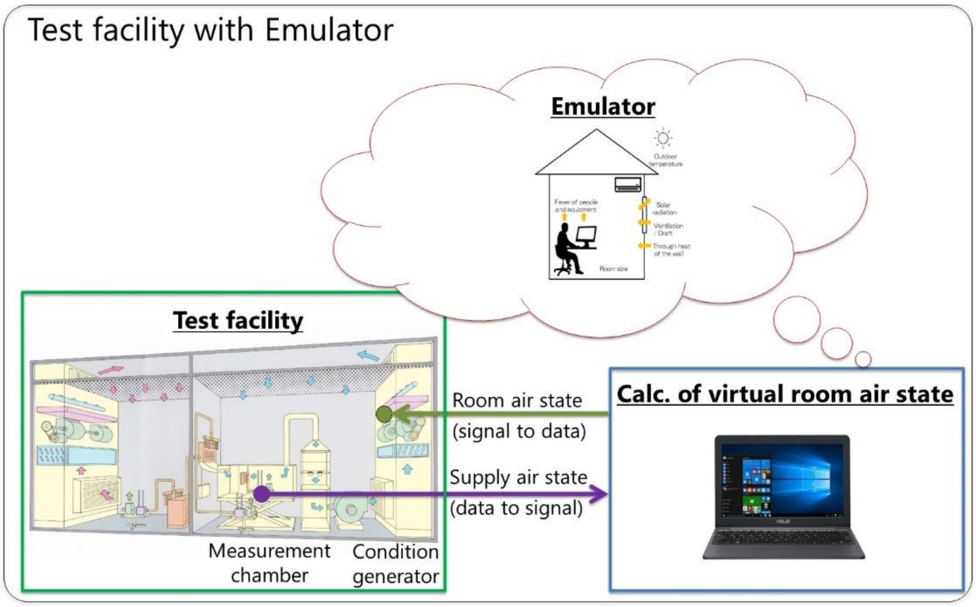

Fig. 4.1.1-8 Proposed hybrid dynamic test facility

(3) Specifications of the dynamic performance test facility

Table 4.1.1-1 provides the specifications of the proposed dynamic performance test facility, Fig. 4.1.1-9 presents an external view of the facility, and Fig. 4.1.1-10 presents the measurement chamber in the indoor unit room. Figs. 4.1.1-11 and 4.1.1-12 respectively depict the airflow diagrams in the indoor and outdoor unit rooms.

Table 4.1.1-1 Specifications of the hybrid dynamic test facility

Measurable capacity range	Up to 5 HP (14 kW)
Settable outdoor temperature range	-7–46 °C
Explosion-proof	Included
Cross wind speed	0.2 ± 0.1 m/s (JIS testing of showcases)
Size	7 m (D) × 8 m (W) × 3 m (H)

The proposed facility has an explosion-proof structure to allow for its use with combustible refrigerants, which are candidates for next-generation low-global warming potential (GWP) refrigerants. Furthermore, given that the proposed facility can test refrigerated display cabinets, a crosswind condition of 0.2 ± 0.1 m/s can be generated in accordance with the test standards in JIS B 8631-2:2011.

As shown in Fig. 4.1.1-11, the blown air from the indoor unit is first sent to the temperature/humidity measurement device through the measurement chamber, then directly to the air volume measurement device installed on the ceiling. The air is pulled by a suction fan to eliminate the pressure loss generated in the duct between the two devices. Air volume measurements are performed by combining four nozzles according to the air volume. These measured blowing conditions are then sent to the emulator. After passing through the airflow measurement device, the air is blown from the ceiling into the indoor unit room, where it is drawn into the condition generator. The indoor air is then generated with the pre-determined temperature and humidity in accordance with the instructions from the emulator. This air is passed through the ceiling duct and evenly blown laterally from the wall through perforated metal.

As shown in Fig. 4.1.1-12, the outdoor unit room is equipped with a measurement chamber, which is uncommon. Air blown from the outdoor unit is released into the measurement chamber, where a temperature/humidity measurement device is installed, and the air volume is measured using a stationary composite pitot tube. The condition signals from the emulator are then applied to the condition generator to achieve the specified temperature and humidity, and the conditioned air is returned to the outdoor unit.

Fig. 4.1.1-9 Overall appearance of test facility

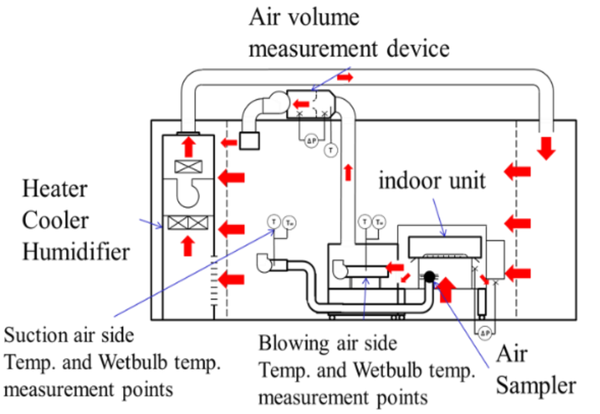

Fig. 4.1.1-11 Air flow diagram of indoor unit room

Fig. 4.1.1-10 Indoor unit measurement chamber

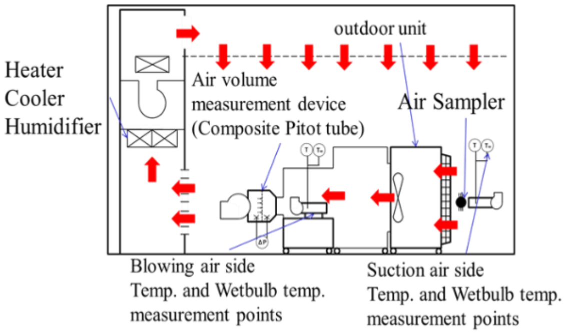

Fig. 4.1.1-12 Air flow diagram of outdoor unit room

(4) Emulator

(a) Standard emulator

As shown in Figs. 4.1.1-13 and 4.1.1-14, we developed emulator software capable of arbitrarily setting conditions such as the building load and heat capacity, which determine the building-side air conditions. As an example, a simple standard emulator used to reflect test standards was developed, in addition to a room emulator reflecting the conditions in an actual building, as detailed in this section.

The standard emulator comprises a continuous single-capacity system and an energy equation as follows:

$$\dot{m}_{out} = \dot{m}_{OA} + \dot{m}_{human} \tag{4.1.1-1}$$

$$M_{Room}\frac{dx_{Room}}{dt} = \dot{m}_{human} \tag{4.1.1-2}$$

$$M_{House}c_{p,a}\frac{dT_{Room}}{dt} = \dot{Q}_{BL} - \dot{Q}_{AC} \tag{4.1.1-3}$$

$$\dot{Q}_{BL} = f(T_{ex}) \tag{4.1.1-4}$$

where M_{House} is the combined mass of the indoor air and furniture. Notably, the empirical value of the heat capacity of a building considering M_{House} is greater than the heat capacity of the indoor air by a factor of approximately 10.

(b) Room emulator

The mathematical model of the room emulator consists of the continuity equation for the indoor air, energy equation, and wall heat transfer equation.

The indoor air continuity is expressed by the mass balance equation, in which the inflow and outflow of air across the boundary of the control volume shown in Fig. 4.1.1-13 are equal, as follows:

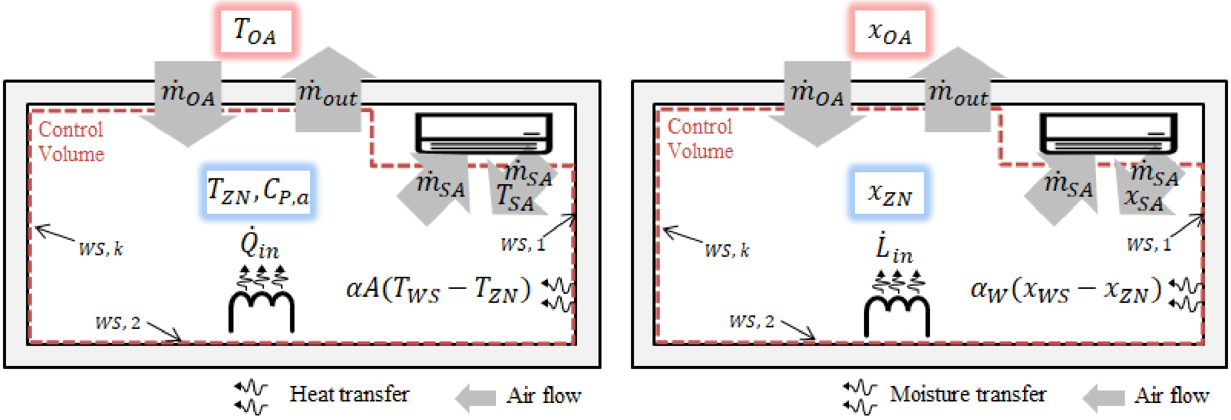

Fig. 4.1.1-13 Mathematical model for room (i) heat transfer and (ii) moisture transfer

:

$$\dot{m}_{out} = \dot{m}_{OA} + \dot{L}_{in} \tag{4.1.1-5}$$

and the mass balance equation for moisture contained in the air is expressed as follows:

$$M_{ZN}\frac{dx_{ZN}}{dt} = \sum_k j_{w,k}A_k\left(x_{WS,k} - x_{ZN}\right) - \dot{m}_{out}x_{ZN} + \dot{m}_{OA}x_{OA} + \dot{m}_{SA}(x_{SA} - x_{ZN}) + \dot{L}_{in} \tag{4.1.1-6}$$

where

$$M_{ZN} = \rho_{w,ZN}V_{ZN} + M_{FN} \tag{4.1.1-7}$$

The moisture that flows across the boundary in Fig. 4.1.1-13 consists of the following four components included in Equation 4.1.1-6:

i) Moisture transmitted from the wall (first term on the right side).
ii) Moisture that flows in and out of the system through ventilation (second and third items on the right side).
iii) Moisture flowing in and out across the system through machines such as refrigerators and air conditioners (fourth item on the right side).
iv) Moisture that dissolves in the air when generated by the human body (perspiration) or humidifier systems (fifth term on the right side).

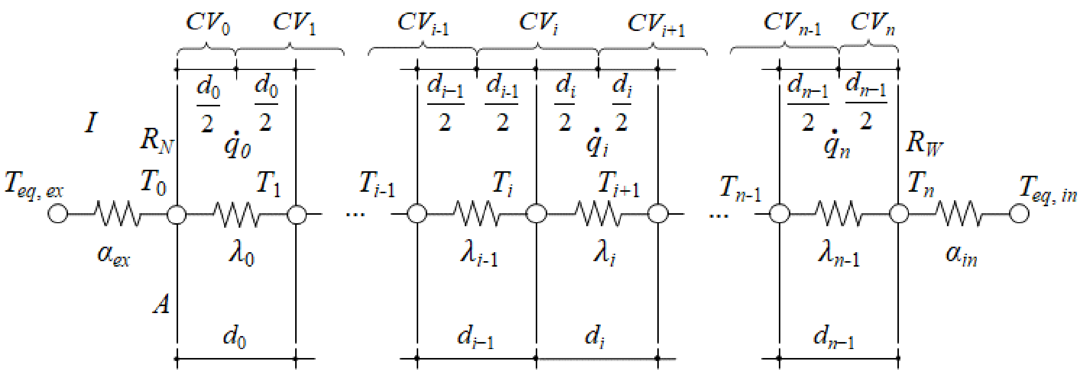

Fig. 4.1.1-14 Mathematical model for room wall

In addition, if moisture flows in and out of the system because of factors such as indoor air circulation, it is added to Equation 4.1.1-6. Equation 4.1.1-7 expresses the mass as the indoor moisture capacity, which is the sum of the moisture content of the indoor air and the moisture capacity of the walls and furniture. The customary value of M_{FN} was reported as approximately 16.7 kg per m^3 of the room volume [13].

The energy equation for the indoor air is then expressed as follows:

$$C_{ZN}\frac{dT_{ZN}}{dt} = \sum_k \alpha_{a,k}A_k\left(T_{WS,k} - T_{ZN}\right) - c_{P,a}\dot{m}_{out}T_{ZN} + c_{P,a}\dot{m}_{OA}T_{OA} + c_{P,a}\dot{m}_{SA}(T_{SA} - T_{ZN}) + \dot{Q}_{in} \tag{4.1.1-8}$$

$$C_{ZN} = c_{P,ZN}\rho_{a,ZN}V_{ZN} + C_{FN} \tag{4.1.1-9}$$

In Equation 4.1.1-8, the following physical phenomena are calculated assuming a real building, as shown in Fig. 4.1.1-13:

i) The heat transfer from the wall due to the difference between the wall surface and indoor temperatures (first term on the right side). When heat transfer occurs across the wall, the indoor air temperature changes as the wall temperature increases.
ii) Energy flowing in and out of the system through ventilation (second and third terms on the right side),
iii) Moisture flowing in and out across the system through machines, such as refrigerators and air conditioners (fourth term on the right side).
iv) Sensible heat and latent heat due to internal heat generation, such as from humans, lighting, and equipment (fifth term on the right side).

Equation 4.1.1-9 expresses the heat capacity as a lumped constant for both air and furniture. The customary value of C_{FN} was reported as approximately 15.2 kJK^{-1}per cubic meter of room volume for offices[14]. If there is energy flow in and out of the system due to indoor air circulation, it should be added to Equation 4.1.1-8.

The equation for heat transfer in a multi-layer wall is expressed as follows:
when $1 \leq i \leq n-1$

$$C_{CV,i}\frac{1}{A}\frac{dT_i}{dt} = \lambda_{i-1}\frac{T_{i-1}-T_i}{d_{i-1}} + \lambda_i\frac{T_{i+1}-T_i}{d_i} \tag{4.1.1-10}$$

when $i = 0$

$$\left(c_{P,0}\rho_0\frac{d_0}{2}\right)\frac{dT_0}{dt} = \alpha_{ex}\left(T_{eq,ex} - T_0\right) + \lambda_0\frac{T_1-T_0}{d_0} \tag{4.1.1-11}$$

when $i = n$

$$\left(c_{n-1}\rho_{n-1}\frac{d_{n-1}}{2}\right)\frac{dT_n}{dt} = \lambda_{n-1}\frac{T_{n-1}-T_i}{d_{n-1}} + \alpha_{in}\left(T_{eq,in} - T_n\right) \tag{4.1.1-12}$$

As shown in Fig. 4.1.1-14, Equation 4.1.1-10 is the energy equation for the *i*-th and *i* + 1 wall materials counted from the outside air side of a multi-layer wall. Equations 4.1.1-11 and 4.1.1-12 are the energy equations for the outside air and wall material adjacent to the room, respectively. In this model, the control volume is considered as a single-mass point system straddling two adjacent wall materials, and the heat capacity of the wall in each system is expressed as follows:

$$C_{CV,i} = \frac{1}{2}A\left(c_{p,i-1}\rho_{i-1}d_{i-1} + c_{p,i}\rho_i d_i\right) \tag{4.1.1-13}$$

To predict the temperature fluctuation inside the wall, the thermal conditions should be determined on both sides of the wall. The heat flow on the wall surface is influenced by the air temperature near the surface and the average radiation temperature from the objects surrounding the wall surface. The values of $T_{eq,ex}$ in Equation 4.1.1-11 and $T_{eq,in}$ in Equation 4.1.1-12 can be expressed using the concept of equivalent temperature. The heat transfer balance around the wall surface on the outside air side can be expressed using the equivalent temperature on the outside air side, as follows:

$$\alpha_{ex}\left(T_{eq,ex} - T_0\right) = \alpha_{ex}(T_{ex} - T_0) + a_s I - \varepsilon F_{sky} E_{ex,N} \tag{4.1.1-14}$$

where the heat transfer due to the difference between the equivalent temperature $T_{eq,ex}$ on the outside air side and the wall surface temperature T_0 is expressed by the convective heat transfer due to the difference between the outside air temperature T_{ex} and T_0 (first term on the right side), the solar radiation near the wall surface (second term), and the radiant heat (third term on the right side).

The heat transfer balance around the wall surface on the inside air side is expressed as follows:

$$\alpha_{in}\left(T_{eq,in} - T_{WS}\right) = \alpha_{in,c}(T_{ZN} - T_{WS}) \quad + \alpha_{in,r}\left(\sum_i \phi_i T_{WS,i} - T_{WS}\right) + R_{in}R_r\dot{Q}_{in} \tag{4.1.1-15}$$

where the heat transfer due to the difference between the equivalent temperature $T_{eq,in}$ inside the room and the wall surface temperature T_{WS} is expressed as the convective heat transfer due to the difference between the room temperature T_{ZN} and T_{WS} (first term on the right side), the radiant heat from other walls (second term on the right side), and the radiant heat emitted by indoor equipment (third term on the right side). The heat received by the indoor wall is summarized in the form of heat transfer using the room equivalent temperature $T_{eq,in}$, as expressed on the left side. Furthermore, ϕ_i in the second term is the absorption coefficient proposed by Gebhart[15] on the *i*-th wall surface. Finally, if $\alpha_{in,c}$ is the same as $\alpha_{a,k}$ in Equation 4.1.1-8; then $\alpha_{in} = \alpha_{in,c} + \alpha_{in,r}$, and α_{ex} are the sum of the convective heat transfer coefficient and the radiative heat transfer coefficient, respectively, which are referred to as the total heat transfer coefficients.

The validity of the proposed models was verified using the Balance Evaluation Systems (BESTest) [16), 17), 18), 19)]. Critically, these models should be considered as simple examples. The greatest advantage of the proposed dynamic performance test method is that the emulation model can be changed as required.

4.1.1.5 Soundness evaluation of dynamic performance test facility

This section verifies the capacity of the proposed dynamic performance test facility to reflect the operating performance of the test equipment with sufficient accuracy.

(1) Static soundness (fixed compressor rotation speed test)

Methods were previously established for the evaluation of the static soundness of performance test equipment. Therefore, we performed a static soundness evaluation based on static tests in which the rotation speed of the compressor was fixed. This was achieved in accordance the procedure for obtaining semi-accreditation, as provided by the Japan Air Conditioning and Refrigeration Research Institute (JATL), who own the only air conditioner test facility in Japan and provide the standards for air conditioner test equipment.

The semi-accreditation provided by JATL stipulates that tests be performed on two air conditioner models with different capacities, and that the measurement results be within 3% of the data measured by JATL under all required test conditions. Therefore, we prepared two models, namely, a 5 hp and 3 hp machine, which were then tested under three conditions: the standard cooling test, standard heating test, and heating low-temperature test, as specified in the JIS B8615 standard. These test conditions are listed in Table 4.1.1-2.

Table 4.1.1-2 Test conditions for validation

Test	Indoor temperature dry/wet ℃	Outdoor temperature dry/wet ℃	Partial load ratio %
Standard cooling test	27/19	35/24	100
Standard heating test	20/15	7/26	100
Low-temperature heating test	20/15	2/1	100

Figs. 4.1.1-15 and 4.1.1-16 present the results of the standard cooling and standard heating tests, respectively, which were conducted in continuous operation. In these tests, the average value of the data acquired over a 35 min period was reported after reaching a sufficiently stable state. The results of the low-temperature heating test, as shown in Fig. 4.1.1-17, depict the average value acquired over three cycles, as the compressor and air volume were stopped periodically to perform the defrosting operation. The results of all tests indicated that the cooling capacity and power consumption were statically measured within 3% of the data reported by JATL. Therefore, the facility acquired semi-certification on October 1, 2020. As a result, it was confirmed that the proposed test facility can determine the performance of air conditioning equipment with the same high accuracy as required for the equipment certification process.

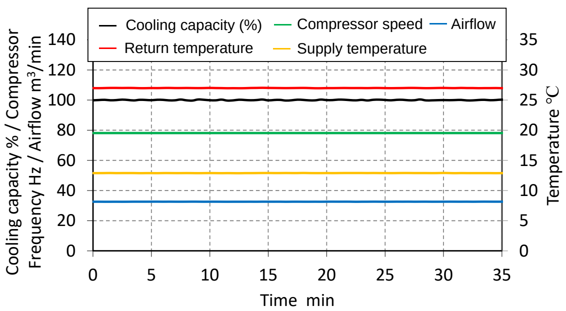

Fig. 4.1.1-15 Results of JIS test
(Standard cooling test)

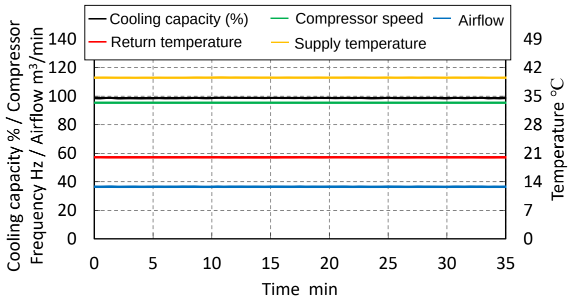

Fig. 4.1.1-16 Results of JIS test

(Standard heating test)

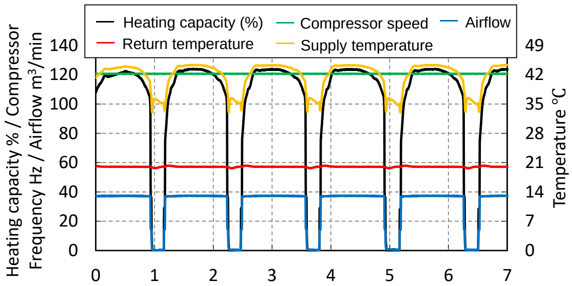

Fig. 4.1.1-17 Results of JIS test

(Low-temperature heating test)

(2) Dynamic soundness

The dynamic soundness of the test equipment was evaluated before conducting the dynamic performance tests in this study. As shown in Fig. 4.1.1-7, the test equipment factors evaluated were those that influence the indoor air temperature control of the building by the air conditioner, as follows:

i) Emulator calculation time lag

ii) Temperature and humidity followability in the condition generator

iii) Time delays of various sensors

This evaluation was based on a 10-kW unit, which is the standard installation size for this test equipment. The standard installation space for the equipment was 147 m^3. The thermal and material time constants (obtained by dividing the mass by the air conditioner volume, as derived from the standard blowing air volume in the test room) used to evaluate soundness were approximately 5000 s and 500 s, respectively.

(a) Emulator calculation time lag

The emulator used to calculate the building air conditions in this study employed a discretized non-linear equation to perform a dynamic analysis on a first-order forward difference equation. Under these conditions, the calculation for a 1 s step was completed in approximately 0.5 s on a normal personal computer. This indicates that the delay in calculation time did not influence the dynamic performance of the test facility.

(b) Temperature and humidity followability in the condition generator

The condition generator should be able to generate the desired air conditions according to the signal provided by the emulator. Therefore, we investigated the capacity of the condition generator to follow periodic fluctuations over a time span of approximately 1 h, such as during start-up or intermittent operation, when the operating conditions changed most abruptly within approximately 0.5–1 h. Table 4.1.1-3 presents the test conditions.

Table 4.1.1-3 Followability test conditions

Test mode	Indoor unit room set temperature		Outdoor unit room set temperature	
	Dry	Wet	Dry	Wet
Start-up in cooling	35 °C →27 °C	24 °C →19 °C	35 °C constant	24 °C constant
Start-up in heating	7 °C →20 °C	6 °C →15 °C	7 °C constant	6 °C constant
Cyclic cooling	27 °C ↔26 °C	26 °C ↔23.5 °C	35 °C constant	24 °C constant

The followability test results are reported in Figs. 4.1.1-18, 4.1.1-19, and 4.1.1-20.

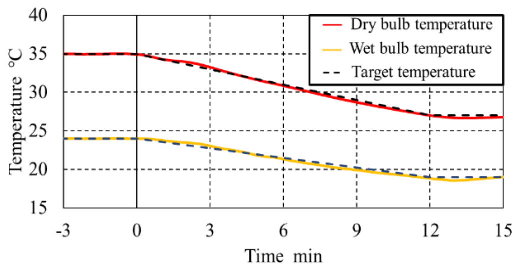

(i) Indoor unit room

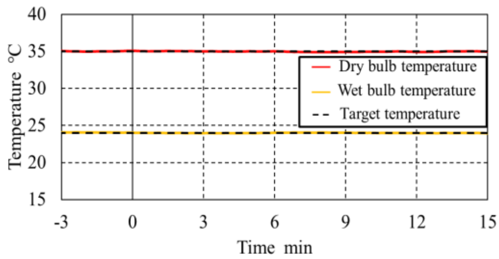

(ii) Outdoor unit room

Fig. 4.1.1- 18 Temperature controllability in cooling start-up mode

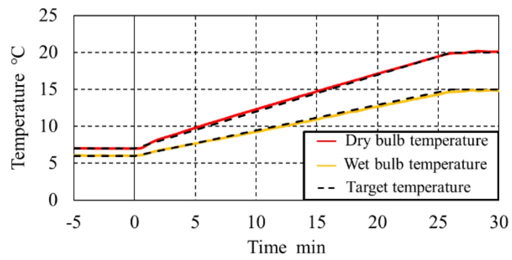

(i) Indoor unit room

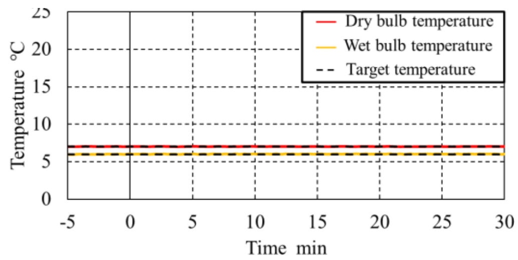

(ii) Outdoor unit room

Fig. 4.1.1-19 Temperature controllability in heating start-up mode

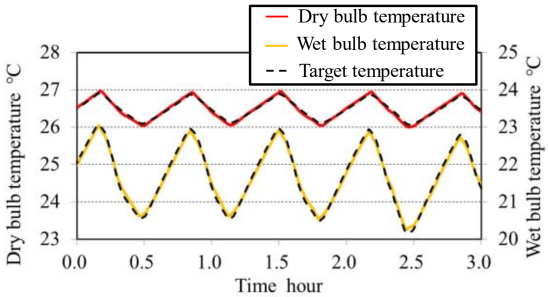

Fig. 4.1.1-20 Temperature followability in intermittent driving

As shown for the cooling operation in Fig. 4.1.1-18, the dry-bulb and wet-bulb temperatures in the indoor unit room rapidly changed within approximately 12 min, thus indicating that the indoor unit started cooling. The dry-bulb and wet-bulb temperature signals provided by the emulator (as indicated by the dashed lines) and the corresponding conditions of the air generated by the condition generator (as indicated by the solid lines) were in good agreement with a delay of only approximately 20 s. In addition, in the outdoor unit room, the heat generated from the outdoor unit was removed, and the dry-bulb and wet-bulb temperatures were kept constant in accordance with the signal provided by the emulator.

Similarly, during the heating operation shown in Fig. 4.1.1-19, the temperature required by the emulator remained unchanged in both the indoor and outdoor unit rooms, even when the temperature in the indoor unit room changed abruptly within approximately 25 min, thus indicating the initiation of heating. The condition generator was in accordance with the humidity signal, with a delay of approximately 20 s.

Finally, as shown in Fig. 4.1.1-20, even when the dry-bulb and wet-bulb temperatures changed rapidly, such as during intermittent operation, the signal provided by the emulator increased or decreased within approximately 30 s. In particular, the emulator responded with a maximum delay of approximately 54 s at the instant of an abrupt change. These values represent approximately 0.6% of the room time constant.

(c) Time delay of various sensors

The test facility was equipped with multiple sensors, including thermometers and hygrometers with measurement delays of less than 10 s.

(d) Summary

The evaluated air conditioning unit was subject to (1) a delay in the intake air temperature/humidity sensor (maximum of approximately 10 s), (2) a delay in the passage of discharged air through the measurement chamber (maximum of approximately 15 s for humidity only), (3) a temperature difference in the discharged air with a delay in the temperature/humidity sensor measurement (maximum 10 s), and (4) a delay in the condition generator response (approximately 20 s), thus totaling a maximum delay of 55 s. Hence, the total temperature delay of the test equipment was approximately 1% of the thermal time constant of the room (5000 s), and the total humidity delay was approximately 10% of the material time constant (500 s). Considering that the static accuracy can be compensated by the verification test, and the period of intermittent operation in which the operating condition of the equipment suddenly changed ranged from approximately 30–60 min, the dynamic performance of the proposed test facility may be dependent on the test time. We therefore plan to conduct a round-robin test in multiple laboratories research to confirm the results reported in this study.

4.1.1.6 Dynamic performance tests of air conditioning equipment

The proposed test facility was used to conduct dynamic performance tests on an air conditioning system. The results of a partial-load performance test are reported using an air conditioner with a rated cooling capacity of 12.5 kW under normal user conditions, that is, without a fixed compressor speed. Table 4.1.1-4 presents the wall material specifications of the room used in the test, Table 4.1.1-5 presents the corresponding thermal parameters, and Table 4.1.1-6 presents the test conditions.

Table 4.1.1-4 Room wall material specifications

Item	Area (m^2)	Material thickness (mm)			
Outer wall	28	Tile	Concrete	Insulation	Gypsum board
		10	175	25	10
Floor ceiling	49	Tile	Concrete	Gypsum board	Sound absorbing board
		3	150	9	15

Table 4.1.1-5 Room wall material thermal parameters

Material	Thermal conductivity (W/(m/K))	Volumetric specific heat (KJ/(m^3・K))
Tile	1.3	2000
Concrete	1.4	1600
Insulation	0.04	33
Gypsum board	0.17	830
Sound absorbing board	0.064	290

Table 4.1.1-6 Test conditions

Item	Value
Rated capacity (kW)	12.5
Outside temperature (℃)	35 / 24, 29 / 19
Indoor temperature (℃)	27 / -
Sensible heat load (W)	9350, 1650
Latent heat load (W)	2230, 430
Room size (m^3)	100, 196, 300

The rated room size for the subject air conditioner was 49 m^2; therefore, the test room was a square-shaped with dimensions of 7 x 7 m. With a ceiling height of 4 m, the room volume was 196 m^3. The emulator was established for two additional room sizes: the first was approximately half the rated size, and the second was greater than the rated size by a factor of approximately 1.5. Experiments were then conducted accordingly. Additionally, experiments were conducted under various air conditioning loads. Representative results are discussed in this section.

First, we set the sensible heat load as 9350 W and the latent heat load as 2230 W using the room emulator, while considering the heat penetrating into the room from the walls, such that the load processed by the air conditioner was 12.5 kW (the rated capacity). The results are shown in Fig. 4.1.1-21. In this case, the compressor rotation speed was nearly constant, and the coefficient of performance (COP) was nearly the same as that obtained by the JIS test using a fixed compressor rotation speed.

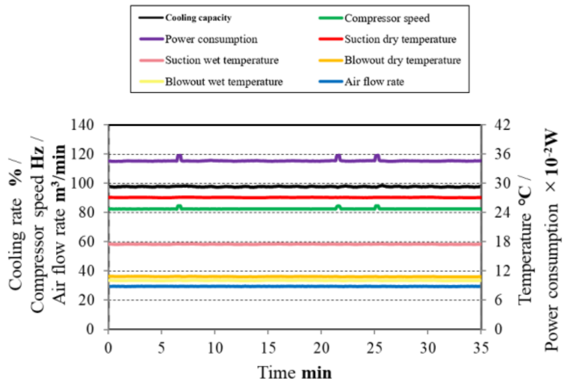

COP＝3.56

Fig. 4.1.1-21 Test results for 35 °C/24 °C at 12.5 kW

If the building load is low, intermittent operation starts, and the compressor speed changes over time. Moreover, to provide a representative result of this condition, the load processed by the air conditioner was set as 3125 W, or 25% of its rated capacity. The room emulator was set as 1650 W for the sensible heat load and 430 W for the latent heat load, considering the heat that penetrated into the room from the walls. The test results are provided in Fig. 4.1.1-22, which reveals that when the compressor rotation speed was not fixed, the room temperature changed by approximately 2 °C due to the intermittent operation of the air conditioner. Given that the outside air temperature remained constant at 35 °C, the heat entering from the wall changed with the temperature of the room. As a result, the air conditioning load in the room changed.

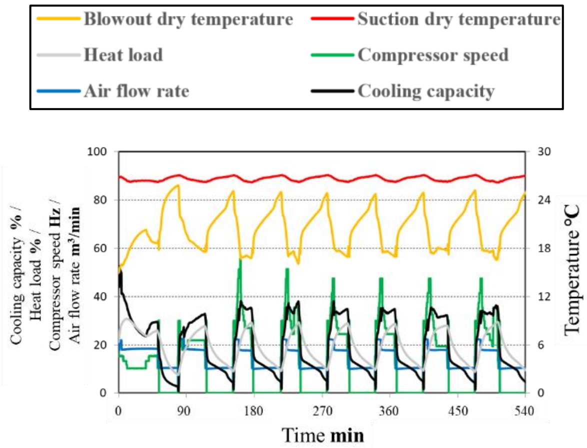

Fig. 4.1.1-22 Air conditioning load for intermittent operation

In addition, the heat capacity given as the “building-side air conditions” changed depending on the size of the room, and the period of intermittent operation of the equipment changed significantly as a result. Fig. 4.1.1-23 presents the test results for the standard (196 m^3), small (100 m^3), and large (300 m^3) room volumes.

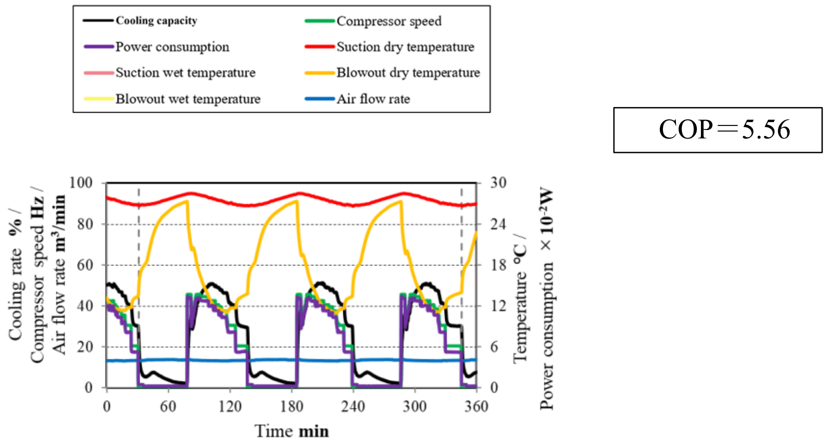

(i) Room volume (standard) (196 m^3)

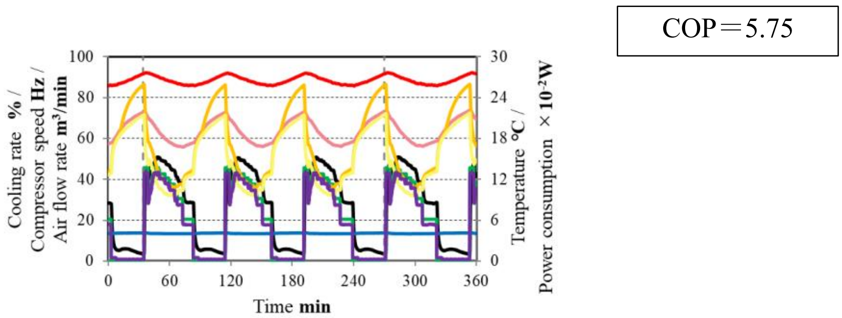

(ii) Room volume (small) (100 m^3)

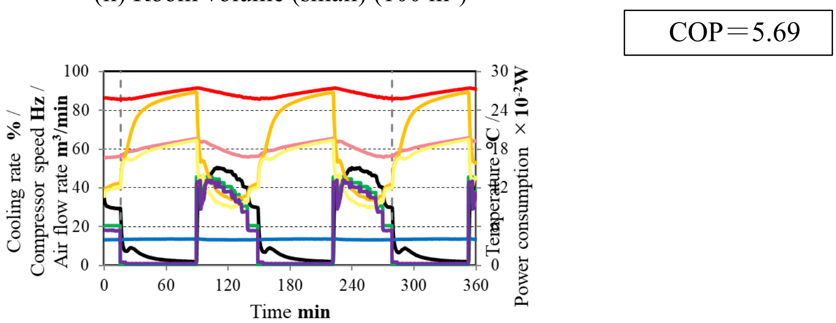

(iii) Room volume (large) (300 m^3)

Fig. 4.1.1-23 Test results for 29 °C/19 °C at 25% of rated capacity

Notably, additional large-scale tests are conventionally required to change the physical size of the test room. However, these results indicate that the dynamic test facility can simulate the changes in the "building-side air conditions" using the emulator, without changing the size of the room; thus representing a major advantage. In particular, the size of the room influences the periodic behavior of the air conditioning system. If the room is small, the operating cycle is shortened because the lower limit of the room temperature is reached at an earlier stage, and the large load present immediately after start-up is reduced. When the room is large, a larger heat capacity is present, which corresponds to a margin in the rate of change before the lower limit of the room temperature is reached. The results of these experiments reveal that, even when the intermittent operation cycle changed due to the simulated change in the size of the room, the behavior of the proposed facility during intermittent operation was maintained; thus, the change in COP was limited to 2–3%. The intermittent operation performance of the air conditioner can differ considerably depending on the size of the room.

This result indicates that the dynamic performance of an air conditioner cannot be accurately determined unless the "building-side air conditions" are the same, including the size of the room. However, the evaluation of the air conditioner performance using the emulator indicates that such tests can be conducted without influence from the physical size of the test room. Thus, the proposed test equipment demonstrated a detailed and diverse dynamic performance, including sufficient equipment control.

4.1.1.7 Summary of emulator-based dynamic performance test facility

In this study, we developed an emulator-based dynamic performance test facility to evaluate the dynamic performance of air conditioning systems; and to therefore establish a performance test method that includes dynamic driving conditions. The proposed approach employs an emulator to virtually derive the air conditions in the building, combined with conventional performance test equipment, thus allowing for the evaluation of the dynamic performance of air conditioners in a highly accurate and reproducible manner without dependency on specific test equipment. The following conclusions were reached:

1) To verify the static soundness of the proposed test facility, the acquired data were compared with the data obtained from a JATL prototype. As the error was suppressed within 3%, a sufficiently accurate performance evaluation was considered.
2) To verify the dynamic soundness of the proposed test facility, the i) calculation time delay of the emulator, ii) temperature and humidity followability in the condition generator, and iii) time delay of the various sensors were comprehensively analyzed. The thermal delay was approximately 1% of the thermal time constant of the room, and no factor significantly influenced the dynamic characteristics of the test facility equipment. In addition, the material delay was approximately 10% of the material time constant of the room.
3) The dynamic performance evaluation of an air conditioner (considered as an example) indicated that when the load reached 25%, the device entered an intermittent operation state, and the heat entering from the outer wall changed with the room temperature, which is similar to the air conditioning load in the room. Furthermore, intermittent operation changed with the emulated room size. These results suggest that the periodic behavior associated with the air conditioner operating state changes, and depending on the control method, its intermittent operation performance may differ considerably depending on the size of the room.
4) The proposed dynamic performance test facility enables simple changes in the air conditions of a building using an emulator. Thus, accurate and reproducible evaluations of air conditioner performance can be conducted, regardless of the physical size of the test room. As a result, the proposed emulator-based dynamic performance test facility can support the standardization of air conditioner testing.

Nomenclature

a_s	: solar absorption rate (-)	$\dot{Q}$	: heat quantity (W)
A	: wall surface area (m^2)	$\dot{q}$	: heat generation inside the wall ($W \cdot m^{-2}$)
C	: heat capacity ($kJ \cdot K^{-1}$)	t	: time (s)
c_p	: constant pressure specific heat ($kJ \cdot kg^{-1} \cdot K^{-1}$)	T	: temperature (K)
E	: radiant heat ($W \cdot m^{-2}$)	V	: volume (m^3)
F	: view factor to the sky (-)	x	: absolute humidity ($kg \cdot kg^{-1}$)
I	: Solar irradiance ($W \cdot m^{-2}$)	α	: heat transfer coefficient ($W \cdot m^{-2} \cdot K^{-1}$)
j	: mass diffusion flux ($kg \cdot m^{-2} \cdot s^{-1}$)	ρ	: density ($kg \cdot m^{-3}$)
$\dot{L}$	: moisture generated ($kg \cdot s^{-1}$)	ε	: long wavelength emissivity (-)
M	: mass (kg)	ϕ	: Gebhart absorption coefficient (-)
$\dot{m}$	: mass flow rate ($kg \cdot s^{-1}$)		

Subscripts

a	: air	*N*	: night
AC	: air conditioner side	*OA*	: outside air
BL	: building	*r*	: radiation
c	: convection	*Room*	: indoor
eq	: equivalent	*SA*	: supply air
ex	: external	*sh*	: degree of superheat
FN	: furniture, etc.	*w*	: water vapor
in	: inside	*WS*	: wall surface
i,k	: serial number	*ZN*	: zone

References

1) Agency for Natural Resources and Energy, Ministry of Economy, Trade and Industry, Annual Report on Energy for 2019 (Energy White Paper 2020) PDF Version, Part 2, pp .112-115.
2) Shinichi, A., Jun, S., Takuya, O. Hiroyuki, I., Yuki, A. Study on State of COP and Regional Characteristics of APF for Room air Conditioners, *AIJ J. Technol. Des.,* 2014, **20**(44), pp. 187-190 (in Japanese).
3) Katsuhiro, K., Technological Innovations of Air Conditioning and their Development into Industry, *Refrigeration*,

2019, **94**(1101), pp. 436-441 (in Japanese).
4) Japan Refrigeration and Air Conditioning Industry Association, Estimation of World Air Conditioner Demand, 2019, pp. 1-8.
5) Keisuke, O. and Kiyoshi, S., Seiichi, Y., Tetsuro, K., Kuniyasu, M., Intermittent Driving Simulation of Compression type Heat Pump－1st Report: Mathematical model and simulation of single-stage vapor compression type heat pump, *Trans.JSRAEngineers*, 2013, **30**(2), pp. 107-122 (in Japanese).
6) Japanese Standards Association, Package Air Conditioner JIS B 861, (2015).
7) Japan Refrigeration and Air Conditioning Industry Association, Practical Performance and Possibilities of Heat Pumps (2010).
8) Masayuki, N., Technologies for Energy −Saving of Room Air−Conditioner, *J.JSME*, 2003, **106**(1015), pp. 464-465. (in Japanese).
9) Fusigi, Y., Create a new breeze! Room Air Conditioner Revolution(Atarasii kaze wo tukure! Ru-mueakon kakumei), *J.JSME,* 2019, **122**(1206), pp. 38-39.
10) Palkowski, C., Zottl, A., Malenkovic, I., Simo, A., Energies, 2019, 12, 1045. doi:10.3390/en12061045.
11) Ban, T., Nakano, D., Ohno, K., Yamaguchi, S., Saito, K., Yamaguchi, H., *Proc. Of 12th IEA Heat Pump Conference* 2017, Rotterdam.
12) OhnishiNetsugaku, https://en.ohnishi.co.jp/.
13) Ozaki, A., Watanabe, T., Takase, H., Tsujimaru, T., Heat-Moisture-Air Coupled Simulation for Buildings Part 1: Temperature and Humidity Calculation Considering Moisture Absorption and Desorption of Walls, *Summaries of Technical Papers of Annual Meeting of Architectural Institute of Japan*, 2004, pp. 439-440.
14) Ishino, H., Kori, K, Measurement and Experimental Study on Thermal Influence of Furniture in Office Buildings, Proc., 1987, Vol. 372, pp. 59-66.
15) Gebhart, B., A new Method for Calculating Radiant Exchanges, ASHRAE Transactions, 1959, Vol. 65, pp.321-332.
16) Judkoff, R., Neymark, J., International Energy Agency building energy simulation test (BESTEST) and diagnostic method, 1995, NREL/TP-472-6231.
17) Design method of general-purpose building heat load calculation class library using immutable interface, Annual Meeting of the Society of Heating, Air-Conditioning and Sanitary Engineers of Japan, Collection of academic lectures, 2009. https://doi.org/10.18948/shasetaikai.2009.3.0_1995.
18) Development of Test Procedure for the Evaluation of Building Energy Simulation Tools, BS, 2019. https://doi.org/10.26868/25222708.2019.210592.
19) Eisuke Togashi: Thermal Environment Calculation Method, ISBN: 978-4990890827, https://www.amazon.co.jp/dp/4990890825.
20) Japanese Standards Association, Package Air Conditioner JIS B 8616:2006 (2006).
21) Ban, T., Nakano, D., Ohno, K., Yamaguchi, S., Saito, K., Yamaguchi, H., Testing facility for unsteady performance of air conditioning system, 12th IEA heat pump conference, Rotterdam, 2017.
22) Harunori, Y., Masato, M., Takao, S., Yasuo, K., Technical papers of annual meeting, *the Society of Heating, Air-Conditioning and Sanitary Engineers of Japan*, 2011, Nagoya, OS31. pp. 1-4.
23) Goo, T., Kenichi Y., Toshiki, I., Mitsuhide, Y., Yasuhiro, S., Masanari, U., Tatsuo, N., *Proc. of 2016 SHASE Annual Conference*, 2016, Kagoshima, 2, pp. B-13.
24) Yoichi, M., Masafumi, H., Yuta, T., Katsuki, N., Takashi, N., *Proc. of 2015 JSRAE Annual Conference*, 2015, Tokyo, pp. B111-1-4 (in Japanese).
25) Hayato, H., Mami I., Eiji, H., Annual Performance and Performance Rating of Air Conditions-1st Report: Packaged Air Conditioners, *Trans. JSRAE*, 2011, **28**(4), pp.393-404.
26) JSRAE, JSRAE Technical Book Series - Refrigeration cycle control, 2018, *JSRAE*, Tokyo, pp.51-53.
27) Ban, T., Nakano, D., Ohno, K., Yamaguchi, S., Saito, K., Yamaguchi, H., *Proceedings of 2016 JSRAE Annual Conference*, 2016, Kobe, B141-1-4 (in Japanese).
28) https://www.ohnishi.co.jp/calorimeter/cal-product01 (Jan, 2021)
29) https://www.ohnishi.co.jp/calorimeter/cal-product02 (Jan, 2021)
30) Togashi, E., The art of thermal environmental computing, Togashi Research Laboratory, Department of Architecture, Faculty of Architecture, Kogakuin University, 2021, Tokyo, pp. 556-569.

4.1.2 Experimental evaluations of various air conditioning equipment

4.1.2.1 Background and purpose of the experiment

When introducing next-generation refrigerants into refrigerating and air conditioning equipment, the safety and environmental GWP (direct impact) of the refrigerant used in the equipment should be considered, in addition to the impact on global warming due to energy-derived CO_2 emissions (indirect impact). Therefore, the actual operating performance of the refrigerant and air conditioning equipment should be evaluated. To fully illustrate the potential of low-GWP refrigerants, an optimized air conditioning unit should be fabricated for each refrigerant and employed to conduct accurate performance tests under actual operating conditions. However, there are several next-generation refrigerant candidates. The corresponding financial and time costs required to produce a series of specifically optimized air conditioning units is impractical. Therefore, in this study [3], the "Simulator development and utilization" objective was to construct various simulators for heat exchangers and air conditioning systems was realized, to decrease the time and costs required for system examination and production. Before using such simulators, the validity and accuracy of the calculated values employed in their construction should be verified. Therefore, the R290 and R454C low-GWP refrigerants were dropped in to air conditioners designed for use with the R22 refrigerant, and their performances were evaluated accordingly.

4.1.2.2 Overview of the air conditioner used in this experiment

Table 4.1.2-1 presents the specifications of the air conditioner used in this experiment. Unless drop-in tests using R290 and R454C are performed in air conditioners intended for low-pressure refrigerants, such as R22, the results will be extremely poor. After consulting with air conditioner manufacturers, we determined that the production of R22 air conditioners was discontinued over a decade ago, and a new inventory could not be obtained. Therefore, we conducted this experiment using a pre-owned R22 wall-mounted room air conditioner with a rated capacity of 2.2 kW. Pressure sensors and thermocouples were installed in the air conditioner after thoroughly cleaning the heat exchangers of the outdoor and indoor units. To measure the refrigerant flow rate, two Coriolis flow meters were installed with valves on the lines, such that they could be switched between cooling and heating. In addition, a tool was provided by the air conditioner manufacturer to enable the free control of the compressor speed, and another tool was installed to enable the free adjustment of the expansion valve opening across 50 steps. Fig. 4.1.2-1 depicts the mounting positions of the pressure sensor, thermocouple, and refrigerant flowmeter; and Fig. 4.1.2-2 presents the test setup in the dynamic performance evaluation facility.

Table 4.1.2-1 Specifications of room air conditioner employed in this experiment

Parameter		Value
Type		Room air conditioner
Year of manufacture		2001
Original refrigerant		R22
Rated capacity (W)	Cooling	2200
	Heating	2500

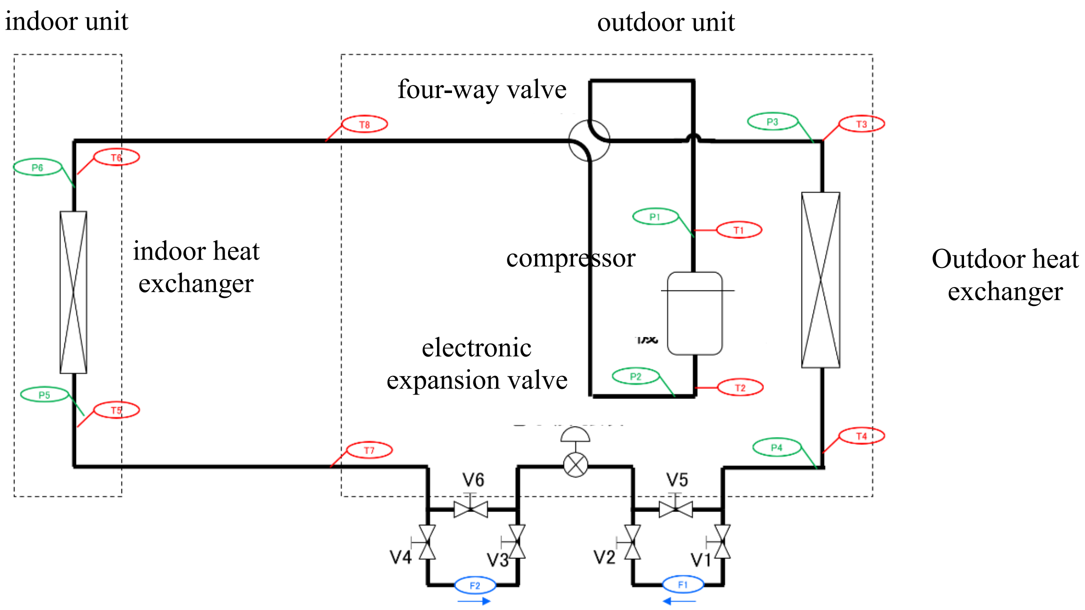

Fig. 4.1.2-1 Mounting locations of pressure sensors, thermocouples, and flow meters

(a) Indoor unit (b) Outdoor unit

Fig. 4.1.2-2 Test setup in the dynamic performance evaluation facility

4.1.2.3 Determination of refrigerant charge

The performance of the air conditioner should be evaluated after maximizing the potential of each refrigerant. Therefore, when R290 and R454C were dropped in, the refrigerant charge was optimized (1) by fixing the compressor speed to the rated value for R22, and (2) fixing the compressor speed to achieve a capacity of 2.2 kW. These refrigerant charge optimization procedures are detailed below.

(1) Optimization of the refrigerant charge by fixing the compressor rotation speed to the rated value for R22.

① Fix the compressor rotation speed of the test machine to the rated value for R22 (48 Hz). At this value, a capacity of 2 kW is realized.

② Set an initial low refrigerant charge.

③ Increase the opening of the expansion valve such that the degree of superheating is 5 °C and the degree of supercooling is 5 °C.

④ Measure the capacity of the air conditioner under cooling-rate test conditions.

⑤ If the degree of supercooling cannot be obtained, increase the refrigerant charge and return to ③.

Accordingly, the refrigerant charge was determined by measuring the degree of supercooling while gradually increasing the refrigerant charge. The final charges for R290 and R454C were determined as 400 g and 730 g, respectively, and the cooling capacity for both was 1,860 W; this corresponds to 84.5% of the rated capacity for R22 (2.2 kW) or 80% of the 2 kW capacity achieved at a compressor speed of 48 Hz.

(2) Optimization of the refrigerant charge by fixing the compressor rotation speed to achieve a capacity of 2.2 kW.

⑥ Set an initial low refrigerant charge.

⑦ Fix the maximum compressor rotation speed of the test machine to achieve a capacity of 2.2 kW.

⑧ Adjust the opening of the expansion valve such that the degree of superheating is 5 °C and the degree of supercooling is 5 °C.

⑨ Measure the capacity of the air conditioner under the cooling-rate test conditions.

⑩ a) If the degree of supercooling cannot be obtained or the capacity does not reach the target capacity, increase the refrigerant charge and return to ⑦.

b) If the capacity exceeds the target capacity, reduce the compressor speed and return to ⑧.

As a result of adjusting the capacity and degree of supercooling while gradually increasing the refrigerant charge, the refrigerant charge was determined as 400 g for R290 and 950 g for R454C when compared with 910 g for R22.

4.1.2.4 Test conditions

Eight test conditions comprising four cooling conditions and four heating conditions were evaluated in accordance with the temperature conditions for the outdoor and indoor units provided by JIS C 9612:2013 [3] for room air conditioners. The specific temperature and load conditions are listed in Table 4.1.2-2.

Table 4.1.2-2 Test conditions

		Test condition	Indoor temperature (℃) Dry/Wet	Outdoor temperature (℃) Dry/Wet	Partial load ratio (%)
①	Cooling	Standard cooling Full-capacity test	27/19	35/24	100
②		Standard cooling Half-capacity test		35/24	50
③		Low-temperature cooling Half-capacity test		29/19	50
④		Low-temperature cooling Minimum-capacity test		29/19	25
⑤	Heating	Standard heating Full-capacity test	20/15	7/6	100
⑥		Standard heating Half-capacity test		7/6	50
⑦		Standard heating Minimum capacity test		7/6	25
⑧		Low-temperature heating Full-capacity test		2/1	100

4.1.2.5 Test results

The results of the four cooling test conditions represented by ①-④ are described below when the refrigerant charge was optimized by fixing the compressor rotation speed to achieve a capacity of 2.2 kW.

Fig. 4.1.2-3 presents a comparison of the COP values achieved when using R22, R290, and R454C; and Table 4.1.2-3 presents a comparison of the rated standard cooling test results when using R22, R290, and R454C.

Table 4.1.2-3 Comparison of rated standard cooling test results for R22, R290, and R454C

Refrigerant type	Refrigerant charge g	Compressor speed Hz	Mass flow rate Kg/h	Degree of superheating ℃	Degree of supercooling ℃
R22	910	55.0	51.0	10.26	1.72
R290	400	62.5	28.2	6.97	4.63
R454C	950	65.0	58.8	6.14	5.70

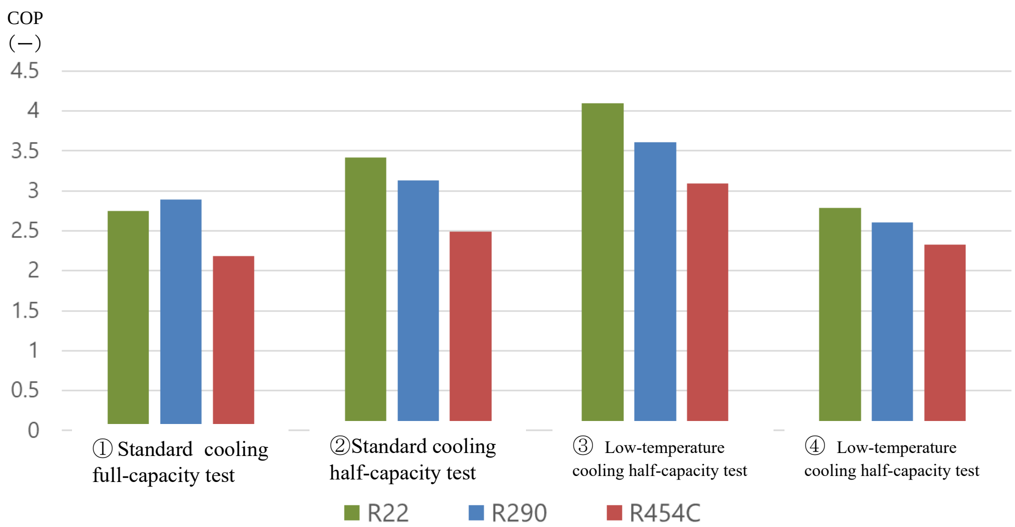

Fig. 4.1.2-3 Comparison of COP values obtained during the cooling tests (adjusted to a cooling capacity of 2.2 kW)

From a comparison of the results for R22 and R290, the COP value for R290 was slightly higher than that for R22 during the standard cooling full-capacity test, and approximately 10% lower than that for R22 during each of the other three tests. Furthermore, the COP values for R454C were consistently 10–25% lower than those for R290 during all the tests.

4.1.2.6 Considerations

First, the COP values of R22 and R290 were considered when the refrigerant charge was optimized by fixing the compressor rotation speed to achieve a capacity of 2.2 kW. In the rated standard cooling full-capacity test, the COP value for R290 was only slightly higher than that for R22 because the latent heat of vaporization for R290 was approximately twice that for R22. Therefore, the amount of circulating refrigerant was reduced when using R290, thus resulting in less pressure loss. We presumed that this decreased pressure loss compensated for the reduced efficiency of the compressor due to the increased compressor rotation speed required to achieve a capacity of 2.2 kW.

Thereafter, the use of R290 and R454C was considered based on the results of the rated standard cooling full-capacity test. The COP value for R454C under Test condition ① was approximately 25% lower than that for R290, given that R1234yf, which is a low-pressure refrigerant, accounts for 78.5% of R454C, and R454C is a low-pressure refrigerant. It was therefore necessary to increase the mass flow rate to obtain the same capacity as that for R290, as follows:

$$Q_c = G_R \Delta h_{EV} \tag{4.1.2-1}$$

As a result, the pressure loss increased when compared with R290, and the pressure difference between the inlet and outlet of the compressor increased, as indicated by the following:

$$\Delta P = f \frac{1}{2d} \rho_R {v_R}^2 \tag{4.1.2-2}$$

$$G_R = \rho_R v_R A \tag{4.1.2-3}$$

Thus, the compressor power consumption increased by approximately 200 W, and the COP for R454C decreased. Figs. 4.1.2-4 and 4.1.2-5 present the test results and *P–h* diagrams, respectively, for R22, R290, and R454C under Test condition ① (standard cooling full-capacity test).

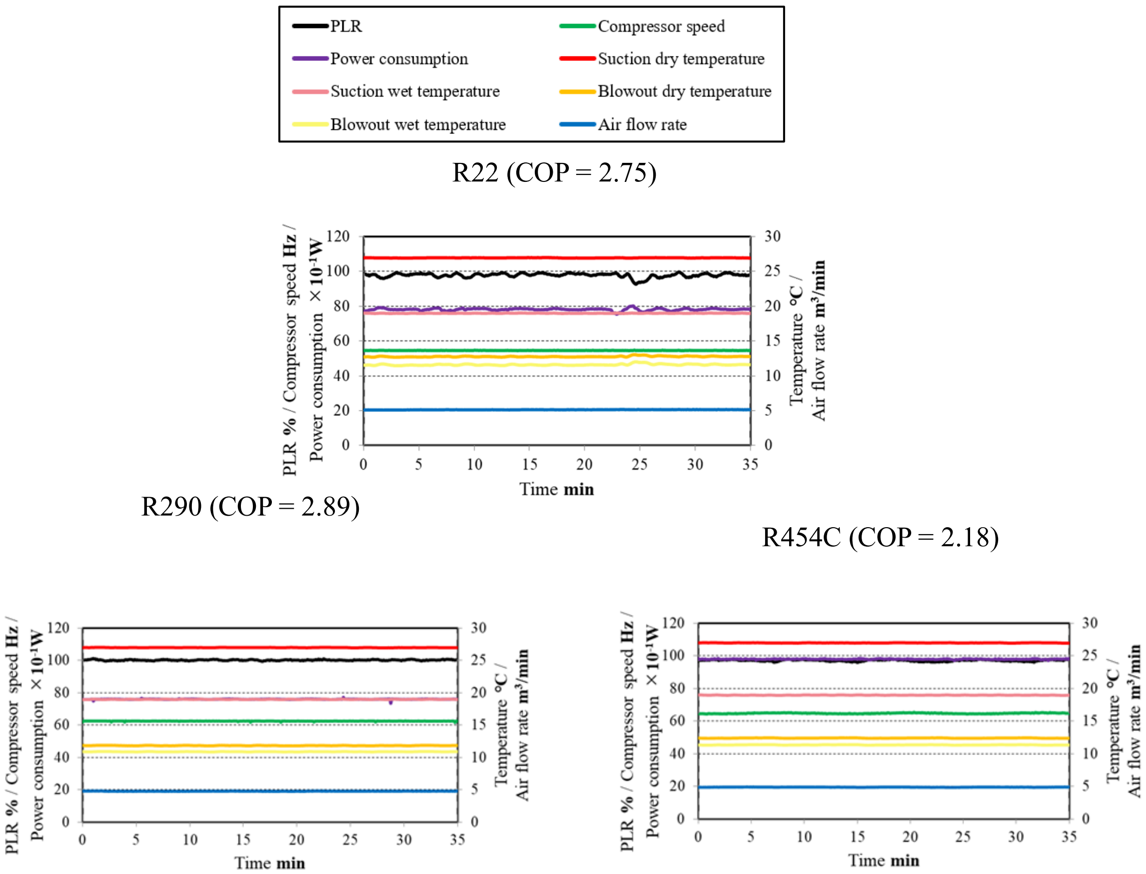

Fig. 4.1.2-4 Test results for R22, R290, and R454C under Test condition ① (standard cooling full-capacity test)

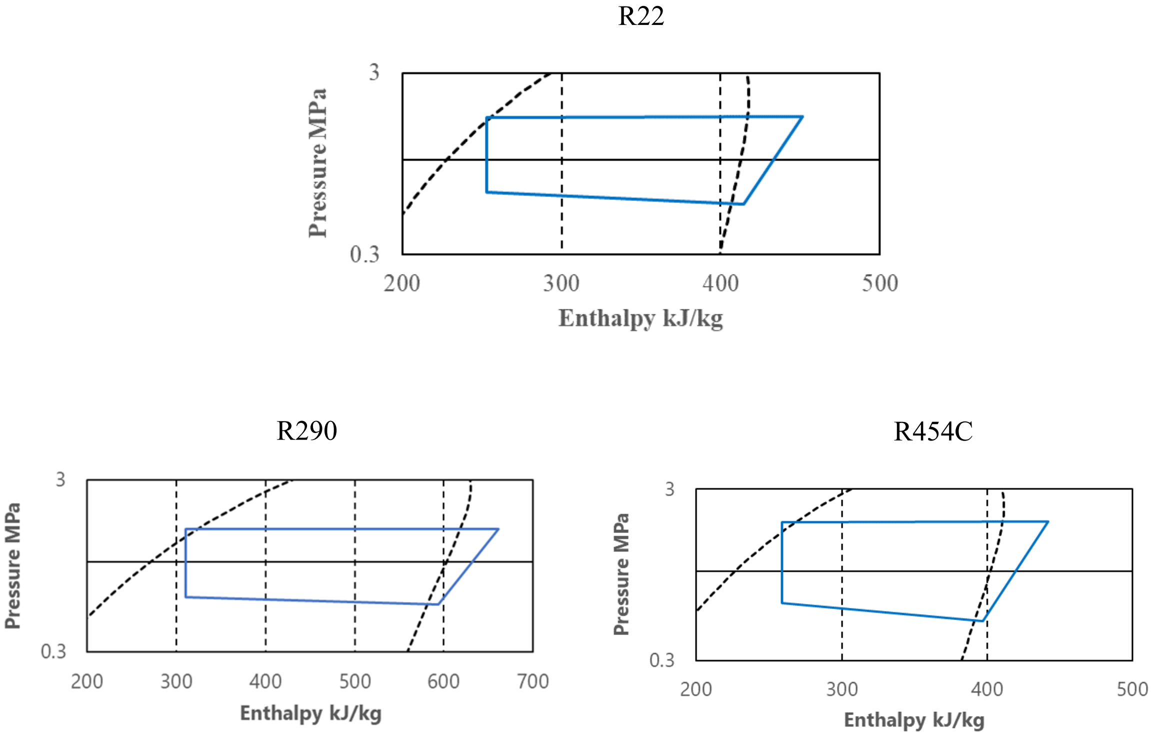

Fig. 4.1.2-5 Comparison of *P–h* diagrams for R22, R290, and R454C

4.1.2.7 Summary of experimental results using various refrigerants

In this study, the low-GWP refrigerants R290 and R454C were dropped in to a room air conditioner designed for use with the R22 refrigerant, and the resulting performances were evaluated. When the refrigerant charge was optimized by fixing the compressor rotation speed to achieve a capacity of 2.2 kW, R290 exhibited nearly the same COP as R22. However, in the partial-load region, the COP for R290 was approximately 10% lower than that for R22. Furthermore, the COP for R454C was 10–25% lower than that for R290.

As mentioned in Section 4.1.3 (Model validation), the calculated values for the developed system simulator were verified based on these experimental results.

4.1.3 Model validation

4.1.3.1 Background and objective of validation

The actual operating performance of refrigeration and air conditioning equipment is the most critical factor in system operation evaluations. As system simulators provide an effective approach for such evaluations, the effects of applying the R290 and R454C low-GWP refrigerants to air conditioners designed for use with the R22 refrigerant, as discussed in Section 4.1.2, were analyzed using the EF + M system simulator, which was developed at our university. The differences between the experimental values and simulation results were then evaluated to validate the simulator.

4.1.3.2 Simulation results for R22 refrigerant

In this section, the simulation results obtained using R22, which was the reference refrigerant, are described for Test condition ① (standard cooling full-capacity test), as presented in Section 4.1.2. The system analysis was performed by first individually simulating the evaporator and condenser. Table 4.1.3-1 lists the conditions of the evaporator unit simulation, Fig. 4.1.3-1 presents the Mollier diagram of the simulation results, Table 4.1.3-2 presents a comparison of the experiment and simulation results at the evaporator outlet, and Table 4.1.3-3 presents a comparison of the experiment and simulation results at the compressor inlet.

Table 4.1.3-1 Conditions of the evaporator simulation (R22)

Atmospheric pressure	kPa	100.9
Indoor dry-bulb temperature	℃	27.00
Indoor wet-bulb temperature	℃	19.00
Indoor absolute humidity	g/kg(DA)	10.50
Indoor fan air flow rate	kg/s	0.1037
Mass flow rate at evaporator inlet	kg/s	0.01307
Evaporator inlet pressure	kPa	693.0
Evaporator inlet enthalpy	kJ/kg	250.8

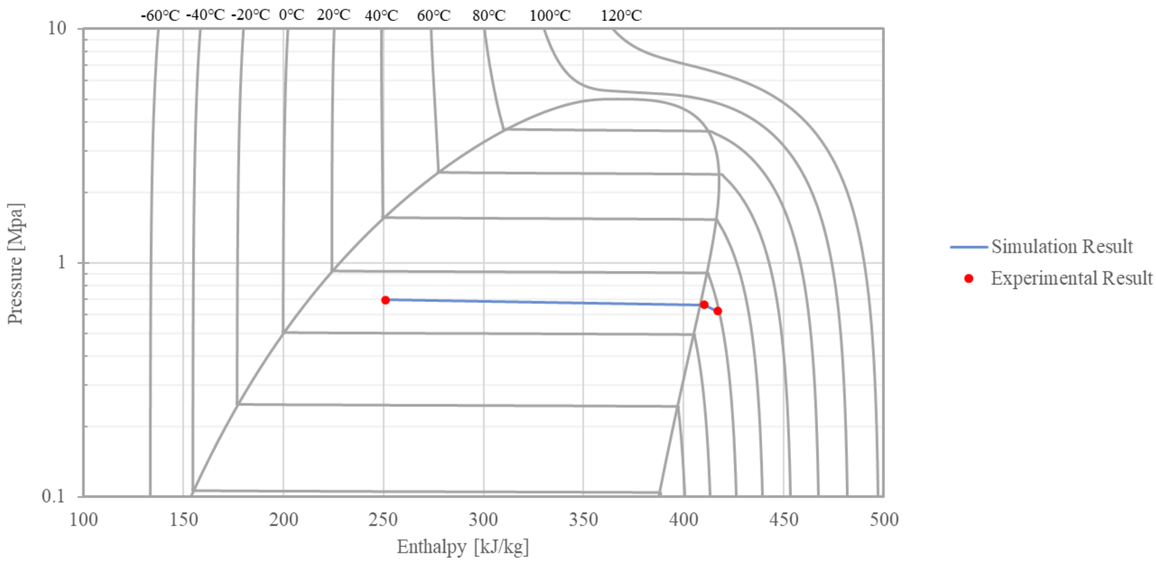

Fig. 4.1.3-1 The *P–h* diagram of the evaporator simulation results (R22)

Table 4.1.3-2 Comparison of experimental and simulation results at the evaporator outlet (R22)

Parameter	Units	Experimental result	Simulation result	Absolute error	Relative error
Pressure	kPa	660	660	-1.14×10^{-4}	-1.72×10^{-2}
Enthalpy	kJ/kg	410	410	-0.123	-0.162
Temperature	℃	11.8	11.6	-2.99×10^{-2}	-1.37

Table 4.1.3-3 Comparison of experimental and simulation results at the compressor inlet (R22)

Parameter	Units	Experimental result	Simulation result	Absolute error	Relative error
Pressure	kPa	621	620	-8.53×10^{-4}	-0.137
Enthalpy	kJ/kg]	417	417	6.98×10^{-2}	1.68×10^{-2}
Temperature	℃	19.3	19.3	7.18×10^{-2}	0.373

Table 4.1.3-4 lists the conditions of the condenser unit simulation, Fig. 4.1.3-2 presents the Mollier diagram of the simulation results, and Table 4.1.3-5 presents a comparison of the experimental and analytical results at the condenser outlet.

Table 4.1.3-4 Conditions of the condenser simulation (R22)

Atmospheric pressure	kPa	100.9
Outdoor dry-bulb temp	℃	35.00
Outdoor wet-bulb temp	℃	21.14
Outdoor absolute humidity	g/kg(DA)	10.06
Outdoor fan air flow rate of condenser 1	kg/s	0.3262
Outdoor fan air flow rate of condenser 2	kg/s	0.08156
Mass flow rate at condenser inlet	kg/s	0.01307
Condenser inlet pressure	kPa	1709
Condenser inlet enthalpy	kJ/kg	447

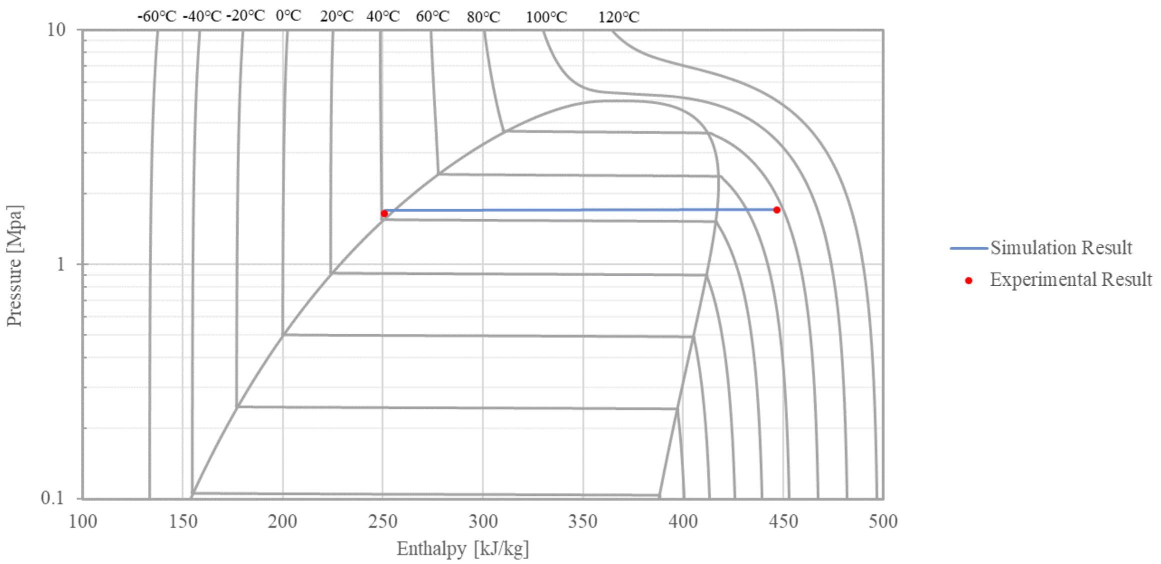

Fig. 4.1.3-2 The *P–h* diagram of the condenser simulation results (R22)

Table 4.1.3-5 Comparison of experiment and simulation results at the condenser outlet (R22)

Parameter	Units	Experimental result	Simulation result	Absolute error	Relative error
Pressure	kPa	1648	1705	56.7	3.44
Enthalpy	kJ/kg	251	252	1.25	0.497
Temperature	℃	40.9	41.8	0.939	2.30

Based on the evaporator and condenser unit simulations, Table 4.1.3-6 presents the conditions for the entire system simulation, Fig. 4.1.3-3 presents the Mollier diagram of the simulation results, and Table 4.1.3-7 presents a comparison of the experimental and simulation results.

Table 4.1.3-6 Conditions of the full system simulation (R22)

Atmospheric pressure	kPa	101.2
Indoor dry-bulb temp	℃	27.00
Indoor wet-bulb temp	℃	19.00
Indoor absolute humidity	g/kg(DA)	10.50
Indoor fan air flow rate	kg/s	0.1037
Outdoor dry-bulb temp	℃	35.00
Outdoor wet-bulb temp	℃	21.14
Outdoor absolute humidity	g/kg(DA)	10.06
Outdoor fan air flow rate of condenser 1	kg/s	0.3262
Outdoor fan air flow rate of condenser 2	kg/s	0.08156
Compressor speed	rps	48

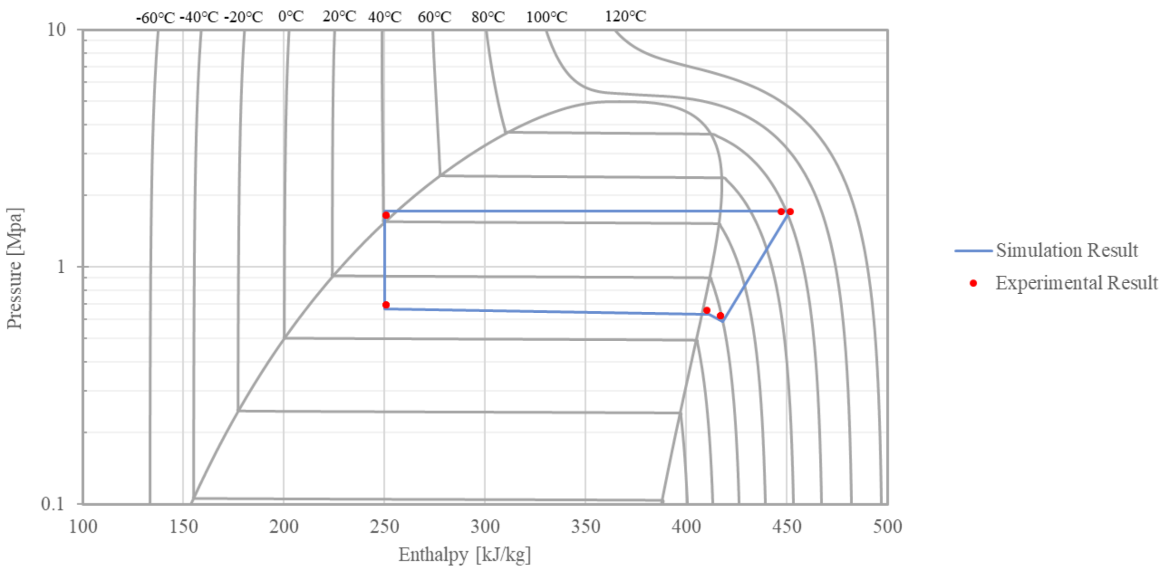

Fig. 4.1.3-3 The *P–h* diagram of the full system simulation results (R22)

Table 4.1.3-7 Comparison of full system experimental and simulation results (R22)

	Cooling capacity %	Power consumption %	Mass flow rate %	Condensing temperature ℃	Evaporating temperature ℃
Experiment	100	100	100	43.0	9.00
Simulation	99.1	99.4	101	44.7	8.4

	Compressor inlet pressure MPa	Compressor outlet pressure MPa	Compressor inlet temperature ℃	Compressor outlet temperature ℃	Degree of superheating ℃	Degree of supercooling ℃
Experiment	0.621	1.71	19.3	81.8	2.83	2.11
Simulation	0.587	1.72	19.8	82.1	2.14	4.32

	Condenser inlet pressure MPa	Condenser outlet pressure MPa	Condenser inlet temperature ℃	Condenser outlet temperature ℃
Experiment	1.71	1.65	76.6	40.9
Simulation	1.72	1.72	77.2	40.4

	Evaporator inlet pressure MPa	Evaporator outlet pressure MPa	Evaporator inlet temperature ℃	Evaporator outlet temperature ℃
Experiment	0.693	0.660	10.7	11.8
Simulation	0.667	0.629	9.31	12.3

4.1.3.3 Simulation results for R290 refrigerant drop-in

The simulation results obtained using R290 are described herein. Table 4.1.3-8 presents the conditions of the evaporator unit simulation, Fig. 4.1.3-4 presents the Mollier diagram of the simulation results, Table 4.1.3-9 presents a comparison of the experimental and simulation results at the evaporator outlet, and Table 4.1.3-10 presents a comparison of the experimental and simulation results at the compressor inlet.

Table 4.1.3-8 Conditions of the evaporator simulation (R290)

Atmospheric pressure	kPa	100.7
Indoor dry-bulb temperature	℃	27.00
Indoor wet-bulb temperature	℃	19.00
Indoor absolute humidity	g/kg(DA)	10.53
Indoor fan air flow rate	kg/s	0.09251
Mass flow rate at evaporator inlet	kg/s	0.008000
Evaporator inlet pressure	kPa	629.6
Evaporator inlet enthalpy	kJ/kg	312.0

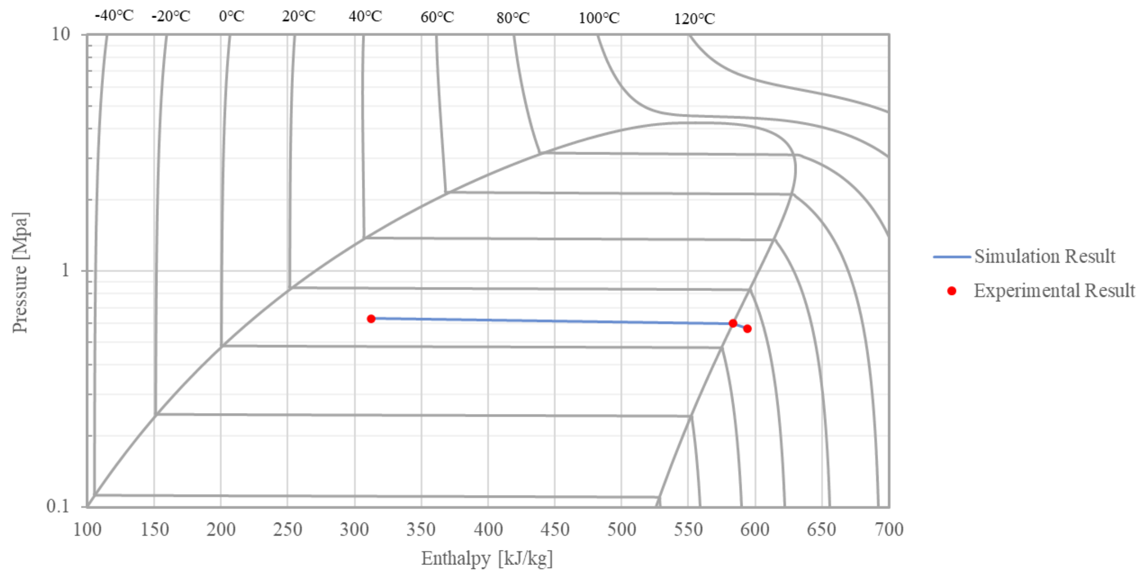

Fig. 4.1.3-4 The *P–h* diagram of the evaporator simulation results (R290)

Table 4.1.3-9 Comparison of experimental and simulation results at the evaporator outlet (R290)

Parameter	Units	Experimental result	Simulation result	Absolute error	Relative error
Pressure	kPa	599	597	-1.75×10^{-3}	-0.292
Enthalpy	kJ/kg	584	584	0.338	5.79×10^{-2}
Temperature	℃	8.00	8.10	0.0997	1.25

Table 4.1.3-10 Comparison of experimental and simulation results at the compressor inlet (R22)

Parameter	Units	Experimental result	Simulation result	Absolute error	Relative error
Pressure	kPa	569	570	1.04×10^{-3}	0.183
Enthalpy	kJ/kg	594	594	1.71×10^{-2}	2.87×10^{-3}
Temperature	℃	13.1	13.1	3.00×10^{-2}	0.229

Table 4.1.3-11 lists the simulation conditions of the condenser unit simulation, Fig. 4.1.3-5 presents the Mollier diagram of the simulation results, and Table 4.1.3-12 presents a comparison of the experimental and simulation results at the condenser outlet.

Table 4.1.3-11 Conditions of the condenser simulation (R290)

Atmospheric pressure	kPa	100.7
Outdoor dry-bulb temperature	℃	35.00
Outdoor wet-bulb temperature	℃	23.99
Outdoor absolute humidity	g/kg(DA)	14.33
Outdoor fan air flow rate of condenser 1	kg/s	0.5078
Outdoor fan air flow rate of condenser 2	kg/s	0.1270
Mass flow rate at condenser inlet	kg/s	0.008000
Condenser inlet pressure	kPa	1564
Condenser inlet enthalpy	kJ/kg	650

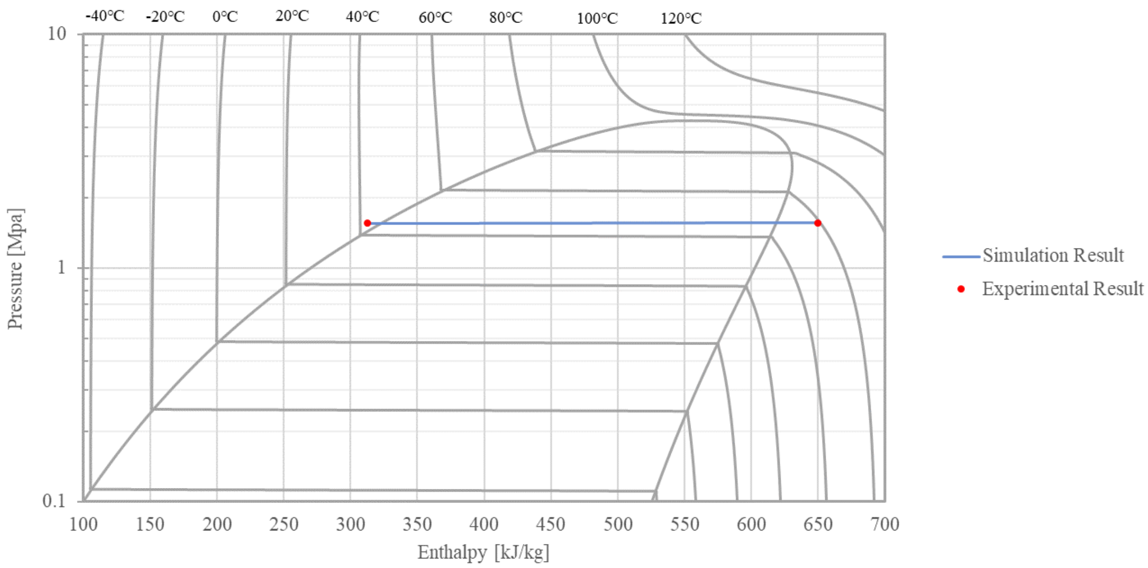

Fig.4.1.3-5 The *P–h* diagram of the condenser simulation results (R290)

Table 4.1.3-12 Comparison of experimental and simulation results at the condenser outlet (R290)

Parameter	Units	Experimental result	Simulation result	Absolute error	Relative error
Pressure	kPa	1560	1560	7.11×10^{-4}	4.56×10^{-2}
Enthalpy	kJ/kg	312	312	-0.495	-0.158
Temperature	℃	41.8	40.7	-1.13	-2.70

Finally, Table 4.1.3-13 lists the conditions for the full system simulation, Fig. 4.1.3-6 presents the Mollier diagram of the simulation results, and Table 4.1.3-14 presents a comparison of the experimental and simulation results.

Table 4.1.3-13 Conditions of the full system simulation (R290)

Atmospheric pressure	kPa	100.7
Indoor dry-bulb temperature	℃	27.00
Indoor wet-bulb temperature	℃	19.00
Indoor absolute humidity	g/kg(DA)	10.53
Indoor fan air flow rate	kg/s	0.09251
Outdoor dry-bulb temperature	℃	35.00
Outdoor wet-bulb temperature	℃	23.99
Outdoor absolute humidity	g/kg(DA)	14.33
Outdoor fan air flow rate of Condenser 1	kg/s	0.5078
Outdoor fan air flow rate of Condenser 2	kg/s	0.1270
Compressor speed	rps	62.37

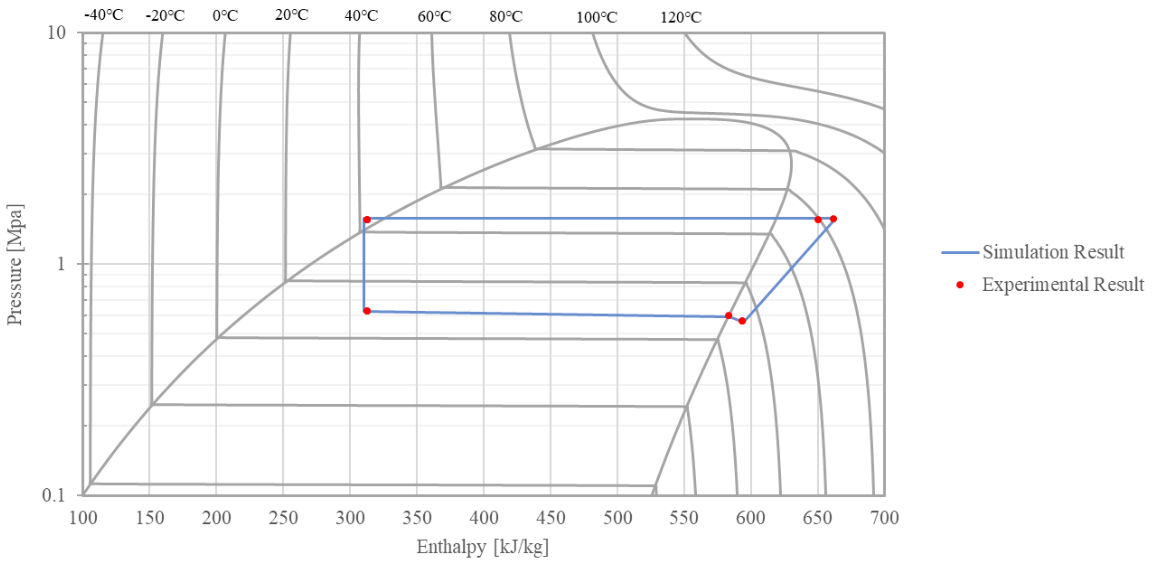

Fig. 4.1.3-6 The *P–h* diagram of the full system simulation results (R290)

Table 4.1.3-14 Comparison of full system experimental and simulation results (R290)

	Cooling capacity %	Power consumption %	Mass flow rate %	Condensing temperature ℃	Evaporating temperature ℃
Experiment	100	100	100	46.0	6.20
Simulation	101	96.5	101	46.2	8.32

	Compressor inlet pressure MPa	Compressor outlet pressure MPa	Compressor inlet temperature ℃	Compressor outlet temperature ℃	Degree of superheating ℃	Degree of supercooling ℃
Experiment	0.570	1.57	12.8	64.5	0.10	2.11
Simulation	0.564	1.58	13.2	65.5	0.82	5.00

	Condenser inlet pressure MPa	Condenser outlet pressure MPa	Condenser inlet temperature ℃	Condenser outlet temperature ℃
Experiment	1.56	1.56	59.5	41.8
Simulation	1.58	1.58	63.4	41.2

	Evaporator inlet pressure MPa	Evaporator outlet pressure MPa	Evaporator inlet temperature ℃	Evaporator outlet temperature ℃
Experiment	0.630	0.601	9.40	7.96
Simulation	0.623	0.592	9.26	8.24

4.1.3.4 Simulation results for R454C refrigerant drop-in

The simulation results obtained using R454C are presented herein. Table 4.1.3-15 lists the conditions of the evaporator unit simulation, Fig. 4.1.3-7 presents the Mollier diagram of the simulation results, Table 4.1.3-16 presents a comparison of the experimental and simulation results at the evaporator outlet, and Table 4.1.3-17 presents a comparison of the experimental and simulation results at the compressor inlet.

Table 4.1.3-15 Conditions of the evaporator simulation (R454C)

Atmospheric pressure	kPa	101.2
Indoor dry-bulb temperature	℃	27.00
Indoor wet-bulb Temperature	℃	19.00
Indoor absolute humidity	g/kg(DA)	10.46
Indoor fan air flow rate	kg/s	0.1040
Mass flow rate at evaporator inlet	kg/s	0.01630
Evaporator inlet pressure	kPa	649.8
Evaporator inlet enthalpy	kJ/kg	258.8

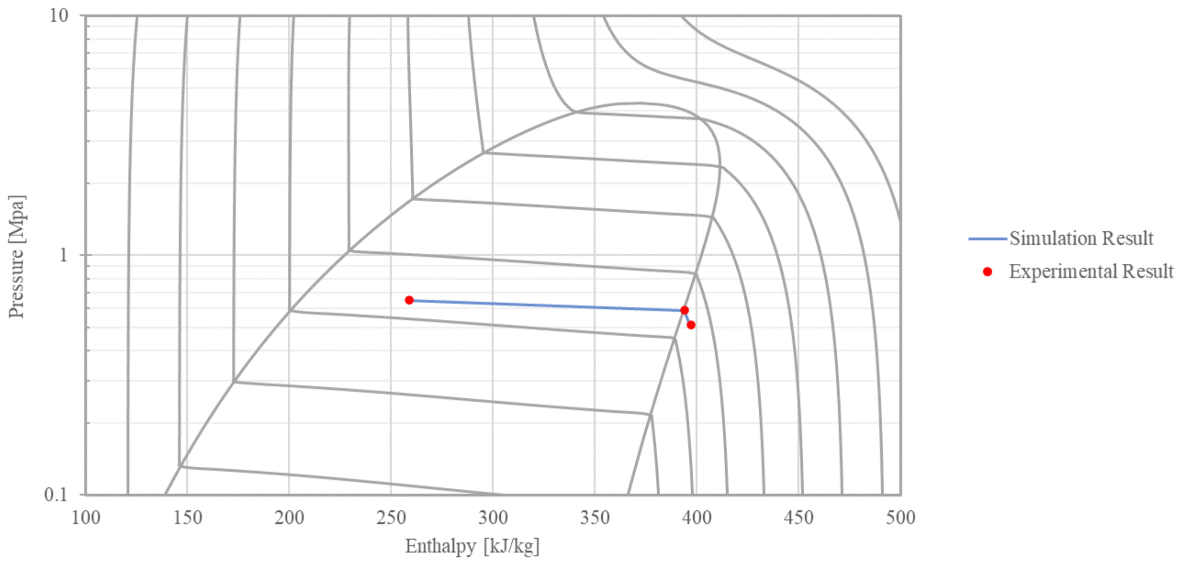

Fig. 4.1.3-7 The *P–h* diagram of the evaporator simulation results (R454C)

Table 4.1.3-16 Comparison of experimental and simulation results at the evaporator outlet (R454C)

Parameter	Units	Experimental result	Simulation result	Absolute error	Relative error
Pressure	kPa	588	590	2.00×10^{-3}	-0.340
Enthalpy	kJ/kg	394	394	-0.125	-3.18×10^{-2}
Temperature	℃	8.40	8.32	-7.21×10^{-2}	-0.858

Table 4.1.3-17 Comparison of experimental and simulation results at the compressor inlet (R454C)

Parameter	Units	Experimental result	Simulation result	Absolute error	Relative error
Pressure	kPa	510	516	5.92×10^{-3}	1.16
Enthalpy	kJ/kg	397	397	-0.502	-0.126
Temperature	℃	9.58	9.21	-0.394	-3.80

Table 4.1.3-18 lists the conditions of the condenser unit simulation, Fig. 4.1.3-8 presents the simulation results in a Mollier diagram, and Table 4.1.3-19 presents a comparison of the experimental and simulation results at the condenser outlet.

Table 4.1.3-18 Conditions of the condenser simulation (R454C)

Atmospheric pressure	kPa	101.2
Outdoor dry-bulb temperature	℃	35.00
Outdoor wet-bulb temperature	℃	25.36
Outdoor absolute humidity	g/kg(DA)	16.46
Outdoor fan air flow rate of Condenser 1	kg/s	0.3239
Outdoor fan air flow rate of Condenser 2	kg/s	0.08098
Mass flow rate at condenser inlet	kg/s	0.01630
Condenser inlet pressure	kPa	1928
Condenser inlet enthalpy	kJ/kg	434.1

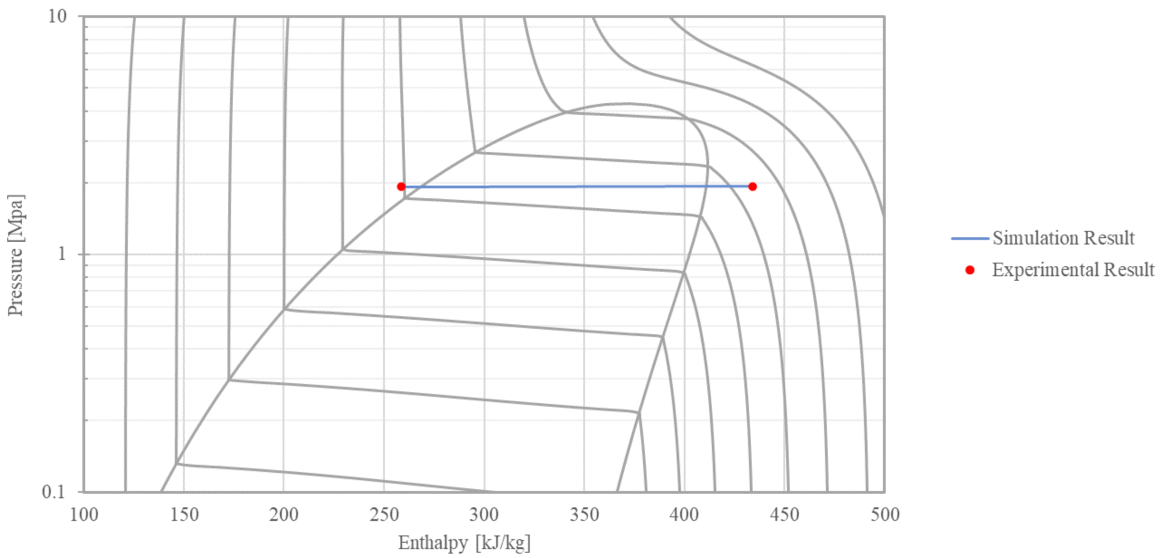

Fig. 4.1.3-8 The *P–h* diagram of the condenser simulation results (R454C)

Table 4.1.3-19 Comparison of the experimental and simulation results at the condenser outlet (R454C)

Parameter	Units	Experimental result	Simulation result	Absolute error	Relative error
Pressure	kPa	1922	1924	1.87×10^{-3}	9.75×10^{-2}
Enthalpy	kJ/kg	259	258	-0.299	-0.115
Temperature	℃	39.1	38.9	-0.181	-0.464

Finally, Table 4.1.3-20 lists the conditions of the full system simulation, Fig. 4.1.3-9 presents the simulation results in a Mollier diagram, and Table 4.1.3-21 presents a comparison of the experimental and simulation results.

Table 4.1.3-20 Conditions of the full system simulation (R454C)

Atmospheric pressure	kPa	101.2
Indoor dry-bulb temperature	℃	27.00
Indoor wet-bulb temperature	℃	19.00
Indoor absolute humidity	g/kg(DA)	10.46
Indoor fan air flow rate	kg/s	0.1040
Outdoor dry-bulb temperature	℃	35.00
Outdoor wet-bulb temperature	℃	25.36
Outdoor absolute humidity	g/kg(DA)	16.46
Outdoor fan air flow rate of condenser 1	kg/s	0.3239
Outdoor fan air flow rate of condenser 2	kg/s	0.08098
Compressor speed	rps	65

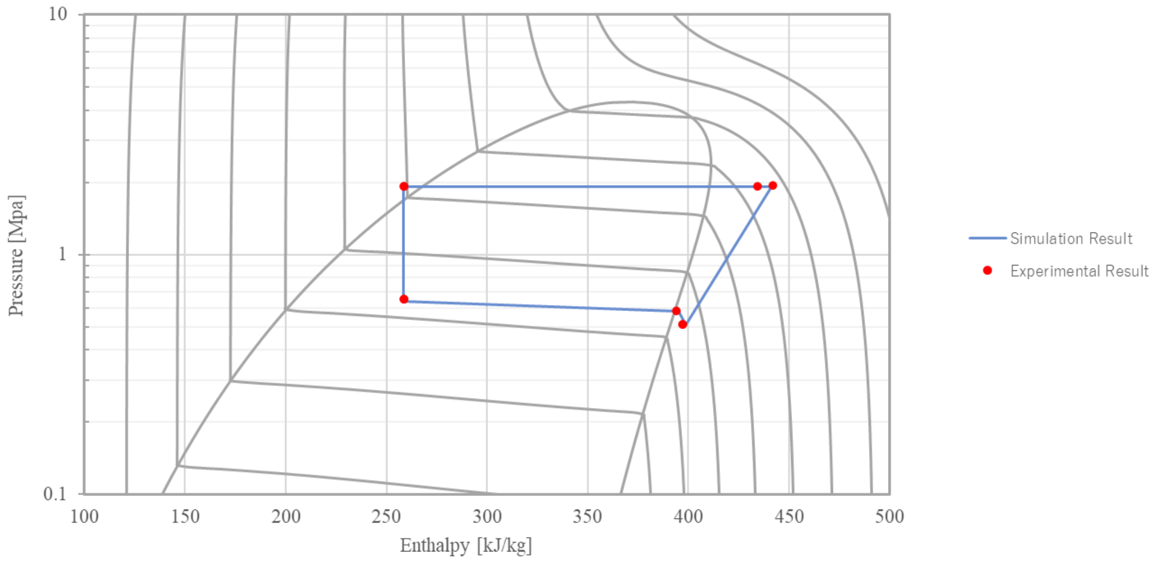

Fig. 4.1.3-9 The *P–h* diagram of the full system simulation results (R454C)

Table 4.1.3-21 Comparison of the full system experimental and simulation results (R454C)

	Cooling capacity %	Power consumption %	Mass flow rate %	Condensing temperature ℃	Evaporating temperature ℃
Experiment	100	100	100	48.0	6.90
Simulation	101	104	96.9	45.0	8.14

	Compressor inlet pressure MPa	Compressor outlet pressure MPa	Compressor inlet temperature ℃	Compressor outlet temperature ℃	Degree of superheating ℃	Degree of supercooling ℃
Experiment	0.510	1.94	9.58	75.0	0.449	5.63
Simulation	0.508	1.92	11.0	74.3	1.94	5.71

	Condenser inlet pressure MPa	Condenser outlet pressure MPa	Condenser inlet temperature ℃	Condenser outlet temperature ℃
Experiment	1.93	1.92	68.7	39.1
Simulation	1.92	1.91	71.8	38.8

	Evaporator inlet pressure	Evaporator outlet pressure	Evaporator inlet temperature	Evaporator outlet temperature
	MPa	MPa	℃	℃
Experiment	0.650	0.581	6.11	8.40
Simulation	0.638	0.580	4.83	9.43

4.1.3.5 Summary of model validation

A system simulator was applied to reproduce the results of a test in which a room air conditioner designed for use with the standard R22 refrigerant was charged with R22, R290, or R454C, the latter two of which are low-GWP refrigerants. Comparisons of the experimental values and simulation results confirmed an acceptable simulation accuracy.

4.2 Simulator development

4.2.1 Heat exchanger simulator development

Heat exchangers are a major component of vapor compression systems, especially with respect to next-generation refrigerants. Non-azeotropic refrigerant mixtures exhibit a significant temperature glide, which should be accounted for when designing the structure of the heat exchanger. Accordingly, the unsuitability of refrigerant performance evaluation by direct refrigerant drop-in in heat exchangers designed for pure or azeotropic refrigerants has been widely recognized. Therefore, a heat exchanger simulator that allows for the optimization of the heat exchanger structure for next-generation refrigerants was developed, thus allowing for a fair comparison between different refrigerants. The user can readily simulate the entire heat exchanger by defining the refrigerant path within the heat exchanger using the graphical user interface (GUI), as shown in Fig. 3-1.1. Moreover, the refrigerant circuitry can be optimized using AI, which is particularly important for refrigerant mixtures with temperature glide.

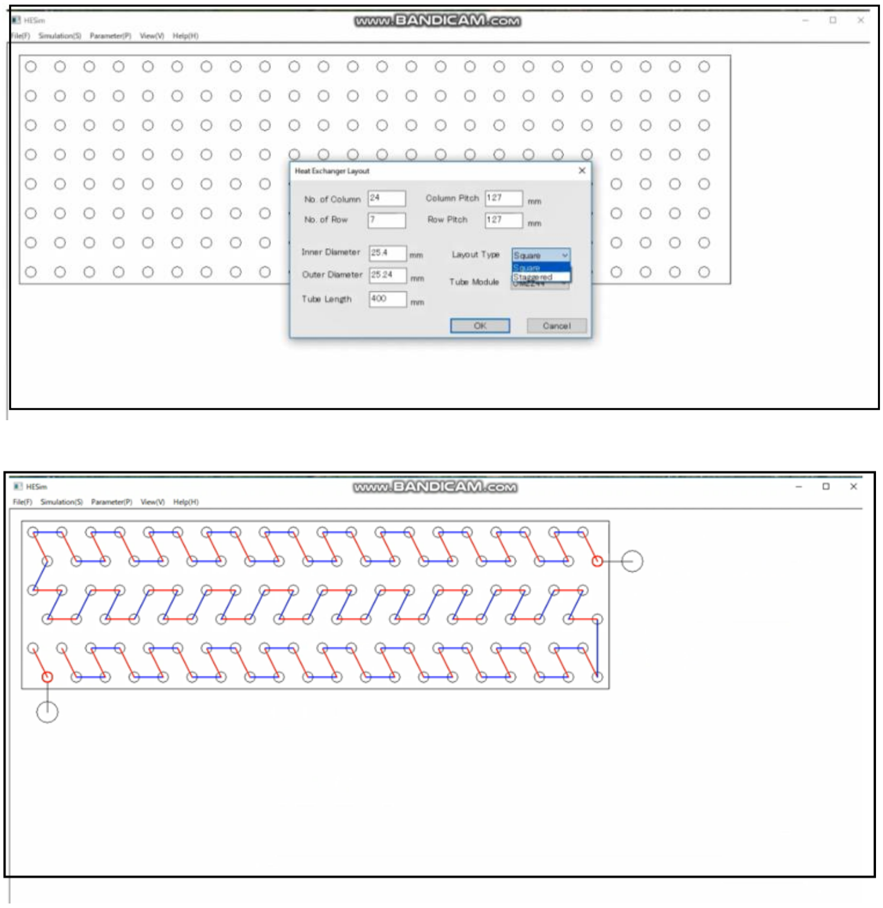

Fig.4.2.1-1 Heat exchanger simulator GUI

This supports the analysis of heat exchangers. Particularly for non-azeotropic mixed refrigerants such as R454C, the path of the refrigerant has a significant influence on the performance of the heat exchanger, and in turn, on the total system performance. Therefore, the refrigerant circuitry within heat exchangers should be comprehensively investigated and optimized for an effective refrigerant evaluation.

4.2.2 Development of the system simulator

With the development of various next-generation refrigerants, it is impractical to experimentally verify their performances as systems. Therefore, simulations have attracted increasing attention. The Waseda University group developed Energy flow + M, which is a general-purpose energy system analysis simulator. This code was recognized as a standard code by the Japan Refrigeration and Air Conditioning Industry Association (JRAIA) and used to evaluate various refrigerant types. However, the Refrigerant Evaluation Working Group established within the Japan Refrigeration and Air Conditioning Industry Association (JRAIA), which promoted the use of this code, suggested multiple modifications to the GUI and calculation method due to the sub-par usability of the simulator. Below are several examples of the major problems:

・The GUI for the heat exchanger section is excessively complex, and significant time is required to set up heat transfer tube connections.

・When the system is complex (e.g., a VRF system), the calculation is slow and generally fails to converge.

・For control tasks, non-stationary calculations are performed although the system is at steady-state, thus requiring a significant computational time.

Researchers and students using the simulator shared the following opinions:

・The simulator is based on Excel; therefore, there is a limit to the number of modules that can be added.

・The code is not appropriately structured; thus, the internal functions interact in a complex manner. This necessitates the re-definition of variables in the code whenever a module is changed. Hence, researchers and students cannot add new modules.

・When analyzing next-generation mixed refrigerants, the internal state of the local refrigerant mixture cannot be accurately calculated. Therefore, average values are used.

In response to these issues that require solutions, the following developments are currently in progress within this project. The theory of system analysis is subject to issues that require solutions, which are addressed in this study. This is described in the section on establishing the systems analysis theory. In addition to the abovementioned modifications, the following fundamental and novel improvements were made in this study:

・In the calculation core, the system analysis, module analysis, convergence calculation, refrigerant properties, and other sections were independent and structured; thus, the code could be readily modified and added to.

・The GUI exhibited a complete tree structure. A new GUI was constructed for the heat exchanger to significantly reduce the time required to input the system flow.

・A new convergence calculation method was used to accelerate the process.

・Refrigerant property information based on the latest REFPROP is the input; accordingly, the refrigerant was mapped to improve the accuracy and speed of the system.

Fig.4.2.2-1 presents the overall structure of the newly constructed code.

Fig.4.2.2-2 presents the GUI structure of the new code.

Fig.4.2.2-3 presents the structure of the computational core. Each function is structured to ensure independence, thus allowing for the modules or entire system to be readily modified. The actual computation part is in accordance with the newly constructed module analysis theory; thus, it is simple to create modules for new devices and readily adaptable to device modifications and changes. In addition, it is highly scalable; thus, it can completely reproduce the data acquired by the evaluation device by performing coupled calculations with the air-conditioning load currently in development for the evaluation device.

Fig.4.2.2-4 presents the module structure. Within the module, the numerical analysis of devices such as heat exchangers is performed. The class structure is described in a simple manner.

Fig.4.2.2-5 presents the connection flow of the modules throughout the system. The icons representing the modules are structured. The calculation results are presented in a P–h diagram, thus facilitating their visual interpretation.

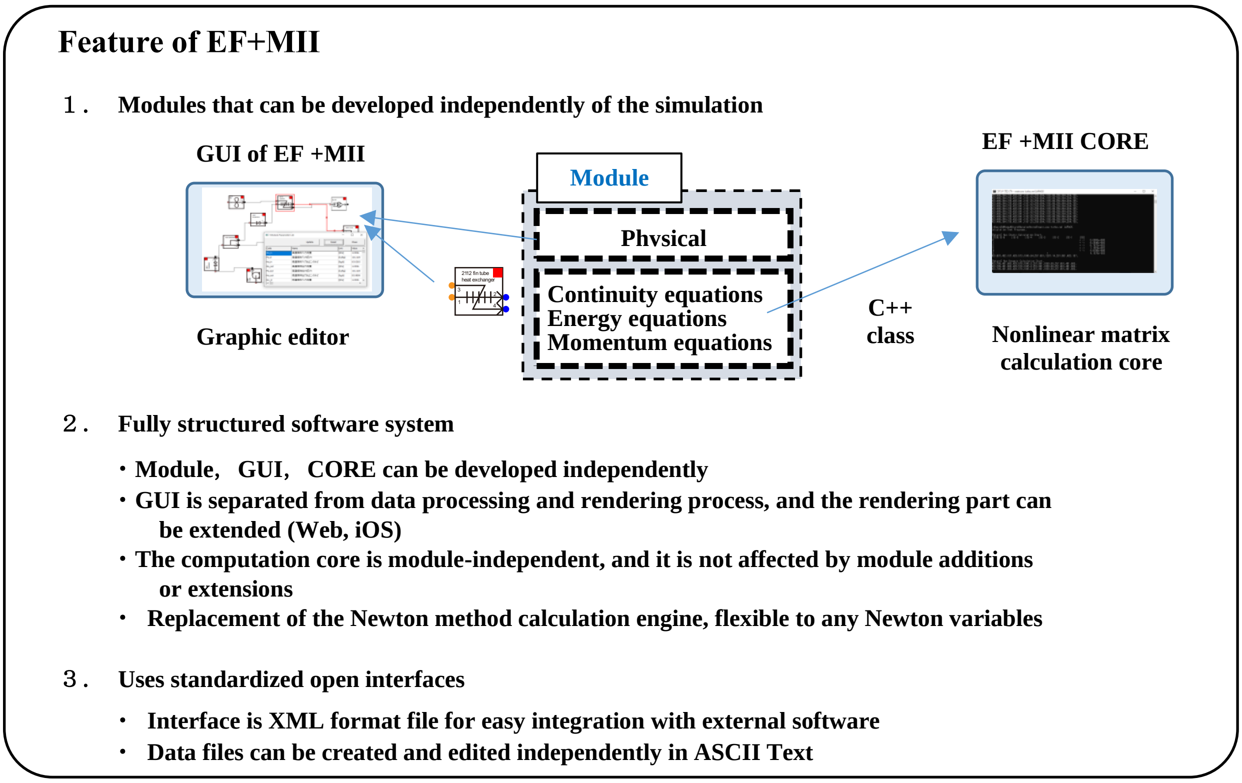

Fig. 4.2.2-1 Overall configuration

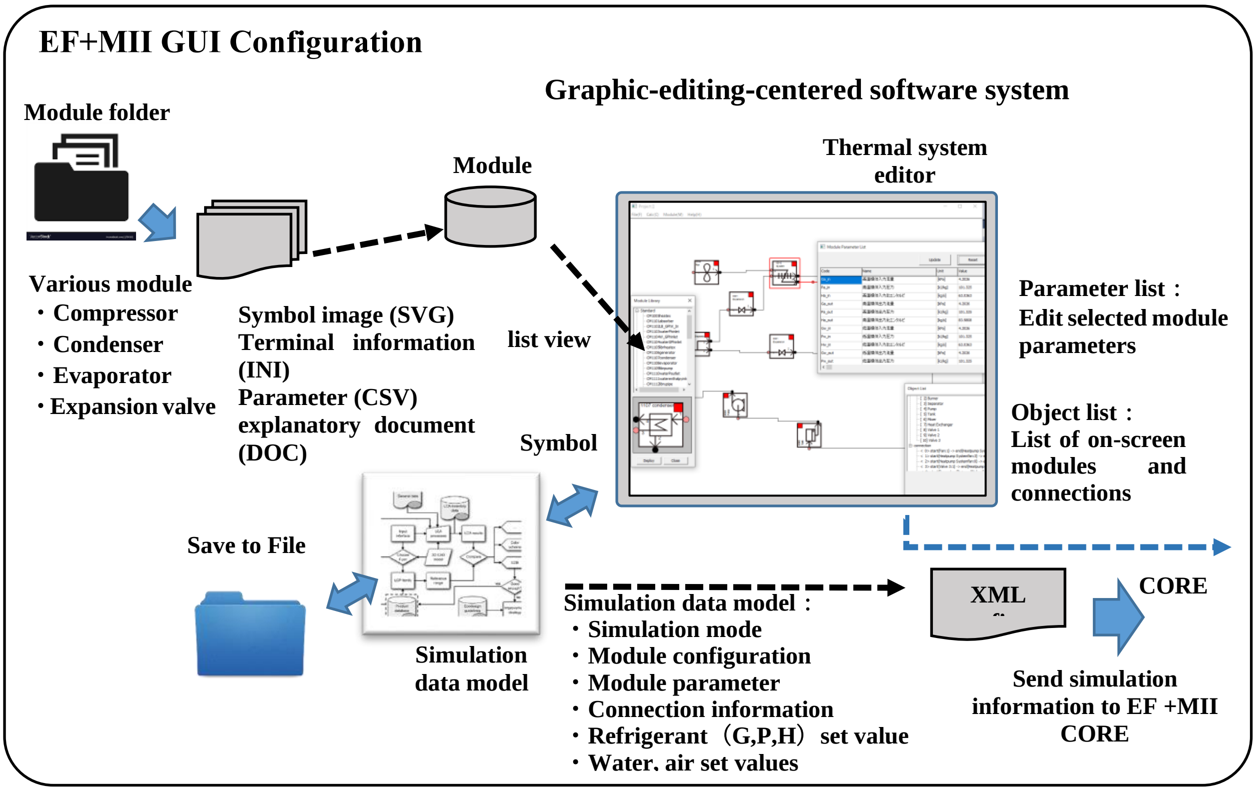

Fig. 4.2.2-2 EF + MII GUI structure

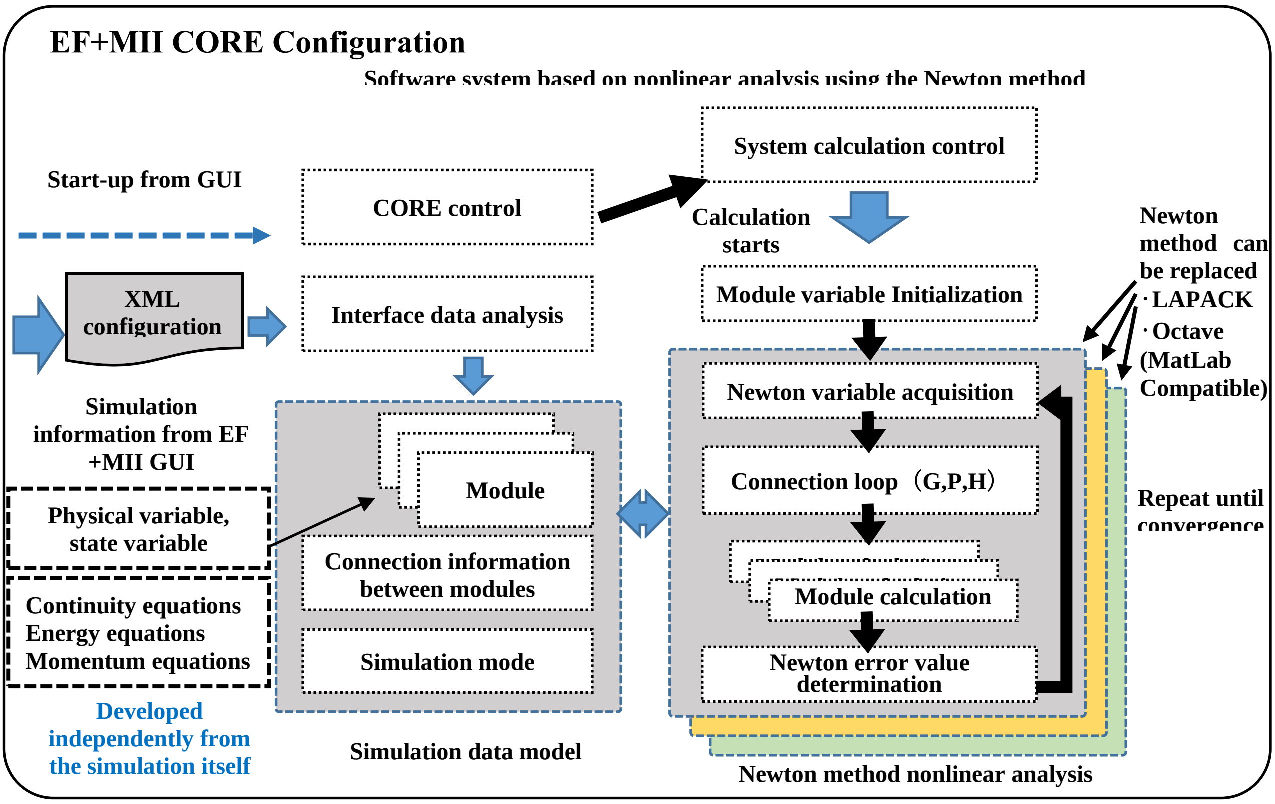

Fig.4.2.2-3 Calculation core structure of EF + MII

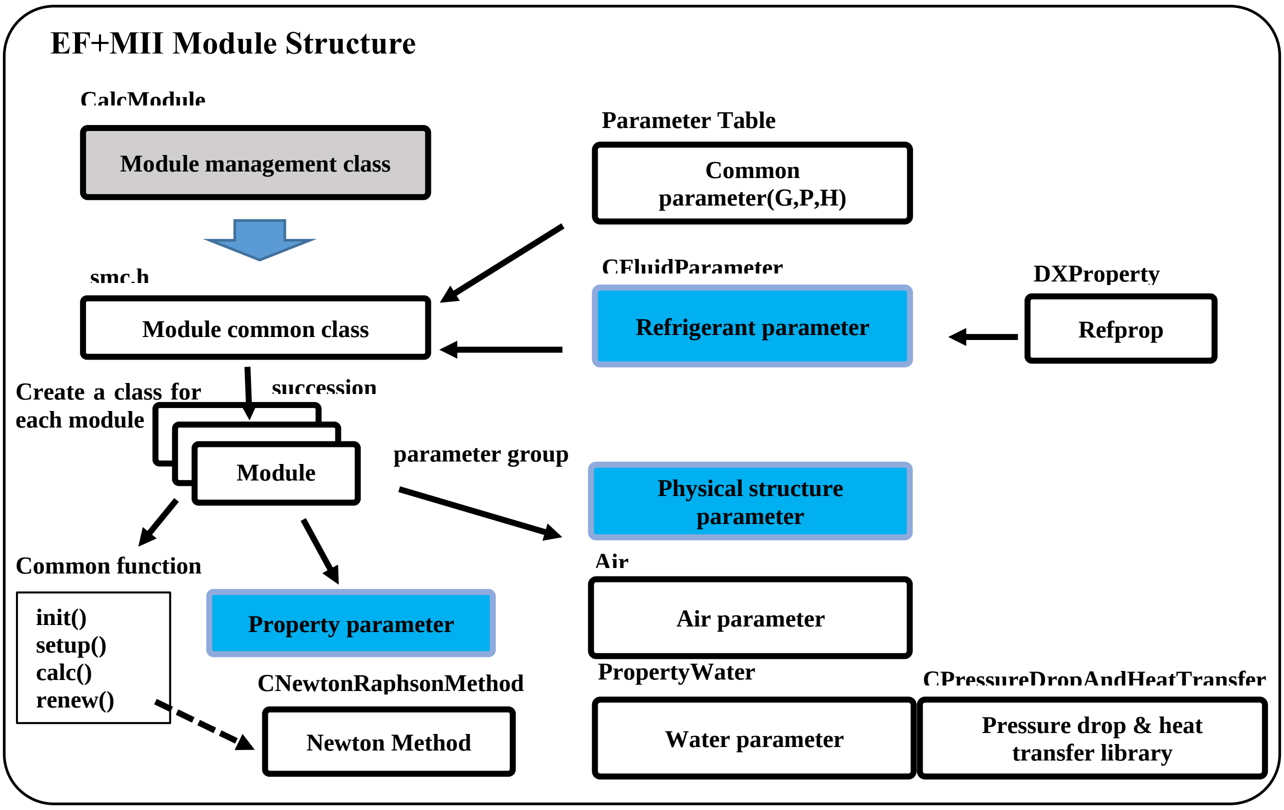

Fig. 4.2.2-4 Module structure of EF + MII

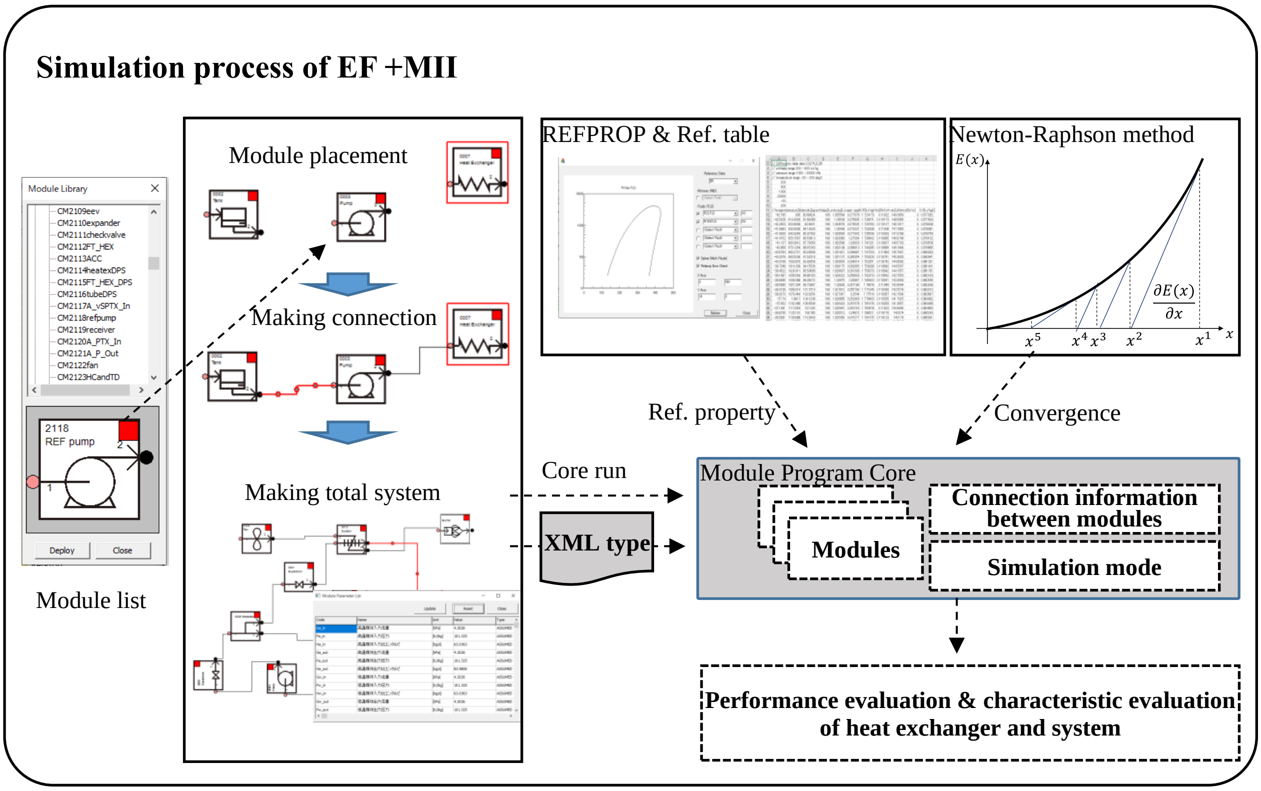

Fig. 4.2.2-5　Simulation process conducted using EF + MII GUI

4.2.3 Development of LCCP simulator

4.2.3.1 Background of LCCP simulator development

The transition to next-generation low-GWP refrigerants is considered necessary to mitigate global warming. However, using the GWP of a refrigerant to evaluate the global warming effect of a heat pump system is not comprehensive, as it does not account for the effects of energy consumption. Therefore, the LCCP, which is an evaluation method that considers direct emissions due to refrigerant leakage and indirect emissions due to energy consumption, has attracted considerable attention. In particular, a time-series LCCP equation was proposed and used to evaluate the global warming effect of air conditioners and heat pump water heaters with increased accuracy. However, the degrees of importance of the various factors and parameters in the LCCP equation require clarification, and should be determined based on parametric studies.

The LCCP was first proposed in the 1990s as a method for assessing impacts on global warming[1)], and in 2018, Stephen et al., as summarized by Andersen[2)], explained that the LCCP evaluation of air conditioning systems comprises two aspects: the global warming impact of refrigerants (direct impact) and the global warming impact of energy consumption (indirect impact). Several parameters such as the annual refrigerant leakage rate and service life of the target equipment are therefore required to conduct the LCCP calculation. However, few studies were conducted on the impact of switching to low-GWP refrigerants on the LCCP, and when the LCCP results were obtained considering multiple parameters, the impact of each on the results was not clarified.

4.2.3.2 Definition of the LCCP

The LCCP equations published in the LCCP V1. 2 guidelines were used in multiple recent studies, and are defined as follows:

$$LCCP = Direct\ Emissions + Indirect\ Emissions \tag{4.2.3-1}$$

$$Direct\ Emissions = C \cdot (L \cdot ALR + EOL) \cdot (GWP + Adp.GWP) \tag{4.2.3-2}$$

$$\begin{aligned} Indirect\ Emissions = {} & L \cdot AEC \cdot EM + \Sigma(m \cdot MM) + \Sigma(mr \cdot RM) + C \cdot (1 + ALR) \cdot RFM \\ & + C \cdot (1 - EOL) \cdot RFD \end{aligned} \tag{4.2.3-3}$$

As expressed by Equation 4.2.3-2, direct emissions are calculated using the leakage rate, GWP, and mass charge. The leakage rate is calculated by summing the recycling leakage rate and the product of the annual leakage rate and lifespan. The GWP of different refrigerants can be obtained from various sources. Equation 4.2.3-3 indicates that indirect emissions originate from five sources: electricity consumption, material manufacturing, material recycling, refrigerant manufacturing, and refrigerant recycling. Emissions due to electricity consumption are calculated from the product life span, annual electricity consumption, and CO_2 emission factor. Emissions due to the manufacturing and recycling of the subject product are calculated from the weight of the product and that of the recycled material. The same method is used to calculate emissions from the manufacturing and recycling of refrigerants.

Previous research revealed that in most cases, emissions due to electricity consumption represent the dominant factor in the LCCP of heat pumps, whereas the manufacturing and recycling of the subject products and refrigerants only contribute slightly to the LCCP.

Fig. 4.2.3-1 presents an example of the display screen of the calculation results obtained using the LCCP V1.2 simulator, which calculates the LCCP of a system from input parameters, and determines the annual power consumption from the results calculated using the system simulator described in Section 4.2.2.

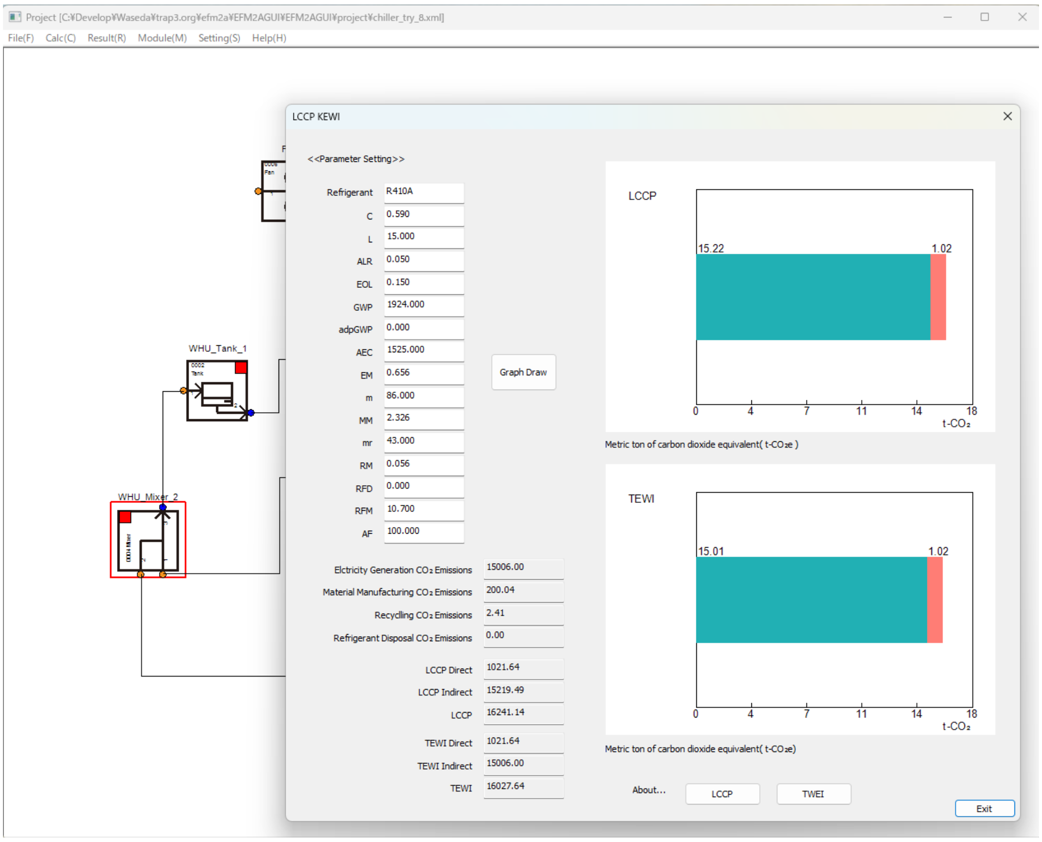

Fig. 4.2.3-1 Calculation result display screen of the LCCP V1.2 simulator

4.3 Analysis of system characteristics

4.3.1 Heat exchanger optimization

4.3.1.1 Overview

This section presents an assessment technique based on the evolutionary optimization of heat exchanger circuitry for the performance evaluation of next-generation refrigerants. To this end, a finned-tube heat exchanger simulator was designed around a bijective mathematical representation of the refrigerant circuitry (tube–tube adjacency matrix) and a formulation of the related constraints, to ensure the coherence and feasibility of the circuitry during the evolutionary search. The "genetic thermal path generator," which is a novel evolutionary algorithm for refrigerant circuitry optimization, is presented. This novel technique can handle the implementation of genetic operators in complex circuitries with unrestrained numbers and locations of splitting and merging nodes, thereby expanding the search space when compared with previous optimization studies. The performances of three representative refrigerants in air conditioning applications, namely, R32, R410A, and R454C, were assessed for the optimized circuitries of a 36-tube evaporator. Larger coefficients of performance improvements (up to 7.26%) were achieved for zeotropic refrigerant mixtures such as R454C, where the appropriate matching of the temperature glide with the temperature variation of the air allowed for a further decrease in the required compression ratio under the corresponding operating conditions. Therefore, as demonstrated, low-global-warming-potential zeotropic mixtures with temperature glide may achieve higher performances than R410A, and comparable performances to R32; whereas, previous drop-in performance analyses yielded opposite conclusions.

Along the path toward carbon neutrality and sustainable development, energy conversion is undergoing a technological revolution with the objective of realizing affordable and clean energy, inclusive and sustainable industrialization and innovation, and immediate action to combat climate change [1]. Within this context, heating, ventilation, air-conditioning, and refrigeration systems are widely installed and extensively operated. Therefore, they have a significant impact on the environment, both directly and indirectly. Accordingly, researchers are focused on mitigating the harmful effects of such systems by improving system efficiency and investigating environmentally friendly working fluid alternatives. The criteria for characterizing these substances, which are contextually referred to as refrigerants, include the GWP, ozone-depleting potential, safety, thermodynamic properties, performance, and cost. Overall, there is no "perfect" refrigerant, and the selection of the most suitable substance differs for each target application. However, increasingly strict requirements promote the development of various low-impact refrigerant mixtures, which have increased the degrees of freedom in the spectrum of available refrigerants, and may provide more appropriate alternatives to conventional substances. Nonetheless, new alternatives such as zeotropic mixtures introduce distinct characteristics and complexities that should be considered when evaluating their performances and considering different component design features. Jakobs and Kruse 1979 [2] demonstrated a substantial energy-saving potential for a zeotropic blend with temperature glide, under the assumption that a corresponding Lorenz cycle may be realized. Kruse (1981) [3] observed energy savings of 5–10% by adjusting the refrigerant blend composition to approach an optimal match between the temperature profile in the evaporator and condenser. This was realized by reducing the mean temperature difference between the refrigerant and external fluid. However, the achievement of these thermodynamic advantages in practice with specific design methodologies has not been demonstrated.

It is common knowledge that analyses based on thermophysical properties or drop-in tests[4] do not provide unbiased perspectives for capturing the actual potential of different refrigerants. System design and operation should be tailored to each specific working fluid. As a result, the effective implementation of these low-GWP refrigerants is closely related to the development of advanced performance assessment techniques that account for the transport performances of these working fluids when interfacing with specific component designs.

Heat exchangers represent the interface of a system with external heat sources and sinks. Heat exchangers are commonly the largest components in vapor compression air conditioners and undergo complex multiphase transport phenomena, which influence the overall system capacity and efficiency. Typically, the refrigerant-side transfer surface interfaces with a phase-changing fluid passing across a wide vapor quality range and different flow regimes with different transfer properties, whereas the external-side transfer surface exchanges heat with an air stream with nearly constant transport properties. The different transfer characteristics between the internal and external fluids result in strong local variations in the relative magnitudes of the internal and external thermal resistances, and are accompanied by large variations in the corresponding temperature difference. These occurrences represent a challenge to the optimal design of this critical component, which is highly sensitive to specific application cases and the properties of different refrigerants.

Various studies were conducted to maximize the air-side transfer performance of condensers and evaporators by compensating for the low air-side heat transfer coefficient [5–11]. However, research and development on the optimal structural design of the air-side transfer surface plateaued owing to conflicting limitations related to pressure drops and the number of geometry-related design variables [8].

Other studies indicated that different features of the refrigerant-side transfer surface may further reduce the corresponding thermal resistance [12–13] and non-investigated benefits to the overall system performance. In particular, owing to the large variability of the heat transfer coefficient in a phase-changing refrigerant stream, enhancing the performance of condensers and evaporators by local action may be an effective method to achieve an equilibrium between thermal resistances and a temperature difference with the airstream that minimizes heat transfer thermodynamic inefficiencies, while controlling local refrigerant-side pressure losses. As demonstrated in previous studies [14–15], refrigerant circuitry optimization, including the splitting and merging of parallel branches, can be used to effectively control the local arrangement of the air-to-refrigerant temperature difference, thermal resistance ratio, and refrigerant-side pressure drops of evaporators and condensers, among other fluidic networks. However, condensers and evaporators typically consist of a large number of tubes arranged in a bundle with innumerable combinations of refrigerant flow paths. Moreover, the transfer performance of each circuitry is directly related to the refrigerant properties and operation requirements of each application case. This renders the search space for optimal circuitries unmanageable from an experimental trial-and-error perspective, especially when different refrigerant varieties are targeted, given that the characteristics of optimal circuitries are dependent on the thermophysical and transport properties of each refrigerant. Additionally, generally accepted analytical methods for the design of refrigerant circuitry are not available [16)]. Therefore, different research groups approached this problem by relying on evolutionary search methods, which are effective at managing complex optimization problems over large search spaces.

The effects of circuitry branching on heat transfer and fluid flow characteristics were investigated by Liang et al. [17)], although the numerical and experimental studies were limited to refrigerant circuitries with two branches. Domanski [18–19)] developed a public-domain software package for the simulation of finned-tube evaporators and condensers. The model [20)] uses a tube-by-tube approach to handle typical complex circuitry arrangements. Lee et al. [21)] further developed this model by considering a two-dimensional airflow distribution. Liang et al. [22)] evaluated the performance of different refrigerant circuits based on exergy destruction analysis.

However, the problem associated with a large solution space remains unresolved, and most studies limited their investigations to simple circuitries defined as tube configurations without splits or merges, and to pre-determined numbers of circuits and split locations [13, 23–24)]. Therefore, excluding the simplified analytical approaches that considered constant transport properties along the refrigerant flow [16, 25)], these studies did not provide a method for defining the number and locations of splits and merges within refrigerant circuitries.

The unresolved limitations are mainly related to the inappropriate mathematical representation of refrigerant circuitry [26)] and the evolutionary technique [27)], which cannot manage the genetic operators used in the search for complex circuitries. Therefore, in this study, a new mathematical representation of complex circuitries and physical constraints [26)] was adopted, and a novel evolutionary method referred to as the "genetic thermal path generator" was developed. This optimization technique can effectively manage unrestrained numbers and locations of splits and merges, thereby expanding the search space when compared with those developed in previous research, while ensuring the feasibility and physicality of the circuitry with topology constraints when applying genetic operators.

The section below presents the application of the proposed method to the assessment of refrigerant performance in an air-conditioning cycle, where the evaporator is optimized to maximize the system COP for a given target cooling capacity, degree of superheating at the compressor suction, and temperature level of the external environment and indoor space.

4.3.1.2 Simulator

Multiple refrigerant circuitries for a finned-tube heat exchanger, such as those shown in 4.3.1-1, are managed using a mathematical representation referred to as the "tube–tube adjacency matrix" [26)], which is based on graph theory concepts in combination with traversal algorithms such as breadth-first search and depth-first search. This approach ensures a one-to-one relationship between any circuitry and its corresponding mathematical representation (Fig. 4.3.1-2), and facilitates the formulation of related relationships to ensure the physicality and feasibility of circuitry during evolutionary searches.

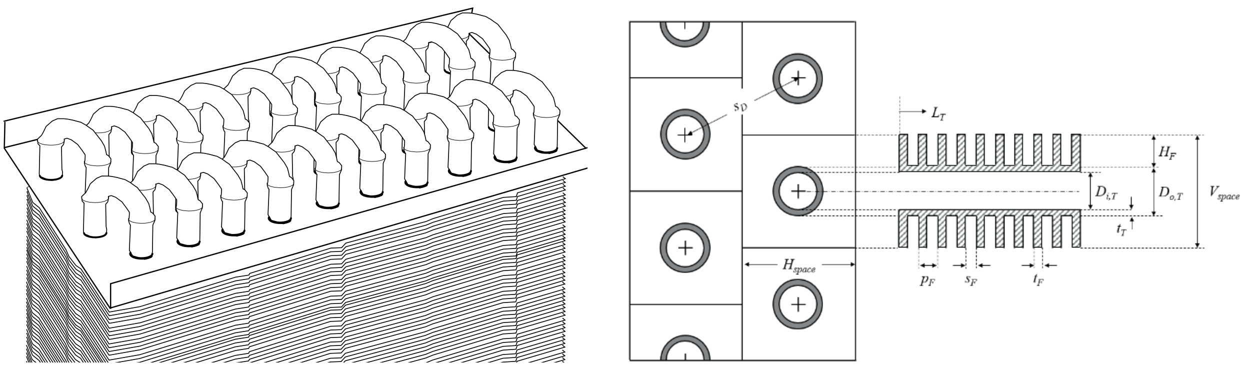

(a) (b)

Fig. 4.3.1-1 (a) Three- and (b) two-dimensional schematic illustrations of a finned-tube heat exchanger

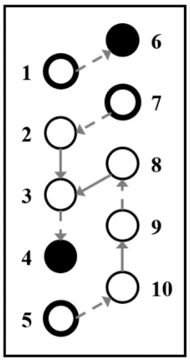

Reference	Connected tubes									
	1	2	3	4	5	6	7	8	9	10
1	0	0	0	0	0	1	0	0	0	0
2	0	0	1	0	0	0	-1	0	0	0
3	0	-1	0	1	0	0	0	-1	0	0
4	0	0	-1	0	0	0	0	0	0	0
5	0	0	0	0	0	0	0	0	0	1
6	-1	0	0	0	0	0	0	0	0	0
7	0	1	0	0	0	0	0	0	0	0
8	0	0	1	0	0	0	0	0	-1	0
9	0	0	0	0	0	0	0	1	0	-1
10	0	0	0	0	-1	0	0	0	1	0

Fig. 4.3.1-2 Tube–tube adjacency matrix

Correspondingly, the physical representation is dependent on a tube-by-tube approach, which is approximated by the numerical convergence mass, energy, and momentum transport equations under the following assumptions. First, the finned-tube heat exchanger is in a steady state. Second, the variation of the kinetic and potential energies is negligible. Third, no heat transfer occurs in the tube bends. Fourth, the air-side velocity is uniform.

The heat transfer coefficient was calculated using the Dittus-Boelter equation [28)] for a single-phase flow, while the correlations proposed by Shah [29)] and Cavallini et al. [30)] were used for two-phase flow in the evaporation and condensation regimes, respectively. The correlation derived by Shah [31)] was adopted in the case of two-phase zeotropic mixtures. The correlation derived by Seshimo and Fujii [32)] for an inline tube arrangement and correlation proposed by Kim et al. [33)] for a staggered tube configuration were used to determine the air-side heat transfer coefficient. The mathematical details were provided in a previous study [26)]. Additionally, a formulation of the pressure drop in the connecting U-bends was included to improve the accuracy of the model. To calculate the pressure drop in the return bends, two essential geometric parameters are the return bend length and return bend radius. The return bend radius is approximated as half of the center-to-center distance of the two connected tubes, whereas the return bend length is the arc length of the 180° return bend. To calculate the return bend pressure drops, the correlations proposed by Popiel and Wojtkowiak [34)] and Domanski and Hermes [35)] were used for single-phase and two-phase flows, respectively.

4.3.1.3 Model validation

The proposed numerical model was validated with reference to the experimental data from a water-to-air commercial coil with 20 tubes and four tube rows [36)], in addition to data from a dedicated experiment on an evaporator circulating R410A within 28 tubes in a single tube row. In the first case, the deviations between the predicted and experimental values were within ± 3%, as indicated by Garcia et al. [26)]. Figures 3(a) and 3(b) reveal the good agreement between the calculated and experimental heat duty and pressure measured in this study. The deviations were within ± 7% and ± 8%, respectively.

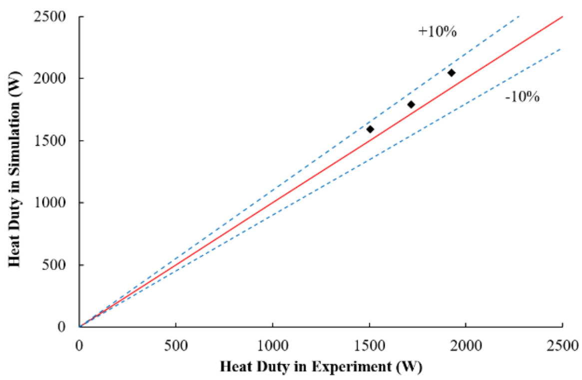

(a)

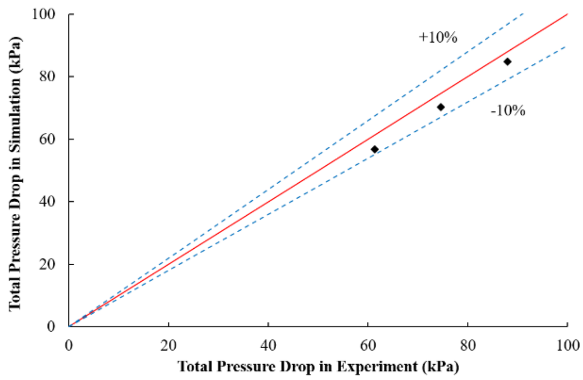

(b)

Fig. 4.3.1-3 Comparison between experimental and calculated values of the (a) heat duty and (b) total pressure drop in a 28-tube evaporator

The refrigerant temperature was measured at multiple locations. Garcia et al. [26)] demonstrated that the corresponding simulated and experimental temperature results were in relatively good agreement.

4.3.1.4 Genetic thermal path generator

Evolutionary algorithms have been widely used to solve optimization problems based on their robustness and flexibility in deriving solutions in complex spaces. In such algorithms, mechanisms based on Darwinian evolution are implemented, including selection, recombination, and mutation. In a basic evolutionary algorithm, a population of candidate solutions is initialized, and the following steps are repeated: (1) the fitness of each individual in the population is evaluated, (2) new children are generated using the fitness information from parent solutions, and (3) candidate solutions to survive in the subsequent generation are selected among parents and children. These three procedures are iterated until a certain condition, such as a maximum number of generations, is satisfied.

The heat exchanger optimization technique developed in this study overcomes the limitations of previous research by extending the evolutionary search to a search space of possible circuitries that covers unrestrained numbers and locations of splits and merges. The management of the number and location of splits and merges in refrigerant circuitry optimization is based on the objective to control the pressure drop, local temperature difference between the air and refrigerant, and equilibrium between the air-side and refrigerant-side thermal resistances. However, the development of chromosomes representing the circuitry, as presented in previous optimization studies, is based on the construction of an array to be acted on by the genetic operators of a genetic algorithm. If it is not modified, this methodology can only handle tube rearrangement. This is because the direct application of genetic operators to an array-type chromosome results in infeasible and non-physical offspring. As a result, infeasible and non-physical circuitries should be excluded based on the formulation of the constraints described below.

(1) Topology constraints

Five categories of infeasible and non-physical circuitry arrangements were considered (Fig. 4.3.1-4): I.) refrigerant circuitry with non-connected tubes, II.) circuitry with an infeasible internal loop, III.) refrigerant circuitry wherein the upstream flows of a merge are opposite flow directions, IV.) connections between tubes limited to a maximum distance of two rows and/or two columns, and V.) heat exchanger outlet flows constrained on the same side.

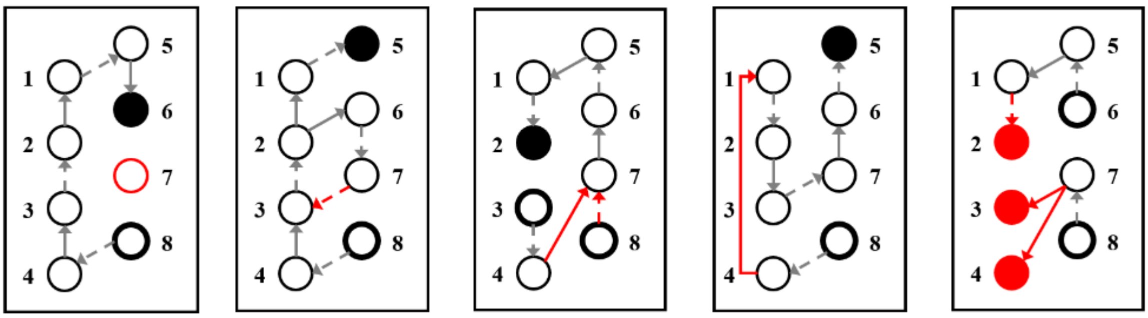

I. II. III. IV. V.

Fig. 4.3.1-4 Feasibility and manufacturing constraints

The details of the formulation of these constraints are presented in a previous study [26]. In particular, limiting the space of possible gene combinations using these constraints can significantly reduce its size and facilitate the convergence of the evolutionary algorithm toward optimal solutions.

(2) Genetic operators

To effectively manage the evolutionary search for optimal configurations of the heat exchanger, a novel optimization algorithm was developed.

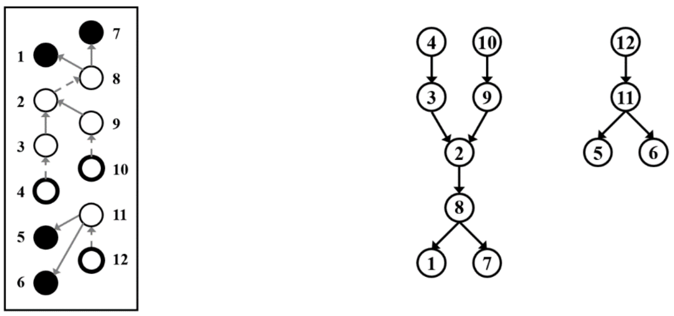

(a) (b)

Fig. 4.3.1-5 (a) Schematic diagram of a refrigerant circuitry and (b) its corresponding tree structure.

The proposed evolutionary search method, which is referred to as the "genetic thermal path generator," is a novel genetic programming technique that can introduce crossover and mutation operations while managing unrestricted numbers and locations of splits and merges. The proposed algorithm applies genetic operators to tree structures, where each node corresponds to a unique tube and is generated according to rules designed to exclude infeasible circuitries. Each tree (circuit) starts with root nodes (inlet tubes) and ends with leaves (outlet tubes). A tree can branch into subtrees if there are splits and merges in a circuit. The depth of a tree is equal to the number of nodes that require traversal to reach a leaf from the root node (Fig. 4.3.1-5).

The proposed algorithm consists of five main phases: I.) initialization, II.) selection, III.) crossover, IV.) mutation, and V.) the application of physical constraints.

I. Initialization

When initializing the population, different refrigerant circuitries are generated until the desired number of members is achieved. However, it should always be ensured that the generated refrigerant circuitries are feasible and comply with a set of manufacturing constraints. The generation of tree structures starts with determining the number of branches N_b, as expressed by Eq. (4.3.1-1), where x is a random value in the range of $0 \le x < 1$ and d_{tree} is the minimum tree depth. The number of nodes in the first branch is greater than or equal to d_{tree}, whereas the numbers of member nodes in the remaining branches are randomly assigned.

$$N_b = 2 + \mathrm{int}\left[x \left(N_{tubes} - d_{tree} - 2 \right) \right] \tag{4.3.1-1}$$

Considering the tube bundle shown in Fig. 4.3.1-5, the heat exchanger has $N_{tube} = 12$, and the tree has a depth $d_{tree} = 5$ in this example. If the value of x is randomly set as 0.3, the number of branches is $N_b = 2 + \mathrm{int}\,[0.3 \times (12 - 5 - 2)] = 2 + \mathrm{int}\,[1.5] = 3$. The different branches generated in this example are presented in Fig. 4.3.1-6.

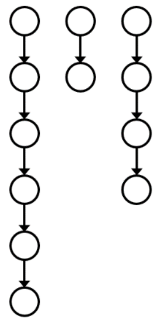

Fig. 4.3.1-6 Branches generated in the initialization of the tree structure

Thereafter, the connections among branches are established such that the first node in a branch can be assigned as an inlet tube, or a random node in a branch is connected to the first node in another branch. The number of times the branch connection process is executed is equal to N_b. Fig. 4.3.1-7 illustrates the following steps in the branch connection process.

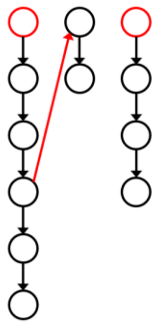

Fig. 4.3.1-7 Branch connections during initialization of tree structures

(1) Assign the first node in Branch 1 as an inlet.
(2) Connect the fourth tube in Branch 1 to Branch 2.
(3) Assign the first node in Branch 3 as an inlet.

The process of assigning inlet tubes and connecting nodes is repeated until the resulting tree structure satisfies all conditions for feasibility and all tube connections meet the requirements of the manufacturing constraints.

II. Selection

When initializing the population, different refrigerant circuitries are generated until the desired number of members is achieved. However, it should always be ensured that the generated refrigerant circuitries are feasible and comply with a set of manufacturing constraints. The generation of tree structures begins with determining the number of branches N_b, as expressed by Eq. (4.3.1-1), where x is a random value in the range of $0 \le x < 1$ and d_{tree} is the minimum tree depth. The number of nodes in the first branch is greater than or equal to d_{tree}, whereas the numbers of member nodes in the remaining branches are randomly assigned.

III. Crossover

Single-point crossover is used in the optimization approach. The crossover point in each parent $node_{cross}$ is a corresponding node in a randomly selected tube number. The upstream node from the crossover point in each parent $node_{up}$ is identified. The crossover point node in Parent A ($node_{cross,A}$) is connected to the upstream node from the crossover node in Parent B ($node_{up,B}$). Similarly, $node_{cross,B}$ is linked to $node_{up,A}$. The feasibility of the resulting offspring are then verified for feasibility (Fig. 4.3.1-8).

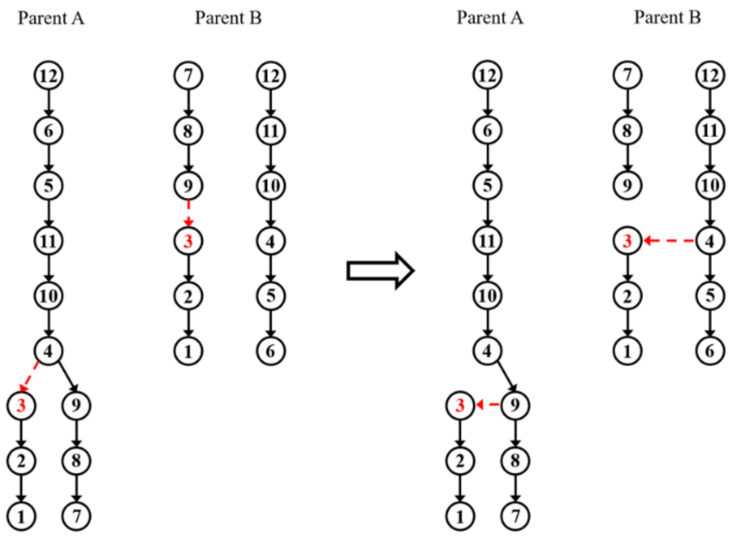

Fig. 4.3.1-8 Single-point crossover

IV. Mutation

Two forms of mutation are implemented in this phase. For subtree mutation, a mutation point is randomly selected in a tree, and a randomly generated subtree replaces the initial subtree. For swap mutation, two randomly selected nodes exchange their assigned tube numbers. The descendants obtained in this manner are verified for feasibility. If they do not satisfy the topology constraints, then they are modified to satisfy the topology constraints (see Section V).

V. Application of topology constraints

Given the probability that the circuitries generated by recombination operators are infeasible, the obtained tree structures are modified to ensure physicality and feasibility according to the constraints described above. In the case where merging upstream flows emerge from opposite sides of a tube, the infeasible link is disconnected if there are more than two upstream flows, or one link is randomly disconnected if there are exactly two upstream flows. Similarly, all outlet tubes should be part of odd-numbered or even-numbered levels. In cases wherein there is a non-connected tube, it is connected to the final node in a branch that can satisfy the conditions for outlet tubes flowing on the same side of the heat exchanger, and not a part of the downstream flow from a split. In cases where mutation and crossover operations result in circuitries with an infeasible internal loop, any link will be removed while the resulting structure satisfies the other feasibility conditions. These processes are illustrated in Fig. 4.3.1-9. Additionally, if the connected tubes do not satisfy the constraint of the U-bend length, the corresponding nodes are interchanged with other tubes that satisfy this manufacturing constraint. This process is repeated until all nodes satisfy the constraint for the return bend length. If several nodes cannot satisfy these conditions after 3000 iterations, the tree structure is discarded.

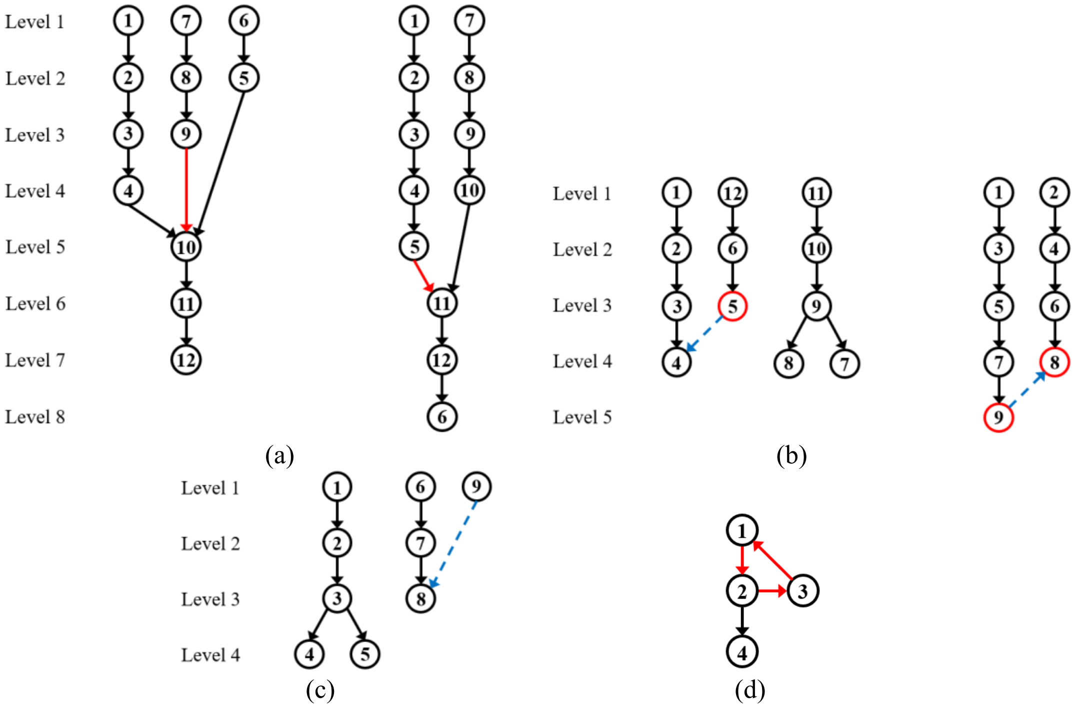

Fig. 4.3.1-9 Modification for cases wherein (a) flows upstream of a merge emerge from opposite sides of a tube, (b) flows from outlet tubes do not exit on the same side, (c) there are non-connected tubes, and (d) there are internal loops

4.3.1.5 Optimization settings

The application of the proposed evolutionary algorithm to the evaporator of an air conditioner can provide a suitable basis for evaluating the potential of different refrigerants with different characteristics, such as azeotropic and zeotropic refrigerant mixtures.

For optimization, the evaporator refrigerant circuitry was considered as a variable parameter to maximize the COP of the system while setting the condenser-side saturation temperature as 45 °C and sub-cooling temperature as 5 K (Table 4.3.1-1). In the case of zeotropic refrigerant mixtures, the saturation pressure was determined with reference to the average temperature between the boiling and dew points. Additionally, the optimization problem was constrained to ensure that the generated refrigerant circuitry achieved the desired evaporator capacity, refrigerant superheating, and air outlet temperature (see Table 4.3.1-1) by converging the refrigerant flow rate, refrigerant inlet pressure, and air flow rate. In this case study, optimization was conducted on an evaporator with 36 tubes and 12 tube rows. The "1.5-circuit" configuration presented by Domanski et al. [13] (see Fig. 4.3.1-10) was used as a baseline for comparison while varying the target capacity within a range of 4–10 kW.

Table 4.3.1-1 Evaporator and condenser operating conditions

Parameter	*Value (unit)*
Air-inlet temperature	26 (°C)
Air-inlet pressure	101.325 (kPa)
Air-outlet temperature	18 (°C)
Degree of superheating	5 (K)
Capacity	4,6,8,10 (kW)
Condensation temperature	45 (°C)
Degree of sub-cooling	5 (K)
Isentropic efficiency	0.85
Motor efficiency	0.85

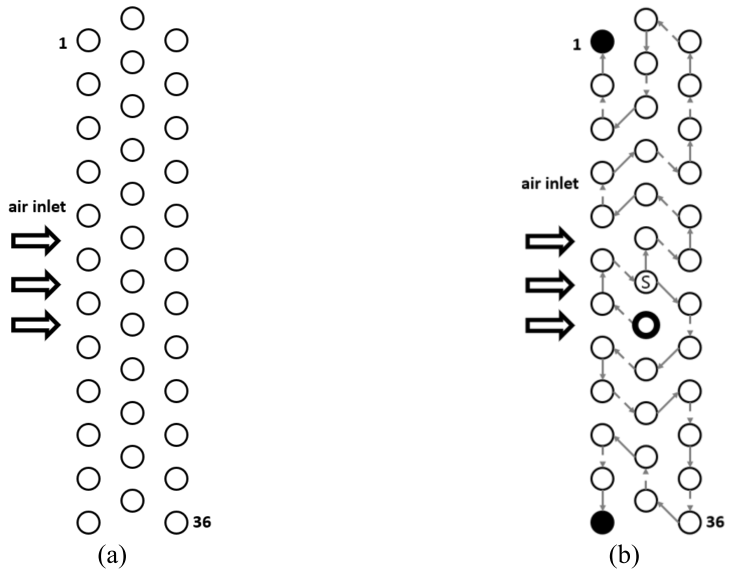

Fig. 4.3.1-10 (a) Evaporator configuration and (b) baseline circuitry from previous research [13)]

The evolutionary search was conducted based on the algorithm settings presented in Table 4.3.1-2 for three representative refrigerants used in air-conditioning applications (R410A, R32, and R454C, and a zeotropic mixture with a relevant temperature glide). The results are presented and discussed in the following sections.

Table 4.3.1-2 Settings for the optimization search

Parameter	*Value*
Population size	500
Number of generations	100
Crossover probability	0.8
Mutation probability	0.005
Elitism probability	0.0005

4.3.1.6 Results and discussion

Figure 4.3.1-11 presents the COP of the system with the optimized evaporator circuitry and COP improvement when compared with the COP of the system with the baseline 1.5-circuit configuration.

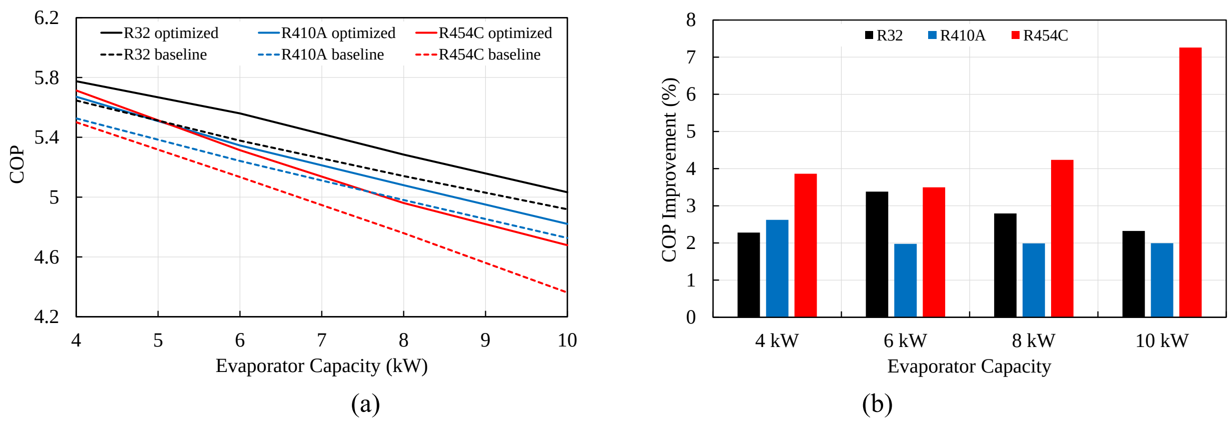

Fig. 4.3.1-11 (a) The COP and (b) COP improvement

There was a 2.28–3.38% increase in the COP of the R32 system with optimized circuitries, 1.98–2.62% increase for the R410A system, and 3.50–7.26% increase for the R454C system. Among the three refrigerants and evaporator capacities considered, the optimized 10 kW R454C circuitry exhibited the most significant COP improvement. This may be because the low-GWP refrigerant mixture with a temperature glide can benefit from the COP improvement achieved by reducing the pressure drop and average temperature difference between the air refrigerant tubes based on the proposed circuitry optimization method.

Figures 4.3.1-12(a) and 4.3.1-12(b) reveal that in general, the COP improvement of the optimized circuitry can be attributed to a higher outlet pressure at the evaporator, thus resulting in a lower compression ratio.

As can be seen from Table 4.3.1-1, a higher evaporator outlet pressure can be achieved with more effective heat transfer characteristics, which allows for an equivalent capacity with a smaller temperature difference between the refrigerant and air (higher inlet saturation temperature), and lower pressure drop inside the evaporator. The optimized circuitry for R410A and R32 mostly operated at a higher inlet evaporator pressure than that of the baseline circuit. Although most of the optimized circuits exhibited high total pressure drops, this was mitigated by operating at higher evaporator inlet pressures, thus resulting in higher evaporator pressures and lower compression ratios. In the case of R454C at capacities of 8 kW and 10 kW, the optimized circuitries exhibited a low inlet pressure, because for correspondingly high refrigerant flow rates, the effects of the pressure gradient were more dominant than possible improvements in the thermal conductance of the heat exchanger. With an increase in the refrigerant mass flow rate at higher capacities, the optimized evaporator circuitry resulted in a large number of parallel circuits that minimized the pressure drop. This eventually resulted in a higher pressure at the evaporator outlet and reduced the required compression ratio. This difference in the trend of R454C when compared with those of R32 and R410A can be attributed to the higher viscosity and lower vapor density of R454C.

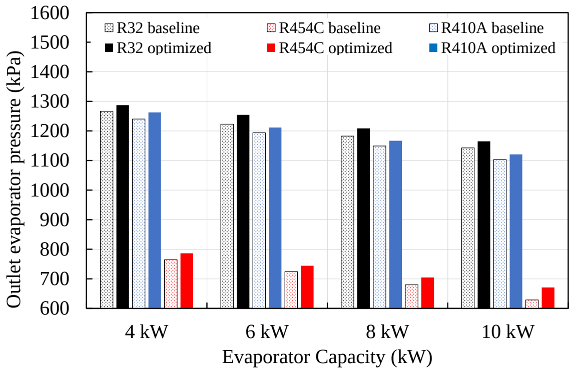

(a)

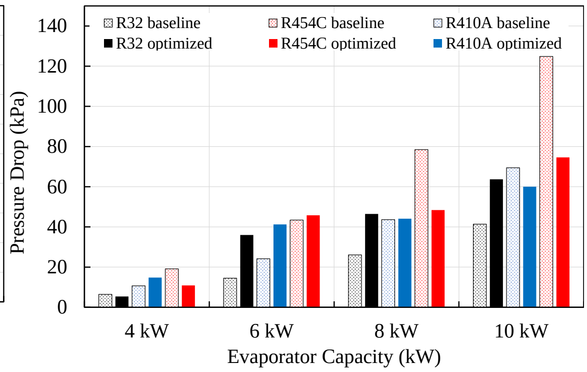

(b)

Fig. 4.3.1-12 (a) Refrigerant outlet pressure of the evaporator and (b) refrigerant pressure drop of the evaporator

The corresponding circuitries of the optimized evaporator for R32, R410A, and R454C are presented in Fig. 4.3.1-13, Fig. 4.3.1-14, and Fig. 4.3.1-15, respectively. In these schematics, the inlet tubes are represented by thick-bordered circles, outlet tubes by “O” symbols, and splits by “S” symbols. The solid lines represent the return bends on the front side of the heat exchanger, whereas the return bends on the back side are represented by dashed lines. The quality of the refrigerant flow is represented by the inner color, as indicated in the legend.

A notable feature of the optimized circuitries when compared with the baseline is the presence of fewer tubes in the superheated refrigerant state. This improves the usage of the transfer surface by minimizing the part of the transfer area that interfaces with a low heat transfer coefficient on the refrigerant side.

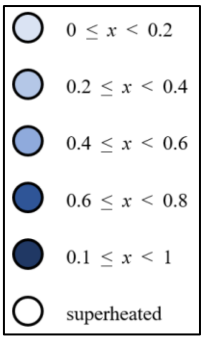

(a)

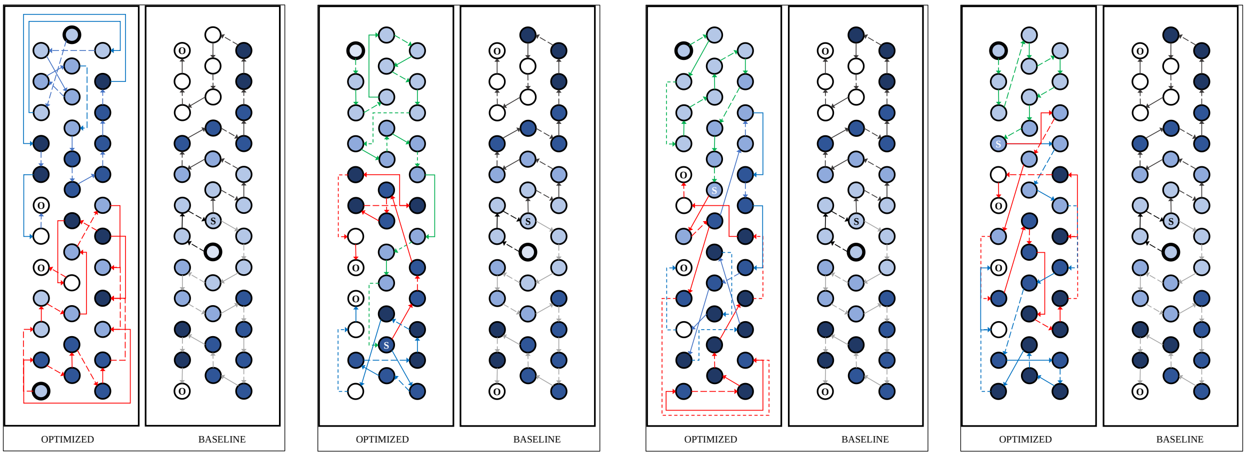

(b) (c) (d) (e)

Fig. 4.3.1-13 (a) Legend for the refrigerant quality state. Comparison of baseline and optimized R32 evaporators at capacities of (b) 4 kW, (c) 6 kW, (d) 8 kW, and (e) 10 kW

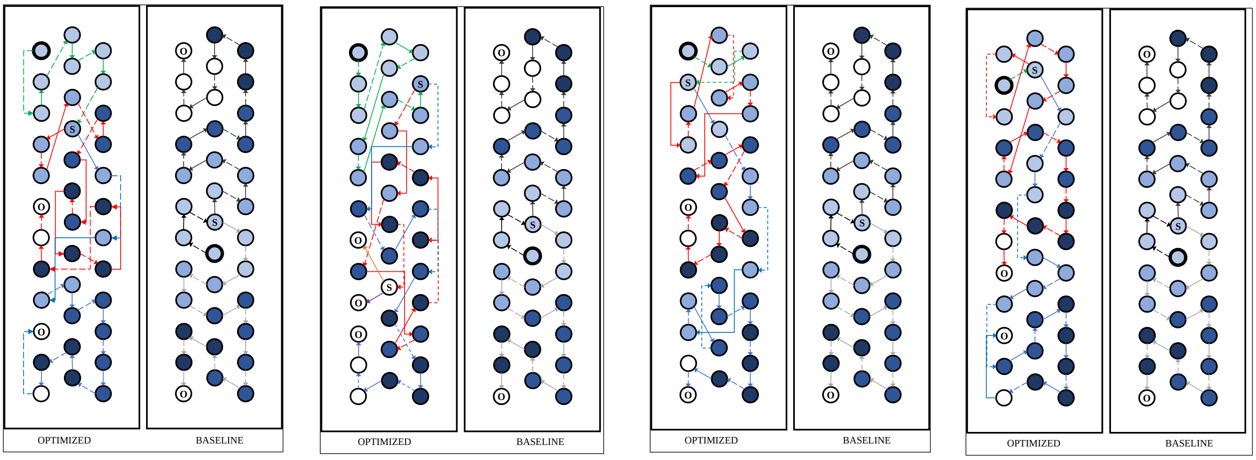

(a) (b) (c) (d)

Fig. 4.3.1-14 Comparison of baseline and optimized R410A evaporators at capacities of (a) 4 kW, (b) 6 kW, (c) 8 kW, and (d) 10 kW

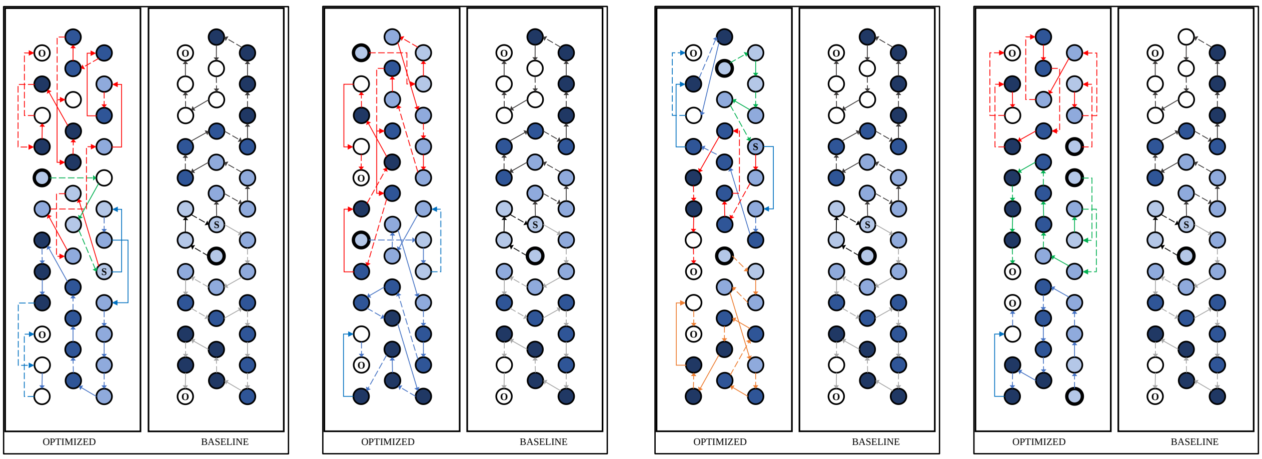

(a) (b) (c) (d)

Fig. 4.3.1-15 Comparison of baseline and optimized R454C evaporators at capacities of (a) 4 kW, (b) 6 kW, (c) 8 kW, and (d) 10 kW

As can be seen from the figures, the number of circuits and split location varied with the refrigerant and target capacity. However, the number of circuits and split location influenced the heat transfer coefficient. As the capacity increased for a given refrigerant, the location of the split shifted, and the number of parallel branches increased to limit the refrigerant pressure drop by reducing the flow rate circulated in each branch. Additionally, the latent heat of vaporization influenced the flow rate required to achieve the target cooling capacity. Based on its large latent heat, among the three refrigerants, R32 required the lowest refrigerant flow rate to achieve the target capacity, whereas R454C required the highest flow rate. Additionally, the variation in the air mass flow rate across refrigerants at a given evaporator capacity was insignificant, given that the refrigerant circuitry had no significant effect on the air-side thermal resistance under the assumption of a uniform air distribution. Regardless, the refrigerant circuitry determined the arrangement of the local temperature difference between the air and refrigerant, which could be optimized to reduce irreversible heat transfer losses related to the refrigerant saturation temperature variation caused by the pressure drop and temperature glide of zeotropic mixtures.

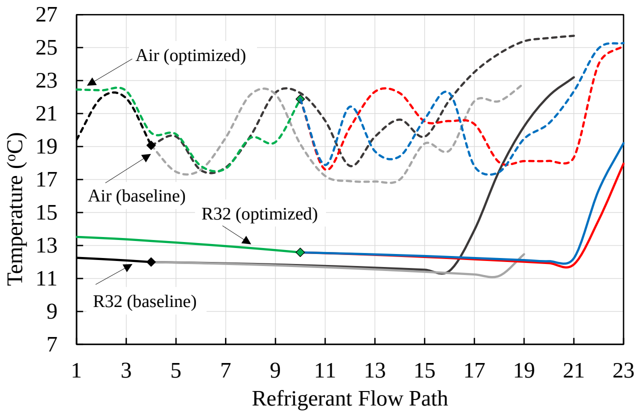

(a)

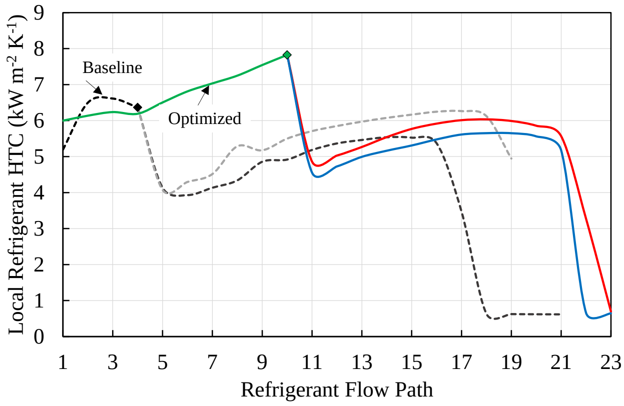

(b)

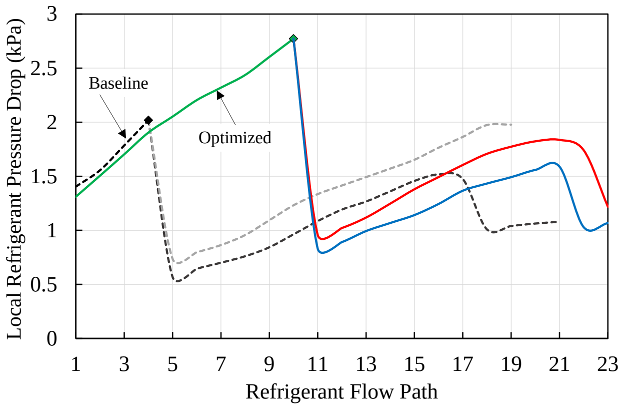

(c)

Fig. 4.3.1-16 Comparison of local (a) temperatures, (b) refrigerant heat transfer coefficients, and (c) refrigerant pressure drops of the baseline and optimized R32 evaporators at a capacity of 10 kW

The horizontal axes in Figs. 4.3.1-16 and 4.3.1-17 represent the flow of refrigerant in each branch of the refrigerant circuitry from the inlet to the outlet, and the number of pipes between the inlet and outlet, respectively. In these figures, the positions of the branches in the two circuitries are represented by diamond-shaped markers. The air-side temperatures shown in Figs. 4.3.1-16(a) and 4.3.1-17(a) are based on the refrigerant path between the inlet and outlet of each branch of the circuitry, and the corresponding air conditions were plotted as dashed lines. This plot was generated to determine the local temperature difference between the air and refrigerant, and the dashed line on the air side does not represent the continuity of the air flow.

The local temperature, heat transfer coefficient, and pressure drop of R32 and R454C in the baseline and optimized circuitries at a capacity of 10 kW are presented as representative cases of the phenomena described above. The case of R32 refrigerant is illustrated in Fig. 4.3.1-16, where the split location in the two circuitries is represented by a diamond marker. As can be seen from Fig. 4.3.1-16(a), the optimized circuit achieved the same 10 kW capacity while maintaining a smaller temperature difference between the refrigerant and air throughout the heat exchanger. Additionally, the optimized circuitry featured only four tubes, in which the refrigerant flowed in a superheated state, whereas the baseline circuitry featured six tubes with a superheated refrigerant and a low heat transfer coefficient.

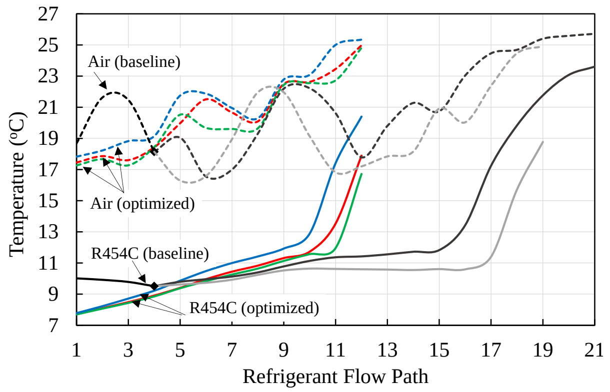

(a)

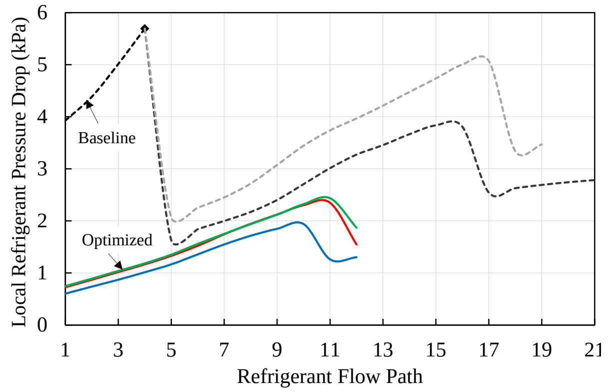

(b)

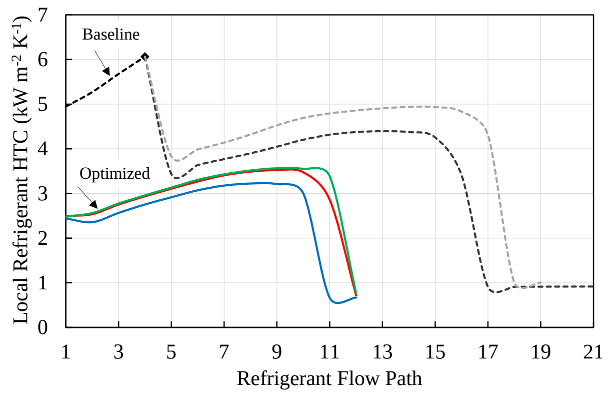

(c)

Fig. 4.3.1-17 Comparison of local (a) temperatures, (b) refrigerant heat transfer coefficients, and (c) refrigerant pressure drops of the baseline and optimized R454C evaporators at a capacity of 10 kW

As a result, the optimized circuitry operated at a higher evaporator pressure. Both the baseline and optimized evaporators had a 1.5-circuit configuration, and the increase in the inlet pressure of the optimized circuitry can be attributed to its split location and improved ordering of tubes for the local arrangement of the temperature difference between the air and refrigerant, particularly in the superheated region. The split in the optimized evaporator was closer to the outlet, which resulted in a higher heat transfer coefficient, as shown in Fig. 4.3.1-16(b). As a result, the effective mean temperature difference between the refrigerant and air was reduced by the improved thermal conductance of the heat exchanger. In contrast, a split farther from the inlet yielded a higher pressure drop (Fig. 4.3.1-16c). The effect of a high-pressure drop on system performance can be mitigated by operating at a higher inlet pressure.

A different trend was observed in the R454C evaporators based on the high temperature glide and different thermophysical properties of the zeotropic mixture. Figure 4.3.1-17 presents the local refrigerant temperature, heat transfer coefficient, and pressure drop of the baseline and optimized R454C evaporators at a capacity of 10 kW.

The optimized R454C circuitry operated at a lower evaporator inlet pressure than the baseline circuitry, which deviated from the general trend of the optimization results. This deviation can be attributed to its greater number of circuits than the baseline. As illustrated in Fig. 4.3.1-17(b), the local pressure drop of the baseline circuitry was significantly higher as a result of the high refrigerant flow rate, low vapor density, and high viscosity of the refrigerant. To reduce the effects of the pressure drop, the optimized circuitry operated in a three-circuit configuration, thus implying that it consisted of three parallel circuits. The increased number of circuits reduced the local refrigerant flow rate and heat transfer coefficient. A larger effective temperature difference between the refrigerant and air was required to achieve the target capacity of the evaporator. Therefore, the optimized circuitry operated at a lower evaporator inlet pressure. Nonetheless, pressure drop minimization resulted in a greater advantage for the optimized circuitry. As shown in Fig. 4.3.1-17(a), the temperature glide cannot be effectively utilized if large pressure drops are encountered on the refrigerant side, as in the baseline case (black and gray lines). The temperature of R454C in the baseline circuitry decreased before the split due to the significant pressure drop. Therefore, the optimized circuitry exploited the temperature glide of R454C by maintaining low values of pressure drop and maximizing the effects of a counter-flow arrangement between the air and refrigerant flows (Fig. 4.3.1-17a).

Figure 4.3.1-18 presents a comparison between the results obtained using different refrigerant assessment methods. Among the different performance evaluation methods, thermodynamic analyses and drop-in tests were the most commonly employed methods in previous studies. Therefore, a comparison of the results is presented for these methods with the performance evaluations conducted using the abovementioned circuitry optimization procedure. Figure 4.3.1-18 presents the results obtained for different refrigerants at an evaporator capacity of 10 kW for each evaluation method.

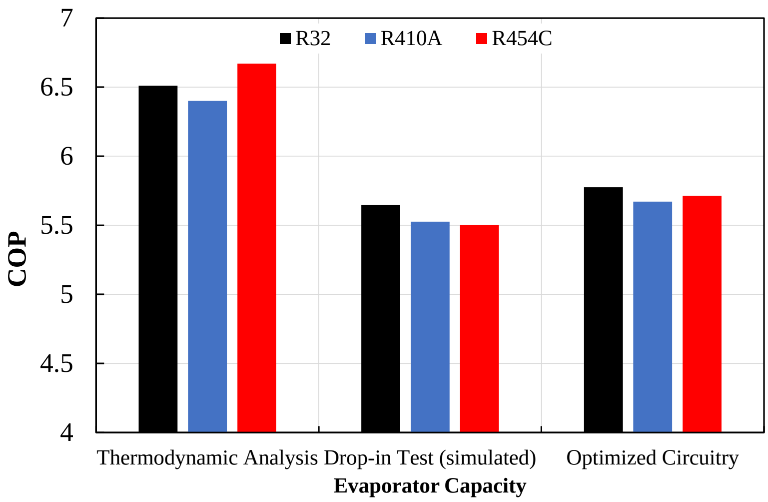

Fig. 4.3.1-18 Results of different refrigerant assessment methods at a capacity of 4 kW

For thermodynamic analysis, the calculations were based on the evaporating and condensing temperatures, degrees of superheating and sub-cooling, and an assumed value of compressor efficiency. The evaporator saturation temperature considered was 12 °C, and the values of the other parameters were set according to the conditions of evaporator optimization (Table 4.3.1-1). It was assumed that there were no pressure drops in the heat exchangers. As can be seen from Fig. 4.3.1-18(a), the refrigerants were ranked based on their critical temperatures, thus demonstrating that a higher COP can be achieved in systems operating far from the refrigerant critical temperature, which can reduce the deviation from the corresponding reversible inverse Carnot cycle.

A different trend was observed for the simulation conducted using the same unmodified system (representative of drop-in test conditions). In this analysis, the refrigerants were compared within the same system, which adopted the baseline evaporator circuitry shown in Fig. 4.3.1-10. In particular, R32 exhibited the highest COP, followed by R410A and R454C. The results indicate that the 1.5-circuit arrangement favored R32 and R410A based on the low viscosity and vapor density of these refrigerants. Therefore, comparing and assessing the potential of refrigerants in the same unmodified system is inappropriate because a given topology of individual components results in different performances with respect to the thermophysical and transport properties of the circulating refrigerant.

In the analysis where the refrigerant circuitry was optimized for each refrigerant, at a capacity of 4 kW, R454C exhibited a higher COP than R410A. The proposed optimization approach can derive a refrigerant path that utilizes the temperature glide of R454C and determine the appropriate number of circuits to minimize the pressure drop for a given target cooling capacity, superheating degree at the compressor suction, and temperature level of the external environment and indoor space. This may be interpreted as thermodynamic cycle optimization under a given temperature and heat capacity of heat sources through the optimization of the refrigerant-side topology of an evaporator, to minimize the thermodynamic losses caused by the pressure drop and the finite-temperature-difference heat transfer between the air and refrigerant. This is realized by considering the local pressure drop, local refrigerant temperature, and refrigerant heat transfer coefficient arrangement by adjusting the tube order and number, in addition to the location of splits and merges, which results in the maximum outlet evaporator pressure for each refrigerant under the conditions listed in Table 4.3.1-1. In the considered cases, the larger improvement observed for zeotropic refrigerant mixtures can be attributed to the possibility of approaching Lorenz-cycle operation for the same temperature levels of indoor and outdoor heat sources and sinks.

4.3.1.7 Summary of heat exchanger optimization

In this section, a novel method for the optimization of heat exchanger circuitry was established and tested for optimizing the circuitries of a 36-tube evaporator under representative conditions of air conditioning applications. The performances of R32, R410A, and R454C were assessed under the given heat source and sink boundary conditions, degree of superheating, and output capacity. This paper proposes the use of this optimization technique as a novel refrigerant evaluation method, which was compared with previous methods and verified according to the evaluation settings considered in this study. The proposed method was recommended for the evaluation of next-generation non-azeotropic refrigerant mixtures, which will be commonly used in the future.

The proposed circuitry optimization algorithm derives efficient heat exchanger topologies by minimizing the pressure drop, mean average temperature difference between the refrigerant and air side, and the number of ineffective tubes in a superheated state.

Given that thermodynamic analysis and drop-in tests are the most commonly employed methods for refrigerant performance evaluations, a comparative study considering these methods and the proposed refrigerant evaluation method was performed. We found that the application of the developed evolutionary algorithm to refrigerant circuitry design reduced the pressure drop and improved the local heat transfer coefficient and thermal matching between the refrigerant and air temperature distribution. As a result, the evaporator outlet pressure was increased, compression ratio was reduced, and COP was maximized under the given optimization constraints.

The main contribution from this study is that low-GWP mixed refrigerants with temperature glide can be leveraged by the proposed circuitry optimization technique by considering the pressure drop and mean temperature difference between the air and refrigerant.

The combination of these novel methods facilitates the search for optimal topologies of heat exchangers in a manner that allows for the thermodynamic benefits of non-azeotropic refrigerants to be exploited by approaching Lorentz cycle operation. The results of the evaluations demonstrated that non-azeotropic refrigerant mixtures with a low GWP may exhibit performances superior to that of R410A and comparable to that of R32.

References

1) https://www.un.org/sustainabledevelopment/ (May, 2022).
2) Jakobs, R., Kruse, H., The use of non-azeotropic refrigerant mixtures in heat pumps for energy saving, International Journal of Refrigeration, 1979, 2, pp. 29–32.
3) Kruse, H., The advantages non-azeotropic refrigerant mixtures for heat pump application, International Journal of Refrigeration, 1981, 4, pp. 119–125.
4) Uddin, K., Saha, B., Thermodynamic analysis of low-GWP blends to replace R410A for residential building air conditioning applications, Environmental Science and Pollution Research, 2021, 28, pp. 2934-2947.
5) Kim, N. H., Kwon, M. H., Go and M. G., An experimental investigation on the airside performance of fin-and-tube heat exchangers having nonsymmetrical slit fins, International Journal of Air-Conditioning and Refrigeration, 2015, 23(2), no. 1550017.
6) Liu, A., Wang, G., Wang, D., Peng, X., Yuan, H., Study on the Thermal and Hydraulic Performance of Fin-and-Tube Heat Exchanger Based on Topology Optimization, Applied Thermal Engineering, 2021, 197, no. 117380.
7) Garcia, J. C. S., Tanaka, H., Giannetti, N., Sei, Y., Saito, K., Houfuku M. and Takafuji, R., Multiobjective Geometry Optimization of Microchannel Heat Exchanger Using Real-Coded Genetic Algorithm, Applied Thermal Engineering, 2022, 202, no. 117821.
8) Huang, L., Aute, V., Radermacher, R., Airflow Distribution and Design Optimization of Variable Geometry Microchannel Heat Exchangers, Science and Technology for the Built Environment, 2015, 21(5), pp. 693-702.
9) Glazar, V., Trp, A., Lenic, K., Optimization of Air-Water Microchannel Heat Exchanger Using Response Surface Methodology, International Journal of Heat and Mass Transfer, 2020, 157, no. 119887.
10) Yang, Z., Ma, Y., Zhang, N., Smith, R., Design Optimization of Shell and Tube Heat Exchangers Sizing with Heat Transfer Enhancement, Computers and Chemical Engineering, 2020, 137, no. 106821.
11) Bacellar, D., Aute, V., Huang, Z. and Radermacher, R., Design Optimization and Validation of High-Performance Heat Exchangers Using Approximation Assisted Optimization and Additive Manufacturing, Science and Technology for the Built Environment, 2017, 23(6), pp. 896-911.
12) Jige, D., Matsuno, T., Inoue, N., Experimental study on condensation heat transfer and flow modes of R245fa on enhanced surface tubes, International Journal of Air-Conditioning and Refrigeration, 2015, 23(2), no. 1550014.
13) Domanski, P. A., Yashar, D. and Kim, M., Performance of a Finned-Tube Evaporator Optimized for Different Refrigerants and Its Effects on System Efficiency, International Journal of Refrigeration, 2005, 28(6), pp. 820-827.

14) Wang, C.C., Jang, J.Y., Lai, C.C., Chang, Y.J., Effect of circuit arrangement on the performance of air-cooled condensers, International Journal of Refrigeration, 1999, 22(4), pp. 275–282.
15) Wu, Z., Ding, G., Wang, K., Fukaya, M., Application of a genetic algorithm to optimize the refrigerant circuit of fin-and-tube heat exchangers for maximum heat transfer or shortest tube, International Journal of Thermal Sciences, 2008, 47(8), pp. 985–997.
16) Lee, W. J., Kim, H. J., Jeong, J. H., Method for determining the optimum number of circuits for a fin-tube condenser in a heat pump, International Journal of Heat and Mass Transfer, 2016, 98, pp. 462-471.
17) Liang, S. Y., Wong, T. N., Nathan, G., Numerical and Experimental Studies of Refrigerant Circuitry of Evaporator Coils, International Journal of Refrigeration, 2001, 24(8), pp. 823-833.
18) Domanski, P. A, Finned-tube evaporator model with a visual interface, presented at the Int. Cong. of Refrig., Sydney, Australia, Sept. 19-24, 1999.
19) Domanski, P. A, EVAP-COND Simulation Models for Finned Tube Heat Exchangers, Gaithersburg, MD, USA: National Institute of Standards and Technology, Building and Fire Research Laboratory, 2003.
20) Domanski, P. A., Simulation of an evaporator with non-uniform one-dimensional air distribution, presented at the ASHRAE Winter Meet, New York, USA, Jan. 19-23, 1991.
21) Lee, J. H., Bae, S. W., Bang, K. H., Kim, M. H., Experimental and numerical research on condenser performance for R-22 and R407-C refrigerants, International Journal of Refrigeration, 2002, 25(3), pp. 372–382.
22) Liang, S.Y., Wong, T.N. and Nathan, G.K., Study on refrigerant circuitry of condenser coils with exergy destruction analysis, Applied Thermal Engineering, 2000, 20(6), pp. 559–577.
23) Ploskas, N., Laughman, C., Raghunathan, A. U., Sahinidis, N. V., Optimization of Circuitry Arrangements for Heat Exchangers Using Derivative-Free Optimization, Chemical Engineering Research and Design, 2018, 131, pp. 16-28.
24) Li, Z., Shen, B. and Gluesenkamp, K. R., Multi-objective Optimization of Low-GWP Mixture Composition and Heat Exchanger Circuitry Configuration for Improved System Performance and Reduced Refrigerant Flammability, International Journal of Refrigeration, 2021, 126, pp. 133-142.
25) Shah, M.M., A general correlation for heat transfer during film condensation inside pipes, International Journal of Heat and Mass Transfer, 1979, 22(4), pp. 547–556.
26) Garcia, J. C. S., Giannetti, N., Varela, D. A. B., Varela, R. J., Yamaguchi, S., Saito, K., Berana, M. S., Design of a Numerical Simulator for Finned-Tube Heat Exchangers with Arbitrary Circuitry, Heat Transfer Engineering.
27) Giannetti, N., Garcia, J. C. S., Varela, R. J., Sei, Y., Enoki, K., Jeong, J. Saito, K., Development of Assessment Techniques for Next-Generation Refrigerants with Low GWP Values - Fourth report: Efforts and outcomes on heat exchanger optimization in FY 2020, Proceedings of 2021 JSRAE Annual Conference, 2021.
28) Dittus, F., Boelter, L., Heat Transfer in Automobile Radiators of the Tubular Type, International Communications in Heat and Mass Transfer, 1985, 12(1), pp. 3-22.
29) Shah, M. M., Chart Correlation for Saturatred Boiling Heat Transfer: Equations and Further Study, AHRAE Transactions, 1982, 88(1), pp. 185-196.
30) Cavallini, A., Censi, G., Del Col, D., Doretti, L., Longo, G., Rosetto, L., Zilio, C., Condensation Inside and Outside Smooth and Enhanced Tubes - A Review of Recent Research, International Journal of Refrigeration, 2003, 26(4), pp. 373-392.
31) Shah, M. M., A method for predicting heat transfer during boiling of mixtures in plain tubes, Applied Thermal Engineering, 2015, 89, pp. 812-821.
32) Seshimo, Y., Fujii, M., Compact Heat Exchangers (in Japanese), Tokyo, Japan: Nikkan Kogyo Shimbun, Ltd., 1992.
33) Kim, N., Youn, B., Webb, R., Air-side Heat Transfer and Friction Correlations for Plain Fin-and-Tube Heat Exchangers with Staggered Tube Arrangements, Journal of Heat Transfer, 1999, 121(3), pp. 662-667.
34) Popiel, C., Wojtkowiak, J., Friction Factor in U-Type Undulated Pipe Flow, Journal of Fluids Engineering, 2000, 122(2), pp. 260-263.
35) Domanski, P. A., Hermes, C., An Improved Two-Phase Pressure Drop Correlation for 180o Return Bends, in 3rd Asian Conference on Refrigeration and Air-Conditioning, 20006, Gyeongju, Korea.
36) Jiang, H., Development of a Simulation and Optimization Tool for Heat Exchanger Design, College Park, Maryland, USA: University of Maryland, 2003.

4.3.2 System simulation

4.3.2.1 Background and purpose

Refrigerants with high global warming potential (GWP) are currently used in heat pumps, and new low-GWP refrigerants have been proposed. To compare the performances of various refrigerants in actual equipment, the performance of the equipment optimally designed for each refrigerant should be evaluated under uniform conditions; however, there are no clear guidelines for this. Therefore, this research group developed the Energy Flow + M to evaluate the performance of new refrigerants. The corresponding results of the comparative study are detailed.

4.3.2.2 Objective system

As shown in Fig. 4.3.2-1, we can assume that the equipment employs a single-stage compression refrigeration cycle, which is used in ordinary air conditioners. The considered system is the most basic air-conditioner cycle, which consists of a compressor, evaporator, expansion valve, accumulator, and piping. The dimensions of the components are presented in Table 4.3.2-1.

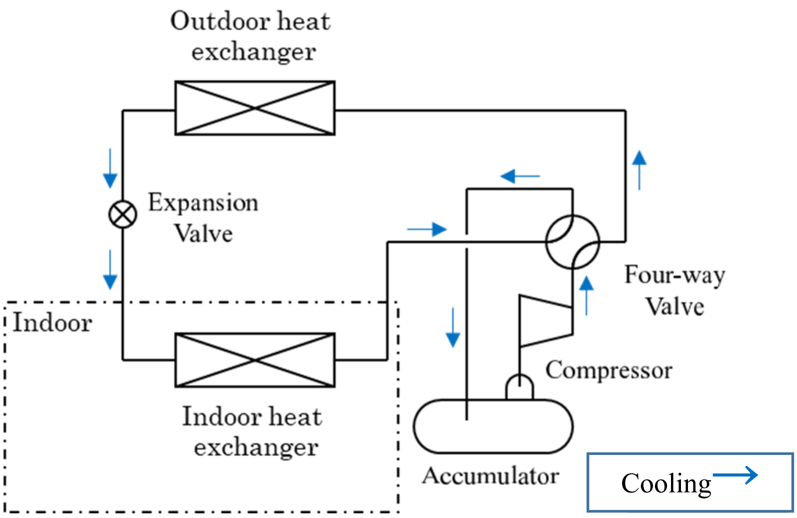

Fig. 4.3.2-1 Room air conditioner

Table 4.3.2-1 Specifications of components in room air conditioner

Components	Parameters	Unit	Values
Compressor	Displacement	mm^3	9200
Outdoor heat exchanger	Length of each straight tube	m	6.90
Accumulator Four-way Valve	Outer diameter	mm	7.50
	Inner diameter	mm,	7.10
	Pipe pitch	mm	22.5
	Width of a row	mm	19.12
	Fin thickness	mm	0.10
	Fin pitch	mm	1.20
	Pass number	-	4
Indoor heat exchanger	Length of each straight tube	m	10.0
	Outer diameter	mm	6.85
	Inner diameter	mm	6.45
	Pipe pitch	mm	15.94
	Width of a row	mm	13.55
	Fin thickness	mm	0.10

	Fin pitch	mm	1.20
	Pass number	-	2
Accumulator	Volume	mm^3	556000
Four-way Valve	High pressure side volume	mm^3	20000
	Low pressure side volume	mm^3	20000

4.3.2.3 Simulation model

The calculations are based on the models of each element proposed in Section 3. The compressor is a scroll type. Accordingly, as stated in Table 4.3.2-2, the adiabatic efficiency, volumetric efficiency, and inverter efficiency are assumed to be constant regardless of the load and refrigerant type.

Table 4.3.2-2 Compressor efficiencies

Components	Adiabatic	Volumetric	Inverter
Room air-conditioner compressor	0.75	0.90	0.95

4.3.2.4 Performance evaluation process by simulation

In this analysis, the changes in performance of a room air conditioner when a low-GWP refrigerant is dropped in were simulated. Moreover, the refrigerant performance was evaluated in terms of the relationship between the capacity and power consumption. The rated cooling capacity of the room air conditioner was 2.5 kW. The first step in the performance evaluation procedure was to determine the rated conditions for the air conditioner. Thereafter, the drop-in refrigerant fill volume was determined; subsequently, the performance of each refrigerant was comprehensively compared at a given set point for the compressor speed and cooling capacity, to clarify the effects of the refrigerant properties on performance. The flow of the drop-in evaluation is illustrated in Fig. 8.2. The performance evaluation conducted in this study was focused on the cooling operation. Specifically, the refrigerant charge was determined such that the COP was maximized under the rated cooling conditions, and the performance comparison was analyzed with emphasis on the cooling operation.

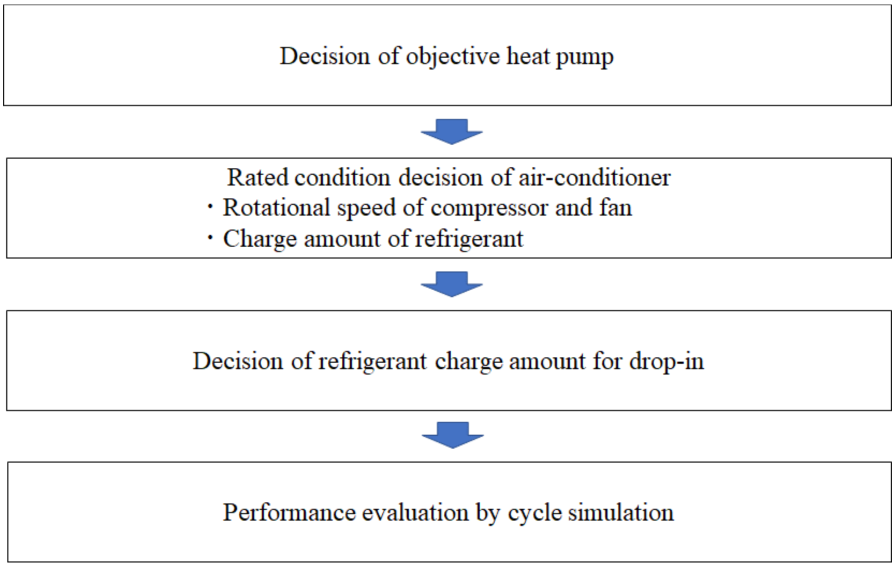

Fig. 4.3.2-2 Drop-in evaluation flow

4.3.2.5 Simulation condition

As reported in Table 4.3.2-3, a refrigerant charge of 0.6 kg for the R32 air conditioner was determined under the operating conditions that maximized the COP by manipulating the evaporator superheat, compressor speed, and refrigerant charge. Fig. 4.3.2-3 presents the relationship between the refrigerant fill volume, COP, and condenser outlet supercooling. Fig. 4.3.2-4 presents the Mollier diagram of the refrigeration cycle when the determined filling volume was used. The indoor and outdoor air conditions are listed in Table 4.3.2-4.

Table 4.3.2-3 エラー！ 参照元が見つかりません。 Simulation conditions

Manipulated variable	Operation method
Expansion valve opening degree	Super heat degree 5 K
Compressor rotational speed	40.7 rps, rated operation
Outdoor unit	20 W, rated operation
Indoor unit	40 W, rated operation

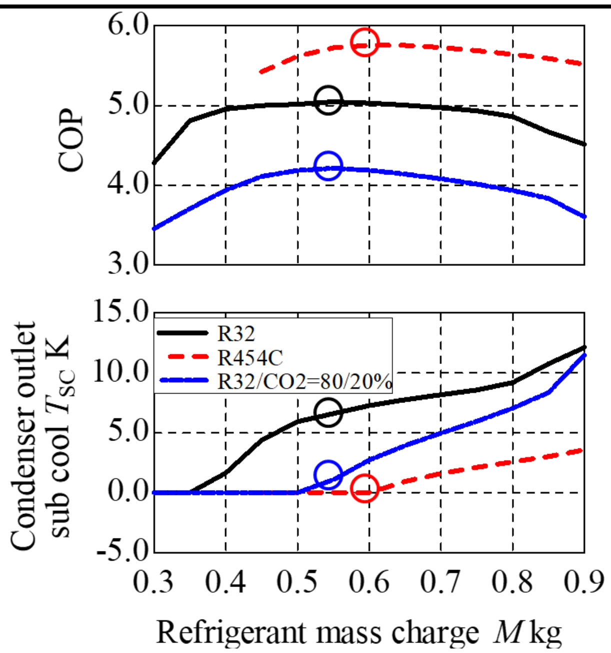

Fig. 4.3.2-3 Relationship between the refrigerant charge amount, COP, and condenser subcooling degree

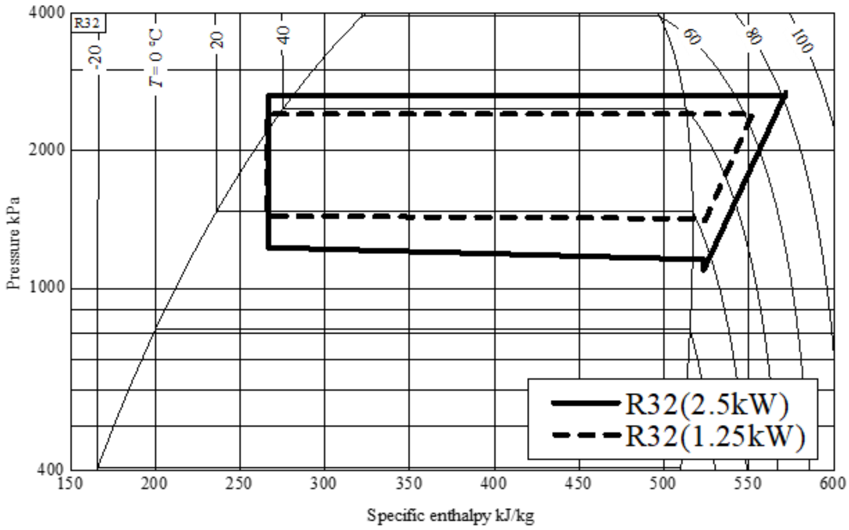

Fig. 4.3.2-4 Operation state on PH diagram (R32) with respect to the determined refrigerant charge amount

Table 4.3.2-4 Air conditions

Parameter	Unit	Value
Indoor unit fan mass flow rate	kg/s	0.214
Outdoor unit fan mass flow rate	kg/s	0.416
Indoor unit temperature	ºC	27 (dry)/19 (wet)
Outdoor unit temperature	ºC	35 (dry)/24 (wet)

4.3.2.6 Simulation results

This section describes the results obtained after comparing the performance of each refrigerant at the same cooling capacity. Figs. 4.3.2-5 and 4.3.2-6 present comparisons of the performance and thermophysical properties at 100% (2.5 kW) and 50% (1.25 kW) of the rated cooling capacity. Fig. 4.3.2-7 presents a Mollier diagram of the cycle at 100% and 50% cooling capacities. The vertical axes of the graphs presented in Figs. 4.3.2-5 and 4.3.2-6 were non-dimensionalized with respect to the physical property of R32.

First, we focused on R454C. As shown in Fig. 4.3.2-5, from a comparison of R32 and R454C at the same cooling capacity, R454C had a lower COP and larger pressure drop in the evaporator than R32. The COP of R454C was 41% lower than that of R32 at the rated cooling capacity standard because of the following reasons. First, its compressor suction density was 36% lower than that of R32. The lower density of R454C was caused by the refrigerant R1234yf with a high-boiling point, which accounted for 78.5% of the composition of R454C. As shown in the Mollier diagram presented in Fig. 4.3.2-7, the R454C cycle shifted to a lower pressure than the R32 cycle. This increased the flow velocity in the evaporator and pipes to achieve the same cooling capacity, in addition to the refrigerant pressure drop, thus resulting in an increase in the compressor power, which lowered the COP.

Second, its latent heat was smaller than that of R32. As shown in the Mollier diagram in Fig. 4.3.2-7, the latent heat of R454C was significantly smaller than that of R32, namely, 43% smaller when compared in terms of the rated cooling capacity. A smaller latent heat implies that a larger amount of refrigerant was required to be circulated to achieve the same cooling capacity, which increased the pressure drop.

The third factor contributing to the lower COP of R454C was its high-temperature glide. This is because the evaporation temperature decreased because of the pressure drop in the evaporator.

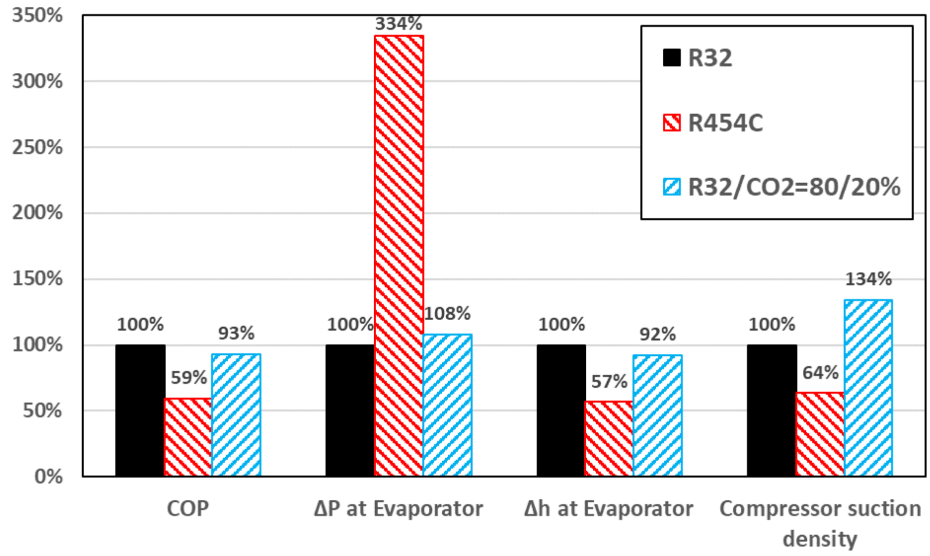

Fig. 4.3.2-5 Comparison of performance (2.5 kW at 100% of the rated cooling capacity)

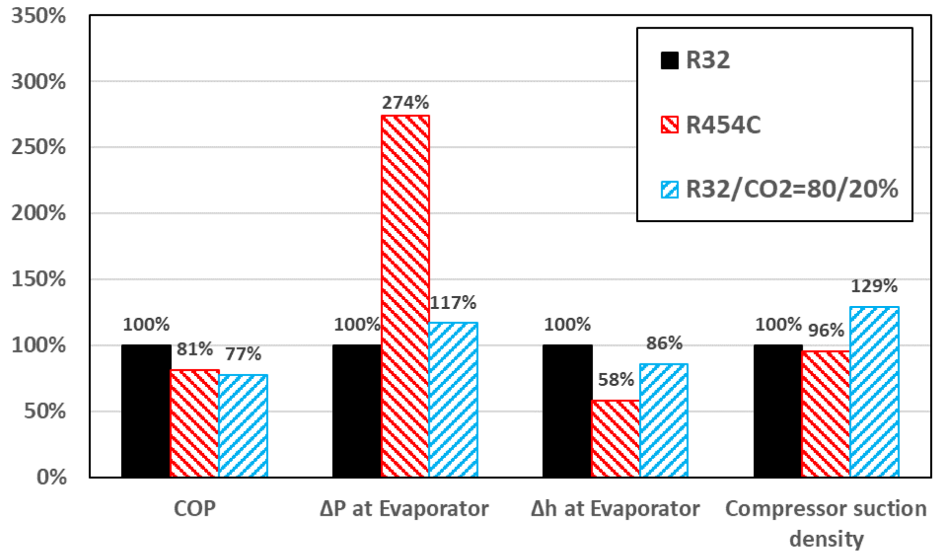

Fig. 4.3.2-6 Comparison of performance (1.25 kW at 50% of the rated cooling capacity)

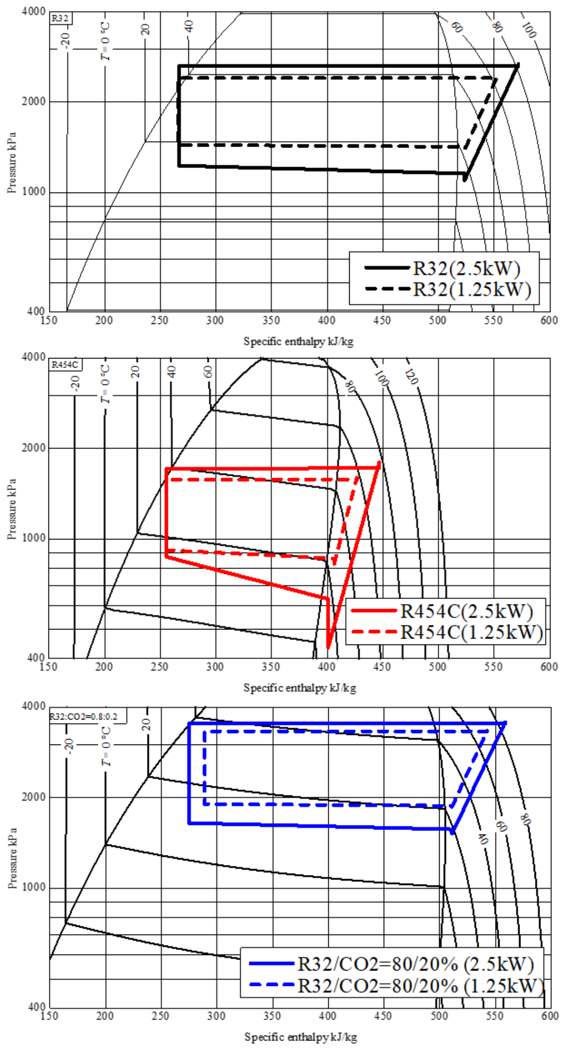

Fig. 4.3.2-7 Pressure–enthalpy diagram

4.3.2.7 Conclusion

The effect of the refrigerant properties on the performance was determined under the conditions of a constant compressor rotation speed and cooling capacity. Three refrigerant properties, namely, (1) the refrigerant density (gas density), (2) latent heat, and (3) temperature glide, were found to have a significant impact on the performance at drop-in.

A comparison was made between R454C and R32 at the same cooling capacity. In particular, R454C exhibited a lower COP than R32 and a larger pressure drop in the evaporator. The COP of R454C was 41% lower than that of R32 at the rated cooling capacity standard. This is because the compressor suction density of R454C was 36% lower than that of R32. The latent heat of R454C was smaller than that of R32. Moreover, R454C had a large temperature glide, which can be attributed to the lower evaporation temperature resulting from the large pressure drop in the evaporator.

4.3.3 Dynamic operation simulation

4.3.3.1 Background and purpose

To determine the next-generation refrigerant, in this study, a technique was developed to analyze the static and dynamic characteristics of an air-conditioning system employing various refrigerants, including a non-azeotropic mixture. All elements, such as the heat exchanger, were modeled based on the finite volume method. Thus, it is a highly versatile model that supports reverse fluid flow. Therefore, a wide range of dynamic analyses, including those involving compressor start/stop characteristics, can be realized. Furthermore, the mathematical model considers the transient and local compositional changes of the non-azeotropic refrigerant mixture and can reproduce their responses. In this study, the constructed high-precision model was used to evaluate the dynamic characteristics of a system using typical non-azeotropic mixed refrigerants (including R454C) during drop-in, and to clarify the underlying mechanism of the system performance and composition change when the cycle operates intermittently.

4.3.3.2 Objective system

This section covers the equipment that employs the single-stage compression refrigeration cycle described in Section 4.3.2. The dimensions of the components are the same as those listed in Table 4.3.2-1.

4.3.3.3 Simulation model

The analytical model is based on that used in Energy Flow + M, which was validated for numerous units. During the intermittent operation analysis, the composition ratio of the non-azeotropic refrigerant mixture should be considered because of the refrigerant flow with respect to time. The mathematical model and simulation method for the analysis of a refrigeration cycle with a two-component non-azeotropic refrigerant mixture are presented in Section 3.1.6. In this mathematical model, the following assumptions can be made for all elements, for practicality, given that the simulation is used to evaluate the performance of the system in terms of static and dynamic characteristics:

(1) The refrigerant flow is considered as one-dimensional.
(2) The two-phase refrigerant is in a vapor–liquid equilibrium.
(3) In the conservation of refrigerant energy, kinetic energy and gravitational potential are neglected.
(4) In the conservation of refrigerant momentum, the acceleration loss and potential loss are neglected, and only the friction loss is considered.
(5) The effect of refrigerant oil is neglected.

4.3.3.4 Simulation conditions

The specifications of the equipment and analysis conditions are listed in Tables 4.3.2-1 and 4.3.2-3. The reference refrigerant was R32, and the refrigerant charge amount was incremented by 50 g, whereas the cooling capacity was set as 2.5 kW and the evaporator outlet temperature as 5.0 °C. The value at which the COP was maximized corresponds to a refrigerant charge amount of 0.55 kg. A compressor speed of 40.7 rps at this instant was set as the rated speed of the system. The drop-in R454C charge was 0.6 kg.

4.3.3.5 Performance evaluation method at intermittent operation

The following is a method for calculating the average cooling capacity, average power consumption, and COP during intermittent operation conditions. One ON/OFF cycle of the compressor is considered as one period T, which is defined by the following equations for three cycles:

$$\bar{Q}_{cool} = \frac{1}{3T}\int_0^{3T} Q_{cool}dt \tag{4.3.3-1}$$

$$\bar{W}_{comp} = \frac{1}{3T}\int_0^{3T} W_{comp}dt \tag{4.3.3-2}$$

$$COP = \frac{\bar{Q}_{cool}}{\bar{W}_{comp}} \tag{4.3.3-3}$$

4.3.3.6 Simulation result

Fig. 4.3.3-1 presents the analysis results. In particular, the figure presents the cooling capacity, compressor power consumption, compressor inlet/discharge pressure, compressor speed, refrigerant mass distribution, R32 component of the circulating composition (compressor inlet and expansion valve inlet), and transient changes in the R32 component of the composition at the gas and liquid sides of the accumulator. For the cooling capacity, compressor power consumption, and compressor inlet/discharge pressure, the results obtained assuming a constant circulating composition at the inlet composition are presented as a solid red line and dashed red line, respectively.

Considering the refrigerant mass distribution, approximately 70% of the charged refrigerant was distributed in the high-temperature, high-pressure condenser during continuous operation; however, after the first compressor stopped operating, 70% of the refrigerant charge amount remained constant at the low-temperature evaporator side. After the compressor operation started, the refrigerant in the evaporator rapidly moved to the accumulator. In the accumulator, the refrigerant was separated into gas and liquid, and only the gas circulated in the cycle. Thus, the mass loss in the accumulator was low. Under the conditions of this analysis, the period of intermittent operation was shorter than the time required for all liquid in the accumulator to vaporize; therefore, approximately 20–50% of the refrigerant remained in the accumulator as a liquid after the first compressor start-up. During intermittent operation, the cooling capacity was lower than the 1.25 kW achieved during continuous operation due to the lack of refrigerant in the entire cycle. Additionally, we focused on the circulating composition of R32 and composition of R32 in the accumulator. Therefore, the R32 composition of the refrigerant that entered the accumulator in liquid form immediately after compressor start-up was lower than the sealed composition. Moreover, the R32 composition of the gas side and the refrigerant circulating inside the cycle were higher than the sealed composition. The R32 composition of the accumulator gas reached its peak immediately after the compressor started up and spread through the compressor to the entire cycle. During intermittent operation, the circulating composition of R32 in the cycle was higher than the contained composition of 0.215, given that the accumulator was always filled with liquid. We compared the analysis results with respect to the cooling capacity, compressor power consumption, and pressure before and after the compressor, assuming that the circulating composition was always the same as the composition in the cylinder. The analysis results were obtained considering the compositional change. The compressor inlet/discharge pressures were higher when the composition change was considered. This is because the composition of the R32 gas component was higher than that of the R454C fluid during intermittent operation. The analysis results reproduced the characteristics of the pure R32 refrigerant.

Table 4.3.3-1 lists the average cooling capacity, average power consumption, and COP from 9–27 min (three cycles). When the composition change was not considered, the cooling capacity and COP were 21.3% and 12.3% lower, respectively, than when the composition change was considered. This is because the analysis with composition change reproduced the phenomenon of the increase in the R32 component of the circulating refrigerant during intermittent operation, and the cycle characteristics approached those of the pure R32 refrigerant. In particular, an analysis that assumes that the circulating composition is always constant with the composition of the contained refrigerant may underestimate the performance of non-azeotropic mixed refrigerants during intermittent operation.

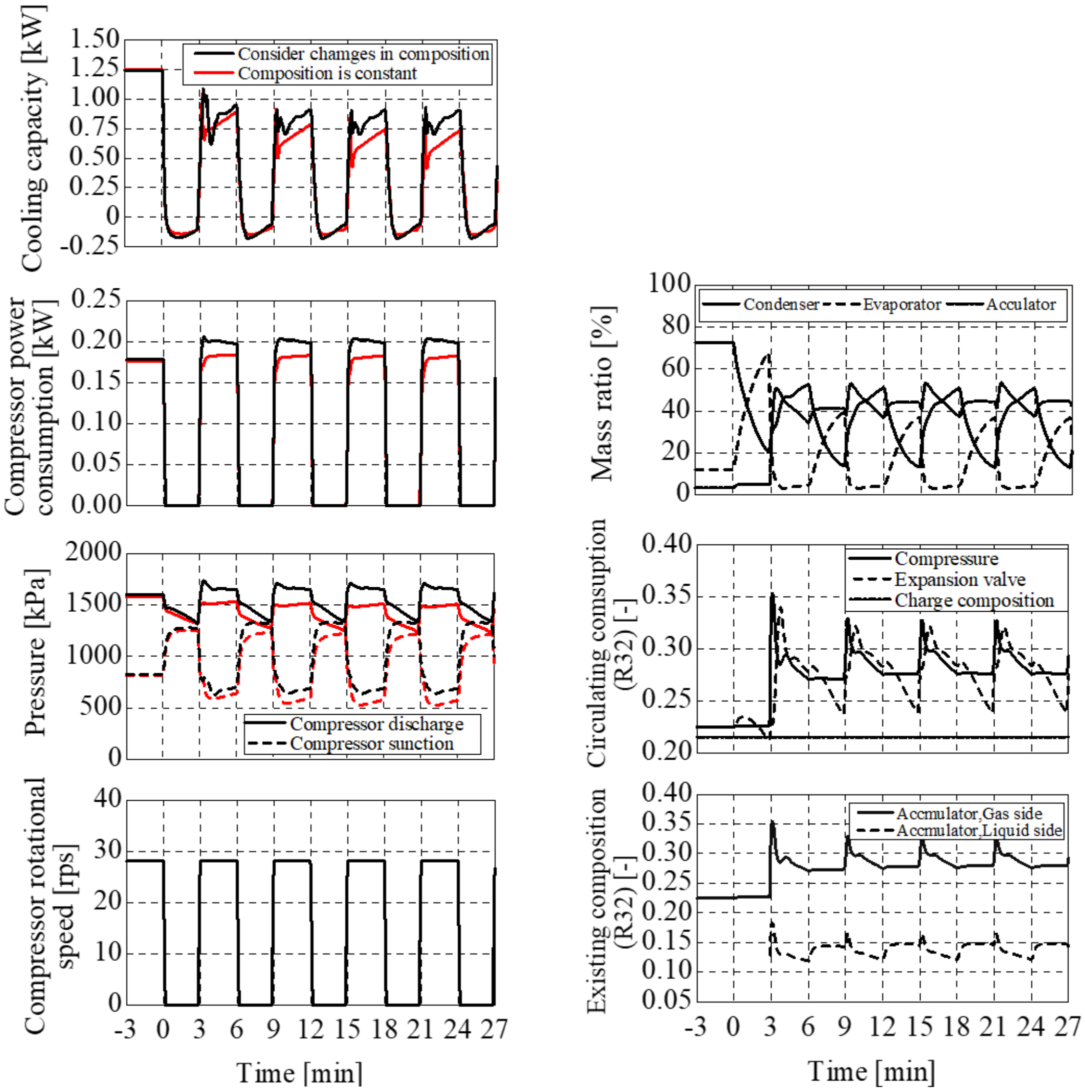

Fig. 4.3.3-1 Intermittent operation of the refrigeration cycle (R454C)

Table 4.3.3-1 Performance during intermittent operation

	Different composition	Constant composition
Cooling capacity, kW	0.395	0.311
Compressor power, kW	0.104	0.0932
COP	3.81	3.34

Subsequently, the average cooling capacity of the system with R454C in intermittent operation was compared with the performance of the two systems when the same cooling capacity was ensured in continuous operation. This allowed for a quantitative evaluation of the decrease in performance or increase in energy consumption due to intermittent operation.

Fig. 4.3.3-2 presents the analysis results, namely, the cooling capacity, power consumption, inlet/discharge pressure, and speed of the compressor. The black solid and dashed lines indicate the results for intermittent operation, and the red solid and dashed lines indicate the results for continuous operation. Table 4.3.3-2 lists the compressor speed, cooling capacity, compressor power consumption, and COP for the two modes. The cooling capacity of 0.395 kW corresponds to a partial load of 15.8% relative to the rated cooling capacity of 2.5 kW.

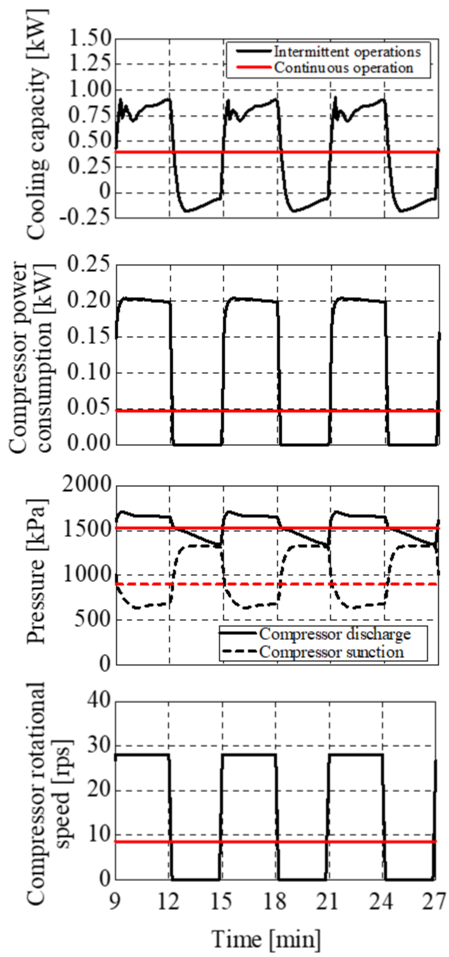

Fig. 4.3.3-2 Comparison between intermittent and continuous operation (R454C)

As reported in Table 4.3.3-2, a performance comparison at the same cooling capacity in continuous and intermittent operation revealed that the COP in intermittent operation was 59.9% smaller than that observed under continuous operation. In this analysis, the various compressor efficiencies were assumed to be constant, regardless of the load and speed. However, in practice, the compressor does not operate continuously at extremely low speeds, and the efficiency decreases significantly. Hence, the performance of the continuous operation in this analysis was overestimated.

The following are possible reasons for the lower performance in intermittent operation when compared with continuous operation in this analysis.

The high-temperature refrigerant flowed from the high-pressure side to the low-pressure side while the compressor was stopped, which led to the combination of thermal energy and increasing entropy, thus resulting in energy loss.

The refrigerant placed on the low-pressure side during the compressor stoppage was moved to the high-pressure side, which consumed excessive input power.

During intermittent operation, a portion of the refrigerant remained in the accumulator as liquid, thus causing a shortage of refrigerant in the entire cycle, which resulted in a low-efficiency operation.

Table 4.3.3-2 Performance comparison between intermittent and continuous operation conditions

Operation	unit	Intermittent	Continuous
Cooling capacity	kW	0.395(Part load 15.8%)	
Compressor rotational speed	rps	28.0(ON/OFF every 3 minutes)	8.61
Compressor power consumption	kW	0.104	0.0475
COP	-	3.34	8.32

4.3.3.7 Conclusion

In this study, we established an analytical technique that considers local and transient compositional changes in non-azeotropic refrigerant mixtures and analyzed the system performance during intermittent operation. The model was used to analyze the dynamic characteristics of systems using non-azeotropic refrigerant mixtures, and the following conclusions were drawn:

The performance of a system using R454C in intermittent operation conditions was analyzed using a model that considers compositional changes and assumes a constant value. Consequently, the cooling capacity and COP were evaluated as high, given that the model considering the composition change reproduced the increase in the R32 composition ratio of the circulating refrigerant immediately after start-up.

The performance of the R454C system when operated at a load factor of 15.8% was analyzed for the continuous and intermittent operation conditions. The results demonstrated that the COP was 59.9% lower in intermittent operation than in continuous operation owing to an energy loss during the system operation.

4.3.4 LCCP analysis

The LCCP analysis portion of this study was focused on room air conditioners and heat pump water heaters, which are two representative product types currently undergoing refrigerant switching, and parametric studies were performed to evaluate the degrees of importance of the various terms in the LCCP equations for each.

Air conditioners are a common subject of LCCP research. Several reports on LCCP evaluations and the energy consumption of air conditioners were published using different standards and calculation methods. Kamel[3] accumulated data describing ambient air temperature and used a data-driven method to calculate the annual air conditioner load. Hanlong[4] calculated the annual load based on the AHRI 210/240 (2017) standard, and then used a validated mathematical model to calculate the annual energy consumption. Troch[5] used the AHRI 210/240 standard with the temperature bin method to calculate energy consumption and perform an LCCP evaluation. Wu[6] compared the results calculated using the Chinese GB 12021.3-2010[7], US ANSI/AHRI 210/240-2008[8], Japanese JIS C9612:2013[9], European BS EN 14825-2012[10], and Australian AS 3823.2-2013[11] standards.

As it is necessary to phase out refrigerants such as R410A to replace them with next-generation low-GWP refrigerants, research was recently conducted on various potential refrigerant types, the corresponding mass charges, and the resulting performances of heat pump systems. Hihara[12] compared the performances and LCCP results for heat pumps using R410A, R32, and R1234yf refrigerants, and concluded that the replacement of conventional refrigerants is essential for heat pump systems that require a large amount of refrigerant mass charge. Chen[13] conducted LCCP evaluations on air conditioners using R22 and R410A as refrigerants. Tian[14] conducted experiments to compare the performances of the R32, R290, and R410A refrigerants. In this study, a simulation was conducted based on JIS C9612:2013[9] and used to predict the annual electricity consumption of air conditioners under the weather conditions of the following cities: Sapporo, Tokyo, and Naha. An LCCP evaluation was then conducted based on the simulation results.

The use of CO_2 (R744) in heat pump water heaters increased consistently from 2001 onward. As a result, previous research on the performance of heat pump water heaters was generally focused on the use of CO_2 as a working fluid[18-22]. Soh and Dubey[20] conducted experiments and collected data indicating that if the hot water outlet temperature is increased from 65 °C to 80 °C, the COP of the system decreases from 5.4 to 3.8; and Nawaz[19] confirmed this inverse ratio between COP and water supply temperature. However, limited research has been conducted on the evaluation the LCCP of heat pump water heaters. In this study, simulations of heat pump water heaters were conducted and applied to predict unit performance under the weather conditions for the cities of Sapporo, Tokyo, and Naha. Notably, unlike air conditioners, heat pump water heaters require hot water storage tanks for operation. Thus, parametric studies were conducted on tank performances. Thereafter, LCCP evaluations were performed, and the results were compared to discuss potential approaches for LCCP minimization.

According to previous research, CO_2 emissions due to electricity consumption are typically the dominant factor in the LCCP evaluations; therefore, the accuracy of this aspect is critical to the accuracy of the overall evaluation. In most previous research that involved LCCP evaluation, the LCCP equation proposed by the IIR Guideline[23] was employed, in which CO_2 emissions due to electricity consumption were calculated as the product of electricity consumption and a CO_2 emission factor, which is typically defined as the annual average value for the target location. The most common method to obtain CO_2 emission factor data is via reports released by the government or electric companies, as recommended by Iran, Islamic Republic (IIR). Additionally, the CO_2 emission factor can be calculated from data describing the composition of power generation methods and the CO_2 emission factor associated with each[24-25]. However, the composition of power generation methods constantly changes. Although several studies were conducted to investigate the variation of the CO_2 emission factor[29-35], this variation was not related to the LCCP evaluation. In this study, a time-series LCCP evaluation method that considers the variation in the CO_2 emission factor with the composition of power generation methods was therefore proposed to enhance the accuracy of the LCCP calculation. The proposed time-series LCCP evaluation method was then applied to air conditioners and heat pump water heaters.

4.3.4.1 Parametric study on the LCCP owing to direct emissions

First, a parametric study was conducted to determine the effects of various system parameters on the direct emissions, which are independent of the operating conditions. Figs. 4.3.4-1, 4.3.4-2, and 4.3.4-3 present the effects of the annual refrigerant leakage rate, refrigerant mass charge, and refrigerant recycling leakage (end-of-life refrigerant leakage (EOL)) on the direct emissions of CO_2.

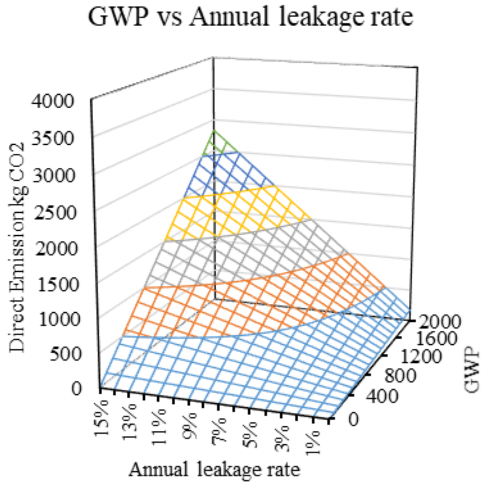

Fig. 4.3.4-1 Effects of annual refrigerant leakage rate and GWP on direct CO_2 emissions

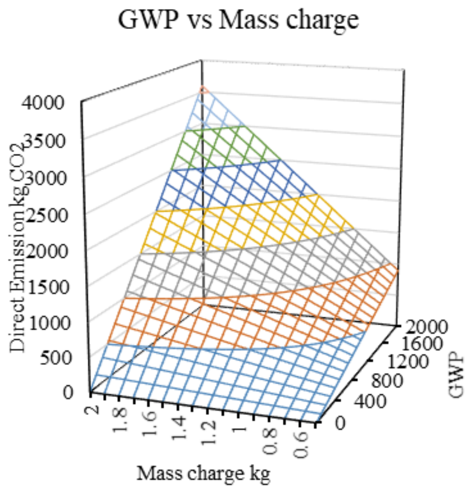

Fig. 4.3.4-2 Effects of refrigerant mass charge and GWP on direct CO_2 emissions

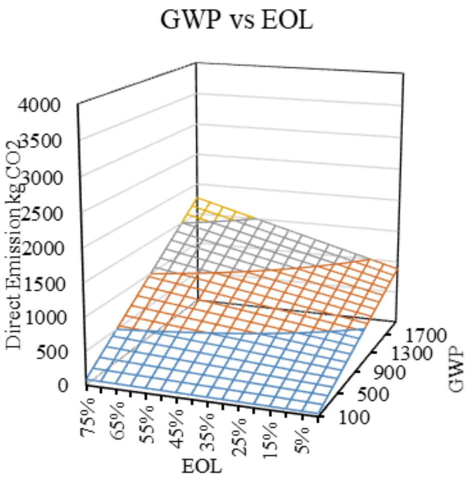

Fig. 4.3.4-3 Effects of refrigerant EOL and GWP on direct CO_2 emissions

The results suggest that direct emissions are more sensitive to the annual refrigerant leakage rate and refrigerant mass charge than the EOL. This is because in the LCCP equation, the annual refrigerant leakage rate and refrigerant mass charge are both multiplied by the life span, whereas the EOL is considered as a one-time leakage event.

Parametric studies of the annual leakage rate and refrigerant mass charge were then conducted using the R1234yf, R32, and R410a refrigerants, which were selected as representative low-, medium-, and high-GWP refrigerants; the results of which are shown in Figs. 4.3.4-4, 4.3.4-5, and 4.3.4-6, respectively.

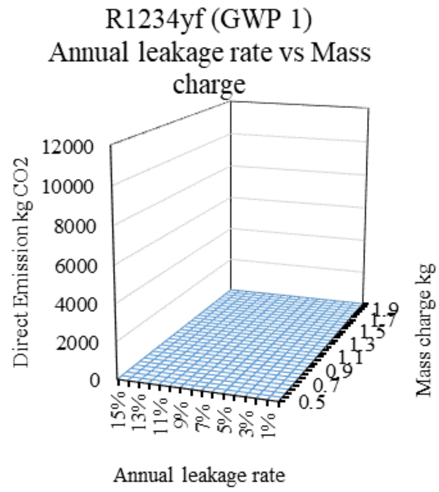

Fig. 4.3.4-4 Effects of refrigerant mass charge and annual leakage rate of R1234yf on direct CO_2 emissions

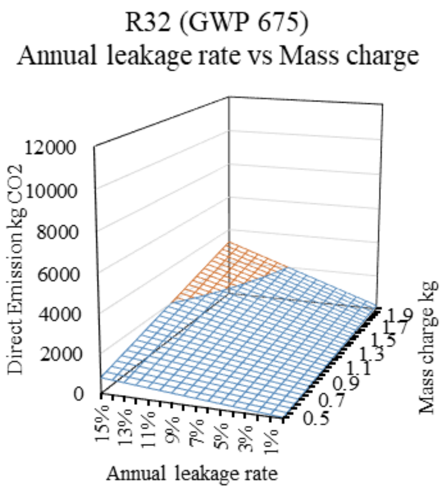

Fig. 4.3.4-5 Effects of refrigerant mass charge and annual leakage rate of R32 on direct CO_2 emissions

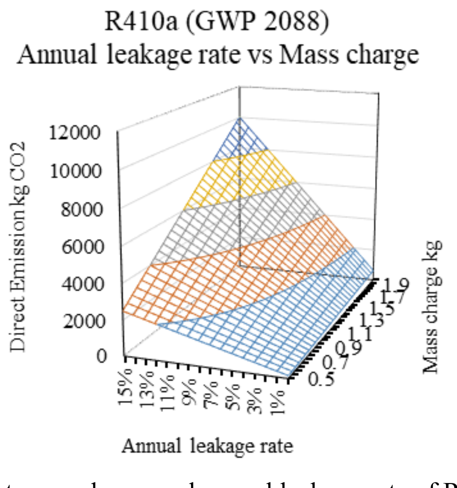

Fig. 4.3.4-6 Effects of refrigerant mass charge and annual leakage rate of R410a on direct CO_2 emissions

The results of the parametric studies suggest that for low-GWP refrigerants such as R1234yf, the direct emissions are significantly small, regardless of the leakage rate or mass charge. For R32, however, minimizing the annual leakage rate and refrigerant mass charge is critical due to its medium-level GWP. Finally, direct emissions are significantly sensitive to the annual leakage rate and mass charge of R410a due to its elevated GWP of 2088. Therefore, the sealing and minimization of the refrigerant mass charge are critical for heat pump systems using R410a as the working fluid.

4.3.4.2 Mathematical model for indirect emissions

In this study, domestic room air conditioners and heat pump water heaters were evaluated to conduct LCCP evaluations using six different refrigerants: R454C, R410A, R466A, R32, R290, and R1234yf. To calculate the annual energy consumption required to determine indirect emissions, an annual performance prediction simulation was constructed for each type of target equipment.

(1) Air conditioner

The heating and cooling loads used in the air conditioner simulation were calculated based on equations from the JIS C 9612:2013 standard using hourly ambient air temperature data from the Japan Meteorological Agency (JMA). These data were then used to construct a thermal dynamic cycle for the calculation of annual electricity consumption. Table 4.3.4-1 presents the conditions and assumptions for the load calculation. 本研

Table 4.3.4-1 Calculation conditions for air conditioner load

Parameter	Condition
Operational time	6:00–24:00
Ambient air temperature	JMA hourly data (8760 data points annually)
Heating/Cooling load	Based on methods in JIS C 9612:2012 Annex B
Rated capacity	2.2 kW

The target locations considered in this study were Sapporo, Tokyo, and Naha, which were selected as representatives of the Japanese winter, interim, and summer seasons. Figs. 4.3.4-7 and 4.3.4-8 present the annual heating/cooling loads and air conditioner operating times, respectively, for the subject locations. Table 4.3.4-2 lists the assumptions used to calculate the annual energy consumption based on the JMA data.

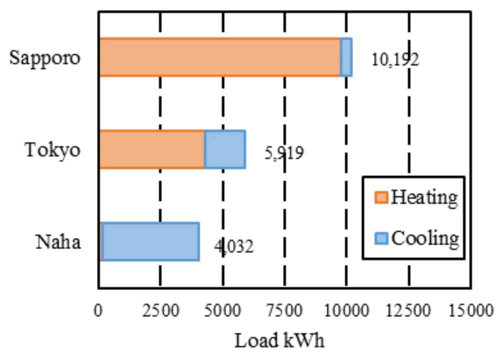

Fig. 4.3.4-7 Annual air conditioner heating/cooling loads (based on JIS)

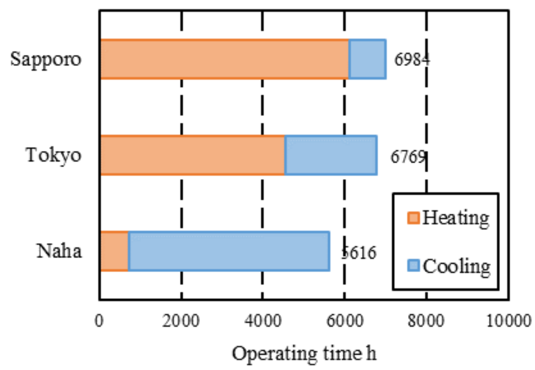

Fig. 4.3.4-8 Annual air conditioner operating times (based on JIS)

Table 4.3.4-2 Conditions and assumptions for the calculation of annual energy consumption

Parameter	Condition
Adiabatic efficiency	0.7
T_{air} - T_{evp}	10 °C (at rated)
T_{con} - T_{room}	10 °C (at rated)
Super heating temp	5 °C
Sub cooling temp	5 °C
Standby power	1 W

Based on research conducted by the Japan Society of Refrigerating and Air Conditioning Engineers (JRA), the average air conditioner operating time in Tokyo was 2272 h, thus suggesting that the annual air conditioner operating time calculated using JIS C9612:2013 is significantly longer than in practice. To compensate for this error, the JRA and JIS results were compared, and 53% of the latter was considered as the annual rate of operation. The annual energy consumption was then corrected using this revised annual rate of operation for the six considered refrigerants, as shown in Figs. 4.3.4-9, 4.3.4-10, and 4.3.4-11.

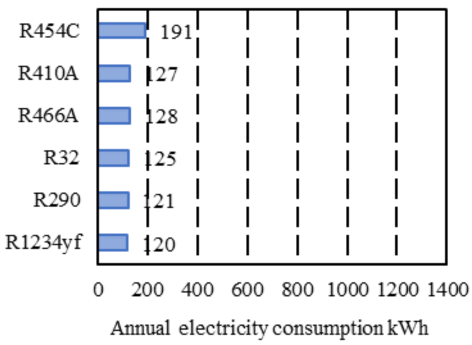

Fig. 4.3.4-9 Annual electricity consumption (Naha)

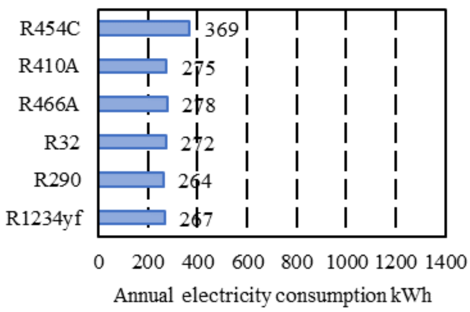

Fig. 4.3.4-10 Annual electricity consumption (Tokyo)

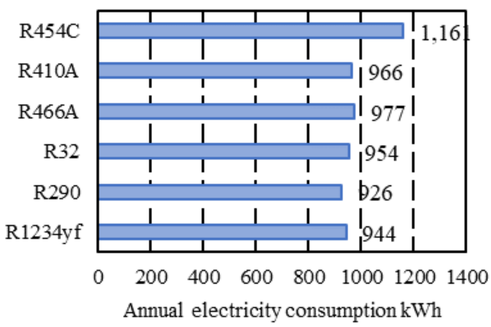

Fig. 4.3.4-11 Annual electricity consumption (Sapporo)

(2) Heat pump water heaters

A simplified mathematical model based on thermal dynamic cycle analysis and a detailed model based on heat transfer were constructed for heat pump water heaters and validated by comparison with experimental results. The detailed model was calculated using the EF + M simulation software, and the simple model was calculated using the pinch mode[138)]. The annual energy consumption and LCCP were then calculated using the weather data for the target cities.

(a) Heating performance experiments

The mathematical model was validated by comparing its results with those obtained from heating performance experiments. The experiments were conducted in accordance with the JIS C9220 standard to evaluate the performance of the subject R32 heat pump water heater under standard winter, interim, summer, and hot climate conditions. Steady heating performance data were obtained during the experiments. Table 4.3.4-3 lists the experimental conditions and Table 4.3.4-4 provides the specifications of the water heater.

Table 4.3.4-3 Air and water temperature settings for the heat pump water heater experiments

Condition	Dry bulb air temperature ℃	Wet bulb air temperature ℃	Water temperature ℃
Winter	7.1	5.9	9.4
Interim	16.7	12.1	17.5
Summer	25.1	21.7	24.9
Hot climate	35.0	25.1	29.7

Table 4.3.4-4 Specifications the of subject heat pump

Parameter	Settings
Mass charge	0.59 kg
Rated capacity	4 kW
Refrigerant	R32
Hot water outlet	65 ℃

Fig. 4.3.4-12 presents the calculated system COP, including the cycle COP of the equipment and the power consumption of the outdoor unit. The results indicate that the COP of the heat pump water heater decreased as the temperature decreased.

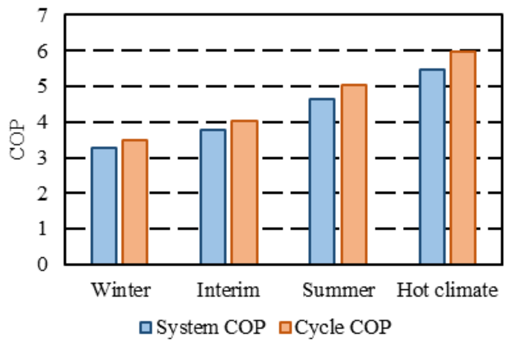

Fig. 4.3.4-12 Experimental heat pump and system COPs

(b) Annual electricity consumption

Fig. 4.3.4-13 presents the simulation results obtained using the detailed and simplified models, in which DS indicates the detailed model and SS indicates the simplified model.

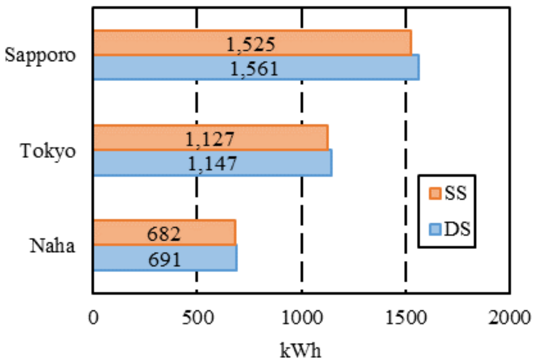

Fig. 4.3.4-13 Electricity consumption of the target heat pump water heater

The detailed model provided only a slightly larger electricity consumption for all three cities. The simplified model was therefore used to calculate the annual electricity consumption when using the six different refrigerants as shown in Figs. 4.3.4-14, 4.3.4-15, and 4.3.4-16.

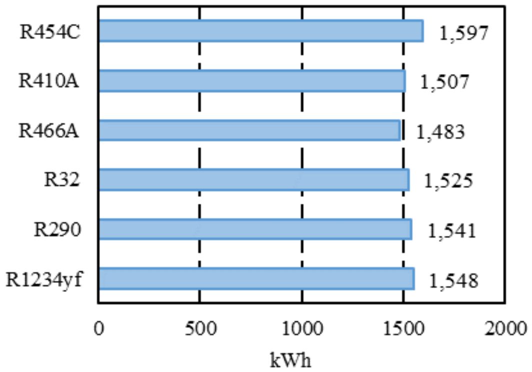

Fig. 4.3.4-14 Annual electricity consumption of the heat pump water heater in Sapporo with respect to the refrigerants

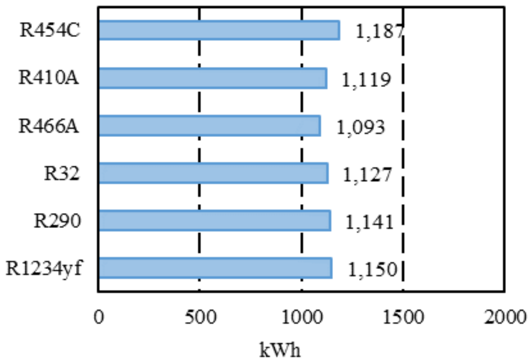

Fig. 4.3.4-15 Annual electricity consumption of the heat pump water heater in Tokyo with respect to the refrigerants

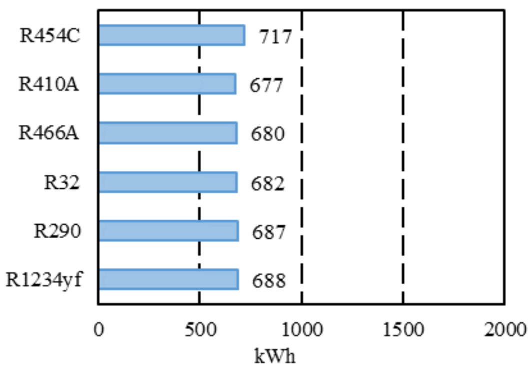

Fig. 4.3.4-16 Annual electricity consumption of the heat pump water heater in Naha with respect to the refrigerants

Based on these results, R466A was determined as the most efficient refrigerant for Tokyo and Sapporo, whereas R410A exhibited the highest efficiency for Naha. Moreover, although the electricity consumption of the water heater was relatively high when using R454C, all other refrigerants exhibited similar performances.

(3) Parametric study on the LCCP

The annual electricity consumptions of the air conditioners and heat pump water heaters described in the previous sections were used to perform the LCCP evaluation using the calculation conditions and factors of each target refrigerant, as presented in Tables 4.3.4-5 and 4.3.4-6, in which AC indicates an air conditioner and HPWH indicates a heat pump water heater.

Table 4.3.4-5 Assumptions and conditions for calculation of LCCP due to indirect emissions

Parameter	Tokyo	Naha	Sapporo
EM (kg CO_2/ kWh)	0.455	0.787	0.656
ALR		5%	
EOL		15%	
m		40 kg	
mr		20 kg	
C		0.59 kg	
L		15 years	
MM (kg CO_2/kg)		2.326	
RM (kg CO_2/kg)		0.056	

Table 4.3.4-6 Target refrigerants and their corresponding *GWP*, *RFM*, and *RFD* values

Refrigerant	*GWP* (kg CO2)	*RFM* (kg CO2/ kg)	*RFD*(2) (kg CO_2/ kg)
R1234yf	1	13.7	0
R290	3	0.05	0
R32	675	7.2	0
R466A	733	7.2(1)	0
R410A	2088	10.7	0
R454C	148	12.3(1)	0

(1) R466A and R454C are mixed refrigerants; therefore, the value of R32 was used for R466A, and the R32:R1234yf ratio was used for R454C.

(2) The refrigerant recycling emission factors were assumed to be zero in this study owing to a lack of available data.

(a) Air conditioners

The assumptions and annual electricity consumptions reported in the previous sections were used as inputs to the LCCP equation, and the results are shown for the three target cities in Figs. 4.3.4-17, 4.3.4-18, and 4.3.4-19.

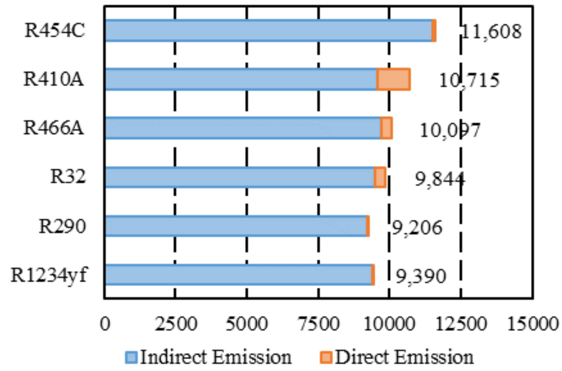

Fig. 4.3.4-17 The LCCP results for an air conditioner in Sapporo with respect to the refrigerants

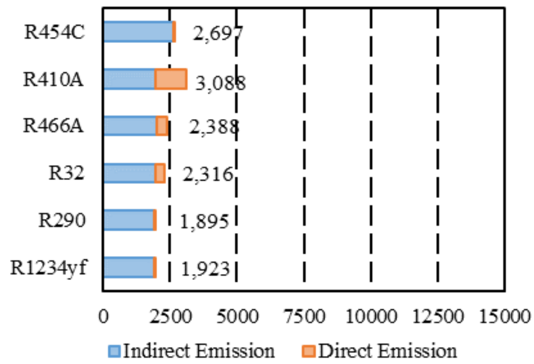

Fig. 4.3.4-18 The LCCP results for an air conditioner in Tokyo with respect to the refrigerants

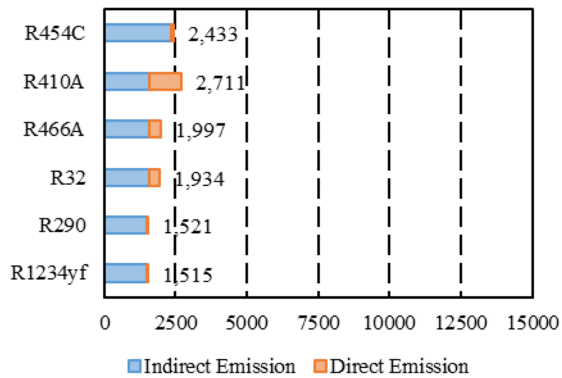

Fig. 4.3.4-19 The LCCP results for an air conditioner in Naha with respect to the refrigerants

Due to higher heating and cooling loads, both the electricity consumption and LCCP were the largest in Sapporo. However, the electricity consumption in Naha was nearly half of that in Tokyo, although a higher CO_2 emission factor in Naha caused the LCCP results for the two cities to be highly similar.

From a comparison of the refrigerant performances, R290 and R1234yf clearly exhibited superior efficiencies, and due to their extremely low GWPs, their corresponding LCCP results were relatively low. In Sapporo, the LCCP of R454C was the highest due to its high associated electricity consumption. In Tokyo and Naha, the indirect emissions were small because the annual load was relatively small, and R410A has a GWP, it provided the highest LCCP results.

(b) Heat pump water heaters

The annual electricity consumption results described in the previous section were used to determine the LCCP results for the heat pump water heaters in the different target cities, as shown in Fig. 4.3.1-20, in which DS indicates the use of the detailed model and SS indicates the use of the simplified model.

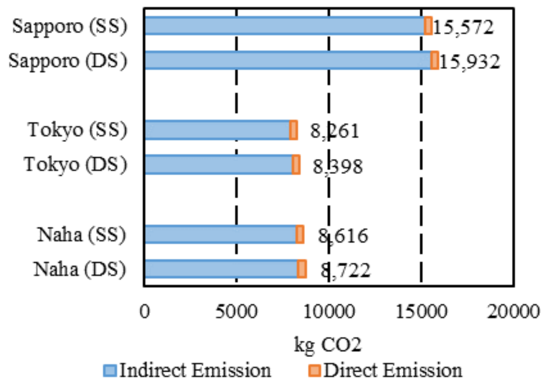

Fig. 4.3.4-20 The LCCP results for heat pump water heaters based on the DS and SS methods

The LCCP was the highest in Sapporo due to its generally low temperature. Although the electricity consumption was the lowest in Naha, it exhibited the highest CO_2 emission factor, thus, its LCCP results were higher than those in Tokyo.

The annual electricity consumption results obtained in Section 4.3.4.2.2.2 were then applied to conduct an LCCP evaluation in each target city with respect to each refrigerant, and the results are shown in Figs. 4.3.4-21, 4.3.4-22, and 4.3.4-23.

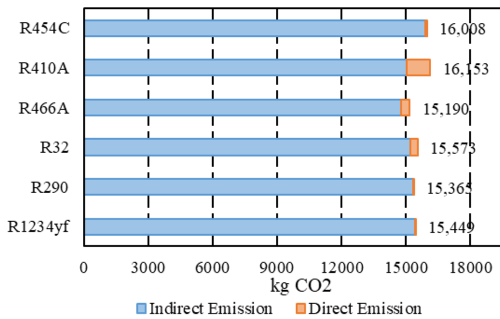

Fig. 4.3.4-21 The LCCP results for a heat pump water heater in Sapporo with respect to the refrigerants

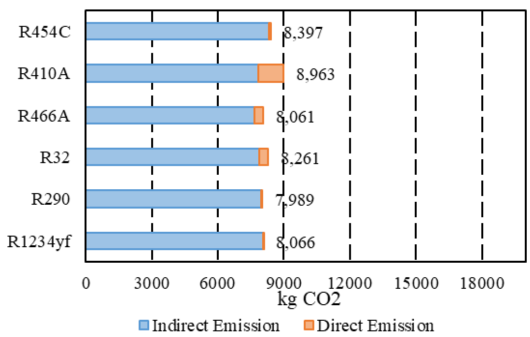

Fig. 4.3.4-22 The LCCP results for a heat pump water heater in Tokyo with respect to the refrigerants

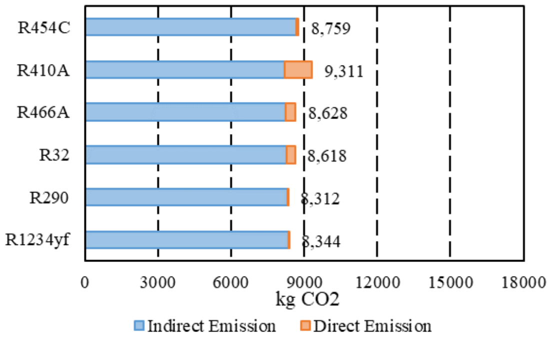

Fig. 4.3.4-23 The LCCP results for a heat pump water heater in Naha with respect to the refrigerants

Given that the use of R454C required a relatively high electricity consumption, the corresponding LCCP results were relatively high. Although R410A exhibited a suitable efficiency, it demonstrated an extremely high GWP; thus, its LCCP was the highest in all three cities.

Notably, a heat pump water heater operates independently of hot water usage, and the performance of the water storage tank influences the overall electricity consumption. To clarify this relationship, a parametric study was conducted by changing the thermal conductivity of the tank insulation material, with the resulting annual electricity consumptions in each target city shown in Figs. 4.3.4-24, 4.3.4-25, and 4.3.4-26.

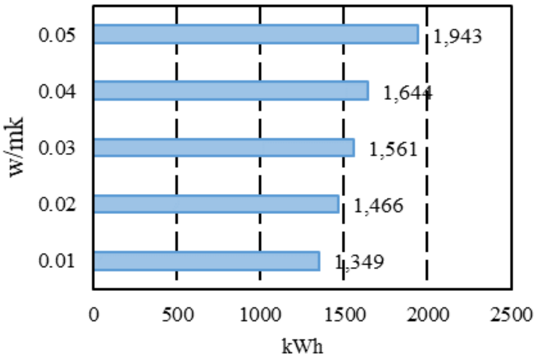

Fig. 4.3.4-24 Effects of insulation material on the electricity consumption of a heat pump water heater in Sapporo

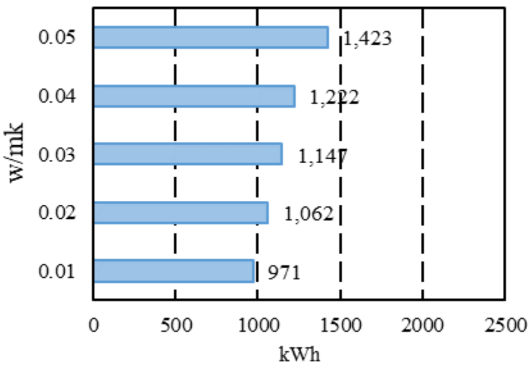

Fig. 4.3.4-25 Effects of insulation material on the electricity consumption of a heat pump water heater in Tokyo

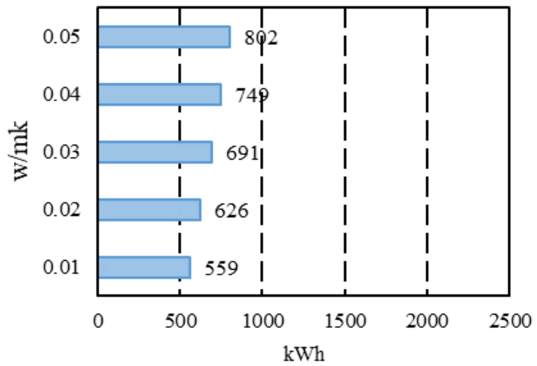

Fig. 4.3.4-26 Effects of insulation material on the electricity consumption of a heat pump water heater in Naha

Thereafter, LCCP evaluations were conducted for the subject locations using the annual electricity consumption results for the different insulation materials. The results are shown in Figs. 4.3.4-27, 4.3.4-28, and 4.3.4-29.

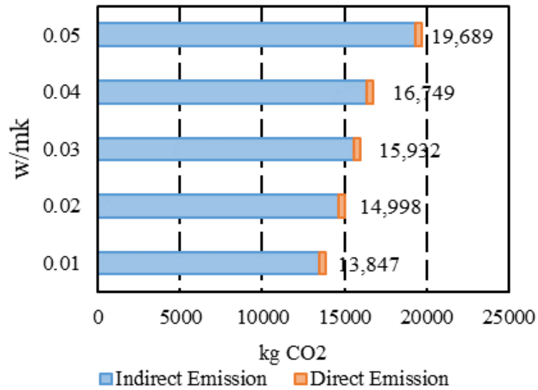

Fig. 4.3.4-27 The LCCP based on annual electricity consumption of a heat pump water heater in Sapporo with respect to the insulation material

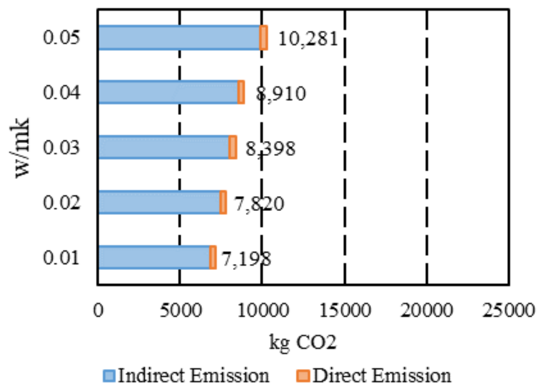

Fig. 4.3.4-28 The LCCP based on annual electricity consumption of a heat pump water heater in Tokyo with respect to the insulation material

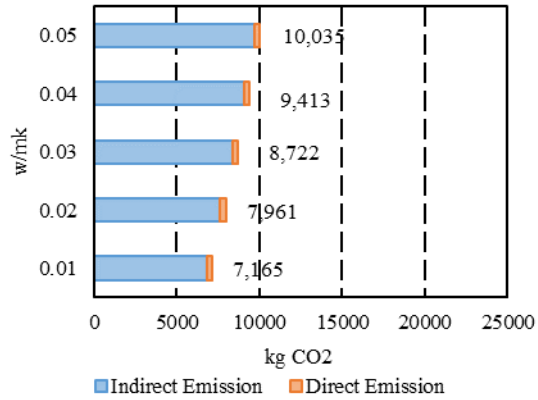

Fig. 4.3.4-29 The LCCP based on annual electricity consumption of a heat pump water heater in Naha with respect to the insulation material

The results of this parametric study indicate that the electricity consumption increased as the thermal conductivity of the hot water tank increased, especially in Sapporo, where the ambient air temperature was lower. Therefore, the performance of the insulation material should be considered as critical when minimizing the electricity consumption and LCCP of a heat pump water heater.

4.3.4.3 Summary of the analysis results obtained using the LCCP simulator

Parametric studies were conducted to analyze the degrees of importance of various factors in the LCCPs for air conditioners and heat pump hot water heaters, to thereby inform the ongoing shift to next-generation low-GWP refrigerants. The results indicated that the annual leakage rate and refrigerant mass charge had a minimal effect on the LCCPs for low-GWP refrigerants such as R1234yf and R290. However, for heat pumps using high-GWP refrigerants such as R410A, the minimization of annual leakage rate and refrigerant mass charge is critical.

The LCCP was indirectly and significantly influenced by the power consumption of the equipment. For both room air conditioners and heat pump water heaters, all the considered refrigerants, with the exception of R454C, demonstrated similar performances with respect to efficiency. In addition, although the power consumption of the heat pump water heater was smaller in Naha than in Tokyo, the LCCP was higher in Naha in Tokyo due to the difference between the CO_2 emission factors for the two cities.

References

1) Andersen., S., The implications to the Montreal protocol of the inclusion of HFCs and PFCs in the Kyoto protocol, 1999, pp. 37-38
2) Andersen., S., Life Cycle Climate Performance Metrics and Room AC Carbon Footprint, 2018, pp. 25
3) Kamel, E., Sheikh, S., Typical meteorological year and actual weather data in data driven machine learning models for residential building energy use, 2020, Proceedings of the 2020 ASHRAE Virtual Conference, ASHRAE, pp. 88-95
4) Wan., H., Comprehensive Investigations on Life Cycle Climate Performance of Unitary Air-Conditioners, 2021, pp. 332-341
5) Troch., S., LCCP evaluation on various vapor compression cycle options and low GWP refrigerants, 2016, pp. 133-134
6) Wu, J., Xu, Z, Jiang, F., Analysis and development trends of Chinese energy efficiency standards for room air conditioners, Energy Policy, 2019, 125, 368–383.
7) GB 12021. 3-2010, 2010a. The Minimum Allowable Value of the Energy Efficiency and Energy Efficiency Grades for Room Air Conditioners. Standards Press of China, Beijing.
8) ANSI/AHRI 210/240-2008, 2008. Performance Rating of Unitary Air-Conditioning & AirSource Heat Pump Equipment. Air-Conditioning, Heating, and Refrigeration Institute, Arlington, VA.
9) JISC 9612:2013, 2013. Room Air Conditioner. Japanese Industrial Standards Committee, Tokyo.
10) BS EN 14825-2012, 2012. Air conditioners, liquid chilling packages and heat pumps, with electrically driven compressors, for space heating and cooling-Testing and rating at part load conditions and calculation of seasonal performance. British Standards Institution, London
11) AS/NZS 3823.2:2013, 2013. Performance of electrical appliances—Air conditioners and heat pumps Part 2: Energy labelling and minimum energy performance standards (MEPS) requirements. Standards Australia International, Sydney; Standards New Zealand, Wellington.
12) Horie, H., Kamiaka, K., Dang, C., Hihara., E., Study on Cycle Property and LCCP Evaluation of Heat Pump Using

Hfo-1234YF, Hfc-32, And Hfc-410a As Refrigerant, 2010, pp. 8.
13) Chen., W., A comparative study on the performance and environmental characteristics of R410A and R22 residential air conditioners, Applied Thermal Engineering, 2007, 28.
14) Tian, Q., Cai, D., Ren, L., Tang, W., Xie, Y., He, G., Liu., F., An experimental investigation of refrigerant mixture R32/R290 as drop-in replacement for HFC410A in household air conditioners, International Journal of Refrigeration, 2015, pp. 216-228.
15) Horie, H., Itoh, M., Hihara, E., Annual Performance and Performance Rating of Air Conditioners 1st Report: Packaged Air Conditioners.
16) Zhang, J., Qin, Y, Wang, C., Review on CO2 heat pump water heater for residential use in Japan, Renewable and Sustainable Energy Reviews, 2015, 50, pp. 1383-1391.
17) Saito, K., Latest heat pump technologies in Japan. In: Proceeding of 13th IEA Heat Pump Conference, Rotterdam, Netterland, 2017, pp. 1-15
18) Alabdulkarem, A., Eldeeb, R., Hwang, Y., Aute, V., Radermacher., R., Testing, simulation and soft-optimization of R410A low-GWP alternatives in heat pump system, International Journal of Refrigeration, 2015, pp. 106-117
19) Nawaz, K., Shen, B., Elatar, A., Baxter, V., Abdelaziz., O., Performance optimization of CO2 heat pump water heater, International Journal of Refrigeration, 2018, 85, pp. 213-228
20) Soh, A., Dubey, S., Performance Study of CO2 Heat Pump under Tropical Conditions of Singapore., Energy Procedia, 2019, 158, pp. 1366–1371
21) Arif Hepbasli, Yildiz Kalinci., A review of heat pump water heating systems, Renewable and Sustainable Energy Reviews., 2019, Vol. 13, pp 1211-1229.
22) Zhang, J., Wang, R.Z., Wu., J.Y., System optimization and experimental research on air source heat pump water heater, 2007, 27, pp. 1029-1035.
23) Life Cycle Climate Performance Working Group, Guideline for Life Cycle Climate Performance. V 1.2, 2016.
24) U.S. Energy Information Administration, 2014. Capacity of Electric Power Plants by Energy Source. http://www.eia.gov/electricity/data.cfm/.
25) Electric Power Statistics Information System, 2016． Facility By Electric Power Source． http://epsis．kpx．or．kr/epsis/.
26) Choi, S., Oh, J., Hwang, Y., Lee., H., Life cycle climate performance evaluation (LCCP) on cooling and heating systems in South Korea, Applied Thermal Engineering, 2017, 120, pp. 88-98.
27) Nuclear Safety and Security Commission, 2014. CO2 Emissions of Power Energy Source. <http://www.nssc.go.kr/nssc/open/opening_data.jsp.
28) Deru, M., Torcellini., P., Source Energy and Emission Factors for Energy Use in Buildings, 2007.
29) Coskun., C., A time-varying carbon intensity approach for demand-side management strategies with respect to CO2 emission reduction in the electricity grid, International Journal of Global Warming, 2019, 19.
30) Beshr, M., Aute, V., Abdelaziz, O.A., Fricke, B.A., Radermacher., R., An Evaluation of the Environmental Impact of Different Commercial Supermarket Refrigeration Systems Using Low Global Warming Potential Refrigerants, 2014.
31) Li., G., Comprehensive investigations of life cycle climate performance of packaged air source heat pumps for residential application, Ingersoll Rand Engineering and Technology Center-Asia Pacific, 2014.
32) Abdelaziz, O., Fricke, B., Vineyard., E.A., Development of Low Global Warming Potential Refrigerant Solutions for Commercial Refrigeration Systems using a Life Cycle Climate Performance Design Tool. International Refrigeration and Air Conditioning Conference, 2012.
33) Khan, I., Jack, M.W., Stephenson., J., Use of time-varying carbon intensity estimation to evaluate GHG emission reduction opportunities in electricity sector, IEEE, 2017.
34) Khan., I., Importance of GHG emissions assessment in the electricity grid expansion towards a low-carbon future: A time-varying carbon intensity approach, 2018, 196, Journal of Cleaner Production, pp. 1587-1599.
35) Khan, I., A Temporal Approach to Characterizing Electrical Peak Demand: *Assessment of GHG Emissions at the Supply Side and Identification of Dominant Household Factors at the Demand Side*, 2018.
36) Comprehensive Evaluation of Life Cycle CO2 Emissions of Power Generation Technology in Japan, Central Research Institute of Electric Power Industry, 2016.
37) Institute for Sustainable Energy Policies. https://www.isep.or.jp/

5. CONCLUSION

The Kigali Amendment to the Montreal Protocol, adopted in 2016, imposes an obligation to reduce the production and consumption of CFC alternatives (especially HFCs). Japan accepted the amendment in December 2018 and has been in compliance since January 1, 2019. Since then, the use of HFC refrigerants, developed as chlorine-free substitutes for CFCs and a solution to ozone layer depletion, has been restricted. However, this has necessitated the development of new refrigerants, similar to the quest for the identification of CFC substitutes. In addition, with global warming progressing, the demand for refrigeration and air conditioning equipment has increased. In particular, countries that were earlier classified as “developing” are now “emerging,” and the development of refrigeration and air conditioning equipment suitable for new refrigerants is desired more than in the past.

This is the final year of the five-year “Development of Technology and Assessment Techniques for Next-Generation Refrigerants with a Low GWP Value” NEDO project for global warming prevention that started in FY2018. Working Group 1 (WG I), led by Kyushu University and Waseda University, has been engaged in two projects: one to identify next-generation refrigerants and evaluate their performance (the responsibility of the Kyushu University group) and the other to acquire data on essential equipment for refrigeration and air conditioning systems and to develop simulation methods and evaluation facilities for system analysis (the responsibility of the Waseda University group). The two groups have been conducting their research in tandem and meet about four times a year to exchange information and check each other’s progress.

The final version of this progress report summarizes the results of these efforts. The results of WG I have already been published as annual progress reports by the Japan Society of Refrigerating and Air Conditioning Engineers. They have also been widely disseminated through domestic and international journals and conferences. Most of these reports contain information on next-generation refrigerants that is yet to be disclosed to the public. We hope that users worldwide will understand how valuable WG I’s results are. We would like to use the various evaluations we receive for future reference.

Research on global warming prevention is a huge task that needs to be tackled from various perspectives. This project, which plays a part in such research, has achieved its initial goal well, but now requires higher-level measures. Furthermore, determining the endpoint is not easy. Even if we develop novel next-generation (green) refrigerants by referring to the process of replacing specified CFCs with CFC alternatives (HFCs), it will not be the end of the project. In other words, the goal of this project is an eternal theme that must continue to move forward at all times, and which Japan must continue to run with as the global frontrunner. We hope that the content of this research project and the collaborative framework it has established will make Japan a global leader in refrigerant and refrigeration and air conditioning equipment development and continue to show the world that Japan is actively working to prevent global warming.

Finally, we would like to thank the many people who have provided support for WG I’s activities. We would like to express our gratitude and respect to all of them and ask for their continued support in the future.

Kyushu university Yukihiro Higashi

Basic Performance, Optimization, and Safety and Risk Evaluation of Next-Generation Refrigerants and Refrigerating and Air Conditioning Technologies

Part 2: Safety and Risk Evaluation of Next-Generation Refrigerants

WG II Final Report

Research Committee for Next-Generation Refrigerants,
Japan Society of Refrigerating and Air-Conditioning Engineers

January 31, 2023

Disclaimer

Copyright

Basic Performance, Optimization, and Safety and Risk Evaluation of Next-Generation Refrigerants and Refrigerating and Air Conditioning Technologies

Part 2: Safety and Risk Evaluation of Next-Generation Refrigerants

Year 2022 Final Report

April 1, 2023

Edited by the Research Committee on Next-Generation Refrigerants, JSRAE

Published by the Japan Society of Refrigerating and Air Conditioning Engineers (JSRAE)

Nihonbashi-Otomi Bldg. 5F, 13-7 Nihon-bashi Odenma-cho,
Chuo-ku, Tokyo, 103-0011 Japan

TEL +81-3-5652-3223 FAX +81-3-5623-3229

TABLE OF CONTENTS

1. INTRODUCTION

1.1 Outline of the New Energy and Industrial Technology Development Organization (NEDO) Project

Under the designated product system of the Freon Emission Control Law, each sector must encourage the broader use of low-global warming potential (GWP) refrigerants. However, no established safety evaluation/risk evaluation methods exist for highly flammable refrigerants, such as hydrocarbons. Accordingly, it is essential to understand the basic characteristics of next-generation refrigerants and establish concurrent safety/risk evaluation methods for their inherent challenges, including the development of domestic safety standards and international standardization. This will support the development of refrigerating and air-conditioning equipment charged with next-generation refrigerants to achieve energy-saving and low greenhouse effects. Considering such circumstances, this project aims to lay the foundation for developing energy-saving refrigerating and air-conditioning equipment running on next-generation refrigerants and contribute to the market launch of refrigerants and refrigerating and air-conditioning equipment products by 2026. For this purpose, this project is geared toward establishing a safety/risk evaluation method for next-generation refrigerants for use in small- and medium-sized refrigerating and air-conditioning equipment, including industrial-use refrigeration and cold storage equipment and residential air-conditioning equipment.

The NEDO project "Development of Refrigerants and Refrigerating and Air Conditioning Technologies and Evaluation Methods for Achieving Energy-Saving and Low-Greenhouse Effects" includes, among others, a development theme entitled "Development of safety/risk evaluation methods for next-generation refrigerants," which was jointly proposed by and commissioned to the University of Tokyo, the Suwa University of Science, and the National Institute of Advanced Industrial Science and Technology (AIST) (Research Institute of Science for Safety and Sustainability). The following are the research themes commissioned to the three institutions for the safety evaluation of fires associated with flammable refrigerants:

[University of Tokyo]

• Evaluation of the risks associated with flammable refrigerant leakage,

• Evaluation of the severity of harm caused by flammable refrigerants from indoor fires,

[Suwa University of Science]

• Screening and modeling of ignition sources,

• Assessment of the physical risk of various ignition sources,

[National Institute of Advanced Industrial Science and Technology (Research Institute of Science for Safety and Sustainability)]

• Case studies of accidental refrigerant leakage from refrigerating and air-conditioning equipment and modeling of leakage conditions,

• Evaluation of the fire-causing abilities of devices in flammable concentration regions,

• Measurement of the diffusion behavior and evaluation of the physical hazards of long-term seepage, and

• Measurement of the diffusion behavior and evaluation of the physical hazards of rapid leakage in indoor units.

Independent of the joint proposals of the three institutions, the National Institute of Advanced Industrial Science and Technology (Research Institute for Sustainable Chemistry) was commissioned by NEDO to perform a safety evaluation of low-GWP low-flammability mixed refrigerants. The research themes are as follows:

• Evaluation of the flammability of mixed refrigerants and

• Evaluation of the practical combustion safety of mixed refrigerants.

R-Map, a method for evaluating the risk presented by home appliances, maps risks in a 6 × 5 matrix, plotting six levels of likelihood and five degrees of harm. This evaluation method was developed by the Union of Japanese Scientists and Engineers under the supervision of the Ministry of Education, Culture, Sports, Science, and Technology. Figure 1-1 shows an example of a typical R-Map.[1-1] Area A (pink area) corresponds to products that require recall. Area B (yellow area) identifies where the level of likelihood needs to be reduced to that of minimum risk. Area C (blue area) represents products that present only negligible risks and can be distributed as is. Regarding the likelihood of accidents, the criteria indicate that consumer products, such as household appliances, can be regarded as safe (deemed as Area C) even if one fatal accident occurs in 100 years. For example, if 100 million units of a product have been distributed, as is the case with room air conditioners in Japan, the acceptable likelihood of accidents is 10^{-10} (cases/unit/year). Figure 1-1 shows an example of the likelihood associated with 100 million distributed units.

Thus, accident likelihood and harm severity evaluations must be performed to evaluate the product risk. For a flammable refrigerant leak from refrigerating or air-conditioning equipment to cause a fire, the three conditions (rapid refrigerant leakage, flammable space, and ignition source) shown in Fig. 1-2 must occur simultaneously. Assuming that the three conditions are independent events, the probability of a fire occurring is obtained as the product of the occurrence probability of each condition. Therefore, to obtain the probability of a fire, the occurrence probability must be determined for each of the three factors.

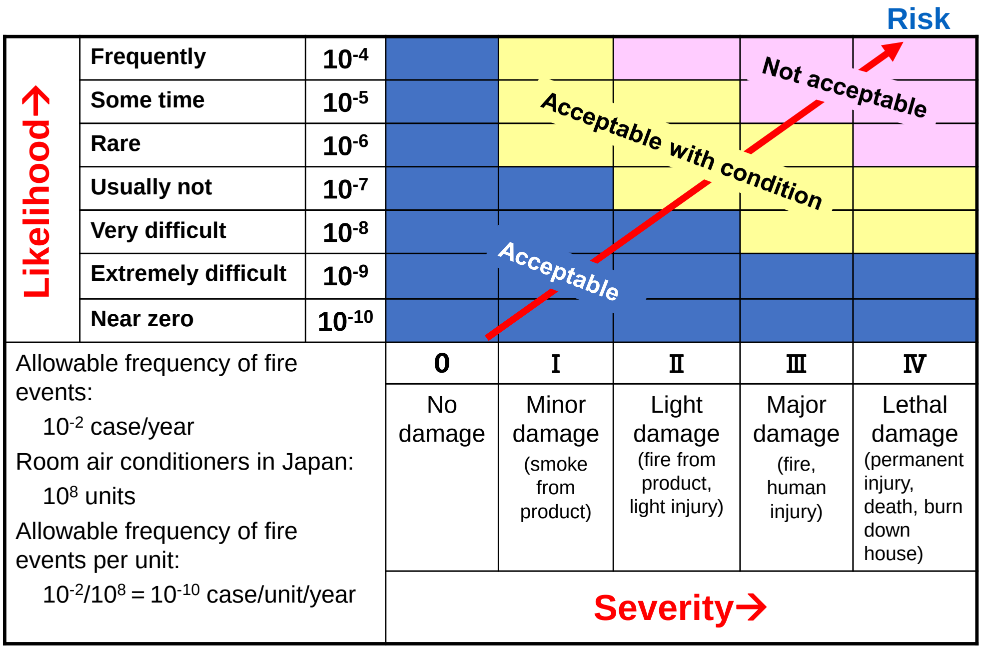

Fig. 1-1 R-Map for consumer products when 100 million units are distributed.[1-1)]

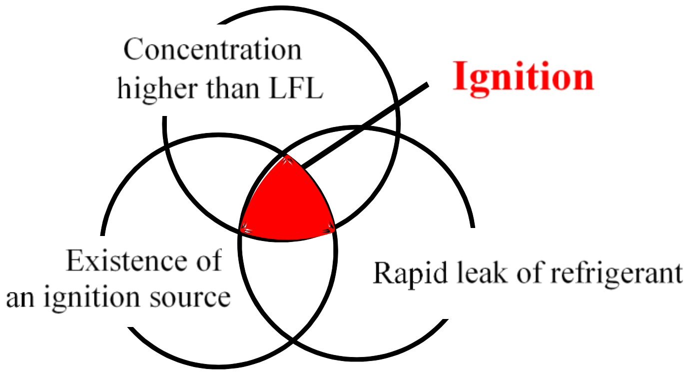

Fig. 1-2 Conditions for fire accident occurrence.

The NEDO project addresses the frequency of fires and investigates the severity of associated damage. Using propane as the refrigerant, we first examined fires associated with refrigerant leakage from room air conditioners and stand-alone display cabinets. Figure 1-3 shows the relationships between the research themes adopted by the three institutions. These three institutions undertook their research through mutual cooperation. The final risk evaluation will be conducted in cooperation with the Japan Refrigeration and Air Conditioning Industry Association (JRAIA).

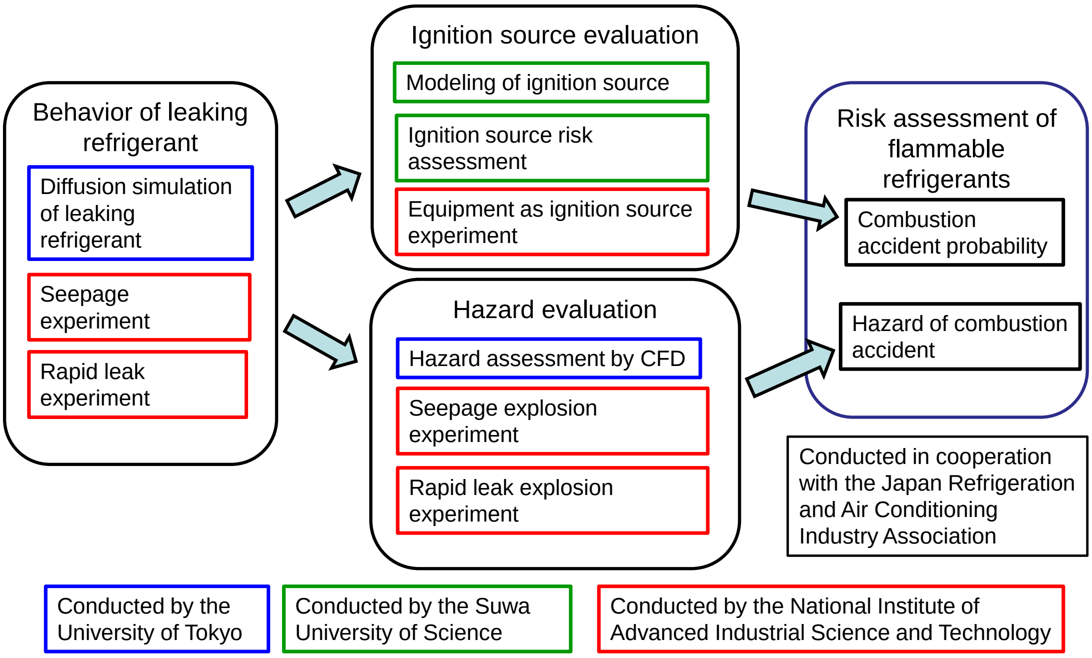

Fig. 1-3 Research flows in this project.

1.2 Activities of Working Group II (WG II) of the Research Committee for Next-Generation Refrigerants

To encourage the wider adoption of low-GWP refrigerants, which are highly flammable, industry stakeholders have highlighted the need for scientific knowledge–based risk evaluation of flammable refrigerants. Research addressing the safety of refrigerants is currently undertaken by various parties, namely the Suwa University of Science, University of Tokyo, and National Institute of Advanced Industrial Science and Technology, as part of the NEDO project “Development of Refrigerants and Refrigerating and Air Conditioning Technologies and Evaluation Methods for Achieving Energy-Saving and Low-Greenhouse Effects” (2018 to 2020). In 2016, JRAIA began to evaluate the risks associated with the application of highly flammable refrigerants (A3 refrigerants) to refrigerating and air-conditioning equipment. JRAIA separately discussed the influence of installation conditions and the existence of ignition sources. To compile the knowledge gained from the above project and perform an objective evaluation from a third-person perspective, the “Research Committee on Next-Generation Refrigerants” was established in 2018 as a NEDO investigation project within the Japan Society of Refrigerating and Air Conditioning Engineers (JSRAE). Deliberations on the safety of flammable refrigerants and the associated risk evaluation are currently being undertaken by the Investigation Committee’s Working Group II (WG II). The WG II deliberation system is built on an industry–government–academia partnership, as shown in Fig. 1-4. The breakdown of committee membership is shown in Table 1-1.

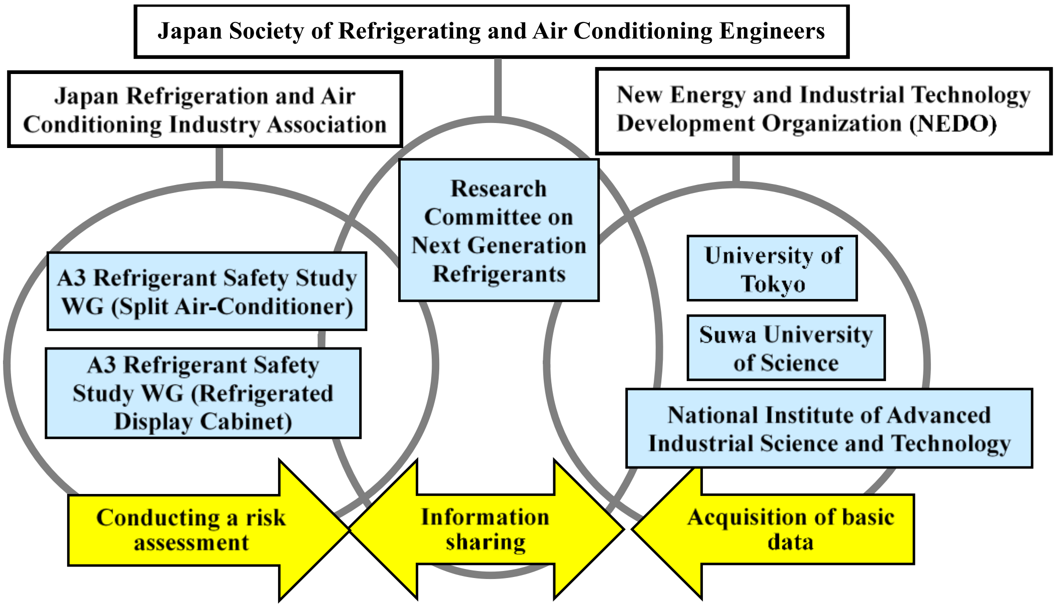

Fig. 1-4 Deliberation system for risk assessment of flammable refrigerants.

Table 1-1 Investigation Committee on Next-Generation Refrigerants, WG II Committee List as of November 1, 2022

	Affiliation	Department	Title	Name
Chair	National Institution for Academic Degrees and Quality Enhancement of Higher Education	Department of Research and Development	Specially Appointed Professor	Eiji HIHARA
Committee member	University of Tokyo	Graduate School of Frontier Sciences	Specially Appointed Researcher	Makoto ITO
	Suwa University of Science	Department of Mechanical-Electrical Engineering, Faculty of Engineering	Associate Professor	Tomohiko IMAMURA
	National Institute of Advanced Industrial Science and Technology	Research Institute for Sustainable Chemistry	Chief Researcher	Kenji TAKIZAWA
	National Institute of Advanced Industrial Science and Technology	Research Institute of Science for Safety and Sustainability	Chief Researcher	Hiroumi SHIINA
Observer	Japan Refrigeration and Air Conditioning Industry Association	Panasonic Corporation		Akiara HIWATA
		Panasonic Corporation		Kenji TAKAICHI
		Mitsubishi Electric Corporation		Koji YAMASHITA
		Toshiba Carrier Corporation		Hiroichi YAMAGUCHI
		Daikin Industries, Ltd.		Shigeharu TAIRA
		Hitachi-Johnson Controls Air Conditioning, Inc.		Toshiharu SASAKI
		Mitsubishi Heavy Industries Thermal Systems, Ltd.		Kenji MATSUDA
		Engineering Department	Department Manager/ Councilor	Takeshi SAKAI
			Councilor	Shunji SASAKI
			Councilor	Koji MUROZONO
			Councilor	Kazuhiro HASEGAWA
	University of Fukui	Division of Engineering Mechanical Engineering	Associate Professor	Chaobin DANG
	Suwa University of Science	Department of Mechanical-Electrical Engineering, Faculty of Engineering	Associate Professor	Kyoko KAMIYA

	Tokyo University of Marine Science and Technology	Department of Marine Electronics and Mechanical Engineering	Professor	Norihiro INOUE
	National Institute of Advanced Industrial Science and Technology	Research Institute of Science for Safety and Sustainability	Research Group Leader	Shiro KUBOTA
	New Energy and Industrial Technology Development Organization	Department of Environment	Senior Chief Researcher	Satoshi FUJIGAKI
			Chief Researcher	Tomokazu MORI
			Chief	Tatsuhiko TAKAHASHI
			Chief	Makoto GOCHO
			Senior Staffer	Takuma OISHI
Secretariat	Japan Society of Refrigerating and Air Conditioning Engineers		Secretary-General	Kyoji KONO
				Shigehiro UEMURA
				Akira NISHIGUCHI

1.3 About this report

This report presents a summary of the achievements made in FY2020 by WG II of the Research Committee on Next-Generation Refrigerants. The authors are grateful to the New Energy and Industrial Technology Development Organization for their economic support in the activities conducted by this study group. Additionally, the authors thank the Committee members and their collaborators for the cooperation they extended.

Table 1-2 Author List

Chapter	Author
1. Introduction	Eiji HIHARA (National Institution for Academic Degrees and Quality Enhancement of Higher Education, NIAD)
2. Progress achieved at the University of Tokyo	Makoto ITO (University of Tokyo), Shizuo SAITOH, Chaobin DANG (University of Fukui), and Eiji Hihara (NIAD)
3. Progress achieved at the Suwa University of Science	Tomohiko IMAMURA (Suwa University of Science)
4. Progress achieved at the National Institute of Advanced Industrial Science and Technology Research Institute of Science for Safety and Sustainability	Hiroumi SHIINA (National Institute of Advanced Industrial Science and Technology), Yoshiaki TAKAHASHI, Ryo MATSUKI, Tei SABURI, and Shiro KUBOTA
5. Progress achieved at the National Institute of Advanced Industrial Science and Technology Research Institute for Sustainable Chemistry	Kenji TAKIZAWA (National Institute of Advanced Industrial Science and Technology)
6. Progress in the risk evaluation of room air conditioners using A3 refrigerant by the Japan Refrigeration and Air Conditioning Industry Association	Kenji TAKAICHI (Panasonic Corporation)
7. Progress in the risk evaluation of built-in refrigerated display cabinets using A3 refrigerant by the Japan Refrigeration and Air Conditioning Industry Association	Koji YAMASHITA (Mitsubishi Electric Corporation)

References

1-1) Risk Assessment Handbook (Practice), Ministry of Economy, Trade and Industry, June 2011.

2. RESULTS OF RESEARCH BY THE UNIVERSITY OF TOKYO

2.1 Introduction

The University of Tokyo is entrusted with research on the safety and risk assessment of flammable refrigerants used in refrigeration and air-conditioning equipment. These include studies on the risk of flammable refrigerant leaking from room air-conditioner indoor units and commercial refrigerated display cabinets, the severity of danger when flammable refrigerant burns in a room, and diesel combustion in pump-down operation.

Regarding research on the risk of flammable refrigerant leakage, we simulated the diffusion of refrigerants when they leak indoors from room air-conditioners and commercial refrigerated display cabinets that use flammable refrigerants. The ignition probability during the leakage of a combustible refrigerant into the room can be determined by calculating the temporal transition of the gas volume with combustible concentration. In this study, first, leakage experiments were conducted using a safe gas with a small global warming potential (GWP), such as carbon dioxide, to validate the simulation model. Next, a simulation of leakage from the indoor unit of the room air-conditioner was conducted, and the relationship between the room area and the required fan air volume was evaluated.

As for the leakage of flammable refrigerant from commercial display cabinets, a leakage experiment using carbon dioxide was conducted, and the results were compared with the simulation results to validate the simulation model. Then, we conducted a leakage simulation and evaluated the maximum charge amount of flammable refrigerant and the airflow of the condenser fan.

When combustible refrigerant leaks indoors and a combustion accident occurs, the severity must be evaluated to assess the risk. Because the degree of danger when flammable refrigerants burn is unknown, fatality is assumed in the current risk assessment. Combustion phenomena were simulated to evaluate the degree of danger when flammable refrigerants burn.

Compressors can explode due to mishandling during the refrigerant pump-down work for relocation or disposal of air-conditioners. A model engine simulated the refrigerant compressor, and an experiment investigated the state of diesel combustion during pump down. The effect of an oxidation reaction inhibitor added to refrigerating-machine oil in suppressing combustion was investigated.

2.2 Refrigerant leakage from a residential split air-conditioner

2.2.1 Background

Several studies have investigated the problem of refrigerant leakage from room air-conditioners. Kataoka et al.[2-1] conducted numerical calculations and experiments on indoor leakage of flammable refrigerants and proposed the maximum charge amount of flammable refrigerants considering the floor area of the leakage space, the lower flammability limit (LFL) of the refrigerant, and the refrigerant leak point height. Hu et al. [2-2] investigated the effects of leak height, refrigerant leak location, and blowing direction when R290 leaks from a wall-mounted air-conditioner. Baba et al.[2-3] conducted numerical calculations to evaluate the risk of R290 leaking from an outdoor unit and evaluated the risk for different methods of installing the outdoor unit on the veranda and the optimal installation method. Colbourne et al.[2-4] conducted a refrigerant leakage experiment using R744 from a wall-mounted air-conditioner and reported a decrease in the concentration near the floor with a decrease in the charging amount and an increase in the average air velocity in the room. Tang et al.[2-5), 2-6] conducted an experiment on R290 for rapid leakage through a hole in the piping inside the air-conditioner. The concentration was measured just below the nozzle, and the concentration significantly exceeded the LFL at a filling amount of 400 g. Hattori et al.[2-7] performed calculations and experiments when R32 leaked from a floor-standing air-conditioner; the correlation between the calculated and experimental concentration distributions could not be confirmed when the fan of the air-conditioner was stopped, but when the fan was turned on, the correlation was evident. Jin et al.[2-8] investigated the leakage from the floor-standing air-conditioner using R32 using calculations considering a room with a ventilation opening. They concluded that the effect of a low ventilation port is significant because the refrigerant stays in the lower regions.

Studies are considering reducing the flammable area by operating the indoor unit fan and stirring the indoor air during refrigerant leakage. Colbourne et al.[2-9] proposed an equation that estimates the fan airflow during the leakage. According to International Electrotechnical Commission (IEC) 60335-2-40:2022[2-10], the fan air volume is expressed as follows:

$$\dot{V}_{\mathrm{o,min}} = \frac{5Y\sqrt{A_0}\dot{m}_{\mathrm{leak}}{}^{3/4}}{h_a{}^{1/4}[FL_{\mathrm{L}}(1-F)]^{5/8}}. \qquad (2-2-1)$$

where A_0 is the airflow discharge area in m^2; $\dot{m}_{\mathrm{leak}}$ is the rrefrigerant leak rate in kg/s; h_a is the release height in m; FL_{L} is the lower flammability limit in kg/m^3; F and Y are constants.

In IEC 60335-2-40:2022, Eq. (2-2-2) provides the maximum charge amount of flammable refrigerant when the indoor unit fan does not operate. Equation (2-2-3) is proposed for the maximum charge amount of flammable refrigerant when the indoor unit fan operates during the leakage.

$$m_{\mathrm{max}} = 2.5 \times FL_{\mathrm{L}}{}^{5/4} \times A^{1/2} \times h_0 \qquad (2-2-2)$$

$$m_{\mathrm{max}} = F \times FL_{\mathrm{L}} \times A \times 2.2 \qquad (2-2-3)$$

where A is the floor area in m^2.

This study numerically evaluated the combustible gas volume during the leakage of R290, which is expected to be a next-generation refrigerant for home air-conditioners and commercial refrigeration equipment. To verify the validity of the calculation model, the numerical results were compared with the experimentally observed temporal changes in the concentration distribution during the refrigerant leakage. We verified that the mesh and discretization scheme are sufficient to reproduce the experimental values. We improved the numerical calculation method to reduce the deviation of the calculated values from the experimental values.

The study aims to evaluate the necessity of operating the fan of the indoor unit to ensure safety when the refrigerant leaks from the indoor unit of the air-conditioner. Although the IEC standard specifies the minimum fan air volume, the effect of airflow direction is not considered. The behavior of combustible gas after a refrigerant leak was calculated considering the installation location of the indoor unit, the airflow speed and direction of the indoor unit fan, and the floor area of the room as parameters.

Generating a circulating flow in the room by operating the indoor unit fan after the refrigerant leaks is important. We considered the relationship between the direction and speed of airflow of the indoor unit fan necessary to eliminate the combustible gas region due to refrigerant leakage at an early stage.

2.2.2 Method of numerical flow analysis

We numerically calculated the diffusion of leaked refrigerant gas (from an air-conditioner indoor unit) while it mixed with indoor air. The basic equations for a 3D-space mixture advection–diffusion problem are the mass conservation equation (2-2-4), the Navier–Stokes equations (2-2-5), the advection–diffusion equation (2-2-6), and the equation of state of an ideal gas (2-2-7). For numerical calculations, we used ANSYS Fluent 2021 R2. Table 2-2-1 summarizes the calculation conditions.

$$\frac{\partial \rho}{\partial t} + \frac{\partial}{\partial x_j}(\rho u_j) = 0, \qquad (2-2-4)$$

$$\frac{\partial \rho u_i}{\partial t} + \frac{\partial}{\partial x_j}(\rho u_j u_i - \tau_{ij}) = -\frac{\partial p}{\partial x_i} + g_i(\rho - \rho_o), \qquad (2-2-5)$$

$$\frac{\partial \rho Y_{\mathrm{m}}}{\partial t} + \frac{\partial}{\partial x_{\mathrm{j}}}\left(\rho u_{\mathrm{j}} Y_{\mathrm{m}} - D\frac{\partial Y_{\mathrm{m}}}{\partial X_{\mathrm{j}}}\right) = 0 \qquad (2-2-6)$$

$$\rho = \frac{p}{RT\left(\frac{Y_A}{M_A} + \frac{Y_B}{M_B}\right)}, \qquad (2-2-7)$$

where τ_{ij} is the stress tensor; X_m is the molar concentration; Y_m, Y_A, and Y_B are mass concentrations; M_A and M_B are the molecular weight; D is the diffusion coefficient.

Additionally, using Eq. (2-2-8)[2-11)], we calculated the molecular diffusion coefficient during refrigerant diffusion and regarded it as a constant, irrespective of temperature and pressure:

$$D_{AB} = \frac{1.5 \times 10^{-5} T^{1.81}}{p(T_{CA} \cdot T_{CB})^{0.1405} \cdot (V_{CA}^{0.4} + V_{CB}^{0.4})^2} \cdot \sqrt{\frac{1}{M_A} + \frac{1}{M_B}}, \qquad (2-2-8)$$

where T_{CA} and T_{CB} are critical temperatures in K; V_{CA} and V_{CB} are the critical specific volumes in cm^3/mol. Table 2-2-2 shows the diffusion coefficients for the refrigerant–air mixtures used in the present study.

Table 2-2-1 Simulation outline

	Room
Software	ANSYS Fluent 2021 R2
Simulation	Unsteady and compressible flow
Species transport	2 components (Air–Refrigerant)
Turbulence model	Realizable k–ε
Solver	SIMPLE
Scheme	2nd order upwind

Table 2-2-2 Diffusion coefficient

	R290–Air	R32–Air	R744–Air
Diffusion coefficient [m^2/s]	1.11×10^{-5}	1.35×10^{-5}	1.59×10^{-5}

2.2.3 Numerical calculation model

An overview of the calculation model is provided in Fig. 2-2-1 and Table 2-2-3. Figure 2-2-2 shows the shape of the wall-mounted indoor unit, and Fig. 2-2-3 shows the shape of the floor-standing indoor unit. In addition to the case with dimensions of the air outlet shown in Fig. 2-2-3. Calculations were also made under conditions where the short side was increased to 100 mm. The floor-standing indoor unit had two air outlets, upper and lower; in the calculation, the air was discharged from one of them, and the other was defined as a wall boundary.

The standard room size was 3200 × 2800 × 2500 mm, and two 100 × 50 mm exhaust ports were defined using pressure boundary conditions on the upper wall facing the air-conditioner. The gap under the door was not set. The mesh was finer near the boundary, and the half area was calculated with the symmetry plane in the center. The leak rate was defined considering the rapid leak condition in which the entire amount was released into the room in 4 min based on IEC 60335-2-40:2022. The IEC standard specifies such a leak rate because a low-speed leak would not generate a flammable region. The refrigerant was R290.

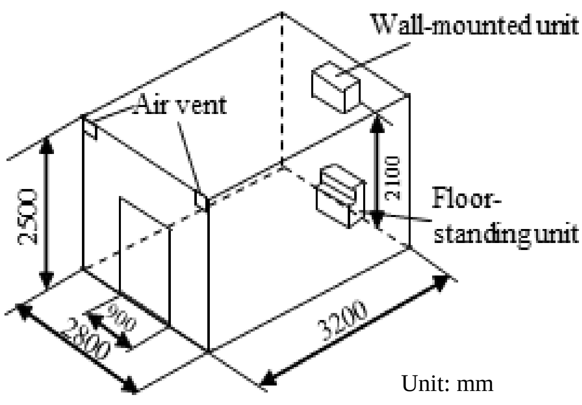

Fig. 2-2-1 Modeled room.

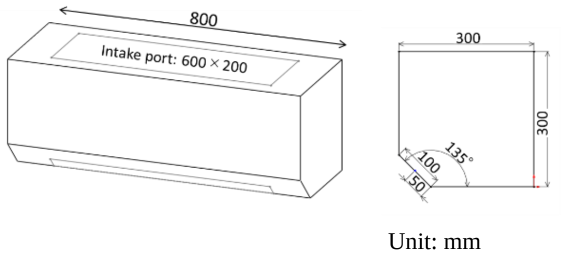

Fig. 2-2-2 Details of the wall-mounted indoor unit model.

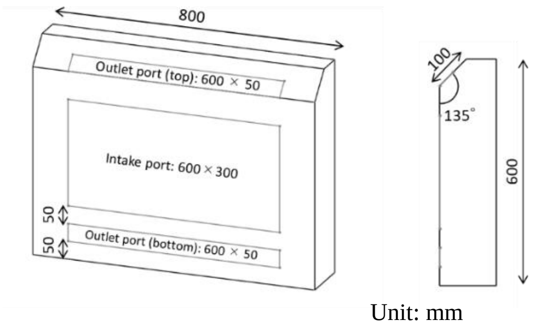

Fig. 2-2-3 Details of the floor-mounted indoor unit model.

Table 2-2-3 Simulation conditions

Refrigerant	R290 and R32
Leak amount	Evaluated
Leak time	4 min
Boundary of A/C model	1 outlet and 1 inlet
Floor Area	Evaluated
Ventilation	Exist (Vent)

2.2.4 Validation of numerical calculation

(1) Verification of mesh independence

To verify the mesh independence of the numerical calculation, Fig. 2-2-4 shows the time integral value until the elimination of combustible gas volume of 50% LFL or more under the condition that 0.286 kg of R290 leaked from the wall-mounted indoor unit. The outlet size was 600 × 100 mm, and the fan airflow speed was 1 m/s. The figure shows that the combustible gas volume converged as the number of cells increased. Based on these results, the number of cells in the room was set to 2.57×10^5, considering the computation time load.

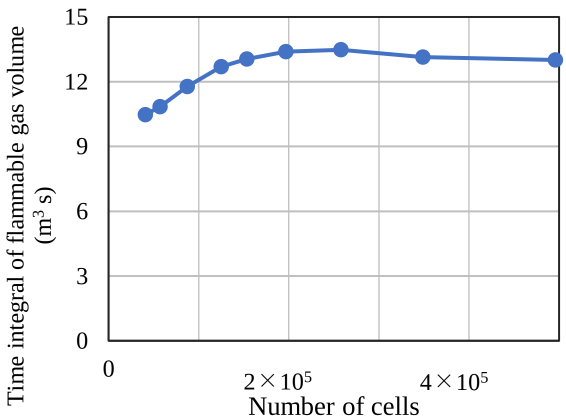

Fig. 2-2-4 Check of mesh dependency.

(2) Validation of the numerical model

To examine the model's validity, we performed concentration distribution measurements using refrigerant leak tests and compared the measured results with the numerically calculated refrigerant concentrations for the same points. The dimensions of the laboratory are shown in Fig. 2-2-5. We fitted heat-insulating boards on the walls as a precaution to prevent drafts. The refrigerants used were R32 and R744. The refrigerant supply system is shown in Fig. 2-2-6. The specifications of the equipment used in this study are summarized in Table 2-2-5. The mass flow controller was intended for R32. Hence, the flow rate coefficient was calibrated via the experiment using R744. We conducted experiments to discharge refrigerant only from the wall-mounted indoor unit. We developed a model to simplify the internal structure and ensure a uniform refrigerant discharge from the air outlet. Figure 2-2-5 is a detailed drawing of this model. The air outlet measured 688 × 100 mm. With no air intake provided, 100% pure refrigerant was discharged at a uniform rate. We used oximeters to estimate the refrigerant concentrations based on the decrease in oxygen concentration, with the aim of using more than one type of refrigerant. The refrigerant concentration X_{ref} was calculated using Eq. (2-2-9) from the oxygen concentration X_{O2} and the initial oxygen concentration $X_{O2,atm}$:

$$X_{ref} = \frac{X_{O2,atm} - X_{O2}}{X_{O2,atm}}. \qquad (2-2-9)$$

The 14 oximeters used in the experiment were calibrated by checking them against the R744 concentration calculated using Eq. (2-2-9) from an R744 concentration reading from an oximeter. We confirmed that the oximeters measured the refrigerant concentrations with an accuracy of ± 2% of full scale. These oximeters were installed at the 14 points shown in Fig. 2-2-8. The experimental conditions are summarized in Table 2-2-6.

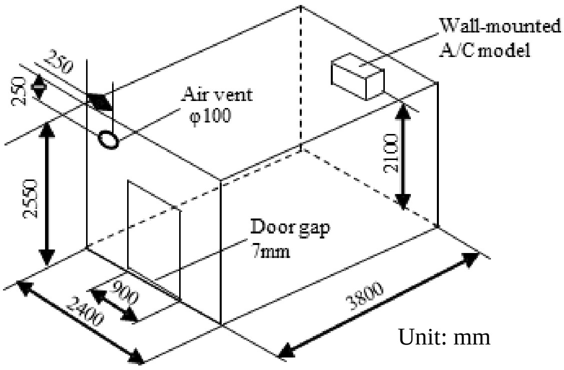

Fig. 2-2-5 Geometry of experimental room.

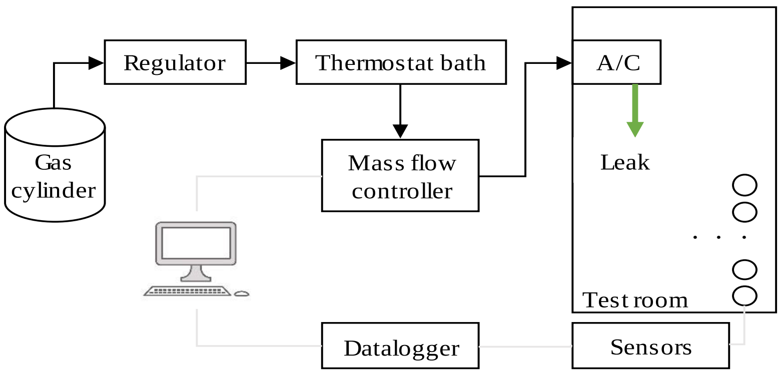

Fig. 2-2-6 Schematic of the experimental setup.

Table 2-2-5 Equipment specification

Name	Type	Specifications
Mass flow controller	Fujikin (FCST1500M)	Gas: CH_2F_2 Range: 0–250 L/min Accuracy: ±2% of full scale
Oximeters	ICHINEN JIKO ($JKO\text{-}O_2$ Ver.3)	Gas: Oxygen Principle: Galvanic battery type Resolution: 0.01% Accuracy: ±0.5% (≥10 vol%), ±0.01% (<10 vol%)

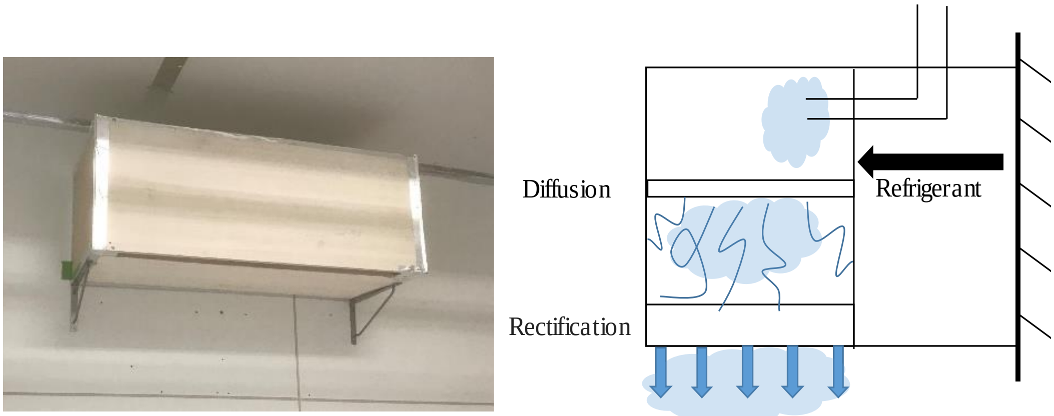

Fig. 2-2-7 Internal structure of wall-mounted air-conditioner.

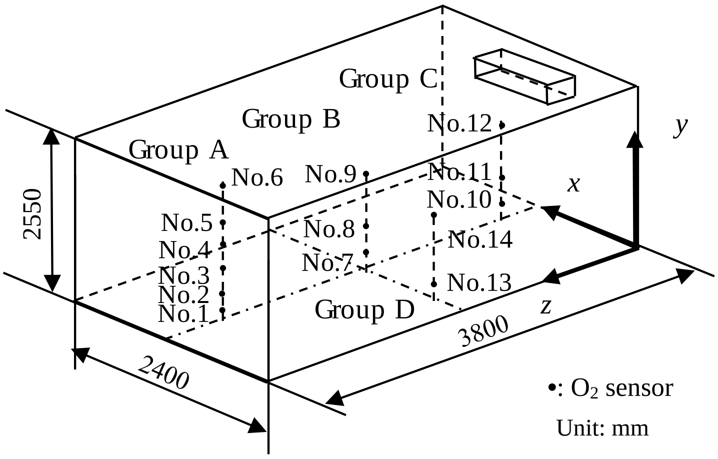

Fig. 2-2-8 Concentration measurement points.

Table 2-2-6 Experimental conditions for validation of computational fluid dynamics model

No.	Refrigerant	Air vent	Refrigerant amount (g)
1-1	R744	exist	200
1-2			300
1-3			400
1-4			500
2	R744	none	500
3	R32	exist	500

(3) Model validity verification results

As shown in Fig. 2-2-9, we compared the calculated and measured values for Group A measurement points under test conditions No. 1-4 and No. 3 (Table 2-2-6). The ordinate axis represents the test gas concentration, and the abscissa axis represents the elapsed time. The figure shows that the refrigerant concentration continuously increased at each point from the start to the end of refrigerant leakage (240 s) and then gradually decreased after 240 s had elapsed. In the early phase of the experiment, we observed discrepancies between the measured and calculated values. After reducing the mesh sizes near the air-conditioner indoor unit’s air outlet, the ventilating opening, and the door undercut and improving the shapes of the walls to allow gas to flow smoothly in or out, we observed fewer and smaller discrepancies. In the final phase of the experiment, as shown in Fig. 2-2-9, the measured and calculated values were consistent with reasonable accuracy, successfully reproducing the actual physical phenomena and thereby validating our calculation model.

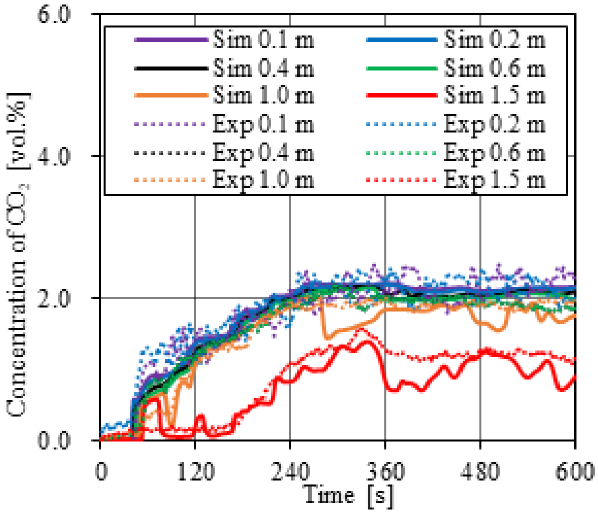

(a) No. 1-4

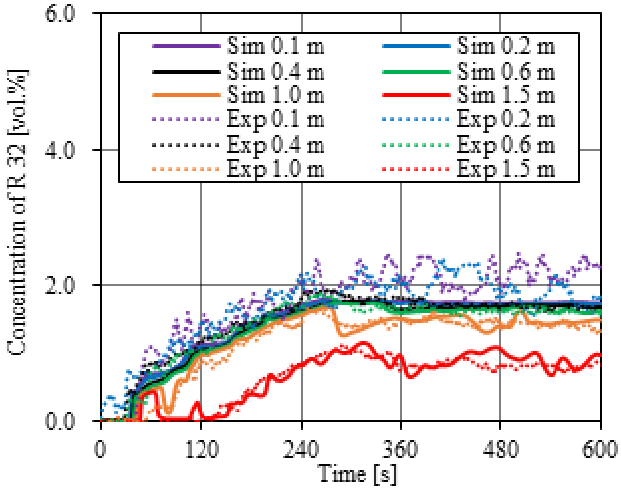

(b) No. 3

Fig. 2-2-9 Comparison between calculation (Sim) and experimental (Exp) results.

2.2.5 Refrigerant leakage simulation

(1) Simulation conditions

Using the calculation model verified in the previous section, we numerically analyzed the diffusion behavior of the refrigerant gas when the refrigerant leaked into the room from the wall-mounted indoor unit and the floor-standing indoor unit. We evaluated the effects of blowing direction and fan airflow speed on flammable region generation. Table 2-2-7 shows the common parameters (regardless of the type of indoor unit), and Fig. 2-2-1 shows the room geometry. In this study, the coefficient F in Eq. (2-2-3), which determines the refrigerant charging amount, and Eq. (2-2-1), which determines the air volume, was 0.382. The simulation assumed the case with no doors to consider the most severe conditions. Therefore, only the 100 × 50 mm vents (pressure boundaries) in the upper corners were provided.

Table 2-2-7 Parameters of computational fluid dynamics simulation

Room dimensions (Width × Depth × Height)	2.8 × 3.2 × 2.5 m (8.96 m^2) 4.0 × 4.5 × 2.5 m (18 m^2) 4.9 × 5.6 × 2.5 m (27.44 m^2)
Refrigerant charge (g)	$m = F \times FL_{\mathrm{L}} \times A \times h$ A: room area (m^2) h: 2.2 m F: 0.382 FL_{L}: lower flammability limit (kg/m^3)
Leakage period	240 s
Fan airflow speed	1–2 m/s (uniform velocity)
Fan operation	Operation started 30 s after the start of leakage

(2) Case in which the wall-mounted indoor unit fan does not operate during the leakage

Figure 2-2-10 shows the results of calculating the volume of combustible gas generated when the indoor unit fan does not operate when the refrigerant leaks from the wall-mounted indoor unit and the floor-standing indoor unit. The floor area was 8.96 m^2, the leaking refrigerant was R290, and the mass m was 0.286 kg. It was assumed that the concentration of the refrigerant discharged from the outlet was 100%, and the flow rate $\dot{m}_{\mathrm{leak}}$ was constant at $\dot{m}_{\mathrm{leak}} = m/240 = 1.19 \times 10^{-3}\ \mathrm{kg/s}$. The shape of the indoor unit is as shown in Figs. 2-2-2 and 2-2-3. The leakage was from the 600 × 100 mm outlet. The size of the floor-mounted indoor unit was 800 × 600 × 150 mm, and a 600 × 50 mm air outlet was provided at the bottom of the front.

The solid line shows the time transition of the combustible gas volume with a concentration of 50% LFL or more. As adopted in the international standard [2-12], considering the safety factor, the area where the concentration is 50% LFL or more was considered as the combustible part. For reference, the transition of combustible gas volume (LFL to upper flammability limit (UFL)) is also shown using a dashed line. The difference between solid and dashed lines indicates the volume of concentration between 50% LFL and LFL. In the case of a floor-standing indoor unit, the difference is small because the highly concentrated gas stays near the floor surface, but in the wall-mounted indoor unit, the gas from the indoor unit is mixed with the surrounding air and diluted as it flows downward due to gravity. Therefore, the region between 50% LFL and LFL becomes large while the volume exceeding LFL is small. This result indicates that the combustible gas region is generated for a long time if the indoor unit fan is not operated.

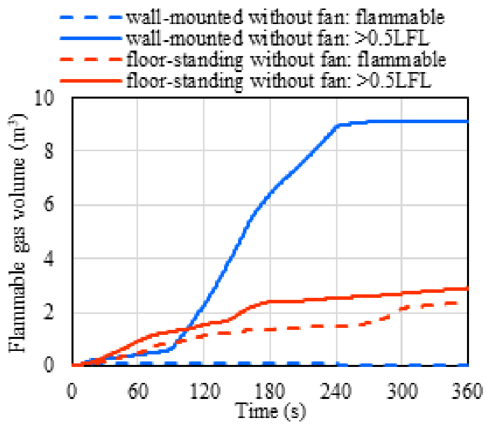

Fig. 2-2-10 Results of flammable gas generation when the fan does not operate.

(3) Case in which the wall-mounted indoor unit fan operates during the leakage

Room air was sucked in through the 600 × 200 mm suction port on the top, and the airflow was discharged from the 600 × 100 mm outlet at the front end of the bottom. The blowing direction was set from horizontal to vertical. The indoor unit fan did not operate for 30 s from the start of refrigerant leakage, and refrigerant gas with a concentration of 100% was discharged from the outlet. After 30 s, the fan of the indoor unit was operated, sucked in the indoor air from the intake port of the indoor unit, and the airflow containing the refrigerant gas was discharged from the outlet port.

Figure 2-2-11 shows the time transition of the combustible gas volume when R290 with a refrigerant charge of 0.286 kg is discharged from the outlet of 600 × 100 mm into a room with an area of 8.96 m^2. The airflow speed calculated from the air volume obtained by substituting $A_0 = 0.06\ \mathrm{m}^2$, $\dot{m}_{\mathrm{leak}} = 1.19 \times 10^{-3}$ kg/s, and $h_a = 2.1$ m into Eq. (2-2-1) was 1.14 m/s. Based on this airflow speed, the time transition of combustible gas volume with a concentration of 50% LFL or

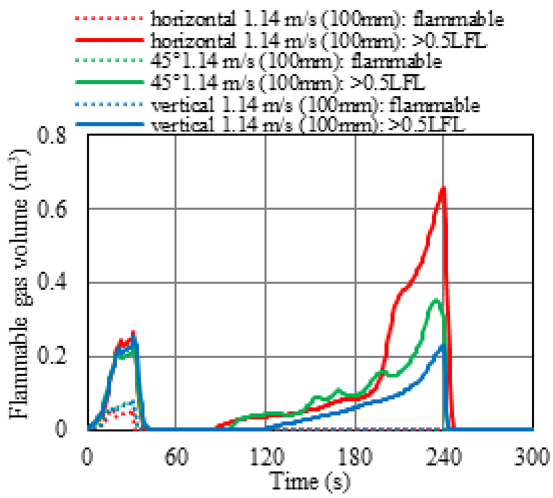

Fig. 2-2-11 Flammable gas volume when the airflow velocity is 1.14 m/s for wall-mounted indoor unit.

more was shown. A small flammable area was formed at the beginning of the leak; however, after 30 s, when the fan started operating, the concentration of the entire area became less than 50% LFL. During the next 120 to 240 s, the 50% LFL concentration region reappeared and increased as the indoor refrigerant concentration increased but was eliminated immediately as the leak ended. The maximum concentration during this period was between 50% LFL and LFL, and no flammable region was formed. As for the airflow direction, the area corresponding to 50% LFL or more was large under the condition of horizontal blowing; however, the difference due to the airflow direction was small when the airflow speed was increased to ~2 m/s.

(4) Case in which the floor-standing indoor unit fan operates during the leakagediagonally upward

The front of the floor-standing indoor unit had a 600 × 300 mm intake port (the lower end was 150 mm from the floor), and a 600 × 100 mm outlet was installed at the upper or lower front end. The direction of the airflow from the air outlet at the top end was horizontal to obliquely upward. The lower side of the outlet at the bottom of the front was set at the height of 25 mm from the floor, and the airflow was horizontal. As with the wall-mounted indoor unit, the indoor unit fan did not operate for 30 s after the start of refrigerant leakage, and refrigerant gas with a concentration of 100% was discharged from the outlet. After 30 s, the fan of the indoor unit was operated, sucked the indoor air from the intake port of the indoor unit, and the airflow containing the refrigerant gas was discharged from the outlet port.

Figure 2-2-12 shows the time transition of the combustible gas volume when 0.286 kg of R290 is discharged from the outlet of 600 × 100 mm into a room with an area of 9 m^2. Based on an airflow speed of 1.14 m/s, the time transitions of the volume with a concentration of 50% LFL or more and the volume of combustible gas (LFL to UFL) are shown. The intensity of the effect of the position and direction of the outlet on the generation of combustible gas is in the order "lower blow" < "horizontal blow from the top" < "diagonally upward blow from the top". The 50% LFL area, when blowing diagonally upward from the top, has approximately the same size as that of the wall-mounted type, but the 50% LFL area is larger in other directions.

Figure 2-2-13 shows the results of expanding the room area to 27.44 m^2 and changing the airflow speed by fixing the airflow direction of the floor-standing indoor unit diagonally upward. The amount of refrigerant charge also increased in proportion to the room area to 0.876 kg. The airflow speed was varied in the range of 1 to 6 m/s. The airflow speed obtained using Eq. (2-2-1) under this condition was 2.6 m/s. Compared to the case with a room area of 8.96 m^2 in Fig. 2-2-12, the combustible gas volume was significantly increased even if the airflow direction was the same. If the airflow speed was not increased by the fan, the airflow had difficulty reaching the wall in front of the equipment, and large convection currents were not formed in the entire room. Therefore, the volume corresponding to > 50% LFL was large in the case of bottom blowing in Fig. 2-2-12 as well.

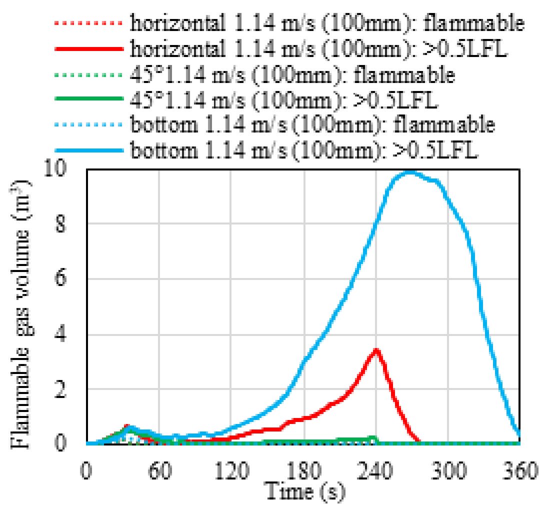

Fig. 2-2-12 Flammable gas volume when the airflow velocity is 1.14 m/s for floor-standing indoor unit.

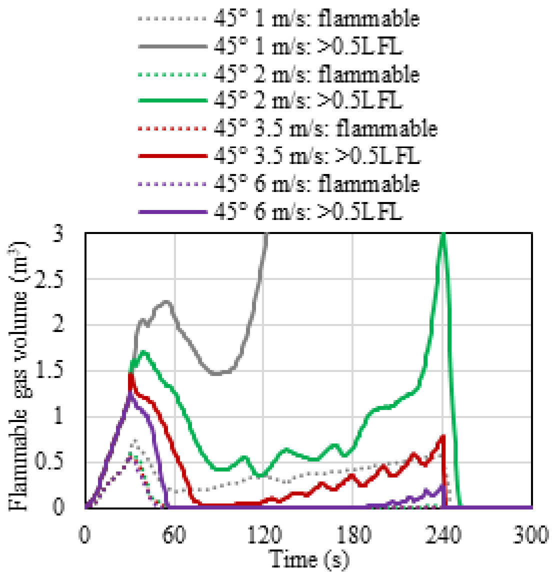

Fig. 2-2-13 Flammable gas volume for 27.44 m^2 of the floor area for floor-standing indoor unit.

2.2.6 Examination of fan air volume formula

Assuming that the filling amount $m_{\max}$ in Eq. (2-2-3) leaks at a constant flow rate and substituting $\dot{m}_{\mathrm{leak}}$ in Eq. (2-2-1) for fan airflow, the following equation for airflow speed is obtained.

$$u_{\mathrm{air}} = \frac{9.03YF^{3/4}}{{t_{\mathrm{leak}}}^{3/4}(1-F)^{5/8}} \times \frac{A^{3/4}F{L_{\mathrm{L}}}^{1/8}}{{h_{\mathrm{a}}}^{1/4}\sqrt{A_0}} \qquad (2-2-10)$$

Judging from the size of the exponents, the air outlet area and the room area have a large effect on the airflow speed; therefore, we examined the validity of these indexes.

(1) Effect of outlet area

A wall-mounted indoor unit leaked 0.286 kg of R290 into a room with an area of 8.96 m^2. Figure 2-2-14 shows the results of calculating the change in combustible gas volume when the fan outlet shape and airflow speed were varied. In the reference case, the outlet size was 600 × 100 mm, and the air was blown downward at 45° with an airflow speed of 1 m/s. The combustible gas volume was calculated when the outlet size was halved (600 × 50 mm), and the airflow speeds were set to 1.41 m/s (as calculated using Eq. (2-2-10)) and 2 m/s. The volume calculation results are shown. Figure 2-2-15 compares the difference in combustible gas volume with variation in airflow speed when the opening area of the floor-standing indoor unit was halved. The airflow was blown upward at 45°. Both figures reveal consistency between the combustible gas volume for the reference case and that for the airflow speed calculated using Eq. (2-2-10). The validity of the exponent for the outlet area in Eq. (2-2-1) was shown.

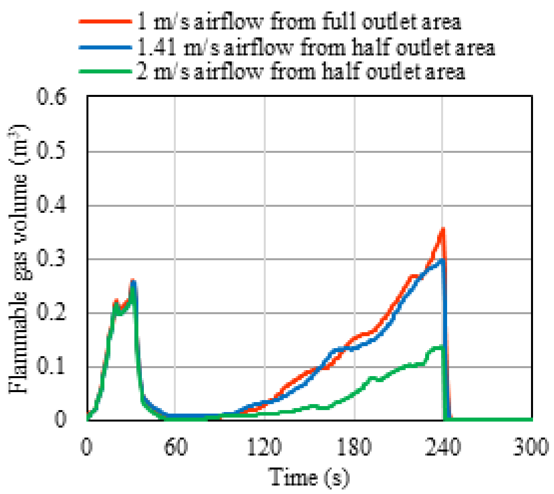

Fig. 2-2-14 Effect of outlet area on flammable gas volume for a wall-mounted indoor unit.

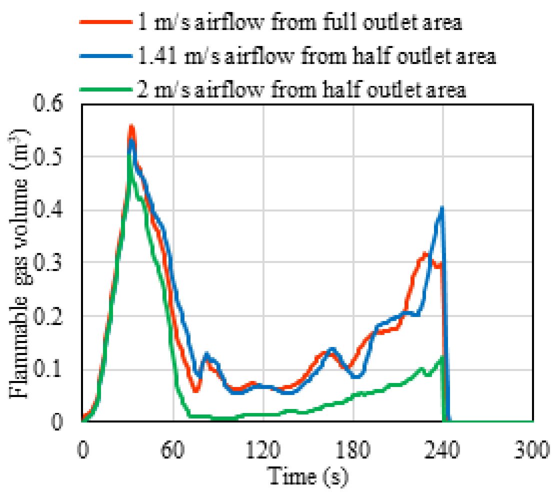

Fig. 2-2-15 Effect of outlet area on flammable gas volume for a floor-standing indoor unit.

(2) Influence of room area

For two types of indoor units, we calculated the change in combustible gas volume by changing the room area to 8.96, 18, and 27.44 m^2 (Fig. 2-2-6). The corresponding leakage amounts of R290 were 0.286, 0.575, and 0.876 kg, calculated by setting the coefficient F in Eq. (2-2-3) to 0.382. The blowing direction of the fan airflow was 45° downward for the wall-mounted indoor unit and 45° upward from the upper opening for the floor-standing indoor unit. These directions were considered because the indoor circulation flows were most likely to be formed in these directions, according to the calculation results of airflow formation with different blowing directions. The vertical axis in Fig. 2-2-16 is the time-integrated value of the combustible gas volume from the start of refrigerant leakage to the elimination of the combustible gas volume divided by the floor area.

The circles in Fig. 2-2-16 indicate the case where the combustible gas volume was eliminated within 15 s after the refrigerant leakage ended, and the triangles indicate the case where the combustible region remained after the end of the leak. Two conditions, Case 1 and Case 2, were considered when considering the lower limit of airflow speed. Case 1 is for the airflow speed at which the vertical axis of Fig. 2-2-16 is 10 m·s, which corresponds to the elimination of the flammable region within 15 s from the end of the leak. Case 2 is for the condition in which the combustible region was eliminated within 1 s after the end of the leak.

Figure 2-2-17 shows the fan airflow velocity that satisfies the conditions of Cases 1 and 2 and the room area dependence of the fan airflow velocity obtained using Eq. (2-2-10). In Cases 1 and 2, the results of wall-mounted indoor units and floor-standing indoor units were similar. Even if the air was blown from a low position as that in the floor-standing type, sufficient agitation could be achieved at a lower air velocity by blowing upwards to form an indoor circulating flow. Therefore, the flammable area could be extinguished as quickly as that in the wall-mounted indoor unit.

The airflow speed given by Eq. (2-2-10) is a function of the outlet height; the fan airflow speed increases as the outlet height decreases. For the height of the floor-standing indoor unit, the minimum airflow speed is generally close to that in Case 2. However, when Case 2 is adopted, the required airflow speed exceeds 3 m/s in a floor area of 20 m^2 or more, causing difficulty in generating a large fan airflow speed in a large area.

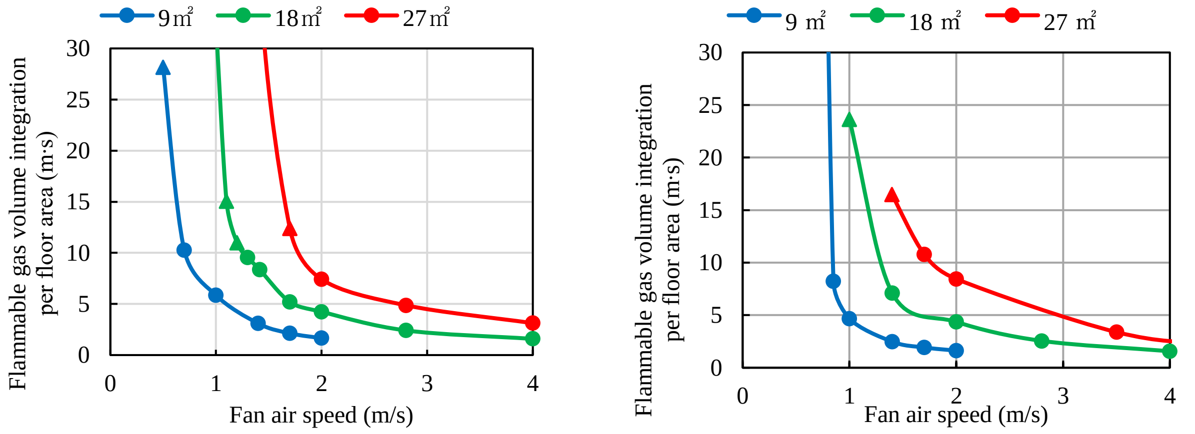

(a) wall-mounted unit (b) floor-standing unit

Fig. 2-2-16 Effect of fan air speed on flammable gas volume integration per floor area at different floor area.

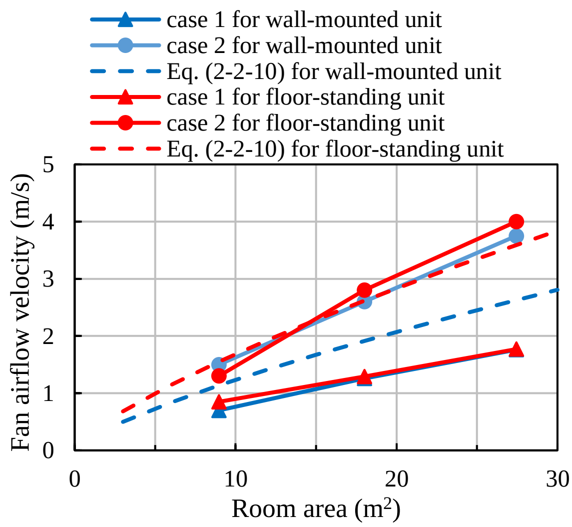

Fig. 2-2-17 Relationship between fan air velocity and room area.

2.2.7 Summary

To assess the risk of indoor leakage of R290, which is a candidate for the next-generation refrigerant for household air-conditioners, we verified the validity of the computational fluid dynamics analysis method and evaluated the stirring effect. The following findings were obtained from this study.

1) The validity of the computational fluid dynamics analysis method used in this study was verified by comparison of the numerical results with the results of refrigerant leakage experiments conducted using R744 and R32.
2) If the combustible gas region is defined as a region with a concentration of 50% LFL or more, when the R290 charge amount given by Eq. (2-2-3) was leaked from the wall-mounted indoor unit or the floor-standing indoor unit, combustible gas remained for a long time even after the leakage ended.
3) As for leakage from the wall-mounted indoor unit, blowing along directions diagonally downward to downward is effective.
4) Regarding leakage from the floor-standing indoor unit, blowing ~45° upward from the upper part is effective.
5) Regarding the effect of the width of the outlet on the fan airflow speed, the fan airflow speed is effective when it is inversely proportional to $\sqrt{A_0}$, as shown in Eq. (2-2-10).
6) If the fan airflow is directed in a direction that facilitates the formation of indoor circulating airflow, the combustible area can be extinguished with the same fan airspeed regardless of the type of indoor unit. In addition, the fan airflow speed obtained using Eq. (2-2-10) is close to the airflow speed required to extinguish the combustible region immediately after the leakage ends.

2.3 Refrigerant leakage from commercial refrigerated display cabinets

2.3.1 background

In this study, a computational fluid dynamics analysis was conducted on the indoor leakage behavior of highly flammable refrigerant R290, which is considered to be a next-generation refrigerant candidate for commercial built-in refrigerators and freezers. To verify the validity of the analysis model and calculation method, we conducted a leakage experiment from a display cabinet and compared the experimental results with the calculation results. In the experiment, we used R744, whose physical properties are close to those of R290.

This study aims to evaluate the safety of a reach-in display cabinet using R290. The international standard for commercial refrigerators and freezers is IEC 60335-2-89:2019 Edition 3.0[2-13)] (hereafter referred to as the “IEC standard”). The maximum charge amount of flammable refrigerant in the refrigeration cycle is specified as the smaller value of 13 times the LFL and 1.2 kg.

$$M_{\max} = 13 \times FL_L \qquad (2-3-1)$$

Because the FL_L of R290 is 0.038 kg/m^3, the maximum refrigerant charge amount is 0.494 kg. The minimum installation floor area for refrigeration equipment filled with combustible refrigerant exceeding 0.15 kg is given by the following formula:

$$A_{\mathrm{lim}} = M/\{2.2 \times (0.25 \times FL_L)\}, \qquad (2-3-2)$$

where 2.2 in the equation is the minimum ceiling height in m, and 0.25 × LFL represents 1/4 of the LFL. The minimum installation floor area for equipment filled with 0.494 kg of R290 is 23.7 m^2. If the equipment is installed in a space narrower than this value, the amount of refrigerant charge should be reduced. In addition, a refrigerant leakage test must be conducted for equipment filled with 0.15 kg or more of flammable refrigerant. In the reach-in display cabinet, the door or lid is opened after all the refrigerant has leaked into the cabinet. The refrigerant concentration around the equipment should be measured at intervals of 5 s or less and should not exceed 1/2 of the LFL after 5 min from the start of measurement.

In this study, to investigate a method to reduce the occurrence of fire accidents, a computational fluid dynamics analysis was conducted assuming a situation in which R290 leaked into a commercial refrigerated display cabinet and then flowed into the room during the opening of the cabinet door, referring to the IEC standard. We investigated the effects of the position of the condenser fan, blowing direction, and airflow speed on the indoor refrigerant concentration distribution and the size and existence time of the flammable area.

2.3.2 Method of computational flow analysis

The computational fluid dynamics analysis method used to simulate refrigerant leakage from a commercial reach-in display cabinet is the same as that used to simulate refrigerant leakage from household air-conditioners described in Section 2.2.2.

2.3.3 Numerical calculation model

The reach-in display cabinet, which uses refrigerant R290, is filled with a maximum charge amount of 0.494 kg as defined by the IEC standard. The minimum floor area of the room where this cabinet is installed is given by Eq. (2-3-2); this value is obtained by dividing the room volume at which the average concentration of the refrigerant leaking into the room is 1/4 LFL by the ceiling height of 2.2 m. Because the LFL of R290 is 0.038 kg/m^3, the minimum room volume is 52 m^3. However, the ceiling height of 2.2 m is a small value, and it is not realistic to use this ceiling height in the computational model. Therefore, the ceiling height was set at 2.5 m, marginally lower than the ceiling height of 2.7 m recommended in the guidelines for opening convenience stores[2-14)]. If the equipment with the maximum charge of R290 is installed in a room with a minimum installation floor area of 23.7 m^2 and a ceiling height of 2.5 m (room volume of 59.25 m^3), the average concentration at the time of leakage is less than 1/4 LFL, and the evaluation can be considered safe. Therefore, in this study, the floor area was set at 20.8 m^2 based on the minimum room volume of 52 m^3 and the ceiling height of 2.5 m. Because the floor area is smaller than the minimum installation floor area in the IEC standard, this is a strict evaluation.

An overview of the laboratory model is shown in Fig. 2-3-1. The room size was 5.2 × 4.0 × 2.5 m. The mesh was finer near the boundary. The initial conditions in the room were a gauge pressure of 0 Pa, a temperature of 300 K, and a refrigerant concentration calculated using the amount of refrigerant charge and the internal volume of the cabinet.

A commercial reach-in cabinet has two doors, and calculations were conducted for the swing and sliding door types. In the swing door type, two doors simultaneously rotate 60° in 3 s according to the IEC standard. In the sliding door type, one door opens sideways. In the calculation, one door on the right side was opened instantaneously, and the refrigerant flowed out. In this study, we considered only the case where the refrigerator was installed at the bottom of the cabinet. To simulate the operation of the condenser fan, we set a uniform speed in the region of the fan and opened the door from the steady state. Figure 2-3-2 is a detailed view of the arrangement with the refrigerator installed at the bottom, and the fan airflow is from the front to the back of the bottom toward the ceiling. The cabinet was installed with the centerline coinciding with that of the laboratory model and was 0.1 m away from the wall. Assuming a state in which multiple cabinets were lined up, we installed cover plates at both ends of the gap between the cabinet and the wall. Therefore, the gas sucked by the lower fan from the front passed through the gap in the rear and returned to the indoor space at the height of the top surface of the cabinet. This study focuses on cabinets in which the airflow is from the lower front to the upper rear.

For reference, we also conducted calculations when the refrigerator was installed at the bottom, and the fan airflow was from the bottom front to the bottom front; Fig. 2-3-3 provides a detailed view. Indoor air was taken in from the left inlet and discharged from the right. The parameters were the position of the condenser fan, blowing direction, and airflow speed.

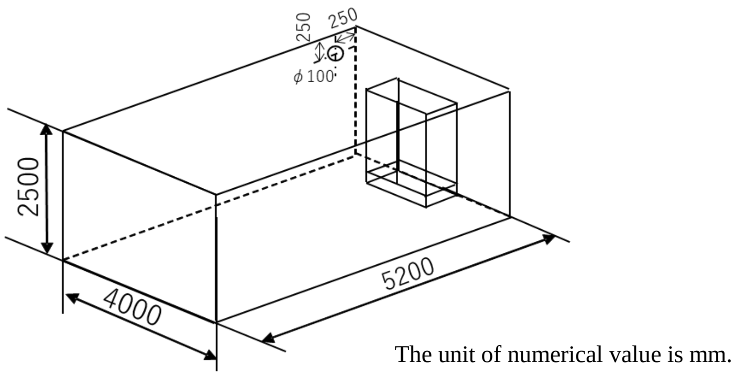

Fig. 2-3-1 Room model.

2.3.4 Validation of numerical calculation

(1) Verification of mesh independence

In this research, we followed the verification of the mesh independence discussed in Section 2.2. As the number of cells increased, the combustible gas volume converged. Based on these examination results, the number of cells in the room with a floor area of 20.8 m^2 was set to 4.0×10^6, considering the calculation time.

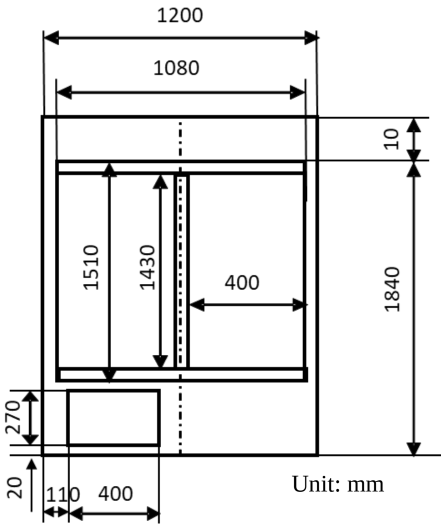

Fig. 2-3-2 Reach-in display cabinet; the condenser is installed at the bottom, and the air flows from the bottom to the top.

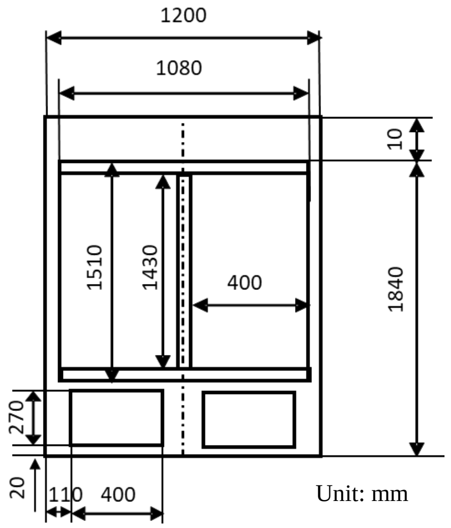

Fig. 2-3-3 Reach-in display cabinet; the condenser is installed at the bottom, and the air flows from the bottom to the bottom.

(2) Validation of the numerical model

In this study, the validity of the model was verified by comparing the numerical calculation and experimental results by measuring the concentration distribution in the refrigerant leakage test. The laboratory had a similar geometry as that of the computational model in Fig. 2-3-1; the dimensions were 5.6 × 3.8 × 2.55 m. Heat-insulating boards were installed on the side of the test room that is in contact with the outer wall to suppress the influence of the outside temperature. The indoor heat source was eliminated by taking in light from the lighting installed outside the test room through a skylight. R744 was used as the experimental gas to avoid any hazards during the experiment. Figure 2-3-4(a) shows the concentration measurement points specified by IEC 60335-2-89, and Fig. 2-3-4(b) shows the indoor concentration measurement points.

A cabinet model was fabricated, as shown in Fig. 2-3-5. The inside of the cabinet was hollow. As shown in Fig. 2-3-6, the doors were opened and closed by linear actuators attached to the two doors. The actuator had a stroke of 300 mm and a maximum speed of 100 mm/s and was adjusted by pulse-width modulation control to open the door by 60° in 3 s. A cushion was attached to the outer periphery of the opening of the main body to prevent gas leakage during gas charging before opening the door.

Refrigerant flowed into the cabinet from a hose installed in the lower rear part. At the time of inflow, the air inside the cabinet had to be removed. Because the R744 used as the refrigerant had a higher density than air, it stayed in the lower

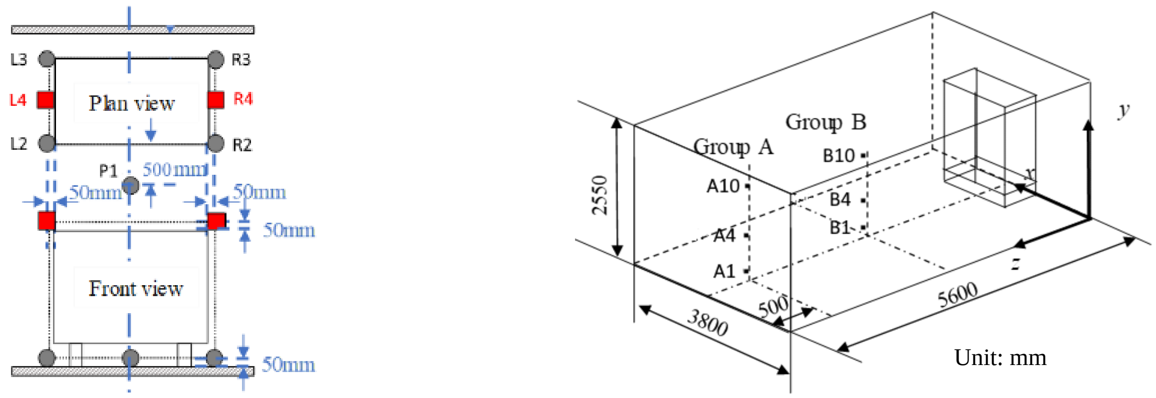

(a) Concentration measurement points specified by IEC 60335-2-89

(b) Concentration measurement points in the laboratory

Fig. 2-3-4 Concentration measurement points.

part of the cabinet, and the air was discharged from the upper part. The discharged gas was guided outside the test room with a hose to prevent it from flowing into the test room. A fan for agitation was installed in the cabinet, and after the filling, the discharge port was closed using a solenoid valve, and the inside of the cabinet was agitated to attain uniform gas composition.

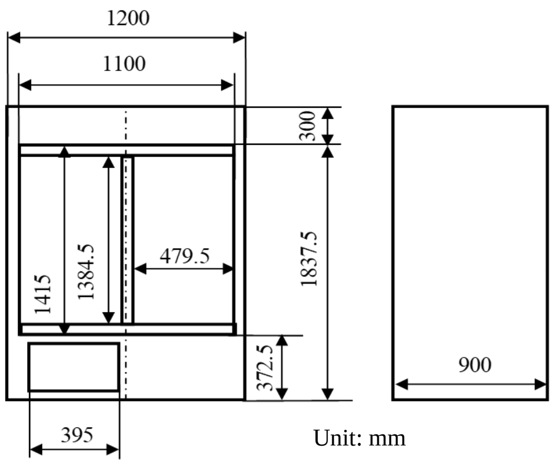

Fig. 2-3-5 Details of the display cabinet.

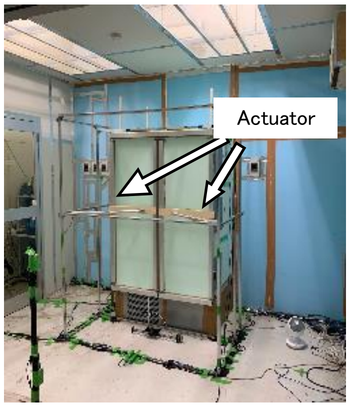

Fig. 2-3-6 Handmade display cabinet.

(3) Numerical calculation validation results

As examples of comparison between the experimental and calculation results, Fig. 2-3-7 shows the case in which the condenser fan is not operating, and Fig. 2-3-8 shows the case in which the condenser fan blows forward from the bottom at 1.3 m/s. Figures 2-3-7 (a) and 2-3-8 (a) provide the results of the measurement points specified in the IEC standard, and Figs. 2-3-7 (b) and 2-3-8 (b) show the values at each point in the room. When the fan did not operate, P1, L2, and R2 near the front attained their maximum values within 10 s immediately after the door opened, and then the values gradually decreased while undulating for 120~180 s. When the fan was operated, the difference in concentration was rapidly reduced by stirring; therefore, the undulation declined after 60 s, and the concentration was uniform. The significant difference between P1 and B1 under these conditions was because the fan was placed to the left in the experiment, as shown in Fig. 2-3-2, assuming an actual machine; in contrast, in the calculation, it was placed in the center to achieve symmetrical conditions. This was because the airflow from the fan hit the sensor directly. In addition, the reason for the longer duration of the rapid increase in the concentration immediately after opening the door in the experiment was presumed to be mainly caused by the response time of the sensor.

Thus, the calculated results were consistent with the experimental results in terms of both trends and values; therefore, we decided to conduct numerical calculations using this model.

2.3.5 Refrigerant leakage simulation results

(1) Effect of fan on generation of combustible gas region

Annexure CC of the IEC standard requires actual measurements at all eight measurement points around the cabinet and the concentration to fall below 50% of the LFL within 5 min of the start of leakage. Therefore, we investigated the effect of stirring with a fan. The condenser was installed at the bottom of the cabinet, and the volumes in which the concentration was over 50% LFL and between LFL and UFL were calculated for the entire room, including the measurement points.

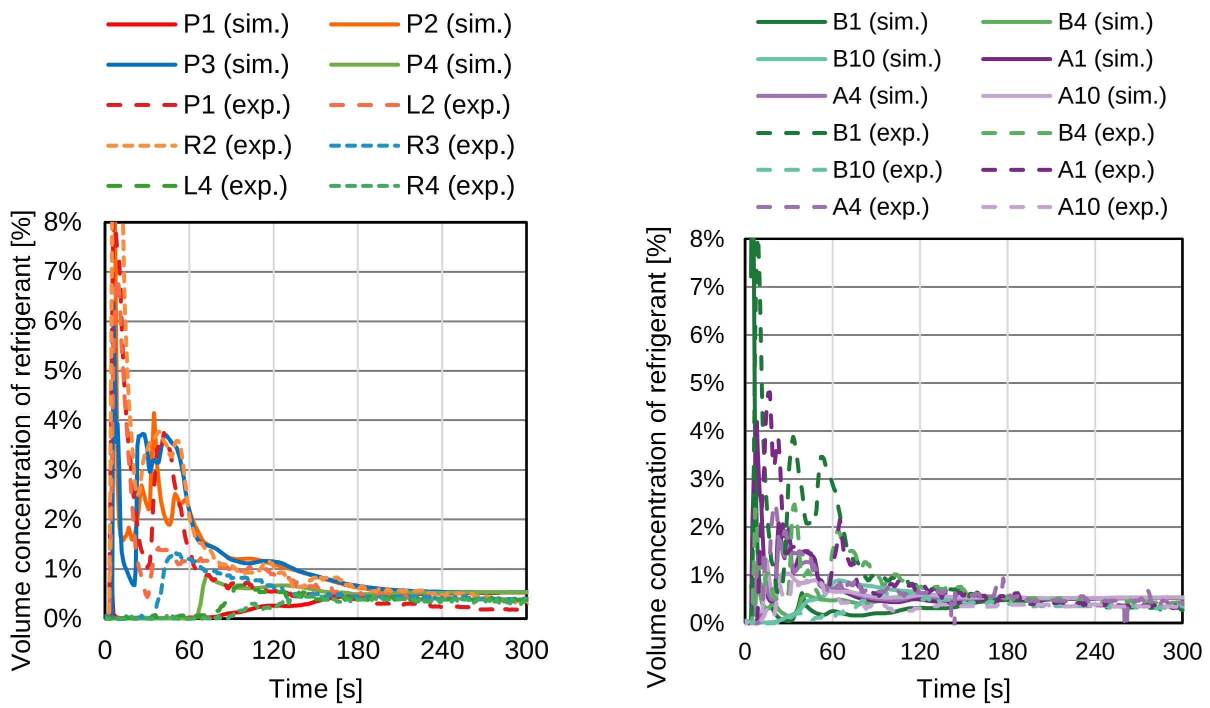

(a) (b)

Fig. 2-3-8 Comparison of simulation (sim.) and experiment (exp.) with a fan with an airflow speed of 1.3 m/s at the bottom when 494 g of R744 is released.

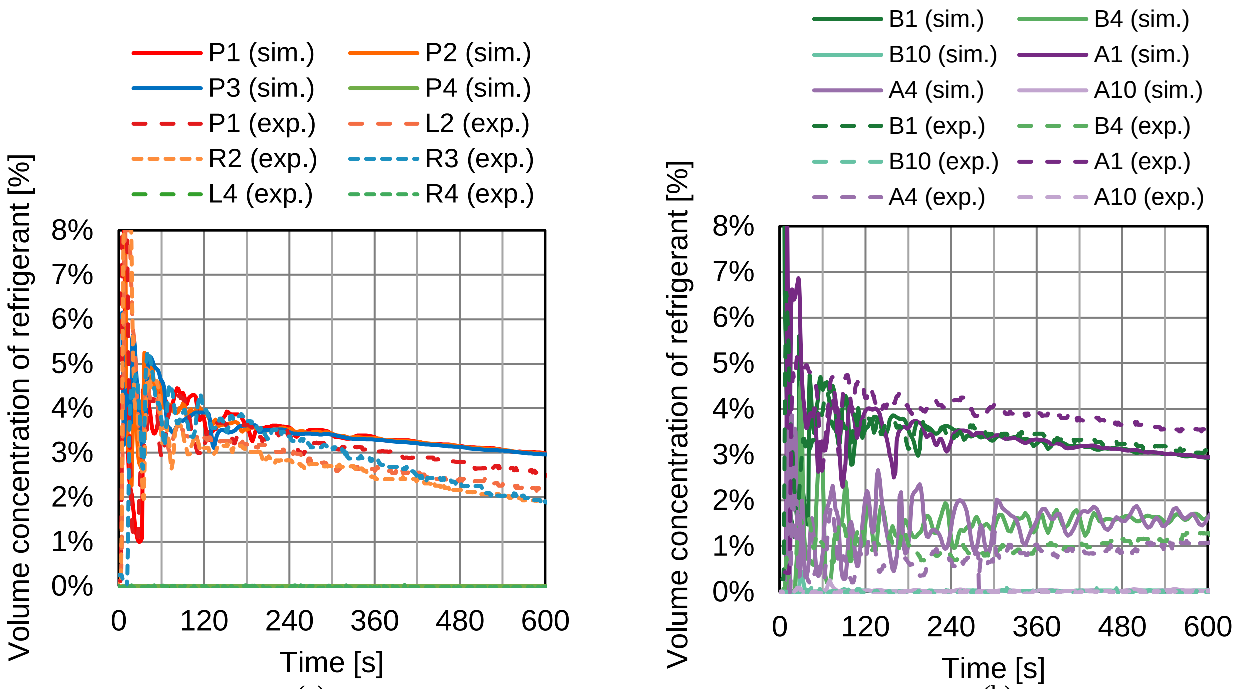

(a) (b)

Fig. 2-3-7 Comparison of simulation (sim.) and experiment (exp.) without fan when 494 g of R744 is released.

Figures 2-3-9 and 2-3-10 show the time transition of the combustible gas region when the air velocity of the condenser fan varies when 0.494 kg of R290 is discharged into a room of 20.8 m^2. In both cases, the condenser fan sucked in air from the bottom of the cabinet and discharged it to the top of the back. Figure 2-3-9 shows the results for the swing door-type arrangement, and Fig. 2-3-10 shows the results for the sliding door-type arrangement. The dashed line shows the change in volume in the region where the concentration was 50% LFL or higher, and the solid line shows the change in

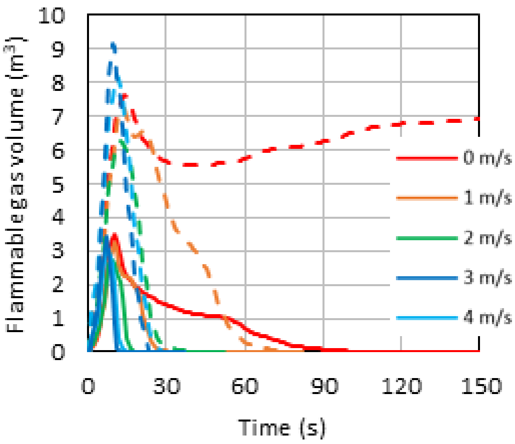

Fig. 2-3-9 Effect of condenser fan on flammable gas volume when 494 g of R290 is released through hinged doors.

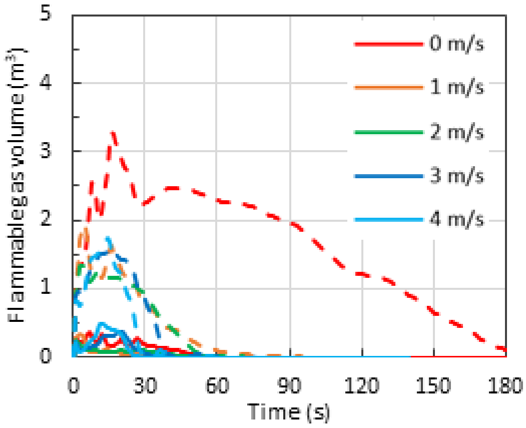

Fig. 2-3-10 Effect of condenser fan on flammable gas volume when 494 g of R290 is released through sliding doors.

volume in the region from LFL to UFL. Refrigerant gas might remain in the refrigerator for a long time; however, because of the absence of an ignition source inside the refrigerator, the volume of combustible gas in the refrigerator was not considered.

In the case of the swing door-type arrangement, because two doors opened, a large amount of refrigerant gas was discharged in a short span of time. In the case of the sliding door-type arrangement, only half of the door was opened; therefore, the refrigerant was released at a slow rate, and less combustible gas was generated.

(2) Time for elimination of combustible gas region using fan

Figures 2-3-11 and 2-3-12 show the elimination time of the combustible gas region when the airflow speed of the condenser fan was varied. This is the condition where 0.494 kg of R290 was discharged into a 20.8 m^2 room. The results are shown for both cases where the target space was the entire room, excluding the inside of the cabinet, and where the 8 measurement points in the IEC standard were used. Figure 2-3-11 shows the results for the swing door type, and Fig. 2-3-12 shows the results for the sliding door type. Even after the door was opened for a long time, the refrigerant gas remaining in the cabinet gradually flowed out, and a small region with combustible gas volume appeared near the opened door. Because this was not a risk, it was judged that the combustible gas region was eliminated when the combustible gas volume was less than 0.01 m^3.

According to Fig. 2-3-11, for the swing door type, if the fan airflow speed was 2 m/s or more, the combustible gas region was eliminated in ~60 s. Regarding the measurement points of the IEC standard, the combustible gas region persisted for the longest time at the front lower part of the open door side; however, the duration was shorter than the combustible gas elimination time in the entire space.

According to Fig. 2-3-12, for the sliding door type, if the fan airflow speed was approximately 1 m/s, the combustible gas volume was eliminated early. Comparing Figs. 2-3-11 and 2-3-12, the duration for the elimination of the combustible gas region was longer in the swing door type, and continuous operation of the condenser fan guaranteed safety.

(3) Influence of condenser fan air path

In this study, the condenser fan induced airflow from the lower front to the rear upper part; the case where airflow entered from the lower front and flowed out through the lower front was also calculated. Therefore, we investigated the effect of the air path of the condenser fan on the generation and elimination of the combustible gas region.

Figure 2-3-13 shows the elimination time of the combustible gas region when the condenser fan sucked from the lower front and discharged through the lower front. The charge amount of R290 and room area were unchanged, and calculations

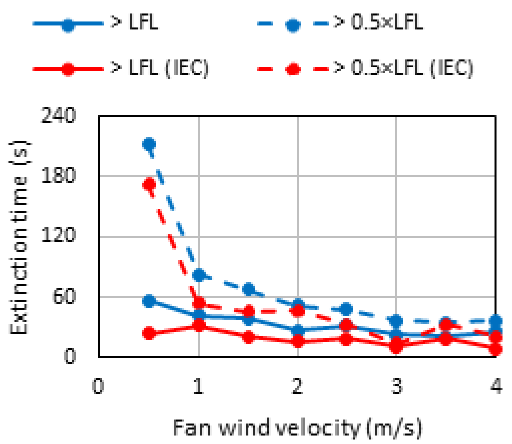

Fig. 2-3-11 Effect of condenser fan on extinction time of flammable gas through hinged doors.

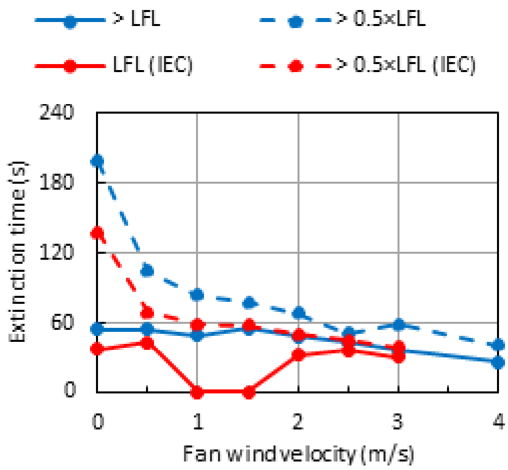

Fig. 2-3-12 Effect of condenser fan on extinction time of flammable gas through sliding doors.

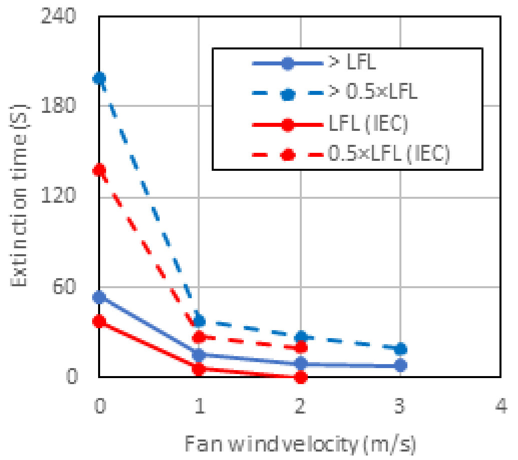

Fig. 2-3-13 Effects of condenser fan flow path on extinction time of flammable gas.

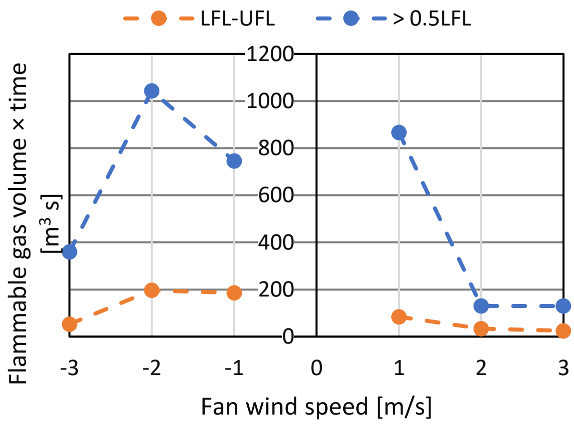

Fig. 2-3-14 Difference in time integration of flammable gas volume due to fan airflow direction.

were performed for the sliding door type. Comparing Fig. 2-3-13 with Fig. 2-3-12, the time required to eliminate the combustible gas region was shorter when the fan blew to the lower front.

Figure 2-3-14 shows the time-integrated value of the combustible gas volume under the condition of a swing door type with a fan at the bottom. A positive value of the airflow speed indicates a backward blow, and a negative value indicates a forward blow. Comparing the cases of 1 m/s, the magnitude of the time integral value was similar.

Thus, the direction of the airflow did not significantly affect the combustible gas generation for the cabinet with the refrigerator installed at the bottom. Notably, the suppression of combustible gas generation is difficult when the condenser is installed on top.

(4) Effect of installation floor space

In the IEC standard, the maximum charge amount of a flammable refrigerant is specified using the LFL of the refrigerant as in Eq. (2-3-1), and the minimum floor area according to the charge amount is specified by Eq. (2-3-2). These equations suggest that even if the equipment filled with the maximum charge amount is installed in a room with a large floor area, the risk does not decrease. To confirm this, we doubled the floor area to 40 m^2 and calculated the elimination time of combustible gas (see Fig. 2-3-14). The conditions other than the floor area were unchanged. The results are for the sliding door type.

Figure 2-3-15 shows that the elimination time of the combustible gas region is shorter than when the floor area is 20.8 m^2; however, the difference is insignificant at an airflow speed of 1 m/s.

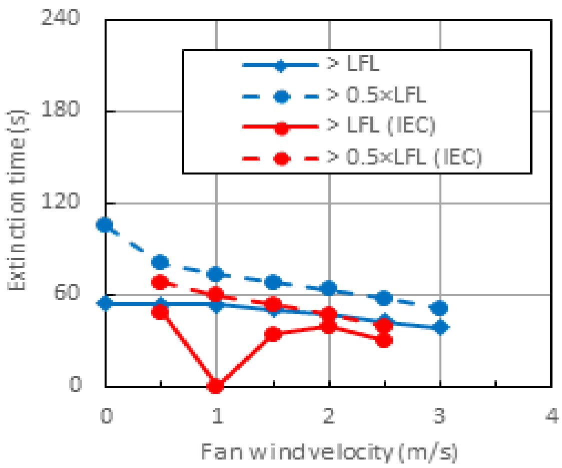

Fig. 2-3-15 Effect of condenser fan on extinction time of flammable gas for 40 m^2 of floor area.

2.3.6 Summary

For the purpose of risk assessment when R290 leaks indoors from a commercial showcase, we evaluated the effect of fan operation on the size of the flammable region using computational fluid dynamics analysis. The findings are as follows.

1) To verify the validity of the computational fluid dynamics analysis method used in this study, a refrigerant leakage experiment was conducted using R744. The transition of the concentration distribution in the room when the cabinet door was opened was measured, and the measured and calculated results were consistent.
2) For the swing-door-type refrigerator, 494g of gas leaked from the inside was combustible for more than 30 min when the condenser fan was not operating. The combustible gas region was eliminated in approximately 1 min when the condenser fan was used to stir at an airflow speed of 2m/s.
3) For the sliding-door-type refrigerator, the opening area of the door was small; therefore, the leakage rate of the refrigerant gas was low, and the volume of the combustible gas region was smaller than that of the swing-door-type refrigerator.
4) When the condenser fan was installed at the bottom, the results regarding the elimination of combustible gas region were similar for the cases of releasing air to the upper part of the rear and releasing air to the front of the lower part.

2.4 Suppression of diesel explosion during pump-down operation of household air-conditioner

2.4.1 Background

In this study, polyolester oil (POE) was used as a base oil for refrigerating-machine oil, and the effect of adding two different types of antioxidants and two stabilizers to suppress diesel combustion was experimentally investigated. The refrigerants used were R22, R32, R1234yf, and R290, which have different degrees of combustibility. R290 is highly flammable (A3), R32 and R1234yf are slightly flammable (A2L), and R 22 is non-flammable (A1). To clarify the mechanism of action, we analyzed the experimentally recovered oil. This study aims to suppress the compressor explosion accident caused by diesel combustion (hereinafter referred to as "diesel explosion") by improving the combustion resistance and oxidation resistance of refrigerating-machine oil.

2.4.2 Experimental equipment and experimental method

(1) Experimental equipment

The experimental equipment used was the same as that used in previous reports[2-15, 2-16]. Figure 2-4-1 shows an experimental device for simulating the inside of a compressor in a split air-conditioner in the event of a compressor explosion. The experimental equipment consisted of a compressor drive unit, refrigerant supply system, air supply system, refrigeration oil supply system, and measurement system. The compressor was simulated by a model airplane engine (R155-4C, 4-stroke, stroke volume: 25.42 cc, compression ratio: 16.0, manufactured by ENYA) and driven by an electric motor connected using an engine crankshaft. The flow rate of the refrigerant was controlled using a mass flow controller, and the refrigerant was supplied to the compressor. A mass flow controller controlled the flow rate of compressed air supplied from the compressor. The airflow from the compressor was passed through a dehumidifier. The refrigerant and air were raised to a predetermined temperature in the mid-section of the tube using an electric heater. These were then supplied to the compressor.

The refrigeration oil supplied from the tank was boosted by a hydraulic pump and injected from the injector of the oil injection system into the intake tube of the engine. The piston phase was tracked by the encoder and stroke sensor, and oil was injected when the phase angle of the piston was 90° (the top dead center position of the intake cycle was set to 0°). The equivalent ratio (φ) is defined as the ratio of the actual oil mass to the oil mass that burns entirely with the air mass in the stroke volume of the engine. The theoretical air–fuel ratio was obtained from the CHO mass fraction of the oil and air mass in the stroke volume of the engine. The oil injection pressure was 100 MPa, and the relationship between the oil injection time and mass was experimentally calibrated in advance. A personal computer controlled the motor by using a servo amplifier. The pressure inside the engine was measured using a piezoelectric pressure sensor. The exhaust gas temperature was measured using a K-type sheath thermocouple (0.5 mm outer diameter) installed in the exhaust tube.

The refrigeration base oil was a POE with an ISO viscosity of 68. A phenolic antioxidant (A1), epoxy stabilizers (A2, A6), and an amine antioxidant (A4) were selected and used as additives to suppress diesel combustion. Additives for refrigeration oils include antioxidants and stabilizers. Because increasing the additive concentration affects the lubricating performance, the additive concentration was set to 1 wt%, and an experiment was also conducted at 5 wt% for reference. R290, R1234yf, R32, and R22 were used as refrigerants to consider the effects of refrigerant flammability. Tables 2-4-1 and 2-4-2 list the experimental conditions and physical characteristics of the refrigeration base oil and additives, respectively.

Table 2-4-1 Experimental conditions

Compressor model engine	ENYA R155-4C (modified)
Compression ratio [-]	16
Stroke volume [cc]	25.42
Engine revolution speed [rpm]	1500
Mixture gas flow rate [L·min^{-1}]	18.8
Oil injection timing [°]	90 (at crank angle)
Inlet gas temperature [°C]	260±5, 270±5
Oil equivalent ratio [-]	1
Refrigerant concentration [vol%]	0–64.9

Table 2-4-2 Properties of base oil and additives

Refrigeration base oil		POE
ISO viscosity grade		68
Ignition point [°C]		408
CHO ratio [wt%]		C:H:O = 70.1:10.8:19.1
Theoretical air-fuel ratio [-]		10.91
Additive	A1	dibutylhydoxytoluene
	A2	glycidyl ester
	A4	aromatic amine
	A6	alicyclic epoxy
Additive concentration [wt%]		0, 1, 5

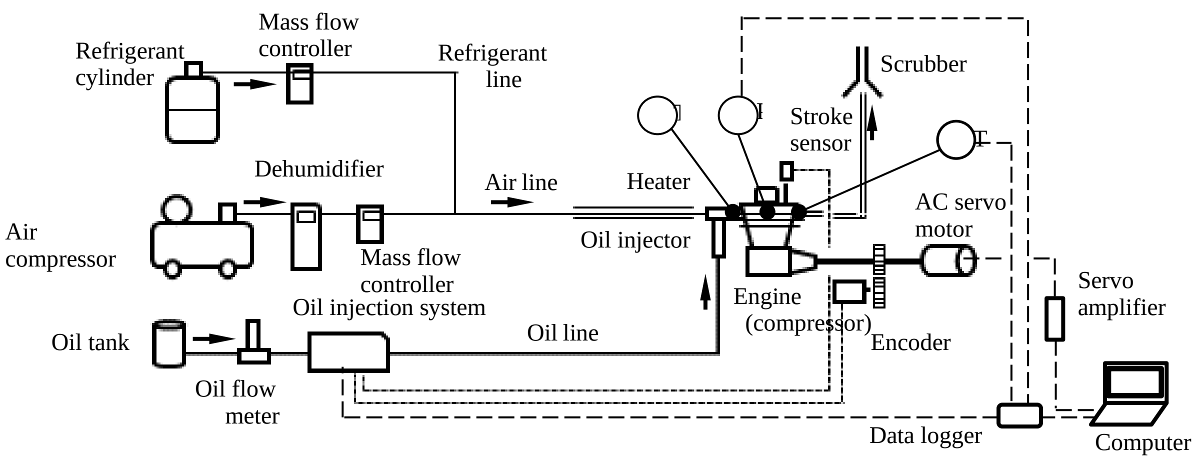

Fig. 2-4-1 Experimental apparatus.

(2) Experimental method

The experiments were conducted in the following order. A specified amount of air was supplied to the engine while operating at an engine speed of 50 rpm. The voltage of the electric heater wound around the tube was increased until the air temperature at the engine inlet reached a predetermined value, after which the temperature stabilized, and a predetermined amount of refrigerant flowed. The oil spray system was operated to inject oil after the engine speed was changed to 1500 rpm. The data were recorded a few seconds after the oil was injected. Experiments were conducted with different refrigerants and additives by varying the refrigerant concentration. The equivalence ratio (φ) was maintained at 1. In a series of experiments, we replaced the engine due to the equipment's engine failure. After confirming the effect of individual engine differences before and after replacement in detail, we changed the mixed gas temperature at the engine inlet from 260±5 °C to 270±5 °C and restarted the experiment under conditions that facilitate combustion. A reference additive was set and compared to ensure consistency with the results before and after replacement.

2.4.3 Experimental results regarding additive effects

(1) Effect of phenolic antioxidant (A1)

Figure 2-4-2 shows the relationship between the refrigerant concentrations of R22, R32, R1234yf, and R290 and the maximum dimensionless pressure with the additive A1. P_0, used for the dimensionless pressure, is the measured maximum pressure when air at 260 °C is adiabatically compressed. Because the gap between the inner wall of the engine cylinder and the piston varied and the rising pressure also varied, P_0 was measured at the beginning of each experiment and was 2.0 to 2.3 MPa. Comparing the refrigerant concentrations at the upper limit of the combustion range of R22 in Fig. 2-4-2 (a), 32 vol% was obtained without the additive, and 22 and 5 vol% were obtained for 1 and 5 wt% of additive A1, respectively. The upper limit of the flammable refrigerant concentration decreased as the additive concentration increased. The combustion range decreased significantly as the additive concentration increased. At additive concentrations of 0, 1, and 5 wt%, the maximum dimensionless pressures were 3.4, 3.2, and 2.0, respectively. The maximum pressure decreased with increasing additive concentration. The combustible refrigerant concentration range of R32 was 0–20 vol%, which was narrower than that of R22 and wider than 0–6 vol% R1234yf. The effect of the additive concentration on R32 and R1234yf was not significant. The combustion range of R290 was as narrow as 0–2.5 vol%, and the dimensionless maximum pressure decreased as the additive concentration increased.

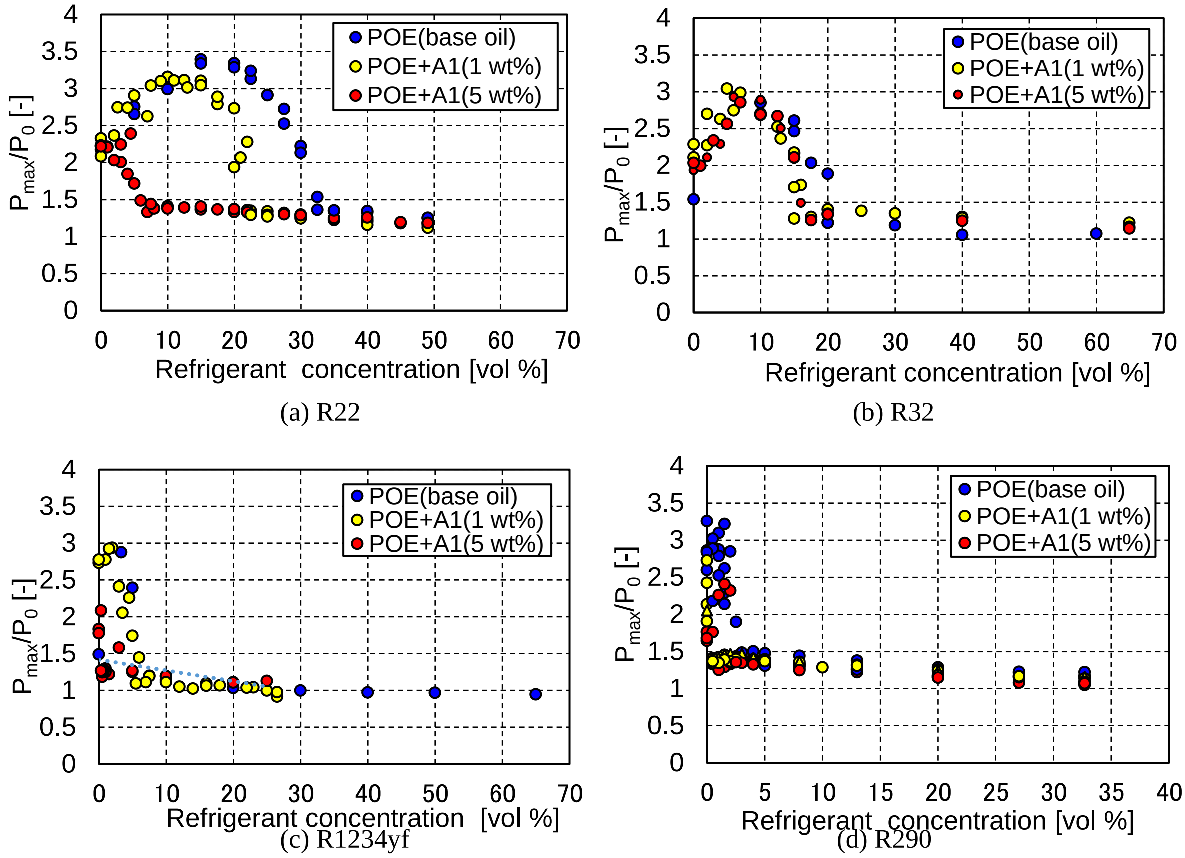

(a) R22 (b) R32

(c) R1234yf (d) R290

Fig. 2-4-2 Relationship between the maximum pressure of mixed gas and the refrigerant concentration for additive A1.

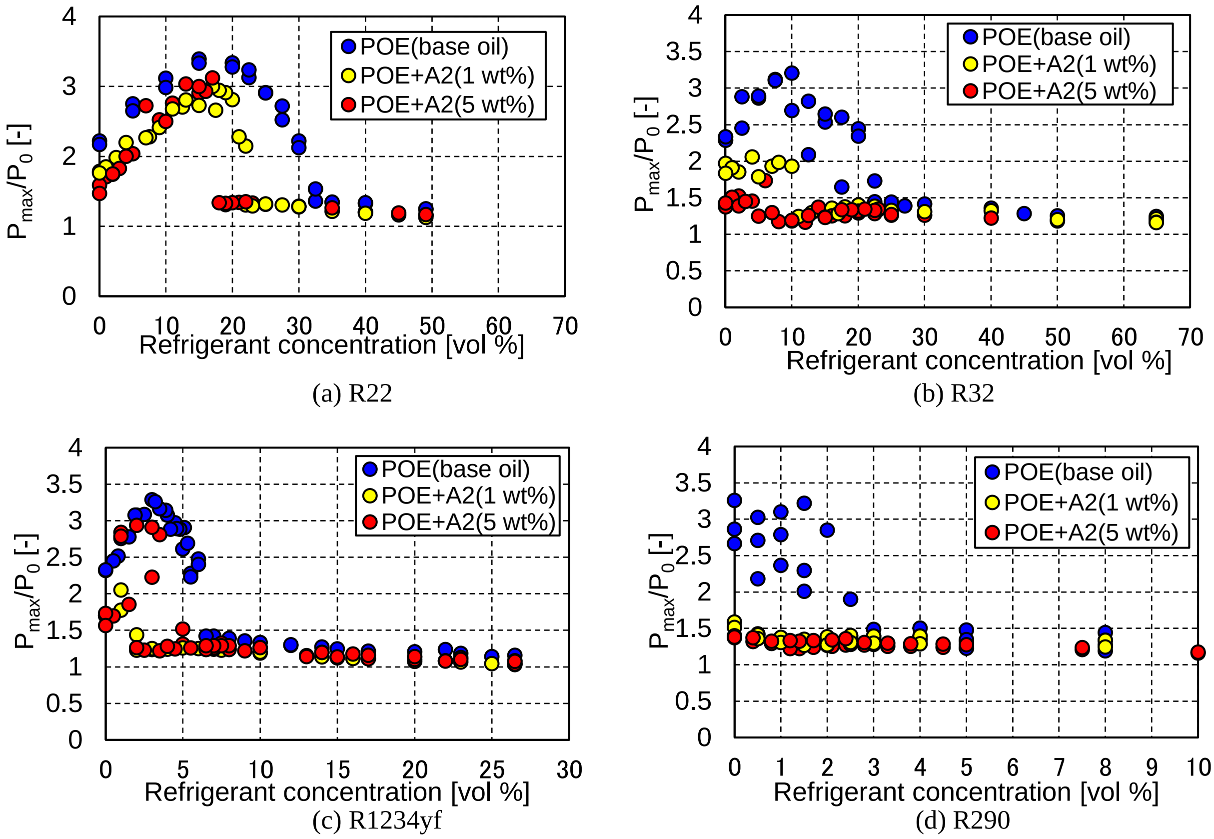

(a) R22 (b) R32

(c) R1234yf (d) R290

Fig. 2-4-3 Relationship between the maximum pressure of mixed gas and the refrigerant concentration for additive A2.

(2) Effect of epoxy stabilizer A2

Figure 2-4-3 shows the relationship between the refrigerant concentrations of R22, R32, R1234yf, and R290 and the maximum dimensionless pressure with the additive A2. In Fig. 2-4-3 (a), the upper limits of the combustible refrigerant concentrations of R22 were 32, 22, and 18 vol% when the additive concentrations were 0, 1, and 5 wt%, respectively. The upper limit decreased as the additive concentration increased. Comparing the upper limit of the combustible refrigerant concentration of R32, it was 20 vol% without the additive and 10 vol% with 1 wt% of additive A2, and the combustion range was eliminated at 5 wt%. The upper limit of the combustible refrigerant concentration for R1234yf did not exhibit a regular trend. For R290, the explosive range was eliminated, even at an additive concentration of 1 wt%.

(3) Effects of additives A4 and A6

In the experiments with additives A4 and A6 after engine replacement, additive A2, which had the greatest combustion suppression effect, was set as the reference additive, and the effects of the three types of additives were compared. Figure 2-4-4 shows the combustion regions of additives A4, A6, and A2. When refrigerant R22 was used, as shown in Fig. 2-4-4 (a), the flammability ranges of A2, A4, and A6 were 0–30 vol%, 0–21 vol%, and 0–30 vol%, respectively. For R32, as shown in Fig. 2-4-4 (b), the flammability ranges of A2, A4, and A6 were 0–19 vol%, 0 to 11 vol%, and 0 to 19 vol%, respectively. For R1234yf, as shown in Fig. 2-4-4 (c), the flammability range of A2, A4, and A6 were 0–7.5 vol%, 0–3 vol%, and 0–8 vol%, respectively. In refrigerants R22, R32, and R1234yf, the flammability range of additive A4 was significantly narrower than that of A2. The flammability range of A6 was approximately the same as that of A2. The maximum pressures in the combustion zones of A2, A4, and A6 were similar. In R290, combustion did not occur in the cases of A2, A4, and A6.

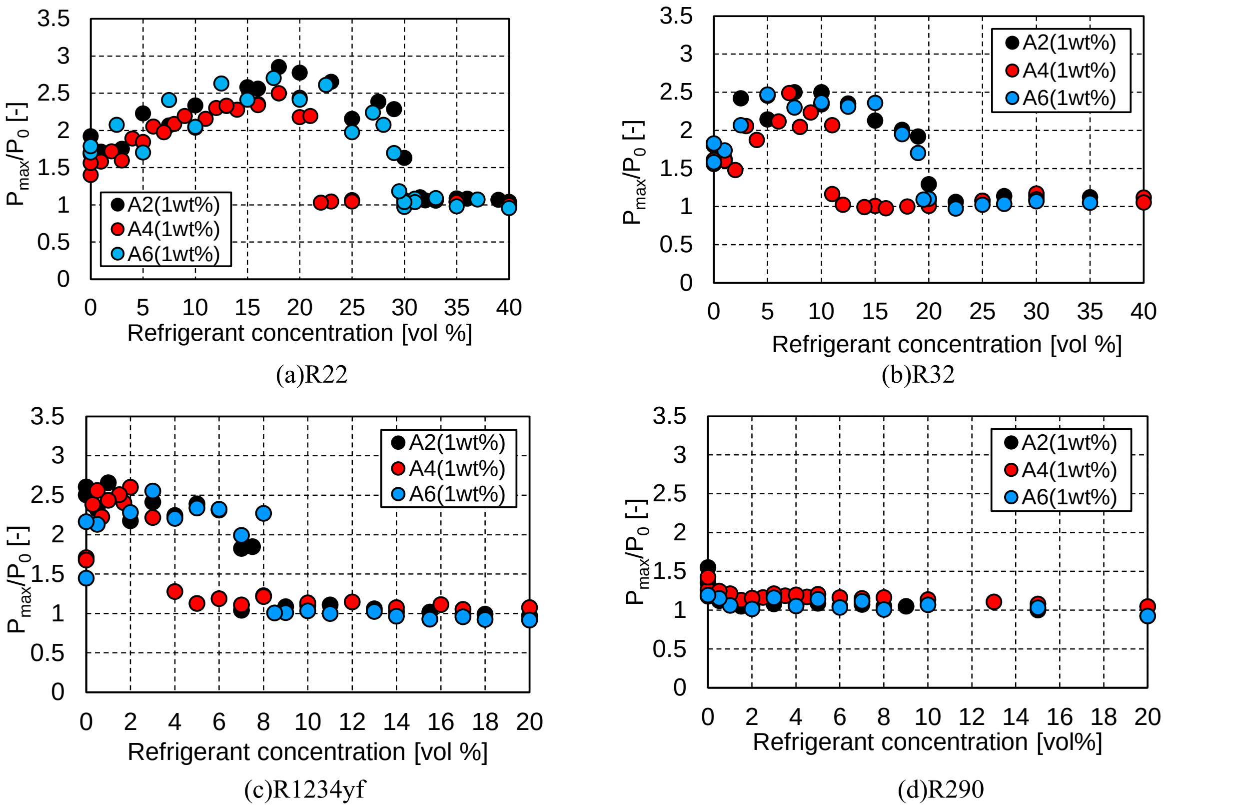

Fig. 2-4-4 Relationship between the maximum pressure and the refrigerant concentration for additives A4 and A6.

(4) Summary of additive effects

The higher the concentration of the additive, the narrower the flammability range of the refrigerant. However, additive concentration affects lubrication performance, and a low additive concentration is desirable. Figure 2-4-5 summarizes the effect of 1 wt% additives A1 and A2 on the upper limit of the flammability range of each refrigerant. As a result, A2 showed superior performance. The addition of A2 inhibited diesel combustion of R1234yf and R290 and significantly reduced the combustion range of R32. However, the effect of suppressing the explosion of R 22 was not significant.

Figure 2-4-6 shows the upper limit of flammability for each refrigerant of additives A2, A4, and A6. The flammable range was wide for the nonflammable refrigerant R22, followed by the mildly flammable refrigerants R32 and R1234yf. Combustion did not occur with highly flammable R290. Regarding the upper limit of flammability for each additive, compared to additives A2 and A6, additive A4 reduced combustion by 30% for R22, 40% for R32, and 50% or less for R1234yf. Antioxidant A4 could substantially suppress the combustion of R1234yf and R290 and considerably limit the combustion range of R22 and R32.

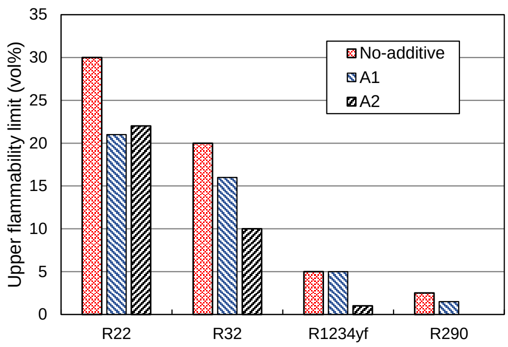

Fig. 2-4-5 Effect of 1 wt% additives on the upper flammable limit of each refrigerant.

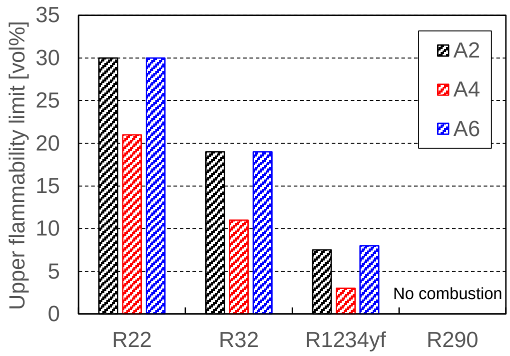

Fig. 2-4-6 Effect of additives on the upper flammable limit of each refrigerant.

2.4.4 Discussions

Based on the self-ignition phenomenon of diesel engines[2-17], the initial process of diesel combustion is assumed to be the self-ignition of refrigerating-machine oil in a high-temperature, high-pressure field, and alkyl radicals and peroxides derived from refrigerating-machine oil are generated. A1 and A4 are radical-scavenging antioxidants, and the radical-scavenging rate of A4 is twice that of A1[2-18]. In this study, the combustion suppression effect of A4 is significantly higher than that of A1, reflecting the radical-scavenging speed. To elucidate the mechanism of action of the epoxy stabilizer, the oil (R22/A2 blended oil/air) was recovered after the combustion experiment, and the structure of additive A2 was analyzed using liquid chromatography, ^{13}C-nuclear magnetic resonance spectroscopy (NMR), and ^{19}F-NMR. When the amount of A2 added was 5 wt%, the A2 in the recovered oil completely deteriorated. The epoxy groups were ring-opened, and the components of the modified product were 1.7 wt% of the hydrate of A2 and 3.3 wt% of reactants such as peroxides and fluorine derived from the refrigerant. From the above, it was inferred that radical-scavenging antioxidants and epoxy-based stabilizers added to POE oil captured the reactive species generated at the beginning of combustion and suppressed diesel combustion.

2.4.5 Summary

To suppress diesel explosions caused by erroneous operation during the pump-down operation of air-conditioners, the effects of four types of additives were investigated through experiments, and the findings are as follows.

1) The flammability range of additive A4 was 30 to 50% narrower than that of A2 and A6 for refrigerants R22, R32 and R1234yf, and A4 had the greatest combustion suppression effect.
2) The flammability ranges of A2 and A6, which were epoxy stabilizers, were almost the same. Combustion did not occur with refrigerant R290 using any additive.
3) The combustion suppression effect of additive A1 was not significant.
4) As for R22, the explosion could not be suppressed using a small amount of additive.

2.5 Research on the degree of hazard when flammable refrigerant ignites indoors

2.5.1 Abstract

To evaluate the degree of hazard when a flammable refrigerant ignites indoors, the flammable range of the refrigerant formed in the room when the refrigerant leaks is needed, along with the indoor temperature and pressure rise rate when the leaked refrigerant burns. Therefore, experimental measurements and numerical simulations of the formation process of the combustible concentration region at the time of refrigerant leakage are being carried out considering the actual operating conditions of air-conditioners. Furthermore, experimental measurement of the pressure change after refrigerant ignition is also carried out using an experimental container and an actual room. However, the research on the combustion/explosion reaction mechanism when the refrigerant ignites is limited, and conducting an experimental evaluation that considers the shape, position, and scale of the leakage space, as well as the location of the ignition source, is difficult. This study aims to clarify the effect of combustibility and the scale law using combustion simulations of refrigerants to evaluate the degree of danger when combustible refrigerants burn.

2.5.2 Combustion simulation model

In the combustion simulation, the mass, momentum, and energy conservation equations that describe the flow and heat transfer are solved along with the chemical species transport equations that describe the chemical reaction to determine the reactant concentration after ignition of the refrigerant, the time and space variation of the product concentration, and the temperature and pressure variation within the computational domain. The temperature and pressure changes are used to evaluate the degree of danger when the refrigerant ignites.

As an example of the combustion reaction of mildly flammable refrigerants, the oxidation reaction of R32 (CH_2F_2) is described by the overall reaction equation below.

$$CH_2F_2+O_2 \leftrightarrow CO_2+2HF \tag{2-5-1}$$

The overall reaction equation omits the detailed process of a chemical reaction and describes only the chemical species of the reactants and the final products. If the chemical reaction to be calculated is rapid, such as the oxidation reaction of hydrogen, analyzing the reactants and products involved in the reaction is possible using the following chemical species transport equation.

$$\frac{\partial}{\partial t}(\rho Y_i) + \nabla \cdot (\rho \boldsymbol{v} Y_i) = w_i - \nabla \cdot (\rho Y_i \boldsymbol{V}_i), \tag{2-5-2}$$

where ρ is the density of the mixture, Y is the mass fraction, v is the velocity, w is the mass production rate, and V is the diffusion velocity vector.

In addition, for premixed combustion, analyzing the concentration change of each chemical species is possible using the following transport equation of the progress variable.

$$\frac{\partial}{\partial t}(\rho c) + \nabla \cdot (\rho \boldsymbol{v} c) = \nabla \cdot \left(\frac{\mu}{Sc} \nabla c\right) + \rho Sc, \tag{2-5-3}$$

where c is the degree of reaction progress; c = 0 represents the unburned gas, c = 1 represents the burned gas, and the isosurface at c = 0.5 is considered as the combustion surface.

Actual chemical reactions cannot usually be entirely represented using the overall reaction as they proceed through many steps. These individual reactions are called elementary reactions. The combustion reaction of mildly flammable refrigerants such as R32 generally has a slow combustion speed, and reproducing the actual phenomenon with a combustion model based on the overall reaction equation is difficult. A detailed reaction model that describes the elementary reactions contributing to the combustion of mildly flammable refrigerants should be developed, and the transport equations of the chemical species involved in each elementary reaction must be solved. However, detailed chemical reaction models for mildly flammable refrigerants have not been studied in detail. In addition, as shown below, depending on the number of models of the chemical species involved in the oxidation reaction of R32, the number of elementary reactions will be tens to hundreds, and the number of elementary reactions will be on the order of hundreds to thousands. The computational load is extremely large to perform three-dimensional and dynamic simulations necessary for evaluating the degree of hazard during combustion.

Part of the elementary reaction model for the oxidation reaction of R32 is listed as follows:

$$CH_2F_2+OH <-> CHF_2+H_2O \qquad (2\text{-}5\text{-}4)$$
$$CH_2F_2+O <-> CHF_2+OH$$
$$CH_2F_2+H <-> CHF_2+H_2$$
$$CH_2F_2+HO_2 <-> CH_2F_2+O_2$$
$$CH_2F_2+HO_2 <-> CH_2F_2+O_2$$
$$CH_2F_2+F <-> CHF_2+HF$$
$$CH_2F_2(+M) <-> CHF+HF(+M)$$
$$CH_2F_2+CHF <-> CHFCHF(Z)+HF$$

…

In this study, we conducted a literature survey and organized the elementary reaction model of mildly flammable refrigerant R32. Using the elementary reaction model, we analyzed the basic characteristics of the combustion reaction of R32 refrigerant. In addition, using ANSYS Fluent, the maximum pressure and pressure rise rate after ignition of refrigerant in containers of different sizes (diameter 0.3, 1, and 3 m) were analyzed. In the future, we will build a simplified elementary reaction model and conduct simulations from refrigerant leakage to ignition to perform simulations with the combustion space scaled up to the size of a living room.

2.5.3 Elementary reaction model

Regarding the combustion reaction model of R32, a detailed reaction model was developed by removing unnecessary parts, such as molecules containing three or more C atoms, from the data compiled by Babushok et al.[2-18]; 99 chemical species and 927 reaction formulas were obtained. This model could calculate the overall combustion reaction of R32 with the degree of reaction progress c as a parameter. We also developed a chemical species transport model considering 99 chemical species simultaneously and confirmed that the flame propagation during the ignition of R32 could be simulated. However, further simplification of the elementary reaction model is necessary due to the large computational load.

Recently, NIST has published detailed chemical reaction models for the combustion reaction of fluorocarbons containing C1-C3 (R-32, R-125, R-134a, R-152a, R-143, R-143a, R-1234yf, R-1234ze(E), R-1243zf) and their mixtures [2-19]. Among them, a more simplified combustion reaction model of R32 (30 chemical species, 111 elementary reaction equations) was proposed [2-20], [2-21]. Using the model, the laminar burning velocity characteristics of R32 were investigated with Chemkin Pro, and the effect of vessel size on the pressure rise characteristics after in-vessel ignition of R32 was evaluated.

2.5.4 Combustion reaction characteristics of R32

(a) Laminar burning velocity and flame speed

A flame occurs when a refrigerant with a combustible concentration range is ignited. Active chemical species (radicals), such as O, H, and OH, are transported from the flame toward the unburned mixture ahead by molecular diffusion, and the flame propagates toward the unburned mixture. The moving speed of the flame front is called the burning speed. A static or lamina mixture has a laminar burning velocity (S_L), and a turbulent mixture has a turbulent burning velocity (S_T). The laminar burning velocity is an index that represents the combustion reaction velocity. In addition, it varies depending on the pressure, unburned gas temperature, and equivalence ratio.

The turbulent burning velocity is a function of the laminar burning velocity and the flow turbulence velocity u'. It can be approximately expressed using the following formula.

$$S_T \cong S_L + u' \qquad (2\text{-}5\text{-}5)$$

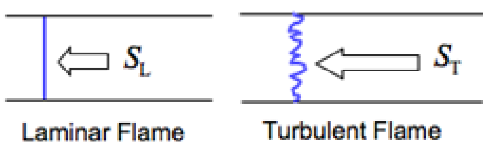

Fig. 2-5-1 Laminar and turbulent burning velocities.

In the flame region, the burned gas expands due to the release of combustion heat, and the actual apparent flame velocity (w_b) is significantly larger than the laminar (or turbulent) burning velocity. Assuming that the pressure difference before and after the flame zone is negligible, the following relation holds between the flame velocity and the burning velocity from the conservation of mass at the flame front.

$$w_b = \left(\frac{\rho_u}{\rho_b}\right) S_L, \qquad (2\text{-}5\text{-}6)$$

where w_b is the flame speed, and ρ_u and ρ_b are the unburned and burned gas densities, respectively.

For example, the laminar burning velocity of R32 is 7.2 cm/s at a temperature of 300 K and a pressure of 1 atm. When R32 inside a container with a radius of 0.5 m is ignited, the flame takes about 1s to propagate to the wall.

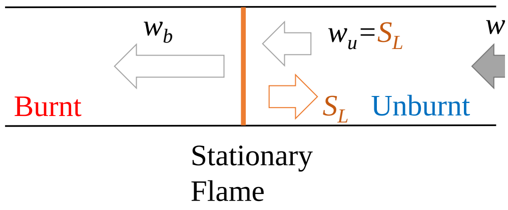

Fig. 2-5-2 Calculation model for laminar burning velocity.

(b) Temperature and pressure dependence of laminar combustion velocity

A one-dimensional model shown in Fig. 2-5-2 is used to calculate the laminar burning velocity. When unburned gas is supplied from the right side of the flow channel at a constant speed and burned at the center position of the flow channel, the gas supply speed w_u when the flame is fixed at the center position is equal to the laminar combustion speed S_L.

Chemkin Pro was used to calculate the laminar burning velocity at unburned gas temperatures of 300 to 900 K, pressures of 1 to 10 atm, and equivalence ratios of 0.5 to 1.5. The results are shown in Fig. 2-5-3.

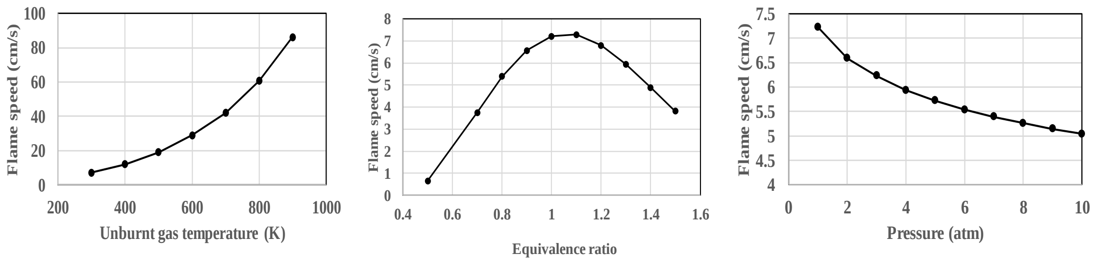

(a) Effect of temperature (b) Effect of equivalent ratio (c) Effect of pressure

Fig. 2-5-3 Laminar burning velocity.

The higher the temperature of the unburned gas, the faster the laminar combustion velocity. The laminar burning velocity calculated at an unburned gas temperature of 300 K was 7.2 cm/s and increased to 86.2 cm/s when the temperature was increased to 900 K. In addition, the laminar burning velocity first increased with the equivalence ratio (molar fraction), and after reaching the maximum value (7.3 cm/s) at the equivalence ratio of 1.1, the laminar burning velocity decreased as the equivalence ratio increased. When the equivalence ratio was 1.5, the laminar burning velocity decreased to 3.8 cm/s. Furthermore, the laminar burning velocity decreased as the pressure increased. The laminar burning velocity calculated at a pressure of 10 atm was 5.0 cm/s. The calculation results of this study are consistent with the experimental results reported in the 2016 Mildly Flammable Refrigerant Risk Assessment Study Group Final Report [2-22].

Table 2-5-1 Experimental results of laminar burning velocity of R32[2-22]

Refrigerant	Equivalence ratio (ϕ)	Temperature (°C)	Moisture	P_{max} (100 kPa)	K_G (100 kPa·m/s)	Flame speed S_f (cm/s)	Buring velocity S_u (cm/s)
R32	1	35	Dry	7.5	7.6	62	7.3
	1.1	35	Dry	7.3	8	65	7.6
		35	Wet (64% RH)	7.2	10.6	71	8.5

(c) Combustion reaction characteristics of R32

Figure 2-5-4 shows the variation in gas temperature and concentrations of major chemical species against the inlet distance.

As shown in Fig. 2-5-4 (a), at the flame front, the concentration drops rapidly due to the combustion reaction of R32 and becomes almost zero at the downstream side. The temperature of the flame front increases rapidly from 300 K of the unburned gas to the temperature of the burned gas, which is approximately 1940 K. On the downstream side, although most of the fuel R32 reacted, the flame temperature continued to rise due to the reaction of its decomposition products and finally increased to the adiabatic flame temperature of 2164 K.

Figure 2-5-4 (b) shows the concentration changes of H_2O and HF. Although H_2O is not involved in the overall reaction shown in Equation 2-10, it is generated by the hydrogen abstraction reaction by the OH radical and CH_2F_2 on the flame front, and the generated H_2O mainly reacts with the F radical to generate OH radical and HF.

Figure 2-5-4 (c) shows variation in CO and CO_2 concentrations. CO is also not included in the oveall reaction, but after generating CO by the decomposition reaction of CFO, CO_2 is generated through the reaction of CO＋OH -> CO2＋H; CO＋O(+M) -> CO2(+M).

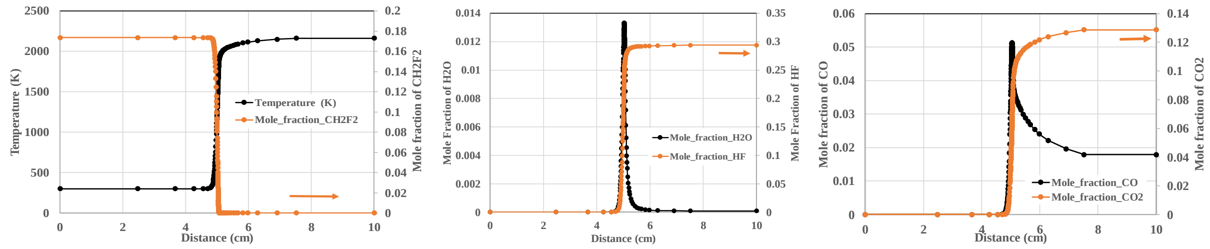

(a) Temperature and R32 concentration (b) H_2O and HF concentrations (c) CO and CO_2 concentrations

Fig. 2-5-4 Variation in each parameter from the entrance (temperature: 300 K, pressure: 1 atm, equivalent ratio: 1).

Using Chemkin Pro's reaction path analysis tool, a chemical reaction path diagram was created under the conditions of a temperature of 300 K, pressure of 1 atm, and equivalence ratio of 1.0. Figures 2-2-5 to 2-2-7 show reaction path analysis and main chemical species and elementary reactions on the upstream, inside, and downstream sides of the flame front. A detailed analysis is avoided; the decomposition reaction of CH_2F_2 on the upstream side of the flame front produces CHF_2 and H_2O through hydrogen abstraction by OH radicals. Several reactions occur simultaneously at the flame front.The CH_2F_2 decomposition reaction is primarily a hydrogen abstraction reaction by F and O radicals. The generated CHF_2 reacts with O, OH, H, and F radicals and is consumed. On the downstream side, HF and CO_2 production reactions are progressing primarily from intermediate products.

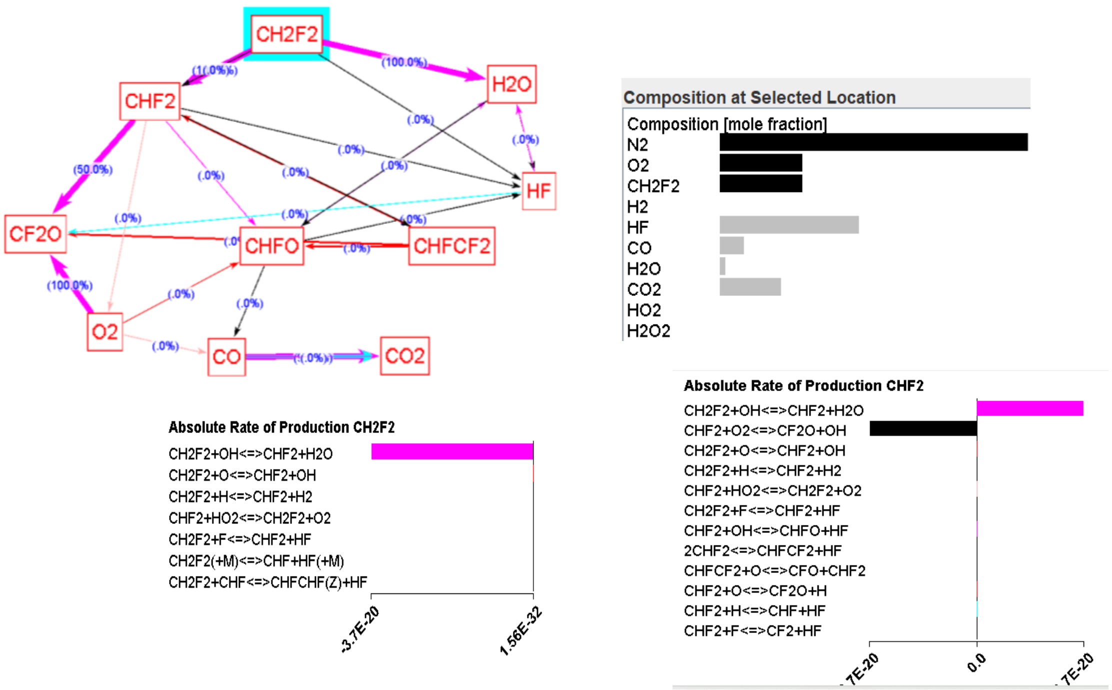

Fig. 2-5-5 Reaction path analysis on the upstream side of the flame surface.

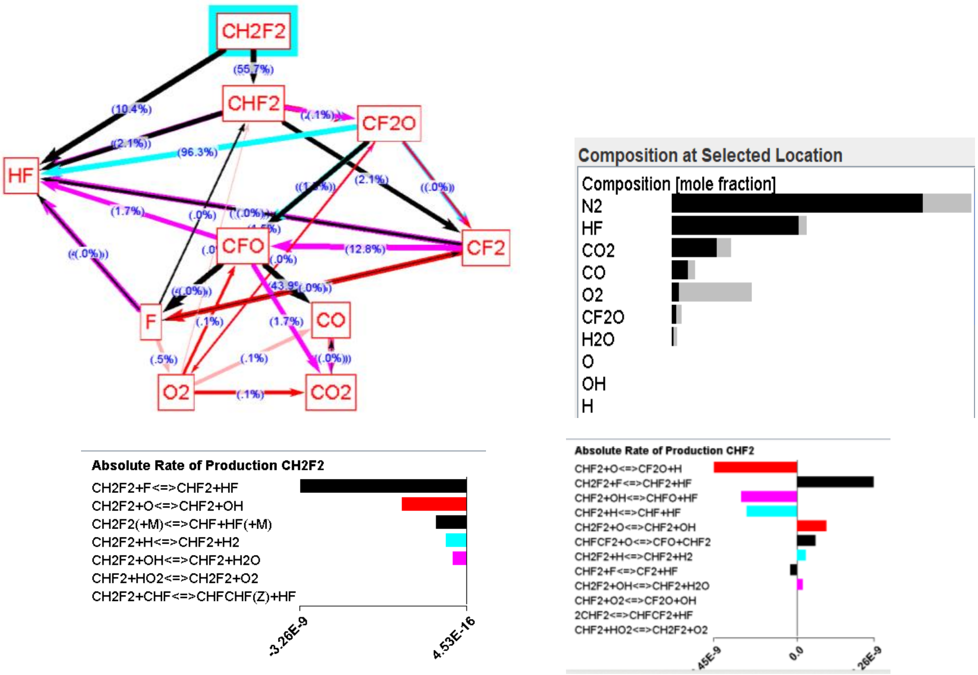

Fig. 2-5-6 In-flame surface reaction path analysis.

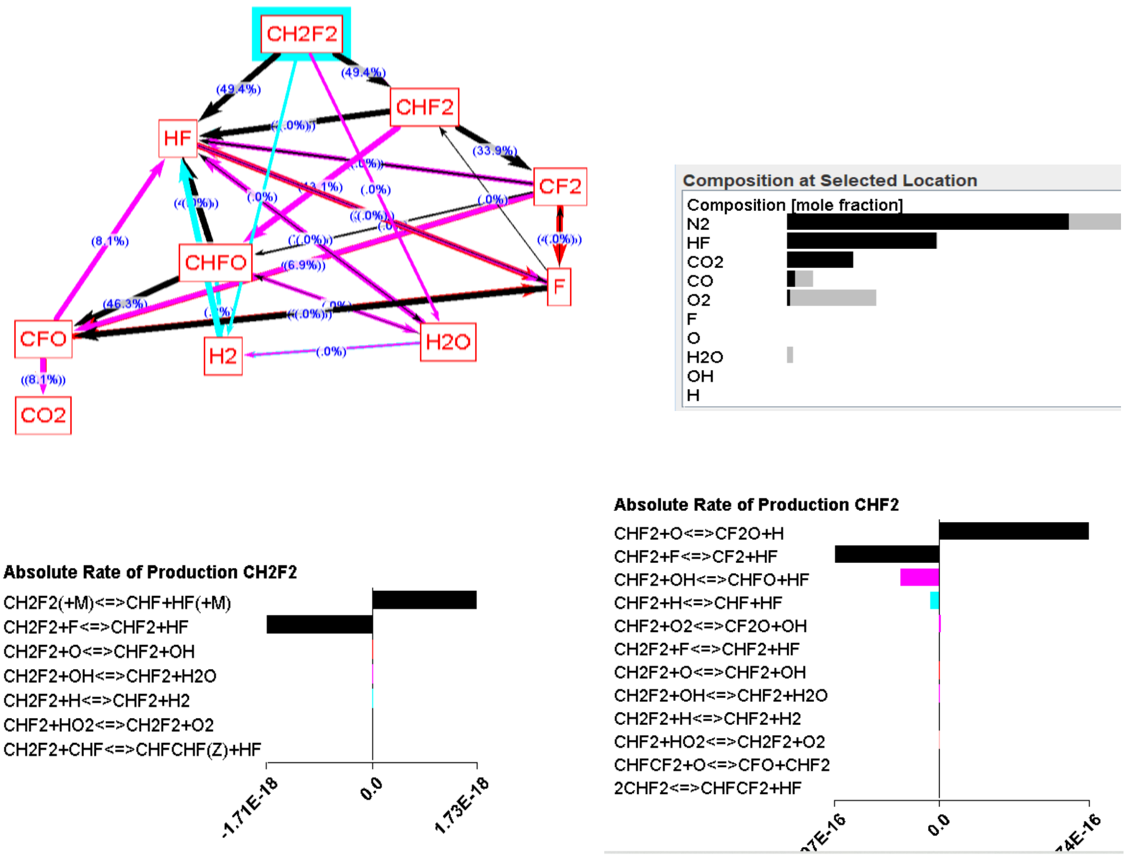

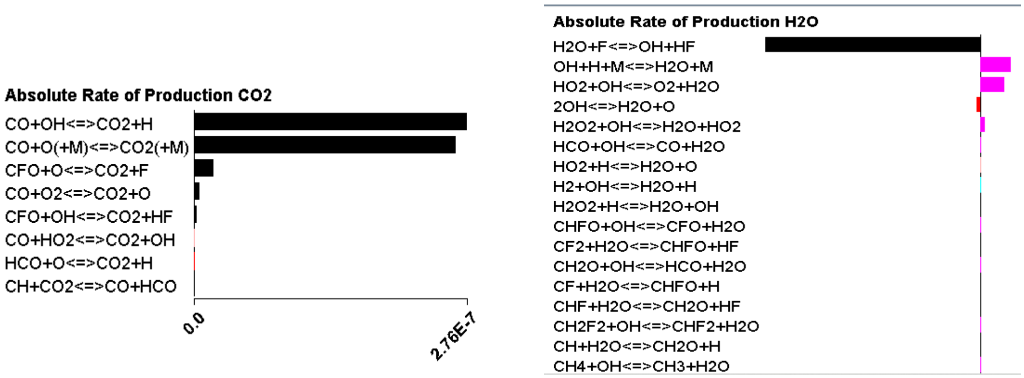

Fig. 2-5-7 Reaction path analysis on the downstream side of the flame surface.

(c) Effect of water vapor on combustion reaction characteristics of R32

Although H_2O is not included in the general reaction equation, as shown in Figs. 2-5-5 and 2-5-7, H_2O, as a product of hydrogen abstraction by the OH radical of CH_2H_2, is involved in the reaction with the F radical to generate HF. Table 2-5-1 also shows that the combustion rate and K_G value increase when water vapor is included in the combustion reaction of R32. Here, we analyze the changes in the laminar burning velocity and reaction path of R32 in the presence of water vapor.

Figure 2-5-8 shows the analysis results of the laminar burning velocity of R32 in the air with 3% water vapor. For comparison with conditions without water vapor, the molar ratio of R32 and O2 was fixed at 1:1, the water vapor mole fraction in the air was adjusted to 3%, and the nitrogen mole fraction was adjusted from 79% to 76%. When water vapor was included, the laminar burning velocity increased when the equivalence ratio of R32 was greater than 0.7. When the equivalence ratio was 1, the laminar burning velocity in the presence of water vapor increased from 7.2 cm/s to 8.4 cm/s. The calculated results are consistent with the experimental results shown in Table 2-5-1.

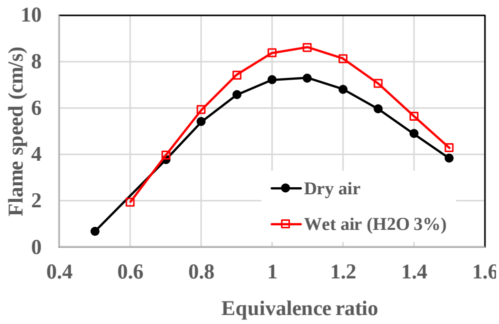

Fig. 2-5-8 Effect of water vapor on laminar burning velocity.

Figure 2-5-9 shows the main reactions of H_2O involved in the upstream and downstream sides and at the flame front in the presence of water vapor. Compared to the conditions without water vapor, the reaction on the upstream side of the flame is almost unaffected; on the downstream side, H_2O+O—>2OH and H_2O + OH- > O_2 + H_2O have higher reaction rates. As a result of the higher production rate of OH radicals, the laminar burning velocity is higher in the presence of water vapor.

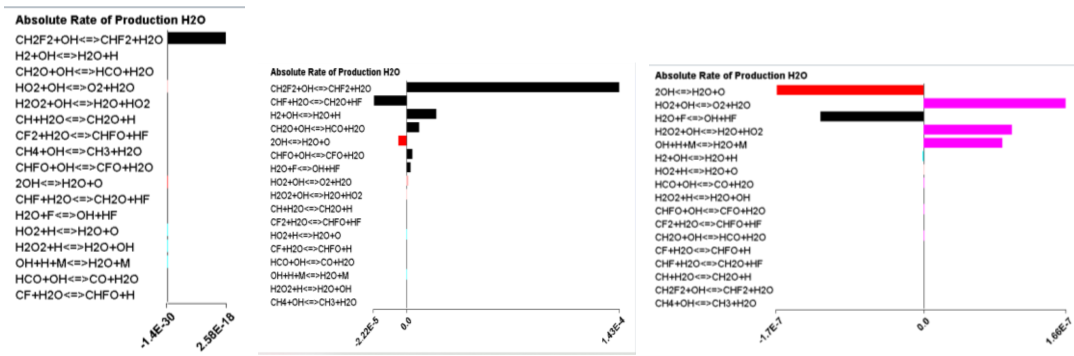

(a) Upstream side of the flame surface (b) Flame surface (c) Downstream of the flame surface

Fig. 2-5-9 Reaction path analysis in the presence of water vapor.

2.5.5 Combustion simulation of R32

To evaluate the degree of danger when a flammable refrigerant burn, a flame propagation simulation was performed after igniting a premixed mixture of R32 and air in a spherical container, and the maximum ultimate pressure and the rate of pressure rise (K_G) were compared for different sizes of the container.

Simulations were performed using ANSYS Fluent 2021. Figure 2-5-10 shows the calculation domain of the simulation. The calculation conditions are summarized below.

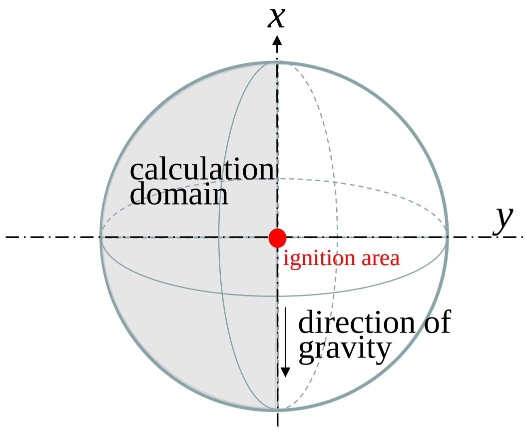

Fig. 2-5-10 Simulation calculation domain.

- The diameters of the spherical container are 0.3, 1.0, and 3 m.
- Axisymmetric two-dimensional model is considered (gravity is also considered).
- Initial conditions: Mass fraction of R32:O2:N2 is 0.26:0.16:0.59 (theoretical air–fuel ratio); initial temperature is set to 300 K; initial pressure is set to 1 atm.
- Ignition is from the center position (applying heat of 20 J to a spherical area with a radius of 2 mm for 10 ms).
- A chemical species transport model, which considers 30 chemical species and 111 elementary reaction equations, is used.
- Flow is laminar.
- To consider the cooling effect of the container, the wall is made of aluminum with a thickness of 5 mm.
- A square mesh of 1 mm or 10 mm square is considered for the entire area. The mesh near the flame front is further divided into 1/16 of the original size.
- Time step is 1 to 10 μs.

(a) Simulation results for a 0.3 m diameter vessel

Figure 2-5-11 shows the time variation of concentration, temperature distribution, and average pressure after the combustion of R32 refrigerant in a relatively small vessel with a diameter of 0.3 m. The left panels of the contour plots show the concentration of R32, and the right panels show the temperature distribution. After ignition, the flame front expands toward the unburned gas region. Furthermore, the flame floats under the influence of gravity.

At the initial stage of combustion, turbulence was observed at the flame front, but the field gradually became smooth as the flame front expanded. The pressure inside the vessel rises rapidly until the flame front reaches the left and right walls. The pressure continues to rise until all the refrigerant is burned, and the maximum pressure is approximately 1 MPa. In addition, the pressure rise reaches its maximum value just before the flame front reaches the left and right wall surfaces. The K_G value at that time is 7.2 (100 kPa·m/s) when calculated from the pressure rise rate.

The K_G value is an index that indicates the intensity of the explosion and is defined as follows.

$$K_G = \frac{dP}{dt}_{max} V^{\frac{1}{3}} \,(100\ \text{kPa·m/s}) \qquad (2\text{-}5\text{-}7)$$

The flame front reaches the left and right wall surfaces in approximately 0.3 s. This is consistent with the prediction results using the flame speed. (Assuming that the radius is 0.15 m and the flame speed is 0.5 m, the arrival time of the flame to the wall is estimated to be ~0.3 s).

The expansion of the flame front and the state of levitation due to gravity observed in this study is similar to the experimental observation results (Fig. 2-5-12) introduced in the final report of the 2016 Mildly Flammable Refrigerant Study Group[2-22]. . The calculated K_G values are consistent with the experimental results shown in Table 2-10.

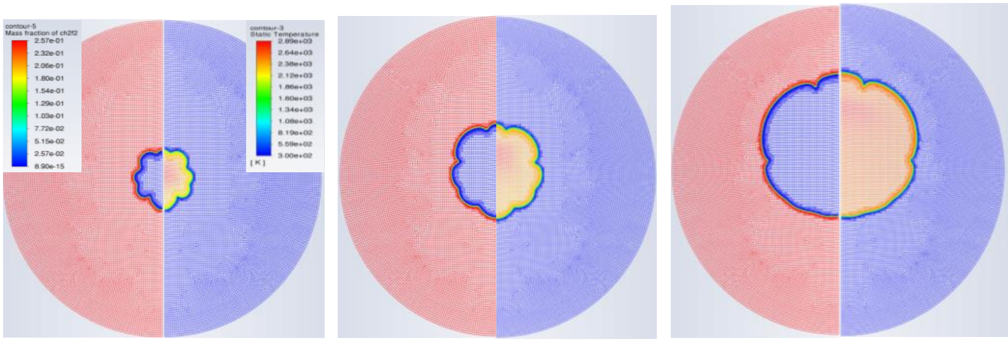

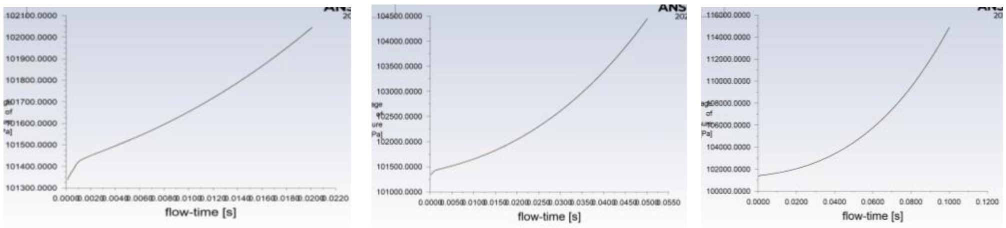

0.02 s 0.05 s 0.1 s

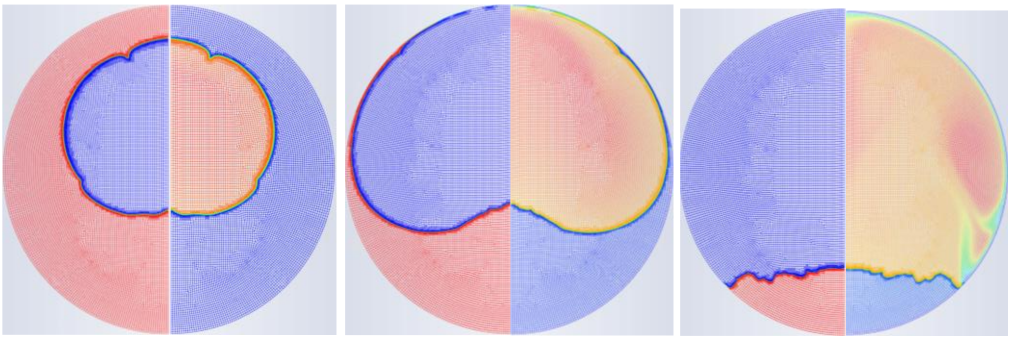

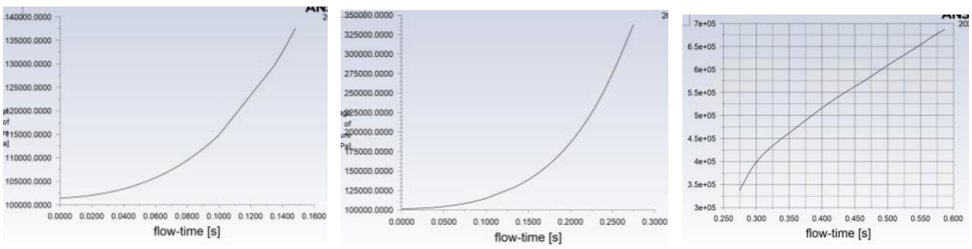

0.14 s 0.27 s 0.6 s

Fig. 2-5-11 Time change of R32 concentration distribution (left panel of the contour plots), temperature distribution (right panel of the contour plots), and average pressure (below the contour plots) (d = 0.3 m).

100 ms 200 ms 300 ms 400 ms

Fig. 2-5-12 Propagation behavior of the flame surface for R32[2-9] (diameter 1 m, equivalent ratio 0.9)

(b) Simulation results for a 1 m diameter vessel

Figure 2-5-13 shows the time variation of concentration, temperature distribution, and average pressure after the combustion of R32 refrigerant in a container with a diameter of 1 m. From ignition to 0.25 s, the flame floats due to the expansion of the flame front and gravity, similar to the state of combustion in the 0.3 m container. In addition, the indentation shape at the bottom of the developing flame front is also reproduced.

After 0.25 s from the ignition, the bottom of the flame was torn apart from the outside by the sudden progress of the depression at the bottom of the flame front, and the flame split into two discontinuous flames. As the length of the flame front increased, more amount of refrigerant was involved in combustion; therefore, the pressure began to increase rapidly. The pressure rise rate reaches its maximum at 0.57, and the K_G value calculated from that pressure rise rate is 12.8 (100 kPa·m/s), which is larger than the experimental result. In addition, the pressure inside the vessel reached the maximum value of 1.02 MPa at 1.2 s after ignition. After that, the pressure decreased due to the cooling effect of the wall surface.

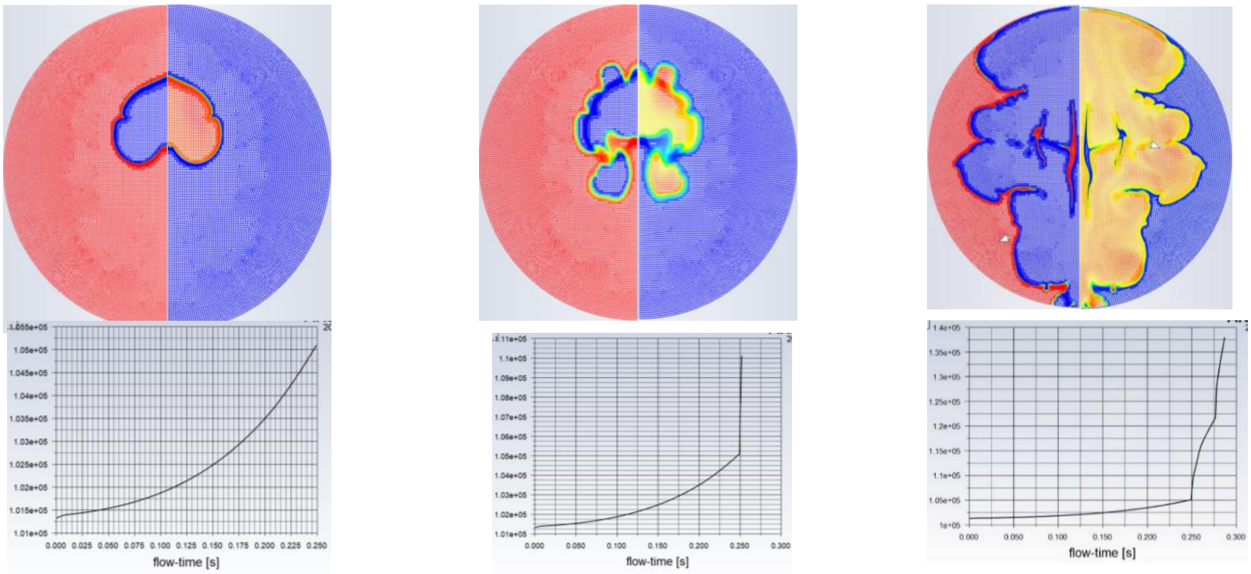

0.25 s (Immediately before the flame split) 0.26 s (Immediately before the flame split) 0.28 s

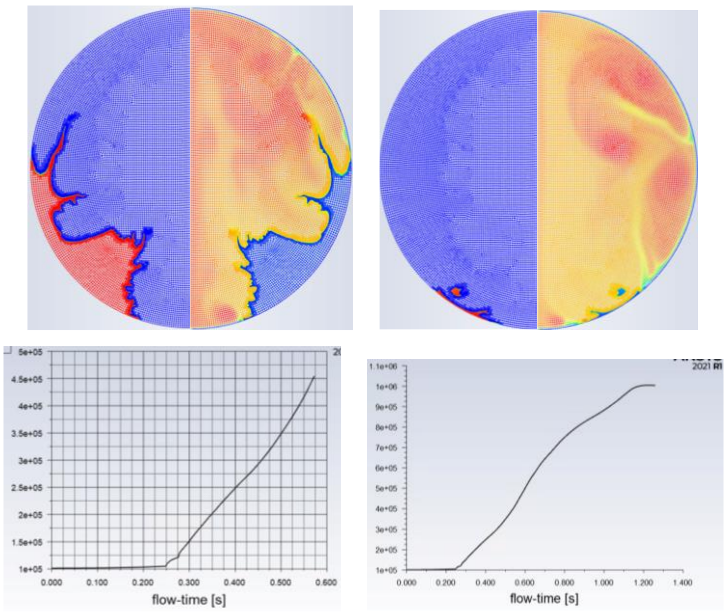

0.57 s (Maximum pressure rise rate) 1.2 s (Maximum pressure)

Fig. 2-5-13 Time change of R32 concentration distribution (left panel of the contour plots), temperature distribution (right panel of the contour plots), and average pressure (below the contour plots) (d = 1 m).

(c) Simulation results for a 3 m diameter vessel

Figure 2-5-14 shows the time variation of concentration, temperature distribution, and average pressure after the combustion of R32 refrigerant in a container with a diameter of 3 m. From ignition to 0.75 s, the expansion of the flame interface and the levitation of the flame due to gravity were observed, similar to the state of combustion in the 0.3 m container. After that, from 0.78 s, the turbulence of the flame front developed, and the flame split into discontinuous flames. At that time, a rapid increase in pressure was observed. The pressure rise rate reaches its maximum at 1.05 s after ignition, and the K_G value calculated from the pressure rise rate is 26 (100 kPa·m/s). The maximum pressure was approximately 1 MPa.

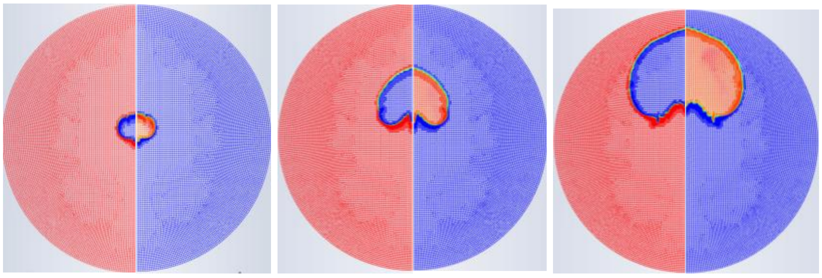

0.22 s 0.52 s 0.75 s

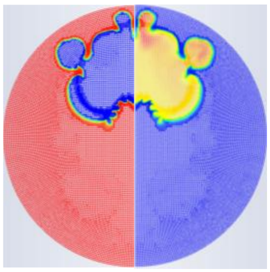

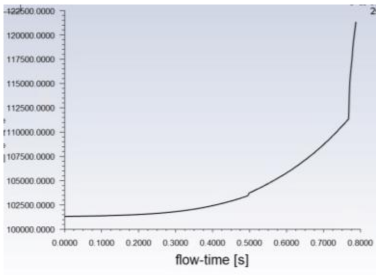

0.78 s

Fig. 2-5-14 Time change of R32 concentration distribution (left panel of the contour plots), temperature distribution (right panel of the contour plots), and average pressure (d = 3 m).

(d) Effects of turbulence models

Cases (a)–(c) were simulated as laminar flow. However, if the vessel is large, the expansion of the flame front may cause a large flow inside the vessel, and the flow field may transition to turbulent flow. To evaluate the effect of turbulence transition, the Reynolds stress (5 equations) turbulence model was used to simulate the combustion after ignition of R32 in a 3 m vessel, and the temperature distribution and mean pressure over time after ignition are shown in Fig. 2-5-15. Compared to the laminar flow results, due to the diffusion effect of turbulent flow, flame splitting does not occur, and a thick flame front is formed. In addition, because turbulent combustion is faster than laminar combustion, the effect of buoyancy is reduced, and the time to reach the wall is approximately half that in laminar combustion. The pressure rise rate reaches its maximum at 0.47 s after ignition, and the K_G value calculated from that pressure rise rate is 86.4 (100 kPa·m/s). The maximum pressure was approximately 0.98 MPa.

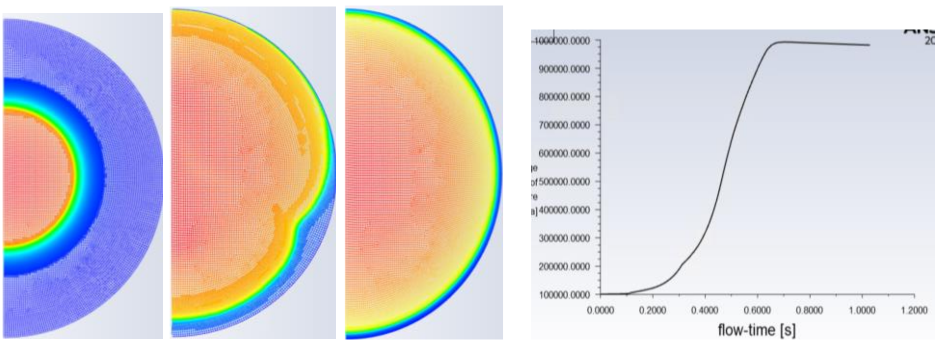

Fig. 2-5-15 Temperature and average pressure over time for R32 (d = 3 m, turbulent model).

2.5.6 Discussion of simulation results

(a) Summary of simulation results

The simulation results are summarized in Table 2-5-2. The variation in maximum ultimate pressure on varying the diameter of the container from 0.3 m to 1 m was marginal. Because the rise in pressure results from the combustion heat release, if the refrigerant concentration is the same in the initial state, the amount of combustion heat released per unit volume will be the same, and the maximum ultimate pressure will also be the same. Also, depending on the conditions, the cooling effect of the wall cannot be ignored; however, because the combustion time is ~1 s, the influence of the heat capacity of the wall is considered to be small.

The K_G value is an index showing the severity of the explosion calculated from the maximum value of the pressure rise rate. The calculated K_G value for the smallest container (d = 0.3 m) is consistent with the experimental results reported in the literature; however, for the larger container, the calculated K_G value is larger than the literature value. This is the result of the flame being violently deformed by buoyancy, splitting the flame into small flames. The calculation results of this flame front instability phenomenon should be further investigated together with experimental observation. Furthermore, when the effect of turbulence is introduced into the simulation model, the diffusion effect of turbulence forms a thick flame interface without flame splitting. A larger K_G value was calculated for laminar combustion.

Table 2-5-2 Summary of simulation results

	Diameter	Laminar/Turbulent	Chemical reaction model	Maximum pressure	K_G (100 kPa·m/s)
1)	0.3 m	Laminar	Species transport model	1 MPa	7.2
2)	1 m	Laminar	Species transport model	1.02 MPa	13.9
3)	3 m	Laminar	Species transport model	1 MPa	26
4)	3 m	Turbulent	Species transport model	0.98 MPa	86.4

(b) Intrinsic instability of premixed flames

Premixed flames tend to be unstable due to thermal expansion, which has been studied since 1959 as the intrinsic instability of premixed flames [2-23]. Hydrodynamic effects, diffusion-thermal effects, and external force effects have been investigated as factors for the inherent instability of premixed flames. Among these, the hydrodynamic effect caused by the thermal expansion of gas is the most important factor. Diffusion-thermal effects caused by the interaction of material diffusion and thermal diffusion play a major role in the instability of lean premixed flames of hydrogen–air and methane–air. External force effects, such as the effects of buoyancy, are important in slow combustion reactions with burning velocities of less than 15 cm/s.

Darrieus and Landau's flame front instability analysis, considering the thermal expansion effect, showed that any small perturbation would cause instability in the flame front; that is, a stable laminar combustion flame could not exist [2-24]. Analysis considering the finite flame front thickness revealed that the amplification factor becomes negative in the large wave number region; that is, the small flame becomes stable, and the large flame becomes unstable. The simulations in this study were performed using a relatively small container for R32, which has a low burning rate. The effect of thermal expansion on flame stability is considered to be small.

Figure 2-5-16 shows the propagation of the flame front in the early stages of the calculation. A smooth flame front was assumed in the initial state; however, unevenness of the flame front appeared at 0.02 s. When the calculation progressed to 0.04 s, the unevenness of the flame front reduced significantly. The reason for this is that the temperature rise of the unburned gas surrounding the burned gas enhances the transport of active chemical species, and the speed of the chemical reaction also increases, resulting in an increase in the combustion speed. When the calculation was advanced to 0.09 s, the flame front became smoother, but due to the effect of buoyancy, the shape of the left and right flame fronts differed. Buoyancy has a significant effect on the shape of the flame front. As shown in Fig. 2-5-13 (0.28 s) and Fig. 2-5-14 (0.78 s), the buoyant force caused a large deformation of the flame front, causing the flame to split and resulting in a sharp rise in the pressure. This effect may be more pronounced for R1234yf, which has a slower burning speed than R32. Because the actual pressure rise rate can be much larger than the pressure rise rate predicted considering laminar flow combustion, a more detailed study of the stability analysis of the flame front considering the type of refrigerant and the scale of the combustion space should be conducted in the future.

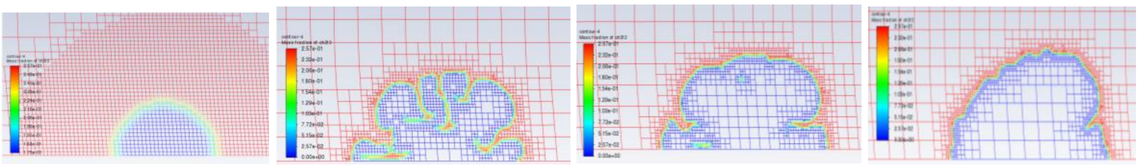

0 s 0.02 s 0.04 s 0.09 s

Fig. 2-5-16 Behavior of flame surface (concentration distribution of R32) (direction of gravity is from right to left).

References

2-1） Kataoka, O., Yoshizawa, M., and Hirakawa, T., Allowable charge calculation method for flammable refrigerants. *Proc. Int. Refrig. Air Cond. Conf.,* Purdue, USA, (2000).

2-2） Hu, M., Li, J., Liu, Z., and Li T.., Experimental and numerical simulation analysis of R-290 air conditioner leak. *Int. J. Refrig.*, 90, (2018), pp. 163-167.

2-3） Baba, A., Takaichi, K., Taira, S., Imoto, T., Itakura, S., Mori, H., Makino, H., Yamashita, K., and Yamaguchi, H., Study on risk assessment of air conditioner using R290. *25th IIR Int. cong. Refrig.*, Montreal, Canada, (2019).

2-4） Colbourne, D., and Suen, K. O., Equipment design and installation features to disperse refrigerant releases in rooms–part I: experiments and analysis. *Int. J. Refrig.*, (2003), 26, pp. 667-673.

2-5） Tang, W., He, G., Zhou, S., Sun, W., Cai, D., and Liu, F., The experiment study of R290 mass distribution and indoor leakage of 2 HP and 3HP split household air conditioner. *Int. J. Refrig.*, (2019), 100, pp. 246-254.

2-6） Tang, W., He, G., Sun, W., Zhou, S., Cai, D., and Zhu, Y., Assessment of leakage and risk reduction of R290 in a split type household air conditioner. *Int. J. Refrig.*, (2018), 89, pp. 70-82.

2-7） Hattori K., Fukuoka M., Murata K., Taira S., and Tomioka K., Numerical method on predicting distribution of leaked refrigerant in indoor space and its experimental observation. *24th IIR Int. Cong. Refrig.*, Yokohama, Japan, (2015), pp. 4782-4789.

2-8） Jin, W., Gao, P., and Zheng, Y., Experimental study on ventilation effect on concentration distribution of R32 leaking from floor type air conditioner. *Energy Procedia*, (2017), 105, pp. 4627-4634.

2-9） Colbourne, D. and Suen, K.O., Airflow to disperse refrigerant leaks from hydrocarbon refrigeration systems, *Int. J. Refrig.*, (2022), 137, pp. 220-229.

2-10） IEC 60335-2-40:2022 CMV, Household and similar electrical appliances – Safety – Part 2-40: Particular requirements for electrical heat pumps, air-conditioners and dehumidifiers. Int. Electrotech. Comm., (2022).

2-11） Shiokawa, J., KIRK-OTHMER Concise Encyc. Chem. Tech., Maruzen, Tokyo, Japan, (1988), p. 1188.

2-12） IEC 60335-2-89, Household and similar electrical appliance –Safety- Part 2-89: Particular requirements for commercial refrigerating appliances and ice-makers with an incorporated or remote refrigerant unit or moter-compressor. Int. Electrotech. Comm., (2019).

2-13） Higashi, T., Dang, C., Hihara, E., and Shitara, Y. Effect of additives to suppress the combustion of oil on pump-down accidents, JRAIA International Symposium on New Refrigerants and Environmental Technology (2018).

2-14） Higashi, T., Saitoh, S., Dang, C., and Hihara, E. Diesel combustion of oil and refrigerant mixture during pump-down of air conditioners. *Int. J. Refrig.*, (2017), 75, pp. 300-310.

2-15） Higashi, T., Tamai, S., Saitoh, S., Dang, C., and Hihara, E. Effect of lubricating oil on explosion accidents of compressor during pump-down of air-conditioner. *Trans. JSRAE,* (2017), 34(3), pp. 181-191. https://doi.org/10.11322/tjsrae.17-17.

2-16） Iijima, A., Autoignition in internal combustion engines. *Journal of Combustion Society of Japan*, (2015), 57, pp. 95-105. (in Japanese)

2-17） Japanese Society of Tribologists, *Tribology Handbook*, Yokendo, 590 (2001). (in Japanese)

2-18） Burgess Jr, D. R., Babushok, V. I., Linteris, G. T., and Manion, J. A. A chemical kinetic mechanism for 2-bromo-3,3,3-trifluoropropene (2-BTP) flame inhibition. *Int. J. Chem. Kinet.*, (2015), 47(9), pp. 533-563.

2-19） Babushok, V., Burgess Jr., D., Kim, D., Hegetschweiler, M., and Linteris, G. Modeling of Combustion of Fluorine-Containing Refrigerants, Technical Note (NIST TN), National Institute of Standards and Technology, Gaithersburg, MD, [online], (2021). https://doi.org/10.6028/NIST.TN.2170.

2-20） Burgess Jr, D. R., Babushok, V. I. and Manion, J. A. A chemical kinetic mechanism for combustion and flame propagation of CH2F2/O2/N2 mixtures. *Int. J. Chem. Kinet.*, (2022), 54(3), pp. 154-187.

2-21） Burgess Jr, D. R., Burrell, R. R., Babushok, V. I., Manion, J. A., Hegetschweiler, M. J., and Linteris, G. T. Burning velocities of R-32/O2/N2 mixtures: Experimental measurements and development of a validated detailed chemical kinetic model.

Combust. Flame, (2002), 236, p. 111795.
2-22) Japan Society of Refrigerating and Air Conditioning Engineers, Mildly Flammable Refrigerant Risk Assessment Study Group 2016 Final Report, 2017. (In Japanese)
2-23) Kadowaki, S. Intrinsic instability of premixed flames: Hydrodynamic effects and diffusive-thermal effects. *Journal of the Combustion Society of Japan*, (2015), 57(181), pp. 167-173 (In Japanese)
2-24) Clavin P., Dynamic behavior of premixed flame fronts in laminar and turbulent flows, *Prog. Energy Combust. Sci.*, (1985), 11, pp. 1-59.

3. RESULTS OF RESEARCH BY SUWA UNIVERSITY OF SCIENCE ON THE IGNITABILITY OF R290/AIR MIXTURES IN THE PRESENCE OF VARIOUS IGNITION SOURCES

3.1 Introduction

An effective approach to reducing the emissions of greenhouse gases is to replace HFC gases with hydrocarbons with lower global warming potential (GWP) in next-generation refrigerants. In particular, refrigerants currently used in room air conditioners (RACs), commercial chillers, and refrigerators produce high levels of emissions. However, most hydrocarbon gases planned for use in next-generative refrigerants, such as propane (R290) and iso-butane (R600a), are flammable and classified as A3 gases under ISO817 (A3 class: LFL$\leq$3.5 vol% or H_c $\geq$19,000 kJ/kg, H_c : heat of combustion)[3-1], making it necessary to assess their physical risks under actual accident scenarios via detailed quantitative methods and to develop countermeasures to ensure their safe use. Dichlorodifluoromethane (R12) had previously been used as a refrigerant, but its production was forbidden in 1996; following detailed risk assessment by the Japan Electrical Manufacture Association (JEMA), it was replaced by R600a as the refrigerant used in household refrigerators [3-2].

The fire/explosion risks of refrigerants originate from situations in which refrigerant leaks and mixes with oxidizers in the air to form a flammable mixture and some source of energy is then supplied to this flammable mixture. However, fire/explosion accidents do not always occur in such risky situations because ignition requires various physical conditions, including an energy-supplying mechanism as an ignition source and a flammable mixture with proper fluid dynamic characteristics. The minimum ignition energy (MIE), quenching distance, and autoignition temperature (AIT) are commonly used to assess ignition probability, but their analysis does not always provide an accurate evaluation of physical risk for the assumed ignition modes; for example, cases in which a flammable mixture is not ignited through the supply of energy an order magnitude higher than the MIE from an arc discharge have been reported[3-3]. These issues suggest the importance of developing more accurate methods for evaluating ignition risks for various ignition sources under actual leakage and usage situations based on academic research. Correspondingly, the aim of this study was to develop a systematic method for evaluating the ignitability of R290 used to replace current refrigerants in RACs, commercial chillers, and refrigerators based on combustion theory.

3.2 Content of this research

This research comprised the following two main subthemes:

(1) Screening of ignition sources in actual accident scenarios

Scenarios involving accidental leakage of refrigerant from RACs, commercial chillers, and refrigerators were developed through in-depth discussion with engineers and academic researchers. Conceivable ignition sources for these accident scenarios were nominated and classified as, e.g., electrical sparks, open flames, hot surfaces, etc.

(2) Development of a method for evaluating the ignitability of various types of ignition sources

The ignitability of R290 under application of the ignition sources nominated under subtheme 1) above was assessed based on theory, experiment, and numerical simulation. From this, a method for evaluating the ignitability of R290 in the presence of various ignition sources was developed.

3.3 Screening of ignitable sources

3.3.1 Nomination and classification of ignitable sources

Fig.3-1 breaks down the number of fire accidents that occurred in Japan in FY2020 by cause of fire[3-4]. In the past, "Arson" was the number one cause but has shown a decreasing trend in recent years, with high-temperature sources such as "cigarette," "bonfire," and "stove" replacing it as top causes. In addition, electrical ignition sources such as "electrical appliances," "cables," "assemblies of plugs and contacts," "electrical equipment," "light," etc., are as important as high-temperature surfaces as the main causes of fire.

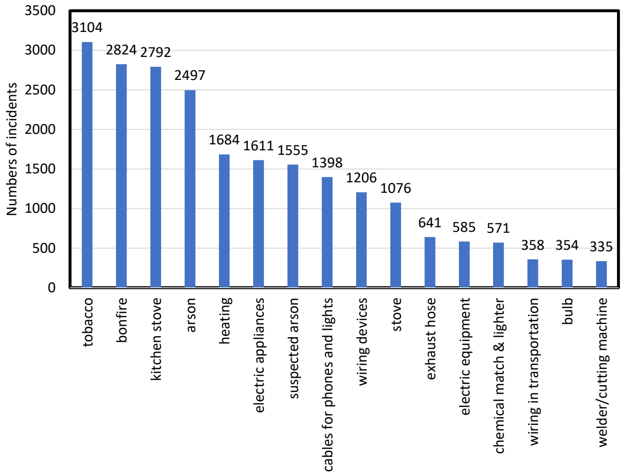

Fig.3-1 Number of fires by major cause in Japan in FY2020[3-4].

Table 3-1 details the history of the numbers of fires caused by electrical appliances from 2018FY–2020FY and Fig.3-2 shows the trend of electrical fire causes[3-5]. Although the number of fires caused by electromagnetic cookers was slightly less than the number of fires caused by other sources, these were nearly the same, indicating that there is a wide variety of potentially fire-causing electric ignition sources.

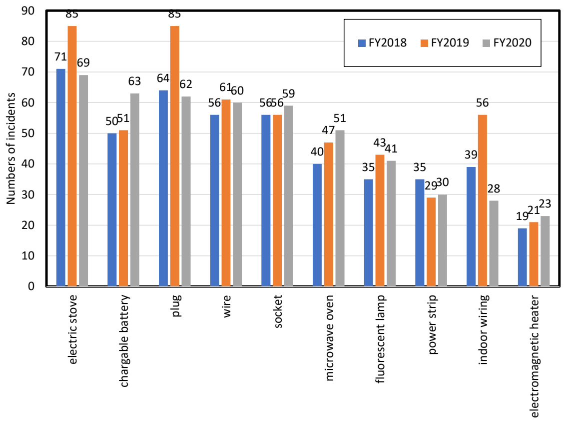

Fig.3-2 Trends in the number of fires caused by household electrical appliances from 2018 to 2020[3-5].

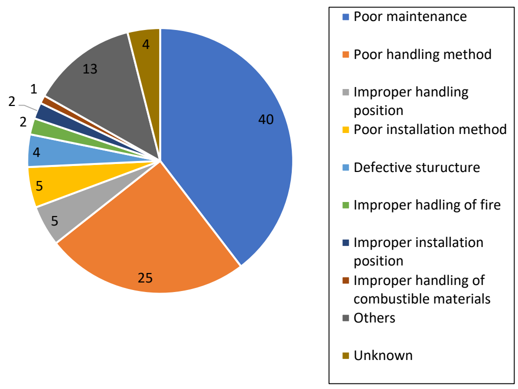

Fig.3-3 Trends of the causes of electrical fires in 2020FY in Japan[3-5].

Table 3-1 Causes of fires in residential occupancies due to electrical wiring and devices[3-6),3-7].

Cause of fire	Percent (individual cause)	Percent (for categories)
Branch circuit wiring		**29**
mechanical damage or improper installation	8	
poor or loose splice	8	
ground fault	3	
use of improper wiring	3	
knob-and-tube encapsulated	3	
miscellaneous overload	2	
unknown	3	
Cords and plugs		**26**
mechanical damage or poor splice	10	
overloaded extension cord	6	
overloaded plug	2	
damaged plug	2	
miscellaneous (short, water, deteriorated insulation, electric blanket cord)	6	
unknown	1	
Service components		**13**
deteriorated insulation	5	
improper installation (ground fault or overload)	4	
fire due to alterations in progress (e.g., contact with HV wire)	2	
unknown	4	
Lamp and lighting fixtures		**13**
loose or poor connection or splice, mis-wiring	5	
combustibles too close	5	
overlamped	3	
deteriorated insulation	1	
Receptacles and outlets		**11**
loose or poor connection	8	
mechanical damage	3	
overloaded	2	
deteriorated, miswired, plug inserted improperly	2	
unknown	3	
Low voltage transformer	**1**	**1**

From Fig.3-3, the main cause of electrical appliance-initiated fire accidents is failure of maintenance. For example, the following situations can be anticipated: the wire insulant around a wire cable breaks down from deterioration and then causes a fire, or the wire itself breaks down from deterioration, generating an arc spark discharge that causes a fire. Table 3-1 lists causes of fires by power-distribution components based on 105 residential fire accidents, as reported by Hall et al. in NBS[3-6), 3-7)], although their data are somewhat old. According to this table, mechanical breakage and contact failure are dominant in each category of fire caused by electrical appliances. In this work, the ignitable sources generally used in living spaces, convenience stores, and supermarkets were used as target sources for the evaluation of ignition risk in cases in which hydrocarbon refrigerant (especially R290) leaks from RACs, commercial chillers, or refrigerators. These are classified in Table 3-2 in the categories of "electrical ignition source," "hot-surface-type ignition source," and "open flame." Flammable sources that could be classified in the category of "open flame" are excluded as evaluation targets because an R290/air mixture will almost certainly ignite when touched to an open flame. Note that this categorization of flammable sources was conducted based on discussion with members of the risk assessment working group established by the Japan Refrigeration and Air Conditioning Industry Association (JRAIA).

Table 3-2 List of candidate ignition sources for propane/air mixtures generally used in refrigeration life cycle.

Major Category	Middle Category	End Category
Electric spark	Electric relay	Refrigerator, Washing machine, Hair dryer, Rice cooker, Microwave oven, Dehumidifier, Vacuum cleaner, Electric carpet, Oven, Fan, Television, Printer, Air cleaner, Audio/Video, Telephone, Fax machine
	Thermostat	Refrigerator, Electric stove, Oven toaster, Electric kettle, Electric Kotatsu, Iron, Hair dryer
	Human operation	Plugging and unplugging, Wall-mounted lighting switch
	Brush motor	Vacuum cleaner, Hair dryer, Electric razor
	Charge	Printer, Electrostatic spark discharge
Hot Surface		Electric heater, Hot plate for cooking, Burnt cigarette
Open flame		Burnt cigarette and lighter, Candles

3.3.2 Screening of ignitability based on literature surveys

Hagimoto et al[3-3)] reported experimentally obtained qualitative behaviors following the ignition of methane/air and R290/air mixtures subjected to arc discharges generated at the gaps of electric contacts when several types of electric switches (key-socket, middle, and embedded type) used for commercial general appliances were opened or closed. They performed their analyses using an incandescent light bulb, fan, fluorescent lamp, and a resistance as electric loads and reported the following findings: (1) flammable mixtures are most easily ignited as the result of opening a key-socket type switch, (2) opening a switch causes ignition more easily than closing a switch, (3) the ignition energy of an inductive circuit is smaller than that of a resistance circuit, and (4) the energy required for ignition depends on the switch type and the characteristics of the electric circuit and covers a wide range of values (several mJ – several J). The reasons for these trends were pointed out as follows. Finding (1) originates from the differences between switch mechanisms, as the electric contact was manually rotated whereas the middle-type and embedded switches were actuated by spring. With respect to finding (2), the gap of electric contact in the cases in which the switch was opened was wider than in the cases in which the switch was closed and, as a result the heat lost from the flame kernel to the electric contact was smaller in the formers cases. With respect to (3), because the induced electromotive force was generated when the switch in the inductive circuit was opened, the voltage supplied to the electric contact in the inductive circuit was larger than that in the resistive circuit. They could, by contrast, find no clear reasons for result (4). They also noted that there were several cases in which the flammable mixture could not be ignited even though the discharged energy was larger than the MIE at the applicable fuel concentration. In these cases, there were limitations on the discharge energy generated at the gap of the electric contact.

Ootori et al.[3-8)] measured the energies of arc discharge produced by a series of experimental circuits comprising an electric relay for a phone, a carbon lamp (resistive electric load), and a DC 48 V power source. They reported that the arc duration was somewhat shorter than 10^{-4} s when the arc current was less than 1.4 A. As this duration corresponds to the critical duration for ignition mentioned by Kinoshita[3-9)] and Strehlow[3-10)], the discharge energy generated over this time would be larger than the MIE, the heat loss could be ignored, and the R290/air mixture could be ignited. On the other hand, a generated arc current somewhat larger than 0.6 A (note that this value might differ with the types of materials used in the electric contact) produced an energy of arc discharge of approximately 0.5 mJ[3-8], which is larger than the MIE of R290/air mixture. Note that, because the relationship between the ignition energy and equivalence ratio followed a downwardly convex curve[3-11]. the energy of arc discharge was not always capable of igniting an R290/air mixture over the entire flammable range, which was limited to within approximately 3.0–6.9 vol% of R290 concentration in air.

The voltages and currents of arc discharges generated at the gap of an electric contact in a circuit containing a power relay or an electromagnetic contact carrying a rated current larger than 2 A were reported in [3-12)-3-14]. The energy generated by arc discharge 4–10 s from commencement of discharge was estimated to be approximately 6–7 mJ, indicating that an R290/air mixture could be ignited over the entire flammable range as the ignition energy at the lower flammable limit (LFL) and upper flammable limit (UFL) were both approximately 4 mJ.

The ignitability of an R290/air mixture by a rectifier spark generated using a brush motor can be estimated using a similar electric contact method. Izato[3-15] measured the voltage and current profiles of a DC motor and the relationships between arc duration, arc voltage, residual current, and revolution rate. The arc duration and residual current decreased as the revolution rate was increased to 3,000 rpm, after which both began to increase. Over this interval, no dependence between revolution rate and arc discharge was found, suggesting that that the energy produced was minimum at 3,000 rpm. The measured arc current, arc voltage, and arc duration at 3,000 rpm were 17 V, 0.55 A, and 37 μs, respectively, corresponding to an energy of 0.35 mJ; as this is larger than the MIE, the ignitability of R290/air mixture could not be ignored in this case.

3.3.3 Screening of ignitable sources

(i) Ink jet printers

As detailed in Section 3.4, the authors disassembled a commercially available ink jet printer (EPSON, EP-806AR) to check for electrical parts that could be potential ignition sources. The printer was found to contain two sheet-feeding brush motors and an ink cartridge-driving brush motor. Although neither of the printer's electronics boards uses contact relays, one each is used for ink discharge control and sheet feed control. It follows from these features that an ink jet printer can cause the ignition of R290 vapors as a result of its use of internal brush motors.

(ii) Electric fan

A commercially available electric fan (manufactured by Mitsubishi Electric, Summer Life R30C-W) was disassembled to check for electrical parts that could serve as potential ignition sources. The appliance contains a brushless motor, which has a low possibility of ignition. However, the fan's operating switch part includes contacts between which electric discharges are likely to occur in a manner similar to an electromagnetic contactor or a contact relay, and the possibility of ignition owing to these contacts cannot be excluded. Incidentally, the electric fan subjected to this disassembly investigation happened to be an older model. Newer models of electric fans in wide current distribution are equipped with electronic operational controls managed by built-in electronics boards, and it is possible that an electronics board of this type, if mounted with a contact relay, could become an electric discharge source that could ignite R290 vapors.

(iii) Microwave oven

A commercially available microwave oven (SANYO, EM-LP1) was disassembled to check for parts that could serve as potential ignition sources. The authors first identified a turn table-driving motor rated to run at 6 rpm, at which arc discharges are unlikely to occur. In addition, the motor is directly connected to a plastic gear, making it even more unlikely to cause ignition-capable electric discharges. Aside from the motor, the oven is equipped with an internal thermostat comprising a bi-metal contact switch. Previously, cases have been reported of the ignition of ethyl ether as a result of sparks from thermostats. Additionally, the oven was found to contain fitted internal contact parts. Accordingly, it is possible for a microwave oven to serve as an ignition source for R290 owing to its internal thermostat.

(iv) Vacuum cleaner

A commercially available vacuum cleaner (TWINBIRD, FW3K167) was disassembled to check for parts that could be potential ignition sources. The tested vacuum cleaner contains a universal motor with a commutator and brush that can produce arc discharges or mechanical sparks. In actual operation, the universal motor was seen to emit electric discharges into the air. Additionally, inspection of a disassembled-view photograph[3-16] from the Internet of another vacuum cleaner revealed a relay mounted on its circuit board, which in turn is located close to the motor and has poor air-tightness. It follows that it is possible for a vacuum cleaner to ignite R290 vapors as a result arc discharges from its brush motor or electric discharges from the relay on its circuit board.

(v) Washing machine

Based on disassembled-view photographs[3-17] of washing machines (TOSHIBA's AW70DG and National's NA-F50Z8) posted on the Internet, we made educated guesses concerning the electrical and electronic parts they contain. In both washing machines, the control panel was located above an electronics board mounted with a contact relay; the electronics board was water-proofed by filling it with resin to prevent electric leakage. The photos posted on the Internet suggest that the electrical parts are not wholly covered with resin but have high degrees of air-tightness. Accordingly, we judged that contact relays used in washing machines are unlikely to become an ignition source.

(vi) Dehumidifier/air purifier

Based on a disassembled-view photograph[3-18] of a dehumidifier (CORONA, CD-J107X) posted on the Internet and the results of actual disassembly of air purifiers (SHARP's KC-Y65 and KC-B50, and Panasonic's f-vxe60), we made educated guesses concerning their internal electrical and electronic parts. As is true for the washing machines investigated, these appliances have control panels mounted above an electronics board, which appear to be mounted with both contact and non-contact relays. Unlike the washing machines, these appliances do not appear to be very well waterproofed. Accordingly, we cannot exclude the possibility of R290 vapor ignition at the contact relays on the electronics board located in these types of appliances.

(vii) Hair dryer

Based on disassembled-view photographs[3-19), 3-20] of hair dryers (National's EH534 and Tescom's Nobby NB1902) posted on the Internet, we made educated guesses regarding the electrical and electronic parts they contained. A circuit board along with a contact relay was found in the handle of each hair dryer. In addition, a brush motor was identified. It follows that the hazard of R290 vapor ignition is present in commercial hair dryers.

(viii) Electric dispensing pot

Based on a disassembled-view photograph[3-21] of an electric dispensing pot (Tiger, PDK-G) posted on the Internet, we made educated guesses concerning its internal electrical and electronic parts. A circuit board and corresponding contact was found in the bottom part of the product. Electric dispensing pots and electric kettles often have poor air-tightness at the bottom and can contain components such as a thermostat or thermistor on the inside. It follows from this that the hazard of R290 vapor ignition is present in electric dispensing pots.

(ix) Electric rice cooker

Based on disassembled-view photographs[3-22] (National's SR-SS18A and Tiger's JAQ-A550) of electric rice cookers posted on the Internet, we made educated guesses regarding their internal electrical and electronic parts. A circuit board and corresponding contact relay were found in the side bottom part of each product. It follows that the hazard of R290 vapor ignition is present in electric rice cookers.

(x) Electrically heated floor mat

In general, electrically heated floor mats often have floor-mounted control units. Photographs of some of these products posted on the Internet[3-23] revealed control units that contain internal relays. As they use internal hot wires to warm their overall bodies, floor mats of this type have high overall circuit resistances and are likely to cause electric discharges between contact elements. Additionally, many products use temperature control thermostats, which have been involved in cases of flammable gas fire accidents. Hence, the hazard of R290 vapor ignition is present in electrically heated floor mats.

3.4 Evaluation of ignitability by electrical ignition source (part 1): electrostatic discharge

3.4.1 Classification of electrostatic discharge phenomena[3-24), 3-25)]

Electrostatic discharge involves the liberation of electrons stored in an insulated conductor or insulator in contact with an grounded conductor and is therefore classified as capacitive discharge. Electrostatic discharges can be roughly classified into the following categories:

(1) Spark discharge: This occurs between an insulated and an earthed conductor. An example of this is the electrostatic discharge between the finger of a charged human body and a metal doorknob. As the discharge energy reaches approximately 1 J, it can ignite most flammable gases, vapors, and powders. This type of discharge should be considered an ignition source for which countermeasure are required in making practical use of flammable gases.

(2) Corona discharge: This occurs between an earthed conductor with a sharp tip (generally with a curvature radius of less than 5 mm [3-26)]) and a charged body (regardless of whether it is a conductor or insulator). As the discharged energy is small (approximately a few microjoules), the ignitability of flammable gas in the presence of corona discharge can be generally ignored except in the case of several gases for which the ignition energy is very small such as hydrogen and acetylene[3-27)]. In short, there are few ignitability issues for hydrocarbon/air mixtures under corona discharge, although the discharge characteristics depend significantly on the polarity of discharging.

(3) Brush discharge: This occurs between an earthed conductor with a high degree of curvature and a charged insulator and is caused when the charge density on the surface of the charged insulator is greater than 3 $\mu C/m^2$ and the surface electric field is also greater than 0.5 MV/m[3-26), 3-28)-3-30)]. A positive polarity discharge in which the insulator is charged negatively will have higher degree of ignitability to flammable gases than a negative polarity discharge. The discharge energy will be at most 1–3 mJ[3-29), 3-31)-3-32)] and will never exceed 4 mJ[3-33)]. Note that all of the charged electrons in an insulator will always be instantly liberated. This type of discharge sometimes behaves as an ignition source depending on the situation.

(4) Creeping discharge: This occurs when a thin insulator glued to an earthed conductor is peeled off. This type of discharge generates very large electrostatic energies of up to 10 J and should be treated as an ignition source.

3.4.2 Evaluation of ignitability by electrostatic discharge under actual accident scenarios

3.4.2.1 Electrostatic discharge between a charged human body and metal doorknob

The ignitability of a capacitive discharge can generally be evaluated through a comparison of the electrostatic energy released and the MIE assuming that all of the electrostatic energy is consumed for ignition. The electrostatic energy of capacitive discharge can be calculated as $E = (1/2)CV^2$, where E [J] denotes the electrostatic energy, C [F] denotes the capacitance, and V [V] denotes the charged voltage. An electrical circuit comprising a human body and another object is generally regarded as an equivalence RC circuit containing 1.5 kΩ of resistance and 100 pF of capacitance[3-10]). Assuming this model, the electrostatic energy stored in the human body released at discharge can be calculated as

$$E = \frac{1}{2}CV^2 = \frac{1}{2}\cdot(100\times10^{-12})\cdot(15\times10^3)^2 = 11.25\ \text{mJ} \tag{3-1}$$

According to Fig.3-8, the MIE of a propane/air mixture is ca. 0.25 mJ. Based on a comparison of these energies, the ignitability of the spark discharge generated between a charged human body and a metal doorknob cannot be ignored.

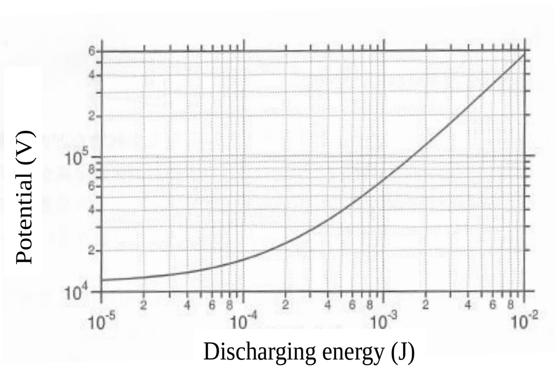

Fig.3-4 Relationship between the charge potential and discharging energy by brush discharge[3-25)].

3.4.2.2 Electrostatic discharge caused by undressing

The type of electrostatic discharge in this case corresponds to a brush discharge because it occurs between an earthed conductor (human body) and insulator (clothes). For example, wearing three layers such as underwear, innerwear, and outerwear generates electrostatic charges through the friction between the human body and underwear, underwear and innerwear, and innerwear and outerwear, respectively.

As a result of this phenomenon, the electric potential of outerwear can be easily increased to more than 10 kV in seasons with low humidity such as winter[3-34]. The amount of electrification produced by the friction between different materials depends on the electrification series, namely, it increases as the distance between the materials on the electrification series increases. It also depends on the motions of undressing and other dynamic factors. For example, very high electric potentials of 60 kV have been reported as the result of undressing from cotton work wear by a man (or woman) who rotated their arms five times before undressing[3-35]. It is also well known that the amount of electrification strongly depends on the humidity and has been reported to significantly decrease at room humidities (RHs) above 50%; an electric potential 60 kV was reported to decrease to 20 and 3 kV at RHs of 50 and 60%, respectively.[3-35]. Furthermore, it seems that the upper limit of electric potential from undressing becomes to decrease in the recent data; for example, there are reports of the potential only being able to reach 10 kV even in the absence of processing for anti-electrification[3-36].

According to Fig.3-4, the electric potential corresponding to the electrostatic energy released by brush discharge exceeds the MIE of R290/air mixture (0.25 mJ) at a discharge potential approximately larger than 20 kV[3-25]. In addition, in the brush discharge process the charges on the surface of charged body are not fully liberated; instead, only a portion of the charge near the earthed electrode is liberated because the charged body is an insulator. Therefore, it would be expected that an electric potential of more than 20 kV would be required to ignite R290/air mixture via brush discharge. Hirakawa[3-37] reported that ignition does not always occur in the presence of hydrocarbon fuel vapors in cases in which the electric potential of the clothes is less than 30 kV. Although estimating the potential needed to reach the ignition limit is not easy, Tabata et al.[3-38] reported the following correlations between the average electric potential ($\bar{V}$) and the electrostatic energy produced by brush discharge (W_d) based on a series of ignition experiments involving hydrogen/air and R290/air mixtures and brush discharge generated between earthed metal spheres of up to 25 mm in diameter and a charged plastic sheet:

$$W_d = k\left(\bar{V}Q_{tm} - \frac{Q_{tm}{}^2}{2C_d}\right),\ k = 0.08,$$
$$Q_{tm} = 1.4 \times 10^{-9} D^{1.7}, \qquad C_d = 9.8 \times 10^{-12} \tag{3-2}$$

where $\bar{Q}_{tm}$ [C] denotes the maximum value of the discharge, C_d [F] denotes the effective capacitance of the discharging circuit, and D [m] denotes the diameter of earthed metal sphere, which is considered to be 20 mm when D > 20 mm. The value of average electric potential ($\bar{V}$) corresponding to $W_d = 0.2$ mJ was calculated to be approximately 22.6 kV.

Based on the above considerations, the ignitability of electrostatic discharge generated by undressing is smaller than that of spark discharge occurring in situations such as contact between a charged human finger and a metal doorknob. However, there remain some risks of ignition because of the possibility that the electric potential induced by undressing exceeds approximately 60 kV, corresponding to a value exceeding the MIE.

3.5 Evaluation of ignitability by electrical ignition source (part 2): arc discharge at the gap of electric contact

3.5.1 Characteristics of arc discharge and ignition

The discharging mechanism of an arc discharge differs from that of a capacitive spark discharge, as explained in Chapter 4. Arc discharge is caused by thermionic emission from part of an electrode at very high temperature as a result of large currents through the circuit. Although a universal definition of arc discharge has not been obtained, it is generally recognized as “a discharge between a pair of opposing electrodes in gases or vapors, which has a cathode drop voltage as large as the minimum ionization voltage or minimum exciting voltage of gases or vapors of electrode materials, and discharge is stable and the sequence of electron emission from cathode is sustained by this arc current”[3-39]. As the characteristics of arc discharge are influenced by variations in the electrode material, as described in Section 3.2, the value of arc current varies slightly but the minimum arc current is within a range of approximately 100 mA –1 A. Arc discharge can be generated at low voltages if there is a very large current; note that there are nearly no limitations on the value of current that can be generated by arc discharge. Fig.3-5 shows the relationship between the arc current and voltage at 100 Pa; Fig.3-6 shows an enlarged figure of the potential distribution of arc discharge[3-40]. It is seen that there are very narrow areas with relatively high electric field strength at both the anode and cathode called the cathode potential drop and anode potential drop, respectively. The characteristics of arc discharge can be derived by investigating these areas near the electrodes and in the arc cylinder separately.

Within the arc cylinder, the average electrical field strength is 10^3 V/m and the current density is $10^6 – 10^7$ A/m^2, unless the arc is forcedly cooled. The steady state of the arc is sustained by the equivalence between the plasma generated by the appearance and its dissipation: thermally, the generation of Joule heat by the current and the heat lost from the arc to the environment from conduction and radiation are equivalent. The temperature of the center of the arc reaches a high

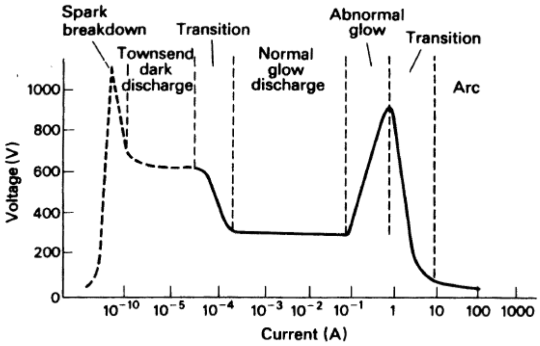

p: 100 N/m^2, showing order of magnitude

Fig.3-5 Steady state voltage-current characteristic of discharge[3-40].

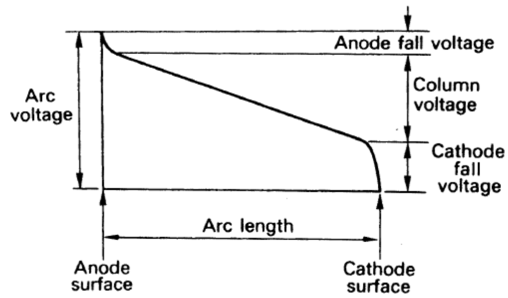

Fig.3-6 Voltage distribution along arc[3-40].

temperature of 10^4 K, as shown in Fig.3-7, from which a temperature gradient to the boundary is generated.

The method for evaluating the ignitability of gases by arc discharge is designated in IEC60079-11[3-41]. In this approach, a metal wire fixed by a movable jig is contacted to a movable metal block with a uniform rotation rate. This type of arc discharge is called "make-arc" because it is generated when an energized metal wire contacts another metal. However, there remain some unknown factors governing ignitability via a "break-arc," which are often generated when electrical contacts are separated[3-42] through, for example, breakage of a wire, opening of electrical contacts, etc. Uber et al.[3-42] investigated the ignition characteristics of hydrogen/air mixtures via arc discharge arising from opening an electrical contact. They proposed a model to explain the ignition criteria of break-arc discharge and found that only 44% of the input electric energy (discharge energy) was consumed by generation of the plasma and that the plasma contributes to the growth of the initial flame kernel when the power it stores exceeds 190 mW. Following this, ignition is achieved when the generated energy, as calculated by the integration of the produced power over time, exceeds the MIE. In short, the MIE is uniform regardless of the type of discharge but the ratio of energy consumed in the growth of the flame kernel to the total discharge energy varies with the type of discharge. Shekhar et al.[3-43] conducted a similar series of experiments in which they observed the process of flame growth using Mach-Zehnder interferometry. They further conducted three-dimensional simulation of element reactions and developed a criterion for achieving ignition namely, that the diameter of the initial flame kernel reaches approximately 200–300 μm within 100–200 μs of initiation of the discharge. However, neither study was able to establish a universal method for evaluating ignitability because too many items needed to be clarified—e.g., the influence of flame stretch caused by the expansion of the flame kernel, the factors affecting extinction, the influence of the speed of contact-breaking, etc.—to predict the ignitability of a break-arc.

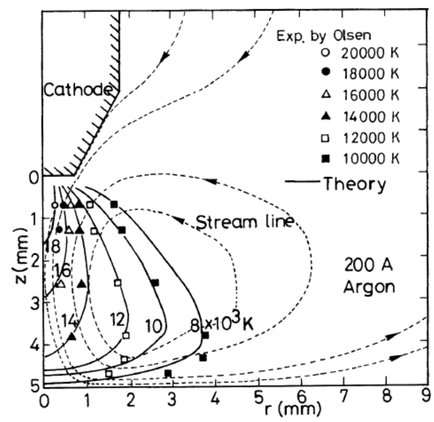

Fig.3-7 Temperature field of gas-tungsten-arc in Ar[3-40].

3.5.2 Evaluation of ignitability by an arc discharge at the gap of an electric contact: experimental procedures

Based on the above background, we experimentally evaluated the ignitability of R290/air mixtures by an arc discharge caused by the opening/closing of a relay electric contact. Fig.3-8 shows a photo and schematic of the experimental setup. A relay (OMRON MK2P) was installed in a combustion chamber fabricated from acrylic boards with thicknesses of 5 mm; the chamber dimensions were 100 mm × 80 mm × 80 mm. An Ag electrical contact with a maximum rated voltage of 250 V and a maximum current of 5 A was fabricated. The acrylic case covering the electric contact was removed and directly exposed to ambient conditions. The concentration of R290 in the combustion chamber was controlled via the volumetric method, with the required volume of R290, as determined by the volume of the combustion chamber and the target concentration, collected using a syringe and then introduced to the chamber. The opening/closing operation was begun 30 s after introducing the R290. A test-load circuit and a circuit for operating the opening/closing of the relay were located on the outside of the chamber. The input voltage to the relay was AC 100 V and the opening/closing operation was controlled by a manual switch.

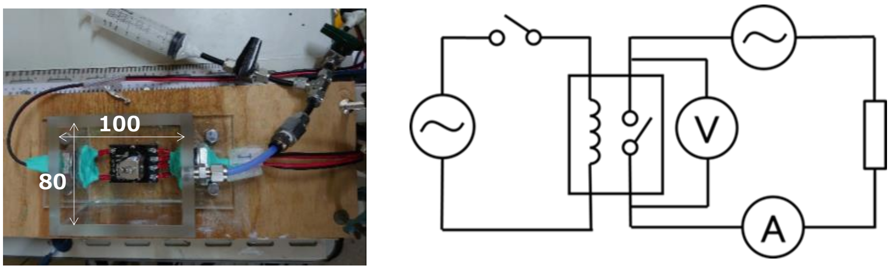

Fig.3-8 Photo and schematic of experimental setup and circuit.

General convenience appliances (hair dryer, electric screwdriver, vacuum cleaner, fan) were used as electric loads in the circuit to replicate an actual leak accident scenario. As there was some bias on the value of the rated consumption power involved in using only four types of appliance, further tests at 200, 500, 700 W of rated consumption power were additionally conducted using a changeable resistance. The specs of these electric loads are listed in Table 3-3. The concentration of R290 and varieties of electric load were set as input parameters. Each combination of R290 concentration and electric load was tested 60 repetitions of opening/closing the relay, with three units of ignition tests conducted at each condition and the number of repetitions of opening/closing needed to obtain ignition counted for each test unit. The number of discharges was used as the denominator because the voltage phase and relay synchronization timing were not synchronized, which allowed for cases in which discharge did not occur when the relay was opened and closed. The number of times was used in the denominator as "the number of times of discharge."

Table 3-3 Specs of test electric loads.

負荷	外観	消費電力	実験対象プロパン濃度
ドライヤー (Panasonic, EH101P)		1200W	3.0, 4.0, 5.0, 6.0, 7.0, 8.0, 9.0 vol%
掃除機 (Panasonic, MC-PJ20G-N)		1150W	3.0, 4.0, 5.0 vol%
電動ドライバー (RYOBI, CDD-1021)		160W	3.0, 4.0, 5.0 vol%
扇風機 (YAMAZEN, FY-J301)		40W	3.0, 4.0, 5.0 vol%
可変抵抗器 (山菱電機，RZ-200-3B)		200W	3.0, 4.0, 5.0 vol%
		500W	3.0, 4.0, 5.0, 6.0, 7.0, 8.0, 9.0 vol%
		700W	

The visible behavior of a premixed mixture of R290/air and the flame kernel around the electric contact was assessed and the associated voltage/current profile was measured. The voltage between the contacts of the test relay was measured using a passive probe (Tektronix, TPP0201) and the current was measured using a current probe (HIOKI, CT6711), and their outputs were logged to a chart recorder (HIOKI, 8860-50). The change in output of the current probe was used as a trigger signal to activate the chart recorder and the trigger signal output from the chart recorder was input to a high-speed camera (Photron FASTCAM NOVA S12) to activate it. The discharge energy was calculated by integrating the measured current and voltage over the period in which a visible discharge was observed:

$$E_d = \int_{t_1}^{t_2} IE dt. \tag{3-3}$$

3.5.3 Evaluation of ignitability by an arc discharge at the gap of electric contact: results and discussion

Fig.3-9 shows the relationship between the ignition frequency and the equivalence ratio. The ignition frequency reaches a maximum near an equivalence ratio of 1.3–1.5. No ignition is observed when the switch closes at an equivalence ratio of 0.75 (3 vol% of R290), which is within the flammable range. Even in the switch-opened case, the ignition frequency is at most 5%. It appears that the ignition frequency is large when the switch is opened and electric load has a large rated consumption power.

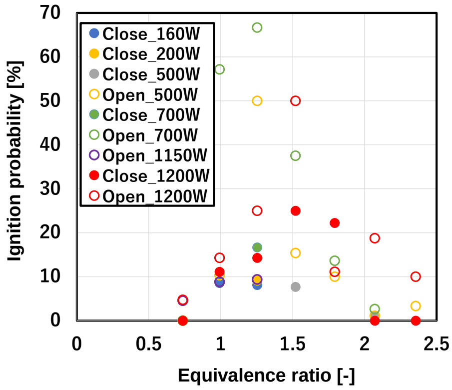

Fig.3-9 Dependence of ignition probability on the equivalence ratio.

Fig.3-10 show examples of the voltage and current profiles of the arc discharge when the switch is opened (called "break-arc"), along with a sequence of images around the electric contact taken by the high-speed camera. The experimental condition of Fig.3-10(a) is a 5.0 vol% R290 concentration and a resistive circuit with a rated consumption power of

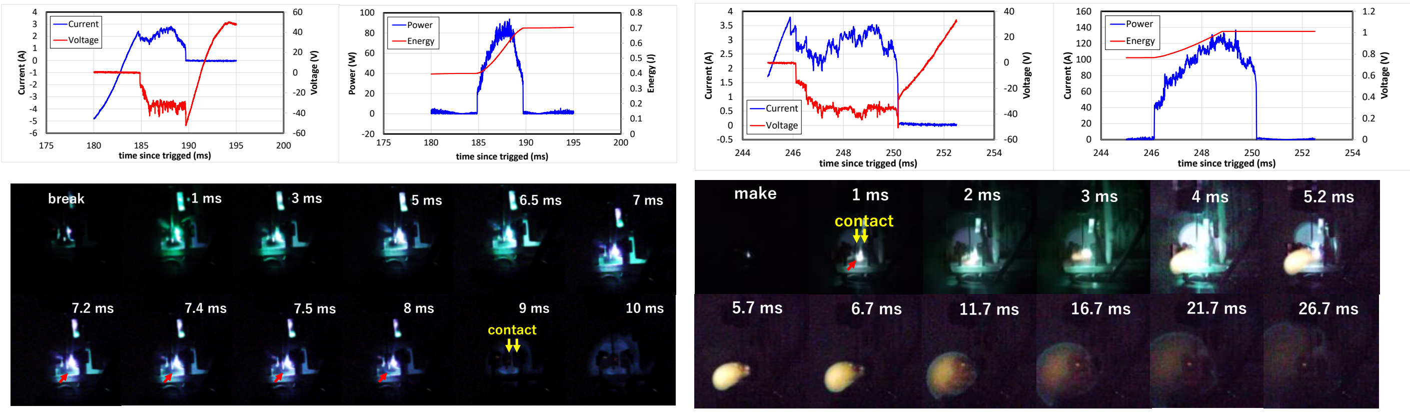

(a)5.0 vol% of R290, resistive circuit, 500 W

(b)7.0 vol% of R290, resistive circuit, 700 W

Fig.3-10 Profiles of voltage and current at break-arc and sequence photos around electric contacts.

500 W; that of Fig.3-10(b) is a 7.0 vol% R290 concentration and resistive circuit with a rated consumption power: of 700 W. The discharged energies, estimated by the integration of voltages and currents over the durations of discharge, are 17.8 and 26.2 mJ, respectively, and the time at which the luminescence of the discharge can be seen is approximately 5–8 ms in both cases. In each case, the voltage remains at a close to uniform value over the period of discharge but the relationship between the power discharged and time follows an upwardly convex curve, with the discharged energy monotonously increasing with time.

Fig.3-10(a) shows the luminescence of discharge from switch-opening. A flame surface can be observed at the downward side of the electric contact starting at 7.2 ms from the commencement of discharge, as shown by the red arrow in Fig.3-10(a). This flame surface gradually grows with time, covering the electric contact at 10 ms. The size of the flame surface observed at 7.2 ms indicates that it had been generated before that time, but this could not be confirmed because the luminescence of discharge was too strong.

Fig.3-10(b) shows some characteristic behavior of the flame discharge. An orange-colored flame kernel, shown by a red arrow, is observed at 1 ms from commencement of discharge. Owing to its orange kernel, we assume that this flame kernel did not originate from the combustion of R290 but through the combustion of metal vapor from the electric contact. The high pressure generated by the high-temperature plasma column pushed the flame kernel outward from the gap of the electric contact, allowing it to grow sustainably because there was no heat loss from contact with obstacles.

Fig.3-11 shows examples of the voltage and current profiles of the arc discharge produced when the switch was closed (called "make-arc") and a sequence of images around the electric contact taken by a high-speed camera. The experimental condition of Fig.3-11(a) is 5.0 vol% R290 concentration and an inductive circuit (hair dryer, rated consumption power: 1200 W, discharged energy: 36.4 mJ); in Fig.3-11(b), the condition is 6.0 vol% R290 concentration and a resistive circuit (rated consumption power: 700 W, discharged energy: 24.3 mJ). When the switch was closed, the following characteristics differing from the switch-opened case were observed: (1) the discharge duration was at least one order of magnitude shorter (approximately 0.5 ms), and (2) the electric contact was re-opened by the bounce of electric contact and the arc discharge was regenerated once the electric contact was closed. Finding (1) has been reported by other researchers[3-42] with nearly the same order of duration. Finding (2) is also well known[3-44].

Fig.3-11(a) shows a make-arc generated by approaching the electric contact, followed by disappearance of the arc at 0.4 ms as a result of complete closing of the electric contact accompanied by orange-colored luminescence at the downward side of the contact.Fig.3-11(b) shows the generation of an arc discharge by approaching the electric contact, followed by its disappearance at 0.4 ms. Although no luminescence from the ignition of R290 is observed, the flame propagates to cover the electric contact at 4.7 ms. Fig.3-12 shows a photo of the electric contact taken after the ignition tests. The surface of the electric contact has been roughened by many melted points. Considering that arc discharges are generated at specific distances from the electric contact in both break-arc and make-arc situations, the roughness of the contact surface can be attributed to probabilistic varying of the ignition behavior under identical conditions of voltage, current, type of circuit load, and contact opening/closing rates.

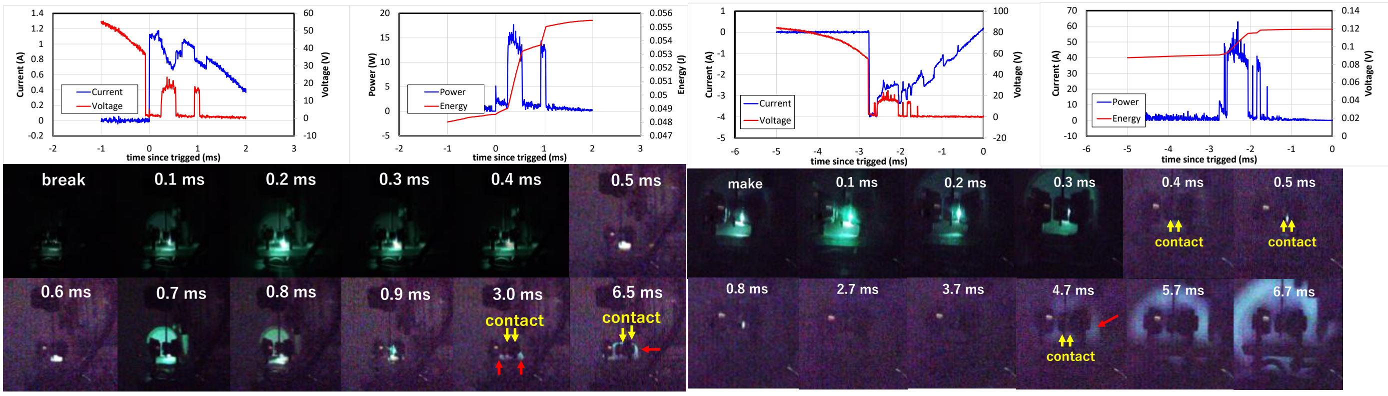

(a)5.0 vol% of R290, inductive circuit (hair dryer), 1200 W (b)6.0 vol% of R290, resistive circuit, 500 W

Fig.3-11 Profiles of voltage and current at make-arc and sequence photos around electric contacts.

Fig.3-13 shows the relationship between the discharged energy and the rated consumption power. The red arrows show the cases in which ignition occurred. Both the discharged energy and the number of ignitions increase with the rated consumption power. No ignition is observed when the fan (rated consumption power: 40 W) is used as the circuit load.

Fig.3-14 shows the relationship between the discharged energy and the equivalence ratio, with the red arrows showing the ignition cases. Data for the MIE of an R290/air mixture under capacitive discharge obtained by Lewis and Elbe[3-11] are shown for comparison. The blue dotted curve shows the minimum values of discharged energies at each equivalence ratio and follows the lower convex curve obtained from Lewis and Elbe. Note that the equivalence ratio at which the discharged energy is minimum is approximately 1.5 and is shifted toward a slightly more fuel-rich composition than that obtained by Lewis and Elbe. The discharged energy obtained in this experiment was at least one order of magnitude larger than the MIE. These trends can potentially be explained as follows.

Fig.3-12 Photo of the electric contact after conducting the ignition

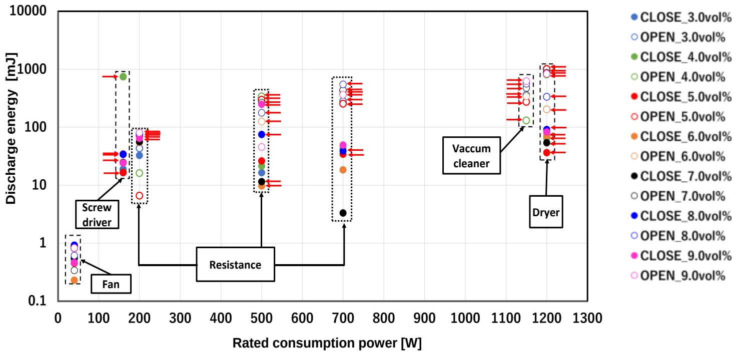

Fig.3-13 Relationship between the discharged energy at the gap of electric contact and the rated consumption power.

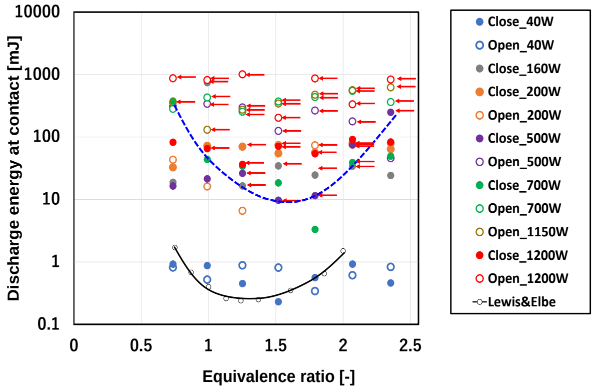

Fig.3-14 Relationship between the discharged energy at the gap of electric contact and the equivalence ratio.

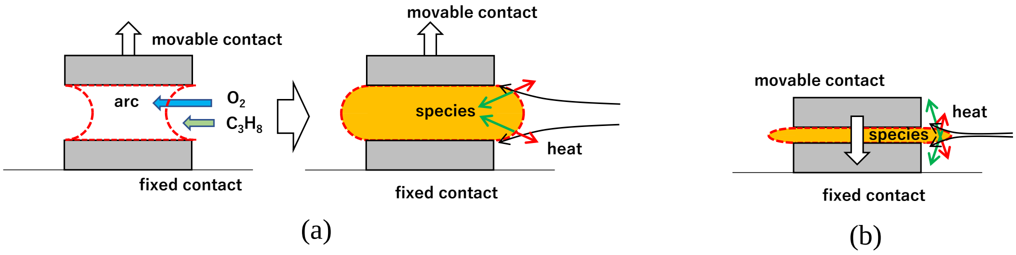

Fig.3-15 Schematic of moving behavior of electrical contact and ignition mechanism.
(a) contact opening (b) contact closing

In the case in which the switch was opened, the R290/air mixture around the electric contact dispersed into the gap of the electric contact after it was opened. As the diffusion coefficient of oxygen is larger than that of R290, the local composition at the flame front that "protruded" to the unburnt gas shifted toward a leaner fuel composition, as shown in Fig.3-15(a). This is generally called the "selective-diffusion effect." The flow tube expanded as a result of the protrusion of the flame front, which in turn increased the supply of chemical enthalpy. By contrast, the heat that increased the unburnt gas temperature was transported from the flame via conduction. If the thermal diffusivity was larger than the diffusion coefficient, the heat balance in the control volume became too negative, causing the flame kernel to be quenched. To evaluate these effects of thermal diffusivity and reactive species diffusion, the Lewis number, which is measured as $\mathrm{Le} = a/D$ (a: thermal diffusivity, D: diffusion coefficient of the insufficient component in the premixed gas) was calculated. The Lewis number of the fuel-lean composition of the R290/air mixture was 1.8 and that of the fuel-rich composition was 0.9; thus, the combustion-weakening effect was sufficient in the fuel-lean R290/air mixture but insufficient to quench ignition in the fuel-rich, making the latter easier to ignite. The equivalence ratio at the minimum value of ignition energy was shifted toward the fuel-rich side because of the interaction between the selective-diffusion and Lewis number effects.

In the case in which the electric contact was closed, the closure was induced by an electromagnetic force; in this case, the discharged column was generated when the gap of the electric contact reached a certain value and a flame kernel was generated by this column. Note that the gap in the electric contact was eventually completely closed, at which point it fully pushed out the flame kernel. As the curvature of the flame kernel protruding from the gap of the electrode was larger than in the switch-opening or gap-fixed cases, the Lewis number effect was more significant and the R290/air mixture was slightly easier to ignite at its fuel-rich composition. On the other hand, the discharged column was smaller and the discharge duration was shorter than in the switch-opened case and, as a result, the ignition frequency was smaller. Given these factors, it was important to estimate the ignition energy in the of switch-closed case to evaluate the ignition potential of an R290/air mixture under arc discharge. To do this, Fig.3-14(a) plots the relationship between the ratio of discharging energy as a dotted curve (called E_{arc}). Similarly, the MIEs obtained by capacitive sparking (called E_{min}) and the corresponding equivalence ratios are shown in Fig.3-16(a). The value of E_{arc}/E_{min} can be expressed as a quadratic function of the equivalence ratio, which can be used to evaluate the ignition energy generated at the electric contact by arc discharge. Note that we obtained no data at an equivalence ratio of 0.7 because no ignition was observed at this point under any

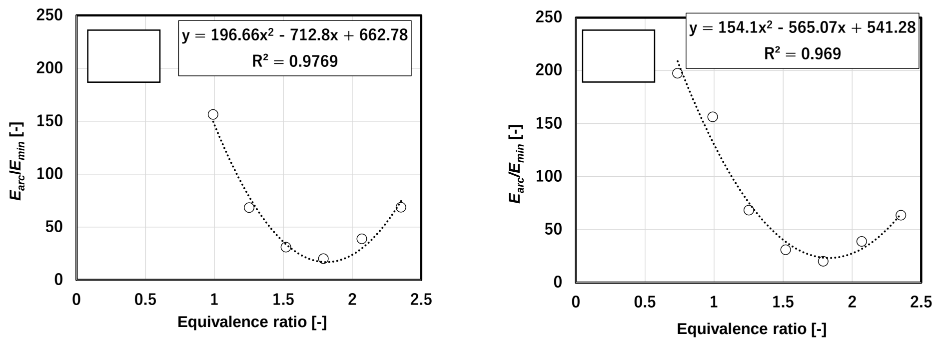

Fig.3-16 Dependence of a minimum arc discharge energy for ignition on equivalence ratio.
(a)data when contact is closing (b) minimum data of ignition energy in each equivalence ratio

switch-closed case, although ignition was observed under several switch-opened cases. Therefore, Fig.3-16(b) was obtained for reference by plotting the minimum discharge energy under which ignition occurred regardless of whether the contact was open or closed. Even in this case, E_{arc}/E_{min} could be expressed as a quadratic function of the equivalence ratio. As the burn rate, which is closely related to the reaction rate, was small near the LFL or UFL, the effects of heat loss or heat diffusion on the growth of the flame kernel increased, causing the value of E_{arc}/E_{min} to increase near the LFL or UFL. The results indicate that tens to hundreds of times the minimum energy is required by an arc discharge generated at the gap of an electric contact to ignite an R290/air mixture. This magnification factor is similar to that reported by Kinoshita et al[3-9].

We note that ignition via arc discharge was generally initiated by the localized thermal-equilibrium plasma[3-45]. In other words, the temperatures of the electrons and gases (molecules) were locally equal, as reflected by the many melted points on the surface of the electric contact shown in Fig.3-12. In this case, the occurrence of ignition depended on whether the flame kernel could grow via the heat supplied by the plasma regardless of whether the cooling effect was induced by convection to the electric contact; i.e., ignition via arc discharge was governed by the thermal explosion theory.

According to previous work investigating ignitability vis arc discharge[3-42], sustainable flame growth will be completed if the diameter of the flame kernel can grow to a certain value within a specific period following commencement of the arc discharge. Uber et al[3-42] proposed 200 µs as this critical duration based on their experimental results for a hydrogen/air mixture and estimated the critical diameter as 500 µm using the following relationship:

$$d_q \sim \sqrt{\frac{MIE}{0.07}}. \tag{3-4}$$

Note that the units of MIE and dq (quenching distance) in Eq.(3-4) are mJ, and mm, respectively. For an R290/air mixture, Eq.(3-4) produces a dq of 1.89 mm at an MIE of 0.25 mJ[3-11]. Therefore ignition of an R290/air mixture occurs if the diameter of flame kernel can grow 1.89 mm within 200 µs. In the case of a make-arc, the diameter of the flame kernel rarely reaches 1.89 mm because the discharge duration is too short (100–500 µs). On the other hand, the energy stored in the plasma column in the case of a break-arc is sufficiently larger than the ignition energy because the discharge duration is one order of magnitude longer than the characteristic duration of the flame kernel growth. However, the flame kernel will not grow if the power supplied to it by the plasma column is too small because the heat loss to the electric contact will become to appear explicitly. Based on the above considerations, the experimental data are arranged to show the relationship between the discharging energy and discharge duration in Fig.3-17. No ignition was observed in situations in which the discharge duration was shorter than 200 µs in either the make-arc or break-arc cases. It is evident that the characteristic duration required for the growth of a flame kernel to the critical diameter under arc discharge is 200 µs. However, the generation of an initial flame kernel just after discharge could not be completely confirmed, making it difficult to further assess the occurrence of ignition in terms of the relationship between the diameter of the flame kernel and the discharge duration. In the make-arc cases in particular, so-called “volumetric ignition” in which flame formation suddenly occurs over a wide region sometime after discharge was observed.

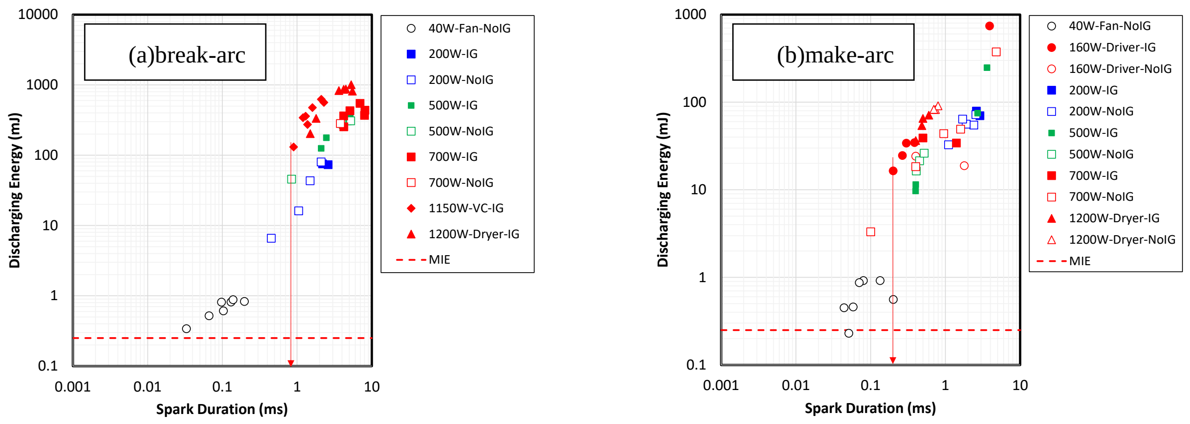

Fig.3-17 Relationship between the discharging energy and spark duration.

Uber et al.[3-42] reported that only 6% of input electric energy contributes to the formation of a flame kernel based on a simulation of ignition via arc discharge in terms of the thermal balance of the heat input between the plasma and the heat lost to the electric contact. Fig.3-18 shows the relationship between the net energy estimated from the production of discharged energy calculated by integrating the electric power, the percentage reported by Uber et al. [3-42], and the equivalence ratio. Although this "net ignition energy" is slightly larger than the MIE obtained by Lewis and Elbe, the orders of magnitude of both energies coincide. In other words, if a certain amount of energy is supplied and the flame kernel reaches a certain diameter within a certain amount of time, the flame will be able to propagate continuously. As the ratio of the energy used for the formation of a flame kernel changes, the energy that can be supplied for ignition increases. Therefore, the occurrence of ignition under arc discharge can be evaluated by comparing the net discharged energy with the MIE. Note that Uber et al.[3-42] pointed out that the probability of ignition when the MIE is supplied is at most 10^{-3}; this is believed to be related to the deterioration of discharge reproducibility owing to wearing of the contacts.

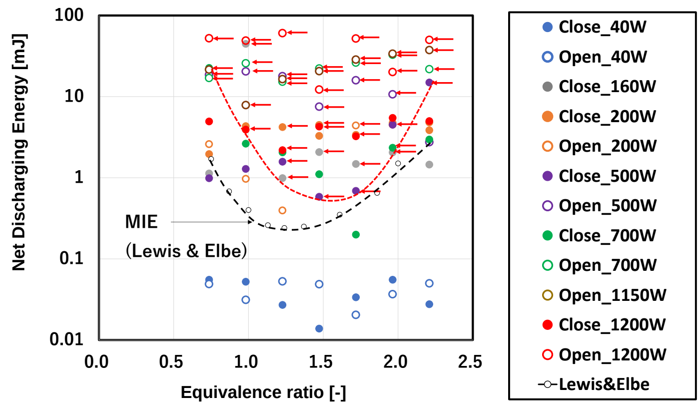

Fig.3-18 Relationship between the net discharging energy and the equivalence ratio.

In addition to the factors discussed above, (1) contact material, (2) circuit elements, and (3) contact opening/closing speed are all expected to affect arc discharge behavior. In terms of contact material, Table 3-4 lists the effects of melting point and resistivity on ignitability. The contact material used in our experiments was silver, which has the lowest ignitability of the materials listed in the table. Therefore, to evaluate other materials it would be necessary to follow criteria stricter than those used in this experiment. In particular, attention would have to be paid to the fact that metals with low melting points are highly ignitable. The effects of circuit elements differ depending on how they are combined but, in general, when an inductive load is used an induced electromotive force is generated when the contacts are opened and closed (especially when the contacts are closed), which causes the voltage to rise. In particular, when the inductance is 95 mH or more the minimum arc current decreases as the inductance increases (that is, arc discharge is more likely to occur). In addition, when the inductance is high, the ignitability is enhanced by opening and closing at high speed. In arc discharge, increasing the electric capacity of the circuit tends to cause the

Table 3-4 List of varieties of materials of electric contact and incendivity of sparks for ignition[3-48].

Metal	Melting point (℃)	Resistivity (nΩ-m)	Incendivity of sparks
tin	232	115	most incendive
cadmium	321	68	
zinc	420	59	
beryllium	1287	35.6	
chromium	1907	125	
aluminum	660	26.5	
nickel	1455	69.3	
iron	1538	96.1	
copper	1085	16.8	
silver	962	15.8	least incendive

voltage at which ignition occurs to decrease whereas the energy tends to increase[3-47), 3-48)].

In this section, we summarized the methods for evaluating ignitability owing to arc discharge at electrical contacts and various effects that govern this process. In practice, these results would be easier to use if the relationship between the rated power consumption and the discharge power at the contact could be evaluated, as is done in Fig. 3-19. From this, it is seen that there is a possibility of ignition when the rated power consumption is 160 W or more and a discharge with an output of approximately 20 W occurs at the contact.

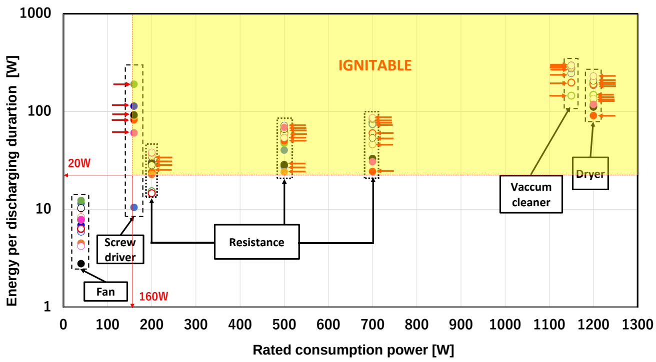

Fig.3-19 Relationship between the power of discharge at the gap of electric contact and rated consumption power.

3.6 Evaluation of ignitability by electrical ignition source (part 3): arc discharge generated at a lighting switch

3.6.1 Study outline

Here, we evaluated one of the ignition scenarios that can occur when a home air conditioner is in use, a refrigerant (R290) leaks into the room to form a propane/air premixture, and ignition occurs as a result of contact sparks generated when a lighting switch is pressed. As mentioned in the previous section, there are studies on the evaluation of the ignitability of various switches in the literature[3-3)]. Therefore, in 2018 we decided to conduct a reproduction experiment using the lighting switch with the highest market share in Japan to evaluate the ignitability hazard associated with its use. Furthermore, considering the global standardization of ignitability evaluation methods, we also evaluated lighting switches covered by overseas standards. First, to confirm whether a combustible propane/air premixture is formed near a contact that can serve as an ignition source, a test space and casing containing the contact (hereafter referred to as the "contact casing") were measured (experiment A). Based on the results, a combustible propane/air premixture was introduced to the test space and the switch was operated to allow us to visually observe the discharge and ignition behavior around the contacts. We then obtained the discharge energy and quantitatively examined the relationship between it and the occurrence or non-occurrence of ignition (Experiment B).

3.6.2 Experimental outline

3.6.2.1 Test A (concentration measurement experiment)

A cubic acrylic pool with a side of length H = 1 m was manufactured and testing locations at 0 H, 1/4 H, 1/2 H, 3/4 H, and H (heights from the bottom of 0, 250, 500, 750, and 1000 mm, respectively) were designated. A copper tube (outer diameter 1/4 inch = 6.35 mmφ, inner diameter 4.0 mmφ) was attached at a height of 1000 mm. From measurements of the gas concentration obtained using five ultrasonic gas analyzers (US-II-T-S, Daiichi Nekken Co., Ltd.), a concentration distribution map was obtained (Fig.3-20(a)). The R290 leak height was set to occur at five levels—0, 1/10 H, 3/10 H, 1/2 H, and H—with the leak rate at each set to 10 g/min. Two leakage amounts—41 and 87 g—were investigated, corresponding to the amounts of leakage at which the concentration of R290 in the pool reached the lower flammability limit (LFL: 2.1 vol%) and the upper flammability limit (UFL: 9.5 vol%) if the entire amount of gas leaked into the pool and diffused uniformly. After obtaining the concentration distribution in the pool from measurements, a switch box and contact casing were attached to the pool wall to investigate whether the R290/air premixture in the pool flowed into the contact casing. The R290 concentration inside each component was measured using an ultrasonic densitometer (Fig.3-20(b)). The switches were installed at heights of 3/4 H, 1/2 H, and 1/4 H.

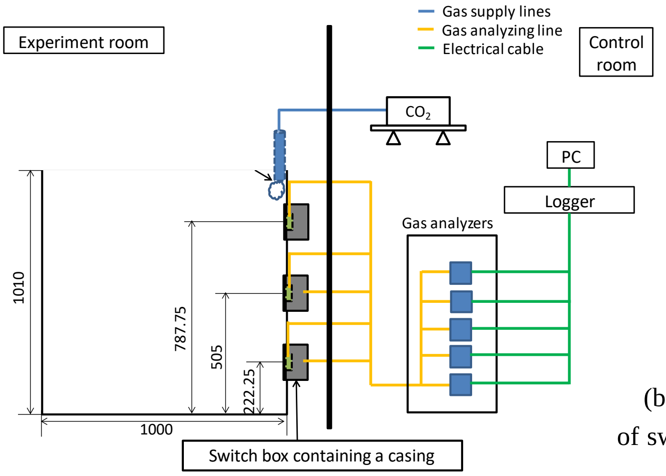

(a) Outline of experimental setup (unit: mm)

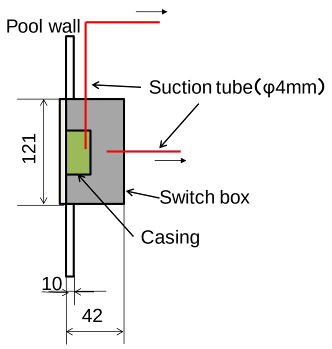

(b) Schematic diagram of cross-section of switch box, casing, and pool wall (unit:

Fig.3-20 Schematic of experimental setup to measure propane flow to the casing containing electrical contacts and the switch box

3.6.2.2 Test B (ignition test)

(i) Test B-1 (ignition experiment: 100 V)

As shown in Fig. 3-21, a premixed R290/air mixture of a predetermined concentration was introduced to the test unit—an acrylic switch box with an attached switch housing—and the contacts were actuated to generate discharge and attempt to cause ignition, which was checked for its presence or absence. R290 was introduced in quantities of 12 and 21 mL, corresponding to the volumes of gas that made the inside of the box reach the lower flammability limit and the stoichiometric composition, respectively. An incandescent lamp (60 W) was used as the circuit load, and only Type B switches were used. Ignition arising from discharge was photographed using a high-speed camera through an observation hole made in the lower part of the contact casing. The discharge energy was calculated using Eq.(3-3).

(ii) Test B-2 (ignition experiment: 230 V)

A pool with an internal volume of 150 mm × 150 mm × 150 mm was fabricated from an acrylic plate with a thickness of 10 mm and used as a combustion vessel. The upper surface of the container was sealed with aluminum foil, which was torn during combustion to dissipate the pressure. A small fan installed in the pool was used to agitate the premixed gas. As with test B-1, an opening was provided in the contact casing to allow R290 to flow between the contacts and the behavior inside the contact casing was photographed using a high-speed camera. The R290 concentration in the combustion chamber was stoichiometric (4 vol%). The circuit load was a 100 W incandescent lamp and a Hf fluorescent lamp (32 W), and the applied voltage was 230 V.

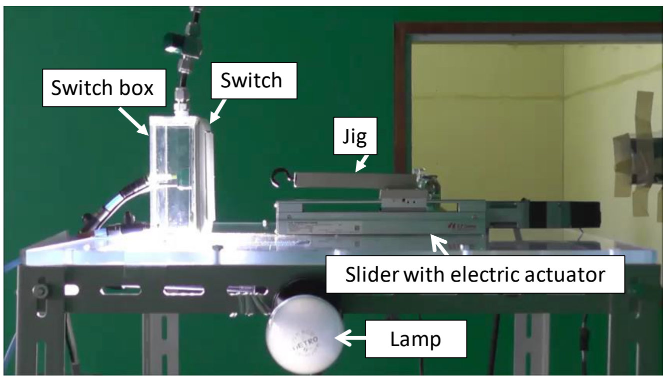

Fig.3-21 Photo of setup for the ignition test of R290/air mixture by a wall-mounted switch for lighting.

3.6.3 Results and discussion

3.6.3.1 Inflow of combustible premixture to the contact casing

Fig. 3-22 shows the concentration distribution in the $1m^3$ pool measured in Experiment A and the measured R290 concentrations in the contact casing and switch box. In tanks constructed using both casings A and B, the inflows of combustible R290/air premixture into the contact casing of switches installed at heights of 1/2H (500 mm) and 1/4H (250 mm) were observed. We presume that the R290 flowed into the switch box through the gaps in the housing plate and into the vicinity of the contacts through the holes in the contact casing.

3.6.3.2 Ignition experiment

Ignition experiments were carried out based on the test setups described above, with ignition observed over 60 (AC100 V experiment: Experiment B-1) and 200 (AC230 V experiment: Experiment B-2) switching operations under each concentration condition. None of the switching operations produced an ignition. Judging from the high-speed camera images of the state during discharge, the distance of the light-emitting region of the arc column was approximately 0.1–0.4 mm, which is approximately 1/10–1/4 of the quenching distance of propane (1.7 mm[3-49)]). The diameter of the contact was approximately 2.0 mm, which is one order of magnitude larger than the distance between the contacts. Based on these facts, ignition was not observed in this experiment because the size of the flame kernel formed by the discharge was larger than the quenching distance; as a result, no heat loss occurred owing to contact between the flame kernel and the contact and the flame could not grow into a sustainable flame.

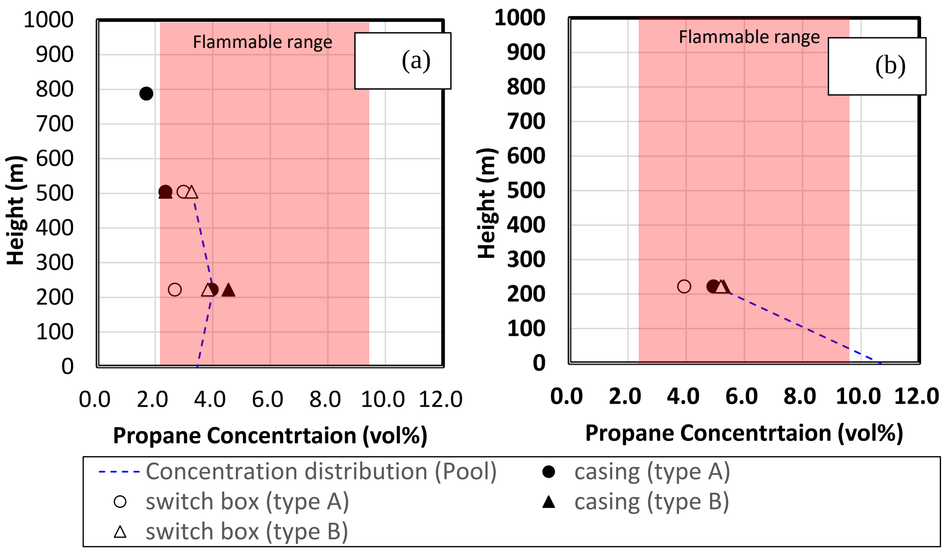

Fig.3-22 Vertical distribution of R290 concentration in the pool and penetration of R290/air mixture in the casing containing an electrical contact. (a) leak height: 1000 mm(H), (b) leak height: 0 mm (H=0)

3.7 Evaluation of ignitability by electrical ignition source (part 4): arc discharge generated by plugging or unplugging

3.7.1 Study outline

As described in the previous section, the MIE can often be measured using a discharge that completes energy release in a relatively short time using capacitive discharge. Although this method can be applied directly to the evaluation of the ignitability of different types of discharges, this is not always possible. Therefore, to evaluate the ignitability of various electrical ignition sources discussed in Section 3.2 in detail, a case-study experiment was carried out in which we evaluated ignitability by simulating the generation of sparks when plugging and unplugging several electrical appliances.

3.7.2 Experimental outline

3.7.3.1 Adaptability experiment for 100 VAC products (Type A)

Fig. 3-23 shows a model in which the commercially available A-type outlet shown in Fig. 3-24 is installed vertically in a container with a side length of 150 mm whose top surface has been sealed with aluminum foil. Because there is no partition between the inside of the outlet housing and the plug insertion port, when gas enters from the insertion port it diffuses and remains inside the overall housing. Two patterns of experiments were conducted: in pattern (1), the power plug was pulled out and inserted 200 times (experiment 1); in (2), the action of pulling out the outlet was repeated 100 times (experiment 2). In experiment (1), the propane introduced into the vessel was replaced each time ignition was observed; in experiment (2), it was replaced each time regardless of whether or not ignition occurred. In both experiments, the most rigorous evaluation was obtained by using a gas composition with an equivalence ratio of 1.31 (propane concentration of 5.18 vol%), which is assumed to have the MIE for a propane/air premixture. The voltage at both ends of the power plug and the circuit current were measured with probes and the discharge energy Ed was obtained from Eq. (3-3).

Table 3-6 List of specification of test devices.

Type of relay	Type of Electrical Load				Consumption Power (W)
Type 1	Inductive & Resistance	Hair dryer	Type A	HIGH	840
				MIDDLE	440
				LOW	40
			Type B	HIGH	1050
				MIDDLE	1000
				LOW	700
	Capacitive & Resistance	Screwdriver	Type A		130
			Type B		210
	Resistance	Electric bulb			50
Type 2	Inductive & Resistance	Hair dryer	Type A	HIGH	840

The circuit loads were a series of commercial home appliances (dryer, electric screwdriver, vacuum cleaner) with the specifications listed in Table 3-6.

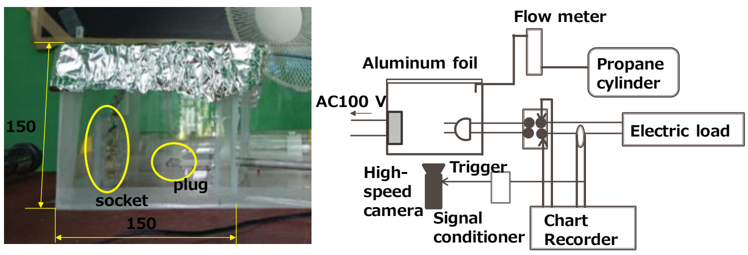

Fig.3-23 Photo of setup for the ignition test of propane/air mixture by plugging or unplugging the power cable of the general electric appliances.

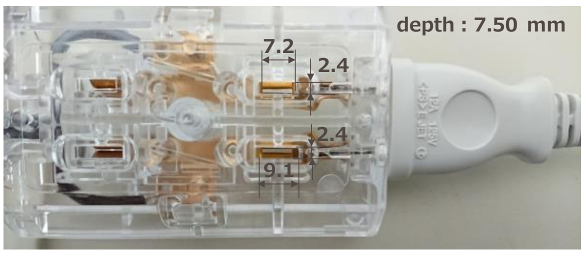

Fig.3-24 Photo of the electrical socket.

3.7.3.2 Adaptability experiment for 230 VAC products (SE Type)

Fig. 3-25 shows photographs of the outlet housing in the normal state (left) and the state in which the cover has been cut to the maximum extent (right: this was used in the ignition experiment). As shown in Fig. 3-26, we constructed a model in which the outlet was attached to a combustion vessel comprising a polycarbonate plate with a side of length 200 mm. The upper part of the combustion chamber was sealed with aluminum foil as in (a). In this experiment, the inside and outside of the outlet housing were airtight, allowing the gas to move freely. The equivalence ratio in the container was set to 1 (propane concentration of 4 vol%). Using resistance loads of 50 and 300 Ω and an applied voltage of 230 V, the voltage across the plug and the circuit current were measured with a probe. The plug insertion/removal speed was proportional to the load applied to the force gauge and was classified into two patterns (slow and quick) based on its magnitude. The number of plugging/unplugging cycles was set to 50 and the discharge energy E_d was obtained from Eq. (3-3).

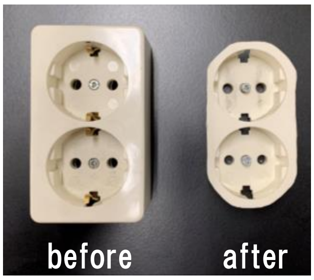

Fig. 3-25 Photo of electrical plug socket (SE type)

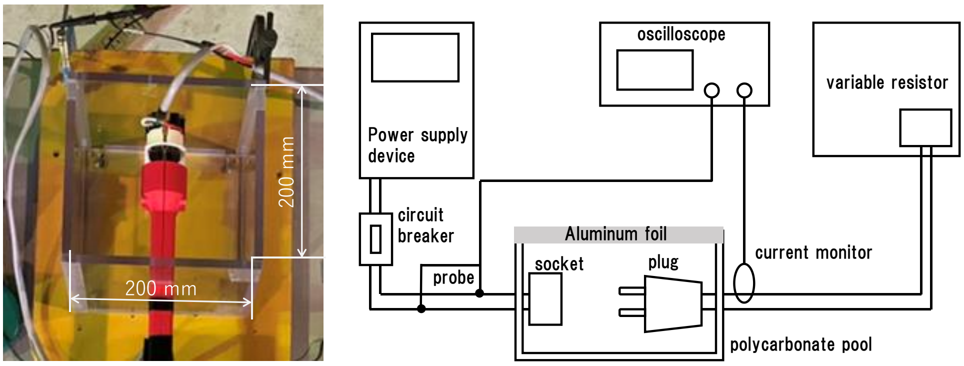

Fig. 3-26 Photo of setup for the ignition test of propane/air mixture by plugging or unplugging the power cable.

3.7.3 Results and discussion

3.7.3.1 Adaptability experiment for 100 VAC products

Ignition was not observed even once in Experiment 2 at any load. As shown in Fig.3-27, the ignition probability tended to increase as the power consumption increased. Fig.3-28 is a high-speed color photograph of the area around the outlet when a Type B dryer was used as the load. The variable t denotes the elapsed time since the luminescence of discharge was observed, and the white frame in Fig.3-28 shows the outer edge of the socket. The load and equivalence ratio are the same in both the upper and lower stages. In the upper photo, the flame starts to blow out from the plug insertion hole of the outlet housing at t = 20 ms and spreads into the chamber at t = 30 ms. In the lower photo, the ejection behavior from the inside of the outlet housing is somewhat unclear but it can be confirmed at t = 70 ms and, at t = 100 ms, the ejection flame spreads and propagates to nearly the same area as in the upper photo at t = 40 ms.

Based on these experimental results and the fact that the gap between the outlet plugs was about 2.4 mm, which is wider than the quenching distance of propane (1.70 mm[3-49]), the ignition mechanism of this phenomenon can be deduced. First, the insertion and removal action (especially the insertion action) entrains the propane/air premixture in the container into the outlet housing. When the propane/air premixture inside the outlet housing becomes combustible by repeated plugging and unplugging, it is ignited inside the plug socket by the discharge energy generated by the plugging and unplugging. As the plug insertion hole was narrower than the quenching distance, the flame passed through the plug insertion hole and spouted into the vessel, following which the heat of the flame propagated to the unburned propane/air mixture in the vessel. Thus, in this experimental system it is presumed that the success or failure of ignition is almost purely determined by the discharge energy produced when plugging in and unplugging from the outlet and, therefore, that ignitability increases depending on the power consumption of the load.

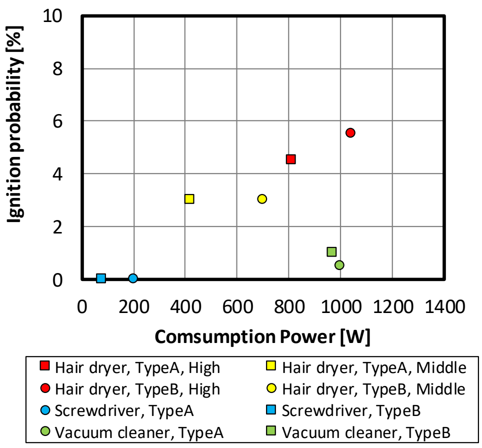

Fig.3-27 Dependence of the ignition probability by plugging/unplugging on the consumption power.

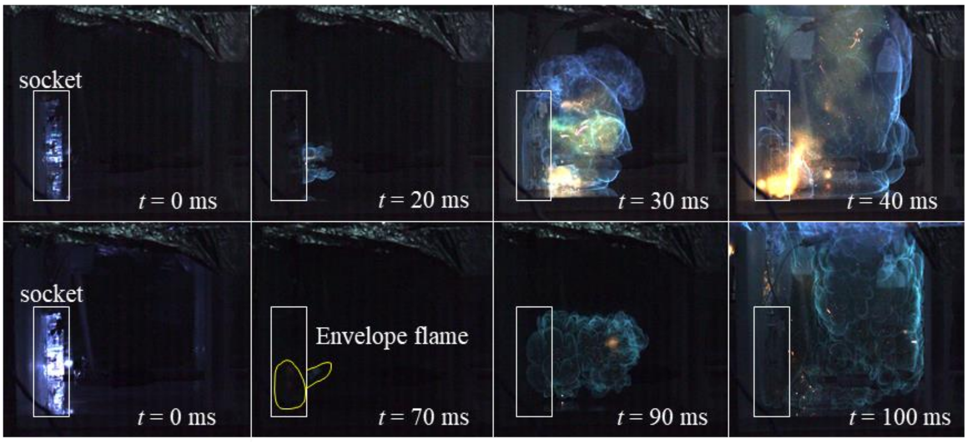

Fig.3-28 Sequence photos of ignition of accumulated R290/air mixture by unplugging of power cable from a socket.

3.7.3.2 Adaptability experiment for 230 VAC products

Fig.3-29 shows a photograph of the surroundings of the outlet when the plug is inserted and removed. Under rapid unplugging applied at a load of 300 Ω, (Fig.3-29(a)) and rapid and slow unplugging applied at 50 Ω (Figs.3-29(b), (c)), light is emitted inside the outlet housing. However, no explosive flame spreads to the unburned propane/air premixture around the outlet. Nevertheless, in Figs.3-29(b) and (c) the emission region is larger than in (a) and yellowish emission is observed. In both cases, this phenomenon was observed at 50 Ω but not at 300 Ω, confirming that it occurs when the circuit current is large. Although it cannot be ruled out that the phenomenon was caused by combustion, it is most likely that the emission comprised fumes from the contact metal as it did not propagate to the unburned air-fuel mixture.

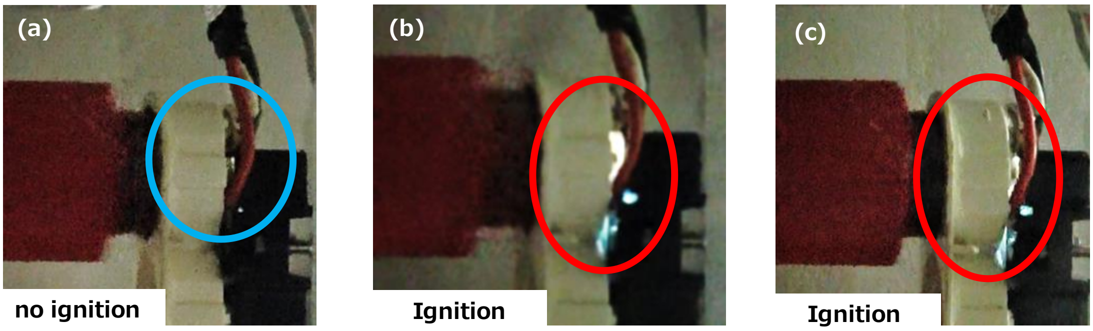

Fig.3-29 Photo of test space around an electrical socket and plug.
(a) 300 Ω– OFF-quick, (b) 50 Ω– OFF-quick, (c) 50 Ω– OFF-slow

3.8 Evaluation of ignitability by hot surface

3.8.1 Evaluation method of ignitability by hot surface

When a flammable mixture is ignited by a hot surface, there are no excited species in the mixture until just before the ignition. Therefore, ignition by a hot surface is simply governed by the heat generation and heat loss rates at the contact volume. The theories of ignition mechanism based on these considerations were established by Semenov and Frank-Kamenetskii. In this chapter, only the outline of the Semenov's theory is described; further details are explained in other works in the literature[3-50)-3-57)].

Here, we focus on a reaction system in which a fuel reacts with an oxidizer and generates products in a vessel. Denoting the volume of the reaction system by V [m^3] and the amount of heat generated by Q [J/m^3], the heat generation rate per time (q_1) assuming that the reaction rate follows Arrhenius's equation can be expressed as

$$q_1 = QVC^n B\exp\left(-\frac{E}{R_0 T}\right), \tag{3-5}$$

where B denotes a pre-exponential factor [1/(s(mol/m^3)^n)] that corresponds to the frequency of collision of molecular or reactive radicals, C [mol/m^3] denotes the mole concentration of fuel, E [J/mol] denotes the activation energy, R_0 [J/(molK)] denotes the universal gas constant, T [K] denotes the temperature, and n [-] denotes the reaction index. Eq.(3-5) shows that the heat generation rate of a reaction (q_1) increases exponentially with a linear increase in temperature.

If there is a temperature difference between the reaction system and the environment, heat transfer will of course occur at a rate depending on this temperature difference. The associated heat loss rate (q_2 [W]) is governed by Newton's cooling law as

$$q_2 = hS(T - T_e), \tag{3-6}$$

where h [W/(m^2・K)] denotes the heat transfer coefficient, S [m^2] denotes the area of heat transfer, and T_e [K] denotes the ambient temperature.

Fig.3-30 shows a schematic of the relationship between temperature and the heat generation/loss rate. The value of the T-segment corresponding to the value of temperature at $q_2 = 0$ coincides with the ambient temperature (T_e). As shown in ① and ② in Fig.3-30, if q_1 is equal to q_2 at the point P at which the temperature is T_P, the temperature of the reaction system can return to T_P even if it decreases slightly from T_P because $q_1 > q_2$. Similarly, it can also return to T_P even if it increases slightly from T_P as a result of some of external heating (as shown in ③-⑤) because $q_1 > q_2$. In this case, the temperature of reaction system endlessly increases because $q_1 > q_2$, i.e., ignition occurs. Consequently, T_P is the "ignition temperature." When the ambient temperature increases, the curve of q_2 shifts to right, allowing q_1 to exceed q_2 over a wider temperature range, as shown in Fig.3-30, which in turn allows the reaction system to attain ignition more easily. Even if the value of h decreases, the temperature range of $q_1 > q_2$ expands because the slope of q_2 becomes smaller as h decreases, which in turn allows the reaction system to be ignited more easily.

From Fig.3-30, $q_1 = q_2$ and $dq_1/dT = dq_2/dT$ at point P, corresponding mathematically to

$$QVC^n \exp\left(-\frac{E}{R_0 T}\right) = hS(T - T_e), \tag{3-7}$$

$$\left(\frac{E}{R_0 T^2}\right) QVC^n \exp\left(-\frac{E}{R_0 T}\right) = hS. \tag{3-8}$$

Based on Eqs.(3-7) and (3-8), T_P can be determined as

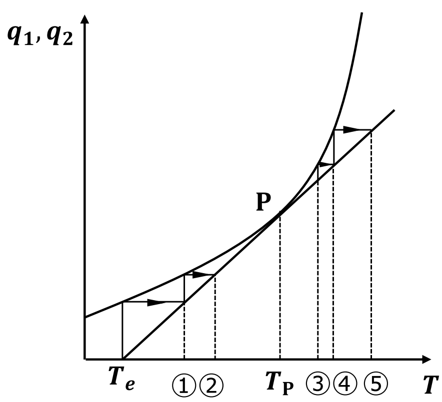

Fig.3-30 Relationship between heat generation rate and heat loss rate[3-52].

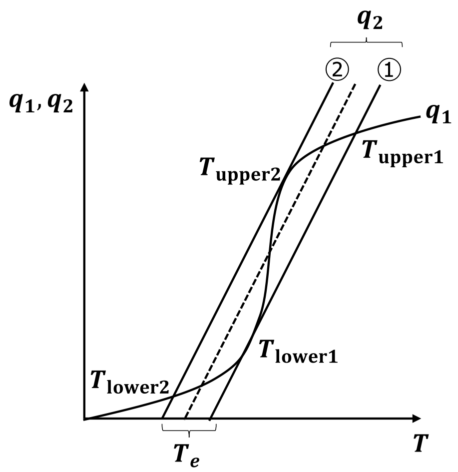

Fig.3-31 Schematic of physical means of double sign of ignition temperature in Eq.(3.5)[3-52].

$$T_P = \frac{E}{2R_0} \pm \frac{E}{2R_0}\sqrt{1 - \frac{4R_0 T_e}{E}}. \tag{3-9}$$

In fact, Fig.3-30 shows only the outlines of q_1 and q_2 over the actual temperature range (~ 2000 K); over a wider temperature range, the curve of q_1 has another inflection point ($= E/2R_0$), as shown in Fig.3-31, because the value of $E/2R_0$ for a general fuel-air mixture is on the order of 10 000 K. Therefore, there are two solutions for temperature that satisfy the equation $q_1 = q_2$ in Eq.(3-9). As is apparent from Fig.3-30, the ignition temperature corresponds to the lower-valued solution of Eq.(3-9). Consequently, the temperature difference between the ignition temperature (T_P) and the ambient temperature (Te) can be expressed by applying a Taylor-expansion to the root term in Eq.(3-9):

$$\Delta T = T_P - T_e \cong \frac{{T_e}^2}{E/R_0}. \tag{3-10}$$

The value of $\Delta T = 5.2$ K can be obtained using Eq.(3-10) by assuming an activation energy of E = 143 kJ/mol[3-58], a universal gas constant of R_0 = 8.314 J/(molK), and an ambient temperature of T_e = 300 K. This means that the reaction system is ignited if its temperature rises by 5.2 K as a result of a self-reaction caused by an ambient temperature of 300 K. However, as the reaction rate of oxidation of an R290/air mixture is nearly zero under most general living situations (~ 40℃), the value of q_1 is generally less than that of q_2. Therefore, the test estimation described above does not mean that the reaction system is ignited when the ambient temperature reaches 305.2 K.

The autoignition temperature (AIT) is generally used to evaluate ignitability. The method for measuring AIT designated in ASTM E659[3-59] involves introducing a test mixture to a 500 cm^3 flask covered with aluminum foil. The flask is then placed in a crucible and gradually heated until the temperature at which ignition is reached can be measured (Fig.3-32). The duration of heating duration is designated to last up to 10 minutes. However, this process produces results that are too severe for actual-scenario-based risk evaluation because the AIT is obtained under an adiabatic and quasi-steady heating condition. For example, the ignition temperature when a flammable mixture flows and contacts a burning cigarette is much greater than the AIT. For cases such as these, the hot-plate ignition test designated in IEC60335-2-40[3-60] (Fig.3-33) is more reasonable than the AIT test. Under the hot-plate test procedure, a 50-mm-diameter planchet composed of stainless-steel is heated to the designated temperature, the test mixture is discharged to the planchet from an upward position, and the occurrence of ignition is determined. However, the ignition criteria for this type of test are influenced by the dimensions of the hot surface[3-61] and as, in particular, the ignition temperature increases as the hot surface area decreases, the ignition temperatures obtained by applying IEC60335-2-40 also produces evaluation conditions that are too severe for addressing the problem of whether an R290/air mixture will be ignited by a burning cigarette. Based on this background, a series of experimental/theoretical studies of the ignition criteria for R290/air mixtures by a hot surface was conducted.

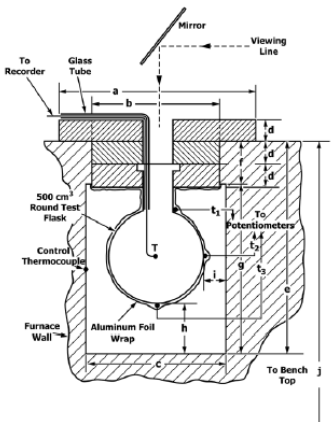

Fig.3-32 Experimental apparatus of autoignition temperature designated by ASTM E659[3-59].

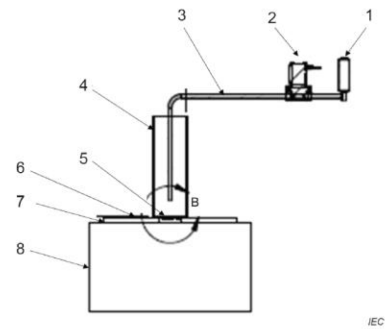

Fig.3-33 Experimental apparatus of hot surface ignition temperature designated by IEC 60335-2-40[3-60].

3.8.2 Model investigation of the criteria for ignition by a hot surface

3.8.2.1 Experimental procedure

A series of laboratory-scale model experiments in which an R290/air mixture was introduced to a loop-shaped combustion chamber and subsequently allowed to flow to a square ceramic heater was conducted. Thus, the experiment focused on the ignition behavior of the stagnation flow of a flammable mixture across a hot surface. A photo of the combustion chamber is shown in Fig.3-34(a); it had a cross-sectional dimension and length of 40 mm^2 and 300 mm, respectively. A propeller was fixed to a brushless motor (Orientalmotor, BMU260-A2) located in the combustion chamber,

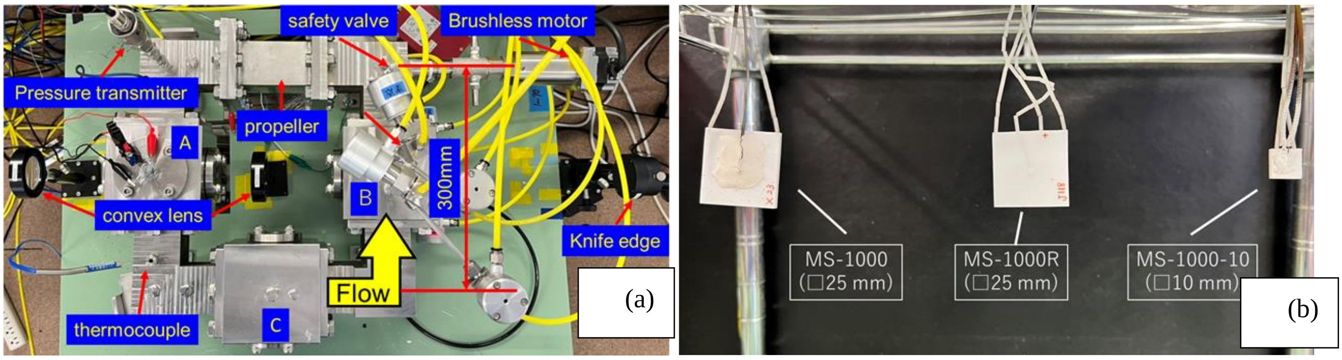

Fig.3-34 Photos of closed-loop-shape combustion chamber and heaters employed for ignition experiment.

and the flow velocity could be controlled by changing the rotational speed of the motor. The flow velocity was measured using a pitot tube (Testo 480) inserted into the chamber, as shown in Fig.3-34(a). Two types of ceramic heater (MS-1000R: 25 mm^2, MR-1000-10: 10 mm^2, Sakaguchi E.H.VOC Corp.) were used as test hot surfaces. The surface temperature of the former was measured using a built-in R-type thermocouple; the temperature of the latter was measured using a sheathed K-type thermocouple (1.0 mm diameter protection tube) pasted to its hot surface using a heatproof adhesive agent. Each test hot surface was hung from the upper side of the chamber with its right-square-side surface facing the flow direction and its power supply cable ran through the connector at the port on the chamber and fixed using epoxy adhesive agent. The energy supplied to each ceramic heater was controlled using an AC power supply (Kikusui, PCR500LE) with a minimum controllable voltage of 0.1 V. A pressure transmitter (KH15-L34, Nagano Keiki Co., Ltd.) was fixed to the chamber and its response was used to determine whether ignition occurred. The visible behavior of ignition was recorded from high-speed images taken via the shadowgraph method using a 75 W Xenon lamp (Kato Koken, Co., Ltd.) as a light source.

Although the focus was on R290/air mixtures as the main test gas, a series of experiments using R290/O_2/N_2/Ar mixtures was also conducted to examine the influence of the thermal properties of the mixture on the ignition criteria. The volumetric concentration of R290 in the mixture was varied over the flammable range (2.1–9.5 vol%); the composition of the inert gas in the R290/O_2/N_2/Ar mixture was varied as Ar:N_2 = 1:2, 1:3, and 1:5. The volumetric concentration of O_2 in the R290/O_2/N_2/Ar mixture was fixed at 21 vol% regardless of the R290 concentration and the N_2 and Ar compositions. The flow velocity was varied over a range of 0.0–4.0 m/s. The heating duration was set to a maximum of 10 min following the guidelines of the AIT test method3-9). If no ignition was observed over this heating

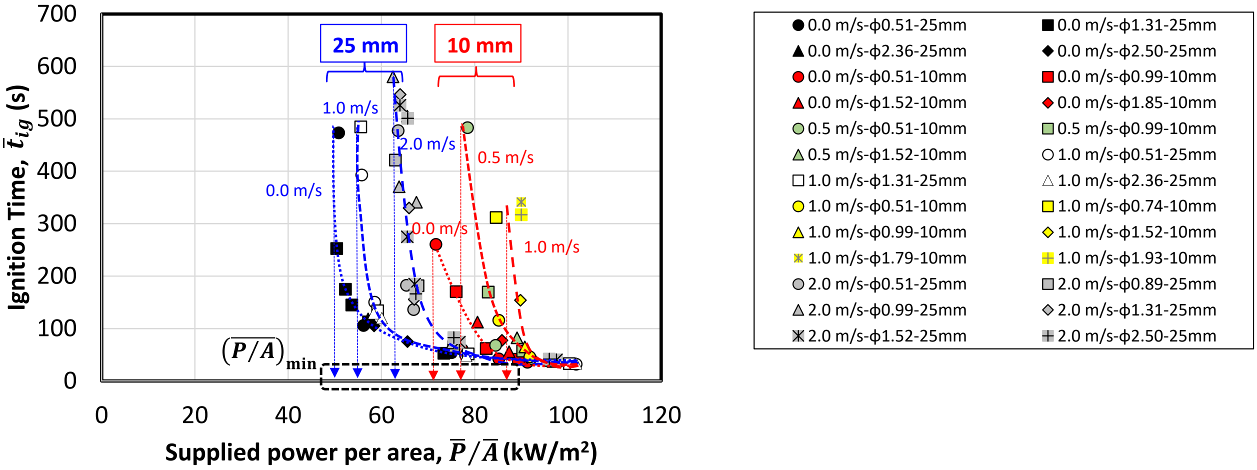

Fig.3-35 Comparison of the relationship between the ignition time and the supplied power per area for R290/air mixtures of various compositions.

duration, the experimental case was determined to be a “no ignition case.” The ignition test was repeated 10 times per combination of flow velocity, equivalence ratio, and input voltage following the method established under ASTM E659[3-59]. If at least one ignition was observed in a set of 10 trials, the combination condition was determined to be an “ignition case.”

3.8.2.2 Experimental results

Fig.3-35 shows the relationship between the time between commencement of heating and ignition ($\bar{t}_{ig}$) of an R290/air mixture and the power input to the hot surface per area ($\bar{P}/\bar{A}$). The symbol $\bar{\ }$ denotes a dimensional variable. Fig.3-36 shows the same relationship for an R290/O_2/N_2/Ar mixture. The following can be deduced from these data:

(1) The dependence of $\bar{t}_{ig}$ on the flow velocity and R290 concentration becomes minimal as $\bar{P}/\bar{A}$ increases to more than approximately 75 kW/m^2.

(2) If $\bar{P}/\bar{A}$ decreases, the value of $\bar{t}_{ig}$ begins to change with the flow velocity; that is, ignition no longer occurs when $\bar{P}/\bar{A}$ is smaller than a critical value. We define this critical power per area for ignition as the critical ignition power, $(\bar{P}/\bar{A})_{\min}$. $(\bar{P}/\bar{A})_{\min}$ begins to increase as the flow velocity increases; in other words, a high amount of power is required to ignite a flammable mixture in cases with increasing flow velocity.

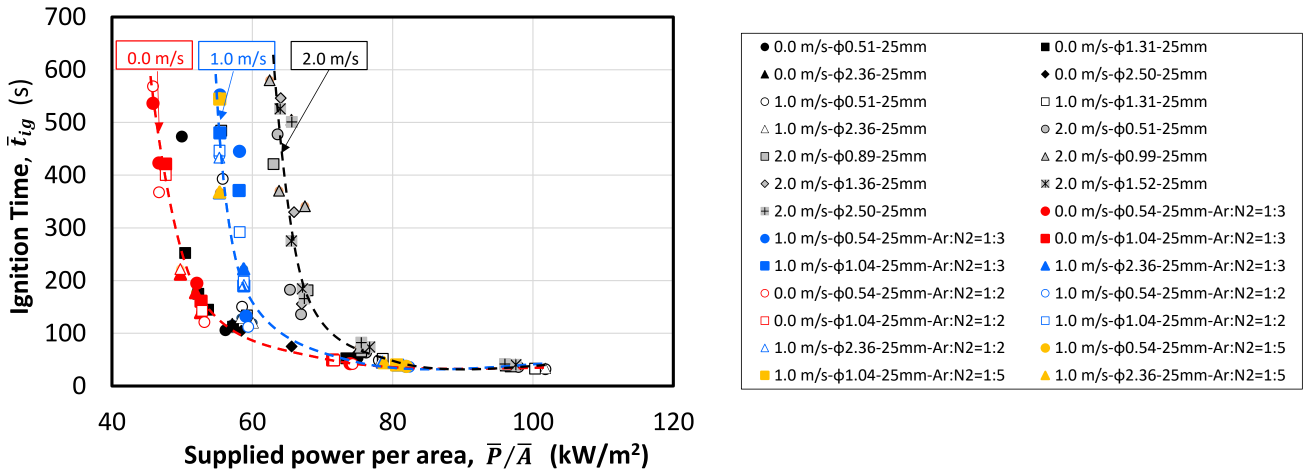

Fig.3-36 Comparison of the relationship between the ignition time and the supplied power per area for R290/O_2/N_2/Ar mixtures of various compositions.

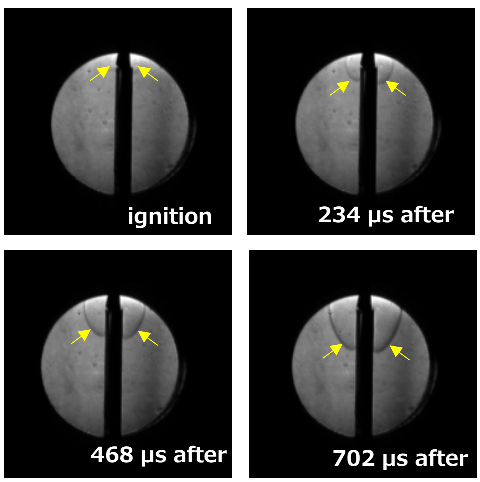

(a) Supplied voltage: 80 V, $\bar{u}_f$ = 0.0 m/s, ϕ = 0.99

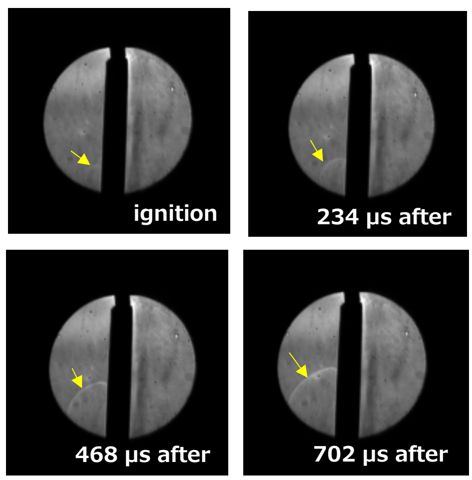

(b) Supplied voltage: 80 V, $\bar{u}_f$ = 1.0 m/s, ϕ = 0.99

Fig.3-37 Visible behavior of ignition and flame propagation for C_3H_8/air mixture with different forced flow velocities. The yellow arrows indicate the flame front.

(3)The R290 concentration in either R290/air or R290/O_2/N_2/Ar mixtures has little effect on the relationship between $\bar{P}/\bar{A}$ and $\bar{t}_{ig}$. The inert gas composition in an R290/O_2/N_2/Ar mixture also has little effect on the relationship.

Fig.3-37 shows a sequence of shadowgraphs taken by a high-speed camera illustrating the R290/air mixture around a hot surface. The following observations can be made:

(1) In the quiescent case, the R290/air mixture was ignited at the top of the hot surface and the resulting flame then propagated downward.

(2) In the case with flow, ignition was observed at the edge of top or bottom at the downstream side of the hot surface.

3.8.2.3 Discussion

To simplify the experimental system, it can be assumed to comprise a one-dimensional stagnation flow colliding with a hot surface, as shown in Fig.3-38. Under this assumption, the length of the hot surface in lateral direction against the flow (y-direction in Fig.3-38) is treated as infinite. In addition, we also assume that the buoyancy can be disregarded relative to the inertial force because neither the flow nor the chemical reaction influence the flow. From these assumptions, a one-dimensional swirl-free potential flow can be assumed, allowing us to express the velocity vector $(\bar{u}, \bar{v})$ as $(-\bar{a}\bar{x}, \bar{a}\bar{y})$, where $\bar{a}$ [s^{-1}] denotes the strain rate of velocity. Under these assumptions, the critical ignition heat flux ($\bar{q}_{w\_c}$) should be expressible as

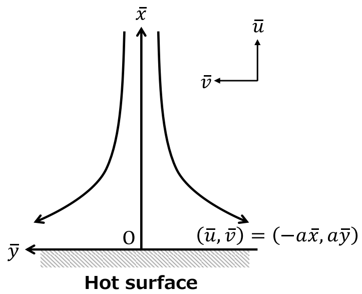

Fig.3-38 Schematic diagram of a stagnation flow impinging to a heated surface assuming one-dimensional potential flow.

$$\bar{q}_{w\_c} = f_1(\bar{\rho}, \bar{c}, \bar{\lambda}, \bar{D}, \Delta\bar{T}, \bar{s}, \bar{a}), \tag{3-11}$$

where $\bar{\rho}$ [kg/m^3] denotes density, $\bar{c}$ [J/(kg・K)] denotes specific heat, $\bar{\lambda}$ [W/(m・K)] denotes thermal conductivity, $\bar{D}$ [m^2/s] denotes the diffusion coefficient, $\Delta\bar{T}$ [K] denotes the temperature increase from the ambient temperature to the adiabatic flame temperature and, $\bar{s}$ denotes burning velocity. The energy balance at the hot surface can be expressed as

$$\bar{q}_w = \frac{\bar{P}}{\bar{A}} - \frac{\bar{C}}{\bar{A}}\frac{d\bar{T}}{d\bar{t}}, \tag{3-12}$$

where $\bar{q}_w$ [W/m^2] denotes the heat flux from the hot surface to the unburned mixture, $\bar{C}$ [J/K] denotes the heat capacitance, and $\bar{t}$ [s] denotes time. As the hot surface temperature can be regarded as constant at just the critical moment of ignition, at which $d\bar{T}/d\bar{t}$ approximately equals zero and $\bar{q}_w \cong \bar{P}/\bar{A}$.

The following non-dimensional relationship can be obtained by applying Buckingham's pi theory to Eq.(3-11):

$$q_{w\_c} = \frac{\bar{q}_{w\_c}}{\bar{\rho}\bar{c}\bar{s}\Delta\bar{T}} = f_2\left(\frac{\bar{\lambda}}{\bar{\rho}\bar{c}\bar{D}}, \frac{\bar{\rho}\bar{c}\bar{s}^2}{\bar{a}\bar{\lambda}}\right), \tag{3-13}$$

The first term on the right-hand side denotes the Lewis number, which is the ratio of the thermal diffusivity to the diffusion coefficient; the second term denotes the Damköhler number (Da), which is the ratio of the specific time of a chemical reaction to that of the residence of the species. In the critical ignition condition between a premixed flammable mixture and a hot surface, it can be assumed that the influence of the Lewis number can be ignored because the species in the flammable mixture are homogeneous and the combustion reaction barely begins just before ignition; correspondingly, the Lewis number in Eq.(3-13) can be considered to be equal to one. Fig.3-39 shows the relationship between $(P/A)_{\min}$, as obtained by substituting $\bar{P}/\bar{A}$ into $\bar{q}_{w\_c}$ in Eq.(3-13), and Da. Note that $\bar{a} = \bar{u}_f/\bar{L}$, where $\bar{u}_f$ denotes the representative velocity of the flow. The black line in Fig.3-39 plots the theoretical solutions of the energy and species conservation equations[3-62), 3-63)]. The experimental data follow a power function in $(P/A)_{\min}$ and Da regardless of the flow velocity, heater size, and inert gases composition. The value of the power exponent obtained from the experimental results is -0.59, which is very close to the value obtained though theoretical analysis (-0.585). If the exponent is assumed to be -0.5, the burning velocity term is eliminated from Eq.(3-13) and it can be assumed that the critical ignition power is not influenced by the burning velocity. As the burning velocity is closely related to the chemical reaction rate, this means that the critical ignition power is independent of the fuel concentration, which coincides with the experimental results. This result can be clearly explained through the realization that the heat transfer process is dominant in the ignition by the hot surface. Table 3-7 lists the methane concentrations that are most ignitable with various ignition sources[3-48),3-64)]. Although the stoichiometric concentration of methane in air is 9.5 vol%, a 4.0–5.0 vol% methane/air mixture is most easy to ignite via electric heating, and the concentration converges on the stoichiometric concentration as the duration of energy supply is reduced. As the chemical reaction rate (in other words, the burning velocity) is fastest at or slightly larger than the stoichiometric composition, a flammable mixture can be easily ignited near its stoichiometric composition when the duration of energy supply is short. On the other hand, as the diffusion coefficient of methane is larger than that of oxygen, methane can reach an ignition source more quickly and, as result, the composition of the flammable mixture near the ignition source shifts toward the fuel-rich side through a phenomenon known as the selective diffusion effect. Therefore, a methane/air mixture can be easily ignited at a fuel-lean composition. Considering that the selective diffusion effect requires a certain amount of time to appear, in an ignition by a hot surface the heat transfer rate is more dominant than the chemical reaction rate. However, as the value of the exponent in the power relation does not exactly equal -0.5, the fuel concentration in fact has little influence on the critical power for ignition. The experimental/theoretical results showing that the critical ignition power increase with the flow velocity correspond to the decrease in Da because the residence time of the chemical species decreases with flow velocity. From the viewpoint of the mechanisms of heat transfer, because the heat loss rate from the hot surface to the ambient flammable mixture increases with flow velocity, a stronger power relation is required to maintain the surface temperature above the ignition temperature.

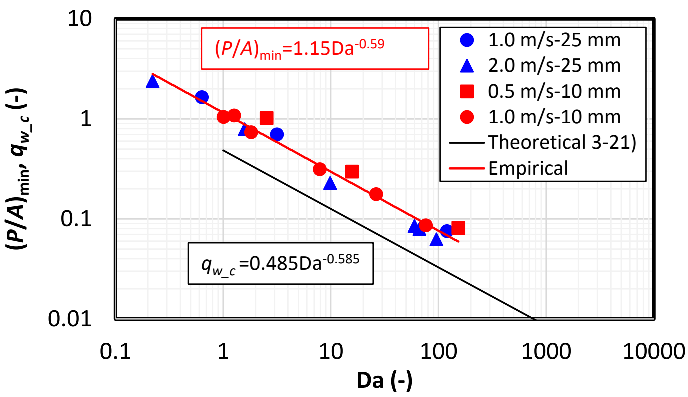

Fig.3-39 Dependence of dimensionless critical power for ignition of R290/air mixture on Damköler number.

Table 3-7 Effects of means of ignition on the most-easily-ignitable concentration for methane.

Means of ignition	**Methane conc. (vol%)**
electrically heated surfaces, large	4.0 – 5.0
heated bomb	5.0
hot gas stream, laminar	5.0
heated plane surfaces, small	5.0 – 6.0
hot quartz tube surface	6.0
sparks from impacts of iron alloys against steel	6.4
wires, electrically heated	6.7
hot jets, pulsed	6.5 – 7.5
sparks from impact of rocks against steel	7.0
hot metal surface, electrically heated	7.0
cannon shots of permissible explosives	8.1
spark, inductive	8.3
spark, capacitive	9.5
flames	9.9

Based on this discussion, the critical ignition power in the heating of a stagnation flow by a hot surface can be evaluated using

$$q_{w\_c} = \frac{\bar{q}_{w\_c}}{\bar{\rho}\bar{c}\bar{s}\Delta\bar{T}} = 1.15\left(\frac{\bar{\rho}\bar{c}\bar{s}^2}{\bar{a}\bar{\lambda}}\right)^{-0.5},$$
$$\therefore \bar{q}_{w\_c} \cong 1.15\sqrt{\bar{\lambda}\bar{\rho}\bar{c}} \cdot \sqrt{\bar{a}} \cdot \Delta\bar{T}. \qquad (3\text{-}14)$$

For example, in cases in which the value of $\bar{P}/\bar{A}$ are known the ignition temperature can be estimated from the thermal properties of the flammable mixture and the strain rate. The term $\sqrt{\bar{\lambda}\bar{\rho}\bar{c}}$ in Eq. 3-14 denotes the thermal inertia, or the degree of difficulty in achieving temperature change against a received heat flux, which depends on the composition of the premixed flammable mixture. As the temperature changes minimally when there is a large thermal inertia, the critical ignition power becomes larger. Because an increase in flow velocity corresponds to an increase in strain rate, the critical ignition power increases with the flow velocity.

3.8.3 A case study of evaluation of ignitability by a hot surface: a burning cigarette

We experimentally investigated whether a R290/air mixture could be ignited by a burning cigarette. Fig.3-40 shows the cubic vessel used as a combustion chamber in these tests. It had a side length of 130 mm and was fabricated from acrylic boards. The top surface of the was covered with aluminum foil that could be ruptured to enable the release of interior pressure generated by combustion. The burning cigarette was inserted into a hole cut into the side of the chamber. Prior to conducting the ignition test, the temperature distribution of the burning cigarette was measured using six K-type thermocouples (0.32 mm diameter). Fig.3-41 shows the time histories of measured temperature, with the distances in the legend denoting the distances between the respective thermocouples and the burning end of the cigarette. Each thermocouple was embedded and then dropped from the cigarette, causing each recorded temperature to suddenly decrease after passing the embedding position.

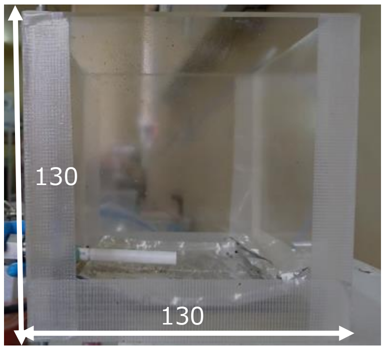

Fig.3-40 Photo of the ignition test by a burnt cigarette to the accumulated R290/air mixture. Unit: mm

Fig.3-42(a) shows a diagram of ignitability illustrating the relationship between $\bar{q}_{w\_c}$ and the size of a hot surface obtained from a series of model experiments using the 4.0 vol% R290/air mixture described in Section 8.2. The red plot shows the estimated values of heat flux from the burning cigarette to the ambient unburned mixture based on Fourier's law. In this estimation, the diameter of the burning cigarette and the temperature of burning are set to 7 mm and 700°C, respectively, based on measurement. The thickness of the temperature boundary layer around the burning cigarette surface is assumed to be 1 mm and the temperature of the unburned mixture is set to 25°C. The plot of the estimated value of heat flux from the burning

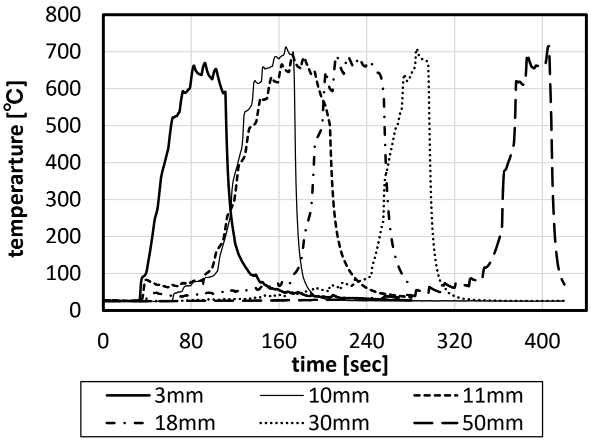

Fig.3-41 Temperatures of burning cigarette.

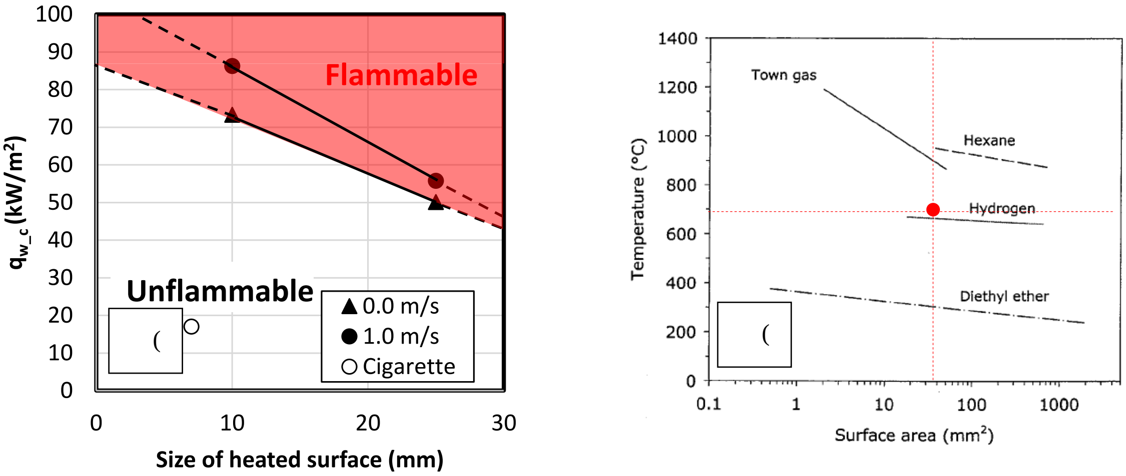

Fig.3-42 Diagram of ignition hazard evaluation by a burning cigarette.

cigarette to the unburned mixture in the non-ignition region in Fig.3-42(a) indicates that the ignitability of an R290/air mixture by a burning cigarette can be ignored under this experimental configuration. Fig.3-42(b) shows the relationship between the critical ignition temperature and the area of the hot surface based on a review by Culter et al[3-65] and compared to our experimental results, which are shown by the red plot. Although the ignition temperature of the R290/air mixture is not shown in Fig.3-42(b), the results suggest that it is difficult to ignite R290/air mixture using a burning cigarette because the critical ignition temperature of the R290/air mixture is estimated to be as large as the city gas used as the hydrocarbon.

3.8.4 A case study of evaluation of ignitability by a hot surface: a hot wire

3.8.4.1 Study Outline

The case examined in this section can be exemplified by a metal wire that has reached a high temperature and is then exposed to a flammable premixed gas as a result of the blowing of an electrical wiring fuse or an overcurrent. In such cases, the ignition mechanism is essentially the same as that in Section 3.8.2 but the risk evaluation index is often determined by factors such as current flow, etc. We obtained data such as the ignition temperature and ignition current of R290/air premixtures experimentally using tungsten wires and the ignition characteristics were considered through comparison with previous studies.

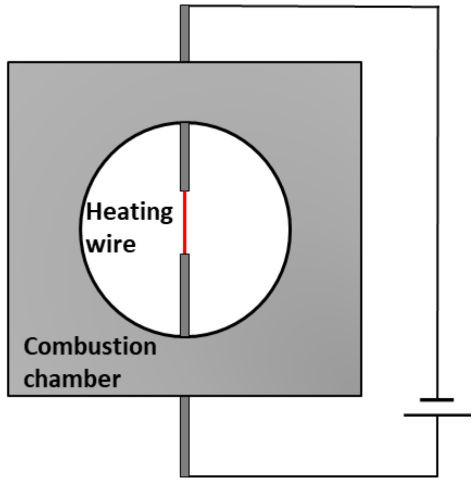

Fig.3-43 Schematic of experimental setup for ignition test to R290/air mixture by a heated tungsten wire.

3.8.4.2 Experimental Procedure and Conditions

Fig. 3-43 shows the experimental setup, in which electrodes were inserted from the top and bottom of an SUS304 cylindrical combustion vessel (inner diameter: 200 mm, height: 200 mm, 6.28 L, pressure resistance: 2 MPa), with both ends of the electrodes connected by a tungsten wire (diameter: 0.5 mm). A tungsten wire was used because tungsten has a high melting point. The target premixtures were R290/air premixtures with equivalence ratios of 0.61, 0.99, 1.25, and 1.52, respectively. Using a regulated DC power supply (PWR401L, Kikusui Denshi Kogyo), measurements were repeated while varying the supply current value to obtain the minimum ignition current value. Ignition behavior was photographed using a high-speed camera (Photron FASTCAM Nova S12 type TDS) with the output of a pressure transducer attached to the top of the combustion vessel used as a trigger signal.

3.8.4.3 Experimental Results and Discussions

Fig.3-44 shows high-speed images of the combustion behavior of a R290/air premixture around the tungsten wire at applied currents of 16.4, 20.0, and 30.0 A, respectively. In this experiment, no ignition was observed at below 16.4 A. The instant at which ignition was recognized was t = 0 ms. At applied currents of 16.4 and 20.0 A, the flame propagated to the outer edge of the orange emission region formed around the hot wire while maintaining a nearly elliptical shape. At 30.0 A, the orange emission band around the tungsten wire increased in size and, in particular, assumed an inverted cone shape, with the flame appearing to spread concentrically through the luminous band. This emission has also been confirmed in nitrogen environments and therefore should not attributed to the combustion of the R290/air premixture but rather to the emission of tungsten fumes caused by the temperature rise of the tungsten wire.

Fig.3-45 shows the relationship between the applied current and the time required for ignition. It is seen that increasing the applied current reduces the time required for ignition. Fig.3-46 shows a photograph of the tungsten wire after the ignition experiment. Areas exposed to R290/air premix have yellow discoloration. It is known that tungsten reacts with oxygen in the air at temperatures above 700°C to form tungsten oxide[3-66], and to verify this we carried out an additional experiment in which tungsten was energized in a nitrogen environment and investigated the relationship between time and temperature, as shown in Fig. 3-47. Under the R290/air premixed gas environment, the temperature of the tungsten wire initially stabilized over time before rising again in a manner that was somewhat discontinuous until just before ignition, after which it maintained a nearly constant temperature. These results suggest that a tungsten oxide developed on the wire; if so, the mass of the wire should have been reduced by the mass of the tungsten in the oxide. In the experiment, the upper and lower ends of the tungsten wire were fixed, so if it is assumed that no axial elongation occurred, the decrease in the mass of the tungsten wire owing to the formation of tungsten oxide led to a decrease in the volume of the wire, in

(a) Input current: 16.4A

(b) Input current: 20.0 A

(c) Input current: 30.0 A

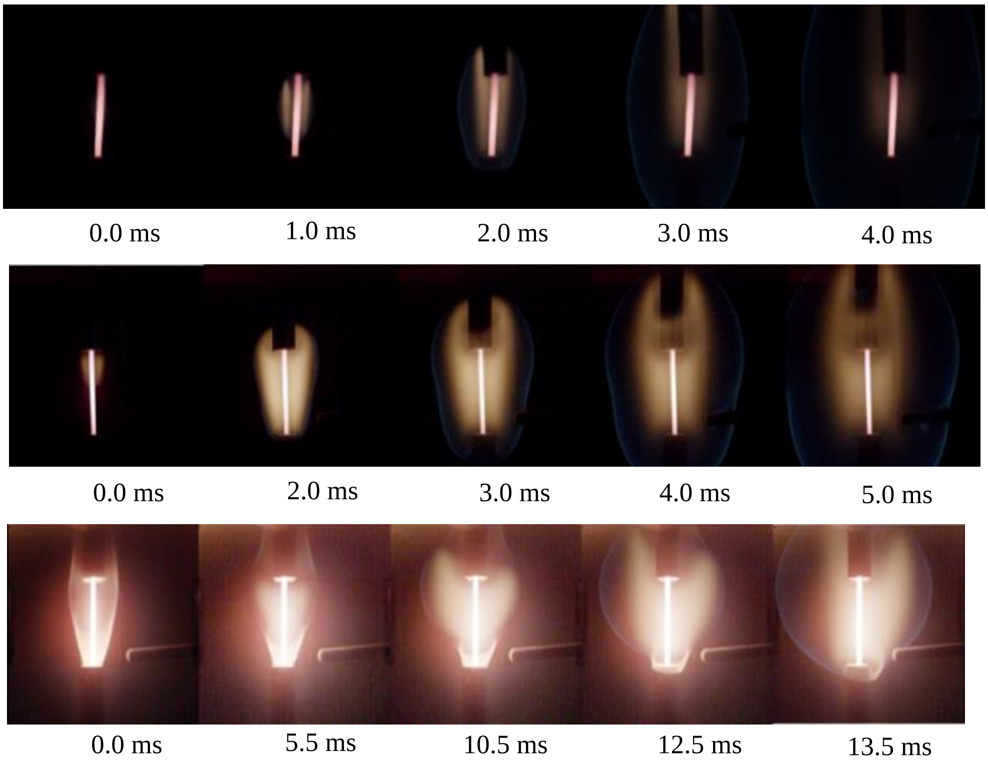

Fig.3-44 Sequence photos of ignition behavior of R290/air mixture ignited by a heated hot wire with various magnitudes of input current.

which case the electrical resistance of the wire would increase. In turn, this would cause the Joule heat to increase as the applied current increases and, considering that the thermal conductivity of the tungsten wire is constant, the temperature gradient in the tungsten would also increase as the applied current increases. Therefore, when the applied current is large, the temperature at the center of the tungsten wire becomes extremely high and expands into a concentric sphere. It is conceivable that, when the applied current is small, the opposite is true and, as the expansion is relatively planar, it is likely that the flame also spreads planarly.

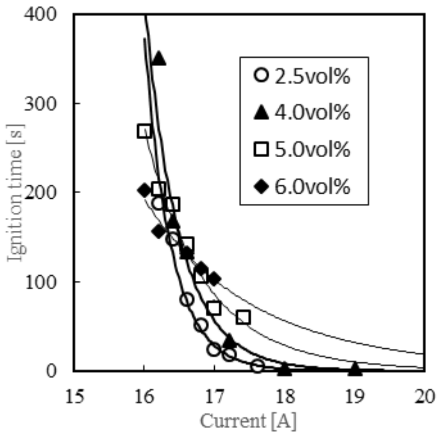

Fig.3-45 Dependences of time since heating to ignition on the input current.

Fig.3-46 Photo of tungsten wire after being used for the ignition test.

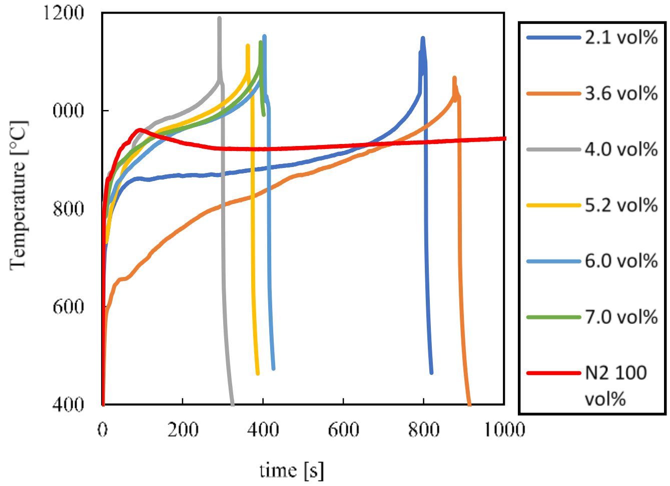

Fig.3-47 Time histories of temperature of tungsten wire in various compositions of R290/air or R290/N_2 mixtures.

3.9 Evaluation of ignitability by laser beam

3.9.1 Outline

Lasers have good light-harvesting capabilities owing to their high monochromaticities and coherence. Therefore, focusing a laser on a gas can cause the electrical breakdown of component gases, generating a plasma column with a high energy density. In this case, ignition is caused by supplying energy to this plasma. When the laser pulse width is longer than nano-seconds, the plasma temperature can nearly equal the gas temperature (i.e., become a thermal equilibrium plasma), in which case ignition acts to balance the heat stored in plasma and the heat lost to the environment. On the other hand, when the pulse duration is shorter than a few pico-seconds, non-thermal-equilibrium plasma often forms. In this case, even though the temperature of the electrons is very high, the gas temperature does not increase very much and ignition is governed by the chain-reaction theory. We experimentally investigated the ignition characteristics of a thermally equilibrated plasma formed by breakdown and evaluated the ignitability of a laser-treated gas by general appliances.

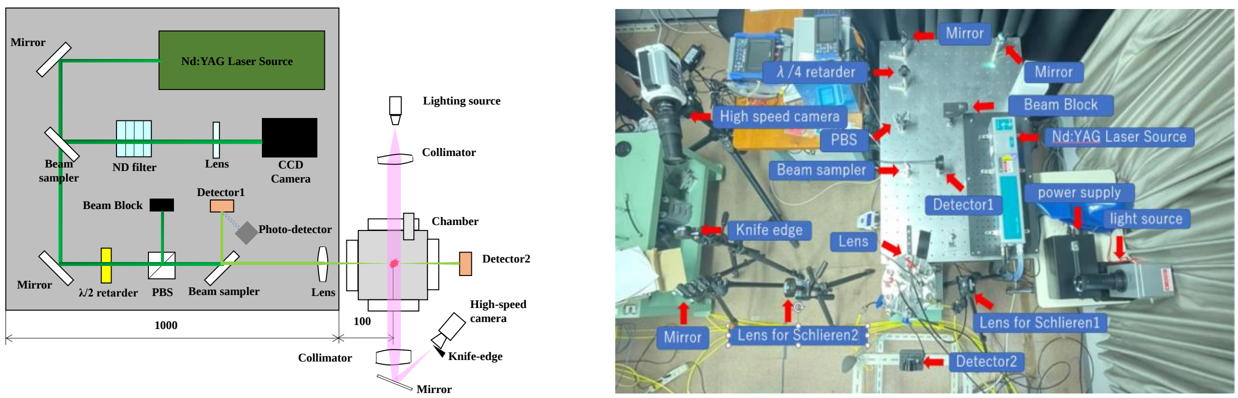

Fig.3-48 Photo and schematic of the experimental setup for ignition experiment by the laser-induced breakdown.

3.9.2 Experimental setup and procedures

Fig.3-48 shows a schematic and photo of the experimental setup. The second harmonic wavelength (532 nm ,100 mJ/pulse) of a Q-switch Nd:YAG laser oscillator (Dawa-200, Beamtech) was used. The direction of the oscillated laser beam was turned by 180° using plane mirrors, the phase difference was given a polarization component using a $\lambda/2$-

wavelength plate, and the S-polarization component was then removed through a polarization beam splitter. By applying this treatment, the power of the laser beam could be arbitrary tuned without changing its spatial and time components by controlling the phase difference[3-67)-3-69)]. The P-polarization component passing through the polarization beam splitter was divided into two beams with equal power. One was fed into a power detector (Newport, 1919-R) and its energy was measured as the incident energy (E_i). The other was fed into a combustion chamber through a focusing lens (focal distance: 100 mm), and a plasma column was generated through electrical breakdown in the chamber. The laser beam passing through the chamber was then fed into a power detector and its energy, referred to as the "transparent energy," was measured (E_{out}). Note that, as the powers of the incident and transparent beam were not exactly equal, the incident energy was corrected based on a comparison of the outputs of E_{in} and E_{out}. The pulse width of the laser beam was measured by feeding the scattered beam into a photodetector (ET-4200) located at an orientation of 45 degrees in front of the beam block. The laser beam diameter was measured by extracting a component of the beam and feeding it into a beam profiler (Ophir, BGP-USB3-SP932U).

The combustion chamber was fabricated from SUS304 stainless steel and had an inner diameter, volume, and pressure resistance of 100 mm, 1.67 L, and 1 MPa, respectively. A propeller fixed at the bottom of the chamber could be arbitrarily controlled using a brushless motor. The pressure of the combustion chamber was measured using a pressure transmitter (KH15, Nagano Keiki Co., Ltd.) fixed to the top of the chamber. The laser beam entered the chamber through a 50-mm-diameter quartz-glass window and passed out of it through a window on the opposite side. Antireflection coating was applied to the quartz-glass windows.

The R290/air mixture was introduced to the combustion chamber using the partial pressure method. After vacuuming out the gases in the chamber, R290 was introduced up to designated pressure and then air was introduced, after which the pressure inside the chamber was maintained at atmospheric pressure. The visible behaviors of dielectric breakdown and ignition were obtained by a high-speed camera via the Schlieren method.

To investigate the characteristics of dielectric breakdown, the thresholds of dielectric breakdown for pure R290, methane, hydrogen, and air were measured. The occurrence of dielectric breakdown was determined from the visible behavior obtained by the high-speed camera and from visible observation. For the ignition experiment, only R290/air mixture was used, with the concentrations varied across the flammable range (2.1–9.5 vol%). To investigate the numerical molecular density, the initial pressure was elevated in five stages ranging from -50 to 50 kPa (gauge pressure). The occurrence of ignition was comprehensively determined from visible behavior obtained using the high-speed camera, direct observation, and the response of the pressure transmitter.

3.9.3 Results and discussions: thresholds of dielectric breakdown

Fig.3-49 shows Schlieren images of gases at the threshold of dielectric breakdown. In these photos, the laser beam entered from the right and departed to the left. The images show the formation of an elliptical plasma in a direction lateral to the laser incidence direction just after the laser enters, following which a surface of density gradients forms around the plasma. This surface is a compressed wave generated by the adiabatic compression caused by the expansion by the dielectric breakdown; the region in which this compressed wave is largest corresponds to the R290. Fig.3-50(a) shows the relationship between the breakdown threshold (E_{i_min}) and the fuel concentration; Fig.3-50(b) plots E_{i_min} against the R290 concentration. As shown in Fig.3-50(a), the threshold of dielectric breakdown for the R290/air mixture began to decrease as the R290 concentration increased. This trend was also

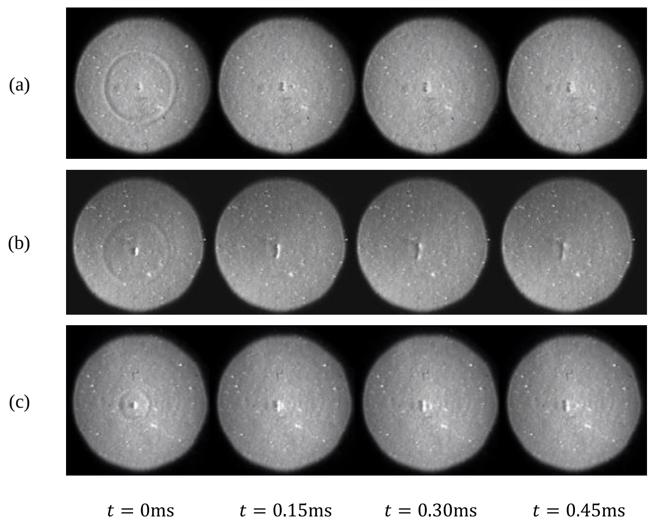

Fig.3-49 Time histories of laser breakdown process.
(a) pure-R290, (b)pure-methane, (c)air

observed for the methane/air mixture. By contrast, for the hydrogen/air mixture the breakdown threshold began to increase with an increase in hydrogen concentration. The breakdown thresholds for the pure material in each fuel were ordered as follows: R290 < CH_4 < Air < H_2. In other words, R290 was the most capable of causing dielectric breakdown.

Dielectric breakdown by laser is caused by the following mechanism. First, electrons are knocked out of their molecules by the multiphoton absorption process caused by the collision of photons with the molecules. These electrons are accelerated by the electric field generated by the laser and enter a high-energy state by receiving thermal energy via an inverse bremsstrahlung process when they collide with neutral and ion particles. The energized electrons then collide with other molecules, causing the number of energized electrons to increase in an avalanche process, which finally produces a plasma[3-70)-3-72)]. Accordingly, the laser breakdown threshold depends on (1) the size of the molecules, (2) the ionization energy of the constituent atoms, and (3) the number of electrons that can be released from the constituent molecules. The size of the R290 molecules and the number of electrons stored in an R290 molecule are larger than the corresponding sizes and numbers for methane, air, and hydrogen, making R290 the best gas for causing dielectric breakdown and ensuring that the region of the compressed wave produced following R290 breakdown and the size of the corresponding plasma column are large. Therefore, the ignitability of R290 by laser breakdown is larger than those for methane or hydrogen.

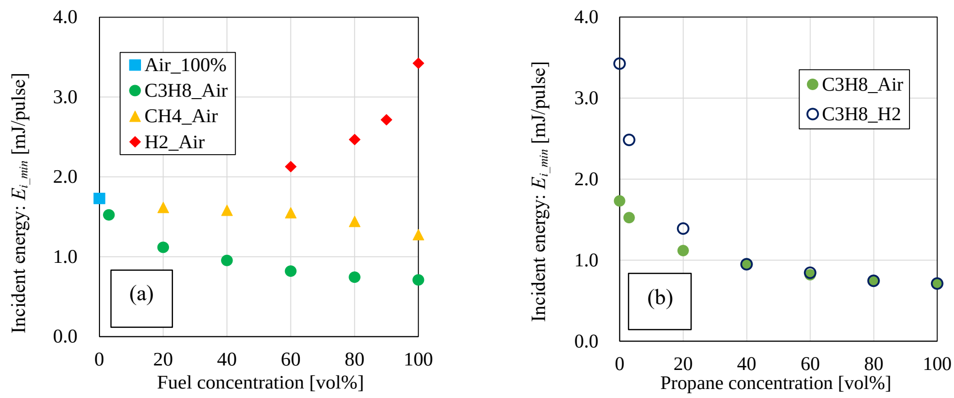

Fig.3-50 Dependence of laser-breakdown threshold on the fuel concentration.

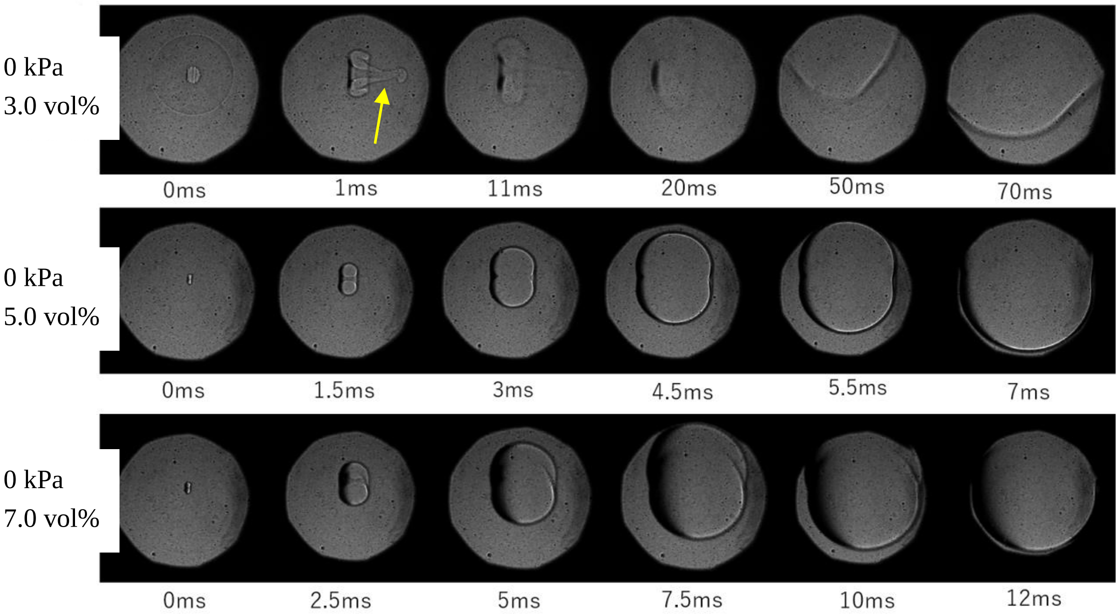

Fig.3-51 Sequence photos of visible ignition behavior of R290/air mixture by laser breakdown in various R290 concentrtaions.

Fig.3-51 shows a series of high-speed Schlieren images of the ignition of R290 with concentrations of 3.0, 5.0, and 7.0 vol% at an initial pressure of 0 kPa (atmospheric pressure). The laser beam enters from the right and exits to the left. The formation of a long and narrow third lobe[3-67] in the incident direction in the 3.0 vol% case (equivalence ratio: 0.74) is shown by the yellow allow in Fig.3-51. The formation of such a third lobe is rarely observed at stoichiometric or fuel-rich compositions. Although the detailed mechanism of third-lobe formation has not been completely clarified, it is believed to be caused by a vortex generated by dielectric laser breakdown. It has been reported that such third lobes grow very fast before finally disappearing[3-67], suggesting that the heat supplied to the unburnt mixture from the plasma generated by dielectric breakdown is fed into the driving force of the third lobe without leading to ignition. Thus, if a third lobe is generated, it is difficult to ignite the unburnt flammable mixture.

Fig.3-52 shows the relationship between the MIE of an R290/air mixture via laser-breakdown and the equivalence ratio. In the fuel-rich region of stoichiometric composition (equivalence ratio: ca.1.0–1.7), the MIE assumes a nearly uniform value regardless of the equivalence ratio; in the fuel-lean region, by contrast, it sensitively increases as the equivalence ratio decreases. Based on this, two observations can be made. First, because the third lobe was generated more easily in the fuel-lean case than in the stoichiometric or fuel-rich cases, additional energy was needed to achieve ignition to make up for the excess heat loss incurred by the formation of the lobe. The second observation is based on the Lewis number effect. In an R290/air mixture, combustion can be strengthened by using a fuel-rich composition and weakened in fuel-lean cases as a result of the Lewis effect, which governs the balance of supplied enthalpy stored in the various species with the thermal diffusivity. In the fuel-rich case, the combustion-weakening effect achieved by increasing the equivalent ratio is canceled by the combustion-strengthening effect caused by the Lewis number effect. In the fuel-lean case, the opposite effect is achieved. Thus, the MIE under laser-breakdown is larger than that under capacitive sparking.

3.10 Summary

This chapter investigated the potential for the ignition of R290 refrigerant installed in home air conditioners, commercial refrigerators, and freezers through contact with igniting agents based on model experiments, theoretical analysis, simulation, and literature survey with the goal of an establishing an ignitability evaluation method suitable for use in a wide variety of leakage scenarios. The following systematic research program was carried out. First, we selected ignition source candidates based on leakage scenarios that can occur in conjunction with R290 refrigerant installed in home air conditioners and commercial refrigeration equipment. For these, we selected and categorized electrical, thermal, and laser ignition sources. We then carried out a detailed evaluation of the ignition sources in each category. The main findings obtained are as follows.

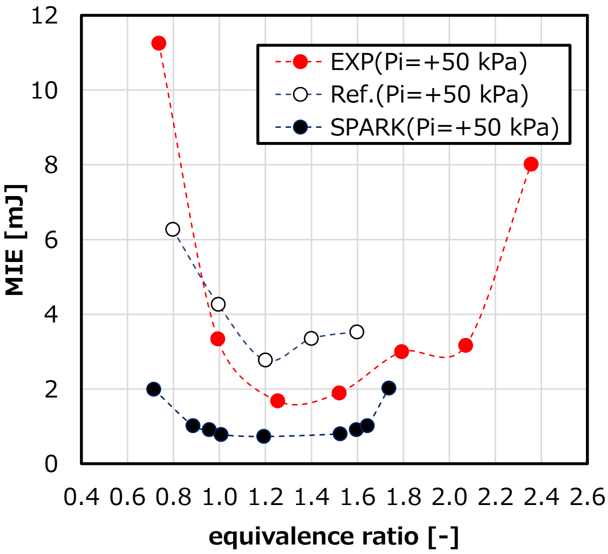

Fig.3-52 Dependence of minimum ignition energies (MIE) in spark discharge and laser breakdown on the equivalence ratio.

A. The following findings were obtained with regard to electrical ignition sources:

(1) Although static electricity cannot be completely excluded as an ignition source, the ignitability resulting from the static electricity generated when undressing can be considered to be small. However, the ignitability from spark discharge occurring between the human body and ground metal cannot be excluded and, to prevent ignition, it is necessary to prevent the R290 concentration in a target space from entering the flammable range in the first place (through, for example, ventilation, etc., as well as the placing of restrictions on the amount of refrigerant loaded).

(2) The arc discharge that occurs when opening/closing contacts can be an ignition source. However, if the discharge time is less than 0.2 ms, the possibility of ignition is extremely small. Furthermore, if the rated power consumption is less

than 160 W, the possibility of ignition is extremely small. Six percent of the energy measured at both ends of a contact is expected to contribute to ignition, and it is possible to evaluate ignitability by comparing this with the generally known minimum ignition energy. However, it should be noted that it has been reported that the ignition probability at the MIE is generally 10^{-3}. In our investigation of a lighting switch, it appears that the light bulb used as the load in this experiment did not ignite because its rated power consumption was less than 160 W.

(3) The arc discharge that occurs when plugging in or unplugging an outlet can ignite depending on the value of the rated power consumption. However, in this case it also seems possible to evaluate ignitability using the same threshold value as that used for contact arcing.

B. The following findings were obtained regarding thermal ignition sources:

(1) To evaluate the ignitability of a hot surface whose surface temperature is controlled by electrical energy, we constructed a model to evaluate the presence or absence of ignition if the input voltage and hot surface area are known. It was also confirmed that reducing the hot surface size reduces the power required for ignition and increases the ignition temperature.

(2) As a case study, we examined the ignitability between R290/air premixture and a lit cigarette. After estimating the heat flux from the hot surface of the tobacco to the unburned R290/air premixture and comparing it with the required power based on the model described in (1), it was determined that no ignition would occur. An experiment in which an ignited cigarette was inserted into a premixed R290/air mixture also failed to produce ignition across multiple trials. These results confirmed the usefulness of the ignitability evaluation method constructed in (1).

(3) We then evaluated ignition by a tungsten wire that has become hot as a result of overcurrent. A minimum ignition current of 16.4 A was obtained for the wire. In the case of metals such as tungsten that undergo surface reactions with oxygen at high temperatures, this reduces the cross-sectional area of the metal, leading to an increase in resistance, which is believed to facilitate a rise in the temperature and lead to ignition.

C. The following findings were obtained regarding laser ignition sources:

(1) Laser breakdown occurs when a laser is focused by a convex lens. The R290 molecule is large and contains a large number of atoms and, therefore, a large number of electrons.

(2) The ignition energy imparted by the laser in our experiment was one order of magnitude larger than the MIE for capacitive discharge.

We believe that the results obtained in this study can be utilized in the evaluation of the ignitability of various equipment that comes into contact with R290/air premixtures.

References

3-1) ISO 817:2014, Refrigerants-Designation and Safety Classification, (2014).

3-2) https://www.jema-net.or.jp/Japanese/ha/reibai/qa.html (Last Accessed: 2022/9/20, in Japanese)

3-3) Hagimoto, Y., Kinoshita, K., Hagiwara, T., Mitsuhashi, N., Shiinoki, J., Sugimoto, R. Possibility of Gas Explosions Caused by the Electric Sparks of Domestic Switches, Journal of JSSE, 20(3), pp.127–132, (1981). (in Japanese)

3-4) Fire and Disaster Management Agency (FDMA)：2021 White Paper on Fire Service，p.64, (2021). (in Japanese)

3-5) Website on Tokyo Fire Department: https://www.tfd.metro.tokyo.lg.jp/camp/2021/202108/data/camp3.pdf (Last Accessed: 2022.9.20, in Japanese)

3-6) Babrauskas, V.: Ignition Handbook, Chapter 14, p.738, Fire Science Publishers, Issaquah, (2003).

3-7) Hall, J.R. Jr., Bukowski, R.W., Gomberg, A.: Analysis of Electrical Fire Investigation in Ten Cities, NBSIR83-2803, (1983)

3-8) Ohtori, S., Watanabe, Y.: Arc Discharge When Contact Opens，IEEJ Transactions, 81(875), pp.1331–1337, (1961). (in Japanese)

3-9) Kinoshita, K.: Study on Fire Caused by Electric Sparks and Heatings, Doctoral Thesis in Kogakuin Univ., p.58, 1997.

3-10) Strehlow, R.A., : Fundamentals of Combustion，TBS，(1968).
3-11) Lewis, B., von Elbe, G.: Combustion, Flames and Explosions of Gases, 2nd Edition, p.334, 1961.
3-12) Hayata. K., Ikegami, T.: Measurement of Arc Discharge Generated at the Gap of Electric Relay with Contacts, https://www.jstage.jst.go.jp/article/jceeek/2005/0/2005_0_138/_pdf/-char/ja (Last Accessed: 2022.2.18, in Japanese)
3-13) Sumire, M. : Influence of Ambient Gases and Pressures on Characteristics of Electric Contact, Report of Research, Nippon Institute of Technology, 46(1), pp.105–108, (2016). (in Japanese)
3-14) https://www.fcl.fujitsu.com/storage/support/relays/relay-technology.pdf (Last Accessed: 2022.2.18, in Japanese)
3-15) Izato, M.: Study on Rectification on High-Speed Rotation of A DC Motor and Brush Wearing, Report of Research, Nippon Institute of Technology, 47(1), pp.154–157, (2017). (in Japanese)
3-16) http://kenshi.air-nifty.com/ks_memorandom/2009/04/post-9deb.html (2019).
3-17) https://blog.alphawave.co.jp/eng/index.php?itemid=1744 (2019).
3-18) http://d.hatena.ne.jp/tomtom1ono/20130128/1359321525 (2019).
3-19) https://rifle.blog.so-net.ne.jp/2014-02-18 (2019).
3-20) http://www.tabogami.tokyo/archives/1284 (2019).
3-21) https://japaneseclass.jp/dictionary/%E9%9B%BB%E6%B0%97%E5%88%86%E8%A7%A3 (2019).
3-22) https://incomprehensiveness.blogspot.com/2014/09/sr-ss18a-nationalpanasonic-ih.html (2019).
3-23) https://insertyourname.blog.so-net.ne.jp/2015-04-09 (2019).
3-24) The Institute of Electrostatics Japan : Handbook on Electrostatics, Ohmsha, p.183, (1998). (in Japanese)
3-25) Technical Recommendations of National Institute of Occupational Safety and Health, JNIOSH-TR-No.42, (2007). (in Japanese)
3-26) Glor, M.: Electrostatic Hazards in Powder Handling, Research Studies Press, Letchworth, (1988).
3-27) Gibson, N.: Electrostatic Hazards in Filter, Filtration and Separation, Filtration and Separation, 16, pp.382–386, (1979).
3-28) Tolson, P.: Assessing the Safety of Electrically Powered Static Eliminators for Use in Flammable Atmosphere, J. Electrostat., 22, pp.57–69, (1981).
3-29) Lövstrand, K.G.: The Ignition Power of Brush Discharges- Experimental Work on the Critical Charge Density, J. Electrostat., 10, pp.161–168, (1981).
3-30) Jones, T.B. and King, J.L.: Powder Handling and Electrostatics: Understanding and Preventing Hazards, Lewis Publishers, New York, (1991).
3-31) Maurer, B.: Discharges due to Electrostatic Charging of Particles in Large Storage Silos, J. Electrostat., 2, pp.189–195, (1979).
3-32) Berta, I., Fodor, I., Clement, G.: Electrostatic Sparks on Charged Insulating Surfaces, J. Electrostat., 10, pp.145–152, (1981).
3-33) British Standard Institution (BSI): BS 5958-Code of Practice for Control of Undesirable Static Electricity, Prat 1-General Consideration, (1991).
3-34) The Institute of Electrostatics Japan : Handbook on Electrostatics, Ohmsha, p.133, p.279, (1998). (in Japanese)
3-35) Tabata, Y.: Prevention of Electrification of Working Wear Using Conductive Fiber, Technical Note of the Research Institute of Industrial Safety, RIIS-TN-71-1, (1971). (in Japanese)
3-36) Kimura, H.: Development of Determination Method for Clothes Using Human Body Voltage, Report on Grant-in-Aid for Scientific Research(C), No.15K00750, (2018). (in Japanese)
3-37) Hirakawa, S.: Prevention Measures for Electrification of Human Body, Journal of JSSE, 30(6), pp.368–372, (1981). (in Japanese)
3-38) Tabata, Y., Masuda, S., Minimum Potential of Charged Insulator to Cause Incendiary Discharges, IEEE Transactions of Industry Applications, IA-20(5), pp.1206–1211, (1984).
3-39) Kettani, M.A. and Hoyaux, M.F.: Plasma Engineering, Butterworth, p.200, (1973)
3-40) Ushio, M. : Arc Discharge and Its Application, Journal of The Iron and Steel Institute of Japan, 73(10), pp.1309–1314, (1987). (in Japanese)
3-41) IEC60079-11: Explosive Atmospheres- Part 11: Equipment Protection by Intrinsic Safety “I”, (2012).
3-42) Uber, C., Franke, S., Bargu, B., Hilbert, M., Berger, F., Uhrlandt, D., Lienesch, F.: Correlation between the Electrical Power of a Slow Contact Break Discharge and the Ignition of an H2/air Mixture, J .Loss. Prev. Proc. Ind., 74, 104620, (2022).
3-43) Shekhar, R., Boeck, L.R., Uber, C., Gerlach, U.: Ignition of a Hydrogen-air Mixture by Low Voltage Electrical Contact Arcs,

Comb. & Flame, 186, pp.236–246, (2017).
3-44) https://faq.fa.omron.co.jp/tech/s/article/faq02246 (Last Accessed: 2022.11.15)
3-45) Tanoue, K., Moriyoshi, Y., Hotta, E.: Non-Thermal Plasma and Ignition, Journal of the Combustion Society of Japan, 55(180), pp.120-126, (2015).
3-46) Ishizuka, S. : Combustion Theory, Morikita Publishing, p.68, (2021). (in Japanese)
3-47) Magison, E.C.: Electrical Instruments in Hazardous Locations, 4th ed., ISA, Research Triangle Park NC (1998).
3-48) Babrauskas, V.: Ignition Handbook, Chapter 4, pp.71–77, Fire Science Publishers, Issaquah, (2003).
3-49) Takizawa, K., Igarashi, N., Takagi, S., Tokuhashi, K., Kondo, S.: Quenching Distance Measurement of Highly to Mildly Flammable Compounds, Fire Saf. J., 71, pp.58–68, (2015).
3-50) Semenov, N.N.: On the Theory of Combustion Processes, Z. Phys. Chem 48, pp.571–582, (1928).
3-51) Kotoyori, T.: Critical Condition of Ignition Proposed by Semenov: Journal of JSSE, 29(3), (1990). (in Japanese)
3-52) Ishizuka, S. : Combustion Theory, Morikita Publishing, pp.14–20, (2021).
3-53) Frank-Kamenetskii, D.A.: Diffusion and Heat Transfer in Chemical Kinetics, 2nd Ed., Prenum Press, (1969).
3-54) Hirano, T. : Combustion Theory, Kaibundo Publishing, pp.100–102, (1986).
3-55) Babrauskas, V.: Ignition Handbook, Chapter 4, pp.46–65, Fire Science Publishers, Issaquah, (2003).
3-56) Willams, F.A.: Combustion Theory, 2nd Ed., Perseus Books Publishing, (1985).
3-57) Law, C.K.: Combustion Physics, Cambridge Press, (2006).
3-58) Bechtold, J.K., Matalon, M: The Dependence of the Markstein Length on Stoichiometry, Comb. and Flame, 127, pp.1906–1913, (2001).
3-59) ASTM E659-15: Standard Test Method for Autoignition Temperature of Chemicals, (2016).
3-60) International Electrotechnical Commission: IEC60335-2-40:2022, Household and Similar Electrical Appliances- Safety-, (2022).
3-61) Kuchta, J.M.: Investigation of Fire and Explosion Accidents in the Chemical, Mining, and Fuel-Related Industries- SA Manual (Bulletin 680), Bureau of Mines, Pittsburgh, (1985).
3-62) Iizuka, H., Kuwana, K., Imamura, T. : Ignition Condition of a Stagnation Premixed Flow Impinging on a Heated Surface, Bulletin of JAFSE, 70(1), pp.1–8, (2020).
3-63) Imamura, T., Uehara, K., Nakata, K., Maruyama, S., Kuwana, K.: Quasi-Steady Characteristics of Flowing Propane/Air Mixture Ignited by a Heated Surface, Fire Safety Journal, 120, 101325, (2021).
3-64) Singer, J.M., Cook, E.B., Grumer, J.: Equivalences and Lower Ignition Limits of Coal Dust and Methane Mixtures (RI 6931), Bureau of Mines, Pittsburgh, (1967).
3-65) Culter, D., Bradley, D.: Frictional Ignition of Dusts and Vapors (IR/L/EC/98/01), HSE, Buxton, UK, (1998).
3-66) Coverdill, A., Delaney, C., Jennrich, A., Krier, H., Glumac, N.G.: Tungsten Combustion in Explosively Initiated W/Zr Mechanical Alloys, Journal of Energetic Materials, 32(3), pp.135-145, (2013).
3-67) Kobayashi, Y.: Research on Ignition of Flammable Gases Generated by Thermal Decomposition of Solid Material in Microgravity, Doctoral Thesis in The University of Tokyo, (2017). (in Japanese)
3-68) Furui, K., Hayashi, J., Okada, T., Nakatsuka, N., Taira, T., Hori, T., Akamatsu, F.: Study on Laser Induced Ignition for Methane-Air Mixtures with Pico-Second Pulse Duration Laser, Transactions of JSME, Series B, pp.1-5, (2012). (in Japanese)
3-69) Hori, T., Akamatsu, F., Shibahara, M., Miyata, D., Katsuki, M.: Laser-Induced Breakdown Analysis Using ND: YAG Laser, Journal of High Temperature Society, 31(1), pp.19-25, (2005). (in Japanese)
3-70) Sunahara, A.: Initial Process of Laser-Plasma Interaction in the Extreme Ultra-Violet Light Source and the Inertial Confinement Fusion Plasmas – Laser Ablation –, Journal of Plasma and Fusion Research, 89(6), pp.416-422, (2013). (in Japanese)
3-71) Takahashi, E., Furutani, H.: Fundamental and Recent Laser Ignition Studies, Journal of the Combustion Society of Japan, 57(180), pp.112-119, (2015). (in Japanese)
3-72) Endo, T.: Introduction to Laser Breakdown, Journal of Plasma and Fusion Research, 94(10), pp.485-495, (2018). (in Japanese)

4. RESULTS OF RESEARCH BY INSTITUTE OF SCIENCE FOR SAFETY AND SUSTAINABILITY AT AIST

4.1 Introduction

The Research Institute of Science for Safety and Sustainability at the National Institute of *Advanced Industrial Science and Technology (*AIST) is responsible for two main research topics: (1) ignitability assessments, in which it is determined whether home appliances can become an ignition source when a flammable refrigerant leaks into the room at flammable concentrations; and (2) real-scale physical hazard assessments of accidental ignition of a refrigerant leakage from an indoor room air conditioner or a reach-in showcase with a built-in refrigerator. Here, we reported the results of ignitability assessments of actual equipment tested under a range of flammable concentrations, as well as diffusion behavior and real-scale physical hazard assessments of indoor room air conditioners and reach-in showcase refrigerators.

4.2 Ignitability assessment of appliances in the flammable concentration range

Propane (R290) is being used as a next-generation refrigerant as it exhibits negligible impact on global-warming. However, because propane is a flammable gas, it is necessary to perform risk assessments to determine the ignition probability of appliances containing this refrigerant in the case of a leakage accident. To observe possible ignitions, we repeatedly and remotely operated appliances in a container filled with a premixed gas mixture of ~5.2% propane–air as this is the concentration at which electrostatic ignition is most likely to occur.

4.2.1 Selection of the assessment appliances and experimental methods

The target appliances for the assessment were determined in consultation with Suwa University of Science (the institute in charge of screening electrical components for their ignition source risk) and the Japan Refrigeration and Air Conditioning Industry Association (who perform risk assessments of A3 refrigerants). In this study, we performed assessment experiments on laser printers, hair dryers, vacuum cleaners, power drills, hot plates, kerosene fan heaters, fans, dehumidifiers, air purifiers, multifunction inkjet printers, hot carpets, and electronic pots.

Excluding the assessment experiment on kerosene fan heaters, all experiments were performed using a container with 1.00 m × 1.00 m × 1.00 m acrylic walls, a steel floor, and a plastic-sheet ceiling. In the case of ignition, part of the appliance might be ejected during an explosion; thus, the acrylic container was placed in the AIST explosion pit. In the experiments with the acrylic container, an air actuator was attached to the appliance inside the container to enable remote operation. The propane and air flows to the container were adjusted accordingly and concentration sensors were used to maintain the propane concentration at ~5.2%. The appliance was remotely operated from outside the explosion pit. Ignitions were observed using a high-speed infrared camera.

4.2.2 Ignitability assessment results

(1) Laser printers

A laser printer model exhibiting high electricity consumption was selected from a group of typical models. 250 two-sided color prints were produced using two laser printers of the same model. No abnormal performance was observed for either printer.

(2) Hair dryers

A hair dryer model with a brushed motor exhibiting high electricity consumption was selected from a group of typical models and four dryers of the same model were tested. Two dryers were set to the hot air setting and power was switched on remotely from outside the container. After 100 cycles of turning the hair dryer ON for 10 s and OFF for 5 s, no ignition was observed for either appliance. For three hair dryers, the air actuator in the container was used to operate the ON–OFF switch of the appliance to activate the hot-air setting. After one or two repetitions, ignition was confirmed. By increasing the duration of the ON–OFF steps, we confirmed that one of the dryers ignited when it was turned off (Fig. 4-2-1). This shows that switching off a hair dryer can provide an ignition source.

a) b) c) d)

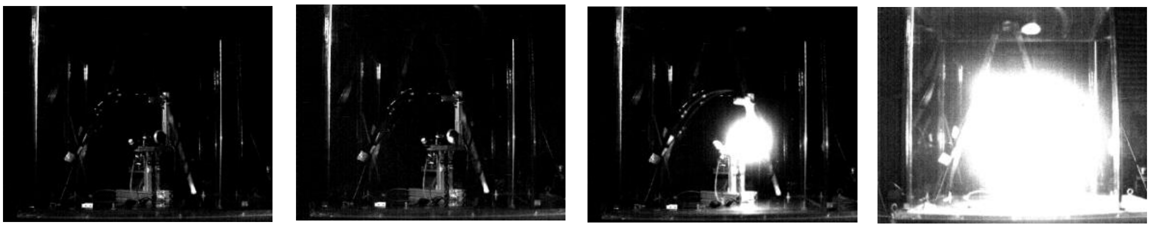

Fig. 4-2-1 Images of the tests with a hair dryer taken by a high-speed near-infrared video camera.

(3) Vacuum cleaners

A vacuum cleaner model exhibiting high electricity consumption was selected from a group of models that use a paper waste bag. Two vacuum cleaners of the same model were tested. One of them emitted smoke after five or six cycles of 7 s at the HIGH setting and 5 s at the OFF setting. Due to the constraints of the experiment, the propane–air mixture was diluted with nitrogen approximately 10 s after the vacuum cleaner started emitting smoke. The flames did not spread to the propane–air mixture and no explosion occurred. The second vacuum cleaner did not exhibit any abnormal behavior, even after 500 cycles (7 s HIGH and 5 s OFF), followed by 5 min at the HIGH setting. The vacuum cleaner that emitted smoke exhibited burned and melted plastic parts from the motor to the exhaust (Fig. 4-2-2).

Fig. 4-2-2 Photographs of the vacuum cleaner that emitted smoke during testing.

(4) Power drills

A power drill model with a brushed motor exhibiting high energy consumption was selected from a group of typical models and experiments were performed on one drill. A cycle of 6 s ON and 4 s OFF was repeated 100 times using the air actuator operated remotely from outside the container under three conditions: high-speed rotation/load, high-speed rotation/no load, and low-speed rotation/no load. No ignition was observed under any conditions.

(5) Hot plates

Hot plate models carrying a bimetal internal temperature control combined with a power switch were selected and one hot plate was tested. When the slide switch was remotely operated with the air actuator, ignition was confirmed after 20 cycles (5 s ON and 5 s OFF).

(6) Kerosene fan heaters

In the assessment of kerosene fan heaters, to assess the ignitability during operation rather than at the time of igniting the heater, the container had to be continuously supplied with air, to burn the kerosene; thus, a greenhouse-style experimental container with a square stainless steel frame of 1.00 m × 1.00 m × 1.00 m with a steel floor and a plastic-sheet ceiling was installed in an outdoor experimental field located at a former mine. To limit the temperature increase within the experimental container, a small heater model was selected and two heaters of the same model were tested.

After confirming that the kerosene fan heater was correctly installed in the container under the aforementioned conditions, it was ignited with an ignition timer. Then, the temperature inside the container started increasing and a pneumatic valve was remotely operated to introduce propane into the container. After rapidly supplying 300 g of propane, or after supplying 150 g of propane at a much lower rate, ignition and tearing of the plastic were observed.

Fig. 4-2-3 shows still images taken at 100 ms intervals from the video recorded by the high-speed camera when 300 g of propane was rapidly supplied. The fire during ignition and tearing of the plastic that occurred with propane discharge (Fig. 4-2-3b) are difficult to visually confirm; thus, ignition may have occurred at the low propane concentration. We confirmed that after ignition and tearing of the plastic, an emission diffusion fire was observed at the propane discharge outlet (Fig. 4-2-3c).

a) b) c) d)

Fig. 4-2-3 Images showing a kerosene fan heater igniting propane.

(7) Fans

A common standing fan with a brushed motor was selected, equipped with a radio switch to set the wind speed and a rotary switch timer. The ON and OFF actions were repeated by activating the rotary switch and an external power source with two fans, but no ignition was observed. During ON and OFF switching using the radio, one of the two fans ignited with the first OFF action while the other fan ignited with the fourth OFF action. This indicates that the brushed motor of the fan was not the ignition source. The different ignition behaviors between the rotary and radio switches were attributed to the better seal of the rotary switch.

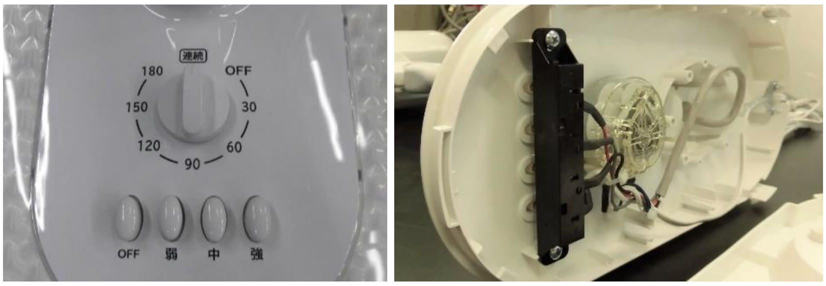

Fig. 4-2-4 Remotely controlled switches of the electric fan.

(8) Air purifiers

An air purifier that captures dust by passing air through a filter was selected. This model has a well-sealed tactile switch, which has become popular recently. Two such air purifiers were tested by remotely operating the power and wind volume switches. The fan of the appliance was switched between OFF and ON (maximum power) 100 times, but no ignition was observed. Even after 10 min of continuous operation, no ignition occurred.

(9) Dehumidifiers

Two dehumidifier models were selected: a desiccant and a compressor type. Both were equipped with a fan for air circulation and a tactile switch for operation. In all models, the tests were performed in the clothes-drying mode where the electric power consumption is the highest. With the desiccant-type dehumidifier, we remotely operated the power switch and repeated the ON and OFF actions 100 times. With the compressor-type dehumidifier, to avoid 3 min of fan operation when the power switch is turned on, we repeated the ON and OFF operations 100 times by switching the external power source. With both models, we repeated the ON–OFF cycle 100 times along with 10 min of continuous operation, but no ignition occurred.

(10) Multifunction inkjet printers

A color printer that can print on A4-size paper was selected as the model multifunction inkjet printer. We repeated the ON and OFF operations 100 times for two identical printers using the switch on the front of the device and produced 200 two-sided color prints, but no ignition occurred.

(11) Hot carpets

Two 60 cm × 60 cm hot carpets of the same model were selected, stored in a normal condition in the experimental container. The ON–OFF cycle was repeated 100 times by activating a sliding power switch, but no ignition occurred. Due to the shape of the switch, it is likely that the premixed gas did not reach the electrical contact.

(12) Electronic pots

An electronic pot model with a magnetic power plug was selected. We repeatedly plugged and unplugged the power connection in two identical pots. After several cycles, both pots ignited during unplugging.

4.2.3 Summary of the ignitability assessments and plan

Ignition was observed with hair dryers, vacuum cleaners, hot plates, kerosene fan heaters, fans, and electronic pots. Even though these experimental results are based on a single model, the ignition probability in the risk assessment should be one when these appliances are operated in the range of flammable concentrations of a refrigerant. All appliances other than the kerosene fan heaters were ignited by an electric spark during the OFF operation of the switch or plug.

No ignition was observed with the other appliances. In the assessment of appliances with a limited number of models and experimental repetitions, the ignition probability in the risk assessment without an explosion-proof structure cannot be zero. However, if we can confirm that ignition does not occur for a certain number of models and experimental trials, the ignition probability in the risk assessment can be reduced with an increasing number of repetitions.

4.3 Diffusion behavior and real-scale physical hazard assessment of indoor air conditioner units

The combustion effect of an accidental leakage was assessed to determine the risk probability in a risk assessment of propane (R290 refrigerant) leakage from an indoor room air conditioner unit. Based on practical usage, we installed an air conditioner unit in a simulation room of realistic size. We measured the leakage diffusion behavior under several possible leakage conditions and assessed the combustion effect in an ignition experiment for conditions with a high ignition risk.

4.3.1 Refrigerant leakage accident and leakage conditions

Room air conditioners that use flammable natural refrigerants are not commercially available nowadays in Japan, though reports of leakage accidents are rare. Thus, we determined the leakage conditions of indoor equipment that use flammable refrigerants as the reference. A risk assessment report of multi-split air conditioning systems for buildings that use flammable refrigerants[4-1)] describes leakage locations, location shapes, and equivalent diameter for leakage accidents reported for such systems that use the R32 refrigerant. Among the reported accidents, the largest equivalent diameter of the corroded area of a heat-transfer tube of the indoor heat exchanger was 0.174 mm. The leakage rate of a liquid at 63 °C is 67 g min^{-1}, which is similar to the discharge rate used to assess the risk of rapid leakage (4 min at full discharge). The reported leakage locations are mostly the heat transfer tube of the heat exchanger and electronic expansion valve. Thus, in this study of the leakage conditions of an indoor air conditioner unit, we mostly used the condition of releasing the entire fill volume in 4 min. In the case of discharging the gas over different durations, we evaluated the situation where gas is discharged by its own pressure at 30 °C from an opening with a diameter equivalent to a break in the pipe. As leakage locations, we used the center of the heat exchanger, near the seam of the heat exchanger and connecting pipes, and joints in the refrigerant pipe inside the unit. Experiments performed in 2016 by our team showed that when there is no direct discharge of refrigerant into an indoor space through pin holes and similar defects, the gas jet promotes the circulation of indoor air and a flammable concentration is not reached.

4.3.2 Diffusion behavior experiments

A wooden simulation room with dimensions of 2.7 m × 5.4 m and a height of 2.4 m (large simulation room) was installed in the large indoor space of the explosion experimental facilities for pipes etc. at the National Institute of Occupational Safety and Health, Japan. A smaller simulation room was constructed by installing indoor walls of 2.7 m × 2.7 m with a height of 2.4 m, to perform experiments involving two room sizes. A multi-split room air conditioner was installed in the large simulation room, with its base being 2.00 m from the floor at the center of the short wall. This is a typical size of a room in which room air conditioners are installed. The fan mechanism was one typically used in Japan. We installed a total of two gaps (800 mm × 4 mm each) under the door in the small simulation room. The gap was covered with aluminum tape when it was not used it. In this manner, we examined the concentration distribution over time.

Catalytic combustion sensors were used to measure propane concentration. A total of 28 sensors were installed; fourteen sensors with a measurement range of 0–6.6 vol% were installed right below the air conditioner unit, on the floor, and 25 cm above the floor. Fourteen sensors with a measurement range of 0–2.2 vol% were installed in other locations.

To determine the amount of discharged propane, we used the maximum fillable mass (m_{max}) obtained by Equation (4-1), as published by Kataoka in IEC60335-2-40:2018,[4-2] which assumes no safety measure, e.g., no airflow. The m_{max} assuming sufficient airflow was calculated using Equation (4-2) as this was anticipated for future use. In the present experiment, we used 2.4 m as the room height (h), where 2.2 m is the upper limit. In the small simulation room, m_{max} was 230 and 340 g with and without airflow, respectively, while in the large simulation room it was 330 and 680 g with and without airflow, respectively.

$$m_{max} = 2.5 \times LFL^{5/4} \times A^{1/2} \times h_0 \qquad (4\text{-}1)$$

$$m_{max} = 0.5 \times LFL \times A \times h \qquad (4\text{-}2)$$

where LFL is the lower flammability limit, A is the floor area, and h_0 is the height of the base of the equipment.

To fully discharge m_{max} in 4 min, a 20-kg cylinder of propane was placed in a water bath at 30 °C and the flow rate of the gas was adjusted using a needle valve. The gas was discharged through a pipe in the air conditioner unit and the flow rate was measured using a mass flow meter. When simulating the leakage of the compressed liquid, we used propane from a 5-kg cylinder placed in a constant-temperature water bath at 30 °C and the entire volume (m_{max}) was discharged. The discharge behavior was remotely controlled to ensure operator safety by monitoring the concentration sensors and a video camera from a room outside of the large simulation room.

4.3.3 Diffusion behavior results

The concentration distribution was measured over time while changing conditions, such as the size of the indoor space, discharge volume (assumed fill volume), discharge locations, discharge rate, condition of air conditioner fan, and under-door gap, and the combustion behavior in the ignition experiments was examined.

After discharge in all experiments (when the m_{max} calculated using Equation 4-1 was discharged), the propane concentration did not reach the flammable range. In all experiments the room air was circulated using the air conditioner fan and no flammable concentrations were measured during fan operation. Therefore, the flammable range was only observed after discharge when the allowable volume was adjusted under the assumption of using the fan but without using the fan.

Small simulation room results

During the experiments in the small simulation room, different m_{max}, discharge locations, discharge methods, air conditioner fan conditions, and under-door gap were tested and the propane concentration distribution was measured over time. The ratio of the m_{max} values calculated using Equations 4-1 and 4-2 was small (approximately 1.5); thus, even when 340 g was discharged without the fan in different discharge positions, the flammable concentration range was barely reached. In the case of 4-min full discharge of gas at the center of the heat exchanger (Fig. 4-2 a), flammable concentrations were measured for approximately 10 min near the floor. In the case of discharge of the gas under its own pressure through a 1.5-mm pin hole at the joint between the heat exchanger and pipes (Fig. 4-2c), flammable concentrations were measured immediately below the air conditioner during discharge and on the floor for approximately 5 min after the start of discharge.

Large simulation room results

During the experiments in the large simulation room, different m_{max}, discharge methods, discharge positions, discharge rates, air conditioner fan conditions, and under-door gaps were tested and the propane concentration distribution was measured over time. In the experiment discharging m_{max} calculated using Equation 4-1, flammable concentrations of propane were measured only at the bottom of the indoor unit during discharge, but not after the end of discharge (Fig. 4-3-1b).

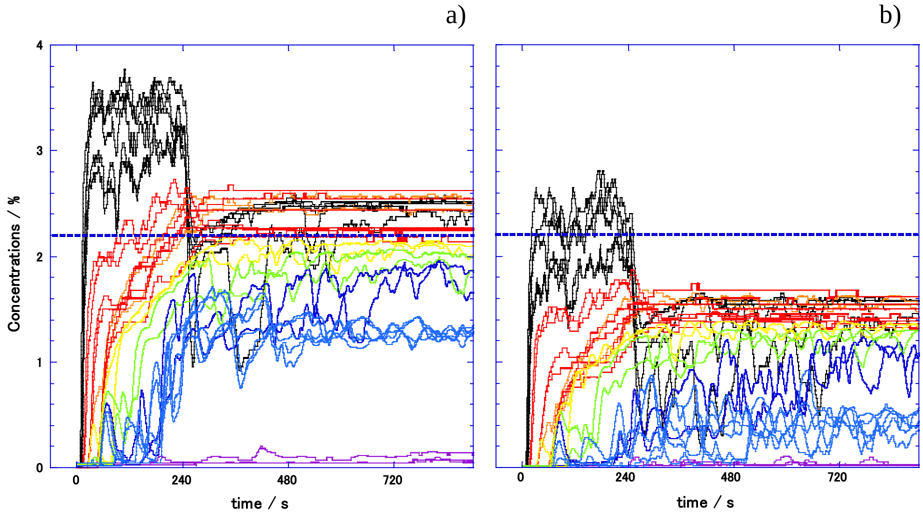

Fig. 4-3-1 Time profile of propane concentrations in the large simulation room: no airflow, no under-door gap, discharge at the center of the heat exchanger, 4-min gas discharge.
a) 680 g and b) 330 g of propane discharged.

Large simulation room/Eq. 4-1 m_{max}: Effect of discharge location and under-door gap

In the case of a 4-min full discharge, flammable concentrations of propane were measured after the end of discharge only when the point of discharge was the center of the heat exchanger and not the heat exchanger–pipe joint or pipe joints of the air conditioner unit. The duration of the flammable concentrations measured without an under-door gap was approximately 80 min. This duration decreased to ~55 min when an 800 mm × 4 mm gap was introduced under the door, whereas the duration was shortened to ~40 min when two such gaps were added. However, no change in the diffusion behavior was observed during or immediately after discharge. The concentration of the propane–air mixture discharged from the gap under the door was measured to be ~2–3% and its volume was approximately the same as that of 100% propane discharged near the unit.

Large simulation room/Eq. 4-1 m_{max}: Effect of discharge method and time

With the discharge point set at the center of the heat exchanger, the duration of the uniform full discharge was set to 3, 4, 5, 6, 8, 12, and 16 min. No notable difference was observed in the propane diffusion behavior in the room when it was fully discharged over 4 and 5 min. Regarding the other durations, the propane concentrations during and after the discharge were low, whereas the time required for the flammable concentration to disappear was short. For discharge over 12 min, flammable concentrations were not observed after the end of discharge. At the same discharge location, when the gas was rapidly discharged at 30 °C under its own pressure, the propane concentration during discharge was high but after discharge, a flammable concentration was not observed. Such a finding was attributed to the circulation of the room's air being promoted by the jet of propane gas. These results confirm that the 4-min full discharge, which is widely used in leakage risk assessments of refrigerants, is the worst condition as it maximizes the size of the space–time product of the flammable concentration of gas.

Large simulation room/Eq. 4-1 m_{max}: Effect of airflow

Regarding the 4-min full discharge of m_{max} (calculated using Equation 4-1) from the center of the heat exchanger and the air conditioner fan in "low/horizontal" continuous operation, propane was diffused into the room, but a flammable concentration was not measured at any point during discharge. Fig. 4-3-2 shows the difference in propane diffusion behavior with or without operating the fan, when 680 g of propane was fully discharged over 4 min. In addition, Fig. 4-3-3 shows the propane concentration diffusion behavior measured with the air conditioner fan at the "highest/downward" setting at 0.5, 1, and 2 min after the start of the 4-min discharge. The gas concentration dropped below the flammable range underneath the unit after 10–20 s of fan operation.

a) b)

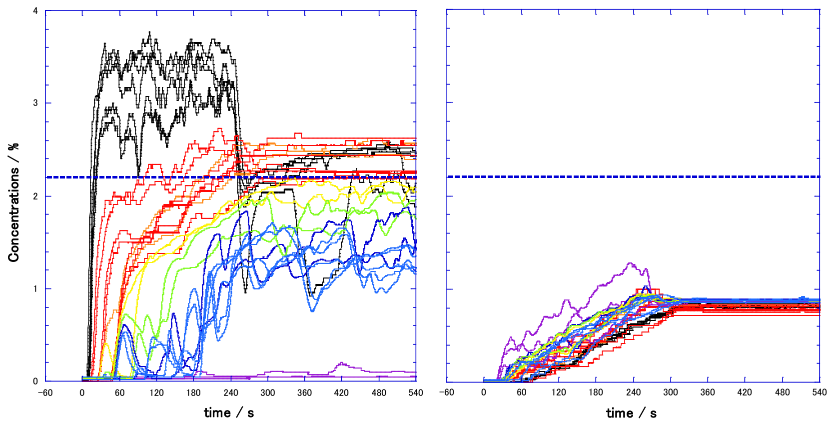

Fig. 4-3-2 Time profile of propane concentrations in the large room:
no under-door slit, discharge at the center of the heat exchanger, 680 g propane gas discharged over 4 min.
a) No airflow and b) continuous airflow at the low/horizontal setting.

a) b) c)

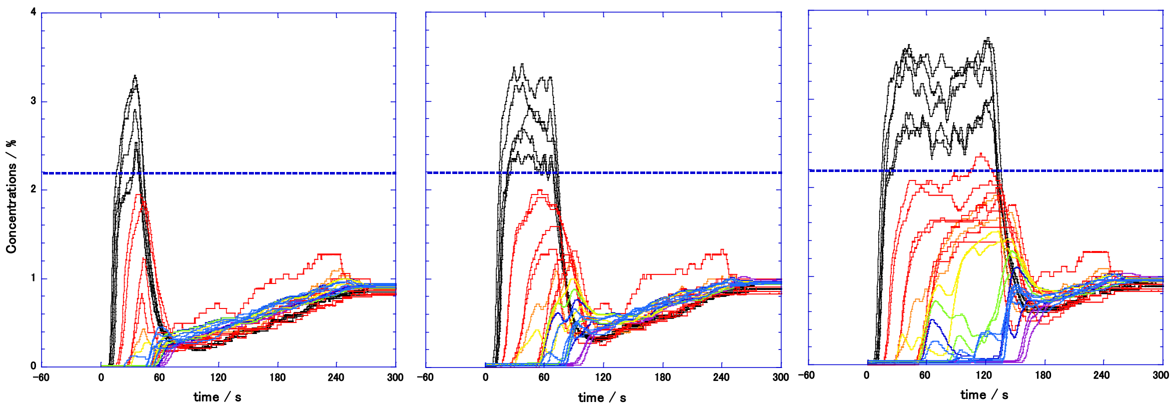

Fig. 4-3-3 Time profile of propane concentrations in the large room:
no under-door slit, discharge at the center of the heat exchanger, 680 g propane gas discharged over 4 min.
Maximum airflow started a) 0.5 min, b) 1 min, and c) 2 min after the end of discharge.

4.3.4 Real-scale physical hazard assessment experiments

A steel simulation room with dimensions of 2.7 m × 5.4 m and a height of 2.4 m was installed at a field test site at the tailings dump of the former Taiheta Mine of Hitachi Cement. Following the same method as that used for the diffusion-behavior measurements, propane was discharged and then intentionally ignited to assess the combustion effect. Since such an effect was observed in a space similar to that of an actual residential room, we installed sliding glass windows with a width of 180 cm at the center of the short wall opposite to that on which the air conditioner unit was installed in the large simulation room. To ignite the gas, we used an electric spark formed by a 100 V AC discharge from a neon transformer powered by a 15 kV generator.

To assess the effect of a leakage accident and combustion on the room, a total of four radiant heat sensors were installed: two indoors and two outdoors. A strain-type pressure sensor was installed in the room, whereas three blast measurement microphones were installed outdoors by the glass window and two on the backside. Three thermocouples were installed: at the top of the air conditioner unit, and the top and bottom of the wall on which the unit was installed. To observe the spread of flames within the room, an acrylic window with a thickness of 50 mm was built at the center of the 5.4-m wall and a visible-range monochromic high-speed camera was installed just outside. To confirm ignition, another high-speed infrared camera was installed outside at 40 m from the glass sliding window. To observe damage to the glass window, color visible-range high-speed cameras were installed outside the room. One camera was placed 40 m on the line extending from the wall with the glass window and another 40 m away at a 45° angle.

4.3.5 Real-scale physical hazard assessment results

Immediately after fully discharging 330 g of propane (mass calculated with Equation 4-1) over 4 min without operating the air conditioner fan, ignition was not observed, even 2 cm above the floor at the center of the simulation room. However, under the same conditions, ignition was triggered 3.5 min into discharge at 150 cm above the floor and directly below the air conditioning unit. When operating the fan of the unit horizontally at a low power, at an m_{max} of 625 g (calculated with Equation 4-2) fully discharged over 4 min, no ignition was observed immediately after discharge (2 cm above the floor).

Regarding the case where ignition was observed, no damage occurred to the glass sliding windows opposite the unit or to the curtains installed on the side wall, whereas the entire air conditioner unit burned. The calculated maximum room pressure was 2.3 kPa and the maximum radiant heat was 7.5 kW m^{-2}. Fig. 4-3-1 shows images from the camera at 200 ms intervals immediately after ignition.

a) b) c) d)

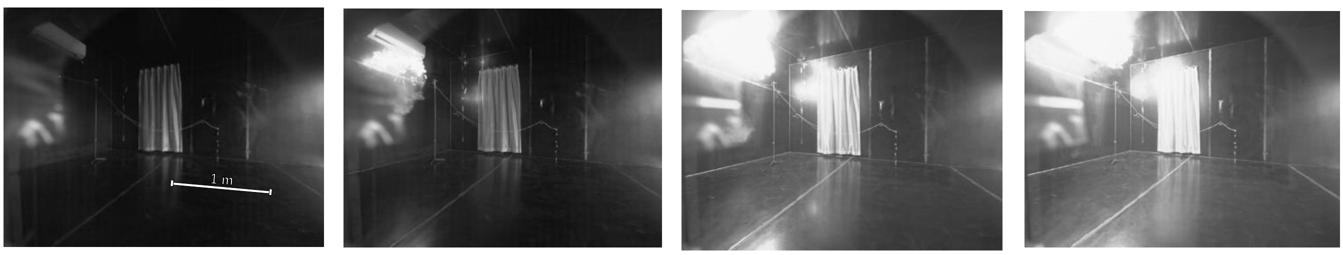

Fig. 4-3-4 Fire observed after ignition and 30 s before blowout (200 ms intervals).

When ignition was attempted immediately after full discharge (m_{max} = 625 g calculated with Equation 4-2) without operating the fan of the unit, ignition was confirmed 2 cm above the floor at the center of the simulation room. The glass and frame of the glass sliding window facing the air conditioner unit were broken and blown outward. The maximum indoor pressure was 5.6 kPa and the maximum radiant heat was 6.1 kW m^{-2}. A maximum blast pressure of 36 Pa was calculated 10 m outside the sliding window. Fig. 4-3-2 shows images from the camera at 200 ms intervals immediately after ignition.

a) b) c) d)

Fig. 4-3-5 Fire observed after ignition and 30 s before blowout (200 ms intervals).

4.3.6 Summary of the real-scale physical hazard assessment

When m_{max} (calculated using Equation 4-1) was released, no ignition occurred. Even when m_{max} adjusted for airflow (from Equation 4-2) was released in a room with few obstacles, no ignition occurred when the air conditioner fan was in operation. In the case of m_{max} discharge with no airflow, if ignition occurs during leakage, there is the possibility that the air conditioner body (made of resin) can combust and spread the fire. In the case of m_{max} corrected for airflow discharge with no airflow, when ignition occurs after discharge is complete, the combustion conditions are strong enough to break the glass windows. The braking of the windows prevents the room pressure from reaching high values, thereby limiting the impact of the combustion on people in the room.

4.4 Diffusion behavior and real-scale physical hazard assessment of a reach-in showcases

The combustion effect of the accidental ignition of a leakage of propane (R290 refrigerant) was assessed from a reach-in showcase with a built-in refrigerator to determine the risk of a leakage accident. Assuming actual usage conditions, we installed a reach-in showcase in a real-size simulation room, measured the leakage diffusion behavior under various possible leakage conditions, and performed an ignition experiment for high-risk ignition conditions.

4.4.1 Diffusion behavior experiments

A wooden simulation room with dimensions of 4.9 m × 4.9 m with a height of 2.8 m was installed in the large indoor space of the explosion experiment facilities at the National Institute of Occupational Safety and Health, Japan. A double-door reach-in showcase with a built-in refrigerator (width of 120 cm, depth of 85 cm, and height of 200 cm) was installed at the center of a wall of the simulation room. Mechanical parts such as compressors were installed at the bottom of the showcase.

It was assumed that the entire volume of propane is discharged as the refrigerant diffuses in the showcase, and that the door would be opened after a constant concentration of propane is reached. This condition assumes the worst case where the propane concentration in the room would be the highest for the same leakage volume. The propane m_{max} values were 100, 500, and 1,000 g. The showcase doors were remotely operated from outside the simulation room using an air actuator installed on the double doors, which open simultaneously at an angle of 60° after 3 s.

A gas thermal conduction propane sensor with a measurement range of 0–100% and catalytic combustion sensors with measurement ranges of 0–2.2 and 0–6.6 vol% were used. A total of 14 thermal conduction gas sensors were installed: two inside the showcase where high concentrations of propane were anticipated, five at 5 cm above the floor near the showcase, and seven at positions 5, 25, and 50 cm above the floor in front of the showcase doors. Six catalytic combustion sensors were placed 5 and 25 cm above the floor close to the side walls (a total of 12), and 16 catalytic combustion sensors were placed 50, 100, 200, and 280 cm above the floor at the center of the simulation room (a total of 28).

4.4.2 Diffusion behavior results

For an m_{max} of 500 g, which was set with the assumption of an airflow, the diffusion behavior was measured while altering the m_{max}, fan operation, and presence of a product within the case to evaluate the situation where the compressor cooling fan at the bottom of the showcase was operating. With the cooling fan on and the doors opened after full discharge of gas into the case, the gas concentration in the simulation room dropped below flammable levels, approximately 5 min after opening the doors (Fig. 4-4-1a). Under the same conditions but with the cooling fan off, flammable concentrations of gas remained in the simulation room for ~90 min. For a small m_{max} of 100 g, the flammable concentration range disappeared within ~1 min, even without operating the fan. Placing a simulated bottle inside the case did not have a significant effect on the diffusion behavior.

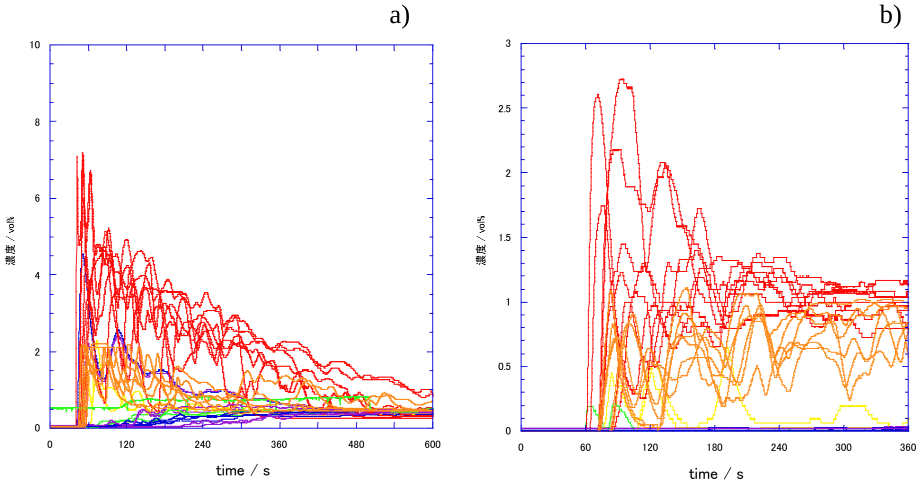

Fig. 4-4-1 Time profile of propane concentrations in the 4.9 m × 4.9 m × 2.8 m room. a) 500 g of propane with the cooling fan operating. b) 100 g of propane with the cooling fan turned off.

4.4.3 Real-scale physical hazard assessment methods

Regarding the air conditioner experiments, a steel simulation room with dimensions of 4.9 m × 4.9 m and a height of 2.8 m was installed in the Taiheta Mine site, for assessment of the combustion effects. To observe the combustion effect under realistic conditions, double sliding glass doors with a width of 240 cm were installed in the wall opposite the showcase to simulate automatic doors. The same ignition conditions as those used for the air conditioner study were used.

To assess the combustion effect, radiant heat sensors were installed (two indoors and two outdoors). A strain-type pressure sensor was also installed in the room, and three blast measurement microphones were installed outside of the glass doors and two behind. A thermocouple was installed inside and above the showcase, and at the top and bottom of the wall. To observe the propagation of the flame in the room, an acrylic window with a thickness of 50 mm was built in the center of a side wall, and a visible-range monochromic high-speed camera was installed just outside the window. To confirm ignition, a high-speed infrared camera was installed 40 m from the glass doors. To observe the damage to the glass window, two color visible-range high-speed cameras were installed, one 40 m from the center of the wall with the glass doors and another 40 m from the center of the wall at 45°.

4.4.4 Real-scale physical hazard assessment results

The propane concentration inside the case was adjusted to 26%, assuming that 500 g of propane leaked inside the case, while operating the compressor cooling fan at the bottom of the refrigerator (same model as that used for the leakage diffusion behavior measurements) of the reach-in showcase. The doors were opened remotely, and the gas was ignited with a spark. When we attempted to ignite the gas 2 cm above the floor at the center of the room 5 min after opening the showcase doors, ignition did not occur. Ignition was achieved 2 cm above the floor and 50 cm in front of the showcase 40 s after opening the showcase door; however, the glass doors of the simulation room were not damaged. When we attempted ignition 2 cm above the floor and 50 cm in front of the showcase doors immediately after opening the showcase doors, ignition occurred and the frame and glass of the window were broken and blown outward.

Fig. 4-4-1 shows images of the flame spreading in the room, taken at 100 ms intervals immediately after the ignition. After opening the doors, a propane–air gas mixture with high specific gravity traveled downward from the showcase, reaching the ignition device where ignition occurred. Fig. 4-4-2 also shows still images of the simulation room glass doors breaking, taken at 200 ms intervals after the time of ignition. The glass doors were blown outward as the pressure inside the simulation room increased, damaging the glass. The maximum measured indoor pressure was 5.0 kPa and the maximum blast pressure 10 m from the sliding windows was 29 Pa. After the glass window was damaged, the increase in the indoor pressure was suppressed to ~5 kPa. Since the combustion rate of propane is low, the impact of the blast pressure propagating outside the room was limited. The maximum radiant heat was approximately 160 kW m^{-2} both inside and outside the room. Although the duration of the explosion was short, the measured conditions are sufficient to cause burn injuries.

a) b) c) d)

Fig. 4-4-2 Fire observed after opening the showcase door under continuous ignition conditions (100 ms intervals).

a) b) c) d) e) f)

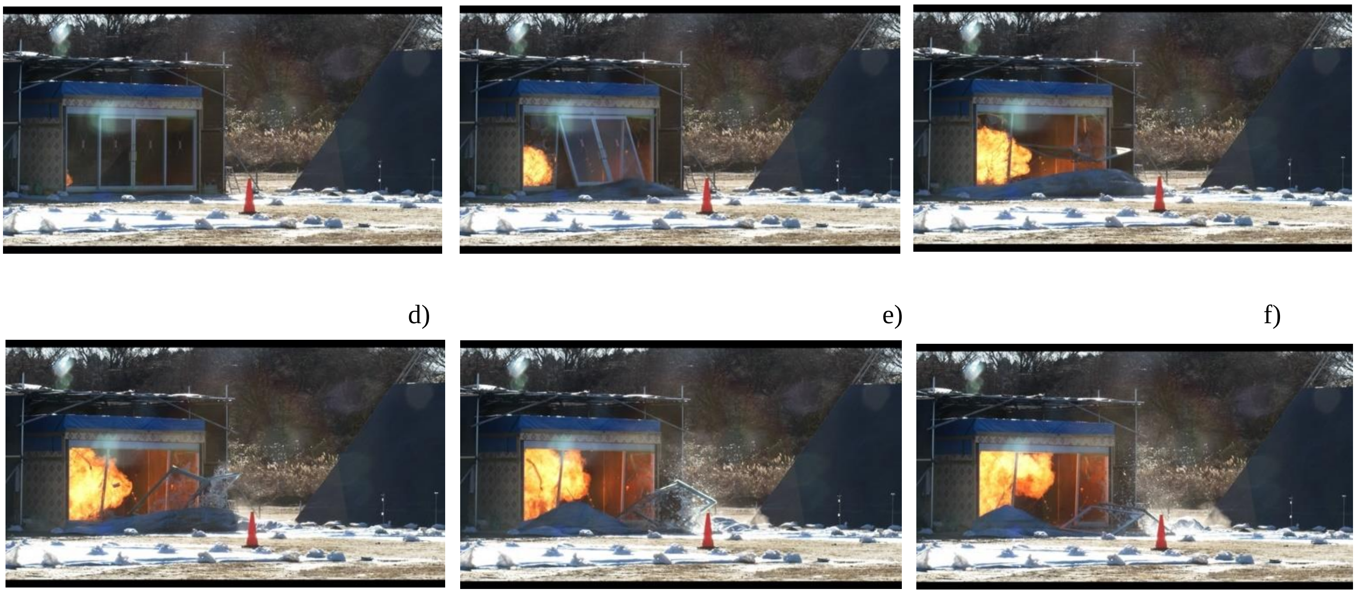

Fig. 4-4-3 Photographs of the glass door after propane gas ignition (200 ms intervals).

The propane concentration in the showcase was adjusted to 5.2% and it was assumed that all 100 g of propane leaked inside the case. The compressor cooling fan at the bottom of the refrigerator was turned off. The showcase doors were opened remotely and propane was ignited 2 cm above the floor and 50 cm in front of the showcase doors using a discharge spark. Ignition and damage to the frame of the glass doors of the simulation room were confirmed, but the glass was not blown out. The maximum indoor pressure was 4.4 kPa and the maximum radiant heat was 8.7 kW m^{-2}. The maximum blast pressure measured 10 m from the sliding windows was 26 Pa. Fig. 4-4-4 shows images of the flame spreading in the room immediately after ignition, taken at 100 ms intervals. Since the concentration of propane was low, the radiation was low as well. Fig. 4-4-5 shows images of the glass doors of the simulation room breaking immediately after ignition, taken at 400 ms intervals. Although the glass doors were blown out, the glass itself was not broken.

a) b) c) d)

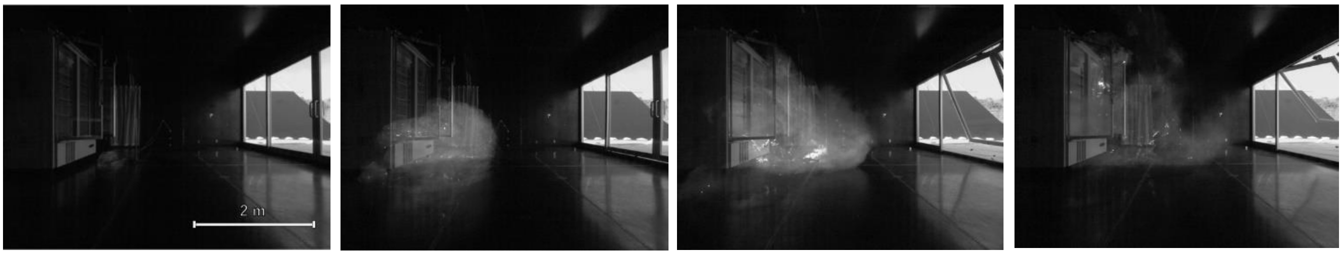

Fig. 4-4-4 Fire observed after opening the showcase doors under continuous ignition conditions (100 ms intervals).

a) b) c) d)

Fig. 4-4-5 Images of the glass door after propane gas ignition (400 ms intervals).

4.4.5 Summary of the real-scale physical hazard assessment

At an m_{max} of 500 g (assuming an airflow) and 5 min after starting the gas leakage, the gas concentration was not within the flammable range. After gas leakage in the reach-in showcase and while the compressor cooling fan was operating, no ignition occurred 5 min after opening the doors. However, ignition occurred immediately after and 40 s after opening the doors. Specifically, the damage to the glass doors from radiant heat was severe when ignition occurred immediately after opening the doors. The damage was higher when m_{max} is calculated assuming an airflow, but an airflow was not used in the experiments. If ignition occurs immediately after opening the doors following gas leakage into the showcase, at a low m_{max} of 100 g, for which safety measures are considered unnecessary, the risk of combustion is relatively low but damage to glass doors is possible.

4.5 Diffusion behavior and physical hazard assessment of an indoor room air conditioner: small-scale experiments

To develop an assessment method to predict and estimate typical (or the highest) physical hazards along with the diffusion behavior during a refrigerant leakage, small-scale experiments were conducted to examine the scalability of the diffusion and combustion results. In this study, propane (R290), R32, and R1234yf refrigerants were used. A leakage was simulated by discharging the gas through a nozzle installed near the short wall of a steel simulation room with a 1/1.8 scale of 9 jou (16.4 m^2) (1.5 m × 3.0 m walls and height of 1.33 m) and the vertical concentration distribution of gas was measured over time. Ignition experiments were conducted under conditions in which the range of flammable concentrations was achieved in the above tests, and for conditions where a flammable range of concentrations close to the stoichiometric ratio of each refrigerant formed above the floor of the simulation room. The combustion effects were assessed by measuring the room pressure and radiant heat.

4.5.1 Diffusion behavior experiments

The leakage diffusion behavior experiment with propane (R290) was mostly performed in the AIST explosion pit. In a real-size test, 1.11 m above the floor correspond to 2.0 m in the 1/1.8 scale (center of a short wall of the simulation room). The gas amount was set as *LFL*/2 when the area up to 1.22 m from the floor (2.2 m in the 1/1.8 scale) is fully circulated[4-1] while changing the internal diameter of the discharge nozzle. In this manner, the nozzle diameter was selected to reproduce the vertical gas concentration distribution measured in the real-scale experiments.

The leakage diffusion behavior experiments with R32 and R1234yf and the combustion effect experiments with all refrigerants were performed in a multi-purpose large chamber at the National Institute of Technology and Evaluation

(NITE) National Laboratory for Advanced Energy Storage Technologies (NLAB). A cylindrical outlet with an inner diameter of 60 mm (selected based on the above-mentioned AIST explosion pit propane experiment) was used to discharge a concentration of *LFL*/2 when the area below a height of 1.22 m from the floor was completely circulated. In addition to the 4-min full discharge that is internationally used to assess the risk of refrigerant leakage, experiments involving other discharge duration times were conducted. To evaluate the concentration distribution of the discharged refrigerants, we used an oxygen meter to measure the oxygen concentration over time. In all experiments, concentration sensors were installed at eight points (0, 14, 28, 42, 55, 83, 111, and 133 cm above the floor) vertically aligned near the center of the long wall of the small-scale simulation room.

4.5.2 Diffusion behavior results

(1) Repetition of the real-scale propane leakage diffusion behavior in the small-scale experiment

A cylindrical discharge nozzle was installed 1.11 m above the floor, equivalent to a height of 2.0 m in the 1/1.8 scale model, which is the height of the bottom of the indoor unit in a real-scale simulation test. The 4-min full discharge experiment was conducted while changing the inner nozzle diameter from 25 to 60 mm. We selected the nozzle diameter that reproduced the vertical concentration distribution measured in the 9-jou (16.4 m^2) real-scale experiment. For nozzle diameters of 35 mm or larger, no notable difference was observed in the vertical concentration distribution; however, a straight cylindrical nozzle with an inner diameter of 60 mm was selected because it best reproduced the real-scale experimental results.

(2) Formation of flammable mixed gas close to the stoichiometric ratio of that in the small-scale propane leakage diffusion experiment

In a leak diffusion behavior experiment with a commercial indoor room air conditioner performed in 2019, we examined the leakage locations that afforded the highest propane concentration near the floor by analyzing three realistic leakage locations within the unit after full discharge in 4 min. However, it is impossible to examine the structure and leakage locations of all practical units, as well as all room conditions where leakage might occur, such as all arrangements of furniture. Thus, to determine an appropriate assessment method for the worst-case combustion effect when ignition occurs after a leakage, we examined the leakage conditions where most air conditioner refrigerants form a layer with a flammable stoichiometric concentration above the floor. Specifically, the discharge nozzle diameter was set at 60 mm. The discharge height was altered to perform a 4-min full-discharge experiment and the vertical concentration distribution after discharge was confirmed. For a nozzle height of 57 cm, gas layers with concentration ranges of 4–5 vol% and 1 vol% formed 28 and 42 cm above the floor, respectively.

(3) Small-scale R-32 leakage diffusion results

A cylindrical outlet with an inner diameter of 60 mm was used (based on the small-scale leakage experiment with propane) to discharge R32 at a concentration of *LFL*/2 assuming that the area below 1.22 m from the floor was fully circulated. The leak duration was 4, 8, 12, and 18 min to achieve full discharge. After the end of discharge, the propane concentration above the floor was 9.5 vol% for the 4-min discharge and 8 vol% for the 18-min discharge. Thus, as the discharge duration increased, the concentration decreased slightly; however, no notable dependence of the vertical concentration on the discharge duration was observed (Fig. 4-2). In all experiments, the concentration did not exceed 13.3 vol% (the *LFL*) at the end of discharge. By setting the height of the discharge nozzle at 60 cm, a flammable concentration of 16–17 vol% was generated, which is close to the stoichiometric ratio of 17.4 vol% in the lower part of the room (up to 14 cm above the floor).

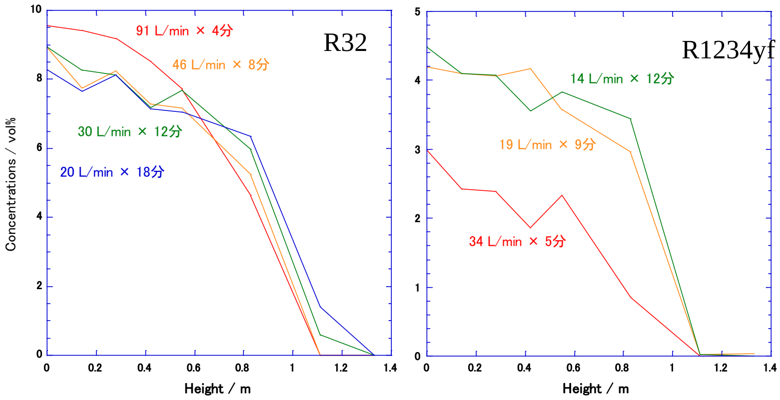

Fig. 4-5-1 Vertical distribution of refrigerant concentration after discharge.

(4) Small-scale R1234yf leakage diffusion results

R1234yf was discharged at a concentration of *LFL*/2 from a cylindrical outlet with a 60-mm inner diameter (selected in the propane experiment), assuming that the area below 1.22 mm from the floor was fully circulated. Leakage durations of 5, 9, and 12 min were used to achieve full discharge. The propane concentration above the floor was ~3 vol% after 5 min of discharge and ~4.5 vol% after 12 min; thus, the concentration increased with increasing discharge time. Although no notable difference was observed in the vertical distribution after 9 and 12 min of discharge, compared to the 5-min discharge, the gas concentration was 1.5 and 3 times higher, respectively (Fig. 4-5-1). In all experiments, a concentration exceeding *LFL* (6.2 vol%) following the end of discharge is unlikely. By setting the height of the discharge nozzle at 65 cm, we were able to achieve a flammable concentration of ~7–8 vol%, close to the stoichiometric ratio of 7.8 vol% in the lower part of the room (up to 28 cm above the floor).

4.5.3 Small-scale combustion effect assessment methods

The leakage conditions were set to obtain the vertical concentration distribution measured in the leakage diffusion experiments for the combustion effect study, where the gas was ignited 2 min after the end of discharge. Ignition was achieved by discharging 1/2 cycle of a 60 Hz AC power supply boosted to 15 kV by a neon transformer with a spark plug installed 2 cm above the floor, at the center of the simulation room.

In the real-scale experiments, on the short wall where the double sliding windows were built, an acrylic plate with a thickness of 1 or 2 mm was installed with a steel frame bolted to an opening, scaled to 1/1.8. The total combustion effect was measured using strain gauge pressure sensors installed on the wall of the simulation room, radiant heat sensors installed inside and outside the room, and blast measurement microphones installed outside the room. A high-speed near-infrared camera was installed to confirm ignition, and a monochromic visible high-speed camera was installed to observe the spreading of the flames.

4.5.4 Small-scale combustion effect results

(1) Comparison of the small-scale and real-scale experiments with propane

The experiment was conducted under the discharge conditions that reproduced the vertical gas concentration distribution in the real-scale experiment. In the small-scale experiment, the maximum indoor overpressure was 13 kPa and maximum radiant heat at the room wall was 26 kW, while these values were 3–4 times lower (5.6 kPa and 6.1 kW, respectively) in the real-scale case. Such an outcome could be because of the differences in the damage behavior of the sliding and acrylic windows and differences in the distance between the radiant heat sensors installed on the wall and the flames. However, it is difficult to apply scaling corrections for these factors.

(2) Effect of the concentration distribution on the small-scale propane combustion effect

The propane concentration in the small-scale experiment described in the previous section was 2.2–2.6 vol%, which is close to the *LFL* of propane up to 55 cm above the floor. However, the discharge nozzle was lowered, and the combustion effect was measured under discharge conditions where the concentration was 4–5 vol% up to 28 cm above the floor. The maximum indoor overpressure was 20 kPa and the maximum radiant heat at the room wall was 87 kW.

In the case where the sealed container was not damaged, the internal pressure of the container after combustion was close to that calculated from the combustion heat assuming combustion is fast and heat transfer to the wall is relatively slow. If the same amount of refrigerant is leaked, results would be similar. In this study, we built an acrylic window to be broken by the internal pressure, to create conditions close to an actual living room space. However, even in an experiment using the same 1-mm-thick acrylic plate, the maximum indoor overpressure during combustion with a gas concentration close to the stoichiometric ratio (where the combustion rate is high), was 1.5 times higher and the maximum radiant heat was at least three times higher. Because there are concentration ranges above the stoichiometric ratio, infrared radiation from soot became significant.

(3) Small-scale R32 combustion results

Under the discharge conditions described in section **4.5.2**(3), the gas was ignited in the flammable range (16–17 vol%) up to 14 cm from the floor, to evaluate the combustion effect. The maximum indoor overpressure was 5.7 kPa, which is approximately half the value measured in the propane experiment with the same 1-mm-thick acrylic window material. The maximum radiant heat at the room wall was 2.6 kW, which is about 1/10 of the value measured in the propane experiment at the room wall.

(4) Effect of the acrylic window thickness on the small-scale R32 combustion effect

Combustion experiments were performed using a 2-mm-thick acrylic window and the discharge conditions described in section **4.5.2**(3). In this case, the maximum indoor overpressure was 33 kPa and the maximum radiant heat at the room wall was 38 kW. The internal pressure and radiant heat measured with the 1-mm-thick acrylic material were five and ten times greater, respectively, than those measured with the thicker acrylic window. In the case of a pressure release that caused damage, the timing of the pressure release had more impact on the room pressure than the combustion rate. Furthermore, the timing of the pressure release had a notable effect on the radiant heat.

(5) Small-scale R1234yf combustion results

The refrigerant was ignited in the flammable concentration range of 7–8 vol% up to 28 cm above the floor under the discharge conditions described in section **4.5.2**(4), to evaluate the combustion effects. The maximum indoor overpressure was 0.8 kPa and the maximum radiant heat at the room wall was 0.3 kW, which are approximately 1/20 and 1/80 of the values obtained in the propane experiment with a 1-mm-thick acrylic window, respectively. The maximum indoor overpressure and radiant heat were about 1/7 and 1/9 of the values measured for R32, respectively. Fig. 4-3-2 shows images taken with a high-speed near-infrared camera where the flame from the combustion of R1234yf slowly spread and rose due to buoyancy and reached the ceiling before propagating horizontally. The flame disappeared before consuming R1234yf in the simulation room.

(6) Effect of added humidity on the small-scale R1234yf combustion effect

Wet paper towels were placed and covered the floor to humidify the simulation room, and ignition was achieved under the conditions described in section **4.5.2**(4). Analysis of the combustion effects showed that the maximum indoor overpressure was 3.2 kPa and the maximum radiant heat at the room wall was 0.7 kW, which are four and two times those obtained without added humidity, respectively.

a) b) c) d) e)

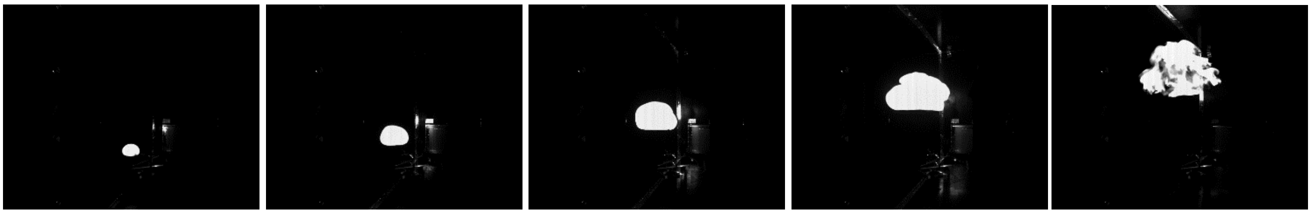

Fig. 4-5-2 Fire observed after ignition of R1234yf began 2 min after finishing discharge (100 ms intervals).

4.5.5 Summary of the small-scale physical hazard assessment

We conducted evaluations of the leakage diffusion behavior and combustion effects for three refrigerants (propane (R290), R32, and R1234yf) in a small-scale simulation room, to examine the possibility of simplifying the combustion effect assessment. We compared the results for propane at small and real scales and revealed the difficulties in applying corrections regarding the scaling of the windows damaged due to combustion and the sensor distances. The pressure resistance of the simulated window and R1234yf were dependent on humidity. In 2022, we conducted real-scale diffusion behavior and combustion effect experiments for refrigerants such as R32 and R1234yf. Please refer to the NEDRO final report for further details.

References

4-1) Risk assessment report on the multi-split air conditioner for buildings that uses flammable refrigerant, The Japan Refrigeration and Air Conditioning Industry Association (2017)

4-2) IEC 60335-2-40: 2018. Household and similar electrical appliance - Safety - Part 2-40: Particular requirements for electrical heat pumps, air-conditioners and dehumidifiers. I.E.C

5. RESULTS OF RESEARCH BY THE RESEARCH INSTITUTE FOR SUSTAINABLE CHEMISTRY AT AIST

5.1 Introduction

The present project aimed to establish practical fire safety criteria and support the development and spread of low-GWP high-safety refrigerants by examining the effects of several factors (e.g., temperature, humidity, refrigerant concentration distribution, and blend composition) on the safety performance indicators (e.g., flammability) of the binary blends of fluorinated refrigerants. Combinations of flammable low-GWP refrigerants with low-flammability ones were considered to determine blend composition ranges affording compliance with domestic and international refrigerant safety standards such as the low flammability class (Class 2L) in the International Standard ISO817 and the specific inert gases specified in the Japanese High-Pressure Gas Safety Act. Additionally, to facilitate future practical use of low GWP refrigerants, we evaluated the effects of temperature, humidity, refrigerant concentration distribution, and other factors on their flammability to establish practical criteria for fire safety.

To accumulate data on blend refrigerants, particularly those related to blend composition, we assessed the flammability of R32/1234yf and R32/152a systems as new low-GWP and conventional blend refrigerants, respectively, and determined the related flammability limits, burning velocities, and quenching distances under both standard and nonstandard (various temperatures and humidities) conditions. Compared to R1234yf and R32, which are classified as *specific inert gases*, R1234yf/R32 blends showed lower flammability at all tested compositions at practical temperatures and humidities. For the R32/152a system, we identified a composition allowing for low flammability and a maximum burning velocity equivalent to or below that of specific inert gases under standard conditions.

In addition, HFO-1123/R32 and HFO-1123/R1234yf blends were assessed in terms of flammability limits, burning velocities, and quenching distances as prospective low-GWP refrigerants under both standard and nonstandard (various temperatures and humidities) conditions.

Regarding flammability limit evaluation, various nonflammable blends and inert-gas blends with lower flammability limits of >10 vol%, including blends containing CF_3I, were experimentally examined.

For the R32/1234yf system, the effects of concentration distribution change were examined using the temporal variation of concentration distribution and flammability upon downward leaking into a large vessel.

5.2 Flammability limits of low-GWP blend refrigerants

5.2.1 Method of flammability limit evaluation

Until 2019, we evaluated flammability limits according to the EN1839B method[5-1)], which was proven to afford results closest to the full-scale flammability limits for various refrigerants, and used a pressure rise rate of $100 \times (P_{\max} - P_0)/P_0 \geq 30\%$ as the judgment criterion. Fig. 5-1 shows the results of pressure and temperature rise measurements performed during the combustion of R32 and R1234yf at concentrations near the lower flammability limit (LFL). LFL was calculated as $(B_1 + A_1)/2$, where B_1 is the highest of the three consecutive concentrations of B_3, B_2, and B_1 required for the pressure rise rate to constantly remain below 30%, while A_1 is the lowest of the three consecutive concentrations of A_1, A_2, and A_3 required for the pressure rise rate to constantly remain above 30%. The LFL of R32 (Fig. 5-1(a)) was estimated as (13.75 + 13.65)/2 = 13.7 vol%, while that of R1234yf (Fig. 5-1(b)) was determined as (7.15 + 6.50)/2 = 6.8 vol%. In the latter case, we observed considerable variation in pressure rise data.

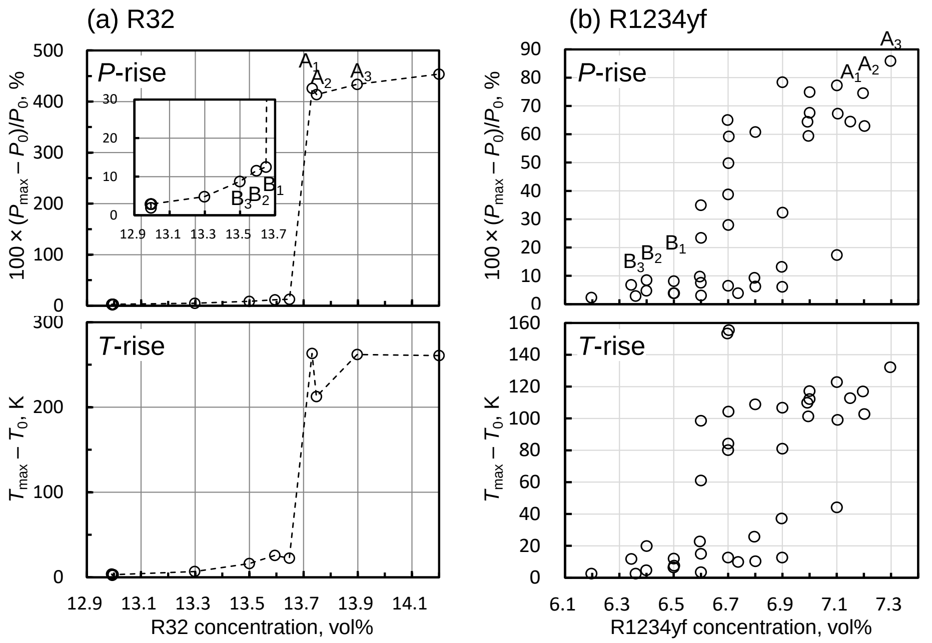

Fig. 5-1 Results of LFL measurements performed for (a) R32 and (b) R1234yf according to EN1839B at 25 ± 2 °C and 101.3 kPa ± 1%.

5.2.2 R32/R1234yf system

The flammability limits of individual R32 and R1234yf were not significantly affected by temperature within the practical temperature range of 15–60 °C and tended to experience greater changes at higher temperatures. The results obtained for the LFL of R1234yf disagreed with the temperature dependence predicted using White's law. Moreover, the flammability limits of the above gases could be expressed as functions of relative humidity (RH) and the H_2O/sample molar ratio.

Next, we examined the effects of temperature on the flammability limits of R32/1234yf blends at 15–60 °C and 0% RH (Fig. 5-2). As in the case of pure R32 and R1234yf, the flammability limits did not significantly change in the investigated temperature range. At 0% RH (dry conditions), both the upper (UFL) and lower (LFL) flammability limits monotonically increased with increasing R32 concentration in almost full agreement with Le Chatelier's formula, and this trend could be approximated using a simple quadratic equation.

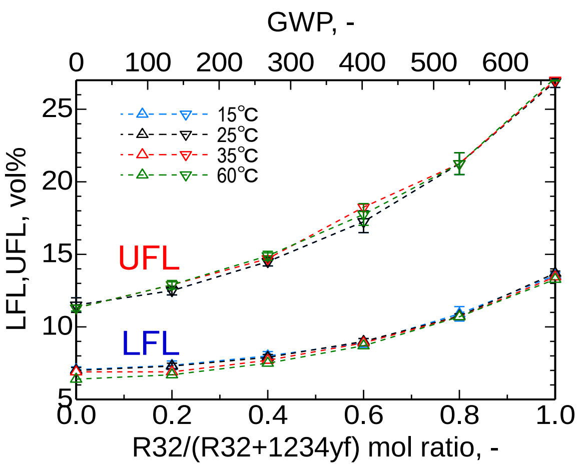

Fig. 5-2 Effects of the molar fraction of R32 on the flammability limits of R32/1234yf blends at 0% RH and 15, 25, 35, or 60 °C. Ordinate intercepts represent the flammability limits of pure R32 and R1234yf.

The effects of RH (10, 35, and 63%) on the flammability limits (LFL and UFL) of R32/1234yf blends were examined at 35 °C (Fig. 5-3) and well agreed with Le Chatelier's formula. The H_2O/sample molar ratio was adjusted to remain constant for each measured value.

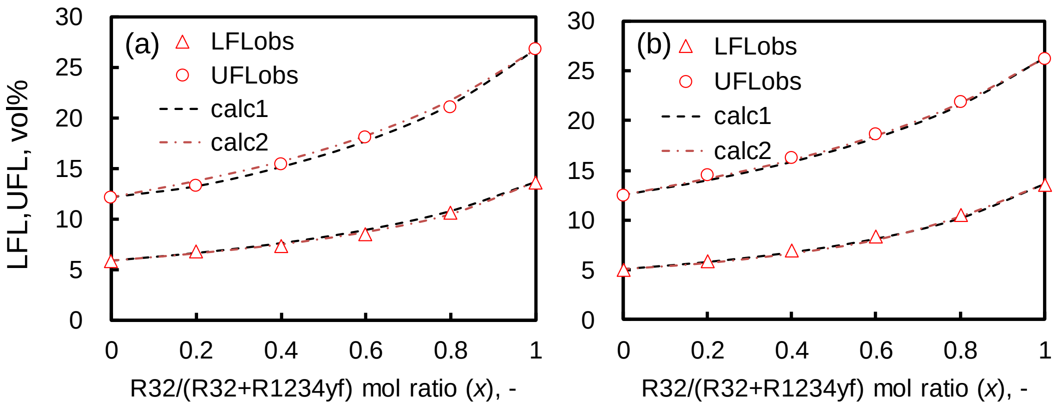

Fig. 5-3 Effects of the molar fraction of R32 on the flammability limits of R32/1234yf blends measured at 35 °C and (a) 10% RH and (b) 63% RH. Curves denoted as calc1 and calc2 correspond to predictions obtained using Le Chatelier's formula and do not show significant deviations from each other and experimental data.

In all cases, the dependence of the flammability limit (y) on the molar fraction of R32 (x) was well approximated by $y = ax^2 + bx + c$. The coefficients a, b, and c depended on normalized relative humidity (r = RH/100 = 0–1), with values obtained using the least-squares method and the related regression equations listed in Table 5-1. These equations allowed the LFL and UFL to be predicted for arbitrary blend compositions and RHs within the practical temperature range, and the predicted results were in close agreement (within the related error margins) with experimental values (Fig. 5-4).

Table 5-1 Coefficients describing the composition-dependent R32/1234yf flammability limit as functions of r.

LFL	0% RH	10% RH	35% RH	63% RH		Regression equation		r = 0.5 (50% RH)
a	6.85	7.47	7.15	7.24	→	$a = -1.95r^2 + 1.49r + 7.03$	→	7.29
b	−0.074	−0.072	0.965	0.961	→	$b = -3.85r^2 + 4.36r - 0.22$	→	0.995
c	6.72	6.07	5.31	5.27	→	$c = 6.37r^2 - 6.25r + 6.69$	→	5.155
UFL	0% RH	10% RH	35% RH	63% RH		Regression equation		r = 0.5 (50% RH)
a	12.68	10.85	9.26	7.83	→	$a = 8.84r^2 - 12.80r + 12.44$	→	8.25
b	2.76	3.61	4.4	5.44	→	$b = -2.28r^2 + 5.45r + 2.88$	→	5.04
c	11.59	11.94	12.55	12.74	→	$c = -3.26r^2 + 3.89r + 11.59$	→	12.715

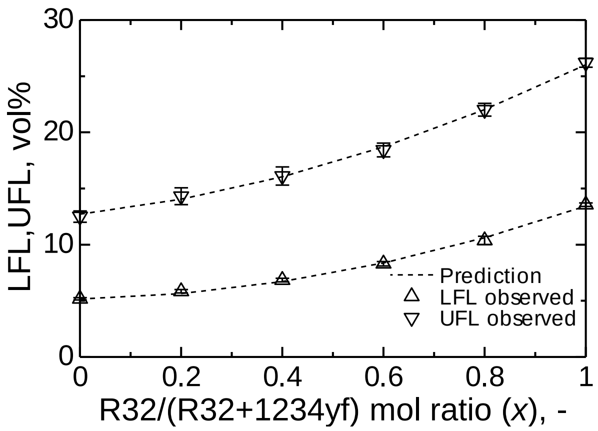

Fig. 5-4 Predicted and measured flammability limits of R32/1234yf blends at 35 °C and 50% RH.

5.2.3 HFO-1123/R1234yf system

The flammability limits of HFO-1123/R1234yf blends were evaluated at temperatures of 35 and 60 °C and RHs of 0, 10, 35, 50, and 63% (Figs. 5-5 and 5-6). In general, with increasing temperature and RH, LFL decreased, and the flammable range expanded. The flammability limits of blends could be well predicted from those of single components at the same [H_2O]/[sample] ratios using Le Chatelier's law, with the deviation between predicted and measured values not exceeding 0.8% and decreasing with increasing RH. Under dry conditions, some blends had LFLs exceeding those of individual components.

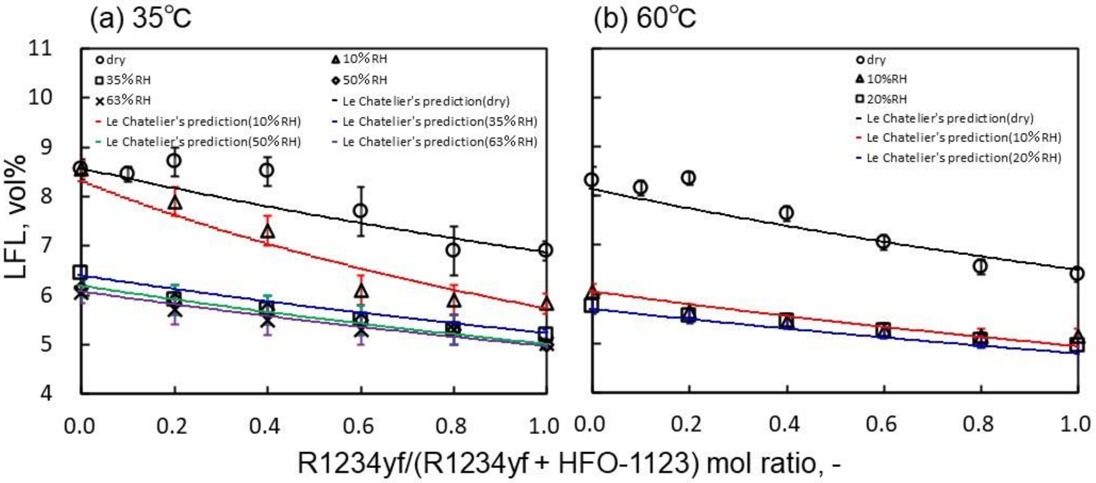

Fig. 5-5 Effects of the molar fraction of R1234yf on the flammability limit of HFO-1123/R1234yf blends measured at various RHs and (a) 35 and (b) 60 °C.

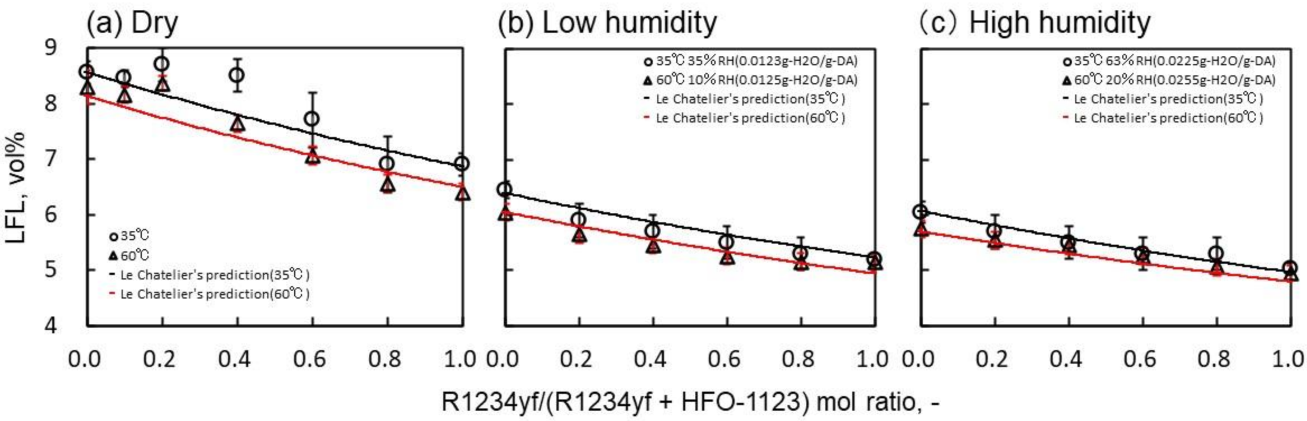

Fig. 5-6 Effects of the molar fraction of R1234yf on the flammability limits of HFO-1123/R1234yf blends measured at 35 and 60 °C under the conditions of (a) zero (dry), (b) low, and (c) high absolute humidity.

5.2.4 HFO-1123/R32 system

The flammability limits of HFO-1123/R32 blends were evaluated for RHs of 0, 10, and 20% at 35 and 60 °C and for RH = 63% at 35 °C (Fig. 5-7). In general, with increasing temperature and RH, LFL decreased, and the flammable range expanded. At R32/HFO-1123 molar ratios above unity, the effect of humidity on LFL was small, probably because the LFL of R32 was almost unaffected by RH. In contrast, at R32/HFO-1123 molar ratios of less than unity, LFL significantly decreased with increasing humidity. Comparison of data obtained at 35 and 60 °C showed that the effect of temperature on LFL decreased with increasing humidity. The flammability limits of this blend, especially at high humidity, could be well predicted from those of individual components (at the same [H_2O]/[sample] ratios) using Le Chatelier's law.

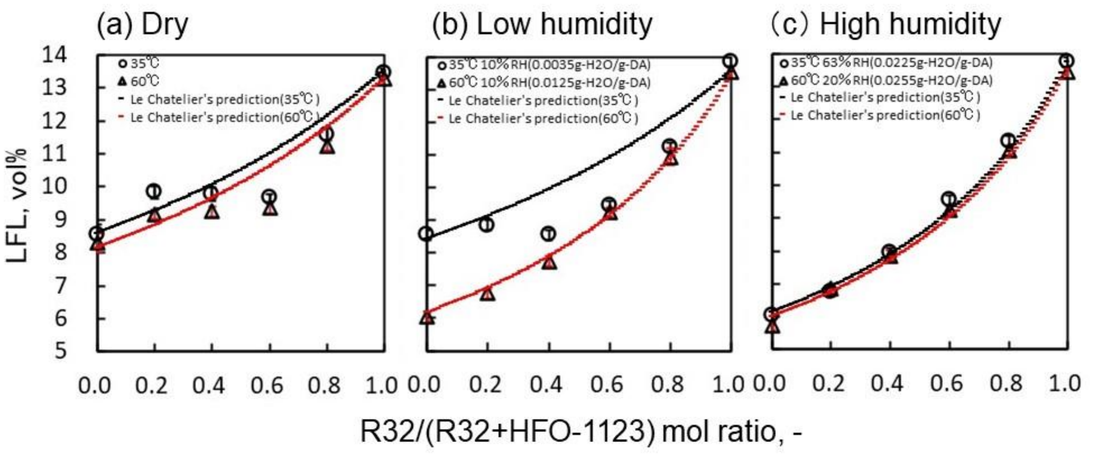

Fig. 5-7 Effects of the molar fraction of R32 on the flammability limits of HFO-1123/R32 blends measured at 35 and 60 °C under the conditions of (a) zero (dry), (b) low, and (c) high absolute humidity.

5.3 Conditions for blend refrigerant inertization

Unless otherwise specified, the conditions of blend refrigerant inertization were determined using B method in EN1839 with a criterion of pressure rise rate of 30%. The results obtained for CO_2/R1234yf and CO_2/HFO-1123 blends are presented in Figs. 5-8(a) and (b), respectively, revealing that the related fuel inertization points (FIPs; i.e., nonflammability onsets) corresponded to R1234yf and HFO-1123 molar fractions of ≤0.683 and ≤0.523, respectively. The condition of LFL ≥ 10 vol% (inert gas under the High Pressure Gas Safety Act) was fulfilled at R1234yf and HFO-1123 molar fractions of ≤0.737 and ≤0.936, respectively.

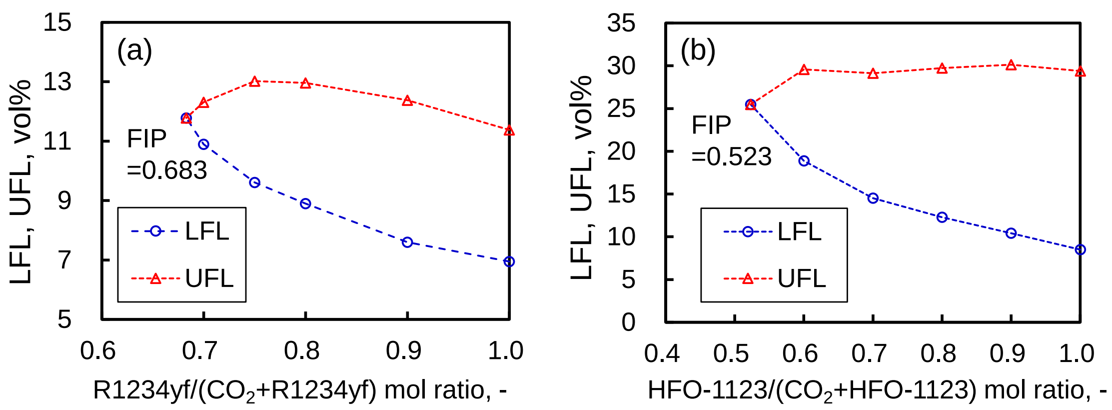

Fig. 5-8 Flammability limits for (a) CO_2/R1234yf blends and (b) CO_2/HFO-1123 blends at 35 °C and 0%RH.

Using the abovementioned method, we obtained the FIPs of various flammable gases and examined the effect of added CO_2 on their behavior. Fig. 5-9 presents a plot of the at-FIP molar fraction of CO_2 vs. the LFL of the flammable blend component, while Table 5-2 lists the related values, including those experimentally determined using the ASHRAE method. Fig. 5-9 reveals that for general flammable gases, the at-FIP CO_2 molar fraction shows a fairly systematic change with LFL, whereas this correlation is considerably disturbed for low-flammability fluorinated compounds such as R1234yf and HFO-1123.

Table 5-2 FIPs of CO_2/flammable gas mixtures at 35 °C and 0% RH.

Flammable	LFL	FIP		
		Fuel ratio	CO_2 ratio	Mixture
	vol%	ratio	ratio	vol%
C3H8*	2.03	0.085	0.915	34.12
C3H6*	2.16	0.087	0.913	37.36
C2H4*	2.74	0.087	0.913	45.98
MeOMe*	3.30	0.118	0.882	39.66
R152a*	4.32	0.170	0.83	35.29
CH4*	4.90	0.206	0.794	31.41
HCOOCH3*	5.25	0.167	0.833	42.51
R1234yf	6.95	0.683	0.317	11.78
HFO-1123/R1234yf (40/60 vol%)	7.70	0.605	0.395	17.81
HFO-1123	8.50	0.523	0.477	25.47
R32/1234yf (60/40 vol%)	8.90	0.557	0.443	20.15

*Measured by ASHRAE method.

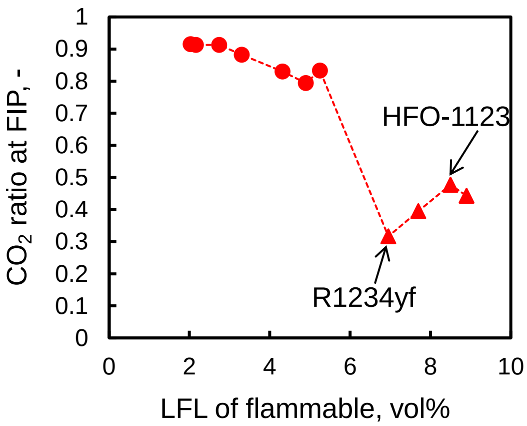

Fig. 5-9 Correlation between at-FIP CO_2 molar fractions and LFLs of CO_2/flammable gas mixtures at 35 °C and 0% RH. Data are taken from Table 5-2. ● = general flammable gas, ▲ = low-flammability Class 2L refrigerant.

Next, we experimentally determined the molar fractions of CO_2 and R32 in mixtures with general flammable gases required to achieve inertization, i.e., LFLs of 10 vol% (Table 5-3 and Fig. 5-10). In the case of CO_2 blends, the CO_2 molar fraction exhibited a good linear correlation with the LFLs of general flammable gases, with slight deviations observed for R1234yf and HFO-1123 (Fig. 5-10). The corresponding regression equation was determined as

$$y = 0.1156(10 - x) - 0.0006(10 - x)^2 - 0.0109(100 - x^2)^{0.5}, \tag{5-1}$$

where x is the LFL (vol%) of the pure flammable gas, and y is the dimensionless molar fraction of CO_2 in the CO_2/gas blend with LFL = 10 vol%. In the case of R32-containing blends, flammability could be fairly well predicted using Le Chatelier's formula for many flammable gases, whereas deviations were observed for R1234yf and HFO-1123. The main reason for this deviation is that the LFLs of pure R1234yf and HFO-1123 are close to 10 vol%, and changes in the related LFL vs. R32 molar fraction plots are therefore small. In this case, confirmation by actual measurements at points near the predicted values is needed.

Table 5-3 CO_2 or R32 molar fraction in (CO_2 or R32)/flammable gas mixtures with LFL = 10 vol% at 35 °C and 0% RH

Flammable	LFL vol%	CO_2 ratio Obs.	CO_2 ratio Linear func.	R32 ratio Obs.	R32 ratio Error	R32 ratio LC's pred.
C_3H_8	2.03	0.774	0.80	0.930	0.005	0.94
C_3H_6	2.16	0.758	0.78			0.93
C_2H_4	2.74	0.700	0.73	0.897	0.007	0.91
MeOMe	3.30	0.644	0.67			0.89
R152a	4.32	0.545	0.57	0.821	0.012	0.84
CH_4	4.90	0.470	0.51	0.762	0.016	0.80
$HCOOCH_3$	5.25	0.453	0.48			0.78
R1234yf	6.95	0.26	0.31	0.723	0.030	0.63
R143a	7.23		0.28	0.586	0.044	0.60
HFO-1123/R1234yf (40/60 vol%)	7.70	0.173	0.23			0.54
HFO-1123	8.50	0.082	0.15	0.656	0.03	0.41
R32/1234yf (60/40 vol%)	8.90	0.109	0.11			0.33
HFO-1123/R32 (90/10 vol%)	9.23	0.050	0.08			0.25

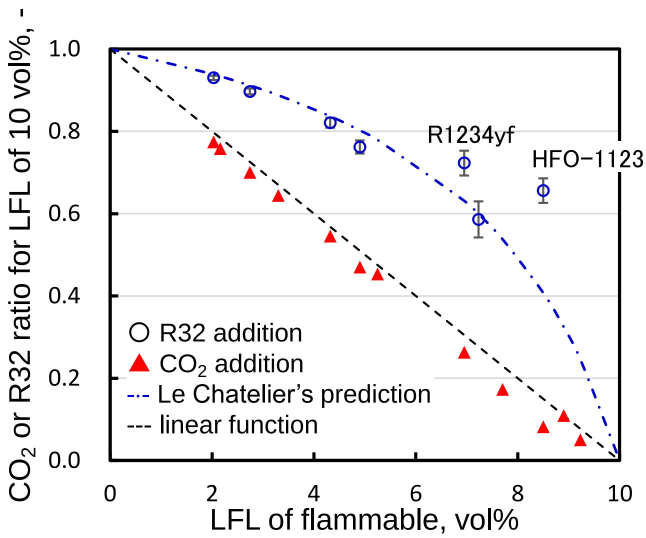

Fig. 5-10 CO_2 or R32 molar fraction in (CO_2 or R32)/flammable gas mixtures with LFL = 10 vol% at 35 °C and 0% RH. Data are taken from Table 5-3.

Subsequently, we measured the flammability limits of mixtures containing CF_3I, which is considered to be a very nonflammable gas. Initially, the flammability limit of pure CF_3I was determined under different conditions. Fig. 5-11 shows the relationship between CF_3I concentration and the pressure rise rate. Using pressure rise rate ≥ 30% as a flammability criterion, we found that in all three cases, flammability developed near a CF_3I concentration of 50 vol%. Next, we determined flammability limits for CF_3I blends. Fig. 5-12(a) compares the effects of diluting methane with CF_3I and CO_2, revealing that whereas a typical change was observed for CO_2, a remarkable expansion of the flammable concentration range with increasing concentration of the nonflammable component was observed for CF_3I. Fig. 5-12(b) shows the effects of diluting R1234yf with CF_3I, revealing that two FIPs were observed. When a small amount of CF_3I was added to R1234yf, the flammability rapidly dropped, and the mixture became nonflammable (FIP①). Conversely, when R1234yf was added to CF_3I, the flammability greatly increased, and nonflammability was achieved only at R1234yf molar fractions of >0.66 (FIP②).

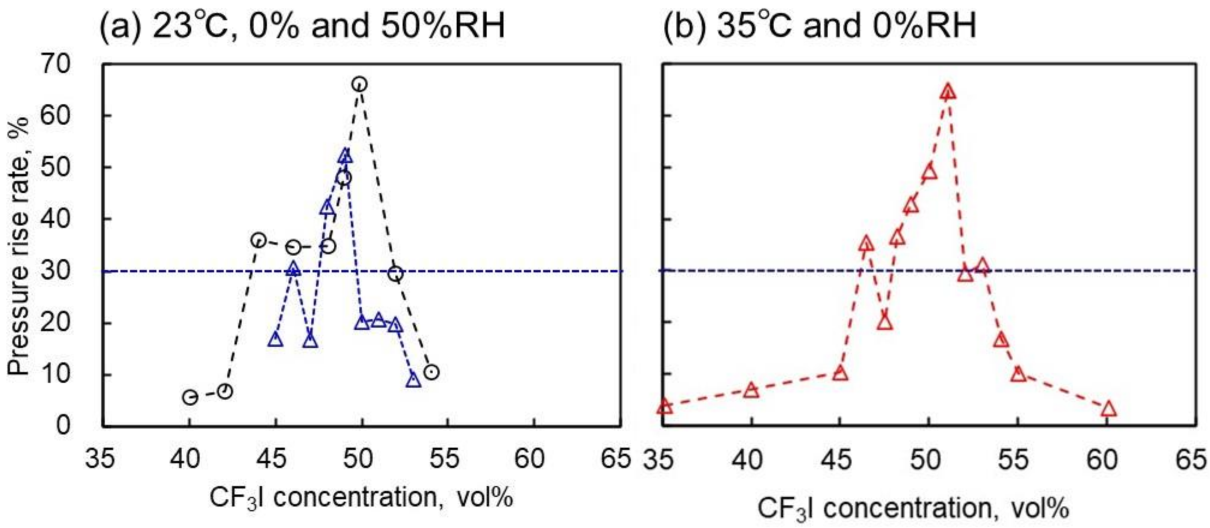

Fig. 5-11 Effects of CF_3I concentration on the maximum pressure rise rate after spark discharge in CF_3I/air mixture determined at (a) 23 °C and 0% RH (circles) or 50% RH (triangles) and (b) 35 °C and 0% RH.

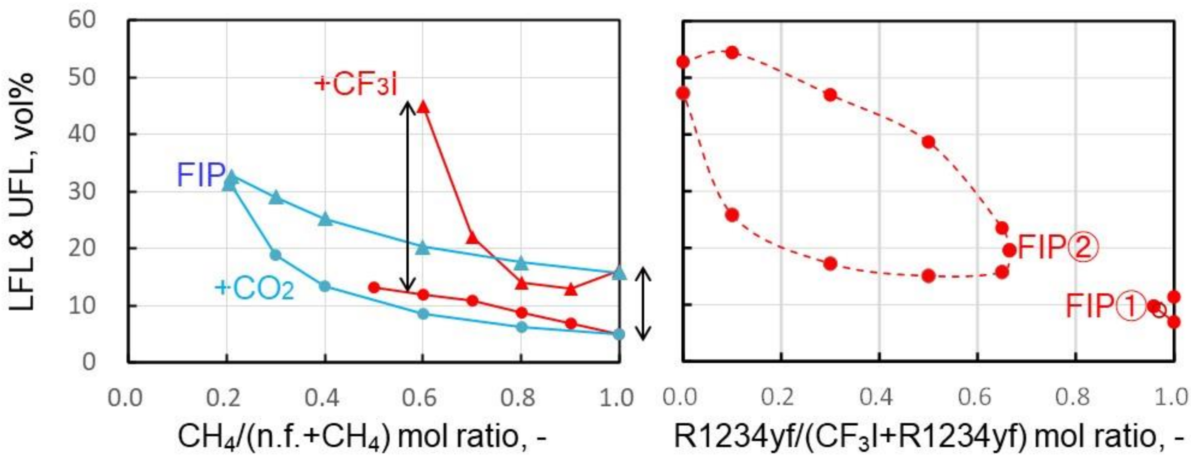

Fig. 5-12 Effects of CO_2 and CF_3I addition on the flammability limit of CH_4 at 35 °C and 0% RH. (b) Effects of CF_3I addition on the flammability limit of R1234yf at 35 °C and 0% RH.

5.4 Burning velocity of low-GWP blend refrigerants

5.4.1 R32/1234yf system

The overall combustion rate can be expressed by the Arrhenius equation. Hence, the mass burning rate ($\rho_u S_u$) is expressed as

$$(\rho_u S_u)^2 \sim \exp(-E_a/RT_b), \tag{5-2}$$

where ρ_u is the unburned gas density, S_u is the burning velocity, E_a is the overall activation energy, R is the universal gas constant, and T_b is the flame temperature represented by adiabatic flame temperature. If the chemical reaction of the system does not change significantly, burning velocity exponentially depends on flame temperature. Accordingly, we initially calculated flame temperatures. Fig. 5-13 shows the flame temperature (T_{ad}; initial temperature (T_0) = 298 K; initial pressure (P_0) = 1 atm) of the R32/1234yf (50/50 vol%) blend as a function of the equivalence ratio (φ), while Fig. 5-14 shows T_{ad} at φ = 1.0 as a function of the molar fraction of R32. Both figures also show values calculated from the flame temperatures of single components using Le Chatelier's equations. Notably, none of Le Chatelier's equations could model the remarkably low flame temperature of this system for any concentration range and mixture composition, which suggested the contribution of between-component interactions.

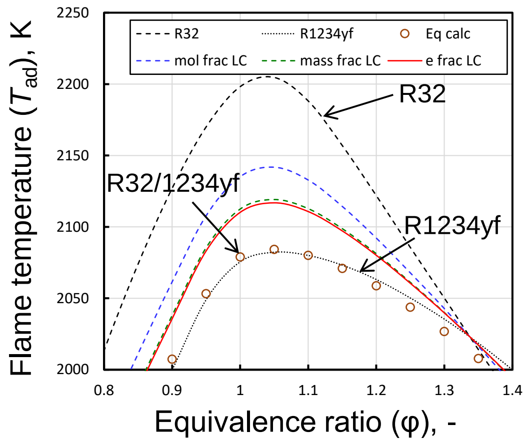

Fig. 5-13 Effects of φ on the flame temperature of the R32/1234yf (50/50 vol%) blend at T_0 = 298 K and P_0 = 1 atm.

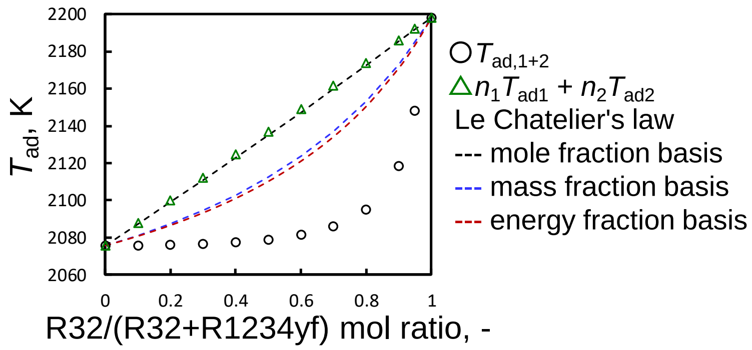

Fig. 5-14 Effects of the R32 molar fraction on the flame temperature of R32/1234yf blends at φ = 1.0, T_0 = 298 K, and P_0 = 1 atm.

Based on the above findings, we evaluated the effects of composition on the burning velocity of R32/1234yf blends at various temperatures and humidities using the Schlieren visualization technique. Initially, we performed measurements over a wide range of temperatures for the entire range of compositions at 0% RH (Fig. 5-15). No significant difference in maximum burning velocity ($S_{u,max}$) were observed within the practical temperature range, similar to the case of flammability limit evaluation. In addition, the burning velocity monotonically increased with increasing R32 concentration at RH = 0%, and no significant increase in burning velocity was observed until the molar fraction of R32 exceeded approximately 0.5, a tendency similar to that observed for flame temperature. Fig. 5-15 also shows that molar-fraction-basis Le Chatelier's equations could not well reproduce the experimental data, although accurate prediction was possible for weight- and energy-fraction-basis equations.

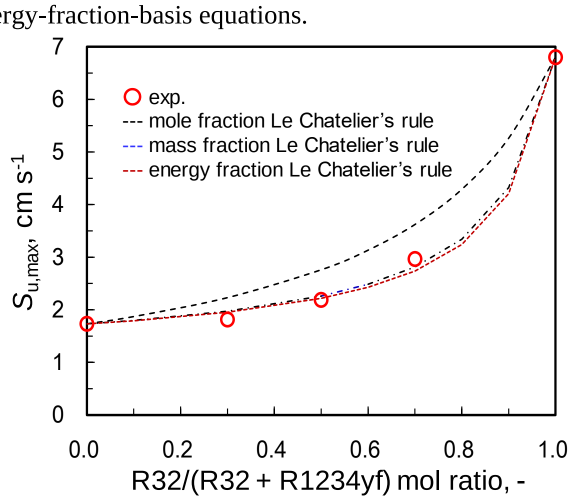

Fig. 5-15 Maximum burning velocity as a function of the molar fraction of R32 in R32/1234yf blends at 35 °C, 1 atm, and 0% RH.

Fig. 5-16 presents the effects of the R32 molar fraction on the burning velocity of R32/1234yf blends at 35 °C and different humidities. Given that the burning velocity of pure R1234yf increased with increasing RH, the burning velocities of the above blends depended on their composition and were always lower than those of individual components under the same conditions.

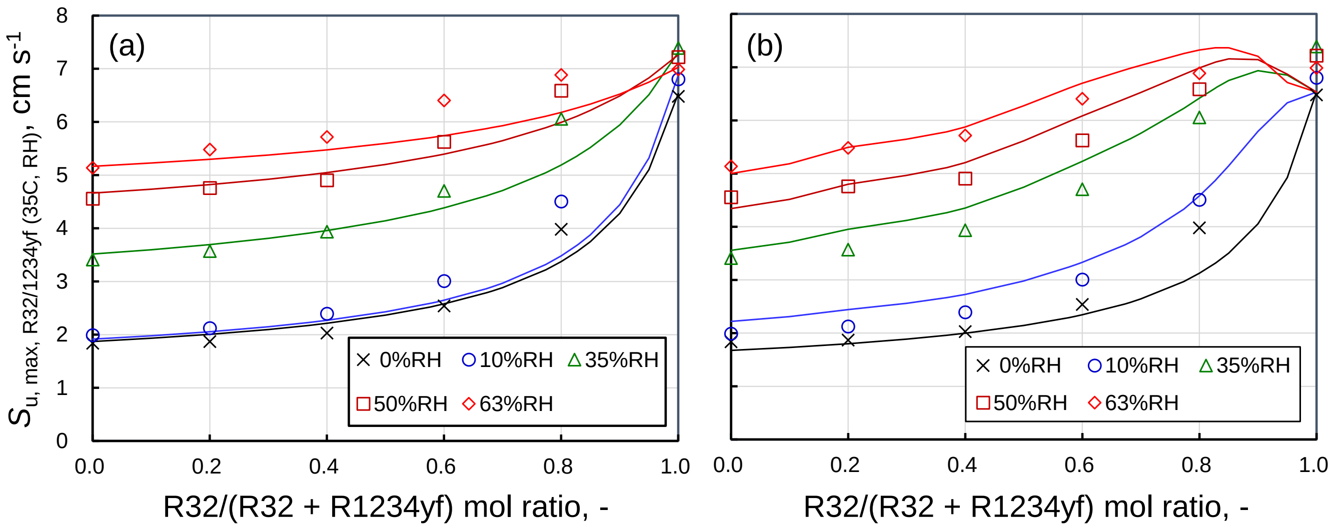

Fig. 5-16 $S_{u,max}$ of R32/1234yf blends measured at various RHs, T_0 = 308 K, and P_0 = 1 atm. (a) Comparison with values calculated using energy-fraction-basis Le Chatelier's equations and $S_{u,max}$ of each component at the same RH. (b) Comparison with values calculated using energy-fraction-basis Le Chatelier's equations assuming that all H_2O reacts with R1234yf.

5.4.2 HFO-1123/R32 system

For the HFO-1123/R32 system, we examined the effect of composition on burning velocity under both standard and nonstandard (various temperatures and humidities) conditions using the Schlieren visualization method. Initially, we evaluated the concentration, temperature, and humidity dependences of the burning velocity of pure HFO-1123. Fig. 5-17 shows that in the practical temperature and humidity ranges (up to ~35 °C and 63% RH, which is equivalent to dew point = 27 °C), the burning velocity was maximized at φ = 1.5. The maximum burning velocity shifted to the vicinity of the stoichiometric concentration at absolute humidities above this level. Finally, burning velocity had almost no pressure dependence, as is the case for ordinary hydrocarbons.

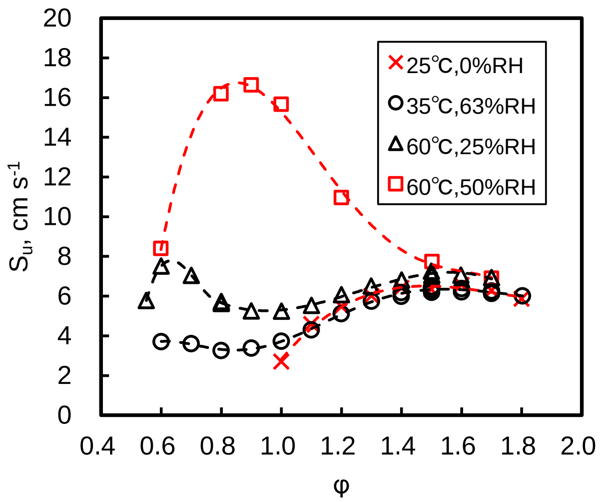

Fig. 5-17 Effect of φ on the burning velocity of HFO-1123.

Next, we fixed φ at 1.5 and measured the maximum burning velocity at temperatures of 18–60 °C and due point temperature of 0–27 °C (Fig. 5-18), obtaining the following regression equation:

$$S_{u,max(T,H)} = S_{u,max(T,0)}[(273.15 + T)/298.15]^{\alpha}(1 + \beta H). \tag{5-3}$$

Here, $S_{u,max(T,H)}$ is the maximum burning velocity at φ = 1.5, temperature T (°C), and humidity H (g-H_2O/g-dry air), and α and β are temperature and humidity dependence coefficients, respectively. Temperature and humidity were assumed to independently influence burning velocity, and a power law similar to that obtained for hydrocarbons was introduced to model temperature dependence, while the humidity dependence was considered to be almost linear within the employed range. Least-squares fitting was performed to obtain $S_{u,max(25,0)}$ = 6.54, α = 1.709, and β = −3.655, as shown in Fig. 5-18. The experimental results were generally well reproduced in the studied temperature range of 18–60 °C and the humidity (dew point) range of 0–27 °C. In this humidity range, β takes a negative value, indicating that burning velocity decreases with increasing humidity.

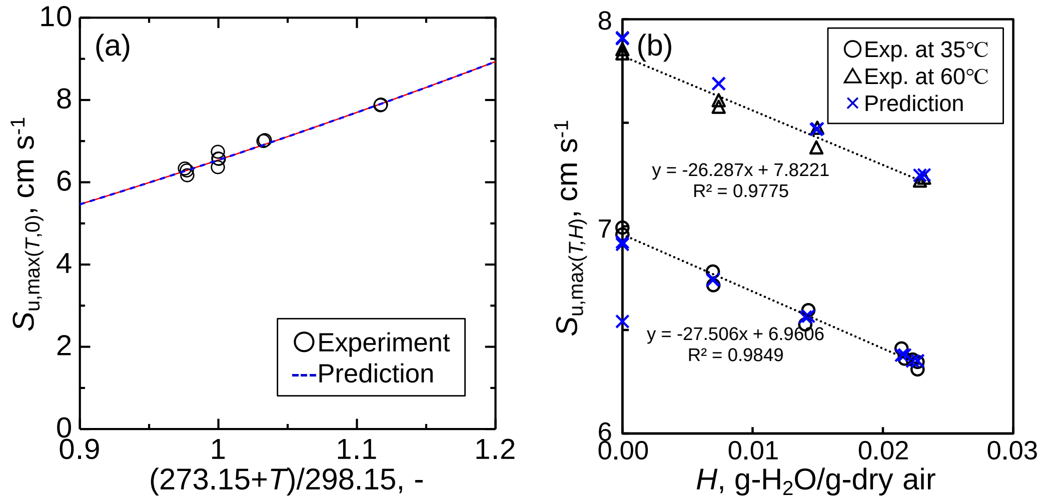

Fig. 5-18 Maximum burning velocities of HFO-1123 (experimental and predicted using Eq. (5-3) as functions of (a) temperature under dry conditions (b) humidity at 35 and 60 °C.

Next, we measured the dependence of he HFO-1123/R32 blend concentration and composition on the burning velocity under the standard conditions of 25 °C and 0% RH (Fig. 5-19). The maximum burning velocity was lower than those of individual components and was minimized at an R32 molar fraction of ~0.69.

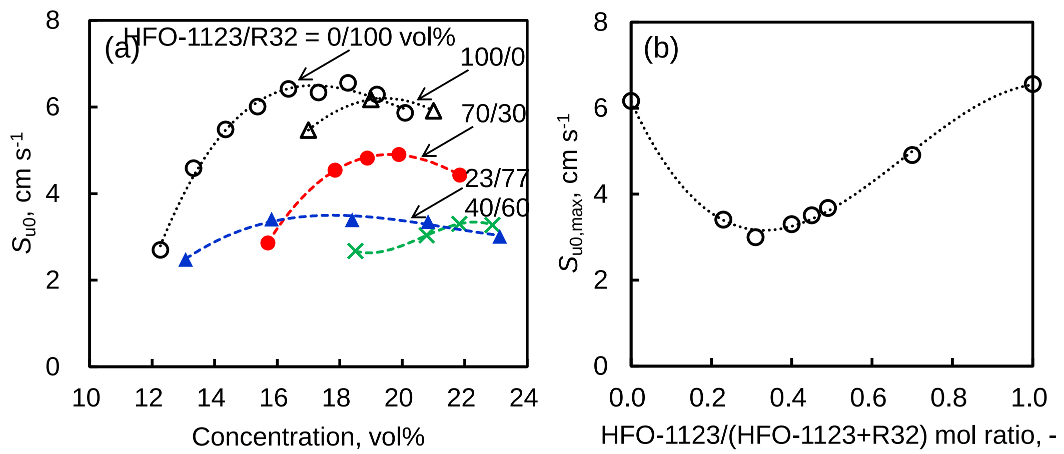

Fig. 5-19 Effects of (a) φ on the burning velocity of HFO-1123/R32 blends and (b) HFO-1123 molar fraction on the maximal burning velocity of HFO-1123/R32 blends.

Subsequently, we probed the dependence of temperature (23–60 °C, φ = 1.5) and humidity (dew point = 0–27 °C, φ = 1.0) on the maximum burning velocity of the HFO-1123/R32 (31/69 vol%) blend. The results (Fig. 5-20) were expressed using Eq. (5-3) in the same way as for HFO-1123 alone. Least-squares fitting was performed to afford $S_{u,max(25,0)}$ = 3.05, α = 2.077, β = 63.019 (α was obtained from the peak at φ =1.5, and β was obtained for the stoichiometric peak). The experimental results were generally well reproduced in the temperature and dew point ranges of 18–60 and 0–27 °C, respectively. In this humidity range, β takes a large positive value, indicating that the burning velocity rapidly increases with increasing absolute humidity. Under dry conditions, the HFO-1123/R32 (31/69 vol%) blend had a very low maximum burning velocity of less than half that of each individual component, with values exceeding that of pure R32 obtained only at high humidities (>0.02 g-H_2O/g-dry air, or dew point ≈ 25 °C).

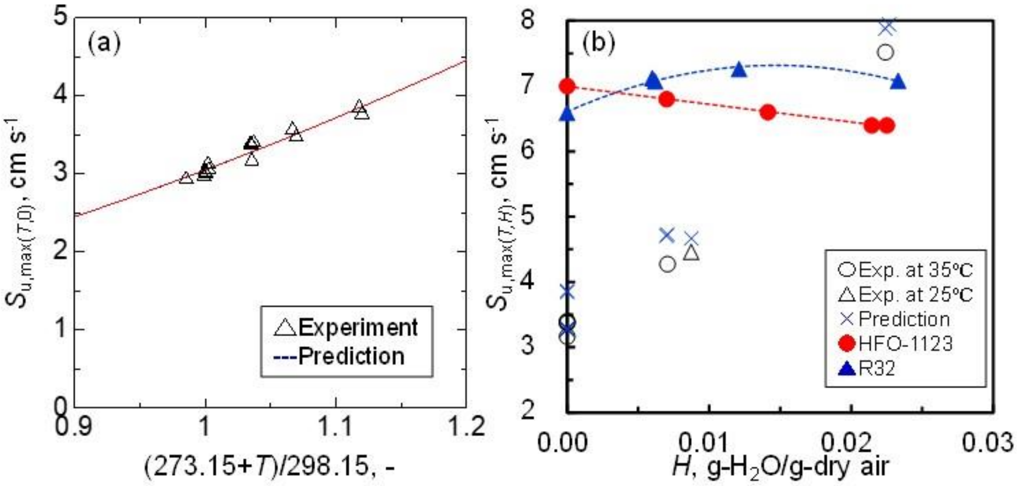

Fig. 5-20 Effects of (a) temperature under dry conditions and (b) humidity at 25 and 35 °C on the maximum burning velocity of the HFO-1123/R32 (31/69 vol%) blend. Panel (b) also shows data for pure HFO-1123 and R32 at 35 °C. The predicted values were calculated using Eq. (5-3).

5.4.3 HFO-1123/R1234yf system

For HFO-1123/R1234yf blends, the dependence of blend concentration and composition on the burning velocity was measured under standard conditions (mixing ratio = 80/20 and 50/50 vol%, temperature = 25 °C, RH = 0%), with the results provided in Fig. 5-21. At a mixing ratio of 50/50 vol%, the flame propagation rate was low, and the flame sphere was greatly distorted because of the buoyancy effect. Therefore, in addition to presenting the results of conventional analysis, we also show those obtained using a flame sphere with a smaller flame radius as well as those of measurements using air with high O_2 concentration. Fig. 5-21(b) reveals that the maximum burning velocity monotonically decreased with the increasing molar fraction of R1234yf, which generally agreed with molar-fraction-basis Le Chatelier's law.

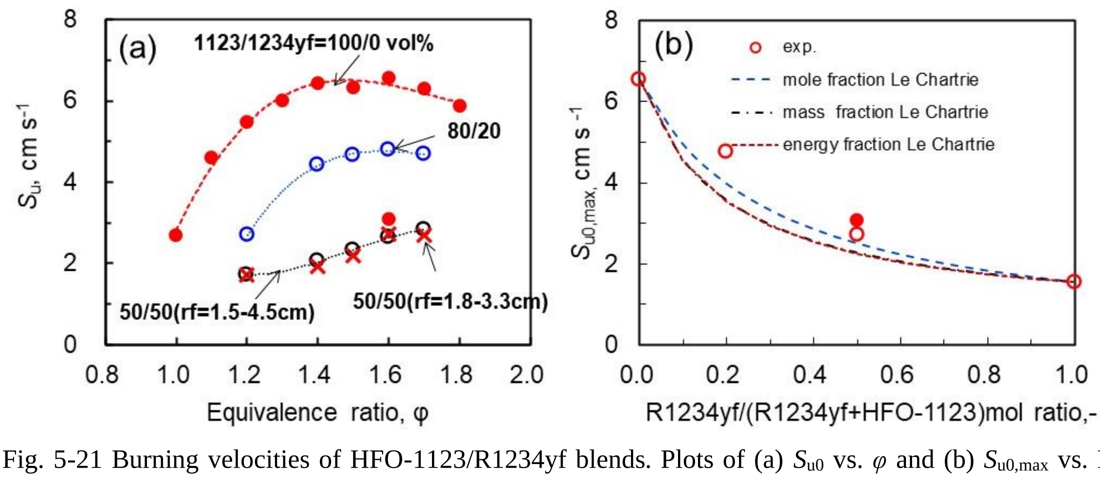

Fig. 5-21 Burning velocities of HFO-1123/R1234yf blends. Plots of (a) S_{u0} vs. φ and (b) $S_{u0,max}$ vs. R1234yf molar fraction.

Fig. 5-22 shows the temperature dependence of the burning velocity of HFO-1123/R1234yf blends, revealing that under dry conditions (Fig. 5-22(a)), this dependence was almost the same as that of each single component. Fig. 5-22(b) shows the temperature dependence of the maximum burning velocity for blends with mixing ratios of 80/20 and 50/50 vol% at high humidity (dew point = 27 °C; equivalent to 63% RH at 35 °C), also presenting the results obtained for pure HFO-1123 (including zero-humidity data). In the employed humidity range, the temperature dependence of maximum burning velocity was almost the same as that of pure HFO-1123, and H_2O addition or mixing ratio change had no effect.

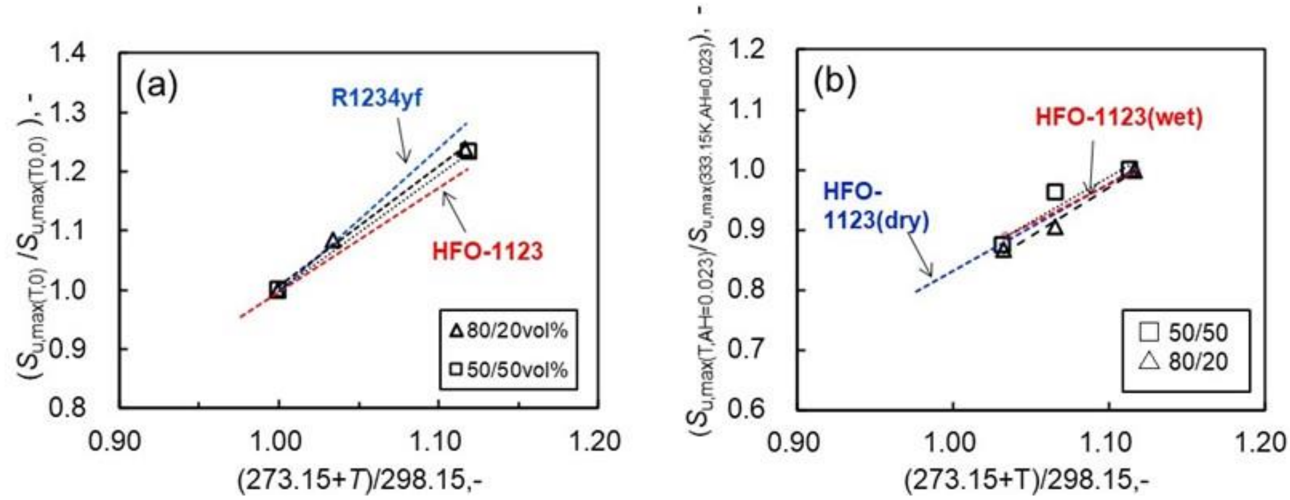

Fig. 5-22 Normalized maximum burning velocities vs. temperature plots for HFO-1123/R1234yf blends and pure blend components obtained at (a) zero humidity and (b) an absolute humidity of 0.023 g-H_2O/g-dry air.

Fig. 5-23 shows the correlation between the burning velocity of HFO-1123/R1234yf blends and humidity, revealing that at a mixing ratio of 80/20 vol% as well as for pure HFO-1123, this correlation was negative. At a humidity corresponding to a dew point of 27 °C (equivalent to 63% RH at 35 °C), the burning velocity was ~10% lower than that under dry conditions. At a 50/50 vol% mixing ratio, burning velocity was negatively correlated with humidity at low humidity, similar to the case of pure HFO-1123 and the 80/20 vol% blend, increasing at high humidity and exceeding the value observed for the 80/20 vol% blend at a dew point of 27 °C (63% RH at 35 °C). This behavior was ascribed to the fact that although burning velocity around $\varphi = 1.6$ hardly changed with increasing humidity, the increase became apparent on the lean side ($\varphi \approx 0.8$). In all cases, the burning velocities of both blends did not exceed that of pure HFO-1123 up to high humidities (dew point ≈ 33 °C).

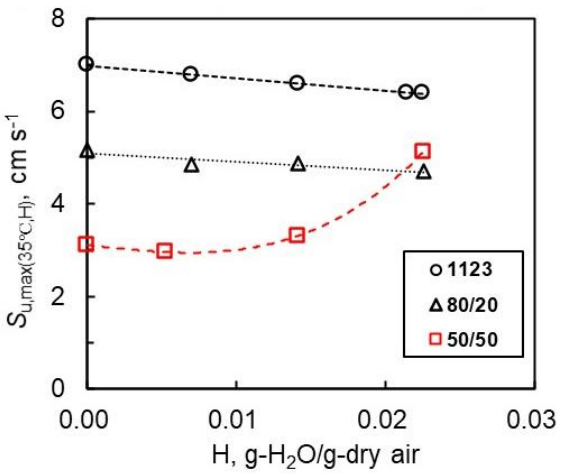

Fig. 5-23 Effects of humidity on the maximum burning velocities of HFO-1123 and HFO-1123/R1234yf blends at 35 °C.

5.5 Fundamental flammability of conventional blend refrigerants

The R32/152a system was selected as a conventional blend refrigerant for comparison with new refrigerants, as it is sufficiently versatile to allow extensive flammability adjustment. Several blend compositions were evaluated in terms of flame temperature, burning velocity, and quenching distance under standard conditions (temperature = 25 °C; pressure = 101.3 kPa; humidity = 0).[5-3] Initially, we calculated the blend's flame temperatures and compared them with values calculated from the flame temperatures of individual components according to Le Chatelier's principles. Figs. 5-24 and 5-25 show the flame temperature of the R32/152a (50/50 vol%) blend as a function of φ and the flame temperature of R32/152a blends (φ = 1.0) as a function of the molar fraction of R32, respectively. Notably, the flame temperature was only weakly affected by blend composition. Additionally, energy-fraction-basis Le Chatelier's principles best reproduced the flame temperature of the blend within all concentration and composition ranges, although reasonable prediction accuracy was also achieved using Le Chatelier's principles on the basis of other parameters.

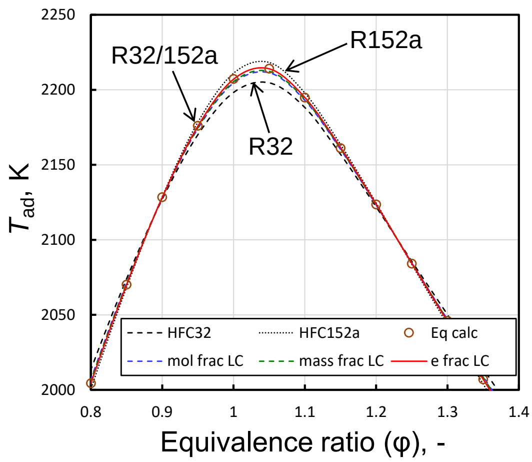

Fig. 5-24 Effects of φ on the flame temperature of the R32/152a (50/50 vol%) blend at T_0 = 298 K and P_0 = 1 atm.

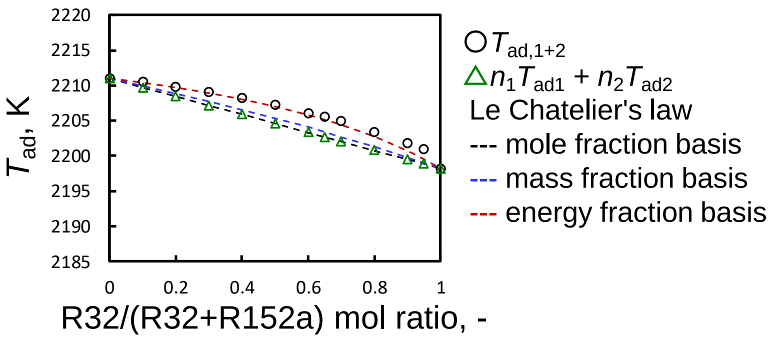

Fig. 5-25 Effects of the molar fraction of R32 on the flame temperature of R32/152a blends at φ = 1.0, T_0 = 298 K, and P_0 = 1 atm.

Based on the above findings, we evaluated the R32/152a system in terms of the dependence of the burning velocity (S_{u0}) on composition under standard conditions using the spherical-vessel (constant-volume) method, with the results presented in Figs. 5-26 and 5-27. A maximum burning velocity of 10 cm s^{-1} or less (*specific inert gas* under the High-Pressure Gas Safety Act) was achieved when the molar fraction of R32 exceeded 0.86. Notably, all Le Chatelier's equations failed to reproduce the compositional dependence of the maximum burning velocity and underestimated the experimental values.

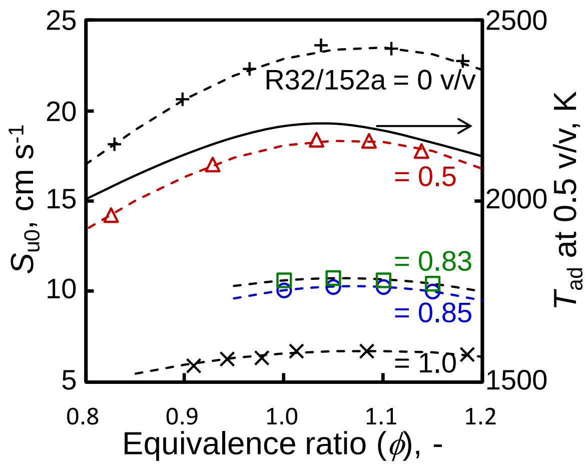

Fig. 5-26 Effects of φ on the burning velocity of R32/152a blends at T_0 = 298 K and P_0 = 1 atm.

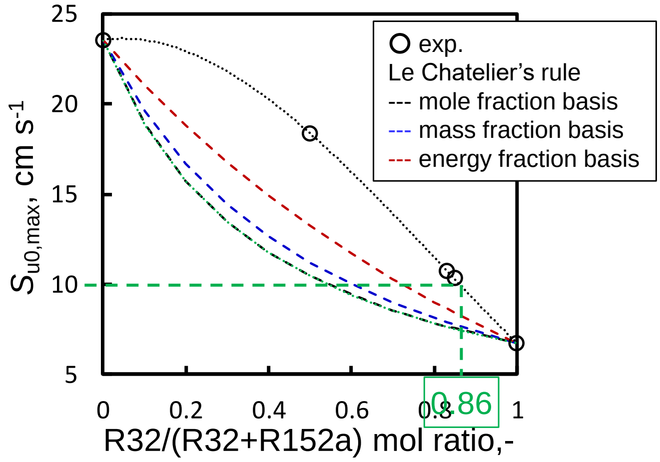

Fig. 5-27 Effects of the molar fraction of R32 on the maximum burning velocity of R32/152a blends at T_0 = 298 K and P_0 = 1 atm.

Subsequently, we evaluated the R32/152a system in terms of quenching distance (d_{q0}) under standard conditions (Figs. 5-28 and 5-29). The results, together with those obtained for burning velocity, revealed that this system fell into the category of specific inert gases when the quenching distance exceeded 5 mm and had the same boundary value as conventional single-component refrigerants. Additionally, the quenching distance of the R32/152a system was approximately expressed according to energy-fraction-basis Le Chatelier's principles, which confirmed that the correlation with the combustion speed was equal to the conventional correlation type. Thus, the quenching distances (known) of single-component refrigerants allowed the estimation of quenching distances and burning velocities for arbitrary blend compositions.

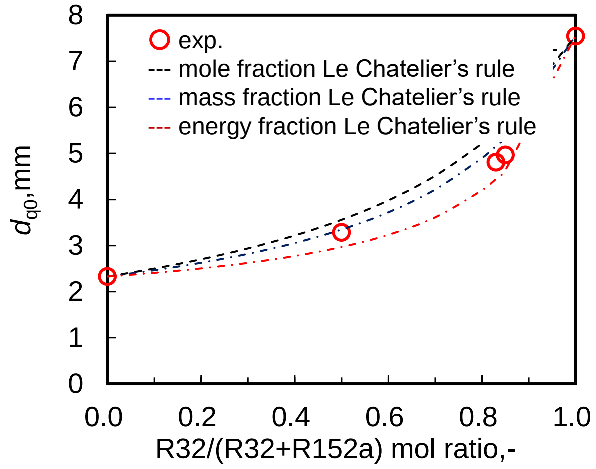

Fig. 5-28 Effects of the molar fraction of R32 on the quenching distance (d_{q0}) of R32/152a blends at T_0 = 298 K and P_0 = 1 atm.

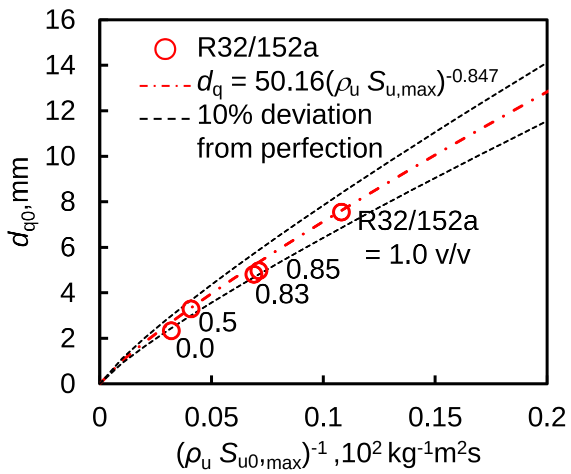

Fig. 5-29 Relationship between the maximum burning velocity and d_{q0} for R32/152a blends.

5.6 Flammability characteristics of low-GWP blend refrigerant with concentration distribution

5.6.1 Evaluation method

In the case of low-flammability refrigerant combustion, the upward force due to buoyancy is significant, and the actual severity degree may be significantly smaller than that predicted from burning velocity data assuming complete refrigerant combustion. Considering refrigerants with different flammabilities and molecular weights as well as different blend systems, we decided to compare and study the contribution of the difference in the flammability of the refrigerant itself to the difference in the severity degree.

When designing our experiment, we assumed downward leakage into a large vessel and downward ignition, in which case the concentration distribution is likely to become apparent. Fig. 5-30 shows a schematic diagram of the employed apparatus. A large-scale vessel with a diameter of 1 m was used, and the refrigerant gas was introduced from the bottom at a flow rate of 1 or 4 L min^{-1} while keeping the ball valve at the top of the vessel open. The gas outlet opening into the vessel has an inner diameter of 10 mm and was softly packed with glass wool to decrease the vertical flow velocity. The total amount of the charged refrigerant gas was ¼ LFL or ½ LFL (for nonflammable gases, 3.4 vol% or 6.8 vol%, respectively, in line with R32). The change in refrigerant concentration with time was measured in advance using an oxygen concentration meter and Fourier transform infrared spectroscopy, and based on the obtained results, combustion experiments were conducted after a given standing time. Prior to ignition, the ball valve at the vessel top was closed. A 15-kV neon transformer was used for ignition, the distance between the two electrodes was 1/4 inch, the spark discharge duration was 0.1 s, and the ignition height was 2 or 10 cm. A high-speed camera equipped with a fish-eye lens was used to record the inside of the vessel after ignition, and the temperature at the top of the vessel and the pressure inside the vessel were measured simultaneously. The initial temperature and pressure was set to 25 °C and 101.3 kPa, respectively.

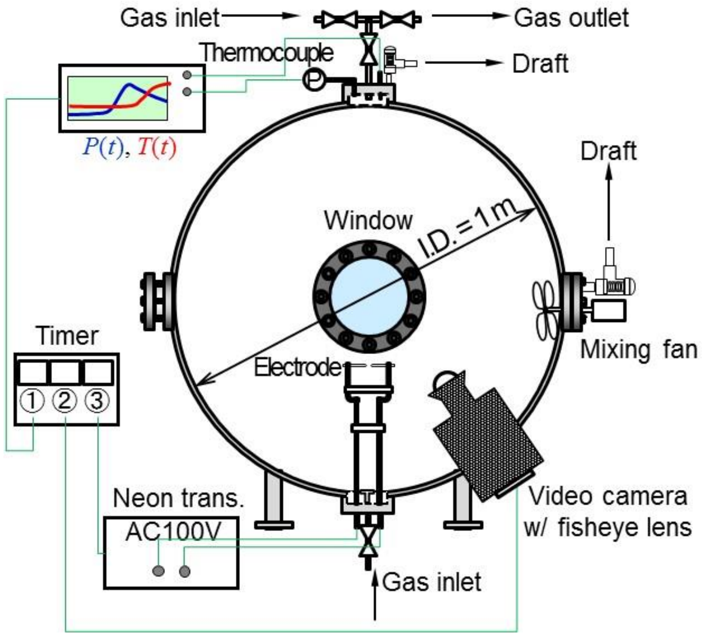

Fig. 5-30 Apparatus used to evaluate the flammability of localized refrigerants in a 520-L vessel.

As an example of concentration distribution measurement, Fig. 5-31 shows the time profiles of the concentration distribution after the bottom charging of small-molecular-weight (R32) and large-molecular-weight (CF_3I) refrigerants. Immediately after the completion of refrigerant charge, the LFL (here, 13.6 vol%) was exceeded only at a height of 20 cm or lower. In view of diffusion, the flammable concentration range disappeared in ~30 min and 1 h in the cases of R32 and CF_3I, respectively.

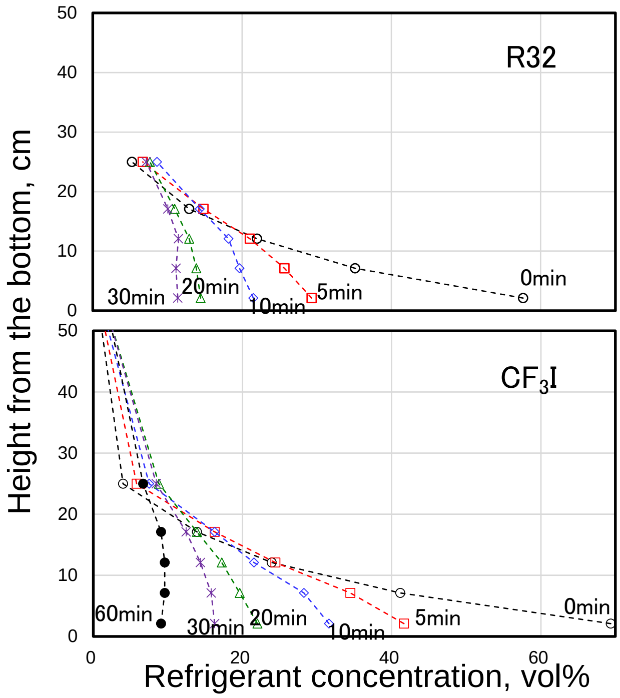

Fig. 5-31 Concentration distribution profiles of R32 and CF_3I charged from the bottom of the vessel (charge amount = 3.4 vol%, charge rate = 1 L min^{-1}).

5.6.2 Evaluation of R32/1234yf blend and comparison with pure components

First, we evaluated the flammability characteristics of pure R1234yf, which is the main component of the R32/1234yf blend, in terms of the local concentration distribution.

Fig. 5-32 shows the results of the concentration distribution evaluation at ¼ LFL. The measured concentration distribution (a) was used to evaluate the gas concentration volume (section volume multiplied by refrigerant concentration) (b) divided in the height direction (position of the sampling ports and sensors) in the vessel, the height of the discharge electrode (2.1 cm), the flammable concentration region (LFL: 6.86% ≤ flammable ≤ UFL: 11.2%) and the flammable gas volume (c), and the change in the flammable volume over time.

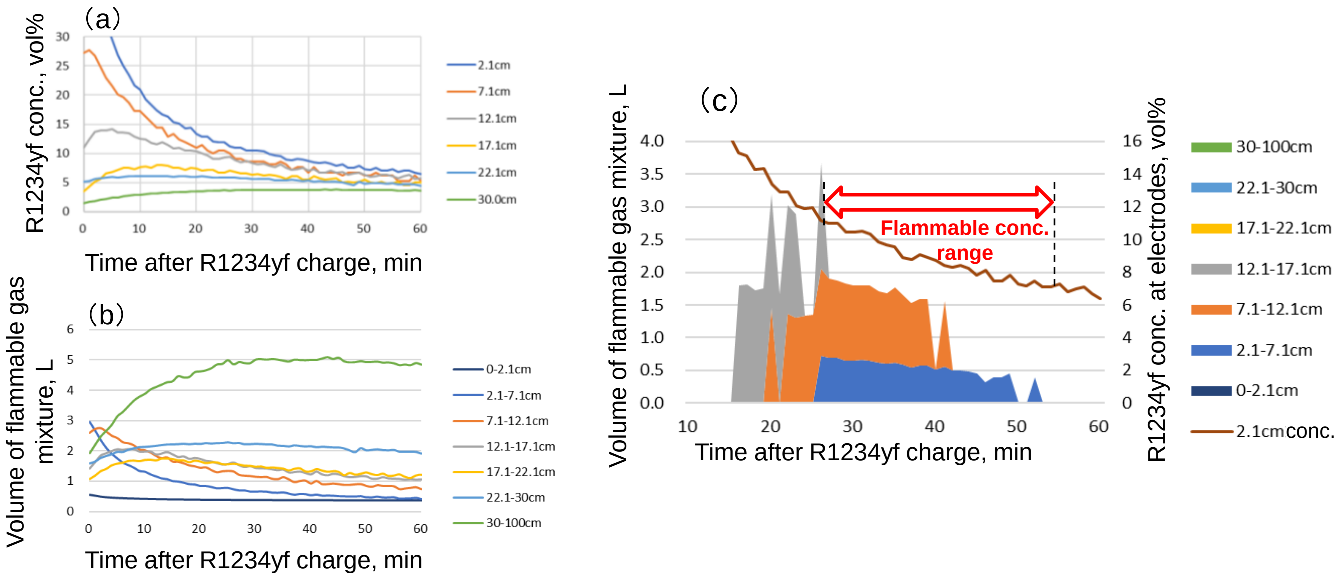

Fig. 5-32 Concentration distribution profile of R1234yf charged from the bottom of the vessel (charge amount = 1.7 vol%, charge rate = 1 L min^{-1}).

Fig. 5-33 shows the results of combustion experiments with R1234yf performed at charge amounts of ¼ LFL and ½ LFL. The deflagration index K_G ($(dP/dt)_{max}V^{1/3}$) [5-4] was calculated from the obtained pressure-time curves. As for the pressure rise tendency, the results were generally consistent with the flammable gas volume shown in Fig. 5-32(c). In addition, the K_G values were much smaller than those obtained for R1234yf (0.8 MPa m/s) and R32 (1.1 MPa m/s) under fully mixed conditions using a large closed vessel of the same shape[5-5].

We also evaluated the R32/1234yf (50/50 vol%) blend, which was prepared beforehand in a 10-L container using the partial pressure method (blend charge amount = ½ LFL (4.18 vol%), charge rate = 1 L min^{-1}). Content analysis was performed using Fourier transform infrared spectroscopy. Fig. 5-34 shows the measured blend compositions at 1800 s (sampling height = 2.1, 22.1 cm), 1860 s (sampling height = 7.1, 30.0 cm), and 1925 s (sampling height = 12.1, 65.0 cm). At a height of 2.1 cm, the R32/1234yf mixing ratio equaled 46.2/53.8 vol%, and the R32 concentration increased with increasing height. Therefore, compared to the combustion characteristics of a homogeneous mixture, we suggested that at the lower part of the vessel, the concentration of R1234yf, which has a lower LFL, is higher, and combustion is likely to occur, whereas at the upper part of the vessel, the concentration of R32, which has a higher burning velocity, is higher, and combustion severity may appear stronger.

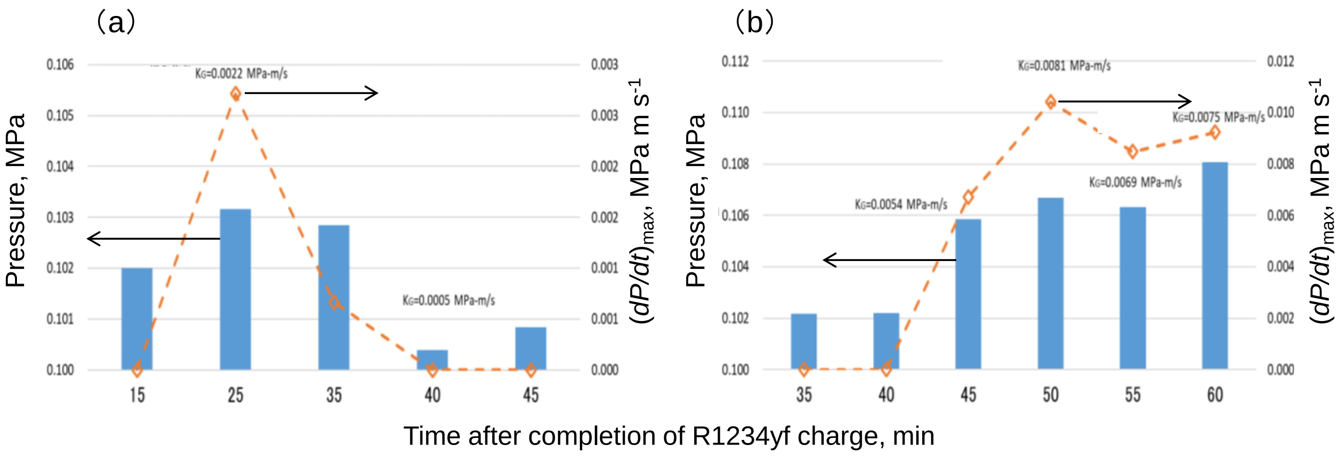

Fig. 5-33 Pressure rise and deflagration index (K_G) for the combustion of localized R1234yf as a function of time after the completion of R1234yf charge. Results obtained for charge amounts of (a) ¼ LFL and (b) ½ LFL.

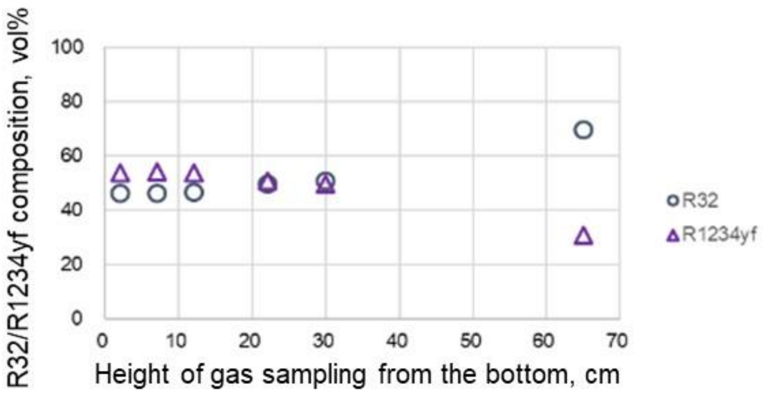

Fig. 5-34 Composition change of the R32/1234yf (50/50 vol%) blend charged from the vessel bottom. Gas sampling was performed ~30 min after charge completion. The charge amount and rate equaled 4.18 vol% (½ LFL) and 1 L min^{-1}, respectively.

Next, we evaluated flammability characteristics for the localized concentration distribution of the R32/1234yf (50/50 vol%) blend at an electrode height of 10 cm (Fig. 5-35). K_G values were obtained from the pressure data of the combustion experiment with a charge amount of ½ LFL and were one order of magnitude smaller than those obtained for pure R1234yf and R32 (0.8 and 1.1 MPa m/s, respectively) under full mixing conditions using a large closed vessel of the same shape[5-5)].

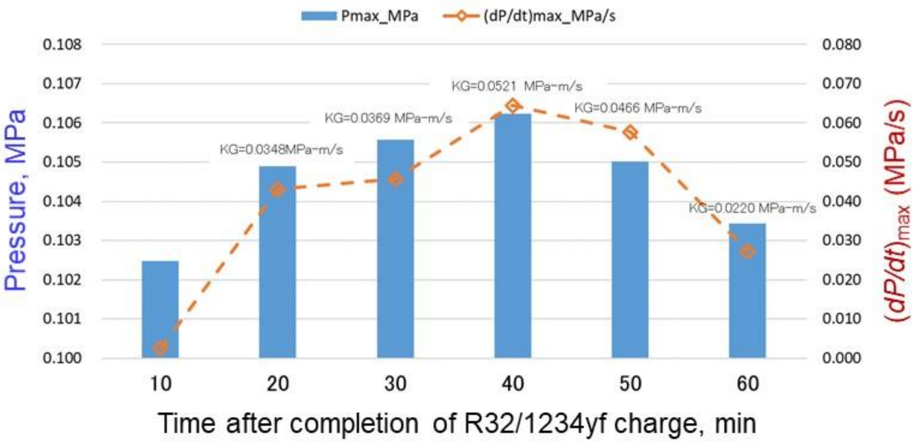

Fig. 5-35 Pressure rise and deflagration index (K_G) for combustion of localized R32/1234yf (50/50 vol%) as a function of time after refrigerant charge completion. Charge amount = ½ LFL.

Fig. 5-36 compares the combustion severity (maximum pressure rise and K_G value) of the R32/1234yf (50/50 vol%) blend and its individual components. Judging from the burning velocities obtained using the homogeneous mixture, this blend (with $S_{u,max}$ = 1.8 cm s^{-1}) showed a slightly higher K_G than R32 ($S_{u,max}$ = 6.7 cm s^{-1}) and R1234yf ($S_{u,max}$ = 1.5 cm s^{-1}). In addition, we suggested that the time during which the meaningful pressure rise was observed may be longer than that for each individual component. The flame sphere shape observed with the high-speed camera suggested that the combustion of this blend resembled that of R1234yf in the first half and that of R32 in the second half. Thus, we concluded that the slow-diffusing component may burn first.

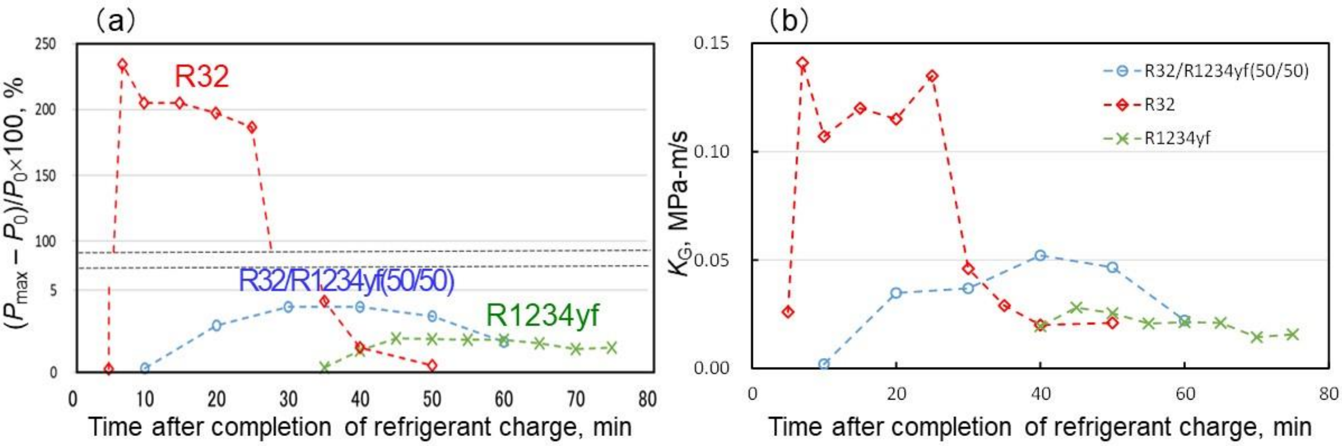

Fig. 5-36 Pressure rise and deflagration index (K_G) of the localized R32/1234yf (50/50 vol%) blend and its pure components as functions of time after refrigerant charge completion. Charge amount = ½ LFL.

References

5-1) EN 1839:2017, "Determination of the explosion limits and the limiting oxygen concentration (LOC) for flammable gases and vapours (2017).

5-2) K. Takizawa, N. Igarashi, K. Tokuhashi, and S. Kondo: Sci. Tech. Built Environ., 24(1), 97(2018).

5-3) K. Takizawa, N. Igarashi, K. Tokuhashi, and S. Kondo: Int. J. Refrig., 120, 370(2020).

5-4) ISO 6184-2: Explosion protection systems - Part 2: Determination of explosion indices of combustible gases in air (1985).

5-5) T. Saburi and Y. Wada: Proc. JRAIA International Symposium on New Refrigerants and Environmental Technology 2014, pp. 85-90 (2014).

6. RISK EVALUATION OF MINI-SPLIT AIR CONDITIONERS USING A3 REFRIGERANT CONDUCTED BY JRAIA

6.1 Introduction

In face of the growing momentum to broaden the use of refrigerants with much lower GWP, triggered by the Kigali Amendment to the Montreal Protocol, the Japan Refrigeration and Air Conditioning Industry Association (hereinafter referred to as "JRAIA") created a working group (hereinafter referred to as the "WG") to conduct risk assessment studies in July 2016. The purpose is to assess the safety of residential air conditioners using A3 refrigerants (hereinafter referred to as "air conditioners"). In conducting risk assessment, safety in each of the air conditioner's life stages has been evaluated to assure safety not only during product use but also during work on the product. IEC 60335-2-40 Ed. 7.0 provides that the volume of refrigerant used in an air conditioner using A3 refrigerant can be increased with use of a fan to circulate leaked refrigerant. The validity of this provision has been examined as well.

This report presents the results of the aforementioned studies and a summary of recommendations in averting unforeseeable event in risk assessment.

6.2 JRAIA and its activities and position in NEDO projects

In the risk assessment activities of the WG at JRAIA, the following are the issues that require attention. Since they exceed the scope of study by JRAIA's member companies, chiefly from the standpoint of the need to conduct actual experimental studies, research by universities and research institutes participating in NEDO has become necessary. The issues are itemized below.

The first is research on safety and risk assessment regarding combustion of flammable refrigerants, namely, quantification of the flammable regions in case of leakage of a flammable refrigerant from the indoor unit of an air conditioner. The research was conducted at the University of Tokyo (Chapter 2).

The second is research into quantification of the flammable region in case of leakage of a flammable refrigerant from the indoor unit of the air conditioner, conducted as safety and risk assessment research pertaining to incineration of flammable refrigerants. The research has been conducted at the University of Tokyo (Chapter 2).

The third is ignition probability of various ignition sources. JRAIA had based its decision on ignition probability on the minimum ignition energy and auto-ignition temperature of propane. However, more detailed study is necessary regarding ignition probability of equipment in actual use. Specifically, the study involves research into academic literature, web research, experimentation, numerical simulation, etc., regarding ignition probability from high-temperature surface of cigarettes or sparks from use of contact relays or switches in the presence of mixture of air with R290 that had leaked from air conditioners and stagnated. This research was conducted at Suwa University of Science (Chapter 3).

The findings of risk assessments conducted at the JRAIA WG have been applied to NEDO research in the respective areas. More specifically, the codes of simulations conducted by JRAIA (Chapters 6.3 and 6.4) were verified through leakage experiments at the University of Tokyo. The findings enabled early action in validating the relaxation of the provisions regarding allowable refrigerant charge for A3 refrigerants to be newly introduced in IEC 60335-2-40 Ed. 7.0. Furthermore, the research findings at Suwa University of Science aided in identifying the electric current/voltage conditions, as well as load conditions, for electrical components that can be excluded from ignition sources. Based on these findings, ignition sources were defined in the risk assessment herein (Chapter 6.6).

Although the content of other NEDO research programs could not be directly applied to the risk assessment study, beneficial knowledges were obtained. Specifically, research results on diesel explosion (Chapter 2) showed that it need not be added as a new risk. Additionally, assessment of physical hazards of true-size equipment (Chapter 4) helped gain knowledge regarding hazards levels at ignition. Furthermore, research in development of refrigerants that excel in safety and at the same time have low GWP (Chapter 5) were found to be effective alternatives to R290 and other A3 refrigerants studied under WG.

6.3 Refrigerant leak simulation in indoor environment

Refrigerant leak simulation was performed in an indoor environment[6-1)]. The study results here are used in risk assessment of air conditioner use and work on the appliance indoors.

As a typical environment of air conditioner use, the floor area was set at 7.0 m² (2.5 m × 2.8 m). Simulation was conducted, assuming use of R290 refrigerant in 200g, the maximum amount permitted under IEC 60335-2-40 Ed. 6.0 (hereinafter referred to as "IEC standard") for the aforementioned floor area when air is not circulated with a fan. Simulation was also performed with refrigerant amount of 500 g of R290, which achieves performance equivalent to a product using 1000 g of HFC refrigerant. The floor area in this case was set at 11.88 m² (3.0 m × 3.6 m) permitted when air circulation by fan is used under the revised IEC standard. In both cases, the ceiling height has been set at 2.2 m, with the indoor unit installed at the height of 1.8 m from the floor. The wall opposite the air conditioner location is assumed to have a gap under the door of width of 800 mm × height of 4 mm, and pressure boundary in size of 200 mm × 200 mm is assumed to be found in two locations on the ceiling surface. The leak rate was set at total amount leakage in 4 min that is adopted in the IEC standard. Analysis of the indoor model is shown in Fig. 6-1.

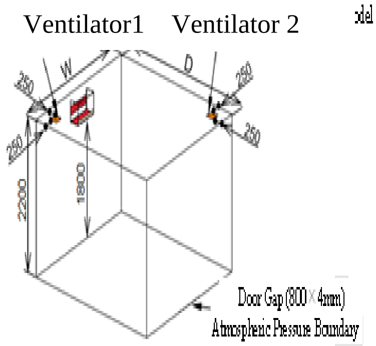

del

		Refrigerant Amount	
		200g	500g
W	m	2.5	3.3
D	m	2.8	3.6
H	m	2.2	2.2
Installation Height	m	1.8	1.8
Floor Area	m²	7.00	11.88

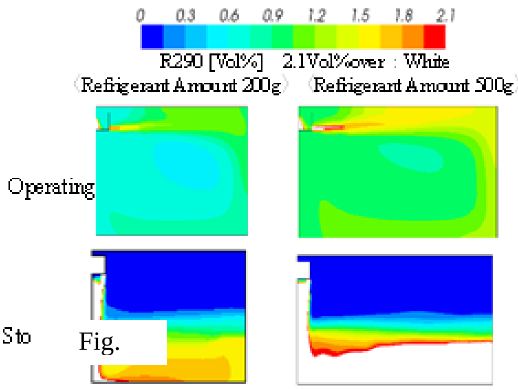

Fig. 2 Refrigerant Concentration Distribution after 4 Minutes

Fig. 6-1 Analysis space model

Refrigerant leakage analysis was performed for both when the air conditioner is not in operation (no air circulation) and during operation (with air circulation by fan). During operation, mixture of air and refrigerant is assumed to leak, and the air flow rate is calculated with Eq. (6-1) proposed by Colbourne et al.

$$\mathbf{Q} = \frac{8Y\sqrt{A_0}}{240}\left(\frac{m_C}{LFL}\right)^{3/4}\left(\frac{F^{1/4}}{1-F}\right) \tag{6-1}$$

Here, Q : Necessary circulation air volume (m^3/s)

A_0 : Air flow discharge surface area (m^2)

mc Refrigerant charge volume (kg)

LFL : Lower flammable limit (kg/m^3)

Y : Constant - Y=1.5 when leakage occurs outside the unit; Y=1.0 elsewhere; 1.0 used in this case

F : Safety coefficient - 0.5

Fig. 6-2 shows the difference in the distribution of refrigerant concentration with and without air circulation after total amount leakage (after 4 min). Without air circulation, flammable region was generated within 0.008 m from the floor surface with the refrigerant amount of 200 g and within 0.326 m with the refrigerant amount of 500 g. With air circulation, flammable region was generated in the range of roughly 0.1 m in the horizontal direction from air outlet opening of the indoor unit with refrigerant amount of 200 g, and in the range of roughly 0.3 m in the horizontal direction with refrigerant amount of 500 g. Without air circulation, refrigerant leaks downward from the indoor unit, resulting in the accumulation of flammable region on the floor surface. For this reason, the height of the flammable region from the floor surface is roughly the value obtained by dividing the flammable volume by the floor area.

As shown above, the indoor refrigerant leak simulation shows that the proposed equation by Colbourne et al., regarding air circulation of leaked refrigerant is effective in preventing generation of flammable region with significant size that could cause an ignition. However, attention is required toward possible hazards, depending on the location of the ignition source, since flammable region of length of roughly 0.1 – 0.3 m is generated near the air outlet opening of the indoor unit.

6.4 Refrigerant leak simulation in outdoor environment

Outdoor refrigeration leak simulation (on a balcony) was performed[6-2]. The study results here are used in risk assessment of use and work in an outdoor environment.

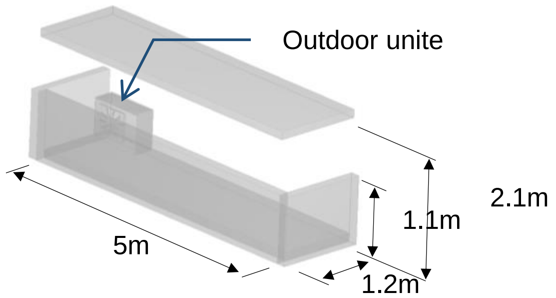

Fig.6-3 CFD model of balcony

Residential housing in Japan consists chiefly of private homes and apartment housing units. Outdoor units of air conditioners are installed in private homes in various ways, such as on the balcony, directly on the ground, mounted on a wall, mounted on the roof or suspended under the eaves. In apartment housing, the outdoor unit may be installed on the balcony, on shared hallway, mini-balcony created specifically for air conditioner installation, etc. Of these locations, leaked refrigerant is most likely to accumulate in a balcony surrounded by walls. Especially in the case of an apartment or condominium unit, the outdoor unit of the air conditioner cannot be installed on shared space in order to assure safety in case of evacuation. For this reason, it is installed on the balcony in many cases. The refrigerant leak simulation was therefore performed assuming that the outdoor unit was installed in a balcony surrounded by walls in 3 directions. Fig. 6-3 shows the simulation model for balcony installation. The balcony is assumed to measure 5 m in width, 1.2 m in depth and ceiling height of 2.1 m, with the handrail located at the height of 1.1 m. If the balcony is connected to the balcony of the adjoining apartment, there is a gap of 100mm at the bottom of the partition between balconies. Although drainage measuring 50 mm in diameter has been created on the floor, the simulation represents leakage without such drainage, which increases the severity of the risk. Three cases of outdoor unit installation were assumed — installation directly on the balcony floor, mounting on the wall and suspension under the eaves.

Refrigerant used is R290, in amounts of 200g, 500g or 1000g and with leak rate set at the value of total amount leakage in 4 min. Refrigerant leakage is assumed to occur uniformly from the air inlet opening of the heat exchanger, with leakage concentration at 100 vol% of R290.

The results of the analysis are shown in Fig. 6-4. If an outdoor unit charged with 500 g of refrigerant is installed on the floor, the duration of the flammable region reached 1900 seconds. If the installation height was higher than the floor surface, the duration of the flammable region shortened to 1206 seconds when mounting on the wall and 939 seconds when suspended under the eaves. When installed on the floor, on the other hand, the mean flammable volume for refrigerant amount of 1000g differed little with the result for refrigerant amount of 500g. This is believed to be due to the formation of concentration higher than the upper flammability level (UFL) closer to the floor surface in the case of 1000g. When the outdoor unit fan is operating at the minimum air flow rate, very small flammable region was generated only when the refrigerant amount was 1000 g.

Installation Condition	Leakage Amount	200 g		500 g		1000 g	
	Time	240 sec	600 sec	240 sec	600 sec	240 sec	600 sec
Floor mounted	Concentration distribution	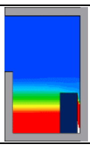	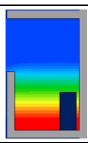	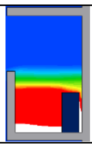	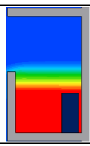	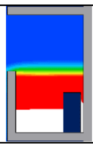	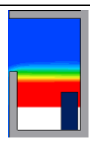
	Duration	776 sec		1900 sec		3546 sec	
	Averaged volume	1.22 m^3		2.96 m^3		2.73 m^3	
Steel stand mounted	Concentration distribution	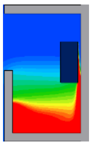	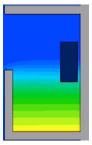	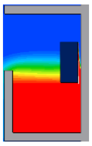	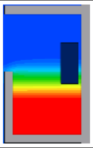	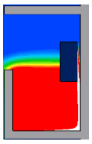	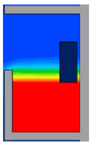
	Duration	292 sec		1206 sec		2126 sec	
	Averaged volume	0.20 m^3		2.83 m^3		3.87 m^3	
Eaves mounted	Concentration distribution	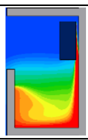	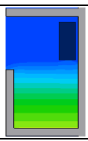	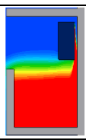	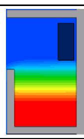	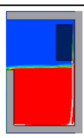	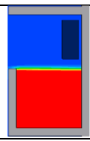
	Duration	260 sec		939 sec		1711 sec	
	Averaged volume	0.05 m^3		2.47 m^3		3.73 m^3	

Fig. 6-4 Concentration distribution, the duration and time averaged volume of flammable region within the balcony for different installation conditions

6.5 Method of risk assessment

6.5.1 Risk assessment process

Risk assessment is a process that involves identifying as many as is possible scenarios that lead to ignition and quantifying ignition probability by multiplying refrigerant leak probability, spatial encounter probability representing the spatial distribution of the flammable region and temporal encounter probability between the ignition source and flammable region. The ignition probability quantified in this fashion then undergoes re-examination until it is reduced to a tolerable level or lower, followed by decision on safety measures that reduce the risks.

This chapter gives the definition of the risk assessment model, the definition of the tolerable level, the refrigerant leak probability and the method of calculating the ignition probability necessary for risk assessment. Explanation will be given also of the product life stages that are covered in risk assessment.

6.5.2 Defining the risk assessment model

This risk assessment model employs the wall-mount type air conditioner chiefly for household use, commonly known as the mini-split air conditioner. The rated cooling capacity was set to be in the 2.2 kW to 5.0 kW class. R290 is assumed to be used as refrigerant. Two installations scenarios were selected — installation of an air conditioner charged with 200 g in a room size of 7m², that IEC standard sets forth as not requiring safety measures, and installation of an air conditioner charged with 500 g, that is equivalent in performance to an HFC refrigerant system with 1000 g charge, in room size of 11.88 m².

6.5.3 Setting the tolerable level

The number of air conditioners in the Japanese market is assumed to be 100 million. Assuming that all ignition accidents are fatal, the tolerable value on usage stage is set at 10^{-10} units/y, which is the level at which ignition accidents occur once every 100 y or less for the number of air conditioners in the market. Regarding product transport and storage, repair and disposal, excluding actual product use, the workers involved undergo specialized training. For this reason, the tolerable value is assumed to be raised by one digit compared to actual usage and is set at 10^{-9} units/y.

6.5.4 Refrigerant leak probability

The refrigerant leak probability was set at 0.4 %/y, based on study results. In terms of types of leakage, the percentages of slow leaks and rapid leaks in an indoor unit were set at 94% and 6%, respectively. In the case of the outdoor unit, the percentages of slow leaks and rapid leaks (including burst leaks) were set at 88% and 12%, respectively, based on the same study results.

Refrigerant leakage caused by work on the product occurs due to working execution error, such as error in pipe connection. Hence, the refrigerant leak probability is calculated from the frequency of human error based on the scenarios.

6.5.5 Calculation of ignition probability

Ignition probability is calculated by multiplying spatial encounter probability, temporal encounter probability and refrigerant leak probability, based on Eq. (6-2). Also, the spatial encounter probability is calculated with Eq. (6-3).

$$P = P_s \times P_t \times P_r \tag{6-2}$$

$$P_s = V_v / V_g \tag{6-3}$$

The symbols used are described as follows.

- P: Ignition probability -
- P_r: Refrigerant leak probability -
- P_s: Spatial encounter probability -
- P_t: Temporal encounter probability -
- V_g : Volume of target space m^3
- V_g : Mean flammable volume m^3

The details in calculating the ignition probability are described in the paper about the risk assessment of built-in refrigerated display cabinets Chapter 7.

6.5.6 Target life stage

Generally speaking, risk assessment covers the product life stages from manufacturing to disposal. Fig. 6-5 shows the scope of study in the risk assessment herein and what is excluded. The scope of study covers transportation and storage, installation, indoor and outdoor usage, repair and disposal. The items italicized in red in Fig. 6-5 are excluded in the risk assessment. The reasons for exclusion are the following.

- Product manufacturing: The manufacturer possessing expertise.
- Air conditioner relocation: Assumed to be basically the combination of transportation and installation.
- Disposal: The disposal process is divided into removal, transportation to the recycling plant and disassembly.

However, the risk assessment study covers removal only.

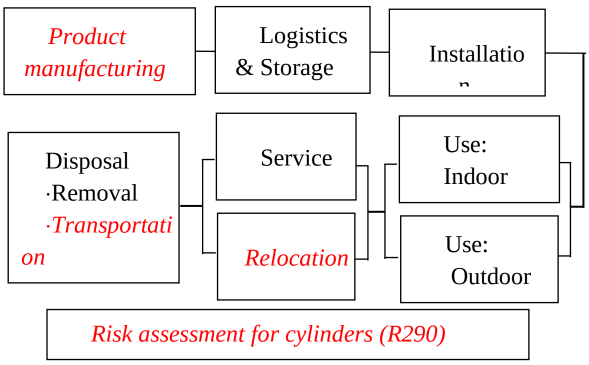

Note: The stages in red area are not included in the JRAIA risk assessment

Fig. 6-5 Life stages covered by risk assessment

6.6 Risk assessment

6.6.1 Calculation of ignition probability and safety measures in product usage

6.6.1.1 Calculation of indoor ignition probability during usage stage

In calculating the indoor ignition probability during product usage, the flammable volume-time integration obtained by refrigerant leak simulation described in Chapter 6.3 has been used. Refrigerant leak simulation was performed with change in the leak rate from a wall-mount indoor unit showed that, in the case of slow leak, the mean flammable volume is smaller by three digits in comparison to total amount leakage in 4 min. Therefore, the mean flammable volume to be used in risk assessment was calculated as the weighted average with attention to this finding. In the indoor environment, there are additional factors to be taken into consideration, such as door opening/closing with human movement, use of electric fans while air conditioner is in use, etc. Although these are inclined to minimize flammable space, they have been excluded since their contribution to the model cannot be quantified.

Ignition sources in the room have been studied. The ignition sources for R290, which is an A3 refrigerant, are the open flame, high-temperature surfaces and sparks. Table 6-1 shows the potential ignition sources in the room. Open flame refers to cigarette lighters, candles and gas cooktops, which ignite without fail when in contact with either A2L or A3 refrigerant. In the high-temperature surface category are electric stoves and cooking plates and grills. Due to low auto-ignition temperature of the refrigerant, A3 refrigerants are highly likely to ignite. Sparks are classified into electrostatic sparks from human body and electric sparks from electrical devices. The electric spark category includes sparks from brush motors in vacuum cleaners, etc., sparks from electrical device thermostats and relay contacts, sparks by plugging/unplugging of power plugs, and sparks from turning light switches on/off. From Table 6-1, ignition sources were identified through comparison of the height of the flammable region found through refrigerant leak simulation and the height of location of the ignition source in the room. When there is no air circulation by fan, the flammable cloud is generated between the space directly below the indoor unit and the floor. For this reason, heat sources used immediately below the indoor unit are likely to become an ignition source. As a result of examination into this matter, the probability of such an ignition source used immediately below the indoor unit was set at 10 %.

The indoor ignition sources during usage were cigarettes, oil stove and candles in the open flame category, electric stove in the high-temperature surface category, and laser printers, electric shavers, electric kotatsu, electric stoves, irons, hairdryers, air purifiers, dehumidifiers, vacuum cleaners, electric carpets, cooking appliances, lighting switches and plugging/ unplugging of power plugs in the spark category. The duration and frequency of each of these ignition sources were determined with attention to lifestyles. Items that were determined not to become ignition sources due to the height of their locations are, for example, gas cooktops, cooking appliances, static electricity spark caused by contact with the doorknob and light switches being turned on/off.

The study showed that the ignition probability was 2.61×10^{-11} when refrigerant amount is 200g, at the tolerable value or lower without air circulation by fan. On the other hand, ignition probability without safety measures exceeded the tolerable value when refrigerant amount was 500 g. However, with air circulation by fan as a safety measure, the ignition probability became 1.32×10^{-11}, at tolerable value or lower.

Table 6-1 Potential ignition sources

Types of Ignition Sources		Potential Ignition Sources
Open flames		Cigarettes during smoking (including lighters), candles (for religious event and aromatherapy)
		Oil stoves, gas cooktops, portable butane stoves
High-temperature surfaces		Electric stoves
Sparks	Charges	Static electricity, laser printers
	Brush motors	Electric shavers, printers
	Thermostats	Kotatsu (tables with electric feet warmers), electric stoves, irons, toasters, hairdryers
	Relays	Air purifiers, dehumidifiers, vacuum cleaners, dryers, electric carpets, rice cookers, microwave ovens
	Others	Plugging/unplugging of power plugs, on/off of lighting switches

In the review conducted by WG for production of a detailed JRAIA report, issues such as those listed below were found in cases of indoor use. Work is underway for recalculation of ignition probabilities.

- Study was conducted on installation space that consists only of a small room and a small kitchen. Although hazards cannot be found in other installation environments, a general ignition probability for indoor usage must be calculated.
- The microwave oven was previously excluded from ignition sources since the height of the ignition source is lower that the height of the location of flammable region. However, there is possibility of the appliance becoming an ignition source, depending of the positional relationship with the air conditioning unit, if it comes in direct contact with leaked refrigerant. For this reason, further review is required.
- Since risk assessment has been conducted alongside NEDO research into ignition sources and the FTA was

based on knowledge obtained up to that point in time, it does not reflect the knowledge gained in NEDO research at its completion. Risk assessment with the additional information is necessary.

- The probability of the air circulating fan stopping in operation stopping is presently referred to as fan failure probability. It is necessary, however, that risk assessment take into account the flammable volume-time integration which covers the time delay from leak detection to fan operation. Additionally, fan operation is triggered by leakage detection by a leakage detector. The detector is to set off alarm in case of failure and to be sensitized with normal aging. However, there are cases of detector losing sensitivity due to oil fume, etc., in the kitchen, and influence of such factors must be taken into account.
- Scenario needed involving the use of a unit containing refrigerant amount larger than the refrigerant amount allowed in relation to floor space.
- Scenario needed in which a user charged with static electricity touches an indoor unit with static buildup, in order to check the cause of poor air conditioner performance or to clean the unit.
- Scenario needed for use of residential air conditioners in a store for commercial use.

6.6.1.2 Calculation of outdoor ignition probability

In calculating the outdoor ignition probability during usage, the flammable volume-time integration obtained by refrigerant leak simulation described in Chapter 6.4 has been used. The factors that are likely to affect the outdoor flammable region are the gap below the balcony partition, natural wind, etc. Of these, natural wind normally blows around the outdoor unit and is a major factor that affection ignition probability. Fig.6-6 shows the annual cumulative time (hours) of wind occurrence for each wind velocity in leading Japanese cities. Although occurrence varies by region, the highest frequency is wind speed of 1.0 m/s to 2.0 m/s. The data shows that window occurrence is 2.5 % for 0.3 m/s or lower, 2.3 % for over 0.3 m/s to 0.5 m/s and 95.2 % for over 0.5 m/s. Refrigerant leak simulation was also performed for wind velocities of 0.3 m/s and 0.5 m/s. Ignition probabilities were calculated for wind speed of 0.3 m/s or lower (represented by 0 m/s), 0.3-0.5 m/s (represented by 0.3 m/s) and over 0.5 m/s (represented by 0.5 m/s). Ignition probability was calculated by using the values as weighted averages,

Potential ignition sources in the outdoor balcony are cigarettes smoked by the user, open flame of gas or oil water heater and electric sparks caused in relation with the outdoor air conditioning unit. Additionally, another probability is electrostatic spark caused when a person touches a doorknob made of metal. Of these, open flame of gas or oil water heater and sparks were excluded from ignition sources due to air being circulated with operation of the incineration fan. Also, the outdoor air conditioning unit was excluded as well, due to a report showing that an outdoor unit in the flammable region does not become an ignition source.

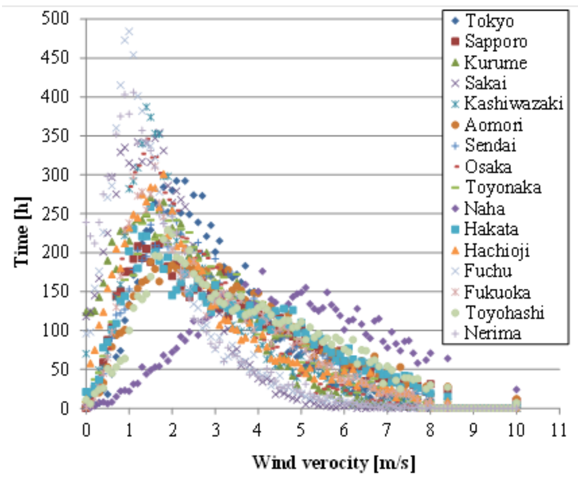

Fig.6-6 The time length of each wind velocity in 16 cities in Japan

As a result, the ignition probability when refrigerant amount is 500g was 1.15×10^{-11}, the tolerable value or lower when without safety measures. This is due to the fact that there are very few ignition sources outdoors. As described in Chapter

6.3, the outdoor balcony holds the possibility of generation of a large flammable region. For this reason, unforeseen installation conditions may lead to extremely dangerous situation.

In the review conducted by WG for production of a detailed JRAIA report, issues such as those listed below were found in cases of outdoor use. Work is underway for calculation of ignition probability once again.

- The case of a balcony without gaps that is regarded to have the highest in risk level was examined. It is necessary, however, to calculate the ignition probability of leakage from a balcony that is connected to that of the next residential unit to form a flammable region also in the next balcony.
- General ignition probability for outdoor usage must be calculated, to also cover installations in locations other than the balcony.
- Attention should also be paid to ignition sources that have emerged with COVID-19 and change in lifestyle (such as camping on the balcony), as well as use of fireworks, candles, barbecuing, golf swing practice (electrical sparks from contact with floor surface). Since risk assessment has been conducted alongside NEDO research on ignition sources and the FTA was based on knowledge obtained up to that point in time, it does not reflect the knowledge gained in NEDO research at its completion. Risk assessment with the additional information is necessary.
- Although flammable region is assumed not created while the air conditioning unit is in operation because of air circulation by the outdoor unit fan, study should be conducted into whether flammable region is created when the wind direction adjusting plate is installed for upward air movement.
- The scenario of refrigerant leakage on the balcony must take into account the possibility of the refrigerant flowing through the rainwater pipe and creating a flammable region at the end of the pipe.
- Review of refrigerant leakage scenarios into whether adequate study has been conducted on possible hazardous situations resulting from the relationship between balcony space and projected refrigerant amount (being too large).
- Review into whether the probability of smoking in the balcony is estimated properly.

6.6.1.3 Summary on usage stage

The ignition probabilities for both indoor and outdoor usage have been compiled in Table 6-2. In the room during usage, taking into account the height location of the ignition source, the magnitude of discharge energy and relationship between leak rate and flammable volume-time integration, ignition probability for 500 g of R290 fell to the tolerable value or lower if air circulation by fan is introduced as a safety measure. In outdoor usage, ignition probability for 500 g of R290 fell to the tolerable value or lower by considering natural wind. Risk assessment was also carried out for 1000 g of R32. The results have been included in Table 6-2 as well.

However, review by WG in production of the detailed JRAIA report showed the issues mentioned earlier and prompted work to recalculate ignition probabilities.

Table 6-2 Ignition probability of usage (Tolerable value; 1×10^{-10})

Refrigerant	R290 with countermeasure		R32
Category	Mini-split AC (wall mounted)		
Refrigerant amount	200 g	500 g	1000 g
Usage (indoor)	2.61×10^{-11}	1.32×10^{-11}	1.68×10^{-13}
Usage (outdoor)	7.03×10^{-14}	1.15×10^{-11}	1.38×10^{-21}

6.6.2 Calculation of ignition probability and safety measures during work on the product

Risk assessment for stages other than usage, namely, transportation and storage, installation, repair and disposal is described here. Since the transportation and storage stage has very few items shared in common with other work-related stages, risk assessment was carried out separately for this stage. Also, flammable volume-time integration calculated in the leak simulation described in Chapters 6.3 and 6.4 (without air circulation by fan) was used for risk assessment of installation, repair and disposal. Because leakage during work is caused by error in pipe connection, etc., and is likely to become rapid leak, the flammable volume-time integration for total amount leakage in 4 min was used. Since there are ignition sources found in all of the work-related stages and those that are unique to each work-related stage, scenarios that lead to ignition were created for each work-related stage. Based on each scenario, the ignition sources were identified for each stage, and the ignition probabilities calculated.

6.6.2.1 Scenario for transportation and storage stage

In the transportation and storage stage, work proceeds in the order shown below, following completion of the product at the factory.

i) Shipment from the factory (truck transportation)
ii) Storage to a medium-sized or large-sized warehouse
iii) Shipment from a medium-sized or large-sized warehouse for delivery to a retail store, etc. (truck transportation)
iv) Storage in a small-sized warehouse at a retail store, etc.
v) Shipment from a small-sized warehouse for delivery to the installation location (transported by a small vehicle)

Of these five steps, the probability of creation of an ignition source and refrigerant leakage from the product (a refrigerant-charged outdoor unit) occurring simultaneously is likely during the storage at the medium-sized warehouse, storage in the small-sized warehouse and transportation by minivan.

Storage locations for air conditioners are classified into medium-sized warehouses (1000 m^2) used for temporary storage following acceptance of shipment from factories in Japan or overseas and small-sized warehouse (15 m^2) used for storage at each sales location. Air conditioners are handled in the warehouse by forklifts or trolleys. In a medium-sized warehouse, it is assumed that 5 people work 8 hours per day for 20 days a month and, in a small-sized warehouse, 2 people work 2 hours per day for 20 days a month.

In transportation by minivan, the internal volume is assumed to be 2.9 m^3, the number of persons necessary for loading and unloading product to be 2 and to be on board the vehicle, the average transportation time to be 2 hours, and the frequency of transportation by minivan to be 100%. In truck transportation, it is assumed that, if flammable region is generated in the transport environment, ignition source is not found within the flammable region and therefore ignition risk does not exist. Also, product unloading has been eliminated in the scenario, due to the fact that indoor air begins to circulate and diffuse immediately with opening of the cargo door, making ignition probability negligible.

In the review conducted by the WG for production of a detailed JRAIA report, however, issues such as those listed below were found in transport and storage. Work is underway for calculation of ignition probability once again.

- Review into possibility of extraction leak in the possible ignition sources.
- Study into the possibility of refrigerant leakage caused by damage of aged pipe from vibrations during transport and storage for reuse or disposal.
- In shipping by truck, ignition sources were previously assumed not to be present in the cargo compartment of a truck. It is necessary, however, to study into scenarios that have not been projected, such as ignition from contact sparks between nails that protrude from pallets or skids and the compartment floor surface. If ignition risk is found, attention is required on the risks involved in transport of equipment piled in stacks and refrigerant flowing out of the compartment when the doors are opened for unloading and creating a flammable region nearby the truck.
- Although it is possible to entrench in workers the work instructions in transportation and warehouses under the control of the manufacturer, it is necessary to consider the possibility that this may not be possible outside the control of the manufacturer.

6.6.2.2 Scenario for installation stage

Installation of an air conditioner is generally executed in the procedure below.

i) Inspection of the installation location and transportation of the indoor and outdoor units to the location

ii) Attachment of the installation panel for the indoor unit, and a hole drilled on the wall

iii) Attachment of circuitry on the indoor unit, pipe connection and installation on the wall

iv) Attachment of circuitry on the outdoor unit and pipe connection

v) Evacuation and refrigerant leakage inspection

vi) Opening of the operating valves in the outdoor unit, and pre-charged refrigerant in the outdoor unit charged into the system

vii) Power turned on for test operation

The frequency of installation is assumed to be once in 10 y, based on the standard usage period defined by the design of the mini-split air conditioner. The work time is assumed to be 1.5 h indoors and 1.5 h outdoors, or a total of 3 h.

In the review conducted by the WG for production of a detailed JRAIA report, however, issues such as those listed below were found in the installation scenario. Work is underway for FTA review and calculation of ignition probability once again.

- Although scenarios have been created for the most hazardous installation environments, the general ignition probability rate for installation must be calculated, to examine into whether there are hazardous situations in other environments.
- In installation, attention is directed on the probability of error, such as mistaken air purge, inadequate flare joint work on existing pipes and flare joint processing error.
- Scenarios are developed for refrigerant leakage caused by failure in hand tightening and ignition caused by sparks from spanners colliding with each other, tools falling, etc.
- Probability of workers being unaware of leakage has been examined. However, attention must be directed to the possibility of formation of a flammable region when a worker notices the leak and tries to tighten with a spanner harder, etc., raising the possibility of ignition.
- Static electricity occurrence must not be limited to those that stem from workers but to include contact with exterior metal objects as well.
- The scenario of electric screwdriver being used for pipe connection by removing the front grille and attaching it later.
- Attention is required to the probability of a portable leakage director not working properly (failure, etc.)
- Study of ignitability of leakage from appliances outside the refrigerator that is not made explosion-proof.
- As an ignition source stemming from installation or maintenance work, attention is required to the use of the vacuum cleaner after completing work involving boring holes.
- Risks involved in damage of pipes during transport, etc., is to be taken into account.
- As ignition source during installation work, study should be conducted into the lack of attention to vacuum pump and contact involving tools.
- In scenarios on refrigerant amount, review should be conducted into whether sufficient study has been conducted on cases of possible hazard caused by the relationship between the floor space of the balcony and projected refrigerant amount (use of large refrigerant amount).

6.6.2.3 Scenario for repair stage

Repair work for the indoor unit is assumed to consist of indoor unit replacement, which refrigerant may be leaked when the pipe is disconnected, circuit board replacement by the service personnel using an electric driver and panel replacement during which electrostatic spark may be created by the worker.

Repair work for the outdoor unit is assumed to consist of compressor and valve replacement that requires brazing and outdoor unit replacement that the refrigerant may be leaked with pipe disconnection.

The frequency of repair is assumed to be 10 % from the study results, and work time is one h for each type of work.

In the review conducted by WG for production of a detailed JRAIA report, however, issues such as those listed below were found in the repair scenario. Work is underway for FTA review and recalculation of ignition probabilities.

- Although attention has been directed to installation environments that are likely to involve high-level risks, study should be conducted on whether there are hazards in other environments and to calculation of general ignition probability in the repair stage.
- Attention is to be paid to the scenario of inadequate refrigerant recovery resulting in leakage of refrigerant remaining in oil, with the removal of the joint on the interior unit side, raising the possibility of contact with an ignition source.
- It is necessary to include the scenario of detecting leakage with a portable leakage detector, in which detection prompts the person to open the window, stop work, etc., and create a flammable region which may come into contact with an ignition source.
- There are ignition sources that have not been examined with application of knowledge from NEDO research regarding final ignition sources. Risk assessment with the additional information is necessary.
- Although brazing conducted in installation work is limited to compressor exchange, attention is required to exchange of heat exchanger and pipe assembly.
- Attention is needed on scenario on work performed by non-professional workers.

6.6.2.4 Scenario for disposal stage

The general workflow for the disposal of air conditioners is shown in Fig. 6-7. The disposal stage is divided into removal, transportation to the recycling plant and disassembly. However, risk assessment here focuses on removal only. The other steps will be described in Chapter 6.6.

In the disposal of an air conditioner, the first step is to collect the refrigerant by pumping down into the outdoor unit. If the air conditioner is damaged and does not operate, operating valves in the outdoor unit are closed, and refrigerant in the indoor unit and the pipe connecting the indoor and outdoor units is released into the atmosphere. Next, the connection pipe is removed, and the indoor and outdoor units are removed from the installation location. The removed air conditioner is moved out of the building and, in compliance with the Japanese recycling law, transported to the recycling plant and disassembled.

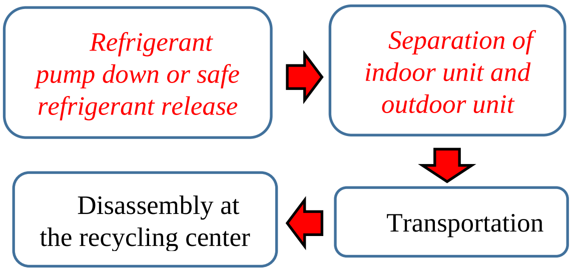

Fig. 6-7 Flow of disposal

Of the steps involved in removal and disposal, the removal work involving pump down and disconnection of the indoor and outdoor units, shown italicized in red in Fig. 6-7, is assumed in risk assessment. The frequency of removal is assumed to be once in 10 y, and work time is one h.

In the review conducted by WG for production of a detailed JRAIA report, however, issues such as those listed below were found in the disposal scenario. Work is underway for FTA review and recalculation of ignition probabilities.

- Although the scenario covers the most hazardous installation environments, it is necessary to examine whether study into other environments is adequate.
- The air conditioner removal environment is limited to a small room with a small kitchen. However, study is necessary into hazards in other removal environments and to the calculation of general ignition probability in the disposal stage.
- Static electrical charge is assumed to become an ignition source only when in contact with the doorknob. Review is necessary into whether there are inadequacies in the scenario.
- Re-examination is necessary into possible problems in the scenarios of refrigerant leakage. There is possibility of refrigerant leakage during work using spanners, as well as probability of workers being unaware of leakage. However, attention must be directed to the possibility of formation of a flammable region when a worker notices the leak and tries to tighten the joint harder with a spanner, etc., raising the possibility of ignition.

- Re-examination into whether the scenario of ignition during refrigerant recovery is adequate.
- When leakage is detected with a portable detector and work is suspended, a flammable region is formed from the time leakage is detected to suspension of work, a scenario of contact of the region with ignition source must be examined.
- Re-examination into problems in projected numerical values caused by, for example, the probability of malfunction of air discharge hose at the joint differing in value with the probability of inappropriate location of the hose tip.
- Re-examination is also necessary for problems in ignition source settings, such as the probability of the gas oil boiler becoming an ignition source.

6.6.2.5 Ignition sources in each work stage

Scenario for each work stage was developed, and possible ignition sources identified. The duration and frequency of the leading ignition sources are shown in Table 6-3. The ignition source shared by all work stages was assumed to be cigarette smoking. However, cigarette smoking is assumed to be prohibited while working indoors. During transportation, electrostatic spark is assumed to be created with ignition key contact. In storage, oil stove is assumed to be used. In addition to the ignition sources during use, circuit connection work, use of electric driver, brazing burner, etc., were assumed to be ignition sources in installation, repair and removal.

Table 6-3 Ignition sources of work

Ignition source		Motion time (s)	Number of motions (times/day)	remarks
Common: Smoking of worker		4.5×10^{1}	1time/h	Number of smokers 1 / person / h, lighter ignition 5 seconds, Tobacco red fire 40 seconds, smoking rate 28.2%
Transport (wagon car)				2 hours, 2 workers
	Static electricity (contact of key and door handle)	1.0×10^{-6}	4 time/person	Key after rubbing the seat, door contact 3 times / person, After undressing key, door contact 1 time / person
Storage (small warehouse)				2 hours, 2 workers, 15 m^2
	Oil stove	3.6×10^{3}	2	Usage period 120 days / year. Oil stove usage rate 25%
Install, repair, removal				1 hours, 1 workers
	Ignition source during use			See "Ignition source during use"
	live-line working	5.0×10^{-3}	1time/h	Occurrence rate of forgetting to check breaker / energization 10^{-4}
	electric screwdriver	3.0	2	Attaching and detaching screws. Incidence 50%
	Brazing burner	1.2×10^{2}	2	Removal and installation 2times

6.6.2.6 Calculation of ignition probability in each work stage and safety measures

The ignition probability for each work stage was calculated. Because the ignition probabilities exceeded the tolerable value, safety measures were studied. In addition to training regarding ignition sources for flammable refrigerants, implementation of safety measures described in Table 6-4 for transportation and storage and those in Table 6-5 for installation, repair and removal reduce the ignition probability to the tolerable value or lower. The ignition probability for each work stage after implementing safety measures is shown in Table 6-6. It became evident that, with appropriate implementation of safety measures during work, the ignition probability can be reduced to the tolerable value (1×10^{-9}) or lower. JRAIA is scheduled to develop standards based on the results in the near future.

Table 6-4 Safety measures for transport and storage

Safety measure	Method	Procedure
Label for fire attention	A fire caution label is displayed on the air-conditioned outdoor unit.	All procedure
Elimination of ignition sources	Education to eliminate ignition sources in the same room in the warehouse according to guidelines etc.	Storage for warehouse
Use of portable leak detector	Regulations for ensuring ventilation, reducing the refrigerant concentration, and carrying and using a portable leak detector by opening windows when a refrigerant leak occurs.	Transportation by wagon car
Measures to prevent electrification and ignition in the car	In order to prevent discharge ignition by a charged human body, a metal start key is insulated, or a discharge plate is installed near the key cylinder on the vehicle body.	Transportation by wagon car

Table 6-5 Safety measures for installation, repair and removal

Safety measure	Method
Use of portable leak detector	If refrigerant leaks during work, the combustible area is reduced by ensuring ventilation by stopping the work and opening windows.
Wearing work gloves against static electricity	In order to reduce the generation of static electricity by workers during work, it is stipulated to wear an antistatic carrier.
Prohibition of using brush motor type electric screwdriver	Prohibition of using a brush motor type electric screwdriver that is an ignition source

Table 6-6 Ignition probability of working with countermeasures

(Tolerable value; 1×10^{-9})

Refrigerant		R290 with countermeasures		R32
Category		Mini-split AC (Wall mount)		
Refrigerant amount		200g	500g	1000g
Logis-tics	Warehouse	5.1×10^{-13}	1.1×10^{-10}	2.3×10^{-14}
	Van	8.9×10^{-11}	1.8×10^{-10}	5.1×10^{-13}
Installation	in	1.2×10^{-12}	1.9×10^{-10}	3.9×10^{-14}
	out	8.5×10^{-12}	4.5×10^{-11}	2.7×10^{-15}
Service/Repair	in	2.7×10^{-15}	4.2×10^{-12}	1.9×10^{-17}
	out	2.6×10^{-10}	2.6×10^{-10}	2.0×10^{-12}
Removal	in	2.7×10^{-12}	1.3×10^{-12}	2.2×10^{-16}
	out	9.2×10^{-13}	2.3×10^{-12}	4.7×10^{-15}

However, review by the WG in production of the detailed JRAIA report showed the issues mentioned earlier and prompted work to recalculate ignition probabilities.

6.7 Consideration and proposal on events unforeseen in the risk assessment study

Risk assessment is carried out on the assumption that operation is executed appropriately, in accordance with the projected scenarios. In reality, however, there is possibility of events unforeseen in the risk assessment study. The consideration and proposal for such events are as follows.

6.7.1 Consideration of events unforeseen in the risk assessment study

The following describes the events that are unforeseen in the risk assessment study. It is easily imaginable that such an event will increase ignition accidents in real-life situations. However, it is difficult to quantify its hazard level.

i) Disposal and recovery

There are cases of the air conditioner being handled through unauthorized channels for disposal. According to a survey by the Ministry of Economy, Trade and Industry and the Ministry of Environment of Japan, nearly 60% of air conditioners are recovered and processed through unauthorized channels. In these cases, whether refrigerants are properly recovered and treated is unclear. In order to avoid the high handling cost after recovery, the possibility of an increase in ignition accidents cannot be denied if refrigerants are emitted to atmosphere in ways other than the approved method. In addition, similar risks emerge when recycled or scrapped by waste material recovery operators.

ii) Installation and repair

The risk assessment assumes that the workers who have received training regarding the knowledge, skills, etc., perform the installation and repair of air conditioners under normal mental state. However, in the case of an enduser installing by himself or a moving company transferring the location of an air conditioner, work may be done by an untrained person. Furthermore, error rate increases if work is performed hurriedly. In risk assessment, human error is generally assumed to be 10^{-3}. However, the ratio of human error is likely to increase beyond the assumed level in such cases.

iii) Unforeseen accidents

Generally, arson of an air conditioner outdoor unit and theft of an installed outdoor unit in use are also not considered in the risk assessment.

6.7.2 Proposals for unforeseen events in risk assessment

Unforeseen events were also not considered in the risk assessment of air conditioners using R32, an A2L refrigerant widely used in the market. Nevertheless, ignition accidents have not occurred in reality. This is believed to be due to the fact that R32 is less flammable than A3 refrigerants for the following reasons.

i) There are fewer ignition sources for R32 in comparison to A3 refrigerants.

ii) The minimum ignition energy for R32 is comparatively larger than that for A3 refrigerants.

iii) The LFL for R32 is 13.5%, which larger than for A3, and therefore does not generate flammable region easily.

On the other hand, R290 has many types of ignition sources and is easily ignited due to its small minimum ignition energy, which is roughly 1/80 of that for R32. Additionally, its LFL is small (2.02%) and therefore can easily generate a flammable region. In order to commercialize air conditioners compatible with R290, it is important how to eliminate the unforeseen events mentioned previously.

The following is a proposal to commercialize R290 as a refrigerant.

i) Reinforcement of the scheme for proper recovery and handling of air conditioner refrigerant

The infrastructure for air conditioner refrigerant recovery and handling, including the Home Appliance Recycling Law, requires further review. It is particularly important to assure safety in case of human involvement.

ii) Qualification scheme for workers who engage in installation and repair of air conditioners

A qualification system involving education and hands-on training must be established for work handling flammable refrigerants. Although the qualifications system may be managed by an organization related to refrigeration and air conditioners, a government-approved program is desirable.

6.8 JRAIA standards

6.8.1 The background of the JRAIA standards

The following describes how the standards are established. Based on the risk assessment findings on air conditioners using A3 refrigerants (highly flammable refrigerants) such as R290, the WG has studied safe operation methods and applied the findings on JRAIA standards to enhance the effectiveness of such methods. Studies into JIS and IEC standards and into Electrical Appliances and Material Act of Japan that were conducted concurrently will be described here in brief in terms of their relevance to this risk assessment study.

The following describes the background that led to the establishment of each of the standards. The risk assessment study by the WG is based on the standard IEC 60335-2-40 Ed. 7.0 that was published in July 2022. On the other hand, JIS C 9335-2-40:2022 published in March 2022 is a standard harmonized with the IEC standard that is the translated version of IEC 60335-2-40 Ed. 6.0 in Japanese that also includes the necessary deviations (differences with its international standard counterpart). However, IEC 60335-2-40 Ed. 7.0 refers to the older version of IEC 60335-1, while JIS standards cannot similarly refer to their older versions. Therefore, JIS standards cannot be established corresponding to IEC 60335-2-40 Ed. 7.0 while referencing the older JIS C 9335-1. To resolve this problem Amendment 1 of JIS C 9335-2-40:2022 was published to fill in the differences between Ed. 6.0 and Ed. 7.0 of IEC 60335-2-40. However, restrictions in text structure were found in the amendment edition, resulting in the limited volume of text that can be introduced.

As a result of deliberations between Japan Electrical Manufacturers' Association (JEMA) Working Group on Air Conditioner Safety JIS and JRAIA's WG, it was decided that JIS Amendment 1 is to set the least minimum provisions regarding A3 refrigerant use, with remaining provisions to be defined under JRAIA standard. Specifically, JIS Amendment 1 is to cover air circulating in case of A3 refrigerant leakage, while provisions on leak detector (Annex LL) and provisions on the location of the leak detector inside the indoor unit (Annex PP) to be established under JRAIA standards. Additionally, Annex PP is expected to be incorporated in JIS when IEC 60335-2-40 Ed. 8 is published in the future and is translated and converted into JIS standard. It must also be noted that Amendment 1 is scheduled for publication in January 2023 and is scheduled to be combined with JIS C 9335-2-40:2022 for submission as standard compliant with the Electrical Appliances and Material Act.

6.8.2 Description of JRAIA standards

JRAIA standards are made up of regulatory standards for equipment that JRAIA member companies must and guidelines that set provisions to be complied with also for non-JRAIA members, such as cautionary notes on air conditioner transport, storage, installation, repair and removal work. JRAIA standard is presently in development, based on JIS C 9335-2-40:2022, JIS Amendment 1, IEC 60335-2-40 Ed. 7.0 and our risk assessment findings. Since JIS requires strict compliance due to its position as standards that comply with the Electrical Appliances and Material Act, the necessary provisions in JIS have been summarized and incorporated into JRAIA standards. Because provisions that could not be covered with JIS Amendment 1 are to be covered by JRAIA standards, compliance with JRAIA standards is likewise essential.

Due to the many issues involved at present in the use of A3 refrigerants for split-type air conditioner, it must be noted that use of A3 refrigerants is not immediately possible for air conditioner. The issues involved in the use of A3 refrigerants are described in a) and b) of 6.7.2. The safe use of A3 refrigerants is believed possible with the resolution of these issues.

6.8.2.1 Equipment standard

(1) Maximum refrigerant charge and refrigerant charge allowable for a single refrigerant circuit

The standard regulates that the maximum refrigerant charge is a quantity calculated by multiplying LFL (kg/m^3) by 26 and refrigerant charge that is allowable for a single refrigerant circuit is less than the maximum refrigerant charge and at the same time is in the following relationship with floor area. Eq. (6-4) is an equation that must be satisfied when the indoor unit is equipped with air circulating fan function for air flow rate set forth in Eq. (6-1). Eq. (6-5) must be satisfied when the indoor unit does not have the air circulating fan function.

$$mc \leq 0.5 \times LFL \times A \times 2.2 \tag{6-4}$$

$$mc \leq 2.5 \times LFL^{5/4} \times h_0 \times A^{1/2} \tag{6-5}$$

Here, A : Floor area of space in which an indoor unit is installed (m^2)

h_0 : Leakage height (the vertical height from the floor surface to the location of refrigerant leakage in the indoor unit) (m); 1.8 m for wall-mounted type, 0.6 m for floor-mounted type and 2.2 m for ceiling-suspended or ceiling-mounted types.

LFL: Lower flammability limit (kg/m^3)

mc : Refrigerant charge for a single refrigerant circuit (kg)

It must be noted that the air flow rate for air circulation for the indoor unit set forth in Eq. (6-1) is found in JIS Amendment 1 but also in the JRAIA's equipment standard.

Furthermore, the indoor unit must be equipped with a leak detector in such a case. The specifications for the detector are set forth in Annex A, nearly identical to the provisions set forth in Annex LL of JIS C 9335-2-40:2022. Also, the location of the leak detector in an indoor unit is set forth in Annex B, based on Annex PP of IEC 60335-2-40 Ed. 7.0.

(2) Labeling on equipment

The JRAIA standards set forth the need of warning labels on equipment regarding flammable refrigerants and cautionary notes regarding securing power source for safety measures to function properly. These regulations are based on those found in JRA 4078[6-3].

6.8.2.2 Guideline

The JRAIA guideline sets forth provisions that require compliance in air conditioner transport, storage, installation, repair and removal.

In the work-related stages, provisions have been set forth to reduce ignition risks during work, such as the use of gloves to prevent static electrical sparks and suspension of work if portable leak detector sets off alarm. Since A3 refrigerants cannot be recovered with refrigerant recovery machine during repair by regulations under the High Pressure Gas Safety Act, provisions have been established regarding the method of refrigerant release into the atmosphere during repair, method of refrigerant charging, etc.

6.9 Conclusions

In the refrigerant leak simulation for air conditioners using A3 refrigerants and risk assessment of the equipment, the findings are as follows.

1) In the indoor refrigerant leak simulation performed, the proposed equation of Colbourne et al., regarding air circulation by fan for leaked refrigerant was found to be effective. However, there is possibility of hazard, depending on the location of the ignition source, since flammable region is generated near the air outlet opening of indoor unit, if air circulation takes place according to the proposed equation.
2) The indoor ignition sources for A3 refrigerants were identified through comparison of the height of the flammable region obtained through refrigerant leak simulation and the height of the location of the indoor ignition source. As a result of a review conducted by the WG for production of a detailed JRAIA report, the issues regarding indoor use such as those listed in each item were identified. Work is underway for repeat calculation of ignition probabilities.
3) The state of generation of a flammable region in the balcony was quantified through refrigerant leak simulation. This showed that generation of a very large flammable region is possible in the balcony. The risk assessment results show there is little risk due to small number of ignition sources in the balcony. As a result of a review conducted by the WG for production of a detailed JRAIA report, the issues such as those listed in each item were pointed out regarding outdoor use. Work is underway for repeat calculation of ignition probabilities.
4) Risk assessments have been performed for each product life stage and have identified the safety measures for each life stage, in order to keep ignition probability below the tolerable level. Also, JRAIA's risk assessments were conducted in accordance with the provisions of IEC 60335-2-40 Ed. 7.0. Part of IEC 60335-2-40 Ed. 7.0 has been established as provisions of Amendment 1 of JIS C 9335-2-40:2022. The remainder is covered by JRAIA standards. Safety will be assured through compliance with both JIS and JRAIA standards. It must be noted that JRAIA standards on equipment and guidelines are shared only by member companies.
5) The considerations in addressing unforeseen events in risk assessment are explained, followed by proposal on the safe management and operation of equipment. For future commercialization and safe operation of air conditioners using R290, one of the A3 refrigerants, it is necessary to strengthen action on assuring proper recovery and handling of air conditioners and to establish a qualification system for workers involved in air conditioner installation and repair. Although the qualification system may be managed by an organization related to refrigeration and air conditioners, a government-approved program is desirable. By eliminating

unassumed events through these efforts, air conditioners using A3 refrigerants can be safely commercialized.

6) It must be noted that JRAIA member companies have pointed out that there are issues such as those listed below that remain to this day. Planning is scheduled to start on whether additional risk assessment is necessary and what are the appropriate actions.

· Issues in flammable volume-time integration assessment in case of outdoor unit leakage (e.g., no review has been conducted on the change in leakage speed regarding the validity of the lack of significant difference when volume-time integration assessment at 500g in case of 1kg leakage and the absence of volume-time integration change during low-speed leakage other than total amount leakage in 4 min, which is the most rigorous condition to date, and observation based on this issue).

· Issues in view of lifestyle changes (the need to take into account the changes in ignition sources on the balcony, stemming from stay-at-home demands spurred by the COVID-19 pandemic, that had not been anticipated in particular at installation of the outdoor unit).

As a result of review into risk assessment studies by the WG, as well as review into the production of a detailed JRAIA report, issues listed in each of the aforementioned sections regarding air conditioner use and work have been pointed out. Work is currently underway to recalculate the ignition probabilities.

Acknowledgments

This report has been jointly authored by Shigeharu Taira, Tomoatsu Minamida (Daikin Industries), Atsushi Baba (Toshiba Carrier), Kazumi Tamura (Johnson Controls-Hitachi Air Conditioning), Shunji Itakura (Fujitsu General), Hiroshi Kanbara (Mitsubishi Heavy Industries Thermal Systems), Kazuhide Yamamoto, Koji Yamashita (Mitsubishi Electric), Madoka Ueno (Sharp), under project leader Kenji Takaichi (Panasonic). Observers from each company are Hiroshi Nakamura, Hiroichi Yamaguchi, Takahiko Hashimoto, Koji Naito, Toshiyuki Fuji and Mitsuru Kawashima who cooperated with this study. The authors would like to deeply appreciate these member’s support.

References

6-1) K. Tamura, et al.: “Ignition Sources at the Stage of Usage for Mini-Split Air-Conditioner using A3 Refrigerant”, Proc. 15th IIR-Gustave Lorentzen Conference on Natural Refrigerants, 1069 (2020).

6-2) A. Baba, et al.: “Study on risk assessment of air conditioner using R290”, Proc. the 25th IIR International Congress of Refrigeration, TS-405. 5 (2019).

6-3) JRA 4078:2021: “Requirements of ensuring safety against refrigerant leakage from commercial built-in refrigerating appliances using flammable refrigerants”, JRAIA (2021) (in Japanese)

7. RISK ASSESSMENT OF BUILT-IN REFRIGERATED DISPLAY CABINETS USING A3 REFRIGERANT CONDUCTED BY JRAIA

7.1 Introduction

Refrigerated display cabinets with incorporated motor compressors (built-in refrigerated display cabinets) used in restaurants, food retailers, supermarkets, etc., use nonflammable refrigerants, such as R404A and R134a, with high global warming potential (GWP) The refrigerant charge ranges from tens of grams to over a kilogram; therefore, it has a huge impact on global warming when leaked into the atmosphere during use or end-of-life disposal. For this reason, shifting to refrigerants with lower GWP becomes important. Most of the refrigerants with low GWP are A3 refrigerants with a low lower flammability limit(LFL) and high flammability. In the case of monobloc refrigerating appliances, such as built-in refrigerated display cabinets, on-site pipe work is not necessary and the refrigerant charge is relatively low. For this reason, A3 refrigerants are believed to be suited for this type of application, in comparison to the split type, thereby generating a strong demand for A3 refrigerants. According to IEC 600335-2-89[7-1)], the international standard for commercial refrigerating appliances, the charge of A3 refrigerant had been limited to a maximum of 0.15 kg. Based on the study results of IEC/61C/WG4, organized in 2015, the standard was revised in Edition 3.0 in June 2019, raising the maximum refrigerant charge to 0.494 kg in the case of R290. This revision was implemented in part due to the strong demand for change, to adapt to refrigerant regulations in other countries. Actual usage requires careful assessment for ensuring safety. The Japan Refrigeration and Air Conditioning Industry Association (JRAIA) has been carrying out risk assessment of built-in refrigerated display cabinets using A3 refrigerants since July 2016. Refrigerant leak analysis was performed to quantify the flammable space, and the ignition probabilities were calculated by developing ignition scenarios for each life stage of the appliance and identifying ignition sources. Furthermore, safety measures based on risk assessment results were established and were reflected in the Japanese standards (JRAIA standards and JIS C 9335-2-89).The maximum charge for flammable refrigerants as stipulated by these standards is 13 times the LFL. In the case of large built-in refrigerated display cabinets, the refrigerant charge limit makes A3 refrigerants (13 times the LFL of R290 which is 0.494 kg) incapable of filling the required charge. Therefore, risk assessment was carried out for the built-in refrigerated display cabinet using A2L refrigerants (13 times the LFL of R1234yf is 3.757 kg) to identify the safety measures for A2L refrigerants, and corresponding Japanese standards were established.

7.2 Refrigerant leak analysis

7.2.1 General

To determine the ignition probability, the duration of the flammable region (the length of time for which the flammable region is present), the mean flammable volume (the mean volume of flammable space in the duration of the flammable region) and flammable volume-time integration (the product of the duration of the flammable region and the mean flammable volume) are necessary and are calculated by analyzing the refrigerant leakage. For the analysis, STAR-CCM+ is used as a solver and a realizable $k\text{–}\varepsilon$ model is used as the turbulence model. The analysis code used in this study was validated by the results of the CO_2 leak measurements, for residential air conditioners, carried out by the University of Tokyo[7-2)].

7.2.2 Analysis of refrigerant leakage from the inside of a reach-in refrigerated display cabinet

Refrigerant leakage analyses were performed after the front door was fully opened suddenly after all the refrigerant charge had leaked into the refrigerated space of a reach-in refrigerated display cabinet. The model of a reach-in refrigerated display cabinet measuring 2.0 m in height, 1.542 m in width, 0.7 m in depth and having an internal volume of 1.08 m^3 (internal dimensions are 1.462 m (W)×0.5 m (D)×1.478m (H)) is shown in Fig. 7-1. A condensing unit consisting of a compressor, condenser and fan is installed in the lower part of the refrigerated display cabinet. The air is sucked from the front of the condensing unit. It then passes through the rear and is expelled from the top of the refrigerated display cabinet. In the condensing unit, the area of the air inlet opening is set at 8.3×10^{-2} m^2, and the air flow rate is set to vary from 0 to 0.249 m^3/s, which corresponds to an air velocity of 0 to3 m/s. The refrigerated display cabinet is assumed to be installed at the center of a wall of a square-shaped enclosed store. Pressure boundaries of size 0.4 m×0.4 m are installed at the two corners of the ceiling and the wall opposite the refrigerated display cabinet. At the start of the calculation, it was assumed that refrigerant concentration was uniformly distributed in the refrigerated space and that there was no door. This condition is considered to approximate the use of sliding doors. The air curtain, with airflow from the top-front of the refrigerated space to the lower part, has an opening area of 6.58×10^{-2} m^2 and an air flow rate of 0.137 m^3/s, which corresponds to an air velocity of 2.08 m/s. This study was conducted with and without considering the air curtain. The store is assumed to have a ceiling height of 2.2 m and varying floor areas of 17.14 m^2 (4.14 m×4.14 m), 24.01 m^2 (4.9 m×4.9 m), 36 m^2 (6 m×6 m), 64 m^2 (8 m×8 m) and 100 m^2 (10 m×10 m). The refrigerant is R290, and refrigerant amount is considered to be either 0.358 kg or 0.5 kg.

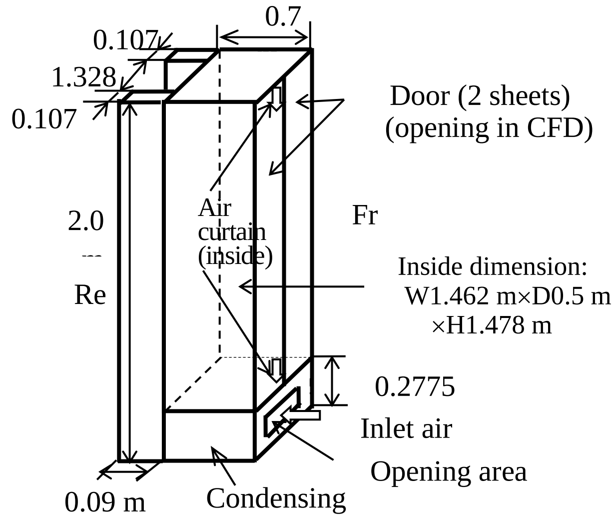

Fig. 7-1 Model of reach-in refrigerated display cabinet

The refrigerant concentration distributions at the center of the refrigerated display cabinet, when refrigerant amount is 0.5 kg and floor area is 24.01 m^2, 5 s and 10 s after the door is opened, are shown in Figs.7-2 and 7-3. The area in red is the flammable region. Fig. 7-2 shows the refrigeration concentration distribution for 0.5 kg of refrigerant, without air curtain and considering an air flow rate of 0 m^3/s. Here, the leaked refrigerant moves linearly from the refrigerated display cabinet towards the facing wall, and the flammable region spreads over a wide area of the floor surface. This is considered to be due to the leak rate being high because the entire refrigerant from the refrigerated space leaks out at once when the door is opened; therefore, the refrigerant diffusion into the periphery cannot keep up with the linear movement of the refrigerant. Fig. 7-3 shows the distribution for 0.5 kg of refrigerant, with air curtain and for an air flow rate of 0.166 m^3/s (air velocity of 2 m/s). In this case too, the flammable region spreads over a wide area of the floor and ceiling surfaces in

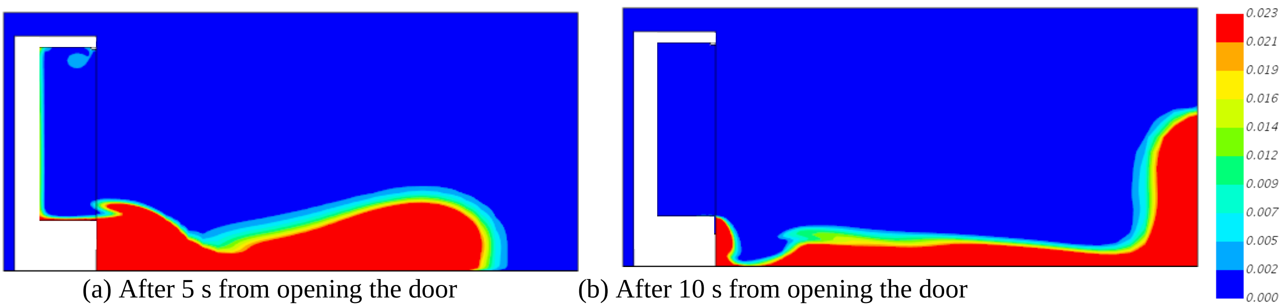

(a) After 5 s from opening the door (b) After 10 s from opening the door

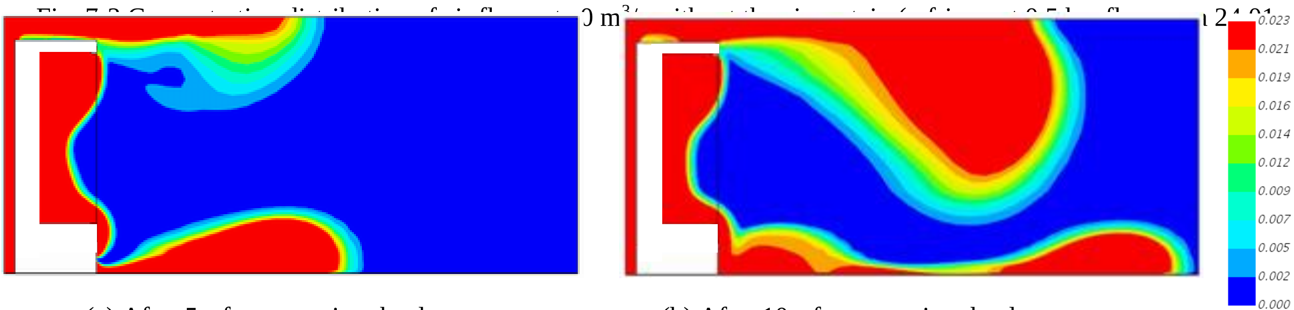

(a) After 5 s from opening the door (b) After 10 s from opening the door

Fig. 7-3 Concentration distribution for air flow rate of 0.166 m^3/s with air curtain (refrigerant 0.5 kg, floor area 24.01 m^2)

a short time. It also shows that owing to the presence of the air curtain some of the refrigerant remains inside the refrigerated space.

Fig. 7-4 shows the change in flammable volume with time when refrigerant amount is 0.5 kg for different condenser air flow rates and floor areas. (a) shows the case when floor area is 24.01 m^2 and without air curtain; (b) when floor area is 24.01 m^2 and with air curtain; (c) when floor area is 100 m^2 and without air curtain; and (d) when floor area is 100 m^2 and with air curtain. When the air flow rate of the condensing unit increases, the duration of the flammable region reduces; however, the flammable region does not disappear, and the maximum value of the flammable volume hardly reduces. When the air flow rate is 0 m^3/s, the change in the flammable volume, with time, is largely dependent on the floor area. When the air flow rate is 0.083 m^3/s (air velocity of 1 m/s) or higher, however, the influence of change in the floor area on flammable volume is not significant. When the air flow rate is 0 m^3/s, the absence of airflow results in the longest duration of the flammable region. When the refrigerant hits the opposite wall, it diffuses in the direction of the width of the refrigerated display cabinet (in direction of the depth shown in Fig. 7-2), increasing the mean flammable volume. When the air curtain is present, the refrigerant is partially retained inside the refrigerated space, resulting in a proportionate reduction in the duration of the flammable region. In cases other than when the air flow rate is 0 m^3/s, the airflow causes the refrigerant to diffuse faster and the duration of the flammable region is shorter. Further, there is less diffusion in the direction of the width of the refrigerated display cabinet. For A3 refrigerants, static electricity and relays of electrical devices are ignition sources. Therefore, if there is an ignition source in the flammable region, there is a possibility of it being ignited easily even if the flammable region is generated only for a short time. According to IEC 60335-2-89[7-1)], however, a flammable region is considered not generated even if a large flammable cloud is generated within 5 min from the start of opening the door.

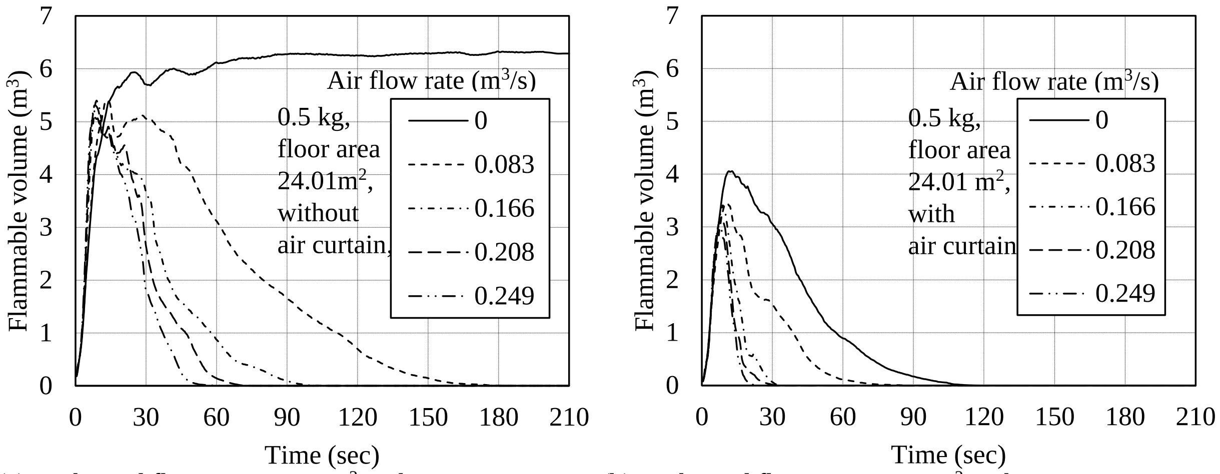

(a) 0.5 kg and floor area 24.01 m^2 without air curtain (b) 0.5 kg and floor area 24.01 m^2 with air curtain

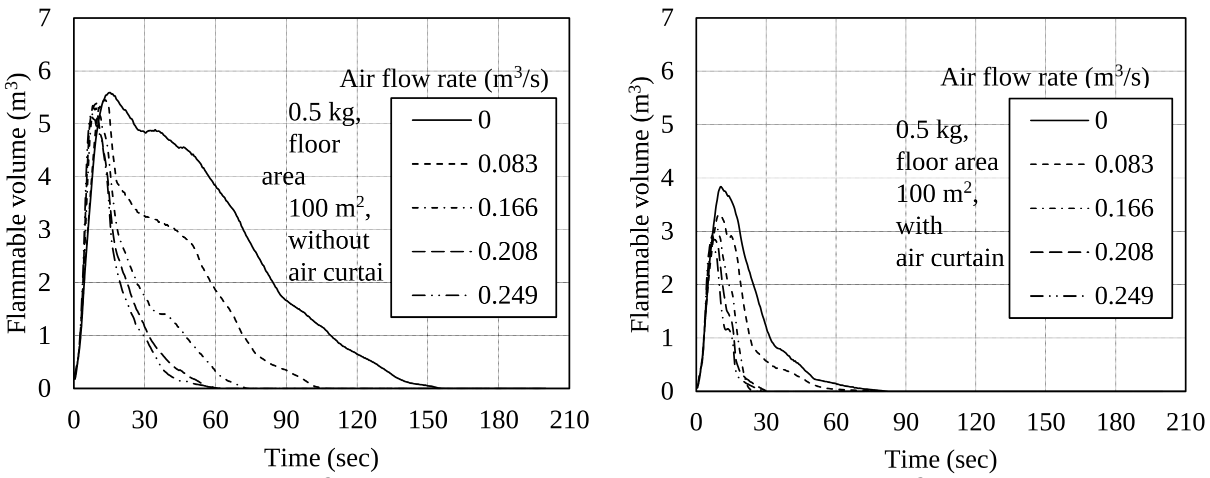

(c) 0.5 kg and floor area 100 m^2 without air curtain (d) 0.5 kg and floor area 100 m^2 with air curtain

Fig. 7-4 Change in flammable volume with time when the floor area and condenser air flow rate are varied.

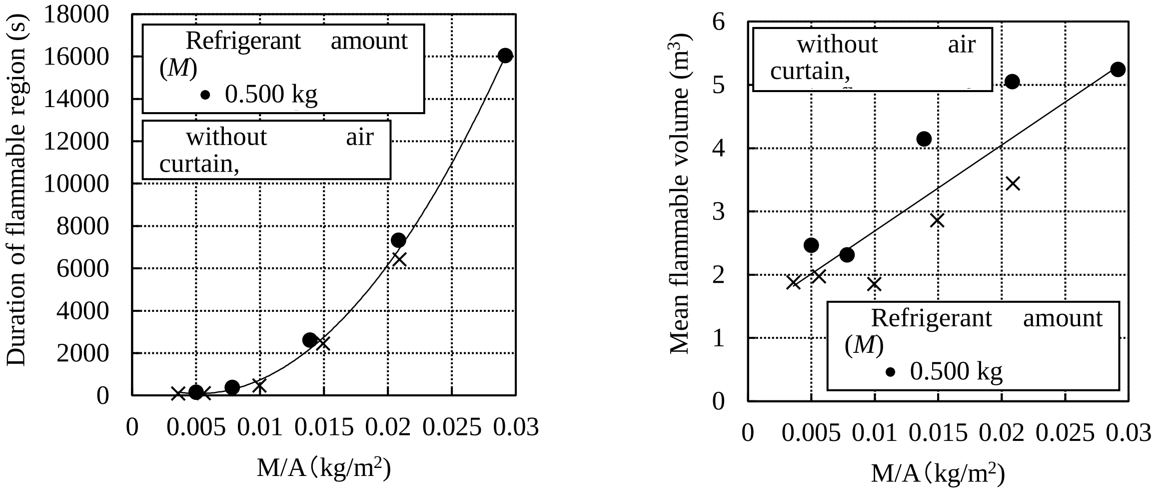

(a) Duration of the flammable region (b) Mean flammable volume

Fig. 7-5 Calculated results for a reach-in refrigerated display cabinet at 0 m^3/s without air curtain

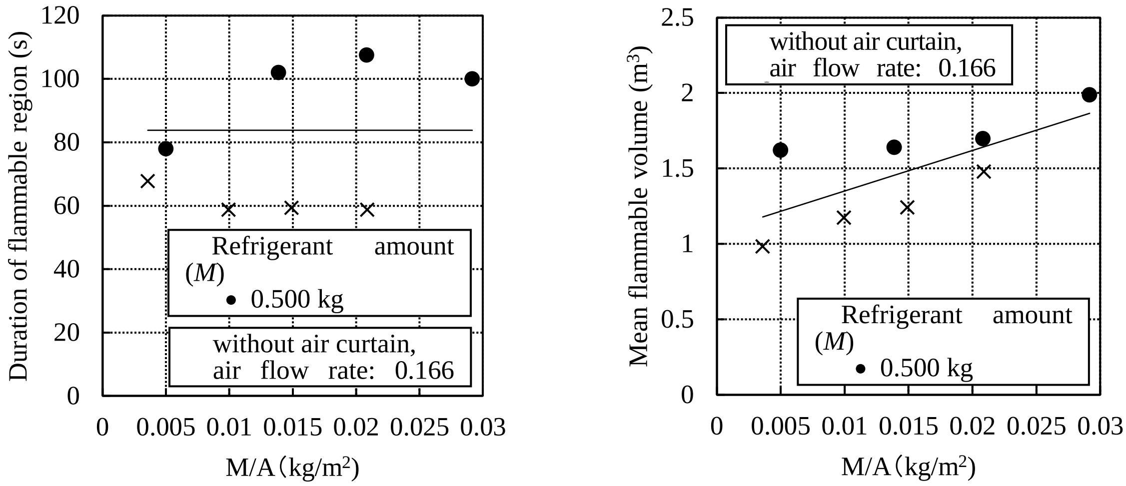

(a) Duration of the flammable region (b) Mean flammable volume

Fig. 7-6 Calculated results of a reach-in refrigerated display cabinet at 0.166 m^3/s without air curtain

Fig. 7-5 and Fig. 7-6 show the results for the duration of the flammable region and the mean flammable volume without an air curtain. These figures show the cases when the air flow rates are 0 m^3/s and 0.166 m^3/s (air velocity of 2 m/s), respectively. In the figures, the horizontal axis shows the value (*M*/*A*) obtained by dividing the refrigerant amount (*M*) by the floor area (*A*). The least squares approximation equations for the duration of the flammable region and the mean flammable volume obtained as functions of *M*/*A* are expressed by Eqs. (7-1) to (7-4) and indicated by solid lines in Figs. 7-5 and 7-6.

$$T_v = 2.76\times10^7\times\left(\frac{M}{A}\right)^2 - 2.86\times10^5\times\left(\frac{M}{A}\right) + 8.30\times10^2 \quad \text{(air flow rate ; 0 m}^3\text{/s)} \tag{7-1}$$

$$V_v = 1.36\times10^2\times\left(\frac{M}{A}\right) + 1.34 \quad \text{(air flow rate ; 0 m}^3\text{/s)} \tag{7-2}$$

$$T_v = 8.38\times10^1 \quad \text{(air flow rate ; 0.166 m}^3\text{/s)} \tag{7-3}$$

$$V_v = 2.68\times10^1\times\left(\frac{M}{A}\right) + 1.08 \quad \text{(air flow rate ; 0.166 m}^3\text{/s)} \tag{7-4}$$

7.2.3 Analysis of refrigerant leakage from the condensing unit of a horizontal refrigerated display cabinet

Analyses were performed on refrigerant leakage from the condensing unit located at the bottom of a horizontal refrigerated display cabinet. The model of the horizontal refrigerated display cabinet measuring 0.81 m in height, 1.8 m in width, 1.09 m in depth is shown in Fig. 7-7. Air is sucked from one side of the condensing unit and expelled from another side. The area of the opening was set as 6.89×10^{-2} m^2 (0.733 m (W)×0.094 m(H)) with an air velocity of 0 to 0.207 m^3/s (air velocity of 0 to 3 m/s). The refrigerated display cabinet is assumed to be installed at the center of a square-shaped enclosed store. Pressure boundaries of size 0.4 m×0.4 m were installed at two corners of the store ceiling and the wall. When the air flow rate was 0 m^3/s, the refrigerant leaked evenly from both the air inlet and outlet, and the refrigerant concentrations at the openings were set at 100 %. When the air flow rate was over 0 m^3/s, the refrigerant leaked from the air outlet, and the refrigerant concentration at the opening was set to the calculated value. The store was considered to have a ceiling height of 2.2 m and the different floor areas assumed were 15.21 m^2 (3.9 m×3.9 m), 24.01 m^2 (4.9 m×4.9 m), 36 m^2 (6 m×6 m), 64 m^2 (8 m×8 m) and 100 m^2 (10 m×10 m). The refrigerant was R290, and the refrigerant amount was either 0.358kg or 0.5kg. The leak rate of the refrigerant was set to a value such that the total refrigerant charge leaked in 4 min (leak rate of 7.5 kg/h).

Fig. 7-8 shows the results of the calculation of the duration of the flammable region and the mean flammable volume when the air flow rate of the condensing unit is 0 m^3/s. In the figure, the horizontal axis shows the value (*M*/*A*) which is amount of refrigerant (*M*) per unit floor area (*A*) of the store. The least squares approximation equations of the duration of the flammable region and the mean flammable volume obtained as a function of *M*/*A* are expressed by Eqs. (7-5) and (7-6) and indicated by the solid lines in Fig. 7-8. The results of the leak analysis using R600a indicate that the flammable volume-time integration was about 10 % greater than that for R290.

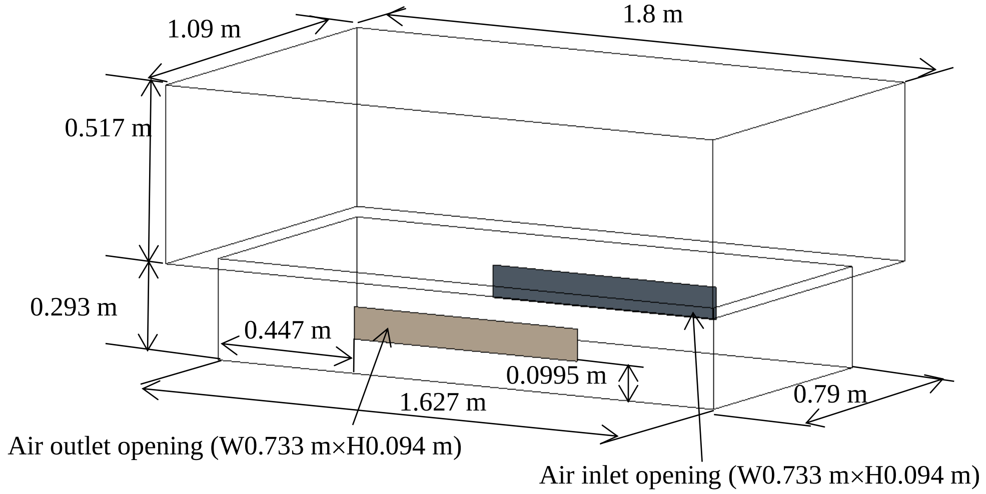

Fig. 7-7 Model of horizontal refrigerated display cabinet

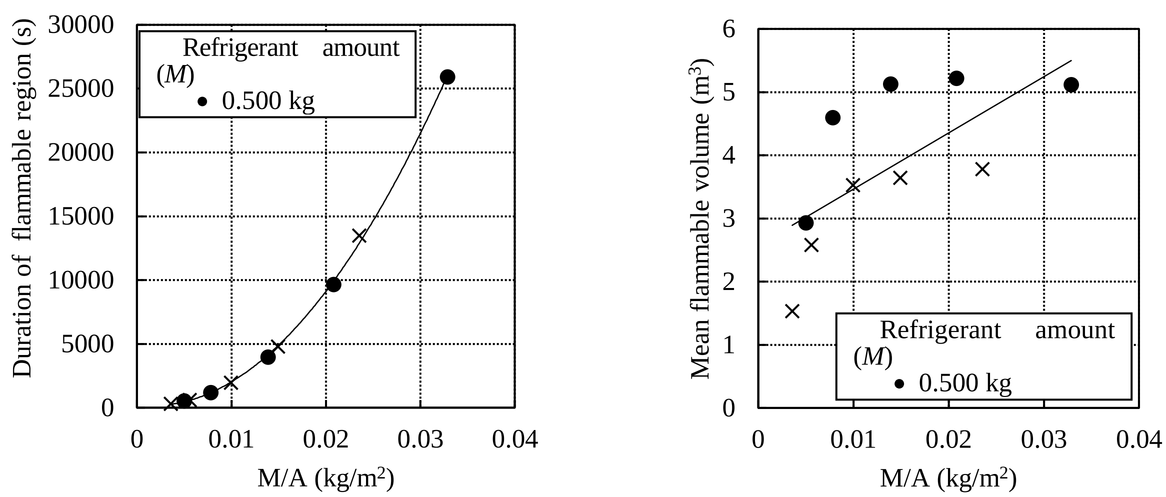

(a) Duration of the flammable region (b) Mean flammable volume

Fig. 7-8 Calculated results for a horizontal refrigerated display cabinet at 0 m^3/s

$$T_v = 2.65\times10^7\times\left(\frac{M}{A}\right)^2 - 8.52\times10^4\times\left(\frac{M}{A}\right) + 2.37\times10^2 \qquad \text{(air flow rate ; 0 m}^3\text{/s)} \qquad (7\text{-}5)$$

$$V_v = 8.90\times10^1\times\left(\frac{M}{A}\right) + 2.58 \qquad \text{(air flow rate ; 0 m}^3\text{/s)} \qquad (7\text{-}6)$$

For the air outlet of the condensing unit, Eq. (7-7) [7-3] is used to determine the air flow rate that does not generate a flammable region. Here, A_o is the area of air outlet (m^2), F is the safety factor of 0.25, G is the LFL (kg/m^3), h_o is the height of the centerline of air outlet (m), Q is air flow rate at the outlet (m^3/s) and w the leak rate (kg/s).

$$Q = \frac{5\times\sqrt{A_0}\times w^{3/4}}{h_0^{\,1/8}\times\{G\times(1-F)\}^{5/8}} \qquad (7\text{-}7)$$

When the floor area was 24.01 m^2, the refrigerant charge amount was 0.5 kg of R290, and the leak rate was 7.5 kg/h, no flammable region was generated at the air flow rate of 0.150 m^3/s (air velocity of 2.182 m/s) calculated with Eq. (7-7). In addition, even when the air flow rate was 0.1378 m^3/s (air velocity of 2.0 m/s), which was 8.4 % lower, a flammable region was not generated. A similar analysis was performed for R600a, and no flammable region was generated with the air flow rate calculated using Eq. (7-7). This value was 9.8% lower.

Next, the calculations were performed when the leak rate was varied from 0.1 to 40.71 kg/h at a floor area of 24.01 m^2, refrigerant amount of 0.5 kg and air flow rate of 0 m^3/s. The results of the mean flammable volume and the flammable volume-time integration are shown in Fig.7-9. The flammable volume-time integration was found to be almost equal to the leak rate of 0.54 kg/h or faster and begins to decrease when the leak rate slows down. Even when the leak rate is 0.1 kg/h, the flammable volume-time integration is approximately 50 % of that obtained with a leak rate of 0.54 kg/h. Therefore, for risk assessment, it is necessary to calculate the ignition probability considering all types of leakages, including slow leakage. The risk assessment is carried out using the flammable volume-time integration at the leak rate of total refrigerant charge leaked in 4 min (7.5 kg/h in the case of R290 for a refrigerant charge amount of 0.5 kg). However, the results of these analyses show that there are no significant problems in risk assessment with this setting.

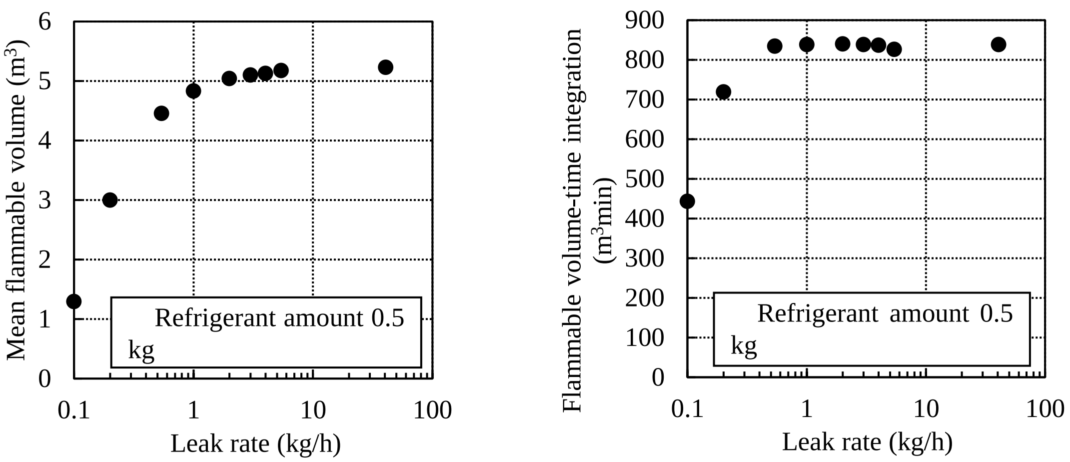

(a) Mean flammable volume (b) Flammable volume-time integration

Fig. 7-9 Calculation results when leak rate varies

7.2.4 Effect of gaps in a store door

Fig. 7-10 shows a store model in which a door with gaps at the top and bottom is installed. The reach-in refrigerated display cabinet (without air curtain and with a condenser air flow rate of 0 m^3/s) shown in Fig. 7-1 is installed at the center of a wall in the square-shaped store. The horizontal refrigerated display cabinet (with a condenser air flow rate of 0 m^3/s) shown in Fig. 7-7 was installed at the center of the store. In the analysis, only one of these refrigerated display cabinets was installed. The two corners of the ceiling above the wall opposite the reach-in refrigerated display cabinet have pressure boundaries of size of 0.4 m×0.4 m. The store door has a width of 0.8 m, and height of 1.875 m (including gaps).

The gaps above and below the store door are10 mm wide. The store door is located at the center of the wall on the opposite side of the reach-in refrigerated display cabinet or in a direction parallel to the longitudinal direction of the horizontal refrigerated display cabinet. In the analysis of the reach-in refrigerated display cabinet, the number of cabinet door openings were varied. When the number of cabinet door openings was 1, it was assumed that the cabinet door on the right was opened suddenly. The ceiling height of the store was 2.2 m, and the store floor area was varied from 24.01 to 100 m^2. R290 was considered as the refrigerant and the refrigerant charge amount was considered to be 0.5kg.

Fig. 7-11 shows the change in the flammable volume of the reach-in refrigerated display cabinet, with time, when the floor area is either 24.01 or 64 m^2. There was almost no difference in the maximum value of the flammable volume for the different floor areas. When floor area is 24.01 m^2, the duration of the flammable region is longer when the number of sudden cabinet door openings is one and there is no gap in the store door. For a floor area of 64 m^2, the difference in this duration, for the store door with and without gaps, was very small. However, there was some difference when the number of sudden cabinet door openings was considered. The relationship between floor area and flammable volume-time integration is shown in Fig. 7-12. When the floor area is 100 m^2, there is nearly no difference in flammable volume-time integration due to the presence of gaps in the store door and the number of sudden cabinet door openings.

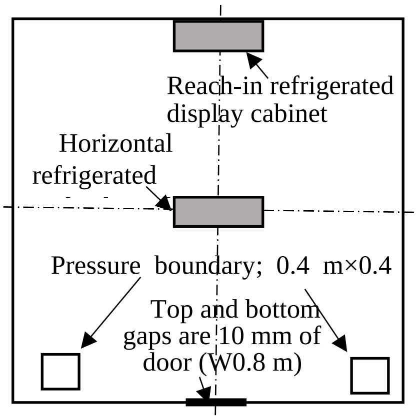

Fig. 7-10 Model of store with door

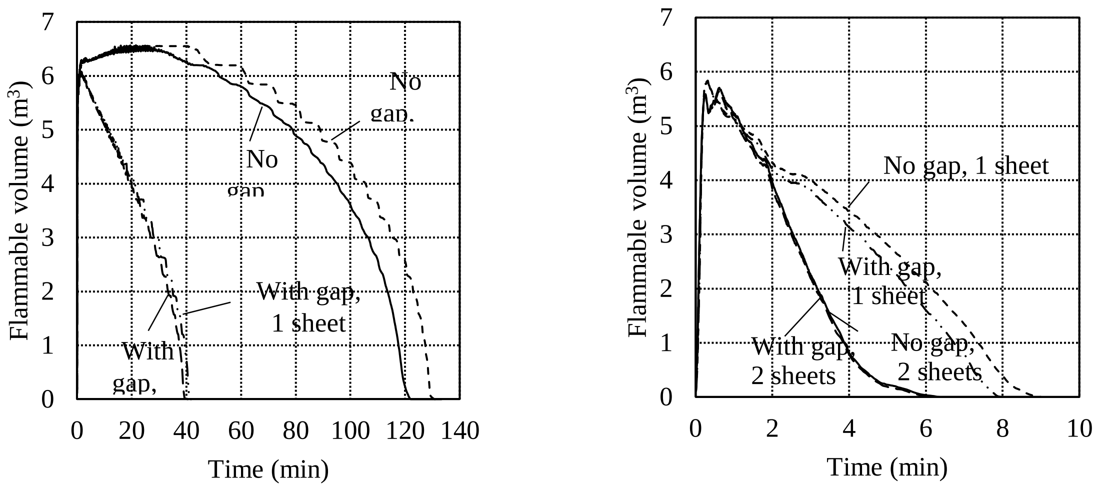

(a) Reach-in refrigerated display cabinet at 24.01 m^2 floor area (b) Reach-in refrigerated display cabinet at 64 m^2 floor area

Fig. 7-11 Variation in flammable volume with time (reach-in refrigerated display cabinet)

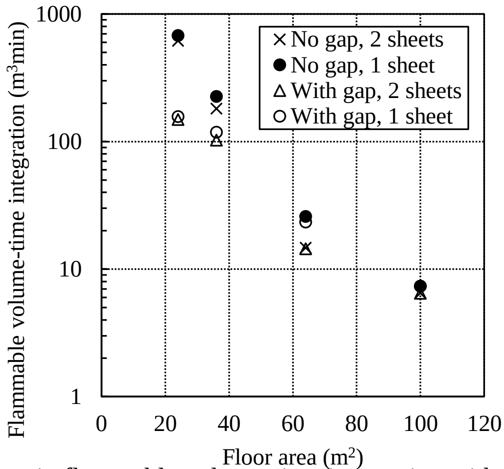

Fig. 7-12 Difference in flammable volume-time integration with and without store door gap (Reach-in refrigerated display cabinet)

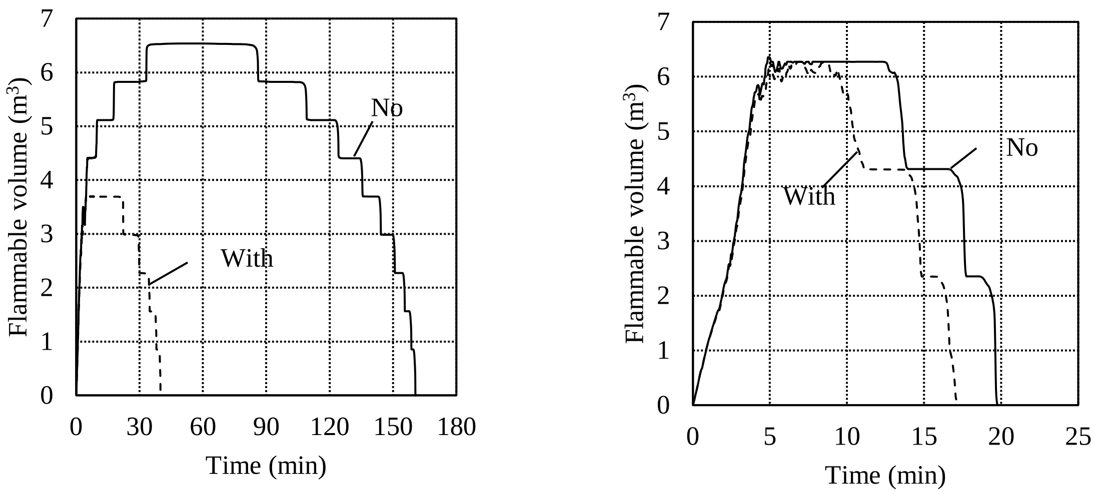

(a) Horizontal refrigerated display cabinet at 24.01 m^2 floor area (b) Horizontal refrigerated display cabinet at 64 m^2 floor area

Fig. 7-13 Variation in flammable volume with time (horizontal refrigerated display cabinet)

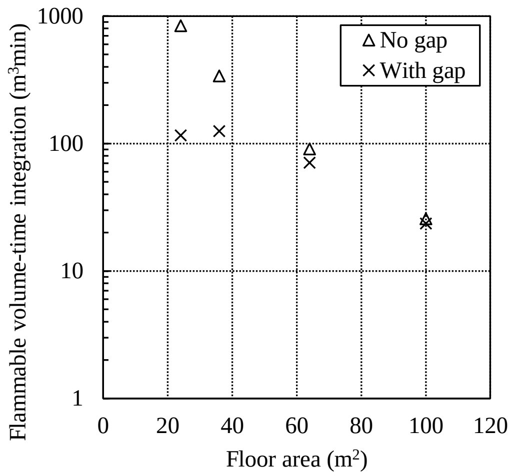

Fig. 7-14 Difference in flammable volume-time integration with and without store door gap (horizontal refrigerated display cabinet)

Fig. 7-13 shows the change in the flammable volume, with time, for the horizontal refrigerated display cabinet when the floor area is 24.01 and 64 m^2. Unlike the calculation results for the reach-in refrigerated display cabinet installed on a floor area of 24.01 m^2, a difference is observed in the maximum values of both the flammable volume and duration of the flammable region, depending on whether there were gaps in the store door. The maximum value of the flammable volume and the duration of the flammable region are 55.4 % and 25.0 % higher, respectively, than those where there are no gaps. When floor area is 64 m^2, the difference in the maximum value of the flammable volume for these two cases is almost eliminated, and the duration of the flammable region for the case with store door gaps is 85.6 % of that with no door gaps, and the difference is not so large. The relationship between floor area and flammable volume-time integration is shown in Fig. 7-14. In the case of 100 m^2 floor area, the difference in the duration of the flammable region when considering the store door with and without gaps is almost eliminated. The convenience store for which risk assessment was carried out has floor area of 84.7 m^2. For that floor area, the store door gaps have a minimal effect on both the reach-in and horizontal refrigerated display cabinets. Therefore, the use of the values obtained for the enclosed store does not pose any problems during risk assessment.

7.2.5 Analysis of refrigerant leakage in the actual store model

Fig. 7-15 shows a store model where an actual convenience store has been recreated. On the left side of the figure, there is a checkout counter (without thickness in the model) of height 0.85 m. The store floor area in the figure is 112 m^2, and the floor area excluding the checkout area is 102 m^2. The ceiling height of the store is 2.2 m. The store has five doors with the following specifications. Door 1 is the door to an office with a width of 0.8 m [top gap of 6 mm, bottom gap of 15 mm]. Door 2 is the door to the backyard with a width of 0.8 m [top gap of 10 mm, bottom gap of 20 mm]. Door 3 is the door to a lavatory with a width of 0.7 m [top gap of 6 mm, bottom gap of 15 mm]. Door 4 is the door of a store entrance with width of 1.6 m [no gap]. The height of these doors is 1.875m. Door 5 is the door to the checkout area with a width of 0.6 m and height of 0.8 m [bottom gap of 75 mm]. A pressure boundary of 0.25 m×0.25 m is located on the left side of the center of the store. The reach-in refrigerated display cabinets are installed on the lower right outside and the upper right outside of the figure, and the horizontal refrigerated display cabinet is installed near the center of the store in the longitudinal direction and parallel to the entrance door. In the analysis, only one of the refrigerated display cabinet types is considered as installed. The analysis was also performed for a smaller store (with store floor area of 75.4 m^2 and floor area excluding the checkout area of 57.4 m^2). The reach-in refrigerated display cabinet considered is the one shown in Fig. 7-1 (without air curtain and with a condenser air flow rate of 0 m^3/s). The right-side door of the two-door cabinet is opened suddenly after the total refrigerant amount has leaked into the refrigerated space. The horizontal refrigerated display cabinet is the one shown in Fig. 7-7 (condenser air flow rate of 0 m^3/s). The leak rate is the leak rate of total refrigerant charge leaked in 4 min. The refrigerant (R290) amount is 0.5 kg.

Calculated results for the reach-in refrigerated display cabinet in the actual store model, with “A” as the floor area excluding the checkout area, as well as the comparison of calculated results for the square-shaped store described in 7.2.4, are shown in Fig. 7-16. The values for the square-shaped store and the actual store model show almost the same tendency. Therefore, for refrigerant leak from the refrigerated space of the reach-in refrigerated display cabinet, the use of floor area excluding that of checkout area is considered adequate in the actual store model. In the case of the reach-in refrigerated display cabinet, the refrigerant in the refrigerated space leaks outside at once and hence the actual leak rate is high. Therefore, the leaked refrigerant moves faster linearly in comparison to the diffusion into the surrounding space. For this reason, the leaked refrigerant stagnating near the floor surface does not flow into the checkout area. If the refrigerant is diluted by the fan of the condensing unit, it gets circulated in the store. Therefore, it is adequate to use the value that includes the checkout area within the floor area.

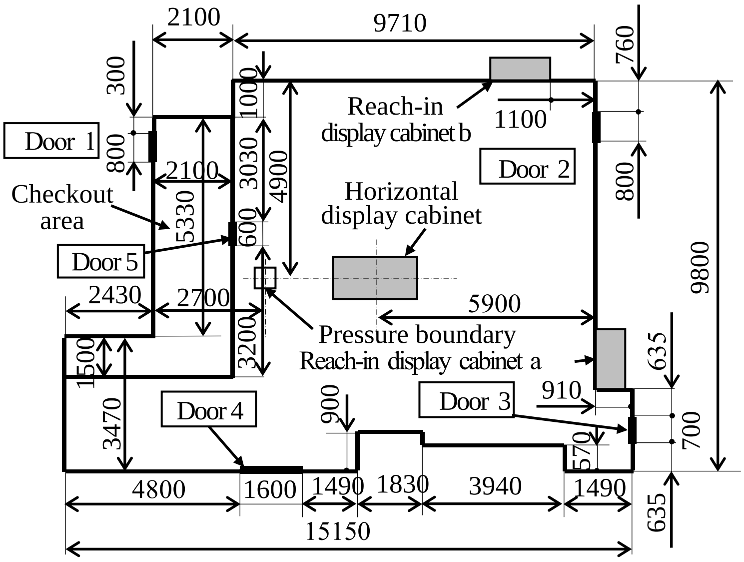

Fig. 7-15 Convenience store model (unit: mm)

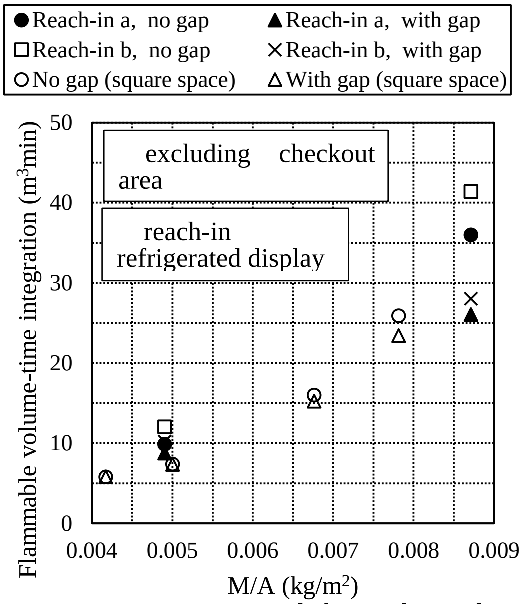

Fig. 7-16 Comparison result for reach-in refrigerated display

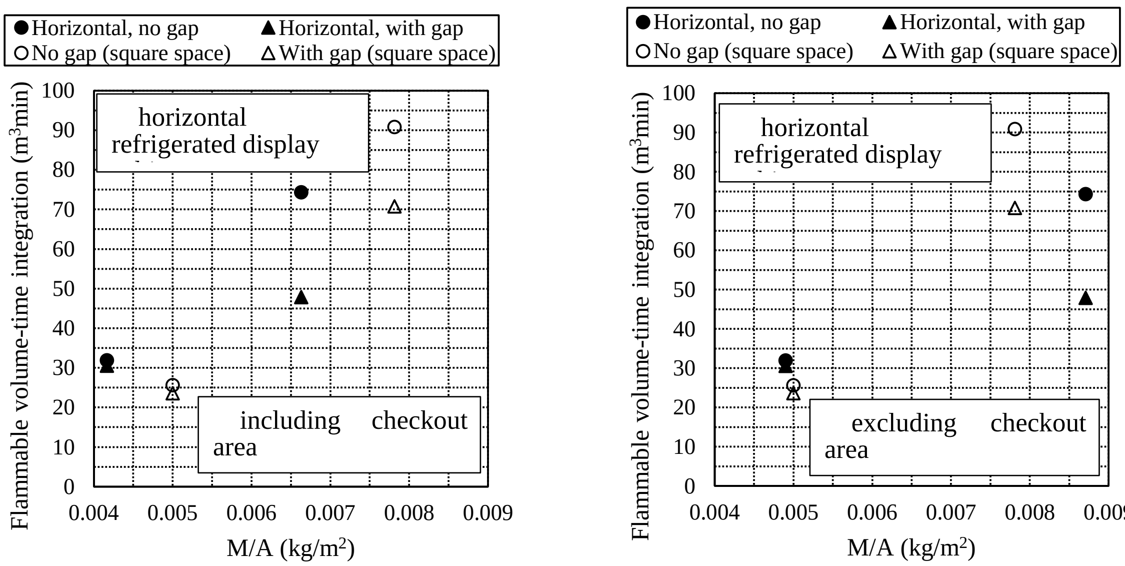

(a) Including checkout area in store floor area (b) Excluding checkout area from store floor area

Fig. 7-17 Comparison results of horizontal refrigerated display cabinet

The calculated results for the horizontal refrigerated display cabinet in an actual store model and the comparison with calculated results for square-shaped store are shown in Fig. 7-17. In Fig. 7-17 (a) "A" denotes the store floor area including the checkout area, and in (b) "A" denotes the floor area excluding the checkout area. From the figure, in the case of the floor area including the checkout area, the values for the square-shaped store tend to be closer to the values for the actual store model when compared with the values for the floor area excluding checkout area, in the case of the horizontal refrigerated display cabinet. Therefore, for refrigerant leaks from the condensing unit of the horizontal refrigerated display cabinet, it seems adequate to use the value including checkout area as the floor area in the actual store model. In the case of the horizontal refrigerated display cabinet, the leak rate is the leak rate of total refrigerant charge leaked in 4 min. For this reason, the refrigerant is considered to have diffused into the surroundings and flown into the checkout area.

Because assessment requires that the floor area used be consistent, the floor area of the store including the checkout area is therefore assumed to be the floor area for both risk assessment and establishing safety standards.

7.2.6 Leak analysis for A2L refrigerant

7.2.6.1 Analysis of refrigerant leakage from the inside of a reach-in refrigerated display cabinet

Refrigerant leak analyses were performed when the front cabinet door was fully opened suddenly after the total refrigerant amount of R1234yf leaked inside the refrigerated space of a reach-in refrigerated display cabinet. The reach-in refrigerated display cabinet and the store model are identical to that shown in 7.2.2. The air flow rate of the condensing unit is 0 m^3/s, and there is no air curtain. The enclosed store has square-shape, with a floor area of 24.01 m^2 and ceiling height of 2.2 m. The refrigerant amount was 3.8 kg of R1234yf, 13 times the LFL of R1234yf (0.289 kg/m^3). When R1234yf is charged into the refrigerated display cabinet using 0.5 kg of R290, the refrigerant charge having the same capacity is approximately 1.0 kg. However, since the maximum refrigerant charge according to standards [7-1] is 13 times the LFL, the refrigerant amount was set to 3.8 kg. Other conditions are identical to those stated in 7.2.2. R1234yf has a molecular weight of 114, which is the highest in A2L refrigerants, and when leaked near the floor, the flammable space becomes the largest.

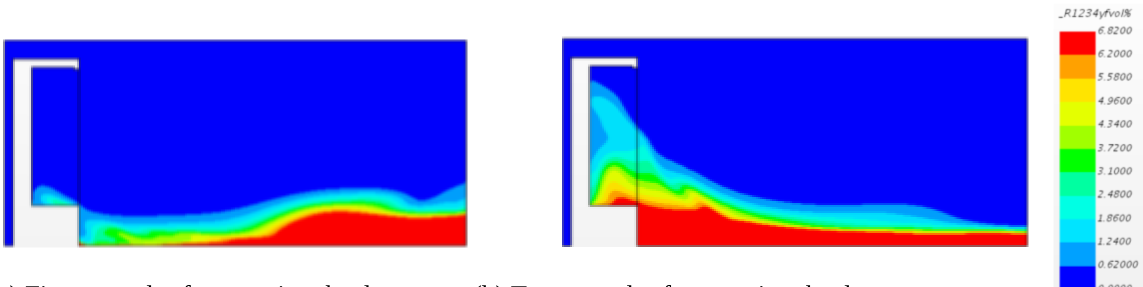

(a) Five seconds after opening the door (b) Ten seconds after opening the door

Fig. 7-18 Concentration distribution for air flow rate of 0 m^3/s at 3.8 kg of R1234yf and floor area of 24.01 m^2

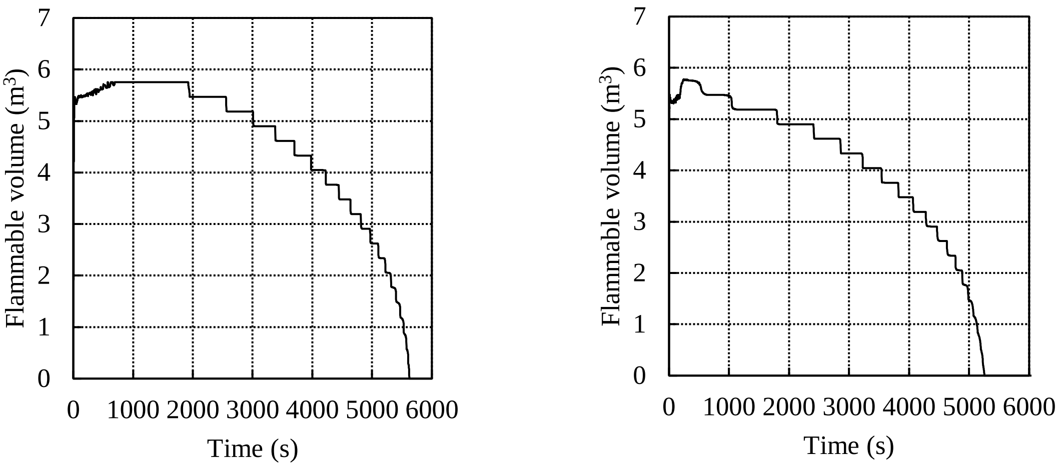

(a) Flammable volume of 0.5 kg of R290 (b) Flammable volume of 3.8 kg of R1234yf

Fig. 7-19 Change in flammable volume for R290 and R1234yf following leakage from a reach-in refrigerated display cabinet with the refrigerant amount of 13 times the LFL and a floor area of 24.01 m^2

The change in refrigerant concentration distribution with time is shown in Fig. 7-18, the red area is the flammable region. As in the case of R290, which is an A3 refrigerant, R1234yf, an A2L refrigerant, shows the generation of a flammable region outside the refrigerated space in a short time with the sudden opening of cabinet door after leakage. The flammable region is generated even for A2L refrigerants which is most likely due to the low leakage height (the height of cabinet door bottom section) which is 0.2775 m and the high leak rate.

Fig. 7-19 shows the change in flammable volume with time. The value of flammable volume in the case of leakage of 3.8 kg of R1234yf was slightly smaller than for 0.5 kg of R290. The duration of the flammable region was also slightly shorter, and the ratio of R1234yf to R290 in terms of flammable volume-time integration was 85.56 %. Since there is no big difference between the values of the flammable volume-time integration for both refrigerants, the values obtained for R290 are used for the leakage from the refrigerated space of the reach-in refrigerated display cabinet in the risk assessment of R1234yf for safety. IEC 60335-2-89[7-1] stipulates that the maximum refrigerant charge be 13 times the LFL or 1.2 kg, whichever is smaller. Japan presented the results of these analyses to the working group of IEC considering the contents of next edition, and as a result, it was decided that the maximum refrigerant charge would be revised to 13 times the LFL (the limit of 1.2 kg or less would be removed) during the next revision.

7.2.6.2 Analysis of refrigerant leakage from a condensing unit of a horizontal refrigerated display cabinet

Analyses were performed on the leakage from a condensing unit located at the bottom of a horizontal refrigerated display cabinet. A horizontal refrigerated display cabinet with a case width and opening area of the condensing unit of 6.84 m and 26.2×10^{-2} m^2 (2.785 m×0.094 m), respectively, which is 3.8 times the size of the model in Fig. 7-7, was installed in the center of a square-shaped enclosed store having a ceiling height of 2.2 m and a floor area of 84.7 m^2. A refrigerated display cabinet of this size is considered a large cabinet, and a refrigerated display cabinet of the size of Fig. 7-7 is considered to be a small cabinet. The refrigerant amount of R1234yf is 3.8 kg (13 times the LFL), the air flow rate of the condensing unit is 0 m/s, and the leak rate is varied from 2 to 57 kg/h. Fig. 7-20 shows the analysis results. The flammable volume-time integration was 83.6 % at a leak rate of 7.5 kg/h against 57 kg/h and 7.2 % for 2 kg/h, and no flammable region was generated at a leak rate of 1 kg/h or less. Therefore, even if the A2L refrigerant leaks from a height of 0.0995 m from the floor surface, a flammable region is not generated if the floor area is 84.7 m^2 or larger. If R1234yf leaks near the floor surface, the flammable space is the largest in A2L refrigerants. Therefore, in the risk assessment of A2L refrigerants, even if the leak height was very low, the refrigerant leak probability from the condensing unit in the store was set to a value excluding slow leak (1.94×10^{-5}). The flammable volume-time integration of R1234yf for rapid leak and burst leak was set to the same value as R290 for safety. Fig. 7-21 shows the changes in the flammable volume, with time, when the leak rates of R1234yf are 15 kg/h, 7.5 kg/h, and 2 kg/h. The flammable region is generated at the beginning of the leak if the leak rate is high; however, if the leak rate is low, the generation of the flammable region is delayed (roughly 90 min after the leakage at 2 kg/h). The analysis was performed for an enclosed store, the refrigerant flows to the outside of the store through openings such as door gaps in the actual store. Therefore, no flammable region is be generated even at a leak rate of 2 kg/h.

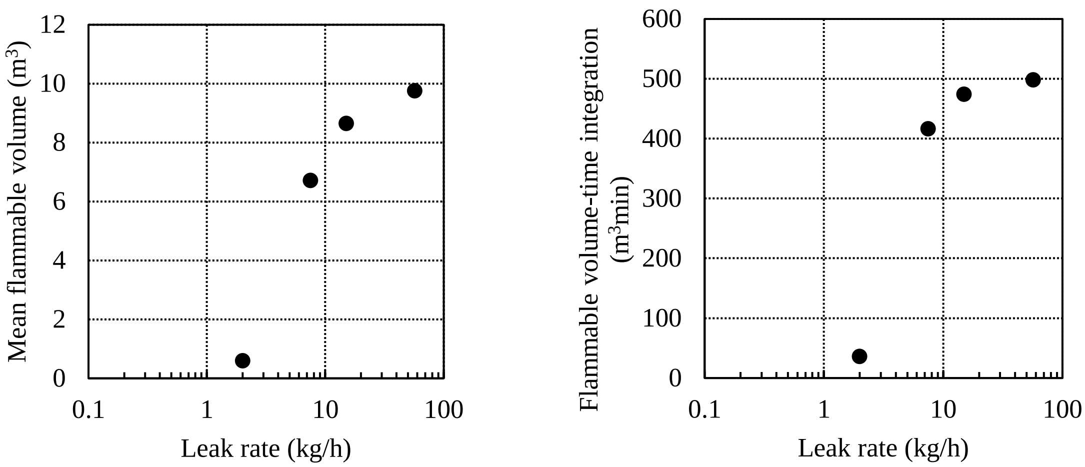

(a) Mean flammable volume (b) Flammable volume-time integration

Fig. 7-20 Calculated results when the leak rate varies for 3.8 kg of R1234yf in a large cabinet with a floor area of 84.7 m^2

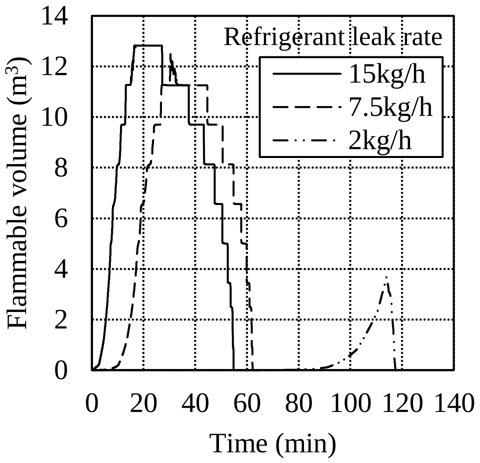

Fig. 7-21 Change in flammable volume for different leak rates for 3.8 kg of R1234yf in a large cabinet with a floor area of 84.7 m^2

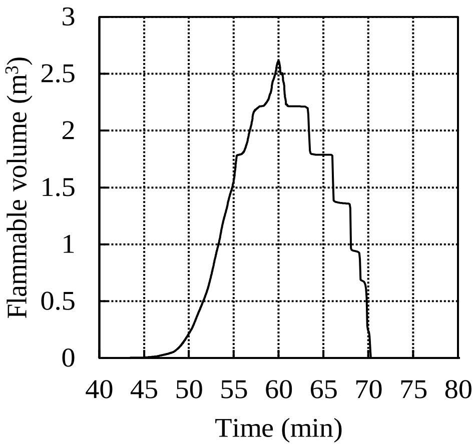

Fig. 7-22 Change in flammable volume for a leak rate of 1 kg/h for 1.0 kg of R1234yf in small cabinet with floor area of 24.01 m^2

When considering an air flow rate of the condensing unit of 0 m^3/s, a small cabinet with 1.0 kg of R1234yf is installed at the center of a square-shaped enclosed store having a ceiling height of 2.2 m and a floor area of 24.01 m^2. Fig. 7-22 shows the analysis result for the flammable volume at a leak rate of 1 kg/h. Although the value was smaller than that for 0.5 kg of R290, the flammable region was generated even at 1 kg/h, which is a slow leak. This is probably because the leak height was very low (0.0995 m) and the floor area was small. The flammable volume, however, was generated roughly 45 min after the leakage, and if it was not an enclosed store, the leaked refrigerant would have flown out to the outside of the store through an opening such as the store door gap, and no flammable region would have been generated. The flammable volume-time integration, when A2L refrigerant leaks from the condensing unit in a small room such as small-sized warehouse, is set to the same value as R290 for rapid leak and burst leak for safety, that is, to the value in Fig. 7-22. Risk assessment is carried out using a value obtained by multiplying the weighted average of these values at the occurrence probability of each leak rate by a coefficient that considers the effect of store door gaps.

In addition, the analysis was carried out when a large cabinet with 3.8 kg of R1234yf was installed at the center of the square enclosed store with a ceiling height of 2.2 m and a floor area of 24.01 m^2. The leak rate was 57 kg/h, which is the leak rate of total refrigerant charge leaked in 4 min, and the air flow rate of the condensing unit was varied. The results showed that R1234yf did not generate a flammable region at an air flow rate of 0.3719 m^3/s (air velocity of 1.42 m/s) that is equivalent to the calculated air flow rate in Eq. (7-7), as well as when the air flow rate is smaller by 30 to 40 %, that is, at 0.2231 to 0.2603 m^3/s (air velocity of 0.853 to 0.995 m/s). R1234yf has the largest molecular weight in A2L refrigerants, and cannot be easily circulated. Hence the Eq. (7-7) was confirmed to be effective for A2L refrigerants also.

7.3 Risk assessment

7.3.1 Method of risk assessment

7.3.1.1 Calculation method of ignition probability

Ignition probability is calculated as a product of the spatial encounter probability that represents the spatial ratio of the flammable region in the target space, the temporal encounter probability which represents the probability of encounter between a flammable region and the ignition source within a specified length of time and the refrigerant leak probability, as shown in Eq. (7-8). The spatial encounter probability is the ratio of the flammable volume to the volume of the target space and is calculated using Eq. (7-9). The temporal encounter probability, which represents the probability in time, of the encounter between the ignition source and the flammable region, is expressed as in Eq. (7-10) by dividing the encounter area by the entire area as seen in Fig. 7-23 and applying the concept of geometrical probabilities[7-4),7-5)]. If the ignition source occurs multiple times, this is expressed using Eq. (7-11). This equation is used to calculate the temporal encounter probability at usage stage. The coefficient k is a coefficient representing the occurrence rate of the ignition source or the degree of concentration of the ignition source in a certain time range. In the case of A3 refrigerants, many ignition sources have short durations, T_i, and high frequencies, n, such as electrostatic and electric sparks. Eq. (7-11) has a high calculation accuracy for this case. Table 7-1 shows examples of calculations when k=1. In Case 1 (assuming a cigarette lighter), when T_v is 3600 s, T_i is 5 s and n is 1 times/day; the calculated values are identical for the conventional equation[7-6)] and Eq. (7-11). In Case 2 (assuming static electricity) when T_v is 3600 s, T_i is 1 μs and n is 24 times/day, however, the result is 1.0 in the conventional equation[7-6)] but 0.64 for Eq. (7-11). For temporal encounter probability at work stage, Eq. (7-14) to Eq. (7-17) are used as deemed appropriate, depending on whether or not the leakage and the ignition source are caused in the work stage. Here, P_a, calculated with Eq. (7-12), is the probability of leakage during work, and set to the value of 1 for leakage caused by work. P_b, calculated with Eq. (7-13), is the probability of ignition source encountered during work time, and set to the value of 1 for ignition sources caused by work. If the ignition source is not caused by work, the exponent used in the equation if replaced by $n\times T_\mathrm{s}/T_\mathrm{d}$, the frequency of ignition sources during work time, as shown in Eq. (7-16) and Eq. (7-17). The duration of the flammable region and the mean flammable volume are calculated using Eqs. (7-1) to (7-6) in an enclosed store because the floor area of a convenience store is less affected by gaps in the store doors (see subsection 7.2.4). Other values are set to values corresponding to the settings of each stage and the characteristics of the ignition source. It must be noted also that the ignition sources for A3 refrigerants are based on research by Imamura[7-7)] of Suwa University of Science.

$$P = P_\mathrm{s} \times P_\mathrm{t} \times P_\mathrm{r} \tag{7-8}$$

$$P_\mathrm{s} = \frac{V_\mathrm{v}}{V_\mathrm{g}} \tag{7-9}$$

$$P_\mathrm{t} = \frac{\dfrac{{T_\mathrm{i}}^2 + {T_\mathrm{v}}^2}{2} + \left\{ {T_\mathrm{d}}^2 - \dfrac{(T_\mathrm{d} - T_\mathrm{i})^2 + (T_\mathrm{d} - T_\mathrm{v})^2}{2} \right\}}{{T_\mathrm{d}}^2} = \frac{T_\mathrm{i} + T_\mathrm{v}}{T_\mathrm{d}} \tag{7-10}$$

$$P_\mathrm{t} = k \times \left[1 - \left\{ 1 - \frac{T_\mathrm{i} + T_\mathrm{v}}{T_\mathrm{d}} \right\}^n \right] \quad \text{(at usage)} \tag{7-11}$$

$$P_\mathrm{a} = \frac{T_\mathrm{s}}{T_\mathrm{d} \times 365} \tag{7-12}$$

$$P_\mathrm{b} = \left[1 - \left\{ 1 - \frac{T_\mathrm{i} + T_\mathrm{v}}{T_\mathrm{d}} \right\}^n \right] \tag{7-13}$$

Table 7-1 Example of temporal encounter probability

Case	T_v	T_i	n	$n\times(T_\mathrm{i}+T_\mathrm{v})/T_\mathrm{d}$ [5)]	Eq.(7-11)
1	3600	5	1	4.2×10^{-2}	4.2×10^{-2}
2	3600	1×10^{-6}	24	1.0	6.4×10^{-1}

(here k=1)

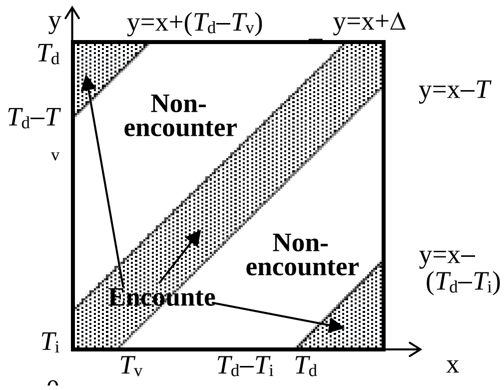

Fig. 7-23 Image of encounter between ignition source and flammable region

$$P_\mathrm{t} = k \times \left[1 - \left\{ 1 - \frac{T_\mathrm{i} + T_\mathrm{v}}{T_\mathrm{s}} \right\}^n \right] \quad \text{(leakage and ignition source caused by work)} \tag{7-14}$$

$$P_\mathrm{t} = k \times P_\mathrm{a} \times \left[1 - \left\{ 1 - \frac{T_\mathrm{i} + T_\mathrm{v}}{T_\mathrm{s}} \right\}^n \right] \quad \text{(leakage not caused by work and ignition source caused by work)} \tag{7-15}$$

$$P_\mathrm{t} = k \times P_\mathrm{a} \times P_\mathrm{b} \times \left[1 - \left\{ 1 - \frac{T_\mathrm{i} + T_\mathrm{v}}{T_\mathrm{s}} \right\}^{n\times T_\mathrm{s}/T_\mathrm{d}} \right] \quad \text{(leakage and ignition source not caused by work)} \tag{7-16}$$

$$P_\mathrm{t} = k \times P_\mathrm{b} \times \left[1 - \left\{ 1 - \frac{T_\mathrm{i} + T_\mathrm{v}}{T_\mathrm{s}} \right\}^{n\times T_\mathrm{s}/T_\mathrm{d}} \right] \quad \text{(leakage caused by work and ignition source not caused by work)} \tag{7-17}$$

Here,	n	frequency of ignition source occurrence per day	times/day
	P	Ignition probability	-
	P_a	Annual work time rate	-
	P_b	Encounter probability between ignition source and work time	-
	P_r	Refrigerant leak probability	-
	P_s	Spatial encounter probability	-
	P_t	Temporal encounter probability	-
	T	Time	s
	T_d	Time per day	s
	T_i	Duration of ignition source presence	s
	T_s	Work time	s
	T_v	Duration of flammable region	s
	V_g	Volume of the Target space	m^3
	V_v	Mean flammable volume	m^3

The ignition probability at usage stage is obtained from the weighted average of the ignition probabilities during operation and non-operation of the fan in the condensing unit. For refrigerant leakage from the refrigerated space of the reach-in refrigerated display cabinet, Eq. (7-1) and Eq. (7-2) are used when it is not in operation, and Eq. (7-3) and Eq. (7-4) are used when in operation. When the refrigerant leaks from the condensing unit at the bottom of the refrigerated display cabinet, Eq. (7-5) and Eq. (7-6) are used when not in operation. When it is in operation, the flammable region is not generated because the air flow rate is assumed to have a value that is not less that obtained using Eq. (7-7)[7-3)]. The value at work stage is calculated by using the equation for non-operation of the fan. Fault tree analysis (FTA) is employed for calculating the ignition probability. When the ignition probability exceeds the tolerable value, safety measures are employed for risk reduction and repeated until the ignition probability falls to the tolerable value or lower[7-8)]. It must be noted that the effects of safety measures were set based on information available in literature[7-9)].

7.3.1.2 Setting the risk assessment model

The model of the store used in risk assessment is a convenience store in which simple cooking such as frying is permitted. Because there are a large number of convenience stores (approximately 56,000), they account for a large proportion of the number of built-in refrigerated display cabinets in the market. A3 refrigerants can be ignited with static electricity and relays of electrical devices in the store; therefore, convenience stores are assumed to be the most dangerous place for A3 refrigerants. In the risk assessment, the refrigerant is 0.5 kg of R290, the ceiling height of the store is 2.2 m, and the store floor area is 84.7 m^2 (this value excludes the separate-type closed refrigerated display cabinets installed inside the store, office, lavatory, etc., but includes the floor area in checkout area).

The built-in refrigerated display cabinet was manufactured in a factory, temporarily stored in a warehouse, transported to the store, and installed at an appropriate location, and then used. Repair of the refrigerated display cabinet was done either at the installed location or the refrigerated display cabinet was taken back to the manufacturer's service center, repaired, and then re-installed. In the risk assessment by JRAIA, transportation, storage, installation, usage, repair, and removal are defined as life stages. All ignition accidents are assumed to be fatal, with the tolerable level defined to be on the level of an ignition accident occurring once or less in 100 years[7-6)]. Based on the number of built-in refrigerated display cabinets in the market in Japan, which is1.9 million, the tolerable value at usage stage is set at 5.26×10^{-9}. At stages other than the usage stage, since workers who normally handle refrigerated display cabinets are professionals who have undergone specialized training, it is assumed that the tolerable value can be raised by one digit compared to that at usage[7-6)], and is therefore set at 5.26×10^{-8}.

7.3.1.3 Leak rate and refrigerant leak probability

Leak rate is classified into burst leak, rapid leak and slow leak, depending on the extent of damage to the pipe[7-6)]. In the case of R32, the rates are 75, 10 and 1 kg/h[7-6)], respectively. When converted to rates for R290, they are 40.71, 5.4

and 0.54 kg/h, respectively. In the risk assessment, however, the leak rate which is the rate of total refrigerant charge leaked in 4 min (7.5 kg/h for 0.5 kg of R290) is adopted here. This is a stipulation of IEC 60335-2-40[7-10)], the international standard for air conditioners. Based on the results of the survey, the refrigerant leak probabilities of the built-in refrigerated display cabinet in the usage stage were set as 5.26×10^{-7}, 1.89×10^{-5} and 9.82×10^{-4}, for burst, rapid and slow leaks respectively. When there is a leakage of refrigerant R290 from the condensing unit at the bottom, a large flammable cloud is generated even for slow leak (see subsection 7.2.3). Hence, in the risk assessment of A3 refrigerants, the refrigerant leak probability at the usage stage was set at 1.0×10^{-3}, which is the total value of all leak probabilities. Refrigerant leak probability at initial installation is set at 2.11×10^{-4}, which is the number of appliances that fail due to refrigerant leaks among the number of initial failures, divided by the number of appliances shipped. This value is used as the refrigerant leak probability from factory shipment to installation. For the transportation and installation stages, this value divided by 3 is used as the refrigerant leak probability. For the storage stage, which includes long-term storage, the refrigerant leak probability until initial installation is used without modification to assure safety. The refrigerant leak probability at repair or removal stage is calculated from the frequency of human error. In general, risk assessment assumes normal working conditions, and hence the value of human error under these conditions is set at 1.0×10^{-3} [7-11)]. The work executed newly to prevent ignition of the flammable refrigerant is different from conventional work and requires caution, and hence the value of human error is set at 5.0×10^{-2} [7-11)].

7.3.2 Calculation of ignition probability and safety measures for A3 refrigerants at usage

Table 7-2 shows the main ignition sources for A3 refrigerants under use at a convenience store. Turning the power of the relay of each electrical device in the store ON/OFF (coffee machine: 186 times a day, deep frying machine, Chinese-style buns steamer and heating appliance for "Oden": 10 times a day), unplugging a vacuum cleaner from the power outlet (twice a day, occurrence rate of 50 %), turning the lighting switch from on to off (twice a day), etc. could generate electric sparks and therefore are assumed to be ignition sources. The brush motor (dissemination rate is 1 %) used in fans for display cabinets other than the one being considered here, was assumed to be an ignition source only when the motor was turned ON, since the airflow around the motor in operation is sufficiently faster than the burning velocity of the refrigerant. In this case, the defrost rate of the evaporator is set at 8.3×10^{-2} (stopped for 2 h/day) and fan failure rate of 2.5×10^{-4} based on research conducted on A2L risk assessment[7-12)]. When safety measures are not implemented, the probability of the fan stopping is assumed to be the sum of the defrost rate and the fan failure rate. The duration of the electric spark is set at 5 ms, assuming maximum wavelength of 1/4 with a 50 Hz power source. Because the difference between the commercial copier and home-use printers is unknown, the commercial copier is assumed to be an ignition source while in use (operates 50 times a day for 3 min at a time), to enhance safety in risk assessment. Static electricity is assumed to occur due to human contact with the metal parts of refrigerated display cabinets. Electrostatic discharge is assumed to occur many times considering all the people in the store. When the entrance door to the store is opened manually it discharges static electricity on entry of each person. Hence, the electrostatic spark occurrence rate is set by taking the product of the probability of 30 % or less in humidity obtained by converting the weather data of Tokyo into the temperature inside the store (18.7 %) and the ratio for automatic doors (50%). The occurrence rate was 44 times a day for the reach-in refrigerated display cabinet and 22 times a day for other display cabinets (×2 cases), the duration of the electrostatic spark was set at 1 μs[7-13], and discharge energy was set at 0.8 to 1.0 mJ[7-14)]. The discharge energy level is maximum for the assumed electrostatic spark from the human body. In the risk assessment, the electrostatic spark is assumed to occur with this energy level every time. Since the static electricity and brush motor of the fan have low discharge energy levels[7-7)] and the ignition area is roughly halfway between the LFL and UFL, for R290, as shown in Fig. 7-24 (created based on literature[7-15)]), the ignition probability was calculated with the flammable volume-time integration assumed to be roughly 1/2. As for the open flame, it was assumed that 5 persons would each try and use cigarette lighters on display in the store for 5 s per day. A combustion-type heater, with dissemination rate 0.01 %, was assumed to be used for 10 h per day. It is assumed that shoppers do not smoke in the store. All high-temperature surfaces are at temperatures that are lower than the auto-ignition temperature for R290 and hence are not ignition sources. If refrigerant leaks from the refrigerated display cabinet, a flammable region is generated in the lower area in the store. If the fan in the condensing unit is operating (Fig.

7-3), the flammable region is not likely to be generated in other areas via the ceiling. Therefore, the height of ignition source present is not taken into account. Fire accidents due to electrical devices were also taken into consideration based on the research data from NITE (National Institute of Technology and Evaluation)[7-16].

The results showed that the ignition probability at usage and without safety measures ("No measures" in Table 7-3) exceeded the tolerable value. For this reason, appropriate measures were reviewed. With the implementation of the following safety measures, the ignition probability ("With measures" in Table 7-3) reduced to the tolerable value or lower. Implementation of the same safety measures for R600a, whose value in flammable volume-time integration is approximately 10 % greater than that of R290, has confirmed reduction in ignition probability to the tolerable value or lower.

(1) The fan in the condensing unit is operated even while defrosting.

(2) Set air flow rate of the fan in the condensing unit to the value calculated with Eq. (17) or higher.

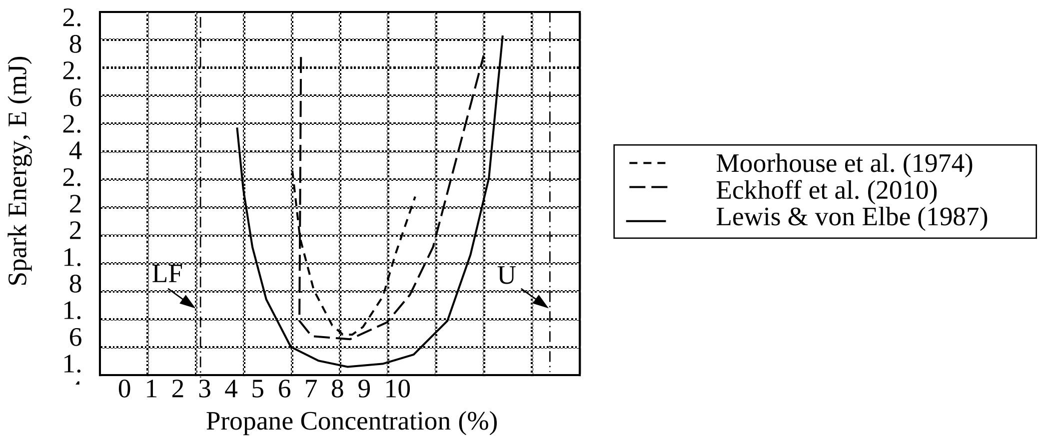

Fig. 7-24 The difference in minimum ignition energy of R290

Table 7-2 Ignition sources for A3 refrigerants at the usage stage

(a) Electric spark

Name	T_i (s)	n	k	Note
Coffee machine	5×10^{-3}	186	1	Relay operates when selling
Switch of deep-frying machine	5×10^{-3}	10	1	Cooking every 4 h in a span of 20 h
Chinese-style buns steamer	5×10^{-3}	10	1	Cooking every 4 h in a span of 20 h
Heating appliance for "Oden"	5×10^{-3}	10	1	Cooking every 4 h in a span of 20 h
Power outlet	5×10^{-3}	2	0.5	Unplugging vacuum cleaner twice a day; occurrence rate: 50 %
Lighting switch	5×10^{-3}	2	1	Switch from on to off twice per day
Copier	180	50	1	50 times a day, usage time 3 min
Brush motors of others	5×10^{-3}	144	0.01	Turn on 6 times in 1 h. dissemination rate: 1 %

(b) Static electricity

Name	T_i (s)	n	k	Note
Door of reach-in display cabinet	1×10^{-6}	44	0.0935	Taking out iced coffee. 10 % of spark encounter flammable region
Exterior of open display cabinet	1×10^{-6}	22	0.0935	Shoppers touch metallic parts
Other doors	1×10^{-6}	22	0.0935	Shoppers touch metallic parts

(c) Open flame

Name	T_i (s)	n	k	Note
Cigarette lighter	5	5	1	5 people trying for 5 s per day
Combustion-type heater	3.6×10^{4}	1	1×10^{-4}	Use 10 h in a day, Dissemination rate: 0.01 %

Table 7-3 Ignition probability for R290 at the usage stage (tolerable value; 5.26×10^{-9})

Stage	No measures	With measures
Usage	2.50×10^{-6}	1.82×10^{-10}

(3) Install functions to detect and turn on the alarm in case of refrigerant leakage in the refrigerated space of the reach-in refrigerated display cabinet and shut off the refrigerant leakage into the refrigerated space in the event of refrigerant leakage.

Here, the failure rate of the shutoff valve is 4.05×10^{-4} according to a study on the risk assessment for A2L refrigerants[7-12)]. It is assumed that the probability of failure with the valve open is less than the probability of failure with the valve closed. For this reason, the shutoff valve failure rate is set at 1.0×10^{-4} and that the refrigerant circuit is not shut off at this probability with the implementation of safety measures. The effectiveness of the alarm was set at 1.0×10^{-1} [7-9)].

7.3.3 Calculation of ignition probability and safety measures for A3 refrigerants during working

Since some ignition sources are commonly found at work, the scenario for each work stage is explained, followed by explanation of ignition sources at work.

7.3.3.1 Scenario for transportation stage

A built-in refrigerated display cabinet installed in a convenience store is generally transported by a truck. When transported by truck there is no ignition source in the freight compartment at the back of the truck. Therefore, risk assessment for the transportation stage assumes transportation by a minivan, in which the cargo compartment and the driver share the same space, and only the condensing unit is transported. On the outbound route, the unused product is transported packed in a wooden crate, and on the return route, the used product is transported without packing. The replacement of the condensing unit is assumed to take place when repairs are required for the refrigerant circuit. The minivan transportation rate is calculated as 4.2×10^{-6} by multiplying 8.39×10^{-4} (see subsection 7.3.3.4), which is the survey result based on the number of repairs required by the refrigerant circuit divided by the number of appliances in the market, by the value 5×10^{-3}, which is the probability that the replaced condensing unit contains the refrigerant. The risk assessment was also carried out when the minivan transportation rate was 1 to enhance safety. It is assumed that the internal volume of minivan is 2.9 m^3, the number of persons on board is two, necessary for the loading and unloading of appliances, the maximum transportation time is 12 h, and the average transportation time is 2 h.

7.3.3.2 Scenario for storage stage

Storage locations for refrigerated display cabinets are classified into medium-sized and small-sized warehouses. Medium-sized warehouses are used for temporary storage following receipt of shipment from factories in Japan or overseas, and are assumed to have space of 1000 m^2. Small-sized warehouses are used for storage at each sales location, and are assumed to have space of 15 m^2. Refrigerated display cabinets are handled in the warehouse by forklifts or trolleys operated personally by workers. In a medium-sized warehouse, it is assumed that five people work 8 h per day for 20 days a month, and in a small-sized warehouse, two people work for 2 h per day for 20 days a month. There are unused and secondhand products stored in the warehouse. Unused products are assumed to be wrapped in plastic or in plastic plus wooden crate, and secondhand products are stored without packing or being wrapped in plastic.

7.3.3.3 Scenario for installation stage

Installation work involves unloading the refrigerated display cabinet located in the freight compartment of the truck to the ground in the open air, carrying the unloaded cabinet to the installation location inside the store and placement consisting of unwrapping and attachment of accessories and parts at the installation location. These tasks require two workers working for 1 h for each refrigerated display cabinet. The time required is broken down into 0.2 h for unloading work, 0.1 h for carrying and 0.7 h for placement. The annual installation rate is same as the annual removal rate, and set at 1.24×10^{-1} (see subsection 7.3.3.5), which is the sum of the probability of replacement at the end of service life, and the probability of removal due to store closing. Installation stage assumes installation of the appliance during new store construction or at a store in operation.

7.3.3.4 Scenario for repair stage

Repair is classified into taken-back repair in which the appliance is repaired at a service center of the manufacturer, etc., outdoor repair in which the appliance is moved temporally outside the store for repairs, and in-store repair to be repaired at the installation location in the store. The annual repair rate of built-in refrigerated display cabinets is 1.0×10^{-2} (the total number of repairs at JRAIA member companies found through survey results for FY2011 – FY2015 divided by 1.9 million units in operation). In on-site repair, the rate of repair requiring refrigerant circuit repair is assumed to be 8.39×10^{-2} (number of repairs on refrigerant circuits at JRAIA member companies found through survey from FY2011 – FY2015 divided by the total number of repairs). Recovery of flammable refrigerant by using a refrigerant recovery machine is substantially impossible because according to the High Pressure Gas Safety Act it requires a notification report to regulatory authorities to be made 20 days in advance. Therefore, when repairing the refrigerant circuit, it is assumed that the refrigerant will be released to the atmosphere (refrigerant disposal), and that it will be released to the atmosphere via a hose, or the refrigerant is transferred to a collection bag and then released to the atmosphere. Further, release into the atmosphere is done at a location away from ignition sources and in well ventilated spaces and must it also be released in small quantities. Regarding time required for repair, it is assumed that 1 h is required for releasing the refrigerant, 1 h for pipe disconnection and replacement of refrigerant circuit parts, 1 h for charging the refrigerant, and 1 h for miscellaneous work not related to the refrigerant circuit.

7.3.3.5 Scenario for removal stage

At the removal stage, it is assumed that the refrigerated display cabinet is removed from the store for disposal. At this time, the built-in refrigerated display cabinet is moved along with the refrigerant contained in the refrigerant circuit. The annual removal rate is set at 1.24×10^{-1}, which is the sum of 7.69×10^{-2} (inverse number of the end of service life of 13 years) and 4.70×10^{-2} (the number of convenience store openings and closings in FY2014 – FY2060, based on survey results, converted into per-year value). The time for removal is assumed to be 1 h. Removal is assumed to take place in case of permanent store closing or from a store in operation.

7.3.3.6 Calculation of ignition probability and safety measures

Table 7-4 shows the main ignition sources at each of the work stages, transportation, storage, installation, repair, and removal. The usage time and frequency of each ignition source were set according to the work pattern in each stage. Ignition sources at usage, shown in Table 7-2, also took into account the working at a store in operation. Regarding cigarette smoking by workers, the smoking time per cigarette is assumed as 5 min, of which the time for the cigarette having the red tip is 40 s and the ignition time of the cigarette lighter is 5 s. Workers are assumed to be male, with smoking rate of 28.2 % and 1.08 cigarettes smoked per hour. At repair or removal, before the work starts, unplugging of the operating refrigerated display cabinet from the power outlet is assumed. The occurring probability is 25 %, obtained by taking the product of the existence rate of the power outlet at the bottom of the display cabinet which is 50 %, and the occurring rate of unplugging which is 50 %. During repair, the vacuum pump and the ON/OFF switch of the refrigerant recovery machine (twice in total) are assumed to be ignition sources. The probability of the erroneous use of the refrigerant recovery machine, which is not permitted for flammable refrigerants under statutory law, is set at 50 %. The duration of the electric spark was set at 5 ms. In the use of the electric screwdriver, the brush motor (existence rate of 5 %) is assumed to ignite, with a discharge duration of 3 s and occurrence frequency of 10. An electrostatic spark is assumed to be generated when a worker touches the metal surface of the refrigerated display cabinet or when a worker touches the ignition key during transportation. The duration of the electrostatic spark is assumed to be 1 μs[7-13]. The frequency of electrostatic spark is set according to the scenario of each work, 1.1 times for transportation (discharge when getting out of the vehicle. 10 % probability of taking breaks), 1 time for storage, 2 times at installation (in removal of vinyl cover and protective film), 2 times for repair (at start of repair and removal of panel at completion), and 1 time at removal (protective covering of the door). In medium-sized warehouse storage and outdoor work (appliance unloading for installation and outdoor repair), the occurrence rate of electrostatic spark is assumed to be 3.2 %, which is a probability of 30 % or less based on humidity in Tokyo based on weather data. For work inside the store, the occurrence rate of electrostatic spark is assumed to be 18.7 %, which is the probability of 30 % or less based in humidity which is the result of converting the said weather data into temperature inside the store. Electrostatic spark caused by clothing removal was not considered to be an ignition source[7-7]. Static electricity and the electric screwdrivers (the brush motor) have small spark energy[7-7], ignition probability is calculated using a value that halves the flammable volume-time integration. In repair work related to the refrigerant circuit, parts from two locations were assumed to be attached and detached using brazing for replacement, each requiring 2 min.

In transportation, refrigerant leakage inside the minivan is assumed to be uniform in concentration due to the small interior space. The mean flammable volume was assumed to be identical to the interior volume, at 2.9 m^3. Further, Eq. (7-18) is assumed to be valid until end of leakage, and Eq. (7-19) valid after the end of leakage[7-6]. Hence, the duration of the flammable region is calculated depending on the length of time for which the concentration is between LFL and UFL. The leak rate was set at the leak rate of total refrigerant charge leaked in 4 min, and the natural draft ventilation volume was set at 1.11×10^{-3} m^3/s[7-17]. Therefore, the duration of the flammable region was 67.1 min. If the exterior air intake mode of the air conditioner is used, the ventilation volume is large[7-18], and flammable region is not likely to be generated inside the vehicle. Based on survey results regarding the rate of exterior air intake mode usage, ventilation rate prior to smoking, etc., the probability of the flammable region not being generated in the vehicle while smoking (probability of ventilation prior to lighting the cigarette) is set at 64.6 %.

$$C = \frac{w}{Q_c} \times \left(1 - e^{-\lambda \times T}\right) \tag{7-18}$$

$$C = \frac{w}{Q_c} \times \left(1 - e^{-\lambda \times M/w}\right) \times e^{-\lambda \times (T - M/w)} \tag{7-19}$$

Here,	C	Refrigerant concentration	kg/m^3
	M	Refrigerant amount	kg
	Q_c	Natural draft ventilation volume	m^3/s
	T	Time	s
	w	Refrigerant leak rate	kg/s
	λ	Ventilation frequency	instances/s

Additionally, the duration of the flammable region and mean flammable volume in the medium-sized warehouse storage and during outdoor work (appliance unloading for installation and outdoor repair) is set based on Eq. (7-1) to Eq. (7-6) for the maximum floor space of 100 m^2 used in the analysis.

The calculated results for ignition probability are shown in the “No measures” column of Table 7-5. The ignition probability exceeds the tolerable value in the case of the highest ignition probability in the scenarios of each stage, that is when minivan transportation rate is 1 at transportation stage, when secondhand products are stored in small-sized warehouse at storage stage and when installation, repair or removal are carried out at a store in operation. Ignition probabilities, shown in “With measures” column in Table 7-5, fell to the tolerable value or lower, by taking the safety measures in Table 7-6 in addition to education and training in handling of flammable refrigerants (ban on smoking, education regarding ignition sources). Taking the same safety measures for R600a, whose value in flammable-volume time integration is approximately 10 % larger than R290, has been confirmed to reduce ignition probabilities to within the tolerable value or lower.

Table 7-4 Ignition sources for A3 refrigerants at the work stage

(a) Common

Name	T_i (s)	n	k	Note
Smoking by workers (Open flame)	4.5×10^{1}	1.08 /h	0.282 /person	Number: 1 /person/h; ignition time with lighter: 5 s; duration of red tip: 40 s; smoking rate: 28.2 %

(b) Transportation

Name	T_i (s)	n	k	Note
Key contact (Static electricity)	1.0×10^{-6}	1.1	0.0468	1.1 times, discharge rate: 25 % (0.25×0.187=0.0468)

(c) Storage

Name	T_i (s)	n	k	Note
Static electricity	1.0×10^{-6}	1	0.064	Contact by worker (secondhand, unpacked) (2 person×0.032=0.064)
Combustion-type heater (Open flame)	7.2×10^{2}	1	0.082	120 days per year; rate: 25 %(0.25×120/365=0.082)

(d) Installation, repair or removal

Name	T_i (s)		k	Note
Ignition source in usage	–		–	See Table 7-2
Power outlet (Electric spark) (at repair or removal)	5.0×10^{-3}		0.25	Unplugging the display cabinet in question; rate: 25 %
Electric screwdriver (Brush motor)	3.0	10	0.05	Opening/closing; existence ratio: 5 %
Electrostatic spark	1.0×10^{-6}	1-2	0.187 /person	Touching display cabinet
Brazing burner (Open flame) (only at repair)	1.2×10^{2}		1	2 min × 4 locations
Vacuum pump (Only at repair)	5.0×10^{-3}		1	Switch ON/OFF
Refrigerant recovery machine (Only at repair)	5.0×10^{-3}		0.5	Switch ON/OFF, Misuse rate 50 %

Table 7-5 Ignition probability for R290 at the work stage (tolerable value; 5.26×10^{-8})

Stage	No measures	With measures
Transportation (For minivan transportation rate set at 1)	1.12×10^{-5}	1.02×10^{-9}
Storage (Secondhand products in a small-sized warehouse)	3.25×10^{-6}	3.65×10^{-8}
Installation (Store in operation)	7.65×10^{-8}	6.85×10^{-9}
Repair (In-store repair)	2.18×10^{-5}	1.23×10^{-8}
Removal (Store in operation)	3.00×10^{-7}	2.81×10^{-8}

Table 7-6 Safety measures for A3 refrigerants at the work stage

Stage	Safety measures
Transportation (By minivan)	1. Marking of warning of risk of fire on the product 2. Using a portable leak detector and ventilation in the event of leakage
Storage	1. Use of gloves to prevent electrostatic discharge 2. Marking of warning of risk of fire on the product and packing
Installation	1. Use of gloves to prevent electrostatic discharge 2. Marking of warning of risk of fire on the product 3. Using a portable leak detector and stopping work in the event of leakage
Repair	1. Use of gloves to prevent electrostatic discharge 2. Using a portable leak detector and stopping work in the event of leakage 3. In in-store repair, cutting off power to all devices likely to become ignition sources and providing ventilation around the refrigerated display cabinet while executing the disposal or charging of the refrigerant
Removal	1. Use of gloves to prevent electrostatic discharge 2. Marking of warning of risk of fire on the product 3. Using a portable leak detector and stopping work in the event of leakage

The effectiveness of training in flammable refrigerant handling and warning labels are both set at 1.0×10^{-1} [7-9]. The effectiveness of the portable leak detector is assumed identical to maintenance inspection and is set at 1.0×10^{-2} [7-9]. The effectiveness of gloves for preventing electrostatic discharge is set at 1.0×10^{-2}, based on JRAIA study findings. In terms of cutting off energization of devices during in-store repair, the presence of persons who failed to implement safety measures is assumed at the rate for human error.

7.3.3.7 Risk assessment for small stores

Risk assessments were also carried out by assuming a small convenience store inside of a station (with floor area of 24.01 m^2 and ceiling height of 2.2 m) in which the built-in refrigerated display cabinet charged with 0.5 kg of R290 was installed. The value of flammable volume-time integration for 0.5 kg of R290 and floor area of 24.01 m^2 and calculated as discussed in Section 7.2 was used. Ignition sources were set in accordance with study results. The existence rate of small stores was set at 0.2 %. The results show that the ignition probabilities were within the tolerable value or lower for all stages following implementation of the same safety measures.

7.3.3.8 Risk assessment of convenience store using A2L refrigerant

Risk assessments were carried out assuming that the built-in refrigerated display cabinet using A2L refrigerant were installed in a convenience store (with floor area of 84.7 m²). The size of the refrigerated space of the reach-in refrigerated display cabinet is the same as the R290. For the condensing unit, the refrigerant is assumed to be 1.0 kg of R1234yf (refrigerant charge with capacity identical to that of 0.5 kg of R290 using identical cabinet size) and the cabinet is assumed to be a small cabinet at transportation and storage stages. At all other stages, the amount of R1234yf is assumed to be 3.8 kg (13 times the LFL) and the cabinet is assumed to be a large cabinet.

At transportation stage, 1.0 kg of R1234yf is assumed to leak in 4 min. As a result of calculation using Eqs. (7-18) and (7-19), the duration of the flammable region was found to be 5.7 min. The flammable volume-time integration for a small room (approx. 15 to 30 m²), such as storage in a small-sized warehouse, was calculated with weighted average, employing the method described in 7.2.6.2. In slow leak, the flammable region is not generated for a floor area of 84.7 m² or larger, even when refrigerant amount is 3.8 kg. For this reason, for medium-sized warehouse storage, installation, usage, repair and removal, the refrigerant leak probability from the condensing unit was set to the value excluding slow leak probability. The ignition sources for A2L refrigerant are shown in Table 7-7. These are the open flames described in Table 7-2 and 7-4. The probability for cigarette lighters, however, was set at 5 %, assuming that ignition is caused only by kerosene lighters[7-6)] except at usage. The cigarette lighters at usage were used as a trial ignition, and all cigarette lighters were assumed to ignite, assuming that the shoppers would definitely ignite cigarette lighters. Also, a brazing burner is assumed not to ignite where the refrigerant is bursting[7-6)], but in the surrounding flammable region.

Table 7-7 Ignition sources for A2L refrigerants

(a) Usage stage

Name	T_i (s)	n	k	Note
Cigarette lighter	5	5	1	5 people try igniting for 5 s per day
Combustion-type heater	3.6×10^4	1	0.0001	Use 10 h in a day, Dissemination rate: 0.01 %

(f) Common for the work stage

Name	T_i (s)	n	k	Note
Smoking by workers (Open flame)	5	1/h	0.0141/person	Cigarette smoked: 1 /person/h; ignition time with lighter: 5 s; smoking rate: 28.2 %; existence rate of oil lighter: 5 %

(b) Storage (2 h, 2 workers, 15 m^2)

Name	T_i (s)	n	k	Note
Combustion-type heater (Open flame)	7.2×10^2	1	0.082	Usage for 120 days per year; usage rate: 25 % (0.25×120/365=0.082)

(c) Install, repair or removal (1 to 4 h, 1 to 2 workers)

Name	T_i (s)	n	k	Note
Ignition source in usage	–	–	–	See (a)
Burner for brazing (Open flame)	1.2×10^2	4	0.5	2 min × 4 locations (not to ignite in the area of burst of refrigerant) (only at repair)

Table 7-8 Ignition probability of commercial freezer, refrigerator and commercial ice-makers for R1234yf (tolerable value; 3.22×10^{-9} for usage stage, 3.22×10^{-8} for work stage)

Stage	No measures	With measures
Installation (In-store operation)	5.64×10^{-8}	3.70×10^{-9}
Repair (In-store repair)	2.47×10^{-7}	1.27×10^{-9}
Removal (In-store operation)	1.46×10^{-7}	1.98×10^{-8}

Table 7-9 Safety measures for A2L refrigerants at the work stage
(No safety measures required at transportation and storage)

Stage	Safety measures
Installation	1. Marking of warning of risk of fire on the product 2. Using a portable leak detector and stopping work in the event of leakage
Repair	1. Using a portable leak detector and stopping work in the event of leakage 2. During in-store repair, prohibit the use of open flames and provide ventilation around the refrigerated display cabinet while recovering the refrigerant by using the recovery machine or charging the refrigerant
Removal	1. Marking of warning of risk of fire on the product 2. Using a portable leak detector and stopping work in the event of leakage

As a result of risk assessment, the ignition probability at usage was 2.63×10^{-8}, which exceeded the tolerable value without safety measures. In addition, by taking identical safety measures as described in Subsection 7.3.2 as with R290, the ignition probability was 2.20×10^{-13}, which was the tolerable value or lower. Risk assessment results at working showed that the ignition probability at transportation (5.03×10^{-8}) and storage (1.34×10^{-9}) were within the tolerable value or lower without safety measures. For this reason, safety measures became unnecessary for these stages. At other work stages, the ignition probability of installation, repair, and removal had the same value as tolerable value or lower without safety measures. Although the ignition source for A2L refrigerant is an open flame, the built-in refrigerated display cabinet is rarely installed in locations where there is a large presence of open flames. IEC 60335-2-89, JIS C 9335-2-89 and JRAIA standards also cover commercial freezers, refrigerators and commercial ice-makers, which are installed in places where there is a large presence of open flame. Therefore, risk assessments were carried out when the equipment was assumed to be installed in commercial kitchens (with floor are of 30.17 m^2). At that time, the effect of door gaps and the effect of the ventilation (0.1 m/s) based on the Building Standard Law were considered by multiplying the flammable volume-time integration by an appropriate coefficient value. The results, shown in Table 7-8, showed that the ignition probability exceeded the tolerable value at installation, repair and removal, and fell to the tolerable value or lower with training in A2L refrigerant handling (ban on cigarette smoking, training in ignition sources, etc.) and implementation of safety measures, as shown in Table 7-9. Safety measures for built-in refrigerated display cabinets were assumed to be identical for these appliances. The differences as compared to safety measures for A3 refrigerants (Table 7-6) are the absence of gloves to prevent electrostatic sparks and the replacement of cutting off the power during in-store repair with the ban on use of open flames. These safety measures are similar to the safety measures for other A2L equipment[7-12)].

7.4 International standards and Japanese standards

7.4.1 International standards

The following is a summary of IEC 60335-2-89 Edition 3.0[7-1)], the international standard for commercial refrigerating appliances. IEC 60335-2-89 refers to A2L, A2 and A3 refrigerants as flammable refrigerants.

7.4.1.1 Maximum refrigerant charge

The maximum amount for flammable refrigerant to be charged into the refrigerant circuit is either 13 times the LFL or 1.2 kg, whichever is smaller. In the case of R290, the LFL is 0.038 kg/m^3, and maximum refrigerant charge is 0.494 kg. Due to the proposal from Japan to the IEC, the upper limit of 1.2 kg is to be removed in the next edition, and it will be possible to charge up to 13 times the LFL for any refrigerant.

7.4.1.2 Minimum room floor area

An appliance charged with more than 0.15 kg of flammable refrigerant shall be installed in a room not smaller than the minimum room floor area, which is 1/4 of the LFL vis-à-vis room volume. The minimum room floor area, which an appliance charged with 0.494 kg of R290 can be installed, is 23.7 m^2.

7.4.1.3 Refrigerant leak test

An appliance charged with a flammable refrigerant of more than 0.15 kg shall carry out designated refrigerant leak tests. For reach-in refrigerated display cabinets, etc., cabinet door or lid shall be opened after the full amount of refrigerant is leaked inside the refrigerated space. The refrigerant concentration around the appliance is measured in intervals of 5 s or less and shall not exceed 1/2 of the LFL after 5 min of measurement.

7.4.2 Japanese standards

JIS C 9335-2-89 [7-19] is a standard developed by translation of IEC 60335-2-89 into Japanese, with addition of necessary deviations (differentials from international standards). It has been revised to correspond to Edition 3.0. JRA 4078[7-20] and JRA GL-21[7-21] are JRAIA standards based on the results of risk assessments of built-in refrigerated display cabinets charged with A3 refrigerants. JRA 4084[7-22] and JRA GL-23[7-23] are JRAIA standards based on the results of risk assessments of built-in refrigerated display cabinets, commercial freezers, refrigerators and commercial ice-makers using A2L refrigerants. These standards are collectively called Japanese standards. The following is a summary of these standards.

7.4.2.1 Maximum refrigerant charge

Although A2L refrigerants are lower in flammability compared to A2 and A3 refrigerants, IEC 60335-2-89 limits the charging up to only 1.2 kg. On the other hand, IEC 60335-2-40, the standard for air-conditioners, allows charging of A2 and A3 refrigerants up to 26 times the LFL, and charging of A2L refrigerants up to 52 times the LFL due to differences in flammability. For this reason, the Japanese standards have removed the limit of 1.2 kg to allow charging up to 13 times the LFL for any of these refrigerants. In the case of R1234yf, the LFL is 0.289 kg/m^3, and maximum refrigerant charge is 3.76 kg.

7.4.2.2 Surface temperature

IEC 60335-2-89 sets forth that temperatures on surfaces that may be exposed to leaked flammable refrigerants shall not exceed the auto-ignition temperature of the refrigerant, reduced by 100 K. On the other hand, however, IEC 60335-2-40, the standard for air-conditioners, accepts up to 700 ℃ in surface temperature for surfaces exposed to A2L refrigerants, due to its low level of flammability. Therefore, the Japanese standards provide that temperature shall not exceed the auto-ignition temperature of A2 and A3 refrigerants, reduced by 100 K, and not to exceed 700 ℃ for A2L refrigerants. Due to the proposal from Japan to the IEC, the specifications regarding surface temperatures will also become the same as those of Japanese standards in the next edition.

7.4.2.3 Deletion of exemption period and measures to prevent flammable region generation

For reach-in refrigerated display cabinets, a large flammable cloud is generated outside the refrigerated space by sudden door opening after the full amount of refrigerant is leaked inside the refrigerated space (see 7.2.2). For A3 refrigerants, static electricity and relays of electrical devices are ignition sources. Hence, there is a possibility of ignition easily if a flammable region is generated even for a short time. In commercial kitchens, even A2L refrigerants can easily be ignited by open flames. In Japanese standards, the 5-minute measurement exclusion period beginning with the start of measurement is deleted, so as not to allow generation of a flammable region. They require that the appliance be equipped with the means of detecting leakage into the refrigerated display cabinet and a device for shutting off the refrigerant circuit. Furthermore, JRAIA standards set forth the operation of a fan with the air flow rate described in Eq. (7-7), in case of leakage from the condensing unit.

7.4.2.4 Marking on appliance and safety requirements at working

JRAIA standards put forth labeling of special warning on appliances. There are also provisions requiring the use of gloves to prevent electrostatic sparks (JRA GL-21), carrying of portable leak detectors, stopping work when the alarm of a portable leak detector is set off and others aimed at reducing ignition risks during work. during in-store repair, thorough ventilation inside the store is required when refrigerants are released into the atmosphere and during refrigerant charging, as well as cutting off the power for all appliances (JRA GL-21). In addition, thorough ventilation is required at refrigerant recovery with a recovery machine for particular inert gases and at refrigerant charging, as well as a ban on the use of open flames inside the store (JRA GL-23). Furthermore, A3 and A2 refrigerants cannot be recovered by using a recovery machine during repair under the provisions of the High-Pressure Gas Safety Act (JRA GL-21).

7.5 Conclusions

Risk assessment was carried out on built-in refrigerated display cabinets using A3 refrigerants. Because the maximum charge for flammable refrigerants is established at 13 times that of LFL, a large built-in refrigerated display cabinet cannot be charged with A3 refrigerant in the required amount. For this reason, risk assessment was carried out on built-in refrigerated display cabinets using A2L refrigerants.

(1) Refrigerant leak analyses for A3 refrigerants were performed. The analysis code was validated by the results of the CO_2 leakage measurements for an air-conditioner conducted by the University of Tokyo. The results showed that when a refrigerant was leaked into the refrigerated space of a reach-in refrigerated display cabinet, and followed by sudden door opening, a flammable region is generated outside the refrigerated space. In the case of the refrigerant leakage from the condensing unit of a horizontal refrigerated display cabinet, the flammable region was not generated when air flow rate was the specified value or higher. When floor area was 84.7 m^2, which is the floor area of the convenience store, store door gaps have little impact, and the calculated flammable volume-time integration for enclosed store can be used for evaluation without any problem. Regarding leakage from a condensing unit, there was little change in the flammable volume-time integration, even with decrease in leak rate. Results of leak analysis of an actual store model showed that it is appropriate to include the checkout area in the floor area used for the evaluation. In addition, results of leak analysis for A2L refrigerant showed that, even if the leak height is near the floor surface, the flammable region is not generated in an enclosed store with 84.7 m^2 floor area in the case of a slow leak. Although the flammable region is generated in an enclosed store with a floor area of 24.01 m^2, in the case of a slow leak, the flammable region will not be generated unless it is an enclosed store.

(2) By assuming scenarios for each life stage of the appliance, ignition probabilities for A3 and A2L refrigerants were calculated, based on the flammable volume-time integration derived from refrigerant leak analysis and the ignition sources were defined by the findings based on the research by Imamura of Suwa University of Science. Further, safety measures were identified to reduce the ignition probabilities to the tolerable value or lower. At usage, continuous operation of the unit fan at an air flow rate of the specified value or higher while the refrigerated display cabinet is energized and functions to detect leakage into the refrigerated space of the reach-in refrigerated display cabinet and other closed cabinets and to shut off leakage into the refrigerated space when detected are prescribed as safety measures. Safety measures during work include warning labeling of appliances to prohibit use of ignition sources, carrying of portable leak detector and appropriate action in case the alarm is set off, use of gloves to prevent electrostatic sparks (in case of A3 refrigerant), thorough ventilation around the appliance in case of refrigerant disposal or charging and cutting off power to all appliances (in case of A3 refrigerant) while conducting in-store repair, and a ban on the use of open flame (in case of A2L refrigerant). The Japanese standards have been developed through comparison with the international standards and risk assessment findings, adding provisions that are believed to be inadequate according to international standards.

Acknowledgments

This report has been jointly authored by T. Kato (Okamura), S. Ikeda (Sanden Retail Systems), S. Sakae (Daikin Industries), S. Ishihara (Toshiba Carrier), A. Kobayashi (Nakano Refrigerators), H. Kaimuma (Panasonic), T. Hasegawa (Fukushima Galilei), H. Deno (Fuji Electric), H. Nagai (Hoshizaki), K. Hosaka (Mitsubishi Electric Applied Refrigeration Systems), under project leader K. Yamashita (Mitsubishi Electric). The authors express their deepest appreciation for the cooperation of K. Hori (Daikin Industries), M. Handa (Toshiba Carrier), F. Hotta (Fukushima Galilei) and H. Maeyama (Mitsubishi Electric) as observers and also to K. Hasegawa (JRAIA) for his secretarial service.

References

7-1) IEC 60335-2-89:2019, "Household and similar electrical appliances - Safety - Part 2-89: Particular requirements for commercial refrigerating appliances and ice-makers with an incorporated or remote refrigerant unit or motor-compressor", (2019.6).

7-2) N. Ashihara, M. Ito, C. Dang, E. Hihara and Y. Chen: "Numerical Simulation of Strongly Flammable Refrigerant Leakage from a Split Air Conditioner", Proc. 14th IIR Gustav Lorentzen Conference on Natural Refrigerants, 1202, Tokyo (2020).

7-3) D. Colbourne and K. O. Suen: "Minimum Airflow Rates to Dilute R290 Concentrations Arising from Leaks in Room Air Conditioners", Proc. 13th IIR Gustav Lorentzen Conference on Natural Refrigerants, 1104, Valencia (2018).

7-4) Y. Okabe: "Probability and Statistics", Asakura Publishing, Tokyo, pp. 131-133 (2010). (in Japanese)

7-5) http://izumi-math.jp/W_Takakura/k_kakuritu/k_kakuritu.pdf, (W. Takakura: "About teaching materials on geometric probability) (2020). (in Japanese)

7-6) R. Yajima, Y. Kiguchi, T. Sekine, S. Sasaki, S. Ito, K. Yamashita, T. Kannon: "Risk Assessment for VRF System with Mildly Flammable Refrigerants", Trans. of the JSRAE, 33(1), pp.23-39 (2016.3). (in Japanese)

7-7) T. Imamura, "Progress achieved at Suwa University of Science", 2020 Progress Report Part 2: Safety and risk assessment of next-generation refrigerants, JSRAE, pp. 29-46 (2021). (in Japanese).

7-8) ISO/IEC Guide51, "Safety aspects - Guidelines for their inclusion in standards", (2014).

7-9) Ministry of Economy, Trade and Industry: "Risk Assessment Handbook - Practical Applications", (2011.6) (in Japanese)

7-10) IEC 60335-2-40:2018, "Household and similar electrical appliances - Safety - Part 2-40: Particular requirements for electrical heat pumps, air-conditioners and dehumidifiers", (2018.1)

7-11) David J. Smith: "Reliability, Maintainability and Risk 8th Edition: Practical Methods for Engineers", Eighth Edition, Elsevier, pp. 395-397 (2011).

7-12) The Japan Refrigeration and Air Conditioning Industry Association (JRAIA): "Report of Risk assessment for variable refrigerant flow using lower flammability refrigerant", https://www.jraia.or.jp/research/pdf/vrf_a0.pdf, (2017.9). (in Japanese)

7-13) T. Yoshida, K. Kubota, T. Sawai and N. Masui: "Time-Frequency Analysis of Discharge Current from Charged Human Body", Journal of the Institute of Electrostatics Japan, Vol. 31 (No. 3), pp. 113-118 (2007). (in Japanese)

7-14) M. Yamaguma: "Hydrogen Properties relating to Safety", Journal of Japan Society for Safety Engineering, 44(6), pp. 386-390 (2005). (in Japanese)

7-15) R. K. Eckhoff, M. Ngo and W. Olsen: "On the minimum ignition energy (MIE) for propane/air", Journal of Hazardous Materials, 175, pp. 293–297 (2010).

7-16) https://www.nite.go.jp/jiko/jiko-db/accident/search/

7-17) Y. Onishi, H. Okuyama, H. Nagayama and H. Oi: "An Engineering Calculation Model for Vertical Temperature Distribution in Vehicle Cabin", Technical papers of annual meeting, the Society of Heating, Air-Conditioning and Sanitary Engineers of Japan, pp.333-336 (2007.9). (in Japanese)

7-18) J. Nakagawa, G. Iwashita, Y. Yoshinami, H. Nagayama and Y. Yokoyama: "Fundamental study of lndoor Air Quality in the car compartment (Part 2) Report on ventilation rate and indoor VOCs concentration", Technical papers of annual meeting, the Society of Heating, Air-Conditioning and Sanitary Engineers of Japan, pp. 537-540 (2007.9). (in Japanese)

7-19) JIS 9335-2-89:2021, "Household and similar electrical appliances - Safety - Part 2-89: Particular requirements for commercial refrigerating appliances and ice-makers", (2021.3). (in Japanese)

7-20) JRA 4078:2021, "Requirements of ensuring safety against refrigerant leakage from commercial built-in refrigerating appliances using flammable refrigerants", JRAIA, (2021.3). (in Japanese)

7-21) JRA GL-21:2021, "Guideline of design construction for ensuring safety against refrigerant leakage from commercial built-in refrigerating appliances using flammable refrigerants", JRAIA (2021.3). (in Japanese)

7-22) JRA 4084:2022, "Requirements of ensuring safety against refrigerant leakage from commercial built-in refrigerating appliances using lower flammability refrigerants", JRAIA, (2022.9). (in Japanese)

7-23) JRA GL-23:2022, "Guideline of design construction for ensuring safety against refrigerant leakage from commercial built-in refrigerating appliances using lower flammability refrigerants", JRAIA (2022.9). (in Japanese)

Basic Performance, Optimization, and Safety and Risk Evaluation of Next-Generation Refrigerants and Refrigerating and Air Conditioning Technologies

Part 3: Survey of Regulations and Standards for Next-Generation Refrigerants

WG III Final Report

Research Committee for Next-Generation Refrigerants,

Japan Society of Refrigerating and Air-Conditioning Engineers

January 31, 2023

Table of Contents

1. Introduction

1.1 Overview of the Survey Project and this Report

The purpose of the research project conducted by the Japan Society of Refrigerating and Air-Conditioning Engineers (JSRAE) is to compile the results of the New Energy and Industrial Technology Development Organization (NEDO) project entitled “Development of technology and assessment techniques for next-generation refrigerants with a low GWP value” in a cross-sectional manner and to disseminate domestically and internationally. In addition, the project aims to investigate the basic characteristics and evaluate the performance of next-generation refrigerants, assess the safety and risk of refrigeration and air-conditioning equipment to which these refrigerants are applied, and propose contents for international standards.

In FY2018, the “WG III” working group was established within the JSRAE Research Committee for Next-Generation Refrigerants to consolidate information through exchange of opinions with experts. First, a survey of the current status of domestic and foreign regulations, types of standards, and contents related to refrigerants, refrigeration, and air-conditioning equipment was conducted.

In FY2019, to comprehend the latest trends, we collected more detailed information and conducted interviews with experts. We also visited relevant organizations in Europe and the US to investigate the trends in revisions of laws, regulations, and standards.

In FY2020, we further investigated the progress in revision of standards related to refrigerant safety and new refrigerant candidates from the perspective of patent applications. We also initiated a survey of standards related to system performance evaluation.

In FY2021, as a continuation of the previous survey, information was collected through published materials of related organizations, symposium materials, hearings, etc., and a trend survey was conducted. In particular, we conducted a survey on refrigerant trends in China that we had not been able to complete in the past.

In FY2022, we aimed to understand the latest trends in related regulations, standards, and policies, as well as add new information on overseas trends and trends among next-generation refrigerant candidates. In addition, we surveyed and summarized how the research and development results have been or are expected to be reflected in standards and norms.

The final edition of this report summarizes the results of WG III (Investigation of Regulations and Standards) of the Investigation Committee on Next-Generation Refrigerants, covering a period of five years.

Table 1.1-1 List of WG III members

	Name	Affiliation
Chief	Tetsuro Kishimoto	Managing Director, Environment and Energy Network 21
Members	Osami Kataoka	Chairman, ISO Domestic Subcommittee, Japan Society of Refrigeration and Air-Conditioning Engineers
	Masato Miyata	Senior Researcher, Building Environment Research Office, Housing Research Department, National Institute for Land and Infrastructure Management
	Kenji Tojo	Waseda University
	Kazuya Matsumoto	Councilor, High-Pressure Gas Department, High-Pressure Gas Safety Institute of Japan
Observer	Norihiro Inoue	Professor, Tokyo University of Marine Science and Technology
	Satoshi Fujigaki	Environment Department, New Energy and Industrial Technology Development Organization
	Tomokazu Mori	
	Tatsuhiko Takahashi	
	Makoto Gocho	
	T 悪魔 Ooishi	
Secretariat	Kyoji Kono	Secretary General, Japan Society of Refrigeration and Air-Conditioning Engineers
	Akira Nishiguchi	Japan Society of Refrigerating and Air-Conditioning Engineers
	Shigehiro Uemura	Japan Society of Refrigerating and Air-Conditioning Engineers

Table 1.1-2 Author list

	Main author	Co-author
1. Introduction	Tetsuro Kishimoto, Environment and Energy Network 21	WG III members (above)
2. Survey on Trends of Domestic and Foreign Regulations and Standards	Akira Nishiguchi, JSRAE	
3. Overseas Trends	Shigehiro Uemura, JSRAE	
4. Trends Related to Next-Generation Refrigerant Candidates	Shigehiro Uemura, JSRAE	

JSRAE: Japan Society of Refrigerating and Air-Conditioning Engineers

---

1.2 Relevant Domestic and Foreign Regulations, Standards, and Norms

International standards related to refrigerants, refrigeration, and air-conditioning equipment, as well as the regulations and standards in Japan, the United States, Europe, and China, are summarized in Table 1.2-1.

Table 1.2-1 Regulations and standards related to refrigerant, refrigeration, and air-conditioning products

	International	Japan	USA	Europe	China
Fluorocarbon regulations (Ozone layer protection, global warming prevention)	Montreal Protocol Framework Convention on Climate Change	-Act on Promotion of Global Warming Countermeasures -Act on the Protection of the Ozone Layer -Act on the Control of Fluorocarbon Emissions	-Clean Air Act -Significant New Alternatives Policy (SNAP) -AIM	-European climate law -F-gas regulation -MAC directive	
Basic properties of refrigerants	ISO 17584		REFPROP		
Refrigerant safety	ISO 817	High Pressure Gas Safety Act	ASHRAE 34	EN 378	GB/T 7778
Safety of refrigeration and air-conditioning in general and of equipment	ISO 5149-1,2,3,4 IEC 60335-2,24,34,40,89	-High Pressure Gas Safety Act -JIS C 9335-2-24,34,40,89	-ASHRAE 15 -UL60335-2-24,34,40,89 -UL 484	-EN 378 -EN 60335-2-24,34,40,89	GB 4706.32 GB/T 9237
Energy saving of refrigeration and air-conditioning equipment	ISO 52000	-Act on the Rational Use of Energy -Building Energy Conservation Act		-Energy-related -Products Directive -EPBD	GB 21455
Performance test method of refrigeration and air-conditioning equipment. Performance evaluation method	ISO 16358-1,2,3 ISO 5151 ISO 15042	JIS C 9612 JIS B 8615-1,2,3 JIS B 8616	AHRI Standard 210/240 AHRI Standard 1230	EN 14511 EN 14825 (BAM Test Guideline)	

In response to global environmental issues, international treaties and regional laws/regulations are being strengthened to protect the ozone layer and prevent global warming. Similarly, new standards and regulations are being considered for refrigerant properties and safety standards, as well as for safety standards for refrigeration and air-conditioning systems and equipment. In addition, energy conservation regulations must be considered when commercializing next-generation environment-friendly refrigerants. For this purpose, the standards for performance test methods and performance evaluation methods for standard refrigeration and air-conditioning equipment need to be reviewed. The above lists the major regulations and standards.

2. Survey on Trends of Domestic and Foreign Regulations and Standards

2.1 Specifications and Standards for Basic Properties of Refrigerants

(1) ISO 17584

The international standard for thermophysical properties of refrigerants and refrigerant mixtures is ISO 17584:2005 “Refrigerant Properties.” The first edition of this standard was published in 2005 and covered refrigerants R12, R22, R32, R123, R125, R134a, R143a, R152a, R717 (ammonia), R744 (carbon dioxide), and mixed refrigerants R404A, R407C, R410A, and R507.

A revised second edition of this document was issued for publication in August 2022. The main changes are as follows:

- Addition of new refrigerants: R290, R600a, R1233zd(E) [1)], R1336mzz(Z) [2)], R1234yf [3)], and R1234ze(E)
- Updated data on ammonia

Several experts from Japan participated in this revision, and the NEDO project results were adopted for the equations of state for the new refrigerants (R1233zd(E), R1336mzz(Z), and R1234yf).

New refrigerant mixtures are expected to be added in future revisions; however, their types and timing have not yet been determined.

(2) REFPROP

REFPROP [4)] is a program published by the National Institute of Standards and Technology (NIST) of the US Department of Commerce to calculate the physical properties of fluids containing refrigerants. It was released in 1989 as a database program called REFrigerant PROPerties, version 1.0. This first edition covered 15 pure substances and mixtures of only two components. Since then, the program has been repeatedly improved and fluids have been added, and now reference fluid properties are also available for fluids other than refrigerants.

Version 10.0 is the latest and was released in 2018. It includes recent refrigerants with low global warming potential (GWP) as well as non-refrigerant fluids, such as natural gas and fluids used in space applications and the general industry, and supports 147 pure fluids, 5 pseudo-pure fluids (such as air), and mixtures containing up to 20 components. Currently, it is widely used as a practical international standard.

Revisions are still being considered, and version 10.1 is expected to be released in 2023. This next edition is expected to incorporate much of the physical property data of next-generation refrigerants obtained in the NEDO project, as well as data on mixed refrigerants that combine these properties.

References

1) Akasaka R., Lemmon E.W., Equation of state for the thermodynamic properties of trans-1-chloro-3,3,3-trifluoropropene (R1233zd(E)), J. Phys. Chem. Ref Data (submitted), 2020.

2) McLinden M. O., Akasaka R., Thermodynamic properties of cis-1,1,1,4,4,4-tetrafluorobutene [R-1336mzz(Z)]: Vapor pressure, (*p, ρ, T*) behavior and speed of sound measurements and equation of state, J. Chem. Eng. Data, (2020).

3) Lemmon E.W., Akasaka R., Equation of state for the thermodynamic properties of 2,3,3,3-tetrafluoropropene (R1234yf), J. Phys. Chem. Ref Data (submitted), 2020.

4) US NIST, https://www.nist.gov/programs-projects/reference-fluid-thermodynamic-and-transport-properties-database-refprop

2.2 Regulations and Standards Related to the Safety of Refrigerants and Appliances

2.2.1 Regulations and Standards Related to the Safety of Refrigerants

The international standards ISO 817 “Refrigerants - Designation and Safety Classification” and ASHRAE Standard 34 “Designation and Safety Classification of Refrigerants” published by the American Society of Heating, Refrigerating, and Air-Conditioning Engineers (ASHRAE) are related to refrigerant safety. Both have established safety standards in terms of flammability and toxicity and have assigned refrigerant numbers and safety class designations to individual refrigerants. The safety class of a refrigerant is an important criterion for applying safety standards to refrigeration and air-conditioning equipment and systems as a whole.

These two standards specify the toxicity class and flammability class as the safety class of the refrigerant.

Table 2.2-1 lists the toxicity classes and their criteria. Both ISO 817 and ASHRAE Standard 34 use the same criteria based on the Occupational Exposure Limit (OEL).

Table 2.2-1 Criteria for toxicity classifications of ISO 817 and ASHRA Standard 34

Grade	Description	OEL *1
A	Lower chronic toxicity	≧400 ppm
B	Higher chronic toxicity	< 400 ppm

*1: Time-weighted average exposure concentrations at which almost all workers in a normal 8-hour-a-day; 40-hour-a-week would not be adversely affected

Table 2.2-2 shows the flammability class and judgment criteria. Four criteria were used: (1) presence of flame spread, (2) lower flammability limit (LFL), (3) heat of combustion (HOC), and (4) burning velocity. When all these conditions are satisfied, the material is judged to be of the appropriate grade. However, a material is judged to be grade 3, that is, “Higher Flammability,” if it satisfies either the LFL or HOC criteria.

Table 2.2-2 Criteria for flammability classifications of ISO 817 and ASHRAE Standard 34

Grade	Description	Flame propagation *1	LFL*2	HOC*3	Burning velocity *4
1	No flame propagation	No	-	-	-
2L	Lower flammability	Yes	>3.5% (ISO) >0.10 kg/m^3 (ASHRAE)	and <19,000 kJ/kg	and ≦10 cm/s
2	Flammable	Yes	>3.5% (ISO) >0.10 kg/m^3 (ASHRAE)	and <19,000 kJ/kg	-
3	Higher flammability	Yes	≦3.5% (ISO) ≦0.10 kg/m^3 (ASHRAE)	or ≧19,000 kJ/kg	-

*1: Test conditions: 60 ℃, 101.3 kPa
*2: Test conditions: 23 ℃, 101.3 kPa. However, if no flame propagation occurs, 60 ℃, 101.3 kPa.
*3: Test conditions: 25 ℃, 101.3 kPa
*4: Test conditions: 23 ℃, 101.3 kPa.

As shown in Table 2.2-2, the reference value for determining the LFL is different in ASHRAE Standard 34, with a volumetric concentration of 0.10 kg/m^3 compared to 3.5% in ISO 817. The main technical differences, including this point, are presented in Table 2.2-3.

Table 2.2-3 Technical differences between ISO 817 and ASHRAE Standard 34

Item			ISO 817	ASHRAE Standard 34
Safety grade	Flammability class boundary LFL		3.5% by volume	0.10 kg/m^3
	Flammability classification		WCF and WCFF	WCFF
	Toxicity classification OEL standards		OSHA PEL, ACGIH TLV-TWA, TERA WEEL, MAK	OSHA PEL, ACGIH TLV-TWA, TERA WEEL
Conc. limit	FCL		20% of LFL	25% of LFL
	ATEL	Anesthetic or CNS effect	NOAEL 100%	NOAEL 80%
		Cardiac sensitization	Allows other similar compounds data	Dose not allow other similar compounds data
Burning test method	Combustion air		Reconstituted air	Standard air
	Humidity		0.0088 g/g, and < 0.00015 g/g	0.0088 g/g
	Temperature		±0.5 K	±5°F（3 ℃）
	Air mixing time		> 5 min	> 2 min
	Mixing static time		60 s	30-60 s
Classification test method	Filling conditions		60 ℃, 100% fill	54.4 ℃, 100% fill
	Leakage test		60 ℃	54.4 ℃
	Leakage/most-filling test		Not needed	Needed

WCF: worst case of formulation for flammability; the nominal formulation, including the composition tolerances, which results in the most flammable concentration of components.
WCFF: worst case of fractionation for flammability; the composition produced during fractionation of the worst case of formulation for flammability that results in the highest concentration of flammable components, as identified in this standard in the vapor or liquid phase.
OHSHA: Occupational Safety and Health Administration (USA)
PEL: permissible exposure limit
ACGIH: American conference of Governmental Industrial Hygienists
TLV: threshold limit value
TWA: time-weighted average
TERA: Toxicology Excellence of Risk Assessment
WEEL: workplace environmental exposure level
ATEL: acute toxicity exposure limit
CNS: central nervous system
MAK: maximale arbeitsplatz-konzentrationen
NOAEL: no observed adverse effect level

ISO 817 and ASHRAE Standard 34, as described above, are in a state of juxtaposition as standards related to the safety of refrigerants, with each having its own adopting country and related standards. The main issues are as follows:

a) Both are parallel standards.
b) Both standards have different processes for naming refrigerants and safety grades.
c) There are technical differences between the two standards, such as the criteria for the safety class and test methods.

Currently, two applications to the two standards are required for one refrigerant, which may result in different refrigerant numbers and safety classes.

To avoid such inconvenience, it would be ideal to eliminate the differences between the two standards and integrate them into a single international standard. However, this requires numerous changes, and integration should be performed step-by-step to avoid confusion. Thus, ISO 817 and ASHRAE Standard 34 are first being considered and coordinated here to resolve the differences in points b) and c) above while maintaining both standards.

(1) ISO 817

ISO 817 is in charge of ISO/TC86/SC8 "Refrigerants and refrigeration lubricants" and is mainly discussed in working group WG5 "Refrigerants - Designation and safety classification." The current ISO 817:2014 was published in May 2014, and the following amendments have been issued since then:

- ISO 817 Amendment 1 (November 2017):

The definition of the auto-ignition temperature (AIT) included in the application data was added, components with concentration below 0.6% were not recognized as components of mixed refrigerants, and the table of refrigerants was moved to the web to allow for periodic updates.

- ISO 817 Amendment 2 (April 2021):

  The use of refrigerant concentration limits (RCLs) as characteristic values for individual refrigerants was removed along with the values from the refrigerant table. The method for determining toxicity data for mixtures was revised, and a new provision setting for an application procedure for harmonization with ASHRAE Standard 34, etc., was established.

Technical alignment with ASHRAE Standard 34 is being discussed in Task Force TF 1 (ISO 817 technical alignment) of ISO/TC86/SC8. In addition, concerning toxicity classes, a new standard combining not only chronic toxicity (OEL) but also acute toxicity (ATEL) is being discussed in Task Force TF 2 “Toxicity safety classification.” Furthermore, given that some substances are being considered as candidates for next-generation refrigerants for which chemical stability is an issue, a proposal was made by Japan to introduce stability as a criterion in addition to toxicity and flammability and to proceed with a study on refrigerant instability.

The ballot for the New Work Item Proposal (NP) for the revision of ISO 817 was held from July 16 to October 8, 2021 and approved. The proposed draft was considered to be a Working Draft. Regarding the future schedule, the targets are registration of the DIS in June 2023 and publication of the International Standard in June 2024.

(2) ASHRAE Standard 34

The latest ASHRAE Standard 34 is ASHRAE Standard 34-2022, published in October 2022, which combines ASHRAE Standard 34-2019 and addenda to it. Certain addenda added new refrigerants, while others changed the contents of the regulations. The following addenda[1)] were issued following ASHRAE Standard 34-2019.

- Addendum a, 2019/11/5

  The method for determining the acute toxicity of a mixture with respect to RCL. If toxicity data for the mixture are available, they are used; otherwise, a weighted average is used.
- Addendum b, 2019/11/5

  For acute toxicity, toxicity data for the mixture, if available, should be included in the submitted data.
- Addendum c, 2019/11/5

  Corrects erroneous values of RCL in Tables 4-1 and 4-2.
- Addendum f, 2019/12/12

  Adds LFL data to Table 4-1 and 4-2.
- Addendum i, 2020/9/1

  Makes it nonessential to submit a material safety datasheet (MSDS) for refrigerant applications.
- Addendum j, 2020/9/30

  Refrigerant numbers and subscripts. In principle, they are assigned in order. However, they can be skipped to avoid confusion with other standards.
- Addendum k, 2020/9/30

  Adds a definition of uniqueness of mixture components.
- Addendum n, 2020/9/30

  Adds a table of recommended significant figures for the application data and an indication of the data source.
- Addendum ag, 2022/8/31

  Changes the application documents for new refrigerants to be submitted electronically instead of manually.

These addenda were reviewed and approved by ASHRAE’s Standing Standard Project Committee (SSPC) 34, which is also working to realize harmonization with ISO 817.

2.2.2 Regulations and Standards Related to the Safety of Appliances

The IEC 60335 series published by the International Electrotechnical Commission (IEC) is an international standard for the safety of refrigeration and air-conditioning equipment. This standard consists of IEC 60335-1 “Household and similar electrical appliances - Safety - Part 1: General requirements” and Part 2, which defines safety standards for individual electrical appliances. Parts 1 and 2 are applied together to the individual devices. The safety standards for the equipment itself overlap with the standards for the general safety of refrigeration and air-conditioning equipment described below; in cases of overlap, the equipment standards take precedence. Part 2 standards related to refrigeration and air-conditioning equipment include the following:

- IEC 60335-2-24: Particular requirements for refrigerating appliances, ice-cream appliances, and icemakers
- IEC 60335-2-34: Particular requirements for motor-compressors
- IEC 60335-2-40: Particular requirements for electrical heat pumps, air-conditioners, and dehumidifiers
- IEC 60335-2-89: Particular requirements for commercial refrigerating appliances and icemakers with an incorporated or remote refrigerant unit or motor-compressor

IEC 60335-2-24, 34, and 89 are handled by the IEC subcommittee IEC/TC61/SC61C “Safety of refrigeration appliances for household and commercial use,” while IEC 60335-2-40 is handled by IEC/TC61/SC61D “Appliances for air-conditioning for household and similar purposes.”

In the United States, Underwriters Laboratories Limited Liability Company (UL) tests, inspects, and certifies the functionality and safety of materials, components, equipment, and products; it has issued the UL 60335 series of safety standards based on IEC standards. In addition, UL 484 is a standard for room air-conditioners.

In Europe, the EN 60335 series of standards was established by the European Committee for Standardization (CEN: Comité Européen de Normalisation).

(1) IEC 60335-2-40

IEC 60335-2-40 is a standard for equipment and does not include requirements for the installation site or provisions for the use of refrigerants based on the occupancy category. It assumes use in general air-conditioning and the like. The standard covers refrigerants A1, A2L, A2, and A3, and the molar mass of flammable refrigerants is limited to 42 kg/kmol or more.

Edition 7.0, published in May 2022, is the latest edition of IEC 60335-2-40, which is a revision of Edition 6.0, published in January 2018.

In Edition 6.0, the requirements for the A2L refrigerant, such as the charge limit, are specified in terms of the refrigerant charge, which is an important factor in the selection of next-generation refrigerants. In addition, the definition of Enhanced Tightness Refrigerating System (ETRS) has been added to ease restrictions on the use of the A2L refrigerant.

Edition 7.0 further relaxes the charge limit for the A2L refrigerant and expands the relaxation requirements to A2 and A3 refrigerants. In other words, requirements for the charge quantity of A2 and A3 refrigerants have been added and the application of airtightness enhancement systems has been expanded to A2 and A3 refrigerants to relax the charge restrictions. In addition, the application of a releasable charge that can be released into the indoor space from a refrigerant system and is limited by methods, such as shutting off with a safety shutoff valve, has also been added.

The requirements for an ETRS, which are important in terms of refrigerant charge mitigation, include: 1) no compressors or pressure vessels containing refrigerant in the occupied space; 2) refrigerant-containing parts in indoor units in the occupied space must be protected from damage caused by rotating parts and other malfunctions; 3) reduced vibration of components containing refrigerant in the occupied space; and 4) requirements to reduce the possibility of leakage into the occupied space, such as freeze protection. Possible systems to achieve this are split air-conditioners and multi-air-conditioning systems for buildings.

The refrigerant charge limits are summarized in Annex GG. The charge limits are constrained by m_1, m_2, and m_3 defined below, using the lower flammability limit concentration LFL (kg/m^3).

For A2, A3 refrigerants:

$$m_1 = 4 \times LFL \quad (2.2\text{-}1)$$

$$m_2 = 26 \times LFL \quad (2.2\text{-}2)$$

$$m_3 = 130 \times LFL \quad (2.2\text{-}3)$$

For A2L refrigerant:

$$m_1 = 6 \times LFL \quad (2.2\text{-}4)$$

$$m_2 = 52 \times LFL \quad (2.2\text{-}5)$$

$$m_3 = 260 \times LFL \quad (2.2\text{-}6)$$

A summary of Annex GG clauses on refrigerant charge is shown in Table 2.2-4, classified by the range of charge limits and systems.

Table 2.2-4 Outline of Annex GG

<table>
<tr><th rowspan="3">Refrigerant charge</th><th colspan="4">Direct system [a]</th><th rowspan="3">Indirect system [b]</th></tr>
<tr><th colspan="3">Indoor space</th><th>Outdoors</th></tr>
<tr><th>Refrigerant charge and room area</th><th>Refrigerant charge, room area and additional requirements</th><th>Additional ventilation</th><th></th></tr>
<tr><td>$m_c \le m_1$ or $m_{rl} \le m_1$</td><td>No room size restriction</td><td></td><td></td><td rowspan="4">No room size restriction</td><td rowspan="4">No room size restriction,
GG.6</td></tr>
<tr><td>$m_1 < m_c \le 2 \times m_1$
(appliances which are not fixed appliances)</td><td>Not allowed</td><td>GG.7</td><td>Not allowed</td></tr>
<tr><td>$m_1 < m_c \le m_2$</td><td>GG.2.1</td><td>GG.2.2[c], GG.2.3[d], GG.9[c], GG.10[c], GG.14[d]</td><td>GG.3, GG.8[c], GG.10[c]</td></tr>
<tr><td>$m_2 < m_c \le m_3$</td><td>Not allowed</td><td>GG.9[c], GG.10[c]</td><td>GG.3, GG.8[c], GG.10[c]</td></tr>
<tr><td>$m_c > m_3$</td><td colspan="5">Beyond the scope of this standard. National standards apply</td></tr>
<tr><td colspan="6">[a] Direct system means a refrigerating system in which a single rupture of the refrigerant circuit results in a refrigerant release to an indoor space, irrespective of the location of the refrigerant circuit.
[b] Indirect system means a refrigerating system in which a single rupture of the refrigerant circuit does not leak into an indoor space, irrespective of the location of the refrigerant circuit.
[c] These clauses are only applicable to appliances with A2L refrigerant.
[d] These clauses are only applicable to appliances with A2 or A3 refrigerant.</td></tr>
</table>

The titles of the Annex GG article numbers classified in the table are as follows:

- GG.2: Requirements for charge limits in unventilated areas
  - GG.2.1: General
  - GG.2.2: Fixed appliances using A2L refrigerants with integral circulation airflow
  - GG.2.3: Fixed appliances using A2 or A3 refrigerant with integral circulation airflow
- GG.3: Requirements for charge limits in areas with mechanical ventilation
- GG.6: Requirements for refrigerating systems employing secondary heat exchangers
- GG.7: Factory-sealed single-package units that are not fixed appliances with a refrigerant charge of $m_1 < m_c \le 2 \times m_1$
- GG.8: Ventilation area requirements for appliances using A2L refrigerants
- GG.9: Charge limits for appliances using A2L refrigerants connected via an air duct system to one or more rooms
- GG.10: Allowable charge for Enhanced Tightness Refrigerating System using A2L refrigerant
- GG.14: Allowable charge for enhanced tightness refrigerating systems using A2 or A3 refrigerant

In Edition 7.0, the requirements of GG.10, which limits the amount of A2L refrigerant charge in ETRS, are relaxed, and GG.14, which specifies the amount of A2 and A3 refrigerant charge in ETRS, is newly established. Tables 2.2-5 and 2.2-6 show the main points of revision from Edition 6.0 to 7.0.

Table 2.2-5 Key points of the revised IEC 60335-2-40

	IEC edition 6 (2018)	IEC edition 7 FDIS (2022)
Warning markings	A2L specific flame mark	Same mark as A3 + grade such as A2L
Countermeasure requirement	Classified by refrigerant charge amount	Classifications by releasable charge amount are also possible
Ignition source regulations	Limits specified for inductive loads (motors)	Inductive load + others (heater)
ETRS	Almost limited to A2L	Relaxed and expanded application to A3
Allowable surface temperature	heating surface ignition temperature (HSIT) of 100 K or auto-ignition temperature (AIT) of 100 K	HSIT or AIT of 100K
Safety shutoff valve leakage	Not specified	4 x LFL (1.2 g/s = 4.32 kg/h) in total
Refrigerant sensor system	Specify countermeasures by refrigerant sensor system and require self-checking	Additional durability (refrigerant + oil spray, etc.), etc. Additional details, such as test tolerances, are specified

Table 2.2-6 Key points of revision for refrigerant charge limit of IEC 60335-2-40

		IEC edition 6 (2018)		IEC edition 7 FDIS (2022)		
Charge limit		A2L is per refrigerant circuit A3 is total amount per unit		All circuit-specific regulations		
ETRS (10 kg/h leakage)		Almost exclusively for A2L refrigerant		Applicable to A3 refrigerant		
ETRS allowable charge		ETRS is newly specified Number of indoor units × m_2 (max. m_2×4)		m_3（A2L）		
CF of ETRS (Charge Factor = Ratio to LFL)		Lowest basement floor	Other	Lowest basement floor	Other	
					>1.8 m or with circulator	<1.8 m with no circulator
	<0.25	No additional measures required	No additional measures required	No additional measures required	No additional measures required	No additional measures required
	0.25-0.5	2 measures	1 measure	No additional measures required	No additional measures required	No additional measures required
	0.5-0.75	Installation prohibited	2 measures	1 measure＋warning	No additional measures required	1 measure
	>0.75	Installation prohibited	2 countermeasures	Installation prohibited	1 countermeasure ＋warning	Warning＋1 additional countermeasure

(2) IEC 60335-2-89

IEC 60335-2-89 is a safety standard for commercial refrigeration equipment and ice manufacturers. The latest edition, Ed. 3.0, was published in June 2019 as a revision of the 2010 edition.

The major point of the revision to Edition 3.0 was the addition of a requirement for equipment containing more than 150 g of flammable refrigerant, which was previously prohibited. Refrigeration equipment are allowed to be charged with flammable refrigerant up to 13 times the LFL or 1.2 kg, whichever is smaller, subject to requirements for protection against damage for components containing refrigerant, configuration and airflow measures to prevent refrigerant

concentration in the event of refrigerant leakage, etc. As a result of this revision, for example, propane R290, a typical A3 refrigerant, can be used up to approximately 500 g, which is 13 times the lower flammable limit concentration (LFL) of 0.038 kg/m^3.
Regarding this standard, the comments on the revision proposals from various countries are still being considered for Edition 4.0, and the CDV is scheduled to be published in December 2022. This will be subsequently published by FDIS, and Edition 4.0 is scheduled for August 2023.

Regarding the safety of next-generation refrigerants, Japan submitted the following proposals:

1) A proposal to delete the 1.2 kg limit for A2L refrigerant from the provision "the maximum charge of flammable refrigerants shall be 13 times the LFL or 1.2 kg, whichever is smaller" as a standard for the charge volume of flammable refrigerants.
   Given that the A2L refrigerant has a larger LFL, the resulting 1.2-kg limit, rather than 13 times the LFL, keeps the A2L refrigerant charge as low as approximately 4 times the LFL. However, the flammability of the A2 refrigerant is low, and in IEC 60335-2-40, the upper limit of multiples of the LFL for the A2L refrigerant is set larger than those for the A2 and A3 refrigerants. Therefore, it is proposed to eliminate the upper limit of 1.2 kg for the A2L refrigerant to correct the lower allowable charge limitation compared to the A2 and A3 refrigerants.
2) Regarding A2L refrigerants, it is proposed that the hot-surface ignition temperature, rather than the auto-ignition temperature, be used as the criterion for defining the upper limit for the hot-surface temperature.
   The A2L refrigerant is more difficult to ignite than the A2 and A3 refrigerants. This proposal introduces the concept of surface ignition temperature adopted in IEC 60335-2-40 and specifies the upper limit temperature of hot surfaces based on this concept.

For proposal (1) above, we presented the results of leakage analysis using an analysis code verified by concentration distribution measurement during refrigerant leakage conducted by NEDO project WGII and explained the results at the IEC committee meeting. Finally, the Japanese proposal was accepted and will be adopted in subsequent revisions.

Proposal (2) is based on the evaluation of ignition sources being conducted by NEDO project WGII.

2.2.3 Regulations and Standards Related to the General Safety of Refrigeration and Air-Conditioning

The international standard for refrigeration and air-conditioning systems in general is ISO 5149 "Refrigerating systems and heat pumps - Safety and environmental requirements." Additionally, ASHRAE Standard 15 "Safety Standard for Refrigeration Systems" published by ASHRAE also has a significant impact on the use of next-generation refrigerants.

(1) ISO 5149

ISO 5149 is the responsibility of ISO/TC86/SC1 "Safety and environmental requirements for refrigerating systems" and is discussed in WG1 "Safety and environmental requirements for refrigerating systems and heat pumps."

ISO 5149 establishes standards for the design, construction, installation, operation, and disposal of equipment and systems to ensure the safety of refrigeration and air-conditioning systems. The current version was published in 2014 as a revision of the 1993 edition, and its basic structure and content are based on the European Committee for Standardization (CEN) standard EN 378, as modified by proposals from countries around the world. The standard is divided into four parts (ISO 5149-1, 2, 3, 4), the contents of which are as follows:

- Part 1: Definitions, classification, and selection criteria
- Part 2: Design, construction, testing, marking, and documentation
- Part 3: Installation site
- Part 4: Operation, maintenance, repair, and recovery

Here, the refrigerant charge limit, which is an important point in selecting the next-generation refrigerant, is defined in Annex A of ISO 5149 - Part 1 and is determined using the following procedure:

(a) Determine which of the three occupancy categories and four installation site types apply.
(b) Apply the classification in (a) to determine the refrigerant charge limit according to the toxicity class of the refrigerant.
(c) Apply the classification in (a) to determine the refrigerant charge limit according to the flammability class of the refrigerant.
(d) The lower values of the toxicity and flammability limits apply to the refrigerant charge limit.

The following three categories of occupancy are defined, as described above.

General occupancy: Rooms, parts of buildings, or buildings where sleeping facilities are provided, people are restricted in their movement, an uncontrolled number of people are present, or to which any person has access without being personally acquainted with the necessary safety precautions.

Supervised occupancy: Rooms, parts of buildings, or buildings where only a limited number of people can be assembled, with some being necessarily acquainted with the general safety precautions of the establishment.

Authorized occupancy: Rooms, parts of buildings, or buildings where only authorized persons have access, who are acquainted with general and special safety precautions of the establishment, and where manufacturing, processing, or storage of material or products take place.

The following four types of locations are defined:

- Class Ⅰ: Refrigerating system or refrigerant containing parts are located in the occupied space
- Class Ⅱ: All compressors and pressure vessels are either located in a machine room or in open air
- Class Ⅲ: All refrigerant-containing parts are located in a machinery room or in open air
- Class Ⅳ: All refrigerant-containing parts are located in ventilated enclosures

Annex A shows how to calculate the refrigerant charge limits by toxicity and flammability classes according to the above occupancy categories and types of locations. Each charge limit is constrained by the limit values m_1, m_2, and m_3 in Equations (2.2-1) through (2.2-6) using the lower flammability limit concentration LFL (kg/m^3), as in IEC 60335-2-40. However, the factor in Equation (2.2-6) for m_3 for the A2L refrigerant is 195 instead of 260.

Considerations for future revisions are also in progress. Figure 2.2-1 shows the process chart for the revision of the ISO 5149 series presented by the working group in charge of the revision (WG1: "Safety and environmental requirements for refrigerating systems and heat pumps") at its subcommittee meeting (SC1: "Safety and environmental requirements for refrigerating systems") held in January 2021.

Part	2013	2014	2015	2016-2018	2019	2020	2021	2022	2023	2024
1	Start mandated work	Publication of ISO 5149-1:2014	Drafting and publication of ISO 5149-1:2014/A1		Drafting and publication of ISO 5149-1:2014/A2					
			Preparing the revision of ISO 5149-1:2014				*NP ballot*	*DIS ballot*	*FDIS ballot*	***Estimated publication***
2	Start mandated work	Publication of ISO 5149-2:2014			Drafting and publication of ISO 5149-2:2014/A1					
			Preparing the revision of ISO 5149-2:2014				*NP ballot*	*DIS ballot*	*FDIS ballot*	***Estimated publication***
3	Start mandated work	Publication of ISO 5149-3:2014			Drafting and publication of ISO 5149-3:2014/A1					
			Preparing the revision of ISO 5149-3:2014				*NP ballot*	*DIS ballot*	*FDIS ballot*	***Estimated publication***
4	Start mandated work	Publication of ISO 5149-4:2014	Preparing revision of ISO 5149-4:2014			NP ballot	*DIS and FDIS ballots*	***Estimated publication***		

Figure 2.2-1 Estimated timeline for amending/revising the ISO 5149 series

A summary of the amendments issued to date is as follows:

- ISO 5149-1 Amendment 1 (October 2015): Amends the definition of concentration limit QLAV with additional ventilation and QLMV with minimum ventilation, etc. in Annex A.5 on charge limits for A1 and A2L refrigerants.
- ISO 5149-1 Amendment 2 (January 2021): In Table A.1, which establishes the requirements for refrigerant charge limits with respect to toxicity, it provides corrections to the scope of Annex A.5 and to the conditions of application of Annex A.5. Additionally, it adds new refrigerants to

Tables B.1 to B.3 of the list of refrigerant designations.

- ISO 5149-2 Amendment 1 (June 2020): Revises Table 1 to address requirements for components and piping, and revises air-tightness testing requirements, labeling requirements, requirements for piping connections for flammable refrigerants, protection requirements for excess pressure, etc.
- ISO 5149-3 FDAMD 1 (February 2021): Modifies machine room and emergency mechanical ventilation requirements, etc.

Future revisions of ISO 5149-1, 2, and 3 are scheduled for publication in 2024; a revised version of ISO 5149-4 is scheduled for publication in 2022; and an FDIS was published in August 2022 and approved in September.

ISO 5149 exists in parallel with safety standards for individual devices, such as IEC 60335-2-40 and IEC 60335-2-89, which take precedence over ISO 5149 when there are individual standards. However, ISO 5149 applies to products related to refrigeration and air-conditioning for which there are no individual standards. Therefore, it is considered necessary to harmonize ISO 5149 with the IEC standard; concerning the next revision of ISO 5149, studies are underway to ensure consistency with IEC standards for individual equipment, such as restrictions on the refrigerant filling volume.

(2) ASHRAE Standard 15

ASHRAE Standard 15 is for the safe design, assembly, installation, and operation of refrigeration systems.

Refrigerant filling limits are established by refrigeration-system occupancy category and system classification. The occupancy classification is defined as the classification of the location where the refrigeration system is installed, as shown in Table 2.2-7. The system classification is defined in Table 2.2-8. For these classifications, the refrigerant charge is limited to the limit of the refrigerant concentration in the case of total refrigerant leakage from the refrigeration system.

Table 2.2-7 Occupancy classification

Classification	Description
Institutional occupancy	A premise or that portion of a premise from which, because they are disabled, debilitated, or confined, occupants cannot readily leave without the assistance of others. Institutional occupancies include, among others, hospitals, nursing homes, asylums, and spaces containing locked cells.
Public assembly occupancy	A premise or that portion of a premise where large numbers of people congregate and from which occupants cannot quickly vacate the space. *Public assembly occupancies* include, among others, auditoriums, ballrooms, classrooms, passenger depots, restaurants, and theaters.
Residential occupancy	A premise or that portion of a premise that provides the occupants with complete independent living facilities, including permanent provisions for living, sleeping, eating, cooking, and sanitation. *Residential occupancies* include, among others, dormitories, hotels, multiunit apartments, and private residences.
Commercial occupancy	A premise or that portion of a premise where people transact business, receive personal service, or purchase food and other goods. *Commercial occupancies* include, among others, office and professional buildings, markets (but not *large mercantile occupancies*), and work or storage areas that do not qualify as *industrial occupancies*.
Large mercantile occupancy	A premise or that portion of a premise where more than 100 persons congregate on levels above or below street level to purchase personal merchandise.
Industrial occupancy	A premise or that portion of a premise that is not open to the public, where access by authorized persons is controlled, and that is used to manufacture, process, or store goods such as chemicals, food, ice, meat, or petroleum.
Mixed occupancy	Two or more *occupancies* are located within the same building. When each *occupancy* is isolated from the rest of the building by tight walls, floors, and ceilings and by self-closing doors, the requirements for each *occupancy shall* apply to its portion of the building. When the various *occupancies* are not so isolated, the *occupancy* having the most stringent requirements *shall* be the governing *occupancy*.

Table 2.2-8 Refrigerant system classification

Classification	Description
High-Probability System	Any system in which the basic design or the location of components is such that a leakage of refrigerant from a failed connection, seal, or component will enter the occupied space. Typical high-probability systems include (a) direct systems or (b) indirect open spray systems in which the refrigerant is capable of producing pressure greater than the secondary coolant.
Low-Probability System	Any system in which the basic design or the location of components is such that leakage of refrigerant from a failed connection, seal, or component cannot enter the occupied space. Typical low-probability systems include (a) indirect closed systems, (b) double indirect systems, and (c) indirect open spray systems where the secondary coolant pressure shall remain greater than refrigerant pressure in all conditions of operation and standby.

The latest ASHRAE Standard 15, the 2022 edition, which is a revision of the 2019 edition of ASHRAE Standard 15-2019, was published in October 2022. Even after the 2019 edition was published, revisions have been continuously reviewed, and the below supplements have been issued. The 2022 edition of ASHRAE Standard 15-2022 is a compilation of ASHRAE Standard 15-2019 and these addenda.

- Addendum a, 2020/2/6

  Addition of capacity factors for new refrigerants and revision of capacity factors for existing refrigerants for pressure-vessel protection devices.

- Addendum b, 2020/2/6

  Change in the definition of the term "listed" and addition of the definition of the term "labeled."

- Addendum c, 2020/2/6

  Change to allow the use of appliances listed in the product safety standard with a limit on the amount of refrigerant other than A1.

- Addendum d, 2022/4/29

  With the publication of ASHRAE Standard 15.2, the scope of the standard excludes residential systems.

- Addendum e, 2022/1/27

  Revision of requirements related to the design, installation, location, and testing of refrigerant piping. The formats and terminology are aligned with building codes.

- Addendum f, 2020/9/30

  New annex for reference information and normative reference information moved into the text.

- Addendum g, 2022/8/31

  Modification to introduce the concept of the amount of refrigerant charge that can be released. Revision of the description of the spatial volume in which the leaked refrigerant is dispersed and the calculation procedure for concentration limits.

- Addendum i, 2020/7/31

  Correction to conform to the regulation of ammonia refrigeration systems to ANSI/IIAR 2. Switching to ANSI/IIAR 2 in the Addendum to ASHRAE Standard 15-2016 as a reference to ammonia was erroneously added to a subsequent addendum.

- Addendum j, 2020/10/30

  Replacement of the terms "flammable" and "non-flammable" for the refrigerant classes when referring to refrigerants classified as A1 or B1.

- Addendum k, 2020/10/30

  Clarification of standards that list product safety. Specifically, UL 484 and UL/CSA 60335-2-40.

- Addendum l, 2022/8/31

  Addition of requirements for commercial systems using flammable refrigerants (A2L, A2, A3).

- Addendum m, 2022/6/30

  Changes in permissible limits for the use of mechanical ventilation in air-conditioning for persons using A2L refrigerant.

- Addendum n, 2022/5/31

Clarification of the description of flow velocities in ducts.

- Addendum o, 2022/4/29

  Clarification of notification when changing refrigerants.
- Addendum p, 2022/8/31

  Change of refrigerant filling quantity limits for air-conditioning when using A2L refrigerant.
- Addendum q, 2022/5/31

  Modification of mechanical ventilation requirements for mechanical rooms using A2L refrigerant.
- Addendum r, 2022/5/31

  Modification of the definition of the term "machine room."
- Addendum s, 2022/8/31

  Revision of refrigerant detection and mitigation requirements in case of leakage of refrigerants other than A1.
- Addendum u, 2022/8/31

  Modified the definition of "approved, nationally recognized laboratory" to align Standard 15 with US Occupational Safety and Health Administration's (OSHA) usage.
- Addendum v, 2022/8/31

  Updated definitions for brazed and soldered joints.
- Addendum w, 2022/8/31

  Updated instructions for use of refrigerant safety groups.

In addition, the North American safety standard for residential products, UL/CSA 60335-2-40, 3rd Edition, was modified to accommodate flammable refrigerants and was published in December 2019. The new ASHRAE Standard 15.2 "Safety Standard for Refrigeration Systems in Residential Applications" was published on April 29, 2022 as the corresponding standard for safe design and installation of residential refrigeration systems. A1 and A2L refrigerants currently regulated by ASHRAE Standard 15.2; other refrigerants are covered by ASHRAE Standard 15.

2.2.4 Regulations and Standards Related to the Safety of Refrigerants and Appliances in Japan

(1) High-Pressure Gas Safety Act

The purpose of the High-Pressure Gas Safety Act is to prevent disasters caused by high-pressure gas. Based on this act, the Refrigeration Safety Regulations, the Container Safety Regulations, and the General High-Pressure Gas Safety Regulations have been established as ministerial ordinances related to refrigeration and air-conditioning. The application of next-generation refrigerants to refrigeration and air-conditioning systems, in particular, has a significant relationship with the Refrigeration Safety Regulations.

While next-generation refrigerants are required to have a low GWP value to prevent global warming, as there is a trade-off between GWP value and flammability, refrigerants with lower GWP values tend to have higher flammability, making safety a major issue. The Refrigeration Safety Regulations classify refrigerant gases into flammable, toxic, and inert gases, and also define the applicable standards. In 2016, R1234yf, R1234ze, and R32, refrigerants with low GWP values but also low flammability, were classified as inert gases in the Refrigeration Safety Regulations under a new designation, and these three gases were further classified as designated inert gases by their names. The amendment also established the classification of designated inert gases as a subgroup among inert gases and further designated these three gases as designated inert gases by their names, thereby defining the applicable standards for these gases.

This allowed the use of designated inert gases with a low GWP under the same standards as inert gases by taking protective measures in the event of refrigerant leakage. Subsequently, in 2017, the classification of gases, which had previously been defined by their names, was revised to include the classification of gases as flammable and inert gases according to the explosive limit of each gas. However, as the designated inert gases are still defined by their names, revisions to the Refrigeration Safety Regulations were unable to keep up with the rapid pace of development and consideration of next-generation refrigerants, making it difficult to advance the practical application of new refrigerants. The flammability standards also differ from the international standards ISO 817 and ASHRAE34, making it a challenge to find a balance between consistency with international standards and continuity with the existing approach of domestic regulations regarding the handling of next-generation refrigerants.

Under these circumstances, a review of flammability standards, particularly those for designated inert gases, including flammability tests, was conducted by the High-Pressure Gas Safety Institute of Japan as a project commissioned by the Ministry of Economy, Trade, and Industry in FY2008[2]. Based on the results of this study, the Refrigeration Safety Regulations were revised in April 2021[3]. This revision defines the criteria for the determination of designated inert gases. Figure 2.2-2 shows a flow diagram of the criteria for determining flammable, inert, and designated inert gases for gases other than those listed in Article 2 of the Refrigeration Safety Regulations before the revision.

First, Criterion A for determining flammable gases through flammability limits is applied, and gases that satisfy this criterion are considered to be flammable gases. However, gases that satisfy Criterion B are excluded from the flammable gas category. Next, for gases excluded from flammable gases by Criterion B or gases excluded from flammable gases by Criterion A that satisfy Criterion C, that is, gases that are fluorocarbons, Criterion D was applied. According to Criterion D, gases with confirmed flame propagation are considered as designated inert gases, while gases with no confirmed flame propagation are simply inert gases. Gases that are not fluorocarbons according to Criterion C are not combustible gases, designated inert gases, or inert gases.

The flammability test method in Criterion A has been revised so that it is determined according to the measurement method in EN 1839:2017 instead of the conventional Method A. The numerical criteria in Criterion B are consistent with the criteria for determining 2L refrigerants in ISO 817:2014. Therefore, the heat of combustion is theoretically calculated under the conditions given in ISO 817:2014 6.1.3.7, and the burning velocity is based on the method given in ISO 817:2014 6.1.3.1. The flame propagation of Criterion D is based on the method given in ISO 817:2014 as the standard.

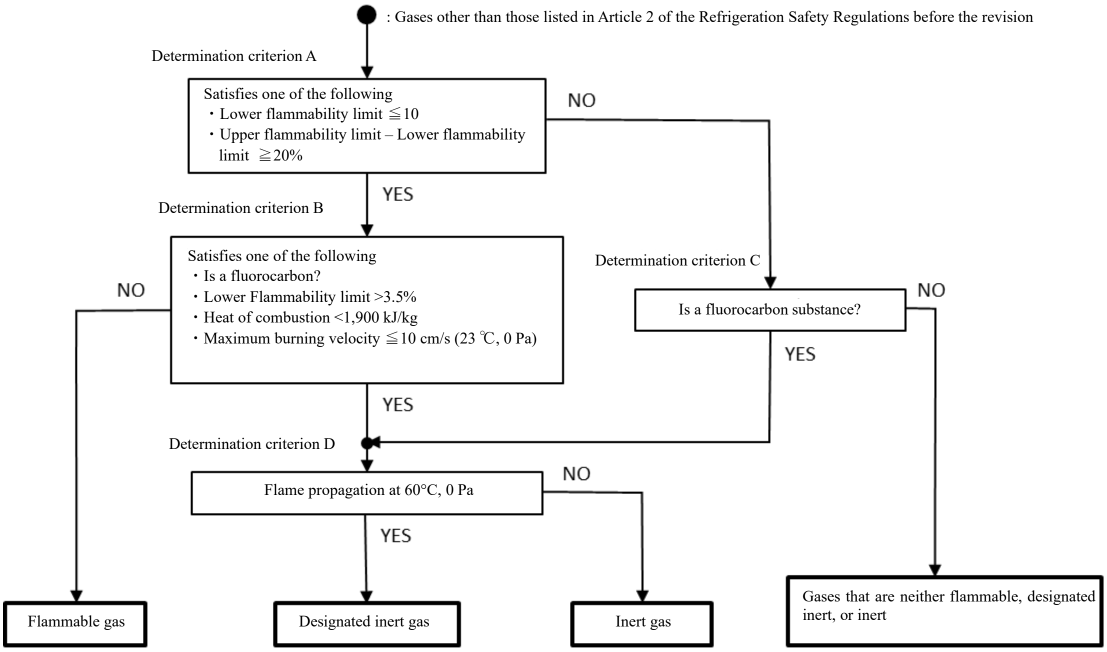

Figure 2.2-2 Flowchart for determining flammable, inert, and designated inert gases according to the amendment

(2) Japan Industrial Standards (JIS)

The following JIS standards are available for the safety of refrigeration and air-conditioning equipment, corresponding to the International Standard IEC 60335 series. These standards are based on IEC 60335, with certain modifications in consideration of the domestic situation. The relevant JIS standards are listed below. Corresponding international standards are presented in [ ].

- JIS C 9335-1:2014 Household and similar electrical apparatus - Safety - Part 1: General requirements [IEC 60335-1:2010]
- JIS C 9335-2-24:2017 Household and similar electrical appliances - Safety - Part 2-24: Particular requirements for refrigerating appliances, ice-cream appliances and ice-makers [IEC 60335-2-24:2010]
- JIS C 9335-2-34:2019 Household and similar electrical apparatus – Safety - Part 2-34: Particular requirements for motor-compressors [IEC 60335-2-34:2010]
- JIS C 9335-2-40:2022 Household and similar electrical appliances – Safety - Part 2-40: Particular requirements for electrical heat pumps, air-conditioners and dehumidifiers [IEC 60335-2-40:2002]

- JIS C 9335-2-89:2021 Household and similar electrical appliances – Safety - Part 2-89: Particular requirements for commercial refrigerating appliances and ice-makers [IEC 60335-2-89:2019]

Work is currently underway to revise JIS C 9335-1 to correspond to IEC 60335-1 Ed. 6.0:2020, with revisions scheduled for March 2023.

JIS C 9335-2-40:2022 was revised to correspond to IEC 60335-2-40 Ed. 6.0:2018, which was published on March 22. However, since Ed. 7.0 of the corresponding International Standard IEC 60335-2-40 was published in May 2022, and a supplement is being prepared to reflect its contents; it is scheduled to be published around January 2023.

3) JRA standards

In Japan, the Japan Refrigeration and Air Conditioning Industry Association (JRAIA) has established two types of industry standards[4)] for products and parts related to refrigeration and air-conditioning: Standard of the Japan Refrigeration and Air-Conditioning Industry Association (JRA) and Guideline of the Japan Refrigeration and Air-Conditioning Industry Association (JRA-GL). JRA 4078 and JRA GL-21 were issued in 2021.

To date, the following standards have been issued regarding the safety of equipment using flammable refrigerants:

- JRA 4070:2020 Requirements for ensuring safety against refrigerant leakage from commercial air conditioners using lower flammability (A2L) refrigerants
- JRA 4072:2017 Safety function requirements for ensuring safety against refrigerant leakage from commercial refrigerating appliances using lower flammability (A2L) refrigerants
- JRA 4073:2020 Safety function requirements for ensuring safety against refrigerant leakage from commercial packaged air conditioners for facilities using lower flammability (A2L) refrigerants
- JRA 4078:2021 Requirements for ensuring safety against refrigerant leakage from commercial built-in refrigerating appliances using flammable refrigerants
- JRA GL-15:2016 Design construction guidelines for ensuring safety against refrigerant leakage from chiller using lower flammability (A2L) refrigerants
- JRA GL-16:2020 Design construction guidelines for ensuring safety against refrigerant leakage from commercial air conditioners using lower flammability (A2L) refrigerants
- JRA GL-18:2017 Design construction guidelines for ensuring safety against refrigerant leakage from commercial refrigerating appliances using lower flammability (A2L) refrigerants
- JRA GL-19:2020 Design construction guidelines for ensuring safety against refrigerant leakage from commercial packaged air conditioner for facilities using lower flammability (A2L) refrigerants
- JRA GL-20:2016 Appropriate measures to prevent combustion against refrigerant leakage from refrigerant-charged equipment using a particular inert gas
- JRA GL-21:2021 Design construction guidelines for ensuring safety against refrigerant leakage from commercial built-in refrigerating appliances using flammable refrigerants

References

1) ASHRAE, https://www.ashrae.org/technical-resources/standards-and-guidelines/standards-addenda

2) High Pressure Gas Safety Institute of Japan, FY 2008 Ministry of Economy, Trade and Industry Commissioned High Pressure Gas Safety Measures Project (1) Study report on legal and technical issues related to test methods for flammability of high-pressure gas and various products using high pressure gas, (2019.3)

3) Ministry of Economy, Trade and Industry, https://www.meti.go.jp/policy/safety_security/industrial_safety/oshirase/2021/04/20210423_kouatsu_1.html

4) The Japan Refrigeration and Air Conditioning Industry Association, https://www.jraia.or.jp/jra/list.html

2.3 Regulations and Standards for Performance Evaluation of Refrigeration and Air-

Conditioning Appliances

Figure 2.3-1 shows the standards for testing and evaluating the performance of refrigeration and air-conditioning appliances. The performance of an equipment was previously referred to by its performance at the rated point. However, approximately 15 years ago, evaluation based on seasonal performance was introduced, and the standardization of the conditions, test methods, and evaluation methods has progressed. In addition, from the viewpoint of energy conservation in buildings, building simulations are required, and standardization of conditions, methods, and evaluation methods is also in progress.

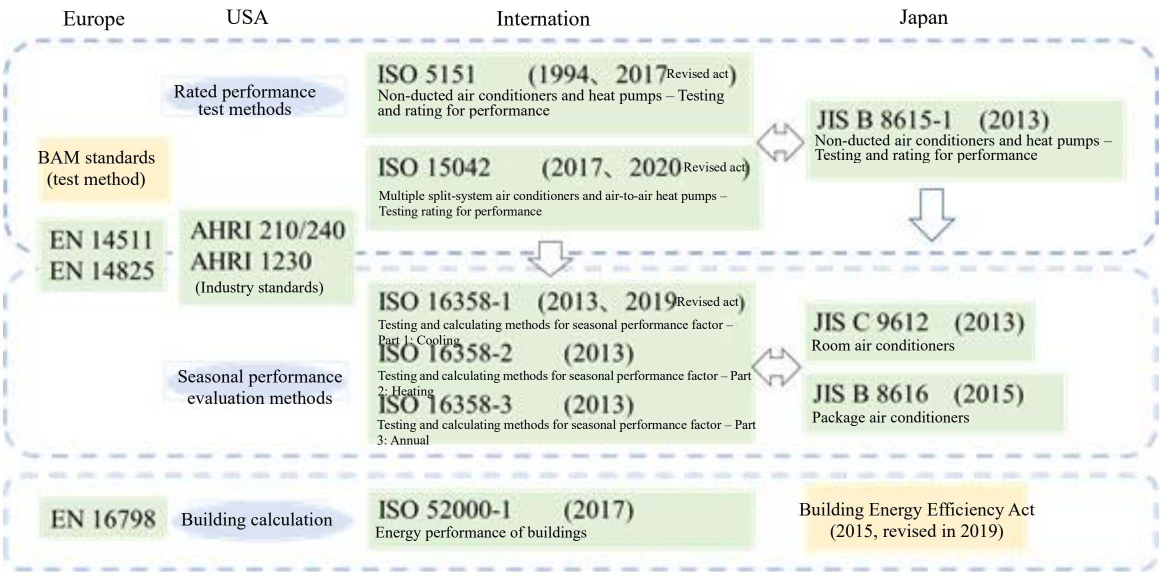

Figure 2.3-1 Standards related with testing and evaluation of performance

2.3.1 International Standards (ISO)

ISO/TC86/SC6 (Testing and rating of air-conditioners and heat pumps) governs international standards for the performance of refrigeration and air-conditioning equipment. It addresses the following standards:

- ISO 5151:2017 Non-ducted air conditioners and heat pumps – Testing and rating for performance
- ISO 15042:2017 Multiple split-system air conditioners and air-to-air heat pumps – Testing and rating for performance
- ISO 16358-1:2013 Air-cooled air conditioners and air-to-air heat pumps – Testing and calculating methods for seasonal performance factors – Part 1: Cooling seasonal performance factor
- ISO 16358-2:2013 Air-cooled air conditioners and air-to-air heat pumps – Testing and calculating methods for seasonal performance factors – Part 2: Heating seasonal performance factor
- ISO 16358-3:2013 Air-cooled air conditioners and air-to-air heat pumps – Testing and calculating methods for seasonal performance factors – Part 3: Annual performance factor

(1) ISO 5151

This standard specifies the test methods and rating conditions for appliance performance. Table 2.3-1 shows the rated temperature conditions. The applicable climatic zone conditions are selected according to the design specifications of the equipment. The room-type calorimeter test method and air enthalpy method are specified as test methods. The room-type calorimeter test method simultaneously measures both indoor and outdoor capacities. The indoor capacity during cooling is measured by balancing the effect of cooling and dehumidification in the evaporator with the amount of heating and humidification on the indoor side. The outdoor capacity is measured by balancing the amount of heat and moisture eliminated by the condenser with the amount of cooling and dehumidification on the outdoor side; it is used as a confirmation test of the indoor cooling capacity.

The air enthalpy test method determines the cooling and heating capacities by measuring the dry-bulb and wet-bulb temperatures of the suction and discharge air of the equipment and the associated airflow rates.

Both are steady-state tests that require a certain equilibrium time, and detailed regulations are available regarding the measurement methods, uncertainty tolerance, and methods for calculating capacity.

Table 2.3-1 Capacity rating conditions

Air conditioners

	T1 (mild climate zone)		T2 (low-temperature climate zone)		T3 (high-temperature climate zone)	
	Dry-bulb temperature DB	Wet-bulb temperature WB	Dry-bulb temperature DB	Wet-bulb temperature WB	Dry-bulb temperature DB	Wet-bulb temperature WB
Indoor	27	19	21	15	29	19
Outdoor	35	24	27	19	46	24

Space heaters

	H1 (standard)		H2 (low temperature)		H3 (extremely low temperature)	
	Dry-bulb temperature DB	Wet-bulb temperature WB	Dry-bulb temperature DB	Wet-bulb temperature WB	Dry-bulb temperature DB	Wet-bulb temperature WB
Indoor	20	15	20	15	20	15
Outdoor	7	6	2	1	-7	-8

(2) ISO 16358

ISO 16358 specifies the test and calculation methods for the seasonal energy efficiency of air-cooled air-conditioners and air-to-air heat pumps. It consists of three parts. Part 1 covers cooling, Part 2 covers heating, and Part 3 covers annual energy efficiency.

The test method conforms to the provisions of ISO 5151 and 15042. The calculation of the seasonal energy efficiency relies on the following procedure:

a. Capacity and power consumption are measured under the temperature and humidity conditions shown in Table 2.3-2. The equipment is classified into four categories: fixed-capacity unit, two-stage capacity unit, multi-stage-capacity unit, and variable-capacity unit. For equipment other than fixed-capacity units, the intermediate (50% capacity) and minimum values are determined by measurement or calculation using coefficients.

b. The assumed air-conditioning load is set. Table 2.3-3 shows the defined air-conditioning load. In the case of cooling, the load is set to zero at an outdoor temperature of 20°C, and the rated capacity value is set to 100% of the load at an outdoor air temperature of 35°C. For heating, the load is zero at an outdoor air temperature of 17°C, and 0.82 times the rated capacity (7°C) at an outdoor temperature of 0°C is considered to be 100% of the load. The air-conditioning load at a given outdoor temperature is obtained as a linear change between zero and 100% loads.

c. The capacity and power consumption characteristics are determined with respect to the outdoor temperature and expressed as a linear change, as shown in Figure 2.3-2. The effect of frost is added in the region where the outdoor air temperature is above -7°C and below 5.5°C during heating.

d. The distribution of the outdoor temperature bin (outdoor temperature and bin hour) is set.

e. The seasonal energy efficiency is calculated as F = seasonal total load L / seasonal energy consumption C. Both the seasonal total load L and seasonal energy consumption C are calculated as the sum of the outdoor temperature appearance frequency (time); however, the seasonal energy consumption C is affected by the intermittent operation range, frosting range, and variable-capacity range.
The annual energy efficiency is calculated as (cooling period total load + heating period total load) / (cooling period energy consumption + heating period energy consumption).

Table 2.3-2 Temperature and humidity conditions for testing

Cooling								Heating							
Rated capacity				Low-temperature capacity				Rated capacity				Low-temperature capacity			
Indoor		Outdoor		Indoor		Outdoor		Indoor		Outdoor		Indoor		Outdoor	
DB°C	WB°C	DB°C	WB°C	DB°C	WB°C	DB°C	WB°C	DB°C	WB°C	DB°C	WB°C	DB°C	WB°C	DB°C	WB°C
27	19	35	24	27	19	29	19	20	15	7	6	20	15	2	1

Table 2.3-3 Defined load

	Cooling		Heating	
	Zero load (0%)	100% load	Zero load (0%)	100% load
AC load (W)	0	Rated capacity (35°C)	0	0.82 × Rated capacity (7°C)
Outdoor temp. (°C)	20	35	17	0

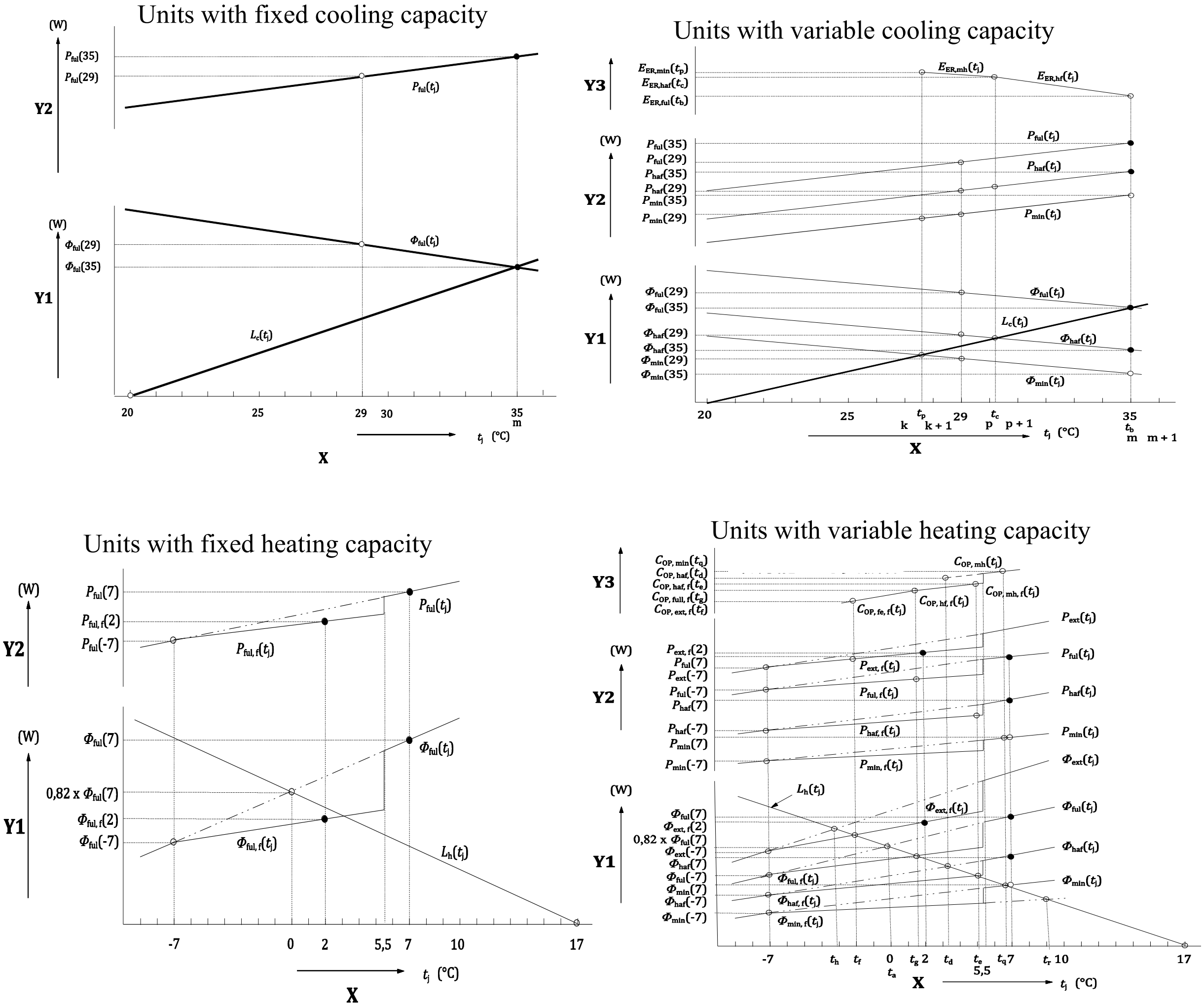

X: Outside air temperature; Y1: Capacity or load; Y2: Power consumption; Y3: Energy efficiency

Figure 2.3-2 Capacity, power input, and load for fixed- and variable-capacity units

2.3.2 Japanese Industrial Standards (JIS)

JIS standards regarding the performance test methods for refrigeration and air-conditioning appliances include the following:

- JIS B 8615-1:2013: Air conditioners -- Part 1: Non-ducted air conditioners and heat pumps -- Testing and rating for performance
- JIS B 8615-2:2015: Air conditioners -- Part 2: Ducted air-conditioners and air-to-air heat pumps -- Testing and rating for performance
- JIS B 8615-3:2015: Air conditioners -- Part 3: Multiple split-system air-conditioners and air-to-air heat pumps -- Testing and rating for performance
- JIS C 9612:2013: Room air conditioners
- JIS B 8616:2015: Package air conditioners

(1) JIS B 8615-1

ISO 5151, the international standard to which this standard corresponds, was revised in 2010, and JIS B 8615-1 was revised in 2013 accordingly. The main revisions are as follows:

− Support for advanced technologies (e.g., inverter air-conditioners)
− Simplification of tests and clarification of requirements, etc.

It was based on ISO 5151 but modified in terms of terminology, temperature conditions, technical content, etc., in consideration of domestic circumstances.

Scope of application:

- Integrated- and separate-type air-conditioners and heat pumps for residential, commercial, and industrial use
- Air-cooled non-ducted-type with a rated capacity of less than 8 kW

(Water-cooled-type equipment were not included. For ducted types, JIS B 8615-2 has been separately established based on ISO 13253.)

Details of standard:

- Cooling test: Type of test and conditions (temperature conditions are the same as those in ISO 5151; Table 2.3-4)
- Heating test: Type of test and conditions (temperature conditions are the same as those in ISO 5151; Table 2.3-4)
- Test method and measurement uncertainty: The room-type calorimeter test method or the air enthalpy test method is used.
- Markings (name plate, rated value)

(2) JIS C 9612

This standard was established in 1964 and has been revised 10 times since then. In particular, it was revised in 2013 in response to a review of energy-efficiency evaluation methods. No corresponding international standard has been established at this time.

Scope of application: Room air-conditioners with a rated cooling capacity of 10 kW or less and multi-type room air-conditioners with a rated cooling capacity of 28 kW or less

Details of standard:

- Operating performance: According to JIS B 8615-1
- Safety performance (temperature, electricity, materials, and structures)
- Operating performance test: According to JIS B 8615-1
- Safety performance test
- Markings (products and packaging)

Standards for the seasonal energy-consumption-efficiency calculation method:

- Standards are based on the technical content of ISO 16358-1.
- The temperature conditions for the capacity test are the same as those in ISO 5151, Table 2.3-2. The variation in capacity and load with outdoor temperature is approximately linear. However, the outdoor temperature at which the load reaches 0% during cooling is 20°C in ISO 5151, while it is 23°C in JIS C 9612. The outdoor temperature at which the load becomes 0% during heating is the same.
- The calculation method for the energy consumption efficiency is essentially the same as that of ISO 5151.
- It is preferable to use the value in Tokyo for the time of occurrence of the outdoor temperature during cooling and heating.

(3) JIS B 8616

This standard was established in 1979 and has been revised four times since then. It was revised in 2015 to match actual usage conditions, harmonize with international standards, and review performance tolerances.

Scope of application: Air-conditioners with a rated standard cooling capacity of 56 kW or less (excluding those for vehicles and other special applications)

Details of standard:

- Operating performance
- Safety performance (temperature, electricity, materials, and structures)
- Refrigerant leakage test: JIS B 8620
- Operating performance test: JIS B 8615-1,2,3
- Safety performance test: This standard, JIS C 9335-2-40
- Inspection
- Markings and instruction manuals

Standards for the seasonal energy-consumption-efficiency calculation method:

- Although not specified as such, the basic calculation method is in accordance with ISO 16358.
- The temperature conditions for testing are in accordance with JIS B 8615 and are the same as those in ISO 5151,

Table 2.3-2.
- The outside temperature at which the load becomes 0% during cooling differs from that of the room air-conditioners mentioned above, being 21°C for stores and 18°C for offices.
- Outside temperature generation times during cooling and heating are presented for 12 regions in Japan, including Tokyo, and the generation times for each outside temperature are different for different stores and offices.

2.3.3 Issues and Revisions of Performance Standards

The contents pertaining to performance standards include methods for measuring capacity and power consumption, and methods for calculating energy efficiency based on these capabilities and power consumption. The following items have been identified and discussed as issues [1), 2)]:

a) Setting a load reference value: This changes the model selection and affects the efficiency calculation.
b) Performance evaluation in the low-load range: Intermittent operation may occur and whether the setting of efficiency reduction factors in that case is appropriate.
c) Setting of outdoor temperature and operating hours: Is there any deviation from actual conditions?
d) Setting of uncertainty in capacity testing
e) Performance evaluation during non-steady-state operation
f) Proposal for fixed-load testing and dynamic testing
g) Evaluation of inverter control
h) Standardization of the seasonal efficiency evaluation method with measured data + simulation
i) Comfort impact evaluation
j) Revision of standards or creation of new standards

As a root cause of these issues, the discrepancy between the indicated performance and actual operational performance of air-conditioning equipment has conventionally been a major problem. ISO/TC86/SC6, which is in charge of international standards for the performance of refrigeration and air-conditioning equipment, proposed the establishment of a new task group, TG 13 (the next generation of performance standards), at its plenary meeting held in January 2021 with the aim of solving these problems, which was subsequently approved. The objective was to propose a future course for the next generation of performance standards and measures for building simulations and to consider the following terms:

1. Discrepancies between evaluated performance and actual performance.
2. Measures to provide performance to the building side.
3. Whether to update ISO 16358 or to create a new standard.
4. Measures to maintain comfort while maximizing performance.

TG13 has held its first meeting (April 12, 2021) through its ninth meeting (January 27, 2022), and the following proposals were made and approved at the SC6 plenary meeting on February 17, 2022.

[A] Create an Ad Hoc Group (AHG) under WG1 to establish seasonal efficiency standards for VRF. The AHG will develop the VRF performance standard under the Air-Conditioning, Heating, and Refrigeration Institute (AHRI) to the ISO standard with necessary modifications.
[B] Create a new working group for the development of standards for data to be provided for building simulations.
[C] TG13 will continue discussions on a new seasonal efficiency rating method, such as test conditions, to minimize the discrepancy between rating seasonal efficiency and real field performance.
[D] Create a new working group to update the measurement methods to the latest technology.
[E] In addition to the above ad hoc and working groups, an informal group will be formed with Waseda University in Japan and research institutes in Europe and the US to discuss load-based test methods.

The schedule for the discussion of each item is shown in Figure 2.3-3.

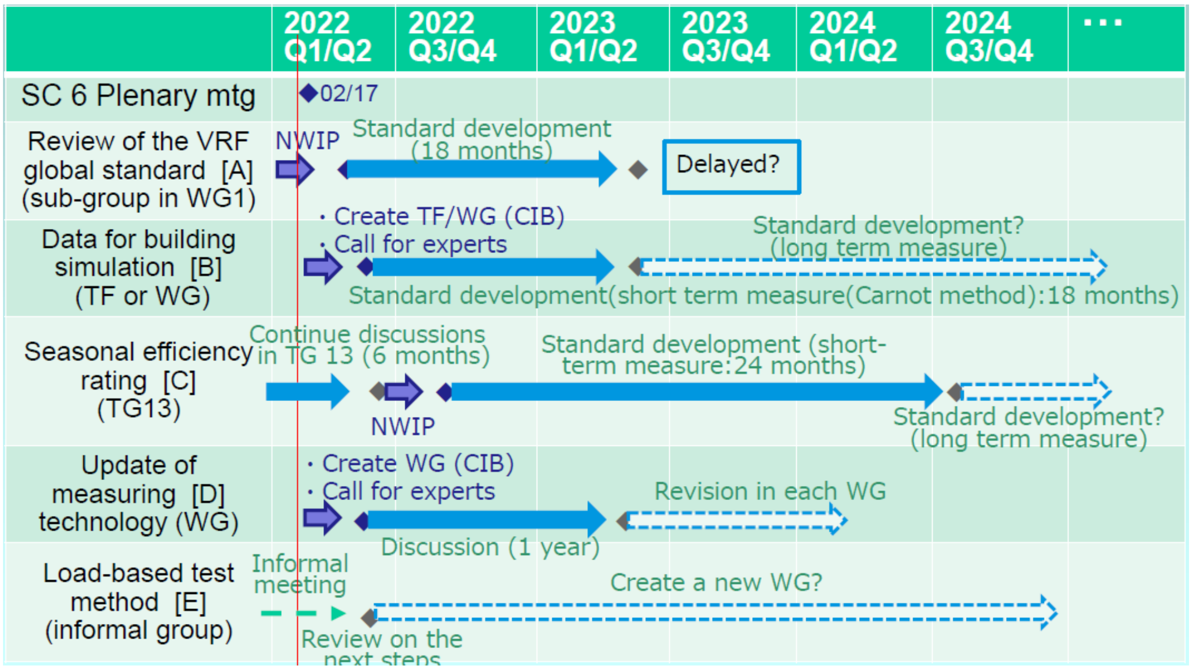

Figure 2.3-3 Schedule to review performance standard in ISO/TC86/SC6

Japan Electrical Manufacturers' Association and JRAIA are also studying the contents of [C] (Figure 2.3-3). The former is considering improving the accuracy of the characteristic curve of equipment performance, particularly in the low-load region, and reviewing the Cd value. JRAIA has been analyzing IoT data on the operating conditions of actual equipment, reviewing load distribution, and studying how to apply the data to performance test conditions and seasonal efficiency evaluations. Japan aims to reflect these results in the TG13 study.

The informal groups in [E] (Figure 2.3-3) include Purdue University, Canadian Standards Association (CSA), Cadeo/IEA, Bundesanstalt für Materialforschung und-prüfung (BAM), Air-conditioning, Heating, & Refrigeration Institute (AHRI), and Waseda University. Experts from Waseda University on load-based tests will participate in sharing their level of technology and recognition of issues.

WGIV on equipment performance evaluation methods was newly established by this committee in FY2021. In addition to Waseda University and the University of Tokyo, the Japan Air Conditioning and Refrigeration Research Institute, Japan Electrical Manufacturers' Association, and Japan Refrigeration and Air-Conditioning Industry Association are participating to study performance evaluation methods, including load-based tests. It is expected that the results of WGIV will be reflected in the discussions at ISO.

2.3.4 The Building Energy Efficiency Act [3)]

There have been multiple reports indicating that the reduction in greenhouse gas emissions is not only due to the warming effect of refrigerants themselves but also to the warming effect of energy consumption by refrigeration and air-conditioning systems, and that the effect of greenhouse gas emissions due to energy consumption is more significant.

While the CO_2 equivalent of domestic consumption of CFCs is 71.52×10^6 t-CO_2 (average value for 2011-13), as shown in Table 2.3-4,[4] the CO_2 equivalent emissions from energy sources are more than one digit higher at $1{,}235 \times 10^6$ t-CO_2 (FY2013). Emissions from the residential and building sectors, in which energy consumption by air-conditioning accounts for a large portion, are 480×10^6 t-CO_2.

Table 2.3-4 Estimated energy-related CO_2 emissions in each sector

Greenhouse gas emissions/absorption (Unit: 100 million t-CO_2)		2013 emission record	2030 emission target	Reduction rate	Conventional target
		14.08	7.60	▲46 %	▲26 %
Energy-origin CO_2		12.35	6.77	▲45%	▲25%
Division	Industry	4.63	2.89	▲38%	▲7%
	Other business division	2.38	1.16	▲51%	▲40%
	Household	2.08	0.70	▲66%	▲39%
	Transportation	2.24	1.46	▲35%	▲27%
	Energy conversion	1.06	0.56	▲47%	▲27%
Non-energy-source CO_2, methane, N_2O		1.34	1.15	▲14%	▲8%
4 fluorocarbon gases (such as HFC)		0.39	0.22	▲44%	▲25%
Absorber		-	▲0.48	-	(▲37 million t-CO_2)
Joint Crediting Mechanism (JCM)		Through public-private partnerships, we aim to achieve a cumulative global emission reduction/absorption amount of approximately 100 million t-CO2 by 2030. The credits acquired by Japan for the achievement of Japan's Nationally Determined Contributions (NDCs) have been appropriately accounted.			-

To reduce the energy consumption in homes and buildings, the Building Energy Efficiency Act, more specifically the "Act on the Improvement of Energy Consumption Performance of Buildings," was promulgated in July 2015.

The Building Energy Efficiency Act requires that the design values of primary energy consumption for air-conditioning, ventilation, lighting, hot-water supply, elevators, and other equipment installed in buildings be lower than the standard values, that is compliance with energy conservation standards [3]. Standard values are defined for each type of equipment, considering the operating conditions and operating characteristics of each application. The energy conservation standards are judged to be compliant if the following equation is satisfied:

$$\mathrm{BEI} \leqq 1.0 \qquad (2.2\text{-}1)$$

Here,

BEI (Building Energy Index):

= (Design primary energy consumption – Other (OA equipment, etc.)) / (Standard primary energy consumption – Other (OA equipment, etc.))

Design primary energy consumption: Sum of the primary energy-consumption design values for air-conditioning + ventilation + lighting + hot-water supply + elevators and escalators + other (OA equipment, etc.) – solar primary energy consumption.

Standard primary energy consumption: Sum of the primary energy-consumption standard values for air-conditioning + ventilation + lighting + hot-water supply + elevators and escalators + other (OA equipment, etc.) – solar primary energy consumption, which are specified for each facility of a building.

In June 2019, an amendment was made to strengthen the regulations in the Building Energy Efficiency Act. An overview of the revisions is shown in Figure 2.3-4[4]. The key point in the revision is the addition of medium-sized buildings (300 m^2 or more) to existing large buildings (2000 m^2 or more) as targets of the obligation to comply with energy conservation standards. In addition, for small buildings and residences of less than 300 m^2, architects are required to explain the energy-efficiency and conservation performance to the owner. If the building does not conform to energy-efficiency and conservation standards, the owner's obligation to make efforts is strengthened by explaining the measures taken to ensure energy-efficiency and conservation performance. The expansion of the scope of the obligation to conform and the obligatory explanation are to come into effect within two years of the promulgation of the act. The act went into effect in April 2021.

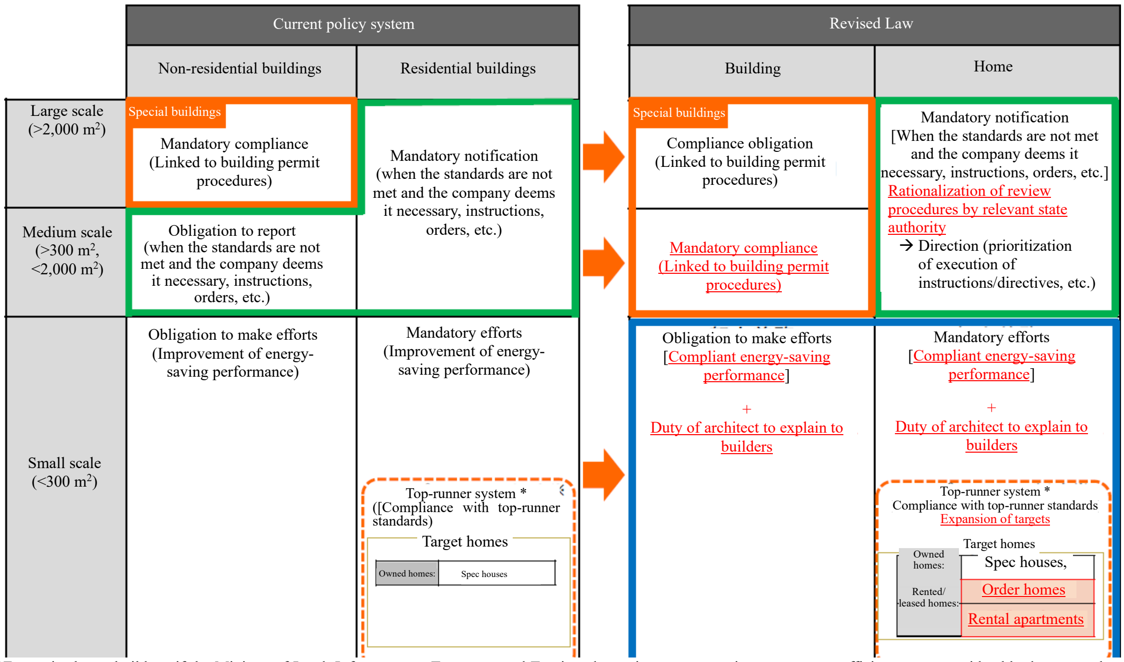

*For major home builders, if the Minister of Land, Infrastructure, Transport, and Tourism deems it necessary to improve energy efficiency to a considerable degree, such as insufficient compliance with the top-runner standards, they will be subject to recommendations and ministerial orders.

Figure 2.3-4 Revision of Act on Building Energy Conservation

During this period, Japan declared its goal of "carbon neutrality by 2050" in October 2020, and efforts toward further energy conservation and decarbonization have become necessary. In light of this situation, the Ministry of Land, Infrastructure, Transport, and Tourism, the Ministry of Economy, Trade, and Industry, and the Ministry of the Environment collaborated to establish the "Study Group on Energy-saving Measures for Houses and Buildings toward a Decarbonized Society"[5] in April 2021 as a forum for discussion on how to further improve energy efficiency in houses and buildings, and in August 2021, a "Roadmap for Energy Efficiency and Conservation Measures in Houses and Buildings Toward a Decarbonized Society" was presented. The roadmap outlines a schedule for strengthening regulations by 2030, including raising energy-efficiency standards and expanding the obligation to comply with energy-efficiency standards. Based on this roadmap, the Building Energy Efficiency Act was revised in June 2022, making it mandatory for all newly built residential and non-residential buildings to comply with energy conservation standards (scheduled for fiscal 2025), expanding the scope of the residential building top runner program, introducing energy conservation performance labeling, promoting the introduction of renewable energy facilities, etc.[6]

Although the primary energy consumption of buildings varies depending on the type of building, the energy consumption for air-conditioning accounts for approximately half of the primary energy consumption of buildings, and the energy efficiency of air-conditioning equipment has a significant impact on the achievement of energy conservation performance of buildings. When selecting a next-generation refrigerant, it is important to consider the balance between the energy efficiency of the equipment and the reduction of the global warming impact, as well as to ensure safety.

References

1) Ministry of Economy, Trade and Industry, "Survey Project for Energy Efficiency and Conservation Policy Planning (Survey concerning Revision of the Toprunner Program, etc.)," https://www.meti.go.jp/meti_lib/report/H29FY/000505.pdf, (2018.2)

2) NEDO, Performance evaluation guidelines for heat pump systems, (2017.1)
3) Ministry of Land, Infrastructure, Transport and Tourism, Detailed explanatory materials: Overview of the Building Energy Conservation Act (2016.12)
4) Ministry of Land, Infrastructure, Transport and Tourism, Outline of revision of the Building Energy Conservation Act and future schedule, etc., (2019.7)
5) Ministry of Land, Infrastructure, Transport and Tourism, https://www.mlit.go.jp/jutakukentiku/house/jutakukentiku_house_tk4_000188.html

2.4 Contribution of R&D Results to the Revision of Standards

Table 2.4-1 shows the status in which the results of research and development conducted under this NEDO project have contributed to the revision of codes and standards and the status in which they are scheduled to contribute in the future.

Regarding the refrigerant properties in WGI, the research results are reflected in the revision of ISO 17584 and REFPROP. Regarding the safety and risk evaluation of WGII, the results are reflected in the international standards IEC 60335-2-40 and IEC 60335-2-89, which are also reflected in the domestic JIS and JRA standards. Meanwhile, the performance evaluation technologies of WGI and WGIV are expected to contribute to the formulation of new international standards in the future.

Table 2.4-1 Contribution of NEDO project results to standard revisions

		Study details	Related regulations, etc.	Contribution to the revision of standards and norms (achievements)			
				Applicable regulations	Contribution details	Proposal date	Effective date
WG I	Kyushu University	Measurement of physical properties of next-generation refrigerants Equation of state	ISO 17584 (Refrigerant Properties) REFPROP	ISO 17584	Registration of R1233zd(E), R1336mzz(Z), R1234yf	2017–2022	Aug. 2022
				REFPROP 10	Provides property definition files for R245fa, R1234ze(Z), R1243zf, R1123, R1224yd(Z), R32/1234yf, R32/1234ze(E)	2013–2018	2018
		Heat transfer data measurement Heat transfer database	(Heat transfer database)	–	Experimental data of boiling heat transfer and condensation heat transfer of new and existing refrigerants can be searched and viewed from all over the world using a Web browser, contributing to the provision of these information	–	–
	Waseda University	Analytical model Development of simulator (heat exchangers, systems, Life Cycle Climate Performance (LCCP))	IEC 60335-2-89	–	–	–	–
			Next-generation ISO seasonal performance standard (successor to ISO 16358)	–	-	–	–
		Performance evaluation facility (emulator-type test lab)	(Real operating performance database)	–	–	–	–
WG II	The University of Tokyo	Refrigerant leakage simulation concentration distribution measurement	ISO 5149-1,2,3,4 (Safety standards for refrigeration and air-conditioning systems) IEC 60335-2-40 (Safety standards for air-conditioners) IEC 60335-2-89 (Safety standards for refrigeration equipment) JIS C 9335-2-40 (domestic edition of IEC 60335-2-40) JIS C9335-2-89 (domestic edition of IEC 60335-2-89) JRA standard	IEC 60335-2-40	The validity of the A3 refrigerant charge relaxation was verified	–	May 2022
				IEC 60335-2-89	The analysis conducted by JRAIA realized the relaxation of the A2L refrigerant charge	Dec. 2019	2023
				JRA 4078 JRA GL-21	The analysis conducted by JRAIA has clarified the danger of forming a flammable zone immediately after A2 and A3 refrigerant leakage in a reach-in showcase, and helped to define the concentration standard in JIS C 9335-2-89 (eliminating the 5-min measurement exemption stipulated in IEC 60335-2-89)	2019–2020	2021
		Suppression of diesel explosion		IEC 60335-2-40	Contributed to the conclusion that no provisions for diesel explosion of A3 refrigerants were necessary	2018	2018
		Autolysis reaction of HFO refrigerant	ISO 817 (safety classes for refrigerants)	–	–	–	–
	Suwa University of Science	Evaluation of ignition sources	ISO 5149-1,2,3,4 (Safety standards for refrigeration and air-conditioning systems) IEC 60335-2-40 (Safety standards for air-conditioners) IEC 60335-2-89 (Safety standards for refrigeration equipment) JIS C9335-2-40 (domestic edition of IEC 60335-2-40) JIS C9335-2-89 (domestic edition of IEC 60335-2-89) JRA standard	–	–	–	–
				JRA 4078 JRA GL-21	The evaluation results of various ignition sources were reflected in the risk assessment, and standards for built-in showcases were established based on them	–	2021
	AIST Science for Safety and Sustainability	Actual-scale hazard assessment		–	–	–	–
	AIST Sustainable Chemistry	Combustion characteristics of low-flammability refrigerants (combustion rate, combustion limit, extinction distance, mixing regulations)	ISO 817 (safety classes for refrigerants) ANSI/ASHRAE Standard 34 (safety classes for refrigerants) High-Pressure Gas Safety Act	High-Pressure Gas Safety Act	The combustion limit evaluation method developed in the NEDO project was adopted as the method for determining the specific inert gases	2020	April 2021
WG IV	The University of Tokyo	Load-based test method	ISO 5151 (Method for testing rated performance of air-conditioners) ISO 15042 (Rated performance test method for multi air-conditioners) ISO 16358-1,2,3 (Seasonal performance evaluation method) JIS B8615-1,2,3 (Rated performance test method) JIS C 9612 (Seasonal performance evaluation method for room air-conditioners) JIS B 8616 (Seasonal performance evaluation method for packaged air-conditioners)	–	–	–	–
	Waseda University			–	–	–	–

Table 2.4-1 Contribution of NEDO project results to standard revisions (continued)

<table>
<tr><th rowspan="2"></th><th rowspan="2"></th><th rowspan="2">Study details</th><th rowspan="2">Related regulations, etc.</th><th colspan="4">Contribution to the revision of standards and norms (forecasted)</th></tr>
<tr><th>Applicable regulations</th><th>Contribution details</th><th>Proposal date</th><th>Effective date</th></tr>
<tr><td rowspan="6">WG I</td><td rowspan="3">Kyushu University</td><td rowspan="2">Measurement of physical properties of next-generation refrigerants
Equation of state</td><td rowspan="2">ISO 17584 (Refrigerant Properties) REFPROP</td><td>ISO 17584</td><td>Mixed refrigerant registration (target mixed refrigerants are TBD)</td><td>TBD</td><td>TBD</td></tr>
<tr><td>REFPROP 10.1</td><td>Provides property definition files for R1336mzz(E), R32/1123, R1123/1234yf, R1234yf/290 and R1123/290</td><td>2018–2023</td><td>2023?</td></tr>
<tr><td>Heat transfer data measurement
Heat transfer database</td><td>(Heat transfer database)</td><td>–</td><td>The new function of setting the authorization level of user accounts and its function and enabling the download of heat transfer data contributes to the acquisition of information necessary for research and development and design</td><td>–</td><td>–</td></tr>
<tr><td rowspan="3">Waseda University</td><td>Analytical model
Development of simulator (heat exchangers, systems, LCCP)</td><td>IEC 60335-2-89</td><td>IEC 60335-2-89</td><td>Contributed to the Japanese proposal for A2L refrigerant by removing the 1.2-kg limit and allowing it to be filled with up to 13 times the LFL of refrigerant.
(The amount of refrigerant required for some A2L refrigerants such as R454C was analyzed using a simulator at the University of Waseda, and it was found that approximately twice the amount of refrigerant of R290 would be enough to ensure the same level of performance. This result contributed to the above Japanese proposal.)</td><td>Dec. 2019</td><td>2023</td></tr>
<tr><td></td><td>Next-generation ISO seasonal performance standard (successor to ISO 16358)</td><td>ISO</td><td>Using the developed simulation as the basis for the next ISO performance standard, it will form the foundation of the standard aiming for digital standardization. By adding the necessary functions, we aim to establish a standard that reduces the burden of measurement, has high accuracy, and is highly convenient.</td><td>2023–2024</td><td>2026</td></tr>
<tr><td>Performance evaluation facility (emulator-type test lab)</td><td>(Real operating performance database)</td><td>ISO</td><td>The emulator-type load test method is gaining recognition as an international standard for load testing and will become mainstream.</td><td>TBD</td><td>TBD</td></tr>
<tr><td rowspan="5">WG II</td><td rowspan="5">The University of Tokyo</td><td rowspan="3">Refrigerant leakage simulation concentration distribution measurement</td><td rowspan="4">ISO 5149-1,2,3,4 (Safety standards for refrigeration and air-conditioning systems)
IEC 60335-2-40 (Safety standards for air-conditioners)
IEC 60335-2-89 (Safety standards for refrigeration equipment)
JIS C 9335-2-40 (domestic edition of IEC 60335-2-40)
JIS C9335-2-89 (domestic edition of IEC 60335-2-89)
JRA standard</td><td>IEC 60335-2-40</td><td>We will propose a general-purpose technology that can easily implement a new fan airflow formula for Edition 7.0 and later international standards through an unprecedented approach in the world focusing on jet velocity.</td><td>TBD</td><td>TBD</td></tr>
<tr><td>IEC 60335-2-89</td><td>This will lead to a safety evaluation for the increase of R290 maximum refrigerant charge from 500 g to 1 kg, which may be proposed in future revisions.</td><td>TBD</td><td>TBD</td></tr>
<tr><td>–</td><td>–</td><td>–</td><td>–</td></tr>
<tr><td>Suppression of diesel explosion</td><td>–</td><td>–</td><td>–</td><td>–</td></tr>
<tr><td>Autolysis reaction of HFO refrigerant</td><td>ISO 817 (safety classes for refrigerants)</td><td>ISO 817</td><td>Promote the risk assessment of the self-decomposition reaction of HFO refrigerants and contribute to proposing the importance of the safety assessment of the self-decomposition reaction to the ISO 817 revision committee. We also discuss the stability of substances such as CF3I. Japan has already explained the main points of the need for a stability index and has reached a basic agreement and has been requested to propose specific provisions.</td><td>2023–2024</td><td>2025</td></tr>
</table>

Table 2.4-1 Contribution of NEDO project results to standard revisions (continued)

		Study details	Related regulations, etc.	Contribution to the revision of standards and norms (forecasted)			
				Applicable regulations	Contribution details	Proposal date	Effective date
WG II	Suwa University of Science	Evaluation of ignition sources	ISO 5149-1,2,3,4 (Safety standards for refrigeration and air-conditioning systems) IEC 60335-2-40 (Safety standards for air-conditioners) IEC 60335-2-89 (Safety standards for refrigeration equipment) JIS C9335-2-40 (domestic edition of IEC 60335-2-40) JIS C9335-2-89 (domestic edition of IEC 60335-2-89) JRA standard	IEC 60335-2-40 IEC 60335-2-89	The voltage/current and load conditions of electrical components that can be excluded as sources of ignition will be summarized and theorized. Convection requirements and heat dissipation mechanisms for high surface temperature ignitability will also be summarized and theorized. Based on this, we propose an international standard that refers to ignitability prediction before implementation.	TBD	TBD
				JRA standards	The results of the evaluation of various ignition sources and determination of whether they are ignited will be reflected in the JRA standard.	TBD	TBD
	AIST Science for Safety and Sustainability	Actual-scale hazard assessment		IEC 60335-2-89	Propose a future revision of the risk of reach-in showcases to be exempted from measurement for 5 mins after the door is opened.	TBD	TBD
	AIST Sustainable Chemistry	Combustion characteristics of low-flammability refrigerants (combustion rate, combustion limit, extinction distance, mixing regulations)	ISO 817 (safety classes for refrigerants) ANSI/ASHRAE Standard 34 (safety classes for refrigerants) High-Pressure Gas Safety Act	ANSI/ASHRAE Standard 34	Provide reference data on combustion characteristics of typical refrigerant mixtures to the ASHRAE SSPC34 Committee, which meets semi-annually, and take the lead in proposing revisions to the standard as part of the review of methods for evaluating combustion characteristics, thereby appropriately addressing the deliberations.	2020	TBD
WG IV	The University of Tokyo	Load-based test method	ISO 5151 (Method for testing rated performance of air-conditioners) ISO 15042 (Rated performance test method for multi air-conditioners) ISO 16358-1,2,3 (Seasonal performance evaluation method) JIS B8615-1,2,3 (Rated performance test method) JIS C 9612 (Seasonal performance evaluation method for room air-conditioners) JIS B 8616 (Seasonal performance evaluation method for packaged air-conditioners)	JIS C 9612	A load-based test method was conducted to measure the performance of air-conditioners by utilizing the control function in the same way as actual operation. A dynamic load test method will also be considered. Based on these, a draft revision of the performance test will be provided to the JIS C9612 Revision Working Team, which is led by Japan Electrical Manufacturers' Association.	TBD	TBD
	Waseda University			ISO	At the informal group meeting of ISO/TC86/SC6, we reported on the load-based test method based on the results of NEDO and continued to participate in solving the remaining problems of this method, promoting and supporting the international standardization of this method. In the future, there are plans for the informal group to shift to a working group and work on standardization, and we will continue to participate in this working group as well, aiming to establish a standard.	June 2021 ~	2026

3. Overseas Trends

3.1 Trends in Europe

(1) Overall

-Based on the European Green Deal announced in 2019/12, the Council of the EU adopted the European Climate Law in June, 2021. The EU's goal to reduce CO_2 emissions by at least 55% below 1990 levels by 2030, as pledged under the Paris Agreement, is now legally binding in the region. The EU also aims to decarbonize (carbon neutral) its economy by 2050.

-The F-gas regulation is scheduled to be revised in 2022 and issued in 2023. To prepare for this, a policy proposal report was released, a stakeholder workshop was held, and a preliminary study report was presented in 2021. After the publication of the draft amendment, public comments will be made and the European Directorate-General for Climate Action (DG-CLIMA) will coordinate the final publication after an impact assessment.

-Europe imports a substantial portion of its refrigerants, and illegal trade has become a problem. Japanese and US-based manufacturers seem to be taking the lead in equipment, and regulatory measures are taking precedence over technological development.

-Europe is a collection of countries and regulatory standards differ from country to country. Therefore, many aspects cannot be judged in a single category.

(2) F-gas regulations

1) Background and Future Plans [1), 2), 3)]

-The first F-gas regulations began in 2006. They mainly focused on reducing refrigerant emissions, including labeling requirements for users, refrigerant leak inspection requirements, and refrigerant recovery requirements when the equipment is disposed. A phase-out of HFCs and a ban on the marketing of products containing certain HFCs was established in 2014 revisions.

-The adoption of new policy consultants, holding of stakeholder workshops, presentation of preliminary study reports, and collection of written opinions have been underway for the second revision starting in 2020.

-After deliberations within the EU Commission, it was expected that the draft revision would be published in April 2020 and issued in the next fiscal year.

Table 3.1-1 presents the progress and status of these plans.

Table 3.1-1 Progress and schedule of F-gas regulations

2006	F-Gas Regulation Issue No 842/2006 - Mainly to curb refrigerant emissions, including mandatory labeling for users, mandatory refrigerant leak checks, and mandatory refrigerant recovery at equipment disposal
2014	F-Gas Regulation Amendment No 517/2014
2015	- Plans to limit the total volume of HFCs (production and imports) in the EU region Total volume for 2015 determined based on actual results for the period 2009–2012. Using this as a reference value, 2016: 93%; 2018: 63%; 2021: 45%; 2024: 31%; 2027: 24%; 2030: 21% - Prohibit the marketing of products containing HFCs 2017: Pre-charge machines with HFC refrigerants not accounted for in the quota system 2020: Portable air-conditioners with GWP of 150 or more 2020: Fixed refrigerators with GWP of 2500 or more (except for cooling below -50°C) 2022: Sealed commercial refrigerators and freezers with a GWP of 150 or more 2024: Single-split air-conditioners containing less than 3 kg of refrigerant with GWP 750 or higher
2020	EU Commission selects Ricardo/Oko-Recherche as Policy Development Consultant EU Commission issues Alternative Refrigerants Report
2021	Stakeholder workshop on revision of F-gas regulations held Ricardo/Oko-Recherche presents a preliminary study report (items to be revised, perspectives, refrigerant condition scenarios, etc.) Industry associations, etc. submit written comments
2022	Deliberations of EU Commission Regulatory Review Committee; Publication of proposed amendments; Consultation between EU Commission, EU Parliament, and EU Council
2023	Publication of revised regulation

2) Key points of the proposed amendments[4)]

Table 3.1-2 lists the policy options proposed in the regulatory review.

Table 3.1-2 List of policy options for further assessment of impact

A: Increased ambition consistent with the European Green Deal	
A1	Raise HFC reduction targets
A2	Prohibit the use of F-gases in products and equipment that no longer require F-gases
B: Pursue harmonization with the Montreal Protocol	
B1	Add new phase-out steps after 2030 for full compliance
B2	Remove some exemptions and thresholds not envisaged in the Montreal Protocol for full harmonization and removal of thresholds
B3	Individual phase-out of HFC production toward full harmonization
B4	Additional flexibility to adapt to future decisions under the Montreal Protocol
C: Improve implementation and enforcement	
C1	Certification of skilled technicians in the use of low-GWP alternatives
C2	Detailed rules to strengthen customs and surveillance offices in EU member states and to promote the use of "EU's Single Window Environment for Customs"
C3	Increasing the stringency of obligations of economic operators to prevent illegal trade
C4	Limiting market participants to legitimate participants
C5	More comprehensive monitoring

The maximum number of HFCs that can be placed in the EU market in a given year is set as shown in Table 3.1-3. Additionally, Table 3.1-4 lists the products and equipment related to refrigeration and air-conditioning, which are banned from the market along with the corresponding date of prohibition.

Table 3.1-3 Maximum amount of HFCs allowed to be placed on the EU market

Year	Allowable market input ($t\text{-}CO_2$)	Compared to baseline year (%)
2024 – 2026	41,701,077	23.6
2027 – 2029	17,688,360	10.0
2030 – 2032	9,132,097	5.2
2033 – 2035	8,445,713	4.8
2036 – 2038	6,782,265	3.8
2039 – 2041	6,136,732	3.5
2042 – 2044	5,491,199	3.1
2045 – 2047	4,845,666	2.7
2048–	4,200,133	2.4

Baseline year: 2015 176, 700, and 479 $t\text{-}CO_2$

Table 3.1-4 Market prohibitions

	Target products and appliances		Prohibition date
1	Residential refrigerators and freezers containing HFCs with a GWP of 150 or more		January 1,
2	Commercial refrigerators and freezers (self-contained units)	Containing HFCs with a GWP of 2500 or more	January 1, 2020
		Containing HFCs with a GWP of 150 or more	January 1, 2022
		Containing other fluorinated greenhouse gases with a GWP of 150 or more	January 1, 2024
3	Self-contained refrigeration units containing fluorinated greenhouse gases with a GWP of 150 or more		January 1, 2025
4	Stationary refrigeration appliances containing or relying on HFCs with a GWP of 2500 or more (except for equipment used in applications designed to cool products to -50 °C or less)		January 1, 2020
5	Stationary refrigeration appliances containing or relying on the function of fluorinated greenhouse gases with a GWP of 2500 or higher, except for equipment used in applications designed to cool products to -50 °C or lower.		January 1, 2024
6	Commercial multipack centralized refrigeration systems with a rated output of 40 kW or more that contain or depend on the function of fluorinated greenhouse gases with a GWP of 150 or more. However, fluorinated greenhouse gases with GWP less than 1500 are allowed in the main refrigerant circuit of cascade systems		January 1, 2022
7	Plug-in room air-conditioners (self-contained equipment) containing HFCs with a GWP of 150 or more that can be moved from room to room by the end user		January 1, 2020
8	Plug-in room and other self-contained air-conditioning and heat-pump equipment containing fluorinated greenhouse gases with a GWP of 150 or more		January 1, 2025
9	Stationary split air-conditioners and split heat-pump equipment		
	(a) Stand-alone split systems containing less than 3 kg of fluorinated greenhouse gases with a GWP of 750 or more fluorinated greenhouse gases or dependent on their function		January 1, 2025
	(b) Split systems with a rated capacity of less than 12 kW that containing or depending on the function of fluorinated greenhouse gases with a GWP of 150 or more (except as required to meet safety standards)		January 1, 2027
	(c) Split systems with a rated capacity greater than 12 kW that containing or depending on the function of fluorinated greenhouse gases with a GWP of 750 or more (except as required to meet safety standards)		January 1, 2027

3) Public comments on the draft amendment[5)]

The public comment period on the draft amendment was held in June 2022, and opinions from 155 organizations and companies were received and published.

The following is a survey and organization of the opinions of six representative industry associations. The appealed points are as follows:

a) Overall

-The existing F-gas regulations contribute to the reduction of greenhouse gases and are highly regarded worldwide.

- Definitions of words in the proposed amendment are ambiguous. Examples include “self-contained,” “rated capacity,” “safety standard,” “national safety standard,” and “sealed container.”

-The basic data and modeling details are unrealistic and unclear.

b) Heat-pump effectiveness

-Conversion from fossil fuel boilers to heat-pump heating has a significant effect on reducing greenhouse gas emissions.

-Heat-pump technology is a major driver for the use of renewable energy.

The deployment and acceleration of heat pumps are in line with the REPowerEU energy policy.

c) HFC reduction

-The plan for HFC reduction is very drastic, and there are concerns that this will have a negative impact on the diffusion of heat pumps.

-Maintaining the current trajectory of gradual reduction until 2034 and reconsidering the trajectory in the subsequent revisions may be preferable.

d) Marketing prohibition

Banning plug-in room air-conditioners and other self-contained AC/HPs containing fluorinated greenhouse gases (GHGs) with GWPs above 150 is technically unfeasible starting in 2025. Equipment using A3 refrigerants is subject to safety restrictions.

-Given the policy option of a GWP limit of 150 for split stationary AC/HPs (12 kW capacity or less), the choice of refrigerants is very limited, including highly flammable refrigerants such as R290. It is not realistic to use these as alternative refrigerants. If the GWP of the refrigerant is to be lowered, the flammability and energy efficiency of equipment will become an issue.

-The use of flammable refrigerants requires harmonization with IEC and EN standards, which takes time.

-The above ban is not an appropriate policy, and GWP limits are not necessary because of challenges related to safety, energy efficiency, equipment, and economic feasibility.

e) Other

To achieve carbon neutrality while ensuring the sustainability and inclusiveness of society, it is important to promote decarbonization and environmental action throughout the entire life-cycle, and refrigerant restrictions should be considered within the same framework.

Service components should not be prohibited from being put on the market.

Policies that promote the proper use of refrigerants (prevention of refrigerant leakage and promotion of steady recovery and reuse of refrigerants) are desirable to promote the phased reduction of refrigerants.

<Surveying Organizations>

EPEE: European Partnership for Energy and the Environment

EUROVENT: Europe's Industry Association for Indoor Climate (HVAC), Process Cooling, and Food Cold Chain Technologies

AREA: Air-Conditioning and Refrigeration European Association

EHPA: European Heat-Pump Association

ASERCOM: Association of European Refrigeration Component Manufacturers

JRAIA: Japan Refrigeration and Air-Conditioning Industry Association

References

1) Japan Society of Refrigerating and Air Conditioning Engineers, Kasahara: Trend of revision of European F-gas regulation, Seminar "Environmental Issues Surrounding Refrigeration and Air Conditioning Fields," (2022.2)

2) European Commission: Evaluation and impact assessment for amending Regulation (EU) No 517/2014 on fluorinated greenhouse gases, Briefing paper for the stakeholder workshop: Preliminary findings, (2021.6)

3) European Commission, The availability of refrigerants for new split air conditioning systems that can replace fluorinated greenhouse gases or result in a lower climate impact, (2020.9)

4) European Commission -, Press release: Green Deal: Phasing down fluorinated greenhouse gases and ozone depleting substances, (2022.4)

5) European Commission, Proposal for a regulation of the European Parliament and of the Council on Fluorinated Greenhouse Gases, amending Directive (EU) 2019/1937 and repealing Regulation (EU) No 517/2014, (2022.4)

3.2 Trends in the United States

(1) Overall

The United States officially returned to the Paris Agreement and announced its acceptance of the Kigali Amendment following a change in administration; however, efforts have been made only on a state-by-state basis for some time. In particular, the state of California is leading the way, with 25 states forming an alliance to deal with global warming.

-The US Environmental Protection Agency (EPA) has been working on HFC reduction plans and estimating the costs and benefits of implementation in accordance with the American Innovation and Manufacturing Leadership (AIM) Act.

The HFC reduction plan is in line with the Kigali Amendment.

-The next-generation refrigerant is an HFO-based mixed refrigerant as an option under the initiative of refrigerant manufacturers, and various proposals have been made, including compliance with related standards; however, no significant changes have been observed in the past year.

-Evaluation of flammable refrigerants is underway by various agencies. However, they may be subject to restrictions imposed not only by international standards but also by national and regional building codes and fire codes.

(2) American Innovation and Manufacturing Leadership (AIM) Act [1), 2)]

- This act was passed with bipartisan vote in 2020 with the aim of reducing HFCs. Based on this, the EPA has issued regulations for HFC production, import quotas, trading programs, etc., which have been in effect since January 2022.

The EPA has also introduced development assistance for related companies and is considering cost and benefit aspects.

-By promoting "HFC Phase Down," US refrigerant and equipment manufacturers will maintain technological leadership in the global marketplace, while new jobs and economic growth are expected as follows:

- 33,000 new manufacturing jobs
- Manufacturing output to increase by $38.8 billion by 2027
- A $12.5 billion improvement in the US balance of trade in equipment and chemicals
- Consumers will benefit from a shift to greener products and more efficient equipment

This initiative is supported by the Alliance for Responsible Atmospheric Policy (AHRI), an industry group, and others.

-The HFC reduction is set at 85% reduction by 2036 (Figure 3.2-1). This is equivalent to the schedule of the Kigali Amendment.

Figure 3.2-1 HFC reduction in US

(3) US Climate Alliance [3)]

-Formed in 2017, a total of 25 states are participating in this study (Figure 3.2-2). Greenhouse gas emission reductions targets include 26–28% reduction by 2025 compared to 2005 levels (US submission to the Paris Agreement). These states cover 55% of the population and 60% of the economy.

- US Climate Alliance members in motion with EPA's Significant New Alternatives Policy (SNAP) rules. Of the 25 states, California, New York, Vermont, and Washington have incorporated the SNAP rule and regulated HFCs, while Connecticut, Delaware, Maryland, and New Jersey have announced HFC regulations. This will result in some states allowing the same devices to be sold, and other states disallowing their sale.

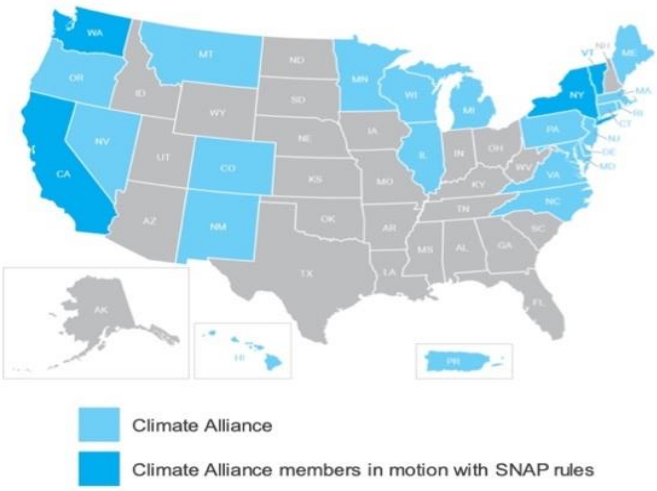

Figure 3.2-2 State initiative in US

(4) California Air Resource Board (CARB) HFC regulations [4)]

The limits placed on GWP are specified as in Table 3.2-1:

Table 3.2-1 California Air Resource Board HFC regulations

Target Systems	Refrigerant Charge Volume	GWP Allowable Upper Limit	Enforcement Year
New stationary refrigeration systems in newly constructed and fully renovated facilities	>50 lb (~23 kg)	150	2022
New refrigeration systems in existing megawatt-hour process refrigeration facilities (excluding chillers)	>50 lb (~23 kg)	2,200	2022
New chillers for industrial process refrigeration in new construction, complete renovation, and existing volume facilities		750–2,200	2024
New chillers for use in air-conditioning circuits		750	2024
New refrigeration systems and chillers for new ice rinks	>50 lb (~23 kg)	150	2024
New refrigeration system and chiller for existing ice rinks	>50 lb (~23 kg)	750	2024
New room air-conditioners and dehumidifiers		750	2023
New residential and commercial stationary air-conditioning units		750	2025
Air-conditioning equipment in VRF or VRV systems		750	2026

CARB also mandated the use of refrigerants with a GWP of 750 or less for room air-conditioners and dehumidifiers manufactured on or after January 1, 2023, among stationary air-conditioning equipment. As next-generation refrigerants are mildly flammable, it is necessary to revise the building code when using them.

Regulations will begin in early 2025 for residential and commercial air-conditioners and in early 2026 for VRF (multi-split air-conditioning systems for buildings). Regarding air-conditioning appliances brought into California in 2023 and 2024, at least 10% of R410A refrigerant must be recovered and used. CARB has also proposed a Refrigerant Recovery, Recycle, and Reuse Program, which will be studied in the future.

References

1) EPA, Protecting our climate by reducing use of HFCs, (2021)
2) EPA, Final rule - Phasedown of hydrofluorocarbons: Establishing the allowance allocation and trading program under the AIM Act, (2021)
3) Chemours Corporate Materials, The Transition to low GWP solutions.
4) JRAIA Refrigeration and Air Conditioning, No. 681, (2021.3)

3.3 Trends in China

(1) Overall

-China is the world's largest CO_2 emitter, accounting for approximately 28% of total global emissions of 33.5 billion tons in FY2018. In 2015, the government announced its Nationally Determined Contributions (NDCs) to the Paris Agreement, establishing voluntary action targets and measures such as a 60–65% reduction in emissions per GDP by 2030 (compared to 2005 levels). Furthermore, at the United Nations General Assembly in 2020, the government announced that it will achieve carbon neutrality by 2060.

-The Kigali Amendment to the Montreal Protocol was accepted by China in June 2021. The phased reduction will be implemented from 2024 in accordance with the reduction schedule of the first group of developing countries.

-The results of the survey on refrigerant trends in terms of patent applications show that in addition to Chinese equipment manufacturers, a large number of applications were filed by academic institutions (universities). Regarding refrigerants, most of the applications are for natural refrigerants, and in recent years, the number of applications for HFO refrigerants has been increasing.

(2) Status of regulations and standards [1), 2), 3)]

(a) Related regulations

-In March 2021, the Fourth Five-Year Plan was formulated, with the goal of reducing emissions per unit of GDP by 18% over a five-year period.

-In the area of fluoro-carbons, the Ozone Depleting Substances Control Regulations were established in June 2010 in compliance with the Montreal Protocol. In June 2020, this regulation was revised and changed to the Ozone Depleting Substances and HFC Control Regulations.

-In compliance with the Kigali Amendment, the production and consumption of HFCs began to be regulated in January 2022.

(b) Related standards

The standards for refrigerants in China include the following:

- GB/T 9237-2017: Air-Conditioning Equipment and Heat-Pump Machines - Safety and Environmental Requirements, July 2018
  - Compliance with ISO 5149-2014
  - Stipulation of standards for use of low-flammability refrigerants
  - Relaxed use of flammable refrigerants, which must be less than or equal to the specified charge volume and must be indicated on the label
- GB 4706.32: Safety of electrical equipment for domestic and similar use - Special requirements for heat pump machines, air conditioners, and dehumidifiers, 2019
  - Compliant with IEC 60335-2-40 (5th edition)
- GB-T 7778-2017: Refrigerant number, safety classification, 2017
  - Compliant with -ISO 817-2014
- GB 21455-2019: Energy efficiency and minimum permissible values for room air conditioners, 2020
  - Grade classification is made according to year-round energy efficiency, etc.

(3) Refrigerant trend survey from the viewpoint of patent applications

(a) Status of applicants

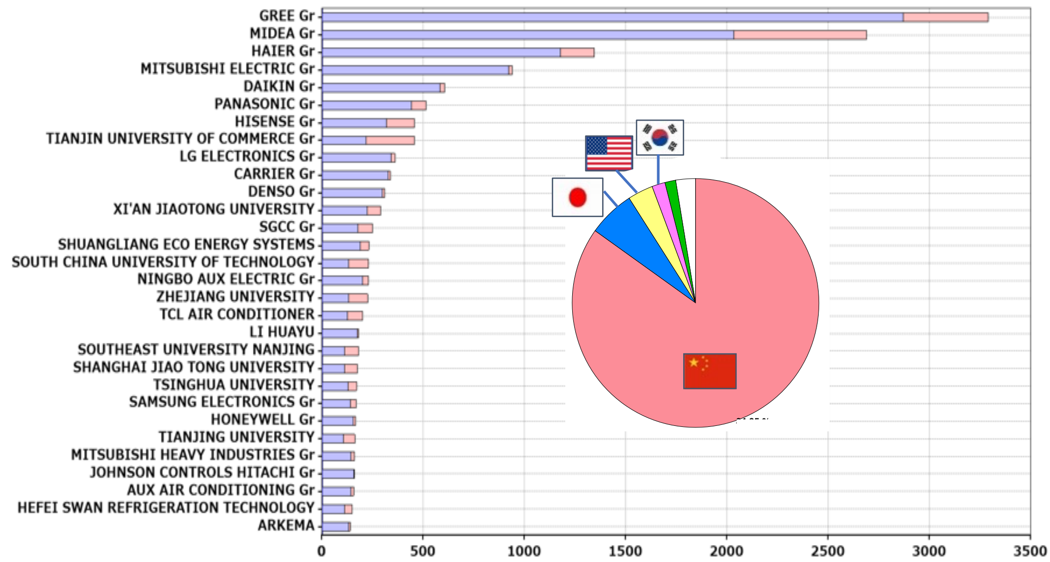

Figure 3.3-1 Applicant ranking

Figure 3.3-1 shows the names of the Top-30 applicants and the number of applications. China accounted for 85% of all applications, while Japan and the US accounted for 6% and 3%, respectively. GREE and MIDEA dominate the Chinese market, followed by HAIER and HISENSE. Eight academic institutions (Chinese universities) were among the top 30, constituting a major force (approximately 13%).

(b) Analysis of refrigerant classification

Figure 3.3-2 shows the results of the analysis of patents with refrigerant numbers used in the application.

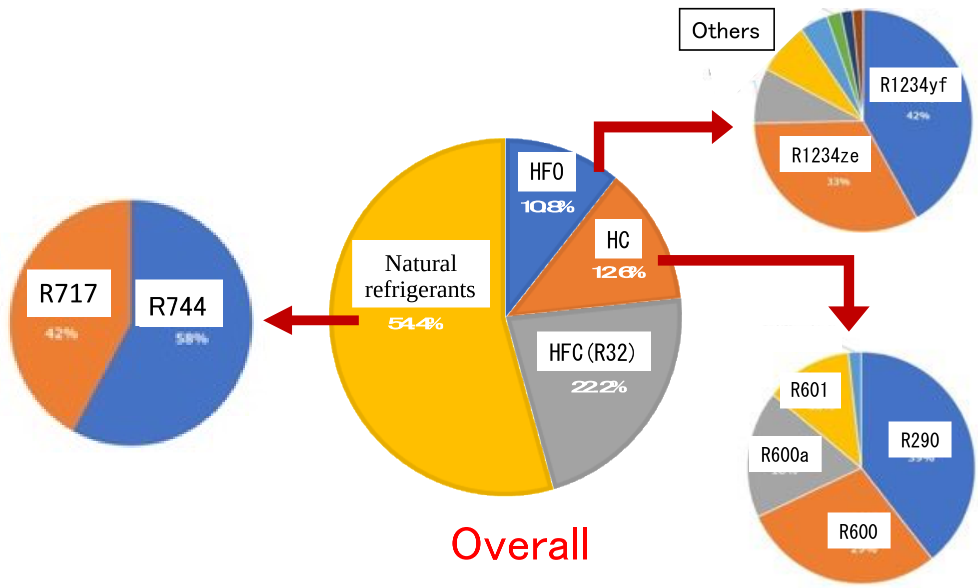

Figure 3.3-2 Classification of patent-filed refrigerants

More than half of the applications were for natural refrigerants (hydrocarbons, ammonia, and carbon dioxide); 22% of the applications were for R32, 13% were for hydrocarbons (HC), and only 11% were for HFO. Among the HFOs, R1234yf and R1234ze constituted the most common applications, followed by R1336mzz. Among the HC-based products, R290 (propane) is the most common, accounting for approximately 40% of all applications. Mixed systems are expected to increase after 2019, with R32 and R1234yf being the most common.

(c) Applications for GWP reduction.

To address next-generation refrigerants, applications containing GWP-related terms in the specifications were extracted and analyzed in terms of applicants, number of applications, and target refrigerants. Figure 3.3-3 shows the number of applicants and applications, and Table 3.3-1 lists the refrigerant type and number of applications.

GREE have the largest number of applications for applicants. Applications from Chinese academic institutions also stand out. There are many applications from Japanese, European, and US companies. In terms of the number of applications of refrigerants, the number of HFO refrigerants is increasing, concentrated in R1234yf and R1234ze, and CF3I is expected to attract attention in 2019. The number of applications for R32 has also been decreasing in recent years, which may be due to the Kigali Amendment.

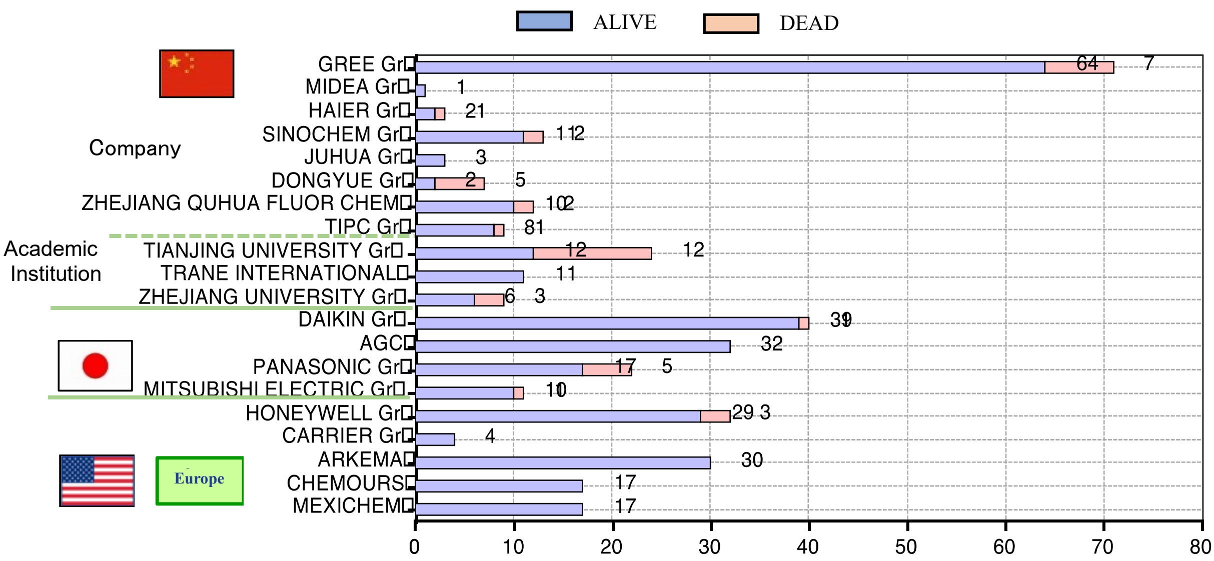

Figure 3.3-3 Applications for the purpose of reducing GWP (applicants and number of cases)

Table 3.3-1 Changes in the number of applications related to GWP

Indeterminate range

Refrigerant no.		2010	2011	2012	2013	2014	2015	2016	2017	2018	2019	2020	2021
HFOs	R1123	2			2	2	3	1	4	7	9		
	R1132a					2		1	1	1	2		
	R1224yd												
	R1233zd	1		1	1		1	2	1			1	
	R1234yf	15	10	5	5	7	7	8	19	23	37	4	2
	R1234ze	13	5	9	5	4	9	8	12	17	27	5	1
	R1336mzz	2	2	1			2		4	5	1	1	1
	R13I1	1	1	2				1	1	3	11	2	
HCs	R290	6	4		2	7	2	3	6	2	5	7	1
	R600	1	1	3	2	4	2		4	2	7	7	1
	R600a		1	2	2	3	1		4	2	7	6	1
HFC	R32	11	7	7	1	8	10	4	22	20	13	8	
Natural refrigerants	CO_2	8	8	7	12	11	11	5	20	14	19	9	5
	NH_3	1	4	4	1	1	2	1	2	5	5	3	

References

1) JETRO, China’s climate change measures and industrial and corporate responses, (2021.5)

2) JARN, February 2018

3) IGES, Commentary on China’s 2060 Carbon Neutrality Declaration, (2020.9)

3.4 Trends in Developing Countries [1)]

Developing countries are taking measures in accordance with the Montreal Protocol's reduction schedule with support from the Montreal Protocol Implementation Fund. To date, conversion to non-ozone-depleting substances, such as HFCs, has been implemented based on HCFC Phase-out Management Plans (HPMPs).

In recent years, activities targeting HFCs have been initiated in response to the Kigali Amendment.

(1) Malaysia, Indonesia, Thailand, and the Philippines are implementing HFC response capacity building activities with the World Bank in 2018–2019. The contents include the following items:
 -Review of existing laws and regulations to control and monitor the import/export of HFCs and HFC blends
 -Holding of training workshops for customs officials, etc.
 -Forecasting of HFC baseline consumption
 -National surveys on HFC consumption
 -Surveys on alternative low-GWP technologies in various sectors
 -Creation of reduction scenarios as a national strategic option for public awareness and implementation phase-out

(2) In Thailand, an investment project was implemented with the World Bank to convert a commercial refrigeration equipment manufacturer from HFC-134a to R-600a.

(3) In Vietnam, the same HFC-ready capacity building activities as above were implemented with UNIDO from 2017 to 2019.
 -Support activities related to the early ratification of the Kigali Amendment
 -Review of existing regulations for the control and monitoring of import/export of HFCs and HFC blends
 Preparation for adding HFC consumption to existing data reporting

HFC reduction is still at the stage of investigation and legislation and depends largely on the activities of European, American, and Japanese companies that are responsible for local production. Additionally, technical assistance measures using the Montreal Fund are still under consideration.

References

1) X Urban Research Institute, Report on the "Project for Promotion of Conversion of Ozone-Depleting Substances in Developing Countries," Report of the Ministry of Economy, Trade and Industry Commissioned Work in FY2020, (2021.3).

4. Trends Related to Next-Generation Refrigerant Candidates

4.1 Current Status of HFC Alternative Refrigerants

(1) HFC consumption reduction plan and measures [1), 2)]

Figure 4.1-1 shows the actual consumption of HFCs (equivalent to domestic shipments) in FY2020. This is approximately 41.15 million t-CO_2, a decrease from the previous year's 48.54 million t-CO_2. Figure 4.1-2 shows a comparison between the reduction projection and consumption limit based on the Kigali Amendment.

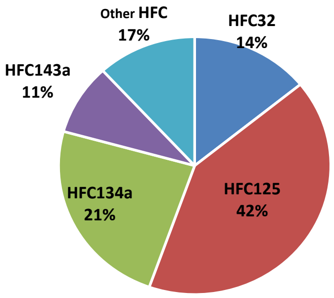

Gas type	10k tons-CO2
HFC32	595.1
HFC125	1726.1
HFC134a	849.0
HFC143a	463.1
Other HFC	482.1
Total	4115.4

Figure 4.1-1 HFC consumption in 2020

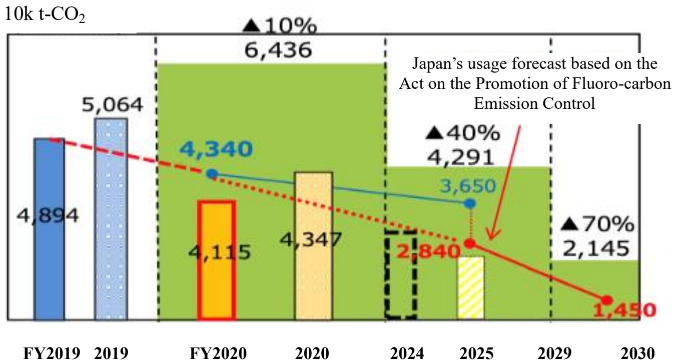

Figure 4.1-2 Contrast with consumption limit based on Kigali Amendment

The following projects are actively undertaken by the government to systematically promote the development and introduction of new refrigerants:

-Project for the development of next-generation refrigerants, refrigeration, and air-conditioning technologies, and evaluation methods that can achieve energy-saving and low-GWP effects (Ministry of Economy, Trade, and Industry)

This project aims to develop the necessary technologies to promote the conversion to green refrigerants, including risk assessment of refrigerants with low greenhouse effect but flammability, evaluation of basic properties of new refrigerants, development of refrigerants and equipment technologies that achieve both safety and energy-saving performance, overseas deployment of technologies, and proposals for international standards.

The research project described in this report was conducted within the framework of this project.

(budget amount for FY2022: 290 million yen; budgeted amount for FY2021: 650 million yen; Period: FY 2018 - FY2022 (5 years))

-Project to accelerate the introduction of energy-saving natural refrigerant equipment for the early realization of a non-fluorocarbon, low-carbon society (Ministry of the Environment)

The project supports the introduction of energy-saving natural refrigerant equipment as an alternative technology to non-fluorocarbons in areas where there are technologies for energy-saving natural refrigerant equipment but where there are also problems such as high initial costs. This will accelerate the introduction of natural refrigerant equipment with high energy-saving performance to promote non-fluorocarbons and transition to a low-carbon society.

(Budgeted amount for FY2022: 7.3 billion yen; budgeted amount for FY2021: 7.3 billion yen; Period: FY 2018-2022 (5 years))

(2) Examples of new refrigerant proposals [3),4),5),6),7)]

A survey was conducted on refrigerants covered in recent years in the following international and national conferences.

- Japan Refrigeration and Air-Conditioning Industry Association: International Symposium on Environment and New Refrigerants (2021)
- JSRAE Annual Conference (2021, 2022)
- International Institute of Refrigeration and Air-Conditioning Engineers (IIR), Japan Society of Refrigeration and Air-Conditioning Engineers HFO2021 Conference (2021)
- Purdue Conference (2022)

New refrigerants were proposed, and their basic properties, cycle performance comparisons, and safety evaluations were discussed.

Many of these studies have focused on HFO-based mixtures. In addition, flammability evaluations and risk assessments of flammable refrigerants continue to be common, while publications on test and evaluation methods for system performance are becoming more prominent.

Table 4.1-1 lists single refrigerants whereas Table 4.1-2 lists new refrigerants for mixtures. In each table, the number of refrigerants discussed in the papers presented at the conference is indicated.

Table 4.1-1 Proposed alternative refrigerants (single)

Name	Chemical formula	Boiling point(℃)	Safety	GWP	Citation frequency	
R1123	CF2=CHF	−56.0	A2L	≒1	★★★	14
R1132a	CF2=CH2	−86.7	A2	≒1	★★★	11
R1224yd(Z)	CF3CF=CHCl	14.5	A1	≒1	★★	8
R1233zd(E)	CF3CH=CHCl	18.1	A1	≒1	★★★★	18
R1234yf	CF3CF=CH2	−29.4	A2L	4	★★★★	19
R1234ze(E)	CF3CH=CHF	−19.0	A2L	≒1	★★★★	16
R1336mzz(E)	CF3CH=CHCF3	9.0	A1	7	★★	8
R1336mzz(Z)	CF3CH=CHCF3	33.4	A1	2	★	3
R13I1	CF3I	−21.9	A1	≒1	★★	10
R32	CH2F2	−52.0	A2L	675	★★★★	17
R600	CH3CH2CH2CH3	0.0	A3	4	★	2
R600a	CH(CH2)2CH3	−11.7	A3	3	★	2
R290	CH3CH2CH3	−42.1	A3	3	★★★	12
R744	CO2	−78.5	A1	1	★★★	12
R717	NH3	−33.3	B2L	≒1	★	1

Citation frequency ★Below5 ★★6-10 ★★★11-15 ★★★Over16

Table 4.1-2 Proposed alternative refrigerants (mixture)

ASHRAE No.	Mixture																Boiling point (℃)	Dew point (℃)	Safety	GWP	Frequency of citation	No. of citations (reference)
	HFC							HFO					HC Hydrocarbons		Carbon dioxide	CF3I						
	23	32	125	134a	143a	152a	227ea	1234yf	1234ze	1130	1132a	1336mzz	600a	290	744	13I1						
R407H		32.5	15.0	52.5													−44.7	−37.6	A1	1,378	☆☆	2
R407I		19.5	8.5	72.0													−39.8	−33.0	A1	1,337		0
R427C		25.0	25.0	40.0	10.0												−45.9	−39.4	A1	2,060		0
R448A		26.0	26.0	21.0				20.0	7.0								−45.9	−39.8	A1	1,387	☆☆☆	4
R448B		21.0	21.0	31.0				20.0	7.0								−44.1	−37.4	A1	1,320		0
R449A		24.3	24.7	25.7				25.3									−46.0	−39.9	A1	1,397	☆☆☆	4
R449C		20.0	20.0	29.0				31.0									−44.6	−38.1	A1	1,250		0
R450A				42.0					58.0								−23.4	−22.8	A1	604	☆	1
R452A		11.0	59.0					30.0									−47.0	−43.2	A1	2,140	☆	1
R452B		67.0	7.0					26.0									−51.0	−50.3	A2L	698	☆	1
R454A		35.0						65.0									−48.4	−41.6	A2L	238	☆☆☆	3
R454B		68.9						31.1									−50.9	−50.0	A2L	465	☆☆☆	3
R454C		21.5						78.5									−46.0	−37.8	A2L	146	☆☆☆☆	10
R455A		21.5						75.5							3.0		−51.6	−39.1	A2L	146	☆☆☆☆	8
R457A		18.0				12.0		70.0									−42.7	−35.5	A2L	139		0
R457B		35.0				10.0		55.0									−46.4	−40.4	A2L	249		0
R459B		21.0						69.0	10.0								−44.0	−36.1	A2L	145		0
R463A		36.0	30.0	14.0				14.0							6.0		−58.4	−46.9	A1	1,494		0
R465A		21.0						71.1						7.9			−51.8	−40.0	A2	143	☆	1
R466A		49.0	11.5													39.5	−51.7	−50.0	A1	733	☆☆☆☆	8
R467A		22.0	5.0	72.4									0.6				−40.5	−33.3	A2L	1,330	☆	1
R468A		21.5						75.0			3.5						−51.3	−39.0	A2L	146	☆☆	2
R468B		13.0						81.0			6.0						−52.4	−36.8	A2L	89	☆	1
R468C		42.0						52.0			6.0						−56.6	−46.2	A2L	284	☆☆	2
R469A		32.5	32.5												35.0		−78.5	−61.5	A1	1,360	☆☆	2
R470A		17.0	19.0	7.0			3.0		44.0						10.0		−62.7	−35.6	A1	277	☆	1
R470B		11.5	11.5	3.0			7.0		57.0						10.0		−61.7	−31.4	A1	749	☆	1
R471A							4.3		78.7			17.0					−16.9	−13.8	A1	140		0
R472A		12.0		19.0											69.0		−84.3	−61.5	A1	354		0
R472B		10.0		32.0											58.0		−82.9	−54.8	A1	526		0
R473A	10.0		10.0								20.0				60.0		−87.6	−83.0	A1	1,830	☆☆☆	5
R475A				43.0				45.0	12.0								−28.8	−28.3	A1	615		0
R513A				44.0				56.0									−29.2	—	A1	630	☆☆☆	3
R513B				41.5				58.5									−29.2	—	A1	594	☆☆	2
R514A										25.3		74.7					29.0	—	B1	2	☆	1
R515B							8.9		91.1								−19.0	—	A1	288	☆☆☆	3
R516A				8.5		14.0		77.5									−21.1	—	A2L	142	☆☆☆	3

Citation frequency: ☆ : 1 ☆☆ : 2 ☆☆☆ : 3–5 ☆☆☆☆ : Over 6

(3) Examples of alternative refrigerant candidates for each product

Table 4.1-3 shows examples of candidate alternative refrigerants for each product, based on a review of last year's table. Most room air-conditioners and small-sized air-conditioners for stores and offices have been converted to R32 from the conventional R410A, while risk assessment of R290 is underway for small-sized equipment such as room air-conditioners and showcases. Although the application of R32 to multi-split-type air-conditioners for buildings is also under consideration, the amount of refrigerant used is large, and discussions are underway to resolve the issue of ensuring the safety of flammable refrigerants. R404A and R410A are still the main refrigerants used in refrigerated showcases and condensing units; however, equipment using R744 (carbon dioxide) are being introduced. R22 is still widely used in refrigeration units for freezer/refrigerated warehouses, and ammonia is becoming more widely used as an alternative refrigerant. Conversion to non-CFC refrigerants is already underway in vending machines, hot-water heat pumps, and household refrigerators. Conversion to R1234yf as a substitute for R134a is planned for passenger-car air-conditioners and is scheduled to be implemented by 2023; however, there are issues in ensuring safety in buses and trucks and more time is needed to resolve these issues.

Table 4.1-3 Examples of alternative refrigerants for each product

Product group	Conventional refrigerant	Alternative refrigerant candidates	GWP	Safety	Development status/issues	Notes
Room air conditioners	R410A R32	R290	3	A3	Risk assessment	
		R454A,B,C	150-470	A2L	Functional assessment	
		R466A	733	A1	Functional/safety assessment	N41 (Honeywell)
Air conditioners for stores and offices	R410A R407C R32	R1123 mixtures R1123/R32 R1123/R32/R1234yf	150-400	A2L	Functional/safety assessment	AGC:AMOLEA
		R466A	733	A1	Functional/safety assessment	N41 (Honeywell)
Air conditioners for buildings	R410A R407C	R32	675	A2L	Partial implementation	
		R466A	733	A1	Functional/safety assessment	N41 (Honeywell)
Chilling unit	R134a R410A R404A	R449A	1397	A1	Functional assessment	XP40 (Chemours)
		R450A	604	A1	--	N13 (Honeywell)
		R465A	143	A2	--	Arkema
		R516A	142	A2L	--	Arkema
		R407H	1378	A1	Partial implementation	Daikin Industries
Turbo chillers	R123 R245fa R134a	R1233zd (E)	1	A1	Partial implementation	(Honeywell)
		R1224yd (Z)	1	A1	--	AGC
		R1234ze (E)	1	A2L	--	(Honeywell)
		R514A	2	B1		
Refrigerator showcase conditioning units	R410A R404A	R463A	1494	A1	Partial implementation	XP41 (Chemours)
		R290	3	A3	Risk assessment	
		R448A	1387	A1	Partial implementation	N40 (Honeywell)
		R449A	1282	A1	--	
		R455A	146	A2L	Functional assessment	L40X (Honeywell)
		R468A	150	A2L	--	Daikin Industries
		R744	1	A1	Practical implementation	
Freezers/refrigerators	R22	R717	1	B2L	Practical implementation	
		R717/R744	1/1	B2L/A1	Practical implementation	
		Air	1	A1	Practical implementation	
Vending machines	R410A R404A	R744	1	A1	Partial implementation	
		R600a	3	A3	--	
Water heat pumps	R744	R454C	146	A2L	Functional assessment	XP20 (Chemours)
Household freezers/ refrigerators	R134a, R600a				Practical implementation (R600a)	
Car air-conditioners	R134a	R744	1	A1	Partial implementation	
		R1234yf	4	A2L	Partial implementation	
		HFO1132(E)/R1234yf	1	A2L	Functional assessment	DIV-140 (Daikin Industries)

*This table is based on publicly disclosed materials, and there are numerous other alternative development candidates that could be considered.

References

1) Working Group on Measures against Fluorocarbons, Status of efforts for “Plan for the Rational Use of Fluorocarbons,” Industrial Structure Council, (2022.4)

2) WG on Measures against Industrial Structure Council, Refrigerants, Direction of Development of New Refrigerants and Equipment, (2022.4)

3) Japan Refrigeration and Air Conditioning Industry Association, International Symposium on Environment and New Refrigerants, (2021.10)

4) Annual General Meeting of the Japan Society of Refrigeration and Air Conditioning, (2021.9)

5) Annual Conference of the Japanese Society for Refrigeration and Air Conditioning, (2022.9)

6) International Society of Refrigeration, Japan Society of Refrigeration and Air Conditioning, HFO2021, (2021.6)

7) Purdue Conference, (2022.7)

4.2 Issues Concerning Next-Generation Refrigerants

In the search for next-generation refrigerants, the selection of flammable substances is inevitable, which is also the biggest challenge. Risk assessment methods have been established to evaluate the risk of applying flammable refrigerants to products, and risk assessments have been conducted to evaluate the occurrence of accidents and degree of hazard. Regarding low-flammability refrigerants (A2L), the Risk Assessment Study Group for Low-Flammability Refrigerants of JSRAE has compiled and issued a report. In addition, a risk assessment of high-flammability refrigerants (A3) is currently being conducted by the JRAIA working group and a report has been issued.

In addition, JSRAE has established the New Refrigerant Evaluation Committee to "evaluate and confirm the classification of the harmfulness of newly developed refrigerant gases" by conducting the following activities.

- Determination of whether the applied refrigerant gas satisfies the inert gas requirements of the Refrigeration Safety Regulations
- If the refrigerant gas satisfies the above conditions, a determination is made regarding the fluorocarbon containers that can be filled

Meanwhile, the global warming impact of refrigeration and air-conditioning equipment is the sum of the direct impact of refrigerant emissions and the indirect impact of energy consumption, which is evaluated on a life-cycle basis by the Life Cycle Climate Performance (LCCP). The indirect impact of energy consumption is generally larger. The direct impact is reduced by reducing the GWP of the refrigerants, improving the recovery rate at disposal, and reducing emissions by preventing leakage during use. In addition, the improvement in the energy-efficiency coefficient of performance (COP) reduces indirect effects. The LCCP evaluation is currently being studied by industry associations.

To apply new refrigerants, it is essential to understand the trend in regulations and standards related to refrigerants and equipment in the future. Further, it is also necessary to pay close attention to the status of regulations on fluorocarbon substances (PFAS, etc.)

Current issues related to next-generation refrigerants include the following:

a) Development of measures to ensure their safe use (risk assessment and related regulations, proposals for revision of standards, standardization, etc.) as low-GWP refrigerants pose issues in terms of flammability, chemical stability, etc.
b) Development of test methods and performance prediction technologies to evaluate equipment performance when new refrigerants are used
c) Global warming impact assessment of equipment as a whole, including GWP values of refrigerants and energy consumption during operation
d) Refrigerant selection and long-term conversion planning according to product group characteristics
   Refrigerants have an infrastructural element; therefore, it is necessary to confirm their reliability, workability, and maintainability.
e) Measures for recovery, recycling, and destruction, etc.

Basic Performance, Optimization, and Safety and Risk Evaluation of Next-Generation Refrigerants and Refrigerating and Air Conditioning Technologies

Part 4: Evaluation methods for the performance of air-conditioning equipment

WG IV Final Report

Research Committee for Next-Generation Refrigerants,

Japan Society of Refrigerating and Air-Conditioning Engineers

January 31, 2023

Table of contents

Introduction

In view of the global demand for carbon neutrality, scientists are striving to identify ways to meet this difficult challenge. Japan has pledged to achieve carbon neutrality by 2050 and is now moving ahead with the goal.

In view of these circumstances, refrigeration and air-conditioning technology have been extensively applied to refrigeration, air conditioning, water heating, and industrial technology as a cold/heat control technology to realize energy conservation. The applications of this excellent technology that can drive the economy are expanding.

In recent years, this technology has been recognized as having the capability to prevent heat strokes by controlling temperatures, even in extreme temperature conditions, and preventing viruses and other infectious diseases from spreading by controlling humidity. The realization of low temperatures and excellent temperature control as the core technology of the cold chain has enabled the provision of safe and secure food. The technology can even produce drinking water from air. Thus, refrigeration and air-conditioning technology have evolved into a technology that protects the environment as well as human life.

Conversely, refrigerants are also causing ozone-layer depletion and global warming problems. Refrigerants were known earlier to cause ozone depletion; only recently has it been discovered that some refrigerants have a greenhouse effect thousands of times greater than that of carbon dioxide. Following the Kigali Amendment to the Montreal Protocol, the reduction in the use of refrigerants has been set as a major goal. Therefore, it has become essential to install equipment that uses low-global-warming-potential (GWP) refrigerants.

In this WG IV, the Waseda University group and the University of Tokyo group joined forces to establish the basic technology that can evaluate an actual system's performance. Accurately evaluating the performance of equipment that uses next-generation refrigerants using conventional performance test facilities at a fixed compressor speed is challenging if not impossible. Particularly, in the case of non-azeotropic mixed refrigerants, a sudden change in operation will cause a change in the composition ratio of the refrigerant and a significant change in the performance of the equipment. Following the recent advances in building insulation and reduced air-conditioning loads, continuous operations with inverters have become difficult for air conditioners, and there is a need for significant performance improvement even when the equipment is repeatedly turned on and off, and the operation of the equipment changes abruptly.

The evaluation of the dynamic performance of the equipment requires the accurate evaluation of the operational performance, including the control system of the equipment, which is considerably affected by the thermal capacity and load of the environmental test room. However, it has been difficult to obtain reproducible, dynamic behavior because test rooms are generally not the same and the size and equipment installed vary greatly depending on the owner of the room.

Therefore, we have established a new method to evaluate equipment performance in a reproducible manner by virtually providing air-conditioning loads and room heat capacities. This will establish a method that can modify the JIS and international standardization organization standards and evaluate the actual operational performance of various equipment types with greater accuracy.

It is hoped that the establishment of a method to evaluate the operational performance of a system will help introduce equipment with high performance at the operational level to the market as quickly as possible, even while employing next-generation, low-GWP refrigerants.

Waseda University Kiyoshi Saito

The composition of WG IV members is shown in Table 1.

Table 1 WG IV members list

	Name	Affiliation
Chair	Kiyoshi SAITO	Waseda University
Committee member	Eiji HIHARA	National Institute for Academic Degrees Quality Enhancement of Higher Education
	Yu CHEN	University of Tokyo
	Makoto ITO	University of Tokyo
	Jongsoo JEONG	Waseda University
	Tatsuya TANI	Japan Air Conditioning and Refrigeration Testing Laboratory
	Ryota HIRATA	Japan Air Conditioning and Refrigeration Testing Laboratory
	Koji MUROZONO	The Japan Refrigeration and Air Conditioning Industry Association
	Satoshi SAKASHITA	The Japan Refrigeration and Air Conditioning Industry Association (Panasonic Corporation)
	Ryoichi TAKAFUJI	The Japan Refrigeration and Air Conditioning Industry Association (Johnson Controls - Hitachi Air Conditioning)
	Hidetomo NAKAGAWA	The Japan Electrical Manufacturers' Association (Mitsubishi Electric Corporation)
	Katsunori MURATA	The Japan Electrical Manufacturers' Association (Daikin Industries, Ltd.)
	Osami KATAOKA	Japan Society of Refrigerating and Air Conditioning Engineers (Daikin Industries, Ltd.)
Observer	Yoichi MIYAOKA	Waseda University
	Shizuo SAITOH	University of Tokyo
	Tomohiro HIGASHI	Central Research Institute of Electric Power Industry
	Akira HIWATA	The Japan Refrigeration and Air Conditioning Industry Association (Panasonic Corporation)
	Shigeharu TAIRA	The Japan Refrigeration and Air Conditioning Industry Association (Daikin Industries, Ltd.)
	Koji YAMASHITA	The Japan Refrigeration and Air Conditioning Industry Association (Mitsubishi Electric Corporation)
	Takehiko SATO	The Japan Electrical Manufacturers' Association
	Tomoko KASE	The Japan Electrical Manufacturers' Association
	Norihiro INOUE	Tokyo University of Marine Science and Technology
	Satoshi FUJIGAKI	New Energy and Industrial Technology Development Organization
	Tomokazu MORI	New Energy and Industrial Technology Development Organization
	Tatsuhiko TAKAHASHI	New Energy and Industrial Technology Development Organization
	Makoto GOCHO	New Energy and Industrial Technology Development Organization
	Takuma OISHI	New Energy and Industrial Technology Development Organization
Secretriat	Kyoji KONO	Japan Society of Refrigerating and Air Conditioning Engineers
	Shigehiro UEMURA	Japan Society of Refrigerating and Air Conditioning Engineers
	Akira NISHIGUCHI	Japan Society of Refrigerating and Air Conditioning Engineers

The authors of this report are listed in Table 2.

Table 2 Author list

		Author
Introduction		Kiyoshi SAITO (Waseda University)
Part 1	1. Development of air-conditioning performance test facility	Kiyoshi SAITO (Waseda University), Niccolo GIANNETTI, Yoichi MIYAOKA
	2. Soundness evaluation of test facility	Kiyoshi SAITO (Waseda University), Niccolo GIANNETTI, Yoichi MIYAOKA
	3. Experimental evaluations of various air-conditioning equipment types	Kiyoshi SAITO (Waseda University), Yoichi MIYAOKA
	4. Results of dynamic test	Kiyoshi SAITO (Waseda University), Yoichi MIYAOKA
Part 2	1. Introduction	Eiji HIHARA (National Institute for Academic Degrees Quality Enhancement of Higher Education)
	2. Results of Japan Air Conditioning and Refrigeration Testing Laboratory	Tatsuya TANI (Japan Air Conditioning and Refrigeration Testing Laboratory), Ryota HIRATA
	3. Results of the University of Tokyo	Makoto ITOH (University of Tokyo), Shizuo SAITOH, Eiji HIHARA (National Institute for Academic Degrees Quality Enhancement of Higher Education)

Disclaimer

Although every effort has been made to ensure the accuracy of the information contained in this report, the authors and JSRAE assume no responsibility for any actions taken by users based on the information contained in this report. Likewise, the authors and JSRAE assume no responsibility for any damages or disadvantage incurred by users resulting from the use of this report.

Part I Progress and Achievements of Waseda University

1. Development of air-conditioning performance test facility

1.1 Development of emulator-based hybrid dynamic air-conditioning performance test facility

The improved performance of devices, such as heat exchangers and compressors, and the progression of various technological innovations, such as inverters[1)2)3)4)5)], has resulted in a significant improvement in the annual performance of air-conditioning systems. Indeed, the annual performance factor (APF)[6)], which expresses the annual energy consumption efficiency [as specified by the Japanese Industrial Standards (JIS)], has exceeded 7.0, and many have conjectured that it has almost reached its limit[7)8)9)]. However, several issues associated with the APF-based evaluation method have been identified. Particularly, an air-conditioner system is operated in a dynamic state by changing its compressor's rotational speed, opening its expansion valve, or other operational features, as required by the current operating conditions according to commands from its control system. However, international standards, such as the JIS, estimate the APF using several discrete points of operating data in the steady state. These points exclude changes owing to indoor air temperature control—the core function of the control system—by keeping the compressor's rotational speed constant. This assumption is made because the performance of an air conditioner is significantly affected by the parameters of the test equipment and control system. As such, the prescribed APF test method prioritizes the ability to assess the performance of air-conditioning equipment rapidly and efficiently in a reproducible manner regardless of the test equipment performance parameters.

Such a simplified quantification of annual performance using only the steady state results in a large discrepancy compared with the actual driving performance. This has been identified as a hindrance to the promotion of effective energy savings and CO_2 emission reductions. The problem extends beyond the limits of the evaluation method; the fact that the actual operating performance is not accurately evaluated has discouraged manufacturers from developing new equipment; it has become a bottleneck in the efforts expended to improve equipment performance. Indeed, this situation is one of the greatest challenges related to the prevention of the realization of carbon neutrality in the refrigeration and air-conditioning industry.

To overcome these issues, the dynamic performance of air-conditioning equipment must be clearly understood so that the same dynamic performance can be consistently obtained across different test facilities. To achieve this objective, the test conditions must be applied on the building side to reflect consistently various characteristics, such as the building load and building heat capacity, both of which considerably affect the dynamic performance of air-conditioning equipment, regardless of the test equipment employed. Naturally, these conditions are nearly impossible to create even when using the same hardware. Although a dynamic performance evaluation method had been previously proposed[10)], the resulting dynamic performance still varies depending on the specific test equipment employed, even when the type of equipment is the same.

Therefore, in this research, we revised the conventional steady-state performance test method to compensate for the building-side test conditions by calculating them virtually using emulator software, thereby realizing a novel, reproducible, dynamic performance test method. To do so, we first developed an epoch-making performance test device equipped with an emulator and evaluated its stability. The realization of a reliable dynamic test method can facilitate the effective use of conventional test equipment to unify air-conditioner product standard performance with its actual operating performance, which is relevant to users once their equipment is installed.

Although we have already studied duct-type test equipment[11)], this research study developed a test facility capable of evaluating the dynamic performance of air-conditioning systems with high accuracy using calorimetric measurements in a test chamber. Accordingly, herein, the concept and configuration of the proposed test facility, an evaluation of its methodological soundness, and the dynamic operation performance of air-conditioning equipment are reported.

1.2 Concept of air-conditioning load and test-facility performance

To study the dynamic performance of air conditioners, we organized the basic concept of energy flow in a building and defined the necessary parameters based on the building energy exchange shown in Fig. 1.2-1. It is assumed that during the summer season, heat enters the building owing to the inflow of air from the outer environment and that by the ventilation, and sun on the walls and windows. Furthermore, human occupants generate heat and steam. These heat sources are collectively referred to as "the building load."

In addition, the conditions inside the building, indicated by the red dashed line in the figure, are affected by the state of the air supplied by the air conditioner, building load, and quantity of indoor air and heat capacity of the building, which includes the fixtures, walls, and room temperature changes. The building-specific conditions that determine the changes in the building load and temperature are referred to as the "building-side air conditions."

On the air-conditioner side, the room air is used as the in-taken air and cooled. This cooled air is blown back into the building as supply air. The cooling provided by the air conditioner at this time is called the "air-conditioning load." The conditions that determine the operational status of the air conditioner (enclosed by the blue-dashed line) are referred to as the "equipment-side air conditions."

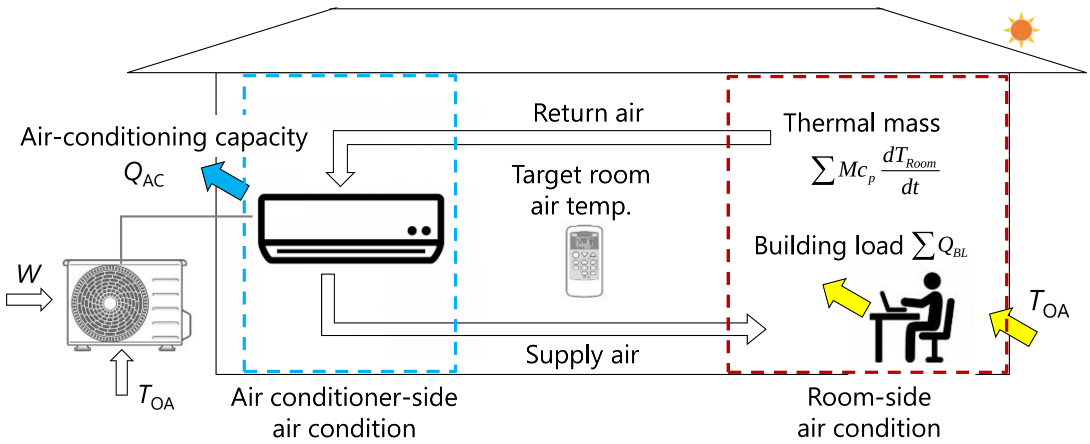

Fig. 1.2-1 Schematic showing the heat flow inside a building during the summer period

Fig. 1.2-2 depicts a series of load–time curves relating the changes in a building, air-conditioning load, and room temperature.

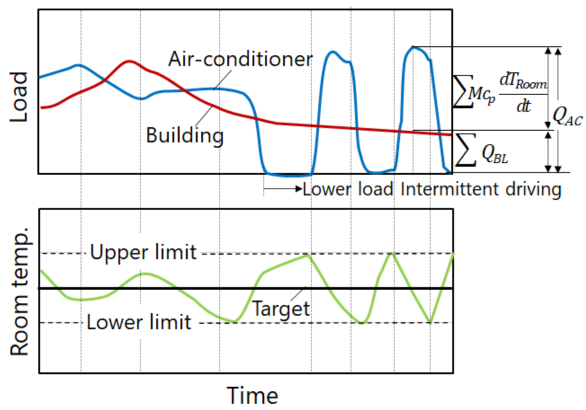

Fig. 1.2-2 Load and temperature changes inside a building

The "building load" and "air-conditioning load" are different in the dynamic state than in the static state. This difference is affected by the heat capacity inside the building, which results in changes in the indoor air temperature.

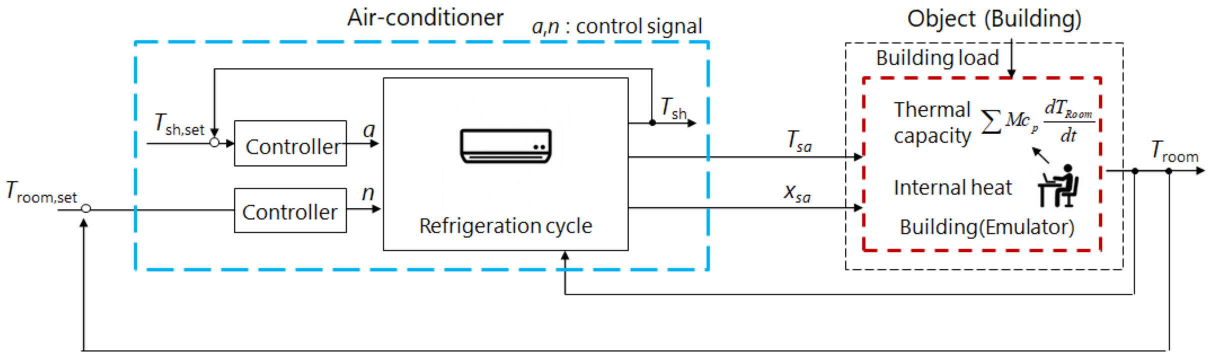

Fig. 1.2-3 Air-conditioner control method

The dynamic performance evaluation also represents an evaluation of the air-conditioning system control performance. As shown in Fig. 1.1-3, indoor air temperature control, which is the primary objective of the air conditioner, is performed for the interior of the building and for the building as a whole; accordingly, the building characteristics exert a significant influence on the control performance. Therefore, the same air-conditioner performance can only be obtained when using the same equipment while the "building-side air conditions" are kept the same. Note that even though this explanation has been provided in terms of heat exchange, because the "building-side air conditions" and the "equipment-side air conditions" have mutual influences on humidity—that is, on the material balance of water—it is also necessary to take this exchange into consideration.

1.3 Current representative performance test facilities

Typical air-conditioner performance tests employ the calorimeter, which was developed for measurements in the steady state at a fixed compressor speed. These tests are typically conducted in "air enthalpy" or "balance" test facilities. Correspondingly, the characteristics, measurement principles, and issues that arise when attempting to determine dynamic performance using each of these test facilities are described in this section.

1.3.1 Air enthalpy test facility

The air enthalpy test facility is shown in Fig. 1.3-1. It comprises an indoor room in which an indoor unit is installed, and an outdoor room in which the outdoor unit is installed. Condition generators are installed in both rooms to control the temperature and humidity to the predetermined levels. The primary feature of this test facility is its ability to measure directly the air-conditioning load by determining the temperature, humidity, and air volume to describe the air conditions. Because the measurement of air volume is difficult, the test results obtained using the air enthalpy facility have been traditionally slightly less accurate than those obtained in the balanced test facility, despite the fact that the former approach has been recently improved to achieve near parity with the latter.

Notably, when analyzing the dynamic performance of an air-conditioning system using the air enthalpy test facility, the performance will differ according to the specific parameters of the facility unless a method is introduced to provide the same "building-side air conditions" regardless of the specific facility employed.

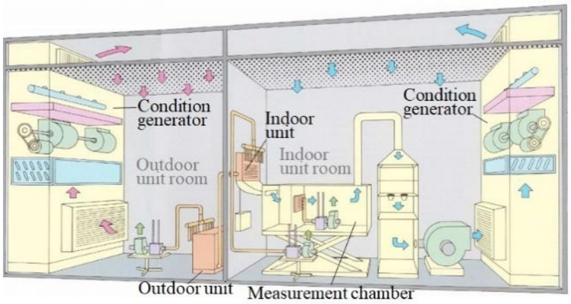

Fig. 1.3-1 Air enthalpy test facility[12)]

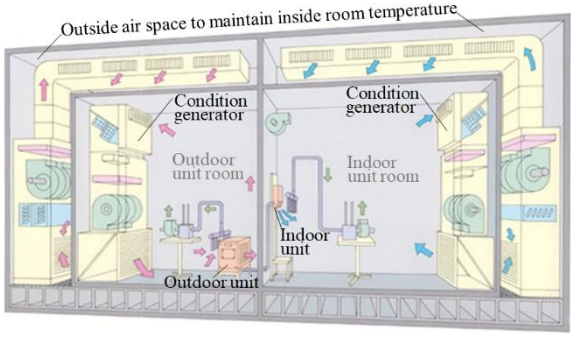

Fig. 1.3-2 Balance test facility[12)]

1.3.2 Balance test facility

Fig. 1.3-2 shows the balance test facility used; it comprises an indoor and outdoor unit room, each of which is equipped with a condition generator to provide a constant room temperature and humidity. A notable feature of this facility is that it enables the measurement of the building load using a condition generator installed in the indoor unit room. If the load is steady, this value is equal to the air-conditioning load, thereby allowing the air-conditioning load to be measured indirectly. The balance between the air-conditioning and building loads justifies the descriptive term “balanced” used for this facility. In addition, a space is provided outside both rooms to prevent heat from leaking through the room walls, thus helping to maintain them at a temperature consistent with the air inside. However, unless measures are taken to ensure that the “building-side air conditions,” which affect changes in the temperature and humidity of the indoor air, are the same even in different test facilities, the performance of the evaluated air conditioner will differ depending on the test equipment employed. This issue is similar to that of the air-enthalpy test facility.

1.4 Proposed dynamic performance test facility

A new emulator-based dynamic performance test facility was developed to address the problems associated with the conventional air-enthalpy and balance test facilities described above.

1.4.1 Basic concept of evaluation equipment

Fig. 1.4-1 illustrates the basic concept underlying the dynamic performance test facility; Fig. 1.4-2 depicts the control system when the air conditioning equipment is dynamically driven by the test equipment. As previously mentioned, the “building-side air conditions,” shown within the red frame, exert considerable influence on the dynamic performance of an air conditioner; thus, different dynamic driving performances will yield different results.

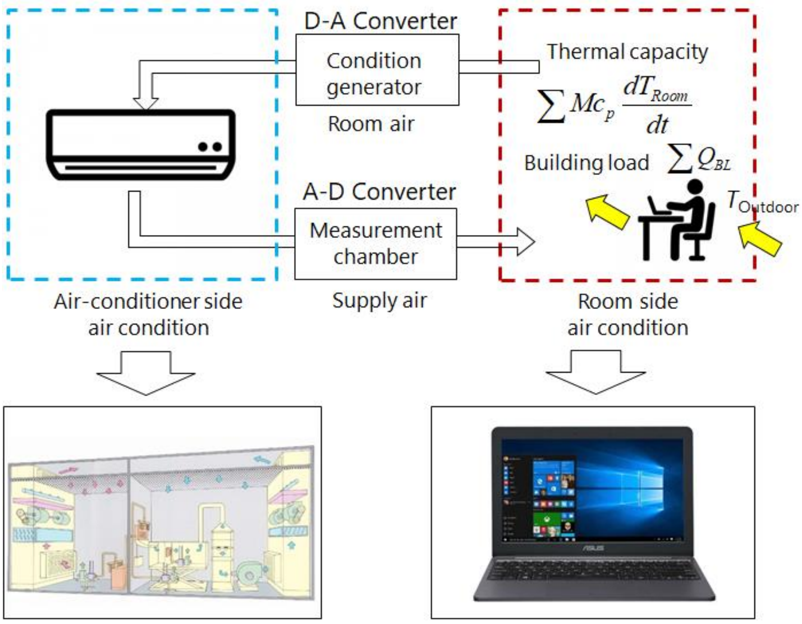

Fig. 1.4-1 Dynamic performance test method for air conditioners

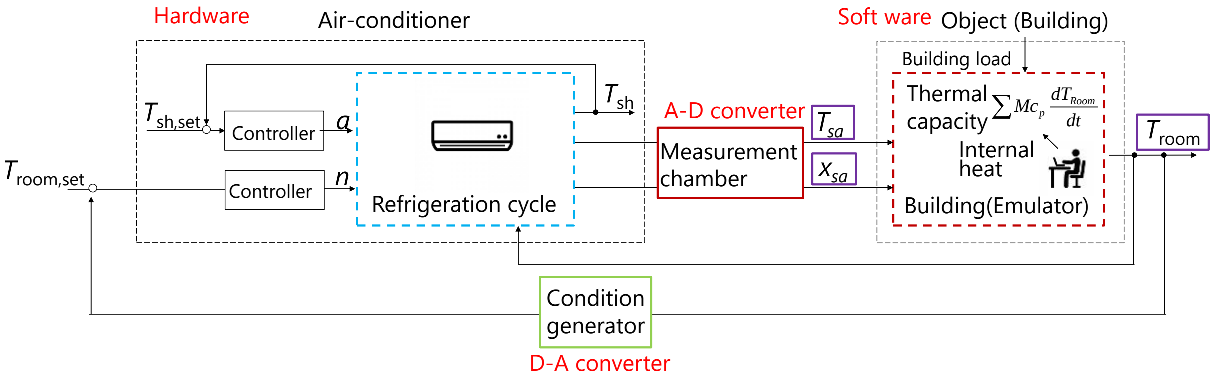

Fig. 1.4-2 Air-conditioner control system considering dynamic conditions

Many factors influence the performance of an air-conditioning system in dynamic operation, such as the walls of the test facility, heat capacity of the installed measurement equipment, and the size of the test equipment; it is impossible to ensure that these hardware conditions are the same in every facility. Therefore, we devised a new test method capable of compensating for the differences owing to the test facility and equipment by virtually deriving the “building-side air conditions” using computer simulations. As it remains necessary to measure directly the load and power consumption of the air-conditioning system, it is physically installed in the test facility and actual measurements are collected, while emulation software virtually calculates the built-in “building-side air conditions.” The “equipment-side air conditions” are then provided in the actual indoor air by the condition generator based on the indoor air conditions calculated by the emulator. The blown air generated by the air-conditioner is measured in the measurement chamber and sent to the emulator as a digital signal.

In this test system, the condition generator and measurement chamber should not be considered as devices that generate loads and measure performance, but rather as devices that play the role of digital-to-analog or analog-to-digital converters mediating between the emulator and performance evaluation device.

The most beneficial feature of the proposed dynamic performance test method is that the test facility can be used as-is when it is based on air enthalpy; balance test-based facilities can be used by introducing a measurement chamber. In addition, by changing the mathematical model employed as the emulator, both the static and dynamic characteristics can be evaluated in various conditions.

Indeed, the proposed method enables the use of conventional test equipment and can also be readily employed to evaluate product development standards by unifying the emulator's architecture for example. In addition, by creating an emulator that reproduces the conditions in an actual building, air-conditioner performance can be quantified in realistic operating conditions. This makes it possible to analyze the actual operating performance of air conditioners in different countries by accounting for their specific building and weather conditions. Thus, the same testing equipment can be used to evaluate everything from product development standards to the dynamic performance required by users in actual operations, thus realizing a unified test facility.

1.4.2 Configuration of the dynamic performance test facility

The evaluation system employed in the proposed dynamic test facility is configured as shown in Fig. 1.4-3. The hardware comprises a test facility and an emulator installed on a computer to calculate the building-side air conditions, which are then physically generated by the condition generator. The air blown by the air conditioner is subsequently measured in the measurement chamber and sent to the emulator as a digital signal.

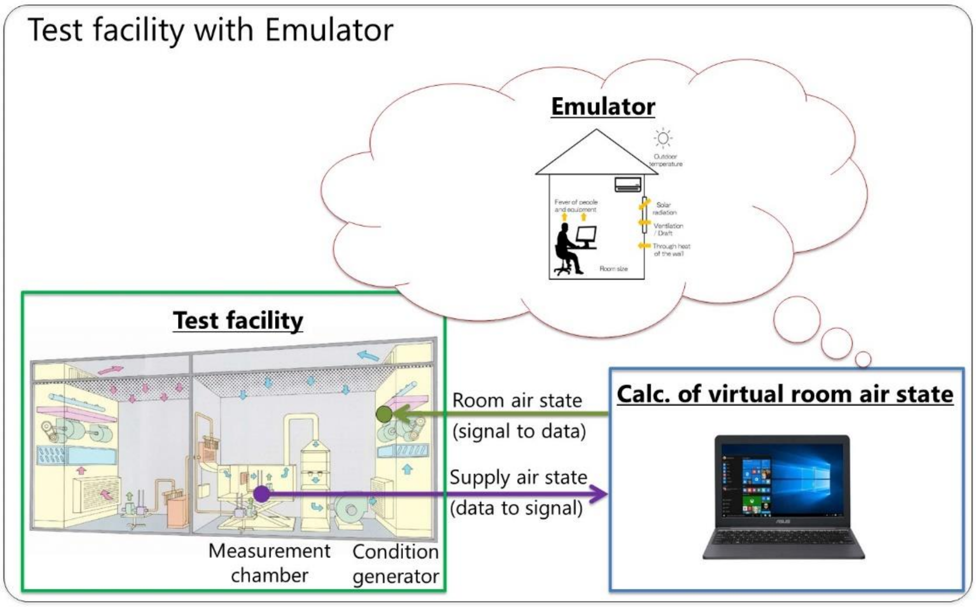

Fig. 1.4-3 Proposed hybrid dynamic test facility

1.4.3 Specifications of the dynamic performance test facility

Table 1.4-1 provides the specifications of the proposed dynamic performance test facility, Fig. 1.4-4 shows an external view of the facility, and Fig. 1.4-5 shows the measurement chamber in the indoor unit room. Figs. 1.4-6 and 1.4-7 respectively depict the airflow diagrams in the indoor and outdoor unit rooms.

Table 1.4-1 Specification listings of the hybrid dynamic test facility

Measurable capacity range	Up to 5 HP (14 kW)
Settable outdoor temperature range	-7−46 °C
Explosion-proof	Included
Crosswind speed	0.2 ± 0.1 m/s (JIS testing of showcases)
Size	7 m (D) × 8 m (W) × 3 m (H)

The proposed facility has an explosion-proof structure to enable its use with combustible refrigerants, which are candidates for next-generation, low-GWP refrigerants. Furthermore, as the proposed facility can also test refrigerated display cabinets, a crosswind condition of 0.2 ± 0.1 m/s can be created in accordance with the test standards in JIS B 8631-2:2011.

As shown in Fig. 1.4-6, the blown air from the indoor unit is first sent to the temperature/humidity measurement device through the measurement chamber and then directly to the air-volume measurement device installed on the ceiling. The air is pulled by a suction fan to cancel out the pressure loss generated in the duct between the two devices. Air-volume measurements are performed by combining four nozzles according to the air volume. These measured blowing conditions are then sent to the emulator. After passing through the airflow measurement device, the air is blown from the ceiling back into the indoor unit room where it is sucked into the condition generator. There, the indoor air is generated at the predetermined temperature and humidity according to the instructions from the emulator. This air is passed through the ceiling duct and evenly blown laterally from the wall through perforated metal.

As shown in Fig. 1.4-7, the outdoor unit room is equipped with a measurement chamber, which is uncommon. Air blown from the outdoor unit is released into the measurement chamber, where a temperature/humidity measurement device is installed and the air volume is measured using a stationary composite pitot tube. The condition signals from the emulator are then applied in the condition generator to achieve the specified temperature and humidity, and the conditioned air is returned to the outdoor unit.

Fig. 1.4-4 Overall appearance of test facility

Fig. 1.4-5 Appearance of measurement chamber

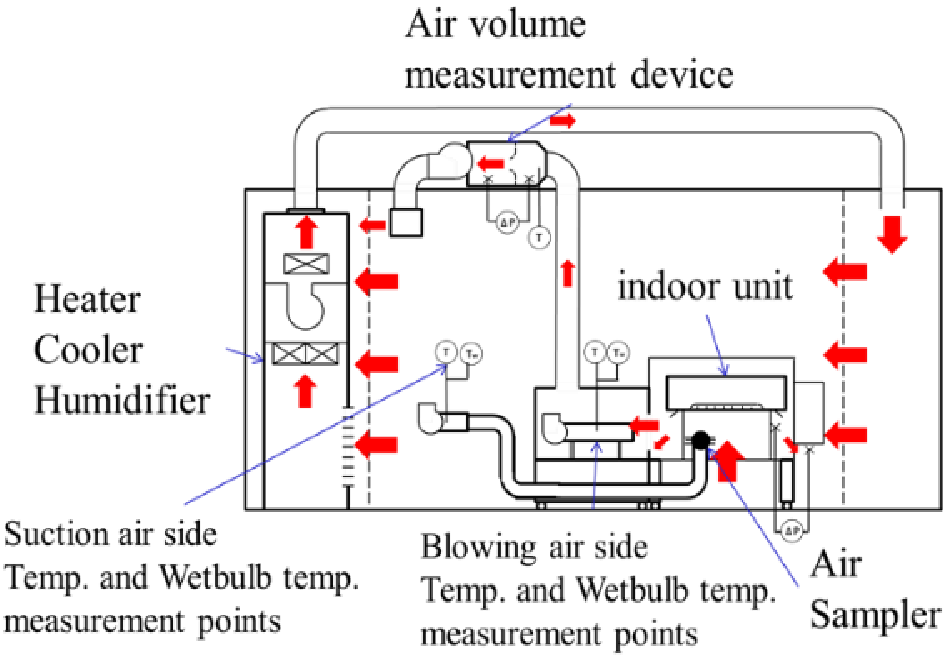

Fig. 1.4-6 Air-flow diagram of the indoor unit room

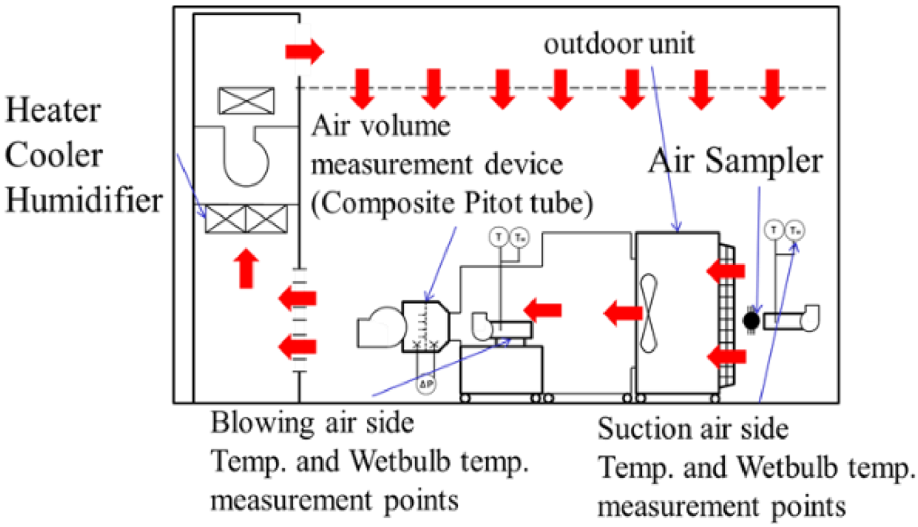

Fig. 1.4-7 Air-flow diagram of the outdoor unit room

1.4.4 Emulator

1.4.4.1 Standard emulator

As shown in Figs. 1.4-8 and 1.4-9, we developed emulator software capable of arbitrarily setting conditions, such as building load and heat capacity, which determine the building-side air conditions. To provide an example, a simple standard emulator, used to reflect test standards, and a room emulator, reflecting the conditions in a real building, were developed. These are described in this section.

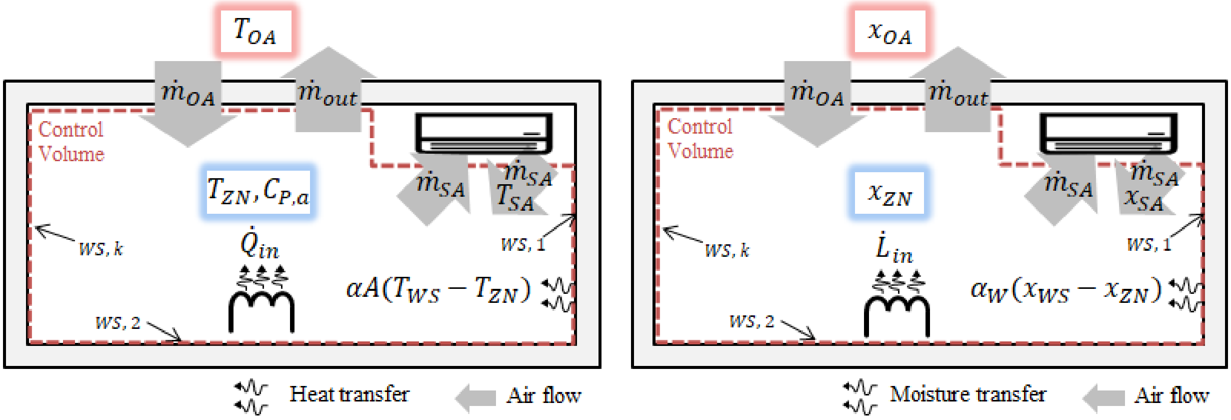

Fig. 1.4-8 Mathematical model for room's (i) heat transfer and (ii) moisture transfer

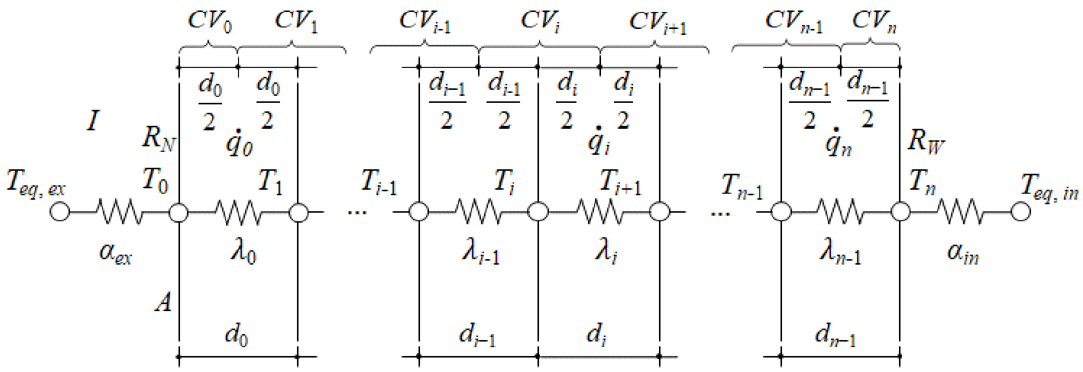

Fig. 1.4-9 Mathematical model for room wall

The standard emulator comprises a continuous single-capacity system and an energy equation, as follows

$$\dot{m}_{out} = \dot{m}_{OA} + \dot{m}_{human} \tag{1.4-1}$$

$$M_{Room}\frac{dx_{Room}}{dt} = \dot{m}_{human} \tag{1.4-2}$$

$$M_{House}c_{p,a}\frac{dT_{Room}}{dt} = \dot{Q}_{BL} - \dot{Q}_{AC} \tag{1.4-3}$$

$$\dot{Q}_{BL} = f(T_{ex}) \tag{1.4-4}$$

where M_{House} is the mass of both the indoor air and furniture. Note that the empirical value of the heat capacity of a building considering M_{House} is approximately ten times the heat capacity of the indoor air.

1.4.4.2 Room emulator

The mathematical model of the room emulator consists of the continuity equation for indoor air, energy equation, and wall heat transfer equation.

The indoor air continuity equation is expressed by the mass balance equation in which the air inflow and outflow across the boundary of the control volume shown in Fig. 1.4-9 are equal,

$$\dot{m}_{out} = \dot{m}_{OA} + \dot{L}_{in} \tag{1.4-5}$$

and the mass balance equation for moisture contained in the air is as follows,

$$M_{ZN}\frac{dx_{ZN}}{dt} = \sum_k j_{w,k}A_k\left(x_{WS,k} - x_{ZN}\right) - \dot{m}_{out}x_{ZN} + \dot{m}_{OA}x_{OA} + \dot{m}_{SA}(x_{SA} - x_{ZN}) + \dot{L}_{in}$$

(1.4-6)

where

$$M_{ZN} = \rho_{w,ZN} V_{ZN} + M_{FN} \tag{1.4-7}$$

The moisture that flows across the boundary in Fig. 1.4-13 consists of the following four components included in Equation 1.4-6:

i) Moisture transmitted from the wall (the first term on the right side)
ii) Moisture flowing in and out of the system through the ventilation system (second and third items on the right side)
iii) Moisture flowing in and out across the system through equipment, such as refrigerators and air conditioners (fourth item on the right side)
iv) Moisture that dissolves in the air when generated by the human body (perspiration) or humidifier systems (the fifth term on the right side)

In addition, if moisture flows in and out of the system owing to indoor air circulation, etc., it is added to Equation 1.4-6. Equation 1.4-7 shows the mass as the indoor moisture capacity, which is the sum of the moisture content of the indoor air and the moisture capacity of the walls and furniture. The customary value of M_{FN} has been reported to be approximately equal to 16.7 kg per m^3 of room volume [13].

The energy equation for the indoor air is then given by

$$C_{ZN} \frac{dT_{ZN}}{dt} = \sum_k \alpha_{a,k} A_k \left(T_{WS,k} - T_{ZN}\right) - c_{P,a} \dot{m}_{out} T_{ZN} + c_{P,a} \dot{m}_{OA} T_{OA} + c_{P,a} \dot{m}_{SA} (T_{SA} - T_{ZN}) + \dot{Q}_{in} \tag{1.4-8}$$

$$C_{ZN} = c_{P,ZN} \rho_{a,ZN} V_{ZN} + C_{FN} \tag{1.4-9}$$

In Equation 1.4-8, the following physical phenomena are calculated by assuming a real building, as shown in Fig. 1.4-13:

i) The heat transfer from the wall is attributed to the difference between the wall surface and indoor temperatures (first term on the right side); when heat transfer occurs across the wall, the indoor air temperature changes as the wall temperature increases

ii) Energy flows in and out of the system through ventilation (second and third terms on the right side),

iii) Moisture flowing in and out across the system through equipment, such as refrigerators and air conditioners (the fourth term on the right side)

iv) Sensible heat and latent heat owing to internal heat generation, such as from humans, lighting, and equipment (the fifth term on the right side)

Equation 1.4-9 expresses the heat capacity as a lumped constant for both air and furniture. The customary value of C_{FN} has been reported to be approximately equal to 15.2 kJK^{-1} per m^3 of the room volume for offices[14]. If there is energy flowing in and out of the system owing to indoor air circulation, it should be added to Equation 1.4-8.

The equation for heat transfer in a multilayer wall can be expressed as follows:

When $1 \le i \le n-1$

$$C_{CV,i} \frac{1}{A} \frac{dT_i}{dt} = \lambda_{i-1} \frac{T_{i-1} - T_i}{d_{i-1}} + \lambda_i \frac{T_{i+1} - T_i}{d_i} \tag{1.4-10}$$

When $i = 0$

$$\left(c_{P,0} \rho_0 \frac{d_0}{2}\right) \frac{dT_0}{dt} = \alpha_{ex} \left(T_{eq,ex} - T_0\right) + \lambda_0 \frac{T_1 - T_0}{d_0} \tag{1.4-11}$$

When $i = n$

$$\left(c_{n-1} \rho_{n-1} \frac{d_{n-1}}{2}\right) \frac{dT_n}{dt} = \lambda_{n-1} \frac{T_{n-1} - T_i}{d_{n-1}} + \alpha_{in} \left(T_{eq,in} - T_n\right) \tag{1.4-12}$$

As shown in Fig. 1.4-14, Equation 1.4-10 is the energy equation for the *i*th and i + 1 wall materials counted from the outside air side of a multilayer wall; Equations 1.4-11 and 1.4-12 are the energy equations for the outside air and wall material adjacent to the room, respectively. In this model, the control volume is considered as a single-mass point system straddling two adjacent wall materials, and the heat capacity of the wall in each system is given by

$$C_{CV,i} = \frac{1}{2}A\left(c_{p,i-1}\rho_{i-1}d_{i-1} + c_{p,i}\rho_i d_i\right) \tag{1.4-13}$$

To predict the temperature fluctuations inside the wall, the thermal conditions must be determined on both sides of the wall. The heat flow on the wall surface is affected by the air temperature near the surface and the average radiation temperature from the objects surrounding the wall surface. The values of $T_{eq,ex}$ in Equation 1.4-11 and $T_{eq,in}$ in Equation 1.4-12 can be expressed using the concept of equivalent temperature. The heat transfer balance around the wall surface on the outside air side can be expressed using the equivalent temperature on the outside air side as follows,

$$\alpha_{ex}\left(T_{eq,ex} - T_0\right) = \alpha_{ex}(T_{ex} - T_0) + a_s I - \varepsilon F_{sky}E_{ex,N} \qquad 1.4\text{-}14)$$

where the heat transfer owing to the difference between the equivalent temperature $T_{eq,ex}$ on the outside air side and the wall surface temperature T_0 is given by the convective heat transfer owing to the difference between the outside air temperature T_{ex} and T_0 (first term on the right side), the solar radiation near the wall surface (second term), and the radiant heat (the third term on the right side).

The heat transfer balance around the wall surface on the inside air side is given by

$$\alpha_{in}\left(T_{eq,in} - T_{WS}\right) = \alpha_{in,c}(T_{ZN} - T_{WS}) \quad + \alpha_{in,r}\left(\sum \phi_i T_{WS,i} - T_{WS}\right) + R_{in}R_r\dot{Q}_{in} \tag{1.4-15}$$

where the heat transfer owing to the difference between the equivalent temperature $T_{eq,in}$ inside the room and the wall surface temperature T_{WS} is expressed as the convective heat transfer owing to the difference between the room temperature T_{ZN} and T_{WS} (first term on the right side), radiant heat from other walls (second term on the right side), and the radiant heat emitted by indoor equipment (the third term on the right side). The heat received by the indoor wall is summarized in the form of heat transfer using the room equivalent temperature $T_{eq,in}$, as shown on the left side. Furthermore, ϕ_i in the second term is the absorption coefficient proposed by Gebhart[15)] on the *i*th wall surface. Finally, and $\alpha_{in,c}$ is the same as $\alpha_{a,k}$ in Equation 4.1.1-8; then, α_{in} = $\alpha_{in,c}$ + $\alpha_{in,r}$, and α_{in} and α_{ex} are the sums of the convective heat and the radiative heat transfer coefficients, respectively, known as the total heat transfer coefficients.

The validity of the proposed models was verified using the BEST TEST [16), 17), 18), 19)]. Critically, these models should be understood as simple examples; the greatest advantage to the proposed dynamic performance test method is that the emulation model can be freely changed as required.

2. Soundness evaluation of test facility

2.1 Soundness evaluation of dynamic performance test facility

In this section, we confirm that the proposed dynamic performance test facility is capable of reflecting the operating performance of the test equipment with sufficient accuracy.

2.1.1 Static soundness (fixed compressor rotational speed test)

Methods had been previously established to evaluate the static soundness of performance test equipment. Therefore, we performed a static soundness evaluation using static tests in which the rotational speed of the compressor was fixed in adherence to the procedure adopted to obtain semi-accreditation provided by the Japan Air Conditioning and Refrigeration Research Institute (JATL); this Institute has the only air-conditioner test facility in Japan and provides the standards for air conditioner test equipment.

The semi-accreditation provided by JATL requires that tests be performed on two air-conditioner models with different capacities and that the measurement results are within 3% of the data measured by JATL in all required test conditions. Therefore, we prepared two models—machines with rated powers at 5 horsepower (hp) and 3 hp—and tested them using the standard cooling, standard heating, and heating low-temperature tests, as specified in JIS B8615. These test conditions are summarized in Table 2.1-1.

Table 2.1.1 Test conditions for validation

Test	Indoor temperature dry/wet °C	Outdoor temperature dry/wet °C	Partial-load ratio %
Standard cooling test	27 / 19	35 /24	100
Standard heating test	20 / 15	7 / 26	100
Low-temperature heating test	20 / 15	2 / 1	100

Figs. 2.1-1 and 2.1-2 show the results of the standard cooling and heating tests, respectively, which were operated continuously. In these tests, the average value of the data acquired over a 35 min period after reaching a sufficiently stable state was reported. The results of the low-temperature heating test, shown in Fig. 2.1-3, depict the average value acquired over three cycles, as the compressor and air volume were stopped periodically to perform the defrosting operation. The results of all tests indicated that the cooling capacity and power consumption were statically measured within 3% of the data reported by JATL; therefore, our facility acquired semicertification on October 1, 2020. As a result, it was confirmed that the proposed test facility can determine the performance of air-conditioning equipment with the same high accuracy as that required for the equipment certification process.

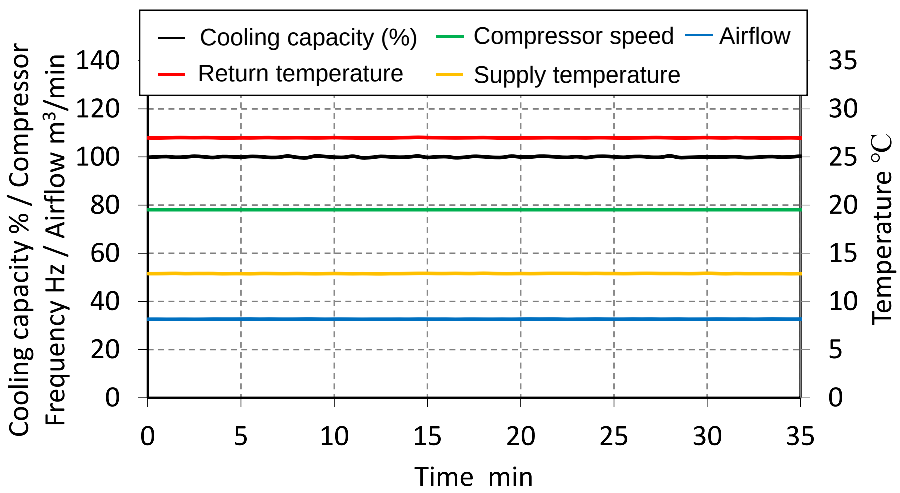

Fig. 2.1-1 Results of Japanese Industrial Standards (JIS) test (Cooling standard test)

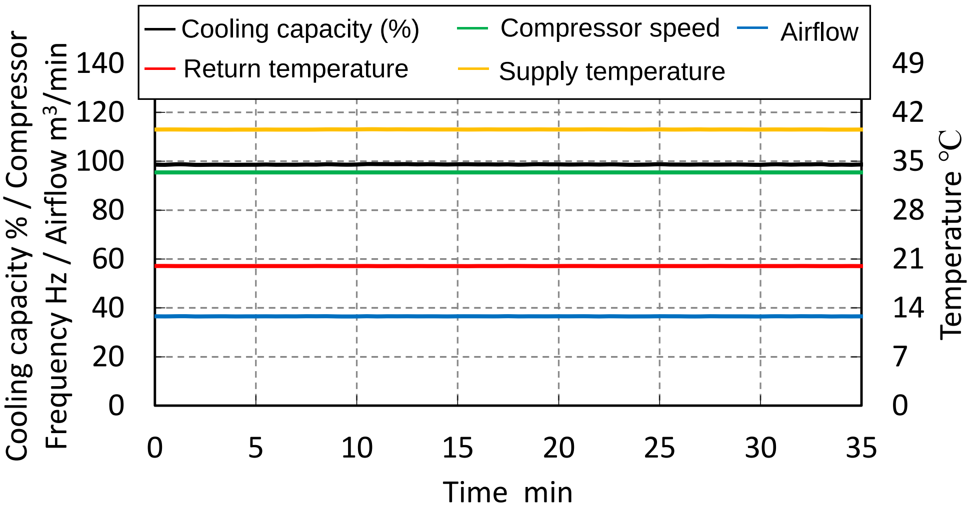

Fig. 2.1-2 Results of JIS test (Heating standard test)

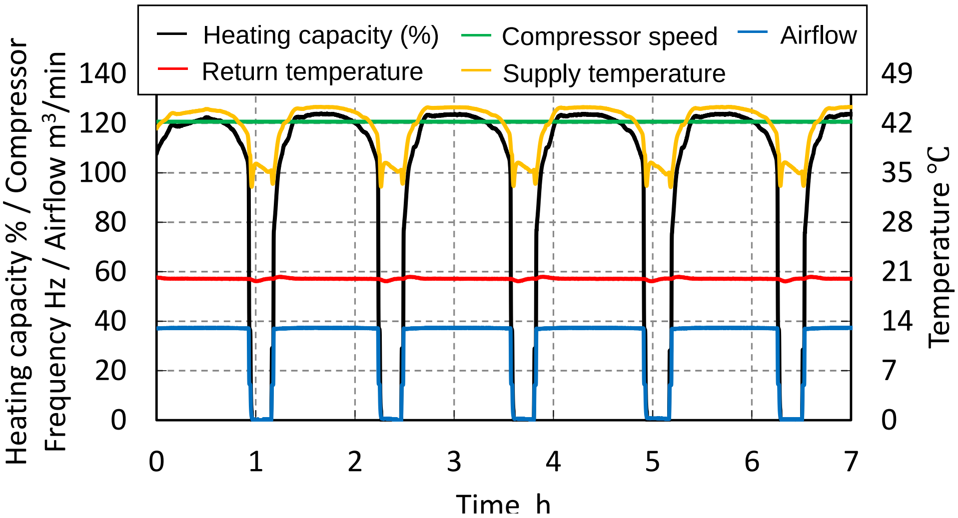

Fig. 2.1-3 Results of JIS test (Heating low temperature test)

2.1.2 Dynamic soundness

The dynamic soundness of the test equipment was evaluated before conducting the dynamic performance tests in this study. As shown in Fig. 1.4-2, the test equipment factors evaluated were those that affected the indoor air temperature control of the building, as follows:

i) Emulator calculation time lag

ii) Temperature and humidity followability in the condition generator

iii) Time delays of various sensors

This evaluation was based on a unit with a rated power of 10 kW, which is the standard installation size for this test equipment. The standard installation space for the equipment was 147 m^3. The thermal and material time constants (obtained by dividing the mass by the air-conditioner volume derived from the standard blowing air volume in the test room) used to evaluate soundness were approximately equal to 5000 and 500 s, respectively.

2.1.2.1 Emulator calculation time lag

The emulator used to calculate the building air conditions in this study employed a discretized nonlinear equation to perform a dynamic analysis on a first-order forward difference equation. In these conditions, the calculation for a 1 s step was completed in approximately 0.5 s on a standard personal computer; this indicates that the delay in calculation time will not affect the dynamic performance of the test facility.

2.1.2.2 Temperature and humidity followability in the condition generator

The condition generator must be able to generate the desired air conditions according to the signal provided by the emulator. Therefore, we investigated the ability of the condition generator to follow periodic fluctuations during an 1 h period (e.g., during start-up or intermittent operation when the operating conditions change most suddenly within a 0.5–1 h period). Table 2.1-2 lists the test conditions.

Table 2.1-2 Followability test conditions

Test mode	Indoor unit Set room temperature		Outdoor unit Set room temperature	
	Dry (°C)	Wet (°C)	Dry (°C)	Wet (°C)
Start-up in cooling	35 →27	24 →19	35 constant	24 constant
Start-up in heating	7 →20	6 →15	7 constant	6 constant
Cyclic cooling	27 ↔26	26 ↔23.5	35 constant	24 constant

The followability test results are reported in Figs. 2.1-4, 2.1-5, and 2.1-6.

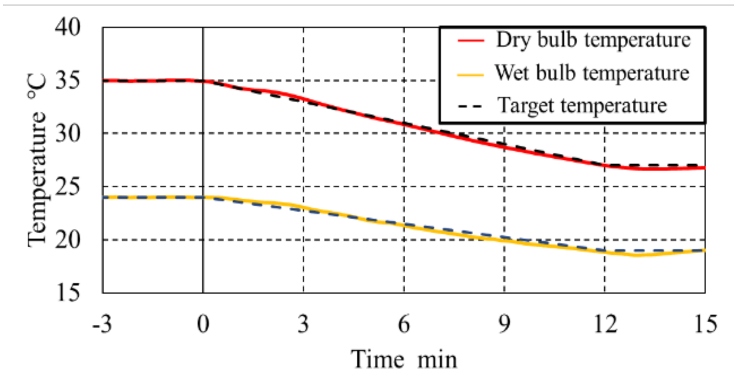

(i) Indoor unit psychrometric room

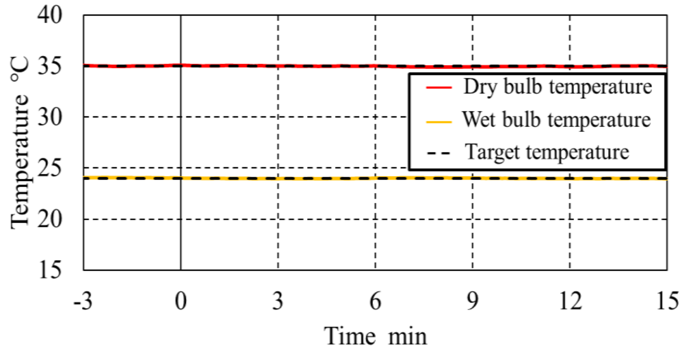

(ii) Outdoor unit psychrometric room

Fig. 2.1-4 Temperature controllability in cooling start-up mode

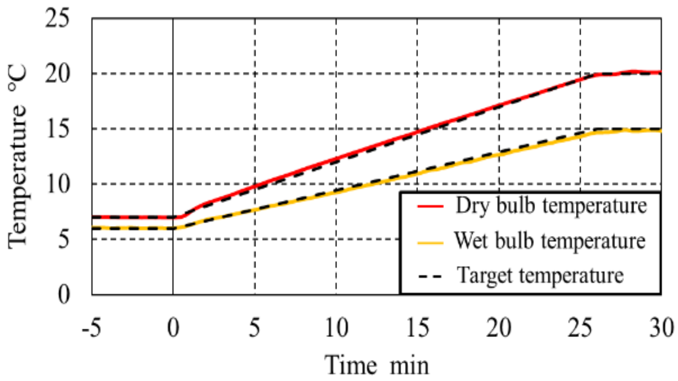

(i) Indoor unit psychrometric room

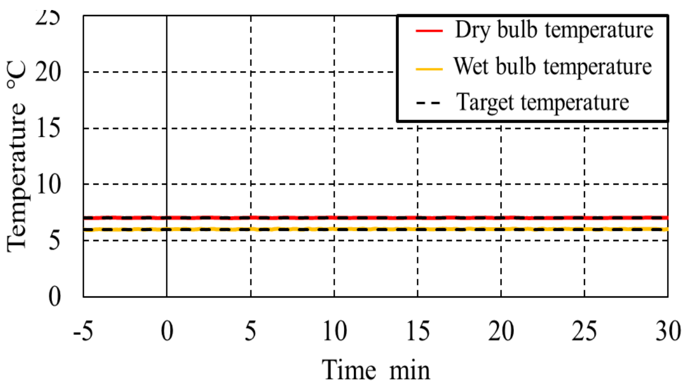

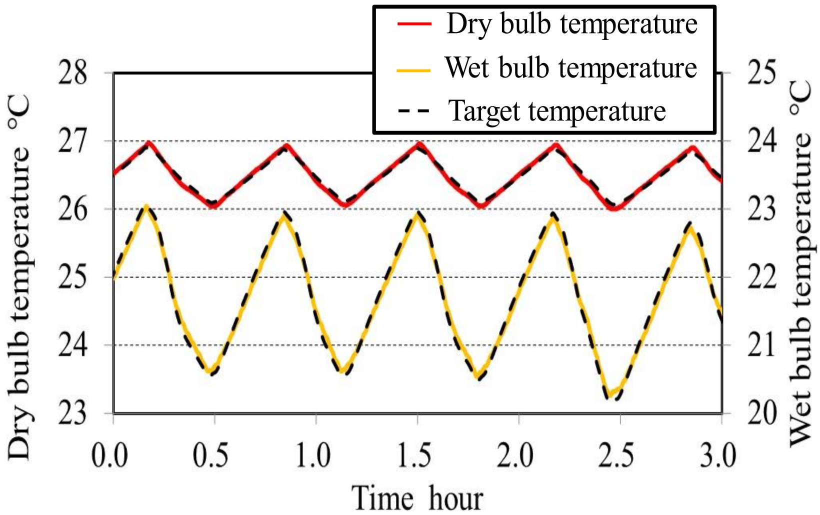

Fig. 2.1-6 Temperature followability in intermittent driving

As shown for the cooling operation in Fig. 2.1-4, the dry-bulb and wet-bulb temperatures in the indoor unit room rapidly changed within approximately 12 min, thus indicating that the indoor unit would start cooling. The dry-bulb and wet-bulb temperature signals provided by the emulator (shown by the dashed lines), and the corresponding conditions of the air generated by the condition generator, shown by the solid lines, are in near agreement with a delay of only approximately 20 s. In addition, in the outdoor unit room, the heat generated from the outdoor unit was canceled, and the dry-bulb and wet-bulb temperatures were kept constant according to the signal provided by the emulator.

Similarly, during the heating operation shown in Fig. 2.1-5, the temperature required by the emulator remained unchanged in both the indoor and outdoor unit rooms, even when the temperature in the indoor unit room changed suddenly within approximately 25 min, thus indicating that heating would be started. The condition generator was able to follow the humidity signal with a delay of approximately 20 s.

Finally, as shown in Fig. 2.1-6, even when the dry-bulb and wet-bulb temperatures changed rapidly, such as during intermittent operations, the signal provided by the emulator normally increased or decreased within approximately 30 s. Indeed, the emulator was able to respond with a maximum delay of approximately 54 s at sudden change instants. These values were approximately equal to 0.6% of the room's time constant.

2.1.2.3 Time delay of various sensors

The test facility was equipped with multiple sensors, including thermometers and hygrometers, with measurement delays < 10 s.

2.1.2.4 Summary

The evaluated air-conditioning unit was subject to (1) a delay in the intake air temperature/humidity sensor (maximum of ~10 s), (2) a delay in the passage of discharged air through the measurement chamber (maximum of ~ 15 s for humidity only), and (3) a temperature difference in the discharged air with a delay in the temperature/humidity sensor measurement (maximum of 10 s), and (4) a delay in the condition generator response (~20 s), totaling a maximum of 55 s. Thus, the total temperature delay of the test equipment was approximately 1% of the thermal time constant of the room (5000 s); the total humidity delay was approximately 10% of the material time constant (500 s). Considering that the static accuracy can be compensated for by the verification test and that the period of intermittent operation in which the operating condition of the equipment suddenly changes is ~30 min to 1 h, it is possible that the dynamic performance of the proposed test facility will depend on the test time. Therefore, we planned to conduct a round-robin test in multiple laboratories to confirm the results reported in this study.

2.2 Verification of the validity of the performance evaluation facility

One of the features of the performance evaluation system developed in this study is that it uses a room emulator to emulate the air-conditioning load of a building and evaluate the dynamic performance of the air conditioner. Therefore, we conducted a test using a room emulator at a third-party organization to verify its validity. Fig. 2.2-1 shows the external and elevation views of the performance evaluation facility of Chubu Electric Power Co., Ltd. where the test was conducted. This figure shows that Chubu Electric Power's equipment is large and was made mainly for testing commercial air conditioners rated at 20–30 hp. In the

2020 academic year, we used a 5 hp R32 refrigerant package air conditioner (ceiling cassette type) owned by Chubu Electric Power Co., Ltd., which we also borrowed and tested.

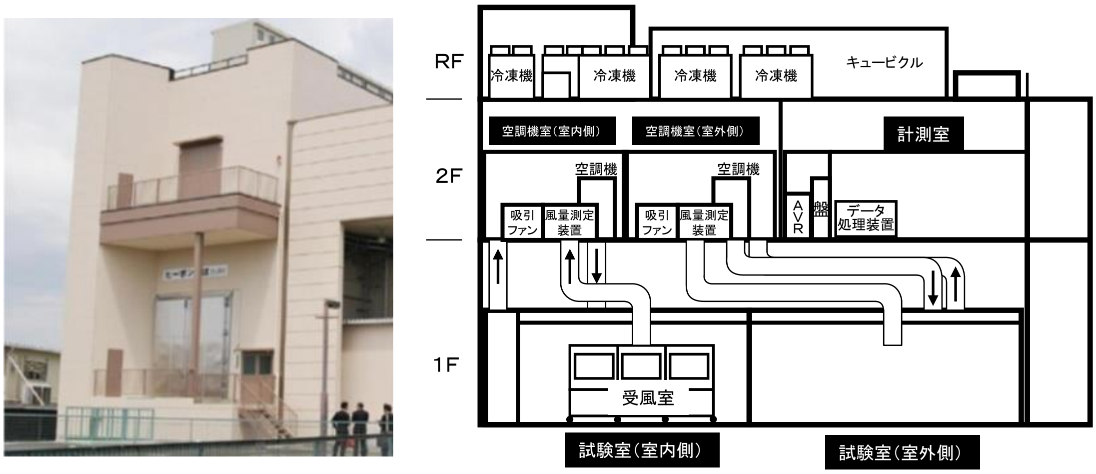

Fig. 2.2-1 Photograph and elevation view of CEPCO's performance evaluation equipment

a) Test results at fixed compressor speed

Figs. 2.2-2–4 show the compressor's test at a fixed rotational speed test performed by Chubu Electric Power Co., Inc. and the University's performance evaluation facility. Fig. 2.2-2 shows the rated cooling standard test (outside temperature 35 °C, load factor 100%). Fig. 2.2-3 is the intermediate cooling standard test (outside temperature 29 °C, load factor 50%). Fig. 2.2-4 is the rated heating standard test (outside temperature 7 °C, load factor 100%). The figure on the left is the result of Chubu Electric Power; and the figure on the right is the result of the performance evaluation facility of the University.

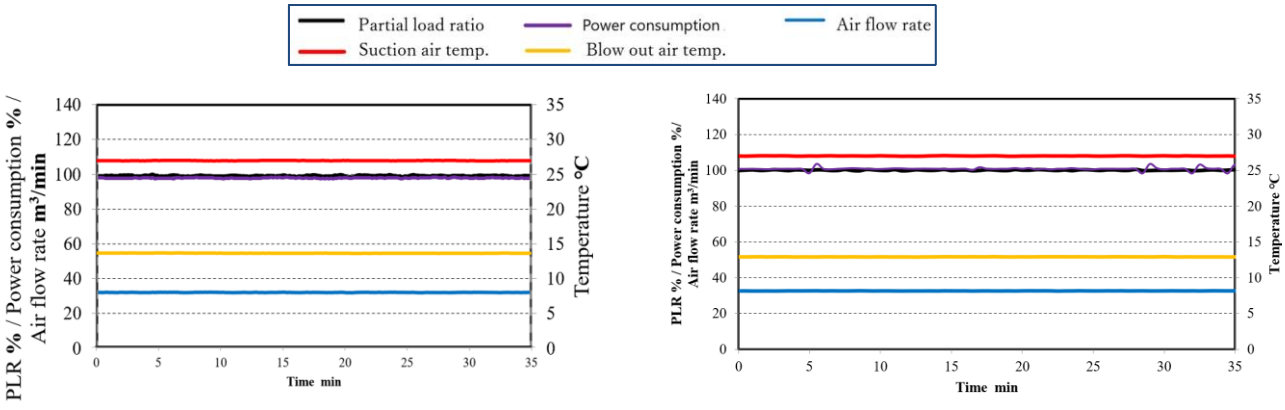

Fig. 2.2-2 Rated cooling standard test

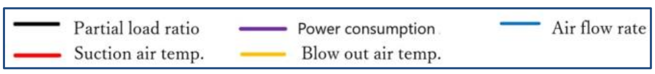

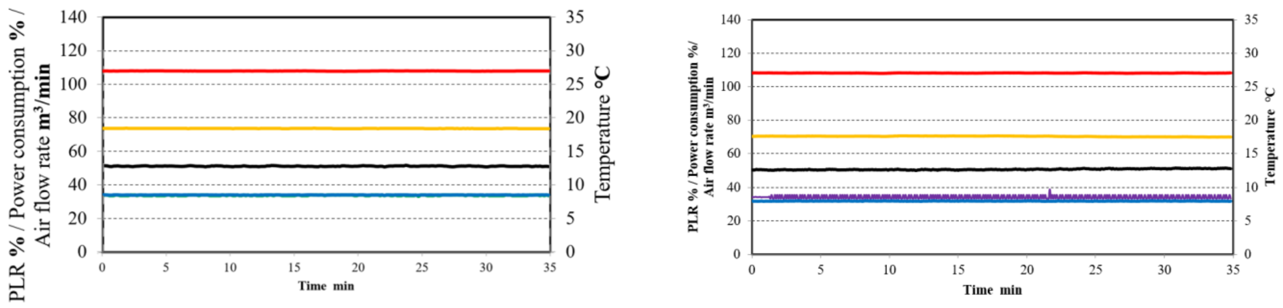

Fig. 2.2-3 Intermediate cooling standard test

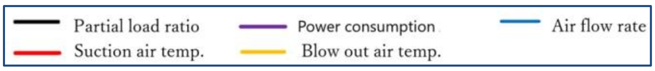

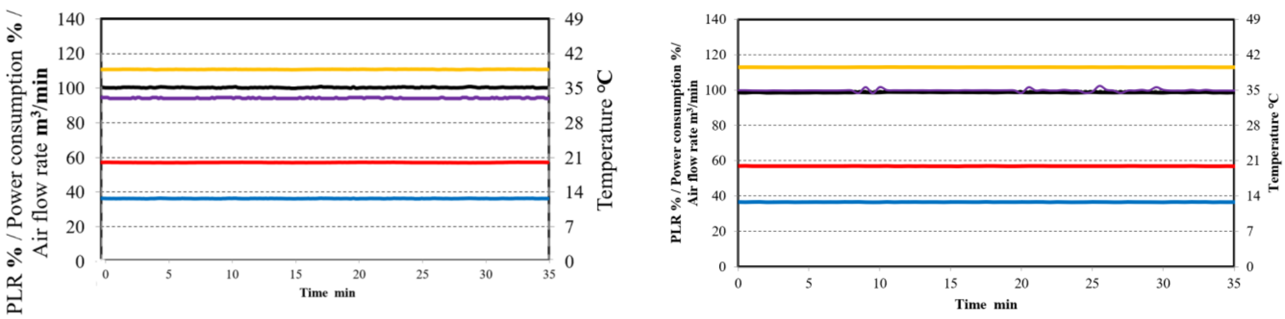

Fig. 2.2-4 Rated heating standard test

Table 2.2-1 shows the coefficient of performance (COP) results of the compressor test at a fixed rotational speed. In tests at a fixed rotational speed, the test results of Chubu Electric Power and Waseda University almost matched.

Table 2.2-1 Coefficient of performance (COP) test results at a fixed compressor rotational speed

	CEPCO	Waseda University
Rated cooling standard test	3.83	3.84
Intermediate cooling standard test	5.73	5.74
Rated heating standard test	4.52	4.45

b) Test results with variable compressor speed

Figs. 2.2-5–7 show the results of tests conducted by Chubu Electric Power Co., Inc., and the University's performance evaluation facility for variable compressor rotational speeds. Fig. 2.2-5 shows an outside cooling temperature of 29 °C, Fig. 2.2-6 shows the outside cooling temperature of 35 °C, and Fig. 2.2-7 shows the outside heating temperature of 7°C; in all cases, the load factor was 50%. The figure on the left shows the result of the test without the use of the emulator at Chubu Electric Power, the figure in the middle shows the result of the test using the emulator at Chubu Electric Power, and the figure on the right shows the result of the performance evaluation facility of the university. In the 2021 academic year, the test results obtained when the air conditioner was in continuous operation (steady operation state) were compared and verified at the university.

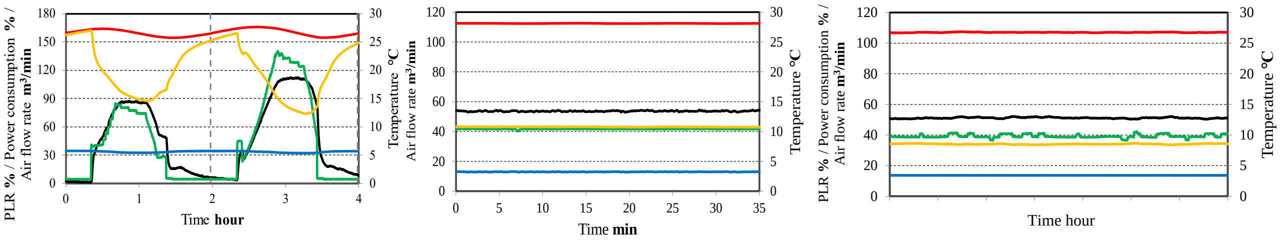

Fig. 2.2-5 Partial-load cooling performance test (29 °C,　50%)

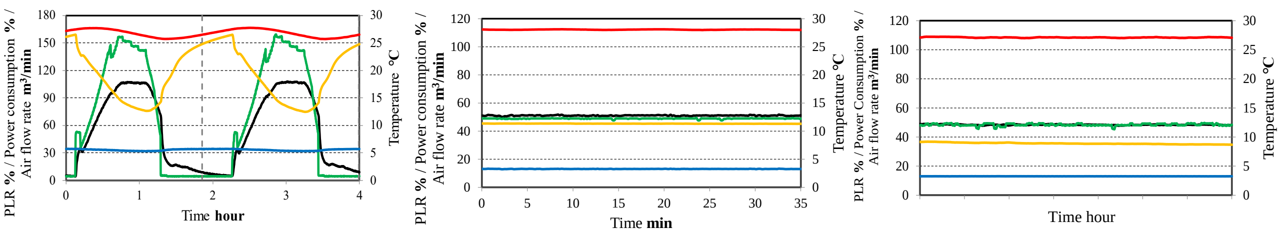

Fig. 2.2-6 Partial-load cooling performance test (35 °C,　50%)

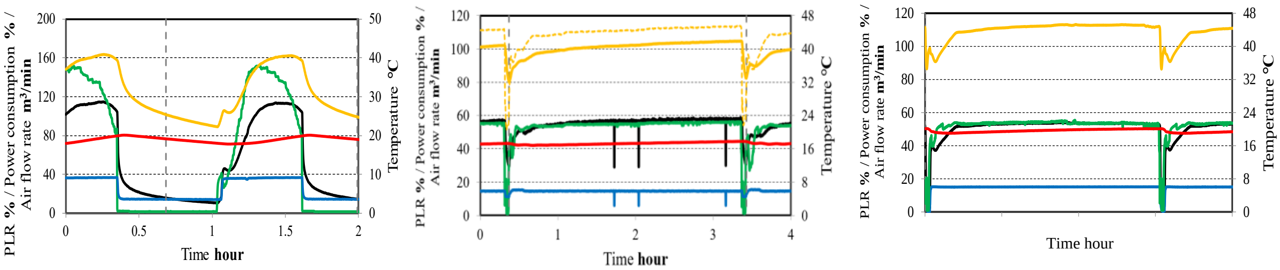

Fig. 2.2-7 Partial-load heating performance test (7 °C,　50%)

Table 2.2-2 shows the COP results of the variable compressor speed test. When Chubu Electric Power does not use an emulator, the tested air conditioners have a small capacity compared with the size of the system, thus resulting in unstable operations. The COP is smaller than that obtained using an emulator and the test results at the University. However, when the emulator was used with Chubu Electric Power's equipment, the behavior was like that during the test at the University, and the COP was similar to the test results at the University. From these results, it was found that the same behavior could be reproduced using the room emulator, even if the equipment was different.

Table 2.2-2 COP test results for variable compressor rotational speed

Partial-load performance test	CEPCO		Waseda University
	Without emulator	With emulator	Without emulator
Cooling (29 °C,　50%)	3.84	5.12	5.22
Cooling (35 °C,　50%)	3.20	4.15	4.00
Heating (7 °C,　50%)	3.73	4.43	4.04

c） Summary of test results

In the fixed-compressor rotational speed test, similar results were obtained even with different equipment types; therefore, reproducible tests were possible. However, in the variable compressor rotation speed test, it was found that reproducible testing was not possible because the operating conditions of the air conditioner changed depending on the device unless an emulator was used.

However, if the device is different, using the emulator yields almost the same results; this finding indicates that reproducible testing is possible. In the case in which the air conditioner was operated intermittently (unsteady operation state), we conducted a test using a room air-conditioner ventilation chamber in 2022.

3. Experimental evaluations of various air-conditioning equipment types

3.1 Background and purpose of the experiment

When introducing next-generation refrigerants into refrigerating and air-conditioning equipment, the safety and environmental GWP (direct impact) of the refrigerant used in the equipment and the impact on global warming owing to energy-derived CO_2 emissions (indirect impact) must be considered. Therefore, the actual operating performance of the refrigerant and air-conditioning equipment needs to be evaluated. To illustrate fully the potential of low-GWP refrigerants, an optimized air conditioning unit should be fabricated for each refrigerant and employed to conduct accurate performance tests in actual operating conditions. However, there are several next-generation refrigerant candidates; moreover, the corresponding financial and time costs required to produce a series of optimized air-conditioning units are unrealistic. Therefore, in this study, objective [3] ("Simulator development and utilization") was pursued to construct various simulators for heat exchangers and air-conditioning systems to shorten the period and cost required for system examination and production. Before using these simulators, the validity and accuracy of the calculated values employed in their construction must be verified. Therefore, the low-GWP refrigerants R290 and R454C were poured into the air conditioners (designed for use with the R22 refrigerant) and their performances were evaluated accordingly.

3.2 Overview of the air conditioner used in this experiment

3.2.1 Air conditioner used in this experiment

Table 3.2-1 provides the specifications of the air conditioner used in this experiment. Unless drop-in tests using R290 and R454C are performed in air conditioners intended for low-pressure refrigerants, such as R22, the results will be extremely poor. After consulting with air conditioner manufacturers, we determined that the production of R22 air conditioners was discontinued over a decade ago, and it was not possible to obtain new inventory. Therefore, we conducted this experiment using a second-hand, wall-mounted, room air conditioner using R22 with a rated capacity of 2.2 kW. Pressure sensors and thermocouples were installed in the air conditioner after the heat exchangers of the outdoor and indoor units were thoroughly cleaned. To measure the refrigerant flow rate, two Coriolis flowmeters were installed with valves on the lines so that they could be switched between cooling and heating. In addition, a tool was provided by the air conditioner manufacturer to enable free control of the compressor's speed, and another tool was installed to enable free adjustment of the expansion valve opening across 50 steps. Fig. 4.1.2-1 depicts the mounting positions of the pressure sensor, thermocouple, and refrigerant flowmeter; Fig. 4.1.2-2 shows the test setup in the dynamic performance evaluation facility.

Table 3.2-1 Specifications of the room air conditioner employed in this experiment

Parameter		Value
Type		Room air conditioner
Year of manufacture		2001
Original refrigerant		R22
Rated capacity (W)	Cooling	2200
	Heating	2500

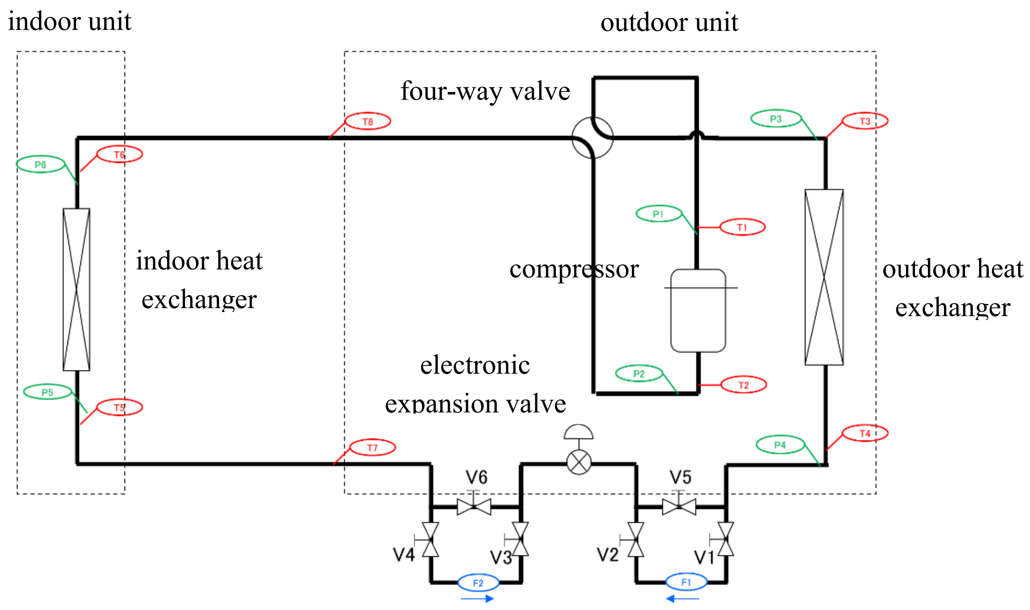

Fig. 3.2-1 Mounting locations of pressure sensors, thermocouples, and flowmeters

(a) Indoor unit

(b) Outdoor unit

Fig. 3.2-2 Test setup in the dynamic performance evaluation facility

3.2.3 Determination of refrigerant charge

The performance of the air conditioner must be evaluated after maximizing the potential of each refrigerant. Therefore, when R290 and R454C were dropped-in, the refrigerant charge was optimized (1) by fixing the compressor speed to the rated value for R22, and (2) the compressor's speed was fixed to achieve a capacity of 2.2 kW. These refrigerant charge optimization procedures are detailed as follows.

(1) Optimizing the refrigerant charge by fixing the compressor's rotational speed to the rated value for R22.

① Fix the compressor rotational speed of the test machine to the rated value for R22 (48 Hz); at this value, a capacity of 2 kW was achieved

② Set an initial low refrigerant charge

③ Increase the opening of the expansion valve such that the degree of superheating is 5 °C and the degree of supercooling is 5 °C

④ Measure the capacity of the air conditioner in cooling-rate test conditions.

⑤ If the degree of supercooling cannot be obtained, increase the refrigerant charge and return to ③.

Thus, the refrigerant charge was determined by measuring the degree of supercooling while gradually increasing the refrigerant charge. The final charges for R290 and R454C were determined to be 400 g and 730 g, respectively, and the cooling capacity was 1860 W for both; this corresponds to 84.5% of the rated capacity for R22 (2.2 kW) or 80% of the 2 kW capacity achieved at a compressor speed of 48 Hz.

(2) Optimizing the refrigerant charge by fixing the compressor's rotational speed to achieve a capacity of 2.2 kW:

⑥ Set an initial low refrigerant charge
⑦ Fix the maximum compressor's rotational speed of the test machine to achieve a 2.2 kW capacity
⑧ Adjust the opening of the expansion valve so that the degree of superheating is 5 °C and the degree of supercooling is 5 °C
⑨ Measure the capacity of the air conditioner in cooling-rate test conditions
⑩ a) If the degree of supercooling cannot be obtained or the capacity does not reach the target capacity, increase the refrigerant charge and return to ⑦
b) If the capacity exceeds the target capacity, reduce the compressor speed and return to ⑧

By adjusting the capacity and degree of supercooling while gradually increasing the refrigerant charge, the refrigerant charge was determined to be 400 g for R290 and 950 g for R454C compared with 910 g for R22.

3.2.4 Test conditions

Eight test conditions comprising four cooling conditions and four heating conditions were evaluated in accordance with the temperature conditions for the outdoor and indoor units provided by JIS C 9612:2013 [3] for room air conditioners. The specific temperature and load conditions are listed in Table 3.2-2.

Table 3.2-2 Test conditions

Test condition			Indoor temperature (°C) Dry/Wet	Outdoor temperature (°C) Dry/Wet	Partial load ratio (%)
①	Cooling	Standard cooling Full-capacity test	27/19	35/24	100
②		Standard cooling Half-capacity test		35/24	50
③		Low-temperature cooling Half-capacity test		29/19	50
④		Low-temperature cooling Minimum-capacity test		29/19	25
⑤	Heating	Standard heating Full-capacity test	20/15	7/6	100
⑥		Standard heating Half-capacity test		7/6	50
⑦		Standard heating Minimum capacity test		7/6	25
⑧		Low-temperature heating Full-capacity test		2/1	100

3.3 Test results and considerations

3.3.1 Test results

The results of the four cooling test conditions represented by ① to ④ are described below when the refrigerant charge was optimized by fixing the compressor's rotational speed to achieve a capacity of 2.2 kW.

Fig. 3.2-3 compares the COP values achieved when using R22, R290, and R454C; Table 3.2-3 compares the rated standard cooling test results when using R22, R290, and R454C.

Table 3.3-1 Comparison of rated standard cooling test results for R22, R290, and R454C

Refrigerant type	Refrigerant charge	Compressor speed	Mass flow rate	Degree of superheating	Degree of supercooling
	g	Hz	Kg/h	°C	°C
R22	910	55.0	51.0	10.26	1.72
R290	400	62.5	28.2	6.97	4.63
R454C	950	65.0	58.8	6.14	5.70

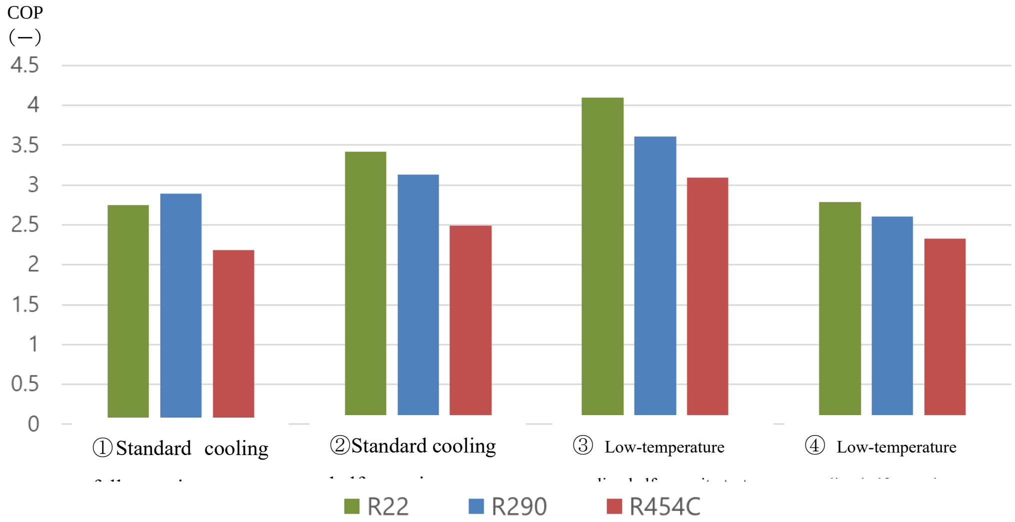

Fig. 3.3-1 Comparison of coefficient of performance (COP) values obtained during the cooling tests (adjusted to a cooling capacity of 2.2 kW)

Comparing the results for R22 and R290 shows that the COP value for R290 was slightly higher than that for R22 during the standard cooling full-capacity test, but was approximately 10% lower than that for R22 during each of the other three tests. Furthermore, the COP values for R454C were consistently 10% to 25% lower than those for R290 during all tests.

3.3.2 Considerations

First, the COP values of R22 and R290 are considered when the refrigerant charge was optimized by fixing the compressor's rotational speed to achieve a capacity of 2.2 kW. In the rated standard cooling full-capacity test, the COP value for R290 was only slightly higher than that for R22 because the latent heat of vaporization for R290 was approximately twice that for R22; therefore, the amount of circulating refrigerant was reduced when R290 was used, and thus resulted in a lower pressure loss. We presumed that this decreased pressure loss canceled out the reduced efficiency of the compressor owing to the increased compressor's rotational speed required to achieve a capacity of 2.2 kW.

The use of R290 and R454C was considered based on the results of the rated standard cooling full-capacity test. The COP value for R454C in test condition ① was approximately 25% lower than that for R290 because R1234yf, which is a low-pressure refrigerant, accounts for 78.5% of R454C, and R454C itself tends to be a low-pressure refrigerant. It was thus necessary to increase the mass flow rate to obtain the same capacity as that for R290 as follows,

$$Q_c = G_R \Delta h_{EV} \tag{3.3-1}$$

As a result, the pressure loss increased compared with that for R290, and the pressure difference between the inlet and outlet of the compressor increased as indicated by

$$\Delta P = f \frac{1}{2d} \rho_R {v_R}^2 \tag{3.3-2}$$

$$G_R = \rho_R v_R A \tag{3.3-3}$$

Thus, the compressor's power consumption increased by approximately 200 W, and the COP for R454C decreased. Figs. 3.3-2 and 3.3-3 show the test results and *P–h* diagrams, respectively, for R22, R290, and R454C in test condition ① (standard cooling full-capacity test).

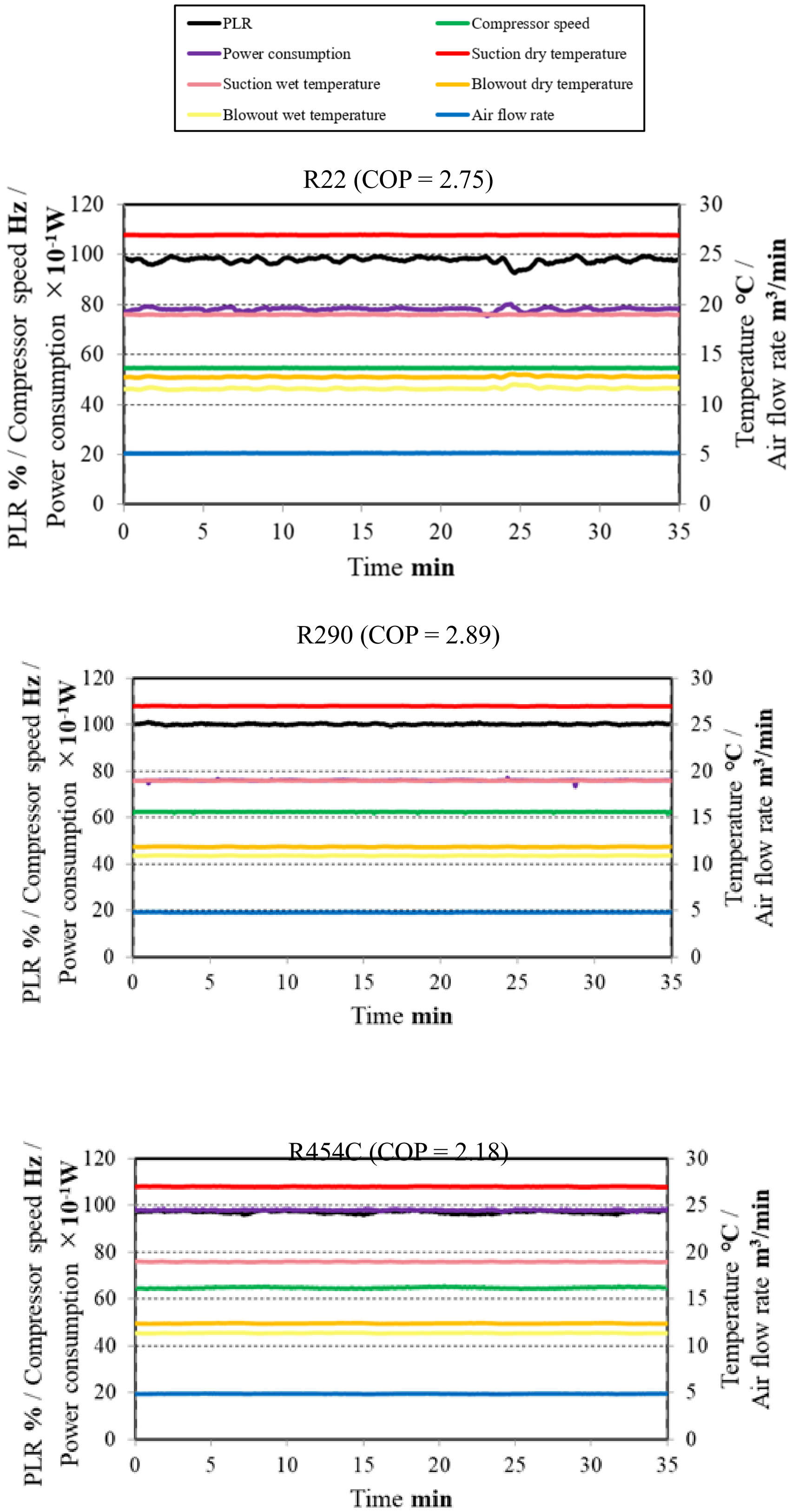

Fig. 3.3-2 Comparison of p-h diagrams of R22, R290, and R454C

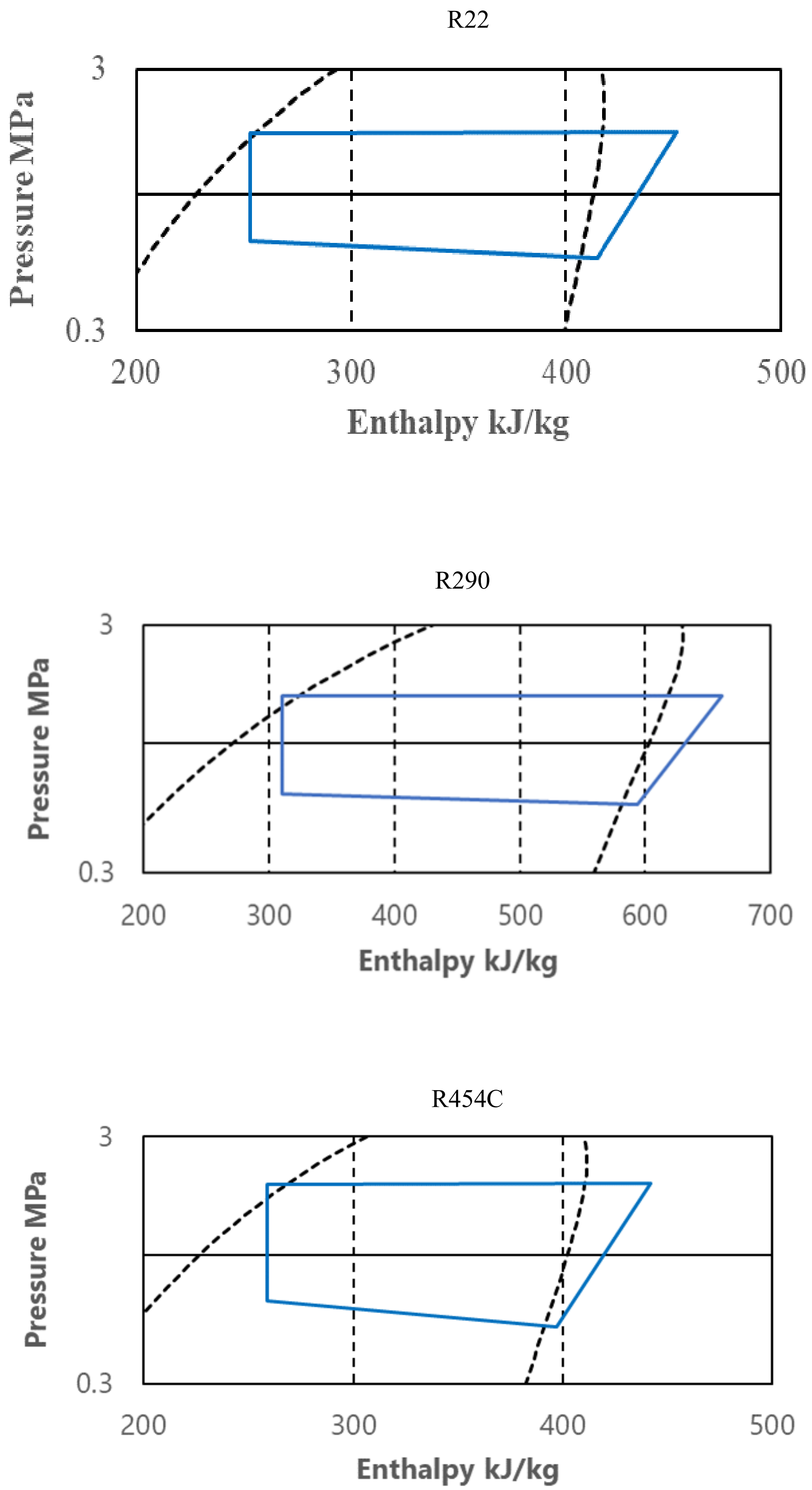

Fig. 3.3-3 Comparison of p-h diagrams of R22, R290, and R454C

3.3.3 Summary of experimental results using various refrigerants

In this study, the low-GWP refrigerants R290 and R454C were poured into a room air conditioner designed for use with the R22 refrigerant, and its resulting performance was evaluated. When the refrigerant charge was optimized by fixing the compressor's rotational speed to achieve a capacity of 2.2 kW, R290 exhibited nearly the same COP as that for R22. However, in the partial-load region, the COP for R290 was approximately 10% lower than that for R22. Furthermore, the COP for R454C was lower than that for R290 by 10–25%.

Note that in Section 4.1.3 (Model validation), the calculated values for the developed system simulator are verified based on these experimental results.

4. Dynamic test results

4.1 Test object

Fig. 4.4-1 shows the target system used in this research study. The test machine was an air conditioner (rated power: 4 hp) manufactured by Company A. In each of the outdoor and indoor units, the dry and wet bulb temperatures of the air were measured at the suction, and the dry and wet bulb temperatures of the air and air volume were measured at the blowout. In addition, the rotational speed of the compressor, power consumption of the fans and compressors of the outdoor and indoor units, and the total power consumption of the entire system were measured.

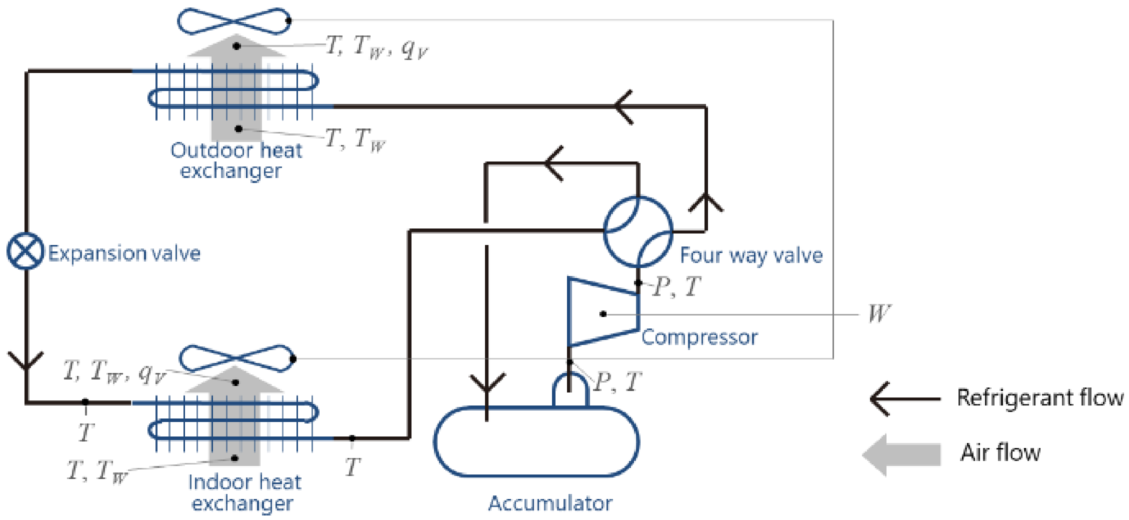

Fig. 4.1.1 Flow of the system and measuring points

4.2 Test conditions

In this test, the compressor's speed and expansion valve opening were maintained to control the air conditioner itself. This is different from the test method defined by current standards in which the compressor's speed was fixed at a constant speed. In addition, as a cooling test, it was conducted in low-load conditions wherein the compressor repeatedly started and stopped (intermittent operation state); this is considered to have a major effect on the controllability of the air conditioner. Furthermore, we conducted tests using an emulator in three conditions in which the volume of the room where the air conditioner was used, was changed. Because the test machine used in this study was a 4-hp machine, assuming the air-conditioning load of a standard building, the standard volume was 147 m^3, which is equivalent to that of a square room with a side of 7 m and a floor height of 3 m. Assuming approximately half the standard volume (i.e., 75 m^3), this is equivalent to the volume of a square with a side of 5 m and a height of 3 m; in turn, approximately doubling the standard volume to a value of 300 m^3 corresponds to the volume of a square room with a side of 10 m and a height of 3 m. Table 4.1-1 outlines the details of the used test conditions.

PLR is the partial load ratio, which is obtained by dividing the load handled by the air conditioner by the rated capacity of the air conditioner. The sensible heat factor (SHF) is the sensible heat ratio of the air-conditioning load and is set to 0.85 as the air-conditioning load of a general building. As aforementioned, this test focused on the performance evaluation of the air conditioner; therefore, the heat load due to the heat intrusion from the wall, which is in turn because the temperature difference between the room and the outer environment, solar radiation, and ventilation, were assumed to be zero, and only internal heat generation was considered.

Table 4.1-1 Test conditions

Parameters	Unit	Value
Indoor temperature (Set temperature)	℃	27
Outdoor temperature	DB℃/WB℃	35/24
Partial load ratio	%	30–40
Sensible heat factor	-	0.85
Room volume	m^3	75, 147, 300

4.3 Test results and discussion

4.3.1 Test results

Figs. 4.1-2–4 show the test results. These indicate that the air conditioner operates variably in a low-load environment. Although the inverter control of the air conditioner reduces the number of revolutions of the compressor, the capacity generated by the air conditioner exceeds the air-conditioning load of the room, thus causing the temperature in the room to continue to decrease and the set temperature to increase. When the temperature fell below a certain level, the compressor’s speed was lowered by controlling the air conditioner. Subsequently, when the air-conditioning load in the room exceeded the air-conditioning capacity, the room temperature began to rise, and when it exceeded the set temperature to some extent, the air-conditioner control again increased the compressor’s rotation speed, thus repeating the cycle. This fluctuating operation of air conditioners is a phenomenon often observed in actual air-conditioner operations, and tests that reproduce this are an important aspect of the simulation of the actual environment in which air conditioners are used.

The COP in Table 4.1-2 was obtained by averaging two to three cycles of variable operations. First, a comparison was made between the different load factors. In general, when the load factor decreases, the heat exchange efficiency of the indoor unit increases; thus, the COP increases. Evidently, the COP is actually higher in the test results with a load factor of 35% than with a load factor of 40%. However, in 30% of the tests, the air conditioner is operated intermittently with starts and stops. When the air conditioner started up, it temporarily operated to generate a certain capacity, but the COP dropped during this operating state. Therefore, the COP of the 30% load factor test result was lower than that of the 35% load factor. In particular, the COP was approximately 15% lower in the condition of 75 m^3.

4.3.2 Discussion

In the intermittent operation test, and given a load factor of 30%, as the room volume increases, the COP increases. Comparing the COPs of rooms with volumes of 75 m^3 and 300 m^3, the latter was approximately 16% higher than that of the former. This is because the intermittent operating cycle changes when the room volume changes. When the air conditioner starts up, it temporarily operates to generate a certain capacity, but the COP drops during this operating state. When the volume of the room is small, the room temperature drops rapidly, owing to the capacity of the air conditioner immediately after starting, and the air conditioner turns off the thermostat within a short time.

In contrast, if the volume of the room is large, the drop in room temperature owing to the ability of the air conditioner immediately after startup will be gradual, and it will be followed by a period during which the compressor will operate at a constant speed. When the compressor was operated at a constant rotational speed, the COP increased. Therefore, in conditions in which the volume of the room is large, the ratio of the time of constant operation in the cycle of intermittent operation increases; as a result, the COP increases. However, in the tests with load factors of 35% and 40%, there were no start-and-stop operations, and no drop in efficiency occurred during startup.

The results of this test show that the dynamic performance of an air conditioner changes when the volume of the room changes. This is the result of proving that to evaluate correctly the dynamic performance of air conditioners, it is necessary to change appropriately the volume of the performance evaluation device according to the rated capacity of the air conditioner. Because it is difficult to change physically the volume of the device, it is suggested that the device used to simulate the air-conditioning load and room volume with software is effective.

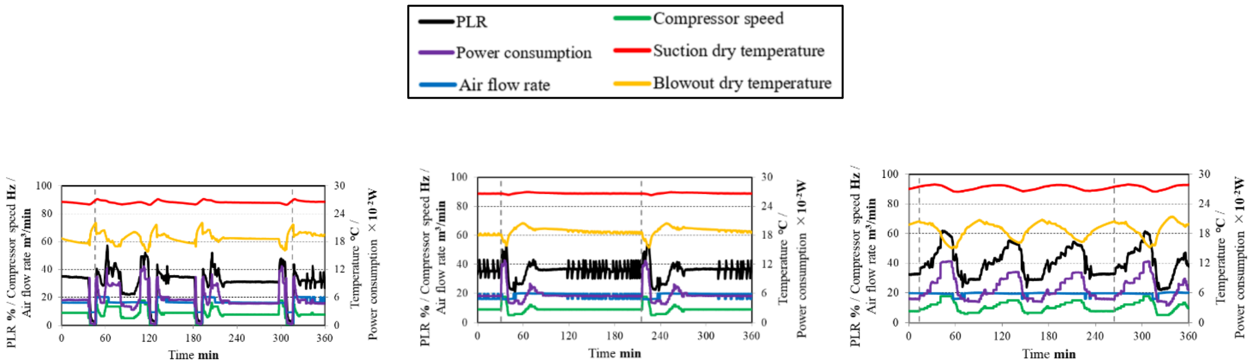

Fig. 4.1-2 Test result (room volume = 75 m^3)
Left: Partial load ratio (PLR) = 30%, Middle: PLR = 35%, Right: PLR = 40%

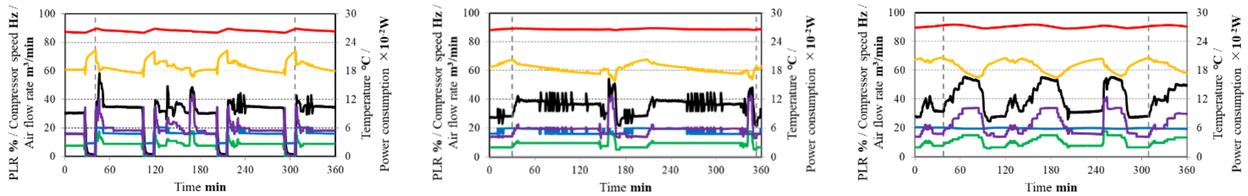

Fig. 4.1-3 test result (room volume = 147 m^3)
Left: PLR = 30%, Middle: PLR = 35%, Right: PLR = 40%

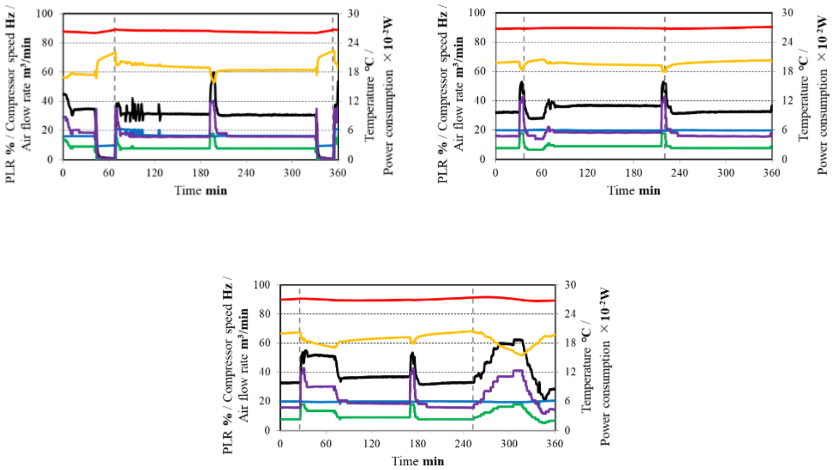

Fig. 4.1-4 test result (room volume = 300 m^3)
Left: PLR = 30%, Middle: PLR = 35%, Right: PLR = 40%

Table 4.1-2 COP test outcomes

		Room volume m^3		
		75	147	300
PLR	30	5.43	5.60	6.22
%	35	6.25	6.13	6.44

40	5.82	5.76	6.09

4.3.3 Summary of dynamic test results

In this study, to establish a new evaluation method for the dynamic performance of air conditioners, we used an "emulator-type performance evaluation device" equipped with an emulator that simulates the air-conditioning load in a room to evaluate intermittent operations. The performance test of the air conditioner was conducted by changing the load factor in low-load conditions. As a result, it was confirmed that a test considering the controllability of the air conditioner was possible, and the relationship between the load factor of the air conditioner and the COP was illustrated. Furthermore, it was possible to confirm that differences in room volume affected the dynamic performance of the air conditioner, thus suggesting the effectiveness of the "emulator-type performance evaluation device" that can reproduce any air-conditioning load.

In a future prospect, we will conduct performance evaluations in various conditions based on the actual operating conditions to establish a new method for evaluating the dynamic performance of air conditioners. In addition, we intend to verify the validity of the emulator by installing the air conditioner in an actual building and conducting a field test while comparing its outcomes with the test results obtained by this device.

Nomenclature

a_s	: solar absorption rate (-)	$\dot{Q}$	: heat quantity (W)
A	: wall surface area (m^2)	$\dot{q}$	: heat generation inside the wall ($W \cdot m^{-2}$)
C	: heat capacity ($kJ \cdot K^{-1}$)	t	: time (s)
c_p	: constant pressure specific heat ($kJ \cdot kg^{-1} \cdot K^{-1}$)	T	: temperature (K)
E	: radiant heat ($W \cdot m^{-2}$)	V	: volume (m^3)
F	: view factor to the sky (-)	x	: absolute humidity ($kg \cdot kg^{-1}$)
I	: Solar irradiance ($W \cdot m^{-2}$)	α	: heat transfer coefficient ($W \cdot m^{-2} \cdot K^{-1}$)
j	: mass diffusion flux ($kg \cdot m^{-2} \cdot s^{-1}$)	ρ	: density ($kg \cdot m^{-3}$)
$\dot{L}$	: moisture generated ($kg \cdot s^{-1}$)	ε	: long wavelength emissivity (-)
M	: mass (kg)	ϕ	: Gebhart absorption coefficient (-)
$\dot{m}$	: mass flow rate ($kg \cdot s^{-1}$)		

Subscripts

a	: air	*N*	: night
AC	: air conditioner side	*OA*	: outside air
BL	: building	*r*	: radiation
c	: convection	*Room*	: indoor
eq	: equivalent	*SA*	: supply air
ex	: external	*sh*	: degree of superheat
FN	: furniture, etc.	*w*	: water vapor
in	: inside	*WS*	: wall surface
i,k	: serial number	*ZN*	: zone

References

1) Agency for Natural Resources and Energy, Ministry of Economy, Trade and Industry, Annual Report on Energy for 2019 (Energy White Paper 2020) PDF Version, Part 2, pp.112–115.

2) Shinichi, A., Jun, S., Takuya, O. Hiroyuki, I., Yuki, A., Study on State of COP and Regional Characteristics of APF for Room Air Conditioners, *AIJ J. Technol. Des.,* 2014, **20**(44), pp.187–190. (in Japanese)

3) Katsuhiro, K., Technological Innovations of Air Conditioning and their Development into Industry, *Refrigeration* , 2019, **94**(1101), pp.436–441 (in Japanese).
4) Japan Refrigeration and Air Conditioning Industry Association, Estimation of World Air Conditioner Demand, (2019), pp.1–8.
5) Keisuke, O. and Kiyoshi, S., Seiichi, Y., Tetsuro, K., Kuniyasu, M., Intermittent Driving Simulation of Compression type Heat Pump－1st Report: Mathematical Model and Simulation of Single-stage Vapor Compression Type Heat Pump－, *Trans. JSRA Engineers*, 2013, **30**(2), pp. 107–122. (in Japanese)
6) Japanese Standards Association, Package Air Conditioner JIS B 8616:2015, (2015)
7) Japan Refrigeration and Air Conditioning Industry Association, Practical Performance and Possibilities of Heat Pumps, (2010).
8) Masayuki, N., Technologies for Energy −Saving of Room Air−Conditioner, *J. JSME*, 2003, **106**(1015), pp.464–465 (in Japanese).
9) Fusigi, Y., Create A New Breeze! Room Air Conditioner Revolution (Atarasii kaze wo tukure! Ru-mueakon kakumei), *J. JSME,* 2019, **122**(1206), pp.38–39.
10) Carsten Palkowski, Zottl, A., Malenkovic, I., Simo, A., Energies, 2019, **12**, 1045. doi:10.3390/en12061045.
11) Toshinori Ban, Daiki Nakano, Keisuke Ohno, Seiichi Yamaguchi, Kiyoshi Saito, Hideki Yamaguchi, Proc. of 12th IEA Heat Pump Conference 2017, Rotterdam, The Netherlands.
12) Ohnishi Netsugaku, https://en.ohnishi.co.jp/.
13) Akihito Ozaki, Toshiyuki Watanabe, Hideyoshi Takase, Tatsunori Tsujimaru. Heat–Moisture–Air-Coupled Simulation for Buildings Part 1: Temperature and Humidity Calculation Considering Moisture Absorption and Desorption of Walls, Summaries of Technical Papers of Annual Meeting of Architectural Institute of Japan", pp.439–440, 2004.
14) Hisaya Ishino, Kimiko Kori, Measurement and Experimental Study on Thermal Influence of Furniture in Office Buildings, *Proc.*, 1987, **372**, pp.59–66.
15) Gebhart, B., A New Method for Calculating Radiant Exchanges, *ASHRAE Trans.* 1959*,* **65**, pp.321–332.

Part II Progress and Achievements of THE University of Tokyo

1. INTRODUCTION

1.1 Introduction

Japan can lead the world in technology to realize energy-saving operations by continuously changing the compressor speed following the air conditioning load. For the development of the Japanese industry, to correctly evaluate the energy efficiency of air conditioners that utilize inverter control technology for compressors, a method must be developed. Furthermore, the method must be disseminated throughout the world. In the JIS C 9612:2013 room air conditioners, the compressor speed was fixed, and the performance was analyzed at two points during the cooling operation and at three points during the heating operation. Based on the results, the year-round energy consumption efficiency (APF) was calculated. However, the method has a few limitations. Even though the compressor speed was variable, the test was conducted at a fixed speed. When the cooling or heating load decreased, the compressor could no longer operate continuously and started intermittent operation. However, the performance degradation at that time could not be determined accurately.

In 2015, the Environmental Protection Agency (EPA) announced that Volkswagen installed fraudulent software that enabled devices to reduce emissions during bench tests for the type approval of diesel vehicles. During actual driving, they were disabled. Therefore, it was suggested that fixing the rotation of compressor while conducting air-conditioner performance tests can result in a situation different from the actual operating conditions in a living room. Additionally, the requirement to obtain technical information from air-conditioner manufacturers to conduct performance tests is an issue. Air conditioner performance tests are becoming increasingly important while they are in use.

Several test methods that do not fix the compressor speed have been proposed. Purdue University has been conducting research on load-based test methods, and several results have been published on test methods that consider the correlation with building load characteristics without turning off the control of air conditioners[1-1)-1-5)]. Furthermore, Federal Institute for Materials Research and Testing (BAM) has proposed a dynamic load test that utilizes air conditioner control without fixing compressor speed[1-6)]. They proposed actively evaluating the quality of air conditioner control by systematically changing the heat load and outdoor temperature conditions while conducting performance tests of an air conditioner. Waseda University developed a hybrid test facility consisting of an emulator capable of simulating an arbitrary environment and equipment for evaluating heat pump performance based on the air enthalpy method for evaluating heat pump performance in an actual operating environment[1-7)].

Based on this background, the compressor was operated freely based on the control algorithm, and the performance of an air conditioner was tested when the outdoor temperature and cooling/heating load changed (hereafter referred to as the “load test”).

The University of Tokyo used its environmental test room for small room air conditioners to study the load test method. In addition, the Japan Air Conditioning and Refrigeration Testing Laboratory used room air conditioner test equipment to examine the issues of the load test method.

References

1-1) Patil, A., Hjortland, A. L., Cheng, L., Dhillon, P., Braun, J. E., & Horton, W. T., Load-Based Testing to Characterize the Performance of Variable-Speed Equipment. International Refrigeration and Air Conditioning Conference, (2018), Paper 2076.

1-2) Hjortland, A. L., & Braun, J. E., Load-based testing methodology for fixed-speed and variable-speed unitary air conditioning equipment. Science and Technology for the Built Environment, 25(2), (2019), 233–244.

1-3) Dhillon, P., Horton, W. T., & Braun, J. E., Comparison of Steady-State and Dynamic Load-Based Performance Evaluation Methodologies for a Residential Air Conditioner. International Refrigeration and Air Conditioning Conference, (2021), Paper 2519.

1-4) Ma, J., Dhillon, P., Horton, W. T., & Braun, J. E., Heat-Pump Control Design Performance Evaluation using Load-Based Testing. International Refrigeration and Air Conditioning Conference, (2021), Paper 2520.

1-5) Dhillon, P., Welch, D., Butler, B., Horton, W. T., & Braun, J. E., Validation of a Load-Based Testing Method for Characterizing Residential Air-Conditioner Performance. International Refrigeration and Air Conditioning Conference, (2021), Paper 210073.

1-6) Palkowski, C., Zottl, A., Malenkovic, I., and Simo, A., Fixing Efficiency Values by Unfixing Compressor Speed: Dynamic Test Method for Heat Pumps, Energies 2019, 12, 1045.

1-7) Saito, K., Hybrid Dynamic test method of air-conditioning systems with next-generation low GWP refrigerants, International Symposium on New Refrigerants and Environmental Technology 2021, Paper M231.

2. RESULTS OF JAPAN AIR CONDITIONING AND REFRIGERATION TESTING LABORATORY

Because air conditioner capacity measurements based on JIS standards are performed with a fixed compressor frequency informed by the manufacturer, from the perspective of users, in Japan and overseas, a trend arises to recommend and consider a test that can be performed only by the user's operation without requiring any information from the manufacturer (hereinafter referred to as “heat load test”)

In this study, we considered the technical issues while carrying out heat load tests in several test facilities in Japan, and the test results were evaluated using room air conditioners.

2.1 Outline of the test facilities

The test equipment was held at Japan Air Conditioning and Refrigeration Testing Laboratory (hereinafter referred to as “JATL”) with the following specifications.

＜Calorimeter No.1＞

・Balanced ambient room type calorimeter in accordance with JIS B 8615-1

・Capacity measurement range 【Cooling】0.9～7.1 kW ・Volume 【Indoor side】 44.1 m^3
【Heating】0.9～8.0 kW 【outdoor side】 44.1 m^3

・Way of cooling for the air in the equipment: Brine chiller

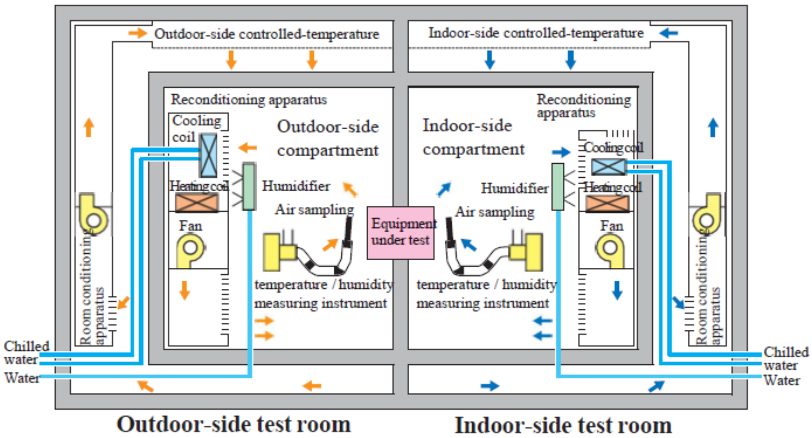

Fig. 2-1 Balanced ambient room-type calorimeter No.1 (elevation)

＜Calorimeter No.2＞

・Balanced ambient room type calorimeter in accordance with JIS B 8615-1

・Capacity measurement range 【Cooling】0.2～16.0 kW ・Volume 【Indoor side】 92.9 m^3
【Heating】0.2～20.0 kW 【outdoor side】 92.9 m^3

・Way of cooling for the air in the equipment: Brine chiller

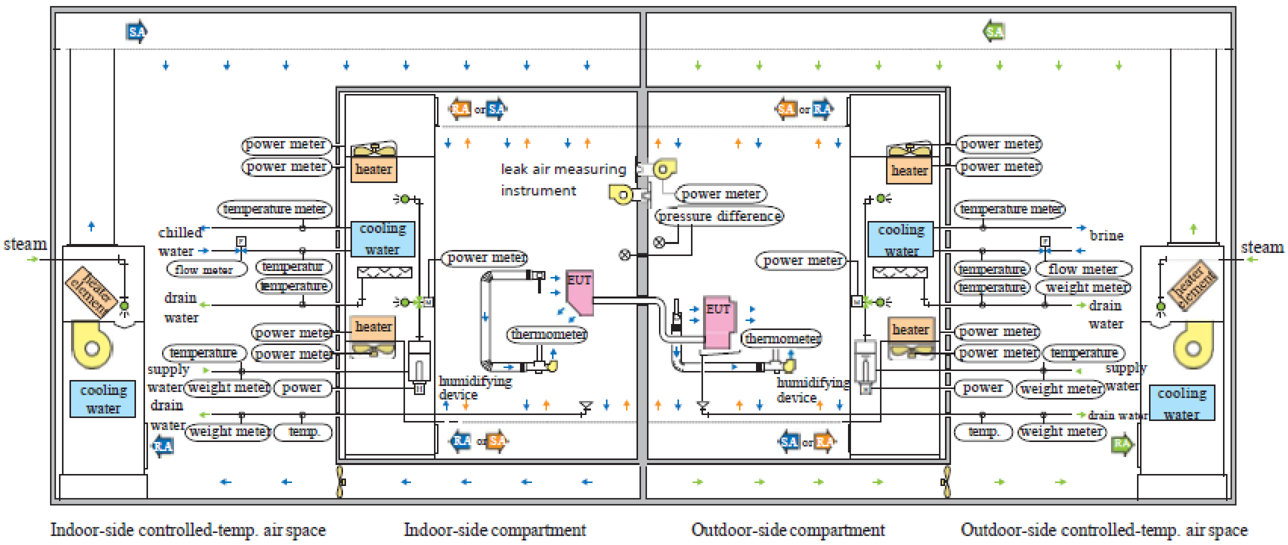

Fig. 2-2 Balanced ambient room-type calorimeter No.2 (elevation)

＜Calorimeter No.3＞

・Tunnel air enthalpy test apparatus in accordance with JIS B 8615-1

・Capacity measurement range【Cooling】0.0～10.0 kW　・Volume　【Indoor side】　139 m^3
【Heating】　0.0～13.0 kW　【outdoor side】　75 m^3

・Way of cooling for the air in the equipment: Direct expansion refrigerator

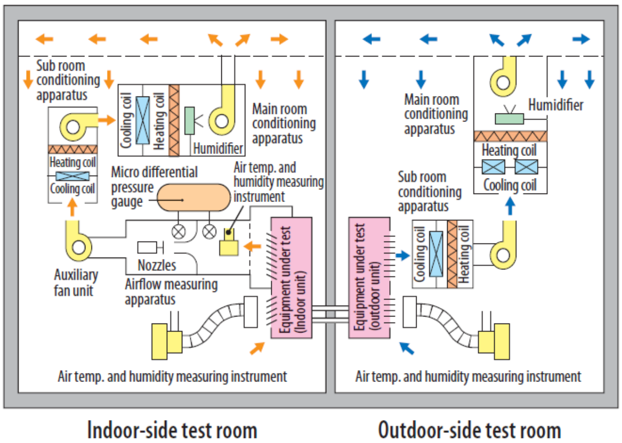

Fig. 2-3 Tunnel air enthalpy test method arrangement (elevation)

The facilities shown in Figs. 2-1, 2-2, and 2-3, which are based on JIS standard capacity measurements, have been certified as original equipment for fiscal 2022 by JRAIA, and test accuracy is recognized.

2.2 Purpose of heat load test

In 2019, BAM in Germany proposed the dynamic test Method (DTM), a test method without fixing the compressor frequency, as a heat load test method in Europe. Furthermore, JRAIA participated in the round-robin test conducted by BAM, and JATL executed the heat load test in that round-robin test. Results suggested that the room temperature control of the equipment under test (EUT) and the heat capacity of the test equipment significantly affected measurement results, and a few issues occurred in reproducibility and repeatability.

The purpose of this study is to examine the influence of the EUT side and other factors that affect the heat load test and technical issues of the test by understanding the disadvantages of the heat load test.

2.3 Test methods

In the balance ambient room-type calorimeter ＜Calorimeter No.1＞ and ＜Calorimeter No.2＞, sensible and latent heat were applied for the rated capacity of the EUT by adjusting the amount of heater, amount of humidifying heater, cooling water temperature, and flow rate of cooling water.

The conditions of the heat load and the settings of the EUT are listed in Table 2-1 and Table 2-2.

Table 2-1 Cooling test conditions (α: temperature adjustment with remote controller)

Cooling load	Settings of EUT		Outdoor temperature (℃)	
(vs. rated capacity)	Setting temp. (℃)	Air flow	Dry bulb	Wet bulb
100%	27±α	Auto ／High	35.0	(24.0)
50%	27±α	Auto ／High	29.0	(19.0)
25%	27±α	Auto ／High	26.0	(16.0)

Table 2-2 Heating test conditions (α: temperature adjustment with remote controller)

Heating load	Settings of EUT		Outdoor temperature (℃)	
(vs. rated capacity)	Setting temp. (℃)	Air flow	Dry bulb	Wet bulb
100%	20±α	Auto ／High	7.0	6.0
50%	20±α	Auto ／High	12.0	10.4
25%	20±α	Auto ／High	14.5	13.2

2.4 Measurement by heat load test and clarifying issues

2.4.1 Heat load test in the different types of calorimeters

Primary specifications of < EUT No.1 > tested in this section are listed in Table 2-3.

Table 2-3 Specifications < EUT No. 1 >

Rated cooling capacity (kW)	2.8	Rated heating capacity (kW)	3.6
Cooling power consumption (W)	800	Heating power consumption (W)	910
EER	(3.50)	COP	(3.96)

First, we verified how the difference between the test equipment appear in the results. Test results using < Calorimeter No.1 > Fig. 2-1 and < Calorimeter No.2 > Fig. 2-1 under the conditions set in Tables 2-1 and 2-2 are compared. Because we could not automatically control the heat loads to the target value in both equipment, they were adjusted manually. In addition, due to the room temperature control of the EUT, adjusting the input of heat load as intended was very difficult when temperature fluctuations occurred. Therefore, the test was conducted to minimize the heat load difference between the equipment as much as possible.

Table 2-4 Comparison between calorimeters, load factor 100% in cooling, <EUT No.1>

	Cooling（set temperature 27／air flow Auto.）	
Test equipment	＜Calorimeter No.1＞	＜Calorimeter No.2＞
Heat load(W)	2,804	2,799
Power consumption(W)	884	863
EER	3.17	3.24
Indoor dry bulb(°C)	27.92	27.05
Indoor wet bulb(°C)	18.61	18.80
Outdoor dry bulb(°C)	35.00	35.01
Outdoor wet bulb(°C)	23.96	24.00
Indoor temperature	Unsteady state cycle	Steady state

Table 2-4 shows the results of < Calorimeter No.1 > and < Calorimeter No.2 > in the cooling operation, and Figs. 2-4 and 2-5 show the trends of room temperature and cooling capacity. No difference was observed in the input heat load between < Calorimeter No.1 > and < Calorimeter No.2 >. However, even if the set temperature of the remote control of the EUT was the same, in < Calorimeter No.1 >, the room temperature fluctuated and the average indoor temperature was higher than that of < Calorimeter No.2 >. A difference was observed in the temperature of the wet-bulb.

The room temperature control characteristics were different for the EUT and could be negatively influenced by air currents around the EUT in the indoor test room. In addition, because the wet-bulb temperature was determined by the evaporation temperature of the heat exchanger of the EUT, the fluctuation of the compressor frequency of the EUT could induce the wet-bulb temperature fluctuation.

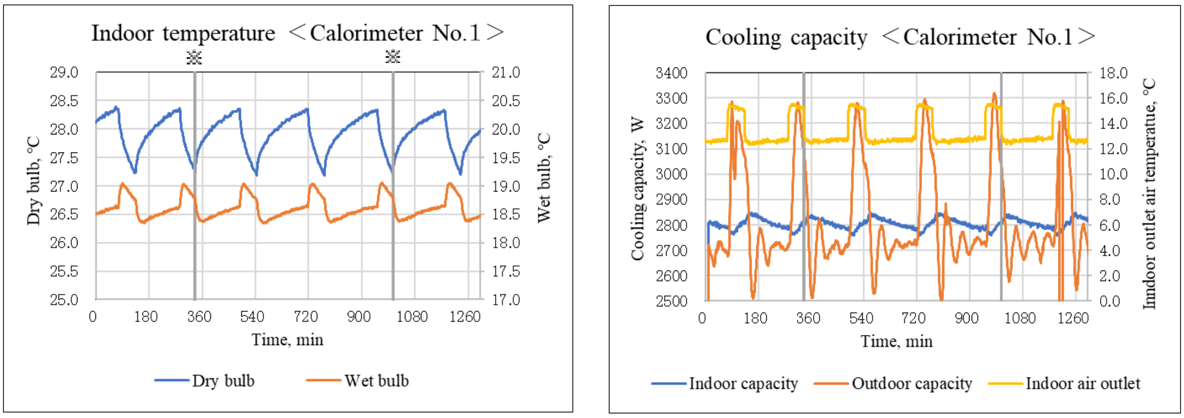

Fig. 2-4 Cooling operation, load factor 100%, indoor air temperature and capacity, calorimeter No.1
（※Average calculated during the period |　| in figures and all figures of this type from the next are with same calculation）

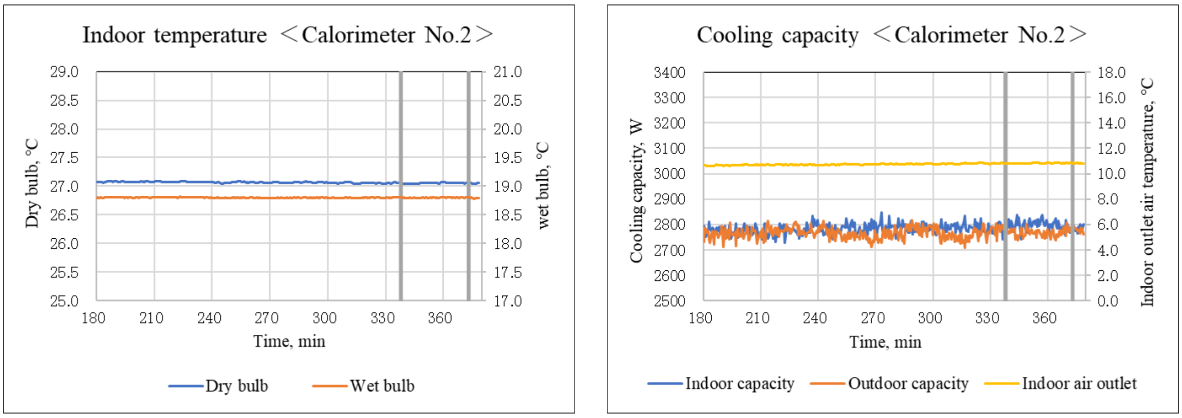

Fig. 2-5 Cooling operation, load factor 100%, indoor air temperature and capacity, calorimeter No.2

Table 2-5 shows the results of < Calorimeter No.1 > and < Calorimeter No.2 > in the heating operation. Similar to the cooling operation, the input heat load in each piece of equipment was adjusted to minimize the difference as much as possible. Steady-state was observed in each piece of equipment and reproducibility was shown for the heat load in the different equipment. In both cases, the room temperature was controlled higher than the temperature setting by the EUT. Furthermore, the difference in room temperature was 0.12 ℃, and the power consumption was 26 W (2.43%). The degree of difference was the limit and issue of repeatability of measurement with manual control of the heat load in the test results.

Table 2-5 Comparison between calorimeters, load factor 100% in heating, <EUT No.1>

	Heating（set temperature 20／air flow High）	
Test equipment	＜Calorimeter No.1＞	＜Calorimeter No.2＞
Heat load(W)	3,600	3,600
Power consumption(W)	1,070	1,044
COP	3.37	3.45
Indoor dry bulb(℃)	21.61	21.49
Indoor wet bulb(℃)	15.86	14.09
Outdoor dry bulb(℃)	6.98	7.00
Outdoor wet bulb(℃)	6.01	6.00
Indoor temperature	Steady state	Steady state

Figures 2-6 and 2-7 show the trends in room temperature and heating capacity. The room temperature was controlled in an steady state and the heat load could be reproduced in both tests with different equipment. < Calorimeter No.1 > and < Calorimeter No.2 > showed no difference in the input heat load.

In a balanced room-type calorimeter, the room temperature control of the EUT significantly affected the results. In particular, when the indoor temperature fluctuated, the heat capacity of the indoor side was one of the factors that caused a difference in the period of an unsteady cycle. However, the number of tests was insufficient for repeatability and reproducibility.

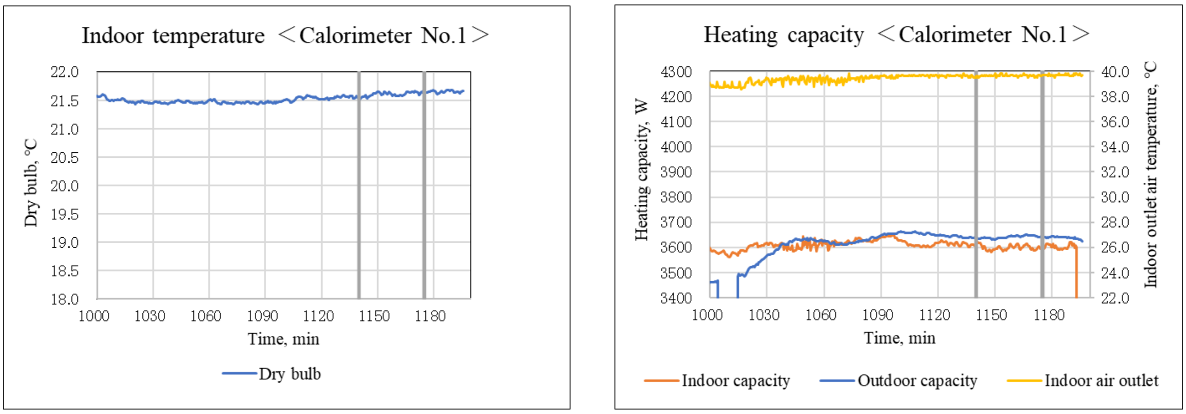

Fig. 2-6 Heating operation, load factor 100%, indoor air temperature and capacity, calorimeter No.1

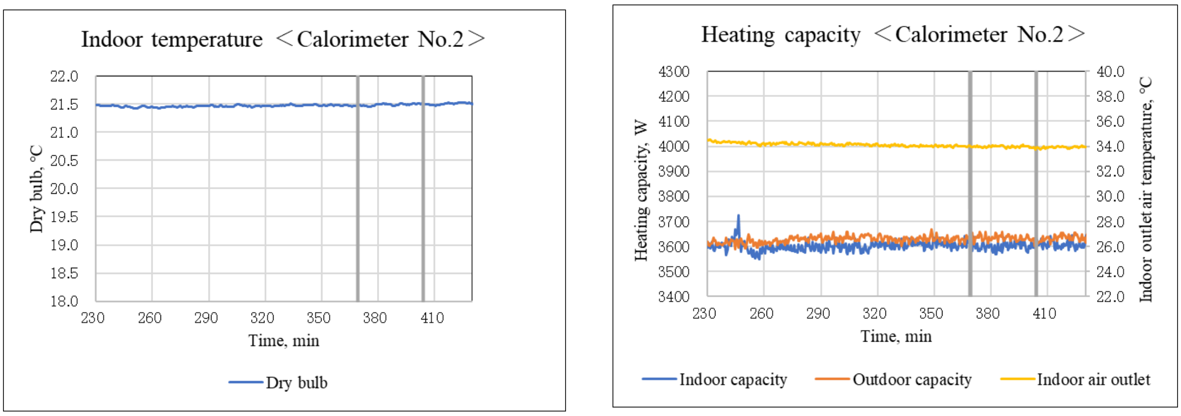

Fig. 2-7 Heating operation, load factor 100%, indoor air temperature and capacity, calorimeter No.2

2.4.2 Comparison of temperature control characteristics on the same test equipment

During the heat load test, the conditions on the consumption side of the load, that is, the operating procedure conducted in the EUT, should be the same as the operation for the consumer on the controller. We selected parameters that might affect the test results and studied the differences due to the heat load test. Here, we conducted a comparison using the same test equipment with the airflow rate setting (High or Automatic) as a parameter that can be selected for remote control.

1）Comparison of air flow setting with the same EUT < EUT No.1 >

We reduced the input heat load to 50% and studied the effect of the airflow setting during the cooling operation. Table 2-6 shows the test results of the difference while changing the airflow setting at the target of 50% heat load of the rated cooling capacity using < EUT No.1 >. A steady state appears in both tests, as shown in Figs. 2-8 and 2-9. The difference in the airflow setting in < EUT No. 1 > affected the indoor temperature and power consumption. Because the impact on EER was large, the number of EUT should be increased, and the method of setting EUT should be studied.

Table 2-6 Comparison between airflow settings, load factor 50% in cooling, <EUT No.1>

＜EUT No.1＞	Cooling Load factor 50% (Set temp. 27)	
Air flow setting	High	Automatic
Heat load(W)	1,414	1,382
Power consumption(W)	213	268
EER	6.63	5.16
Indoor dry bulb(°C)	26.73	27.34
Indoor wet bulb(°C)	18.72	19.05
Outdoor dry bulb(°C)	28.98	28.99
Outdoor wet bulb(°C)	19.36	19.42
Indoor temperature	Steady state	Steady state

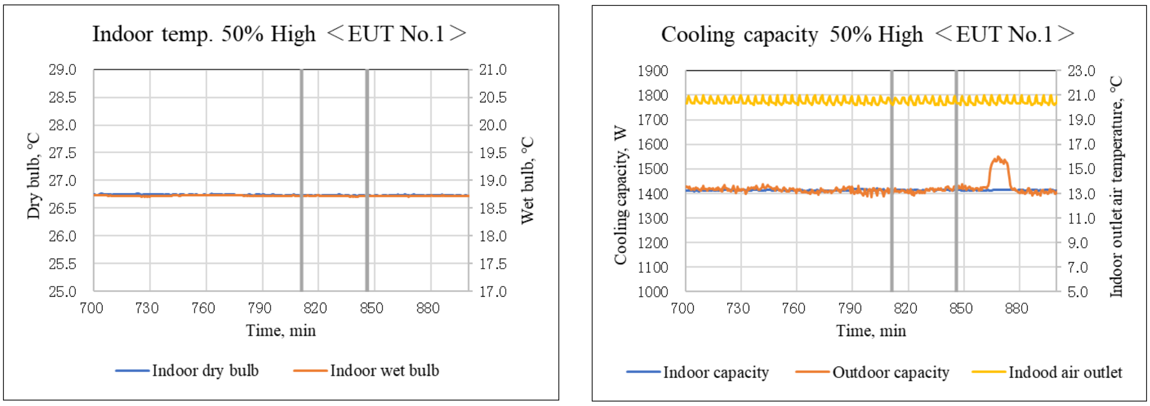

Fig. 2-8 Cooling operation, load factor 50%, airflow High, indoor air temperature and capacity <EUT No. 1 >

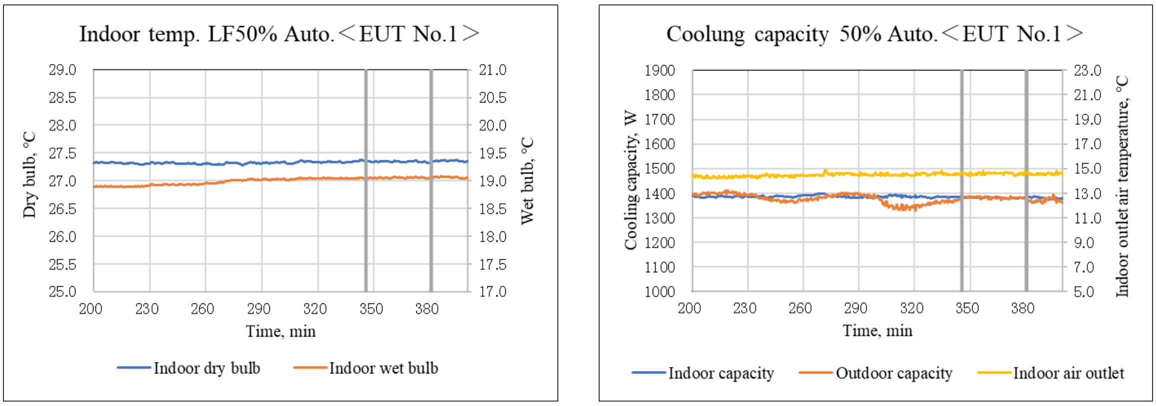

Fig. 2-9 Cooling operation, load factor 50%, airflow Automatic, indoor air temperature and capacity < EUT No. 1 >

2）Comparison of airflow setting in the intermittent operation range

We reduced the input heat load to 25% and studied the effect of the airflow setting during the heating operation. Table 2-7 shows the results of the difference while changing the airflow setting at the target of 25% heat load of the rated heating capacity using < EUT No.1 >. The intermittent operation of the compressor appears at 25% of the full heat load, as shown in Figs. 2-10 and 2-11. Practically the same heat load could be applied, and the reproducibility of the average room temperature was good. The difference in the airflow setting affected the power consumption, COP, and the period of one intermittent operation cycle. However, as the results were from < EUT No.1 > and did not represent all of them, the differences should be confirmed by changing the EUT.

Table 2-7 Comparison between airflow settings, load factor 25% in heating, < EUT No.1 >

＜EUT No.1＞	Heating Load factor 25%（Set temp. 18）	
Air flow setting	High	Automatic
Heat load(W)	880	879
Power consumption(W)	166	178
COP	5.30	4.94
Indoor dry bulb(°C)	21.78	21.78
Indoor wet bulb(°C)	14.27	14.24
Outdoor dry bulb(°C)	14.53	14.40
Outdoor wet bulb(°C)	13.20	13.13
Compressor operation	ON/OFF	ON/OFF
One cycle time(min)	30.5	74.8

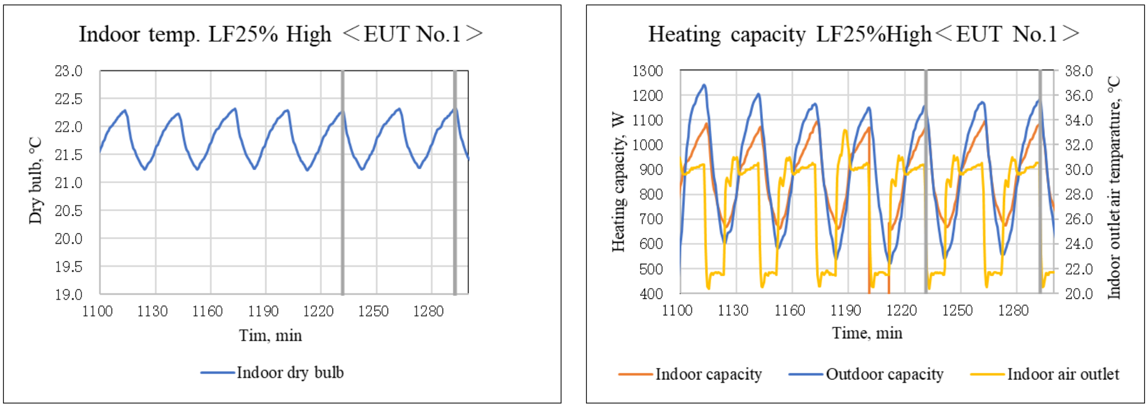

Fig. 2-10 Heating operation, load factor 25%, airflow High, indoor air temperature and capacity <EUT No. 1 >

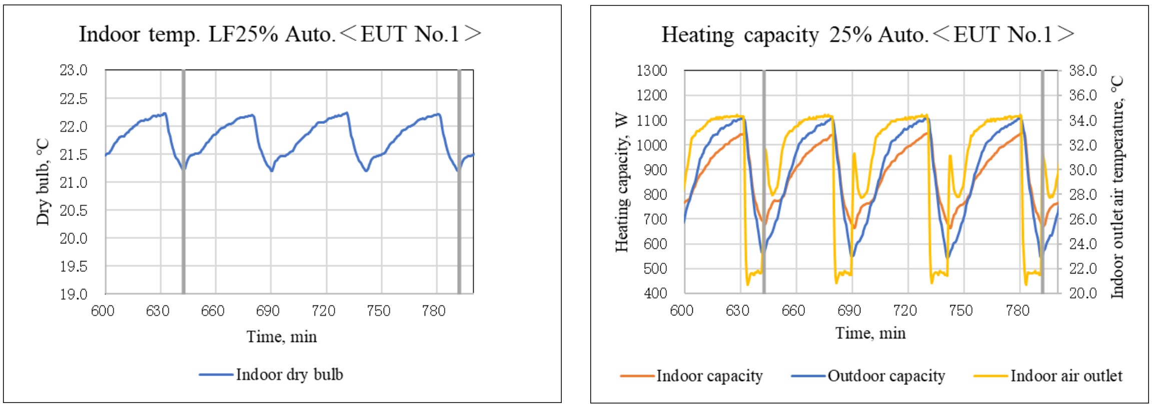

Fig. 2-11 Heating operation, load factor 25%, airflow Automatic, indoor air temperature and capacity < EUT No. 1 >

3）Comparison of airflow settings in the different EUT

The settings in EUT on the consumption side of the heat load were the parameters that can be selected by the test person as the position of the consumer. As they strongly affected the characteristics of room temperature control, we prepared another EUT, which was made by other manufacturer (hereinafter referred to as “EUT No.2”) for further study. Table 2-8 shows the specifications of < EUT No.2 >.

Table 2-8 Specifications ＜EUT No.2＞

Rated cooling capacity (kW)	2.8	Rated heating capacity (kW)	3.6
Cooling power consumption (W)	750	Heating power consumption (W)	865
EER	(3.73)	COP	(4.16)

Table 2-9 shows the heat load test results of < EUT No.2 > with the different airflow settings in the cooling operation using < Calorimeter No.1 >. The Input heat loads were adjusted based on the JIS standard test results added to Table 2-9 as a reference. The temperature control is practically in a steady state, as shown in Figs. 2-12 and 2-13.

Table 2-9 Comparison between airflow settings, load factor 100% in cooling, < EUT No.2 >

＜EUT No.2＞	Cooling operation Full load 100%（Temperature setting 27）		
Air flow setting	High	Automatic	(※reference) JIS
Heat load(W)	2,906	2,870	2,894
Power consumption(W)	752	742	704
EER	3.86	3.87	4.11
Indoor dry bulb(°C)	26.82	28.55	27.01
Indoor wet bulb(°C)	18.87	19.02	19.02
Outdoor dry bulb(°C)	35.00	35.00	34.99
Outdoor wet bulb(°C)	23.99	23.99	23.98
Indoor temperature	Steady state	Steady state	Steady state

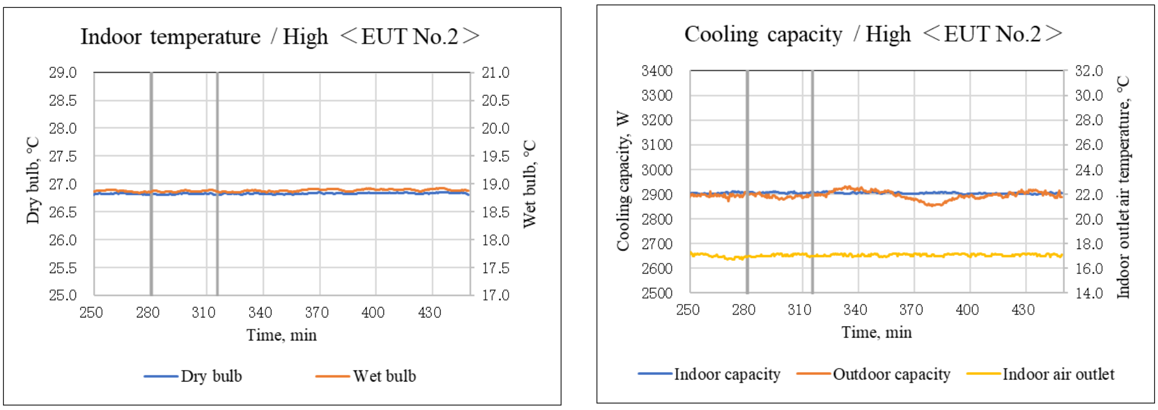

Fig. 2-12 Cooling operation, load factor 100%, airflow High, indoor air temperature and capacity <EUT No.2>

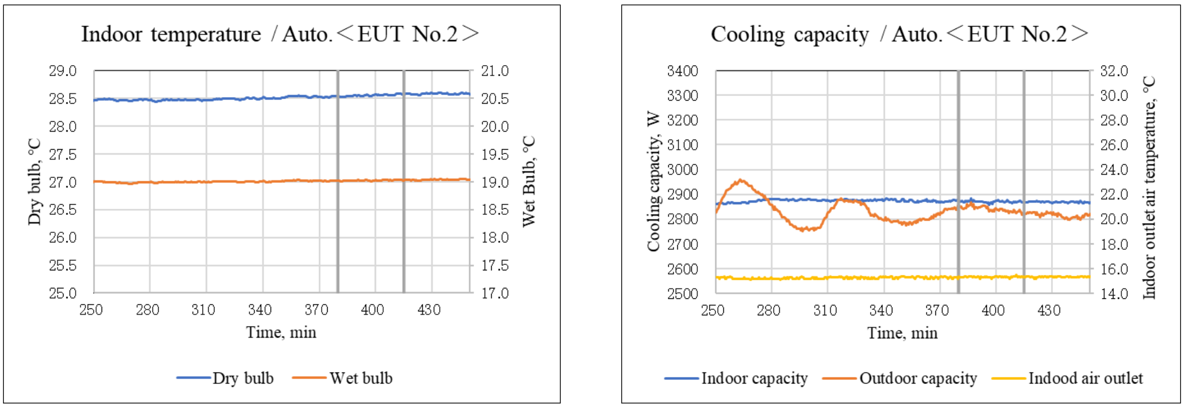

Fig. 2-13 Cooling operation, load factor 100%, airflow Automatic, indoor air temperature and capacity <EUT No.2>

Table 2-10 shows the result of the difference while changing the airflow setting at the target of 50% heat load of the rated cooling capacity of < EUT No.2 > using < Calorimeter No.1 >. Figures 2-14 and 2-15 show the operating states.

Table 2-10 Comparison between airflow settings, load factor 50% in cooling, < EUT No.2 >

＜EUT No.2＞	Cooling Load factor 50%（Set temp. 27.5）	
Air flow setting	High	Automatic
Heat load(W)	1,423	1,501
Power consumption(W)	170	233
EER	8.37	6.44
Indoor dry bulb(℃)	27.32	26.69
Indoor wet bulb(℃)	19.17	18.71
Outdoor dry bulb(℃)	29.00	29.01
Outdoor wet bulb(℃)	19.36	19.42
Indoor temperature	Steady state	Steady state

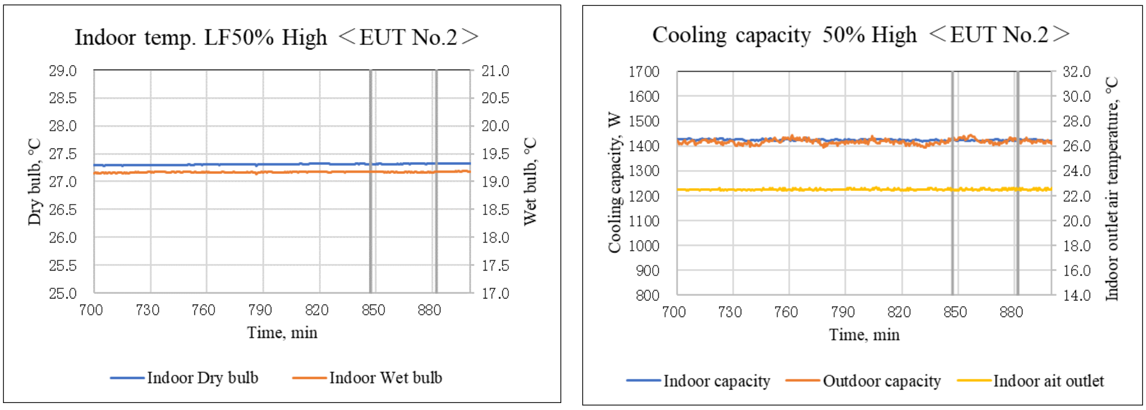

Fig. 2-14 Cooling operation, load factor 50%, airflow High, indoor air temperature and capacity <EUT No.2>

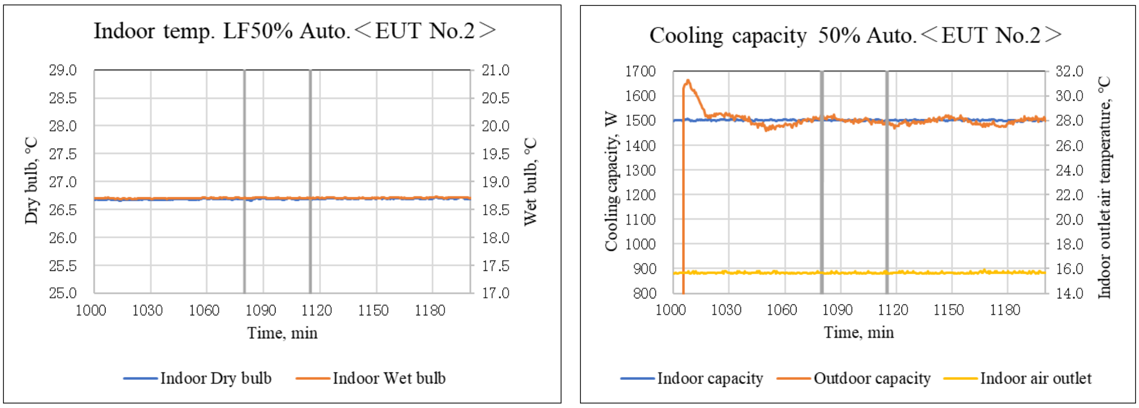

Fig. 2-15 Cooling operation, load factor 50%, airflow Automatic, indoor air temperature and capacity <EUT No.2>

Table 2-11 shows the result of the difference while changing the airflow setting at the target of 25% heat load of the rated cooling capacity of < EUT No.2 > using < Calorimeter No.1 >. Figures 2-16 and 2-17 show the operating states. The temperature setting of the remote control was different because the indoor temperature must be approached at 27°C.

Table 2-11 Comparison between airflow settings, load factor 25% in cooling, < EUT No.2 >

＜EUT No.2＞	Cooling Load factor 25% (Set temp.)	
Air flow setting	High (28.5)	Automatic (28)
Heat load(W)	792	763
Power consumption(W)	112	110
EER	7.07	6.93
Indoor dry bulb(°C)	26.98	27.29
Indoor wet bulb(°C)	17.50	17.63
Outdoor dry bulb(°C)	26.00	26.00
Outdoor wet bulb(°C)	17.30	17.25
Indoor temperature	Steady state	Steady state

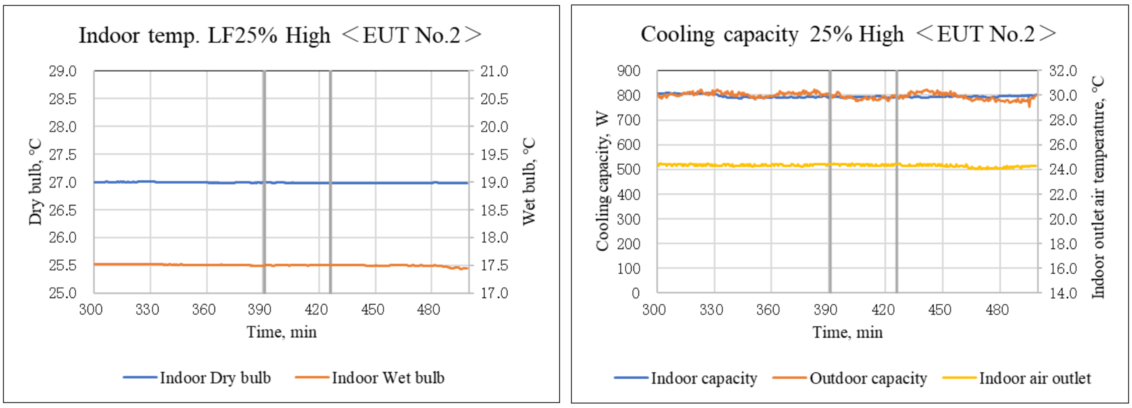

Fig. 2-16 Cooling operation, load factor 25%, airflow High, indoor air temperature, and capacity < EUT No.2 >

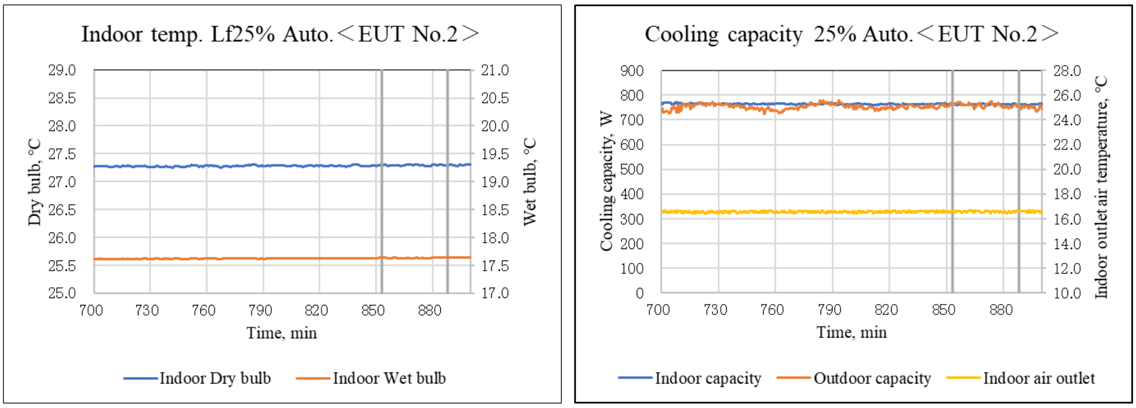

Fig. 2-17 Cooling operation, load factor 25%, airflow Automatic, indoor air temperature, and capacity < EUT No.2 >

< EUT No.2 > was operated steadily at loads of 50 and 25% of the rated cooling capacity. The operating characteristics were different from < EUT No.1 >, and we considered that this difference was affected by the control characteristics of the EUT to get the indoor room temperature to the target. Furthermore, we attempted to reduce the load until the ON/OFF state of the compressor appeared.

Table 2-12 shows the results of studying the difference by changing the airflow setting at the target of 15% heat load of the rated cooling capacity of < EUT No.2 > using < Calorimeter No.1 >. Figures 2-18 and 2-19 show the operating states.

< EUT No.2 > was running under the ON/OFF cycle of the compressor at a heat load of 15% of the rated cooling capacity and that one cycle time varied depending on the airflow setting.

Table 2-12 Comparison between airflow settings, load factor 15% in cooling, < EUT No.2 >

＜EUT No.2＞	Cooling Load factor 15%（Set temp.29）	
Air flow setting	High	Automatic
Heat load(W)	394	417
Power consumption(W)	54	64
EER	7.30	6.52
Indoor dry bulb(°C)	26.78	26.79
Indoor wet bulb(°C)	18.18	18.10
Outdoor dry bulb(°C)	24.79	24.79
Outdoor wet bulb(°C)	16.11	16.11
Compressor state	ON/OFF	ON/OFF
One cycle period (min)	20.0	33.0

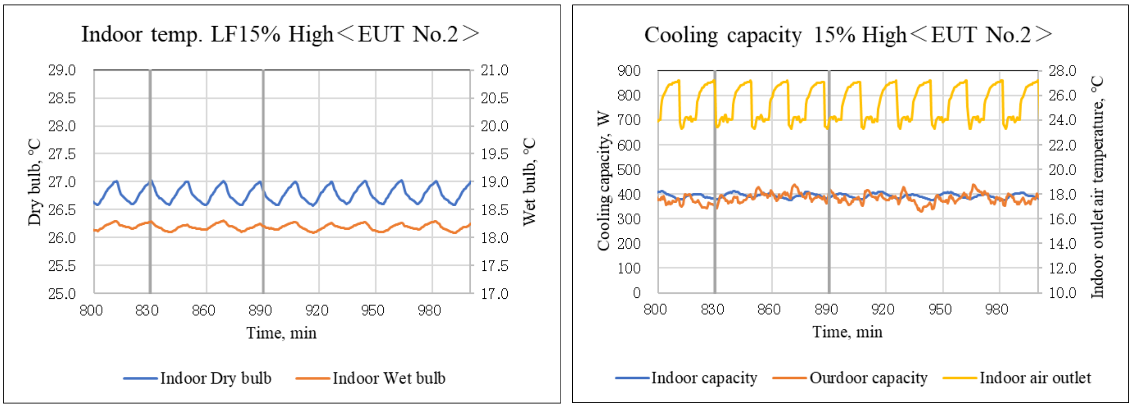

Fig. 2-18 Cooling operation, load factor 15%, airflow High, indoor air temperature and capacity <EUT No.2>

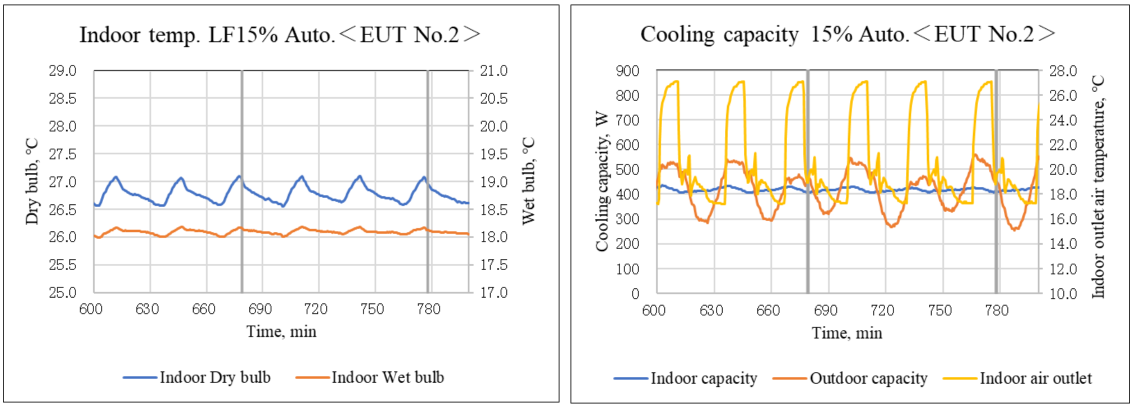

Fig. 2-19 Cooling operation, load factor 15%, airflow Automatic, indoor air temperature and capacity < EUT No.2 >

Table 2-13 shows the heat load test results of < EUT No.2 > with the different airflow settings in the cooling operation using < Calorimeter No.1 >. The input heat loads were adjusted based on the JIS standard test results added to Table 2-13 as a reference. The temperature control is nearly in a steady state, as shown in Figs. 2-20 and 2-21.

Table 2-13 Comparison between airflow settings, load factor 100％ in Heating, <EUT No.2>

＜EUT No.2＞	Heating operation Full load 100%（Temperature setting 18.5）		
Air flow setting	High	Automatic	(※reference) JIS
Heat load(W)	3,684	3,725	3,741
Power consumption(W)	804	906	826
COP	4.59	4.11	4.53
Indoor dry bulb(°C)	19.66	20.14	20.01
Indoor wet bulb(°C)	14.05	12.57	14.72
Outdoor dry bulb(°C)	6.99	6.99	7.00
Outdoor wet bulb(°C)	6.00	6.01	6.00
Indoor temperature	Steady state	Steady state	Steady state

In the heating operation, we observed that the indoor temperature was slightly warmer than the temperature setting on the remote control. Therefore, we changed the temperature setting on the remote control to 18.5°C to enable the indoor temperature to reach 20°C, which was the JIS heating standard condition. From the figures, we observed that the operating state was stable around the rated heating capacity.

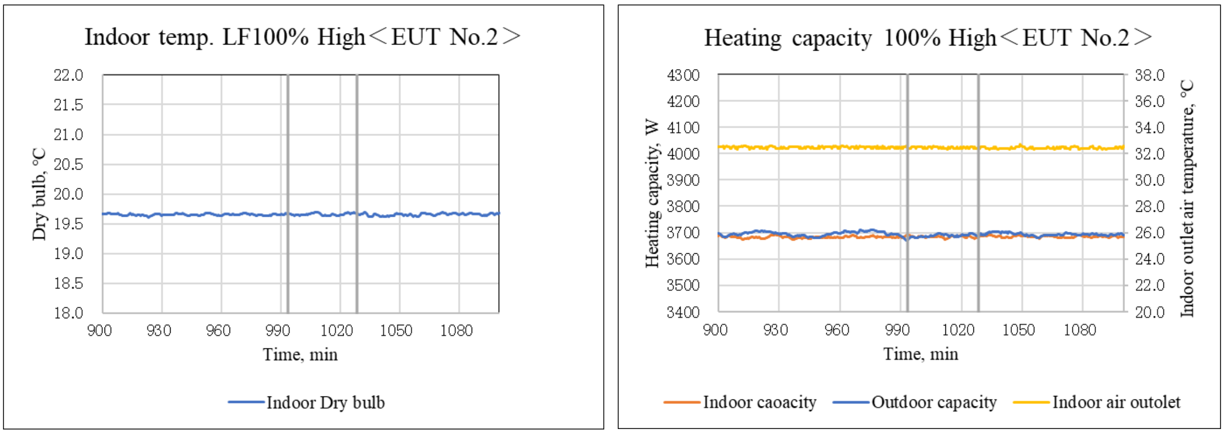

Fig. 2-20 Heating operation, load factor 100%, airflow High, indoor air temperature and capacity <EUT No.2>

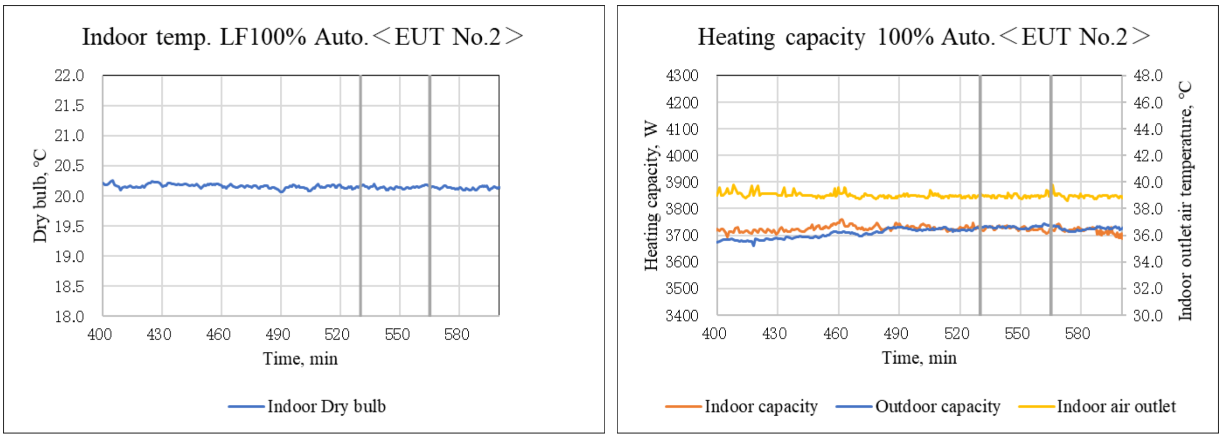

Fig. 2-21 Heating operation, load factor 100%, airflow Automatic, indoor air temperature and capacity <EUT No.2>

Table 2-14 shows the result of the difference while changing the airflow setting at the target of 50% heat load of the rated heating capacity of < EUT No.2 > using < Calorimeter No.1 >. Figures 2-22 and 2-23 show the operating states.

Table 2-14 Comparison between airflow settings, load factor 50% in Heating, <EUT No.2>

＜EUT No.2＞	Heating Load factor 50%（Set temp.18.5）	
Air flow setting	High	Automatic
Heat load(W)	1,873	1,884
Power consumption(W)	268	271
COP	6.99	6.93
Indoor dry bulb(°C)	19.73	20.00
Indoor wet bulb(°C)	14.33	14.61
Outdoor dry bulb(°C)	11.99	11.99
Outdoor wet bulb(°C)	10.33	10.33
Indoor temperature	Steady state	Steady state

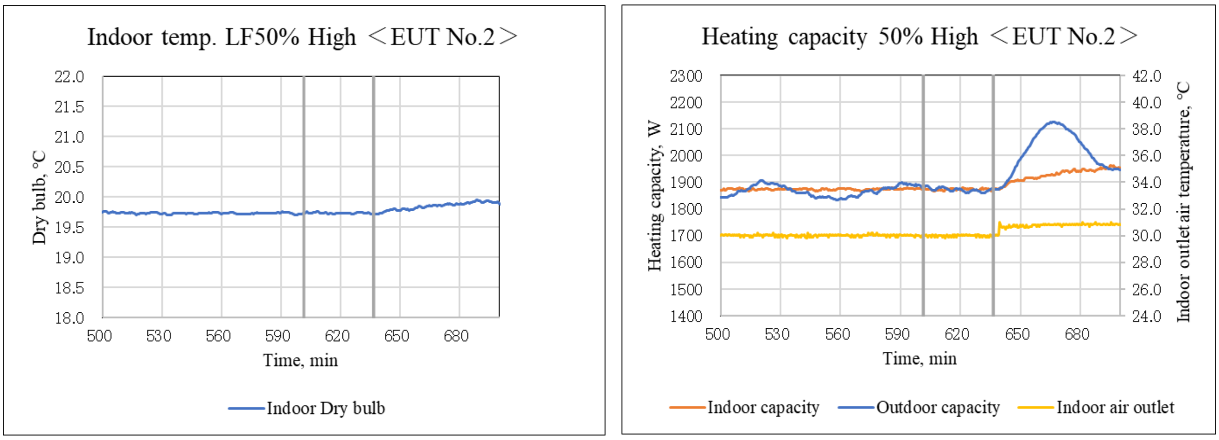

Fig. 2-22 Heating operation, load factor 50%, airflow High, indoor air temperature and capacity < EUT No.2 >

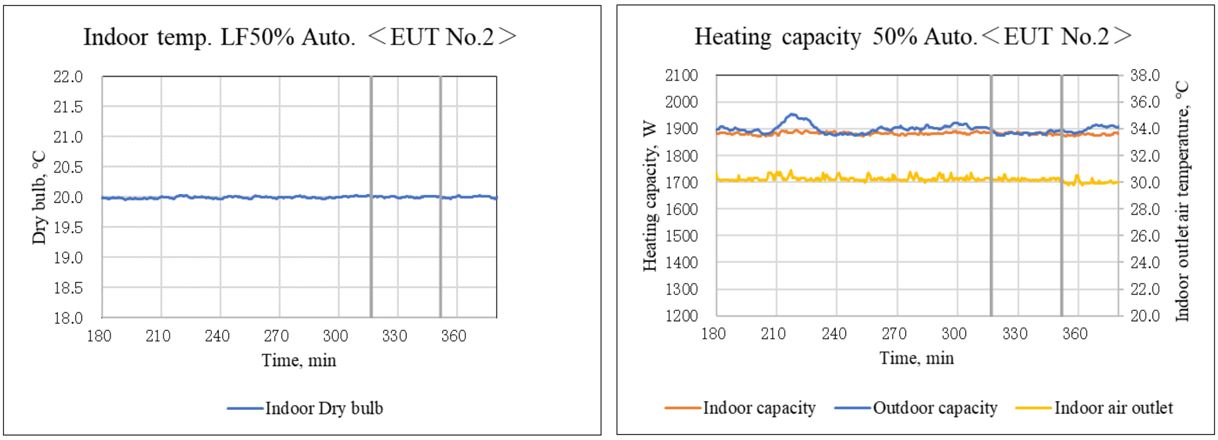

Fig. 2-23 Heating operation, load factor 50%, airflow Automatic, indoor air temperature and capacity < EUT No.2 >

Table 2-15 shows the result of the difference while changing the airflow setting at the target of 25% heat load of the rated heating capacity of < EUT No.2 > using < Calorimeter No.1 >. Figures 2-24 and 2-25 show the operating states.

Table 2-15 Comparison between airflow settings, load factor 25% in Heating, <EUT No.2>

＜EUT No.2＞	Heating Load factor 25% (Set temp.18.5)	
Air flow setting	High	Automatic
Heat load(W)	936	966
Power consumption(W)	128	132
COP	7.31	7.32
Indoor dry bulb(°C)	20.00	20.00
Indoor wet bulb(°C)	14.14	14.70
Outdoor dry bulb(°C)	14.50	14.50
Outdoor wet bulb(°C)	13.20	13.20
Indoor temperature	Steady state	Steady state

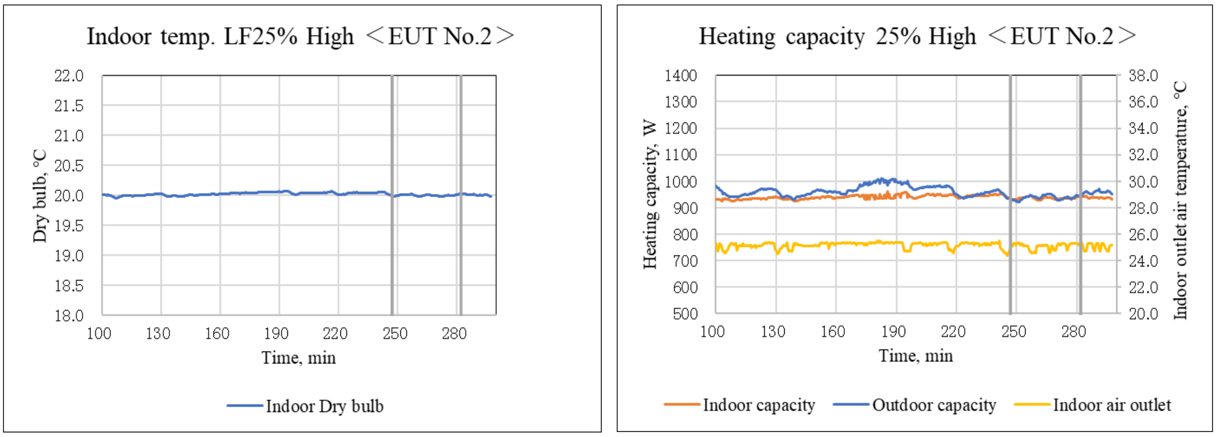

Fig. 2-24 Heating operation, load factor 25%, airflow High, indoor air temperature and capacity < EUT No.2 >

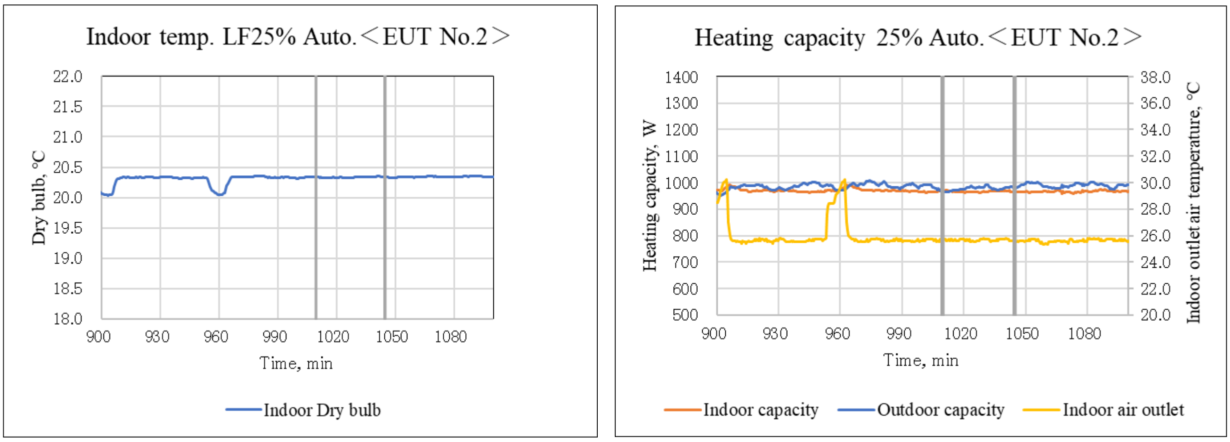

Fig. 2-25 Heating operation, load factor 25%, airflow Automatic, indoor air temperature and capacity < EUT No.2 >

< EUT No.2 > performed steady operation up to a 25% load in the heating and cooling operations. Therefore, to check the ON/OFF operation of the compressor, we reduced the input load further and confirmed the operating state.

Table 2-16 shows the result of the difference while changing the airflow setting at the target of 15% heat load of the rated heating capacity of < EUT No.2 > using < Calorimeter No.1 >. Figures 2-26 and 2-27 show the operating states.

Table 2-16 Comparison between airflow settings, load factor 15% in Heating, < EUT No.2 >

＜EUT No.2＞	Heating Load factor 15%（Set temp.）	
Air flow setting	High(17.5)	Automatic(18.5)
Heat load(W)	541	565
Power consumption(W)	93	112
COP	5.82	5.04
Indoor dry bulb(°C)	20.64	21.64
Indoor wet bulb(°C)	13.77	14.01
Outdoor dry bulb(°C)	15.51	15.56
Outdoor wet bulb(°C)	14.24	14.16
Compressor state	ON/OFF	Steady state
One cycle period (min)	95.0	-

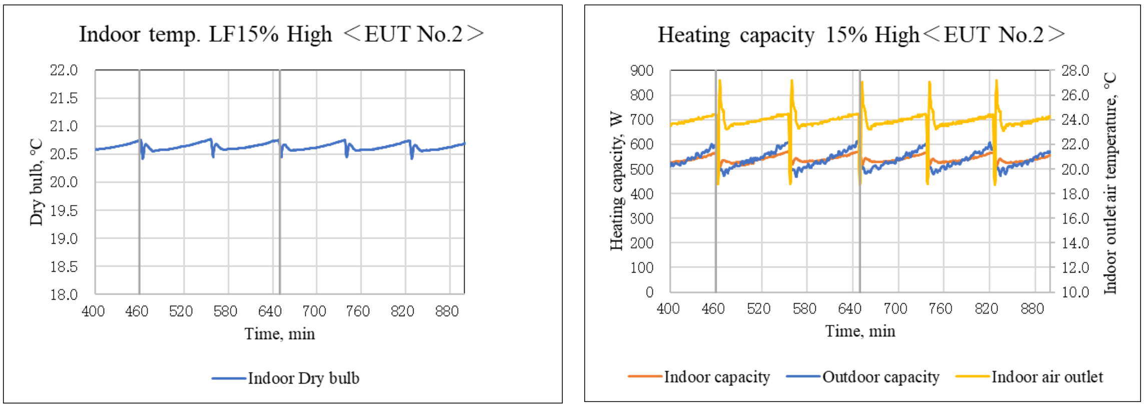

Fig. 2-26 Heating operation, load factor 15%, airflow High, indoor air temperature and capacity <EUT No.2>

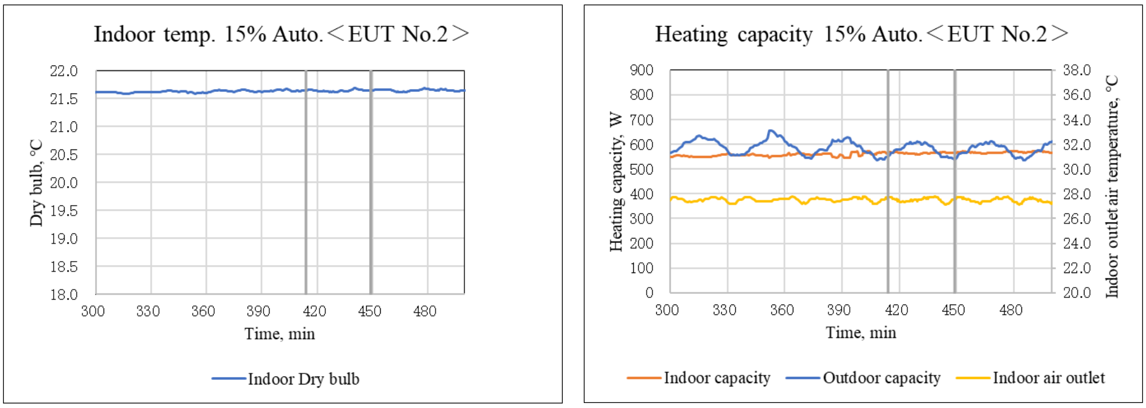

Fig. 2-27 Heating operation, load factor 15%, airflow Automatic, indoor air temperature and capacity <EUT No.2>

At a heat load of 15% of the rated heating capacity, a difference in the operating state depending on the airflow setting was observed. We attempted to reduce the input heat load further to confirm the ON/OFF operation of the compressor. Regardless of the airflow setting, the compressor turned ON/OFF when the heat load was reduced to 10% of the rated heating capacity. The period of one ON/OFF cycle on the intermittent operation was 13 min. with a high airflow setting and 15 min. with automatic operation.

4）Difference analysis depending on EUT

We compared the differences between the characteristics depending on the remote control settings of the EUT using the same balanced room-type calorimeter. We observed that the heat capacity of the equipment affected the results when the EUT was operated in unsteady cycles and intermittent operation. However, the operating characteristics of the EUT in a stable range can be compared. Therefore, we compared the energy efficiency of < EUT No.1 > and < EUT No.2 > measured with the balanced room-type calorimeter < Calorimeter No.1 >.

In the heat load test, the inlet air temperature (dry bulb/wet bulb) of the EUT cannot easily match within the JIS standard tolerance. However, we adjusted the inlet air temperature to be as close to the JIS standard temperature as possible by changing the temperature setting on the remote control. However, the wet-bulb temperature was measured without adjusting if the load factor in the cooling operation was 50% or less and the outlet air temperature of the EUT was higher than the dew point of indoor temperature.

Tables 2-17 and 2-18 show the representative data of the heat load test in the cooling and heating operations of < EUT No.1 > summarized based on the airflow settings and energy efficiency for the load factor at each operating point. To compare the difference between the airflow settings of the EUT in each load factor set for the input heat load target, we manually controlled the test equipment so that the input heat load matched the target heat load as much as possible.

The temperature setting on the remote control at the same load factor in each table was the same setting at high airflow and automatic airflow. However, the indoor temperature was adjusted by the temperature setting to approach the JIS standard conditions (cooling 27°C/heating 20°C) for each load factor. Therefore, the temperature setting during the test was not set at the same temperature. Consequently, the input heat load can be significantly matched and we observed that the difference between the operating characteristics appeared.

Table 2-17 Comparison between airflow settings in cooling < EUT No.1 >

Indoor average temperature（Dry bulb/Wet bulb）Cooling ＜EUT No.1＞						
Airflow setting	High			Automatic		
Load factor %	Heat load(W)	Indoor temp.(°C)	EER	Heat load(W)	Indoor temp(°C)	EER
100(2.8kW)	-	-/-	-	2,809	26.74/18.55	3.09
50(1.4kW)	1,414	26.73/18.72	6.63	1,382	27.34/19.05	5.16
25(0.7kW)	705	26.73/17.77	6.18	713	26.69/17.24	6.09

Table 2-18 Comparison between airflow settings in heating < EUT No.1 >

Indoor average temperature（Dry bulb）Heating ＜EUT No.1＞						
Airflow setting	High			Automatic		
Load factor %	Heat load(W)	Indoor temp.(°C)	COP	Heat load(W)	Indoor temp(°C)	COP
100(3.6kW)	3,600	21.61	3.37	3,600	19.55	3.08
50(1.8kW)	1,901	19.92	5.89	1,875	19.88	4.77
25(0.9kW)	880	21.78	5.30	879	21.78	4.94

Figure 2-28 compares energy efficiency with the load factor on the horizontal axis. Differences were observed in the operating characteristics depending on the airflow setting.

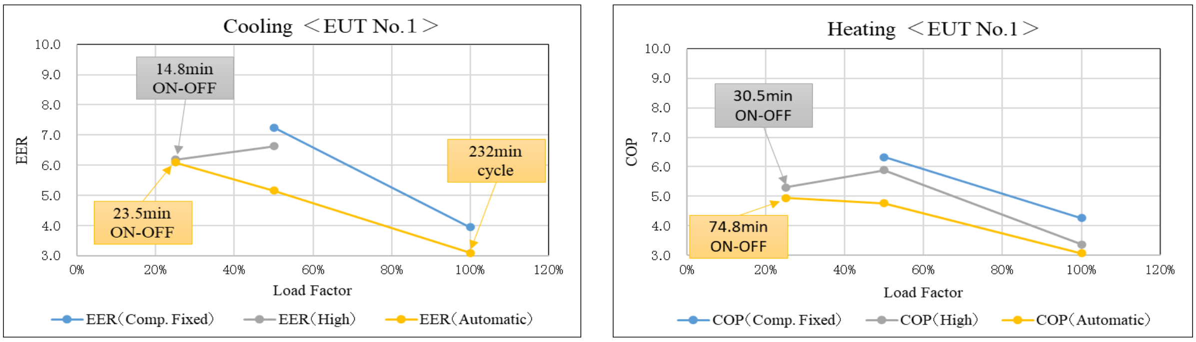

Fig. 2-28 Energy efficiency comparison <EUI No.1>

Tables 2-19 and 2-20 show the representative data of the heat load test in the cooling and heating operations of < EUT No.2 > at each operating point, summarized based on the airflow settings and energy efficiency for the load factor. Owing to the manual adjustment of the input heat load, a difference was observed between the heat loads from 0.5 to 5%. Furthermore, approaching the heat load to target load was challenging.

Because the indoor temperature was adjusted by the temperature setting on the remote control, matching the JIS standard conditions exactly was challenging. However, we could conduct tests for dry- and wet-bulb temperature for a range of approximately ±0.3 for dry- and wet bulb-temperatures, respectively. However, in the range where the load factor was small during the cooling operation, because the outlet air temperature of the EUT was higher than the dew point, the wet-bulb temperature should not be controlled to maintain a stable input heat load in the range such that the cooling capacity was not affected by the wet-bulb.

Table 2-19 Comparison between airflow settings in cooling < EUT No.2 >

Indoor average temperature（Dry bulb/Wet bulb）Cooling ＜EUT No.2＞						
Airflow setting	High			Automatic		
Load factor %	Heat load(W)	Indoor temp.(℃)	EER	Heat load(W)	Indoor temp.(℃)	EER
100(2.8kW)	2,906	26.82/18.87	3.86	2,892	28.21/19.11	3.86
50(1.4kW)	1,423	27.32/19.17	8.37	1,501	26.69/18.71	6.44
25(0.7kW)	792	26.98/17.50	7.07	763	27.29/17.63	6.93
15(0.42kW)	394	26.78/18.18	7.30	417	26.79/18.10	6.52
10(0.28kW)	282	26.80/17.86	7.62	280	26.72/17.85	6.36

Table 2-20 Comparison between airflow settings in heating < EUT No.2 >

Indoor average temperature（Dry bulb）Heating ＜EUT No.2＞						
Airflow setting	High			Automatic		
Load factor %	Heat load(W)	Indoor temp.(℃)	COP	Heat load(W)	Indoor temp.(℃)	COP
100(3.6kW)	3,684	19.66	4.59	3,725	20.14	4.11
50(1.8kW)	1,873	19.73	6.99	1,884	20.00	6.94
25(0.9kW)	936	20.00	7.31	966	20.33	7.32
15(0.54kW)	541	20.64	5.82	565	21.64	5.04
10(0.36kW)	345	20.73	4.26	325	20.75	4.01

Figure 2-29 compares the energy efficiency with the load factor. Differences were observed in the operating characteristics depending on the airflow setting. In particular, a difference was observed in the operating characteristics between cooling and heating under intermittent operation in the range of lower load factors.

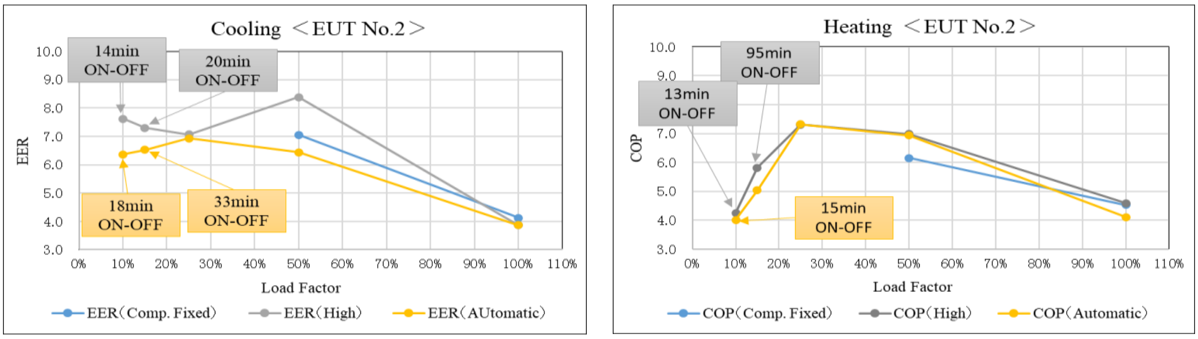

Fig. 2-29 Energy efficiency comparison <EUI No.2>

5）Results and summary

In heat load tests using a balanced room-type calorimeter, the heat capacity of the test equipment affected the test results when unsteady cycles of indoor temperature and compressor ON/OFF cycle appeared owing to the control characteristics of the EUT. Therefore, the issue of quantitative evaluation remains, and this issue cannot be solved at present. The issue depends on the test equipment. However, if it can be solved in the near future, the next crucial aspect is the setting of conditions on the side of the subject of evaluation, which is the best setting for the EUT operation.

Various operating patterns are available on the market. However, after determining the operating mode (cooling/heating), then, the combinations of temperature setting, airflow rate and wind direction are selected. In this study, a relative comparison was executed by a heat load test with different EUT airflow rates. The conclusions are as follows:

A) The airflow setting affects the test results and it is a crucial factor in the evaluation because a difference is present in the characteristics of the temperature control between the maximum air volume of the EUT and the air flow rate selected most practically as the operation setting.

B) Due to the difference in the indoor temperature distribution between the actual installation situation on the market and the installation situation in the test equipment, and the differing relationships between the room temperature control of the EUT and the temperature setting of the remote control, we must change the temperature setting on the remote control several times to adjust to the measurement conditions.

C) A relative evaluation is possible if the room temperature is controlled steadily by the EUT. Although, accurate temperature conditions cannot be easily obtained, as in the JIS standard test, it should be considered a test for evaluating the overall operating characteristics.

D) The manual load adjustment performed in this study can be automated. However, indoor temperature control is performed by the ETU, and the indoor temperature state is determined by the control specification of the EUT. Therefore, the indoor temperature under the JIS standard conditions cannot be easily obtained.

2.4.3 Possibility of heat load test with an air enthalpy test device

To study how to conduct the heat load test and to investigate how to measure the performance without fixing the compressor frequency using an air enthalpy test device, we have conducted a study to determine if there is a method that can be conducted efficiently, as the heat load test with a balanced room-type calorimeter takes a lot time.

Assuming the difference between the temperature setting of the EUT and the inlet air temperature as a parameter, we compared the performance of the EUT that was operated by remote control only using the air enthalpy test device < Calorimeter No.3 >. The air enthalpy test device used in this study is standard equipment that uses a direct expansion refrigerator as a cooling device for room-temperature control. It cannot be fixed on the cooling capacity for room-temperature control, such as a balanced room-type calorimeter. Therefore, although the amount of heat load input into the equipment is unknown, we evaluated the enthalpy difference between the inlet and outlet airs as the load consumed by the EUT while operating under certain conditions without fixing the compressor frequency.

1） Test conditions

Table 2-21 shows the condition settings for the EUT and test equipment. The EUT was operated without fixing the compressor frequency, and the dry- and wet-bulb temperatures of the inlet air were adjusted by the temperature controller of the test equipment.

Table 2-21 Test conditions with air enthalpy measuring equipment

＜EUT No.2＞	Indoor temperature condition	Outdoor temperature condition
compressor : non-fixed frequency	controlled by test equipment	controlled by test equipment

Various operating patterns are conceivable, even when the EUT is operated without fixing the compressor frequency using an air enthalpy test device. First, to consider the effects of the characteristics of the test equipment, the setting conditions on EUT were determined only by the difference between the temperature setting of the remote control and the inlet air temperature of the EUT. The airflow rate was set to a high volume, and the other settings were not changed. Tests were conducted to evaluate the validity of this difference as a parameter.

2） Tests results of cooling operation

Table 2-22 shows the test method and the procedure for the cooling operation. We considered the running state of the EUT and room temperature stability with the difference between the temperature setting of the EUT and inlet air temperature as a parameter.

Table 2-22 Procedure of air enthalpy in cooling operation

Temperature setting	27℃
Indoor inlet air temperature	｜inlet air temperature－temperature setting｜used as a parameterand and varied between 0 and 3 (deg) as a guide. （Wet bulb : adjusted to relatiive humidity of standard condition）
Outdoor temperature	Dry bulb 35℃ ／ Wet bulb 24℃
Capasity mesurement	Measuring air enthalpy (by integration if the indoor temperature fluctuates)

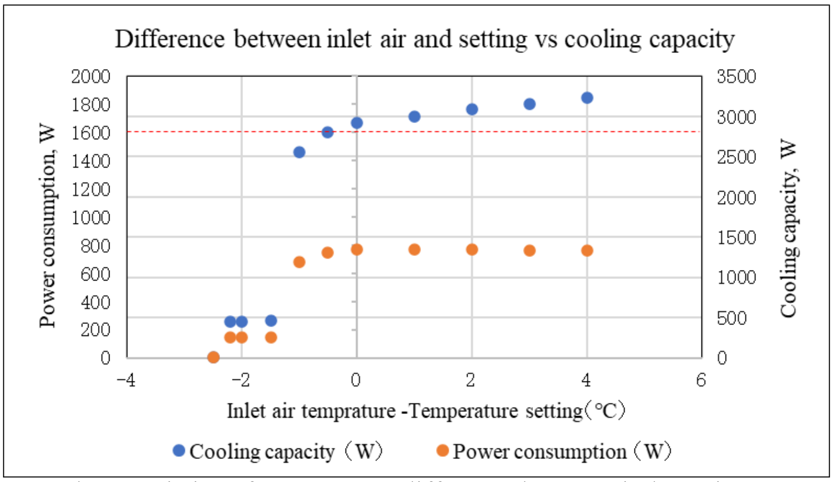

Fig. 2-30 Characteristics of temperature difference between indoor air temperature and setting vs. cooling capacity, airflow High

Figure 2-30 shows the results of the performance characteristics of < EUT No.2 > in the cooling mode. Even if the inlet air temperature of the EUT was below the temperature setting of the remote control, the cooling capacity was near the rated capacity (red dashed line in the figure). The cooling capacity did not reduce remarkably unless the inlet air temperature was lower than the temperature setting by 1.5℃ or more. However, if the inlet air temperature minus setting of the remote control was higher than -0.5 ℃ or more, the EUT was running near or above the rated capacity.

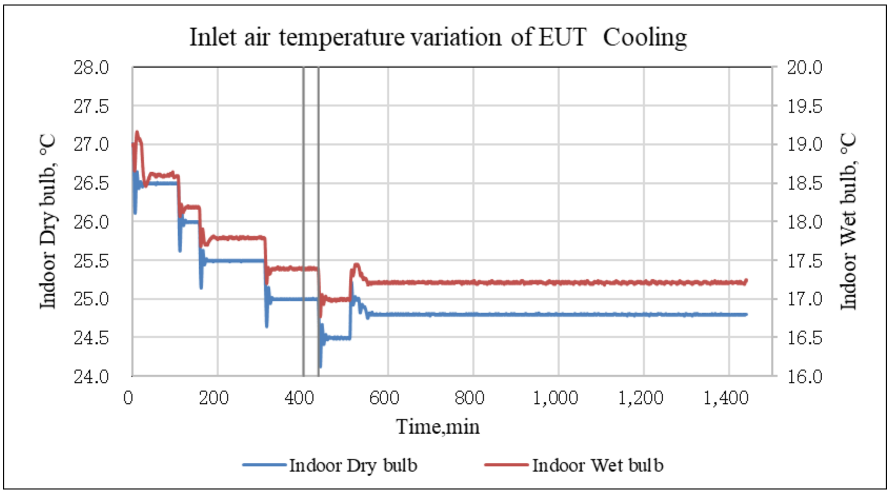

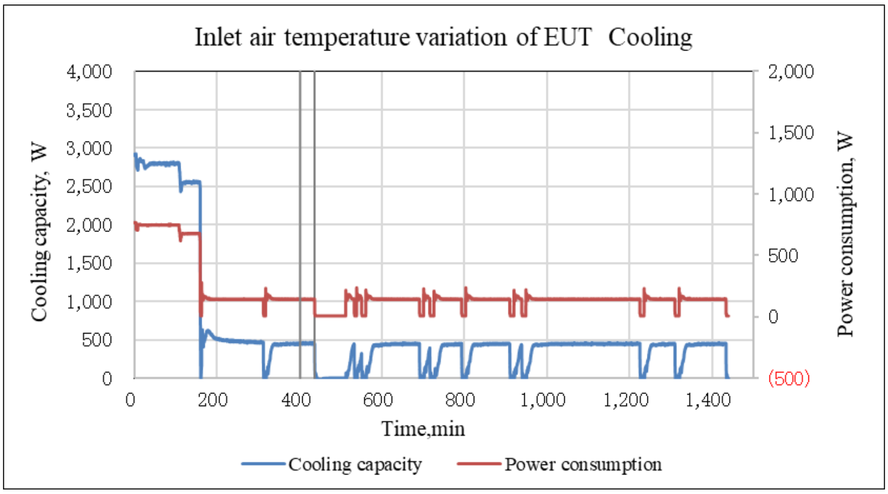

Fig. 2-31 Characteristics of indoor air temperature variation vs cooling capacity, airflow High

Figure 2-31 shows the operating state when the inlet air temperature of the EUT was lowered in increments of 0.5 ℃ from the temperature setting (27 °C) of the remote control. The EUT stopped when the inlet air temperature was lowered to 24.5 °C. In addition, the cooling operation was restarted by raising the inlet air temperature to 24.8 °C. The cooling capacity between | | in the figure was 454 W, and the power consumption was 144 W, which was considered to be near the minimum cooling capacity of the EUT. Based on the results, the following conclusion were drawn:

A) The EUT is in steady operation up to a temperature difference of -2 ℃, and maintains a steady state in terms of room temperature control.
B) Because the control on the test equipment kept the inlet air temperature constant, the difference between the setting of the remote control and inlet air temperature of the EUT was always maintained.
C) Because the difference between the temperature setting of the remote control and inlet air temperature does not change in the control of the EUT, the EUT is operated by continuously recognizing the lack of capacity or excess capacity.
D) The difference between the inlet air temperature of the EUT and temperature setting is adjusted in increments of 0.5 ℃, However, this adjustment range may have been significantly large. The cooling capacity near the intermediate performance did not appear.

However, EUT was selected as an arbitrary model for testing from the manufacturers, and the results might not be representative. The above conclusions include speculation about the results.

3）Tests results of the heating operation involving defrost

Table 2-23 shows the test method and procedure in heating operation. We intended to consider the running state of the EUT and the room temperature stability the same as in cooling by the difference between the temperature setting of the EUT and the inlet air temperature as parameters.

Table 2-23 Procedure for air enthalpy in heating operation

Indoor inlet air temperature	Dry bulb 20℃ ／ Wet bulb 14.5℃
Temperature setting	｜inlet air temperature－temperature setting｜used as a parameterand and varied between 0 and 3 (deg) as a guide.
Outdoor temperature	Dyr bulb 2℃ ・Wet bulb 1℃ ／ Dry bulb 7℃ ・Wet bulb 6℃
Capasity mesurement	Measuring air enthalpy (by integration if the indoor temperature fluctuates)

Figure 2-32 shows the results of the heating capacity of < EUT No.2 > under the low-temperature heating condition by changing the difference between the temperature setting on the remote control and inlet air temperature.

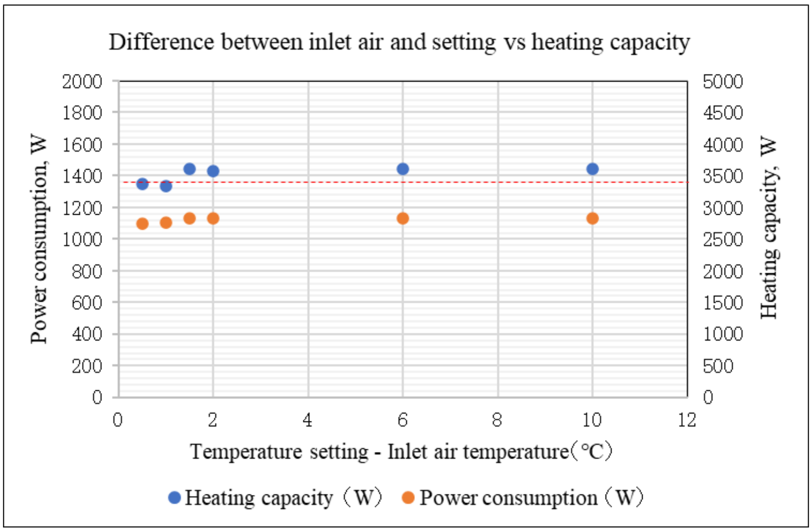

Fig. 2-32 Characteristics of temperature difference between indoor air temperature and setting vs heating capacity with defrosting, airflow High

The heating capacity was measured by setting the inlet air temperature constant and setting the remote control to be higher in the range of +0.5 to 10 ℃. In the range where the temperature was set on the remote control minus the inlet air temperature of the EUT ≥ 1.5 ℃, practically no change was observed in the heating capacity. When the difference was lowered to 1 ℃ or less, the heating capacity decreased, and the defrosting interval increased from 42 to 72 min. However, the decrease in the heating capacity was small, and the heating capacity was near the rated heating low-temperature capacity (red dashed line in the figure) in the region where the temperature setting on the remote control was higher than the inlet air temperature. Based on the results, we have the following considerations:

A) As we observed that the EUT controlled the room temperature slightly higher (slightly warmer) than the temperature setting during the heating operation, as measured by the balanced room-type calorimeter, the same situation was maintained even under low-temperature heating conditions.
B) Because the inlet air temperature of the EUT is automatically controlled to be constant on the test equipment, the difference between the temperature setting on remote control and inlet air temperature is always left in the control of the EUT. Therefore, the heating operation continues as the result of continuously recognizing the insufficient heating capacity on the EUT side.

4）Tests results of heating operations not involving defrost

Figure 2-33 shows the results of the heating capacity of ＜EUT No.2＞ under the heating standard condition by changing the difference between the temperature setting on the remote control and the inlet air temperature.

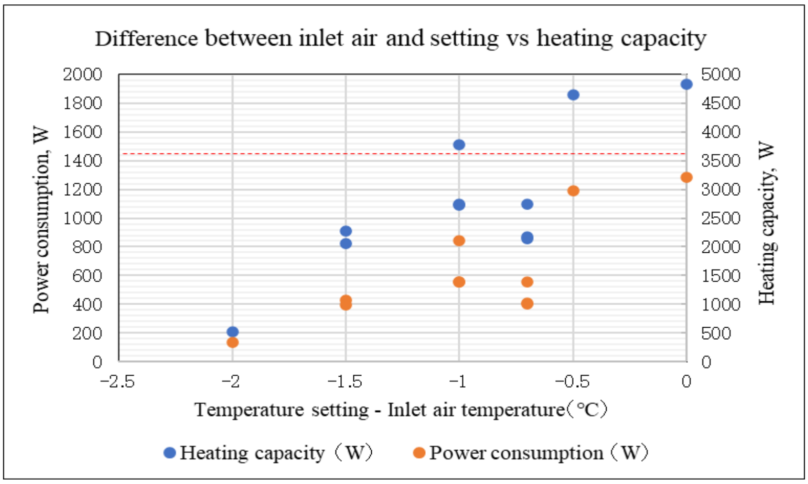

Fig. 2-33 Characteristics of temperature difference between indoor air temperature and setting vs heating capacity without defrosting, airflow High

During the heating operation, the EUT controlled the room temperature slightly higher (slightly warmer) than the temperature setting, as determined by the balanced room-type calorimeter. The heating capacity was measured in the range where the temperature setting on the remote control was lower than the inlet air temperature of the EUT. Therefore, the heating operation was performed until the temperature setting on the remote control minus inlet air temperature of the EUT was ≥ -2 ℃. Based on the results, we have following consideration:

A) The EUT is constantly operating until the temperature setting on the remote control minus inlet air temperature of the EUT is ≥ -1.5 ℃, and the room temperature control is stable.
B) When the temperature setting on the remote control is lowered to a temperature difference of -2 ℃, the heating capacity fluctuates. The EUT seems to be operated in near the minimum heating capacity.
C) Because the inlet air temperature of the EUT is controlled by the controller on the test equipment so that it remains constant, the difference between the temperature setting and inlet air temperature is always left in the room-temperature control of the EUT. However, unlike the cooling operation, an intermediate performance range smaller than the rated standard heating capacity of the red dashed line in the figure appeared because of this temperature difference. This is due to the difference between the room temperature control of the heating and cooling operation.
D) Compared to the cooling operation, a variation in the heating capacity is observed at the same temperature difference. The phenomenon occurs when the air conditioner is restarted, or the temperature setting is changed. However, the cause cannot be estimated.

5）Results and summary

We considered the heat load to air conditioners as the difference between the temperature setting and inlet air temperature of the EUT and evaluated the characteristics of the performance measured by this difference as the variable. Owing to the small number of EUT samples, the results are not representative. However, a correlation was observed between the variable and the cooling or heating capacity. However, we could not quantify the relationship.

The room temperature control of the EUT significantly affects the tests. However, in addition to the characteristics of inverter air conditioners, in which the capacity is adjusted based on the difference between the inlet air temperature and temperature setting of the remote control, if there are various technical specifications of the control, taking into consideration how it is used in the market that are unique to the manufacturer, we should determine the degree of influence from both sides of the test equipment and how to operate the EUT.

In the mathematical performance evaluation method [2-1] developed by Waseda University, an air enthalpy test device was used for measurement, and the indoor inlet air condition was inputted to the EUT by a virtual indoor model that calculates the indoor air condition. Although, the measurement was the same as that measured at a certain equilibrium point in both methods, a large difference was observed between the system and measurement method in this study regarding whether the input heat load was predicted in the temperature control.

For example, in the verification of the cooling operation, when the inlet air temperature is lowered based on the method in this study with respect to the temperature setting of the remote control, EUT stops the cooling operation at a certain temperature (24.5°C in this study), However, it does not resume its operation (Fig. 2-31). Furthermore, in the indoor virtual model mentioned previously, when EUT stops, the indoor air temperature rises in the calculation of the indoor virtual model. Therefore, EUT restarts.

2.4.4 Issues with heat load tests using an air enthalpy test device

1）Test equipment

The air enthalpy test device can measure a wide range of capacities from room air conditioners to multi-split systems for buildings. Although, a few factors can increase the uncertainty value instead of a balanced room-type calorimeter, in terms of equipment, the double structure of test rooms is unnecessary, and a direct expansion refrigerator can be used for cooling. Therefore, equipment costs can be maintained. Thus, the heat load test must be a test method that can be measured with an air enthalpy test device.

2）Identifying Issues and handling

The test equipment used in this study is a typical air enthalpy test device, and the issues from the test results can be extracted as common issues for several kinds of equipment in the country. The primary issues are as follows:

A) Because a direct expansion refrigerator is used for cooling equipment, the input heat load cannot be constant, and the value of the input load is unknown.

B) It is not a test equipment, instead a balanced room-type calorimeter that uses a measurement system that considers heat leakage.

To address the two issues, the target value of the heat load input to the air conditioner must be set and controlled. When the air enthalpy test device, which is made in various sizes, can measure the heat load input into the test equipment, then, we need to build a new test method and concept that ensures that the heat capacity of the test equipment does not affect temperature control of the EUT when using a balanced room-type calorimeter. In this study, the heat load was replaced by the difference between the temperature setting of the EUT and the inlet air temperature. However, the latent heat was not considered. In addition, the relationship between the degree of this difference and cooling or heating capacity cannot be quantitatively evaluated. We will continue our efforts from the perspective of a test method that does not fix the compressor frequency.

References

2-1) JSRAE, https://www.jsrae.or.jp/committee/jisedai_R/jisedai_R.html

3. RESULTS OF THE UNIVERSITY OF TOKYO

3.1 Overview of the environmental test room

The calorimeter for the room air conditioners of the University of Tokyo was installed in the test building, and the temperature in the building could be controlled. The calorimeter can perform tests specified in JIS B8615-1:1999 and JIS C 9612:2005 (hereafter referred to as standard tests) and load tests for room air conditioners with a rated cooling capacity of 4 kW. The capacity of the test machine can be measured by both the air-enthalpy method using a wind tunnel and the heat balance method. Tables 3-1, 3-2, and 3-3 summarize the size, specifications, and types of tests of the calorimeters at the University of Tokyo, respectively.

Table 3-1 Calorimeter dimensions

Indoor unit room	Heat balance type	3 900W×3 450D×2 800H（37.67 m^3）
Outdoor unit room	—	3 900W×3 450D×2 800H（37.67 m^3）

Table 3-2 Calorimeter specifications

Indoor unit room temperature (°C)	20 – 27
Outdoor unit room temperature (°C)	-7 – 35
Applied load (kW)	・Cooling: 0.6 – 4.0 (SHF: 0.6 – 1.0) ・Heating: 0.6 – 5.0
Accuracy (difference between processed heat and applied load heat)	Within ±5% at standard test Within ±10% at load test
Air conditioner capacity measurement method	・Air-enthalpy method ・Heat balance method

Table 3-3 Test types

Load test (Test in which the amount of heat load is controlled under constant temperature and humidity conditions)	・Unsteady test (Cooling/Heating)
Performance test	・Steady test (Cooling/Heating) ・Unsteady test (Defrost test)
Calorimeter test	・Heat balance test ・Heat leakage coefficient test

Figures 3-1 to 3-4 show images of the interior of the calorimeter, outdoor unit test room, indoor unit test room in the test building, and wind channel for measuring the capacity of the test machine.

Fig. 3-1　Calorie meter, outdoor unit test room (left), and indoor unit test room (right)

Fig. 3-2 Outdoor unit test room

Fig. 3-3 Indoor unit test room

Fig. 3-4 Wind receiving chamber in the indoor unit test room

3.2 JIS test results

The test machine used for the JIS test was a general-purpose room air conditioner. The specifications of the test machine are presented in Table 3-4. Two test machines of the same model were purchased from the suppliers at the same time. One was used for the JIS tests at the JATL, and other at the University of Tokyo.

The test machine was installed in the test room based on JIS (B 8615-1:2013). The cooling-rated/intermediate capacity tests and heating-rated/intermediate capacity tests of the JIS tests were conducted under the cooling and heating capacity test conditions shown in Tables 3-5 and 3-6. Each test was conducted at a fixed compressor rotation speed in accordance with the JIS standard (B 8615-1:2013). The capacities were measured using the air enthalpy and heat balance methods. An advanced tachometer FT-7200 made by Ono Sokki was used to measure the compressor rotation speed, and a sensor was attached to the outer wall of the compressor to measure the compressor rotation speed.

Table 3-4 Test machine specifications

<table>
<tr><td colspan="4">Inverter-type room air conditioner</td></tr>
<tr><td rowspan="2">Cooling</td><td colspan="2">Rated capacity (kW)</td><td>2.8</td></tr>
<tr><td colspan="2">Electric power consumption (W)</td><td>800</td></tr>
<tr><td rowspan="4">Heating</td><td rowspan="2">Rated capacity (kW)</td><td>Standard</td><td>3.6</td></tr>
<tr><td>Low temperature</td><td>3.5</td></tr>
<tr><td rowspan="2">Power consumption (W)</td><td>Standard</td><td>910</td></tr>
<tr><td>Low temperature</td><td>1 320</td></tr>
<tr><td colspan="3">Annual performance factor (APF)</td><td>5.8</td></tr>
</table>

Table 3-5 Cooling test conditions

Standard cooling test (JIS B 8615-1:2013)			
Colling	Indoor unit room air	Dry-bulb temperature (°C)	27
		Wet-bulb temperature (°C)	19
	Outdoor unit room air	Dry-bulb temperature (°C)	35
		Wet-bulb temperature (°C)	24
Air temperature outside the environmental test room (°C)		27	

Table 3-6 Heating test conditions

Standard cooling test (JIS B 8615-1:2013)			
Heating	Indoor unit room air	Dry-bulb temperature (°C)	20
		Wet-bulb temperature (°C)	15
	Outdoor unit room air	Dry-bulb temperature (°C)	7
		Wet-bulb temperature (°C)	6
Air temperature outside the environmental test room (°C)		24	

Tables 3-7 and 3-8 show the JIS test results for the rated and half-cooling capacity tests, respectively. For comparison, the test results of the RAC2 (balanced room type calorimeter) of the JATL are shown. In comparison of the rated capacity test, when the catalog value of the cooling capacity was used as the standard, the values of JATL, air-enthalpy method at the University of Tokyo, and heat balance method were 1.038, 1.046, and 1.052, respectively. Electric powers were 0.922, 0.896, and 0.919, and COPs were 1.126, 1.169, and 1.146, respectively. Based on the cooling capacity, power consumption, COP values of the JATL, values obtained by the air-enthalpy method at the University of Tokyo were 1.01, 0.97, and 1.04, respectively. Similarly, the values obtained using the heat-balance method were 1.01, 0.997, and 1.02, respectively. In the JIS test of rated capacity, we observed that the difference between the value determined by the air-enthalpy method at the University of Tokyo and the value obtained by JATL was within ±4%, and that of the heat balance method at the University of Tokyo was within ±2%.

A similar comparison was made in the half-cooling capacity test. Based on the cooling capacity, power consumption, and COP values of the JATL, the values of the air enthalpy method at the University of Tokyo were 1.04, 0.987, and 1.05, respectively. The values obtained using the heat balance method at the University of Tokyo were 1.03, 0.996, and 1.03, respectively. In the half-capacity JIS test, we observed that the difference between the values obtained by the air enthalpy method at the University of Tokyo and values obtained by JATL was within ±5%, and that of the heat balance method was within ±3%.

Tables 3-9 and 3-10 show the JIS test results for the rated and half-heating capacity tests, respectively. In a comparison of the rated capacity test, using the catalog value of the heating capacity as the standard, the values of the JATL, air-enthalpy method at the University of Tokyo, and heat balance method were respectively 1.031, 0.995, and 1.016. Electric powers were 0.956, 0.948, and 0.942, and COPs were 1.078, 1.048, and 1.078, respectively. Based on the cooling capacity, power consumption, COP values of the JATL, values obtained by the air-enthalpy method at the University of Tokyo were 0.965, 0.992, and 0.972, respectively. Similarly, the values obtained using the heat balance method were 0.986, 0.986, and 1.0, respectively. In the JIS test of the rated capacity, we observed that the difference between the value obtained by the air enthalpy method at the University of Tokyo and the value obtained by JATL was within ±3.5%, and that of the heat balance method at the University of Tokyo was within ±1.4%.

A similar comparison was made in the half-cooling capacity test. Based on the cooling capacity, power consumption, COP values of the JATL, and values of the air-enthalpy method at the University of Tokyo were 0.973, 0.989, and 0.984, respectively. The values obtained using the heat balance method at the University of Tokyo were 0.993, 0.981, and 1.013, respectively. In the half-capacity JIS test, we observed that the difference between the values obtained by the air enthalpy method at the University of Tokyo and JATL was within ±2.7%, and that of the heat balance method was within ±1.9%.

Table 3-7 Results of rated cooling capacity test

	Catalog value	JATL (Heat balance method)	This research	
			Air-enthalpy method	Heat balance method
Cooling capacity (W)	2800	2907	2930 (1.01)*	2946 (1.01)
Electricity consumption (W)	800	737.5	717 (0.97)	735 (0.997)
COP	3.5	3.94	4.09 (1.04)	4.01 (1.02)
SHF	–	1.0	1.0	1.0
Blowing temperature from the test machine (°C)	–	17.9	17.1	–
Airflow rate (m^3/min)	–	–	13.9	–
Compressor speed (Hz)	–	–	65.0	65.0

*Values in parentheses indicate the ratio with the JATL value.

Table 3-8 Results of half-cooling capacity test

	JATL (Heat balance method)	This research	
		Air-enthalpy method	Heat balance method
Cooling capacity (W)	1321	1368.8 (1.04)*	1356.1 (1.03)
Electricity consumption (W)	208.1	205.4 (0.987)	207.3 (0.996)
COP	6.35	6.66 (1.05)	6.54 (1.03)
SHF	1.0	1.0	1.0
Blowing temperature from the test machine (°C)	22.1	21.4	–
Airflow rate (m^3/min)	–	11.5	–
Compressor speed (Hz)	–	23.9	23.9

*Values in parentheses indicate the ratio with the JATL value.

Table 3-9 Results of heating rated capacity test

	Catalog value	JATL (Heat balance method)	This research	
			Air-enthalpy method	Heat balance method
Heating capacity (W)	3600	3710	3581 (0.965)*	3658.5 (0.986)
Electricity consumption (W)	910	869.5	862.5 (0.992)	856.9 (0.986)
COP	3.96	4.27	4.15 (0.972)	4.27 (1.0)
Blowing temperature from the test machine (°C)	–	32.4	32.9	–
Airflow rate (m^3/min)	–	–	13.6	–
Compressor speed (Hz)	–	–	94.2	94.2

*Values in parentheses indicate the ratio with the JATL value.

Table 3-10 Results of heating half-capacity test

	JATL (Heat balance method)	This research	
		Air-enthalpy method	Heat balance method
Heating capacity (W)	1659	1614.2 (0.973)*	1647.3 (0.993)
Electricity consumption (W)	261.9	259.0 (0.989)	256.9 (0.981)
COP	6.33	6.23 (0.984)	6.41 (1.013)
Blowing temperature from the test machine (°C)	27.3	27.5	–
Airflow rate (m^3/min)	–	10.5	–
Compressor speed (Hz)	–	40.0	40.0

*Values in parentheses indicate the ratio with the JATL value.

The above results are summarized as follows.

1) In the JIS test of the rated and half-cooling capacity, the test results of the heat balance method at the University of Tokyo were within ±3% of the JATL values (air conditioner capacity, power consumption, and COP). The results of the test using the air-enthalpy method at the University of Tokyo differed from the JATL values by within ±5%.
2) In the JIS test for the standard/intermediate heating capacity, the difference between the results of the test by the heat balance method at the University of Tokyo and value of JATL was within ±1.9%. The air enthalpy test results at the University of Tokyo differed from the JATL values within ±3.5%.
3) Comparing the JIS test results for air conditioning using the calorimeter at the University of Tokyo with the JATL values, the difference from JATL was within a few percent, indicating that the accuracy of the calorimeter at the University of Tokyo was sufficiently good.

3.3 Test without fixing compressor rotation speed by the heat balance method

A heating and cooling load test was conducted by the heat balance method without fixing the compressor speed of a room air conditioner. The load test was conducted as follows: Under the dry- and wet-bulb temperature conditions listed in Tables 3-11 and 3-12, the air conditioner was operated after applying a predetermined heat load to the indoor test room. The air conditioner was operated based on the settings of the remote controller and led the room to an equilibrium state. When obtaining the air conditioner capacity, we processed the data when the equilibrium state was reached. The remote controller settings for the load test were set as listed in Table 3-13.

The trend graphs for the rated and half-cooling load tests are shown in Figs. 3-5 and 3-6, respectively. For the rated cooling load test in Fig. 3-5, damped oscillations of the power consumption and compressor rotation speed with a period of approximately 180 min were generated, and the indoor dry- and wet-bulb temperatures oscillated in opposite phases. The equilibrium condition was reached in more than 20 h. At the half-cooling load in Fig. 3-6, the oscillation was dampened in one and a half cycles and reached equilibrium in approximately 4 h.

Table 3-11 Cooling load test conditions

Cooling	Heat load (kW)	2.8 (1.4)*	
	Indoor unit room air	Dry-bulb temperature (°C)	27
		Wet-bulb temperature (°C)	19
	Outdoor unit room air	Dry-bulb temperature (°C)	35
		Wet-bulb temperature (°C)	24
Air temperature outside the environmental test chamber (°C)		25	

Table 3-12 Heating load test conditions

Heating	Heat load (kW)	3.6 (1.9)*	
	Indoor unit room air	Dry-bulb temperature (°C)	20
		Wet-bulb temperature (°C)	15
	Outdoor unit room air	Dry-bulb temperature (°C)	7 (12)
		Wet-bulb temperature (°C)	6 (10.34)
Air temperature outside the environmental test chamber (°C)		20	

*Values in parentheses indicate values of the half-load test.

Table 3-13 Remote control settings

Operation	Cooling/Heating
Airflow mode	Strong
Wind direction (1 – 5)	3
Temperature (°C)	27 (18, 20)*

* Values in parentheses indicate the values for heating operations.

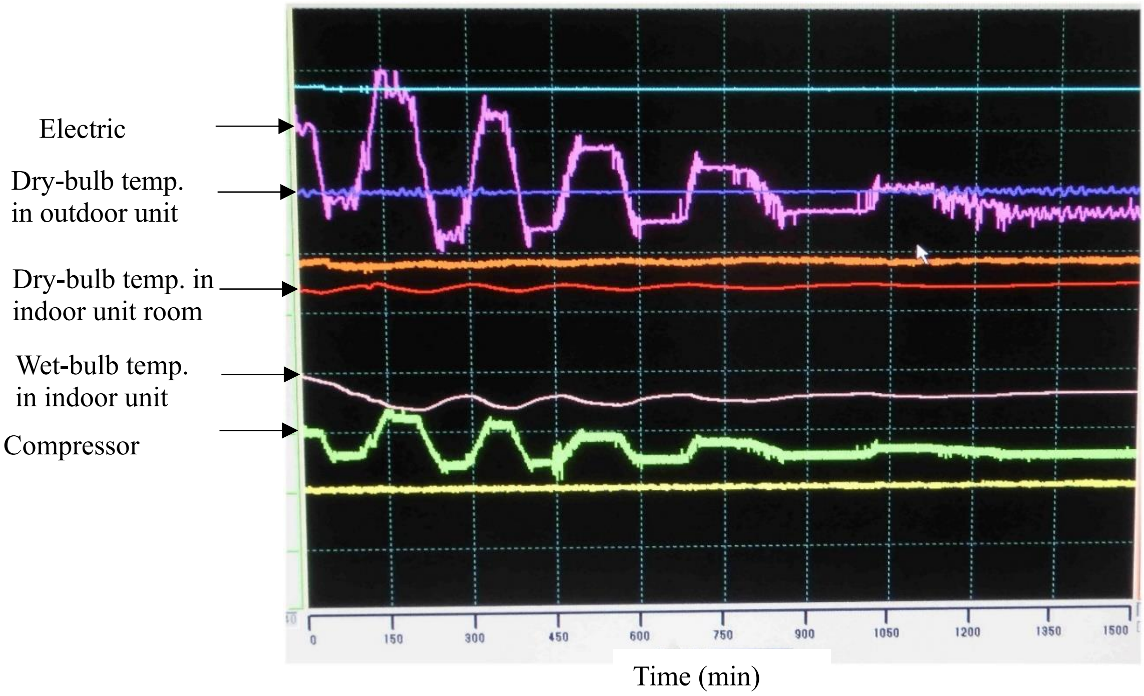

Fig. 3-5 Trend graph of rated cooling load test (2.8 kW)

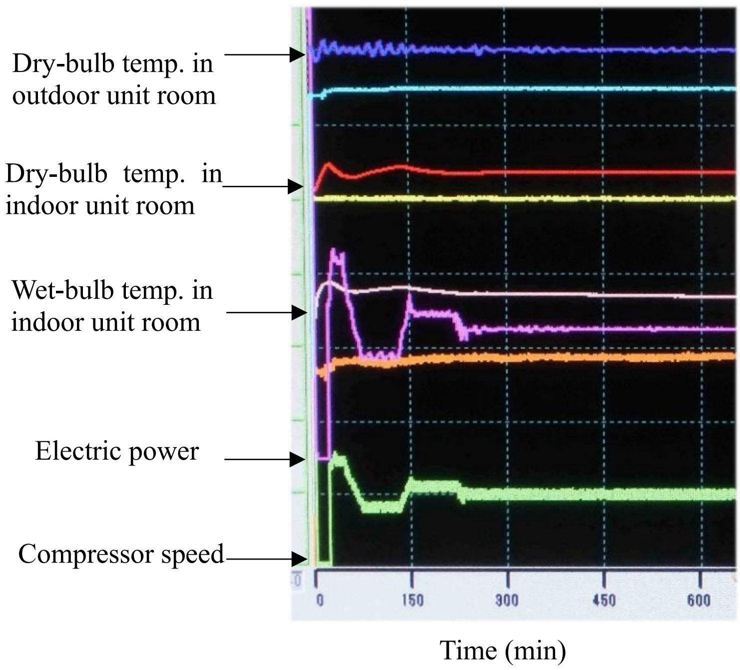

Fig. 3-6 Trend graph of half-cooling load test (1.4 kW)

Tables 3-14 and 3-15 show the rated and half-cooling-load test results. The indoor dry-bulb/wet-bulb (DB/WB) temperatures in Table 3-14 were stable at the temperatures and humidity shown in the table under equilibrium conditions. In addition, while the vibration persisted under the same conditions at JATL, the test at the University of Tokyo reached an equilibrium state after the damping oscillation. In the test conducted by JATL, the wind speed setting by the remote controller was powerful. Based on the cooling capacity, power consumption, and COP of the JATL, the values at the University of Tokyo were 1.042, 0.898, and 1.161, respectively. The half-cooling load test achieved equilibrium state at both JATL and the University of Tokyo. Based on the values of the cooling capacity, power consumption, and COP of the half-cooling load test of JATL, the values at the University of Tokyo were 1.022, 1.352, and 0.757, respectively. In the rated and half-cooling load tests, we observed that the differences between the COP of the University of Tokyo and that of JATL were 16.1 and −35.2%, respectively. The indoor dry-bulb temperature in the equilibrium state was slightly >27 °C in the rated load test and slightly lower in the half-load test.

Tables 3-16 and 3-17 show the standard and half-heating load test results, respectively. No vibrations were observed in the standard and half-heating-load tests. In the standard load test, the values of the University of Tokyo were 1.031, 0.989, and 1.024, respectively, based on the heating capacity, power consumption, and COP values of the JATL. The difference between the values of the University of Tokyo and JATL was within ±3.1%. In the half-heating load test, the values of the University of Tokyo were 1.011, 0.975, and 1.036, respectively, based on the JATL values. Therefore, the difference in COP between the University of Tokyo and JATL was within ±3.6%. The indoor dry-bulb temperature was 1–2 °C higher than the remote controller set temperature.

Table 3-14 Results of rated cooling load test (2.8kW)

	JATL	This study
Heat load (W)	2804	2922 (1.042)*
Electricity consumption (W)	884	794 (0.898)
COP	3.17	3.68 (1.161)
SHF	0.8	1.0
Indoor DB/Wb temperature (°C)	27.9/18.6	27.2/18.0
Airflow rate (m^3/min)	69.7	70.6
State	Cyclic	Stable

*Values in parentheses indicate the ratio with the JATL value.

Table 3-15 Results of half-cooling load test (1.4 kW)

	JATL	This study
Heat load (W)	1414	1444.6 (1.022)*
Electricity consumption (W)	213	287.9 (1.352)
COP	6.63	5.02 (0.757)
SHF	0.99	1.0
Indoor DB/Wb temperature (°C)	26.7/18.7	26.8/18.4
Airflow rate (m^3/min)	22.9	27.9
State	Stable	Stable

*Values in parentheses indicate the ratio with the JATL value.

Table 3-16 Results of standard heating load test (3.6 kW)

	JATL	This study
Heat load (W)	3600	3647 (1.031)*
Electricity consumption (W)	1070	1058 (0.989)
COP	3.37	3.45 (1.024)
Remote control temperature setting (°C)	20	20
Indoor DB/Wb temperature (°C)	21.6/15.9	21.1/16.6
Airflow rate (m^3/min)	89.6	98.4
State	Stable	Stable

*Values in parentheses indicate the ratio with the JATL value.

Table 3-17 Results of half-heating load test (1.9 kW)

	JATL	This study
Heat load (W)	1901	1921 (1.011)*
Electricity consumption (W)	323	315 (0.975)
COP	5.89	6.10 (1.036)
Remote control temperature setting (°C)	18	18
Indoor DB/Wb temperature (°C)	19.9/14.8	19.3/14.5
Airflow rate (m^3/min)	39	42.3
State	Stable	Stable

*Values in parentheses indicate the ratio with the JATL value.

The above results are summarized as follows:

1) Rated- and half-cooling load tests were conducted using the heat balance method without fixing the compressor speed, and the results were compared with those of JATL. Vibration occurred during the rated cooling load test. The differences between the COP values of the University of Tokyo and JATL in the rated and half-cooling load tests were 16.1 and −35.2%, respectively.
2) Standard and half-heating load tests were conducted using the heat balance method without fixing the compressor speed, and the results were compared with JATL results. The differences in the COPs between the University of Tokyo and JATL in the standard and half-heating load tests were within ±3.1 and ±3.6%, respectively.

3.4 Improvement of the air-enthalpy type environmental test room

3.4.1 Overview of environmental test room improvements

The air conditioner test room (calorimeter) installed at the University of Tokyo was capable of both air enthalpy and heat balance measurements. In the air enthalpy measurement, a wind channel was installed in the indoor unit test room, air blown out from the indoor unit was collected, and dry-bulb temperature, wet-bulb temperature, and flow rate of the air were recorded. The enthalpy of the air was calculated from the dry- and wet-bulb temperatures. The performance of the air conditioner can be measured from the difference between the enthalpies of the air in the indoor unit test room, air blown of the indoor unit, and airflow rate. While conducting a performance test with a fixed compressor rotation speed, such as the air conditioner performance test specified in JIS C 9612:2013 (hereafter referred to as the "JIS test"), the COP was calculated by measuring the power consumption and cooling or heating capacity. The air enthalpy measurement method is suitable for tests with a fixed compressor speed and is widely used. Because the air enthalpy measurement system cannot apply a heat load, a load test cannot be performed without fixing the compressor rotation speed. In this study, we improved the operation of the test room to conduct load tests. Figure 3-6 shows an outline of the air enthalpy test room at the University of Tokyo. The environmental test room complies with JIS B 8615-1 with a cooling capacity of 0.6 to 4.0 kW and a heating capacity of 0.6 to 5.0 kW.

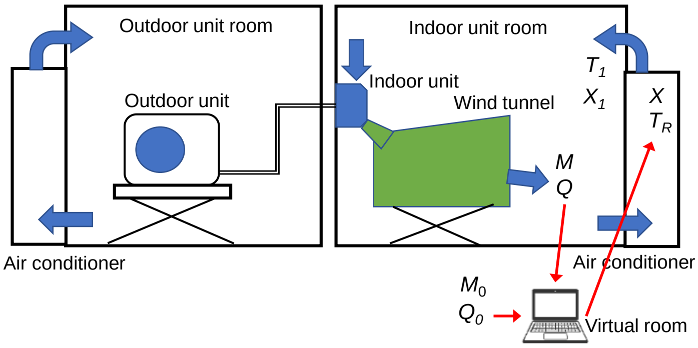

Fig. 3-6 Outline of calorimeter of air enthalpy

3.4.2 Environmental test room control

To conduct a load test in an air enthalpy measurement test room, a virtual air conditioner installation room was considered, and a constant heat load was assumed to be applied to the room. We assumed that an air conditioner was installed in the virtual room, and its performance was measured using a wind channel. Furthermore, the temperature of the virtual room changed based on the difference in the heat load and capacity of the air conditioner. Therefore, the operating software of the test room was modified so that air with the same temperature as the calculated virtual room temperature was blown into the indoor unit room. When such operations were conducted, the heat load of the virtual room and the capacity of the air conditioner were matched, and the temperature of the indoor unit room was stabilized. However, for a stable indoor room temperature unit to approach a specified temperature, the set temperature of the remote controller was adjusted. For humidity control, the amount of moisture in the virtual room was calculated from the difference between the dehumidification load and dehumidification result of the air conditioner, and the humidity of the blown air in the test room was controlled.

A block diagram of the operation method of the air-enthalpy test room is shown in Fig. 3-7. The change in temperature of the virtual room during cooling is expressed by Eq. (3-1).

$$C\frac{dT_R}{dt} = (Q_{C0} - Q_{L0}) - (Q - Q_L) \qquad (3\text{-}1)$$

The change in room temperature T_R in the virtual room with heat capacity C was considered due to the difference between the sensible heat of heat load Q_0 and sensible heat of capacity Q provided by the air conditioner. Q_{L0} is the latent heat load and Q_L is the latent heat capacity provided by the air conditioner. Because the JIS test does not specify the sensible heat ratio of the load, the humidity in the virtual room cannot be controlled. Therefore, in this study, we considered $Q_{L0} = Q_L$, and Eq. (3-2) is obtained.

$$C\frac{dT_R}{dt} = Q_{C0} - Q \tag{3-2}$$

Because no latent heat treatment is performed during the heating operation, the temperature change in the virtual room is given by Eq. (3-3).

$$C\frac{dT_R}{dt} = Q - Q_{H0} \tag{3-3}$$

The change in the absolute humidity X of the air in the virtual room during the cooling operation is calculated from the difference between the required dehumidification amount M_0 and dehumidification amount M of the air conditioner, as expressed by Eq. (3-4).

$$C_M\frac{dX}{dt} = M_0 - M \tag{3-4}$$

As JIS C 9612:2013 has no provisions for latent heat treatment, if we consider $M_0 = M$, the absolute humidity of the air in the virtual room does not change with time and remains constant.

As shown in the block diagram of Fig. 3-7, while calculating the temperature and humidity in the virtual room and specifying the outlet temperature and humidity in the environmental test chamber, depending on the scale and structure of the environmental test room, we can observe a time delay in the changes in the actual indoor room temperature and humidity. Because the time delay in the indoor room temperature was <1 min, no control measures were taken.

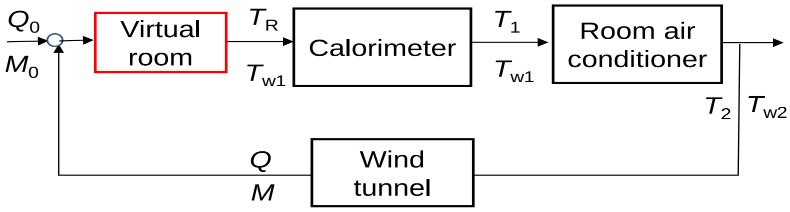

Fig. 3-7 Block diagram of calorimeter

3.5 Static load test method

3.5.1 Test conditions

The test air conditioner is a popular model with a rated cooling capacity of 2.8 kW and a rated heating capacity of 3.6 kW. It has five modes of air volume setting: automatic, strong, medium, weak, and powerful. The powerful mode is used for rapid cooling or heating and is presumed to be the mode used in the JIS tests. When the test air conditioner was installed in a standard 10 tatami room (2.7 m high), the room volume was 49.2 m^{3,} and the heat capacity of the air in the room was only 58 kJ/K. As the actual room is surrounded by walls, floors, and ceilings, the heat capacity of the space that provides the load of the air conditioner is larger than the air heat capacity. The larger the heat capacity, the slower the room temperature change, stabilizing the environmental test room operation. By increasing the heat capacity of the virtual chamber, three calculations were conducted with heat capacities of 200, 400, and 600 kJ/K. A list of test conditions is presented in Table 3-18. The values specified in JIS C 9612:2013 were used for outdoor and indoor air temperature and humidity conditions. In addition, low-temperature heating tests were performed.

Table 3-18 Experimental conditions

Capacity	Airflow mode	C = 200 kJ/K	C = 400 kJ/K	C = 600 kJ/K
Rated capacity	Powerful	○ □	○ □	○ □
	Strong			○ □
	Automatic			○ □
Half capacity	Powerful	○ □	○ □	○ □
	Strong	○ □	○ □	○ □
	Automatic			○ □
25% capacity	Powerful	○	○	○ □
	Strong	○	○	○ □
	Automatic	○	○	○ □

Symbols ○ and □ mean the cooling and heating experiments, respectively.

3.5.2 Influence of the heat capacity of the virtual room

Even if the size of the room where the air conditioner is installed changes, if the heat load and temperature conditions are the same, performance, such as COP, does not change. Therefore, changing the heat capacity of the virtual room affects the stability of the environmental test room operation. However, it does not affect the COP when the heat load and temperature conditions are the same, and stable operation is achieved. In this study, information such as the structure of the virtual room is not necessary, and only the heat capacity is required.

Because the influence of the heat capacity of the virtual room was significant in the half-capacity test, the effect was examined in the half-capacity test of cooling and heating. Table 3-19 shows the results for C = 200–600 kJ/K in the powerful airflow mode of the half-cooling load test, and Table 3-20 shows the results for the strong airflow mode. The controller set temperature T_{set} was adjusted so that the room temperature T_{in} of the indoor unit was 27 °C. However, T_{in} could not be adjusted completely, and the room temperature could not be finely adjusted because the set temperature increment of the remote controller was 1 °C. In the powerful airflow mode, the air volume was 13.7 m^3/min, which is >11.5 m^3/min in the JIS test. However, the COP in the load test was 1.5 to 1.8 smaller than that in the JIS test. Because the compressor speed was low and the power consumption was small, the COP of C = 200 kJ/K was slightly higher than those of the others (C = 400 and 600 kJ/K). In the strong-airflow mode, the air volume was 10 m^3/min, which was smaller than the air volume of 11.5 m^3/min in the JIS test. At C = 200 kJ/K, the compressor became intermittent, whereas at C > 400 kJ/K, the air conditioner became stable. The COP at C = 200 kJ/K increased to 4.33, while the steady-state COP at C = 400 and 600 kJ/K increased to 5.18 and 5.04, respectively. Here, "stable" implies a state in which the compressor speed fluctuates slightly, while it is operating without large fluctuations, and "unstable" implies that the compressor speed vibrates. Intermittent operation (ON-OFF) indicates that the compressor repeatedly starts and stops. The values shown in the tables were averaged over time. In the unstable state and intermittent operation, the three fluctuation cycles were averaged.

Table 3-21 shows the results of C = 200–600 kJ/K in the powerful airflow mode in the half-heating load test, and Table 3-22 shows the results of the strong airflow mode. In the powerful airflow mode, the air volume was 12.5 m^3/min, which was higher than the air volume of 10.5 m^3/min in the JIS test. The COP was greater in the powerful airflow mode than in the strong airflow mode. Both the COPs were smaller than those in the JIS test. In both cases, the increase in C changed from an oscillating state to a damped oscillation, and then to a stable state while increasing the fluctuation period. The attenuation of vibration led to a decrease in power consumption and an increase in COP. Vibration was suppressed when C = 600 kJ/K.

Table 3-19 Effect of heat capacity for powerful airflow mode at half cooling capacity operation

Test mode	JIS test	Load test		
Heat capacity (kJ/K)	-	200	400	600
Cooling load (W)	1368	1367	1355	1386
Power consumption (W)	205	265	277	285
COP	6.66	5.15	4.89	4.86
SHF	0.971	0.95	1.03	1.02
Airflow rate (m^3/min)	11.5	13.7	13.7	13.6
Indoor DB temp. (°C)	27.0	26.6	27.6	27.6
Indoor WB temp. (°C)	19.0	19.0	19.2	19.6
Outdoor DB temp. (°C)	35.0	35.0	35.0	35.0
Outdoor WB temp. (°C)	24.1	24.0	24.0	24.1
Compressor speed (Hz)	24	24	26	26
Controller set temp. (°C)	-	27	27	27
Airflow mode	-	Powerful	Powerful	Powerful
State	Stable	Stable	Stable	Stable

Table 3-20 Effect of heat capacity for strong airflow mode at half cooling capacity operation

Test mode	JIS test	Load test		
Heat capacity (kJ/K)	-	200	400	600
Cooling load (W)	1368	1349	1373	1353
Power consumption (W)	205	312	265	269
COP	6.66	4.33	5.18	5.04
SHF	0.971	0.95	0.96	1.01
Airflow rate (m^3/min)	11.5	9.8	10.2	9.9
Indoor DB temp. (°C)	27.0	26.7	26.8	27.1
Indoor WB temp. (°C)	19.0	20.6	19.8	19.7
Outdoor DB temp. (°C)	35.0	35.0	35.0	35.0
Outdoor WB temp. (°C)	24.1	24.0	24.0	24.0
Compressor speed (Hz)	24	31	26	26
Controller set temp. (°C)	-	26	26	26
Airflow mode	-	Strong	Strong	Strong
State	Stable	On-off	Stable	Stable

Table 3-21 Effect of heat capacity for powerful airflow mode at half heating capacity operation

Test mode	JIS test	Load test		
Heat capacity (kJ/K)	-	200	400	600
Heating load (W)	1614	1651	1650	1628
Power consumption (W)	259	323	319	313
COP	6.23	5.11	5.17	5.19
Airflow rate (m^3/min)	10.5	12.5	12.5	12.5
Indoor DB temp. (°C)	20.0	20.5	20.4	20.3
Indoor WB temp. (°C)	15.0	15.2	15.1	15.1
Outdoor DB temp. (°C)	7.0	7.0	7.0	7.0
Outdoor WB temp. (°C)	6.0	6.0	6.0	6.0
Compressor speed (Hz)	40.0	42	43	42
Controller set temp. (°C)	-	19	19	19
Airflow mode	-	Powerful	Powerful	Powerful
State	Stable	Unstable	Unstable	Stable

Table 3-22 Effect of heat capacity for strong airflow mode at half heating capacity operation

Test mode	JIS test	Load test		
Heat capacity (kJ/K)	-	200	400	600
Heating load (W)	1614	1657	1659	1609
Power consumption (W)	259	346	333	320
COP	6.23	4.79	4.98	5.02
Airflow rate (m^3/min)	10.5	8.0	8.0	8.6
Indoor DB temp. (°C)	20.0	20.6	19.4	20.1
Indoor WB temp. (°C)	15.0	15.2	14.8	15.1
Outdoor DB temp. (°C)	7.0	7.0	7.0	7.0
Outdoor WB temp. (°C)	6.0	6.0	6.0	6.0
Compressor speed (Hz)	40.0	44	44	42
Controller set temp. (°C)	-	20	19	19
Airflow mode	-	Strong	Strong	Strong
State	Stable	Unstable	Unstable	Stable

3.5.3 Effect of airflow setting

For cooling, the relationship between the airflow mode and airflow rate is shown in Fig. 3-8, and the relationship between the airflow mode and COP is shown in Fig. 3-9 with the load as a parameter. The airflow rate decreased in the order of the powerful, strong, and automatic airflow modes. The airflow rate of the JIS test at the rated heat load matched that of the powerful airflow mode. However, the half JIS test had an airflow rate in between the powerful and strong modes. Except for the rated load, the relationship between the COP and airflow mode was unclear. At half the load, COP was high, followed by a 25% load. At the rated load, the decrease in airflow coincided with a decrease in COP. The difference in COP between the rated capacity of the JIS test and the load test was small. However, the COP of the half-capacity load test was considerably lower than that of the JIS test.

For heating, Fig. 3-10 shows the relationship between the airflow mode and airflow rate, and Fig. 3-11 shows the relationship between the airflow mode and COP. The airflow rate decreased in the order of the powerful, strong, and automatic airflow modes. The airflow rates in the rated and half-capacity tests of the JIS tests were slightly smaller than in the cooling tests. The COPs of the half and 25% load tests were practically the same in the powerful and strong airflow modes, a decrease in the automatic airflow mode was observed (Fig. 3-11). The COPs of the rated loads in the strong and automatic airflow modes were considerably lower than those in the powerful airflow mode. The COP of the half-load test was considerably lower than that of the JIS test, which was the same as that of cooling. In the JIS test, it appeared that the compressor rotation speed and expansion valve opening are adjusted to achieve an optimum cycle that maximizes the COP. However, optimal control is not necessarily achieved in operating conditions such as load tests, where users are assumed to be using the machine in a living room. The COP of the half-capacity load test was lower than that of the JIS test because of the operational control of the test machine.

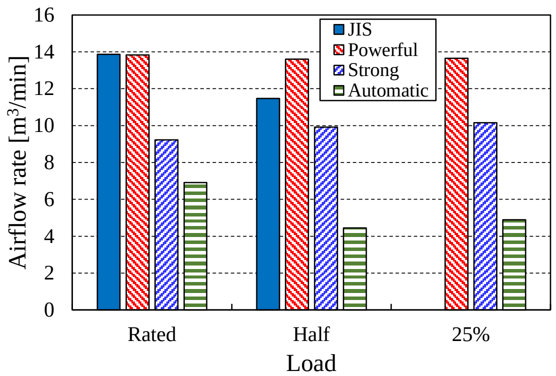

Fig. 3-8 Relationship between airflow mode and airflow rate for cooling operation at C = 600 kJ/K.

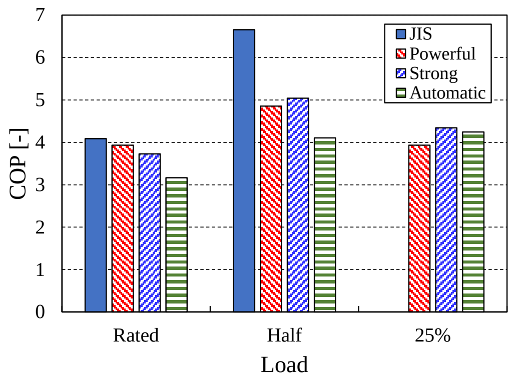

Fig. 3-9 Relationship between airflow mode and COP for cooling operation at C = 600 kJ/K.

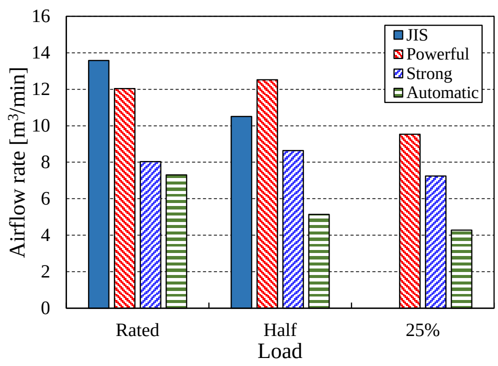

Fig. 3-10 Relationship between airflow mode and airflow rate for heating operation at C = 600 kJ/K.

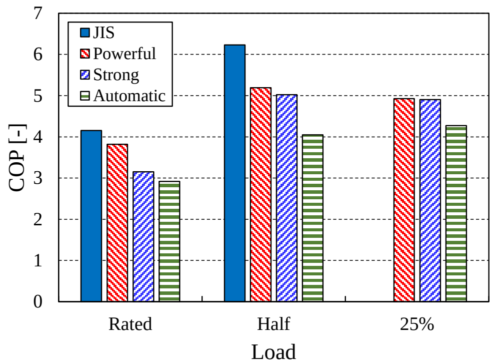

Fig. 3-11 Relationship between airflow mode and COP for heating operation at C = 600 kJ/K.

3.5.4 Measurement of intermittent operation at low heat load

Figure 3-12 shows the trend graph of intermittent operation at a 25% cooling load. In the figure, the range of C = 200, 400, and 600 kJ/K, and the data processing periods, which cover three cycles corresponding to C are indicated by numbers 1 to 3. Table 3-23 shows the average data. At a 25% cooling load, the compressor turned ON and OFF intermittently. However, no significant change was observed in the airflow rate from the air conditioner, regardless of whether it was ON or OFF. Regarding the effect of the heat capacity C, the amplitude of variation decreased (Fig. 3-12), power consumption decreased, and COP increased (Table 3-23) with increasing C. The COP increased with an increase in C.

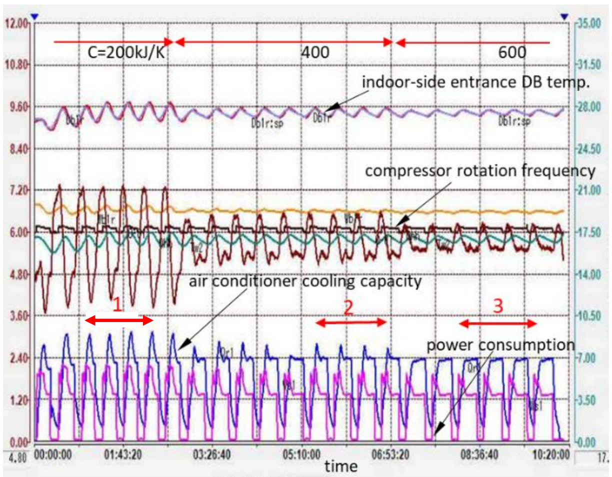

Fig. 3-12 Trend graph for 25% cooling load operation

Table 3-23 Performance at 25% cooling load operation

Cycle number	1	2	3
Heat capacity (kJ/K)	200	400	600
Cooling load (W)	724	729	737
Power consumption (W)	196	188	183
COP	3.69	3.89	4.04
SHF	1.00	1.00	1.00
Airflow rate (m^3/min)	5.2	5.2	5.2
Indoor DB temp. (°C)	27.5	27.5	27.5
Indoor WB temp. (°C)	19.4	19.2	19.2
Outdoor DB temp. (°C)	35.0	35.0	35.0
Outdoor WB temp. (°C)	24.0	24.0	24.0
Compressor speed (Hz)	20	20	19
Controller set temp. (°C)	26	26	26
Controller set airflow	Automatic	Automatic	Automatic
State	ON-OFF	ON-OFF	ON-OFF

3.5.5 Low-temperature heating test

Figure 3-13 shows the trend graph of the heating test when the heat load is 2.6 kW (93% of the rated cooling capacity) under low-temperature conditions (outdoor air dry-bulb temperature is 2 °C, wet-bulb temperature is 1 °C). The heat load was close to 88% of the rated cooling capacity, which was the assumed load at an outdoor air temperature of 2 °C according to JIS B 8615-1:2013. The heat capacity of the virtual room was set at 600 kJ/K. In the low-temperature heating test, the outdoor air temperature was 2 °C. Therefore, in the outdoor unit, frosting and defrosting were repeated. The value of air conditioner performance was the average of three cycles of frosting and defrosting. The time to start defrosting was left to the operation of the air conditioner, and the cycle lasted 82 min. The average values are listed in Table 3-24. Power consumption was included during defrosting. The heating capacity did not include the heating capacity during defrosting. Based on the results, stable measurements were achieved, and no issue was observed.

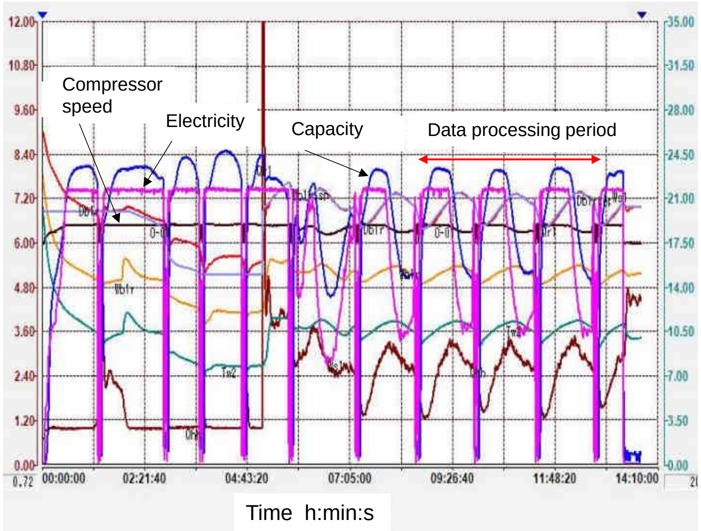

Fig. 3-13 Trend graph for low-temperature heating operation

Table 3-24 Performance at low-temperature heating operation

Heat capacity (kJ/K)	600
Heat load (W)	2601
Power consumption (W)	964
COP	2.70
Airflow rate (m^3/min)	7.6
Indoor DB temp. (°C)	20.3
Indoor WB temp. (°C)	15.1
Outdoor DB temp. (°C)	2.0
Outdoor WB temp. (°C)	0.9
Compressor speed (Hz)	94
Controller set airflow	Strong
Controller set temp. (°C)	21
State	ON-OFF
On/off period (min)	82
Defrost period (min)	4.1

3.5.6 Summary of the static load test

A load test was conducted using the air enthalpy method with the heat capacity model of a virtual room. An air conditioner with a rated cooling performance of 2.8 kW was used as a test machine, and the results are as follows:

1) An existing air-enthalpy-type environmental test room was refurbished, and a static load test was conducted.
2) If the heat capacity of the virtual room was small, the follow-up time was short. However, oscillatory behavior was easy.
3) For the performance test of the air conditioner with a rated cooling capacity of 2.8 kW used this time, the heat capacity of the virtual room should have been 400 kJ/K or more, and 600 kJ/K was appropriate, considering intermittent operation at low heat load during cooling.
4) The refrigeration cycle performance could be improved by increasing the heat transfer performance by increasing the airflow rate of the indoor and outdoor units. This test confirmed that the airflow rate affects the COP. It was suggested that a standard should be established for the airflow rate used in the performance test.
5) Regarding the COP of the half-capacity tests for cooling and heating, we observed that the load test results were considerably lower than the JIS test results. The cause is unclear. However, it may be due to the operation control of the air conditioner used in this study.
6) The fluctuation amplitude, period, and COP were affected by the heat capacity of the virtual room during intermittent operation. If the heat capacity was increased to a certain extent, the effect became less significant.
7) A low-temperature heating test with frosting and defrosting was performed, and no major issues were observed.

3.6 Dynamic load test method

3.6.1 Test conditions

A dynamic load test was conducted by Palkowski et al. in BAM, Germany. The object was a hot water supply heat pump for space heating, using an underground heat source (water heat source) or an air heat source. The relationship between the heat source temperature, part load factor (PLR), and hot water supply temperature is set according to EN 14825, as shown in Fig. 3-14. The load factor varied linearly between 100–3% with respect to the heat source temperature of −10–15 °C. The parameters were changed systematically, as shown in Fig. 3-15 to test the performance of the heat pump. The heat source temperature was changed by approximately 1.4 °C in one step, and the measurement was performed by maintaining one heat source temperature for more than 5 h. The test took six days.

In this study, we set the relationship between the outdoor temperature and load factor, as shown in Fig. 3-16 in accordance with JIS B 8616:2015. The heat load was obtained by multiplying the vertical axis by the rated cooling capacity. The profile of the dynamic heat load test is as follows:

(1) For both cooling and heating, we divided the heat load rate between 15 and 100% into four parts and conducted the test. Five measurement points were considered sufficient to examine the COP characteristics over the entire range of outdoor air temperatures.

(2) With respect to the order of the test, the part-load factor started from a state close to 100%, and the part-load factor was gradually decreased to 15%. Subsequently, the part-load factor was increased, and the process ended when

the load factor returned to a state close to 100%. The same load factor test was performed twice to check if the results of increasing the heat load and the results of decreasing the heat load had the same values. The reproducibility of the measurements was evaluated.

(3) Measurements were taken after maintaining the outdoor temperature for 3 h because holding the temperature for 5 h, as in the BAM test, was considered the same as the static load test. In addition, as described in (2), nine points were continuously recorded. The test was completed in a day.

(4) Regarding the heating test, we examined whether to perform the test with frost formation and defrosting when the outdoor air temperature was in the frost formation temperature range or to prevent frost formation and set the outdoor air temperature to 7 °C. Figure 3-16 shows the two test points at an outdoor temperature of 7 °C to avoid frost formation. If the test was performed at an outdoor temperature that avoided frost formation, the heat load should be corrected because of the change in the outdoor temperature and performance deterioration caused by frost formation and defrosting. This led to unreliable results. Therefore, in this study, we conducted frosting and defrosting tests.

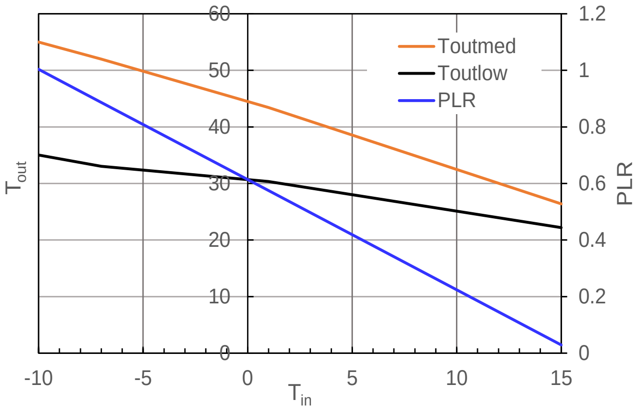

Fig. 3-14 Relationship between the outdoor temperature and supply temperature, and the part load ratio.

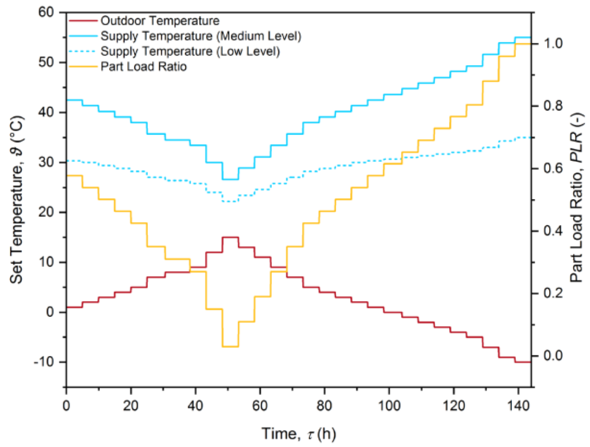

Fig. 3-15 Profiles of the outdoor temperature, supply temperature at medium and low levels, and the part load ratio.

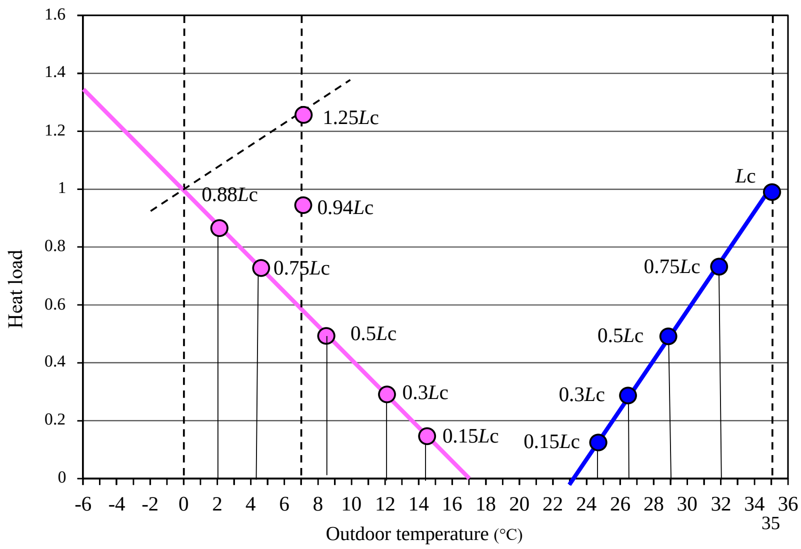

Fig. 3-16 Relationship between the outdoor temperature and the heat load.

Tables 3-25 and 3-26 show the cooling and heating test profiles set based on the aforementioned policy, respectively. In Table 3-25, the outdoor temperature is the dry-bulb temperature, and in Table 3-26 the dry-bulb temperature is the wet-bulb temperature. L_c is the rated cooling capacity. The test machine was the same as that used for the static load test.

Table 3-25 Profiles of cooling test

	Process	Heat load	Outdoor temperature
Cooling	1	*Lc*	35
	2	0.75*Lc*	32
	3	0.5*Lc*	29
	4	0.3*Lc*	26.6
	5	0.15*Lc*	24.8
	6	0.3*Lc*	26.6
	7	0.5*Lc*	29
	8	0.75*Lc*	32
	9	*Lc*	35

Table 3-26 Profiles of heating test

	Process	Heat load	Outdoor temperature
Heating	1	0.88*Lc*	2/1
	2	0.75*Lc*	4.3/3.3
	3	0.5*Lc*	8.5/7.5
	4	0.3*Lc*	11.9/10.9
	5	0.15*Lc*	14.5/13.5
	6	0.3*Lc*	11.9/10.9
	7	0.5*Lc*	8.5/7.5
	8	0.75*Lc*	4.3/3.3
	9	0.88*Lc*	2/1

3.6.2 Results of the cooling condition test

The results of the static load test indicate that a stable test can be performed by setting the heat capacity of the virtual room to 600 kJ/K. The set temperature of the air conditioner remote controller was adjusted for each heat load such that the room temperature of the indoor unit was close to 27 °C. However, because the heat load, virtual room heat capacity, outdoor temperature, and remote controller temperature settings for all tests were programmed in advance, and the tests were conducted fully automatically, in a few cases, the indoor unit room temperature deviated from 27 °C.

Figure 3-17 shows the trend graph of the test measurements. Nine processes were set every three hours. The time when the data were acquired, as displayed. Considering the air conditioner capacity and power consumption of processes 1, 2, 8, and 9 with a heat load of 75% or more, damp oscillations were observed. In contrast, half-load processes 3 and 7 were nearly stable, although there were times when they fluctuated momentarily. An ON-OFF operation was observed in processes 4 to 6, where the heat load was <50%. Table 3-27 shows the results of the time-averaged characteristic values. The average of one cycle was obtained when the signals vibrated over long periods, and the average of three cycles was obtained when the ON-OFF operation was observed for short periods.

Additionally, to speed up the load following of the room air conditioner, the heat capacity of the virtual room was set to 200 kJ for the first hour and 600 kJ/K for the remaining two hours. The trend graph of the test results is shown in Fig. 3-18. The time-averaged values of the test data are listed in Table 3-28. The results show that the fluctuations in the heat load and power consumption immediately after changing the heat load did not decrease significantly and did not contribute to stabilization.

Table 3-27 Results of a dynamic load test for cooling with the constant heat capacity of the virtual room.

Process	1	2	3	4	5	6	7	8	9
Heat capacity [kJ/K]	600	600	600	600	600	600	600	600	600
Cooling load (W)	2832	2108	1402	843	422	846	1406	2107	2822
Sensible heat load (W)	2476	1860	1212	690	287	668	1164	1727	2265
Latent heat load (W)	357	249	190	154	135	179	241	380	557
Electricity consumption (W)	640	349	189	115	61	115	183	316	552
COP	4.43	6.05	7.44	7.34	6.93	7.38	7.67	6.67	5.11
SHF	0.87	0.88	0.86	0.82	0.68	0.79	0.83	0.82	0.8
Airflow rate [m^3/min]	9.7	10.1	10.0	10.1	10.0	10.1	10.2	10.3	10.1
Indoor dry-bulb temp. [ºC]	28.5	27.7	26.3	26.4	25.9	26.4	26.3	27.5	28.1
Indoor wet-bulb temp. [ºC]	20.0	20.4	19.7	20.0	19.7	19.9	19.6	20.4	20.6
Air conditioner outlet dry-bulb temp. [ºC]	16.2	18.8	20.5	23.1	24.5	23.2	20.8	19.4	17.3
Air conditioner outlet wet-bulb temp. [ºC]	15.3	17.1	17.5	52.9	53.9	52.6	21.3	20.2	18.3
Outdoor dry-bulb temp. [ºC]	35.0	32.0	29.0	26.6	24.8	26.6	29.0	32.0	35.0
Outdoor wet-bulb temp. [ºC]	25.0	22.0	19.0	17.1	15.5	16.8	19.0	22.0	25.0
Compressor speed [Hz]	60	37	23	15	7	15	23	34	52
Airflow mode	Strong	Strong	Strong	Strong	Strong	Strong	Strong	Strong	Strong
Controller setting temp. (ºC)	26	26	26	27	27	27	26	26	26
State	Vibration	Vibration	Stable	on/off	on/off	on/off	Stable	Vibration	Vibration
Averaging period	1	1	1	3	3	3	1	1	1

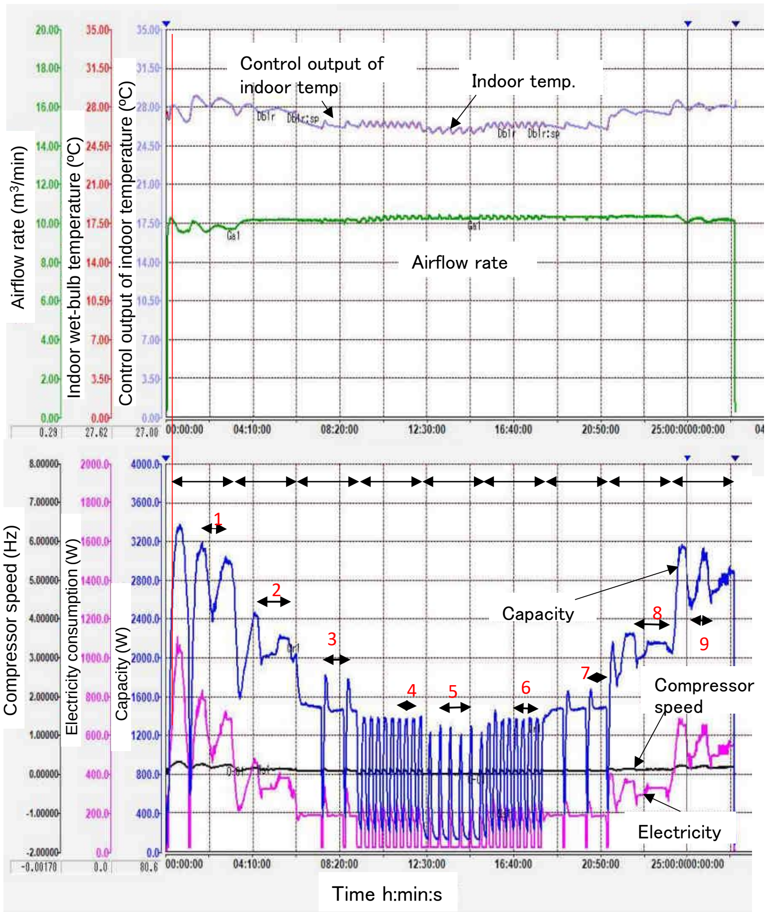

Fig. 3-17 Trend graph of a dynamic load test for cooling with the constant heat capacity of the virtual room.

Table 3-28 Results of a dynamic load test for cooling with the variable heat capacity of the virtual room.

Process	1	2	3	4	5	6	7	8	9
Heat capacity [kJ/K]	200/600	200/600	200/600	200/600	200/600	200/600	200/600	200/600	200/600
Cooling load (W)	2819	2188	1437	879	423	877	1447	2031	2829
Sensible heat load (W)	2303	2067	1448	934	504	921	1446	1994	2314
Latent heat load (W)	515	121	-11	-55	-81	-44	2	37	515
Electricity consumption (W)	818	479	209	139	82	139	217	409	783
COP	3.45	4.56	6.87	6.33	5.16	6.29	6.68	4.96	3.62
SHF	0.82	0.94	1.01	1.06	1.19	1.05	1	0.98	0.82
Airflow rate [m^3/min]	8.5	9	9.4	10	9.9	10.1	10.2	10.3	8.8
Indoor dry-bulb temp. [ºC]	26.9	27.5	27.3	26.7	27.3	26.7	27.1	26.8	26.8
Indoor wet-bulb temp. [ºC]	19	19.5	20	19.8	20.3	19.7	19.7	19.3	19.1
Air conditioner outlet dry-bulb temp. [ºC]	13.9	16.3	19.9	22.2	24.8	22.3	20.2	17.4	14.2
Air conditioner outlet wet-bulb temp. [ºC]	13.3	15.4	17.6	52.3	56.2	52	20.9	18.3	15.6
Outdoor dry-bulb temp. [ºC]	35	32	29	26.6	24.8	26.6	29	32	35
Outdoor wet-bulb temp. [ºC]	24	20.8	18.8	16.7	15.5	16.6	18.1	21.1	24
Compressor speed [Hz]	71	48	26	19	11	19	26	42	70
Airflow mode	Strong	Strong	Strong	Strong	Strong	Strong	Strong	Strong	Strong
Controller setting temp. (ºC)	24	25	26	27	28	27	26	25	24
State	Vibration	Vibration	Stable	On/off	On/off	On/off	Stable	Vibration	Vibration
Averaging period	1	1	35min	3	3	3	35min	1	1

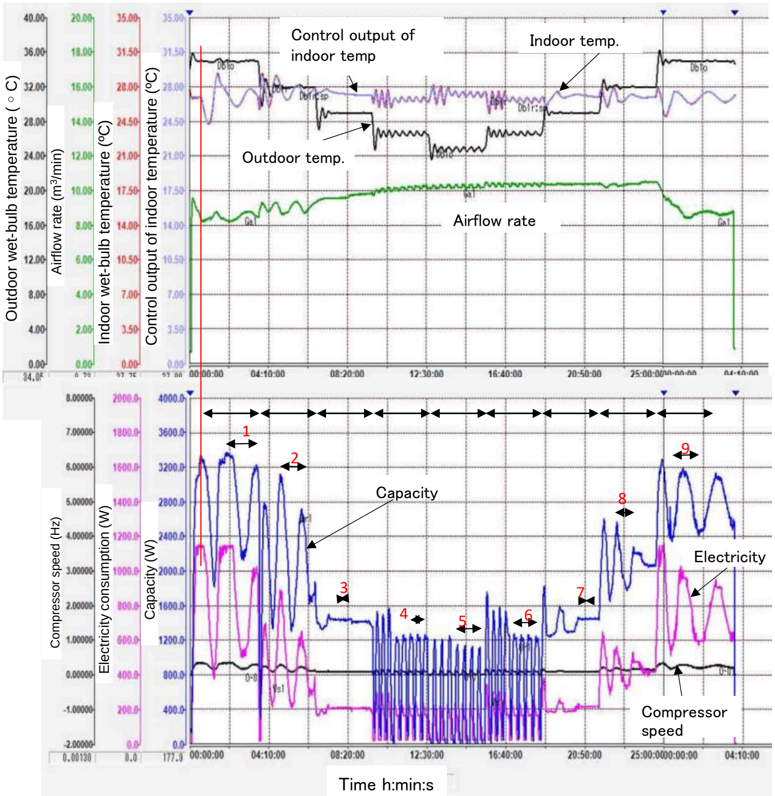

Fig. 3-18 Trend graph of a dynamic load test for cooling with the variable heat capacity of the virtual room.

Figure 3-19 summarizes the cooling test results when the heat capacity of the virtual room was maintained at 600 kJ/K. Figure 3-20 summarizes the cooling test results when the heat capacity of the virtual room was changed from 200 to 600 kJ/K. In the former case, the set temperature of the remote controller did not change significantly depending on the heat load. Therefore, the room temperature of the indoor unit exceeded 27 °C in the process with large heat loads. In the latter test, the room temperature of the indoor unit was set to 27 °C because the temperature setting of the remote controller was finely adjusted based on the heat load. Each point was measured twice: once to decrease the heat load and again to increase it. The difference between them increased when the variation was large (when the heat load was large) because of the deterioration of the measurement accuracy due to fluctuations. Figures 3-19 and 3-20 show a significant difference between the COPs. The cause is unknown. However, the reliability is low.

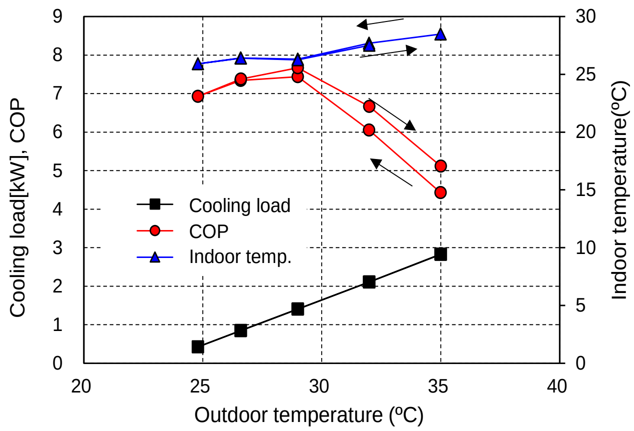

Fig. 3-19 Results of the dynamic load test for cooling with the constant heat capacity of the virtual room.

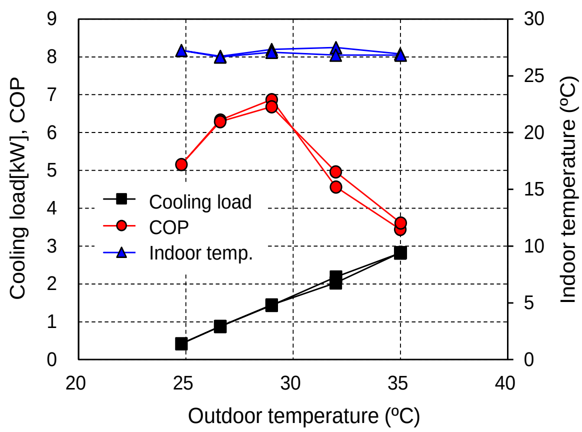

Fig. 3-20 Results of the dynamic load test for cooling with the variable heat capacity of the virtual room.

3.6.3 Results of heating condition test

Figure 3-21 shows the trend graph of the results of the heating test, in which the heat capacity of the virtual room was set to 200 kJ/K for the first hour and 600 kJ/K for the remaining two hours. The time-averaged values are listed in Table 3-29. The results show that the heat load and power consumption fluctuated immediately after changing the heat load when the heat load was large similar to the cooling test, and they were unstable. Frost formation and defrosting occurred under the conditions (processes 1, 2, 8, and 9) where frost formation could occur at low temperatures.

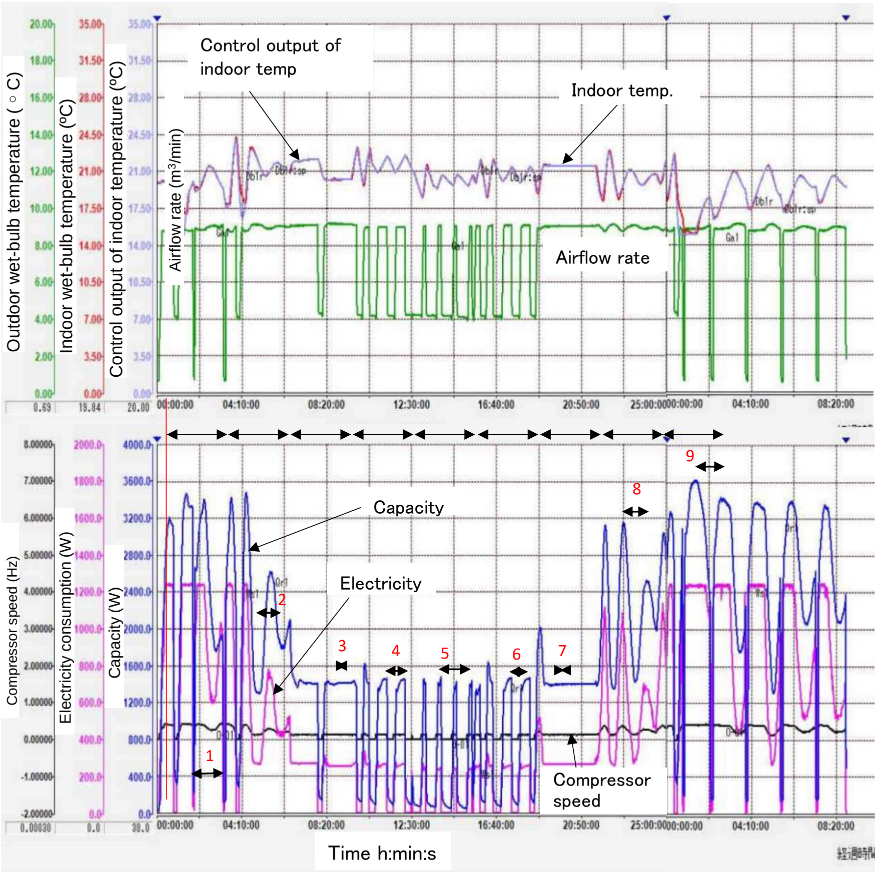

Fig. 3-21 Trend graph of a dynamic load test for heating with the variable heat capacity of the virtual room.

Table 3-29 Results of a dynamic load test for heating with the variable heat capacity of the virtual room.

Process	1	2	3	4	5	6	7	8	9
Heat capacity [kJ/K]	200/600	200/600	200/600	200/600	200/600	200/600	200/600	200/600	200/600
Cooling load (W)	2373	2095	1415	849	419	849	1401	2136	2623
Electricity consumption (W)	916	544	258	161	76	155	269	532	1071
COP	2.59	3.85	5.48	5.27	5.49	5.47	5.22	4.02	2.45
Airflow rate [m^3/min]	8.2	8.6	8.9	6.6	5.1	6.6	8.7	8.6	7.8
Indoor dry-bulb temp. [ºC]	20.3	21.3	20.3	21.7	20.2	20.7	21.5	20.4	20.3
Indoor wet-bulb temp. [ºC]	15.2	15.5	15.1	15.6	15.1	15.2	15.5	15.2	15.1
Air conditioner outlet dry-bulb temp. [ºC]	34.2	33.1	28	27	23.2	25.9	29.3	32.5	36
Air conditioner outlet wet-bulb temp. [ºC]	20.1	19.7	18	48.9	45.1	47.8	28.3	31	33.9
Outdoor dry-bulb temp. [ºC]	2	4.3	8.5	11.9	14.5	11.9	8.5	4.3	2
Outdoor wet-bulb temp. [ºC]	1.1	3.3	7.5	10.9	13.5	10.9	7.5	3.3	1
Compressor speed [Hz]	96	62	35	22	12	22	35	61	105
Airflow mode	Strong	Strong	Strong	Strong	Strong	Strong	Strong	Strong	Strong
Controller setting temp. (ºC)	21	20	19	18	17	18	19	20	21
State	Vibration	Vibration	Stable	On/off	On/off	On/off	Stable	Vibration	Vibration
Averaging period	1	2	35min	1	2	1	35min	1	1

Figures 3-22 and 3-23 show the heating test results when the heat capacity of the virtual room was kept constant at 600 kJ/K and changed from 200 to 600 kJ/K. In Fig. 3-22, the indoor room temperature could not be set to 20 °C. In Fig. 3-23, the indoor unit room temperature could be set to 20 °C because the set temperature of the remote controller was finely adjusted based on the heat load. Each point was measured twice, once to decrease the heat load and again to increase the heat load, and a difference was observed between the two. Comparing the COP in Figs. 3-22 and 3-23, the difference was not significant as in cooling. However, it was not highly reliable.

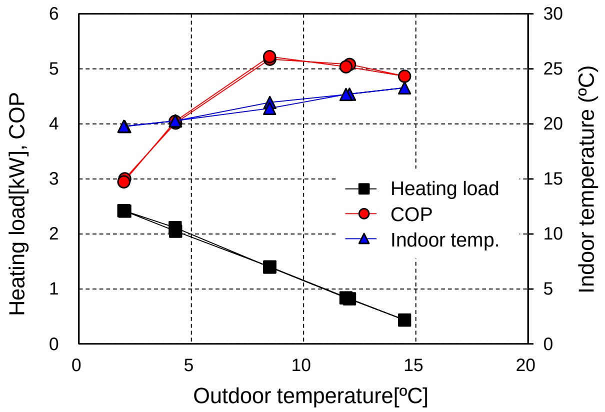

Fig. 3-22 Results of the dynamic load test for heating with the constant heat capacity of the virtual room.

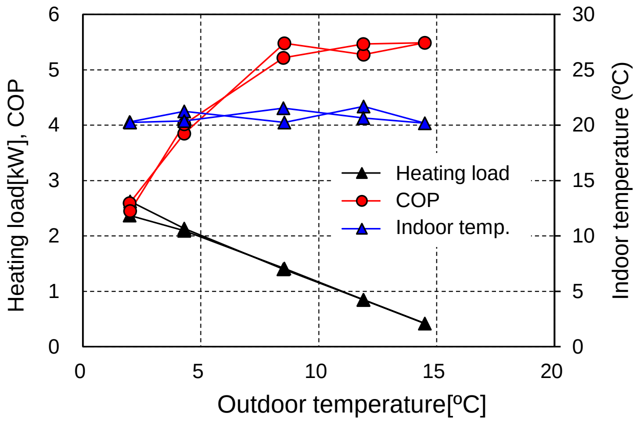

Fig. 3-23 Results of the dynamic load test for heating with the variable heat capacity of the virtual room.

3.6.4 Summary of the dynamic load test

Dynamic load tests were conducted using an air conditioner with a rated cooling capacity of 2.8 kW. The following results were obtained using the dynamic test method.

1) A dynamic load test was conducted with a test time of 3 h. When the load following speed of the air conditioner was slow, the difference between the heat load and supply capacity of the air conditioner increased, causing the fluctuation of the air temperature in the virtual room. The tendency became stronger, especially when the heat load was large. One of the reasons for the oscillatory behavior observed in this study is the load-following speed of the air conditioner.
2) Measurements were possible under ON/OFF operation with a heat load of <50% because the thermo-off cycle was sufficiently <3 h.
3) In the process of increasing and decreasing the heat load, we noticed that no significant difference was observed in a few cases. However, a difference was observed when the operation of the air conditioner fluctuated.
4) In tests involving frosting and defrosting, a holding time of 3 h was insufficient.
5) The tests were conducted with a constant and varying heat load of the virtual room. A large difference was observed in the measured COP during the cooling test. Currently, it cannot be concluded that the results of the dynamic load test are highly reliable.
6) To increase the reliability of the dynamic load test, the test method and operation control of the air conditioner should be improved.

3.7 Conclusion

Here, a load test is conducted, which is expected to replace the current JIS test in which the compressor speed is fixed. The static load test is crucial for future research. However, the test method and air conditioner control method for the dynamic load test should be improved.

The following issues should be considered in the future.

1) Only one air conditioner was tested in this study. However, a few conclusions were not general. For practical application of the load test method, various devices must be tested in environmental test chambers with different specifications to accumulate data.
2) In the beginning of the load test, the selection of airflow mode was an issue. In this study, we selected three modes from the airflow modes implemented in the air conditioner and conducted tests. Therefore, the way of setting an airflow in the performance test should be determined.
3) The heat capacity of the virtual room affects the stability of the test conditions and test time. In the future, the way of providing the heat capacity of the virtual room to conduct efficient tests should be determined.

4) Currently, there are several issues associated with the dynamic load test method. In the dynamic load test, one of the reasons that the vibrational behavior could not be suppressed is that the load-following speed of the air conditioner is slow. However, fast load-following control is not always necessary for practical use. We must consider the difference between the control required for the dynamic load test and that suitable for actual use.
5) In the future, if performance tests is conducted using the load test method, the operation control method for air conditioners evolve rapidly. We consider that the issues identified in this research will be solved simultaneously.

References

3-1) Palkowski, C., Zottl, A., Malenkovic, I., and Simo, A., Fixing Efficiency Values by Unfixing Compressor Speed: Dynamic Test Method for Heat Pumps, Energies 2019, 12, 1045.